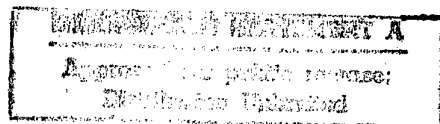

**NINTH INTERNATIONAL SYMPOSIUM ON
APPLICATIONS OF LASER TECHNIQUES TO FLUID MECHANICS**

VOLUME II



19980924 136

**July 13th - 16th 1998
Lisbon, Portugal**

DTIC QUALITY INSPECTED 1

AQF98-12-2562

REPORT DOCUMENTATION PAGE			Form Approved OMB No. 0704-0188
Public reporting burden for this collection of information is estimated to average 1 hour per response, including the time for reviewing instructions, searching existing data sources, gathering and maintaining the data needed, and completing and reviewing the collection of information. Send comments regarding this burden estimate or any other aspect of this collection of information, including suggestions for reducing this burden to Washington Headquarters Services, Directorate for Information Operations and Reports, 1215 Jefferson Davis Highway, Suite 1204, Arlington, VA 22202-4302, and to the Office of Management and Budget, Paperwork Reduction Project (0704-0188), Washington, DC 20503.			
1. AGENCY USE ONLY (Leave blank)	2. REPORT DATE 10 July 1998	3. REPORT TYPE AND DATES COVERED Conference Proceedings	
4. TITLE AND SUBTITLE Ninth Int'l Symposium on Applications of Laser Techniques to Fluid Mechanics		5. FUNDING NUMBERS F61775-98-WE015	
6. AUTHOR(S) Conference Committee			
7. PERFORMING ORGANIZATION NAME(S) AND ADDRESS(ES) Instituto Superior Tecnico Av. Rovisco Pais Lisboa Codex 1096 Portugal		8. PERFORMING ORGANIZATION REPORT NUMBER N/A	
9. SPONSORING/MONITORING AGENCY NAME(S) AND ADDRESS(ES) EOARD PSC 802 BOX 14 FPO 09499-0200		10. SPONSORING/MONITORING AGENCY REPORT NUMBER CSP 98-1011	
11. SUPPLEMENTARY NOTES Two volumes.			
12a. DISTRIBUTION/AVAILABILITY STATEMENT Approved for public release; distribution is unlimited.		12b. DISTRIBUTION CODE A	
13. ABSTRACT (Maximum 200 words) The Final Proceedings for Ninth Int'l Symposium on Applications of Laser Techniques to Fluid Mechanics, 13 July 1998 - 16 July 1998 Turbulent Flows; Unsteady Flows; Hydrodynamic and Aerodynamic Flows; Reacting Flows; Two Phase Flows and Related Instrumentation; Particle Sizing; Developments of Instrumentation for Laser Anemometry; Whole Field Velocimetry; Optical Methods for Temperature, Density, Concentration; Imaging Methods for Scalar Fields			
14. SUBJECT TERMS Combustion, Fluid Mechanics, Laser Measurements Techniques		15. NUMBER OF PAGES Too many to count.	
		16. PRICE CODE N/A	
17. SECURITY CLASSIFICATION OF REPORT UNCLASSIFIED	18. SECURITY CLASSIFICATION OF THIS PAGE UNCLASSIFIED	19. SECURITY CLASSIFICATION OF ABSTRACT UNCLASSIFIED	20. LIMITATION OF ABSTRACT UL

NSN 7540-01-280-5500

Standard Form 298 (Rev. 2-89)
Prescribed by ANSI Std. Z39-18
298-102

**NINTH INTERNATIONAL SYMPOSIUM ON
APPLICATIONS OF LASER TECHNIQUES TO
FLUID MECHANICS**

VOLUME II

July 13 - 16, 1998

Lisbon, Portugal

PREFACE

These proceedings volumes I and II comprise the papers accepted for presentation at the *Ninth International Symposium on Applications of Laser Techniques to Fluids Mechanics*, which is to be held at The Calouste Gulbenkian Foundation in Lisbon, during the period July 13 to 16, 1998. The prime objective of this Ninth Symposium is to provide a forum for the presentation of the most advanced research on laser techniques for flow measurements, and reveal significant results to fluid mechanics. The applications of laser techniques to scientific and engineering fluid flow research is emphasised, but contributions to the theory and practice of laser methods are also considered where they facilitate new improved fluid mechanics research. Attention is focused on laser-Doppler anemometry, particle sizing and other methods for the measurement of velocity and scalars, such as particle image velocimetry and laser induced fluorescence.

The papers comprising the formal record of the meeting were selected following high standard reviews, by members of the Advisory Committee, from approximately 300 extended abstracts submitted for presentation at this meeting.

Volume I comprises the papers to be presented in sessions 1 to 20 during the first and second days of the Symposium, namely July 13 and 16, while Volume II includes the papers included in sessions 21 to 39, which will occur in the following days, Wednesday, July 15, and Thursday, July 16.

We would like to take this opportunity to thank those who assisted in the Organization of the Symposium and in particular the members of Advisory Committee. We are highly indebted for the financial support provided by the Sponsoring Organisations that made this Symposium possible. Many thanks are also due to the Secretariat of the Symposium, Graça Pereira, Tibéria Valente, Luisa Martins, Anabela Almeida and Ana Nunes.

THE ORGANIZING COMMITTEE

ORGANIZING COMMITTEE

- **Ronald J. Adrian**
Department of Theoretical and Applied Mechanics
University of Illinois at Urbana - Champaign
Urbana, Illinois 61801
USA
- **Diamantino F. G. Durão**
Department of Mechanical Engineering
Instituto Superior Técnico
Av. Rovisco Pais
1096 Lisboa Codex
PORTUGAL
- **Franz Durst**
Lehrstuhl für Strömungsmechanik
Erlangen Universität - Nuremberg
Egerlandstraße 13
D-8520 Erlangen
GERMANY
- **Manuel V. Heitor**
Department of Mechanical Engineering
Instituto Superior Técnico
Av. Rovisco Pais
1096 Lisboa Codex
PORTUGAL
- **Masanobu Maeda**
Department of Mechanical Engineering
Keio University
1-14-1 Hioshi, Kohuku
Yokohama 223
Japan
- **James H. Whitelaw**
Imperial College of Science, Technology and Medicine
Department of Mechanical Engineering
Exhibition Road
London SW7 2BX
England, United Kingdom

ADVISORY COMMITTEE

R. A. Antonia	W. Merzkirch
C. Arcoumanis	J. F. Meyers
W. D. Bachalo	E. A. Müller
A. Boutier	T. Nakajima
A. Cartallier	N. Nakatani
A. Cenedese	A. Naqwi
A. Coghe	K. Ohba
W. J. A. Dahm	T. Obokata
D. Dopheide	J. C. Pereira
M. Escudier	H. J. Pfeifer
L. Fingerson	F. Pinho
J. Fitzpatrick	M. L. Riethmüller
M. Gharib	D. Rockwell
G. Gouesbet	X. Shen
I. Grant	R. L. Simpson
J. A. C. Humphrey	M. Sommerfeld
D. A. Jackson	R. N. Syred
T. Jacobsen	A. Taylor
R. Karlsson	E. P. Tomasini
K. Hishida	M. Trinité
J. Kompenhans	C. Tropea
L. Lading	J. E. S. Venart
F. Lance	G. Wigley
B. Lehmann	P. O. Witze
A. Leipertz	M. Yianneskis
W. Lempert	
A. Melling	

SPONSORING ORGANISATIONS

- Calouste Gulbenkian Foundation
- European Research Office:
United States Army,
Navy and Air Force Departments
- Expo'98
- FCT – Fundação para a Ciência e Tecnologia, Portuguese Ministry of Science
and Technology
- FLAD, Portuguese-American Foundation for the Development
- IST - Instituto Superior Técnico
- TAP, Air Portugal

LOCAL SECRETARIAT

Graça Pereira

Tibéria Valente

Anabela Almeida

Luisa Martins

Ana Paula Nunes

Instituto Superior Técnico

Department of Mechanical Engineering

Av. Rovisco Pais, 1096 Lisboa Codex

Portugal

Telephone: (351 1) 841 73 79

Fax: (351 1) 849 61 56

EMail: symp98@tercomb.ist.utl.pt

LIST OF CONTENTS

VOLUME I (SESSIONS 1-20)

SESSION 1. PLENARY SESSION

- 1.1 Instantaneous rotor wake measurements using Doppler global velocimetry
J. F. Meyers, G. A. Fleming, S. A. Gorton and J. D. Berry
- 1.2 Effect of sensor geometry on the performance of PIV interrogation
J. Westerweel
- 1.3 Effect of variable liquid properties on the flow structure within shear-driven liquid films
A. Elsässer, W. Samenfink, J. Ebner, K. Dullenkopf, S. Wittig

SESSION 2. WAKES

- 2.1 A Study of the near-wake region of a circular cylinder
R. Elavarasan, L. Djenidi and R.A. Antonia
- 2.2 LDV measurements in the near wake behind a egg-formed body close to a stationary and a moving wall
M. S. Kim and D. Geropp
- 2.3 LDA measurements and visualization of the supersonic flow around a longitudinal cylinder with different surface roughness
F. Leopold, E. Augenstein, S. Damp, F. Christnacher and E. Bacher
- 2.4 Laser Doppler velocimetry (LDV) and particle image velocimetry (PIV) measurements of the time dependent flow behind a circular cylinder and comparison with results obtained by numerical simulation
O. Stenzel and C. Lund
- 2.5 The structure of subsonic air wakes at high Reynolds number
F. Barreras, A. Lozano, A. Yates and C. Dopazo
- 2.6 Characterization of a bluff body wake using LDV and DPIV techniques
Ö. Karatekin, F. Y. Wang, and J.-M. Charbonnier
- 2.7 LIF measurements in a turbulent far-wake
H.Rehab, L. Djenidi and R.A. Antonia

SESSION 3. COMBUSTION I

- 3.1 Three-dimensional LDA measurements in a turbulent precessing jet flame
G.M. Schneider, G.L. Nathan, R.E. Luxton and N. Syred
- 3.2 Quantitative characterisation of the precessing vortex core and the vortex breakdown phenomena using particle image velocimetry
W. Fick, A.J. Griffiths, G. Schoepf and T. O'Doherty
- 3.3 On the extension of a laser-Doppler anemometer to the analysis of oscillating flames
E. C. Fernandes and M. V. Heitor
- 3.4 Liquid-fuelled flames with imposed air oscillations
Y. Hardalupas, A. Selbach and J.H. Whitelaw
- 3.5 Phase locked velocity measurements in an excited transient pressure field
J. R. Dawson, A. Beale, T. O'Doherty and N. Syred
- 3.6 Measurements of unsteady combustion in a simple combustor configuration
S. Dawson and J.A. Fitzpatrick

SESSION 4. VORTICES

- 4.1 Experimental study by white light laser tomoscopy and P.I.V. of the interaction of a vortex ring with a flat wall
P. Dupont, O. Werquin, S. Le Mironet and M. Stanislas
- 4.2 Vorticity evolution of a vortex ring using high resolution CCDPIV
J. Cater, J. Soria and T.T. Lim
- 4.3 The application of laser diagnostics to cyclonic flow with vortex precession
A.J. Hoekstra, A.T. Israel, J.J. Derksen and H. E.A. van den Akker
- 4.4 On the advantages and pitfalls of statistical PIV analysis in the measurement of confined vortex breakdown
J.M.M. Sousa and C. Freek
- 4.5 Analysis of orderlines in higher instabilities towards the occurrence of chaos in a Taylor-couetter flow system
N. Ohmura, K. Matsumoto, T. Aoki and K. Kataoka
- 4.6 LDV measurements on baroclinic waves
B. Sitte and C. Egbers

SESSION 5. MANUFACTURER'S TECHNICAL PRESENTATION

SESSION 6. PIV OPTICS

- 6.1 Multilayer PIV technique with high power pulse laser diodes
M. Abe, N. Yoshida, K. Hishida, M. Maeda

- 6.2 Gas flow visualization by laser diode light sheet imaging
B. Nath, W. Löber, W. Baetz, W. Holzapfel
- 6.3 Fibre optic beam delivery of high peak power, short pulse laser light for PIV
D. P. Hand, D. P. Wiles, A. Kuhn, J. Jones, J. D. Entwistle and C.A. Greated
- 6.4 Diagnostic techniques for microfluids research
C. D. Meinhart, J. G. Santiago, S. T. Wereley, and R. J. Adrian
- 6.5 Design and calibration of a stereoscopic PIV system
D. C. Bjorkquist
- 6.6 Investigation of a turbulent boundary layer flow using LDV and PIV
S. Kerrigan, W. Lai, C. Tomkins, K. Sharp, Z.-C. Liu, R. Adrian

SESSION 7. SPRAYS IN ENGINES

- 7.1 LDA-based measurements of instantaneous and integrated flow rates in high-pressure gasoline injection system
M. Ismailov, T. Ishima, T. Obokata, M. Tsukagoshi and K. Kobayashi
- 7.2 Characteristics of sprays from gasoline injectors
C. Brehm, M. Posylkin and J. H. Whitelaw
- 7.3 Comparison of different drop sizing techniques on direct injection gasoline sprays
J.-F. Le Coz
- 7.4 Characterization of a diesel spray head by different laser based techniques
L. Araneo, A. Coghe, and G. E. Cossali
- 7.5 Application of two-component phase Doppler anemometry to the study of transient diesel spray impingement
H. G. C.-Góngora and M. Brun
- 7.6 Diesel spray-wall impingement characterization by means of PDA and high speed visualization
J.M. Desantes, J. Arregle, J.V. Pastor and U. Gonzalez

SESSION 8. COMPLEX FLOWS I

- 8.1 Laser velocimetry measurements in a cyclone separator
M. J. Fisher and R.D. Flack
- 8.2 Investigation of internal flows by means of the stereoscopic PIV method
J. Schabacker and A. Bolcs
- 8.3 Effects of centrebody rotation on the laminar flow of a shear-thinning liquid through an eccentric annulus
M. P. Escudier and I.W. Gouldson
- 8.4 Energy losses on a 90° tee junction
R. Maia, P. Miranda, F. T. Pinho and M. F. Proença
- 8.5 Microchannel flows: whole-field optical measurements of velocity and mixing after merging three laminar channel flows
D.R. McCluskey, J. A. van de Konijnenberg, J. J. Rasmussen and B. Stenum

- 8.6 3D LDV measurements in a rotating cooling channel
P. Gicquel, Y. Servouze and B. Tanguy

SESSION 9. 2-PHASE FLOWS INSTRUMENTATION I

- 9.1 Refractive index measurements with phase Doppler anemometry in the size range 0.3 to 20 μm
P. Volkholz, A. Melling and F. Durst
- 9.2 Velocity, size and concentration in suspension measurements of cylindrical jets and spherical droplets
F. Onofri, L. Bergounoux, J-L. Firpo and J. M.-Ripault
- 9.3 Principle of statistical dependence and its application to sizing of irregular particles using phase Doppler technique
A. Naqwi and C. Fandrey
- 9.4 A high power, high resolution LDA/PDA system applied to dense Gasoline Direct Injection Sprays
G. Wigley, G.K. Hargrave and J. Heath
- 9.5 A new approach to eliminate the measurement volume effect in PDA measurements
H. Qiu and C. T. Hsu

SESSION 10. PIV SIGNAL PROCESSING

- 10.1 Advanced evaluation algorithms for standard and dual plane particle image velocimetry
O. Ronneberger, M. Raffel and J. Kompenhans
- 10.2 Particle tracking velocimetry using an image relaxation method
K. Ohmi and D. H. Lam
- 10.3 Fast sub-pixel precision PIV using SSDA algorithm
T. Uemura, T. Tosiyaasu and K. Katayama
- 10.4 A new algorithm for the evaluation of PTV data using point matching distance measures and deterministic annealing
A. Kuzmanovski and K. Obermayer
- 10.5 An advanced MQD tracking algorithm for PDIV
L. Gui and W. Merzkirch
- 10.6 Evaluation of the spring model tracking algorithm using standard images for PIV
K. Okamoto

SESSION 11. WALL FLOWS

- 11.1 Turbulent boundary layer investigations with convential and stereoscopic PIV
C.J. Kahler, R.J. Adrian and C.E. Willert
- 11.2 Experimental study of a high Reynolds number turbulent boundary layer using DPIV
J. M. Foucaut, P. Dupont, J. Carlier and M. Stanislas

-
- 11.3 Reynolds number dependence of near wall turbulent statistics in channel flows
M. Fischer, F. Durst and J. Jovanovic
- 11.4 LDV analysis of temporal intermittency in pipe flow
E. Nino and C. Serio
- 11.5 Streamwise vortex production by an array of inclined jets
X. Zhang and A. Rona

SESSION 12. 2-PHASE FLOWS INSTRUMENTATION II

- 12.1 PIV in two-phase flows: Simultaneous bubble sizing and liquid velocity measurements
I. Dias and M. L. Riethmuller
- 12.2 PIV application for spray characteristic measurement
Y. Ikeda, N. Yamada and N. Kawahara
- 12.3 Advanced measurement techniques for injector validation
W. Scheuerpflug and S. Funke
- 12.4 Measurement of particle size and velocity in two phase flows using PIV
W.T. Martin, J.R. Kadambi and M.P. Wernet
- 12.5 Directionally resolved two phase flow measurements using PIV with fluorescent particles and colour recording
D.P. Towers, C.E. Towers, C.H. Buckberry and M. Reeves
- 12.6 Multi-intensity-layer PIV for spray measurement
Y. Ikeda, N. Yamada and T. Nakajima

SESSION 13. PIV DATA PROCESSING

- 13.1 On the accuracy of a DIC-PIV system based on massive sampling
C. Freek, J. M. M. Sousa, W. Hentschel, W. Merzkirch and J.M.F. Raposo
- 13.2 Wavenumber Spectrum Estimation from Irregularly Spaced Data: Application to PIV Data Processing
W. Hubner, C. Tropea and J. Volkert
- 13.3 The Elimination of Correlation Errors in PIV Processing
D. P. Hart
- 13.4 Particle imaging velocimetry standard images for transient three-dimensional flow
T. Kobayashi, T. Saga, S. Nishio and K. Okamoto
- 13.5 Measurement of velocity field spectra by means of PIV
L.M. Lourenco, M. B. Alkislar and R. Sen
- 13.6 International activities for cooperation, comparison, and standardization at the development and application of particle image velocimetry
J. Kompenhans, M. Stanislas, M. Gharib and T. Kobayashi

SESSION 14. MIXERS

- 14.1 A study of vorticity and dissipation around a Rushton turbine using particle image velocimetry
K.V. Sharp, K.C. Kim and R.J. Adrian

-
- 14.2 Visualisation of the trailing vortex system produced by a pitched blade turbine using a refractive index matched automated LDA-technique
M. Schafer, P. Wachter, F. Durst and M. Yianneskis
- 14.3 Measurement of the mixing characteristics of a stirred vessel with a liquid crystal technique
K.C. Lee
- 14.3 Laser pulsed holography applied to three-dimensional two-phase-flow in aerated stirred vessels
O. Feldmann and F. Mayinger
- 14.4 Phase-resolved three-dimensional LDA measurements in the impeller region of a turbulently stirred tank
J. J. Derksen, M. S. Doelman and H. E. A. van den Akker
- 14.5 Turbulence energy dissipation rate estimation in stirred vessels
P. Saarenrinne, Mika Piirto, Heimo Ihalainen and Osmo Kaleva
- 14.6 Synchronised LDA and interfacial wave height measurements in a model of continuous casting moulds
M. Keicher, H. Morikita and A. M. K. P. Taylor

SESSION 15. LDV OPTICS I

- 15.1 Investigation of a two-component LDA using integrated optical devices
C. Resagk, J. Grabow and S. Voigt
- 15.2 A compact LDV System for high resolution flow measurements
L. Berkner and A. Naqwi
- 15.3 Compact achromatic laser Doppler anemometer employing novel powerful fiber lasers and diffraction optics
Jürgen W. Czarske, H. Zellmer, K. Plamann, H. Welling
- 15.4 Optical preamplification of 1064 nm LDA radiation
H. Tobben, H. Muller and D. Dopheide
- 15.4 Analysis of the three-dimensional fringe patterns formed by the interference of ideal and astigmatic Gaussian beams
E.B. Li and A.K. Tieu

SESSION 16. HOLOGRAPHIC PIV

- 16.1 Decomposition of Turbulent fields and Visualization of vortices
K.T. Christensen, R.J. Adrian, S.M. Soloff, C.D. Meinhart and Z.C. Liu
- 16.2 Instantaneous 3-D velocity measurement of a thermal plume using HPIV
K. Yamaguchi, M. Maeda and K. Hishida
- 16.3 An advanced off-axis holographic particle image velocimetry (HPIV) system
Ye Pu, Zhijian Huang and H. Meng
- 16.4 New advances in holographic interferometry as a fluid velocimetry technique
M.P. Arroyo, M. P. Alvarez, I. J. Sola and N. Andrés
- 16.5 Development and Application of a Defocusing Three Dimensional DPIV Technique for the Mapping of Two Phase Bubbly Flows
M. Gharib, D. Modares, D. Dabiri, F. Pereira and F. Taugwalder
-

SESSION 17. FREE FLOWS I

- 17.1 A PIV study of compressible shear layers
W. D. Urban and M. G. Mungal
- 17.2 Experimental determination of the turbulent kinetic energy and the dissipation rate in variable density turbulent jets
J. Pagé, B. Sarh and I. Gökalp
- 17.3 Turbulent scalar mixing in coaxial Jet flows
F. Caldas, P. Ferrão, M. V. Heitor and M. Matos
- 17.4 PIV and PLIF investigation of mixing by model filter-feeders
U. Ullmum, R. J. Adrian and P. S. Larsen

SESSION 18. 2-PHASE FLOWS INSTRUMENTATION II

- 18.1 Planar particle image analyzer
C. Hess
- 18.2 Droplet sizing by interferometric method based on Mie scattering
O. Pajot and C. Mounaïm-Rousselle
- 18.3 Aerosol size measurement using a laser Doppler probe and acoustic excitation of the fluid flow
V. Strunck, H. Muller, G. Grosche and D. Dopheide
- 18.4 Measurement of size and velocity of particles by optical based spatial filtering technique
D. Petrak, K. Rosenfeld and E. Przybilla
- 18.5 A new laser method for aerosol concentration measurements
G. Cognet, P. Falgayrettes and Y. Brenier
- 18.6 Rainbow thermometry with a pulsed laser
J.P.A.J. van Beeck and M. L. Riethmuller
- 18.7 Non-orthogonal optical spray pattern analysis
R. Sellens and R. Deljouraves

SESSION 19. AERODYNAMIC FLOWS

- 19.1 LDV-measurements on a high-lift configuration with separation control
F. Tinapp and W. Nitsche
- 19.2 Flow measurements on a large delta wing using particle image velocimetry
L. Dieterle, J. Raffel, K. Ehrenfried and J. Kompenhans
- 19.3 Flow field in the vicinity of a thick cambered trailing edge
G. Pailhas, Y. Touvet, P. Sauvage and E. Coustols
- 19.4 Reconstruction of 3-D steady incompressible flow field out 2-D PIV measurements in wind tunnels
N. Lang and W. Limberg

- 19.5 Embedded LDV methodology for boundary-layer measurements on oscillating models
C. Allain, E. Berton, D. Favier and C. Maresca
- 19.6 Instantaneous flow field measurements for propeller Aircraft and Retorcraft research
**M. Raffel, C.E. Willert, F. De Gregorio, K. Ehrenfried, J. Kompenhans
K. Pengel and C. Kähler**

SESSION 20. COMPLEX FLOWS II

- 20.1 Three-dimensional effects of turbulent flow in an in-line tube bundle
K. E. Meyer
- 20.2 Detailed LDV flow field measurements on a model of bayonet tube equipped with heat transfer augmenting devices
A. Cattanei, N. Elia, S. Razore, A. Sciacchitano, M. Ubaldi and P. Zunino
- 20.3 LDA and PIV measurements on thermal convection in spherical shells
C. Böhm, C. Egbers and H. J. Rath
- 20.4 Study of Hairpin Vortex Dynamics and Turbulence Statistics of a surface-mounted mixing tab wake using PIV
Jian Sheng, W. Yang , H. Meng
- 20.5 A Fence flow with periodic cross-flow forcing
H. A. Siller and H. H. Fernholz
- 20.6 Measurements in the shear-layer behind a surface-mounted obstacle for the determination of coherent structures
T. Baur and J. Köngeter
- 20.7 Measurements of the Spatial coherence of the flow around two cylinders
V. Valeau and J.A. Fitzpatrick

VOLUME II (SESSIONS 21-39)

SESSION 21. 2-PHASE FLOWS I

- 21.1 Molten metal atomization by inert gases: Off-line and on-line metal powder characterization by PDA
J. Raimann, G. Wolf, J. Domnick, G. Brenn and F. Durst
- 21.2 Investigation of rebounding droplets from a heated cylinder in spray cooling using PDA
H -H Qiu and Y. F. Yeung
- 21.3 Experimental study on the behaviour of a spray in the model of a fuel preparation duct
A.N. Barros and A.L.N. Moreira

- 21.4 Some aspects of electrohydrodynamic spraying in cone-jet mode
K. Ohba, P. H. Son and Y. Dakemoto
- 21.5 Characteristic measurement of electrostatic fuel spray
Y. Ikeda, J. H. Kim and T. Nakajima

SESSION 22. SEPARATED FLOWS

- 22.1 Reynolds number effect and laminarisation of turbulent flow in axisymmetric sudden-contraction pipe flow
K. T. Ajayi and F. Durst
- 22.2 A flow structure at reattachment region of a two dimensional backward-facing step
N. Furuichi, T. Hachiga, K. Hishida, and M. Kumada
- 22.3 A non-newtonian turbulent sudden expansion flow
A. S. Pereira and F. T. Pinho
- 22.4 PIV measurements of turbulence statistics in the three-dimensional flow over a surface-mounted obstacle
J.M.M. Sousa, C. Freek and J. C. F. Pereira
- 22.5 Turbulence analysis on the BFS with iterative multigrid PIV image processing
F. Scaramo and M. L. Riethmuller

SESSION 23. SCALAR MEASUREMENTS I

- 23.1 Evaluation of flowfield temperatures and pressures using broadband excitation and detection
J. Mendoza, I. Catton and M. Azzazy
- 23.2 Measuring water temperatures by means of Linear Raman spectroscopy
J. Karl, M. Ottmann and D. Hein
- 23.3 Development of a fluorescence-based temperature measurement technique for two-phase flashing propane jets
J.T. Allen and R. J. Bettis
- 23.4 Combined measurement of velocity, temperature, and pressure in compressible gas flows using laser-induced iodine fluorescence
M. Havermann and A. E. Beylich
- 23.5 Density and temperature measurements in a nitrogen jet at supercritical pressures using spontaneous Raman scattering
M. Oswald and A. Schik

SESSION 24. 2-PHASE FLOWS II

- 24.1 On the frequency analysis of the disintegration of planar liquid films
I. S. Carvalho, M.V. Heitor and D. Santos
- 24.2 The velocity field in an air-blasted liquid sheet
A. Lozano, I. Garcia Pallacin and F. Barreras

- 24.3 Measurements of film characteristics along a stationary Taylor bubble using laser induced fluorescence
J.P. Kockx, R. Delfos, J.L.J. Zijl, T.D. Tujeehut and R.V.A. Oliemans
- 24.4 Experimental analysis of a confined bluff body flow laden with polydispersed solid particles
T. Ishima, J. Boree, P. Fanouille and I. Four
- 24.5 Experimental analysis of spatial and temporal two-phase flows structures in circulating fluidized beds using particle images velocimetry and phase Doppler anemometry
F. Onofri, T. Van den Moortel, L. Tadrist and J. Pantaloni
- 24.6 Investigation of a particle laden wake flow by means of particle image velocimetry
T. J. Möller and K. A. Bütefisch

SESSION 25. COMBUSTION II

- 25.1 Experimental investigation of spatio-temporal correlation between aerodynamic and flame front location in an axisymmetric non premixed bluff body burner flame
A. Susset, M. Trinite, D. Honore, D. Jaffre and M. Perrin
- 25.2 Simultaneous PIV and PLIF measurements in nonpremixed transverse jet flames
E. F. Hasselbrink, M. G. Mungal, and R. K. Hanson
- 25.3 Simultaneous PIV and OH planar LIF in the stabilization region of a lifted-turbulent jet flame
C. Maurey, A. Cessou and D. Stepowski
- 25.4 Detection of 3D temperature gradients in turbulent premixed flames with the dual-sheet laser Rayleigh scattering technique
A. Soika, F. Dinkelacker and A. Leipertz
- 25.5 On the effect of rotation on bluff-body stabilized flames
D. Duarte and P. Ferrão
- 25.6 Simultaneous planar OH and temperature measurements for the detection of lifted reaction zones in premixed bluff-body stabilized flames
D. Most, V. Holler, A. Soika, F. Dinkelacker and A. Leipertz
- 25.7 A laser-Doppler analysis of flame stabilisation in a lean premixed prevaporised research combustor
P. Anacleto and M.V. Heitor

SESSION 26. SCALAR MEASUREMENTS II

- 26.1 Measurement of free surface inclination using specklegram
K. Okamoto, G. Tanaka and H. Madarame
- 26.2 Non-linear effects in planar scattering techniques: Proofs of existence, simulations and numerical corrections of extinction and multiple scattering
P. Voigt
- 26.3 CT-type 2DLaser concentration meter with no rotating parts-Application of virtual-load method to an inverse problem
M. Hino and Y. Sato

- 26.4 Applications of laser in the study of thermodynamical properties of heavy oils and petroleum in water emulsions
G. Da Costa
- 26.5 Application of non-linear containing infrared spectrograph for researching of the methane flows
A.B. Britan, P.V. Kozlov, V.A. Levin, S.Y. Mitichkin and V.G. Testov
- 26.6 Concentration measurement by molecular absorption using narrow band tunable infra-red laser
T. Kawaguchi, K. Hishida and M. Maeda

SESSION 27. 2-PHASE FLOWS III

- 27.1 Thermocapillary Bubble Experiments Using Liquid Crystals
G. Wozniak
- 27.2 Simultaneous measurements of continuous and dispersed phase in bubble columns by PDA
D. Bröder and M. Sommerfeld
- 27.3 The Determination of the Bubble Growth Rate in Boiling Heat Transfer by Phase-Doppler Anemometry
T. I. Nonn
- 27.4 3D measurements of wake interaction in a bubbly two-phase flow using Scanning PIV (SPIV) and Stereo-Imaging
Ch. Brücker
- 27.5 Investigation of three-dimensional bubbly flow measurement using displacement particle image velocimetry technique
Y.A. Hassan, W. D. Schmidt and J. Ortiz-Villafuerte

SESSION 28. LDV OPTICS II

- 28.1 Instantaneous velocity profile capturing by a scanning laser velocimeter
M. D. Matovic and O. LeRudulier
- 28.2 First breadboard study about the operation of miniaturized laser Doppler anemometry (LDA) in view of an application on test container level of the future fluid science laboratory (FSL)
J. Immohr, C. Egbers and H. J. Rath
- 28.3 Development of fiber optic laser Doppler velocimetry sensor for measurement of local blood velocity
K. Ohba, M. Nishiyama and K. Korenaga
- 28.4 Integrated laser Doppler velocimeter for wall friction measurements: new prototypes and performance
P.L. Auger, A. Cartallier, P. Bench and I. Schanen-Duport

SESSION 29. BIOLOGICAL FLOWS I

- 29.1 Visualizations of pulsatile flows in bifurcation and stenosis models
S. Yongda, Y. Lixin, G. Changsong, Y. Xianqiu, Z. Liubao and C. Jingui
- 29.2 DPIV measurements of pulsative flow in a constricted tube
A. Borg, J. Bolinder and L. Fuchs
- 29.3 Steady and unsteady LDV and PIV investigations of flow within lung bifurcation
A. Ramuzat, S. Day and M. L. Riethmuller
- 29.4 Spectral and instantaneous flow characteristics of vascular junctions using continuous DPIV
Y. Grad and S. Einav
- 29.5 Low coherence interferometry for flow measurement
A.G. Podoleanu, J.A. Rogers and D.A. Jackson

SESSION 30. OPEN FORUM

SESSION 31. ENGINES 1

- 31.1 Investigation of in-cylinder flow inside a small two stroke engine using PIV in conjunction with endoscopic optics
J. Gindele and U. Spicher
- 31.2 Application of cross correlation particle image velocimetry to the characterisation of unsteady rotating flow
M. Mouqallid , A. Belghit and M. Trinité
- 31.3 Visualization and PIV- Measurements inside the intake port an IC-Engine
G. Rottenkolber, K. Dullenkopf and S. Wittig
- 31.4 Influence of axial compression on a strongly swirling cylinder flow
J. Keller, C. Tropea and J. Volkert
- 31.5 Development of a 2 Colour PIV system for in-cylinder spark ignition engine flows
D.P. Towers, C.H. Buckberry and M. Reeves

SESSION 32. LDV SIGNAL PROCESSING

- 32.1 Correlation estimate for two-channel, non-coincidence laser Doppler anemometry
E. Muller, H. Nobach and C. Tropea
- 32.2 Improved reconstruction of turbulent velocity fluctuations from laser-Doppler anemometry data
H.R.E. van Maanen and F. J. Nijenboer
- 32.3 Determination of Doppler frequencies and characteristic frequency modulation phenomena in laser Doppler signals
P. Lehmann
- 32.4 Quadrature demodulation as advantageous Doppler signal processing technique
J. W. Czarske and O. Dölle

- 32.5 The measurement of structure functions with laser Doppler anemometry
G. P. Romano
- 32.6 Benchmark Tests for the Estimation of power spectra from LDA Signals
C. Tropea and L. Benedict

SESSION 33. COMPLEX FLOWS III

- 33.1 DPIV- Measurements for examination of transient flow Phenomena
J. Reuber and J. Köngeter
- 33.2 A comparison of velocity-field data behind a double-swirl nozzle measured by means of Doppler-global and conventional three-component LDA techniques
B. Lehmann and I. Röhle
- 33.3 Characteristics of transverse dispersion and fluid flow at the exit of short ceramic foams inside a pipe
J.C.F. Pereira and J. Raposo
- 33.4 Interaction of swirling flows from two adjacent coal burners
A. Aroussi, S. Tarr and S. J. Pickering
- 33.5 LDA measurements in a flash smelting furnace model
B. Chiné and A. Barrientos
- 33.6 Flow induced vibration of a scale model of the flow in a scale model of the Flixborough "by-pass" pipe
R. Teng-yang, K.F. Sollows and J. E.S. Venart

SESSION 34. MULTI-POINT METHODS

- 34.1 Quantitative unseed molecular velocimetry imaging
P. A. Drbarber, L. A. Ribarov, J. A. Wehrmeyer, F. Batliwala and R. W. Pitz
- 34.2 Recent applications of three-component Doppler global velocimetry in turbo-machinery
I. Röhle, C. Willert, and R. Schodl
- 34.3 The use of diode array velocimetry for the measurement of turbulent pipe flow
E. Huckle, I. Catton and M. Azzazy
- 34.4 A novel approach to measuring the instantaneous velocity of flow density gradients
G. Papadopoulos and W. M. Pitts
- 34.5 Application of digital holographic interferometry to visualize buoyancy convection
B. Skarman, K. Wozniak and J. Becker
- 34.6 Measurement of the velocity distribution of turbulent flow by the laser photothermal effect with a CCD-LD-interferometer
N. Nakatani
- 34.7 Fluid image velocimetry for unseeded flow
Y. Levy, B. Golovanevsky and T. A. Kowalewski

SESSION 35. COMBUSTION III

- 35.1 PIV and OH LIF imaging of flame-vortex interactions in an opposed-jet burner
J. R. Gord, J. M. Donbar, G. J. Fiechtner, C. D. Carter and J. C. Rolon
- 35.2 Three-dimensional mapping of turbulent flame fronts
M. Lawes, C. G. W. Sheppard and R. Woolley
- 35.3 Application of new light collecting probe with spatial resolution to a spark-ignited spherical flames
S. Tsushima, F. Akamatsu and M. Katsuki
- 35.4 Size, Shape, velocity and temperature measurement of burning coal particles with a newly designed optical measurement technique - TOSCA
G. Hackert, S. Wirtz and H. Kremer
- 35.5 Devolatilization of Single Carbon Particles
B. Zhao, I. Kantorovich, and E. Bar-Ziv
- 35.6 Laser ignition of single magnesium particles
J. F. Zevenbergen, A. E. Dahoe, A. A. Pekalski, B.R. de Ruiter and B. Scarlett
- 35.7 PIV in spherically expanding laminar cellular flames
C. G. W. Sheppard, R. Woolley and M. Lawes

SESSION 36. TURBO MACHINERY

- 36.1 Measurements of rotating machinery flows under steady and transient operating conditions using LDV and PIV
Rajan K. Menon, Wing T. Lai, Steve D. Hoff and Tim P. Mahon
- 36.2 Detailed measurements of the internal flow of a backswept centrifugal impeller
El Hajem M., Morel R., J. Y. Champagne and F. Spettel
- 36.3 Measurements of instantaneous flow structures in turbomachinery using PIV
Draciana Udrea, M. Burnett, W. K. Lee and P. Bryanston-Cross
- 36.4 Unsteady boundary layers on the diffuser blades of a centrifugal stage due to rotor blade wake interaction
A. Cattanei, M. Ubaldi and P. Zunino
- 36.5 Experimental and numerical investigation of the unsteady flow in an axial turbine at different points of operation
C. Gentner, G. Lein and E. Göde
- 36.6 Secondary flow field measurements with a LDV in the vaned diffuser of a high subsonic centrifugal compressor
D. Stahlecker, E. Casartelli and G. Gyarmathy
- 36.7 Velocity measurement downstream an axial blade wheel using LDV-PIV
L. Girardot, F. Lanzetta, J. P. Prenel, J. Stefanini and R. Menon

SESSION 37. ENGINES II

- 37.1 PIV measurements during combustion in a reciprocating internal combustion engine
D. L. Reuss and M. Rosalik
- 37.2 In-cylinder measurements of mixture composition for investigation of residual gas scavenging
P. Miles
- 37.3 Laser diagnostics of nitric oxide inside a two-stroke DI diesel engine
G. Stoffels, E. van den Boom, C. Spaanjaars, N. Dam, W. Meerts and J.J. ter Meulen
- 37.4 Investigation of oil transport mechanisms in the piston ring pack of a single cylinder diesel engine, using two-dimensional laser induced fluorescence
B. Thirouard and D. P. Hart

SESSION 38. FREE FLOWS II

- 38.1 Weakly interacting two parallel plane jets
J. C. S. Lai and A. Nasr
- 38.2 An image processing approach to the study of turbulent structures with a jet in a crossflow
S. McCusker, N. Toy and E. Savory
- 38.3 PTV analysis of jets in cross-flow
G. Carlomagno, A. Cenedese and G. De Angelis
- 38.4 A 30° inclined wall jet
J. C. S. Lai and D. Lu

SESSION 39. COMPLEX FLOWS IV

- 39.1 Energy dissipation study of submerged breakwaters using velocity measurements
F. T. Pinto, M. F. Proença and F. V. Gomes
- 39.2 LDV measurements of turbulence length scales generated by swell downstream to a structure
A. Arsié, L. Maison and M. Bêlorgey
- 39.3 Classification of tsunami wave to runup transition using laser-induced fluorescence technique
K.M. Mok and H. Yeh
- 39.4 Characterisation of the interaction between a boundary layer and a cavity using digital particle image velocimetry with optical flow
G. Quénot, A. Rambert, P. Gougat and T. Kowalevski

SESSION 21

TWO-PHASE FLOWS I

MOLTEN METAL ATOMIZATION BY INERT GASES: OFF-LINE AND ON-LINE METAL POWDER CHARACTERIZATION BY PDA

G. Brenn [§], J. Raimann [§], G. Wolf [%], J. Domnick [&] and F. Durst [§]

[§] Lehrstuhl für Strömungsmechanik (LSTM)

Universität Erlangen-Nürnberg, Cauerstr. 4, D-91058 Erlangen, FRG

[%] Applikations- und Technikzentrum für Energieverfahrens-, Umwelt und Strömungstechnik (ATZ-EVUS)

Rinostr. 1, D-92249 Vilseck, FRG

[&] Fraunhofer-Institut für Produktionstechnik und Automatisierung (FhG-IPA)

Nobelstr. 12, D-70569 Stuttgart, FRG

ABSTRACT

Modern metal powder processing techniques have a continuous demand for decreasing the mean particle size of powders and increasing quality in terms of, e.g., powder particle surface structure and morphology. The industrial processes of gas or inert gas assisted atomization (IGA) of molten metals must therefore be optimized to yield these required high quality powders at competitive prices.

In the present work it was attempted to reach this optimization by two steps: first, the search for a deeper understanding of the IGA process through detailed off- and on-line PDA measurements and, second, on-line process control for the adjustment of the dominant process parameter, the atomizing gas pressure, to an optimized level.

It was found that a droplet velocity measurement at a single specific location inside the molten metal spray of IGA is sufficient to characterize the mean droplet diameter of the whole spray and, hence, to predict the essential characteristics of the metal powder produced.

1 INTRODUCTION

Although metal powders cover only a small part of the worldwide market for metal raw materials, powder metallurgy shows increasing importance for many production processes. Following White (1997), powder metallurgy is the most promising way for developing new metals and creating new material characteristics.

Metal powders required by the processing industries over the last years have shown tendencies for very small mean particle diameters (Capus 1996). In order to deliver these fine powders at competitive prices, the powder production process via IGA has to be optimized.

The gas-assisted atomization of molten metals has been investigated by several groups worldwide (e.g. Anderson et al. 1991, Miller et al. 1992) in order to optimize the atomizer geometries and process parameters. The on-line measurement of particle sizes in this process was first performed using Fraunhofer diffraction-based techniques (e.g. Ridder et al. 1992). Stagnation in the dissemination of this technique to industrial application showed that this technique is only partly applicable for characterizing the dense sprays of IGA. Early investigations by Bauckhage et al.

(1989) proved that PDA is more suitable for such measurements in the gas-assisted atomization of metals.

In this paper, the steps in the application of PDA for the control of IGA are described. First a short overview of the applied PDA measurement technique is given. The off- and on-line investigations are then described in detail, together with the resulting setup of a closed control circuit for this process (Domnick et al. 1996). In addition to the PDA characterization of the metal sprays in IGA, a method to characterize the atomization process by a one-component LDA measurement is presented. The paper ends with a summary of the work and an outlook.

2 PDA MEASUREMENT TECHNIQUE

A commercial fiber-based two-component AEROMETRICS PDA system, using an ILT argon-ion laser and a DSA processor, was used to investigate the metal sprays produced by IGA. The system offers the necessary velocity bandwidth and the robustness of optical and electronic components required in the hostile environment near a metal atomization chamber. The optical setup of the system and the resulting measurement ranges are summarized in Tables 1 and 2.

Table 1: Optical setup of the used PDA system

transmitting optics	symbol	value
laser power in probe volume	P_L	40 mW
focal length	f_{tr}	500 mm
beam separation	d_{sp}	78 mm
beam diameter	D_{e-2}	7.8 mm
wavelength	λ	514.5 nm
receiving optics	symbol	value
focal length	f_r	500 mm
slit width	s	150 μ m
detector separation	$(d_1-d_2) / (d_1+d_3)$	14.71 mm / 38.01 mm

Tab. 2: Resulting PDA characteristics

characteristic dimensions of the probe volume	value
diameter	42.0 μm
length	554.0 μm
distance of the fringes	3.3 μm
number of fringes	13
measurement range	
velocity	-66.0 - +260.5 m/s
size (reflection)	4.8 - 216.9 μm

3 OFF-LINE PDA CHARACTERIZATION

There are two major reasons for performing an off-line characterization of metal powders before applying a PDA system on-line in an atomization process: first, the capability of the PDA to measure solid powder particles as well as liquid droplets has to be verified, and second, these tests allow a direct comparison of PDA and Fraunhofer diffraction measurements of the powders. According to Bauckhage et al. (1989), the surface structure of solid particles makes PDA measurements of the particle size more difficult and uncertain than drop size measurements. In an application, this might affect the small particles most strongly, since the smallest droplets solidify most quickly. Any correlation between the rejection rate of the PDA and the size of the particles would lead to a systematic difference between on-line PDA results and the real particle size distribution, which is usually measured using the Fraunhofer technique as a reference.

3.1 Laboratory setup

These reference measurements were performed with a SYMPATEC HELOS particle size analyzer. Metal powders produced by IGA are highly spherical, and therefore the SYMPATEC results agree reasonably well with sieving results for the powders tested. Based on a scanning electron microscope (SEM) analysis of the powders produced, approximately 95% of the mass is represented by spherical particles. Additionally, it must be noted that the SYMPATEC particle sizer is widely accepted by the consumers of metal powders as a reference measurement technique. In general, typical mean diameters of metal powders, as the volume median $D_{V0.5}$, are accepted by customers only if this measurement technique has been used.

In a typical SYMPATEC setup, the powder sample is passed through the probe volume by a quasi two-dimensional gas flow. The probe volume has a diameter of approximately 2 cm. The setup is chosen to allow for the analysis of the powders with minimized effects of multiple scattering of the incident laser light (Vielhaber 1989).

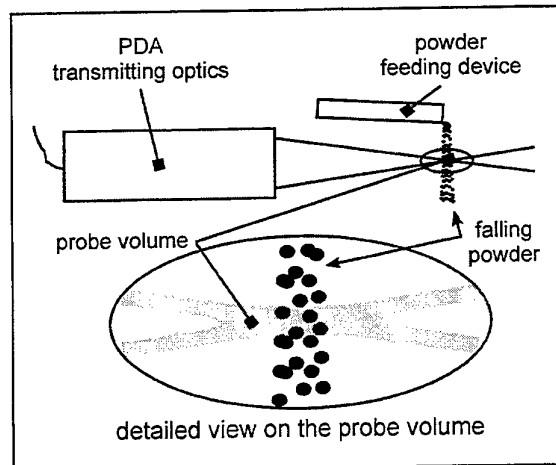


Fig. 1: Experimental setup for the off-line characterization of metal powders by PDA

It is evident that PDA results comparable to the SYMPATEC data can only be obtained if a representative fraction of the powder passes the small probe volume of the PDA. Here it must be kept in mind that the PDA measures a temporal mean size (flux weighting), while the Fraunhofer diffraction result is a spatial mean (concentration weighting). Good results were achieved by simply feeding the powder to the PDA probe volume in a stream driven by gravitation (Fig. 1). The distance between the tip of the feeding device and the probe volume location was kept very short in order to prevent aerodynamic separation of the powders and size dependence of the measured velocities. It was found that 10000 single particle measurements were necessary to ensure statistical stability of the measured mean values.

In Figs. 2 and 3 the measurement results obtained from the two techniques for a sieving fraction of copper powder and iron-nickel alloy powder of nominally the same

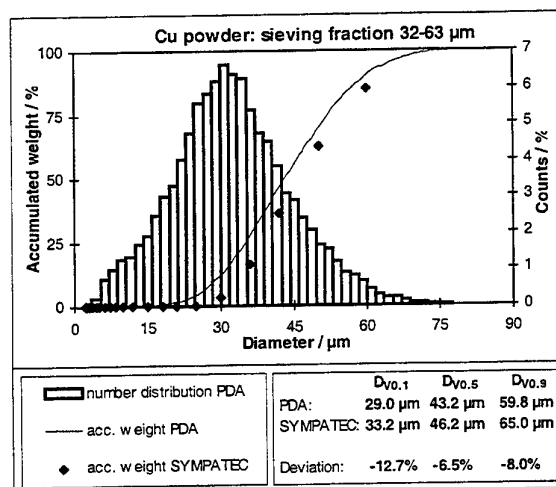


Fig. 2: Off-line characterization of copper powder, sieving fraction 32 - 63 μm : comparison of PDA and SYMPATEC results

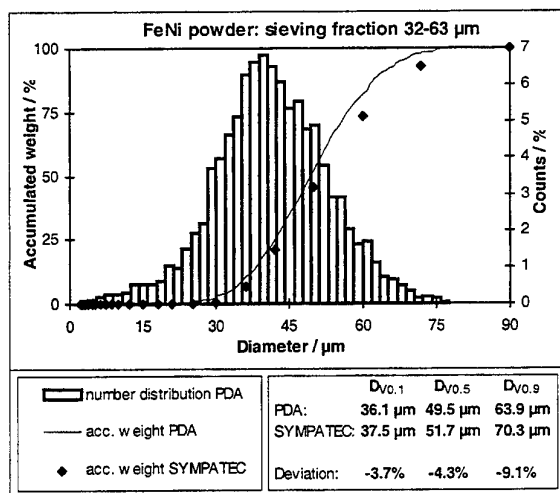


Fig. 3: Off-line characterization of iron-nickel alloy powder, sieving fraction 32 - 63 µm: comparison of PDA and SYMPATEC results

sizes are presented. In general, the results obtained with the two techniques agree quite well. In the case of the copper powder (Fig. 2), the PDA yields the same shape of the cumulative distribution as the SYMPATEC, but slightly shifted towards smaller sizes. For the FeNi powder (Fig. 3), however, the deviations between PDA and SYMPATEC increase for particle sizes above 50 µm. This difference may be due to slightly inaccurate sieving and differences in the surface structure.

According to Göbel et al. (1997), surface irregularities of the particles lead to broadened size distributions in PDA measurements. Hence it is worth examining the surface structure of the powder particles. Examples of surface structures on different metal particles produced by IGA are presented in Figs. 4 - 7. In Fig. 4 the surface of a copper powder particle with a diameter of 36 µm is shown. Apparently, the surface is very smooth. In general, IGA atomized copper particles of any diameter show practically no irregularities with length scales larger than 1/5000 of the particle size. The structures visible on the iron-nickel parti-

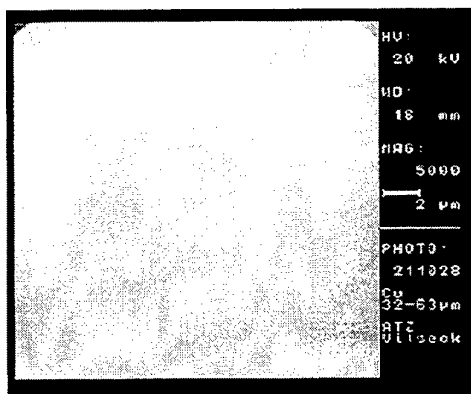


Fig. 4: SEM picture of a copper powder particle of approximately 36 µm diameter

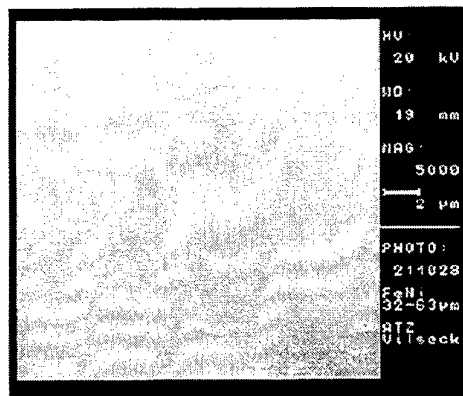


Fig. 5: SEM picture of an iron-nickel alloy powder particle of approximately 42 µm diameter

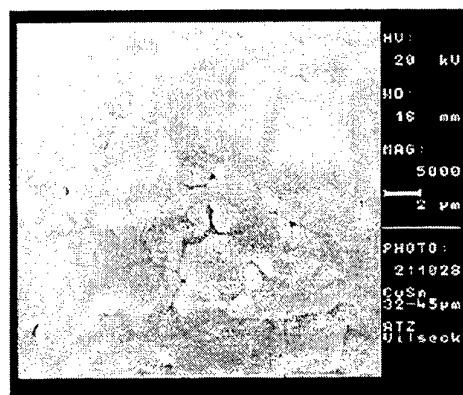


Fig. 6: SEM picture of a copper-tin alloy powder particle of approximately 38 µm diameter

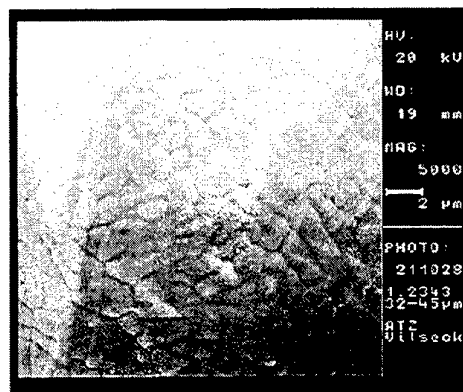


Fig. 7: SEM picture of a tool steel powder particle of approximately 40 µm diameter

cle are clearly larger than 300 nm. However, these disturbances are smaller than the wavelength of the laser light applied for the PDA measurements (Table 1). It can be assumed that such surface irregularities of the particles have no effect on the PDA measurements.

The SEM photographs of a copper-tin alloy and a tool steel powder particle in Figs. 6 and 7 reveal larger surface irregularities with length scales clearly greater than

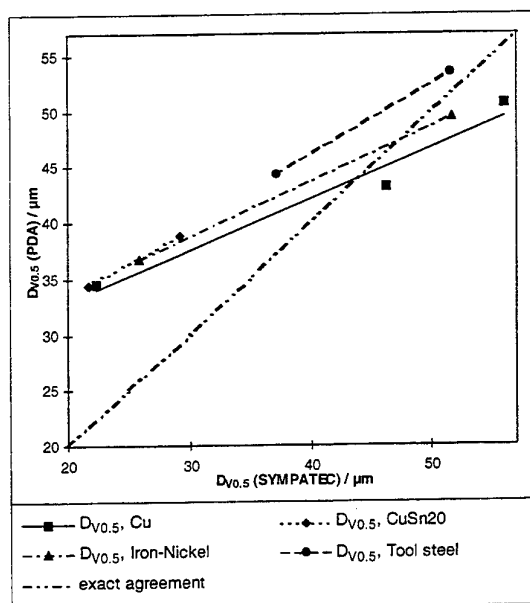


Fig. 8: Comparison of mean diameters of different alloy and pure metal powders: $D_{V0.5}$ measured by PDA versus $D_{V0.5}$ measured by SYMPATEC

the incident laser light wavelength. However, these structures are smaller than the fringe spacing in the PDA probe volume. Owing to the integration effect of the photodetectors used for the investigations, no systematic influence of the surface structures on the measurement results was found.

Figure 8 depicts the analysis results for different sieving fractions of the four powder materials corresponding to Figs. 4 - 7. The data given are the mean diameters $D_{V0.5}$ from the PDA measurements versus $D_{V0.5}$ from SYMPATEC analysis. The double dotted line represents the exact agreement of the two techniques. The results for $D_{V0.5}$ calculated from the PDA measurements compared with the SYMPATEC results for all four powders show no systematic effect of the different surface structures on the PDA measurements. All materials show a linear relationship of the measurement results.

Although the surface structures of the powders seem to have only slight influences on the size measurements, the detected light intensities are, in fact, affected by these structures. In Fig. 9 the correlation between the PDA measured diameter and the detected signal intensity of the copper and iron-nickel powders already discussed in Figs. 2 and 3 is depicted. The curves show the well-known relationship between particle size and scattered light intensities: larger particles yield higher intensities. The fluctuations of the detected intensities are depicted as error bars on the mean values. The larger fluctuations in the light intensities from the FeNi particles, which even increase with the particle size, give rise to the assumption that this kind of powder may lead to slightly larger measurement uncertainties with optical techniques than the copper powder. In the present case this leads to a slight underestimation for the coarse particles.

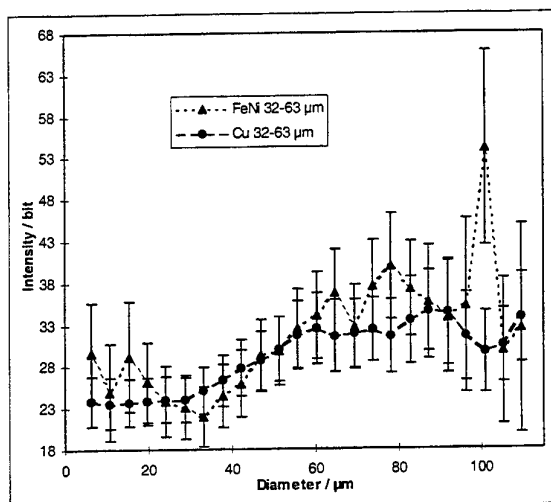


Fig. 9: Correlation between PDA measured diameter and intensity of the signals for the powders of copper and iron-nickel melts

4 ON-LINE CHARACTERIZATION

The on-line characterization of the IGA process should be understood as an investigation of the fluid dynamics of the metal spray inside the atomization chamber. In addition to on-line measurements in the melt atomization process, the present contribution also presents results of experiments performed in a model flow field of the IGA. These model experiments were performed in order to obtain information about the correlation between locally measured particle sizes and velocities with the overall powder size distribution.

In this section, both liquid melt droplets and solidified particles are called "particles", basically because it is impossible to distinguish between the two disperse fractions in the metal spray.

4.1 Laboratory setup

The adaptation of the PDA to the IGA system was based on detailed Mie calculations (Domnick et al., 1996). In addition to the construction of windows which was necessary to allow optical access to the measurement region in the spray about 12 cm below the atomizing nozzle, a set of baffles was introduced into the atomizing chamber.

In Fig. 10 the PDA system is shown together with the cross-section of the atomization chamber and the windows. The off-axis angle of 60° was chosen since it is also appropriate for melt spray experiments with liquefied gases and water, where extended phase-Doppler anemometry has to be applied (Domnick et al. 1995, Raimann et al. 1997). In Fig. 11 the effect of the baffles is explained schematically. By an appropriate layout of the geometry of these baffles, the recirculation of small powder particles was minimized. It was found that the application of such baffles is necessary for the production of powders with a $D_{V0.5}$ of less than $20 \mu\text{m}$. In the production of coarser powders, the baffles show no effect on the measurement results.

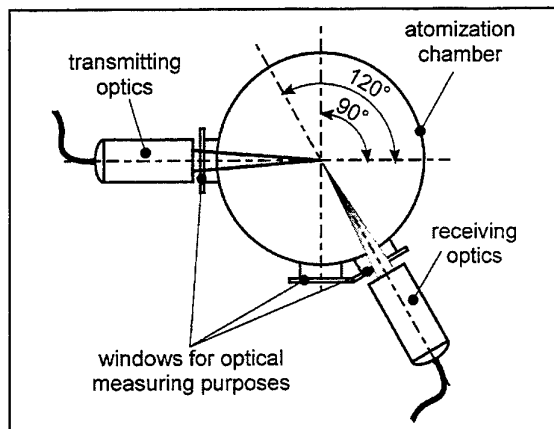


Fig. 10: PDA system adapted to the atomization system

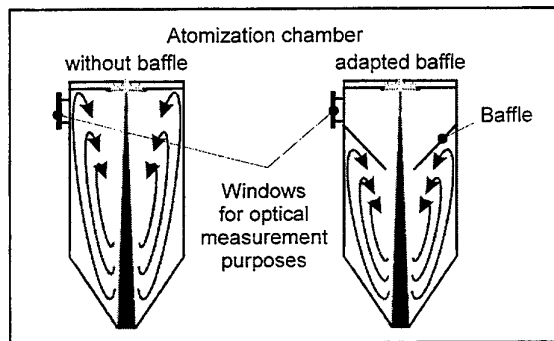


Fig. 11: Effect of the baffle adapted to the atomization system

4.2 On-line measurements in melt atomization

On-line PDA measurements were performed in a melt spray facility equipped with a close-coupled atomization nozzle as drawn schematically in Fig. 12. The melt is fed through a tube surrounded symmetrically by individual gas nozzle holes. The gas pressure ratio between the gas ring chamber and the atomization chamber lies beyond the critical pressure ratio, so that the gas jets leave the gas nozzles underexpanded.

The high-speed gas flow outside the melt tube causes a very low static pressure at the edges of the tube. Owing to this pressure field, the melt flows as a thin film from the center towards the edge of the melt tube tip, where the primary atomization occurs. The disintegration process of the melt at the edge of close-coupled atomizers was visualized using the PCO technique, confirming previous results of Anderson et al. (1991), Miller et al. (1992), and Kuntz et al. (1995).

The PDA measurements at a location of 12 cm below the atomizer exit were performed in a number of experiments under constant process conditions. These experiments with a typical run time of 5 - 10 min allowed complete radial profiles in the spray cone to be measured.

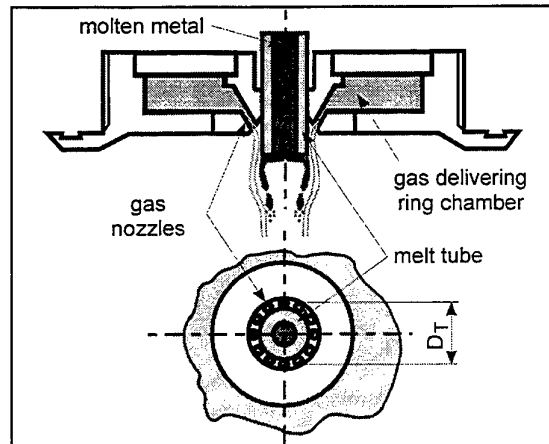


Fig. 12: Close-coupled atomizer applied to IGA

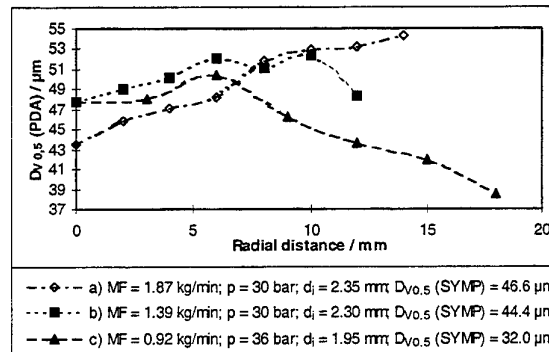


Fig. 13: Particle mean diameter profiles in the spray at a distance of 12 cm from the nozzle (legend also for Fig. 14)

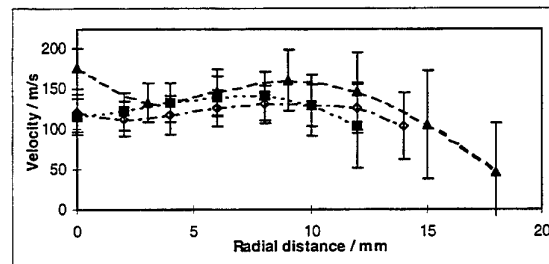


Fig. 14: Axial particle velocity profiles in the spray. Error bars represent the RMS velocities (legend see Fig. 13)

In Figs. 13 and 14, results of three experiments are depicted as radial profiles of the volume median $D_{V0.5}$ and the mean axial particle velocity. Comparing cases a) and b), it is remarkable that experiments under nominally identical test conditions result in different melt flow rates MF, but in similar $D_{V0.5}$ values, as determined by means of the SYMPATEC technique. The radial profiles of $D_{V0.5}$ from the PDA measurements correspond to the global $D_{V0.5}$ measured by SYMPATEC. The application of a smaller melt outlet tube and a higher gas pressure (experiment c)) results in a finer powder. Owing to the high drop concen-

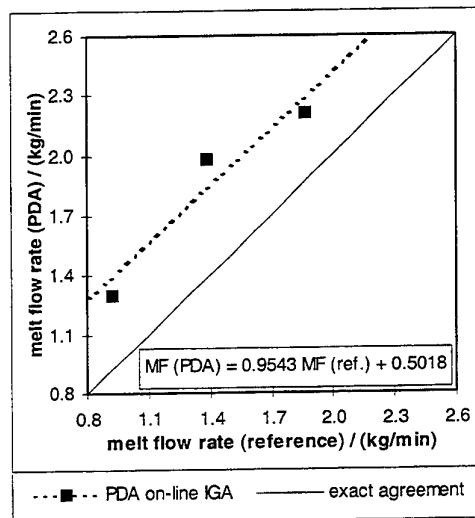


Fig. 15: Mass flow rate measured with PDA versus reference mass flow rate

tration in the spray, many fine particles are not detected by the PDA, which leads to too high $D_{v0.5}$ as compared with the SYMPATEC result. The measured velocity, however, corresponds to the gas pressures applied (Fig. 14). The importance of this result will be shown in the next section.

Using these measurement results, the mass flow rate of the melt was calculated. In Fig. 15 the melt flow rate computed from the PDA measurement data is plotted ver-

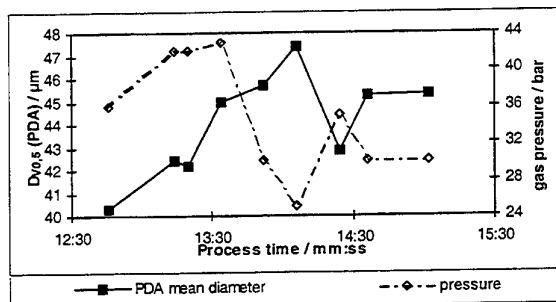


Fig. 16: Particle mean diameter measured by PDA as a function of process time at different gas pressures during an IGA process

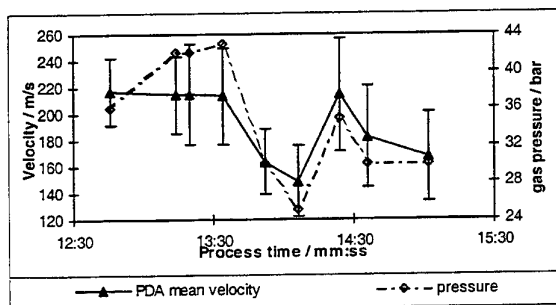


Fig. 17: Particle mean velocity measured by PDA as a function of process time at different gas pressures during an IGA process

sus the melt flow rate determined after the experiment by dividing the mass of the powder obtained by the process run time. The results show that the PDA results overestimate the flow rate. This may be caused by the fact that the PDA overestimates the mean diameter used for the flow rate calculation.

Finally, experiments with variations of the dominant process parameters were performed. It was found that changes in the melt temperature in the relevant range between 100 and 300 K melt superheat, which are believed to affect the fluid parameters, seem to be irrelevant for the atomization process. From stepwise gas pressure variations, a much stronger effect was obtained. In Figs. 16 and 17, the volume median $D_{v0.5}$ and the axial mean and RMS velocities measured by PDA during such an experiment are shown. RMS velocities are represented by error bars. The mean particle size shows a tendency to decrease with increasing gas pressure, whereas the mean particle velocity increases, as expected.

4.3 Model Experiments

It was indicated above that the velocity of the particles measured at a given location in the spray is correlated with the atomization process itself. However, both the results of the off-line characterization by PDA and the on-line measurements during the powder production process revealed certain differences between the local PDA particle size measurements and the results of the reference measurements. It is therefore obviously useful to incorporate additional particle information to improve the on-line analysis by PDA. Useful information for this purpose is the particle velocity.

In order to establish the use of the particle velocity, model experiments were performed, combining the technique of off-line PDA characterization (Fig. 1) with the on-line measurement in the flow field of the atomizing nozzle in the chamber. Powders of well-defined mean particle diameters and size distributions were fed through the melt feeding tube of the atomizer and entrained into the gas flow.

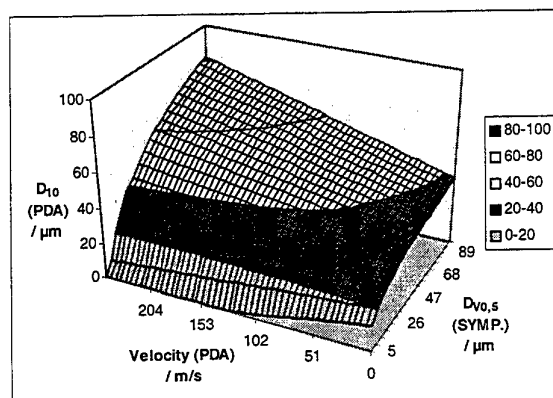


Fig. 18: Correlation between local PDA measurement of size and velocity and global powder size measured by the SYMPATEC system

The PDA measurements in this two-phase flow field were performed at a position 12 cm below the nozzle at an arbitrary radial distance of 4 mm. The gas pressure applied varied between 0 bar (free falling powder particles) and 40 bar, resulting in particle velocities around 200 m/s. The correlation of the arithmetic mean diameter and the mean particle velocities measured by PDA and the mean diameter of the inserted powder fraction measured with the SYMPATEC system is shown in Fig. 18. The relationship between the three variables can be approximated by

$$D_{V0.5, SYMPA} = C_0 \exp \left(\frac{D_{10, PDA} - (C_1 U_{PDA} + C_2)}{C_3 U_{PDA} + C_4} \right) \quad (1).$$

The empirical constants in this equation are listed in Table 3.

Tab. 3: Constants of eq. (1)

constant	value	dimension
C_0	1	μm
C_1	-0.275	$\mu\text{m}/(\text{m/s})$
C_2	1.3565	μm
C_3	0.0965	$\mu\text{m}/(\text{m/s})$
C_4	8.1428	μm

4.4 Global characterization of the spray by a single PDA measurement

Using this correlation, the local on-line PDA measured mean particle sizes may be related to the global mean powder size measured by the SYMPATEC system. In Fig. 19, the volume medians $D_{V0.5}$ calculated by means of Eq. (1) from the PDA data are plotted versus the off-line characterization results ($D_{V0.5}$ SYMPATEC). The open symbols represent the "raw" PDA measurement data and the filled

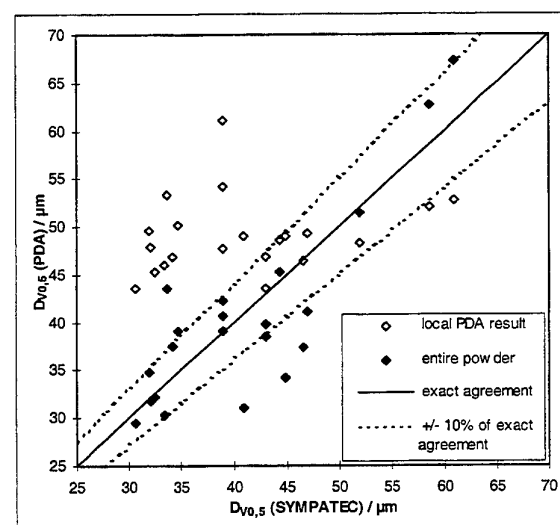


Fig. 19: Characterization of the IGA sprays (copper, copper-tin and silver melts)

symbols represent the values calculated from Eq. (1). In general, the agreement is satisfactory and indicates that the local PDA measurement can characterize the global powder size with an uncertainty of only $\pm 10\%$ in most of the experiments. It should be noted that Fig. 19 includes measurements with melt tube diameters between 1.9 and 4 mm and gas pressures between 25 and 70 bar.

5 CHARACTERIZATION OF THE ATOMIZATION PROCESS BY LDA MEASUREMENTS

It was shown above that the velocity of the particles in the spray is an important parameter for the spray characterization. As an alternative to the method described in Sections 4.3 and 4.4, the pure velocity information of the particles at a given distance from the nozzle can be used for the characterization of the overall mean particle size of the spray in IGA. This method is based on the aerodynamic behavior of the powder particles in the gas flow field.

In Fig. 20 the axial velocity of the particles produced by IGA processes is plotted versus the particle diameter of the produced powders determined off-line. The diagram represents results for different inner diameters of the melt tube, but constant outer diameter of the tube and constant geometry of the gas nozzles. At inner diameters of the melt tube of 2.3 mm or less, it was found that a unique correlation between the locally measured velocity of the particles and the mean particle diameter $D_{V0.5}$ measured by SYMPATEC exists. Basically, the mean velocity decreases with increasing mean diameter, as already shown above. At melt tube inner diameters of more than 2.3 mm the situation changes completely, probably due to a change in the pressure field at the melt tube outlet. For these tubes, no useful correlation was found.

Using the correlation between velocity and global mean particle size of the powder shown in Fig. 20, the prediction of the powder obtained is possible by calibrating the correlation function with on-line LDA measurements in a set of calibration processes. With this calibration, prediction of the mean diameter of the powder production is possible within $\pm 10\%$ agreement (Fig. 21), using a single com-

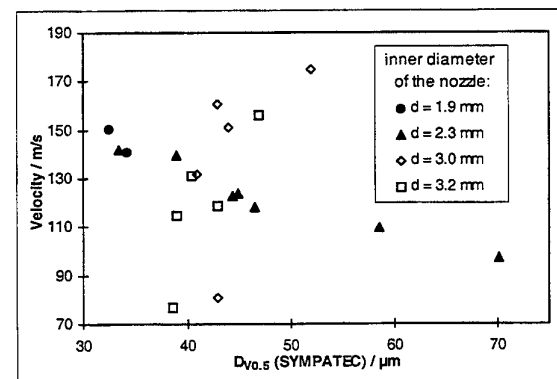


Fig. 20 Correlation between measured droplet velocity in the spray and the IGA powder mean sizes measured by SYMPATEC (Copper melts)

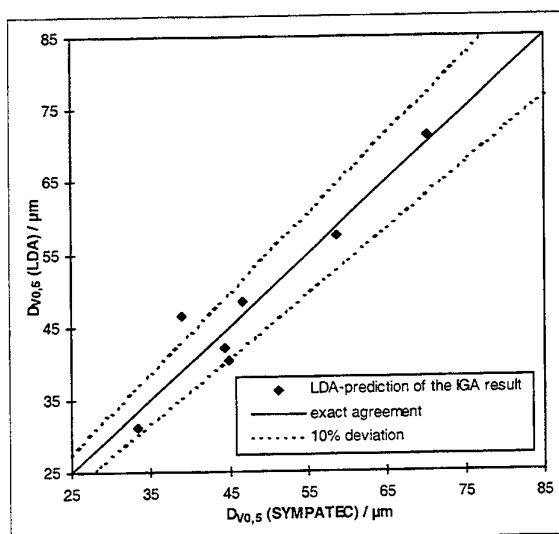


Fig. 21: LDA characterization of the IGA sprays (copper melts)

ponent LDA system.

6 SUMMARY AND OUTLOOK

A deeper understanding of the IGA process of molten metals was obtained through detailed off-line and on-line particle size and velocity measurements using the PDA technique. A correlation between the results of local PDA measurements and off-line particle size measurements characterizing the entire powder yield was found for a specific atomizer geometry. Thus the characterization of the whole spray by a single PDA measurement is possible with an uncertainty of $\pm 10\%$ in the volume median particle diameter. In addition, it could be shown that, for well defined conditions, a single LDA measurement can be sufficient to characterize the whole spray with the same degree of uncertainty. This method is based on a sufficient stability of the two-phase flowfield in the atomization chamber.

In the future, detailed optimization tests of the close-coupled nozzles applied in IGA must be performed. This optimization must be based on detailed investigations of the (gas) flow field near the nozzle with experimental and numerical methods. Furthermore it is necessary to develop a technique for measuring the melt flow rate on-line.

ACKNOWLEDGMENTS

The financial support of the present work from the EU in the frame of the BRITE/EURAM project 8209 entitled "On-line process control of liquid gas and water atomization by extended phase-Doppler anemometry" is gratefully acknowledged.

REFERENCES

- D. Ridder, S. A. Osella, P. I. Espina, F. S. Biancaniello 1992, Intelligent Control of Particle Size Distribution During Gas Atomization, *Int. J. Powder Metallurgy* **28**, No. 2, pp. 133-147.
- D. G. White 1997, Challenges for the 21st Century, *Int. J. Powder Metallurgy* **33**, No. 5, pp. 45-54.
- J. M. Capus 1996, METAL POWDERS: A Global Survey of Production, Applications and Markets 1992-2001, Elsevier Science Ltd, Oxford, UK.
- K. Bauckhage, P. Schreckenber 1989, Control of Powder-Metal Production: A New Application of Phase-Doppler-Anemometry, *Proc. of the Int. Conf. on Mech. of Two-Phase Flows*, pp. 267-272, Taipei, Taiwan.
- J. Domnick, J. Raimann, G. Wolf 1996, Application of Extended Phase-Doppler Anemometry in Liquid Gas Atomization; *Proc. of the 8th Int. Symp. on Appl. of Laser Techniques to Fluid Mechanics*, pp. 20.4.1-20.4.8, Lisbon, Portugal.
- J. Domnick, J. Raimann, G. Wolf, E. Schubert, H.W. Bergmann 1995, On-Line Characterization of Particle Jets During the Atomization of Molten Metal by High Velocity Cryogenic Liquid Gas Jets, *Proc. ILASS-95*, pp. 137-146, Nürnberg, Germany.
- J. Raimann, G. Brenn, J. Brito Correia, J. Domnick, N. Shohoji 1997, On-line measurement of powder size and velocity in the water atomization process, *Proc. of the European Conference on Advances in Structural PM Component Production*, pp. 415-422, Munich, Germany.
- D. W. Kuntz, J. L. Payne 1995, Simulation of powder metal fabrication with high pressure gas atomization, *Advances in Powder Metallurgy and Particulate Materials* **1**, No. 1, pp. 63-77.
- S. A. Miller, R. S. Miller 1992, Real Time Visualization of Close-Coupled Gas Atomization, *Advances in Powder Metallurgy and Particulate Materials* **1**, No. 1, pp. 113-125.
- I. E. Anderson, R. S. Figliola, H. Morton 1991, Flow mechanisms in high pressure gas atomization, *Materials Science and Engineering A* **148**, pp. 101-114.
- U. Vielhaber 1989, Genauigkeit der Partikelgrößenmessung mit Laserbeugungsspektrometern, *Sonderdruck Verfahrenstechnik. Interkarma-Report*.
- G. Göbel, A. Doicu, T. Wriedt, K. Bauckhage 1997, Influence of surface roughness of conducting spheres on the response of a phase-Doppler anemometer, *Particle & Particle Syst. Char.* **14**, No. 6, pp. 283-289.

INVESTIGATION OF REBOUNDED DROPLETS FROM A HEATED CYLINDER IN SPRAY COOLING USING PDA

H. -H Qiu and Y. -F. Yeung

Department of Mechanical Engineering
Hong Kong University of Science and Technology
Kowloon, Hong Kong

ABSTRACT

Water droplets impinging onto a cylindrical fin was investigated. Experimental investigations and analysis were performed to determine the mechanisms causing transition to critical heat flux (CHF). The diameter and velocity of impacting and rebounding droplets were measured to investigate their effect to the critical heat flux. The number of rebounding droplets (secondary sprays) by the impact angle, droplet velocity and diameter, surface tension of working fluid, and surface temperature of the substrate were studied in detail by using phase-Doppler anemometry (PDA) which indicate that the CHF is caused in rebounding droplets from the heated surface. By optimizing the droplet velocity, size and mass flux, as well as the surface property of the cylinder, the rebounding droplets may be reduced. Hence, the critical heat flux of the cylindrical surface by spray impingement can be improved.

INTRODUCTION

Because of recent emphasis on removing high dissipated heat $1.0 \times 10^7 \text{ W/m}^2$ (Sehmbey *et al.* 1995) from electronic devices, spray cooling has become a subject of intense interest as an effective cooling technique. The heat transfer process of spray cooling is complex because it involves the dynamics of droplet deformation, heat transfer and phase change of such droplets. For the case of droplets impacting on a hot surface the heat transfer process involves transient boiling heat transfer together with the complex droplet dynamics. The interaction between droplets in a spray during the impacting process has further complicated the heat transfer mechanisms.

Yao and Choi (1987) developed a monodispersed spray generator which allowed the liquid mass flux, droplet size and droplet velocity of the spray to vary independently. The progress in understanding the dynamics of droplets has relied on experimental investigation due to the complexity of impact spray cooling process. It is only recently that much advances have been achieved when the phase-Doppler anemometry (PDA) becomes available. Durst and Zare (1975) first introduced phase-Doppler anemometry (PDA) for particle sizing. In the past few years, various developments have been introduced for improving the performance and extending the functional capabilities of PDA. The experimental studies of Tilton and Chow (1987), Sommerfeld and Qiu (1992), Lee *et al.* (1994) and Sehmbey *et al.* (1995) have provided the droplet velocity and size information by using laser phase-Doppler anemometry in spray evaporation and impact. Through these investigations, preliminary understanding of the heat transfer of spray cooling has been achieved. Although these studies provided some information on impacting spray heat transfer, the results could not be generalized and, sometimes, contradictory trends were observed. This is due to the complexity of spray cooling process and the lack of detailed information such as the rebounding spray characteristics and film thickness. The heat removal capability of the spray can be estimated from the total latent and sensible heat contents (Tilton and Chow 1990). In their experiments, the sensible heat removal capability was estimated by using the arbitrary assumption that all of the liquid expelled (rebounding droplets) is raised fifty percent of the

way to the saturation temperature, therefore, the effect of the temperature of incoming and outgoing droplets was not studied. It was found that the mass flux of rebounding droplets could reach to 70% of the total impinging mass flux. Furthermore, as a full cone spray nozzle usually has a Gaussian mass flux distribution in the downstream of the spray, the group model should take the local droplet mass flux into account. Unfortunately, this was not be paid attention at previous studies. At the present time, spray cooling is not a well understood process. To the authors knowledge, no study on the effect of rebounding droplets on a cylindrical surface due to the surface temperature and heat flux has been conducted. For a better understanding of the spray characteristics to optimize the heat transfer process in spray impact cooling, accurate measurements of droplet velocity, size, temperature, mass flux and film thickness under realistic flow conditions are necessary. In this paper, a nozzle impinging water droplets onto a cylindrical fin was described. The size and velocity of impacting and rebounding droplets will be measured by using PDA to investigate mechanism of spray cooling.

EXPERIMENTAL DESCRIPTION:

Experimentation was conducted to understand the spray cooling process and identify the important governing factors. Figure 1 shows the schematic diagram of the PDA measurement facilities. The PDA system is mounted on a XYZ moving table so that the measurement volume can be moved along different direction in spray. The measurement distance between the cylinder surface and the measurement volume is 2mm.

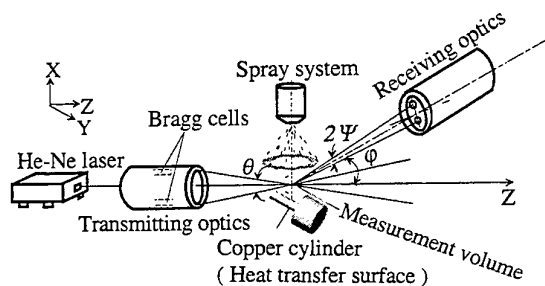


Fig. 1: Measurement Facilities

The effect of rebounding droplets (secondary sprays) by the impact angle, droplet velocity and size, and surface temperature were studied experimentally by

using a Dantec/Invent PDE system. The optical parameters of the PDA system are shown in table 1.

Table 1: Optical parameter of the PDA system

wavelength	632.80 nm
beam diameter	1.10 mm
beam spacing	20.07 mm
transmitting lens	400.00 mm
receiving lens	400.00 mm
detector spacing	40.00 mm
scattering angle	30°
refractive index cont. phase	1.00
refractive index particle	1.33
shift frequency	2.00MHz

The evaporative cooling test apparatus is shown in Figure 2. For both test cases, the heated surfaces were horizontally placed solid copper cylinders with 10mm and 7mm in diameter, and 35mm in length respectively. A 143-Watt heater ring and a 1000-Watt cartridge heater were inserted into the heat blocks as shown in Fig a) and b). The heaters was controlled by a PID controller so that a variable power input may be obtained. It maintained the temperature at some preset value by regulating the power to the cartridge heater. The power of the heater and the temperature reading were displayed from the meter in the controller. The temperature reading of the other five positions was recorded continuously by the data acquisition system at the rate equal to 0.5s. The data was then stored in the PC. To get higher thermal conductivity of the heat block, copper is used as the substrate. When the cylinder reach critical heat flux, cool water was allowed to pass through the pipe surrounding the cylinder so as to protect the component inside the cartridge heater. A level spirit was used to make sure that the cylinder align in horizontal position and the cylinder is supported by an aluminum frame. For the both cases, there 3 thermocouples were embedded under the top surface of the cylinders for the measurements of the surface temperature of the cylinders. For case 2, additional three thermocouples were mounted at the heat supply side of the cylinder center so that the total heat flux removed by the spray can be calculated from the temperature gradients of the materials.

The spray generating system consisted of a pressurized water tank and a spray nozzle. The tank outlet was connected to the nozzle and the inlets to the compressed air which had a maximum supply pressure of 6 bar. To simulate the actual cooling

environment, a full-cone nozzle made of stainless steel with orifice diameter equal to 0.51mm was used. The supply pressure was adjusted to 3bar to achieve a mass flow rate of 0.22 l/min. The center of spray was coincidentally aligned with the center of the hot cylindrical surface.

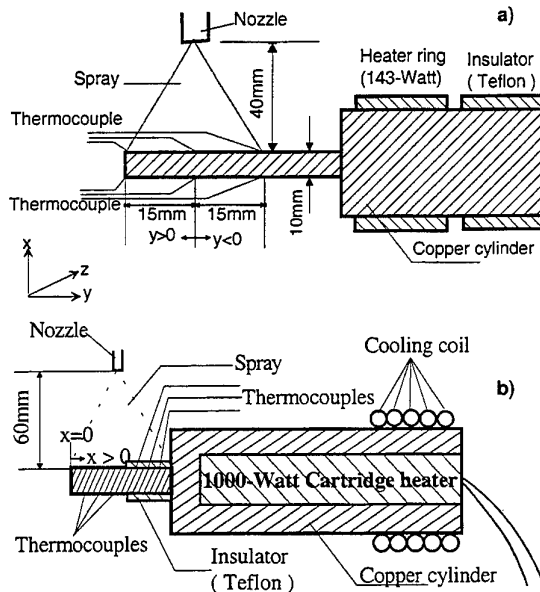


Fig. 2: Geometry of Heaters

Before starting the measurements, the PDA system was calibrated by the TSI monodispersed droplet generator. The test surface was polished by "Brasso" solution and then rinsed with distilled water to remove any oxide formed on the surface, which may affect the behavior of the rebounding droplets. Distilled water was used as cooling liquid throughout the experiments. The distances between the spray nozzle and the surface were 40mm and 60mm for cases 1 and 2 respectively. The cone angle of spray is about 53.67° for both cases. After the setup was aligned properly, the droplet size and velocity of both the impinging droplet and rebounding droplet was measured. Experiments started at room temperature and the surface temperature increased step by step until the critical heat flux was reached. The temperature reading was recorded by a PC computer and the heat transfer characteristics were obtained. By controlling the XYZ table, the position of measurement volume was relocated from one to another. Measurements of droplet size, velocity, surface temperature and heat flux were performed simultaneously and conducted for different positions until rebounding droplets at all the 3 positions ($y=5, 10, 15\text{mm}$) were obtained.

RESULTS AND DISCUSSION:

Test Case 1:

Figures 3-4 presents experimental results obtained by the measurements of test case 1. It is observed that with heating of the cylinder, the mean droplet diameters show an asymmetric distribution along the cylinder axis (see Fig. 3) while the original impacting droplets are symmetrically distributed along to the cylinder axis.

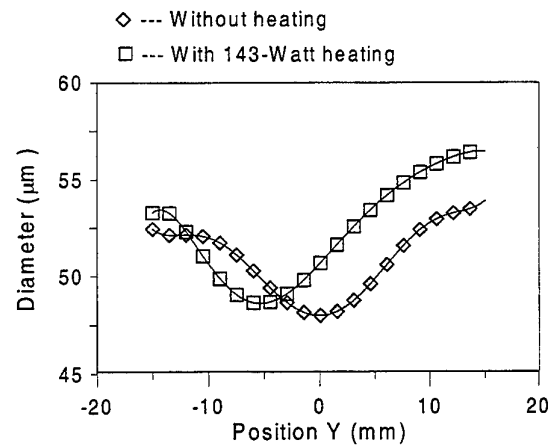


Fig. 3: Overall droplet mean diameter distribution with and without heating (Case 1)

This phenomena may be explained that the measured mean droplet diameter is an overall average of impinging and rebounding droplets. Although the distribution of droplet diameters was shifted towards to the heater size, the velocity distribution was only slightly changed. This explanation was conformed by separating the positive and negative velocities for each particle in test case 2. Another interesting phenomena was found by comparing the size of droplets with heating and without heating of the cylinder. The overall mean diameter of droplets measured without heating is smaller than that with heating which seems to be conflict with the expected phenomena. Because the rebounding droplets are generated from the breakup of impinging droplets on the hot surface, the rebounding droplets were expected smaller the impinging droplets. There are three possibilities that can be drawn from this measurements. The first one is some kind of droplet collision occurred at the heated surface and the surface temperature enhanced this kind of collision.

The second possibility is the small droplets evaporated faster than the large droplets and therefore, only the large droplets will be rebounded from the hot surface. The third possibility could be some condensation of the evaporated vapor happened on the impinging droplets. If the third phenomena is true, it could be much easier to observe it when the surface temperature is at higher condition. However, the ring heater selected (143-Watt) could not supply sufficient power to the heated cylinder and therefore, a larger power (1000-Watt) cartridge heater was then used to further investigate the effect in the test case 2.

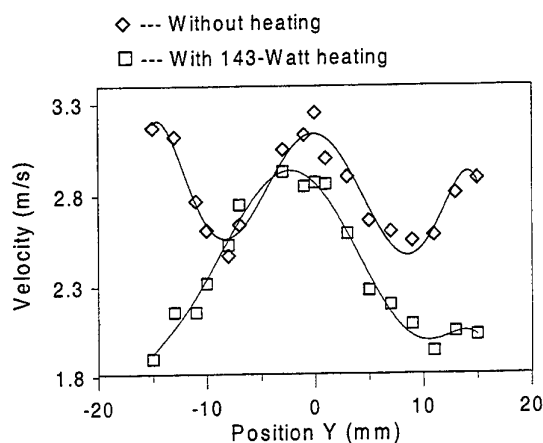


Fig. 4: Overall droplet mean velocity with and without heating (Case 1)

Test Case 2:

The test apparatus has been shown in Fig. 2b. Because a droplet with negative velocity can be considered as a rebounding droplet, the impinging and rebounding droplets can be separated by the measured velocities. To compare the influence of the surface temperature, the results for velocity and diameter, as well as the rebounding droplets, under the surface temperatures $T=22^{\circ}\text{C}$ (unheated) and $T=100^{\circ}\text{C}$ are shown in Figs. 5 to 8.

Mean velocity of the rebounding droplets

Figs. 5 to 8 show similar correlation for both the impinging and rebounding droplets. No significant difference between the droplet velocities and the

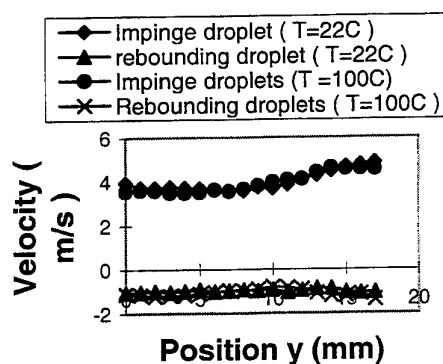


Fig. 5: Comparison of the velocities of impinging and rebounding droplets at (i): unheated cylinder ($T = 22^{\circ}\text{C}$), (ii): mean surface temperature $= 100^{\circ}\text{C}$

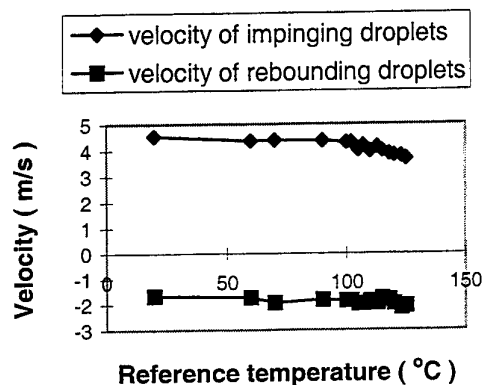


Fig. 6: Velocities of droplets via surface temperature, at the edge of the spray ($y=5\text{mm}$)

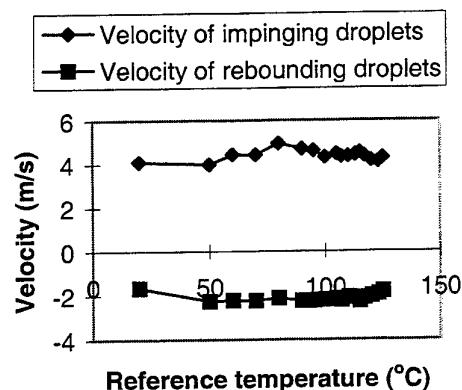


Fig. 7: Velocity of droplets on different surface temperature, at the middle part of the exposed fin ($y=10\text{mm}$)

surface temperatures for impinging and rebounding droplets was found. The droplet velocities also only increase slightly after the critical heat flux. This

seems contradictory to our expectation that the droplets should gain more kinetic energy away from the surface when the surface temperature increases and so increases the rebounding velocity.

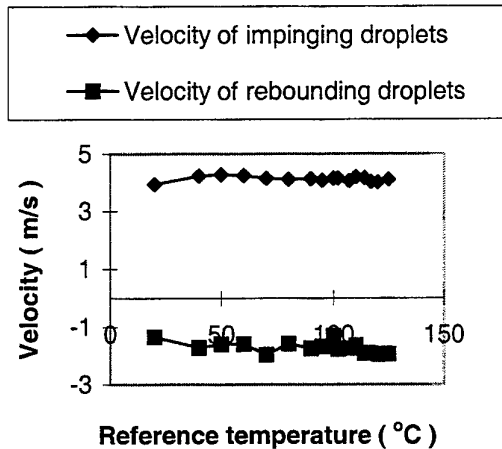


Fig. 8: Velocity of droplets on different surface temperature, at the center of the spray ($y=15\text{mm}$)

There are two possible reasons. When water droplets impinge on the surface, they form a thin water film on the surface. The followed droplets will impact on the water film rather than directly impact on the hot substrate. Especially, before reaching the critical state, the water film remains and droplets can only rebound from the water film. Since water is a poor conductor, the surface temperature of water film does not change much with the substrate temperature. As a result, droplets can only impinge upon the water film which has nearly constant surface temperature despite a large increase in surface temperature. Therefore, it seems that droplet velocity does not show any obvious change as the surface temperature increases.

Another possibility is the droplets rebound once they gain enough kinetic energy. They will not stay longer to absorb more heat even if the surface reach critical heat flux, at which direct contact between droplet and copper surface is possible. That means droplets rebound from the surface just when their rebounding velocity is large enough to overcome the gravitational force and the surface tension of water, as kinetic energy is a function of mass and velocity. This is why the velocity increase only slightly after critical heat flux.

Critical heat flux

Fig. 9 shows the correlation between the heat flux and the reference temperature. The reference temperature was measured at the center of the fin which is proportional to the surface temperature. The temperature recording began when it reached to 50°C . The results showed that the temperature range at which critical heat flux occurs is more narrow than that of spray cooling on a flat surface. This is because the curvature of the fin affects the impact angle of the droplets which has shown a great effect to the critical heat flux in the following experiments which was not be paid attention in the previous research. Flooding was not so serious on a fin and only a thin layer of water film formed on the surface. When the surface temperature reaches to the critical value, very little increase in surface temperature can cause the rapid reduction of the wettability of the hot surface and, consequently, result in completely drying the water film.

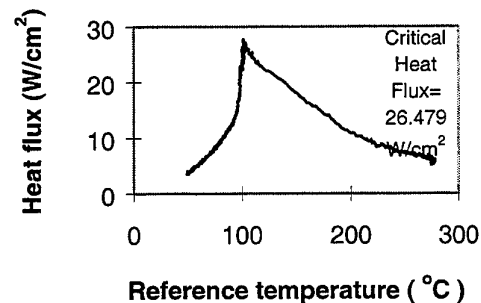


Fig. 9: Heat transfer characteristics of a copper cylinder, reference temperature was taken at the middle of the fin

In Fig. 9, it is shown that there was no obvious change until the substrate is heated to about 110°C . When the surface exceeded 110°C , the film became much thinner and then completely dried out. After the water film dried out, the surface temperature increased abruptly. In this case, the droplet will be rebounded directly from the hot substrate and by the splashing, transient nucleation boiling and expelling.

Mean diameter of the rebounding droplets

The rebounding droplets were measured at different surface temperatures as shown from Figs. 10 to 13. In Fig. 10, the droplet diameter increased slightly for the most of impacting angles. However, it fluctuated around the position $y=10\text{mm}$ before reaching the critical heat flux. Therefore, there should be some kind correlation between the impacting angle and the

diameter of rebounding droplets remained which should be further investigated. As the surface temperature of the substrate increases, more heat transfer to the droplets, so the average temperature of the droplets increases and so the surface tension and viscosity of the droplets decreases. Hence, the droplets can evaporate more quickly or less impacting force required to break the film and the droplets. As described previously, before reaching the critical heat flux, the copper surface was covered by a water film and most of the droplets can only rebound from it.

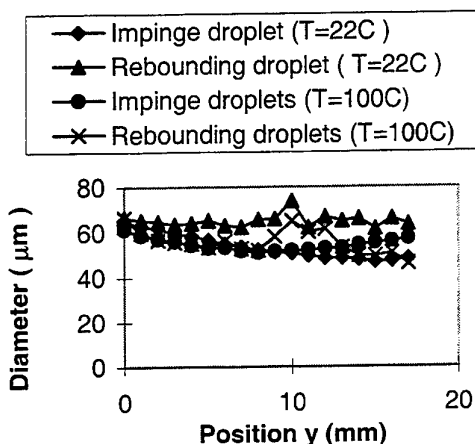


Fig. 10: Diameter of impinging droplets and rebounding droplets at (i): unheated cylinder, (ii): mean surface temperature = 100 °C

The water film has low conductivity and little heat transfers to the droplets before it rebounds. This means that the temperature and surface tension of the rebounding droplets remain more or less the same despite the large increase in surface temperature. The correlation between the surface temperatures and the droplet diameters are shown in Figs. 11-13 for positions 5, 10, 15 mm on the the top surfaces. For all cases, the diameters of droplets decrease significantly after reaching the critical heat flux (T_c is about 110 °C). The reason is that after reaching critical heat flux, water film evaporate quickly from the surface. Now the impinging droplet impact directly on the hot copper surface some of the mass may be evaporated before rebounding from the surface. Since water film is no longer an obstacle for spray evaporation, heat flux increase abruptly during critical heat flux.

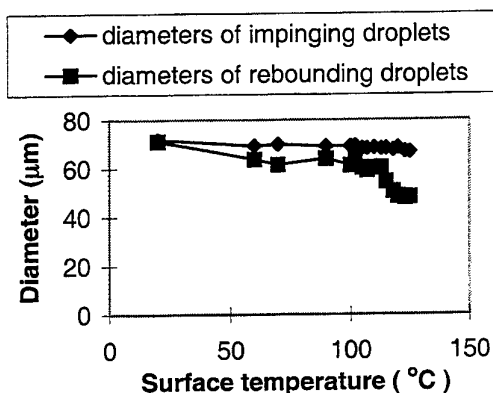


Fig. 11: Diameter of droplets on different surface temperature, at the edge of the spray ($y=5\text{mm}$)

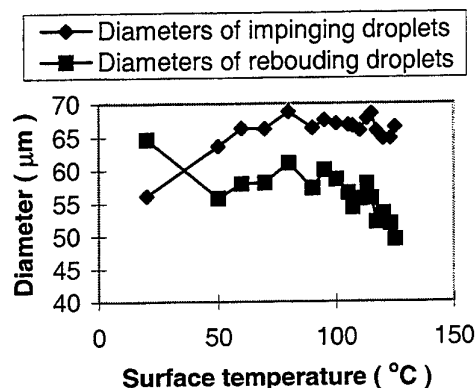


Fig. 12: Diameter of droplets on different surface temperature, at the middle part of the exposed fin ($y=10\text{mm}$)

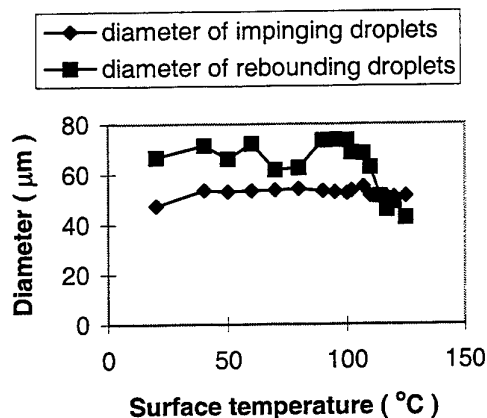


Fig. 13: Diameter of droplets on different surface temperature, at the center of the spray ($y=15\text{mm}$)

One of the interesting phenomena was found when comparing size of rebounding droplets at different positions. Near the center of spray (i.e. at $y=15\text{mm}$), the average diameter of the impinging droplets was smaller than the diameter of the rebounding droplets (see Fig. 10). But near the edge of spray (i.e. at $y=5\text{mm}$), the diameter of the impinge droplets was found to be larger than the diameter of rebounding droplets. Since the droplets near the edge impacted with a large contact angle while the droplets near the center impacted on the surface perpendicularly, the droplets near the center ($y=15\text{mm}$) had low rebounding rate than that of the droplets near the edge of spray ($y=5\text{mm}$) as it has also been indicated in Fig. 14.

Because small droplets have relatively lower terminal velocity and, therefore, lower Weber's number than that of large droplets, the droplet rebounding rate for small droplets should be less than that for large droplets (See also Fig. 14). Hence, only large droplets can be rebounded from the surface and measured by PDA. This may be one of the reasons for the diameter of the rebounding droplets measured larger than that of the impinging droplets.

But the situation was very different near the edge of spray. Near the edge of the spray, the horizontal velocity component of the droplets was much larger than that of the droplets in the center of the spray. This horizontal velocity component was coming from the impact angle of the droplets. The smaller droplets could be also rebounded from the surface due to this horizontal component. A larger droplet may continue its horizontal motion and swept away by the water more easily. This is why larger droplet is more reluctant to rebound at the periphery.

Number of rebounding droplets

Refer to Figs. 13 to figure 14, the number of droplets increases slightly with increasing temperature before reaching critical heat flux. This is caused by the effect of water film as explained previously. However, it is interesting to note that the rate of the rebounding droplets at the location of $y=10\text{mm}$ showed the largest value than the other positions ($y=5$ and 15mm). This suggested that there exists a critical impacting angle where the rebounding rate reaches the maximum. In this study, the angle is in the position of $y=10\text{mm}$ where the impacting angle is about 5 degree. However, due to lack of more detailed data, the correlation of this angle with the

spray characteristics is still not clear and should be further investigated in the future.

Fig. 14 also proved that relatively fewer droplets were able to be rebounded at the center location. However, when the temperature reach to the critical temperature, the rebounding rates for all of three cases increase drastically. This phenomenon can explain why the heat flux drop abruptly after reaching critical heat flux, since many droplets were rebounded from the surface and much less latent heat was removed through the evaporation of water droplets. This will be mainly constraint for the spray cooling. To improve the spray, one suggestion is to develop the spray nozzle so that the droplets can impinging onto the hot surface perpendicularly.

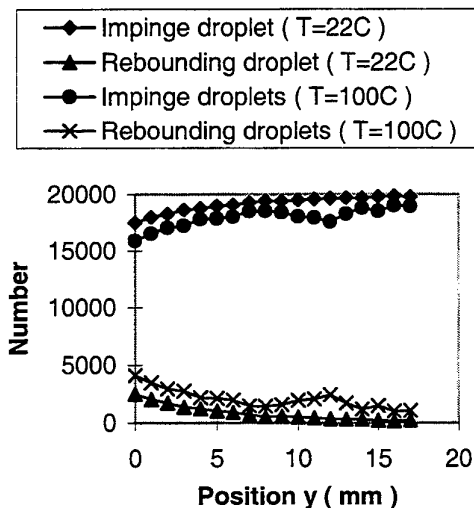


Fig. 13: Number of impinging droplets and rebounding droplets at (i): unheated cylinder, (ii): mean surface temperature = 100°C

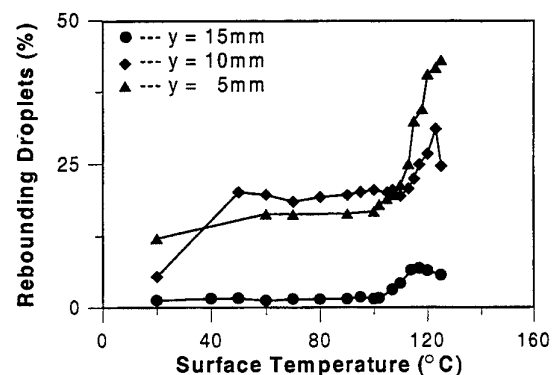


Fig. 14: Percentage of rebounding droplets via surface temperature

CONCLUSION

By using PDA measurements, it was found that the characteristics of rebounding droplets depend not only on the surface temperature, mass and velocity of droplets, but also on the impinging angle. Since the heat transfer process of spray cooling is complex, some of the results is out of prediction. Nevertheless, the heat transfer characteristics can still be explained from the droplet characteristics detected. Therefore, further investigation of droplet characteristics is necessary in order to improve critical heat flux of cylindrical surface by spray impingement.

REFERENCE

1. Durst, F. and Zar6, M. 1975: "Laser-Doppler measurements in two-phase flows", *Proc. LDA Symp. Copenhagen*, 403-429.
2. Lee, S. L., Yang, Z. H. & Hsyua, Y. 1994: "Cooling of a heated surface by mist flow", *Journal of heat transfer*, vol. 116, pp. 167-172.
3. Sankar S. V., K.M. Ibtahim, D.H. Buermann, M.J. Fidrich, and W.D. Bachalo 1993: "An integrated phase Doppler/rainbow refractometer system for simultaneous measurement of droplet size, velocity, and refractive index", *The 3rd. Int. Congress on Optical Particle Sizing*, Yokohama, 275-284.
4. Sehmbe, M. S., Chow, L. C., Hahn, O. J., and Pais, M. R., "Spray Cooling of Power Electronics at Cryogenic Temperatures", *Journal of Thermophysics and Heat Transfer*, Vol.9, No. 1, January-March 1995. pp. 123-128.
5. Sommerfeld, M. and Qiu, H.-H. 1992: "Experimental studies on spray evaporation in a turbulent flow", *Proceedings of the 6th Workshop on Two Phase Flow Predictions*, Erlangen 167-185.
6. Tilton, D. E. & Chow, L. C. 1987: "High power density evaporative cooling", *Paper No. AIAA87-1536*.
7. Yao, S. C. & Choi, K. J. 1987: "Heat transfer experiments of mono-dispersed vertically impacting spray", *Int. J. Multiphase Flow*, vo. 13. No. 5, pp. 639-648.

SOME ASPECTS OF ELECTROHYDRODYNAMIC SPRAYING IN CONE-JET MODE

K. Ohba, P.H. Son and Y. Dakemoto

Department of Mechanical and Systems Engineering
Kansai University, Japan

ABSTRACT

Herein we report an experimental study on the electrohydrodynamic (EHD) spraying in cone-jet mode. The effects of electric field strength, surrounding ambient fluid, surface tension of the working fluid, pressure head in the working fluid supply line and the electrodes configuration of the apparatus for spraying were investigated. The working fluid, ethanol or water, of different surface tension was issued out into the surrounding fluid, air or CO₂ gas, by using a needle-plate apparatus for EHD spraying. The formation of the cone-jet at the needle tip was monitored by using a hypervideo microscope. The droplet size and velocity were measured by using a Phase Doppler Particle Analyzer. The results indicate that a stable cone formed in CO₂ gas in a certain range of the applied voltage for either ethanol or water, while it takes place for only ethanol sprayed in air. The droplet size decreased with increasing applied voltage and is of order of 2-4 microns for both ethanol and water when produced in stable cone-jet mode.

1. INTRODUCTION

The electrohydrodynamic (EHD) atomization is a process of producing a droplets spray by imposing a strong electric field or electric charge on the liquid. This atomization method has a great potential in producing droplets of small size and provides additional controlling parameters such as the applied voltage and the electric charge on the droplet. The EHD spraying is employed in a number of technologies, among which are ink-jet printing, crop spraying, paint spraying and surface coating. Despite the extensive practical applications of the method, the droplet

formation process still remains elusive. There is a number of modes of droplet formation depending on the electric field strength and its configuration, the physical properties of the working fluid and its ambient medium. A comprehensive review on the EHD spraying modes is given by Cloupeau and Prunet-Foch (1994). Among those modes, the EHD spraying in cone-jet mode is one of the most important, since it can produce a monodispersed spray of very fine droplets of micrometer order. However the conditions for the formation of a steady cone-jet are not clarified. This work does not seek to answer fundamental questions about the mechanism of the cone-jet formation, but rather to define the effects of electric field strength, ambient fluid, surface tension of working fluid and hydrostatic pressure of liquid supply line on the cone-jet formation. In the present experiments, the characteristic parameters of the spray such as the droplet size and its velocity were acquired by using a Phase Doppler Particle Analyzer (PDPA). Also, the process of cone-jet formation at the capillary tip was monitored. The experimental droplet size then is compared to the theoretical one, which was calculated based on our theoretical and experimental work (1998).

2. DROPLET FORMATION IN CONE-JET MODE

A striking feature of producing droplet spray in cone-jet mode is that a monodispersed spray of very fine droplets of some microns can be obtained. In the present experiments, the liquid is gravitationally supplied from the reservoir to the needle at a specific pressure head. In the absence of an electric field, a pendant meniscus of pear shape forms at the needle tip. The meniscus grows in size with time until it detaches and falls from the needle tip under action of the

gravitational force. The application of a DC voltage to the needle and its increase cause the reduction in the droplet size and the increase in droplet emission frequency. In general, the diameter of droplets formed in this so-called dripping mode remains greater than the needle diameter. With further increasing the applied voltage, the meniscus attains a conical form. At a certain voltage, a very small jet compared to the capillary diameter emanates from the vertex of the conical meniscus with subsequent disintegration to form a spray of fine droplets.

It would be a difficult task to conduct an analytical description for the complete EHD spray. Therefore, an EHD spray in cone-jet mode can be split into three interacting regions with quite distinct behavior (see figure 1):

- 1) Conical meniscus, which forms at the needle tip;
- 2) Liquid jet, which breaks up into droplets by the wellknown Rayleigh's capillary instability;
- 3) Droplets spray, where the information on the droplet size and velocity, as well as the droplet charge is important.

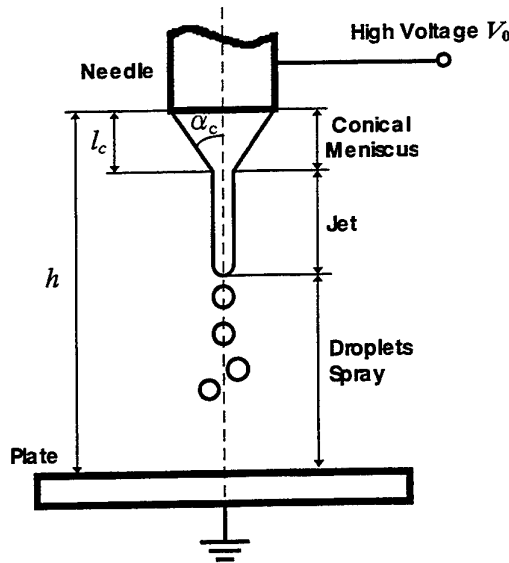


Figure 1 Sketch of an EHD spray in cone-jet mode.

The effects of the surface tension, pressure head in the liquid supply line and electric field strength can be estimated in the light of the normal pressure balance at the meniscus surface, which is expressed as

$$\sigma \left(\frac{1}{R_1} + \frac{1}{R_2} \right) - \rho_1 g H - \frac{1}{2} \epsilon_0 E_n^2 = 0 \quad (1)$$

where σ is surface tension of liquid in contact with air, R_1 and R_2 are principle radii of surface curvature, ρ_1 is liquid density, H is height level between liquid surface in reservoir and needle tip, ϵ_0 is permittivity of surrounding air and E_n is normal electric field strength at the liquid surface.

The breakup of jets is thought to occur due to the Rayleigh's capillary instability. We have carried out the linear analysis on the instability of an electrically charged liquid jet. By using the basic equations of fluid mechanics and electromagnetism, Son and Ohba (1998) have derived the following equation for the dimensionless growth rate of the disturbances developed on the surface of the jet.

$$\omega^{*2} = - \frac{k^{*2} \rho^* I K}{(I - \rho^* K)^2} We + \frac{k^*}{I - \rho^* K} \left[\left(1 - m^2 - k^{*2} \right) - \alpha^2 Bo_E \left(1 + k^* \frac{1}{K} \right) \right] \quad (2)$$

where

$$\rho^* = \frac{\rho_2}{\rho_1} : \rho_1 \text{ and } \rho_2 \text{ are density of continuous}$$

and dispersed phase, respectively;

$$I = \frac{I_m(k^*)}{I'_m(k^*)} \quad \text{and} \quad K = \frac{K_m(k^*)}{K'_m(k^*)} : I_m(k^*) \quad \text{and}$$

$K_m(k^*)$ are modified Bessel functions of the 1st and 2nd kind;

$k^* = ka$: Dimensionless wavenumber, where a denotes the radius of undisturbed liquid jet;

$$We = (U_1 - U_2)^2 \frac{\rho_1 a}{\sigma} : \text{Weber number, } U_1 \text{ and}$$

U_2 are velocities of continuous and dispersed phase;

$$Bo_E = \frac{\epsilon_0 E_n^2 a}{\sigma} : \text{Electrical Bond number; } \alpha \text{ is a}$$

constant and equal to 0.707 in our work.

The calculation results of this equation have revealed that the varicose mode of instability takes place at low electric field strength and the kink mode of instability is enhanced at high electric field strength. The kink instability causes the lateral motions of the jet, while the varicose instability causes the breakup of the jet. By assuming the jet breaks up with the wave of maximum growth rate, we can calculate the droplet diameter according to the following formula.

$$d = (12\pi)^{1/3} (\lambda_{cr}^*)^{1/3} a \quad (3)$$

where $\lambda_{cr}^* (= 1/k_{cr}^*)$ is dimensionless critical wavelength. The equation 3 is used for theoretically predicting the droplet size.

3. EXPERIMENTAL APPARATUS AND PROCEDURE

In the present experiments, an electrohydrodynamic spraying was produced by establishing a high electric field between the tip of a needle, from which liquid is emanated, and a washer-plate. The experimental apparatus is shown schematically in figure 2. The main components of the system included a liquid delivery system, an electrical charging system, a CO₂ gas supply system, a laser measurement system and a visualization system.

The fluid delivery system consisted of a liquid reservoir, where the liquid surface level was maintained at the heights H of 15 and 20 mm above the surface of the needle tip. The working fluids were distilled water and ethanol with surface tensions of 0.0728 and 0.0228 N/m, respectively. Liquid was fed to the needle under gravity. The mass flow rate was measured by defining the mass reduction of liquid in one minute with the help of an electronic balance. The needle is made of a stainless steel with 260 μ m I.D. and 510 μ m O.D. Two kinds of needle were used: one with flat tip and another with conically tapered end with semivertex angle 30°. A Glassman High Voltage Power Supply with variable voltage of 0-10 kV was used to apply to the needle a high DC voltage of

positive polarity with respect to an electrically grounded plate of washer type. This aluminum washer-plate with outer diameter of 18 mm and hole diameter of 8 mm was placed perpendicularly below the needle at the distance of 1 mm from the needle tip. Another electrically grounded plate of aluminum with diameter of 40 mm was placed further downstream at 20 mm from the needle tip to collect the droplets. Coaxial with the needle, a flow of CO₂ gas with 3 l/min flow rate isolated the needle tip from the ambient air in order to suppress the onset of corona discharge. The droplet size and its axial component of velocity at 5 mm far from the needle tip were measured by using an Aerometrics Phase Doppler Particle Analyzer (PDPA). The PDPA was configured to receive the scattered light in the 30° off-axis forward scattering mode. A Keyence Hypervideo Microscope with exposure time of 1/50000 sec was used to monitor the shape and behavior of the meniscus formed at the needle tip with the aid of a halogen lamp.

In a typical run, the applied voltage was increased by 10 V step starting from zero and finishing at corona discharge occurrence. At each value of applied voltage, the droplet size and its axial component of velocity, mass flow rate were measured and the video recording was taken.

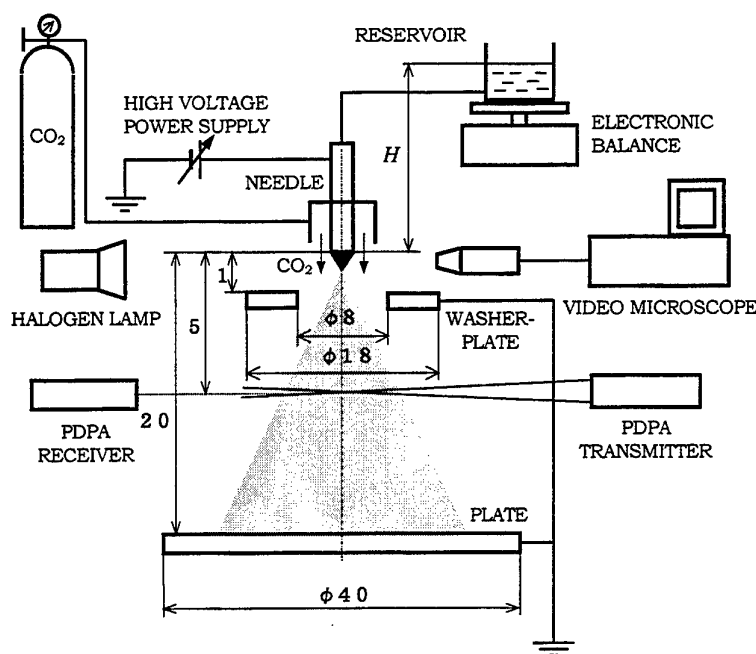


Figure 2 Schematic diagram of experimental apparatus.

4. EXPERIMENTAL RESULTS AND DISCUSSION

4.1. Cone-Jet Configuration

Taylor was the first to make a theoretical prediction of the cone angle. Considering the case of an isolated drop located in a strong electric field, Taylor has showed that the half-angle at the apex of the cone is equal to 49.3° . However our experiments showed stable conical menisci formed at the needle tip for a certain range of applied voltage and hydrostatic pressure. Moreover, the value of the cone angle and its length is variable. The generatrix of the cone may be either concave or convex.

Ethanol. Since ethanol has a low surface tension, the pendant drop forms at the needle tip for H of both 15 and 20 mm. These specific heights were selected based on the initial observations identifying those at which the formation of the cone-jet mode was best characterized for both ethanol and water. The photographs showing the shape of the meniscus at various applied voltages are given in figure 3(a). At 2.6 kV, the meniscus attains a convex conical form and a jet begins emitting from the apex of the cone. With increasing applied voltage, the cone length shortens, the cone angle becomes larger, cone generatrix becomes concave and the jet diameter decreases. At about 3.7 kV, a second jet forms as a result of abundant

accumulation of charge at the meniscus surface. The number of jets formed at the rim of the needle tip in this so-called multi-jet mode increases with further increasing in applied voltage. The process of cone-jet formation is almost similar for spraying of ethanol in either CO_2 gas or air.

Water. No spray of water in the air in cone-jet mode could be obtained. Since the surface tension of water is relatively high, the corona discharge occurs before the electric field becomes high enough to create the electrostatic pressure that exceeds the pressure due to surface tension. The spraying in cone-jet mode was obtained only in CO_2 gas. For needle with flat tip, the cone-like meniscus forms with strong lateral oscillation. By contrast, a stable cone occurs for needle with cone ending, as shown in figure 3(b). Although the cone length shows a little change compared to that for ethanol at various applied voltages, it increases with increasing applied voltage. We could not define whether the jet formed by the video microscope used in the present experiments. There are two possible mechanisms of droplet emission from the apex of the cone. In one mechanism, the droplets are emitted directly from the cone apex due to strong electric field present there by the growth of unstable surface deformations. In another mechanism, the liquid jet is ejected and subsequently breaks up into droplets.

When the electric field becomes high enough to create the electrostatic pressure that exceeds the pressure due to surface tension. The spraying in cone-jet mode was obtained only in CO_2 gas. For needle with flat tip, the cone-like meniscus forms with strong lateral oscillation. By contrast, a stable cone occurs for needle with cone ending, as shown in figure 3(b). Although the cone length shows a little change compared to that for ethanol at various applied voltages, it increases with increasing applied voltage. We could not define whether the jet formed by the video microscope used in the present experiments. There are two possible mechanisms of droplet emission from the apex of the cone. In one mechanism, the droplets are emitted directly from the cone apex due to strong electric field present there by the growth of unstable surface deformations. In another mechanism, the liquid jet is ejected and subsequently breaks up into droplets.

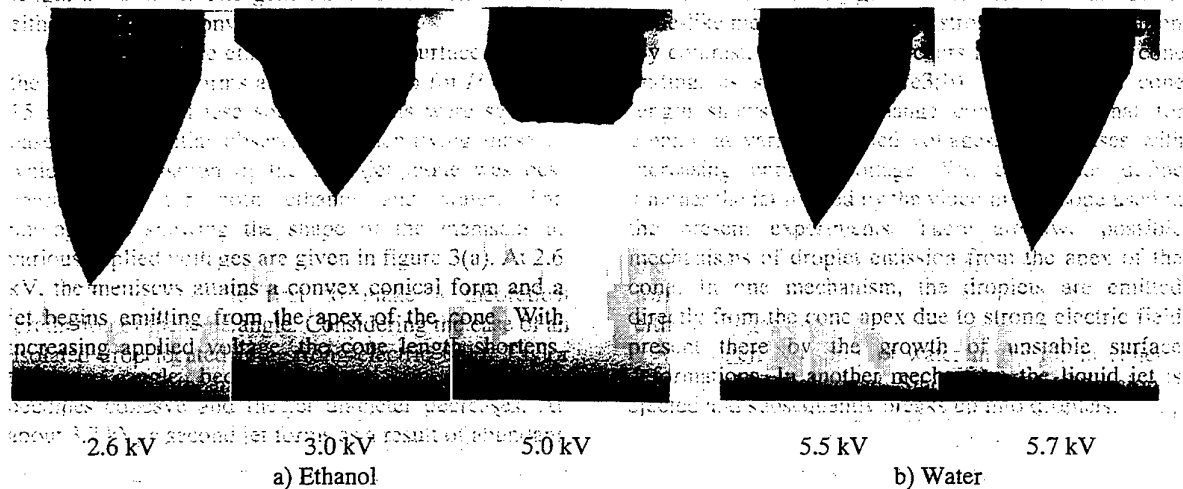


Figure 3 Photographs of conical menisci at the needle tip at various applied voltages.

4.2. Droplet Size

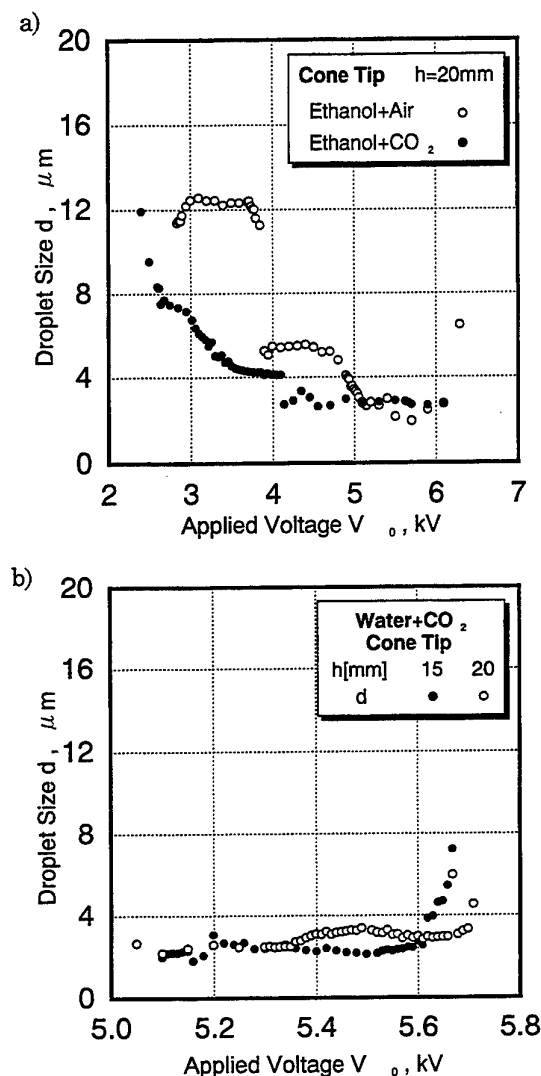


Figure 4 Droplet size variation with applied voltage.

For ethanol, the increase in applied voltage reduces the jet diameter and its breakup wavelength, and thus, the droplet size as well. For the case of ethanol issued in CO_2 gas, droplet size decreases with increasing applied voltage and stays unchanged at about 3 microns at applied voltage above 4 kV for needle with cone tip, as shown in figure 4(a). For ethanol issued in air, with increasing applied voltage, droplet size stays constant at 12 microns until 3.7 kV, then sharply decreases in size down to 5 microns. It is constant at about 3 microns from 5 kV until corona

occurs. For the flat tip, the droplet size is a little larger and about 4 microns at applied voltage above 5 kV. Reducing the height level between liquid surface in reservoir and the needle tip from 20 mm to 15 mm resulted in higher voltage range where the droplet size remains unchanged and minimum. The comparison between the experimental droplet size and calculated one according to formula (3) for ethanol is shown in figure 5. A relatively good agreement is achieved.

For water, droplet diameter is almost constant at 2-3 microns for the whole range of applied voltage where the cone is stable, as shown in figure 4(b). But this range of voltage is more narrow compared to the case of ethanol and is from 5.1 to 5.7 kV. Droplet size is of the same magnitude for two different pressure heads ($H=15$ and 20 mm) in the present experiments.

4.3. Axial Component of Droplet Velocity

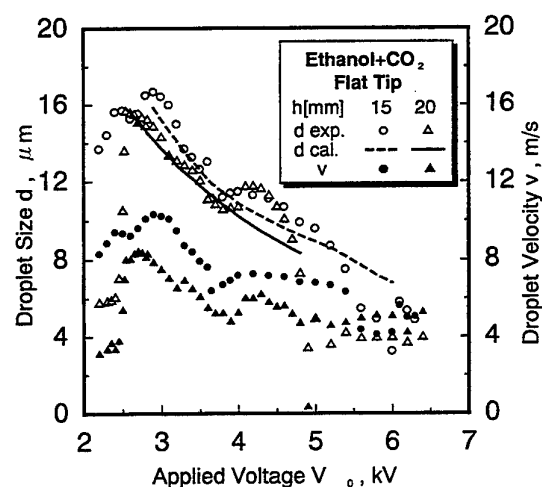


Figure 5 Variation of droplet size and its axial component of velocity.

The variation of the axial component of droplet velocity has a similar tendency of droplet size variation with increasing applied voltage. The value of velocity changes within the interval 2-10 m/s depending on the applied voltage and droplet size, as shown in figure 5 for the case of ethanol sprayed in CO_2 gas. The larger the droplet, the higher its momentum. Besides, the larger droplets are thought to carry a larger amount of charge, which results in a greater electrostatic force acting on the droplet in the direction of electric field and attracting the droplet downward to the grounded plate.

4.4. Flow Rate

In the present experiments, instead of keeping the flow rate constant we kept the hydrostatic pressure in the liquid supply line constant. For needle with cone tip, flow rate is small and almost constant at nearly 0.01 ml/min (see figure 6). However, for needle with flat tip, the flow rate increases with increasing applied voltage and reaches the maximum of about 0.16 ml/min at 6 kV where the corona discharge occurs.

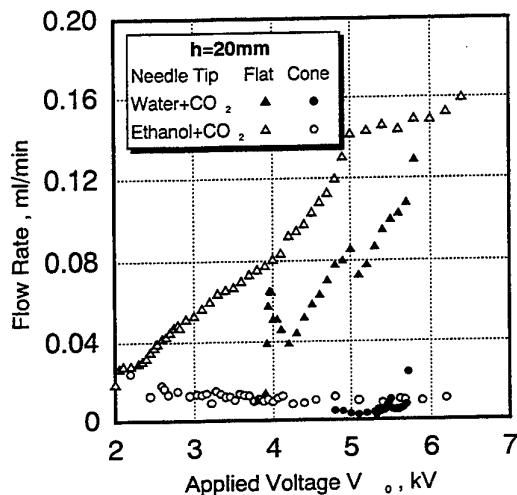


Figure 6 Variation of volumetric flow rate with applied voltage.

5. CONCLUDING REMARKS

The experimental study on the EHD spraying in cone-jet mode has showed that:

- The surface tension plays an important role in the formation of cone-jet. The cone-jet mode was established in a large region of applied voltage for liquids with low surface tension such as ethanol. For water, the cone-jet mode took place only in CO₂ gas and within a narrow range of applied voltage.
- In cone-jet mode, very fine droplets of 2-4 microns were obtained for both ethanol and water.
- A comparison between the experimental droplet size and that calculated by our theoretical result of instability analysis of charged liquid jets shows a relatively good agreement.

REFERENCES

- Cloupeau, M. & Prunet-Foch, B. 1994, Electrohydrodynamic Spraying Functioning Modes: A Critical Review, *J. Aerosol Sci.*, vol. 25, pp.1021-1036.
- Son, P.H. & Ohba, K. 1997, Instability of a Perfectly Conducting Liquid Jet in Electrohydrodynamic Spraying: Perturbation Analysis and Experimental Verification, *J. Phys. Soc. Japan*, vol. 67 (3), pp.825-832.

CHARACTERISTIC MEASUREMENT OF ELECTROSTATIC FUEL SPRAY

Jeong Heon KIM, Yuji IKEDA and Tsuyoshi NAKAJIMA

Department of Mechanical Engineering
Kobe University

Rokkodai, Nada, Kobe 657 JAPAN

ABSTRACT

The characteristics of an electrostatic spray were investigated by detailed measurements by phase-Doppler techniques. Droplet size, axial and radial velocity, and number density were measured throughout the spray field. Experiments were carried out using heptane doped with an anti-static additive to enhance its electric conductivity.

The droplet sizes were characterized as a two-peak distribution in the whole spray field and affected the spray characteristics. The droplets behaved differently with droplet sizes. The number density, mean diameter and mean velocity of droplets were more strongly affected by the behavior of small droplets.

1. INTRODUCTION

Liquid jets break up to form sprays of charged droplets when intense electric fields are applied, because Coulombic repulsion on the surface of a charged droplet overcomes a surface tension that holds the droplet. An electrostatic atomization is an essential process in the current technologies of spray painting, ink jet printing, crop spraying, space-vehicle propulsion and other applications. Particularly, in spray combustion, electrostatic atomization can offer good mixing and low agglomeration, and control over the droplet size and dispersion [Chen (1992), Gomez (1994), Thong(1971)]. This electrostatic atomization was first studied theoretically by Rayleigh and has been studied by many other researchers [Rayleigh (1882), Mutoh (1979), Hayati (1987)] and so on. Despite of its advantages and wide application, the fundamental mechanisms of electrostatic atomization are not well understood.

The purpose of this study was to experimentally investigate the structural characteristics of an

electrostatic spray. For the purpose, a series of detailed measurements was taken in a spray field. The droplet size, velocity, velocity-size correlation, and droplet number density were measured using two dimensional phase-Doppler techniques.

In a previous study, we understood already that a electrostatic atomization was dependent on charged voltage and liquid-flow rate [Kim (1998)]. The droplet size was decreased with charged voltage. The size distribution was varied with flow-rate of liquid. For the very low flow-rate, the size distributions were one-peak histogram of mono-disperse droplets. Then, droplet sizes were characterized as a two-peak distribution with increasing a flow-rate. Then, this present study was focused on the structural characteristics of an electrostatic spray with a two-peak size distribution.

2. EXPERIMENTAL

The electrostatic atomization system consisted of a 0.2 mm stainless steel capillary tube and a 6.5 mm inner diameter grounding ring positioned 5 mm away from the tube. The capillary was charged to several kilovolts and a liquid fuel was fed from a metal tank through the capillary using pressured nitrogen. A sketch of the electrostatic atomization system is shown in Fig. 1.

Heptane (C_7H_{16}) was used as liquid fuel of these experiments, due to its well-established properties. the fuel was doped with an anti-static fuel additive (0.5 w%, Du Pont Stadis 450) to raise its conductivity to a value of 10^{-5} mho/m, which was measured by a high resistance meter. For this study, the pressure in the fuel tank and the fuel flow-rate was fixed at 24.5 kPa and 2.5 cm^3/min , respectively. The capillary was constantly charged to 5 kV.

Detailed single-point measurements were taken using a two dimensional phase-Doppler measurement system to achieve simultaneous

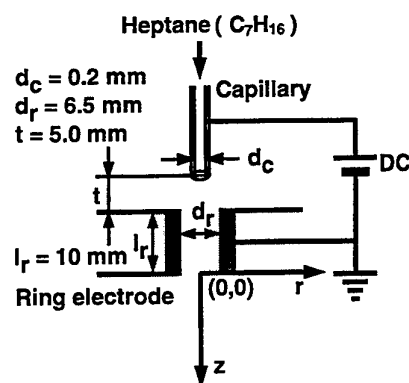


Fig. 1 Electrostatic atomizer.

Table 1 Set-up parameters of phase-Doppler measurement.

	Axial	Radial
Wave length (nm)	514.5	488
Focal length (mm)	600	
Spot diameter (μm)	291.2	276.2
Fringe spacing (μm)	8.13	7.71
Fringe number	36	36
Maximum diameter (μm)	157	
Maximum velocity (m/s)	7.31	6.94
Minimum velocity (m/s)	-2.44	-2.31
where		
Focal length of receiving optics	: 310 mm	
Frequency shift	: 40 MHz	

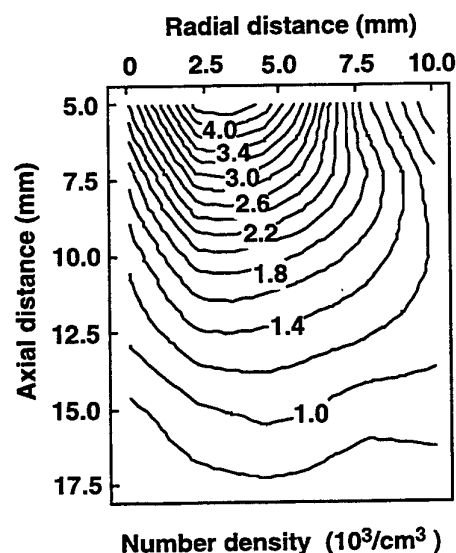


Fig. 2 Profile of droplet number density.

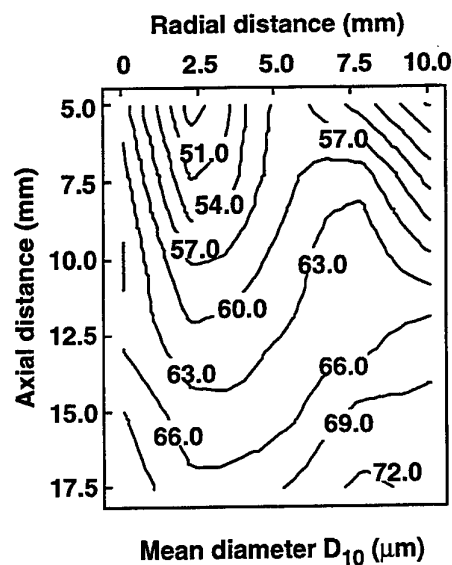


Fig. 3 Profile of droplet size.

measurement of the size and velocity of droplets. The measurements were taken through all of the spray field below the grounding ring.

A 72° offset angle was used in the phase-Doppler measurement to improve the S/N ratio. This angle was determined from Brewster condition, using the refractive index of heptane. Brewster angle was found to give the best linearity of phase shift versus droplet diameter [Naqwi (1991)]. Optical set-up parameters used for the phase-Doppler measurement are shown in Table 1.

3. RESULTS AND DISCUSSION

3.1 Number Density and Mean Diameter

Figure 2 shows the profile of droplet number density in a spray field. The droplet number density was calculated from the results of phase-Doppler measurement by following equation.

$$ND = \frac{1}{t} \sum_i \frac{t_{\text{tran}(i,j)}}{PV_i}$$

Where, ND : number density, t : total sampling time, $t_{\text{tran}(i,j)}$: particle transit time for size class i, PV_i : corrected maximum probe volume for size class i.

The number density was high in up-stream of the spray and decreased monotonically with axial distance. However, we can observe that it had no a

monotonic tendency with the radial distance. The peak of droplet number density was at a finite distance, about $r = 2.5$ mm away from the centerline of spray axis.

Figure 3 shows the profile of arithmetic mean diameter (D_{10}) in the spray field. The profile of mean diameter had the reversed tendency to the case of droplet number density. D_{10} was monotonically increased with the axial distance. D_{10} was minimum at a finite distance, about $r = 2.5$ mm away from the centerline of spray axis, where was also the axis of the maximum number density.

From results, we can estimate that droplets were dispersed outward and small droplets gathered at a finite distance away from the centerline of spray axis. It is considered that droplets were dispersed differently with droplet size.

3.2 Two-peak Droplet Size Distribution

Figure 4 shows the droplet size distribution at a representative measured location ($r = 0$ mm, $z = 5$ mm). The droplet size distribution had a two-peak histogram and its cumulative number distribution had two-steps. Small droplet group under $5 \mu\text{m}$ occupied 13% of the total number of measured droplets. The number of droplets from $10 \mu\text{m}$ to $50 \mu\text{m}$ was very low. The large droplet group from $50 \mu\text{m}$ to $100 \mu\text{m}$ accounted for a major portion of the total number of measured droplets.

Considering the cumulative mass distribution,

however, the small droplet group accounted for only about 1% of the total mass. The D_{10} was $61.5 \mu\text{m}$ and the D_{32} (Sauter Mean Diameter) was $89.3 \mu\text{m}$. The difference between D_{10} and D_{32} was comparatively large. It is apparent that the difference will be increased with the portion of small droplets.

Figure 5 shows correlation of axial velocity and droplet diameter at several locations. We could observe that a two-peak histogram of droplet sizes was distributed in almost the whole spray field. The portion of small droplet group was maximum at the axial locations of $r = 2.5$ mm and decreased with the axial direction. We consider that the two-peak size

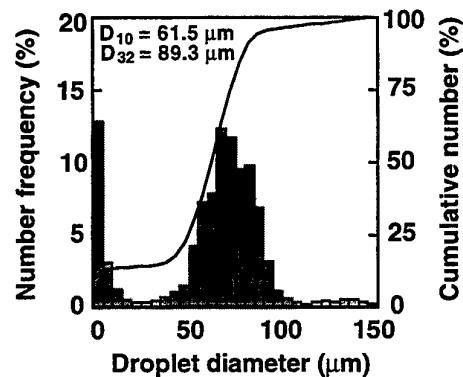


Fig. 4 Typical droplet size distribution.

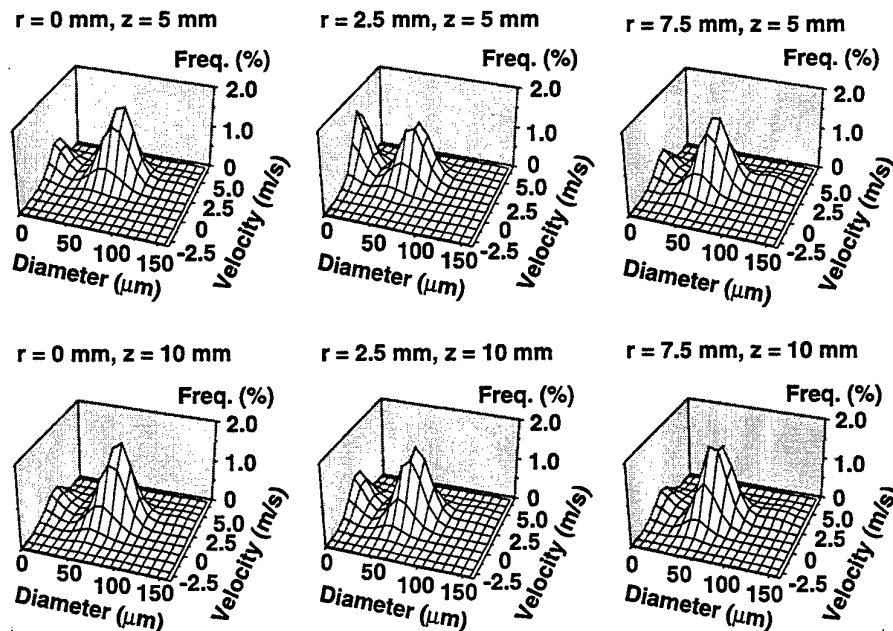


Fig. 5 Correlation of axial velocity and droplet diameter at selected locations.

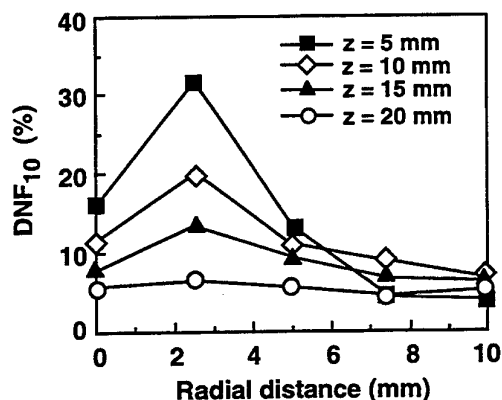


Fig. 6 Radial profile of small size droplets at axial locations.

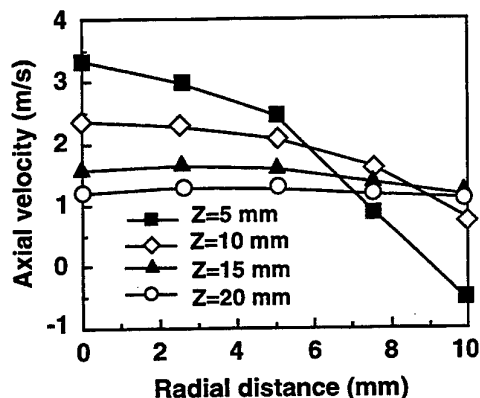


Fig. 7 Profile of axial mean velocity.

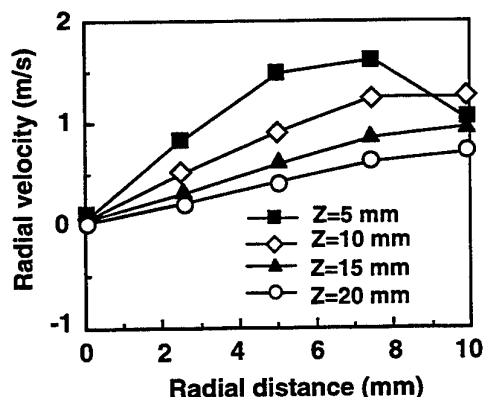


Fig. 8 Profile of radial mean velocity.

distribution is characteristically originated from a fissionable disruption of an electrostatic charged droplet.

It was already observed that the shape of droplet size distributions was dependent on the flow-rate of liquid [Kim (1998)]. Then, with the flow-rate of liquid, the size distribution got to be transformed from one-peak histogram to two-peak histogram. For this reason, it is necessary to verify the characteristics of the electrostatic spray with a two-peak size distribution.

The portion of small droplets under $10\text{ }\mu\text{m}$ to total droplets (DNF_{10}) as a function of the radial distance was examined as shown in Fig. 6. As discussed, DNF_{10} had a maximum value more distinctively at $r = 2.5\text{ mm}$ away from the centerline, and was decreased with the axial distance. We consider that small droplets were attracted more strongly by the grounding ring. Then, we investigated the axial and radial velocity, and the behavior of each group of size-classified droplets.

3.3 Mean Velocity and Behavior of Droplets

Figures 7 and 8 show the axial and radial velocity as a function of the radial distance, respectively. Axial velocity was decreased with axial and radial distances decreased except for a recirculation region. From the intervals between velocities, we can know that the deceleration was also decreased. We can observe that there was a recirculating flow after $r = 7.5\text{ mm}$ at $z = 5\text{ mm}$. The radial velocity was monotonically decreased with the axial distance, but increased with the radial distance. It is considered that the axial dispersion of droplets was decelerated by a drag force and electrostatic force to axial direction. However, owing to the ground ring, the radial velocity was accelerated to the radial direction.

The axial and radial velocities of each group of size-classified droplets were examined as shown in Figs. 9 and 10, respectively. The droplets were classified by droplet size, and then the validation of each size interval was considered by the droplet number frequency. For the groups of large droplets over $30\text{ }\mu\text{m}$, the larger droplets were faster. However, we can observe that the droplet group under $30\text{ }\mu\text{m}$ differed from the other groups.

This tendency was definitely confirmed by the droplet size-velocity correlation as shown in Figs. 11 and 12. Firstly, we can observe three islands of droplets in each figure of size-velocity correlation. In Fig. 11, droplets over $30\text{ }\mu\text{m}$ had a tendency that the larger droplets was increased with the droplet size. However, the very small droplets under $20\text{ }\mu\text{m}$ behaved with different tendency. The velocity of very

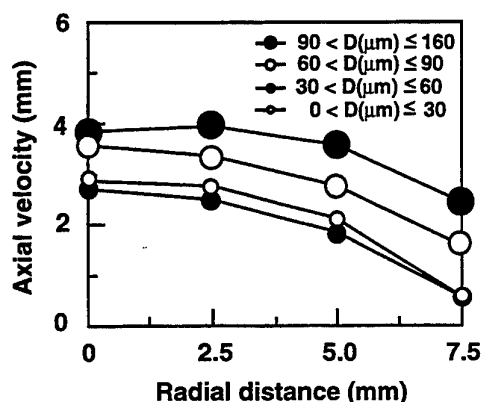


Fig. 9 Axial velocity of size-classified droplets with radial distance at $z = 5$ mm.

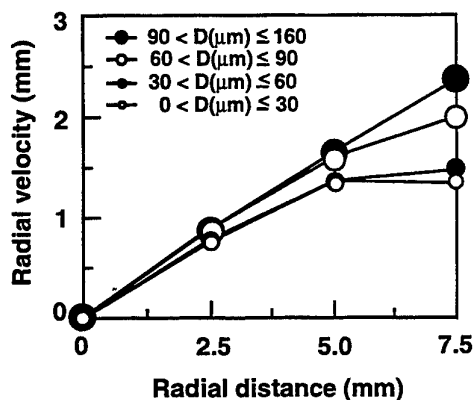


Fig. 10 Radial velocity of size-classified droplets with radial distance at $z = 5$ mm.

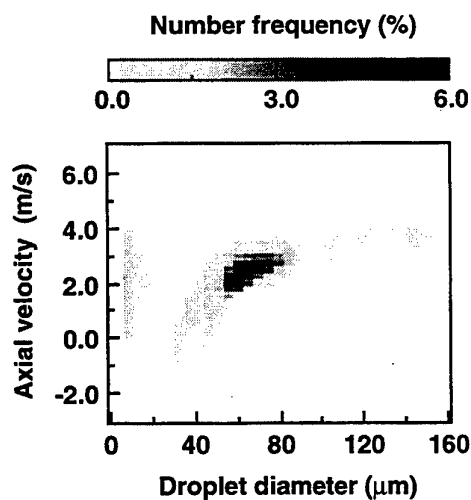


Fig. 11 Correlation of axial velocity and size at $r = 5$ mm, $z = 5$ mm.

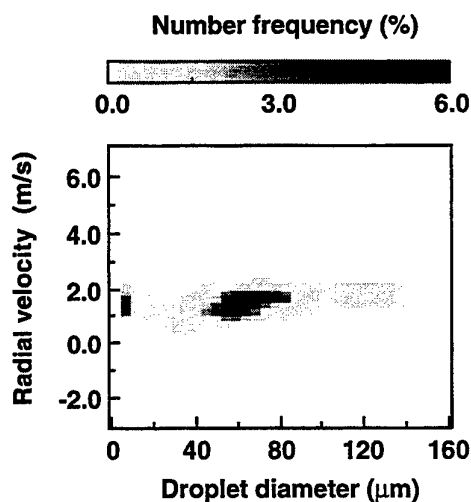


Fig. 12 Correlation of radial velocity and size at $r = 5$ mm, $z = 5$ mm.

small droplets was near to the large droplets. We consider that the very small droplets were more strongly accelerated in breaking up from the large droplets by an electrostatic fission.

4. CONCLUSIONS

The findings from this experimental determination of the structural characteristics of an electrostatic spray can be summarized as follows:

The droplet sizes were distributed with two peaks in the whole spray field and affected the spray structure. At a finite distance near to the centerline of spray axis, the number density was maximum, mean diameter was minimum, and the portion of small droplets was distinctively maximum. The droplets dispersed outward and the axial and radial velocities were decelerated with the axial distance. The droplets, however, dispersed differently with droplet size. This behavior of droplets was reflected in the profiles of number density, mean diameter and mean velocity.

REFERENCES

Chen, G. & Gomez, A., 1992, Counterflow Diffusion Flames of Quasi-Monodisperse Electrostatic Sprays, *Proc. 24th Symp. (Int.) on Comb.*, The Combustion Institute, pp.1531.

Gomez, A. & Tang, K., 1994, Charge and Fission of Droplets in Electrostatic Sprays, *Phys.*

Fluids, Vol. 6, No.1, pp.404.

Hayati, I., Bailey, A. I. & Tadros, TH. F., 1987, Investigations into the Mechanisms of Electrohydrodynamic Spraying of Liquids, Journal of Colloid and Interface Science, Vol. 117, No.1, pp.205.

Kim, J.H., Ikeda, Y. & Nakajima, T., 1998, Dependence of Atomization on Charging Voltage in Electrostatic Sprays, Proc. 5th Int. Cong. on Optical Particle Sizing, Minnesota, in printing.

Lord Rayleigh, 1882, On the equilibrium of liquid conducting masses charged with electricity, Philos. Mag., Vol. 14, pp.184.

Mutoh, M., Kaieda, S. & Kamimura, K., 1979, Convergence and Disintegration of Liquid Jets Induced by an Electrostatic Field, J. Appl. Phys., Vol. 50, No. 5, pp.3174.

Naqwi, A.A. & F. Durst, 1991, Light scattering applid to LDA and PDA measurements. Part 1: Theory and numerical treatments. Part. Part. Syst. Charact., 8 : pp245.

Shrimpton, J.S., Yule, A.J. & Watkins, A.P., 1996, Spray Visualization and Phase Doppler Anemometry Measurements of Charged Hydrocarbon Sprays, Proc. 8th Int. Symp. of Laser Tech. to Fluid Mech., Lisbon, pp.20.2.1.

Thong, K.C. & Weinberg, F.J., 1971, Electrical Control of the Combustion of Solid and Liquid Particulate Suspensions, Proc. Roy. Soc. Lond., A324, pp.201.

SESSION 22

SEPARATED FLOWS

REYNOLDS NUMBER EFFECT AND LAMINARISATION OF TURBULENT FLOW IN AXISYMMETRIC SUDDEN-CONTRACTION PIPE FLOW

K. T. Ajayi and F. Durst

Lehrstuhl für Strömungsmechanik
Universität Erlangen-Nürnberg Cauerstrasse 4, D-91058 Erlangen, GERMANY

ABSTRACT

This paper presents the study of Reynolds number effect and laminarisation of turbulent flow in a pipe with sudden contraction having a fixed upstream-to-downstream area ratio of four. The influence of Reynolds number on the dynamics of flow with this type of area discontinuity were investigated for Reynolds numbers in the range 2000 - 12000 based on upstream flow conditions. Information on the laminarisation effect and the subsequent positional influence on the resulting overshoot due to flow acceleration are also reported.

1. INTRODUCTION

A wide variety of applications in engineering practice involve the flow of fluid through pipes with changes in cross-sectional area, which could either be expansion or contraction, gradual or sudden. Such discontinuities give rise to a complicated flow pattern that is characterized by flow separation, recirculation, and reattachment. In axisymmetric sudden contraction, which is the focus of this study, the performance of various equipment, such as, mixing vessels, combustion chambers, hydraulic flow systems and heat exchangers, is dependent on good understanding of the flow field, since as a result of flow separation there exist significant changes in pressure loss, erosion rates, as well as, heat and mass transfer rates. Because of the complexity of such flow, the theoretical analysis is virtually impossible, hence paving the way for experimental and numerical analysis.

A schematic representation of the problem definition for this geometry is shown in Fig. 1. As the flow enters the contraction it experiences a bulk velocity increase, which results into a static pressure drop. The contraction to the vena contracta is

accompanied with inlet losses arising from velocity distribution changes due to local flow acceleration, while subsequent expansion from the vena contracta promotes instability and turbulence giving rise to expansion related losses. Thus, the flow past a sudden contraction experiences favourable and adverse pressure gradients with corresponding velocity overshoot, which result in energy losses, other than those due to friction.

Although a substantial amount of effort had been made in recent times to study the flow characteristics in the vicinity of sudden contraction experimentally (Durst et al., 1989) and/or numerically (Jones and Launder, 1972; Patankar and Spalding, 1967), nevertheless the nature and characteristics of the flow have not been fully explored, owing to the limitations of either measuring instruments or computers. In particular, there do not yet exist LDA measurements that cover the near-step proximity in the vicinity of a sudden contraction for turbulent flow, hence there still persist the inability to locate correctly the velocity overshoot and the subsequent effect on the nature of flow in this region and downstream of it. Lack of reliable measurements can be attributed to the difficulty involved in matching the refractive index of the containment wall with the working fluid. A further difficulty occurs as a result of the inability to resolve spatially the recirculating flow regions in the concave and convex corners in the plane of contraction owing to the large relative size of the measuring control volume. Moreso, extensive computational resources are needed, and even then much uncertainty exists in the ability of the present turbulences models to capture the phenomena that may occur in a sudden contraction due to local flow acceleration. Improving predictive tools require extensive experimental data, and this need has motivated the present investigation. In the present paper, highly resolved velocity measurements for turbulent flow past a circular sudden contraction are

presented. Furthermore, results from computations of the flow using a finite-volume scheme incorporating a $k - \epsilon$ turbulence model are compared with the experimental data.

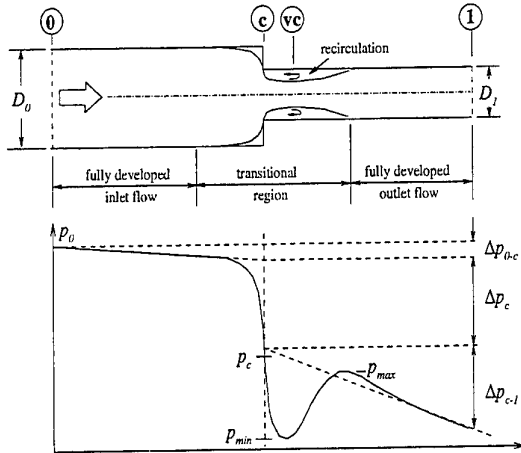


Fig. 1: Schematic representation of flow characteristics in the vicinity of sudden contraction

2. EXPERIMENTAL AND NUMERICAL METHODS

A highly resolved velocity measurements and numerical computation for a fully developed flow in a pipe with axisymmetric sudden contraction with contraction area ratio $n_c = 4$ were performed for a Reynolds number range of 2000 to 12000.

2.1 Velocity Measurements

A specially designed one-component, forward scatter laser-Doppler system consisting of 17mW helium-neon laser, double Bragg cells, beam splitter, transmitting lenses, receiving lenses and avalanche photodiode showed in Fig. 2, was used to measure the velocity. The test section which was centrally mounted in a rectangular box to permit laser-Doppler measurements, consisted of two Duran glass pipes with internal diameters of 50 mm and 25 mm, thus resulting in a fixed contraction area ratio of $n_c = 4$ and a fixed forward step height of 12.5 mm. Necessary provision was made to eliminate the air bubbles trapped within the sudden-contraction recirculation region during the start-up operation of

the facility. In order to ensure fully developed flow upstream of the contraction after initial tripping, a total length of about 80 diameters of pipe was used upstream of contraction. The working fluid consisted of two mixed diesel oils of slightly different refractive indices matched with the Duran glass at suitable working temperature. The temperature of the fluid, which was monitored by an RT-100 resistance thermometer located just downstream of the test section and directly after the heater, was controlled by heating and cooling elements installed in the downstream settling chamber of the test rig. A secondary pump was used to bypass some working fluid into the region between the pipe and the enclosing rectangular box, thus eliminating any thermal effects on the refractive index. The rectangular box surrounding the pipe was made from Duran glass.

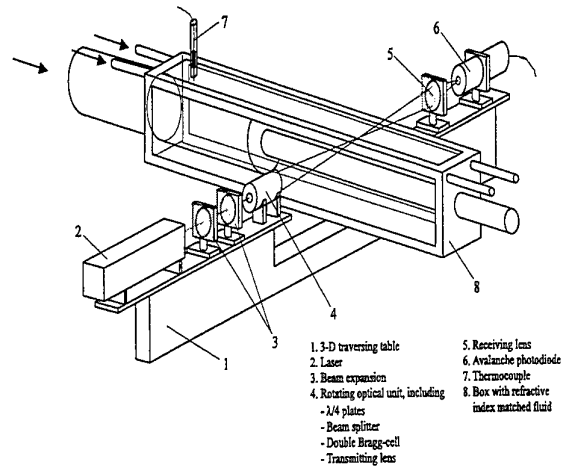


Fig. 2: Schematic layout of LDA system.

The arrangement of the LDA system with a beam expansion of 2.5 yielded an effective measuring control volume of $72 \mu\text{m}$ in diameter and $250 \mu\text{m}$ in length. The Bragg cell driver was set up to provide a frequency shift of 200 kHz. Scattered light was collected by the receiving optics and directed onto a $100 \mu\text{m}$ diameter pinhole that was placed in front of an avalanche photo-diode. The signal from this diode was bandpass filtered prior to being processed by a TSI Model 1990 counter, which operated in the total burst mode with a minimum of 16 cycles/burst. Sufficient particles were present in the oil to yield acceptable data rates (50-100 Hz close to the wall; 300-500 Hz away from the wall). For every measurement point 10,000 to 30,000 samples were obtained with a sampling rate of 10 Hz to 30 Hz, the

former close to the wall. These sampling conditions ensured statistically reliable measurements even for the fourth-order moments. The statistical uncertainty in the mean velocity was estimated to be less than 1%.

2.2 Numerics

A finite volume approach was used to solve the two-dimensional, incompressible, steady Reynolds-averaged Navier-Stokes equations. In general coordinates, the equations are:

$$\frac{\partial \bar{U}_i}{\partial x_i} = 0; \quad i = 1, 2 \quad (1)$$

$$\rho \bar{U}_i \frac{\partial \bar{U}_i}{\partial x_j} = \frac{\partial \bar{p}}{\partial x_j} + \frac{\partial}{\partial x_j} \left(\mu \frac{\partial \bar{U}_i}{\partial x_j} - \rho \overline{u_i u_j} \right); \quad i, j = 1, 2 \quad (2)$$

To achieve closure, several turbulence models for the Reynolds stress terms, $\overline{\rho u_i u_j}$, are available, such as, the mixing-length or zero equation model, the one-differential-equation model, the two-differential-equation model and the more complex Reynolds stress models. The two-equation $k - \varepsilon$ model was considered in the present effort because of its simplicity, hence low cost of computing. The Reynolds stress terms are modelled using the turbulent viscosity (μ_t) and turbulent kinetic energy (k)

$$-\overline{\rho u_i u_j} = 2\mu_t \frac{\partial \bar{U}_i}{\partial x_j} - \frac{2}{3} \rho \varepsilon \delta_{ij} \quad (3)$$

where $\mu_t = \rho C_\mu \frac{k^2}{\varepsilon}$ and $k = \frac{1}{2} \overline{u_i u_i}$. The transport form of the turbulence kinetic energy and its dissipation rate (ε) are

$$\frac{Dk}{Dt} = \frac{1}{\rho} \frac{\partial}{\partial x_j} \left(\frac{\mu_t}{\sigma_k} \frac{\partial k}{\partial x_j} \right) + \frac{\mu_t}{\rho} \left(\frac{\partial \bar{U}_i}{\partial x_j} + \frac{\partial \bar{U}_j}{\partial x_i} \right) \frac{\partial \bar{U}_i}{\partial x_j} - \varepsilon \quad (4)$$

$$\frac{D\varepsilon}{Dt} = \frac{1}{\rho} \frac{\partial}{\partial x_j} \left(\frac{\mu_t}{\sigma_\varepsilon} \frac{\partial \varepsilon}{\partial x_j} \right) + \frac{C_1 \mu_t}{\rho} \frac{\varepsilon}{k} \left(\frac{\partial \bar{U}_i}{\partial x_j} + \frac{\partial \bar{U}_j}{\partial x_i} \right) \frac{\partial \bar{U}_i}{\partial x_j} - C_2 \frac{\varepsilon^2}{k} \quad (5)$$

with values for the constants used given in Table 1.

Table 1: Applied constants in $k - \varepsilon$ turbulence model

C_μ	C_1	C_2	σ_k	σ_ε
0.09	1.44	1.92	1.0	1.3

The generalized transport equations of the aforementioned governing equations and a detailed description of the discretization and implementation, together with a multigrid method for accelerating the convergence to the steady state condition, was reported by Ajayi (1997). The solution of the coupled set of equations was based on the SIMPLE algorithm for collocated grids. A detailed description was given by Peric et al. (1988). Boundary conditions were imposed along the wall (no-slip), the axis of symmetry, and at the inlet and outlet of the test section. At the inlet to the pipe a uniform profile was assumed, with the velocity at each point along the section equal to the bulk velocity. This profile approximated the inlet condition realised in the experimental investigation. At the outlet boundary a zero gradient was assumed for all dependent variables. The computation was first carried out on a coarse grid of 23482 control volumes and refined to a grid of 93928 control volumes. An almost infinite time step was considered for stationary calculations. A preliminary check on the validity of the numerical procedure was performed by computing and comparing the normalised centerline velocity with DNS and experimental data for fully developed pipe flow. The results of Table 2 indicate good agreement. The decay of U_{cl}/U_b with increasing Re is in agreement with the expected behavior (see Papadopoulos et al., 1997).

Table 2: Comparison of measured and predicted normalized centerline velocity upstream of the contraction with DNS and experimental data.

Case	Method	ReD	Ucl/U _b
Eggels et al. (1994)	DNS	5300	1.31
	PIV	5400	1.30
	LDA	5450	1.32
	HWA	5600	1.31
Present	LDA	5300	1.30
	LDA	7500	1.28
	LDA	10000	1.26
	k - ε	5300	1.28
	k - ε	7500	1.27
	k - ε	10000	1.25

3. RESULTS

In this study, some flow properties measured for a Reynolds-number range from 2000 to 12000 for a u-velocity component are, the mean velocity (\bar{U}), central moment (u'), turbulence intensity ($\frac{u'}{\bar{U}}$) and two statistical parameters often used in the description of turbulent flow, namely skewness (S) and flatness (F) factors. These properties were analysed respectively as follows: $\bar{U} = \bar{U}_{\theta=0}$; $u' = \sqrt{\overline{u'^2}}$;

$$\frac{u'}{\bar{U}} = \frac{\sqrt{\overline{u'^2}}}{\bar{U}_{\theta=0}}; \quad S(u) = \frac{\overline{u'^3}}{(\overline{u'^2})^{3/2}}; \quad F(u) = \frac{\overline{u'^4}}{(\overline{u'^2})^2};$$

where $\overline{u'^2} = \overline{u'^2}_{\theta=0}$, $\overline{u'^3} = \overline{u'^3}_{\theta=0}$ and $\overline{u'^4} = \overline{u'^4}_{\theta=0}$.

3.1 Lower-Order Turbulence Statistics

Distribution of the rms values of the turbulence velocity fluctuations at the centerline of the flow, normalised by the centerline mean velocity along the centerline position are shown in Fig. 3. The strong effect the sudden contraction has on the flow at the position $X/H \approx -4$ is obvious. Before the decrease, the turbulence intensity shows the well known distribution for fully developed pipe flow, in which the local turbulence intensity at the centerline decreases with increasing Reynolds number. This trend is also apparent at the location far downstream of contraction.

It is interesting that there is nearly no Reynolds number dependence in the region where the turbulence intensity decreases due to the flow acceleration occurring in front of the sudden contraction. In the

redevelopment region after the contraction, a Reynolds number dependence on the turbulence intensity is present, yielding higher turbulence intensities for the higher Reynolds number, hence requiring longer streamwise length for attaining full recovery from the plane of contraction.

Detailed investigations of Reynolds number effect based on positional variation for both upstream and downstream of contraction are presented in Figs. 4a and 4b respectively. Upstream of contraction, when X/H is increased from the step, u'/U correspondingly increases for any given Reynolds number. At $X/H \approx -5$ the flow is already fully developed, as shown by curve of u'/U at $X/H \approx -20$ coinciding with the selected DNS data for pipe and channel flows. Also very obvious in Figure 4a is the laminarisation effect close to the step, with $u'/U \approx 0.012$ at $X/H \approx -0.3$. Irrespective of any position upstream of contraction, turbulence intensity is a weak function of Reynolds number, becoming virtually independent of Reynolds number in regions close to the step. On the other hand downstream of contraction, Figure 4b indicates that the turbulence intensity is completely independent of Reynolds number at $X/H \approx +0.4$.

Contrary to upstream condition, increasing turbulence intensity results from increasing Reynolds number at higher stations up to $X/H \approx +24$ resulting in fairly constant positive gradient. At about $X/H \approx +43$, the gradient is found to reverse to negative.

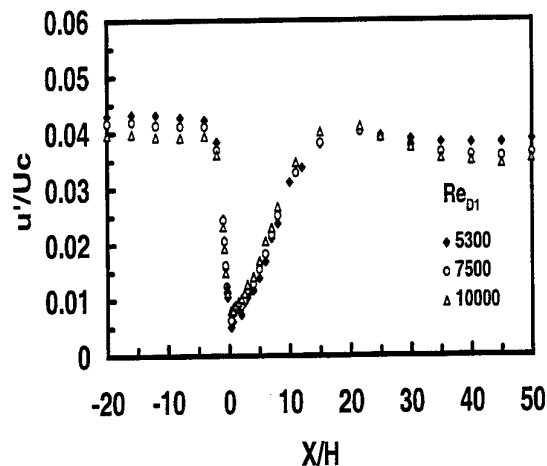
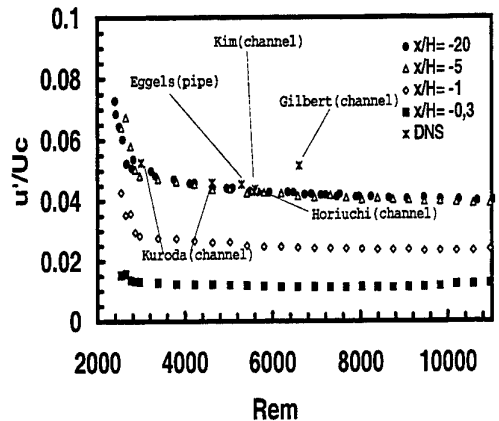
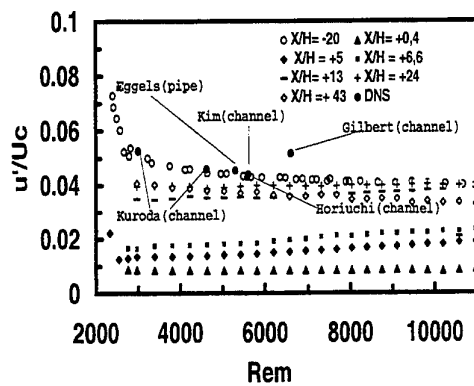


Fig. 3: Streamwise centerline turbulence intensity



(a)



(b)

Fig. 4: Dependence of turbulence intensity on Reynolds number (a) upstream of contraction (b) downstream of contraction.

The mean statistics of turbulence shown in Fig. 5 indicate the position of velocity overshoot, positional influence on this overshoot and the laminarisation effect within the separation region upstream and downstream of contraction. The influence of the step on the u -velocity profile upstream and downstream of contraction is shown in the selected profiles in Fig. 5a. As the flow approaches the step with decreasing X/H , severe acceleration is noted in the central core of the flow upstream of the contraction. The closer the flow is to the step, the more severe the acceleration, resulting in a reverse transition as pointed out previously. Although the influence of the step on the oncoming flow is severe, nevertheless, no velocity overshoot is noted at any section upstream of the contraction. On the other hand, at $X/H \approx +0.32$ downstream of the contraction, the velocity profile is

seen to have severe overshoot, resulting in a convex flow profile in the direction of flow. This velocity overshoot decays with increasing centerline velocity up to $X/H \approx 0.96$, where the core of the streamwise velocity profile is approximately flat. At $X/H \approx 1.12$, the profile resumes a concave curvature in the direction of flow. From $X/H \approx 1.12$ to 1.6 the profiles reduces in the streamwise direction with subsequent reduction in the heavily retarded region of flow.

The representation of turbulence intensity in Fig. 5b indicates very interesting features, which are regions of laminar, turbulent and secondary flows. At any cross-section normal to the streamwise direction and close to the step upstream and downstream of the contraction, there always exists turbulent flow between the core of the flow, which is laminar, and the wall of the pipe. Therefore, the laminarisation effect is limited only to the central core of the flow in the streamwise direction. Regions of secondary flow at the concave corner between the upstream and downstream pipes are also very noticeable, together with that present at the convex corner immediately downstream of the contraction. Fig. 5c indicates at $X \approx -20\text{mm}$ ($X/H \approx -1.6$) conventional profiles of u' having a maximum value close to the pipe wall. The effect of contraction is very obvious, with decreasing X/H in the direction of flow resulting in higher values of u' downstream of the contraction.

3.2 Higher-Order Turbulence Statistics

In Figures 6 and 7 the behaviour of the higher order moments of the streamwise centerline turbulence velocity fluctuations are presented. The skewness shows the well known negative values of approximately -0.4 on the axis of turbulent pipe flows, for all Reynolds numbers, and increases just before the plane of sudden contraction. It reaches a maximum at about $X/H \approx -4$ before decreasing to a minimum value at about $X/H \approx -9$ and thereafter redevelops to a value approximately the same as that of the incoming flow. Similarly, strong distortions occur close to the sudden contraction for the flatness factor. It has a centerline value just above 3 for the oncoming flow and results in strong distortions just after the plane of contraction. The dependance of the third-order statistics on Reynolds number upstream and downstream of contraction presented in Figures 8a and 8b confirms the laminarisation effect of the flow close to the step. This effect becomes more pronounced with the fourth-order moment presented in Figures 9a and 9b.

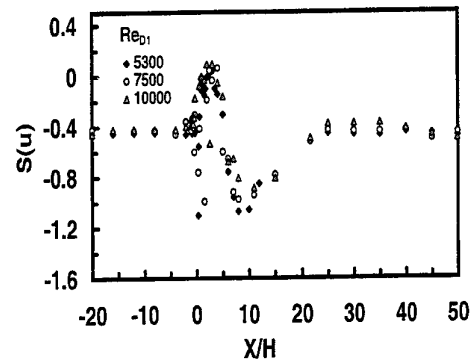
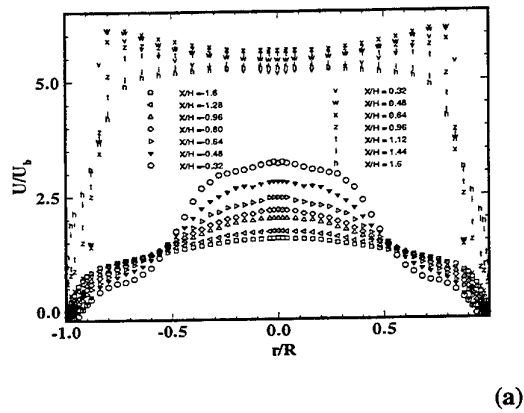


Figure 6: Streamwise centerline skewness factor

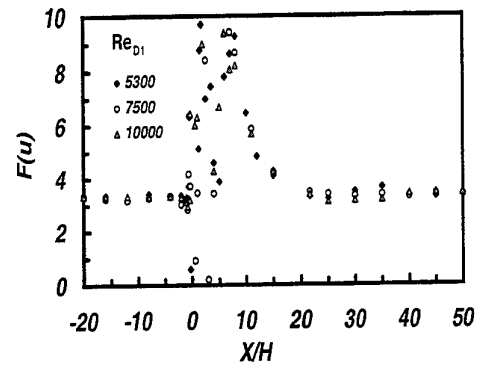
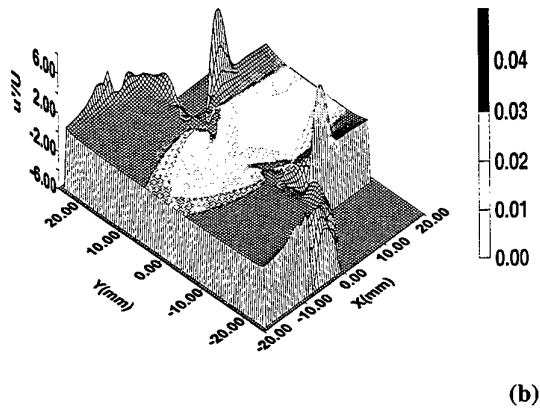


Figure 7: Streamwise centerline flatness factor

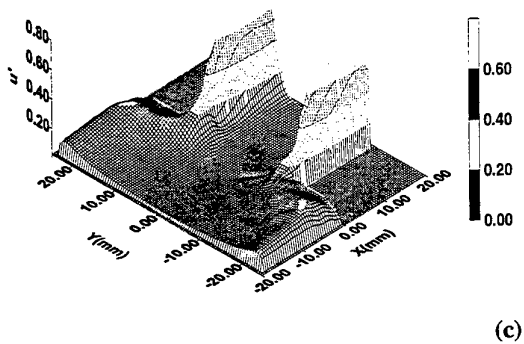
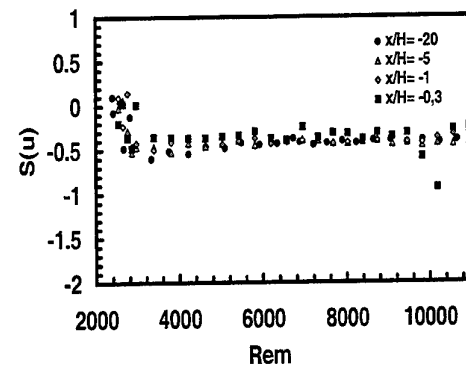


Fig. 5: Profile measurements of u-velocity component in the vicinity of sudden contraction (a) mean values (b) turbulence intensity © rms values



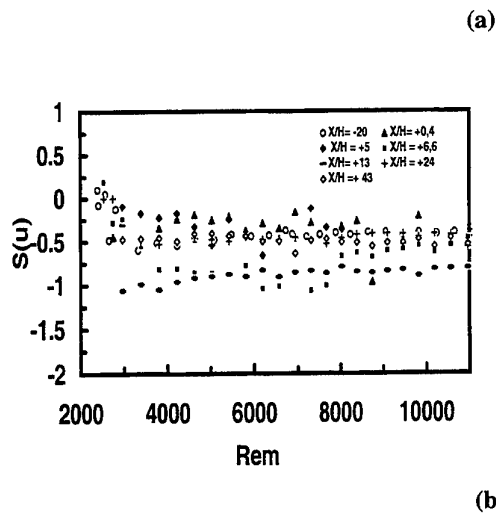


Fig. 8: Dependence of skewness factor on Reynolds number (a) upstream of contraction (b) downstream of contraction.

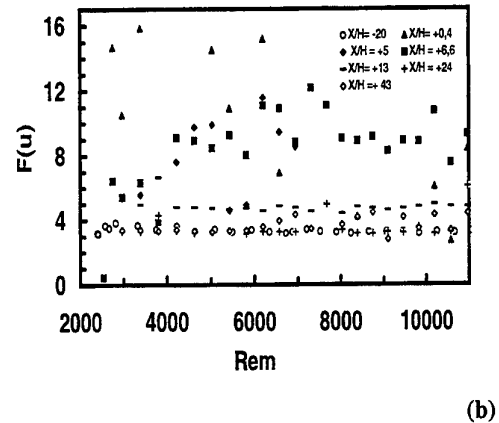
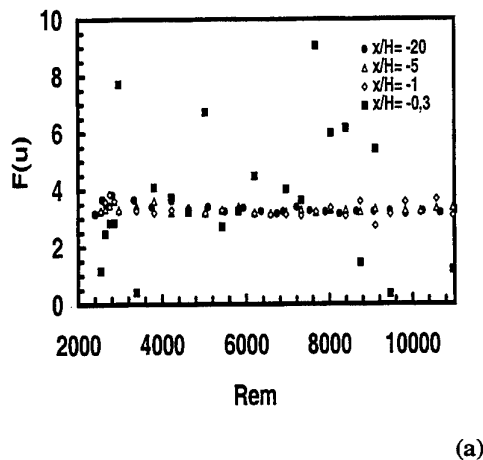


Fig. 9: Dependence of flatness factor on Reynolds number (a) upstream of contraction (b) downstream of contraction

3.3 Comparison of Experimental and Numerical Results

Figure 10a clearly shows the good agreement between the experimental and numerical velocity profiles upstream of the contraction without the presence of any overshoot, even up to $X/H \approx -0.32$, hence eliminating any doubt about the non-existence of velocity overshoot upstream of the contraction. On the other hand, as indicated in Fig. 10b, an acceptable level of agreement exists from upstream of the contraction to $X/H \approx 1$ and from $X/H \approx 10$ to the limit of the centerline investigation downstream of the contraction. The discrepancies between the experimental and numerical results are obvious in the region $1 < X/H < 10$, where the experimental centerline velocity decays more rapidly than the numerical to the minimum value at $X/H \approx 3$ and then increases to coincide with the numerical profile at $X/H \approx 10$ for the three Reynolds numbers considered.

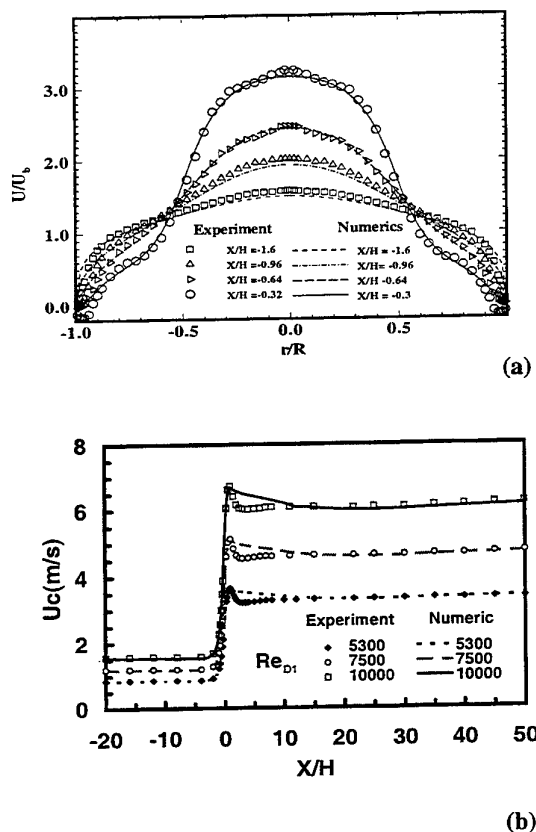


Fig. 10: Comparison of experimental and numerical data for (a) mean velocity profiles upstream of sudden contraction (b) streamwise centerline velocities.

4 CONCLUSION

The influence of Reynolds number on the nature of flow in the vicinity of sudden contraction indicated independence of turbulence intensity on Reynolds number immediately before and after the plane of contraction. Laminarisation was seen to persist for the range of Reynolds numbers considered in this region. As the distance X/H increases from the step upstream and downstream of contraction for any given Reynolds number, the value of the turbulence intensity increases, reaching an asymptotic state already at $X/H \approx -5$ upstream of the contraction, but requiring a longer recovering length downstream of the contraction. The comparison between the experimental and numerical results showed an acceptable level of agreement. The area of discrepancies between these results may be associated with the assumptions of the turbulence model and the refinement of the grid immediately downstream of the

plane of contraction. Therefore, efforts should be made to resolve these discrepancies by accounting for low Reynolds number effects on the turbulence model and further refining the grid downstream of the contraction.

REFERENCES

- Ajayi, K.T. 1997, Laminare und Turbulente Strömungen in Rohrleitungen mit plötzlichen Verengungen, Ph.D thesis, Universität Erlangen-Nürnberg, Germany.
- Durst, F., Founti, M., Wang, A.B. 1989, Experimental Investigation of the Flow through an Axisymmetric Contraction, *Proceedings of Turbulent Shear Flows 6*, Vol. 18.
- Eggels, J. G. M., Unger, F., Weiss, M. H., Westerweel, J., Adrian, R. J., Friedrich, R., and Nieuwstadt, F. T. M. 1994, Fully Developed Turbulent Pipe Flow: A Comparison between Direct Numerical Simulation and Experiment, *Journal of Fluid Mechanics*, Vol. 268, pp 175-209.
- Jones, W. P. and Launder, B. E. 1972, The Prediction of Laminarisation with a Two-Equation Model of Turbulence, *Int J. Heat Mass Transfer*, Vol. 15, pp 301-313.
- Papadopoulos, G., Lekakis, I. and Durst, F. 1997, Reynolds Number Asymptotic Covariance for Turbulent Pipe Flow past a Sudden Expansion, *ASME FEDSM97-3323*, June.
- Patankar, S. V. and Spalding, D. B. 1967, Heat and mass transfer in boundary layers, Morgan-Grampian Press, London.
- Peric, M. Kessler, R. and Sheuerer, G. 1988, Comparison of Finite Volume Methods with Staggered and Colocated Grids, *Computers and Fluids*, Vol. 16, pp 389-403.

A Flow Structure at Reattachment Region of a Two-Dimensional Backward -Facing Step

Noriyuki Furuichi^{*1}, Tadashi Hachiga^{*2}, Koichi Hishida^{*3}, and Masaya Kumada^{*1}

^{*1} Department of Mechanical and Systems Engineering, Gifu University, Yanagido 1-1, Gifu 501-1193, Japan

^{*2} Department of Automotive Engineering Takayama College, Shiobayashi 1155, Takayama, Gifu 506-8577, Japan

^{*3} Department of System Design Engineering, Keio University, Hiyoshi 3-14-1, Kohoku-ku, Yokohama 223-8522, Japan

ABSTRACT

A temporal data of instantaneous velocity profile of a two-dimensional backward-facing step flow was measured by multi-point LDV, and was discussed with a special focus on the details of the motion of the separated shear layer and the phenomena of reattachment. As a result, the instantaneous velocity profile was found to be very different from the time-averaged velocity profile. The dividing stream line oscillates because of vortex concentration in the separated shear layer. The phenomenon of reattachment was seen to follow two patterns, one when the separated shear layer reattaches, the other when the separated shear vortex reattaches.

1. INTRODUCTION

Experiments have been performed to study the flow structure around the reattachment region behind a two-dimensional backward-facing step with a turbulent shear layer (Eaton et al. 1981 and Armly et al. 1983). This flow field exhibits a three-dimensional, unsteady structure involving oscillation of the reattachment point and the large scale vortex (Eaton et al. 1980). Very few other studies on this configuration have been performed with the aim of investigating the unsteady structure of the flow field. Hijikata et al. (1991) visualized the pressure field in a backward-facing step using a holographic method and velocity-pressure cross-correlation. They clarified that the motion of the high cross-correlation region corresponds to the motion of the pressure fluctuation lumps obtained in the holographic visualization. By direct numerical simulation, Hungel et al. (1997) have shown that the fluctuation in the reattachment location was caused by a large-scale roll-up of the shear layer extending to the reattachment region, which is composed of many small counter-rotating vortices. In terms of spatial measurement, Kasagi and Matsunaga (1995)

measured velocity vector using a 3-D PTV, then calculated detailed turbulence statistics and an energy budget.

As mentioned above, many studies have shown that the three-dimensional flow structure caused by the transformation of the shear layer vortex governs the fluid dynamics near the reattachment region. However, none of these studies provided quantitative experimental data on the three-dimensional flow structure. This lack of quantitative data was a result of the absence of a method of measurement for spatial and temporal velocity distributions over an unsteady, three-dimensional flow field. Measuring simultaneous and spatial velocity profiles across the dividing stream line in the separated shear layer is especially important for clarifying the process of vortex concentration, shedding of large-scale vortices and vortex deformation near the reattachment point. Up to now, there exist several methods for measuring multi-point velocity, for example, ultrasonic velocity profile method (Takeda 1991), the particle image velocimeter (Sakakibara et al. 1993), and others. But these methods have limitation in terms of sampling interval and spatial measurement. We developed the advanced multi-point LDV using a 1-bit FFT approach that had been described in a previous paper (Hachiga et al. 1998), and were able to improve the measurement of reverse flow in the present study. We accumulated the instantaneous velocity profile by setting up this LDV system spatially in the flow field and considering the flow structure of the 2-D backward-facing step. We paid particular attention to clarifying the fluid flow motion of the separated shear layer and the phenomenon of reattachment.

2. EXPERIMENTAL APPARATUS

2.1 Backward-Facing Step

The flow field and coordinate system are shown in Fig.1. The closed-loop water channel used in this experiment has a working section of 240×60mm in cross-sectional area

and 2300mm in length. The backward-facing step (with a step height h of 20mm) was formed below the floor plate at a point 250mm downstream from the construction nozzle exit. The expansion ratio is $ER=1.5$, and the aspect ratio is $AR=12$. The main flow velocity is fixed at $U_c=0.25\text{m/s}$ in all experiments (Reynolds number of $Re_h=5000$). The turbulence intensity of the main flow is $Tu=0.6\%$. The distribution of u -component mean velocity upstream of the step is in agreement with Blasius theory. The boundary thickness upstream of the step is about 4.6mm.

2.2 LDV system

A velocity profile was measured by an advanced multi-point LDV system which was reported in a previous paper (Hachiga et al., 1998). For measuring the backward-facing step flow, this LDV has been improved on two points mentioned below. One is that this LDV can measure reverse flow by double Bragg cell system and another one is that can

be measure simultaneous 24-point data.

The optical system of this LDV is shown in Fig.2. This LDV is made very compact by using semiconductor laser with a maximum power of 40mW and a wavelength of 685nm, and optical fiber unit with 96 plastic fibers with a diameter of ϕ 0.25mm. Two Bragg cells are used to introduced frequency shifts of 80MHz and 79.9MHz respectively. Therefore Doppler burst signal is shifted 0.1MHz, and it is possible that reverse flow is measured. Two Bragg cells role like a beam splitter by using two shifted beam. After two shifted beam are detached by two mirrors, these beam are deformed to a fan-like shape by rod lens. Non-shifted beam is cut before this rod lens. The process after two shifted laser beam of fan-like shape are made into rectangular-like light sheet by cylindrical lens is similar to the process in the previous paper.

The hardware system block diagram of an advanced multi-point LDV used in the present study is shown schematically in Fig.4. The hardware system was modified that 24-point scattered light signal could be measure simultaneous as mentioned above. A scattered light signal is converted into an individual Doppler burst signal by Si-APD. This signal is digitized to one bit using a comparator. The raw one-bit data sampling frequency is 250KHz, and the velocity data sampling interval is about 1.024ms with frequency analysis by FFT of 256 points. Therefore, data sampling rate is about 976/s. The data processing is similar to that performed in the previous paper (Hachiga et al., 1998). In present study a lack of data is interpolated by adjacent measuring point in spatial. The rate of capture for temporal velocity data in all experimental data is over 70%. The spatial resolution of each point set up in the x - z plate is $0.22 \times 1.40\text{mm}$ from cross angle of the laser light sheet, and of those in the y plate it is ϕ 0.24mm, which corresponds to the core diameter of the receiving optical fiber. In this experiment, the optical fiber for measurement is selected 24-point out of 96-point, and the distance between adjacent

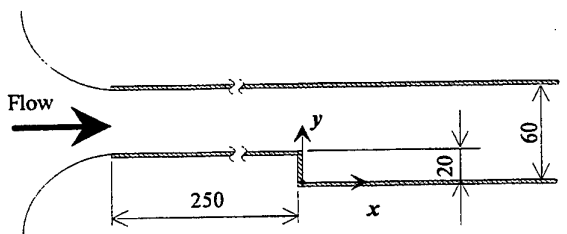


Fig. 1 Experimental apparatus

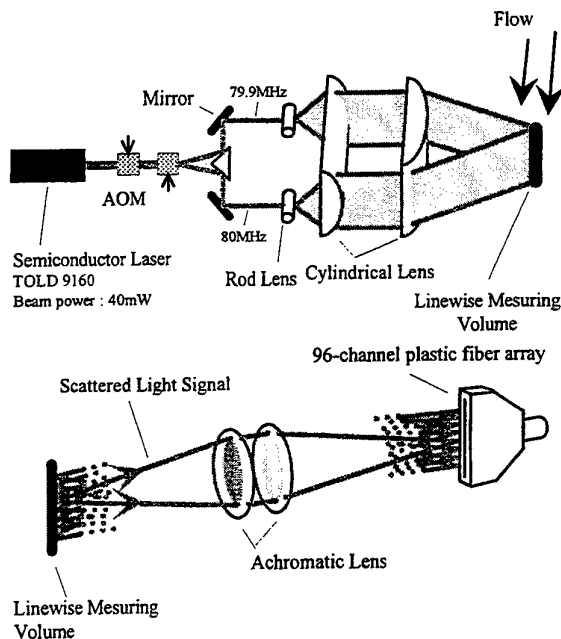


Fig. 2 Optical system

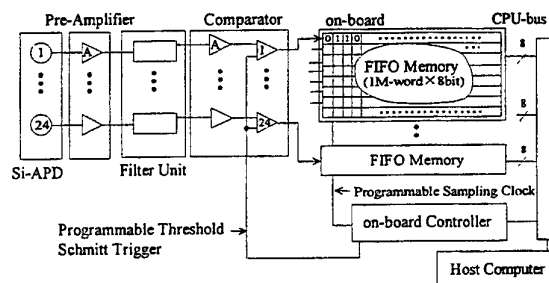


Fig. 3 Hardware system block diagram

measuring points is 1mm. Besides about seeding, polystyrene particles of $5\ \mu\text{m}$ in mean diameter were used as the tracer particles for measuring of velocity.

3. Results and Discussion

3.1 Instantaneous velocity profile

Typical time series velocity profiles at $x/h=3$ and $x/h=6$ are shown in Fig.4. Each profile interval is 0.5 in dimensionless time tU_c/h (about 40msec) and the dotted lines mean 0 point of each profile. The distribution of u -component mean velocity and turbulent intensity behind the step which calculated by these velocity profile is shown in Fig.5. In this figure the dotted line represents the time-averaged dividing stream line. Each distribution is in good agreement with the other previous studies. The time-averaged reattachment length, determined by the fraction of forward flow at $y/h=0.05$, is $x_R=6.0$ in this experimental

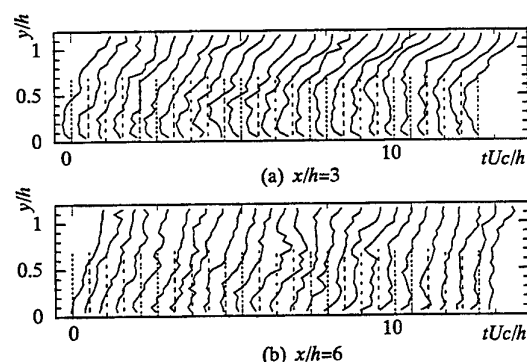


Fig. 4 Typical time series velocity profiles at $x/h=3$ and $x/h=6$

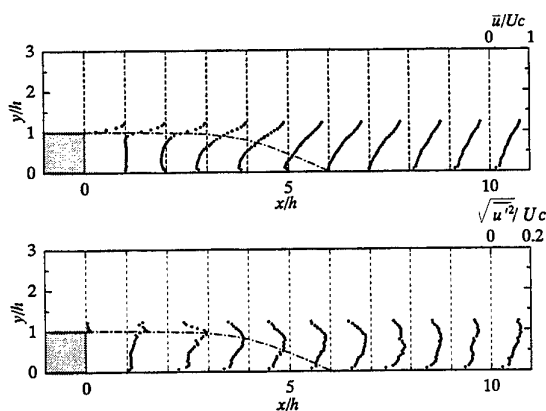


Fig. 5 Distribution of mean u -component velocity and turbulent intensity

apparatus.

Contour maps of instantaneous u -component velocity are shown in Fig.6, where velocity is measured at streamwise locations of $x/h=1-10$. The measuring point of the bottom is where $y/h=0.05$ and the top is where $y/h=1.15$, therefore the measuring width is 22mm. The interval between the each measuring points is 1mm. Time progresses from left to right. At $x/h=1$, an oscillatory motion of the separated shear layer, caused by shear vortex concentration, can be observed. Under the step height, the flow is almost stagnated. Specifically, the flow direction is negative at $y/h=0.4-0.8$, and the flow direction is only slightly positive at $y/h<0.3$ near the step wall. In the vicinity of $y/h>0.8$ in the separated shear layer, the flow direction is seen to change periodically due to the shear vortex concentration, which is the stripe-shaped structure in this figure. At $x/h=2$, the velocity distribution of the separated shear layer is almost identical to that at $x/h=1$. However, the structure in the separation bubble at $x/h=2$ is different from that at $x/h=1$ on toe points mentioned below, the stripe-shaped structure, which forms the dark red section of the figure, grows as the separated shear vortex increases, and the flow direction near the step wall is almost negative.

The governing frequency of velocity fluctuation in the separated shear layer from $x/h=1$ to $x/h=2$ is about 3Hz. This fluctuation is caused by the concentration of the shear vortex. But the governing frequency can not be observed clearly between the location at $x/h=3$ and at $x/h=6$, and it disappears at the downstream of the reattachment region. This means that it is difficult to extract the periodicity from the velocity fluctuation as measured at only one point in the measuring area, because the boundary region between forward flow and reverse flow is largely oscillating at the downstream of $x/h=3$, as seen in the figure.

The separated shear layer with vortex concentration is largely oscillating with the increasing reverse flow in the separation bubble. The forward flow of the stripe-shaped structure from the separated shear layer is inclined to streamwise and reaches the step wall more and more frequently. Time of forward flow in succession is longer at the step wall than upstream. This fluid motion indicates the dynamic phenomena of reattachment. A larger reverse flow is detected at $y/h=0.3-0.8$ than near the wall. It is not clear that this phenomena is caused by separated shear vortex or by another factor. This reverse flow is not detected downstream of the reattachment region $x/h=6$, only near the wall. A structure of the stripe-shaped structure, that is detected at $x/h=7$, is not detected at the downstream of $x/h=7$. On the other hand, large-scale velocity fluctuation of

forward flow is detected over the measuring cross-section.

It can be seen a phenomenon of reattachment from a behavior of reverse flow near the step wall around the time-averaged reattachment region. The area ① in Fig.6 (e) shows a flow motion that the separated shear layer reattaches to the step wall. It is found clearly that the separated shear flow which approach to the step wall reattaches maintaining velocity gradient with increasing a reverse flow near the step wall. The area ② in Fig.6 (f) shows a flow motion that the separates shear vortex reattaches to the step wall. It should be noted that reverse flows are detected at two region at the same time, near the wall and at $y/h=0.5$, as shown in this velocity profile. This phenomenon is suspected to result from the reattachment of the separated shear vortex. Up side reverse flow is caused by the separated shear vortex, and down side reverse flow occurs because of the reattachment

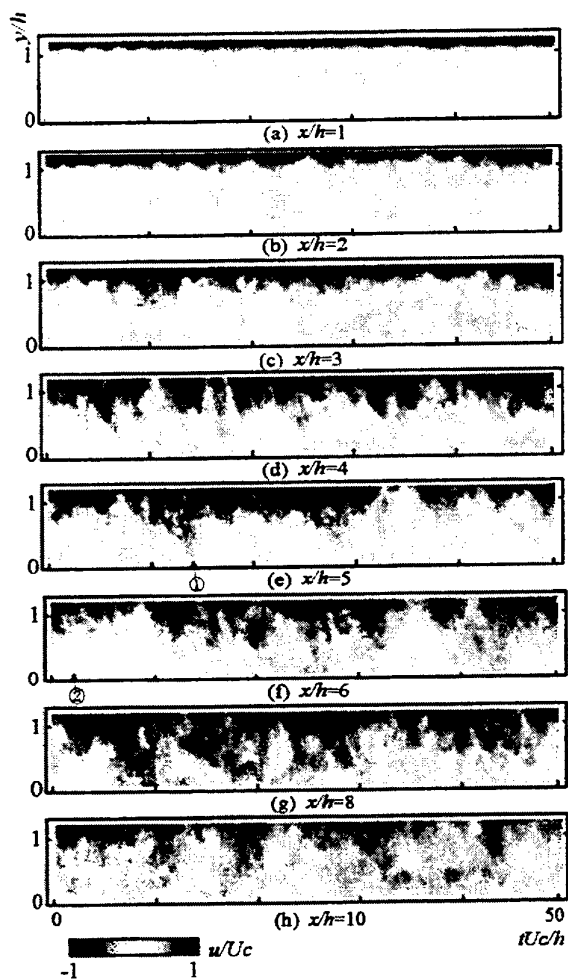


Fig. 6 Contour maps of instantaneous velocity at each streamwise location

point downstream from the measuring point.

As mentioned above, the phenomenon of reattachment have two patterns. One is the case that separated shear layer reattaches and the other one is the case that separated shear vortex reattaches.

In this experiment, continuous time over of measurements of velocity profile is 4.2msec. If there is large scale fluctuation in the flow dynamics beyond this measuring time, it is impossible for the frequency of this fluctuation to be detected. Fig.7 shows another two contour maps of instantaneous velocity profile at $x/h=3$ ((a) and (b)) where instability is seen to be increase and at $x/h=6$ ((c) and (d)) where is time averaged reattachment region, in order to check whether there is large scale fluctuation in the flow field. At $x/h=3$, the extent of boundary region between forward flow and reverse flow is similar to that all profile, else but a forward flow reaches the step wall in profile (a) at nearly $tUc/h=50$. Therefore, there is no typical large scale fluctuation at $x/h=3$. But at $x/h=6$, the flow field is unsteady because of the reattachment region, there is a possibility that large scale fluctuation exists in this region.

3.2 Spatial correlation

To clarify the flow structure of the separated shear layer, a two-point correlation of velocity fluctuation in space is given by the following formula,

$$R_u(x, y_1, y_2, \tau) = \frac{\overline{u'_1(t, x, y_1) u'_2(t + \tau, x, y_2)}}{\sqrt{\overline{u'^2_1(t, x, y_1)} \sqrt{\overline{u'^2_2(t + \tau, x, y_2)}}}$$

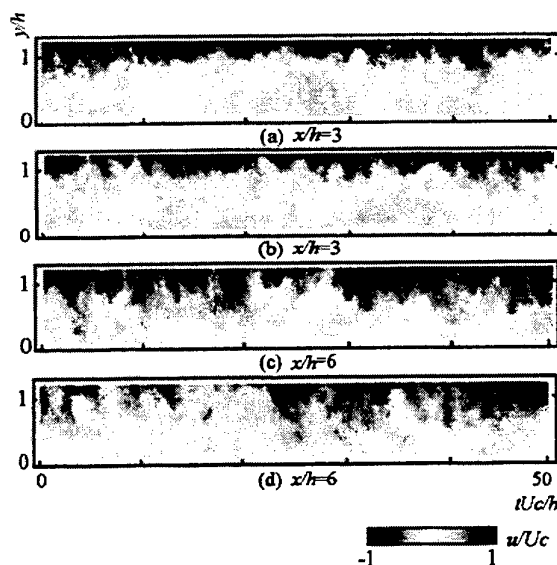


Fig. 7 Contour maps of instantaneous velocity at $x/h=3$ and $x/h=6$

where τ is a lag time, and y_1 and y_2 are the vertical locations of a fixed-point and a moving-point, respectively. In Fig.8, a two point correlation map of each streamwise location are shown, with a fixed-point located at $y/h=1.0$ corresponding to the step height. Solid and dotted line contours represent

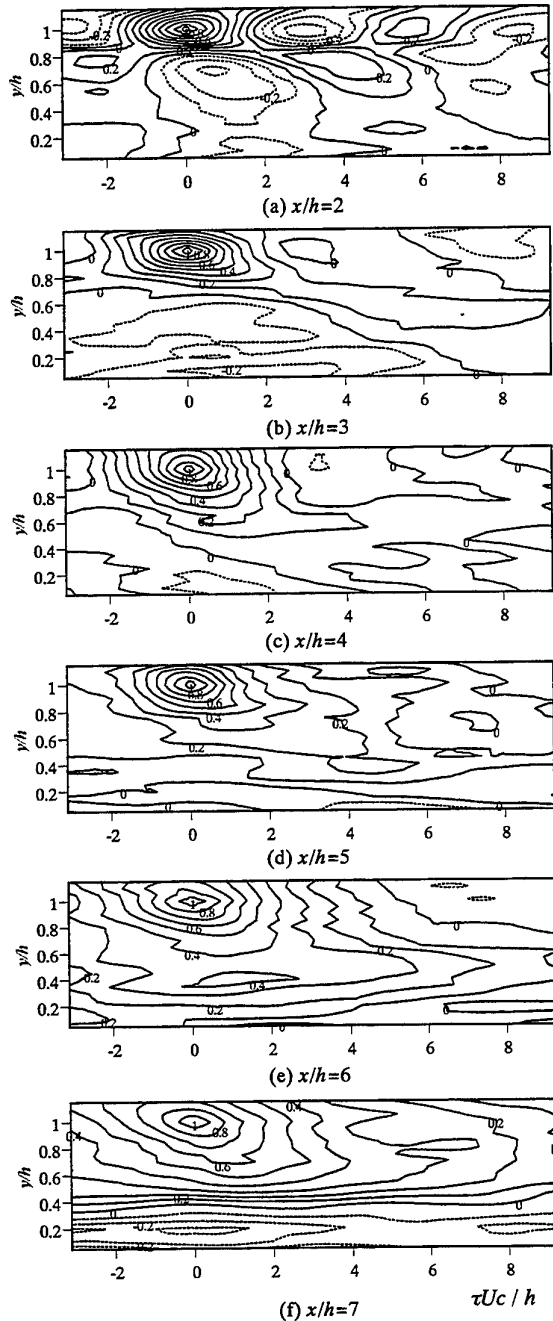


Fig. 8 Spatial correlation between fixed-point $y/h=1$ and moving-point over a measuring cross-section

positive and negative signs, respectively. The interval between contours is set at 0.1. At $x/h=2$, the positive high correlation area around the fixed-point is relatively small, and a negative correlation area is detected around $y/h=0.8$. This means that the velocity fluctuation in the separated shear layer and in the separation bubble are correlated with 180° out-of-phase. A correlation at $y/h=1.0$ means auto-correlation, and fluctuation is relatively frequent so that the negative correlation region appears $\tau U_c / h = 3$. It is difficult to detect this periodical motion downstream of $x/h=3$, as mentioned above.

The positive high correlation area of $R_{uu} > 0.4$ around a fixed-point remains roughly at the same size until $x/h=5$. At the downstream of $x/h=6$, this area gets gradually larger. As a whole, much as positive correlation area approach to the step wall, it is suspected that the flow structure does not change at the upward of separated shear layer as the flow proceeds downstream to the reattachment region, and the flow structure changes downstream around reattachment region.

As the flow proceeds downstream, the positive high correlation region become to incline because a correlation under step height is more larger at some lag-time with vortex growing up. As shown in figure of contour maps of velocity profile, the correlation map indicates that a stripe-shaped area among two vortices passes a measuring cross section with inclining to streamwise direction. The angle of this flow structure becomes slightly larger until $x/h=6$. A negative correlation region is detected near the step wall at $x/h=7$. This correlation means that there is a large scale structure corresponding to the step height after the reattachment region.

3.3 Dividing stream line

Temporal variation of dividing stream line are shown in Fig.9 (correspond to Fig.6(a)-(f)) with the boundary point of instantaneous velocity between forward flow and reverse flow that is furthest from the step wall (hereafter, this point will be referred to as the 0 velocity point), so that the motion of the separated shear layer with the vortex concentration is clear. The dividing stream line is defined as the point at which the integrated value of the instantaneous velocity from the step wall upward changes from minus to plus at first as follow dividing stream line definition. Note that there are several velocity profiles for which it is difficult to calculate the dividing stream line. For example, at $x/h=1$, there exists a "dividing stream line" in the separation bubble because the flow direction is forward near the step wall. Although this profile includes these problematic points, the motion of the separated shear layer is still represented well.

At $x/h=2-3$, the dividing stream line oscillates around $y/h=1$ in the separated shear layer. The interval between the dividing stream line and the 0 velocity point becomes narrow when the 0 velocity point and the dividing stream line go down immediately. This means that the reverse flow in the separation bubble becomes slow when a forward flow

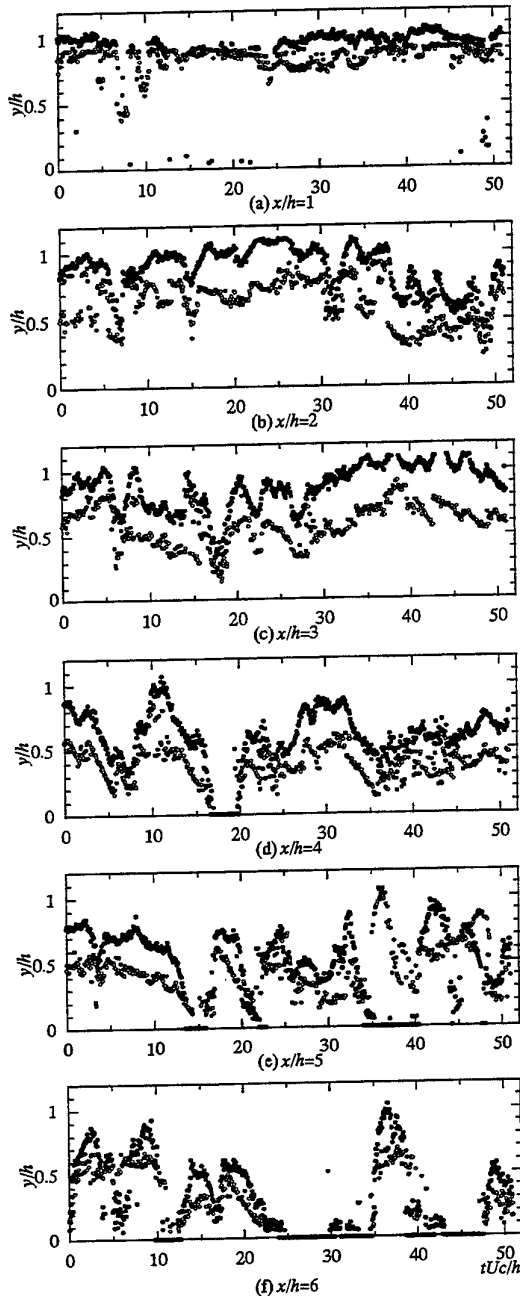


Fig. 9 Temporal variation of the dividing stream line (●) and boundary point between forward flow and reverse flow (○)

simultaneously enters the separation bubble from the separated shear layer. This phenomenon of the dividing stream line immediately going down can also be observed at $y/h=4$. The interval between the 0 velocity point and the dividing stream line, which represents, so to speak, a thickness of the separated shear layer, it grows gradually larger as the flow proceeds downstream to $x/h=3$. The thickness remains unchanged in spite of the oscillation of the separated shear layer. The time averaged dividing stream line approaches the step wall gradually.

At $x/h=4-5$, there is a tendency that the dividing stream line, that is oscillating around $y/h=0.5-0.8$ for some time to approaches the step wall immediately. When the dividing stream line can not be detected for a time, this means that the dividing stream line reattaches to the step wall behind the measuring point. The velocity at which the dividing stream line descend to the step wall is about 100mm/s. After this reattachment, the dividing stream line ascend immediately to 0.3-0.8h from the step wall. These flow dynamics mean that the instantaneous reattachment point moves to the downstream of the measuring point.

At $x/h=6$, the oscillations at $y/h=0.5-0.8$ of dividing stream line that appeared show at $x/h=4,5$ are not detected. Much as an approach to the step wall of dividing stream line is detected as approach to the separated shear layer, there is a tendency for the dividing stream line to immediately ascend to $y/h=0.5-0.8$ from the step wall and to reattach after 5 times in dimensionless time (about 400msec).

The probability density of the dividing stream line for each streamwise location are shown in Fig.10. As mentioned above, it must be noted that the dividing stream lines are detected in the separation bubble at $x/h=1-2$ as a result of the velocity profile in which it is difficult to define the dividing stream line. The oscillation width of the dividing stream line is limited near the separated shear layer until the point where $x/h=3$. This width becomes larger as the flow proceeds downstream from the step wall to upper side of the separated shear layer. The highest peak is on the time-averaged dividing stream line at $x/h=1-2$, but there is a slight down side at $x/h=3$. Two peaks appear at $x/h=5$, where the time-averaged dividing stream line is on a saddle of two peaks. The peak of $x/h=3,4$ is $y/h=0.8$ and $y/h=0.75$ respectively, and upside peak of $x/h=5$ is $y/h=0.7$, and the vertical location of these peaks are almost same. This histogram profile means that the dividing stream line that oscillates around the time-averaged dividing stream line approaches to the step wall immediately as mentioned above.

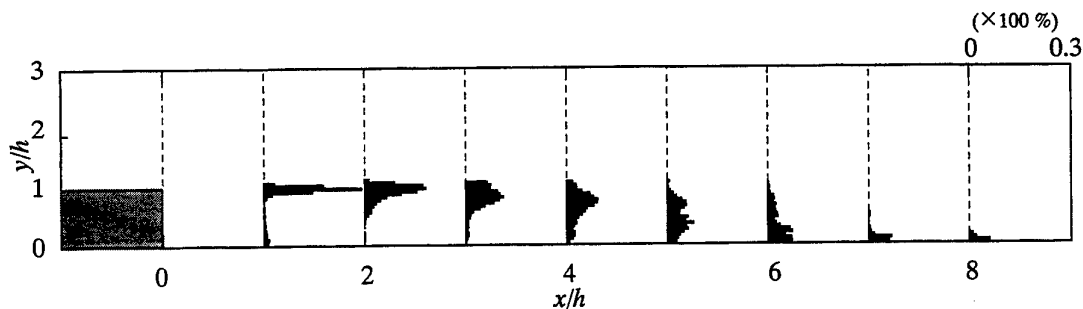


Fig. 10 Probability density of the dividing stream line

4. Conclusion

A temporal data of instantaneous velocity profile from the bottom to the main flow behind a two-dimensional backward-facing step was measured by multi-point LDV, and was discussed with a special focus on the details of the motion of the separated shear layer and the phenomena of reattachment.

As a result, the instantaneous velocity profile is extremely different from the time-averaged velocity profile. The dividing stream line that was calculated in this velocity profile oscillates as vortex concentration in the separated shear layer. But the thickness of the separated shear layer does not show large oscillation in spite of the dividing stream line oscillation. The most notable feature of the dividing stream line oscillation is that the dividing stream line that oscillated around the time-averaged dividing stream line approached to the step wall immediately.

The phenomenon of reattachment have two patterns. One is the case that separated shear layer reattaches and another one is the case that separated shear vortex reattaches.

5. Reference

- Armly, B. F., Durst, F., Pereira, J. C. F., and Schonung, B., "Experimental and theoretical investigation of backward-facing step flow", *J. Fluid Mech.* 127(1983), 473-496
- Eaton, J., and Johnston, J. P., "Turbulent flow reattachment : An experimental study of the flow and structure behind a backward-facing step", Rep. MD-39, Thermoscience Division, Dept. of Mech. Eng., Stanford University (1980)
- Eaton, J., and Johnston, J. P., "A review of research on subsonic turbulent flow reattachment", *AIAA J.*, 19(1981), 1092-1100
- Hachiga, T., Furuichi, N., Mimatsu, J., Hishida, K., and Kumada, M., "Development of multi-point LDV by using semiconductor laser with FFT-based multi-channel signal processing", *Experimental in Fluids* 24(1998), 70-76
- Hijikata, K., Mimatsu, J., and Inoue, J., "A study of wall pressure structure in a backward step flow by a holographic / velocity-pressure cross-correlation visualization", *Experimental and Numerical Flow Visualization*, 128(1991), 61-68
- Hungel, Moin, P., and Kim, J., "Direct numerical simulation of turbulent flow over a backward-facing step", *J. Fluid Mech.*, 330(1997), 349-374
- Kasagi, N., and Matsunaga, A., "Tree-dimensional particle-tracking velocimetry measurement of turbulence statistics and energy budget in a backward-facing step flow", *Int. J. Heat and Fluid Flow*, 16(1995), 477-485
- Sakakibara, J., Hishida, K., and Maeda, M., "Measurement of thermally stratified pipe flow using image-processing techniques", *Experimental in Fluids* 16(1993), 82-96
- Takeda, Y., "Development of an ultrasound velocity profile monitor", *Nuclear Engineering and Design*, 126(1991), 277-284

A NON-NEWTONIAN TURBULENT SUDDEN EXPANSION FLOW

A. S. Pereira

Departamento de Engenharia Química, Instituto Superior de Engenharia do Porto
Rua de S. Tomé, 4200 Porto CODEX, Portugal

F. T. Pinho

Departamento de Engenharia Mecânica e Gestão Industrial
Faculdade de Engenharia, Rua dos Bragas, 4099 Porto CODEX, Portugal

ABSTRACT

A miniaturised fibre optic Laser-Doppler anemometer was used to carry out a detailed hydrodynamic investigation of the flow downstream a sudden expansion with 0.1% to 0.2% by weight shear-thinning aqueous solutions of xanthan gum.

Upstream of the sudden expansion the pipe flow was fully-developed and the xanthan gum solutions exhibited drag reduction with the corresponding lower radial and tangential normal Reynolds stresses, but a higher axial Reynolds stress near the wall and a flatter axial mean velocity profile.

The recirculation bubble length was reduced by more than 20% relative to the high Reynolds number Newtonian flow, and this was attributed to the higher levels of maximum turbulence and their earlier occurrence in space for the non-Newtonian solutions. This happened as a result of the advection of the upstream inlet condition leading to both higher initial values of axial turbulence in the free shear layer and higher turbulence production.

1. INTRODUCTION

The vast majority of turbulent flow research with non-Newtonian fluids has concentrated on understanding wall-dominated flows with polymer solutions and more recently surfactants (Gyr and Bewersdorff, 1995), but a better knowledge of turbulent flow behaviour requires also the investigation of wall-free flows, preferably with the same fluids. The axisymmetric sudden expansion flow is easily implemented for liquid flows of non-Newtonian fluids and has been investigated in the past by a few researchers. Pak et al (1990,1991) showed the influences of fluid viscosity and elasticity on the mean flow characteristics of Carbopol and Separan solutions under laminar, transitional and turbulent flow conditions, but failed to report detailed turbulent measurements in the latter case. More recently, Castro and Pinho (1995) have mapped the mean and turbulent fields in the sudden expansion flow of weakly elastic 0.4% and 0.5% by weight aqueous solutions of Tylose (molecular weight of 6,000 kg/kmole), which were previously investigated by Pereira and Pinho (1994) on their fully-developed turbulent pipe flow characteristics. These solutions were found to be inelastic in conventional

rheometric shear tests, but showed drag reductions of less than 24% and 27% in turbulent pipe flow, respectively. In the sudden expansion flow they yielded small variations in the recirculation bubble length and reductions of the normal Reynolds stresses of up to 30%, especially in the tangential and radial directions.

The extension of this research to other fluids exhibiting a higher degree of elasticity in shear rheological flows, and higher levels of drag reduction in turbulent pipe flow, such as the axial solutions of xanthan gum tested by Escudier et al (1995) or the CMC solutions of Pinho and Whitelaw (1990), are deemed necessary to enhance our understanding of turbulent flows of polymer solutions and constitutes the objective of the present work.

In the next section the rig and instrumentation are described, and that is followed by the presentation and discussion of results. The characteristics of the fluids are presented before the hydrodynamic results and the paper ends with a summary of the main conclusions

2. EXPERIMENTAL SET UP

The flow configuration is similar to that used in the pipe flow experiments of Pereira and Pinho (1994) except for the test section and the ensuing duct leading to the tank. The installation consisted of a vertical closed loop with a 100 litre tank and a centrifugal pump located at the bottom. The descending pipe before the test section was 26 mm in diameter and more than 90 diameters long, leading to a transparent sudden expansion test section from 26 mm to 40 mm in diameter and 700 mm in length. Downstream of the test section there is a further pipe of 40 mm diameter which is fitted with a valve and leads the flow to the tank. The test section is represented schematically in Fig. 1 with the coordinate system and it had a square outer cross section to reduce diffraction of light beams. To help ensure a fully developed flow at the inlet of the sudden expansion, a honeycomb was placed at the inlet of the descending 26 mm pipe, i.e., 90 diameters upstream of the sudden expansion plane.

Fourteen pressure taps were located in the pipe downstream of the sudden expansion and two taps were drilled upstream, in the region of fully-developed flow. One of the upstream taps was drilled in the perspex test section whereas the other was located in the brass pipe. The rising

pipe had an electromagnetic flowmeter and two valves which, together with a bypass circuit, allowed the flow rate to be properly monitored. The connection between the brass pipe and the test section was well done and within the machining tolerances of $\pm 10 \mu\text{m}$, causing no detectable harm to the flow condition.

The pressure drop in the sudden expansion was measured by means of differential pressure transducers from Validyne (models P305D) and its output was sent to a computer via a data acquisition board Metrabyte DAS-8 interfaced with a Metrabyte ISO 4 multiplexer, both from Keithley. The overall uncertainty of the pressure measurements varied between 1.6% and 7.2% for high and low pressure differences, respectively.

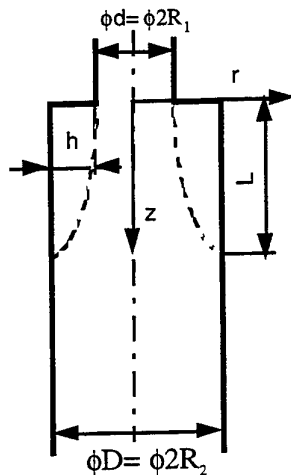


Fig. 1 - Schematic representation of the sudden expansion test section.

Table I - Laser-Doppler characteristics

Laser wavelength	827 nm
Laser power	100 mW
Measured half angle of beams in air	3.68
Size of measuring volume in water (e^{-2} int.)	
minor axis	37 μm
major axis	550 μm
Fringe spacing	6.44 μm
Frequency shift	2.5 MHz

For the velocity measurements a miniaturised fiber optics laser-Doppler velocimeter from INVENT, model DFLDA, similar to that described by Stieglmeier and Tropea (1992), was used, with a 100 mm front lens mounted onto the 30 mm diameter probe. Scattered light was collected by a photodiode in the forward scatter mode, and the main characteristics of the anemometer are listed in Table I and described by Stieglmeier and Tropea (1992). Measurements of the radial velocity component were limited to the inner 70% of the pipe radius due to excessive refraction of light beams outside that region.

The signal was processed by a TSI 1990C counter interfaced with a computer via a DOSTEK 1400 A card, which provided the statistical quantities. The data presented in this paper have been corrected for the effects of the mean gradient broadening and the maximum uncertainties in the

axial mean and rms velocities at a 95% confidence level are of 1.0% and 2.2% on axis respectively, and of 1.1% and 5.2% in the wall region. The uncertainty of the radial and tangential rms velocity components is 2.5% and 5.9% on axis and close to the wall, respectively.

The velocimeter was mounted on a milling table with movement in the three coordinates and the positional uncertainties are of $\pm 200 \mu\text{m}$ and $\pm 150 \mu\text{m}$ in the axial and transverse directions, respectively.

3. FLUID PROPERTIES

Water and aqueous solutions of xanthan gum grade Keltrol TF from Kelco, a polysaccharide of high molecular weight ($2 \cdot 10^6 \text{ kg/kmol}$), at weight concentrations of 0.1% and 0.2% were used. This additive produced solutions of higher elasticity than those of CMC of Pinho and Whitelaw (1990) and Tylose of Castro and Pinho (1995), but at the same time the solutions were more shear-thinning, especially at low shear rates. The polymer was dissolved in Porto tap water and 0.02% by weight of the biocide Kathon LXE from Rohm and Haas was added to help prevent bacteriological degradation. The rheological characterisation was carried out in the Physica MC100 rheometer implementing a double gap concentric cylinder geometry.

The viscometric viscosity of the solutions are plotted in Fig. 2 together with the curve-fitted Sisko model equation (Eq. 1), whose parameters are listed in Table II.

$$\eta = \eta_{ref} (\lambda_s \dot{\gamma})^{n-1} + \eta_{\infty} \quad (1)$$

Table II- Sisko model parameters for Keltrol solutions at 25°C.

Solution	η_{ref} [Pas]	η_{∞} [Pas]	λ_s [s]	n
0.1%	10.52	0.0012	1970	0.4299
0.2%	58.06	0.001589	1900	0.3434

To assess the elasticity of the solutions creep and oscillatory tests were carried out. In the creep tests the ratio of the stored shear deformation to the total deformation of the 0.1% and 0.2% xanthan gum solutions was less than 0.04% and 0.15%, respectively for a range of applied stresses between 0.3 and 3 Pa. In the oscillatory shear tests it was not possible to get reliable data for amplitudes of deformation below 0.2. For this amplitude of deformation the ratio of the storage to the loss moduli G'/G'' was less than 0.7 for the 0.1% solution and about 1 for the 0.2% solution.

In spite of the low elasticity shown in the rheological tests, these two solutions exhibited drag reduction in turbulent pipe flow as shown in Fig.3. In a pipe of 26 mm and for maximum wall Reynolds numbers of 40,100 and 28,100, the measured drag reductions of 45% and 59% for the 0.1% and 0.2% xanthan gum solutions represent over 1/2 and 3/4 of the maximum predicted by Virk's asymptote (Virk et al, 1970). Note that these values are substantially higher than those reported by Pereira and Pinho (1994) for identical concentrations of Tylose, but are similar to those of Pinho and Whitelaw (1990) for identical concentrations of CMC.

4. RESULTS AND DISCUSSION

Five flow conditions were investigated in detail and allowed the analysis of the effects of Reynolds number and additive concentration. The Reynolds number Re is defined on the basis of the upstream pipe flow characteristics such as the upstream bulk velocity and wall viscosity. However, for the sake of comparisons with other works in the literature, a generalised Reynolds number (Eq. 2) is also recorded in Table IV which lists the main characteristics of the investigated flows.

$$Re_{gen} = \frac{\rho D_1^n U_1^{2-n}}{K} \quad (2)$$

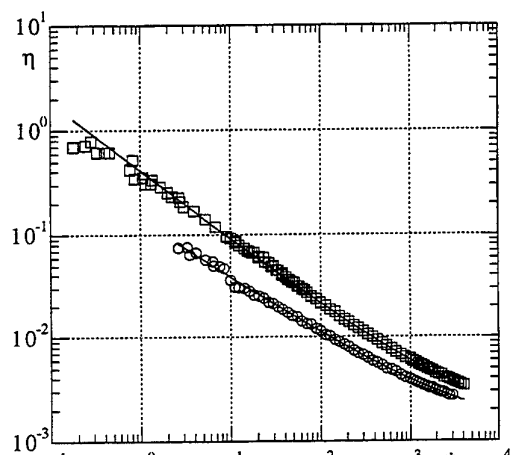


Fig. 2- Viscometric viscosity of the xanthan gum solutions and the corresponding curve fitted Sisko models. O 0.1% Xanthan gum, □ 0.2% Xanthan gum.

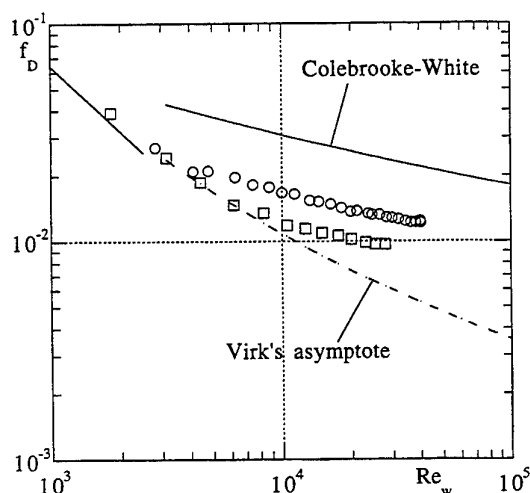


Fig. 3- Darcy friction factor as a function of the wall Reynolds number in a fully developed pipe flow. O 0.1% Xanthan gum, □ 0.2% Xanthan gum.

Note that Eq. (2) requires the power index n and consistency index K of the Ostwald de Waele power law fit to the measured viscosity.

The largest Reynolds number Re flows in Table IV correspond to the maximum flow rate in the rig. The Table lists also the recirculation length L normalised by the step height h . To measure the recirculation length the axial velocity was measured twice in a fine grid around the estimated location of flow reattachment and the data interpolated. The nodes of this grid were spaced axially and radially by 3 mm and 0.2 mm, respectively and the overall uncertainty of the eddy size measurement, due to positional and mean velocity uncertainties, is better than 5%.

Table IV- Main flow characteristics of the investigated flows of water and xanthan gum (XG)

Run	Fluid	Re	Re_{gen}	L/h
1	water	133,000	133,000	8.64
2	water	50,000	50,000	8.47
3	0.1% XG	19,300	7,950	6.61
4	0.2% XG	26,600	10,380	6.42
5	0.2% XG	19,100	7,530	6.64

4. 1. Mean flow

The mean flow measurements showed the flow field in all cases to be similar in that we could identify a core flow, a free shear-layer downstream of the upstream wall pipe, a recirculation region delimited by the step, the downstream pipe wall and the shear layer, a reattachment region and a redeveloping boundary layer, in accordance to the flow field definition of Prorichick and Kline, (1983).

Our measurements with water compare well in all respects with data from the literature pertaining to Newtonian fluids. In particular the normalised recirculation lengths plotted in Fig. 4 are in good agreement with data from other researchers, especially the values measured by Khezzar (1985), although a small expansion ratio effect in the slightly normalised eddy sizes for the lower expansion ratios is observed. Note also that the values are very similar to those measured by Castro and Pinho in 1995.

Quite unexpected, considering previous non-Newtonian measurements from the literature, is the shorter recirculation observed with the xanthan gum solutions. To the authors knowledge there has been only two investigations of this quantity and their results, together with the present measured lengths, are plotted in Fig. 5. So far it was thought that polymer solutions of non-Newtonian rheology would exhibit unchanged or longer eddy sizes in comparison to the Newtonian values, at identical Reynolds numbers, but this work shows that shorter bubbles can also occur.

As we shall see below the different behavior can be explained by the turbulent flow field, especially by the location and magnitude of the maximum normal Reynolds stresses. However, before analysing in detail the flow downstream of the expansion it is convenient to assess well the inlet flow condition.

Pressure gradients measured between the two upstream pressure taps were in agreement with the measured pressure gradients obtained for the same fluid flow in the pipe flow rig described in Pereira and Pinho (1994). Fig. 6-a) shows the fully developed radial profiles of the mean axial velocity u in the pipe upstream of the sudden expansion. The velocities were normalised by the maximum velocity

and the profiles at higher Reynolds numbers are flatter than those pertaining to lower Reynolds number flows. The mean and turbulent Newtonian velocity profiles are in agreement with those of the literature (Laufer, 1954 and Lawn, 1971), thus confirming a fully developed flow condition at the inlet of the expansion.

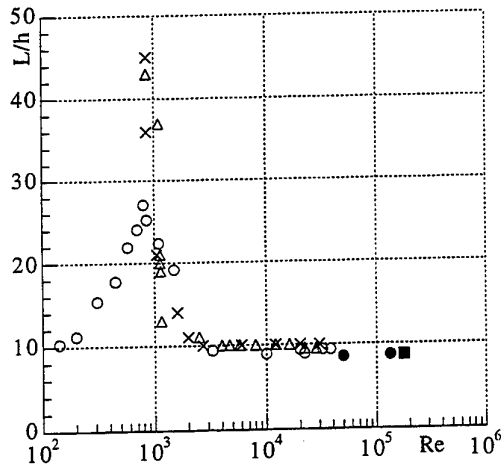


Fig. 4- Normalised recirculation length for Newtonian fluids. O Khezzar (1985) $D/d=1.749$; X Pak et al (1990) $D/d=2.0$; Δ Pak et al (1990) $D/d=2.667$; \blacksquare Castro and Pinho (1995) $D/d=1.538$; \bullet Present work $D/d=1.538$.

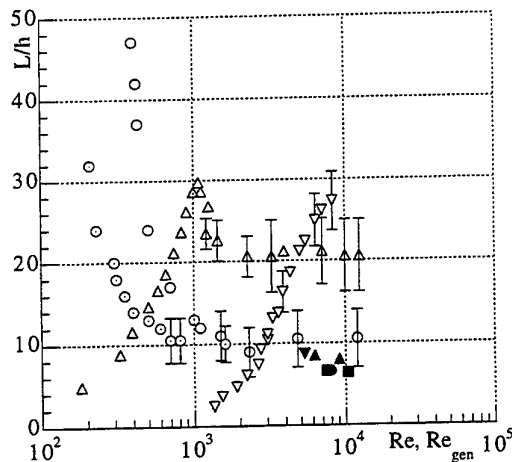


Fig. 5- Normalised recirculation length for non-Newtonian fluids. Pak et al (1990) $D/d=2.667$: O Carbopol 5000ppm, \circ Carbopol 15000 ppm; Pak et al (1990) $D/d=2.0$: Δ Separan 200 ppm, ∇ Separan 1000 ppm; Castro and Pinho (1995) $D/d=1.538$: \blacktriangle 0.4% Tylose, \blacktriangledown 0.5% Tylose; Present work $D/d=1.538$: \bullet 0.1% Xanthan gum, \blacksquare 0.2% Xanthan gum.

The profiles for the 0.1% Xanthan gum solution at $Re=19,300$ and the 0.2% Xanthan gum solution at $Re=26,600$ are flatter than any of the Newtonian profiles, in spite of their higher Reynolds numbers. In our view this helps to explain the observed shorter recirculation bubble, as we shall see below.

The non-Newtonian turbulent velocity profiles in Figs. 6-b) to -d) are typical of fluids which exhibit drag reduction. Both transverse turbulence intensities (v' and w') are considerably dampened in relation to that of their Newtonian counterparts, especially when we take into account that a reduction in the Reynolds number in fully-developed pipe flow is equivalent to an increase in the turbulence (compare data for Newtonian flows at $Re=50,000$ and $Re=131,000$). However, the axial turbulence of the xanthan gum solutions is only slightly reduced in the central part of the pipe whereas near the wall the maximum turbulence becomes considerably higher than for Newtonian fluids. This different behaviour means that there is decoupling between the axial and transverse turbulence which explains the reduced friction.

Fig. 7 shows radial profiles of the axial mean velocity at various axial planes downstream of the expansion. Near the expansion ($x/d=0.25$ to 0.75) the flow of the non-Newtonian solutions have a flatter profile in the core and higher negative velocities within the recirculation region, consequently they exhibit a stronger shear layer. This feature is especially relevant as it contributes to higher turbulence production and higher levels of turbulence in the free shear layer, as will be shown in the next section. It is also worth mentioning that the ratio of the velocity on axis to the bulk velocity increases until about $x/D=0.5$ to 1.0 , with that effect more pronounced with the Newtonian fluid.

As the flow proceeds further downstream the mean velocity of all solutions seem to collapse, but we continue to observe anticipated features for the non-Newtonian flows in space relative to the water flows.

4. 2. Turbulent flow

Table V shows the maximum values of the normalised normal Reynolds stresses and of the turbulent kinetic energy. Note that the maximum normal stresses do not occur at the same location, therefore their sum does not yield the maximum kinetic energy. Everywhere else in the flow field, the axial Reynolds stress is always the highest turbulent stress followed by the tangential and then the radial components.

Table V- Maximum values of the normal Reynolds stresses

Run	$\overline{u_{\max}^2}/U_1^2$	$\overline{w_{\max}^2}/U_1^2$	$\overline{v_{\max}^2}/U_1^2$	k_{\max}^2/U_1^2
1	0.0495	0.0324	0.0227	0.0513
2	0.0440	0.0271	0.0221	0.0480
3	0.0417	0.0312	0.0195	0.0461
4	0.0552	0.0337	0.0242	0.0556
5	0.0470	0.0333	0.0225	0.0505

It is clear that a reduction of the Reynolds number, at low Reynolds numbers, leads to lower maximum turbulence whereas an increase in polymer concentration increases it. For instance, the 0.2% xanthan gum at Re of 26,600 has maximum values of the axial Reynolds stress 10% higher than that of the water flow at Re of 133,000 and about half that for the other two components of turbulence.

The whole turbulent flow field is shown in the contour plots of the normalised axial, tangential and radial normal Reynolds stresses of Figs. 8, 9 and 10, respectively. At first look the various plots look identical, but closer inspection shows the following differences: the non-Newtonian solutions develop the maximum Reynolds stresses earlier in space than the Newtonian flows and for some cases those quantities attain higher values as pointed out above. Then, on moving downstream the Reynolds stresses of the non-Newtonian solutions decay at a faster rate than those of the Newtonian flows, and this is particularly clear for the radial, and less so for the tangential components. Some of these differences could be better observed with x-y plots but these had to be omitted for reasons of space.

Initially we would think that a stronger turbulence dampening of the Reynolds stresses of these drag reducing, non-Newtonian fluids would lead to longer recirculation lengths, a result which would agree with the literature data in Fig. 5, but instead a reduction in eddy size was measured.

The mean and turbulent velocity plots show that the xanthan gum solutions initially develop turbulence in the

shear layer at a faster rate than the Newtonian flows, and reach higher values of the maximum Reynolds stresses, whereas the strong dampening of turbulence, especially of its transverse components, becomes effective in lowering the Reynolds stresses below the Newtonian level at the end of the reattachment and in the flow redevelopment regions only. This pronounced effect of the polymer additive upon transversal turbulence has been observed before in sudden expansion free-shear layers with Tylose solutions (Castro and Pinho, 1995) and in jets with polyacrilamide and polyethylene oxide solutions (Berman and Tan, 1985) and is also typical of wall dominated turbulent flows.

This apparent contradiction is explained as follows: the faster increase of turbulence in the free shear layer observed with the xanthan gum solutions is consistent with differences measured in the fully-developed pipe inlet condition. The flatter axial mean velocity profiles of the xanthan gum solutions (Fig. 6) lead to higher mean velocity gradients in the free shear layer (Fig. 7). The Reynolds shear stress was not measured but it is expected that in the upstream pipe it will be lower than for the Newtonian fluids because of the axial-transverse turbulence decoupling typi-

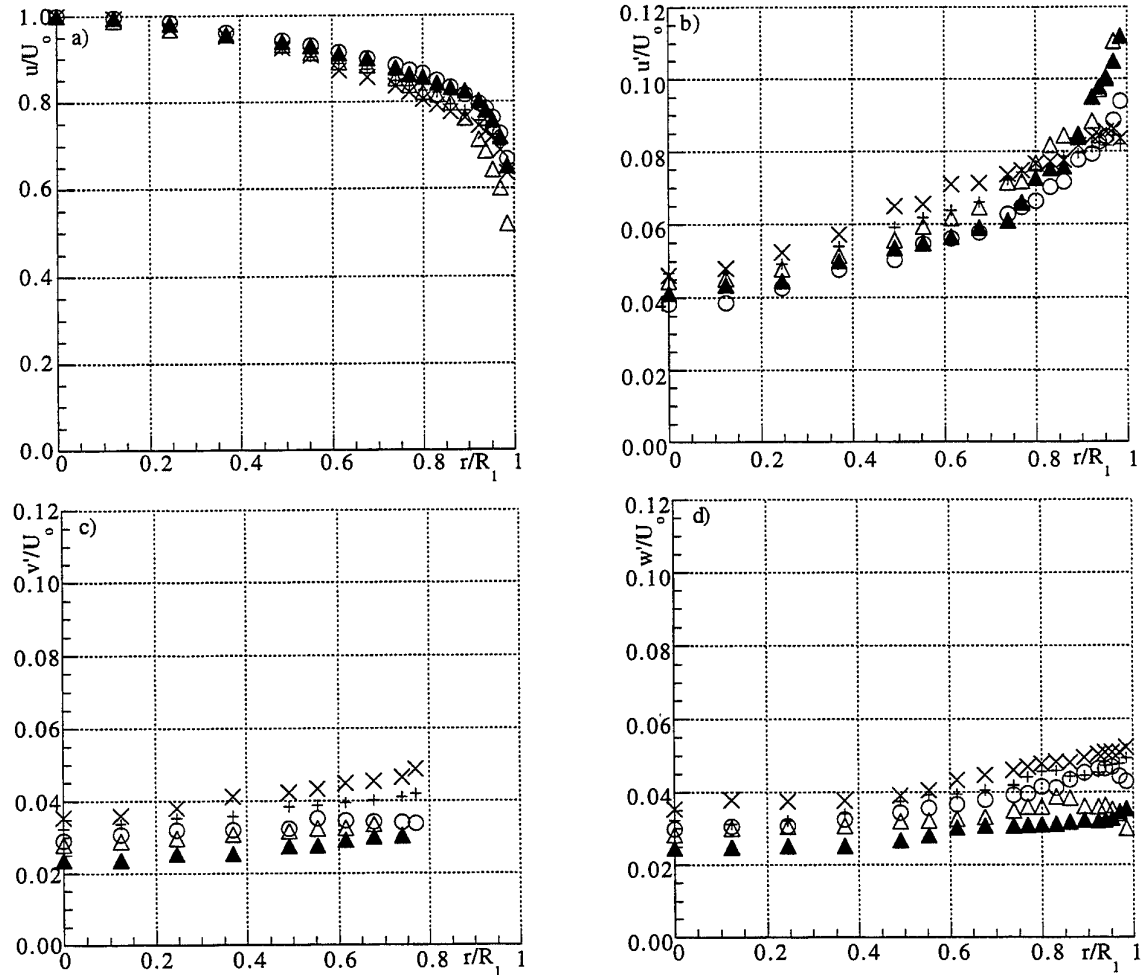


Fig. 6- Radial profiles of normalised mean and turbulent velocities at $x/d=0.25$ upstream of the expansion. X water $Re=50,000$; + Water $Re=131,000$; O 0.1% Xanthan gum $Re_w=19,300$; Δ 0.2% Xanthan gum $Re_w=19,100$; \blacktriangle 0.2% Xanthan gum $Re_w=26,600$. a) Axial mean velocity; b) Axial rms velocity; c) Radial rms velocity; d) Tangential rms velocity.

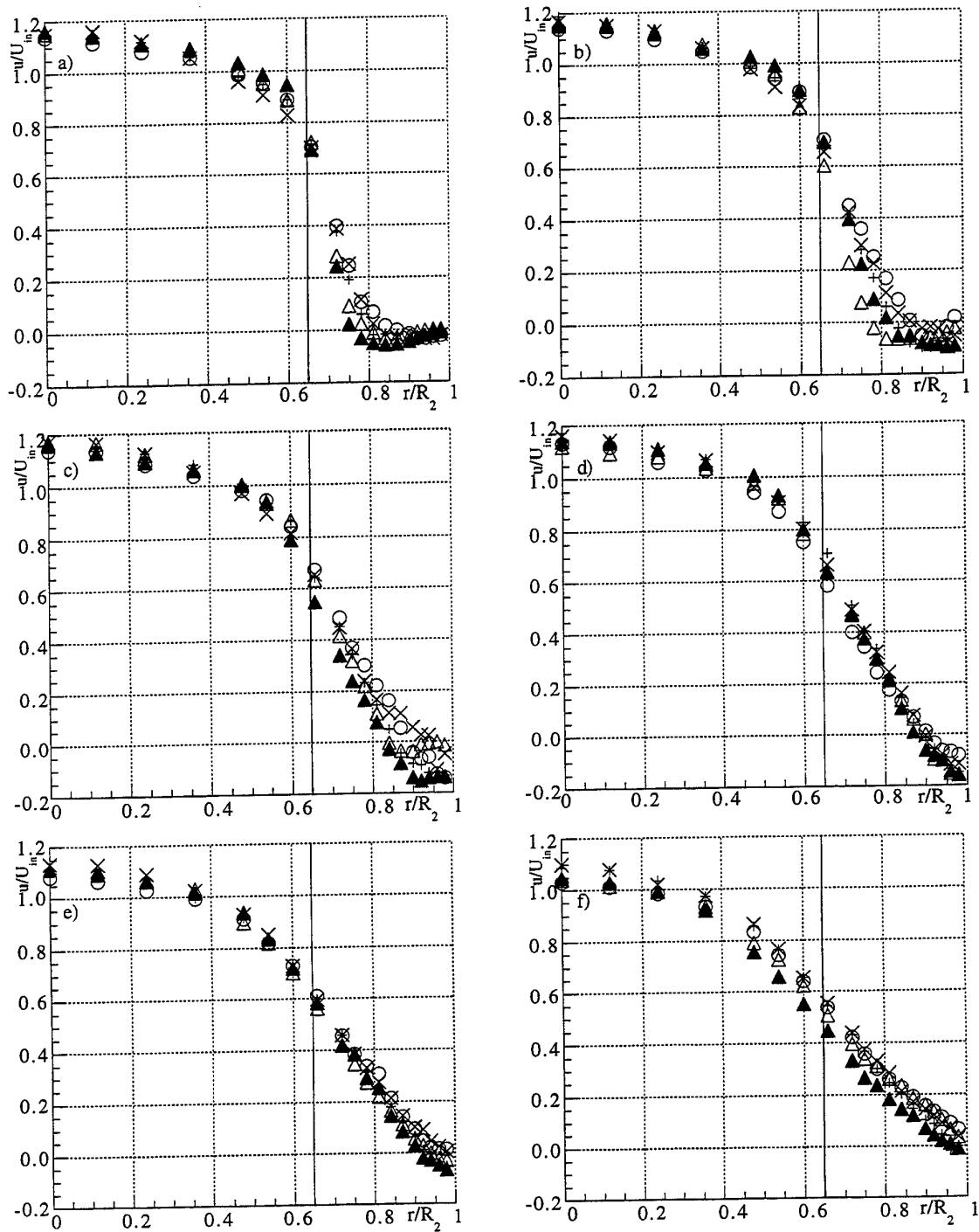
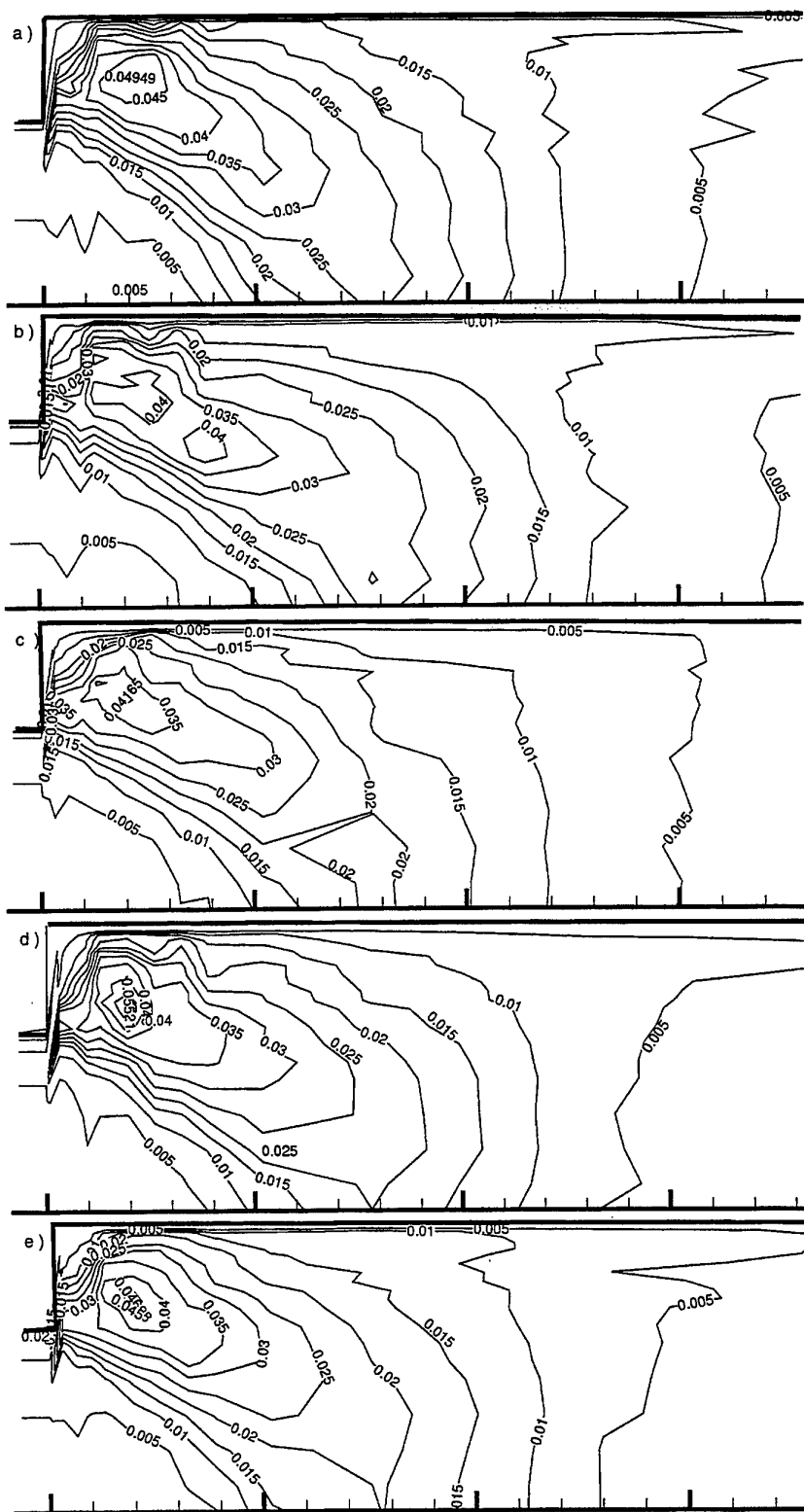
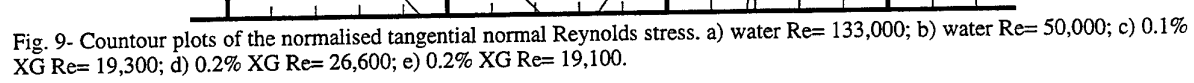


Fig. 7- Radial profiles of normalised mean velocity downstream of the expansion. X water $Re = 50,000$; + Water $Re = 131,000$; O 0.1% Xanthan gum $Re_w = 19,300$; Δ 0.2% Xanthan gum $Re_w = 19,100$; \blacktriangle 0.2% Xanthan gum $Re_w = 26,600$. a) $x/d = 0.25$; b) $x/d = 0.5$; c) $x/d = 0.75$; d) $x/d = 1.0$; e) $x/d = 1.5$; f) $x/d = 2.0$. Staright line marks the location of the inlet pipe wall.



Figs. 8- Countour plots of the normalised axial normal Reynolds stress. a) water $Re=133,000$; b) water $Re=50,000$; c) 0.1% XG $Re=19,300$; d) 0.2% XG $Re=26,600$; e) 0.2% XG $Re=19,100$.



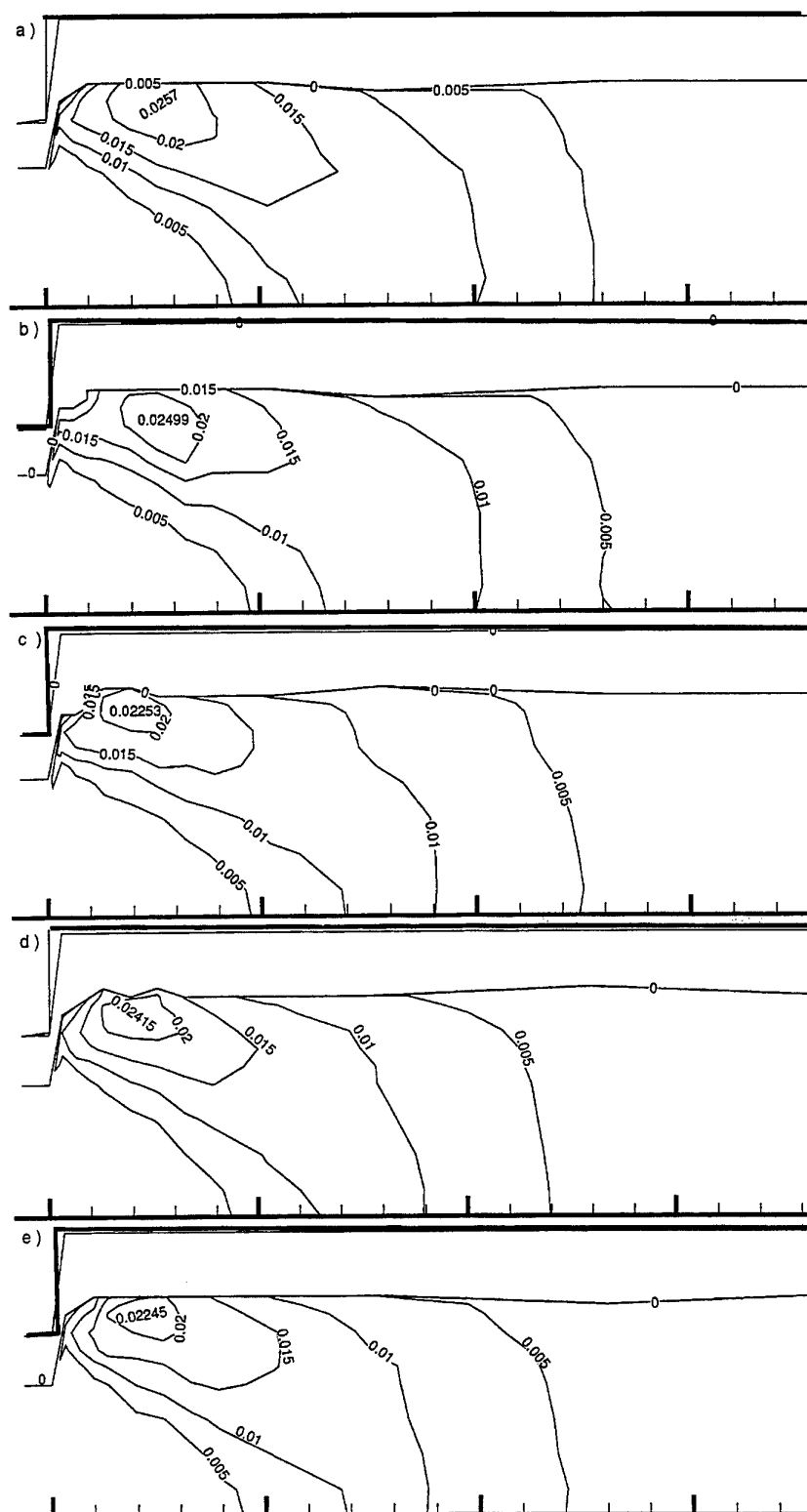


Fig. 10- Countour plots of the normalised radial normal Reynolds stress. a) water $Re = 133,000$; b) water $Re = 50,000$; c) 0.1% XG $Re = 19,300$; d) 0.2% XG $Re = 26,600$; e) 0.2% XG $Re = 19,100$.

cal of drag reducing fluids. So, production of $\overline{u_1^2}$

$$Pr od = \overline{u_1^2} \frac{\partial U_1}{\partial x_1} + \overline{u_1 u_2} \frac{\partial U_1}{\partial x_2} \quad (3)$$

via the second term on the right-hand-side of Eq (3) could be similar to that in Newtonian fluids because of the compensating variations in the shear velocity gradient and shear Reynolds stress. Then, the higher axial turbulence in the wall region of the upstream pipe is advected downstream and should increase the production of $\overline{u_1^2}$ via the first term on rhs of Eq. (3) but, more important, it leads to a higher initial level of axial turbulence in the free-shear layer. The higher maximum values of axial turbulence found in the shear layer for the xanthan gum solutions and its redistribution by the pressure strain also increase the other two normal Reynolds stresses.

The higher levels of turbulence in the middle of the shear layer enhance momentum transfer to the downstream pipe wall region, thus reducing the eddy size.

Further research with different polymer additives, inlet conditions and expansion ratios are deemed necessary to a full and comprehensive understanding of this type of flows for non-Newtonian solutions.

5. CONCLUSIONS

Measurements of the mean and turbulent flow fields downstream a sudden expansion were carried out for a Newtonian and two elastic xanthan gum aqueous solutions at Reynolds numbers between 19,000 and 133,000.

Addition of polymer resulted in drag reduction in the upstream pipe flow which was characterised by flatter axial mean velocity profiles and higher axial normal Reynolds stresses in the wall region which was then advected downstream by the mean flow. These resulted in enhanced velocity gradients and higher axial turbulence in the shear layer downstream of the expansion plane, thus increasing turbulence production. The maximum values of normal Reynolds stresses pertained to the non-Newtonian solutions and the eddy size was reduced by a factor of 20% relative to the water flows.

ACKNOWLEDGEMENTS

The authors would like to thank the financial support of the Stichting Fund of Schlumberger, of project PBIC/CEG/2427/95 of the Portuguese Research Council JNICT and the laboratories of INEGI- Instituto de Engenharia Mecânica e Gestão Industrial- where the whole work was carried. The authors are listed alphabetically.

REFERENCES

- Berman, N. S. and Tan, H. 1985. Two-component Laser-Doppler Velocimeter Studies of Submerged Jets of Dilute Polymer Solutions. *A. I. Ch. E. J.*, vol. 31, pp 208-215.
- Castro, O. S. , and Pinho, F. T. 1995. Turbulent Expansion Flow of Low Molecular Weight Shear-Thinning Solutions. *Exp. in Fluids*, vol. 20, pp. 42-45.
- Escudier, M. P., Gouldson, I. W., and Jones, D. M. 1995. Flow of Shear-Thinning Fluids in a Concentric Annulus., *Exp. in Fluids*, vol. 18, pp 225-238.
- Gyr, A. and Bewersdorff, H.- W. 1995. Drag reduction of turbulent flow by additives. Fluid Mechanics and Its Application Series, Kluwer Academic Publishers.
- Khezzar, L. 1985. An experimental study of flows through round sudden expansions. Imp. College of Science and Technology, Mech. Eng. Dep., Fluids Section Report, London.
- Laufer, J. 1954. The structure of turbulence in fully developed pipe flow. National Bureau of Standards, Report 1154.
- Lawn, C. J. 1971. The determination of the rate of dissipation in turbulent pipe flow. *J. Fluid Mech.*, vol. 48, pp 477-505.
- Pak, B., Cho, Y. I., and Choi, S. U. S. 1990. Separation and Reattachment of Non-Newtonian Fluid Flows in a Sudden Expansion Pipe. *J. Non-Newt. Fluid Mech.*, vol. 37, pp. 175-199.
- Pak, B., Cho, Y. I., and Choi, S. U. S. 1991. Turbulent Hydrodynamic Behaviour of a Drag- Reducing Viscoelastic Fluid in a Sudden Expansion Pipe. *J. Non-Newt. Fluid Mech.*, vol. 39, pp. 353-373.
- Pereira, A. S. and Pinho, F. T. 1994. Turbulent Pipe Flow Characteristics of Low Molecular Weight Polymer Solutions. *J. Non-Newt. Fluid Mech.*, vol. 55, pp 321-344.
- Pinho, F. T., and Whitelaw, J. H. 1990. Flow of Non-Newtonian Fluids in a Pipe. *J. Non-Newt. Fluid Mech.*, vol. 34, pp. 129-144.
- Pronchick, S. W., and Kline, S. J. 1983. An Experimental Investigation of The Structure of Turbulent Reattachment Flow Behind a Backward- Facing Step, *Report MD-42*, Thermosciences Div., Mech. Eng. Dept., Stanford University.
- Stieglmeier, M. and Tropea, C. 1992. A Miniaturized, Mobile Laser- Doppler Anemometer, *Applied Optics*, vol. 31, pp. 4096.
- Virk, P. S., Mickley, H. S. and Smith, K. A. 1970. The Ultimate Asymptote and Mean Flow Structure in Tom's Phenomena. *J. Appl. Mech.*, vol. 37, pp. 488-493.

PIV MEASUREMENTS OF TURBULENCE STATISTICS IN THE THREE-DIMENSIONAL FLOW OVER A SURFACE-MOUNTED OBSTACLE

J.M.M. Sousa¹, C. Freek² and J.C.F. Pereira¹

¹ Instituto Superior Técnico/Technical University of Lisbon, Mechanical Engineering Department,
Av. Rovisco Pais, P-1096 Lisboa Codex, Portugal

² Volkswagen AG, Research and Development, EZMM-1785, D-38436 Wolfsburg, Germany

ABSTRACT

The primary objective of this work is to show that Particle Image Velocimetry (PIV) can be used to provide reliable turbulence measurements in flows where homogeneous directions do not exist. As in any other measuring system based on sampling, the key to the success of such procedure lies in the acquisition of a statistically large number of samples. The use of compression of digital PIV images strongly facilitates this task.

In the present work, the flow over a surface-mounted cube is studied employing digital PIV. Turbulence data is computed by ensemble averaging, based on 2000 PIV images acquired at a frequency of 25-Hertz. Instantaneous views of the flow field provide additional information regarding large-scale dynamics of turbulent structures.

1. INTRODUCTION

Experimental studies of the flow over sharp-edged obstacles mounted in channels have been mainly focused on two-dimensional geometries. These are obviously easier to handle and, consequently, there already exist a large number of reported investigations on two-dimensional surface-mounted obstacles. In contradistinction, quantitative data for turbulent flows over three-dimensional obstacles are still scant. Nevertheless, a very significant amount of information on the topology and turbulent characteristics of the flow around cuboids with various shapes has been provided by Castro and Robins (1977) and Hunt *et al* (1978), for a boundary-layer-type of approach flow, and by Martinuzzi and Tropea (1993), for plane channel flow. Despite their geometrical simplicity, these flows exhibit remarkable topological complexity,

making them very attractive to basic fluid mechanics researchers. On the other hand, the dynamics of large-scale turbulent structures, typically present in the aforementioned type of flows, is a matter of potential practical application in various engineering processes.

As a rule in the assessment of turbulent flow characteristics, a statistical analysis is required when employing any measuring device based on a sampling procedure. Regardless of the fact that Particle Image Velocimetry (PIV) has been traditionally used in the characterization of instantaneous flow patterns, this technique does not constitute an exception to that rule when the aim is to quantitatively describe a turbulent flow. It must be noted that very few attempts have been made in this direction in virtue of the large quantity of data involved in such a statistical analysis of PIV images. However, Freek *et al* (1997) have recently shown that Digital Image Compression can be successfully applied as a sensible solution to abate the inherently high data stream and storage requirements. As a result, full statistical characterization of turbulent flows may be easily accomplished, retaining all the advantages of PIV techniques.

The recent awakening of numerical researchers towards the application of Large Eddy Simulation (LES) to complex geometries has also set an urgent need for detailed experimental data on test cases that may be successfully tackled by this technique. This fact is substantiated by the organization of a number of workshops, such as the "Workshop on Large Eddy Simulation of Flows past Bluff Bodies" by Rodi *et al* (1997) and the "Sixth ERCOFTAC/IAHR/COST Workshop on Refined Flow Modelling" by Hanjalic and Obi (1997). It follows that the requirements on experimental data to validate LES (spatial resolution, temporal resolution, ...) can, in general, be easily met by PIV. As a consequence, a fruitful symbiosis will

certainly be established between these two techniques in a near future.

In the present work, turbulence statistics are calculated from PIV measurements in the three-dimensional flow over a cube mounted on the floor of an open-surface water channel. Instantaneous views of the flow field are presented as well. Section 2 provides information regarding the experimental setup. The results are shown in Section 3. Finally, Section 4 summarizes the main findings of this investigation.

2. EXPERIMENTAL ARRANGEMENT

The unperturbed flow at the test section was a turbulent boundary-layer characterized by a Reynolds number based on momentum thickness $Re_\theta = 770$. The mass flow rate recirculated inside the channel produced a surface velocity $U_o = 0.07$ m/s. A detailed description of the open-surface (water) channel facility employed in these experiments was given by Freek *et al* (1997). The surface-mounted obstacle was a 4-cm cube made of Perspex. Thus, the presently investigated obstacle flow was characterized by a Reynolds number $Re_L = 3210$.

The digital PIV system employed to map the flow field is based on CCD camera recording and Ar-ion laser illumination. MJPEG compression of PIV images is also implemented with the aim of easing the handling of large quantities of data. A thorough description of the present system as well as a meticulous discussion on the advantages and pitfalls of using MJPEG compression was presented by Freek *et al* (1998).

A sequence containing 2000 PIV images was collected at the channel centerplane in the test section area, as shown in Figure 1. Digital image compression allowed on-line recording of the data at a sampling frequency of 25-Hertz (only 80 seconds to acquire all the data), maintaining storage needs low. Flow maps were obtained by off-line processing of PIV images interrogated in sub-images of size $IA = 32 \times 32$ pixels. The spacing between interrogation windows was prescribed as 16 pixels (i.e., a 50% IA overlap), producing 47×35 vectors per vector field. An overview of relevant experimental parameters is shown in Table 1.

Turbulence statistics were calculated by using single-point, ensemble averaging. Following Raffel *et al* (1998), the total measurement error in displacement PIV vectors can be written as the sum of a bias error ϵ_{bias} and a measurement uncertainty ϵ_{rms} (random error). Unbiased values of the correlation function were obtained by dividing out the corresponding weighting

factors prior to estimation of fractional displacement, as suggested by Westerweel (1993). A Gaussian estimator of fractional displacement was used to achieve sub-pixel accuracy, leading to negligible values of *rms* tracking error associated with the estimator. The use of high seeding densities has also allowed minimizing the error due to the presence of displacement gradients in the images. Additionally, spurious measurements were removed from all vector

Channel:			
type	open-surface		
length	2.5	m	
width	0.20	m	
Flow:			
fluid	water		
temperature	28	°C	
depth	0.11	m	
surface velocity, U_o	0.07	m/s	
obstacle height, L	0.04	m	
Reynolds number, Re_θ	770		
Reynolds number, Re_L	3210		
Seeding:			
type	polyamid		
nominal diameter	60	µm	
Illumination:			
type	light sheet		
source	cw Ar ⁺ laser + Bragg cell		
maximum power	5	W	
thickness	1	mm	
pulse separation	10	ms	
number of exposures	2		
Recording:			
type	electronic (CCD)		
resolution	576 x 768	px	
lens focal length	26	mm	
numerical aperture	2.0		
image magnification	0.21		
image compression	5.5		
Interrogation:			
resolution, IA	32 x 32	px	
spacing	16	px	
multi-grid levels	2		
Data set:			
vectors/image	1645		
images/data set	2000		
size	160	Mb	

Table 1 Summary of relevant experimental parameters fields employing a median-based procedure similar to that indicated by Westerweel (1994). Increased values of dynamic spatial range and data yield have been

obtained by the implementation of window offset coupled with a multi-grid/pass procedure (see, e.g., Raffel *et al*, 1998). This has allowed further reductions in measurement noise. Nevertheless, the statistical evaluation of turbulent flow quantities introduces additional uncertainties. Based on the analysis proposed by Yanta and Smith (1973), the statistical uncertainties in mean and variance values for a 95% confidence level can be quantified as 0.4% and 3%, respectively.

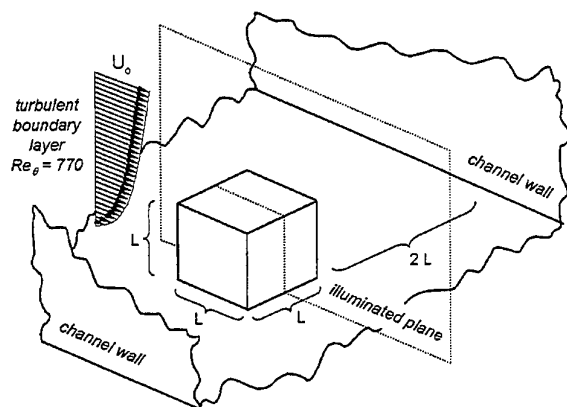


Fig. 1 Geometry of test section and measured plane

3. RESULTS

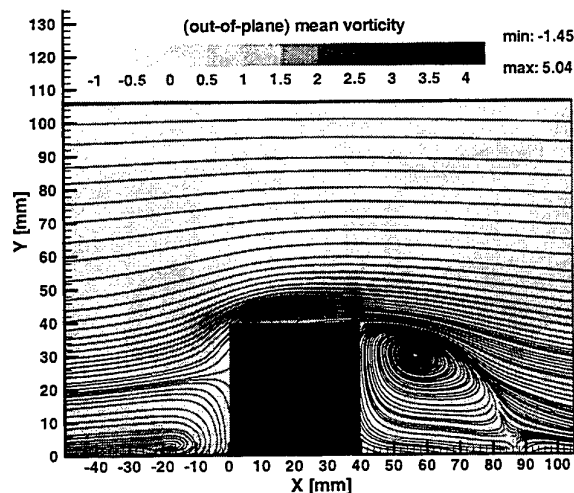
First, the mean flow topology obtained by the application of the digital PIV system is analyzed. All flow quantities have been non-dimensionalized using U_0 and L , respectively as velocity and length scales. Figure 2 shows the mean flow streamlines in the measured plane, computed from U - and V -velocity components. The overall mean streamline pattern agrees satisfactorily with the sketches reported by Hunt *et al* (1978). Differences in complexity, namely with respect to the horseshoe vortex system, can be attributed to distinct characteristics of the approaching boundary-layer flow. The present experiments have been carried out at a much lower Reynolds number and the obstacle was totally immersed in the boundary-layer, which markedly differs from the flow conditions indicated by the aforementioned authors. Surprisingly, better agreement was found between the presently studied flow field and that corresponding to a surface-mounted cube placed in a turbulent channel flow. The latter geometry was investigated in detail by Larousse *et al* (1991) and by Martinuzzi and Tropea (1993), utilizing laser-Doppler anemometry (LDA) and flow visualization. Yet, they could not find any evidence

supporting the existence of the hierarchy of horseshoe vortices reported by Hunt *et al* (1978) either, which is in accordance with the flow features depicted in Figure 2. Even the secondary corner vortex (upstream the obstacle) is not clearly observed in the figure, due to the small dimensions displayed by this structure at low Reynolds number.

A direct comparison between the detailed LDA mean flow maps provided by Larousse *et al* (1991) and the mean streamline pattern represented in Figure 2 enhances the main difference between these two flows. It essentially results from the strong flow acceleration promoted by the sudden contraction (2:1) formed by the obstacle and the top channel wall in the former case. As a consequence, the size of separated flow regions over and behind the cube is significantly smaller for a boundary-layer-type of approach flow. Additionally, the corresponding vortex core centers are located closer to bottom walls in this case also.

Fig. 2 Mean streamline pattern and vorticity contours

Contours of the out-of-plane component of vorticity have been superimposed to mean flow streamlines in Figure 2. It must be noted that the calculation of vorticity involves differentiation of basic flow quantities. However, vorticity estimates were obtained here by employing Stokes' theorem of circulation (see, e.g., Raffel *et al*, 1998), which seemed to perform better than conventional schemes. Important values of positive vorticity were found in the separated shear-layers formed over and behind the obstacle. It can be seen that the area of the horseshoe vortex is not



characterized by large values of mean vorticity, which indicates that this mean flow structure is not very intense at the present Reynolds number.

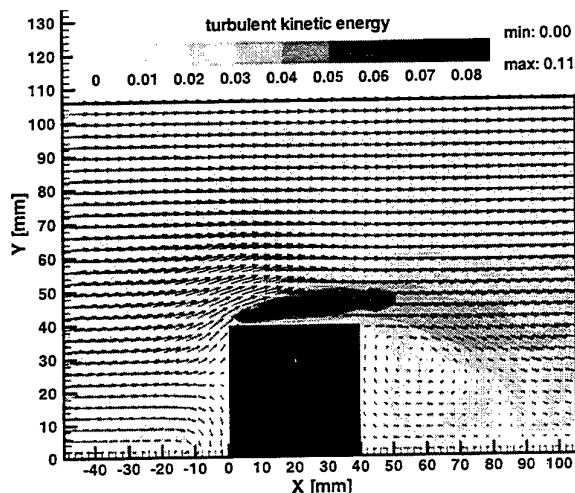
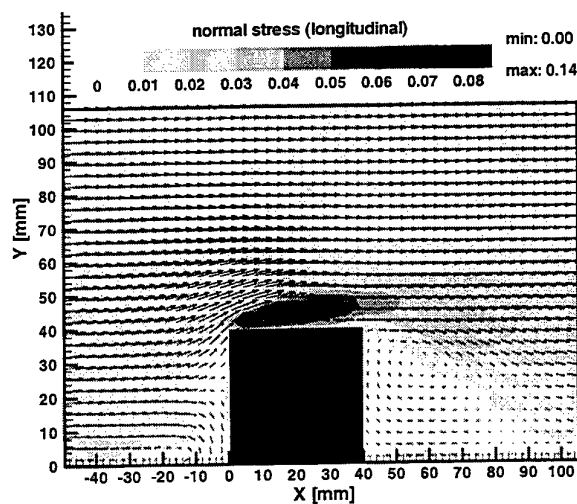
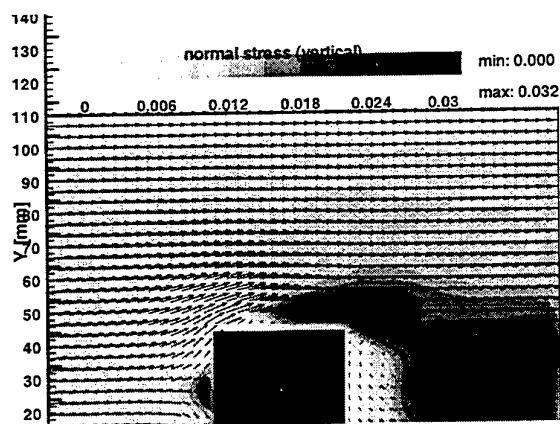


Fig. 3 Contours of turbulent kinetic energy

The maxima in turbulent kinetic energy were also found in the separated shear-layers, as shown in Figure 3. In order to keep track of the relative position of mean flow structures, contours maps are presented here simultaneously with mean velocity vectors (this procedure will be used throughout the remainder of the paper). It must also be mentioned that, as only in-plane quantities were measured by the PIV system, the values of turbulent kinetic energy in the flow were estimated by the use of the following expression:

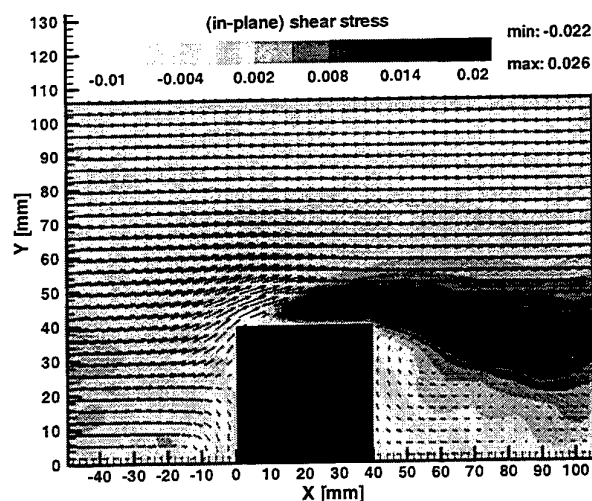
$$k = \frac{3}{4} (\overline{u'^2} + \overline{v'^2}). \quad (1)$$

The contribution of normal-stresses $\overline{u'^2}$ and $\overline{v'^2}$ to k is depicted in Figures 4a and 4b, respectively. It can be seen that, while the longitudinal component of normal-stresses reaches peak magnitudes in the first stages of development of the separated shear-layer over the cube, the vertical component is characterized by moderate values in this area. The intense mean shear established as the fluid flows over the obstacle is the main responsible by the large values associated with the longitudinal component. In contradistinction, the vertical component reaches its peak values (always



smaller than those for the longitudinal component) farther downstream, essentially as a result of large-scale unsteadiness. This observation will be further substantiated later in the paper. Thus, two major sources of large-scale structures can be identified in the flow field, corresponding to the recirculation

Fig. 4 Contours of Reynolds-stresses: a) and b) normal-stress components; c) shear-stress



regions over and behind the cube. Again, little energy seems to be contained in the flow structures defining the horseshoe vortex upstream the obstacle. The contours of (in-plane) shear-stress corroborate the above assertions (see Figure 4c). Two large local maxima can be found slightly upstream the peaks in the vertical component of normal-stresses, indicating intense turbulence production in these areas. Consequently, it seemed reasonable to conclude that very organized motions can be found there, leading to

highly correlated u - and v -velocity fluctuations. On the other hand, it is also interesting to note that a sharp peak of negative shear-stress occurs in the vicinity of the upper left corner of the cube.

Aiming to analyze some of the flow features with better detail, transverse profiles of mean and turbulent quantities, respectively at $X = 20$ mm and $X = 55$ mm (i.e., crossing the recirculation regions on top and behind the cube, respectively), have been represented in Figures 5a, 5b, 6a and 6b. These

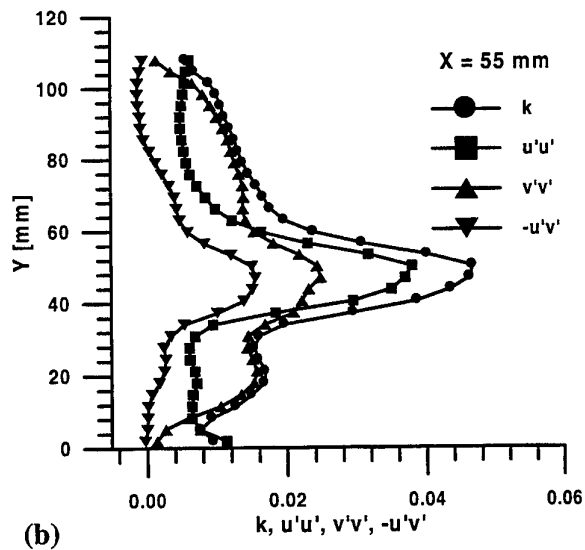
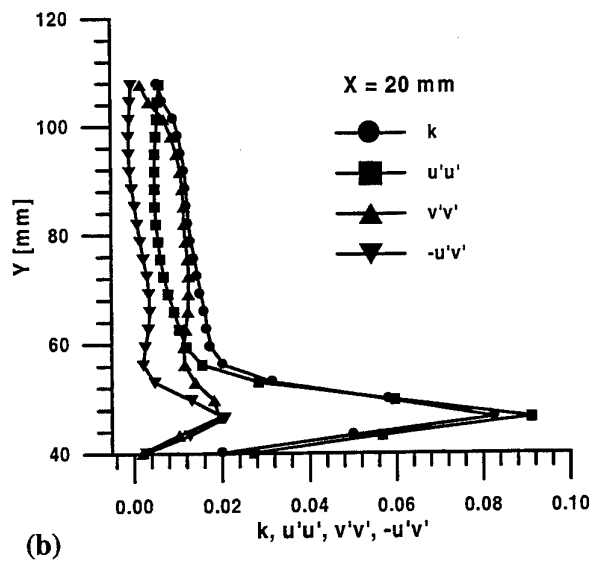
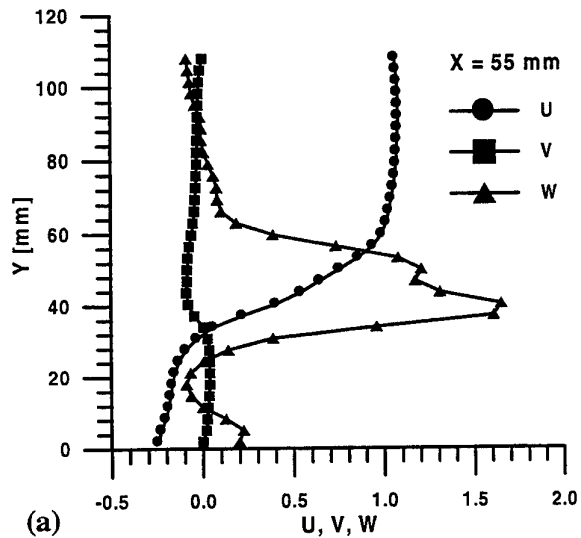
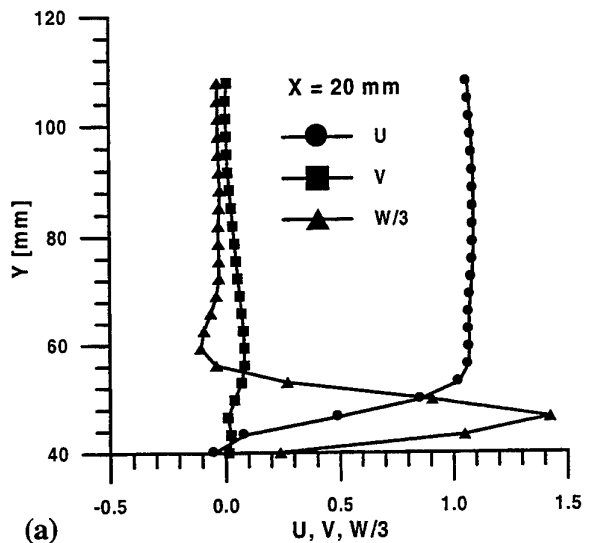


Fig. 5 Transverse profiles at $X = 20$ mm: a) mean velocities and vorticity; b) turbulent kinetic energy and Reynolds-stresses

Fig. 6 Transverse profiles at $X = 55$ mm: a) mean velocities and vorticity; b) turbulent kinetic energy and Reynolds-stresses

profiles also facilitate a discussion of the results with reference to measurements reported in the literature.

As noted before, Figure 5a shows that the flow acceleration over the cube is much more modest in the present flow configuration than in channel flow, which naturally influences the strength of the recirculation eddy traversed by this profile. At this location ($X = L/2$), Martinuzzi and Tropea (1993) measured longitudinal velocities that were about 30% in excess of the reference velocity. Additionally, the magnitude of reversed flow was reported to reach 50% of the reference velocity. Present values do not exceed 10% of the surface velocity in either case. Martinuzzi and Tropea (1993) did not compute the vorticity field. However, it is quite obvious that the aforementioned differences in longitudinal velocity component would be reflected by vorticity maxima as well (note that vorticity values have been scaled down to one third in Figure 5a, i.e., $W/3$, for the sake of figure clearness only). As immediate consequence of these smaller mean gradients, Reynolds-stresses levels in the separated shear-layer over the obstacle (see Figure 5b) are also characterized by lower values than in channel flow. Nevertheless, it is important to emphasize that all present peak values closely preserve the various ratios between Reynolds-stress components indicated by the above-referred LDA measurements (a scaling factor of approximately 3.5 was found). The foregoing result strongly supports the credibility of these PIV measurements of turbulence statistics.

A direct comparison for profiles located inside the recirculation region behind the cube is much more difficult, due to the difference in the values of reattachment length. The profiles shown in Figures 6a and 6b are located slightly upstream $X = 3L/2$ (where LDA data are available for channel flow), in an attempt to account for a smaller reattachment length. It is not surprising that, once again, the measured velocity excess in the longitudinal component is clearly lower than the characteristic values for channel flow reported by Martinuzzi and Tropea (1993). The maximum intensity of the reversed flow is, of course, larger in this area, but still limited to approximately 50% of the corresponding values obtained in channel flow. However, the main point of interest in Figure 6a is the "kinked" profile of mean vorticity, which indicates a multiple layer structure. An explanation for such shape can only be found by recognizing this feature as the reminiscence of the existence of two individual (separated) shear-layers. In fact, besides portraying the trend of convergence between the peak values of measured normal-stresses (again in total agreement with the findings for channel flow), Figure 6b also shows that the multi-layer structure is exhibited by the

vertical component of those stresses as well. It should be mentioned that this feature can also be detected in some of the LES calculations performed by M. Breuer in the framework of the "6th ERCOFTAC/IAHR/COST Workshop on Refined Flow Modelling" (Hanjalic and Obi, 1997).

As earlier asserted in this paper, organized large-scale motions associated with vortex-shedding

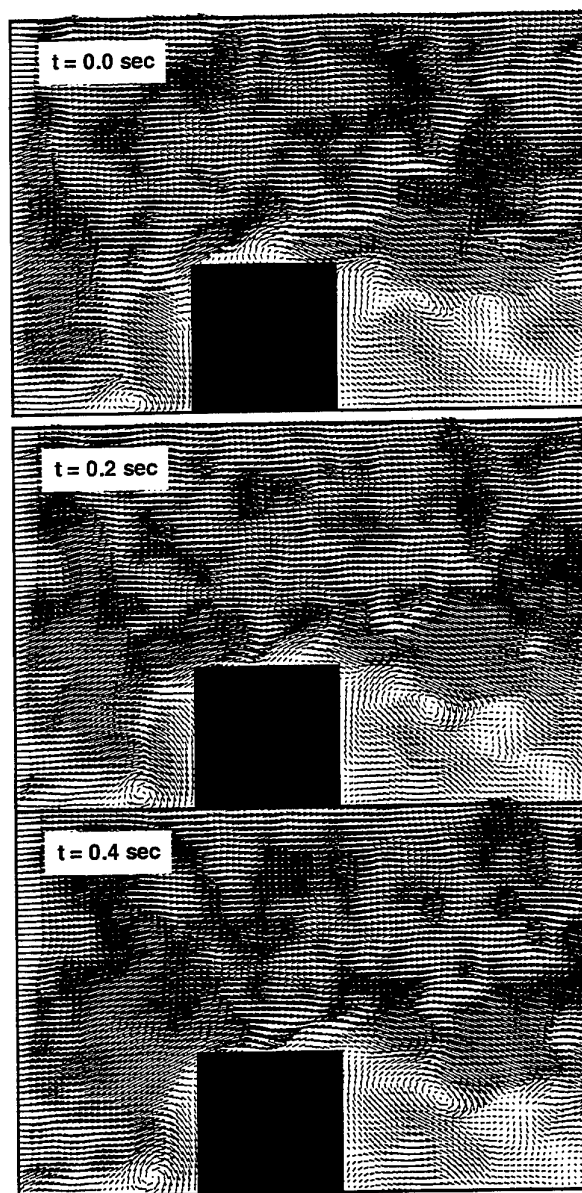


Fig. 7 Sequence of snapshots showing the formation of organized large-scale motions (75% IA overlap)

from recirculation regions are in the origin of the process. Figure 7 illustrates the formation of notably coherent turbulent structures in a series of snapshots portraying instantaneous velocity fields (75% IA overlap was used). During the depicted time instants, one eddy drags over the top of the obstacle. The region in the back of the cube sheds another eddy, which is convected downstream closely following the path defined by the curved shear-layer. The vertical component of normal-stresses naturally receives an important contribution from these two "springs" of organized motions that, meeting in the near-wake of the obstacle, ultimately give rise to the establishment of a multi-layer structure in this area of the flow.

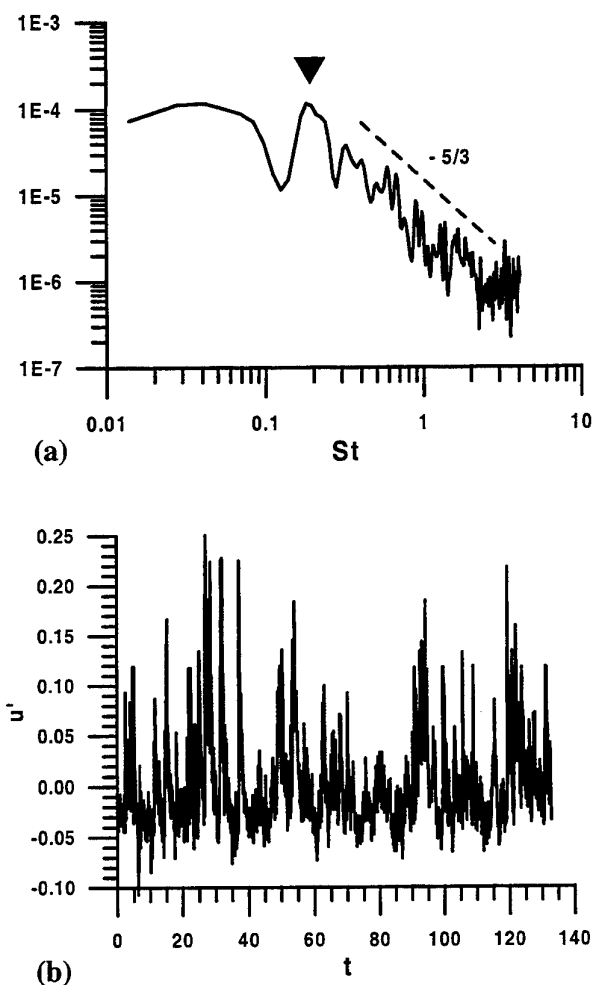


Fig. 8 Analysis of u' -velocity in the vicinity of the lower corner upstream the obstacle: a) power spectrum (power scale is arbitrary); b) time series

One may still note that the flow in the region of the horseshoe vortex is not quiescent either. However, the excursions traced out by the associated large-scale structures are rather limited in the present case, which explains the moderate values of Reynolds-stresses measured in this portion of the flow field. From this observation it can be inferred that, in contrast with the findings of Larousse *et al* (1991) for a much higher Reynolds number, the horseshoe vortex does not constitute here the dominant source of large-scale unsteadiness. In fact, the spectral analysis of a time series acquired in this area produces a broad peak, without bringing out any dominant frequency (Strouhal number in the graph). Figure 8a shows the above result and Figure 8b portrays the corresponding time-trace of the (fluctuating) longitudinal velocity component u' . Similar measurements taken in the separated shear-layer over the cube exhibited a bi-modal character in probability-density functions (PDF) of vertical velocity, heralding the appearance of a dominant frequency (or range of frequencies, as broadband behavior is also a characteristic of natural instability of free shear-layers; see Husain and Hussain, 1983).

In addition, a few more observations can be made regarding Figure 8. Firstly, one may note that a significant portion of the power spectrum in Figure 8a closely reproduces an evolution consistent with the so-called inertial sub-range of turbulence. Although good results have been obtained in the present flow, which was characterized by low fluid velocities, the sampling frequency imposed by the video system is a strong limitation for a more general application of this analysis. It becomes particularly stringent if we keep in mind that Adrian and Yao (1987) suggested that, as a guideline for LDA measurements, the mean data rate should be about twenty times the largest frequency at which undistorted measurements are desired. Secondly, the measured time-trace in Figure 8b firmly suggests that the PDF of the (fluctuating) longitudinal component of velocity at the indicated location must be strongly skewed. Aiming to investigate this issue in further detail, higher-order moments of the probability distributions were computed. The results have been expressed in non-dimensional form, in terms of skewness and kurtosis factors.

Figures 9a and 9b show contour maps of skewness factor, respectively for longitudinal and vertical velocity components. With respect to the former component, it can be seen that the bulk of the flow field is characterized by values close to zero, which corresponds to a normal random process. However, clearly negative values can be found in the separated shear-layer evolving over the obstacle, while even stronger positive values occur in a very limited

area in the vicinity of the lower corner upstream the cube. This last observation confirms the hypothesis formulated in the previous paragraph. Concerning the latter component of velocity (see Figure 9b), it can be seen that the maximum levels of positive skewness are always more modest than those observed in Figure 9a.

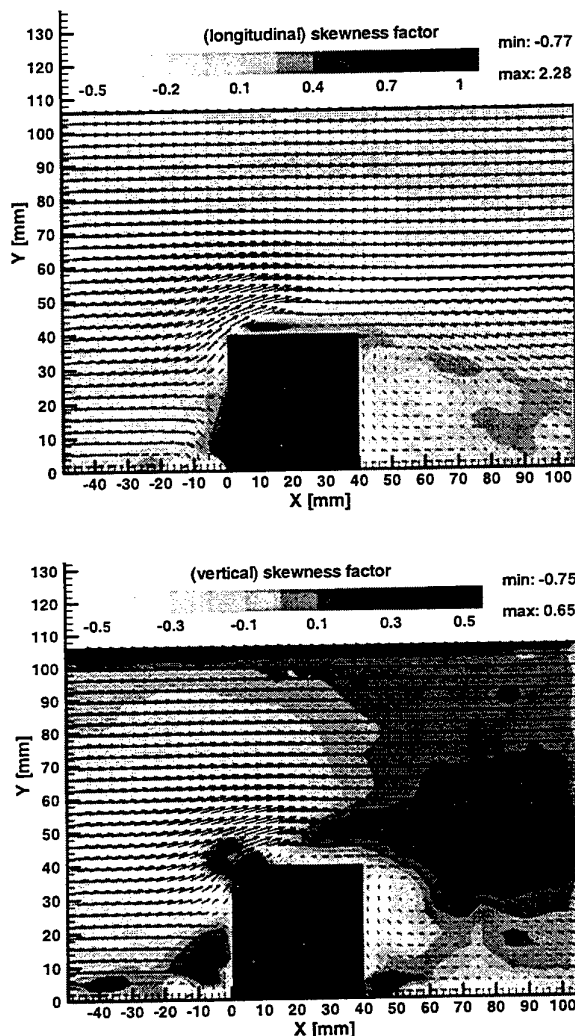


Fig. 9 Contours of skewness factor: a) longitudinal velocity; b) vertical velocity

The contour maps of kurtosis factor are shown in Figures 10a and 10b, respectively for longitudinal and vertical velocity components. Contour levels have been chosen with the aim of evincing the so-called "excess". For this reason, the scale of contour levels always starts at the value reflecting a normal random process (i.e., at the value of three). Consistently with the observations made for the skewness factor of

longitudinal velocity distributions, very large values of "excess" can also be found in the lower corner upstream the cube. On the other hand, with respect to vertical velocity component, the regions of maximum "excess" are located inside the back recirculation zone adjacent to the reattachment at the wall (negative skewness; see Figure 9b) and encircling the front edge of the obstacle (essentially positive skewness). Naturally, for both velocity components, large values of kurtosis are always observed where extreme values (negative or positive) of skewness occur.

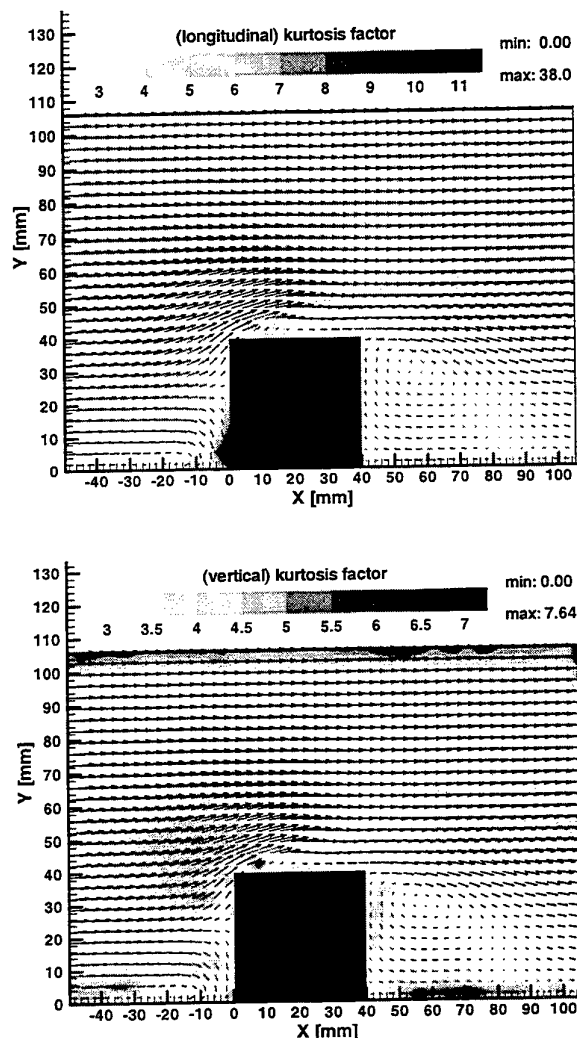


Fig. 10 Contours of kurtosis factor: a) longitudinal velocity; b) vertical velocity

From the viewpoint of a statistical description of turbulent flows, the main advantage of PIV over LDA probably resides in the fact that the former technique

may readily provide estimates of spatial correlations. In the present study, some estimates of Taylor microscales have been obtained. Hence, an assessment of the size of the eddies mainly responsible for dissipation in the flow under investigation could be carried out. The definition of the various dissipation scales is given, e.g., by Hinze (1975). In this paper, only λ_{fu} and λ_{gu} were evaluated, using the following

$$\lambda_{fu}^2 = \frac{\overline{2u'^2}}{\left(\frac{\partial u'}{\partial x}\right)^2}; \quad \lambda_{gu}^2 = \frac{\overline{2u'^2}}{\left(\frac{\partial u'}{\partial y}\right)^2}. \quad (2)$$

The results obtained for these two quantities are shown in Figures 11a and 11b. At this stage, one should recall that the reference scale employed here in the non-dimensionalization of lengths was $L = 0.04$ m. A general conclusion drawn from the examination of the contour maps is that the spatial resolution set in the interrogation of the video images ($\Delta x = \Delta y \approx 0.08$) seems adequate. However, this fact was confirmed "a posteriori" only. Additional findings can be deduced through a closer inspection of the aforementioned figures. Namely, it can be seen that, as expected, a good correlation can be found between the locations where λ_{fu} reaches minimum magnitudes and the areas where peak values of negative shear-stress were measured. The minima of λ_{gu} occur in the vicinity of the edges of the cube and in the area where the separated shear-layer develops over the obstacle. It is also interesting to note that the strong decrease in the measure of the latter dissipation scale over the obstacle, mainly as a result of longitudinal stretching, is accompanied by the formation of a very localized area of large λ_{gu} in the precise location where the minimum in shear-stress was found (see Figure 4c). Finally, Figure 12 illustrates the spatial distribution of

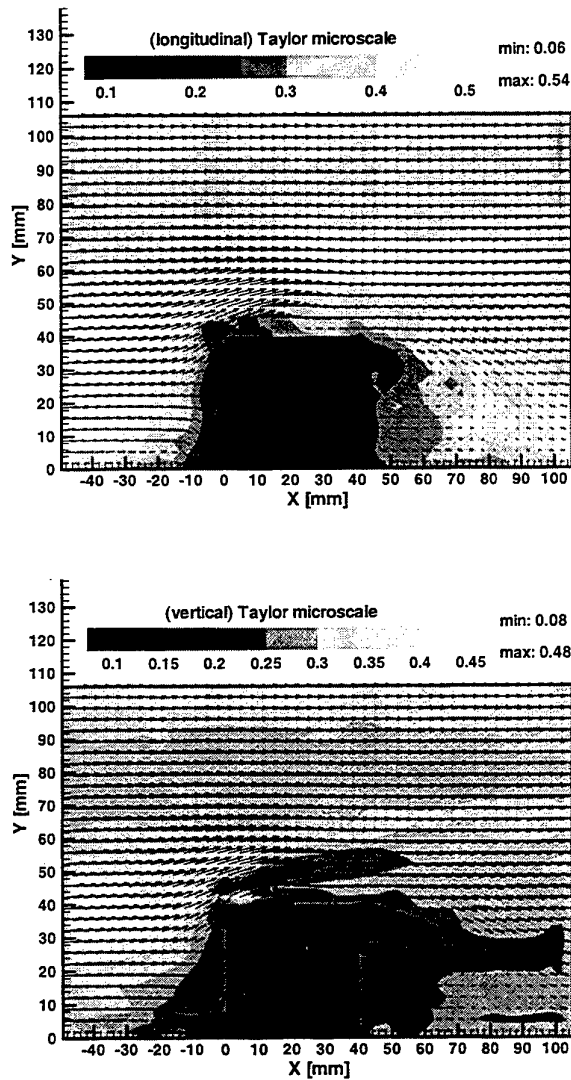


Fig. 11 Contours of magnitude of Taylor microscales: a) λ_{fu} ; b) λ_{gu} expressions:

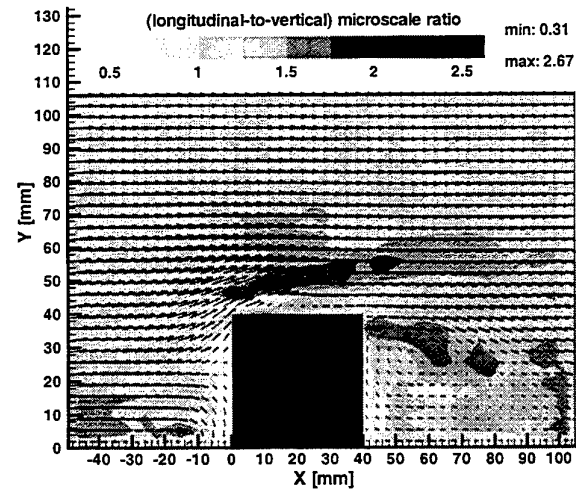


Fig. 12 Contours of the ratio $\lambda_{fu} / \lambda_{gu}$. The contour map shows that, except for the regions where shear-layers are present,

the values are not far from the known relation for isotropic turbulence, i.e., $\lambda_f = \sqrt{2}\lambda_g$. In fact, it can be seen that this ratio becomes notably different from the aforementioned value only in areas dominated by attached shear-layers (smaller) and separated shear-layers (larger). The maximum magnitude can be found in the separated shear-layer developing over the cube.

4. CONCLUSIONS

The turbulent flow over a cubical obstacle mounted in the bottom of an open-surface, low-Reynolds number, water channel was thoroughly investigated. A digital PIV system employing MJPEG image compression was the tool that allowed whole-field quantification of turbulence characteristics in the centerplane of the channel, namely, mean velocities and vorticity, Reynolds-stresses, skewness factors, kurtosis factors and Taylor microscales. The study of the time-dependent characteristics of the flow was carried out using spectral analysis of time series and visualization of large-scale dynamics of turbulent structures.

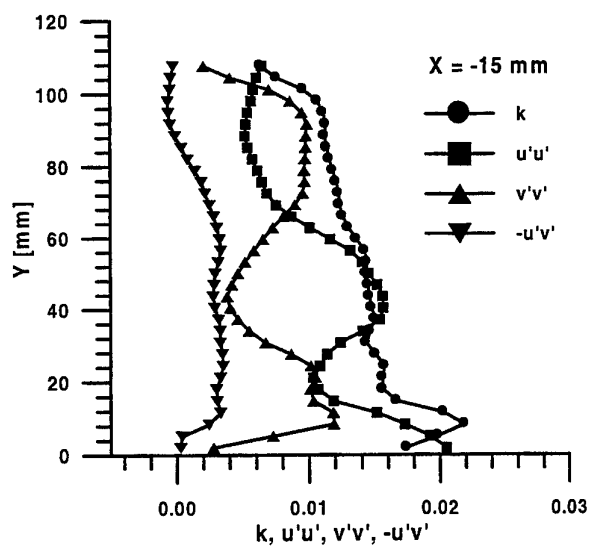
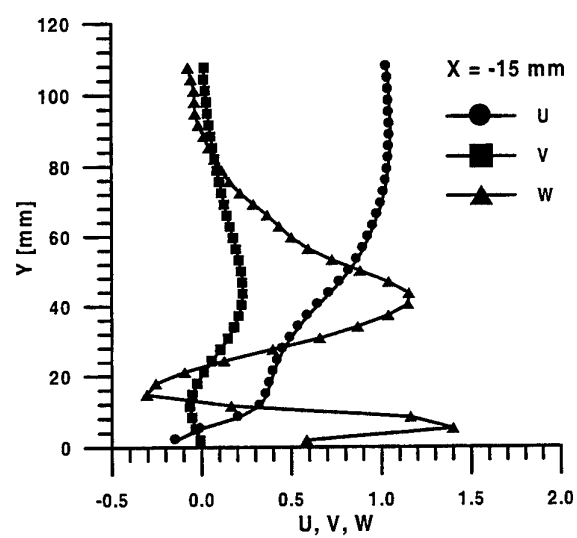
The feasibility of using digital PIV in the statistical investigation of turbulent flows without homogeneous directions was demonstrated in the paper. Furthermore, a detailed characterization of turbulence statistics allowed bringing out additional insight about turbulent flows over surface-mounted, sharp-edged obstacles.

PIV recordings of a complete set of planes distributed around the obstacle are currently under analysis. These results will be presented in a forthcoming paper.

REFERENCES

- Adrian, R.J. & Yao, C.S. 1987, Power Spectra of Fluid Velocities Measured by Laser Doppler Velocimetry, Exp. Fluids, vol. 5, pp. 17-28.
- Castro, I.P. & Robins, A.G. 1977, The Flow Around a Surface-Mounted Cube in Uniform and Turbulent Streams, J. Fluid Mech., vol. 79, pp. 307-335.
- Freek, C., Sousa, J.M.M., Hentschel, W. & Merzkirch, W. 1997, Digital Image Compression PIV: a Tool for IC-Engine Research, Proc. 7th Int. Conf. on Laser Anemometry Advances and Applications, Karlsruhe, pp. 455-464.
- Freek, C., Sousa, J.M.M., Hentschel, W. & Merzkirch, W. 1998, On the Accuracy of an MJPEG-based Digital Image Compression PIV-system, submitted to Exp. Fluids.
- Hanjalic, K. & Obi, S. 1997, Flow Around a Surface-Mounted Cubical Obstacle, Proc. 6th ERCOFTAC/IAHR/COST Workshop on Refined Flow Modelling, Delft, vol. 4.
- Hinze, J.O. 1975, Turbulence, McGraw-Hill.
- Hunt, J.C.R., Abell, C.J., Peterka, J.A. & Woo, H. 1978, Kinematical Studies of the Flows Around Free or Surface-Mounted Obstacles; Applying Topology to Flow Visualization, J. Fluid Mech., vol. 86, pp. 179-200.
- Husain, Z.D. & Hussain, A.K.M.F. 1983, Natural Instability of Free Shear Layers, AIAA J., vol. 21, pp. 1512-1517.
- Larousse, A., Martinuzzi, R. & Tropea, C. 1991, Flow Around Surface-Mounted, Three-Dimensional Obstacles, Proc. 8th Symposium on Turbulent Shear Flows, Munich, vol. 1, pp. 14.4.1-14.4.6.
- Martinuzzi, R. & Tropea, C. 1993, The Flow Around Surface-Mounted, Prismatic Obstacles Placed in a Fully Developed Channel Flow, J. Fluids Engng., vol. 115, pp. 85-92.
- Raffel, M., Willert, C. & Kompenhans, J. 1998, Particle Image Velocimetry: a Practical Guide, Springer-Verlag.
- Rodi, W., Ferziger, J.H., Breuer, M. & Pourquié, M. 1997, Status of Large Eddy Simulation: Results of a Workshop, J. Fluids Engng., vol. 119, pp. 248-262.
- Westerweel, J. 1993, Digital Particle Image Velocimetry: Theory and Application, Ph.D. thesis, Delft University of Technology, the Netherlands.
- Westerweel, J. 1994, Efficient Detection of Spurious Vectors in Particle Image Velocimetry Data, Exp. Fluids, vol. 16, pp. 236-247.
- Yanta, W.J. & Smith, R.A. 1973, Measurements of Turbulent-Transport Properties with a Laser Doppler Velocimeter, 11th Aerospace Science Meeting, Washington, AIAA paper 73-169.

PLOTS NOT USED IN THE PAPER



TURBULENCE ANALYSIS ON THE BFS WITH ITERATIVE MULTIGRID PIV IMAGE PROCESSING

F. Scarano⁺, M. L. Riethmuller

von Kármán Institute for Fluid Dynamics, Chaussée de Waterloo 72
1640-B Rhode-St-Genèse, Belgium

ABSTRACT

An advanced PIV processing technique is applied to investigate the turbulent flow over a Backward Facing Step (BFS). This constitutes a traditional test case for experimental techniques and for numerical codes development. The results are compared with Direct Numerical Simulation (DNS) and LASER Doppler Velocimetry (LDV) data available on the subject.

The work proposes an appropriate algorithm to evaluate the PIV recordings. This procedure performs a local relative displacement of the areas to be correlated and optimises it with an iterative procedure. The local particle displacement, due to the in-plane motion, is compensated by means of such a discrete offset.

Moreover, during the iterative procedure the size of the interrogating areas is gradually reduced yielding a finer resolution in space if compared with one step interrogation methods.

A brief section explains the expected improvements in terms of dynamic range and resolution. The accuracy is assessed analysing images with imposed displacement.

1. INTRODUCTION

To perform PIV measurements in turbulent flows, it is necessary to reach a resolution in space that will allow the small scales of the turbulence spectrum to be detected. In addition to this, a high accuracy is required to correctly measure the small velocity fluctuations. Finally, in order to determine the statistical flow properties, it is necessary to acquire and analyse a large number of images.

To fulfil the first requirement, the primary step is to reduce as much as possible the size of the interrogation areas where the cross-correlation is to be calculated.

The problem of loss-of-pairs as shown by Keane and Adrian (1991) strongly limits the possibility of

reducing the size of the interrogation areas once the time interval Δt between the subsequent acquisitions is chosen.

The displacement of the second exposure interrogation area as already proposed by Keane and Adrian (1993) and further deeply analysed by Westerweel et al. (1997) allows to retrieve most of the particle image pairs lost for the in-plane motion.

Single-step processing methods are not appropriate to take advantage of the local displacement. Many works proposing advanced interrogation algorithms are iterative. Huang et al. (1993) and Jambunathan et al. (1997) proposed techniques for a complete compensation of the in plane motion, Keane et al. (1995) introduced the Super-Resolution concept with a coupled PIV/PTV algorithm. The present work proposes the application of a multigrid analysis to the PIV images.

The multiple interrogation with refinement of the window size allows maximising the spatial resolution for the cross-correlation analysis of images.

The separated flow over a BFS is frequently proposed as a test case for techniques under development as well as for code validation. This is motivated by the simple geometry, the stability of the separation region and the high turbulence levels experienced in the shear layer. The results of the present work are compared with DNS (Le et al. 1997) and LDV (Jovic and Driver 1994) available on this subject with a similar test configuration.

2. PIV ANALYSIS ALGORITHM

WIDIM stands for *Window Displacement Iterative Multigrid*. The ratio between the signal peak and the noise level in the correlation map is a crucial parameter in PIV measurements; it has already been found to be strongly dependent on the loss-of-pairs due to the in-

⁺ Also -DETEC- Department of Applied Energetics and Thermo-Fluid Dynamics to Environmental Control.
University of Naples - Facoltà di Ingegneria. Piazzale V. Tecchio, 80 I-80125 Napoli.

plane motion (Keane and Adrian 1993). Nevertheless as referred by many authors, other parameters also do contribute to the degradation of the signal like high velocity gradients, turbulent motion or loss-of-pairs due to out-of-plane motion. The present method has been conceived with the purpose of compensating for the loss-of-pairs due to in-plane motion. The correlating windows are provided with a degree of freedom in terms of pure translation one respect to the other.

A schematic of the situation is shown in figure 1: regions *a* and *b* correspond to the same physical area where particles are detected at two successive instants of time. Due to the motion some particles (black) present in *a* are no more included in *b* and some new particles (white) enter this last.

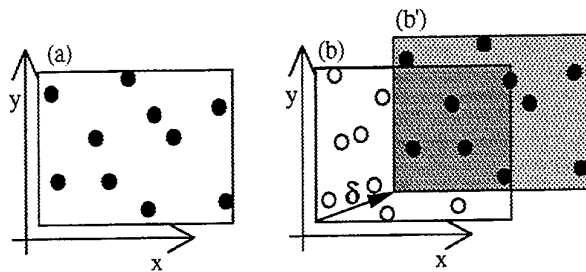


Fig.1-Principle of the window displacement.

The local displacement of each interrogation area (δ in fig. 1) is made on the basis of a flow pattern prediction. The predicted displacement, is obtained by the previous interrogation of the set of two images, therefore it is necessary to adopt an iterative procedure (fig.2).

Each iteration starts from a predicted displacement field (exception made for the first interrogation which is made with an appropriate window size) and yields a correction for this. At each iteration, the size of the interrogation areas is halved leading to the multigrid concept (fig. 3).

The displacement field is obtained as a sum of the predicted value and a small correction:

$$\delta(x, y) = \delta_p(x, y) + \delta_c(x, y) \quad (1)$$

In the first box the *windowing* consists in splitting each of the two pictures into sets of interrogation areas. In particular, the application of the displacement predictor on the second picture translates each window according to the distribution of $\delta_p(x, y)$. In the second box, the cross-correlation is applied and yields the correction distribution $\delta_c(x, y)$. The result is validated and can either constitute the final output, or the input for a new interrogation based on a finer grid. Hence the iterative form for eq. 1 is

$$\delta^k(x, y) = \delta_p^k(x, y) + \delta_c^k(x, y) \quad (2)$$

where the predictor is updated by the relation

$$\delta_p^{k+1} = \text{integer}(\delta^k) \quad (3)$$

At the start of the process, no information on the flow pattern is considered available and the first predictor is set uniformly to zero (no relative offset is applied). The window size for this interrogation is set respecting the *one quarter rule* for the in-plane motion (maximum in-plane displacement $< 1/4$ window linear size).

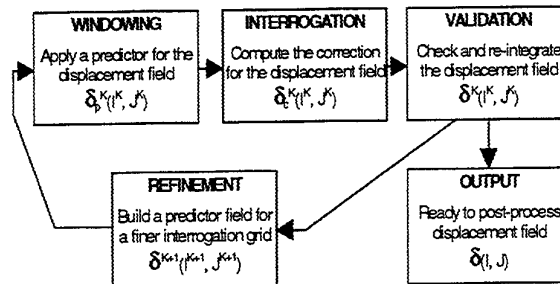


Fig.2-Image processing flow diagram.

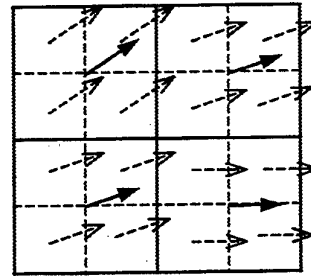


Fig. 3 –Coarse interrogation grid result (continuous line vectors and areas) and finer displacement predictor (dotted line vectors and areas).

After this interrogation, the coarse result (solid line arrows and windows in fig. 3) will be used as a predictor. A finer windowing is made halving the windows in both directions and the predictor is applied to the window offset by means of simple substitution of the previous iteration result.

As a consequence, in the subsequent steps the *one-quarter rule*, related to the in-plane displacement, does not limit anymore the size of the windows and the pictures can be interrogated with a better resolution.

The end of the process is reached when, after various refinements, the maximum possible resolution is achieved (according with the limits of application for the cross-correlation operator on PIV images).

2.1 Resolution And Dynamic Range

The main improvement obtained with this method consists in the de-coupling of two important parameters namely maximum in-plane displacement and interrogation window size. This last is no more

constant during the whole processing and a subscript will indicate the refinement step to which it is referred. The dynamic range of the technique refers to its ability to represent large velocity differences in the flow field. The lower end of the dynamic range is determined by the requirement that the corresponding displacement will be distinguished from the one corresponding to the noise level. Calling l_{min} such a minimum displacement that can be resolved, the consequent minimum measurable velocity is given by:

$$U_{min} = \frac{l_{min}}{\Delta t} \quad (4)$$

For single-step methods, the limit on the maximum measurable velocity is therefore related to the ratio c_1 between the maximum in-plane displacement l_{max} and the window linear size W_s

$$c_1 = \frac{l_{max}}{W_s} \quad (5)$$

Such a coefficient should not exceed values of 0.2~0.3 if a high confidence level is required in the measurement (Keane and Adrian 1993), thus:

$$U_{max} = \frac{l_{max}}{\Delta t} = \frac{c_1 \cdot W_s}{\Delta t} \quad (6)$$

Combining the expressions (4) and (6) one obtains:

$$\frac{U_{max} - U_{min}}{U_{min}} = c_1 \frac{W_s}{l_{min}} - 1 \quad (7)$$

This expression reads as the accuracy-resolution trade off. In fact, the dynamic range can be increased with a larger window size, but lowering the spatial resolution. Other authors (Adrian 1991, Willert and Gharib 1991) already investigated the dependence of l_{min} from the experimental parameters. It has been found to be associated with the particle image size, with the window size and, in digital PIV, with the type of sub-pixel interpolation that is used to determine the location of the correlation peak.

A typical value of $l_{min} = 0.1$ pixel can be assumed in agreement with Willert and Gharib (1993), (three-point gaussian fit, particle image two or three pixels diameter, displacements not exceeding 10 pixels and window size of 32x32 pixels). With the previous considerations eq.7 yields the following result: the choice of a window size of 32x32 pixels will allow distinguishing about 100 different velocity levels.

The method being presented aims at de-coupling space resolution and accuracy leading to a significant increase of the dynamic range of the technique.

Eq. 7 yields for the present case

$$\frac{U_{max} - U_{min}}{U_{min}} = \frac{l_{max}}{l_{min}} - 1 = \frac{c_1 \cdot W_0}{l_{min}} - 1 \quad (8)$$

where W_0 represents the window size at the first interrogation. A refinement ratio can be defined as

$$R(k) = \frac{W_0}{W_k} \quad k=1,2,\dots,K$$

Eq. 8 is rewritten as

$$\frac{U_{max} - U_{min}}{U_{min}} = \frac{l_{max}}{l_{min}} - 1 = \frac{c_1 \cdot R \cdot W_k}{l_{min}} - 1 \quad (9)$$

It is possible to appreciate that, fixed the window size, the dynamic range can be amplified in proportion with the refinement ratio R .

Moreover, the maximum displacement can even exceed the window linear dimension (exception made for the first iteration). Of course other factors may limit the maximum displacement: out-of-plane motions and/or high vorticity levels constitute the principal sources for loss-of-pairs. Huang et al. (1993) investigated the limitations in vorticity measurement with PIV and proposed an algorithm that compensates for the relative deformation between the two interrogation windows. Further developments of the current work will be directed to couple these corrections with the window refinement.

Comparisons with the performances of a basic interrogation method (see next sect.) showed that with the *WIDIM* algorithm the maximum displacement could be increased by a factor four ($R=4$ was achieved).

A further extension of the dynamic range is expected on the lower end too; previous studies conducted by Westerweel et al. (1997) demonstrated how the discrete window offset has a beneficial effect on the accuracy of the determination of the peak location in the cross-correlation analysis.

The above-cited authors found that for highly turbulent flows, the application of a discrete offset to window location yields a noise reduction (NR) of about three. Therefore the superposition of the extension of l_{max} and the refinement of l_{min} leads to a widening for the dynamic range of about one order of magnitude.

2.2 Accuracy Assessment

The procedure presented hereafter aims at analyzing the effect, on the measurement accuracy, of a compensation for the *in-plane* motion of the tracers. Starting from PIV images taken under ordinary experimental conditions, synthetic displacement fields were obtained for simulating uniform flows. The reason for this choice was to obtain information related as close as possible to the real experimental conditions. The first image is a real PIV image while the second image was obtained as a 45° shifted version of the first one. The seeding density in the light sheet is of about 15 (particles/mm²). To allow displacements of non-integer number of pixels, bilinear interpolation was applied to the first image.

A range of displacements from zero to ten pixels was covered with steps of 0.1 pixels.

After the displaced images were generated, the basic and advanced interrogation methods were applied. The results are compared with the expected data.

The correlation peak position is established using a three-point gaussian interpolation for both methods. Areas of 32 by 32 pixels overlapped for 50% of their extension were used as interrogation windows.

The average error relative to the WIDIM method exhibits an oscillation with a wavelength of one pixel. This behavior is caused principally by the averaging effect of the bilinear interpolation in the reconstruction of the second image. Fig. 4 shows the result of a moving average filter applied to the averaged patterns of the error. For the basic method, a bias error is present. The same is not found when the improved algorithm is applied. Even though such a bias does not exceed one tenth of a pixel, it leads to underestimate systematically the displacements. About this bias, Lecordier (1997) reports the presence of this effect comparing the cases of discrete window offset and sub-pixel window transformations. The asymptotic trend shows that even for large imposed displacements this component of the relative error does not vanish. One should therefore expect an increase of the absolute bias error with the displacement. The source for this can be found in the distortion of the peak shape due to the *loss-of-pairs*. The less the number of particles which contribute to build the correlation peak, the lower the corresponding intensity in the peak region.

A straight conclusion is that a higher level of accuracy can be reached enlarging the maximum displacement as much as possible.

The higher limit to the maximum displacement (viz. Δt) comes from other sources of error as the following ones: in presence of a non-zero acceleration level in the flow field, the error associated to the approximation of the Eulerian velocity in PIV is a linear function of the particle displacement (Boillot and Prasad 1996).

Out-of-plane motions cause loss-of-pairs and degradation of the signal peak (Keane, Adrian and Zhang 1995).

Loss-of-pairs is also due to strong vorticity levels in the flow (Huang, Fielder and Wang 1993).

Comparing the two patterns in fig 5 for the basic method, at the higher end of the analyzed range of displacements, the standard deviation can exceed one tenth of a pixel; while the value corresponding to the application of WIDIM keeps below 0.04 pixels.

Also in this case it has to be remarked that the periodic scattering has a main source in the degradation of the second image. This leads to overestimate the uncertainty level.

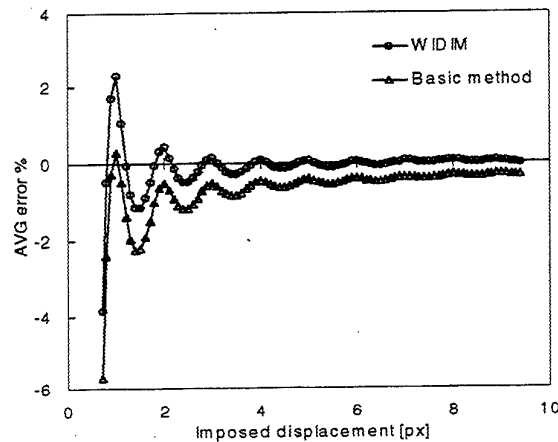


Fig. 4 - Measurement error: $U_{\text{meas}} - U_{\text{exact}} / U_{\text{exact}}$. DPIV results relative to a uniform spatial shift in both directions.

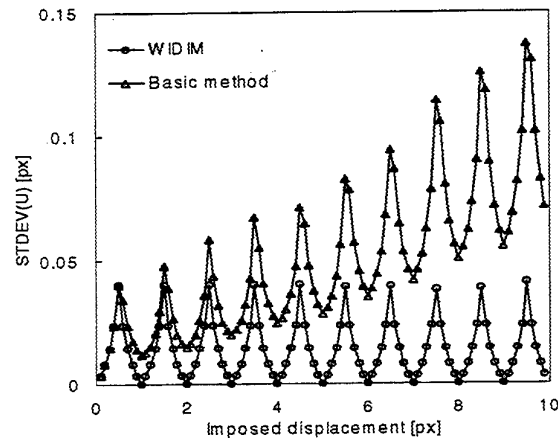


Fig. 5 - Measurement uncertainty: standard deviation of the measured displacement distribution.

3. EXPERIMENTAL INVESTIGATION

Fig. 6 shows a sketch of the experimental section.

The primary elements of the facility are:

- * the wind tunnel

- * the LASER cavities
- * the seeding device
- * the acquisition system

Wind tunnel and model

The experiments have been conducted in a VKI subsonic wind tunnel 20x20 cm² test section. An horizontal flat plate divides the test section into two channels: the backward facing step is installed in the upper channel (fig. 6).

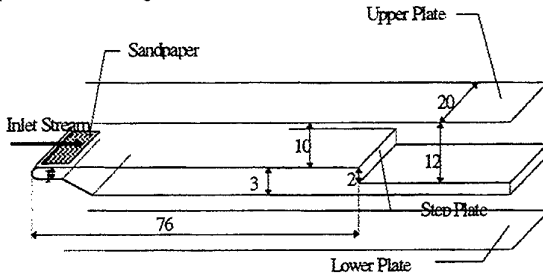


Fig. 6 - Geometry of the test section (quotes in cm).

The resulting test section is 20(w)x10(h) cm². The flow is supplied by a centrifugal fan driven by an asynchronous motor. Air is blown through filters into a settling chamber. The contraction ratio between the sections of this chamber and that of the wind tunnel is equal to 6. The nominal turbulence intensity at the inlet is of 0.3%.

At the leading edge of the flat plate, a rough sand paper is placed to trigger the transition of the boundary layer. The step occurs at 76 cm from the leading edge of the plate. The step height is $h=2$ cm. The expansion ratio is defined as:

$$ER = \frac{L_y}{L_y - h} \quad (10)$$

where L_y is the channel height downstream the step. For the present case $ER=1.2$.

The surface of the step and downstream of it is made of polished stainless steel in order to fulfill two needs: 1) to avoid that the laser beam penetrates into the Plexiglas, 2) to reflect the laser sheet back into itself. This also allows to increase the light intensity in the measurement region yielding a final enhanced contrast of the pictures.

LASER and optics

The light source was a double cavity pulsed Nd: Yag LASER. A 5mm diameter light beam passes through a first semi-cylindrical lens that opens the beam in the horizontal plane, then a spherical lens of appropriate focal length makes the light paths parallel to the optical axis, but it also concentrates the beam in the vertical plane. A second semi-cylindrical lens, turned at 90° from the first one, deviates the rays in parallel directions. The laser sheet, horizontal at first, is finally reflected vertically towards the test section by a prism.

Seeding device

A VKI built-in oil smoke generator has been used.

A nozzle sprays oil droplets on a hot plate (~150 C), the oil vaporizes, exits the chamber and enters the wind tunnel blower through a flexible pipe. The condensed oil droplets in the test section have a mean diameter of 1 μ m.

Acquisition system

To acquire, display and record digital images, use has been made of a commercial PIV system "INSIGHT", developed by TSI. The system is composed of: CCD video sensor (640x480pixels, 256 gray levels) able to acquire couples of images at a rate of 10 or 15 Hz; PC with acquisition board and equipped with a dedicated PIV software; LASER synchronizer.

3.1 Measurement Conditions

A sketch of the region over which the measurements have been performed is shown below.

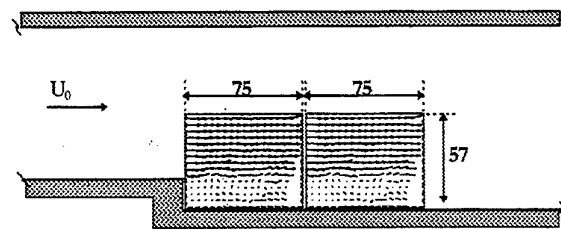


Fig. 7 - The two measurement areas (quotes in mm).

In order to reach a high resolution and to adapt the aspect ratio of the sensor FOV (4/3) to the one of the region of interest, it has been decided to split the acquisition over the entire measurement domain into two sessions pointing the sensor on two adjacent regions as shown in fig. 7. Adding together the data coming out of the two acquisitions all the region of recirculation has been investigated, including the region of reattachment.

The Reynolds number for this configuration is defined as:

$$Re_h = \frac{U_o \cdot h}{\nu} \quad (11)$$

During the experiments $Re_h=5000$, $U_o=3.8$ m/s and $\nu=1.52E-5$ m²/s.

The separation between the two LASER pulses has been chosen in order to obtain a relatively large particle displacement distribution between the two pictures.

This is a fundamental requirement to achieve a good accuracy. With a pulse separation of $\delta t=300$ μ s, the corresponding maximum displacement over the whole field was of about ten pixels.

4. RESULTS

Since the PIV technique is a field measurement technique, it can yield data sets comparable to the ones

coming from the most recent and sophisticated computational techniques.

In the following paragraphs the results of the PIV measurements will be presented and a special attention is devoted to the quantitative comparison of the experimental data with the ones coming from DNS (Le et al.) and from LDV (Jovic and Driver) who studied the same case.

Inlet conditions

The mean inlet velocity and the turbulence intensity profiles have been experimentally determined by means of Hot Wire measurement ($x = -3h$). The boundary layer thickness was found to be $\delta_{99}=1.2h$ with a maximum turbulence intensity level $TI_b=0.11$ inside the BL and a free stream level $TI_\infty=0.008$. These values

find a good correspondence with both DNS and LDV inlet data.

Processing parameters

The processing of the acquired images makes use of a three point gaussian interpolation for the estimation of the peak location with sub-pixel accuracy and the following sequence of window sizes in the grid refinement: (I) 64x32 pixels, (II) 32x16 pixels, (III) 16x8 pixels. A 50% final overlap factor is applied yielding a grid spacing of 8x4 pixels ($0.9 \times 0.48 \text{ mm}^2$).

Instantaneous velocity field

A typical instantaneous flow pattern is shown in fig. 8. The velocity is normalized by U_o . Intense span-wise vortices are visualized in fig. 9 where the fluctuating velocity field is plotted.

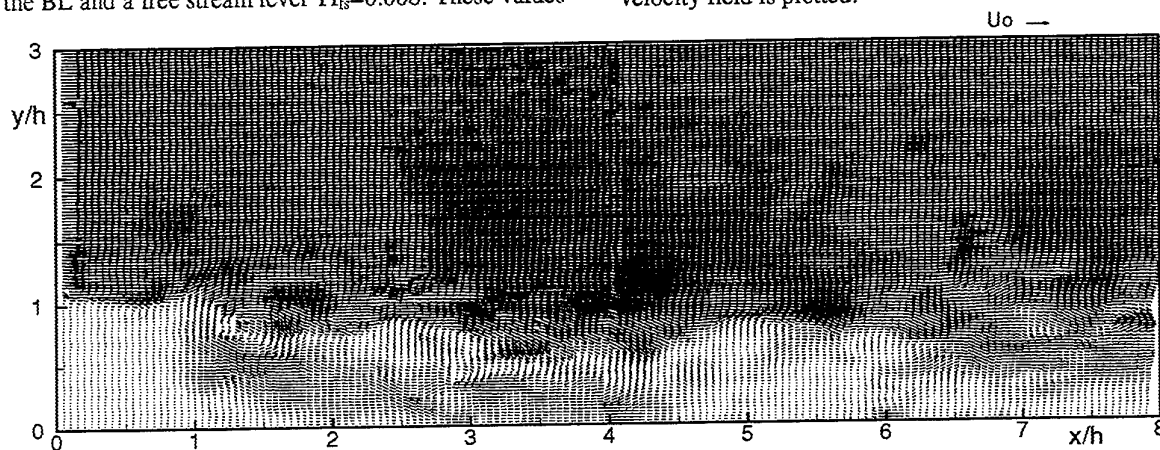


Fig. 8 - Instantaneous velocity distribution.

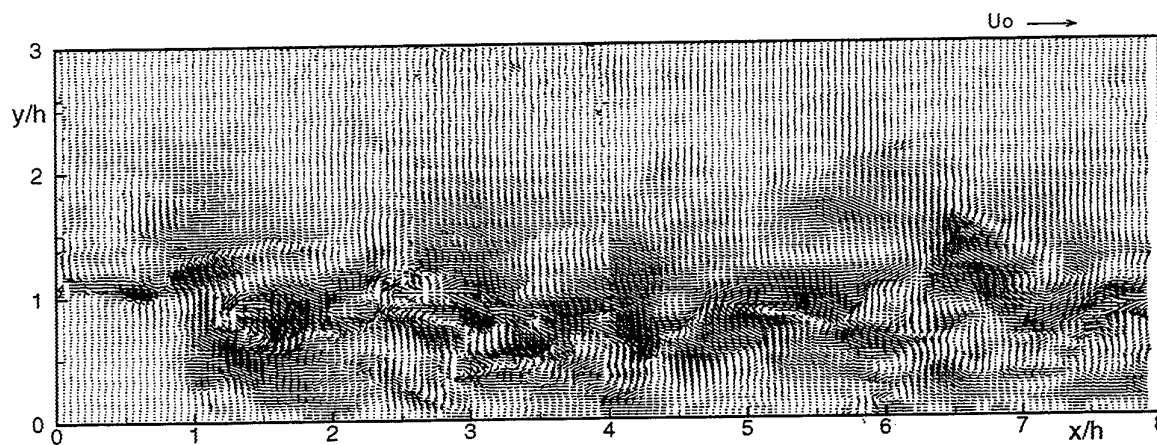


Fig. 9 - Instantaneous fluctuating velocity distribution.

Statistical flow quantities

A statistical analysis of the turbulence has been conducted considering 208 available sample fields. The measurement conditions allow to consider each velocity field independent of the following and preceding one. Fig. 10 shows the average velocity and

vorticity fields. It is possible to visualise the mean shear inversion at the wall ($x/h \sim 6$). A small set of stream traces aid the detection of the mean reattachment region. A minor inversion is also noticed in the bottom step corner ($x/h < 1$) where a secondary mean re-circulation region has been detected.

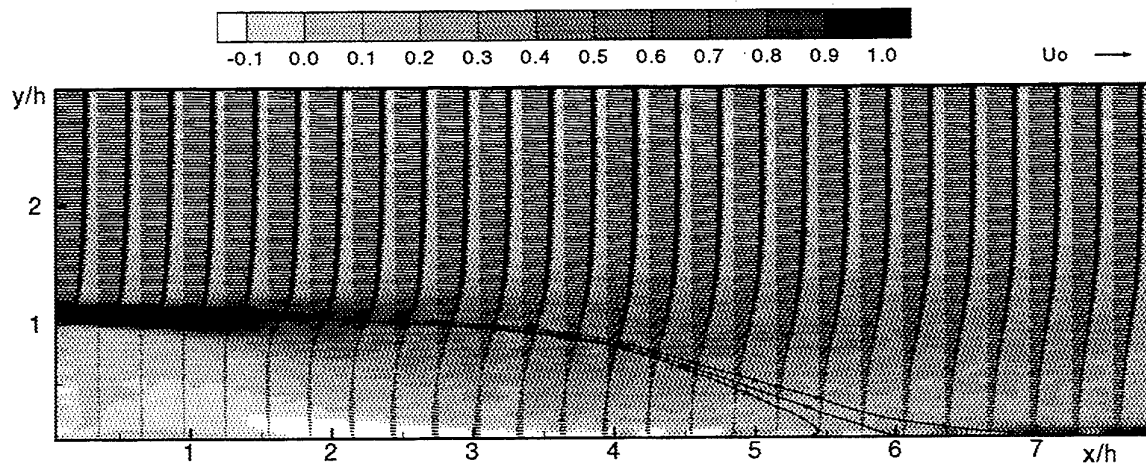


Fig. 10 - Mean velocity and span-wise vorticity. Velocity profiles are represented one over six for clarity. Vorticity values are normalised with the field maximum value. Positive values refer to clockwise vorticity.

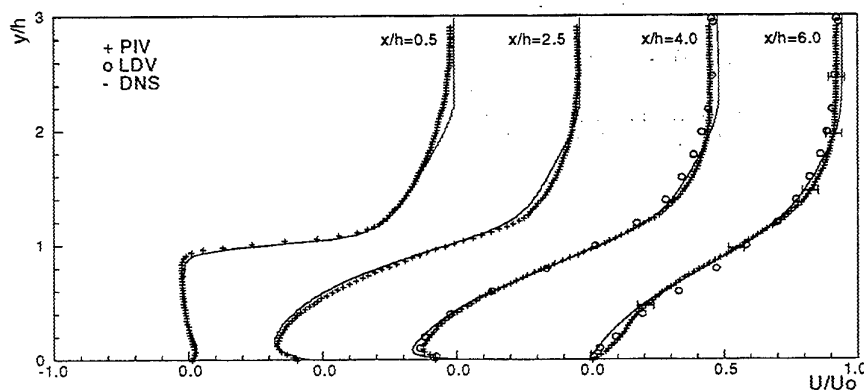


Fig. 11 - Mean stream-wise velocity component at different abscissae.

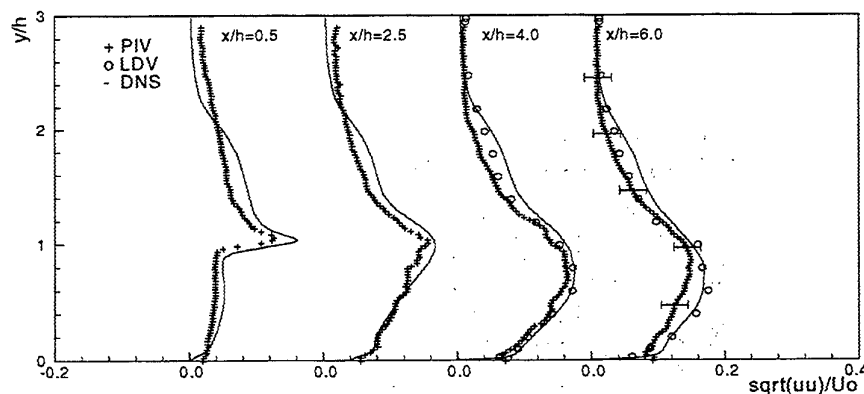


Fig. 12 - Stream-wise component turbulence intensity.

The comparison between PIV, LDV and DNS data is presented in figs. 11, 12 and 13 where vertical profiles of mean and fluctuating quantities have been extracted from the whole field PIV data available. It is possible to appreciate that the resolution reached in

the PIV interrogations leads to the detailed description of the shear region downstream the step. This is particularly evident observing the steep velocity profile at $x/h = 0.5$. PIV data agree with DNS as well as LDV results within the estimated uncertainty level (5% of the free stream velocity U_o).

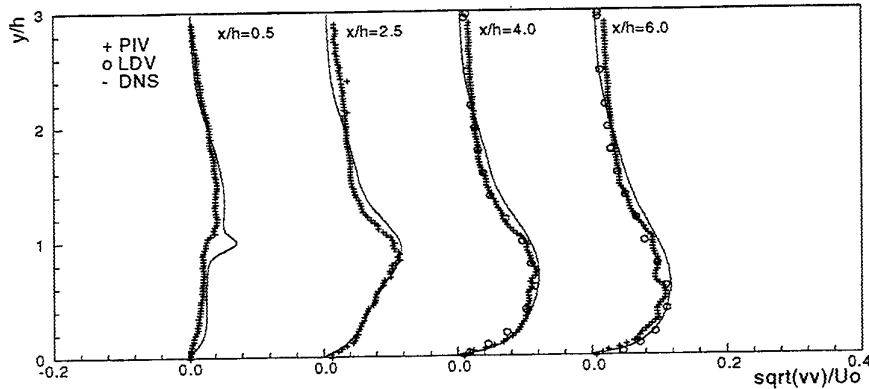


Fig. 13 - Vertical component turbulence intensity.

5. CONCLUSIONS

An improved algorithm to interrogate digital PIV recordings has been proposed. The performances of the technique in terms of dynamic range and spatial resolution have been evaluated. The application of successive (cross-correlation) analysis steps with window refinement showed an enlargement of the dynamic range taking as a reference a one-step algorithm.

The measurement of the turbulent flow on the BFS allowed the detailed characterisation of the flow field over the whole separation region. The estimated uncertainty of the measurement of the instantaneous velocity is of 0.5% of the free stream value. The measurement error increases for the statistical quantities (3% for the mean quantities and 6% for the Reynolds stress terms) due to the limited number of flow samples.

The spatial resolution of $0.9 \times 0.48 \text{ mm}^2$ grid spacing and the above-mentioned uncertainties assessed the capability of the technique of analysing successfully this kind of flow. The comparison with numerical and experimental data available on the same test case showed a good quantitative agreement.

The whole image processing procedure did not make use of image pre-processing. As a consequence the additional computational load due to the multiple iterations grew linearly with the number of iterations and a speed of about 300 vectors/s was achieved with an ordinary PC (Pentium 200).

The authors are currently working on further improvements of the technique. Schemes allowing full windows transformations (translation + rotation + stretching) are in assessment phase.

REFERENCES

- Adrian, R.J. 1991, Particle-imaging techniques for experimental fluid mechanics, *Ann. Rev. Fluid Mech.*, vol. 23, pp. 261-304.
- Boillot A. and Prasad A. K. (1996) Optimization procedure for pulse separation in cross-correlation PIV. *Exp. Fluids* 21: 87-93
- Huang H. T., Fielder H. F. and Wang J. J. 1993a Limitation and improvement of PIV, part I. Limitation of conventional techniques due to deformation of particle image patterns. *Exp. Fluids* 15 168-174
- Huang H. T., Fielder H. F. and Wang J. J. 1993b Limitation and improvement of PIV, part II. Particle image distortion, a novel technique. *Exp. Fluids* 15 263-273
- Jambunathan K., Ju X. Y., Dobbins B. N. and Ashfort-Frost S (1997) An improved cross correlation technique for particle image velocimetry. *Meas. Sci. Technol.* 6: 507-514
- Jovic S. and Driver D. M. (1994) Backward facing step measurement at low Reynolds number, $Re_\tau=5000$. *NASA technical memorandum* No. 108807.
- Keane R. D. and Adrian R. J. (1993) Theory of cross-correlation analysis of PIV images. *Flow visualization and image analysis*, 1-25. Kluwer academic Publishers
- Keane R. D. and Adrian R. J and Y. Zhang. (1995) Super-resolution particle imaging velocimetry. *Meas. Sci. Technol.* 6, 754-768
- Le H., Moin P. and Kim J. (1997) Direct numerical simulation of turbulent flow over a backward facing step. *IFM* 330: 349-374
- Lecordier B. (1997) Etude de l'interaction de la propagation d'une flamme prémélangée avec le champ aérodynamique, par association de la tomographie Laser et de la Vélocimétrie par Images de Particules. *Thèse de doctorat de l'Université de Rouen*.
- Westerweel J., Dabiri D. and Gharib M. (1997) The effect of a discrete window offset on the accuracy of cross-correlation analysis of digital PIV recordings. *Exp. Fluids* 23: 20-28.
- Willert C. E. and Gharib M. (1991) Digital particle image velocimetry. *Exp. Fluids* 10: 181-193

SESSION 23

SCALAR MEASUREMENTS I

EVALUATION OF FLOWFIELD TEMPERATURES AND PRESSURES USING BROADBAND EXCITATION AND DETECTION

J. Mendoza, I. Catton

Mechanical and Aerospace Engineering Department
University of California, Los Angeles

and

M. Azzazy

Azzazy Technologies
Aliso Viejo, California

ABSTRACT

A nonintrusive method to measure temperature and pressure utilizing broadband excitation and detection of oxygen fluorescence is presented. The required finely-tuned laser excitation source is replaced by a more rugged and less bulky Xenon flashlamp. As a tradeoff, more lines are excited and hence more fluorescence lines need to be monitored. Using a numerical fluorescence model, temperature and pressure sensitive bins of varying sizes (5,10,15,20 nm) between 200 and 300 nm are determined. By scaling the bin values with a relatively pressure insensitive bin, a pressure insensitivity parameter was found that allowed the determination of the 5 nm bin centered about 222.5 nm to be the most temperature sensitive for 200-1500 K.

1. INTRODUCTION

Current mechanical instrumentation used in temperature and pressure measurements are more suited for studying surface conditions. However, even then they are usually exposed to the flow and so could be potentially damaged by adverse flow conditions. Also, if flowfield values are desired, their placement within the flow introduces errors due to flowfield disturbances initiated by the instrumentation. Optical methods offer resolutions to these shortcomings and, thus, have sparked considerable interest.

Among optical methods, laser-induced fluorescence (LIF) has been a popular technique in the measurement of temperature and pressure in various environments. The fluorescence emitted by a molecule is dependent on its ground state population distribution. This distribution is in turn dependent on temperature and pressure. In obtaining this distribution, one can determine temperature and pressure.

The unavailability of a light source for excitation in the ultraviolet (UV) regime was a primary deterrent to UV fluorescence. However, with the advent of the ArF and KrF laser, many techniques utilizing UV fluorescence have been developed. Lück and Müller (1977) used a frequency double continuous wave (CW) dye laser and the combustion product OH to take advantage of the temperature dependence in the Doppler broadening component of a spectral linewidth. Seitzman, Kychakoff, and Hanson (1985) used a constant mole fraction of NO as a seeding material in premixed methane-air flames with temperatures between 300 and 2500 K to derive a fluorescence expression as a function of temperature. Non-intrusiveness was maintained by adding only a small amount of NO to the flow. Rensberger, Jeffries, Copeland, Kohse-Höinghaus, Wise, and Crosley (1989) measured the fluorescence output of OH, NH, CH, and CN and fitted it to a synthetic spectrum with temperature and Gaussian linewidth as parameters.

Two-line techniques where the ratio of fluorescence from two separate lines are taken to remove the number density dependence and so result in a ratio dependent only on temperature have also been investigated. Smith, Price, and Williams (1993) proposed a two-line technique using calibration curves and two ArF excimer lasers temporally separated 100 ns apart. Massey and Lemon (1984) also proposed a two-line method using a single laser and two temporally separated laser excitations of O₂ lines to determine temperature and density fluctuations. Other authors who have investigated the use of two-line excitation O₂ fluorescence are Lee, Paul, and Hanson (1986) and Grinstead, Laufer, and McDaniel (1993). The latter group used a KrF laser and two- and four-line excitation techniques in their measurements.

Another technique using an ArF laser combines LIF with Raman scattering as a density indicator.

Laufer, McKenzie, and Fletcher (1990) proposed this innovative method for low to moderate temperatures (60-500 K). However, for higher temperatures the Raman scattering is overshadowed by the air fluorescence and, thus, limits the temperature range.

All of the above methods, however, require accurate excitation of specific spectral lines. To get around this, Lee and Hanson (1986) proposed that a method utilizing broadband excitation of O₂ using an ArF laser source could be developed due to the molecule's large absorption coefficients. However, this still requires the use of a bulky laser. Thus, we propose to use broadband excitation and broadband detection of the O₂ molecule with a durable and, relatively small, Xenon flashlamp as the excitation source. In this paper, the oxygen fluorescence spectrum due to broadband excitation is calculated via a numerical program. A segment of the O₂ Schumann-Runge band (185-200 nm) is used for the excitation range due to its strong absorption coefficients. The resulting fluorescence spectrum between 200 and 300 nm is recorded. This range is then divided into bins of 5 (10, 15, 20) nm widths and their pressure and temperature sensitivity evaluated. The central wavelength of each bin is incrementally varied one nm at a time such that there are 5 (10, 15, 20) bin distributions. Since oxygen fluorescence is dependent on both pressure and temperature, at least two bins are required. One window being designed to be sensitive to temperature while the other is sensitive to pressure. The resulting bins will then be used in a pending experiment to validate the technique.

The paper is divided into three sections. Section one gives a brief background on the theory behind the technique. Section two describes the O₂ fluorescence numerical model. Section three discusses the determination of the temperature- and pressure-sensitive spectral regions along with the results.

2. Numerical Fluorescence Model

The premise behind the use of LIF lies in the temperature and pressure dependence of the ground state population distribution and the fluorescence intensity being proportional to this population. The temperature and pressure can therefore be derived from the population distribution. For the cases taken here, oxygen in air is the molecule of interest such that the O₂ mole fraction is known and so does not pose as an additional unknown. Also, the oxygen fluorescence is ideally modeled. Attenuation in the optical paths and inefficiencies in the optical components are presently not accounted. These effects will be included in the

final program for the experiment. Presently, importance is placed on whether or not temperature and pressure sensitive bins can be found. If they are found, then a layout of the optical components will be designed utilizing these bins. The required pathlengths would then be known and included in the numerical model. Furthermore, due to a focus on highly predissociated states, as will be seen later, rotational and vibrational redistribution was assumed negligible such that the two-level absorption model used here sufficed.

The numerical program written simulates the oxygen absorption and fluorescence utilizing spectroscopic constants found in literature. The primary task addressed by this paper is the determination of fluorescence regions sensitive to temperature or to pressure which will aid in the design of a pending experiment. The program requires, as input, the following parameters: 1) temperature, 2) pressure, 3) exciting wavelength bandcenter, and 4) exciting bandwidth. However, to ensure adequate energy input from the source, the latter two parameters are fixed. In the original design, a 1 nm excitation bandwidth was to be taken between 185 and 200 nm. However, to maximize light energy and due to the low end cutoff of the flashlamp (190 nm), a 10 nm bandwidth (190-200 nm) with the bandcenter at 195 nm was taken. The fluorescence between 200 and 300 nm was then recorded. This reduces elastic contributions from Rayleigh and Mie scattering. With temperature and pressure as variables, the code calculates the resulting number of fluorescence photons as a function of wavelength.

The individual rotational line wavenumber, $w_{JJ'}$ [cm⁻¹], of the allowed O₂ transitions is the first to be calculated. Schumann-Runge system spectroscopic constants B, D, and G are taken from (Creek and Nicholls, 1975) along with the following relation for the wavenumber,

$$\begin{aligned} w_{JJ'} &= w_{v'v''} + m(B_{v'} + B_{v''}) + m^2(B_{v'} - B_{v''} - D_{v'} + D_{v''}) - \\ &\quad 2m^3(D_{v'} + D_{v''}) - m^4(D_{v'} - D_{v''}) \\ w_{v'v''} &= G_{v'} - G_{v''} \end{aligned} \quad (1)$$

$$\begin{aligned} m &= J'' \quad \text{P-Branch} \\ m &= J'' + 1 \quad \text{R-Branch} \\ \Delta J &= +1 \rightarrow \text{P-Branch} \quad \Delta J = J'' - J' \\ \Delta J &= -1 \rightarrow \text{R-Branch} \end{aligned}$$

J'' and J' represent the ground and excited rotational state quantum numbers while v' and v'' apply to the ground and excited vibrational state quantum numbers, respectively. The program evaluates transitions from v''=0-21 to v'=0-21.

Once the line wavenumbers are calculated, the Boltzmann population distribution ($N_{v'J'}$) is found,

$$N_{v''J''} = \frac{F_{v''J''}}{kT} P \chi_{O_2} \quad (2)$$

χ_{O_2} = mole fraction of O_2

$F_{v''J''}$ is the Boltzmann Fractional Population of the v'' vibrational level and J'' rotational level and k is the Boltzmann constant (1.381×10^{-23} J/K). It is given by,

$$F_{v''J''} = \frac{2J''+1}{Q_e Q_r Q_v} e^{-\frac{hc}{kT}[T_e(n) + G(v'') + F(J'')]} \quad (3)$$

with Q_e , Q_r , Q_v being the electronic, rotational, and vibration partition functions, respectively. The terms within the brackets of the exponential account for the electronic, vibrational, and rotational energy contributions, respectively. In the ground state, $T_e(n)$ is equal to zero. The values for the G term (cm^{-1}) are tabulated by Creek and Nicholls (1975). The rotational contribution (cm^{-1}) is given by,

$$F(J) = B_v(J''+1)J'' - D_v(J''+1)^2 J^2 \quad (4)$$

with the B and D values taken from Creek and Nicholls (1975).

The individual absorption line strength ($cm^{-2} atm^{-1}$) is next calculated by the following relation,

$$k_{v''J''} = \frac{\pi e^2}{m c^2} \frac{N_{v''J''} f_{v''J''} S_{J''} T_{J''}}{P \chi_{O_2} 2J''+1} \quad (5)$$

$T_{J''}$ is a correction factor to account for vibration-rotation interaction and is unity in this case. $S_{J''}$ is the Hönl-London factor (Tatum, 1966) evaluated at J'' for absorption.

The oscillator strengths, $f_{v''J''}$, is related to the Einstein spontaneous emission coefficients through the following relation,

$$f_{v''J''} = \frac{A_{v''J''} \lambda_{v''J''}^2}{6.670 \times 10^{15}} \quad (6)$$

Here the $\lambda_{v''J''}$ is in angstroms and is found via the Bohr frequency rule. The A (sec^{-1}) coefficients are taken from Allison, Dalgarno, and Pasachoff (1971).

Line broadening is accounted for next. The effects are included through the broadening widths associated with natural uncertainty (b_N), collision (b_c), predissociation (b_{pre}), and Doppler (b_d). The "a" coefficients required to calculate the predissociation linewidths are taken from Lewis, Berzins, Carver, and Gibson (1985). The broadening terms (cm^{-1}) are given by the following relations:

$$b_c = 0.2P \left(\frac{298}{T} \right)^{0.7}$$

$$b_{pre} = a_1 + a_2 X + a_3 X^2 + a_4 X^3 + a_5 X^4$$

$$\text{where } X = J'(J'+1), J' \leq 40 \quad (7)$$

$$b_d = \left(\frac{2kT \ln 2}{m c^2} \right)^{\frac{1}{2}} w_{ij}$$

$$b_N = \frac{A_{ij}}{4\pi c}$$

P is the pressure (atm), T is the temperature (K), c is the speed of light (cm/sec), w_{ij} is the wavenumber of the transition (cm^{-1}), and A_{ij} is the Einstein spontaneous emission coefficient. Natural line broadening is considered negligible in the program in comparison to the other broadening terms. The broadening terms affect the shape of the spectral line and are modeled following the description of Penner and Kavanagh (1953). Collision broadening is pressure dependent and is inversely proportional to the square root of the temperature. Predissociation broadening is very prevalent in the Schumann-Runge band. Doppler broadening is important at higher temperatures since it varies directly with the square root of temperature. Thus, these three components need to be included in the model.

Doppler broadening requires a Gaussian lineshape while predissociation and collision result in a Lorentzian lineshape. The Lorentzian lineshape is similar to the Gaussian except that it drops off more slowly than the latter and, hence, models the lineshape at the wings (edges) poorly. To account for these broadening contributions, the Voigt lineshape, which combines the Lorentzian and Gaussian lineshapes, is used. The Voigt lineshape is numerically modeled following the approximation of Whiting (1968) and using the correction factors of Olivero and Longbothum (1977).

Once the lineshape function ($\Phi(w)$) [cm] is found, the calculation of the upper population is straightforward and is given by the following relation:

$$N_{v''J''} = \int I_L k_{v''J''} P_{O_2} \Phi(w) dw \quad (8)$$

$$\int \Phi(w) dw = 1$$

I_L is the number of photons per unit wavenumber from the flashlamp (photons/ cm^{-1}) and is taken from spectroscopic data supplied by EG&G Corporation. L_{vol} is the length of the probe volume/slab which is taken to be 1 mm. Calculation of the emission fluorescence photons then involves the multiplication of the above population by the Stern-Volmer factor (fluorescence yield):

$$S_f = N_v r \left(\frac{A_{21}}{A_{21} + Q_{pre} + Q_{col}} \right) \quad (9)$$

Predissociation dominates the deexcitation processes in the Schumann-Runge band but the collision quenching rate (sec^{-1}) is still accounted for in the program. The A terms are the Einstein spontaneous emission coefficients.

3. Determination of Sensitive Bins

Before calculating the oxygen fluorescence, the code was validated by comparing its calculation of the individual line strengths and spectral absorption coefficients to those of Lee and Hanson (1986). For these runs, the Xenon flashlamp was replaced with a broadband ArF laser at 193 nm. The results compared very well.

As stated earlier, the primary task is to find temperature- and pressure-sensitive bandwidths. Ideally, it is desirable to find bandwidths that are highly temperature dependent with no pressure dependence and vice versa. Furthermore, to make this method as robust as possible, the applicable temperature and pressure range would be made as large as possible.

The oxygen fluorescence was calculated for temperatures from 200 K to 2000 K at 100 K increments for pressure values of 0.1, 0.5, and 0.5 atm increments to 5 atm. The fluorescence spectrum for oxygen at a pressure of 1 atm for a few different temperature values are plotted in Figure 1. Note that each plotted fluorescence value encompasses a band of 0.5 nm. As can be seen, the fluorescence spectrum becomes cluttered with numerous lines after 500 K and so makes isolation of a specific spectral line very difficult.

Although there are many temperature sensitive spectral lines to choose from, spanning a larger band would be easier and would make the technique more robust. Several bin widths (5, 10, 15, and 20 nm) were investigated and the fluorescence within the encompassing wavelengths summed and assigned to the midpoint of each bin. The initial wavelength for the first distribution was set at 200 nm and increased 1 nm at a time for each following distribution. This resulted in 5 (10, 15, 20) bin distributions for bin widths of 5 (10, 15, 20) nm. The collection wavelength range was taken to be 200-300 nm to reduce the effects of elastic scattering. Maximum sensitivity was taken to be the bin with the largest change in fluorescence photon sum.

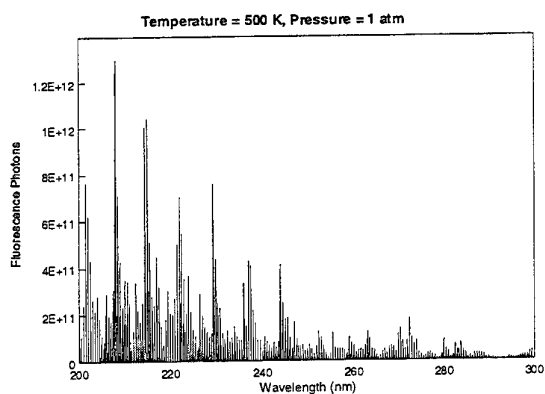


Figure 1b: Fluorescence Photons at 500 K

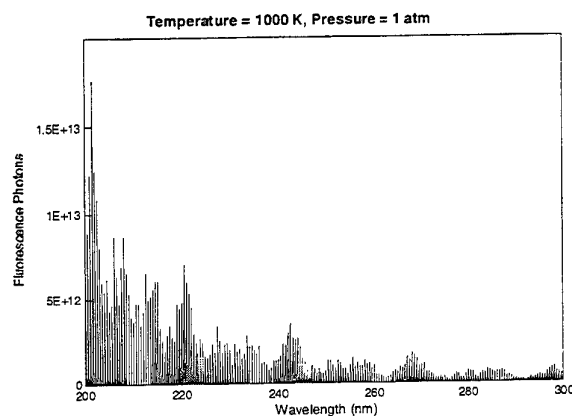


Figure 1c: Fluorescence Photons at 1000 K

During an initial analysis of the data, highly temperature sensitive bins were found. However, after a check for pressure sensitivity, it was realized that these bins were also highly sensitive to pressure. A check of all the bins turned up no single bin to be sensitive to temperature or to pressure alone. This led to a different approach. The fluorescence output for various pressures at 500 K is shown in Figure 2. It became evident from the plots that the line spectra do not appear to change other than in magnitude. No significant new peaks are developed as the pressure is varied. It was surmised that the pressure effect on the fluorescence was basically

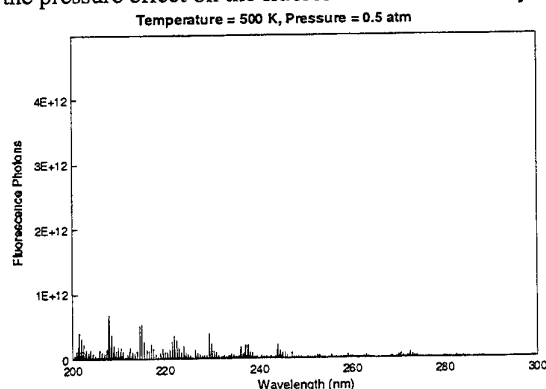


Figure 2a: Fluorescence Photons at 0.5 atm

linear. Thus, if a ratio of two bins were to be taken, the effects of pressure would be removed and the remaining ratio would be a function of temperature only. This was attempted and the results for a 5 nm bin width are shown in Figure 3. As can be seen, this pressure linearity was predominantly the case except at the larger temperature values. This will be discussed in more detail later. A note to consider is that even if the pressure dependence is removed, the resulting ratio would still need to be single-valued with temperature if only two bins are monitored.

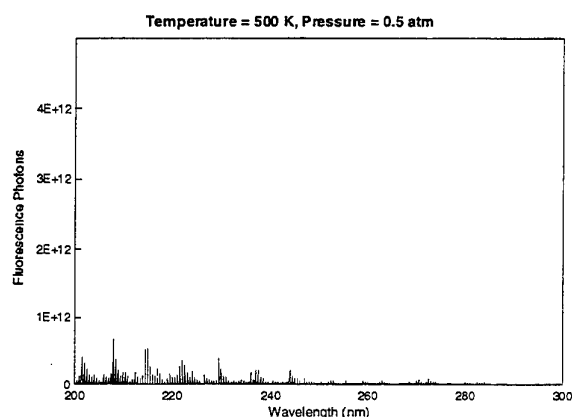


Figure 2a: Fluorescence Photons at 0.5 atm

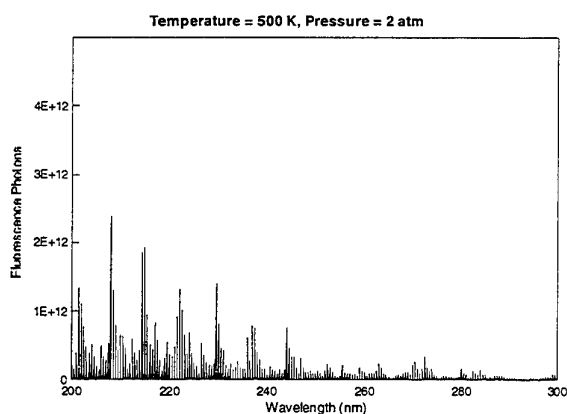


Figure 2b: Fluorescence Photons at 2 atm

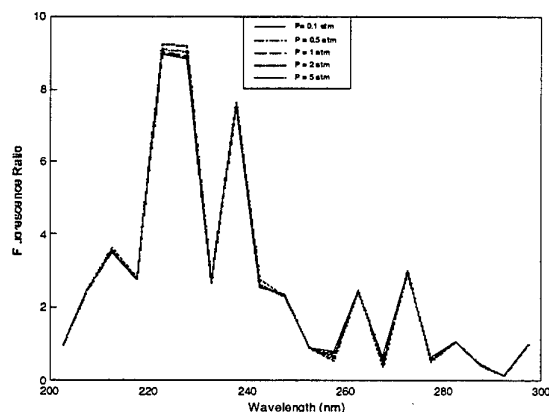


Figure 3a: Scaled Bin Fluorescence Values at 300 K

In the choice of the temperature sensitive bandwidths of the scaled fluorescence and due to the slight pressure sensitivity at higher temperatures, it was still necessary to check for pressure independence. The bin location showing the least pressure sensitivity was chosen to be the scaling parameter for the other bins. After an evaluation of the summed fluorescence, the last bin was found to be consistently the one with the least variation and, so, it was used as the scaling component.

The pressure dependence of the fluorescence for the investigated pressure range is almost linear. At higher pressure values, the pressure influence will be seen through the collisional quenching rate as it becomes comparable to the predissociation rate. It will also appear in the evaluation of the spectral linewidths (Equation 7) and in the calculation of the number of excited particles (Equation 8). The first two cited effects are relatively small if the excited states are highly predissociated such that collisional relaxation becomes negligible as in low temperatures. At 300 K, most of the fluorescence comes from the $v'=4-8$ vibrational states which are all dominated by predissociation (Lewis et al., 1985). Thus, as seen in Figure 3, the fluorescence is basically pressure independent. However, at higher temperatures, other excited states ($v'=9, 10, 12, 13, 14$) become a factor. These states are not as strongly predissociated and, so, collision broadening and quenching are no longer negligible. Thus, the fluorescence becomes a nonlinear function of pressure. At still higher temperatures (1500 and 2000 K), although the collision linewidth decreases due to its $T^{-1/2}$ dependence, contributions from higher, less predissociated excited states result in the slight increase in the fluorescence nonlinearity with pressure (Figure 3). Thus, to ensure pressure linearity, the choice of the collection band must be carefully made such that it encompasses transitions from highly predissociated states.

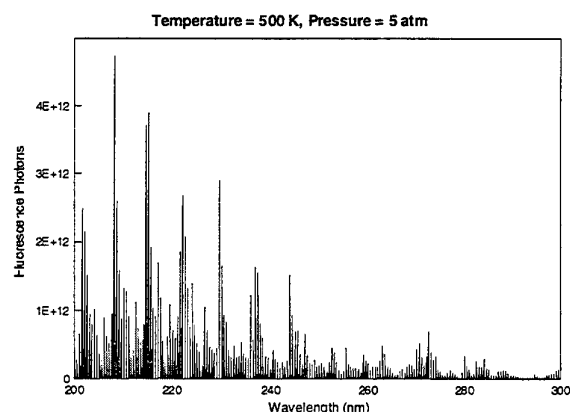


Figure 2c: Fluorescence Photons at 5 atm

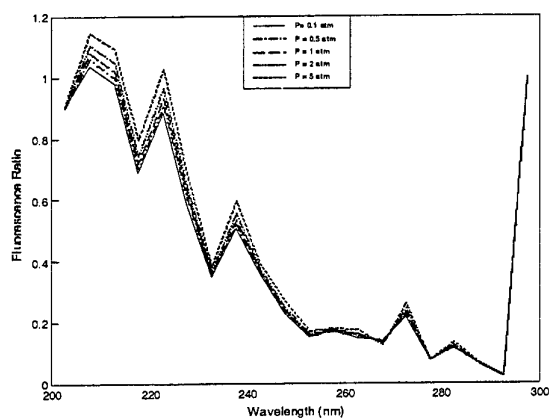


Figure 3b: Scaled Bin Fluorescence Values at 500 K

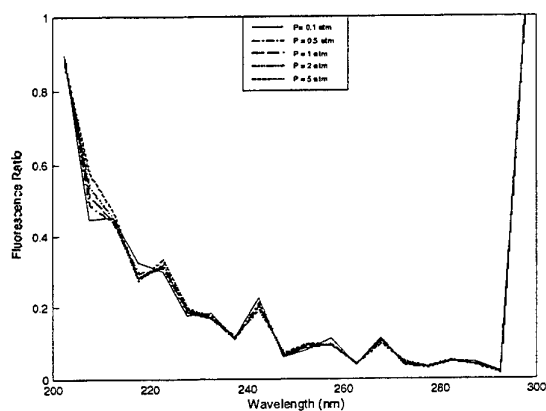


Figure 3c: Scaled Bin Fluorescence Values at 1000 K

This led to three criteria necessary for the bin choice. These criteria are, pressure insensitivity, temperature sensitivity, and the fluorescence ratio being single-valued with temperature. The pressure insensitivity was determined via the ratio described above. Dividing the standard deviation of the scaled fluorescence values for different pressures at a specific temperature by their arithmetic average resulted in a parameter that measured the pressure insensitivity. The smaller the value, the smaller the pressure dependence of the bin. The temperature sensitivity was determined through the slope of the scaled fluorescence versus temperature at constant pressure. The greater the slope, the larger the temperature sensitivity. A plot of the scaled fluorescence versus temperature for five bins is shown in Figure 4. The one-to-one correspondence in the fluorescence ratio with temperature involved making sure the slopes between each temperature points never changed signs or went to zero. A check on this resulted in no bins satisfying it until 2000 K. Thus, it was decided to set the upper temperature limit for all bins at 1500 K. If higher temperatures are required, the

temperature range would need to be subdivided and a selection of a more appropriate bin within each subdivision could be done by simply going through the three criteria mentioned above. In this way, even more temperature sensitive and pressure insensitive bins may be found. However, for a very general and robust technique, it was decided to set the upper temperature limit to 1500 K.

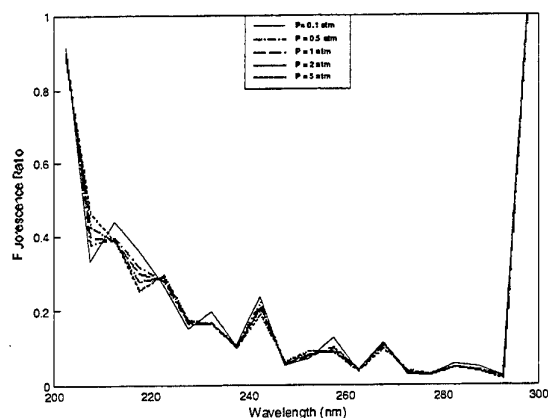


Figure 3d: Scaled Bin Fluorescence Values at 1500 K

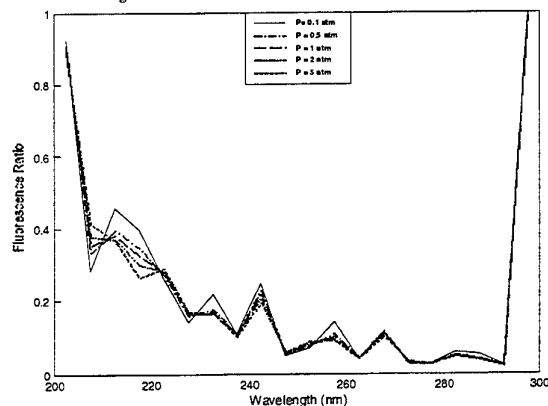


Figure 3e: Scaled Bin Fluorescence Values at 2000 K

Beginning with the first criteria of pressure insensitivity and using 10% as the cutoff, 45 bins were chosen. Reducing the cutoff tolerance to 5% reduce this number to 23. These bins are shown in Table 1.

Table 1: Pressure Sensitivity

Bin	Width (nm)	λ_{mid} (nm)	Average STD/Ave
1	5	222.5	0.031
2	5	227.5	0.034
3	5	239.5	0.025
4	5	243.5	0.030
5	5	244.5	0.015
6	5	245.5	0.012
7	5	264.5	0.023
8	5	284.5	0.034
9	10	216	0.032

10	10	217	0.034
11	10	237	0.013
12	10	262	0.013
13	10	263	0.028
14	10	275	0.032
15	15	226.5	0.010
16	15	240.5	0.012
17	15	241.5	0.009
18	15	242.5	0.011
19	15	243.5	0.019
20	15	245.5	0.021
21	15	246.5	0.024
22	15	271.5	0.021
23	20	210	0.003

A sample plot of the fluorescence ratios for five of the above bins which show the largest temperature sensitivity is given in Figure 4. Examining the plot shows that the second criteria is satisfied most by bin 1, especially at moderate temperatures.

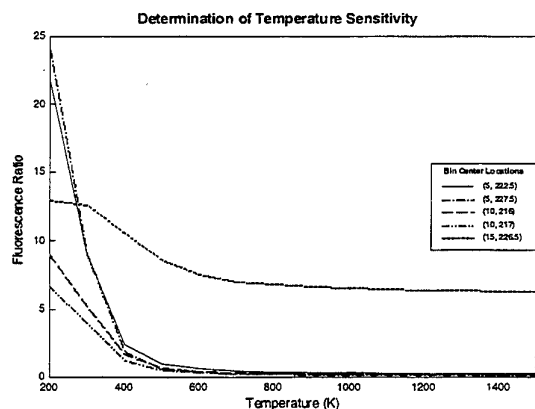


Figure 4: Averaged Scaled Bin Fluorescence Values

Note that after 800 K, the temperature sensitivity is almost nil. Thus, it appears that the temperature range should be broken down further. If the entire temperature range of 200 - 1500 K is still necessary, more temperature sensitive bins within each sub-range would need to be found and monitored.

Once temperature is known, the pressure would be determined from the (at least) two measured fluorescence bin values (centered about 222.5 nm and 297.5 nm). These values will be scaled with the input intensity to remove flash-to-flash variations in the input source. The pressure would then be inferred from a calibration curve constructed with results of the code for a range of temperatures and pressures.

4. Conclusion

The feasibility of using a Xenon flashlamp to measure temperature and pressure by fluorescing oxygen molecules has been discussed. It has been shown that for the bins evaluated, there is no single bin that is either solely dependent on temperature or on pressure. However, due to the almost linear dependence of fluorescence on pressure, a ratio could be taken that effectively remove the pressure dependence for bins that encompass excited states with predissociation dominating the relaxation processes. The only other criteria to take note of is that this ratio needs to be single-valued with temperature. From the above analysis, the 5 nm bin centered about 222.5 nm scaled by the 5 nm bin centered about 297.5 nm gives the best sensitivity to temperature with low sensitivity to pressure. This along with the ratio's one-to-one correspondence with temperature allows the determination of temperature up to 1500 K. Once the temperature is found, the pressure is arrived at using the two absolute fluorescence bin counts (normalized by input energy) and a calibration curve.

ACKNOWLEDGMENTS

The research presented in this report was fully supported by NASA Dryden Flight Research Facility under contract No. FDP NASA Dryden NCC 2-374.

REFERENCES

- Allison, A.C., Dalgarno, A., and Pasachoff, N.W. 1971, Absorption by Vibrationally Excited Molecular Oxygen in the Schumann-Runge Continuum, Planetary and Space Science, Vol.19, pp. 1463-1473.
- Creek, D.M. and Nicholls, R.W. 1975, A Comprehensive Re-Analysis of the O_2 ($B^3\Sigma_u^- - X^3\Sigma_g^-$) Schumann-Runge Band System, Proceedings of the Royal Society of London Series A, Vol.341, pp. 517-536.
- Grinstead, J.H., Laufer, G., and McDaniel, J.C. Jr. 1993, Rotational Temperature Measurement in High-Temperature Air Using KrF Laser-Induced O_2 Fluorescence, Applied Physics B, Vol.57, pp.393-396.
- Laufer, G., McKenzie, R.L., and Fletcher, D.G. 1990, Method for Measuring Temperatures and Densities in Hypersonic Wind Tunnel Air Flows Using Laser-Induced O_2 Fluorescence. Applied Optics, Vol. 29, No. 33, pp. 4873-4883.

- Lee, M.P. and Hanson, R.K. 1986, Calculations of O₂ Absorption and Fluorescence at Elevated Temperatures for a Broadband Argon-Fluoride Laser Source at 193 nm, Journal of Quantitative Spectroscopy and Radiative Transfer, Vol. 36, No. 5, pp. 425-440.
- Lee, M.P., Paul, P.H., and Hanson, R.K. 1986, Laser-Fluorescence Imaging of O₂ in Combustion Flows Using an ArF Laser, Optics Letters, Vol. 11, No. 1, pp. 7-9.
- Lewis, B.R., Berzins, L., Carver, J.H., and Gibson, S.T. 1986, Rotational Variation of Predissociation Linewidth in the Schumann-Runge Bands of ¹⁶O₂, Journal of Quantitative Spectroscopy and Radiative Transfer, Vol. 36, No. 3, pp. 187-207.
- Lück, K.C. and Müller, F.J. 1977, Simultaneous Determination of Temperature and OH-Concentration in Flames Using High-Resolution Laser-Absorption Spectroscopy, Journal of Quantitative Spectroscopy and Radiative Transfer, Vol. 17, pp. 403-409.
- Massey, G.A. and Lemon, C.J. 1984, Feasibility of Measuring Temperature and Density Fluctuations in Air Using Laser-Induced O₂ Fluorescence, IEEE Journal of Quantum Electronics, Vol. QE-20, No. 5, pp. 454-457.
- Olivero, J.J. and Longbothum, R.L. 1977, Empirical Fits to the Voigt Line Width: A Brief Review, Journal of Quantitative Spectroscopy and Radiative Transfer, Vol. 17, pp. 233-236.
- Penner, S.S. and Kavanagh, R.W. 1953, Radiation from Isolated Spectral Lines with Combined Doppler and Lorentz Broadening, Journal of the Optical Society of America, Vol. 43, No. 5, pp. 385-388.
- Rensberger, K.J., Jeffries, J.B., Copeland, R.A., Kohse-Höinghaus, K., Wise, M.L., and Crosley, D.R. 1989, Laser-Induced Fluorescence Determination of Temperatures in Low Pressure Flames, Applied Optics, Vol. 28, No. 17, pp. 3556-3566.
- Seitzman, J.M., Kychakoff, G., and Hanson, R.K. 1985, Instantaneous Temperature Field Measurements Using Planar Laser-Induced Fluorescence, Optics Letters, Vol. 10, No. 9, pp. 439-441.
- Smith, M.S., Price, L.L., and Williams, W.D. 1993, Laser-Induced Fluorescence Diagnostics Using a Two-Line Excitation Method, AIAA Journal, Vol. 31, No. 3, pp. 478-482.
- Tatum, J.B. 1966, Hönl-London Factors for ³Σ⁺-³Σ⁺ Transactions, Canadian Journal of Physics, Vol. 44, pp. 2944-2946.
- Whiting, E.E. 1968, An Empirical Approximation to the Voigt Profile, Journal of Quantitative Spectroscopy and Radiative Transfer, Vol. 8, pp. 1379-1384.

MEASURING WATER TEMPERATURES BY MEANS OF LINEAR RAMAN SPECTROSCOPY

J. Karl, M. Ottmann, D. Hein

Lehrstuhl für Thermische Kraftanlagen
Technische Universität München
Germany

ABSTRACT

In many cases it is necessary to measure local water temperatures with high local resolution. The usage of common thermocouples limits the local resolution, affects the temperature field and may cause incorrect readings.

The paper presents a new technique to measure temperatures of liquid water in situ, using an optical measurement method - linear Raman spectroscopy. The shape of liquid water Raman spectra changes with temperature and this allows to measure water temperatures one dimensionally - that means along a laser beam - with good accuracy.

Two dimensional measurements miss one of the major advantages of one dimensional Raman measurements. The spectral information about the fluorescence background will be lost and this reduces accuracy. But it might be a valuable method to locate and evaluate local temperature differences.

INTRODUCTION

Raman spectroscopy is a well established method to measure concentrations in gases or liquids, to investigate the molecular structure of pure substances and to measure temperatures in flames or high temperature gas flows.

There are two different effects which can be used to measure temperatures by means of Raman spectroscopy.

The first effect originates from the ratio between gas molecules which are in a vibrational excited state and gas molecules in the vibrational ground state. This ratio depends on the gas temperature according to Boltzmann's law. The effect requires gas temperatures above 1000 K, because there won't be a significant number of molecules in an excited state otherwise. The most common application of Raman spectroscopy is to measure temperatures in flames, therefore. In this case flame temperatures can be calculated from the ratio between Stokes and anti-Stokes peak of a certain component like nitrogen for example or from the shape of the vibrational line of nitrogen for

example (Schrader, 1995)

A completely different effect allows to measure the temperature of liquid water by means of Raman spectroscopy.

The shape of Raman spectra of liquid water is quite different to the shape of Raman spectra of water vapor, because hydrogen bonds affect the O-H-stretching vibration. The number of hydrogen bonds depends on the temperature and the shape of liquid water Raman spectra changes with temperature, too, therefore.

Walrafen et al. (1986) described the influence of the hydrogen bonds to the vibrational line near 3652 cm^{-1} already in 1967. He notified a temperature dependence of the shape of the Raman peak in the region between 3000 and 3800 cm^{-1} . Walrafen and Fujita and Ikawa (1989) used this effect to determine the molecular structure of liquid water and to determine the bonding energy of hydrogen bonds by means of Raman spectroscopy and infrared spectroscopy.

Leonard et al. (1979) started a first attempt to use this effect for water temperature measurements in the early seventies. He developed an airborne LIDAR system to measure ocean water temperatures over large ocean areas. He measured water temperatures 100 m below the water surface. Within a depth of 3 m he got an accuracy of $\pm 1,2\text{ K}$. Schwaiger (1992) used the effect to measure temperatures of water droplets.

Leonard used Raman spectroscopy to determine water temperatures from discrete points without investigation of local temperature distributions.

In our previous work we applied Raman spectroscopy to measure the water temperature distribution along a laser beam. We measured water temperatures simultaneously with concentration profiles in a steam-nitrogen boundary layer during condensation in the presence of a non condensable gas (nitrogen) to calculate condensation heat transfer coefficients (Karl, 1997). With another experimental set-up we focused the laser beam vertically through a water layer and measured the water temperature distribution along the laser beam.

We obtained one dimensional temperature profiles, therefore, which allowed to calculate local heat transfer

coefficients during direct contact condensation (Karl and Hein, 1997)

Our recent work was aimed at possibilities to measure water temperatures in two dimensions to get in situ detailed two dimensional images of a temperature distribution in liquid water flows.

The best way to evaluate Raman signals is to register the entire spectral information using a spectrograph.

The main advantage of Raman spectroscopy for various applications is, that the required Raman signal can be separated from any Mie-, Rayleigh- or Fluorescence signal. But separation of those signal components requires that the spectral information is available completely.

Using a spectrograph together with a CCD camera allows to get one dimensional temperature distribution for example along the laser beam. As shown in Fig. 1 the images provided by the a CCD chip can be used to get spectral information simultaneously to local information. Each pixel row provides a spectrum corresponding to a certain location of the laser beam, then.

Of course it is not possible to get two dimensional information for flow field measurements with such a configuration, simultaneously, because one dimension of the two dimensional CCD detector is necessary to provide the spectral information.

Measuring water temperatures in two dimensions causes the loss of the spectral information and reduces the accuracy inevitably. But in case not absolute temperatures but temperature differences are looked for, two dimensional measures can make valuable results.

RAMAN SPECTRA OF LIQUID WATER

Raman scattering is an inelastic light scattering process. A molecule may scatter light of any wavelength either elastically - that means without wavelength shift - or inelastically. In that case the scattered light is shifted to a different wavelength. The first case is called Raleigh scattering and the second case is called Raman scattering. Inelastic scattering of incident light means, that a certain amount of energy remains in the molecule. The energy

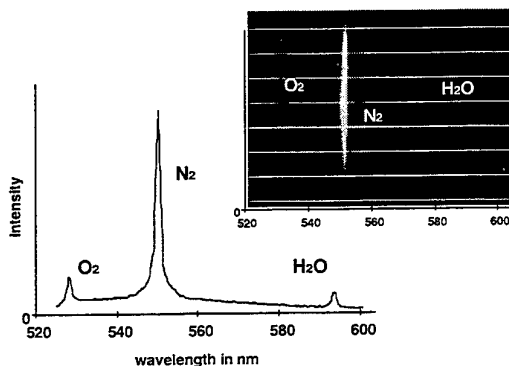


Fig. 1: Raman spectrum of air

loss of the scattered light quantum corresponds to the energy of a certain molecule vibration caused by the scattering process.

Those molecule vibrations, for example stretching or rotational vibrations, are specific for the molecule. This allows to use Raman spectroscopy in quantitative chemical analysis or to investigate the molecule structure.

The Raman shift of a certain molecule depends on the energy of a molecule vibration and on the structure, the atomic distance and the atomic weights of a molecule, therefore.

A typical spectrum of air is shown in Fig. 1. We used an argon-ion laser operating in single line mode at 488 nm to obtain this spectrum. This laser wavelength caused an oxygen peak at 528 nm, a nitrogen peak near 550 nm and a single narrow water-vapor peak near 594 nm. This water peak is caused by the ν_s O-H-stretching vibration of the water molecule:

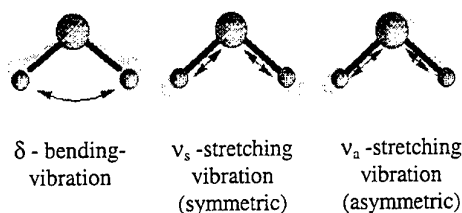


Fig. 2: Vibrational modes of water molecules

It is a single narrow peak like the peaks caused by two atomic nitrogen or oxygen molecules.

As shown in Fig. 3 the Raman spectrum of liquid water is quite different. The same O-H-bond is now affected by hydrogen bonds, which increase the atomic distance between the oxygen and the involved hydrogen atom.

This effect decreases the energy of the O-H-stretching vibration and reduces the Raman shift. The liquid water peak is much wider then the vapor peak, because the angle between the O-H-bond and the hydrogen bond may differ. The influence of the hydrogen bonds to the O-H-stretching vibration depends on the angle between the hydrogen bond and the O-H-bond.

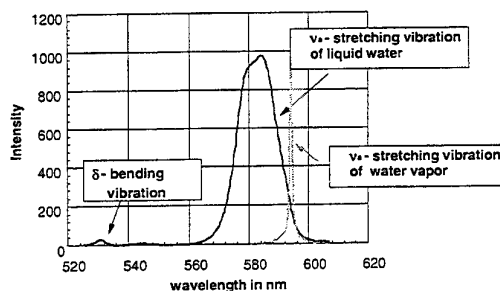


Fig. 3: Raman spectra of Liquid and vaporous water

The shape of the liquid water peak changes with the temperature as shown in Fig. 4

Walrafen explained this effect with a temperature dependent equilibrium between hydrogen-bonded and non hydrogen-bonded O-H stretching oscillators in liquid water. The number of established hydrogen bonds decreases with higher temperatures.

This effect can be used to measure water temperatures with an accuracy of about ± 2 K using an algorithm described in (Karl and Weiss, 1997)

Fig. 4 shows the shape of measured Raman spectra of liquid water at temperatures between 30 and 100 °C. After base line extraction the normalized water peaks cross at the same point (*isosbestic point*) as documented by Walrafen.

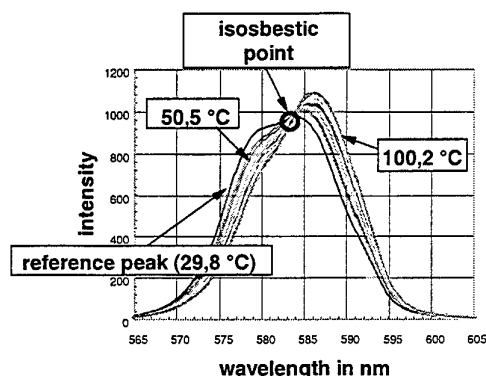
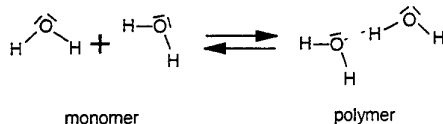


Fig. 4: Temperature dependence of the ν_s - Stretching region of liquid water

The real molecular structure of liquid water is quite complicated, but in simplified terms it can be said that the water peak consists of two peaks with a maximum at 577,6 nm and 589,4 which represent the hydrogen bonded O-H-bonds and the non hydrogen bonded O-H bonds.

The shape of those difference spectra proved to be useful to get the intensity ratio between the peak of the hydrogen bonded and the non hydrogen bonded molecules.

Assuming a temperature dependent equilibrium between hydrogen-bonded and non hydrogen-bonded ν_1 -stretching oscillators, this equilibrium may also be interpreted as an equilibrium between hydrogen-bonded (polymer) and non hydrogen-bonded (monomer) water molecules



The concentration ratio of the established bonds represents the equilibrium constant of that equilibrium. This constant can be expressed by the enthalpy of the hydrogen bonds ΔH^0 and the entropy (Atkins, 1986)

$$\ln\left(\frac{[\Pi]}{[M]}\right) = \frac{\Delta H^0}{R \cdot T} + R \cdot \Delta \Sigma^0 \quad (1)$$

Assuming that the hydrogen-bonded and the non hydrogen-bonded water O-H-bonds cause peaks in the Raman spectra with a differential cross section S_M and S_P , Eq. (1) may be written as

$$\ln\left(\frac{\Sigma_M \cdot I_\Pi}{\Sigma_\Pi \cdot I_M}\right) = \frac{\Delta H^0}{R \cdot T} + R \cdot \Delta \Sigma^0 \quad (2)$$

or

$$\ln\left(\frac{I_\Pi}{I_M}\right) = \chi_1 \cdot \frac{1}{T} + \chi_2 \quad (3)$$

A linear least squares fit to measured temperature and intensity data provided the coefficients c_1 and c_2 . We used Vant'Hoffs principle to compute the enthalpy of the hydrogen bonds ΔH^0 from coefficient c_1 and obtained a value of $10.47 \cdot 10^3$ KJ/kmol. This value is in good agreement to the enthalpies published elsewhere.

If the intensity ratio $\frac{I_\Pi}{I_M}$ is known from measured data the liquid water temperature can be calculated from

$$T = \frac{\chi_1}{\ln\left(\frac{I_\Pi}{I_M}\right) - \chi_2} = \frac{1259.66 \text{ K}}{\ln\left(\frac{I_\Pi}{I_M}\right) - 3.92} \quad (4)$$

TEMPERATURE EVALUATION PROCEDURES

There are two different ways to obtain that intensity ratio.

The first method requests a monochromator or a spectrograph as mentioned above and uses the whole spectral information for temperature evaluation. The spectrograph or monochromator provides a complete Raman spectrum, which allows to calculate the intensity ratio $\frac{I_\Pi}{I_M}$ with best reliability.

The main advantage of this method is, that any Rayleigh-, Mie or fluorescence signal can be separated and discharged easily.

A base line extraction can be done automatically using a line fitting procedure which separates the signals of the spectrum. The image processing procedure presented by Karl and Weiss, 1997 provided water temperatures with an accuracy of less than ± 2 K within a temperature range between 20 and 180 °C as shown in Fig. 5.

Raman spectroscopy has proved to be an adequate method to get one dimensional temperature profiles, therefore. But there are various applications where two dimensional measurements might be more useful. The second method to obtain water temperatures uses narrow band width interference filters. The idea is to use two narrow band bandpass filters which transmit mainly the Raman signals of hydrogen bonded and non hydrogen

bonded O-H bonds.

The laser beam can be expanded to a light sheet. A CCD camera samples the scattered light with or without a spectrograph. Two images of the light sheet taken with different interference filters are necessary to evaluate the water temperature distribution.

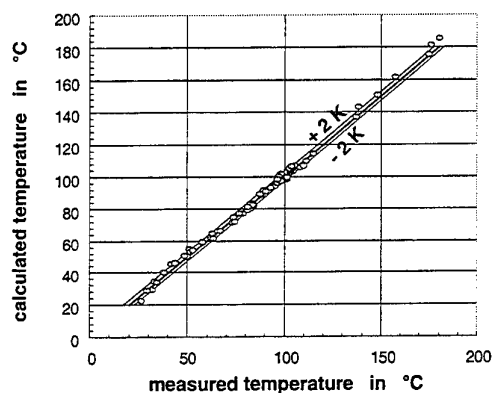


Fig. 5: Water temperatures calculated from Raman spectra (using a spectrograph)

Using two interference filters with a central wavelength at the wavelength of the hydrogen-bonded and the non hydrogen bond Raman wavelength makes it possible to get the intensity ratio $\frac{I_H}{I_M}$ from two separate

measurements with that filters. Using the blue line of an argon ion laser at 488 nm requires two bandpass filters near 577 nm and 589 nm. We used two interference filters with a central wavelength of 578 nm and 590 nm and a full width at half maximum (FWHM) of ± 10 nm. Fig. 6 shows the liquid water spectra transmitted by those filters:

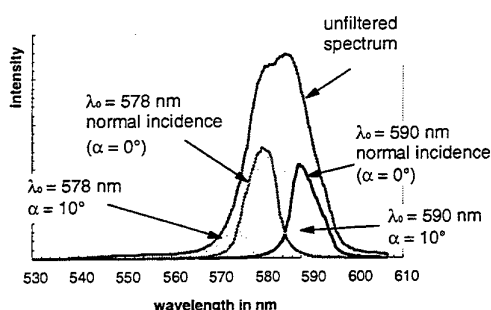


Fig. 6: Spectrum of liquid water transmitted by narrow band interference filters

Fig. 7 shows the spectra of water at different temperatures obtained with both filters. It is obvious that the ratio of the intensities transmitted through the filters depends on the water temperature. Integration of the spectra gives the total intensity transmitted through the filters. The spectra shown in Fig. 7 represent the light

which will meet the pixels of CCD chip corresponding to certain location of the water flow with two dimensional measurements.

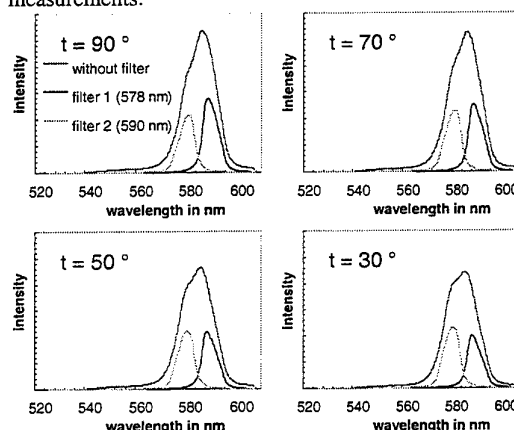


Fig. 7: Influence of the water temperature on the spectra transmitted by the bandpass filters

This integration of the spectra leads to a characteristic line which can be used to calculate water temperatures from two dimensional intensity data according to Eq. (4). The same characteristic can be achieved without experiments only using the transmission curves of the filters and the knowledge of the shape of the water peak with respect to the temperature. The accuracy is much lower as the accuracy achievable with a spectrograph:

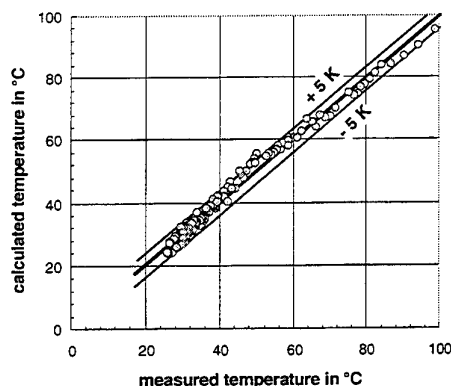


Fig. 8: Water temperatures calculated from Raman signals ('two color method', without spectrograph)

This 'two-color-method' has to deal with two major problems. The first is shown in Fig. 6 and Fig. 9. Narrow band interference bandpass filters are usually Fabry-Perot-filters, which operate with the same principle as the Fabry-Perot interferometer. A Fabry-Perot filter consists of coated surfaces with a well defined distance which

corresponds to a certain wavelength. The transmission of light with a certain wavelength depends on this distance. The central wavelength of the filter is given for normal incidence. The real central wavelength depends on the angle of incidence according to the equation

$$\lambda_{0,\alpha} = \lambda_{0,\alpha=0^\circ} \cdot [1 - \text{const.} \cdot \sin^2(\alpha)] \quad (5)$$

The central wavelength is shifted to lower wavelengths and alters the transmitted spectrum as shown in Fig. 9 for an angle of incidence of 10° . It is obvious that this effect will cause severe errors and it is only valid to calculate water temperature values from the intensity ratio $\frac{I_\Pi}{I_M}$ if

the angle of incidence is very small. But especially for laboratory scale applications, if the distance between laser beam and detector is small this angle of incidence might be very large. Optics with small focal lengths cause the angle of incidence to be 10 degree or more as shown in Fig. 9.

The second problem of the two filter method is caused by fluorescence. High fluorescence rates increase the intensities of the 578 nm and 590 nm peaks and distort the intensity ratio $\frac{I_\Pi}{I_M}$, therefore.

With pure water most of the fluorescence signal originates from the water surface. Reflection and scattering of laser light on solid surfaces water causes additional fluorescence which enhances the total fluorescence rate. For any technical applications the third effect will be the most important. Any solvents or particles cause additional fluorescence which might be even more intense than the Rayleigh signal. Dirtiness of the laser windows and mirrors will enhance fluorescence, too. The best way to eliminate the error caused by fluorescence

is to measure it using a spectrograph. For two dimensional measurements there are two methods to get the fluorescence level. The first possibility is to use a third bandpass filter at a suitable wavelength. If the shape of the fluorescence spectrum is given for a certain optical setup, the intensity measured at a single wavelength will be enough to estimate the fluorescence rate which distorts the Raman signals obtained with the 578 and 590 nm filters. But of course this method increases the number of images which are necessary to get the temperature. If the fluorescence signal does not vary, for example if the particles content or the dirtiness of the water flow keeps constant, it is not necessary to get the fluorescence intensity for each temperature measurement.

A second way which is often used to reduce errors caused by fluorescence can not be used for the presented measurements. Especially for Raman spectroscopy in gases, where high fluorescence or Mie signals superimpose the Raman signal, it might be useful to rotate the polarisation of the laser beam using half wave plates. Mie scattering and fluorescence depend on the polarisation of the laser light only weakly. The difference obtained with two images taken with vertical and horizontal polarisation can be used to eliminate the fluorescence signal, therefore.

But we observed different depolarisation rates for the hydrogen bonded and non hydrogen bonded Raman signals. Rotation of the polarisation plane affected the intensity of both Raman peaks differently. Elimination of fluorescence by rotation of the laser beam polarisation will change the intensity ratio $\frac{I_\Pi}{I_M}$ and will cause additional errors, therefore.

The third method to eliminate fluorescence uses the different time scales of Raman and fluorescence processes. The Raman signal arises spontaneous without retardation. The fluorescence process will last some nanoseconds. Short laser pulses and a intensified CCD camera can be triggered with very short time gates to enhance the ratio between Raman and fluorescence signal.

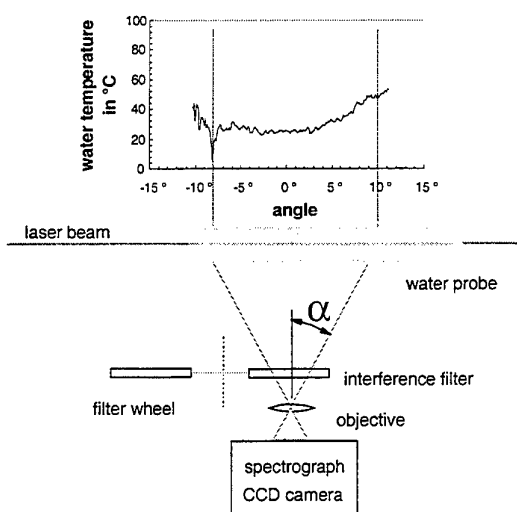


Fig. 9: Influence of the optical set-up to the measured temperature

EXPERIMENTAL APPLICATIONS

In earlier experiments we used Raman spectroscopy to measure concentration profiles in condensation boundary layers during condensation in the presence of non condensable gases. We investigated the condensation of nitrogen steam mixtures at system pressure levels from 0,2 to 2,0 MPa at a thin water layer. The experiments were aimed at measuring local heat transfer coefficients by measuring local concentration profiles. We designed the pressure vessel shown in Fig. 10 to simulate the boundary conditions of one dimensional film theory.

The laser beam was focused vertically onto the water layer and an objective focused the image of the laser beam to the entrance slit of a 125mm - spectrograph. This spectrograph separated shifted Raman signals from unshifted Rayleigh and Mie signals. A CCD chip of an intensified CCD Camera detected the weak Raman signals

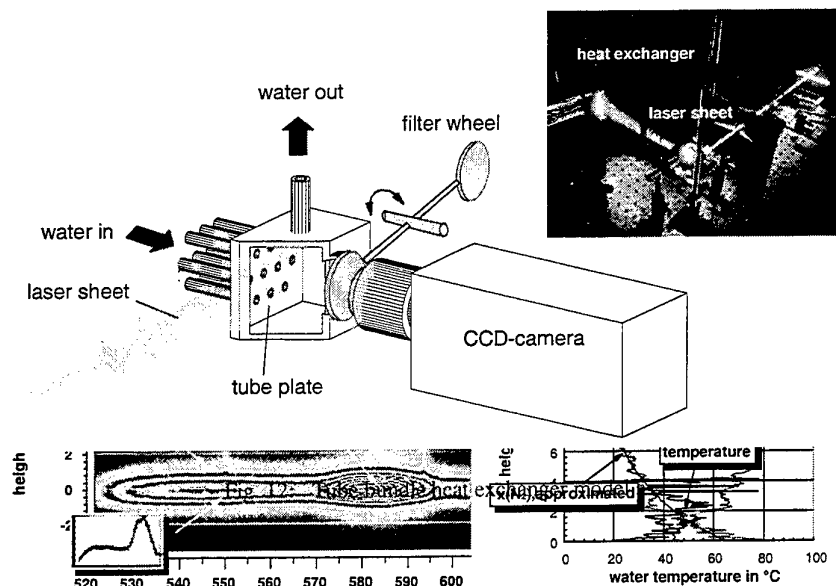


Fig. 10: Raman image of a condensation boundary layer and calculated concentration profiles

and the image processing system provided images of the mass transfer boundary layer as shown in Fig. 10.

Fig. 10 shows two images of the same laser beam, shifted to different wavelengths by the spectrograph. The line located at a wavelength of 550,6 nm is caused by light

scattered at nitrogen molecules and the line located at 594 nm is caused by light scattered at water vapor molecules.

Each pixel row corresponds to a certain position at the laser beam and yields an intensity profile or a Raman spectrum, therefore, to calculate local concentrations from measured intensities.

The steam water interface caused an intense fluorescence signal and a very strong Raman signal of the liquid phase which provided the temperature of the water layer.

The concentration profiles calculated from those images are in good agreement to film theory and the presented method has proved to be suitable to measure heat and mass transfer rates.

With another experiment we tried to get not only a single temperature value but a complete temperature profile in a water layer.

We focused the laser beam of a Coherent SabreFred argon ion laser with a single line output power of about 10 W_{cw} onto a water layer flowing in a rectangular duct inside of an autoclave. The same software which processed the image shown in Fig. 10 calculated temperature profile as shown in Fig.11 from the images provided by the image processing system.

The experiment shown in Fig. 12 was designed to get two dimensional water temperature measurements. We performed the experiments with a small model of a tube bundle heat exchanger and without spectrograph. The CCD camera sampled the scattered light of a light sheet which was focused along the tube plate.

Single tubes were heated and caused different temperatures at those positions where the exit water passed the light sheet. An image of the tube plate without laser light sheet is shown in Fig. 13.

The exit temperatures were measured together with the

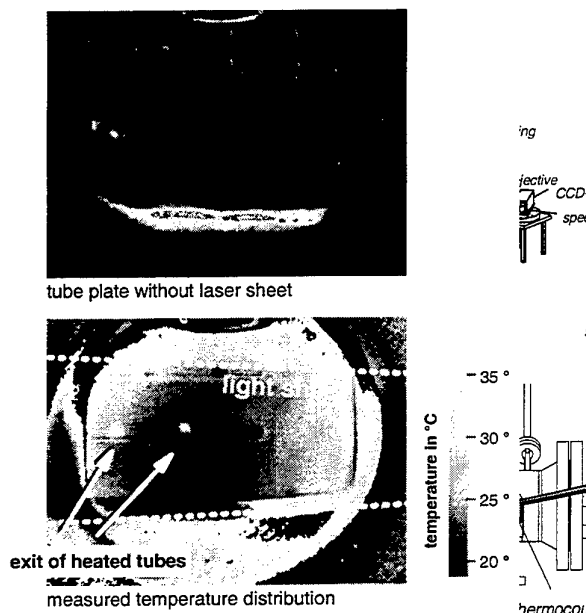


Fig. 13: Image of the tube plate of the heat exchanger model (without laser sheet) and temperature image

Fig. 11: Experimental set-up to measure temperature profiles in stratified flows

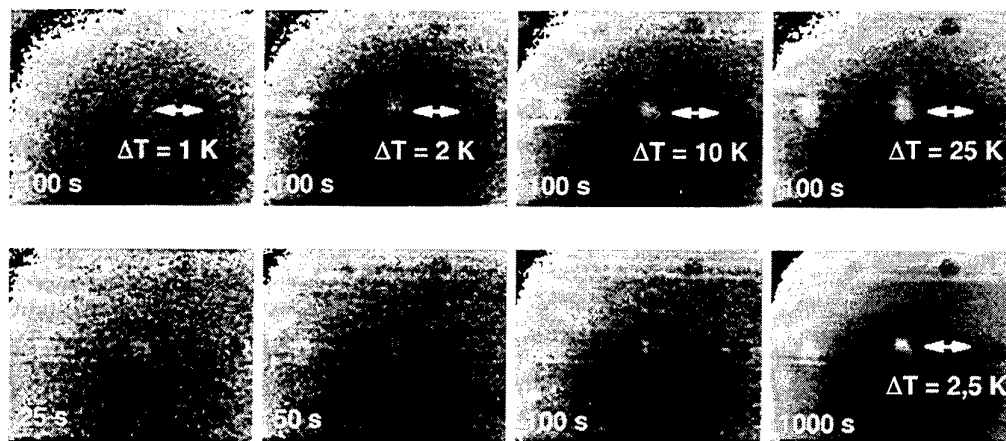


Fig. 14: Temperature images of the water flow in front of the tube plate of the heat exchanger model with different temperature differences and measuring times

camera readings by thermocouples. The exit temperature differences of the tubes in the middle of the tube plate varied between 1 and 30 K.

We sampled the scattered light with each filter for a certain time and used the characteristic to compute a temperature image from the images taken with different filters. We had to measure for a certain time to reduce the statistical errors caused by particles or variation of the laser power.

It is obvious, that the absolute accuracy of this method is not acceptable. Above all the error caused by the angle of incidence has proved to be very high. This effect made the temperature seem to rise from the middle of the image to the edges. But it is significant that temperature differences can be recognized very precisely. This can be skillful to locate or evaluate local temperature differences. Fig. 14 shows the influence of measuring time and the variance of the images with respect to the temperature difference. It is possible to measure absolute temperatures only for normal incidence with an accuracy of about ± 5 K but it is possible to detect local temperature differences of 1 K even with measuring times less than 2 minutes.

CONCLUSION

Measuring water temperatures by means of Raman spectroscopy requires an expensive experimental setup. If flame temperatures shall be measured Raman spectroscopy is a good choice, because there are only few other possibilities to measure temperatures of about 2000 K with sufficient accuracy.

Water temperatures can be measured very simple and with few costs by means of thermocouples.

For that reason water temperature measurements by means of Raman spectroscopy will be useful only for special applications, if very detailed local information is needed - in example for heat transfer applications - or if a

thermocouple will disturb the measurement, in example with micro scale heat transfer applications.

If only low accuracy is required two dimensional measurements may be quite useful to supervise any chemical or thermal processes with a 'two color method' set-up. Because the intensity of the Raman signal is very high it is not necessary to use high sensitive CCD-cameras or high laser power.

Another possible application of the water temperature effect might be to do remote temperature sensing with a LIDAR set-up for example to get ocean water temperatures.

Linear Raman spectroscopy has proved to be an optical measurement method which provides the possibility to measure temperatures of liquid water with highest local resolution even in two dimensions without affecting the fluid flow, therefore. The local resolution is only limited by the optical setup and the resolution of the CCD-chip.

LITERATURE

B. Schrader, Infrared and Raman Spectroscopy, VCH, Weinheim, 1995.

G. Walrafen, M.R. Fisher, M.S. Hokmabadi, W.H. Yang, Temperature dependence of low- and high-frequency Raman scattering from liquid water, J. Chem. Phys., Vol. 85, No. 12, pp. 6970-6971, 1986.

Y. Fujita, S. Ikawa, Effect of temperature on the hydrogen bond distribution in water as studied by infrared spectra, Chemical Physics Letters, Vol. 159, No. 2,3, pp. 184-188, 1989

Leonard, B. Caputo, F.E. Hoge, Remote sensing of subsurface water temperature by Raman scattering, Appl. Opt., vol. 18, No. 11, pp 1732-1746, 1979.

G.Schwaiger, Optische Konzentrationen und Temperatur-Messung in Aerosolen und Sprays, Chem.-Ing.Tech., Vol. 64, No. 1, pp 41-47, 1992. (in German)

J. Karl, Untersuchung des Wärmeübergangs bei der Partialkondensation mittels linearer Ramanspektroskopie, Herbert-Utz-Verlag, München, 1997 (in German)

J. Karl, D. Hein, Measuring water temperature profiles at stratified flow by means of linear Raman spectroscopy, Proceedings 2nd Japanese German Symp. on Multi- Phase Flow, Tokyo University, 1997

J. Karl, T. Weiss, Measurement of condensation heat transfer coefficients at stratified flow using linear Raman spectroscopy, J. Flow Visual. and Image Processing, Vol. 4, No. 3, 1997, pp. 231-245

P. Atkins, Physical Chemistry, Oxford University Press, 1986

Development Of A Fluorescence-Based Temperature Measurement Technique For Two-Phase Flashing Propane Jets

J T Allen and R J Bettis

Health and Safety Laboratory, Harpur Hill, Buxton, Derbys, UK. SK17 9JN.

ABSTRACT

A novel fluorescence-based system has been developed for the non-intrusive measurement of liquid phase temperature in two-phase flashing propane releases.

It is believed that the application of this technique can generate non-intrusive temperature measurements with an accuracy of better than $\pm 1^\circ\text{C}$, over the temperature range of -70°C to 20°C , and will allow comparison with conventionally obtained temperature data.

The technique, in its current format, should be applicable to a range of non-polar alkanes, especially pressure-liquefied gases, subject to calibration.

1. INTRODUCTION

There is a strong interest in two-phase flow in many areas of science and engineering. In the safety field, the interest lies in the accidental releases of pressure-liquefied gases, primarily propane/LPG (flammable) and toxic materials, such as chlorine. Of specific interest, in this area, are the mathematical models and predictive computer codes which may be applied to such releases. At present only the latter regions of a jet, where atmospheric dispersion is dominant, are adequately modelled. It is hoped that these codes may be ultimately employed to mitigate the consequences of accidental releases through a better understanding of the processes, resulting in improved transport and storage design, storage site placements, and other safety features.

For accurate prediction of the likely consequences of any two-phase release, it is desirable that all regions may be modelled from known initial storage conditions, i.e. the source terms. In the momentum driven regions of the propane jet, where the system is furthest from its equilibrium state and measurement is most difficult, little or no experimental

work has been published. There is, therefore, a need for accurate and reliable data from these regions in order to generate and/or refine useful predictive computer codes.

Due to the non-equilibrium nature of the near-field regions however, accurate data measurement is not possible with intrusive techniques, for instance thermocouples. Non-intrusive methods, therefore, such as laser-based techniques present the only possibility for obtaining accurate data measurements in this environment.

The work described in this paper forms part of a project, co-sponsored by the CEC and the Major Hazards Assessment Unit of the Health and Safety Executive, to provide quality data from the near-field regions of two-phase flashing propane releases. Its aim is to investigate flashing two-phase propane jets by the use of conventional and laser-based measurement techniques, and to develop and refine predictive codes from the data for use in risk assessment.

2. EXPERIMENTAL PROJECT

Part of the Health and Safety Laboratory's work has been concerned with obtaining laser-based and conventional measurements in a two-phase flashing jet, utilising a small-scale purpose built facility. Techniques employed have included Laser Doppler Anemometry (LDA), Diffraction-based particle sizing, conventional temperature measurements, and fluorescence-based temperature determination. Data from the full range of experiments has been published in the open literature, or will be in the near future [1, 2, 3, 4].

Earlier work in this project involved the determination of the jet temperature profile by conventional means [5], i.e. thermocouples, although the non-equilibrium nature of the near-field regions of such a jet calls into question the accuracy of the data. It was, therefore, decided to attempt to measure the liquid phase temperature by the use of a non-intrusive

technique. This should generate more accurate temperature profiles and allow direct comparison of the two techniques. Furthermore, the accuracy of other conventional temperature measurements made in two-phase releases could then be re-assessed.

This paper details the development of that technique, and is believed to be the first measurement of liquid propane temperature by this means [6].

3. FLUORESCENCE TECHNIQUE

The technique employed in this work was initially used by Melton to obtain liquid phase temperature in two-phase diesel sprays [7, 8, 9] and then extended to lower boiling-point materials by Ewan [10, 11].

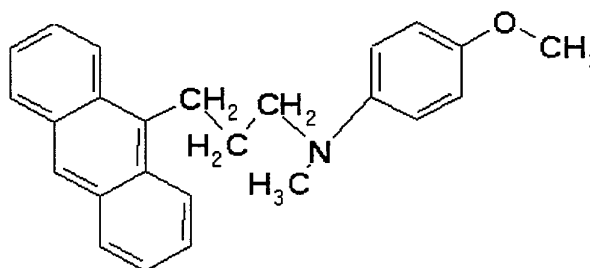
Briefly, the technique is based on the fact that the temperature of a compound effects the population of its various energy levels. The variation of the energy level population in some fluorescing materials, termed fluorophores, affects the intensity and position of peaks in its emission spectrum. If this phenomenon can be reliably calibrated then the intensity at a given wavelength can be used to determine its temperature.

4. FLUOROPHORE IDENTIFICATION

One of the major problems associated with this technique, in relation to propane, is the fact that propane does not itself exhibit fluorescent properties. However, if it can be assumed that, when dissolved in a host material, a temperature-dependent fluorescent material achieves the same temperature as its host then its fluorescent signal can be used to measure the temperature of the host.

A material had, therefore, to be found that exhibited temperature dependent fluorescence, was soluble in liquid propane, and would mimic the behaviour of its host, especially its temperature characteristics. A suitable fluorophore had to meet all these criteria over the range of temperatures expected from the conventional study.

A literature survey revealed little information with regards to solubility and fluorescent properties of materials in propane. Some information was available on materials in other alkane solvents, but very few exhibited the temperature dependence required. One series of papers, however, presented a chemically related group of compounds containing a compound which was shown to have the type of temperature dependence required and was soluble in alkanes [12, 13, 14]. The particular compound was:



1-(N-p-anisyl-N-methyl)-amino-3-anthryl-(9)-propane (referred to in this document as NpaNmaap for brevity)

The spectrum of NpaNmaap had been shown to exhibit a temperature-independent wavelength, and two relatively high intensity temperature peaks [12]. The two high intensity peaks showed, respectively, direct and inverse proportionality to temperature, giving the possibility of high accuracy temperature determination. It had also been shown to be soluble in hexane, making it highly likely to be soluble in other lower order non-polar alkanes such as propane and liquefied petroleum gas (LPG).

Synthesis of the material was undertaken by the Chemistry Department at the University of Sheffield. The synthesis was initially based on the route reported by Pragst et al [13], but a more efficient synthesis route was developed [15], and small quantities were synthesised and supplied.

A more detailed description of the technique, and the properties of the chosen fluorophore, can be found elsewhere [16].

5. PRELIMINARY WORK

5.1 Preliminary Work Experimental Layout

The system utilised for the preliminary work, which is shown schematically in Figure 1, basically comprised a double monochromator and focusing lens system, a photomultiplier tube (PMT), an excimer laser, a calibration cell, and a data acquisition system. These components and their function are described in detail below.

5.2 Experimental Equipment

Monochromator and Associated Components: Two single monochromators, both operating at the same wavelength and containing identical 1200 lines/mm holographic gratings with a blaze wavelength of 500nm, were combined to produce a double monochromator. The advantage of such a system is that it produces a greater spectral accuracy. Light, from the calibration chamber, was focussed onto the entry slit of the double monochromator system by the use of a suitable lens, mounted on a traverse system for ease of use.

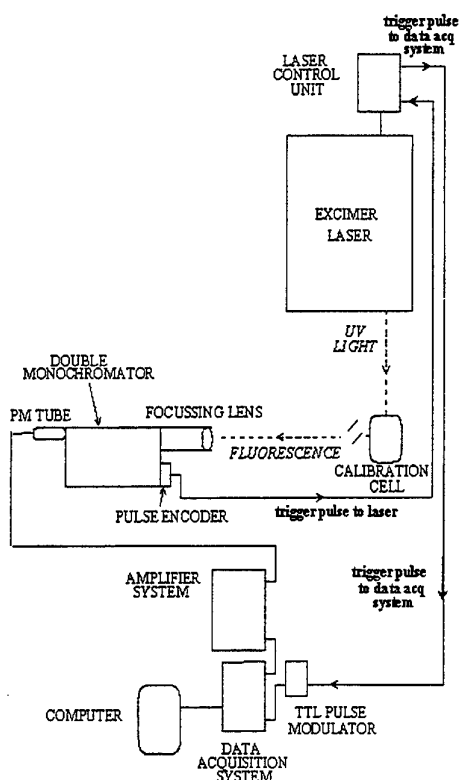


Figure 1 - Schematic Of Initial Experimental Layout

A suitable PMT, for the wavelength range under consideration, was attached to the exit port of the double monochromator. This in turn was connected to the data acquisition system, via an amplifier system. The PMT was powered from a single dual-output stabilised voltage PMT power supply, at between -999 and -1000V.

A purpose-built pulse encoder was attached to the wavelength indicator mechanism of the monochromator system, and was set up such that the laser was triggered to fire a single pulse at fixed wavelength intervals ($<1\text{nm}$) as the monochromator was manually traversed across the wavelength range of interest.

Excimer Laser: The laser employed for this work was a Xenon chloride excimer laser, manufactured by the Estonian Academy of Science, generating pulsed emission at 308nm . The laser could be manually or externally triggered to give variable pulse rates, or could be internally triggered at fixed rates of 10, 25 or 40Hz . In this case the laser was triggered by the pulse encoder attached to the monochromator system, as detailed above.

The laser unit produces an electronic output pulse at the start of each laser pulse. This was utilised to synchronise the data acquisition system with the laser. As the output pulses from the laser were very short and electrically noisy, they were first used to trigger a longer and more stable TTL pulse from a signal generator, and this 'clean' pulse was used to trigger the data acquisition.

A pulse counter was additionally paralleled into the laser output pulse system in order to indicate the number of laser shots fired. The Excimer laser and calibration chamber can be seen in Figure 2.



Figure 2 - Excimer Laser and Calibration Chamber

Calibration Chamber: The calibration chamber is shown schematically in Figure 3, and can be seen in the preliminary experimental layout in Figure 2. It is of stainless steel construction, with a UV quality input window and two UV quality output windows. The output windows are situated opposite each other and are above, and at 90° , to the axis line of the input window. Thus the fluorescence signal was collected at right angles to the line of excitation by the monochromator system. The chamber was fitted with a k-type thermocouple, situated close to the bottom face when the chamber was positioned in the experimental layout, to allow the liquid propane temperature to be determined. The temperature was read shortly before and immediately after any fluorescence measurement.

Extensive tests were undertaken prior to this work to ensure the suitability of this chamber both to contain propane under the range of temperatures and pressures required, and for its optical inactivity in terms of unwanted fluorescence generation.

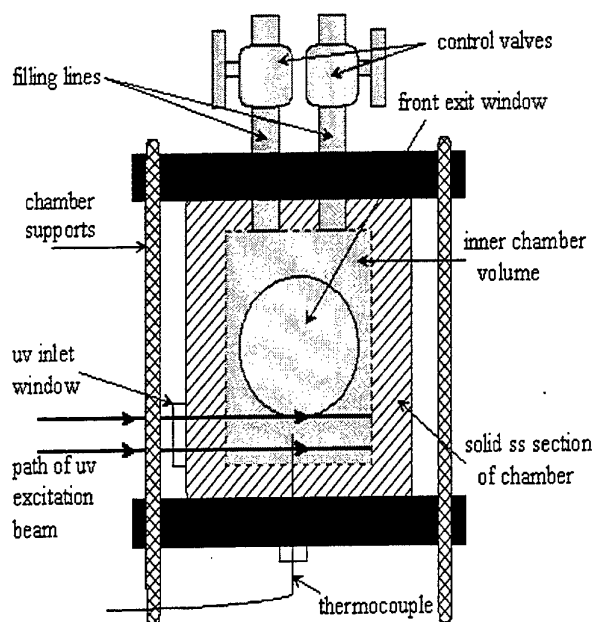


Figure 3 - Schematic Of Calibration Chamber

For the range of experiments detailed in this report, the chamber contained liquid propane doped with a known concentration, $3.0 \times 10^{-4}M$, of NpaNmaap. To obtain the temperature ranges required the chamber was cooled to around $-45^{\circ}C$ in a freezer unit and allowed to warm up by natural convection from the laboratory air.

Data Acquisition System: The output from the PMT, following each laser pulse, was recorded by a Biodata Microlink data capture unit, running under Windmill's Streamer software on a standard personal computer. Subsequent data analysis and manipulation was undertaken using Jandel Scientific's Sigmaplot software.

5.3 Preliminary Work

After simple tests with the calibration chamber to confirm the solubility and fluorescence of the fluorophore in propane, the fluorescence emission spectrum and preliminary temperature dependence was determined, using the system detailed in Section 5.1.

A spectrum of NpaNmaap, obtained from averaging of four independently obtained spectra, is shown in Figure 4. These spectra were obtained at a liquid propane temperature of $-20^{\circ}C$. The two emission peaks expected from the literature can be clearly seen, as can the UV excitation peak at 308nm. The second harmonic of the excitation peak is also evident at 616nm.

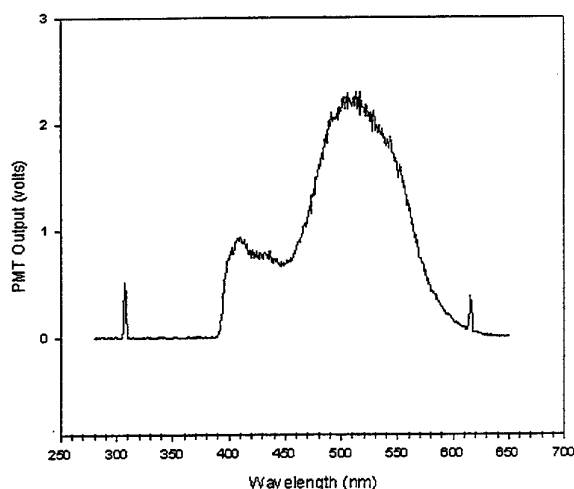
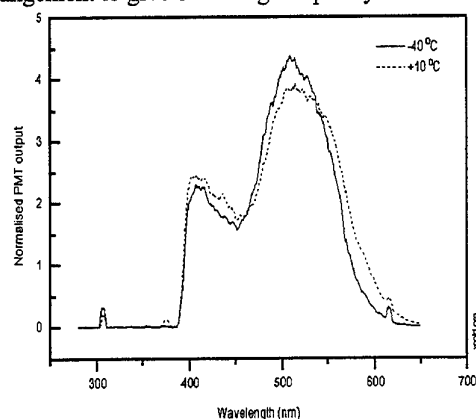


Figure 4 - Spectrum of NpaNmaap at $-20^{\circ}C$

The temperature dependence was studied by taking full spectra, in the manner described above, at a range of temperatures from $-40^{\circ}C$ to $10^{\circ}C$. A temperature dependence was observed, but was not as clear as reported previously [12]. The system was improved by the addition of a nitrogen jet, applied to the measurement (front exit) window, to ensure that ice formation did not occur. This resulted in improved quality spectra at lower temperatures.

The two main peaks were observed, but did not seem to be indirectly proportional to one another with respect to the temperature. The overall level of fluorescence measured across the spectrum was also seen to change with temperature.

The data acquisition system was modified by adding a signal amplifier and improving the wiring arrangement to give better signal quality.



**Figure 5
Temperature Dependence Plot of NpaNmaap**

With this revised system, subject to normalisation of the spectra against the temperature-independent wavelength intensity value, the expected behaviour was observed, as shown in Figure 5.

This plot demonstrates a definite temperature dependence in the fluorescence spectrum. It also suggests that accurate measurement of the temperature effect could be achieved by determination of the fluorescence intensity ratio of two wavelengths, one representative of each of the two peaks present in the spectrum. Study of the spectra resulted in the choice of 410nm and 510nm as the representative wavelengths for the two peaks.

6. CALIBRATION DETERMINATION

6.1 Full Calibration Experimental Layout

In order to undertake the full calibration measurements, the double monochromator was disassembled into its two component single monochromators, each one fitted with an identical model PMT at its exit port.. This allowed the simultaneous measurement of intensity of the two chosen wavelengths, 410nm and 510nm. The emitted fluorescence signal was split between the two monochromators, after focusing by the lens system, by the use of a 50:50 beam splitter, as shown schematically in Figure 6.

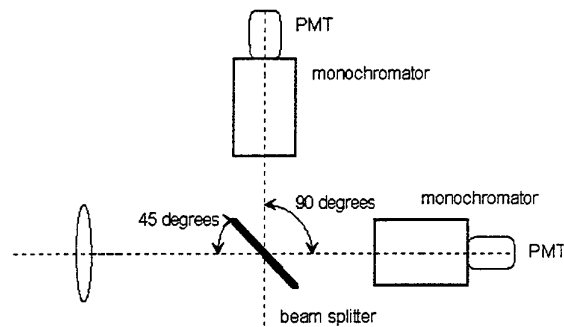


Figure 6 - Schematic of Dual Single Monochromator System and Beam Splitter

Care was taken to ensure that the fluorescence beam path lengths were equal for both monochromators, and that each split beam was therefore identically focussed onto the input slit of its respective monochromator.

For the full calibration experiments, where the monochromators were set at fixed wavelength values, the pulse encoder was removed from the system and the laser was triggered by its internal system at a pulse rate of 10Hz, with a final few pulses being triggered manually by the operator so as to obtain a constant number of pulses.

All experiments were undertaken in a totally dark environment, with the lens and monochromator system being enclosed to further reduce any effect of stray light. The experimental layout of the monochromator system can be seen, without enclosure, for the full calibration experiments in Figure 7. All other pieces of equipment used for the full calibration are the same as that used for the preliminary work and detailed in Section 5.2

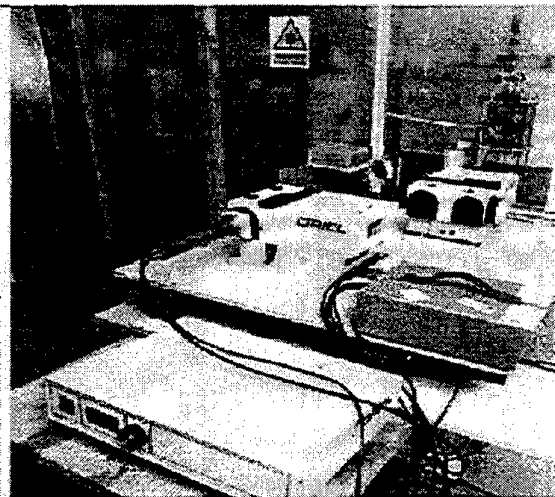


Figure 7 - Dual Single Monochromator System and Calibration Chamber

6.2 Initial Full Calibration

A full calibration was then undertaken using the system outlined in Section 6.1. The number of laser pulses fired, and hence fluorescence intensity measurements taken, at each temperature was 200 in order to provide a statistically viable average for use in the ratio calculation.

Calculation Of Fluorescence Intensity Ratio: As detailed previously, NpaNmaap possessed two fluorescence intensity emission peaks, one with direct and one with inverse proportionality to temperature. from the preliminary work, two wavelength values were chosen as representative of these two peaks; 410nm and 510nm. For the full calibration experiments, one monochromator was set to measure the intensity of the 510nm fluorescence emission, and the other 410nm emission.

The calibration plot was determined from the relationship between the ratio of these two wavelengths and temperature. This method of calibration has the advantages of removing the effects of any laser power variation from the equation, and increasing the accuracy of the temperature calibration process, as suggested elsewhere [16].

The value of the fluorescence intensity ratio for the two wavelengths at any given temperature was calculated using the following equation:

$$\text{Ratio} = \text{PMT1 (410nm)} / \text{PMT2 (510nm)}$$

6.3 Relative PMT Output Problems

It was noted in system trial runs that, with the monochromators set to the same wavelength, a significant change of ratio was obtained with small changes to the set up, particularly those resulting in a change in access for ambient light and fluorescence emission.

Further investigation showed that the two PMTs were exhibiting different responses (i.e. voltage outputs) in relation to each other with respect to varying input light intensities. As this effect would render the system inoperable, it was necessary to try and remove it.

6.4 PMT Intensity Sensitivity Tests

A series of tests were undertaken, using neutral density (ND) filters to simulate varying light intensity inputs, to try and find a solution to the problem.

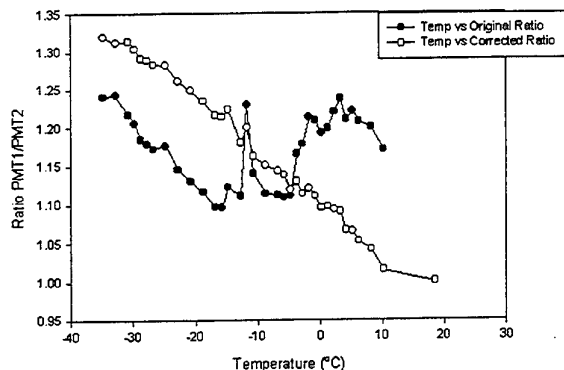


Figure 8 - Comparison Of Corrected and Uncorrected Ratio Data

It was found that a correction factor, in the form of a quadratic equation, could be applied to one of the PMT voltage readings in order to give intensity independent ratio values at the two chosen wavelengths. The effect on the calculated ratio of applying the correction factor is shown in Figure 8, where it has been applied to the data from an initial calibration run.

As can be seen, the inclusion of the correction to the PMT output makes a most significant difference to the results obtained. The fact that the corrected results show a reasonably good fit to a linear relationship between Ratio and Temperature across the measured range suggests that the change has improved the quality of the data.

6.5 Final Calibration

Having determined suitable normalisation parameters for the two PMTs, a final calibration was undertaken. This was undertaken with the dual single monochromator system as detailed previously. After application of the normalisation parameters, and suitable data manipulation, a relatively good plot was obtained. It was however noticed that, at about -15°C and 0°C , deviations from the approximately linear temperature/fluorescence intensity occurred, as can be seen in Figure 9.

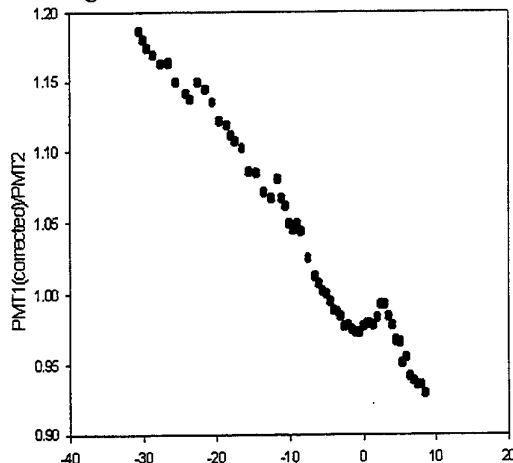


Figure 9 - Calibration Data Showing Anomalous Deviation

Consideration of the problem suggested that this may be due to the formation and melting of ice occurring on the back window of the chamber. This process could result in an unequal transmittance/reflectance of the two measured wavelengths, giving rise to further variation in wavelength ratio, in addition to that generated by the temperature dependency of the fluorescence process.

To test this hypothesis, the outer surface of the back exit window was coated with a white non-fluorescing material. A plate was then attached over the window, the remaining volume being taken up with hygroscopic crystals to further reduce the likelihood of any ice formation. The calibration process was then repeated. In this final calibration determination, presented in Figure 11, the anomalous fluorescence/temperature dependence is not evident.

6.6 Conclusions From Normalised Calibration Data

After application of the PMT normalisation parameters, a good temperature/fluorescence ratio relationship was obtained. Although not linear in its form, the calibration can be considered linear over a wide range of the temperatures studied. It should be noted however that the calibration will have to be

extended down to $\sim 80^{\circ}\text{C}$, the approximate minimum temperature determined by the conventional studies [5], in order to be usefully applied to a free jet situation. The pseudo-linear relationship is unlikely to be prevalent across this extended range, and a suitable mathematical fit to the relationship will need to be found.

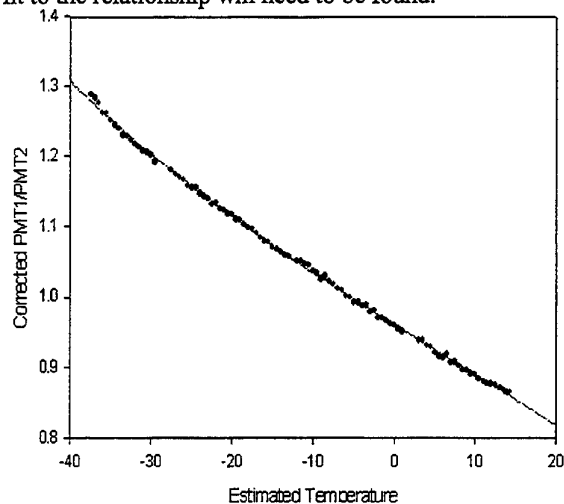


Figure 10 - Final Calibration Data

7. OVERALL CONCLUSIONS

The material and system was found to be suitable for use in two-phase propane releases, and possibly other low boiling point (non-polar) alkanes of interest, e.g. butane, LPG giving a potential accuracy of $\pm 1^{\circ}\text{C}$.

The system should provide a way of making non-intrusive temperature measurements in the near-field regions of two-phase flashing propane releases. The next part of the work will involve the application of the technique to determine temperature profiles in a jet release, utilising the purpose built small-scale release facility.

Prior to the undertaking of any free jet measurements, consideration will have to be given to the consequences and safety implications of the release of NpaNmaap into the atmosphere and its possible deposition inside the small-scale jet release facility.

A number of potential experimental problems, such as the effects of droplet number density, droplet boiling, and possible fluorescence scattering and re-absorption, with respect to the fluorescence signals may also need to be addressed before the technique can be practically applied to a laboratory scale free jet.

A more detailed and comprehensive report on the work presented in this paper, and its attendant theory, can be found elsewhere [16].

ACKNOWLEDGEMENTS

Acknowledgement is given to Doz. Dr. sc. nat. F Pragst, Institut Fur Gerichtliche Medizin, Charite der Humboldt-Universitat, Berlin, for information on the properties of NpaNmaap and related compounds, and the supply of small quantities of the same.

Acknowledgement is also given to Dr B Ewan, University of Sheffield, for technical advice in relation to the exciplex fluorescence technique.

REFERENCES

- [1] Allen J T and Bettis R J, 'Valid Data Abstraction From LDA Measurements In Two-Phase Flashing Propane Releases', Proceedings of the Seventh International Conference 'Laser Anemometry - Advances and Applications', 8th-11th September 1997, Karlsruhe, Germany, pp509-516.
- [2] Allen J T, 'Laser-Based Measurements In Two-Phase Flashing Propane Jets: Part One - Velocity Profiles' J. Loss Prev. In preparation.
- [3] Allen J T, 'Laser-Based Measurements In Two-Phase Flashing Propane Jets: Part Two - Droplet Size Distributions' J. Loss Prev. In preparation.
- [4] Allen J T, 'Optical Measurement and Data Manipulation of Droplet Size Distribution in Two-Phase Flashing propane Jets', Int. Conf. on Optical Methods and Data Processing in Heat and Fluid Flow, 16th-17th April, 1998, City University, London, UK, pp 97-112.
- [5] Allen J T, 'Conventional Temperature Measurements in Small Scale Two-Phase Flashing Propane Jet Releases', HSL Section Report IR/L/FR/95/5, 1995.
- [6] Allen J T, 'The Application Of Laser-Based Measurement Techniques To Two-Phase Releases' HSE Internal Report IR/L/FR/93/10, 1993.
- [7] Murray A M, and Melton L A, 'Fluorescence Methods For Determination of Temperature in Fuel Sprays' App Opt, Vol. 24, No. 17, 1985.
- [8] Murray A M and Melton L A, 'Exciplex Visualisation Systems for Low Boiling Hydrocarbons'
- [9] Gossage H E and Melton L A, 'Fluorescence Thermometers Using Intramolecular Exciplexes' App Opt, Vol. 26, No. 11, 1987.
- [10] Ewan B C R, 'The Development of Spray Diagnostics Instrumentation', RLSD Section Report, IR/L/FR/89/26, 1989.

[11] Ewan B C R, 'The Development of Equipment for the Optical Investigation of Evaporating Sprays', RLSD Section Report, IR/L/FR/90/24, 1990.

[12] Pragst F, Hamann H-J, Teuchner K, Naether M, Becker W, and Daehne S, 'Steady State And Laser Spectroscopic Investigations On The Intramolecular Exciplex Formation Of 1-(N-p-Anisyl-N-Methyl)-Amino-3-Anthryl-(9)-Propane', Chem Phys Lett, Vol. 48(1), 36-40, 1977.

[13] Hamann H-J, Pragst F, Jugelt W, 'Preparation and electrochemical properties of N,N-disubstituted 1-amino-3-(9-anthryl)-propane derivatives' J. prakt. Chem. 318, (8) pp369-380, 1976.

[14] Hamann H-J, Jugelt W, Pragst F, 'Intramolecular exciplex formation of some 1-(N-methyl-N-phenyl)-amino-3-(9-anthryl)-propane derivatives' Z. Chem. 14, (12) pp475-477, 1974.

[15] Spivey A C, Bissell A J, and Stamman B, 'A Practical Synthesis of N-p-Anisyl-N-methyl-amino- 3-(9-anthryl)-propane: An Exciplex Fluorescence 'Thermometer'', Synthetic Communications, Vol. 28(4), 623-632, 1998.

[16] Allen J T, 'Development Of a Fluorescence-Based Temperature Measurement Technique For Two-Phase Flashing Propane Releases', HSL Section Report, FS/98/02, 1998.

COMBINED MEASUREMENT OF VELOCITY, TEMPERATURE AND PRESSURE IN COMPRESSIBLE GAS FLOWS USING LASER-INDUCED IODINE FLUORESCENCE

Marc Havermann and Alfred E. Beylich

Lehrgebiet Electric Propulsion, Shock Wave Laboratory, RWTH Aachen
Templergraben 55, D-52056 Aachen, Germany

ABSTRACT

A laser-induced fluorescence (LIF) measurement system has been developed to study compressible gas flows. Iodine molecules are seeded into the flow and excited by an argon ion laser at 514.5 nm. A combined measurement of velocity, temperature and pressure is possible for velocities down to 30 m/s, temperatures below 300 K and pressures lower than 15 kPa. Experimental results are presented for supersonic free jets. The results agree well with theory and the absence of any velocity slip proves that this method is well suited for the study of high speed flows with strong gradients.

1. INTRODUCTION

The accurate measurement of flow properties in gasdynamic flowfields is a challenging task. Intrusive measurement techniques like Pitot tubes, for example, have a limited spatial resolution and can disturb inner supersonic flows considerably through the formation of shock waves.

The schlieren method is a typical example of an established non-intrusive technique. It yields a fast and global survey of the flowfield, providing, however, only little quantitative information.

The most common laser-based measurement technique is laser Doppler velocimetry. This method is suited to measure velocity and turbulence components, but measurements can be incorrect in areas with strong velocity gradients such as shock waves or shear layers due to the inertia of seeding particles.

Laser-induced fluorescence (LIF) is a measurement technique which has the potential to overcome the mentioned problems because of molecular-size tracers. Additionally, since the fluorescence signal is related to the thermodynamic state (Demtröder (1996)), a

simultaneous measurement of velocity, temperature and pressure is possible. Iodine LIF was first used for flow measurements 15 years ago at Stanford University by McDaniel et al. (1983). The technique was perfected at the University of Virginia, where Donohue and McDaniel (1996) performed accurate planar measurements of velocity, temperature and pressure in complex flowfields.

A similar, single-point iodine LIF measurement system has been developed for the study of supersonic mixing flows and is presented in this paper.

2. LASER-INDUCED FLUORESCENCE (LIF) MEASUREMENT TECHNIQUE

If electronic transitions of atoms or molecules are excited and if the lifetime is of the order of microseconds or less, spontaneous emission of light, called fluorescence, can occur. In LIF measurements, a tunable narrowband laser is normally used to scan the excitation spectrum, whereas the broadband spontaneous emission signal is recorded.

The iodine molecule is a good choice for a seed molecule for gas flow measurements at low pressures, because it has a dense absorption spectrum with a strong emission signal in the visible. It can easily be seeded into gas flows by means of crystal sublimation because of its high vapour pressure (40 Pa at room temperature). Two blended, strong absorption lines can be excited with the 514.5 nm line of a tunable, single mode argon ion laser (Fig. 1). The lines are assigned by their rotational branches (P or R), their rotational quantum numbers and, in brackets, their vibrational quantum numbers of the excited electronic and the ground state, respectively (Hiller and Hanson (1990)).

The fluorescence signal for each absorption line is proportional to:

- Fluorescence efficiency factor (Stern-Volmer factor), which depends on the lifetime of the excited state and on the quenching rate which is related to the thermodynamic conditions
- Laser power (in the unsaturated regime)
- Absorption line shape function which depends on temperature and pressure and which is a convolution of both Doppler and collisional broadening
- Number density of iodine molecules which is proportional to the seeding fraction
- Fractional population of iodine molecules in the absorbing energy level
- Rotational and vibrational line strengths.

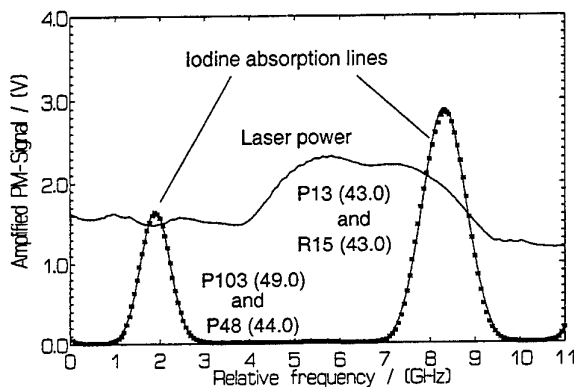


Figure 1. Measured LIF excitation spectrum from reference cell containing iodine at vapour pressure ($T=295$ K, points: measurement, line: Gaussian-fit).

A measured LIF spectrum at a low pressure shows that the absorption line shapes look like Gaussian functions (Fig. 1). The single mode argon ion laser line width is not narrow enough in frequency to resolve the hyperfine structure of the iodine molecule.

The principle of velocity measurements is explained in Fig. 2. A molecule moving at a velocity u is excited by the laser beam at an angle of incidence α .

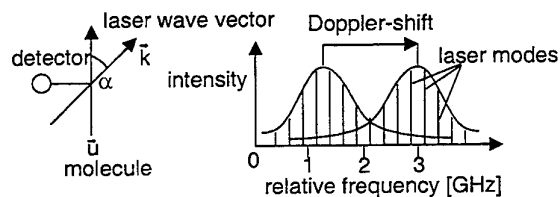


Figure 2. Principle of LIF velocity measurements.

The molecule acts as a moving receiver and receives a shifted excitation frequency according to the Doppler effect. If the LIF signal in the flow is compared to a static reference signal, the frequency shift is given by

$$\Delta\omega = 2\pi\Delta\nu = \vec{k} \cdot \vec{u} = \frac{2\pi}{\lambda} u \cos \alpha. \quad (1)$$

The rotational temperature (which for thermodynamic equilibrium corresponds to the static flow temperature) can be measured by exciting two different absorption lines (two-line method, see Ni-Imi et al. (1995)). If the ratio of the two LIF signals is used, all factors mentioned above cancel out except for the fractional populations and the rotational and vibrational line strengths (Hönl-London and Franck-Condon factors, respectively). The fractional population is assumed to have a Boltzmann distribution, since flows at thermodynamic equilibrium are studied here. The total fractional population can be written as the product of the vibrational and the rotational fractional populations:

$$f = f_R \cdot f_V = \frac{(2J''+1) \exp\left(-\frac{\Theta_R}{T} J''(J''+1)\right)}{Q_R} \cdot \frac{\exp\left(-\frac{\Theta_V}{T} (v''+0.5)\right)}{Q_V}. \quad (2)$$

Additionally, a degeneracy factor for the hyperfine structure has to be considered, see Hiller and Hanson (1990).

The calculated intensity ratio has been plotted against the temperature and shows a high sensitivity for cold temperatures (Fig. 3).

Experiments in a supersonic free jet and with a heated iodine cell, however, showed that the theory is not consistent. If the temperature exceeded 90 K the measured intensity ratio was higher than the theoretical one so that temperatures were underpredicted considerably.

The same phenomenon was observed by Donohue (1997). He argued that a probable reason for this discrepancy is that the fluorescence efficiency from the upper to the lower state (Stern-Volmer factor) is not the same for all lines as assumed in the two-line method. He corrected the fluorescence model empirically and a similar approach has been applied here by multiplying

the theoretical intensity ratio by a linear temperature dependent coefficient (Fig. 3).

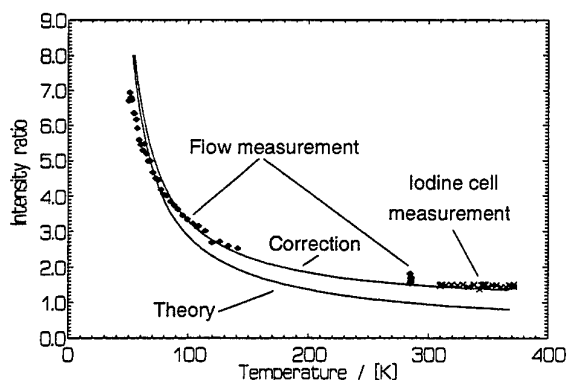


Figure 3. Calculated and corrected temperature dependence of the intensity ratio of the absorption lines (P13/R15 to P103/P48).

For the pressure measurements the absorption linewidth of the P13/R15 absorption line is taken into account. As shown in Fig. 4, the halfwidth of the absorption lines is increased at a higher pressure.

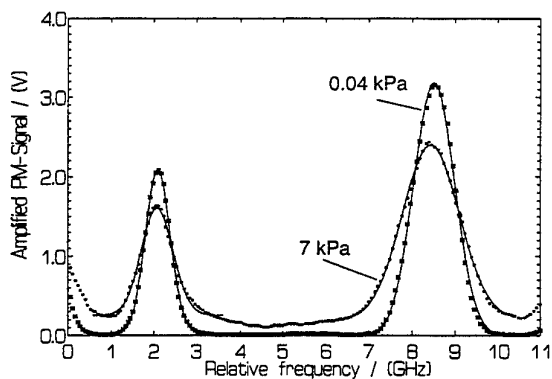


Figure 4. LIF spectrum at different pressures.

An analytical description of the linewidth, however, leads to complicated calculations because iodine absorption lines exhibit a hyperfine structure. A convolution integral which considers the different line broadening effects has to be calculated for every hyperfine line, see Hirai and Teshima (1998).

A simplified, semi-empirical approach has been developed here.

The thermal motion of the molecules leads to an inhomogeneous line broadening which is expressed by the Doppler width (Demtröder (1996)):

$$\Delta\nu_{DW} = \lambda \sqrt{\frac{8 \ln(2) kT}{M}} \quad (3)$$

Collisions between the molecules cause a homogeneous line broadening which is called collisional or pressure broadening. It depends on the total number density of the iodine-air mixture which corresponds approximately to the total number density of air molecules:

$$N = \frac{P}{kT} \quad (4)$$

Collision broadening parameters are rarely available in the literature, however. Therefore, a calibration measurement with a variable pressure cell was conducted to determine the variation of the linewidth at room temperature. Fig. 5 shows that the halfwidth depends linearly on the pressure in the range from 0 to 15 kPa. A linear regression is applied to the datapoints and the slope is used to calculate the pressure broadening.

The contribution of the hyperfine structure is assumed to have a constant value of 0.8 GHz, as measured by Levenson and Schawlow (1972).

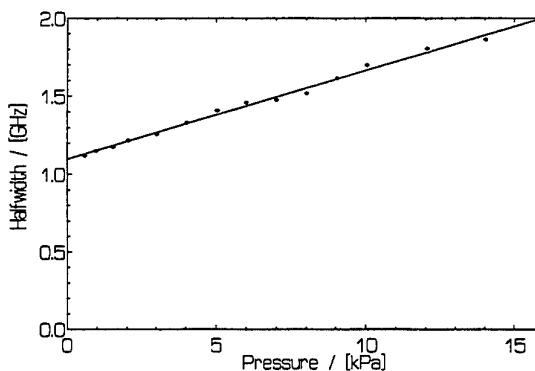


Figure 5. Absorption line halfwidth versus pressure.

The three line broadening effects are combined to Eq. (5) for the calculation of the linewidth. The constant factors are given in Table 1.

$$\Delta\nu_w = A \frac{P}{T} + B\sqrt{T} + C \quad (5)$$

Table 1. Constants used in Eq. (5).

A	B	C
13.7 GHz K/kPa	0.02 GHz/K ^{0.5}	0.8 GHz

Molecular collisions not only cause line broadening but also a frequency shift of absorption lines. The collisional impact shift has to be subtracted from the measured frequency shift to obtain the Doppler shift for the velocity calculation.

An empirical relation was obtained by Donohue and McDaniel (1996):

$$\Delta\nu_I = D \frac{P}{T^{0.7}}, \quad (6)$$

with $D = -0.39 \text{ GHz K}^{0.7} / \text{kPa}$.

The minus sign accounts for the fact that the collisional impact shift leads to a downshift of the line center frequency.

3. EXPERIMENTAL FACILITIES

Experiments have been performed using a low density wind tunnel running with atmospheric air. Test sections can be attached to a large vacuum tank (28 m³) connected to several vacuum pumping systems. A vacuum pressure down to 1 kPa can be obtained for a reasonable test section size. The wind tunnel can be operated either in a continuous or in an intermittent mode depending on the mass flow through the test section.

The experimental set-up for LIF measurements is shown in Fig. 6.

The incoming air is dried by means of silica gel and flows through a mixing chamber where iodine molecules are seeded into the flow by sublimation from crystals. An iodine seeding fraction of 10 ppm has been measured, which yields good fluorescence signals. The seeding fraction is well below the saturation limit of 400 ppm. A high seeding fraction is not desirable for two reasons: First, the air-iodine mixture becomes optically thick which would result in a non linear response of the fluorescence signals. Second, iodine is corrosive and should only be used in a small amount.

A Coherent Innova 200-15 argon ion laser is operated in single mode by inserting an air spaced intra-cavity etalon (Spectra Physics Model 589, free spectral range 10 GHz). As a result, the laser line width

is narrowed from 10 GHz (8.8 pm) in multi mode operation down to 20 MHz (0.02 pm) in single mode operation. This is sufficiently narrow to analyse an absorption line profile with a typical halfwidth of 1.5 GHz (1 pm).

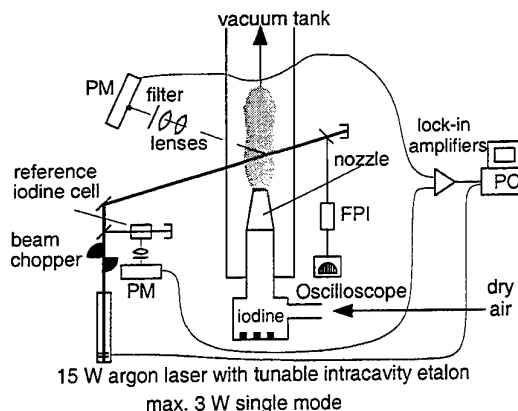


Fig. 6. Experimental set-up for LIF measurements.

The etalon acts as a bandpass filter and selects one of about 120 longitudinal modes (80 MHz apart) in the laser cavity. It is possible to tune the etalon by varying the optical path length in the filter which is achieved by smoothly tilting the etalon with a small DC motor.

The laser beam is adjusted to intersect the test section axis at an angle of 70°. An angle not equal to 90° is necessary for the detection of the Doppler shift according to (Eq. 1). While the laser is tuned over an absorption line, the broadband fluorescence emission of the excited iodine molecules is imaged on a photomultiplier (measuring volume size ~ 1 mm³) and the absorption line is reconstructed. The fluorescence emission is shifted to longer wavelengths because the excited energy level decays to all possible ground states. Therefore, the emission signal can be detected by blocking the excitation laser wavelength with a longpass filter positioned in front of the detector (530 nm cut-off frequency).

A part of the laser beam is split to the reference iodine cell containing iodine crystals under vapour pressure. Both photomultiplier signals are amplified by lock-in amplifiers, then digitised using a 12 bit AD-card, and processed by a PC which controls also the etalon tuning and traversing mechanism. The laser mode structure can be observed using a Fabry-Perot interferometer and an oscilloscope.

An example of a typical measurement is plotted in Fig. 7. The measured data of the LIF signals in the flow

and reference cell are normalised to the laser power which is recorded simultaneously with an amplified photodiode. The absorption lines are fitted with Gaussian functions in order to determine the maximum value which is used to calculate the Doppler shift for the velocity measurement.

The ratio of the maximum intensity of the P13/R15 line to the maximum intensity of the P103/P48 line yields the temperature (Fig. 3). The temperature and the halfwidth of the P13/R15 line is used in (Eq. 5) to determine the pressure. The tuning and data acquisition process takes about 6 s so that only time averaged values can be obtained.

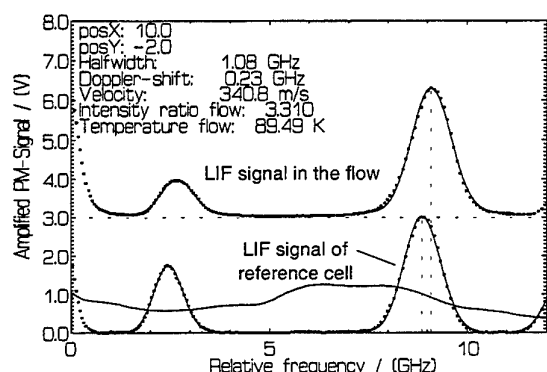


Figure 7. Plot of LIF measurement.

4. EXPERIMENTAL RESULTS

A supersonic free jet issuing from a small round orifice into a low pressure is used to test the LIF system (Fig. 8). This kind of flow is an ideal test case for two reasons: First, it offers a wide range of thermodynamic flow property values with a strong gradient after a normal shock at the end of the expansion process (Mach disk). Second, a Mach number relation for the isentropic expansion along the free jet centreline axis which is valid for the distance of one orifice diameter from the exit up to the Mach disk was presented by Ashkenas and Sherman (1966). The location of the Mach disk can be computed with an empirical formula:

$$x_M = 0.67 \sqrt{\frac{p_0}{p_b}} d \quad (7)$$

If the stagnation conditions are known, the velocity, pressure and temperature can be calculated according to the Mach number distribution and the isentropic Mach number relations (Liepmann and Roshko

(1957)), so that a comparison of experimental and theoretical results is directly possible.

The state after the Mach disk is computed with the normal shock relations and the flow properties are assumed to be uniform for a short distance after the Mach disk.

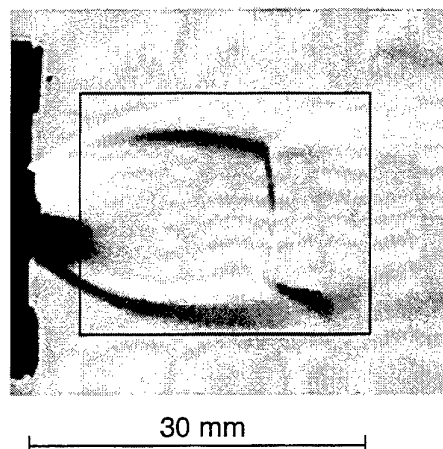


Figure 8. Schlieren picture of a free jet expanding from an orifice. Frame: Cf. Figs. 12, 13, 14.

Centreline axis measurements for the velocity, temperature and pressure distribution are presented for a free jet with an orifice diameter of 7.5 mm and a pressure ratio of 20.7 (stagnation to background pressure). The maximum Mach number before the Mach disk is 4.85 corresponding to a velocity of about 700 m/s, a temperature of 60 K and a pressure of 0.23 kPa. Downstream of the Mach disk, the Mach number is reduced to 0.42 which corresponds to a velocity of 142 m/s, whereas the temperature and pressure rise to 290 K and 6.16 kPa, respectively. The theoretical location of the Mach disk is found at 22.9 mm from the orifice exit.

In the following pictures, measurements are denoted by points and the theoretical distribution is plotted as a smooth line.

The velocity measurements have been corrected with the collisional impact shift calculated from the theoretical pressure. Fig. 9 shows that the impact shift plays a significant role only up to a distance of 10 mm from the orifice exit.

The measurement is consistent with the theoretical distribution and the velocity drop after the Mach disk is represented very clearly. After the Mach disk, the flow

is slightly reaccelerated. The average absolute error is ± 20 m/s.

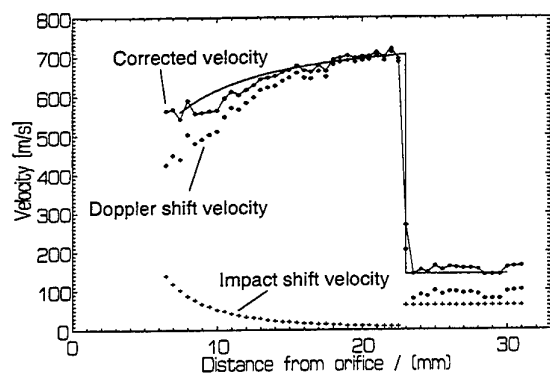


Figure 9. Centreline axis velocity measurement of the free jet.

The temperature measurements prove to be in good agreement with the theoretical temperature distribution especially at cold temperatures ($T < 100$ K), where the sensitivity of the two-line method is high (Fig. 10). The average absolute error is ± 10 K (calculated up to a distance of 25 mm).

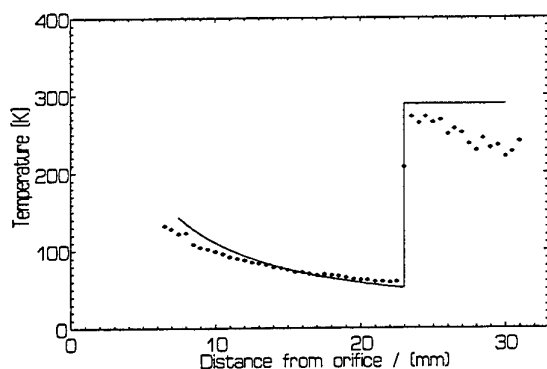


Figure 10. Centreline axis temperature measurement of the free jet.

Directly after the shock, the measured temperature agrees well with the theory. The lower temperatures downstream of the shock can be explained with the reacceleration of the flow.

Fig. 11 shows that the pressure measurement corresponds to the theoretical distribution especially for pressures lower than 5 kPa. After the Mach disk, the measured pressure rises to the theoretical pressure. An average absolute error of ± 0.5 kPa was calculated up to a distance of 25 mm.

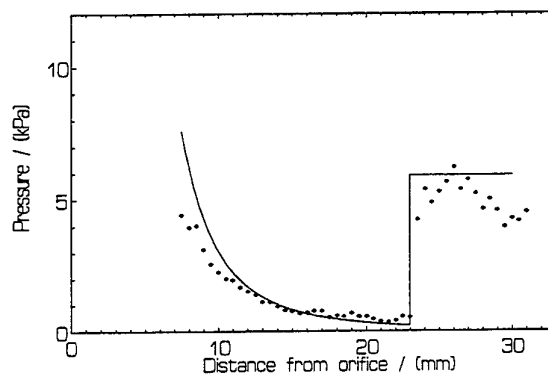


Figure 11. Centreline axis pressure measurement of the free jet.

Figs. 12, 13 and 14 show flow field measurements of the free jet expansion (cf. Fig. 8). The impact shift has been calculated from the measured pressure. A smooth flowfield the can be observed inside the barrel shocks and the Mach disk can be clearly seen in the contour plots.

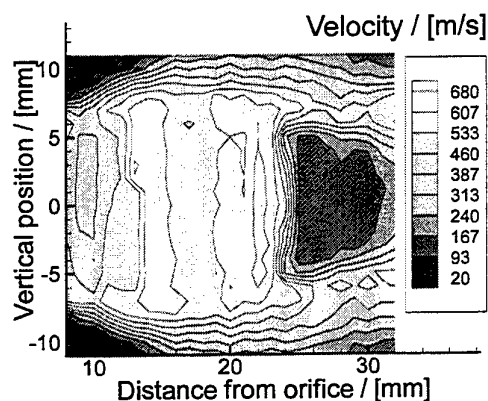


Fig. 12. Velocity field measurement of the free jet.

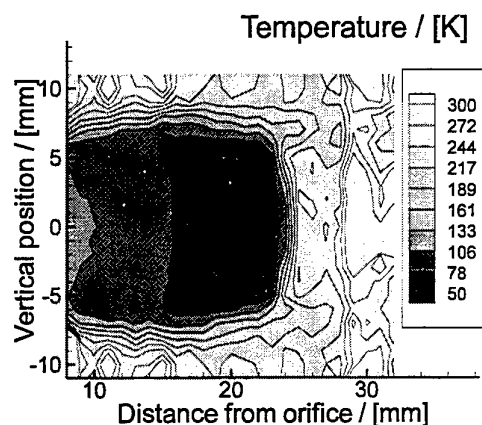


Fig. 13. Temperature field measurement of the free jet.

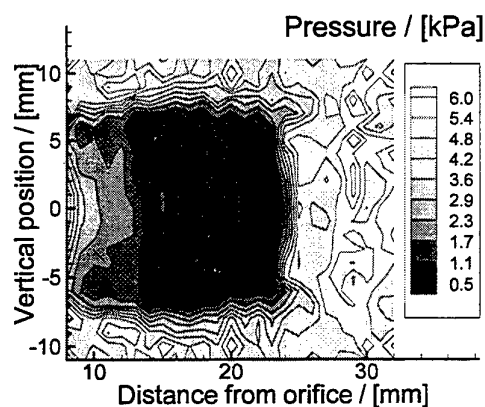


Fig. 14. Pressure field measurement of the free jet.

5. CONCLUDING REMARKS

Laser-induced fluorescence offers the possibility to perform a combined measurement of velocity, temperature and pressure in compressible gas flows for velocities above 30 m/s, temperatures below 300 K and pressures lower than 15 kPa. High gradients are represented correctly. Velocity measurements agree well with theory, but they have to be corrected at higher pressures with the collisional impact shift. The temperature can be measured correctly between 60 K and 300 K if a linear correction is applied to the theoretical fluorescence model. Pressure measurements based on a semi-empirically derived relation show a reasonable agreement with theoretical results. It is necessary to account for the temperature in this relation, so that errors in the temperature measurement affect also the pressure measurement.

The application of the iodine LIF method is limited to pressures below 30 kPa, however, because of line broadening and signal quenching. Furthermore, it yields only time averaged values and one velocity component per measurement because of the scalar product in (Eq. 1).

The combined LIF measurement technique will be applied to supersonic mixing flows with shear layers to study the evolution of mixing layers.

NOMENCLATURE

Latin symbols:

A	: Constant	[Ghz K/kPa]
B	: Constant	[GHz/K ^{0.5}]
C	: Constant	[GHz]
d	: Orifice diameter	[m]
D	: Constant	[Ghz K ^{0.7} /kPa]
f	: Fractional population	[%]
J''	: Rotational quantum number of the groundstate	[-]
\bar{k}	: Wave vector of laser beam	[1/m]
k	: Boltzmann constant	[J/K]
M	: Molecular mass	[amu]
N	: Number density	[1/m ³]
p	: Pressure	[Pa]
T	: Temperature	[K]
u	: Velocity	[m/s]
V''	: Vibrational quantum number of the groundstate	[-]

Greek symbols:

θ	: Angle between laser wave vector and velocity vector	[°]
λ	: wavelength	[m]
ν	: Light frequency	[Hz]
$\Delta\nu$: Frequency shift	[Hz]
$\Delta\nu_w$: Linewidth	[Hz]
Θ	: Characteristic temperature (molecular constant)	[K]
ω	: frequency	[Hz]

Subscripts:

0	: Stagnation
b	: Background

D : Doppler
 I : Impact
 p : Pressure
 R : Rotational
 V : Vibrational

ABBREVIATIONS

FPI : Fabry-Perot interferometer
 LIF : Laser-induced fluorescence
 PM : Photomultiplier

ACKNOWLEDGEMENTS

Financial support through the *Graduiertenkolleg Transportvorgänge in Hyperschallströmungen* at the RWTH Aachen is gratefully acknowledged.

REFERENCES

- Demtröder, W. 1996, Laser Spectroscopy, Second Enlarged Edition, pp. 5-98, Springer-Verlag, Berlin.
- Donohue, J.M., McDaniel Jr., J.C. 1996, Computer-Controlled Multiparameter Flowfield Measurements Using Planar Laser-Induced Iodine Fluorescence, AIAA Journal, vol. 34, no. 8, pp. 1604-1611.
- Donohue, J.M., 1997, Dept. of Mechanical Engineering, Santa Clara University, Santa Clara, Calif., USA, personal communication.
- Hiller, B., Hanson, R.K. 1990, Properties of the Iodine Molecule Relevant to Laser-induced Fluorescence Experiments in Gas Flows, Exp. in Fluids, vol. 10, pp. 1-11.
- Hirai, E., Teshima, K. 1998, Fluorescence Intensity Distribution in I₂-LIF Flow Visualization Considering I₂-Hyperfine Structure, Colloquium on Nonequilibrium Phenomena of Low-Density Jets in Space, Kyoto, Japan, pp. 61-65.
- Levenson, M.D., Schawlow, A.L. 1972, Hyperfine Interactions in Molecular Iodine, Physical Review A, vol. 6, no. 1, pp. 10-20, 1972.
- Liepmann, H.W., Roshko, A. 1957, Elements of Gasdynamics, pp. 39-61, John Wiley & Sons, New York.
- McDaniel Jr., J.C., Hiller, B., Hanson, R.K. 1983, Simultaneous Multiple-Point Velocity Measurements Using Laser-Induced Iodine Fluorescence, Optics Letters, vol. 8, no. 1, pp. 51-53.
- Ni-Imi, T., Fujimoto, T., Ishida, T. 1995, Selection of Absorption Lines for I₂-Planar Laser-Induced Iodine Fluorescence Measurement of Temperature in a Compressible Flow, Applied Optics, vol. 34, no. 27, pp. 6275-6281.
- Sherman, H., Ashkenas, F.S. 1966, The Structure and Utilization of Supersonic Free Jets in Low Density Wind Tunnels, Proceedings of the 4th International Symposium on Rarefied Gas Dynamics Toronto 1964, vol. 2, pp. 84-105, Academic Press.

DENSITY AND TEMPERATURE MEASUREMENTS IN A NITROGEN JET AT SUPERCRITICAL PRESSURES USING SPONTANEOUS RAMAN SCATTERING

M. Oschwald, A. Schik

Deutsches Zentrum für Luft- und Raumfahrt, Raumfahrtantriebe
Lampoldshausen, Germany

INTRODUCTION

Rocket motors working with cryogenic oxygen and hydrogen are operated at pressures above 10MPa, higher than the critical pressure of oxygen (5.0MPa) and hydrogen (1.3MPa). Whereas hydrogen is behaving like an ideal gas, oxygen shows real gas behaviour at injection conditions. The Cryo-Injector-Experiment at the DLR Lampoldshausen is dedicated to investigate the fuel injection under the conditions of supercritical pressures at idealized experimental conditions. LN_2 and GH_2 are injected through a coaxial injection element in a pressurized reservoir. Real gas behaviour is resulting in a strong variation of the nitrogen density in the temperature range from 100K to 140K. This non-reactive system is used to clarify the phenomenology and to validate modelling and CFD-codes, allowing the interpretation of experimental and numerical results without the complex interaction of reaction and flow. Spontaneous Raman-scattering which at ambient pressure suffers from its low signal intensity becomes a diagnostic tool of high potential at high pressures. Quantitative analysis of signals generated by spontaneous Raman-scattering is straight forward compared to other spectroscopic techniques like LIF or CARS where collisions between molecules requires adequate modelling of line broadening and quenching.

The breakup of a cryogenic nitrogen jet has been investigated using spontaneous Raman scattering. In this paper the experimental set-up for applying spontaneous Raman-scattering for density measurements under high pressure conditions is described. Results for nitrogen injection without and with coaxial injection of hydrogen are presented. For several injection conditions radial density profiles of nitrogen and hydrogen has been obtained as a function of location downstream the injector.

EXPERIMENTAL SET-UP

The coaxial injector was designed to be as representative as possible to the situation in rocket combustion chambers in terms of non dimensional numbers (e.g. Reynolds numbers, reduced temperatures and pressures, Mayer (1996)). The diameter of the nitrogen-post was 1.9mm, the inner and outer diameter of the annular hydrogen slit was 2.4mm and 3.2mm respectively. The fluids are injected in a reservoir filled with nitrogen at ambient temperature that can be pressurized up to 6MPa. Experiments have been done at 4MPa, a factor of 1.18 above the critical pressure of nitrogen of $P_C=3.39\text{MPa}$. Nitrogen is injected at cryogenic temperatures, injection of hydrogen is optional. Table 1 summarizes the test cases that are presented in this paper. Test cases A and B/C differ in the density ratio between the cryogenic nitrogen injected and the nitrogen in the reservoir. The critical temperature of nitrogen is $T_C=126.3\text{K}$. In case A nitrogen is injected at temperatures above this value, in cases B and C at temperatures below this value.

A sketch of the optical set-up is shown in figure 1. An Ar-ion laser beam (1.5Watt, 488nm) is focused with a $f=50\text{mm}$ lense into the measurement volume. The radiation emitted by the laser has some small contribution from emission lines from the laser plasma. Since part of the plasma emission is laying in the spectral region of the Raman lines it could be a source of interference. The laser beam was therefore spectrally cleaned by passing it through two prisms and through a spatial filter in front of the entrance window of the flow channel.

The high density gradients between the injected cryogenic nitrogen and the reservoir gas at ambient pressure results in strong gradients of the index of refraction. At this gradients the laser beam will be efficiently reflected. For measuring the weak Ra-

case	P [MPa]	$v_{N_2, Jet}$ [m/s]	$T_{N_2, Jet}$ [K]	$\rho_{N_2, Jet} / \rho_{Res}$	v_{H_2} [m/s]	T_{H_2} [K]
A	4	5	140	3.34	-	-
B	4	5	119	12.5	-	-
C	4	20	100	15.7	-	-
D	4	5	140	3.34	60	270

Table 1: test cases

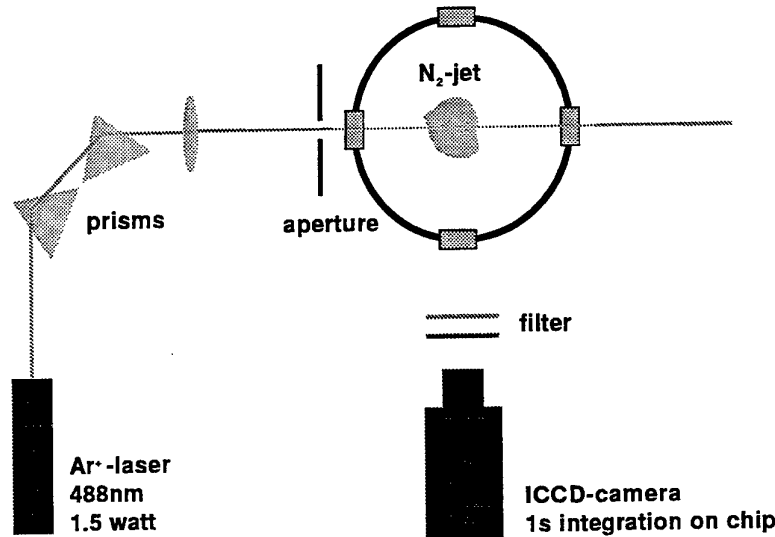


Figure 1: Sketch of the optical set-up

man lines filters with high absorption at the wavelength of the laser line and high transmission at the Raman lines have to be used. With a combination of a high pass filter (SCHOTT OG550) and narrow-band interference filters at the Raman wavelengths a transmission on the laser wavelength less than 10^{-12} could be achieved.

Laser light reflected on the surface of the cryogenic nitrogen jet was scattered in all directions leading to a bright illumination of all walls in the flow channel. The effect becomes more serious when the temperature of the injected nitrogen is decreased. Density gradients and hence gradients of refraction are much more pronounced in this case. The illumination of the walls results in a broadband emission in a wide spectral range covering the positions of the Raman-lines. The use of narrow-band filters is therefore necessary to discriminate the Raman lines from broadband background radiation.

The Raman-signal generated in the 1D measurement volume was detected with an intensified

CCD-camera. The signal was integrated on the CCD-Chip during 1s. For a density of 40 amagat a S/N-ratio about 40 could be achieved in this experiments.

From the Raman-signal intensity the probe molecule density was determined by the assumption of proportionality of Raman-signal intensity to probe molecule density, any density dependance of the Raman cross section as discussed for example by Schrötter (1979) has been neglected. The signal was calibrated by the Raman signal in the reservoir on the entrance side of the laser beam where temperature and pressure and hence the density are known. With the tabulated values of the dependence of density on temperature from Younglove (1982) temperature profiles were determined from the temporally averaged density profiles.

EXPERIMENTAL RESULTS

Typical density profiles for test cases A and C are shown in figure 2 and 3. In all test cases the laser beam was deflected at the refraction index gradients. In case A the beam was slightly divergent after it passed the nitrogen jet. In cases B and C, when the nitrogen density was much higher due to the lower injection temperature, the divergence of the laser beam becomes very strong on the exit side of the N_2 -jet and the significance of the Raman data is reduced at that location, especially in the region near the injector exit.

Profiles for case D where hydrogen and nitrogen are injected coaxially are shown in figures 4 and 5. Near the injector (fig. 4) the hydrogen signal drops nearly to zero on the central jet-axis. The hydrogen signal is not approaching zero at large value of r/d since the nitrogen gas in the reservoir is enriched with the injected hydrogen during the experiment. At radial positions of maximum hydrogen density minima in the nitrogen density can be observed as expected. Further downstream mixing of the two fluids leads to a decrease of the hydrogen peak density and to an increase of the hydrogen level on the central axis (fig. 5).

The measured profiles for test cases A and C were analyzed in respect to the maximal and minimal values of density and temperature respectively (see fig. 6, 7). Further parameters were determined to characterize the shape of the density and temperature profiles which change downstream in a characteristic way. The slope dT/dr has been derived from the measured profiles (fig. 8) which should give information on the heat entrainment from the reservoir gas at ambient temperature to the central axis on which cryogenic nitrogen has been injected. Near the injector the density profiles have a rather rectangular shape with constant plateau at the level of the injection conditions (see for example fig. 2). Further downstream the shape is more Gaussian. To quantify this change of the shape a function of the form $1 - \tanh^2((r/r_0)^n)$ has been fitted to the radial profiles. Rectangular shaped profiles yield a fitted parameter $n > 1$. $n = 1$ corresponds to a profile used to describe free jets in the similarity region (Schlichting (1979)). Figure 9 shows the behaviour of n down-streams the injector for cases A and C.

DISCUSSION

In figures 6 and 7 density maxima and temperature minima of the radial profiles are shown normalized

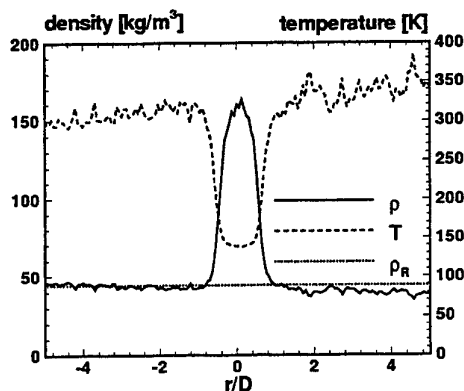


Figure 2: Radial N_2 -density profile, test case A, 2mm downstream of the injector

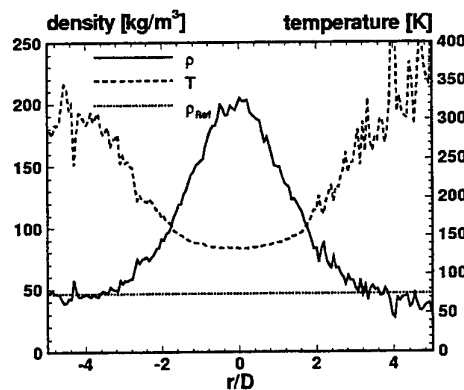


Figure 3: Radial N_2 -density profile, test case C, 53mm downstream of the injector

to the difference between injector exit and reservoir conditions. A normalized value of 1 corresponds to injector exit conditions, a value of 0 to reservoir conditions. Note that a decrease in normalized temperature corresponds to an increase of jet temperature.

The maximum of the radial density profile decreases in case A and approaches nearly reservoir conditions for $x/D \approx 20$ (fig. 6). For case C in which nitrogen is injected at much lower temperature a linear decrease with smaller slope is observed. The reservoir density is still not reached at the end of the field of observation at $x/D = 30$.

The different jet behaviour in cases A and C is much more pronounced in respect to the radial temperature distribution. In case A the normalized temperature is constant for $x/d \approx 6$ and then decreasing, corresponding to an increase of the jet-

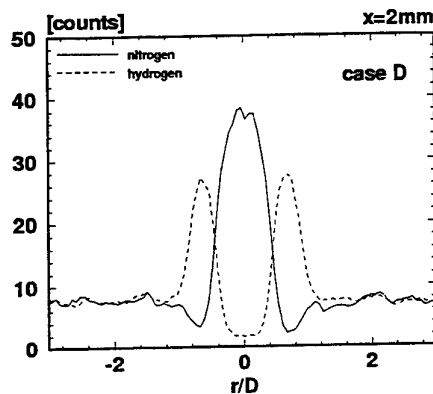


Figure 4: Radial density profile for nitrogen and hydrogen, test case D, 2mm downstream the injector

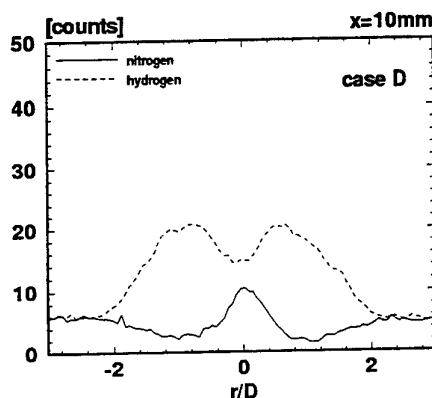


Figure 5: Radial density profile for nitrogen and hydrogen, test case D, 10mm downstream the injector

temperature T_{jet} due to heat transfer from reservoir gas at ambient temperature. At the end of the field of observation the temperature of the jet and of the reservoir are rather equilibrated. At the injection temperature of 100K (case C) real gas behaviour is much more pronounced than at 140 K (case A). In case C temperature is rather constant up to $x/d \approx 30$. The fluid at supercritical pressure and subcritical temperature is behaving similar to a boiling liquid: the density of the jet is decreasing strongly while the temperature of the fluids remains nearly constant on a level corresponding to the boiling temperature at the phase transition of a liquid.

The radial temperature gradients as a function of the distance from the injector shown in figure 8 can be fitted well by exponential decays. As can be seen the slope of the temperature profile smooths

much more slowly in case C than in case A.

In case A and C the parameter n , which is characterizing the shape of the radial density profile is decreasing linearly up to $x/D \approx 10$. In case A at this position n reaches a value of about 1, reflecting a similarity profile of a free jet. Although the data indicate that n may increase again for $x/D > 10$ again, the scatter of the data is too high to make definitive statements. In case C the decrease of n ends at $x/d \approx 10$ at a level significantly higher than 1, indicating a more rectangular shaped profile. The value of n stays constant up to $x/D \approx 19$ and is then approaching values near 1. The change in the behaviour of n near $x/d \approx 10$ in both test cases is remarkable. More experimental work has to be done to proof whether and how this behaviour can be linked to the phenomenology of the mixing process.

A comparison of the radial density profiles for nitrogen in test cases A and D clearly shows the increase of the atomization efficiency with coaxial hydrogen injection. Whereas the peak density of nitrogen is reduced to about 50% of the injection level at $x/D \approx 10$ without coaxial injection (case A, see figure 2) the nitrogen density has decreased to almost the reservoir value with coaxial hydrogen injection (test cases D, see figure 5).

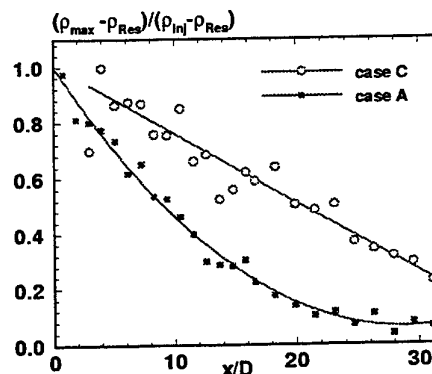


Figure 6: Normalized maximum of the radial density distribution

CONCLUSION

1D-Raman diagnostics with a CW-laser has been shown to give reasonable signal-to noise ratio when acquiring temporal averaged data in high pressure flows. Density gradients in the flow may result in refraction index gradients limiting spatial resolution and measurement accuracy.

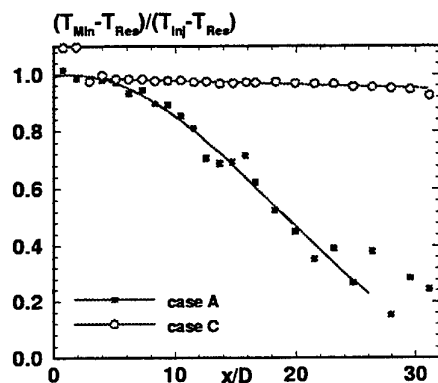


Figure 7: Normalized minimum of the radial temperature distribution

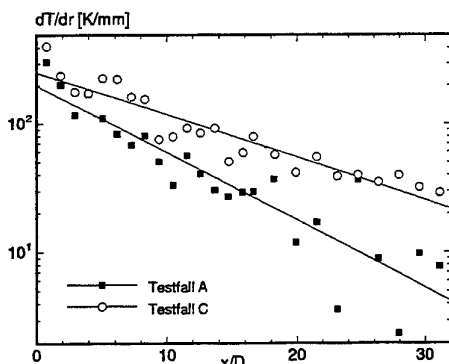


Figure 8: Temperature gradient in the slope of the radial temperature profile

The experiments showed that although at supercritical pressure at subcritical temperatures real gas behaviour results in a phenomenology similar to a boiling fluid. Heat entrained from the warm reservoir gas into the cold jet results in a expansion of the fluid rather than in a temperature increase. For large distances downstream the detector the jet profile approaches that of a ideal gas free jet.

ACKNOWLEDGEMENT

This work was supported by the Deutsche Agentur für Raumfahrtangelegenheiten (DARA) under the contract 50TT9627.

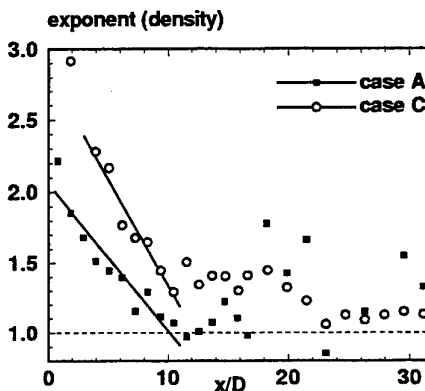


Figure 9: Fit parameter n (see text) of the radial density profile

REFERENCES

- Mayer, W., Schik A., Schweitzer C. & Schaeffler, M. (1996), Processes in high pressure LOX/GH₂ rocket combustors, AIAA 96-2620, 32nd AIAA/ASME/SAE/ASEE Joint Propulsion Conference, July 1-3, 1996, Lake Buena Vista, FL
- Schrötter H. W. & Klöckner H. W. (1979), Raman Scattering Cross Sections of Gases and Liquids, Raman Spectroscopy of Gases and Liquids, edited by A. Weber, Springer 1979

Younglove B. A. (1982), Thermophysical Properties of Fluids, J. Phys. Chem. Ref. Data, Vol. 11, Suppl. 1, 1982

Schlichting H.T. (1979), Boundary Layer Theory, McGraw-Hill

SESSION 24

TWO-PHASE FLOWS II

ON THE FREQUENCY ANALYSIS OF THE DISINTEGRATION OF PLANAR LIQUID FILMS

I.S. CARVALHO, M.V. HEITOR and D. SANTOS

Technical University of Lisbon
Instituto Superior Técnico
Department of Mechanical Engineering
Lisbon, Portugal

ABSTRACT

The frequency analysis of the disintegration process of a planar liquid film injected in the shear layer formed between two air flows is realised by means of two different experimental techniques, namely strobelight illumination and a laser attenuation technique. The experiments were conducted for a liquid velocity between 0.55 and 6 m/s ($425 \leq Re_L \leq 4986$) and an air velocity up to 40 m/s ($Re_a \leq 17647$), with the velocity ratio between the two air flows in the range 1 to 4. The results quantify the limits of application of the two techniques, and includes analysis of the process of liquid disintegration as function of the liquid velocity. In addition, back light and laser light sheet illumination are used to measure the instability amplitudes, which leads to the liquid film disintegration and the spray formation.

1. INTRODUCTION

In a previous paper we have identified the periodic nature of the process of liquid break-up and described the atomisation regimes of a flat liquid film surrounded by a mixing layer for variable strain levels (Carvalho et al., 1997). The work followed previous studies on the disintegration of a thin liquid sheet in a cocurrent air stream (e.g., Drombrowski and Johns, 1963; Fraser et al; 1963, Rizk and Lefebvre, 1980; Mansour and Chigier, 1990, 1991; Lozano et al, 1996), which have been particularly motivated by the need to improve understanding of the process of liquid atomisation, namely for low-emission combustors. Although a range of tests in axisymmetric geometries have been reported in the literature (Adzic et al, 1994; Carvalho and Heitor 1995; Karl et al, 1996), the particular complexity of the airblast geometry requires

fundamental studies on planar liquid sheets. In this context, the present paper is aimed to improve on understanding of the periodic nature of the liquid break-up process and assess the use of optical diagnostics for this purpose.

Analysis of the liquid disintegration process has been based on the aerodynamic interaction between liquid and air, which gives rise to the formation of waves (dilatational or/and sinusoidal) on the liquid surface, that grow up to a critical point. Then, ligaments and/or liquid clusters separate from the liquid sheet, which subsequently fragment into droplets (Drombrowski and Johns, 1963). Those waves are characterized by a wave length, a wave amplitude rate and a frequency, which depend on the working conditions (Eroglu and Chigier, 1991; Chigier and Dumouchel, 1996).

Arai and Hashimoto (1985) studied a planar liquid film and report similar results for the break-up frequency, making use of strobelight illumination, and the liquid film oscillation frequency, which was measured with a laser dispersion technique. The oscillating frequency of a planar liquid film was later analysed by Mansour and Chigier (1991) and Lozano et al. (1996), for different geometries and working conditions. All these studies show that the disintegration frequency slightly increases with the liquid velocity, but strongly increases with the air velocity. The resulting wave amplitudes and spray angles were particularly studied by, Eroglu and Chigier (1991), Mansour and Chigier (1991) and Lozano et al (1996) using several visualisation techniques, making comparison difficult to achieve.

In this context, this paper aims to discuss and compare two different experimental techniques for the frequency analysis of the disintegration process, and two visualisation techniques for wave amplitude and spray angle measurements.

The next section describes the liquid generator and the measuring techniques used through this work. The main results are presented and discussed in section 3, and the last section summarises the main conclusions of the work.

2. EXPERIMENTAL METHOD

2.1 The liquid film generator

Figure 1 shows the liquid film generator used in this work, which consists of: i) an inner part, for liquid flow, with an exit thickness of $t = 0.7$ mm, and an aspect ratio of $L/t = 114$; and ii) an outer part, for air flow, with a thickness of 7 mm. The width of the generated liquid sheet is 80 mm. Air can be fed through the left and right channels separately, thus allowing the air velocity ratio to be varied between 1 and 4, with absolute average velocities up to 40 m/s ($Re_a \leq 17647$). Water was used as a test liquid, and the results reported here are for a liquid velocity between 0.55 and 6 m/s ($425 \leq Re_l \leq 4986$).

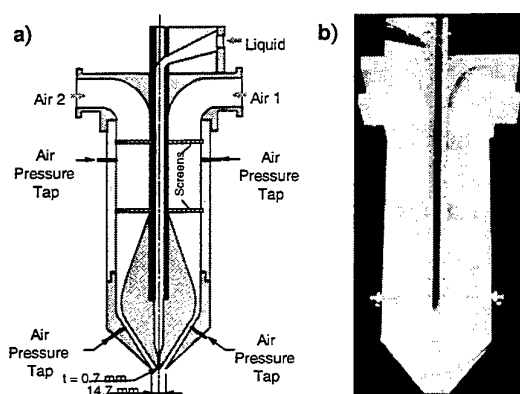


Figure 1. Liquid film generator
a) schematic diagram of the liquid film generator;
b) vertical cut - side view

2.2 Frequency measurements

The frequency analysis of the disintegration of the liquid film was achieved by means of two different techniques, as shown in figure 2: one of them makes use of a strobelight with a variable frequency illumination, as previously used by Arai and Hashimoto (1985). The characteristic frequency of the disintegration process, or break-up frequency, is measured as

the illumination frequency which freezes the phenomena near the exit region. This procedure allows to identify the fundamental and related harmonics and sub-harmonics.

The other technique used is similar to that described by Mansour and Chigier (1991) and makes use of the light attenuation caused by the flow when crossing a laser beam. A 30 mW He-Ne laser was used and positioned parallel to the flow in a 180° arrangement with the photodiode detector. For the results presented here, the system was located in the break-up region. The current of the photodiode is converted into voltage, which is fed to a digital oscilloscope to visualise the wave form, and simultaneously transferred to a 16 bits acquisition board. For each point, 10 series of 16 304 points were acquired and Fourier analysed (Fernandes and Heitor, 1997). The maximum relative error of these measurements is estimated to be 1%.

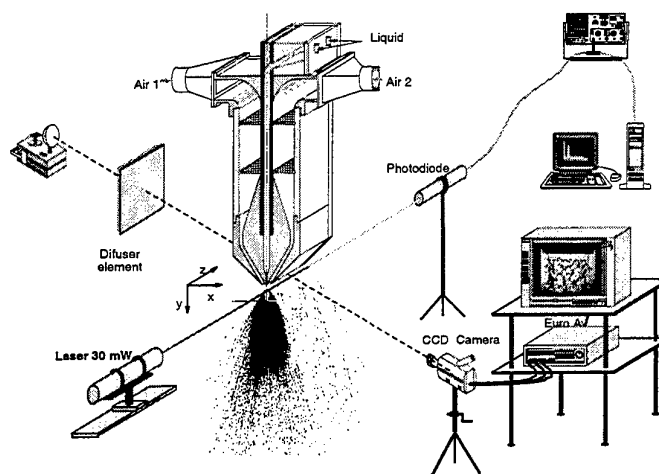


Figure 2. Optical configuration used for frequency measurements

Figure 3 shows a typical power spectrum obtained for similar (figure 3a) and different air velocities from each side of the liquid film (figures 3b, c), together with electronic noise, which can be observed only in the log-log representation (figures 3a2, b2 and c2). A fixed noise frequency at 286 Hz, due to the acquisition board itself, is always present. The spike corresponding to that frequency can be

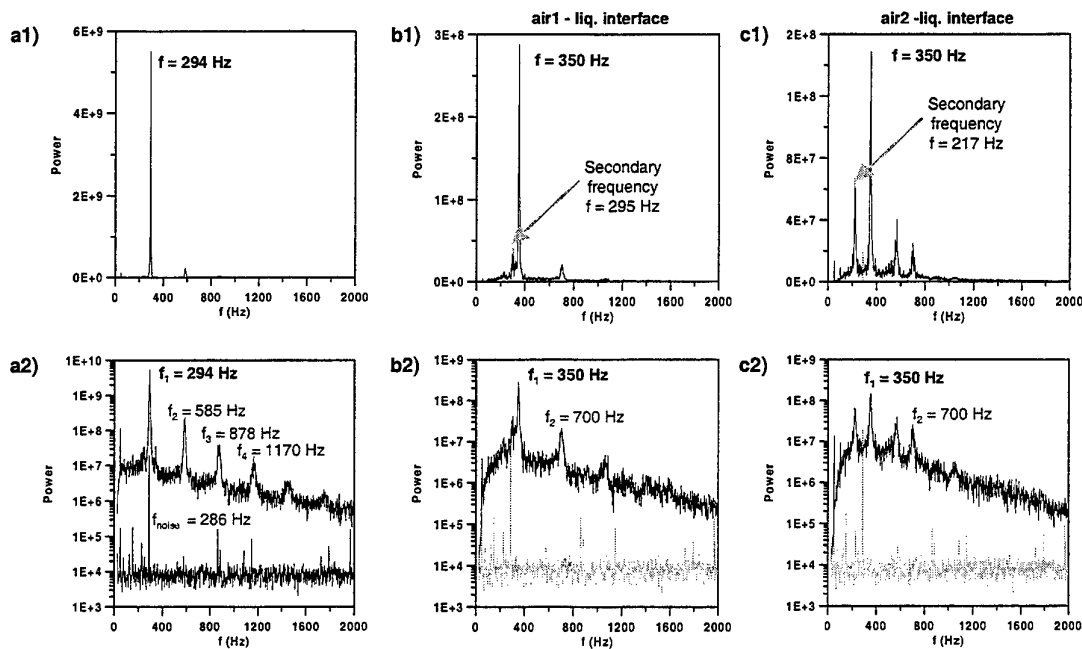


Figure 3. Typical power spectrum for $U_L = 2$ m/s:

- a1) $U_{a1} = U_{a2} = 30$ m/s (linear scale); a2) $U_{a1} = U_{a2} = 30$ m/s (log-log scale)
- b1) $U_{a1} = 40$ m/s, $U_{a2} = 10$ m/s (air1/liq interface; linear scale);
- b2) $U_{a1} = 40$ m/s, $U_{a2} = 10$ m/s (air1/liq interface; log-log scale)
- c1) $U_{a1} = 40$ m/s, $U_{a2} = 10$ m/s (liq/air2 interface; linear scale);
- c2) $U_{a1} = 40$ m/s, $U_{a2} = 10$ m/s (liq/air2 interface; log-log scale)

observed only in the log-log representation and it does not affect the frequency analysis presented here.

Analysis shows that when the air velocity ratio is different from unity, a second predominant frequency, lower than the dominant, appears. In addition, when the control volume is in the air/liquid interface of lower relative velocity (**liq – air2**), that secondary frequency has a significantly lower value. If the control volume is positioned in the air/liquid interface of higher relative velocity (**air1 – liq**), then the secondary frequency appears for values only slightly lower than the fundamental. The results also show that the energy of these secondary frequencies are dependent on the axial position and on the liquid velocity.

Despite the existence of secondary frequencies for air velocity ratios different from unity, the overall frequency analysis shows that the fundamental frequency is not dependent on either the axial or transversal measuring locations. The control volume position in the flow affects only the signal to noise ratio, SNR, as previously observed by Mansour and Chigier

(1991). The SNR was found to be minimum for the control volume positioned along the central plane (higher attenuation), and maximum in the wave crest region. In addition, regarding the axial position of the control volume, analysis shows that the SNR is maximum in the break-up region, which is in agreement with Eroglu and Chigier (1991).

In fact, the axial position of the control volume determines the “meaning” of the measured frequency. If it is positioned upstream of the break-up region, an oscillating frequency is measured, while the result is closed to the break-up frequency when the control volume is located downstream of that region. As the fundamental frequency does not depend on the axial position, it is confirmed that the break-up and the oscillating frequencies are similar. This conclusion is also supported by the comparison between the results obtained with the different frequency measuring techniques, as in figure 4.

As referred before, the strobelight technique allows to “freeze” the break-up phenomena for different frequency values. As a consequence, three different measurements were always recorded for each operating condition, and three

curves were obtained as shown in figure 4. On the other hand, the laser attenuation technique allowed to identify the fundamental frequency, and the results show maximum relative

deviations between the values measured with two techniques below 3%.

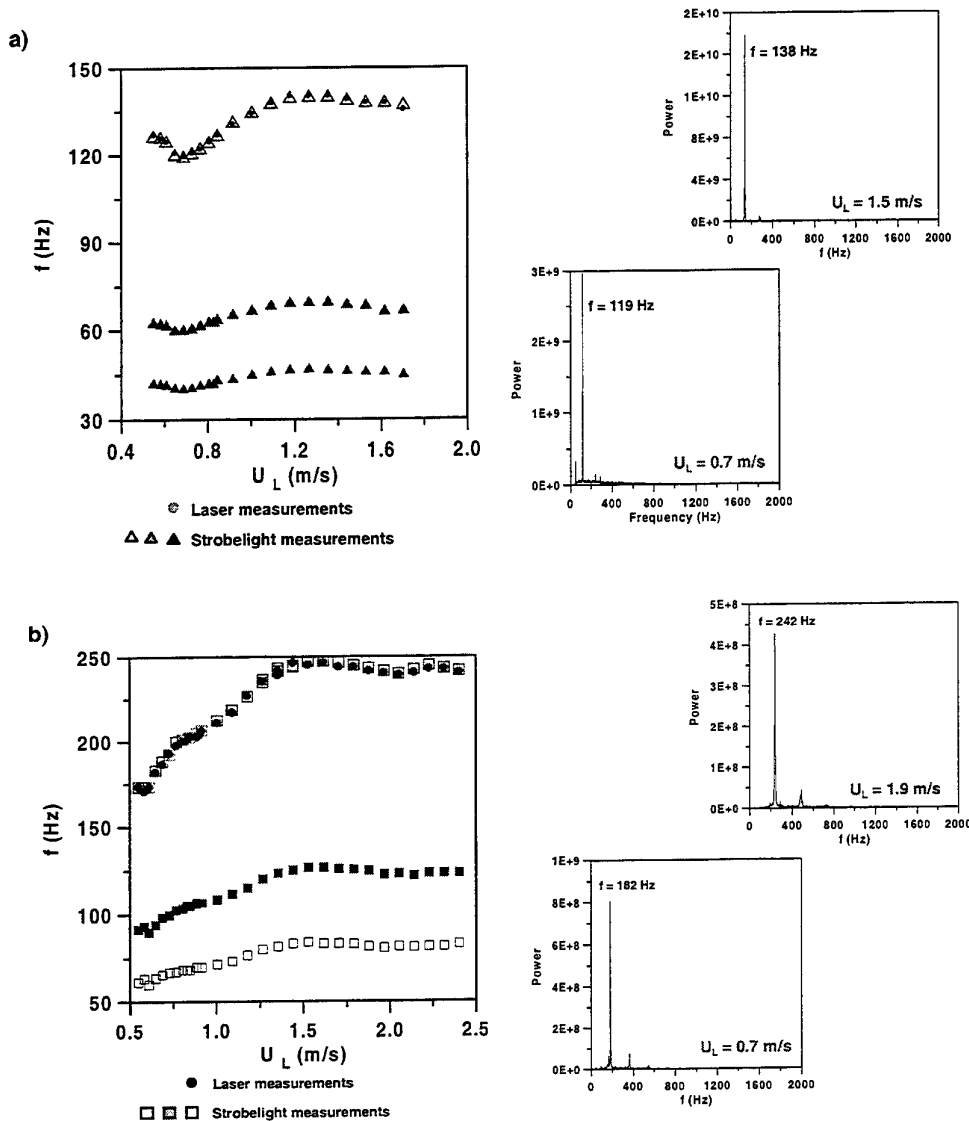


Figure 4. Frequency measurements obtained with strobelight and laser attenuation technique
a) $U_{a1} = U_{a2} = 15$ m/s; b) $U_{a1} = 30$ m/s; $U_{a2} = 10$ m/s

2.3 Instability amplitudes and spray angle measurements

The critical amplitude of the instabilities for which the break-up occurs determines the angle of the spray, and several techniques can be used to measure these characteristics (e.g., Mansour and Chigier, 1990, 1991; Lozano et al, 1996). In the present work two different visualisation

techniques were used. The first makes use of laser light sheet illumination obtained by spreading a laser beam with a cylindrical lens. Individual images were acquired by a 35 mm camera operating with 400 ASA films, and exposure time varying between 4 ms and 66 ms. The second uses a back white lighting of the flow, obtained with a strobe light illumination. Flow images were acquired by a CCD video camera, each frame corresponding to an

individual image of the flow, with an exposure time of $1.2 \mu\text{s}$.

Figure 5 shows sample results obtained for $U_{a1} = U_{a2} = 15$ and 30 m/s with laser light sheet and back light illumination. In the case of the laser light sheet illumination, the spray angle is measured making use of a visually observed average value of contrast between the "white" spray and the "black" background. For the back light illumination the criteria was to follow the crests of the major disturbances. The surrounding droplet mist was not generally considered. In both cases the uncertainty of the measurements is estimated to be 5%.

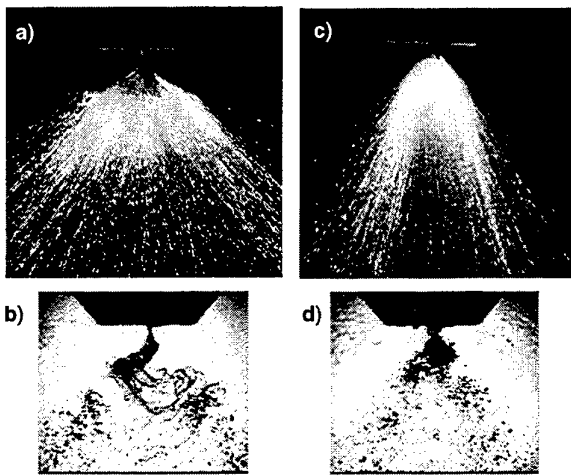


Figure 5. Side view of the flow for $U_L = 1.3 \text{ m/s}$:
a) laser light sheet ($U_{a1} = U_{a2} = 15 \text{ m/s}$);
b) back light illumination, same working conditions;
c) laser light sheet ($U_{a1} = U_{a2} = 30 \text{ m/s}$);
d) back light illumination, same working conditions;

Figure 6 shows the results obtained with both techniques for $U_{a1} = U_{a2} = 30 \text{ m/s}$ and $U_{a1} = 39 \text{ m/s}$ and $U_{a2} = 20 \text{ m/s}$. It is observed that the results obtained with the laser light sheet are 40% higher, when compared with the back light illumination technique. This is related with the exposure time used, which was about 33 ms for the laser light sheet, and between 1.2 and $0.8 \times 10^{-3} \text{ ms}$ for the back light illumination. In addition, the differences observed are also related to the droplet mist that surrounds the "wave crests" (see figure 5) and which is not considered for spray angle measurements in the back light illumination, and is obviously accounted for with the laser light sheet technique.

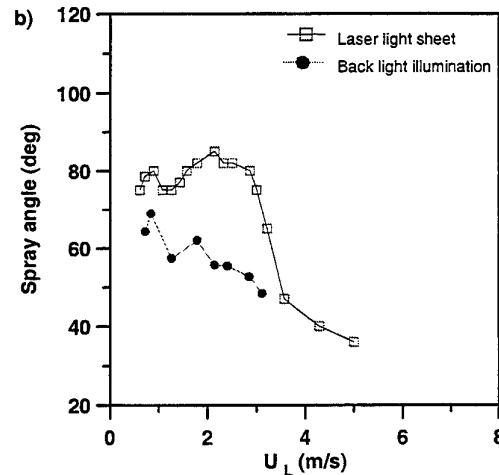
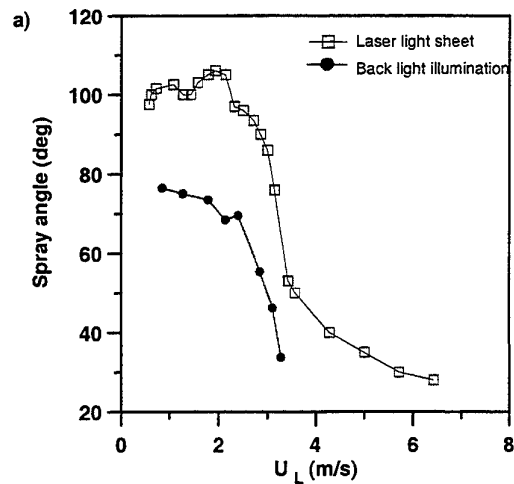


Figure 6. Laser light sheet *versus* back light illumination : a) $U_{a1} = U_{a2} = 30 \text{ m/s}$; b) $U_{a1} = 39 \text{ m/s}$ and $U_{a2} = 20 \text{ m/s}$

When comparing both techniques, it is suggested that the values obtained with the laser light sheet quantify better the spray angle, and that the back light illumination technique is more adequate for instability amplitude measurements. This is because spray angle measurements require some level of temporal integration, as provided by the laser light sheet technique.

3. RESULTS AND DISCUSSION

The following paragraphs present and discuss the frequency and spray angle results obtained by means of the techniques discussed above.

Based on the strobelight measurements, sample results are plotted in figure 7 as function of the

liquid velocity. Figure 7a quantifies the wave frequencies, f , for $U_{a1} = U_{a2}$, while the results for $U_{a1} \neq U_{a2}$ are presented in figure 7b. The dashed lines define three distinct regions (A, B and C), as proposed in previous works of Chigier and co-workers. Analysis shows that the expected wave frequency increases with the liquid flow rate and, in particular, with the air

velocity. At low liquid flow rates (region A), the energy transferred aerodynamically is sufficient to make the sinusoidal oscillations to prevail, resulting in long wavelengths (or low frequencies).

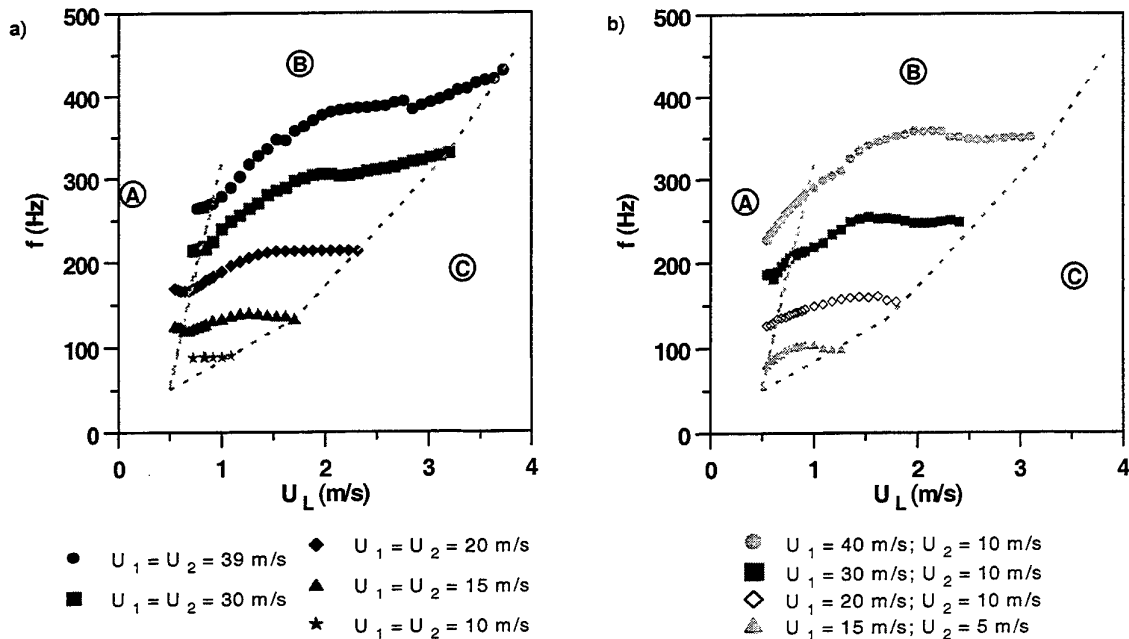


Figure 7. Wave frequencies as function of the liquid velocity: a) $U_{a1} = U_{a2}$; b) $U_{a1} \neq U_{a2}$

On the other hand, region B is characterised by combined sinusoidal and dilatational oscillations (Mansour and Chigier, 1991). As the liquid flow increases, the dilatational mode becomes more and more important, and the frequency still increases with U_L . However, for higher liquid velocities, the sinusoidal mode is still present, but the dilatational mode increases its relative influence. It should be noted that in regions A and B the oscillating frequency of the liquid sheet is highly stable and the bandwidth of these oscillations is very narrow (the evidence is that similar results to those of figure 3 are obtained).

The transition to region C corresponds to the onset of a dominant dilatational mode (Mansour and Chigier, 1991). This region is characterised by low wave amplitude growth rates, and are lacking energy to be transferred to the liquid film by the aerodynamic forces. In region C, no dominant frequency was identified. With the

strobelight it is no longer possible to “freeze” the flow and the power spectrum obtained with the laser attenuation technique do not allow the identification of a fundamental frequency, due to the total widening of the bandwidth of frequency spikes.

Figure 8 shows measured spray angles making use of the laser light sheet technique. For all operating conditions, regardless the air velocity, a region of maximum spray angle occurs, followed by a sharp decrease for higher values of liquid velocity. The maxima of the spray angles are displaced for higher values of liquid velocity, with the maximum value decreasing with air flow rate, as observed before by Mansour and Chigier (1991) and Lozano et al (1996), in the case of symmetric co-flowing air streams.

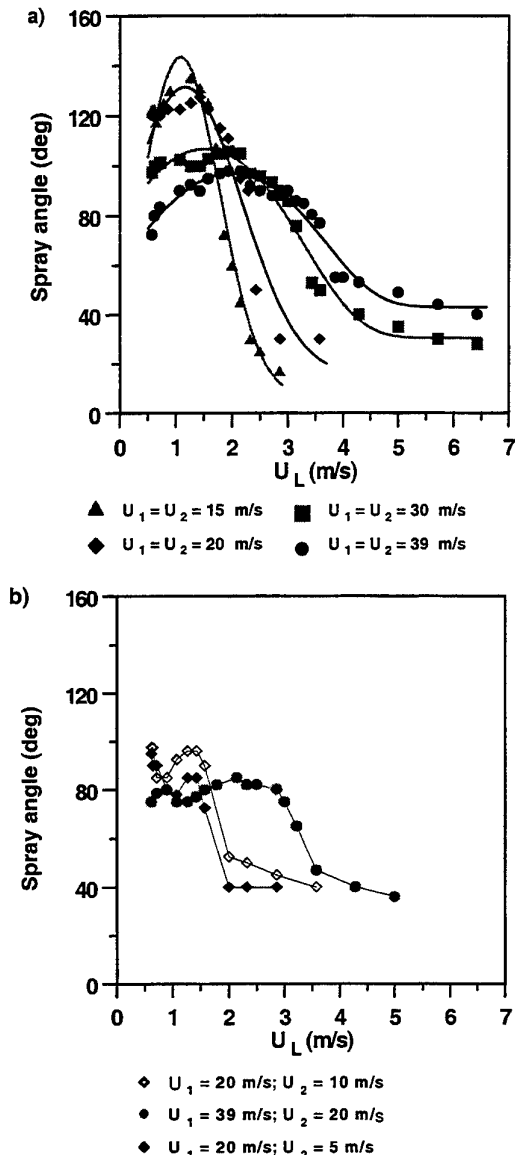


Figure 8. Spray angles as function of the liquid velocity: a) $U_{a1} = U_{a2}$; b) $U_{a1} \neq U_{a2}$

The present results show that for the region corresponding to the sharp decrease of the spray angle, a "transition flow" appears for specific liquid velocity values. This transition flow is characterised by a spray angle oscillation in a range of about 15 to 20 deg. For a small increase in the liquid velocity, very poor atomisation is obtained and the spray angle assumes very small values.

Figure 9 shows the break-up frequencies and the spray angles obtained for two different air flow conditions. It is observed that a better

atomisation quality is obtained in region A of the frequency diagram. The maximum spray angle (maximum amplitude of the instabilities) is obtained in the region B, after a zone of a sharp linear increase of the wave frequency, where a "plateau" is observed. For this "plateau", the spray angle slowly decreases up to the point where the "transition flow" occurs together with the transition to the region C of the frequency diagram. After this point, the spray angle assumes very small values and it is no longer possible to measure break-up frequencies for the reasons mentioned above.

The analysis of the results suggests that the disintegration of a planar liquid film, under the range of operating conditions studied, is mainly dependent on the "energy" transferred in the air-liquid interface, although the gas-to-liquid momentum ratio is the dominant parameter in the atomisation process, namely under two different co-flows of air. Also, the results show a close relation between the break-up frequency and the corresponding spray angle, the latter being dependent on the exposure time used with measuring instrumentation.

4. CONCLUSIONS

Frequency analysis of the disintegration of a planar liquid film is reported by means of strobe light illumination and a laser attenuation technique. The latter allowed to identify the fundamental wave frequency of the instability which leads to break-up, confirming the values measured by strobe light illumination with a maximum deviation of 3%. When comparing both techniques, it is also possible to show that the oscillation frequency of the liquid film before the disintegration, equals the "release" frequency of clusters of ligaments and droplets, or the break-up frequency.

Two visualisation techniques were also used to quantify the spray angle and the amplitude of instabilities on the liquid film. Although both characteristics are closely related (the spray angle directly depends on the amplitude of the instability, which leads to the break-up), analysis shows that the laser light sheet technique allows a more reliable measurement of the spray angle, due to the higher temporal integration period used. The back light illumination technique, with a much shorter

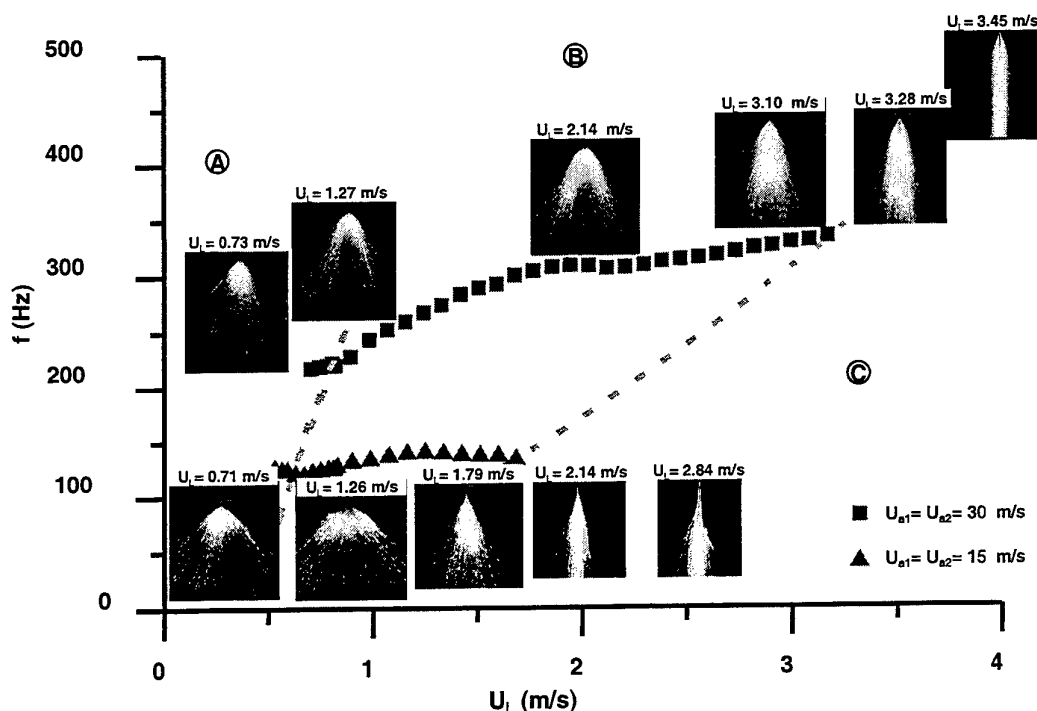


Figure 9. Break-up frequency and spray angles for $U_{a1} = U_{a2} = 15$ m/s and 30 m/s

exposure time, is proved to be more adequate for wave amplitudes.

ACKNOWLEDGEMENTS

The several discussions with Mr. E.C. Fernandes are grateful acknowledged.

Financial support has been provided through the BRITE/EURAM program of the European Commission under the contact AERO-CT95/0122

The authors are pleased to acknowledge the research grant of Dina Santos from the PRAXIS XXI program of the Portuguese Ministry of Science and Technology.

REFERENCES

- Adzic, M., Carvalho, I.S. and Heitor, M.V. (1994). Laser Shadowgraphy of Break-up of a Liquid Sheet Downstream of a Model Prefilming Airblast Atomizer. 7th International Symp. Applications of Laser Anemometry to Fluid Mechanics, 11-14 July, Lisbon, Portugal.
- Arai, T. and Hashimoto, H. (1985). Disintegration of a Thin Liquid Sheet in a Cocurrent Gas Stream. ICLASS-85, Paper VIB/1, 9-10 July, London, UK.
- Carvalho, I.S. and Heitor, M.V. (1995). On the Analysis of the Break-up of an Annular Liquid Sheet Downstream of an Airblast Prefilming Atomizer", ILASS Europe, 21-23 March, Nurnberg, Germany.
- Carvalho, I. S., Heitor, M.V. and Santos, D. (1997). On the Analysis of Shear-Driven Liquid Break-Up Processes. Proc. 11th Symposium on Turbulent Shear Flows, 8-11 September, Grenoble, France, pp. 27.6-27.11
- Chigier, N. and Dumouchel, C. (1996). Atomization of Liquid Sheets. In: Recent Advances in Spray Combustion: Spray Atomization and Drop Burning Phenomena, Volume

I, Progress in Astronautics and Aeronautics, Vol.166, pp.241-259.

Dombrowski, N. and Johns, W.R. (1963). The Aerodynamic Instability and Disintegration of Viscous Liquid Sheets. Chemical Engng. Sci., 18, pp.203-214.

Eroglu, H. and Chigier, N. (1991). Liquid Sheet Instability in Coflowing Air Stream. ICLASS-91, 15-18 July, Gaithersburg, MD, USA, pp. 679-686.

Fernandes, E.C. and Heitor, M.V. (1997). Simultaneous Measurements of Velocity, Pressure, Temperature and Heat Release in an Oscillating Flame. 90th Symp. of Propulsion and Energetics on the Advanced Non Intrusive Instrumentation for Propulsion Engines. AGARD 20-24 October, Bruxelles, Belgium.

Fraser, R.P. (1956). Liquid Fuel Atomization. 6th Symp. Intl. Combustion, pp.687-701.

Fraser, R.P., Dombrowski, N. and Routley, J.H. (1963). The Atomization of a Liquid Sheet by an Impinging Air Stream. Chemical Engng. Sci., 18, pp.339-353.

Karl, J., Huilier D. and Burnage H. (1996) "Mean behavior of a Coaxial Airblast Atomized Spray in a Co-flowing Air Stream" Atomization and Sprays, 6, pp 409-433.

Lozano, A., Call, C.J., Dopazo, C., Garcia-Olivares, A. (1996). Experimental Study of the Atomization of a Planar Liquid Sheet. Atomization and Sprays, 6, pp.77-94.

Mansour, A. and Chigier, N. (1990). Disintegration of Liquid Sheets. Phys. Fluids A, 3(12), pp. 2971-2980.

Mansour, A. and Chigier, N. (1991). Dynamic Behavior of Liquid Sheets. Phys. Fluids A, 2(5), pp. 706-719.

Rizk, N.K. and Lefebvre, A.H. (1980). The Influence of Liquid Film Thickness on Airblast Atomization. Trans. ASME, J. Engng. Power, 102, pp.706-710.

THE VELOCITY FIELD IN AN AIR-BLASTED LIQUID SHEET

Antonio Lozano*, Ignacio García Palacín°, Félix Barreras°

* *LITEC/CSIC, Maria de Luna, 3, 50015-Zaragoza, Spain*

° *Centro Politécnico Superior de Ingenieros, Area de Mecánica de Fluidos
Universidad de Zaragoza, Maria de Luna, 3, 50015-Zaragoza, Spain*

ABSTRACT

The instability growth that causes a liquid sheet break up when it is subjected to high velocity parallel air streams has been analyzed in some recent experimental studies. Most of them have been based on visual observations from instantaneous spray images or oscillation frequency measurements. The purpose of this work is the study of the air field near the sheet interfaces to improve the understanding of the air/liquid interaction. To this end, flow visualization and particle image velocimetry (PIV) have been used to ascertain the flow structure and to obtain two-component velocity maps of planar sections of the air streams.

1. INTRODUCTION

Two-dimensional liquid sheets are becoming increasingly popular as a test flow to study instability growth and atomization processes. Large aspect ratio configurations facilitate the study of transverse perturbations in regions close to the nozzle exit, and edge effects are minimized. Results can, thus, be extrapolated to axisymmetric geometries that are more common in industrial applications. Experiments and simulations regarding large aspect ratio sheets have their earliest precedent in the work of Hagerty and Shea (1955), where perturbations were introduced by oscillating the liquid nozzle. In that analysis the water sheet was exiting in a quiescent atmosphere. In the present work, atomization is produced with the aid of a high speed air coflow, in a configuration similar to those of Rizk and Lefevbre (1980) or Arai and Hashimoto (1985).

It might be interesting to add that although initial interest in the liquid sheet problem has been mostly academic, recent papers describe applications

where the specific two-dimensional characteristics of this flow are especially advantageous (e.g. Mansour et al. 1998).

2. DESCRIPTION OF THE EXPERIMENT

The design of the experimental set up used in the present study is similar to that described in Mansour and Chigier (1990) and Lozano *et al.* (1996). It differs, however, in that both water and air nozzle profiles have been contoured fitting 6th order polynomials to ensure uniform and parallel air and water velocity profiles at the exit. Water injected at the top of the nozzle head exits vertically through a 0.35 mm wide slit. The nozzle has a 23:1 contraction ratio. The span of the sheet is 80 mm, yielding an aspect ratio of 230. Air is also introduced from the top following a settling chamber with two honeycombs and a wire mesh screen to smooth the flow. The air channels located at both sides of the liquid nozzle contraction ratios of 15:1 and exit widths of 3.45 mm.

This geometry is not likely to provide the most efficient atomization, as air impinging at an angle with respect to the liquid sheet would probably produce a faster break up. Its simplicity, however, is an advantage in order to be compared with numerical simulations and to identify basic break up mechanisms. For the conditions under study, water velocities have ranged from 0.6 to 6 m/s, while air velocities have been varied between 15 and 35 m/s.

To visualize the air field and measure the velocity using particle image velocimetry (PIV), one of the air channels has been seeded with glycerin/water droplets from a commercial seeder. To illuminate, a double cavity Quantel Nd:YAG laser has been used, capable of producing 6 ns, 125 mJ pulses at 532 nm. The temporal spacing between the pulses has been adjusted according to the

velocity of the flow, being on the order of 30 μ s. Images have been obtained either with a slow-scan 16 bit Princeton Instruments CCD camera, or with a cross-correlation 1000x1000 pixels TSI PIVCAM 10-30 camera with Kodak array. With the appropriate TSI synchronizer, this second camera is capable of working in "frame straddling" mode, with a minimum temporal delay of 25 μ s between each image in a pair.

3. VISUALIZATION RESULTS

Images have been acquired for longitudinal sections of the flow, perpendicular to the exit nozzle. Special attention has been devoted to the near field region, close to the nozzle, to study the triggering mechanisms of the instabilities. Several fields of view have been imaged: 4.3 x 4.3 cm with a resolution of 43 μ m/pixel, 2 x 2.6 cm with a resolution of 70 μ m/pixel, and 1 x 2 cm with resolution of 20 μ m/pixel.

Initial test images without water flow have been registered to ensure proper seeding levels and air flow characteristics. The experimental conditions substantially change when water is added. The large density difference between air and water produces the growth of longitudinal perturbations. The air/water interface interaction results in a Kelvin-Helmholtz instability which quickly causes the sheet break-up. Increasing the air velocity with respect to that of water, the sheet breaking point recedes to the nozzle exit, hindering the study of the instability waves. For this reason, only moderate air velocities have been considered.

The presence of the liquid sheet also modifies the image recording process due to the different intensities between the seeded glycerin droplets and the spray droplets from the atomized sheet. Trying to increase the registered signal from the air can cause a total image saturation if water droplets are present because they have much larger diameters.

It has to be noted that although it is possible to seed both air channels, the illuminating sheet becomes so distorted after crossing the liquid curtain that only the air stream closer to the laser source can be analyzed.

Instantaneous images for a fixed air velocity of 15 m/s and decreasing water velocities (0.9, 1.5 and 2.1 m/s) are depicted in Figs. 1 a), b) and c). Figure 2 shows similar images for the same water velocity values, but for an air velocity of 25 m/s. In the images, the water flows from left to right

although in the experiment it was moving downwards.

As has been reported in other works, until the air/water velocity ratio exceeds a limit, no atomization occurs. As air velocity increases, the sheet starts oscillating, initially with a dominant dilatational or varicose mode. At some point, the dominant mode becomes antisymmetric, and when this happens, the growth rate is highly enhanced resulting in a quick break-up at a distance of a few wavelengths from the nozzle exit. The oscillation frequency increases linearly with the air velocity, with a much weaker dependence on water velocity. The spray angle, however, presents a relatively sharp maximum when varying the water velocity for a fixed air flow.

Comparing Figs. 1 and 2 it can be noticed how the higher air velocity causes the sheet break up to occur closer to the nozzle exit. The quick atomization in Fig. 2 originates a cloud of water droplets impeding the visualization of the glycerin air markers. For higher air speeds, not shown in the images, atomization is almost immediate and more efficient, resulting in a spray formed by smaller droplets.

The seeded air is clearly visible in Figs. 1 a) and b). The mixing layer between the air stream and the quiescent room air results in vortical structures with scales smaller than the sheet oscillation wavelength. In the air/water interfaces no vortical structures are clearly discernible. The air gets decelerated by the liquid sheet, and the possible vortices that could be shed from the splitter plate seem to be washed out by the water. This is an important point to clarify the origin of the instability waves, and the mechanisms that could contribute to their growth.

The water displacements are followed by the air streams. As the liquid sheet oscillation amplitude increases, the transverse component of the movement is also increased. Although the water is flowing downwards, under the effect of the surface tension it moves like a pendulum, and the sinusoidal wave degenerates in a zigzag shape with pointy edges that are curved upwards. The air following this movement is also turned upwards and separates creating large recirculation rollers, and occasionally small vortices detached from the sharp vertices of the wave (see Lozano et al. 1997). When this situation takes place close to the nozzle head, the

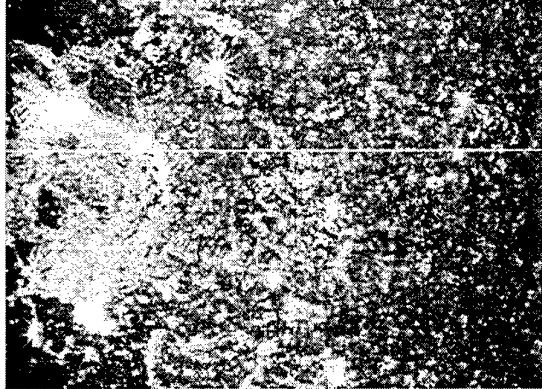
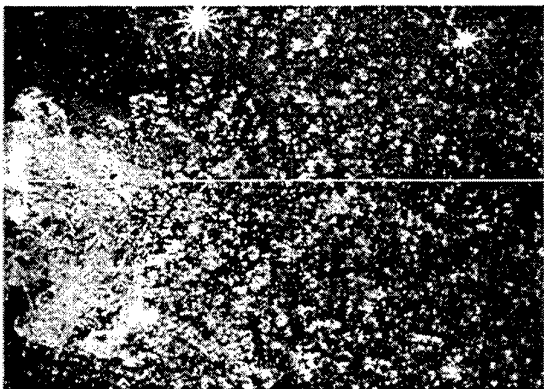
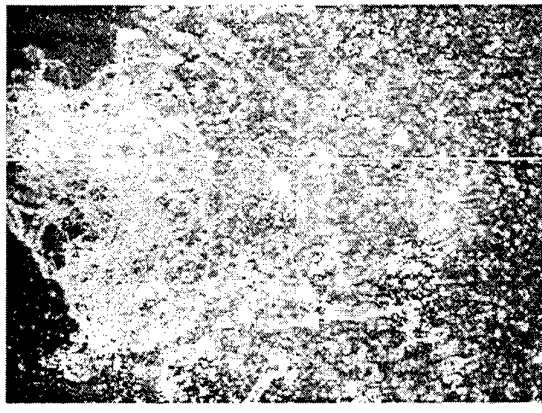
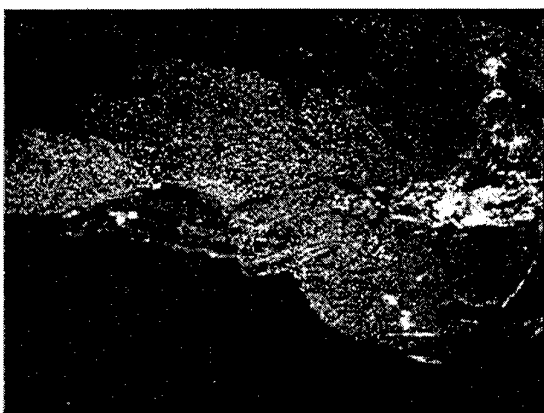
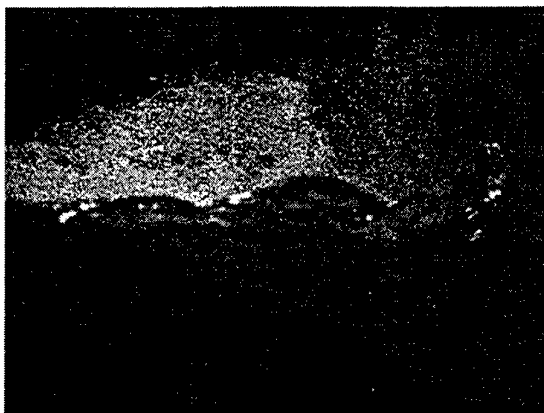


Fig. 1: liquid sheet images. Air velocity: 15 m/s. Water velocities: 0.9 m/s (upper), 1.5 m/s (middle) and 2.1 m/s (lower). Field of view 4.3 x 3.2 cm. In the experiment, the sheet was flowing downwards.

Fig.2: liquid sheet images. Air velocity: 25 m/s. Water velocities and field of view as in Fig. 1

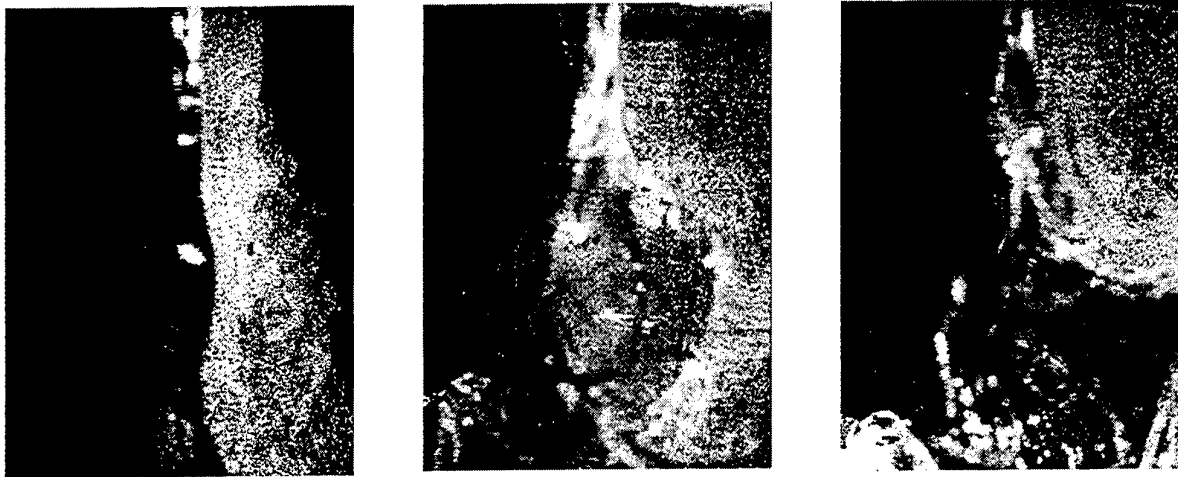


Fig. 3: liquid sheet images. Air velocity: 15 m/s. Water velocities: 2.1 m/s (left), 1.5 m/s (middle) and 0.9 m/s (right). Field of view 2.6 x 2 cm

recirculation effect is enhanced by the presence of the plate where the exit slits are located, that partly blocks the entrance of room air. The air deflected upwards collides with the plate and is reingested by the stream. This recirculation zone could contribute to the fast amplitude growth of the instability waves and to the steep increase in the spray angle for determinate values of air and water velocities.

This process can be clearly seen in Fig. 3 where again, a sequence of frames with decreasing water velocities (2.1 m/s, 1.5 m/s and 0.9 m/s) for a fixed air speed (15 m/s) is presented. For the higher water velocity, the wave amplitude is small, and the air stream can follow the oscillations without problems. For 1.5 m/s, although the amplitude is larger, the wave maintains its sinusoidal shape, and the air is capable of flowing along the curve maximum. When the velocity reduces to 0.9 m/s, the zigzag shape is apparent, although the curve vertex is out of the image. The air stream turns upwards, generating the recirculation zone.

4. VELOCITY MEASUREMENTS

The data set acquired with higher resolution has been used to study in more detail a region extending 2 cm from the nozzle, that yields a resolution of 20 $\mu\text{m}/\text{pixel}$. Only a low air velocity, 15 m/s, has been considered, to increase the length of the intact sheet.

Images have been acquired in frame straddling mode, and analyzed by cross-correlation.

A window 32 pixels wide has been used, with an offset of 15 pixels. Some results are shown in Figs. 4 and 5 for a fixed air velocity (15 m/s) and the following decreasing water exit velocities: 1.8 m/s (Fig. 4 upper), 1.5 m/s (Fig. 4 lower), 1.2 m/s (Fig. 5 upper) and 1.15 m/s (Fig. 5 lower). Velocity maps in the right hand side of the figures correspond to the images in the left. No vectors have been interpolated in these maps.

Apparently, no clear vortical structures can be identified in the air/water interface, which suggest that the sheet oscillation is not imposed by vortex shedding. Possible influences by the smaller vortical structures formed in the air/air interface in the outer side of the air stream do not seem to alter the wavelength or amplitude of the sheet movement, although from the lower regions of the images it can be seen how the entrained room air can get directly in contact with the sheet. The influence of this entrainment could be analyzed by varying the width of the air streams.

The large recirculation zone visible in Fig. 3 appears also in Fig. 5. The presence of recirculation structures is sometimes masked by the flow mean velocity. In order to identify them more clearly, the velocity of the vortex center should be subtracted. After subtraction, the upper velocity map in Fig. 5 transforms into the one presented in Fig. 6, where the recirculation is apparent. Alternatively, the vorticity field can be analyzed, as vorticity is galilean invariant. At present, work is in progress to calculate and study the vorticity obtained from the velocity maps.

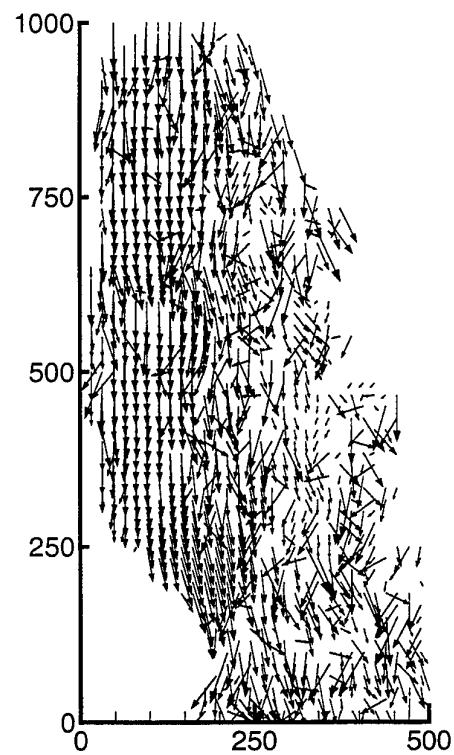
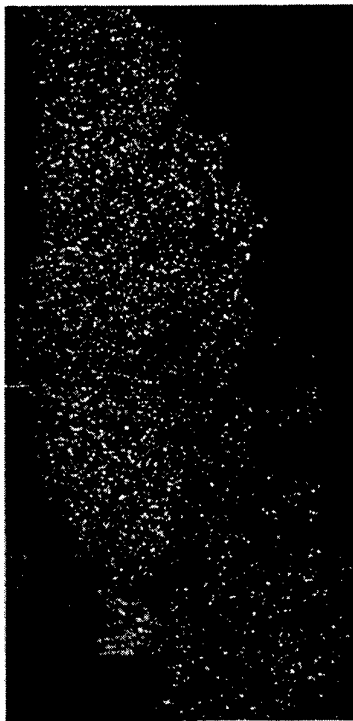
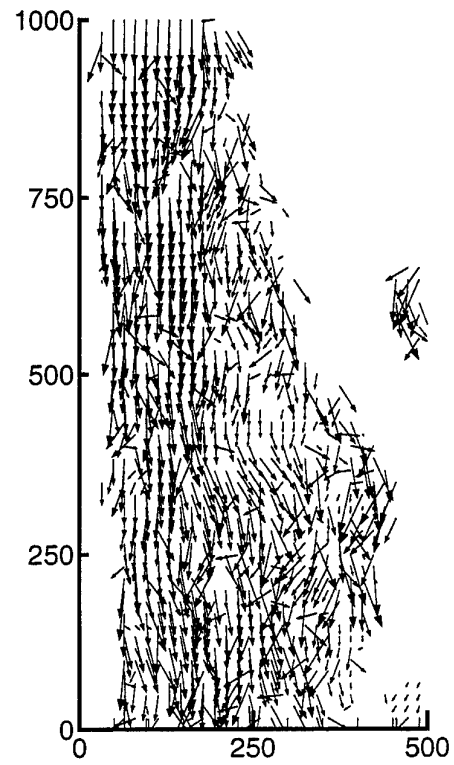
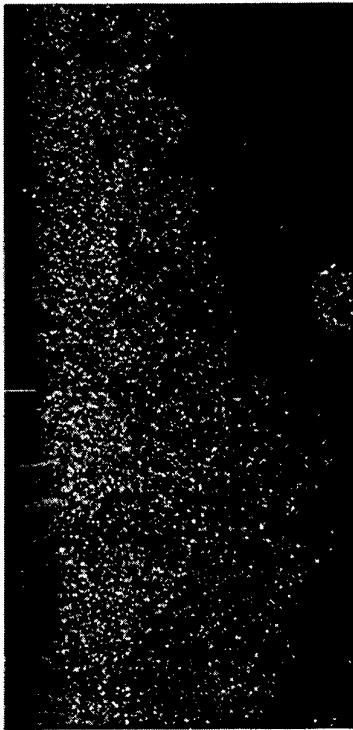


Fig.4: caption explained in text

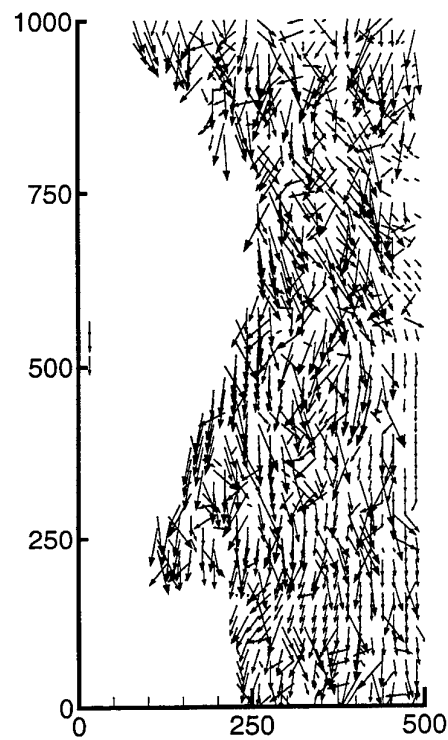
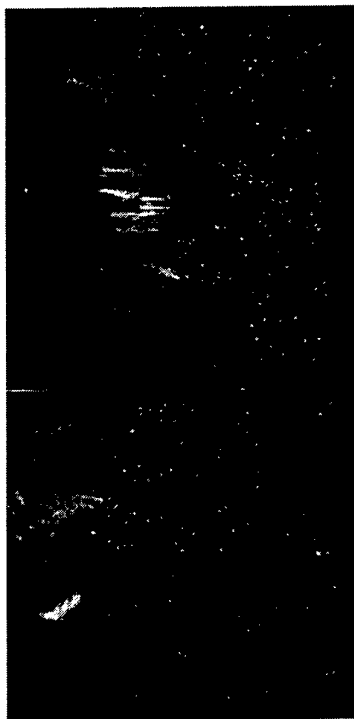
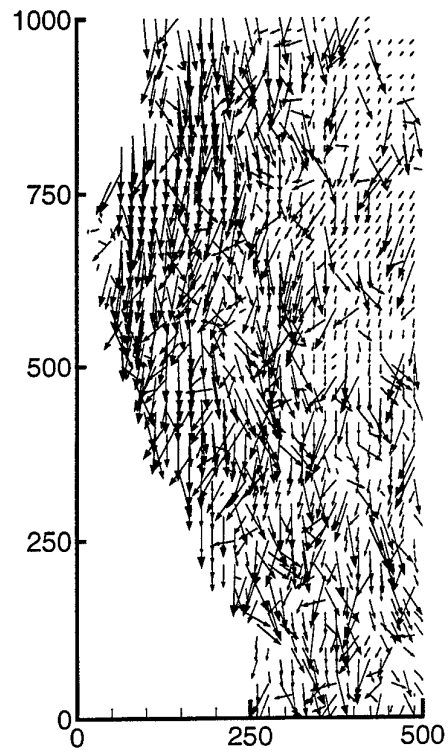
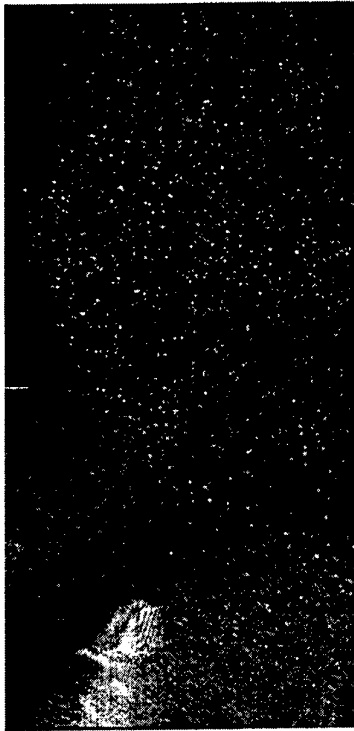


Fig. 5: caption explained in text

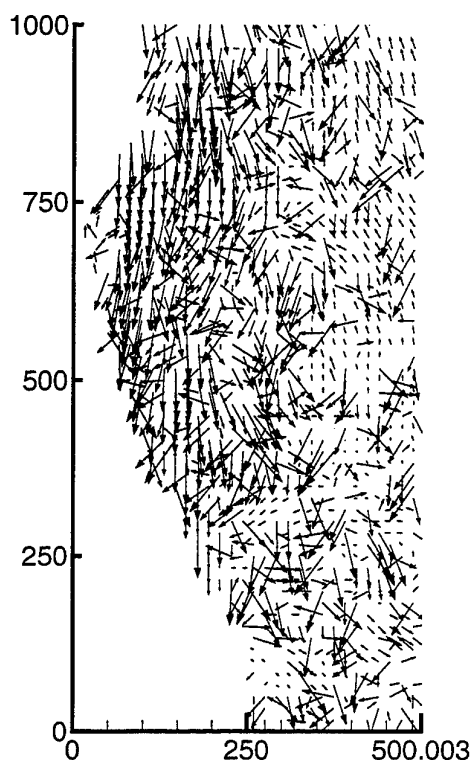


Fig. 6: velocity map in Fig. 5 upper, with mean velocity of the recirculation structure subtracted

5. CONCLUSIONS

The behavior of the air streams surrounding a liquid sheet has been studied seeding them with glycerin droplets and illuminating the flow with a laser sheet. The longitudinal waves formed in the water sheet by Kelvin-Helmholtz instability have been visualized simultaneously to the coflowing air. Fast acquisition of image pairs by frame straddling has enabled the calculation of the 2-D air velocity field by PIV cross correlation.

Small vortical structures are observed in the air/air interface between the coflowing air streams and the quiescent room atmosphere. The water/air interfaces present different characteristics. The liquid sheet which flows with slower velocity than the air does not curl in rollers due to its much higher density. Sinusoidal oscillations can, however, be

subjected to very high amplification ratios that cause the film break up into small droplets.

The air streams follow the displacements of the liquid sheet. For large oscillation amplitudes, which ultimately result in the atomization, the liquid surface is curved upwards, and the air is "pushed" by the flapping sheet. In these cases, separation between the two layers can occur. It has also been observed in this study that when large amplitude oscillations take place close to the nozzle head, the concave curvature of the sheet forces the air into a recirculation bubble, that might in turn contribute to the fast growth of the longitudinal instability waves. Work is in progress to calculate the out-of-plane component of the vorticity field from the velocity maps.

As a final consideration, it has to be pointed out that to completely explain the phenomena that produce the final atomization of the liquid sheet, the three dimensionality of the flow has to be taken into account, as transverse waves also develop in the interfaces.

ACKNOWLEDGMENTS

This project has been partially supported by the Comisión Interministerial de Ciencia y Tecnología and the Dirección General de Estudios Superiores of the Spanish Government under contracts AMB96-0427-C03-01 and PB96-0739-C03-03.

REFERENCES

- Arai, T. and Hashimoto, H., 1985, Disintegration of a thin liquid sheet in a concurrent gas stream. Proc. ICLASS-85, London.
- Hagerty, W.W., and Shea, J.F., 1955 A study of the stability of plane fluid sheets, *J. Appl. Mech.* December, 509-514.
- Lozano, A., Call, C.J., Dopazo, C. García-Olivares, A., 1996, An Experimental and Numerical Study of the Atomization of a Planar Liquid Sheet, *Atomization and Sprays*, 6, 77-94.
- Lozano, A., Barreras, F., Yates, A., García, I., Andrés, N., 1997, Experimental study of the near field of a breaking liquid sheet, Proc. ICLASS-97, Aug. 18-22, Seoul, Korea
- Mansour, A. and Chigier, N., 1990, Disintegration of liquid sheets. *Phys. Fluids A*, 2,(5), 706-719.

Mansour, A., Chigier, N., Shih, T, Kozarek, R.L., 1998, The Effects of the Hartman Cavity on the Performance of the USGA Nozzle Used for Aluminum Spray Forming, *Atomization and Sprays* 8, (1), 1-24.

Rizk, N.K., and Lefebvre, A.H., 1980, The Influence of Liquid Film Thickness on Airblast Atomization, *J. Eng. Power* 102, 706-710.

Measurements of film characteristics along a stationary Taylor bubble using laser induced fluorescence

J.P. Kockx, R. Delfos and R.V.A. Oliemans

J.M. Burgers Centre, Laboratory for Aero & Hydrodynamics
Delft University of Technology, Rotterdamseweg 145, 2628 AL Delft, the Netherlands

Abstract

In this study we consider the film characteristics of a stationary Taylor bubble. A Taylor bubble is a large gas bubble in a vertical tube that spans the tube diameter and rises with a high speed through a liquid with dispersed gas bubbles. There are three gas fluxes into and out of the Taylor bubble. The entrainment flux, by which small gas bubbles are torn off the bottom of the Taylor bubble, is not yet fully understood. According to Delfos (1996) fluctuations in the thickness of the liquid film surrounding the Taylor bubble play a dominant role in this entrainment process. The objective of the present study is to measure the characteristics of the falling film and based on these data validate the model of Delfos (1996).

The experiment is carried out in a set-up in which a Taylor bubble is kept at a fixed position in a downward water flow in vertical tube with a diameter $D_i = 100$ mm. To measure the film thickness, we developed a Laser Induced Fluorescence (LIF) technique, which allows us to measure the instantaneous film thickness with an accuracy of 0.1 mm.

The film along the initial part of the Taylor bubble agrees with the results for a laminar film falling along a vertical wall. At a Taylor bubble length of about 0.7 m, the laminar flow inside the film changes into turbulence. The mean film thickness then should grow at a different rate which is confirmed by the experiments. As soon as the film becomes turbulent the surface of the film exhibits undulations, which can be considered as footprints of the turbulent eddies. In accord with the hypothesis of Delfos (1996) the entrainment process starts as soon as these undulations appear. For small Taylor bubbles ($D_i < 10$) the entrainment model of Delfos agrees reasonably well with our observations. For large Taylor bubbles ($D_i > 10$) the model seems to overestimate entrainment.

1 Introduction

Liquid-gas flow in a vertical pipe is one of the fundamental flow categories in the field of two-phase flow. Depending on the flow rates of the gas and liquid, the flow patterns in this case can differ considerably. One of these flow patterns is slug flow.

A slug flow is characterised by a liquid flow in combination with a series of large axis-symmetric bullet-shaped gas bubbles, so-called Taylor bubbles. These bubbles occupy

most of the cross-section of the pipe and move upward with a constant speed. Between the Taylor bubble and the tube wall the liquid flows downwards as a thin free-falling film. The Taylor bubbles are separated by regions of continuous liquid phase which contain small gas bubbles. These regions are denoted as liquid slugs. A schematic picture of a vertical slug flow is given in Fig. 1.

Vertical slug flow is encountered in many industrial two-phase flow applications. For instance it occurs during oil production and in various process equipment. The strongly in-stationary flow conditions during slug flow may have a large mechanical impact on the equipment in which this flow occurs. For industrial applications it is therefore important to determine the conditions for which slug flow can appear. A required parameter to predict this, is the void fraction, the fraction of gas, in the liquid slug. To predict the void fraction various models have been proposed. For a review see Fabre & Liné (1994).

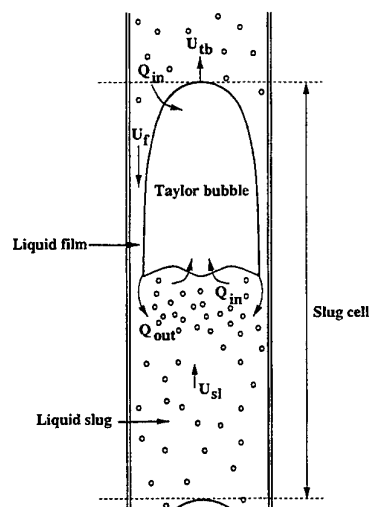


Figure 1: A schematic picture of slug flow in a vertical tube. U_{tb} , U_f , U_{sl} are respectively the Taylor bubble velocity, the film velocity and the superficial liquid velocity.

In their model, based on a description in terms of a slug cell, Fernandes *et al.* (1983) predict the void fraction in the liquid slug by considering the gas fluxes into and out of the Taylor bubble, as indicated in Fig. 1. As the liquid

flows around the nose of the Taylor bubble it deforms into a film too thin to accommodate the bubbles carried within the liquid slug. As a result bubbles coalesce with the nose of the Taylor bubble, which results in a gas flow rate into the Taylor bubble. At the bottom of the Taylor bubble small bubbles are torn off due to the falling film which plunges into the liquid slug. This gas flow rate out of the Taylor bubble is indicated as the entrainment flux. A part of these entrained gas bubbles re-coalesces back into the Taylor bubble at its trailing edge, which results in a re-coalescence flux. For a stationary Taylor bubble these gas fluxes are in balance.

The detailed mechanisms behind entrainment and re-coalescence are not yet fully understood (Dukler & Fabre, 1991). In particular the mechanism by which small bubbles are torn off from the Taylor bubble, i.e. the entrainment process, remains unclear. Delfos (1996) has suggested that the entrainment occurs due to the fact that the liquid interface at the bottom of the Taylor bubble is not able to follow the variations in thickness of the downward falling liquid film. Based on this hypothesis he has proposed a model for the entrainment flux. Given the uncertainties in the entrainment process and the role of the falling liquid film in this process, our objective here is to measure the characteristics of this falling film. In particular the mean film thickness, film thickness fluctuations and intermittency. For this purpose we developed a method to measure the film thickness based on a Laser Induced Fluorescence (LIF) technique.

In the present paper some theory of the falling film is explained in section 2. The experimental set-up as well as the measurement method are described in section 3. Finally results are presented and conclusions are drawn.

2 Theory

In preparation for the analysis of our experimental data, we concentrate in this section on some theoretical aspects of a Taylor bubble. Using potential flow, Dumitrescu (1943) has calculated the shape of a Taylor bubble. He finds for the radius of curvature R_n at the nose of the bubble

$$R_n = 0.375D \quad (1)$$

where D is the diameter of the pipe in which the Taylor bubble rises. The liquid layer alongside the Taylor bubble far from its nose is sufficiently thin to be described as a falling film. Based on this result the shape of the Taylor bubble below the nose can be calculated.

The rise velocity of the Taylor bubble is given by Nicklin (1962) as

$$U_{tb} = 1.2U_{sl} + 0.35\sqrt{gD} \quad (2)$$

where U_{sl} is the superficial liquid velocity. In our experiment, to be described in section 3, we consider a Taylor bubble kept at a fixed position by a downward liquid flow. According to (2) the downward velocity of this liquid flow is equal to

$$U_{lexp} = 0.2U_{sl} + 0.35\sqrt{gD} \quad (3)$$

2.1 The falling film

Let us consider the falling film surrounding the Taylor bubble in a frame where the Taylor bubble is fixed. Within this reference frame the film flows downward and it behaves as a free-falling film, i.e. the shear across the interface between film and bubble is assumed to be negligible. For a thin film ($h_f \ll D$) we can approximate this case as a two-dimensional film flowing along a flat vertical plate. In the simplest case of a free-falling, laminar film without friction on the wall, the velocity profile will be uniform. As a result of conservation of mass, the downward liquid flow rate must be constant at each position along the vertical pipe. This implies that the liquid flow rate above the fixed Taylor bubble must be equal to the liquid flow rate in the falling film:

$$\frac{\pi}{4}D^2U_{lexp} = \frac{\pi}{4}(D^2 - [D - 2h_f(z)]^2)U_f(z) \quad (4)$$

$$h_f(z) = \frac{D}{2} \left(1 - \sqrt{1 - \frac{U_{lexp}}{U_f(z)}} \right) \quad (5)$$

where $h_f(z)$ is the mean film thickness and $U_f(z)$ the mean film velocity. The z denotes the axial position (taken positive downwards) along the pipe where the origin of z is chosen at the top of the Taylor bubble.

The velocity of a free-falling film in our reference frame reads

$$U_f(z) = \sqrt{2gz}. \quad (6)$$

If we take friction with the wall into account, a laminar boundary layer will develop on the wall. The boundary-layer thickness for the case of a two-dimensional accelerating laminar flow reads (Delfos 1996, Appendix A):

$$\delta(z) = 3.41\sqrt{\nu\sqrt{\frac{z}{2g}}}$$

with ν the kinematic viscosity of the liquid. The accelerating boundary layer causes a non-uniform velocity profile within the film. As a consequence we have to correct the free-falling film thickness (5) by adding to h_f the displacement thickness δ^* due to the boundary layer (Delfos 1996, Appendix A), given by

$$\delta^* \approx 0.252 \delta \quad (7)$$

A final point to consider is the transition from laminar to turbulent flow inside the liquid film. In our experiment with $Re = \frac{4U_f h_f}{\nu} = 3.8 \cdot 10^4$ this transition takes place at about 0.5 m from the nose of the Taylor bubble. When the turbulent flow is fully developed across the whole film, the film should reach a stationary thickness. The friction factor for such a fully developed turbulent film has been measured by Belkin (1959). Based on a balance between the friction at the wall and the gravity force, the stationary film thickness can be computed. For our Reynolds number this results in a film thickness of 3.0 mm.

2.2 The entrainment flux

Delfos (1996) suggests that the entrainment flux, the gas flow out of the Taylor bubble into the liquid slug, occurs due to disturbances on the surface of the falling film along the Taylor bubble.

The proposed mechanism for entrainment is now the following: The falling film along the Taylor bubble becomes turbulent at a certain Taylor bubble length, L_{onset} . The turbulent eddies in the film then deform the film surface. Due to these surface disturbances, advected by the film flow, the free surface at the bottom of the Taylor bubble sees, so to speak, a transversely oscillating wall. The transverse acceleration of this oscillation is proportional with the rate $\frac{h_w}{\lambda} \frac{U}{L}$, with h_w the amplitude of the wave and λ the wave length of the wave. When this acceleration a_t becomes much larger than the gravitational acceleration g , the pool surface is not able to follow these oscillations (disturbances) of the incoming film flow (Delfos, 1996). As a result an air gap is generated between the vertically falling film and the liquid slug at the bottom of the Taylor bubble. This gap may be closed by crest of the next disturbance and as a result air is trapped inside the liquid. The entrained gas is then approximately equal to the volume of air enclosed between the crests of the disturbances.

To come to an expression for the entrainment flux we have to make some assumptions. First we assume that the disturbances are sinusoidal waves. Further more we suppose that the velocity of the waves is approximately equal to the bulk velocity. Finally we assume that the disturbances on the surface occur intermittently with an intermittency factor, I , which can be interpreted as the percentage of Taylor bubble circumference on which disturbances occur. The model for the entrainment flux then becomes

$$Q_{ent}(z) = I\pi(D_i - 2h_f(z))U_f(z)h_w(z) \quad (8)$$

To calculate the entrainment flux we need to measure the mean film thickness, the intermittency, the film velocity and the amplitude of the waves on the surface of the liquid film.

3 Experiment

3.1 Experimental set-up

The details of the experimental set-up that we have used, are described by Delfos (1996). Here we will summarise only the main characteristics. A schematic layout of the experimental set-up is illustrated in Fig. 2. It consists of a vertical, cylindrical pipe made out of perspex and with an inner diameter $D_i = 100$ mm. In this tube, a Taylor bubble is generated by an injection of air through a small tube with diameter D_t . At the end of this tube a spherical cap is attached. The purpose of this spherical cap is to stabilise the bubble in the centre of the main vertical pipe. The radius of curvature of this cap is the same as that of the nose of a theoretical Taylor bubble as given in (1).

The bubble is kept at a fixed position by a water flow moving downward with a velocity equal to U_{lexp} given by (3). Above the Taylor bubble a flow straightener, made

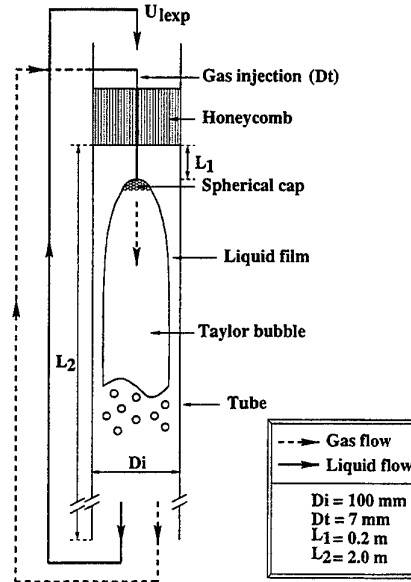


Figure 2: A schematic drawing of the experimental set-up. D_t is the external diameter of the gas injection tube.

out of honeycomb material, is placed to obtain a uniform velocity profile. Such a profile is representative for flow conditions encountered by a rising Taylor bubble in a stagnant liquid. Apart from creation of a flat velocity profile, the flow straightener also decreases the turbulence intensity in the flow in front of the Taylor bubble.

The part of the pipe where the Taylor bubble can be observed, is called the test section. The test section is enclosed by a rectangular, water-filled, box to provide a good optical access.

3.2 The LIF-technique to measure film thickness

The measurement of film thickness has to be performed without disturbing the flow, since a disturbance can change the behaviour of the film, e.g. it can promote transition from laminar to turbulent flow. In this experiment we have chosen to measure the film thickness with a Laser Induced Fluorescence (LIF) technique (Hewitt, 1964). This method allows instantaneous observation of the film thickness at a given position and as a function of time. From these measurements statistical information, such as the mean and variance of the film thickness, can be obtained.

The principle of this LIF-technique is illustrated in Fig. 3. Blue light ($\lambda_L = 488$ nm) from an Argon-ion laser illuminates via a small circular mirror, $D_m = 3$ mm, the liquid film, which contains a constant concentration of a fluorescent dye, Uranine AP, $[C_{20}H_{14}Na_2O_5]$. When the dye is excited by the incident beam, a green fluorescence ($\lambda_F = 515$ nm) results. This green light is observed by an optical system which is positioned at the same side of the pipe as the incoming blue laser light. After passing a collimating lens, the fluorescent light is first separated from the reflected blue light by a bandpass filter (XM-535 Corion).

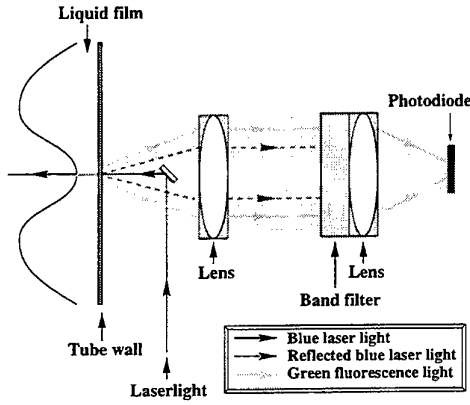


Figure 3: Schematic figure of film thickness measurement with the Laser Induced Fluorescence technique.

Subsequently, it is focused on a photo-diode by means of a second lens. The signal of photo-diode is proportional to the intensity of the fluorescent light.

The intensity of the fluorescent light depends on the intensity of the incoming blue light I_0 , the concentration of the dye C , the film thickness h_f (i.e. the light path through the fluorescence solution) and the properties of the detector. The relation reads (Guilbault, 1973)

$$I_f = k_1 I_0 (1 - e^{-k_2 C h_f}) \quad (9)$$

where k_1 and k_2 are material properties. During the experiment the concentration of the fluorescent dye and the intensity of the incoming laser light are kept constant. The measured intensity of fluorescence can thus directly be interpreted as a measure for the film thickness.

For sufficiently dilute solutions and small film thicknesses, (9) can be simplified to the following relationship

$$I_f \approx k_1 k_2 I_0 C h_f - \frac{1}{2} k_1 k_2^2 I_0 C^2 h_f^2 \quad (10)$$

where the non-linear second term is called the inner-cell effect (Guilbault, 1973). Its explanation is that the portion of fluorescence solution nearest to the light source absorbs radiation, so that less is available for the rest of the solution. The dye concentration is $C = 1.10^{-3} \text{ gl}^{-1}$. It is chosen such that the fluorescence intensity is sufficiently high for the photo diode to detect, but sufficiently low to avoid the inner-cell effect.

The relationship (10) must follow from a separate calibration procedure in which the intensity of fluorescence is determined for a set of given film thicknesses. For this we have designed a special calibration set-up, which is shown schematically in Fig. 4. It consists of a rectangular container, made out of perspex, which is filled with the fluorescent solution. In this container a ladder-shaped perspex beam with holes is placed on the bottom. The holes are closed on the bottom side with thin glass plates ($d_g = 0.2 \text{ mm}$). These thin glass plates replace the free surface (water-air) in the experiment (during calibration we correct for the fact that this surface reflects about 2

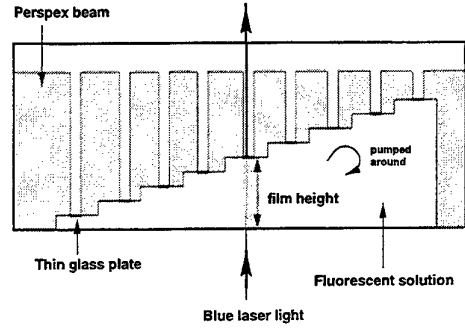


Figure 4: Schematic side-view of the calibration set-up.

% more than an air-water interface). Between these thin glass plates and the bottom of the container a range of liquid layers with well-defined thicknesses are present. The bottom of the container consist of two perspex walls with a water layer in between, to imitate the construction of the test section in the experiment. The distance between the laser and the liquid layers is taken the same as in the experiment. During the calibration, the fluorescent solution is circulated by a pump to prevent photo decomposition (Guilbault, 1973) of the dye. The calibration procedure now consist of measuring the thickness of the liquid layers by means of the LIF-technique. The voltage of the photo-diode (which measures the fluorescence intensity) is found to fluctuate during the calibration measurement. These fluctuations occur since the laser itself fluctuates with 50Hz and its harmonics. The intensity of this ripple is 2 % of the total measured intensity at a given film height. These Nx50Hz fluctuations are deleted during signal processing. The error in the calibration voltage is the sum of the inaccuracy in the thickness of the liquid layer ($\approx 0.02 \text{ mm}$) and the error in the curve fitted to the calibration data (which is 3 %). For a typical film thickness of 3 mm this leads to an error of about 0.1 mm. An example of a calibration curve is shown in Fig. 5. The curve is almost linear which confirms that the inner-cell effect is small.

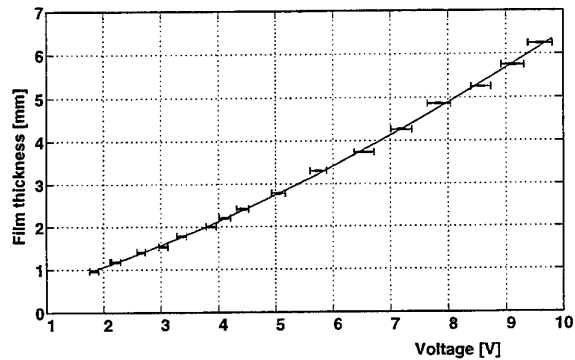


Figure 5: The calibration curve, which gives the relation between the film thickness and the voltage of the photo-diode (i.e. the fluorescence intensity).

After calibration the laser and detector are mounted on a traversing system along the test-section, so that we could measure the film thickness at different points along the Taylor bubble. At every measuring point the intensity of fluorescence is sampled during 15 seconds with at a frequency of 4000 Hz.

3.3 Determination of intermittency and wave height

To determine the intermittency and wave height, we have to look at the continuous film thickness signal. An example of such a signal at a Taylor bubble length of 0.7 m, where the film is already turbulent and entrainment occurs, is shown in Fig. 6.

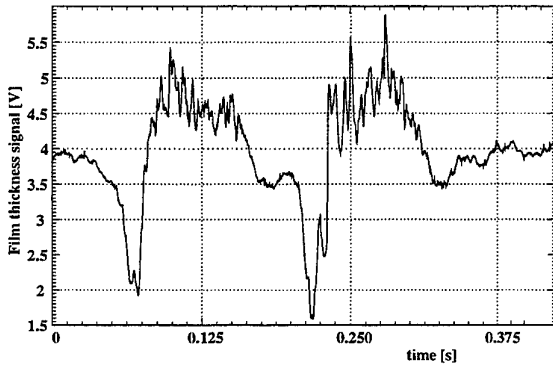


Figure 6: An example of the continuous film thickness signal at a Taylor bubble length of 0.7 m (in a wavy part).

In this figure we see two kind of waves. Very large waves, $\lambda \approx 0.38$ m and $h_w \approx 1.0$ mm and small waves, $\lambda \approx 6$ mm and $h_w \approx 0.5$ mm. In the power spectrum we find the large waves at a frequency of about 10 Hz and the small waves about 200 Hz. The criterion for entrainment, $\frac{a_t}{g} \gg 1$, can in our case only be satisfied if the rate $\frac{h_w}{\lambda} \gg 0.03 \text{ m}^{-1}$. The large waves do not conform to this requirement. Thus, to determine the relevant wave height and intermittency for the entrainment, the film signal is filtered by a high pass filter with a cut off frequency of 30 Hz.

The intermittency, which in our case is defined as the percentage of time that waves occur on the film surface, is computed by applying the VITA-technique (Johansson, 1983). In the VITA technique, shown in Fig. 7, the (local) standard deviation is calculated for small time intervals of the signal (in our case 2.5 msec). The time period that this local standard deviation exceeds a threshold value, is then defined as the time interval T_d which is the time period that waves due to turbulence are present on the film interface. The threshold value is found by taking the mean local standard deviation of a known smooth surface (the case of a laminar film). In our experiment the threshold value is 0.09 V, which is 0.1 mm at a mean film thickness of 3 mm. The intermittency is then obtained as the ratio between T_d and the total time interval, T_{tot} .

The standard deviation of the interface disturbances,

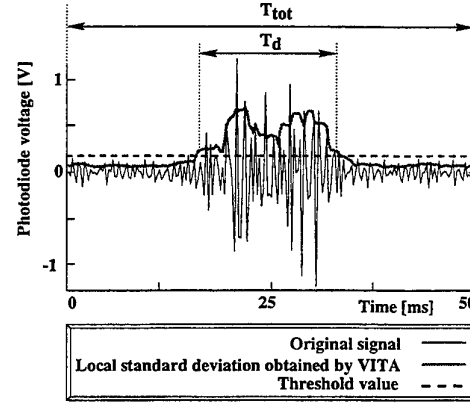


Figure 7: Definition of the intermittency with the VITA-technique. T_d is the time that disturbances on the film surface are present and T_{tot} is the total time interval.

σ_w , is now obtained from the standard deviation of the filtered film thickness signal σ_{tot} corrected for intermittency. This leads to the following expression

$$\sigma_w^2 = \frac{\sigma_{tot}^2 - (1 - I)\sigma_0^2}{I} \quad (11)$$

where σ_0 is the standard deviation of the signal without waves (noise). If we assume that the disturbances are sinusoidal waves, the wave height becomes

$$h_w \approx \sqrt{2} \sigma_w. \quad (12)$$

4 Results

4.1 Mean film thickness

In Fig. 8 we give the measured mean film thickness as function of the distance from the Taylor-bubble front. These data have been obtained with a gas influx $Q_{co} = 0.36 \text{ ls}^{-1}$ and a downward liquid velocity of $U_{lexp} = 0.35 \text{ ms}^{-1}$. The film thickness profile is only given for this particular case of the gas influx, because the profile is independent of the incoming gas flux.

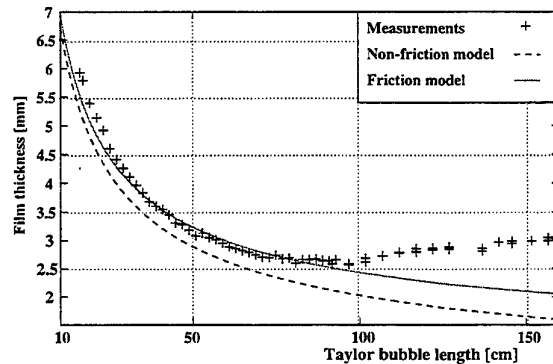


Figure 8: The measured film thickness at $Q_g = 0.36 \text{ ls}^{-1}$ and $U_{lexp} = 0.35 \text{ ms}^{-1}$ compared with the models for a free-falling laminar liquid film with and without friction.

In Fig. 8 we also show the theoretical results for the thickness of a free-falling film with and without friction as discussed in section 2.1. We find that the measured film thickness agrees rather well with the theoretical film thickness for the case of a laminar free-falling film with friction until a bubble length of about 0.7 m. The difference between the measurements and the friction model after this point is probably caused by the development of turbulence. The turbulent friction at the wall causes a decrease of the mean velocity in the film which results in thicker film. Eventually the film thickness seems to reach a constant value of ± 3 mm, which is in agreement with the stationary turbulent film thickness determined from the empirical correlation of Belkin (1959).

4.2 Intermittency distribution and wave height

The intermittency distribution along the Taylor bubble, determined as described in section 3.3, is shown in Fig. 9. From our measurements we see that the intermittency is zero until the bubble reaches a length of about 0.5 m. This point is called 'the onset of entrainment' and we interpret this as the transition point. Beyond this point the intermittency grows rapidly to 1 at about 1 m.

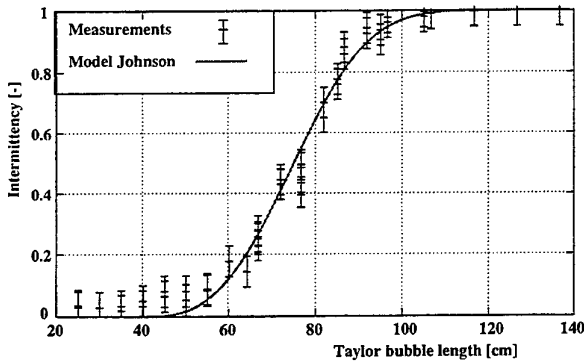


Figure 9: Measured intermittency distribution along the Taylor bubble at $U_{lep} = 0.35 \text{ ms}^{-1}$ compared with the model by Johnson (1994) for intermittency distribution in a boundary layer on a flat plate.

In the same figure the intermittency of the surface of the falling film is compared with a model for the intermittency distribution in a boundary layer during transition. In this latter case the intermittency is equal to the percentage of time that turbulent spots occur in the boundary layer (Johnson & Fashifar, 1994). Their model agrees well with our measurements, which is consistent with our hypothesis that the disturbances are caused by turbulence.

The wave height of the disturbances on the falling-film surface, computed according to (11) and (12) is shown in Fig. 10. The wave height increases from 'the onset of entrainment point' at about 0.5 m till a height of about 0.55 mm at a Taylor bubble length of 1.4 m. From the trend in the data shown in this figure, it seems that the wave height will increase even more after this length.

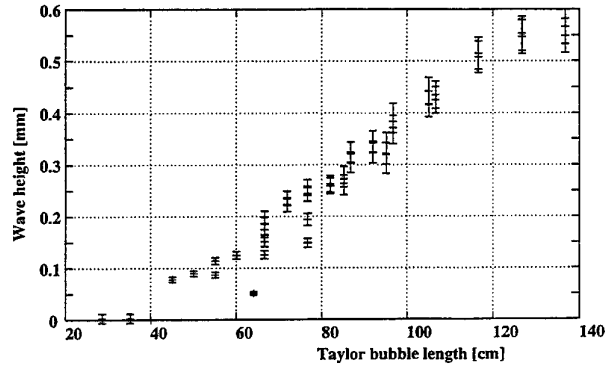


Figure 10: The wave height of the waves on the surface of the falling liquid film.

4.3 Derivation of the entrainment flux

We finally calculate the entrainment flux. For this we need an estimate for all the parameters in (8) which are respectively the mean film velocity U_f , the mean film height h_f , the intermittency I and the height of the waves on the falling film surface h_w . Apart from the mean film velocity, these parameters can all be obtained directly from our measurements. The remaining parameter, i.e. the mean film velocity, is calculated with help of the measured film thickness by means of conservation of mass given by (5).

In Fig. 11 we give the entrainment flux, Q_{ent} obtained from (8) as a function of the bubble length. In the same figure we also show the incoming gas flux at the top of the Taylor bubble, which is equal to the entrainment flux if we neglect the re-coalescence flux.

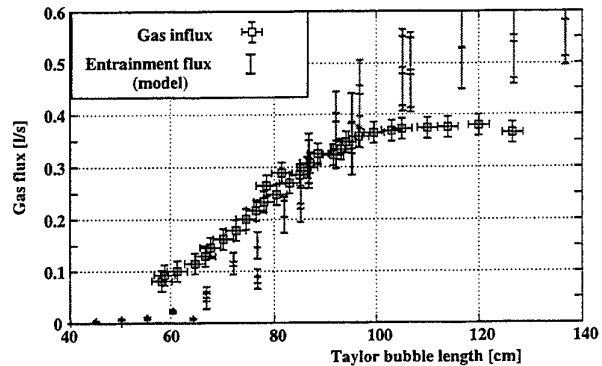


Figure 11: The modelled entrainment flux compared with the gas influx at $U_{lep} = 0.35 \text{ ms}^{-1}$

The results in Fig. 11 show that for bubble lengths smaller than 0.9 m the theoretical model slightly underestimates the observational value. Given the various assumptions made in our theoretical model we consider this agreement to be a confirmation of our entrainment hypothesis, i.e. entrainment is caused by disturbances on the free-falling film surface. After the Taylor bubble has reached a length of 1.0 m, the entrainment according to the theoretical result (8) still increases, while the entrainment based

on the incoming gas flux reaches a maximum value. This behaviour suggest that our entrainment model, where all air in between the disturbances on the film surface is entrained in the slug flow, might no longer be valid for large Taylor bubbles. Further study for this particular case is therefore warranted.

5 Conclusions

Based on the results presented in this study we can draw the following conclusions

- We have applied a technique to measure the film thickness based on Laser Induced Fluorescence and found the results to be reliable. The film thickness can be measured within an accuracy of 0.1 mm.
- The measured mean film thickness along a stationary Taylor bubble agrees with the model for a laminar free-falling film with friction on the wall until the Taylor bubble reaches a length of 0.7 m. After this bubble length the change of slope in the film-thickness curve indicates that there is a transition from laminar to turbulent flow in the liquid film. From a length of 0.9 m the film thickness increases slowly to a constant thickness of 3 mm, which agrees with the stationary film thickness determined with the empirical correlation of Belkin (1959).
- The film surface changes from smooth to rough at a Taylor bubble length of 0.5 m. As soon as the film surface becomes rough entrainment is observed, which is in agreement with the hypothesis of Delfos (1996) that disturbances on the film surface are responsible for entrainment. The area of the film surface covered by disturbances grows as function of the bubble length. This is described by the intermittency which increases from a value 0 at a bubble length of 0.5 m to 1 at a length of 1.2 m.
- The simple model for the entrainment flux (Delfos, 1996) is found to be in reasonable agreement with observations for Taylor-bubble lengths smaller than 1 m. For larger Taylor bubble lengths, i.e. above 1 m, the model for the entrainment flux shows a trend which is not in agreement with the experimental data. Further study is therefore needed.

Acknowledgements

The authors thank T.D. Tuijthut and J.L.J. Zijl for their work on the experimental part of this research. We also thank Prof. dr. ir. F.T.M. Nieuwstadt for his useful discussions.

References

- BELKIN H.H., MACLEOD A.A., MONRAD C.C., & R.R., ROTHFOS. 1959. Turbulent liquid flow down vertical walls. *AIChE Journal*, **5**, 245-248.
- DELFO, R. 1996. *Experiments on air entrainment from a stationary slug bubble in a vertical tube*. Ph.D. thesis, Delft University of Technology.
- DUKLER A.E., FABRE J. Gas-liquid slug flow; knots and loose ends. *Third int. workshop on Two-Phase fundamentals, ICL, june 1992*.
- DUMITRESCU, D.T. 1943. Strömung an einer Luftblase im senkrechten Rohr. *Z. angew. Math. Mech.*, **23**(3), 139-149.
- FABRE J., LINÉ A. 1994. Advancements in two-phase slug flow modelling. *Proc. of the Univ. of Tulsa Cent. SPE Symp, Tulsa*.
- FERNANDES R.C., SEMIAT R., DUKLER A.E. 1983. Hydrodynamic model for gas-liquid slug flow in vertical pipes. *AIChE Journal*, **29**, 981-89.
- GUILBAULT, G.G. 1973. *Practical Fluorescence*. Marcel Dekker Inc., New York.
- HEWITT G.F., LOVEGROVE P.C., NICHOLLS B. 1964. Film thickness measurement using fluorescence technique. *Atomic Energy Research, Harwell, AERE - R4478*.
- JOHANSSON A.V., ALFREDSSON P.H. 1983. Effects of imperfect spatial resolution on measurements of wall-bounded turbulent shear flows. *J. Fluid Mech.*, **137**, 409.
- JOHNSON M.W., FASHIFAR A. 1994. Statistical properties of turbulent bursts in transitional boundary layers. *Int. J. Heat Fluid Flow*, **15**, 283-290.
- NICKLIN D.J., WILKES J.O., DAVIDSON J.F. 1962. Two-phase flow in vertical tubes. *Trans. Inst. Chem. Engs.*, **40**, 61-68.

EXPERIMENTAL ANALYSIS OF A CONFINED BLUFF BODY FLOW LADEN WITH SOLID PARTICLES

T. Ishima^{*,†}, J. Borée^{*}, P. Fanouillère^{**} and I. Flour^{**}

^{*} Institut de Mécanique des Fluides ; UMR CNRS/INPT-UPS 5502
Allée du Professeur Camille Soula ; 31400 TOULOUSE ; France

[†]Gunma University ; Tenjin, KIRYU 376, Japan

^{**} EDF – DER – LNH , 6, Quai Watier , 76400 CHATOU, France

ABSTRACT:

An experimental study of the two-phase flow downstream a confined bluff body is presented in this paper. This situation is interesting for the development of gas-solid flow turbulence closures. Measurements are made with a phase Doppler anemometer. Glass beads are added to the inner jet. The initial particle size distribution covers a wide range of size classes from 20 μm to 110 μm with a mean value of 60 μm . The single phase configuration is chosen to establish a stagnation point in the recirculating region. This configuration emphasises the role of the inertia of the particles. This study shows particularly well that one has to write and solve transport equations for the fluctuating velocity of the particles and that no local equilibrium with the fluid turbulence can be assumed. In particular, production and transport effects are clearly observed. Contrasted mass-loading ratio of the inner jet ranging from 22 % to 110 % are selected in order to show the two-way coupling between continuous and discrete phases. We show that it has a noticeable effect on the organisation of the flow downstream the bluff body and on the spatial distribution of the particulate phase.

1. INTRODUCTION

Particle-laden gas flows are common in the industry and receive presently a lot of attention in the laboratories. Significant efforts are developed to improve numerical predictions of engineering complex situations with Lagrangian (Berlemont, Desjonqueres, and Gouesbet 1990) or Eulerian (Elgobashi and Abou-Arab 1983; Simonin 1991) predictions. Owing to the large number of new dimensionless parameters involved when one adds particles in a flow, development of turbulence models require a large amount of accurate experimental data in basic homogeneous or inhomogeneous flows.

Laser based measurements now provide insight into dispersed two-phase flows. A large number of basic experiments are reported in channel flows (Kulick, Fessler, and Eaton 1994) , boundary layer flows (Rogers and Eaton 1991) and in simple free shear flows as shear layers (Hishida, Ando, and Maeda 1992; Ishima, Hishida, and Maeda 1993) and jets (Hardalupas, Taylor, and Whitelaw 1989; Modaress, Tan, and Elgobashi 1984; Prévost, Borée, Nuglisch, and

Charnay 1996) . The role of the Stokes number of the particles, which compares the particle Stokesian time scale to the time scale of the large eddy motion seen by the particles is largely discussed in the shear flows where a typical turbulent time scale is easy to define. Modifications of the turbulence for moderate mass-loading (defined as the ratio of particles mass fluxes to air mass fluxes) is clearly demonstrated in these works. Fluid particle correlations are measured in (Prévost *et al.* 1996) and used to analyse the contrasted evolution of the particles Reynolds stresses along the jet.

These basic situations present essential test cases for numerical predictions. For instance, jet flow studies have clearly shown that the influence of ejection conditions and the local production by the mean particle velocity gradients are dominant mechanisms for the dispersed phase fluctuating motion (Hardalupas *et al.* 1989) that have to be taken into account in models (Simonin 1991) . The bluff body flow presented in this paper was designed as a severe test case for the modelling. This configuration is typical of an industrial application where the objective is to control the mixing of a fuel (pulverised coal) with the air. However and contrary to practical situations, the outlet velocity of the inner jet is chosen low enough in order to obtain two stagnation points (see figure 1) in single phase. Polydispersed glass particles are added to the inner tube flow only. The stagnation point configuration obtained here is therefore interesting as inertia properties of the particles and fluid/particle coupling in the inner jet are expected to play a dominant role. The initial particle size distribution covers a wide range of size classes from 20 μm to 110 μm with a mean value of 60 μm . Measurements obtained with a Phase Doppler anemometer will be presented. A size class analysis will illustrate the contrasted evolution of the fluid and particle turbulence.

The experimental configuration and the measurement method are first described. The evolution of the fluid and particles mean and fluctuating velocity field for two typical size classes is presented in part 3. The air flow in the presence of particles obtained for two different mass-loading ratio of the inner jet $M_j = 22\%$ and $M_j = 110\%$ is then compared with the single-phase flow data. The consequences as spatial distribution of the particulate phase is concerned are finally discussed.

2. EXPERIMENTAL SET-UP

2.1 Flow Configuration

The experiment presented here has been performed in the flow loop Hercule of EdF-LNH. The vertical axisymmetric air flow downstream the bluff body is shown in figure 1. The outer and inner radius of the annular outer region are respectively $[R_2 = 150 \text{ mm} ; R_1 = 75 \text{ mm}]$. The maximum velocity of the annular flow is 6 m/s and the Reynolds number of the flow is $Re = U(R_2 - R_1)/\nu \approx 30000$. This relatively low value of the external velocity was chosen in order to use a reasonable external volume flux and to overcome seeding problems. The external volume flux is kept constant at $Q_e = 780 \text{ Nm}^3/\text{h}$ for a relative static pressure at $x=0$ of $\Delta p = 10 \text{ mbar}$. The length of the straight annular section upstream the test section is $L_e = 2 \text{ m}$. Several honeycomb structures are added in order to remove any swirl motion. An inner tube jet $[R_j = 10 \text{ mm} ; U_j(r=0) = 4 \text{ m/s}]$ is generated by compressed air flows on the axis of the recirculation as shown in figure 1. With $L_e/D_j = 100$, the tube flow is established. The volume flux of the jet is $Q_j = 3.8 \text{ Nm}^3/\text{h}$ at the relative static pressure $\Delta p = 10 \text{ mbar}$. This corresponds to a mean velocity $\bar{U}_j = 3.4 \text{ m/s}$. The ratio of the jet volume flux to the annular flow volume flux is very low (0,5%). The maximum velocity $U_j = 4 \text{ m/s}$ was chosen in order to get a single phase flow with stagnation points in the recirculation. The Reynolds number of the pipe flow is $(Re = \bar{U}_j D_j / \nu \approx 4500)$, the flow is turbulent with $\bar{U}_j / U_j(r=0) = 0,85$. Moreover, we could check that the velocity profile at the exit is well fitted by a power law of exponent approximately (1/7).

A particular care was devoted to seed both outer and inner single phase flows. Two water injectors designed for spreading water mist as tracer particle are located upstream the establishment region and are used to seed the annular flow. Smoke tracers generated by a smoking machine (produced by Dantec) are added to the central jet flow.

The test section is 1500 mm in length. For further descriptions, The origin is set on the edge of the bluff body and at the centre of the inner jet. The measurements on the axis were made at 3mm, 10mm, 20mm and after every 20mm up to 500mm. Flow characteristics were also measured in planes of 3, 80, 160, 200, 240, 320 and 400mm. The flow will be described henceforth using a cylindrical coordinate system (x, r, θ) to indicate the axial (downward), radial and azimuthal directions. The components of the mean and fluctuating velocity field are denoted respectively by (U, V, W) and (u, v, w) where V is the radial component and W is the azimuthal component. No swirling motion was detected to within our measurement precision. Subscripts "f" and "p" indicate respectively fluid and particles properties. The symbol $\langle \rangle_f$ and $\langle \rangle_p$ indicates averaging operators associated respectively to fluid and particle phases. The expressions u' and v' stand respectively for longitudinal and radial standard deviation.

2.2 Glass Particles

Glass particles are released in the conducting pipe of the inner jet by a particle feeder. All flow conditions and particle mass loading are monitored on a work station. The mass loading is controlled accurately in closed loop by weighting continuously the particle feeder. Two mass flux of particles of 1 kg/h (resp. 5 kg/h) corresponding to contrasted inner jet mass loading ratio M_j of $M_j = 22\%$ (resp. $M_j = 110\%$) have been selected in order to show the coupling between continuous and discrete phases. Note that the mass loading ratio of the global flow is in each case very weak: $M_t = 0,1\%$ (resp. $M_t = 0,5\%$).

The material density of the glass particle is $\rho_p = 2470 \text{ kg/m}^3$. The initial particle size distribution covers a wide range of size classes from 20 μm to 110 μm with a mean value of 60 μm . The Stokes number of a particle size class is defined as the ratio of the particle aerodynamic time constant τ_p to an appropriate turbulent time scale τ_j . The Stokesian particle relaxation time was chosen for $\rho_p \gg \rho_f$: $\tau_p = \rho_p d_p^2 / 18\mu$ where d_p is the median diameter of the particle size class, ρ_p is the particle density and μ is the fluid viscosity. While the assumption of Stokes flow around an isolated particle is not satisfied for many cases in our experimental conditions, this characteristic time calculation remains interesting for particle Reynolds number up to order of unity. The particle time scale varies significantly. For size classes 20 μm , 60 μm and 110 μm , its value is respectively $\tau_p = 3. \text{ ms} ; 27,5 \text{ ms}$ and 92 ms .

2.3 PDA Settings

For making measurement with a Laser Doppler system, 15 optical windows consisting of thin plastics sheets with a thickness of 0.3 mm are located along the test section. A two components phase Doppler anemometer produced by Dantec (particle Dynamics Analyser: PDA) was used. For accuracy and convenience of the displacement, optical fiber system was preferred. Total inter section angle of incident beam was 1.5 degree. The receiving optics was settled at 67 degrees of off-axis angle from the incident beam to minimise the contribution of the reflected light.

The optical windows were put only on the incident beam side. The actual off-axis angle was therefore changed from the 67 degree at the outer side of the measuring range because of the refraction effect on the cylindrical wall of the test section. The off-axis angle error by this reason was checked before making diameter measurement. It is less than 3% and is thus not significant for diameters measurements.

The used refractive index was set as 1.51 which is for normal glass particle. In this experiment, water droplet and smoke were used as the tracer particles. Their refractive indexes are not equal to that of glass particle. However, the result from the single phase flow measurement with only seeding particle indicates that the mean diameter of the water droplets is less than 5 μm and that of smoke is 2 μm , where the values were obtained with the refractive index of the glass particle. In addition, the results from two-phase flow without tracers show that very few glass particles with less than 10 μm in diameter exist in the experimental region. Therefore, all the

particles with less than $5\text{ }\mu\text{m}$ in diameter were treated as tracer particles in the present experiment. We have verified that all the particles in this size-class can be considered as good tracers of the continuous phase. Measurements are carried out for the continuous and dispersed phases simultaneously. Unless specified, we perform statistical averaging of at least one thousand independent samples in each size-class. Consequently, estimated statistical absolute errors for mean values (resp. relative errors for standard deviation values) are respectively $\Delta U \approx 0.06u'$ (resp. $E_\sigma \approx 5\%$) with a 95% confidence level.

3. TWO-PHASE FLOW AT MODERATE MASS LOADING $M_j = 22\%$

3.1 Qualitative Description of the Flow

The sketch of the confined bluff body flow presented in figure 1 was derived from systematic axial and lateral mean velocity profiles in single phase configuration (Ishima and Boree 1998). The flow is schematically decomposed into three longitudinal regions. Region A ranges from the jet nozzle to the first stagnation point S_1 with $x_1 \approx 120\text{ mm}$ or $x_1/D_j \approx 6$. The jet is therefore rapidly stopped by the recirculating flow. Note also that the positive pressure gradient due to the section increase should play an important role. In A, the central jet is surrounded by a recirculation upward flow which "feeds" both the initial entrainment in the jet and the annular shear layer developing at the edge of the bluff body. Region B ranges from S_1 to S_2 and represents the recirculation region. An intense upward flow on the axis is detected (see profiles of U_f in fig. 4a). The second stagnation point S_2 is located approximately at $x_2 \approx 220\text{ mm}$ or $x_2/D_j = 11$. Profiles measured further downstream at $x = 200\text{mm}$, 240mm , 320mm and 400mm show that region C downstream S_2 corresponds to the development of a wake flow.

For small particles much denser than the surrounding fluid, a first step is to compare the particle stokesian time τ_p with representative time scales of the turbulent flow.

We can characterise qualitatively important features of this configuration :

- With $\tau_j = D_0/U_0 \approx 5\text{ms}$, most particles are only partly responsive to the initial inner jet flow.

- The time scale of the strong longitudinal velocity decrease about the stagnation point S_1 represent the deceleration imposed to the particles.

$\tau_{dec} = (\partial U_f / \partial x)^{-1} \approx 15\text{ms}$ can be obtained from figure 3a. Only the smallest particles can therefore recirculate.

- The annular shear layer developing at the edge of the bluff body or the downstream wake are characterised by $\tau_s = (\partial U_f / \partial r)^{-1}$ (Hishida *et al.* 1992). τ_s is evaluated from measurements (Ishima and Boree 1998) resulting in $\tau_s = 4\text{ms}$ at $x=80\text{mm}$, $\tau_s = 7\text{ms}$ at $x=160\text{mm}$ and $\tau_s = 20\text{ms}$ at $x=400\text{mm}$. Most particles are therefore not responsive and dispersion of the largest particles is expected to occur later in the far wake.

3.2 Exit Velocity Profiles of the Two-Phase Flow

The fluid and particle mean velocity profiles at $x=3\text{mm}$ (nozzle exit) are displayed in figure 2. The $60\mu\text{m}$ particles differs slightly from the continuous phase. They should experience rebounds on walls which have an obvious signature on mean longitudinal velocity profile.

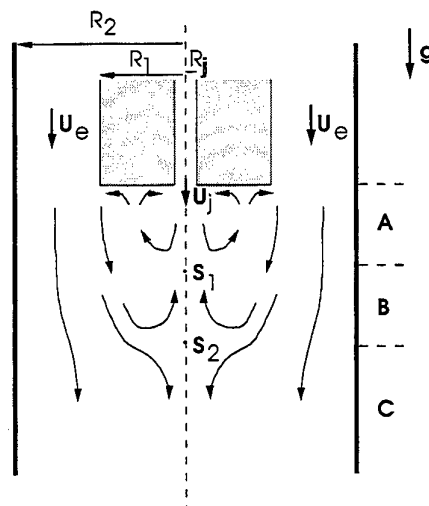


Figure 1: Sketch of the confined bluff body flow

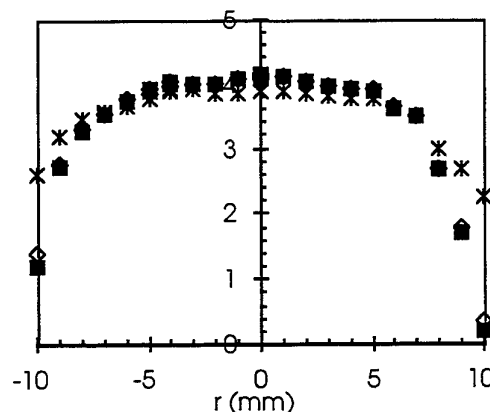


Figure 2: Fluid and particle mean velocity profiles at nozzle exit ■, Tracers ; ◇, $d_p = 20\mu\text{m}$; *, $d_p = 60\mu\text{m}$

3.3 Axial Evolution of the Two-Phase Flow

Figures 3a, b and c compare respectively the axial evolution of the mean axial velocity, rms axial velocity and rms radial velocity for the air and for the two contrasted size classes $d_p \in [15\mu\text{m}, 25\mu\text{m}]$ and $d_p \in [55\mu\text{m}, 65\mu\text{m}]$ noted for simplicity $d_p = 20\mu\text{m}$ and $d_p = 60\mu\text{m}$. Figure 3a shows that particles lag the fluid behaviour so that their axial velocity decreases more slowly. The difference induced by particle inertia is particularly striking just downstream the fluid stagnation point where the two size classes exhibit mean velocities of opposite signs. This trend increases with the size

class and no mean negative velocity is detected in the downstream evolution of particles larger than $60 \mu\text{m}$ not displayed here.

Quite high relative Reynolds number based on the mean velocities differences are reached (The effect of a drift velocity (Simonin 1991) is not considered) in the recirculation corresponding to $\max(\text{Re}_p)=1$ for $d_p = 20 \mu\text{m}$ and $\max(\text{Re}_p)=6$ for $d_p = 60 \mu\text{m}$.

A clear maximum of the fluid and particle axial fluctuating velocity is detected. Let's focus first on the fluid behaviour. The particular configuration with two stagnation points is interesting for turbulence studies. S_1 and S_2 have very different natures : At S_1 , $\frac{\partial U}{\partial x} \approx -75 \text{ s}^{-1} < 0$ and at S_2 , $\frac{\partial U}{\partial x} \approx +29 \text{ s}^{-1} > 0$. On the axis of an axisymmetrical flow, mean continuity equation tells us that $\frac{\partial V}{\partial r} = -\frac{1}{2} \frac{\partial U}{\partial x}$. At S_1 , turbulence is therefore submitted to an axial compression and radial strain while axial strain and radial compression occur at S_2 . The axial evolution of longitudinal and radial fluctuating components (see profiles of u'_f and v'_f in figures 3b and 3c) show clearly that turbulence react strongly to these solicitations. For an axisymmetrical turbulent flow, productions terms for the longitudinal, radial and azimuthal fluctuating components are respectively :

$$\text{Pr } od_{u_f} = -2 \left[\langle u_f^2 \rangle_f \frac{\partial U_f}{\partial x} + \langle u_f v_f \rangle_f \frac{\partial U_f}{\partial r} \right] \quad (1)$$

$$\text{Pr } od_{v_f} = -2 \left[\langle u_f v_f \rangle_f \frac{\partial V_f}{\partial x} + \langle v_f^2 \rangle_f \frac{\partial V_f}{\partial r} \right] \quad (2)$$

On the axis, using mean continuity equation, they reduce to :

$$\text{Pr } od_{u_f}(r=0) = -2 \langle u_f^2 \rangle_f \frac{\partial U_f}{\partial x} \quad (3)$$

$$\text{Pr } od_{v_f}(r=0) = \langle v_f^2 \rangle_f \frac{\partial U_f}{\partial x} \quad (4)$$

S_1 is associated with an intense production of u'_f and destruction of v'_f which explains the sharp peak and the very strong anisotropy $\max(u'_f/v'_f) \approx 2.2$ at $x_1 \approx 140 \text{ mm}$. S_2 is associated with a moderate destruction of u'_f and production of v'_f . Moreover, mean and turbulent transport terms are known to be important contributors to v'_f balance on the axis. Downstream S_2 , v'_f exceeds u'_f with a quasi constant value of $u'_f/v'_f \approx 0.7$ which increases slowly downstream.

A clear maximum of the axial fluctuating velocity of the particle is also detected in figure 3b. The maximum corresponds to the location of maximum production of u_p' by mean longitudinal velocity gradients

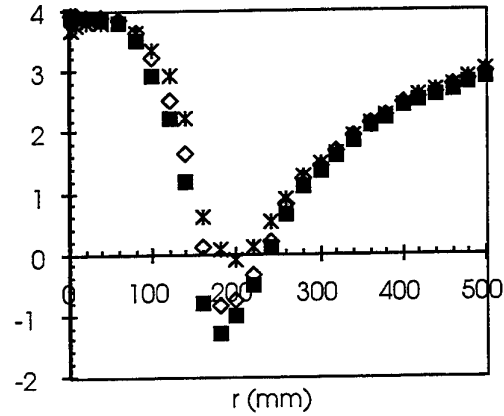


Fig. 3a : Mean longitudinal velocity

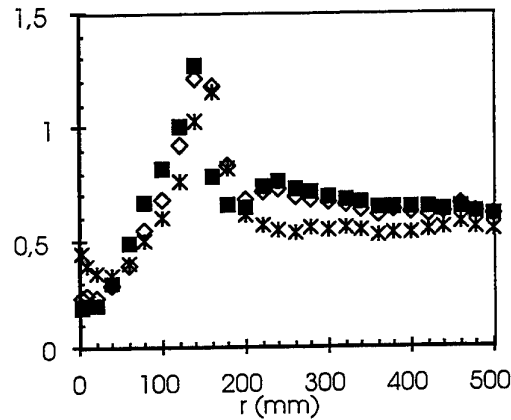


Fig. 3b : Rms longitudinal velocity

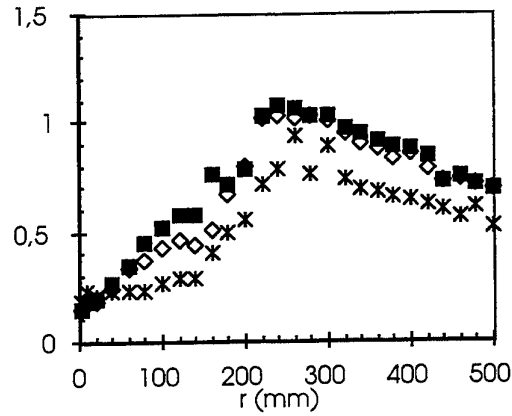


Fig. 3c: Rms radial velocity

Figure 3: Longitudinal evolution on the axis.
■, Tracers ; ◇, $d_p = 20 \mu\text{m}$; *, $d_p = 60 \mu\text{m}$

(see (Simonin *et al.* 1995) for the corresponding equations) and is shifted downstream of u'_f maximum. The evolution of the radial fluctuating velocity of the particles (fig. 3c) is significantly different. The initial increase of v'_p is slow, particularly for the largest particles. The anisotropy of the bead fluctuating motion is very high in the recirculation zone with $\max(u'_{p20}/v'_{p20}) \approx 2.8$ and $\max(u'_{p60}/v'_{p60}) \approx 3.6$ at $x_1 = 140$ mm. v'_p increases sharply at the downstream end of the recirculation zone about point S_2 and exceeds the longitudinal fluctuating motion. Qualitatively, this high level of v'_p is believed to be associated with a global unsteadiness of the end of the recirculation bubble. Any lateral or azimuthal flapping of this region will indeed result in a high level of radial rms velocity on the axis. A slow decrease of the radial rms velocity is measured in the early wake flow ($x > 240$ mm). The memory of the recirculation zone is of course important. Noticeably, the anisotropy u'_p/v'_p of the bead fluctuating motion is very similar to the fluid one. These results show clearly that any assumptions of local dragging of the particulate phase by the turbulence in such flow put aside the dominant mechanisms.

3.4 Radial Evolution of the Two-Phase Flow

To emphasise the previous discussion concerning the influence of inertia, the whole set of radial evolution at $x=160$ mm is drawn in figure 4. The role of the inertia of the particles is particularly clear as mean longitudinal velocities are concerned (fig. 4a). A local maximum is detected on the axis for U_{p20} and U_{p60} at $r=0$ is still positive while U_f is typical for a recirculating flow. Note that, in this highly intermittent region, the downward movement of particles is also probably associated with downward moving fluid pockets. It would be very interesting to draw profiles of the mean fluid velocity seen by the particles which may also exhibit a jet-like behaviour near the axis. More work is presently devoted to this point using the method of (Prévost *et al.* 1996). The mean movement of the large particles (fig. 4a, b) differs from the mean movement of fluid and 20 μ m particles. In the outer region, their mean longitudinal velocities is significantly lower than the fluid velocity while their mean radial velocity shows an outward motion. Two reasons can contribute to this observation. First, the estimated turbulent time scale in the shear layer is $\tau_t = (\partial U_f / \partial r)^{-1} \approx 7$ ms which is larger than $\tau_{p20} = 3$ ms but smaller than $\tau_{p60} = 27.5$ ms. Due to their inertia, large particles can cross the shear layer (for $x < 80$ mm) and are convected downstream by the external flow. A second explanation comes when one looks at the radial evolution of the pdf of particle size measured at $x=160$ mm. The probability of finding a 55/65 μ m particle decreases sharply from $r=60$ mm to $r=90$ mm. The presence of large particles is therefore associated only with outward fluid motion of low longitudinal velocity which also contributes to the results. Note also that the statistical convergence associated with large particles in the outer region ($r > 80$ mm) is not so good as less than two hundred samples were used to limit duration of data acquisition in this region.

The radial evolution of the fluctuating velocities deserve a lot of comments. The longitudinal fluctuating velocities u'_{p20} and u'_{p60} are much greater than u'_f on the jet axis with $u'_{p20}/u'_f \approx u'_{p60}/u'_f \approx 1.7$. Production of the particle longitudinal fluctuation by the longitudinal mean particle velocity gradient is maximum on the axis and explains the important peak. The lateral evolution of u'_f is typical for a recirculating flow with an obvious signature of the shear layer. Local production terms (relations (1) and (2)) were inferred from the data. The maximum value of $Prod_{uf}$ correspond closely to the region of maximum shear rate ($\max(Prod_{uf}) = 150 \text{ m}^2 \text{ s}^{-3}$ at $r \approx 50$ mm) and to the peak detected in figure 4c. Contrary to what is observed classically in quasi parallel shear flows, a significant maximum of v'_f production

$$\left(\max(Prod_{vf}) = 110 \text{ m}^2 \text{ s}^{-3} \right)$$

$\approx 0.75 \max(Prod_{uf})$ is located at $r=40$ mm. This location corresponds to the radial edge of the recirculation zone (fig. 4a), to the maximum value of $(\partial v_f / \partial r)$ and to the peak value of v'_f .

Peak values of u'_p and v'_p are detected at these radial locations also and are believed to be associated with production mechanisms. An interesting result can be obtained if one draws the radial evolution of the correlation coefficient $R_{uv} = \overline{u'v'}$ (fig. 4f). R_{uvp} and R_{uvf} have opposite signs as expected near the flow axis. The large scale time scale of the shear layer is $\tau_t \approx 7$ ms and the 20 μ m particles follow closely the evolution of the fluid phase. On the contrary, one sees that the fluctuating velocities of the 60 μ m particles are highly correlated and that R_{uv60} is quasi constant throughout the whole shear layer. This value corresponds to recent theoretical results by (Fevrier and Simonin 1998).

4. INFLUENCE OF THE MASS LOADING OF THE INNER JET

The value of the mass loading provides information about the proportion of the momentum flow rate carried by the particles to that carried by the gaseous phase in the inner jet. Particles have a mean slip velocity that causes momentum transfer from the dispersed phase to the fluid. In two phase jets, (Hardalupas *et al.* 1989; Modaress *et al.* 1984) have shown that this exchange and the particle/turbulence interaction depend strongly on the particle Stokes number that separates fully responsive, partly responsive and unresponsive particles. Our polydispersion ranges from responsive to unresponsive glass beads and a strong two-way coupling is therefore expected.

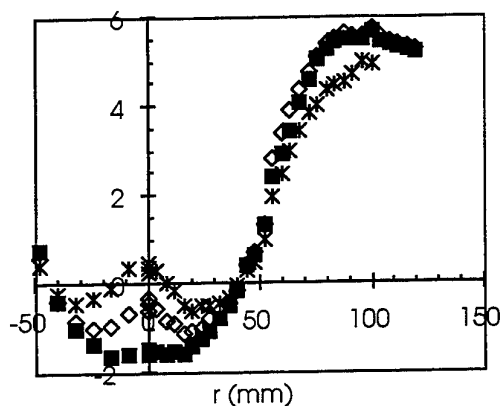


Fig. 4a : Mean longitudinal velocity

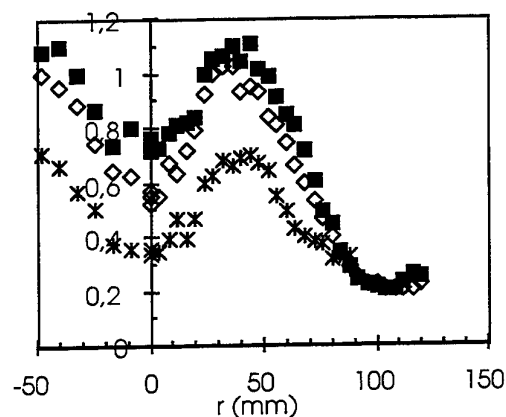


Fig. 4d : Rms radial velocity

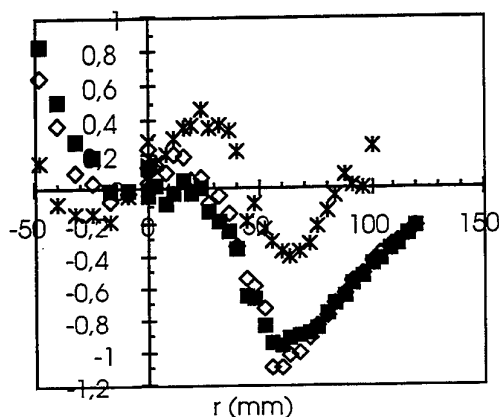


Fig. 4b : Mean radial velocity

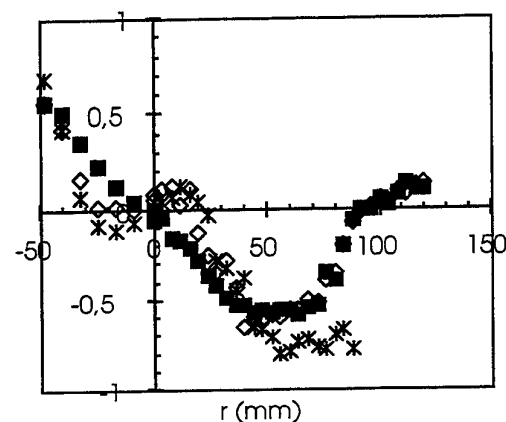


Fig. 4e : Correlation coefficient

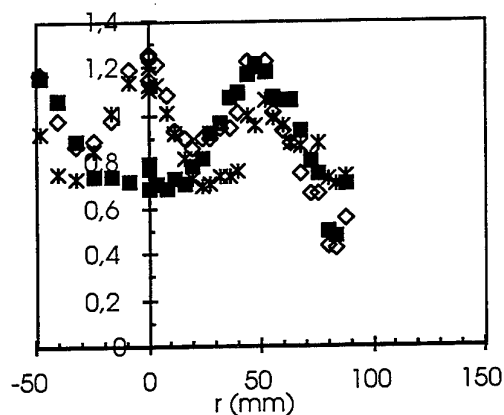


Fig. 4c : Rms longitudinal velocity

Figure 4: Radial evolution at $x=160$ mm.
■, Tracers ; ◇, $d_p = 20\mu m$; ×, $d_p = 60\mu m$

Note that the central jet in region A (fig. 1) is the only dense region of the two-phase flow while the other parts of the flow are very dilute. M_j has however here a strong effect on the whole organisation of the mean flow. The axial evolution of the gas phase velocity in presence of particles is plotted in figure 5. Figure 5a shows that the axial evolution of the air mean axial velocities for $M_j = 0$; 22 % and 110 % differ significantly. One notes in particular that the region of strong velocity decrease is shifted downstream when M_j increases and that no mean stagnation point is found for $M_j = 110$ %. The initial strong longitudinal increase of u'_f and v'_f seems to be delayed after 4 jet diameters at higher mass loading. This is not surprising as the relative motion between the fluctuating velocities of the particles and the fluid provides an additional mechanism for turbulent energy dissipation. Moreover, an estimation of the inter-particle

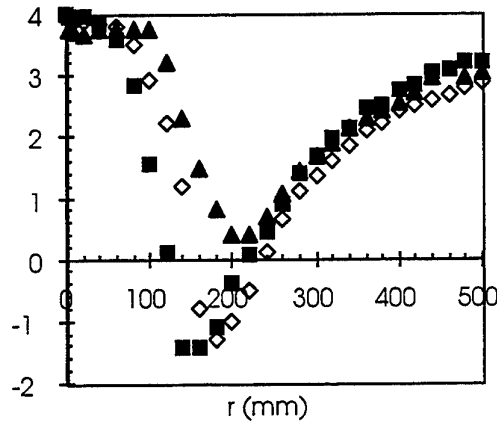


Fig. 5a : Air Mean longitudinal velocity

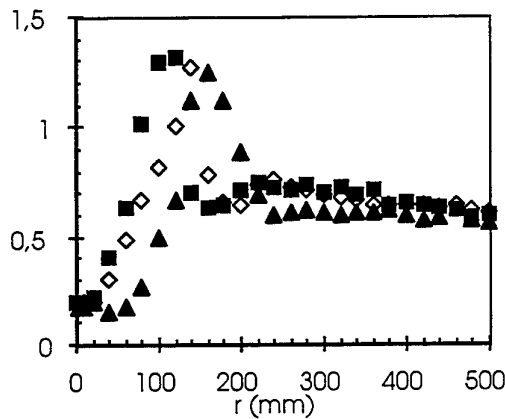


Fig. 5b : Air Rms longitudinal velocity

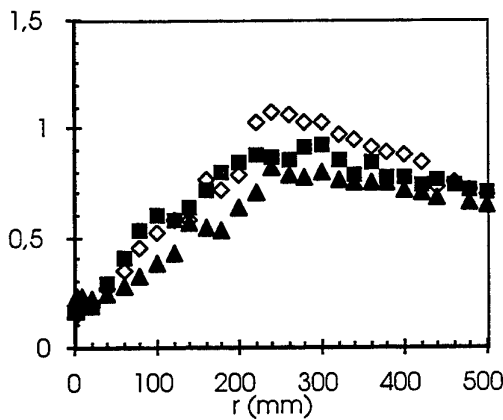


Fig. 5c : Air Rms radial velocity

Figure 5: Longitudinal evolution on the axis. ■, Single phase flow; ◇, Air at $M_j = 22\%$; ▲, Air at $M_j = 110\%$

collision time τ_{coll} (Lavieville et al 1997) for $M_j = 110\%$ leads to $\tau_{coll} \approx 15\text{ms}$. Inter-particle collisions should therefore be important near the jet outlet at the highest loading.

Elsewhere in the flow, the local mass loading becomes very weak as the two streams mix. At first order, the modification of the fluid mean flow in presence of the glass beads will thus be responsible for turbulence modifications. As an example, figure 5b shows that the location of the peak of axial rms velocity is shifted downstream together with the shift of maximum longitudinal gradient of the mean axial velocity (fig. 5a). Radial profiles not shown here would lead to similar observations.

These changes in the flow evolution have important consequences on the distribution of the particulate phase in the flow. Figure 6 presents three (qualitative) pdf of particle size measured on the axis of the flow for $M_j = 22\%$ at respectively $x=10\text{ mm}$, $x=200\text{ mm}$ and $x=320\text{ mm}$. The probability of finding a particle belonging to a given size class at the measurement point displayed in figure 7 was estimated by dividing the number of detected particles of the given size class by the total number of particles detected. This method supposes that the proportion of valid data is the same in each size class. This statement is not true because it is well known that the probability of detection depends on the size class. The presented results are therefore biased toward large particles. No correction is attempted here (Sommerfeld and Qiu 1995) and results are only qualitative.

$x=200\text{ mm}$ is located in the recirculation zone. We see clearly that the probability of detection of particles larger than $60\text{ }\mu\text{m}$ is greater. This is natural if one realises that the particle of largest class should not experience any return flow on the axis. The small particles are therefore dispersed while big ones go straight forward. The situation (not shown here) is very different at $M_j = 110\%$ (Ishima and Boree 1998). The probability of finding larger classes increases regularly when one moves downstream. This is due to the absence of any recirculation on the axis and to radial dispersion of the small classes. Predictions of these distributions by turbulent two-phase flow models are

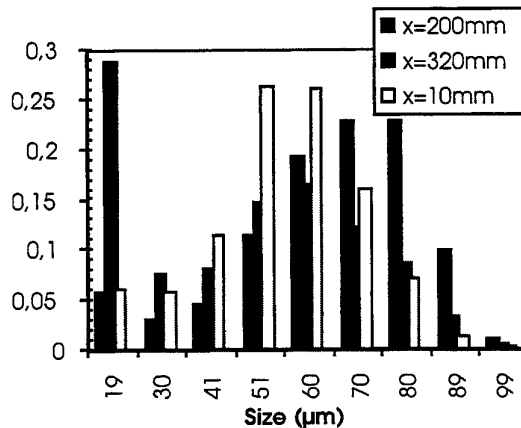


Figure 6: Qualitative pdf of particle size measured along the axis

particularly important in combustion chambers or streams of pulverised solid fuels to ultimately predict accurately the combustion phase.

5. CONCLUSION

An experimental study of two-phase flow behind a confined bluff body has been presented in this paper. This configuration has direct links with typical industrial applications in coal combustion. Such situation is also very interesting for the development of two phase flow turbulent closures.

The initial particle size distribution covers a wide range of size classes from 20 μm to 110 μm with a mean value of 60 μm . Dealing with a polydispersion is possible when phase Doppler measurements are made. A size class analysis was presented. This analysis is necessary for such a wide range of particles time scale. Moreover, contrasted inner jet mass loading ratio M_j ranging from 22 % to 110 % have been selected in order to show the coupling between continuous and discrete phases.

For the chosen ejection velocity of the inner jet, we have shown that three different longitudinal zones can be distinguished in the flow characterised on the axis by respectively a jet flow, a recirculating flow and the establishment of a wake flow. Two stagnation points separate these regions. These stagnation points have different nature described by the sign of the longitudinal rate of deformation. The reaction of the turbulent field is clear : a very high anisotropy is measured and explained on the flow axis.

This study shows particularly well that one has to write and solve transport equations for the fluctuating velocity of the particles and that no local equilibrium with the fluid turbulence can be assumed. Production effects due to either mean axial strain near the stagnation points or more classically to high shear in the initial jet, in the annular shear layer and in the "wake like" flow is clearly observed. The locations of these maxima can be highly dependant of the diameter of the particles when the influence of the inertia is dominant and the polydispersion has to be taken into account. This is expected to be a major difficulty for models, particularly when two-way coupling is significant.

The effect of mass loading was discussed and is clear when one looks at the axial evolution of the mean longitudinal velocities of the fluid in the presence of particles. The region of strong velocity decrease is shifted downstream when M_j increases and no mean stagnation point is found for $M_j = 110$ %. Moreover, the significant initial increase of rms velocities is delayed at $M_j = 110$ %. The mass loading has therefore a global effect on the flow organisation in the wake of the bluff body. By changing the flow organisation, it also modifies the region of turbulence production and the spatial distribution of the particulate phase. A bad prediction of the effects of the mass loading will thus result in a wrong prediction of the whole two-phase flow and eventually of the resulting combustion phase.

This situation is believed to be a severe test case for turbulent two-fluid models. Measurements of fluid/particle correlated motion in relevant part of the flow and comparison with model predictions are presently on their way.

Acknowledgements

We want to express a special acknowledgement for O. Simonin who initiated this research and to G. Balzer who accepted to keep on the long way necessary to obtain reliable experimental results.

REFERENCES

- Berlemont, A., Desjonqueres, P. & Gouesbet, G. 1990 Particle lagrangian simulation in turbulent flows. *Int. J. Multiphase Flow* **16**, 19-34.
- Elgobashi, S.E. & Abou-Arab, T.W. 1983 A two-equation turbulence model for two-phase flows. *Phys. Fluids* **26**, 931-938.
- Fevrier, P. & Simonin, O. 1998 Constitutive relations for fluid-particle velocity correlations in gas-solid turbulent flows. In *Third International Conference on Multiphase Flows, ICMF'98*, Lyon, June 8-12.
- Hardalupas, Y., Taylor, A.K.M.P. & Whitelaw, J.H. 1989 Velocity and particle-flux characteristics of turbulent particle-laden jets. *Proc. R. Soc. Lond. A* **426**, 31-78.
- Hishida, K., Ando, A. & Maeda, M. 1992 Experiments on particle dispersion in a turbulent mixing layer. *Int. J. Multiphase Flow* **18** (2), 181-194.
- Ishima, T. & Boree, J. 1998 *Presentation of a two-phase flow data base obtained on the flow loop Hercule*, IMFT /EEC- 68.
- Ishima, T., Hishida, K. & Maeda, M. 1993 Effects of particle residence time on particle dispersion in a plane mixing layer. *J. Fluids Eng.* **115**, 751-759.
- Kulick, J.D., Fessler, J.R. & Eaton, J.K. 1994 Particle response and turbulence modification in fully developed channel flow. *J. Fluid Mech.* **277**, 109-134.
- Lavieville, J., Simonin, O., Berlemont, A. & Chang, Z. 1997 Validation of inter-particle collision models based on large eddy simulation in gas-solid turbulent homogeneous shear flow. In *ASME FEDSM'97*, June 22-26.
- Modaress, D., Tan, H. & Elgobashi, S.E. 1984 Two-component LDA measurement in a two-phase turbulent jet. *AIAA J.* **22** (5), 624-630.
- Prévost, F., Borée, J., Nuglisch, H.J. & Charnay, G. 1996 Measurements of Fluid/particle correlated motion in the far field of an axisymmetric jet. *Int. J. Multiphase Flow* vol. **22**, n° 4, 685-703.
- Rogers, C.B. & Eaton, J.K. 1991 The effect of small particles on fluid turbulence in a flat-plate, turbulent boundary layer in air. *Phys. Fluids A* **3**(5), 928-937.
- Simonin, O. 1991 Prediction of the dispersed phase turbulence in particle-laden jets. In *Proc. 4th Int. Symp. on gas solid flows, ASME FED*, vol. 121, 197-206.
- Simonin, O., Deutch, E. & Boivin, M. 1995 Large eddy simulation and second moment closure model of particle fluctuating motion in two-phase turbulent shear flows. In *Selected Papers from the Ninth Int. Symp. on Turbulent Shear Flows, Springer-Verlag*, 85-115.
- Sommerfeld, M. & Qiu, H.H. 1995 Particle concentration measurements by phase-doppler anemometry in complex dispersed two-phase flows. *Experiments in fluids* **18**, 187-198.

EXPERIMENTAL ANALYSIS OF SPATIAL AND TEMPORAL TWO-PHASE FLOW STRUCTURES IN A CIRCULATING FLUIDIZED BED USING PARTICLE IMAGE VELOCIMETRY AND PHASE DOPPLER ANEMOMETRY

F. Onofri, L. Tadrist, T. Van den Moortel

IUSTI, UMR CNRS 6595-Université de Provence
Technopôle de Château-Gombert, 5 rue E. Fermi, Marseille 13008, France
Email : Onofri@iusti.univ-mrs.fr, Fax : (33) 4 91 10 69 69

ABSTRACT

The gas-solid flow structure in the riser of a cold laboratory scale fluidized bed reactor has been investigated. Phase Doppler Anemometry is used to provide local information highly resolved in time and space. A Particle Image Velocimetry system has been developed to investigate the spatial flow structures and to obtain a better understanding of the related information obtained from PDA time series and pressure fluctuations in the flow. A review is made on the new possibility offers by this system to investigate mechanisms induce by gas bubbles on the solid phase heterogeneity

1. INTRODUCTION

Thermal power stations using a Circulating Fluidized Bed (CFB) furnace have attracted much attention since the 1970s and 1980s due to their excellent heat and mass transfer properties and because they permit controlled transfer of solids into, out of, and within the system. Their relatively low temperature operation (840 to 890°C), which limits NO_x formation, and their capability of neutralizing of sulfur oxide emissions by calcaire calcination, make them efficient for environmental requirements too. Basically, one of the main properties of the fluidization process, which make it absolutely essential for processes requiring a high conversion and close control of temperature is the high solids to gas contacting surface obtained, which is itself closely connected to local concentration homogeneity in solids. In spite of this idealistic description of the gas-solid flow characteristics in CFB the existence of a segregated gas/solid two-phase flow structure is now well accepted for the upper dilute region. The mezzoscale structures can be described as clusters and strands of higher solid volume concentrations suspended in continuous suspension phase of low density, where the particle clustering seems to have significant influence on the gas-solid momentum transfer and on development of macroscopic flow structures including the core-annulus flow, (Horio 1997). It probably has a lot of influence on chemical processes and thus on gas pollutant formation too.

Nevertheless, very few reliable data are found in the literature on cluster formation mechanisms and interaction with the gas flow, although there is a growing interest in these mechanisms from a practical and theoretical point of view. Experimentally, a variety of measuring techniques for CFB local flow analysis, such pressure, capacitance or fiber-optical probe systems have been extensively used. Laser Doppler Anemometry or Phase Doppler Anemometry has also been used for mean velocity or flux profile measurements. Nevertheless, although these techniques provide useful statistical data on some local flow characteristics, they do not allow non-stationary physical phenomenon (in space and time) to be understood.

The present paper reports on the experimental setup developed and the preliminary results obtained on the study of gas-solid flow structures in LFCs and more particularly, particle cluster formation mechanisms, with an approach combining a local and a spatial analysis. Local and time resolved analysis is performed with a Phase Doppler Anemometer (PDA), giving access to the particles velocity, size, and mass flux. The spatial analysis of flow structures is based on a Tomographic and Particle image Velocimetry (PIV) system, giving access to spatial solid distributions, and 2D velocity. Note that PIV is applied here, for the first time as known by the authors, to the study of the hydrodynamics of CFB. Static and dynamical pressure measurements, which are classically used in industrial processes, have also been used for comparison with optical techniques.

2. EXPERIMENTAL SETUP

2.1 Fluidization loop

Experimental studies have been carried out on a laboratory scale cold circulating fluidized bed with a height of 2 meters (=H) and a cross section of 0.2*0.2 (=L*L), see Figure 1. A pump located at the outlet of the cyclone sucks the air (ambient temperature, humidity and pressure) through layers of closely-packed glass beads 200 mm thick. Two grids are placed immediately above the layers of packed beads. The first one, with circular

holes 3 mm in diameter, it has a 30% clear aperture and is used to supply a uniform plug flow of gas in the riser even when there are no particles in the riser. The second one is a square grid plate with a 40 μm opening which is used to retain the particles in the riser. Various superficial gas velocity conditions (U_f , between 0 to 1.5 m/s) can be considered. Fluidized particles are glass beads, with known size distribution, and different mean diameters from 60 to 250 μm for a total solid hold-up down to 3 % in volume. With increasing superficial gas velocity the bed evolves from a dense bed to bubbling, slugging, turbulent and circulating bed, with an increasing concentration of particles in suspension. Particles that go out from the risers are separated from the gas flow by a cyclone and recycled via a recirculation loop and reintroduced at the basis of the riser. The pump releases the air into the atmosphere. The superficial gas velocity is measured at the pump outlet, see Catthiew (1994).

2.2 Optical setup

Phase Doppler Anemometry, PDA system

The PDA is a one component system based on a 10mW He-Ne laser, from Aerometrics Inc. A classical forward scattering collection angle of 30° was used, with a trans-

mitting and collection optics focal lens of 500mm. The probe volume size versus particle diameter is set to 3, when possible, which is the minimum to limit Trajectory Effects (TE) with a classical Phase Doppler geometry, see Gréhan et al. 1996, Onofri 1995. The transmitting and receiving optics were mounted on a motor driven table such that the probe volume could be accurately moved in all three orthogonal directions. The starting data acquisition control is controlled either from software or from an external trigger event.

Tomographic, Particle Imaging Velocimetry, PIV system

A PIV system that operate in two ways has been fully developed. One with video frequency acquisition of large fields, see Figure 2, and the other one, for high speed acquisitions but with severely limited field resolution, see Figure 3.

(1) The video frequency acquisition Tomographic/PIV system is based on a double pulse Laser YAG, from Quantel, giving 140mJ per pulse with a 25 Hz repetition rate. The laser beam output is directed to the riser with a periscopic translating system. Three cylindrical high power lenses are used to produce a laser sheet of a thickness of 1.5 mm at the measurement location, and

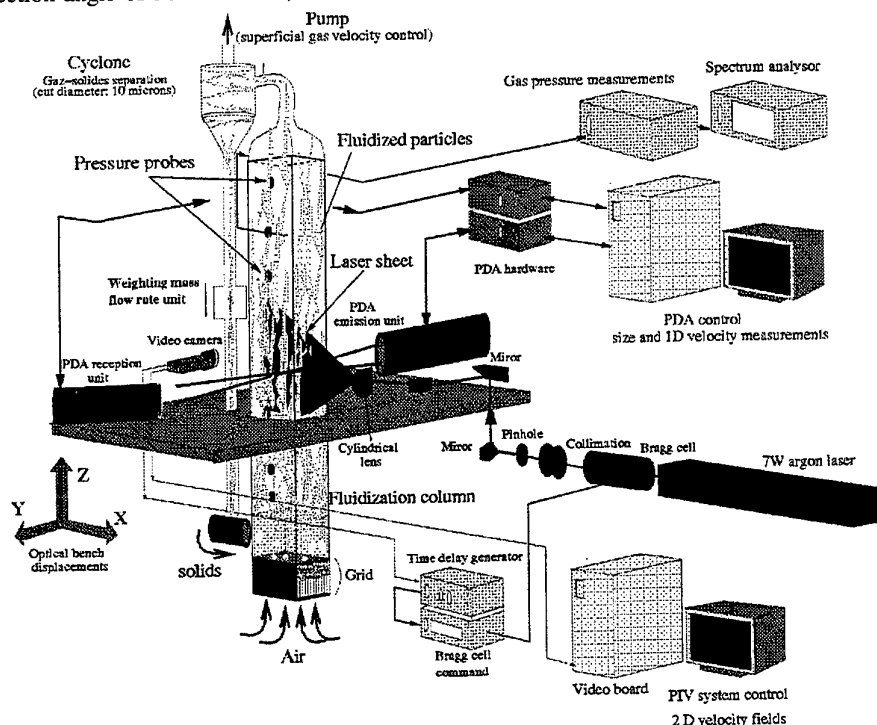


Figure 1 Experimental setup: the glass column of the fluidized bed is 2 meters high ($=H$) and has a 0.2×0.2 cross section ($=D \times D$). Fluidized particles are glass beads of known size. A phase Doppler system, a Particle Image Velocimetry and pressure probe system mounted on a motorized optical bench are used for the hydrodynamics studies. The axial velocity component is along the Z axis, and the transverse velocity component measured with PIV is along the X axis.

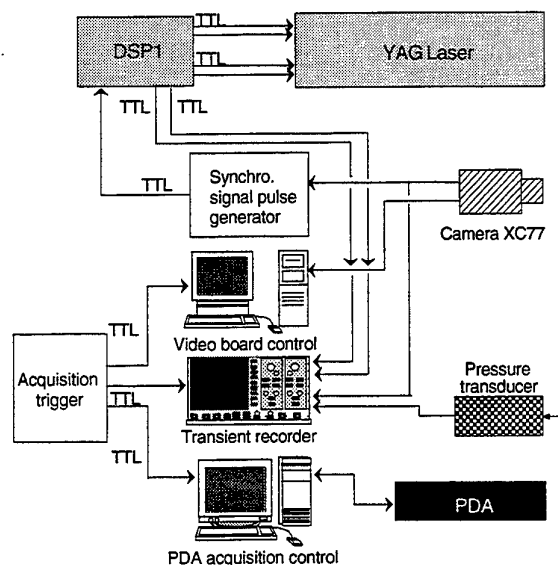


Figure 3 Experimental setup for PIV system working at high frequency acquisition rate.

with a 30° cone angle. The periscopic system has been designed to obtain a laser sheet that can be moved with the motorized table without significant modifications of its characteristics. The imaging system is constituted by a XC77 camera from Sony, operating in FIELD integrating and interlaced mode (the processing algorithm use an intercorelation scheme). The output signal parity of the FIELD mode is directed to special electronics that have been developed to produce one or two trigger pulse with controlled delay and duration. One of these pulses is used to trigger the laser control panel (DSP1) which generates four TTL signals, with controlled delay, to trigger the laser flash lamps and control quenching. The TTL output of the flashes lamps are registered on a transient recorder for further verification of synchronization delays. The analog video output signal is directed to an imaging board, Pulsar L.C. from Matrox. Over 250 images, with a size of 752×572 pixels, can be registered at video frequency, which corresponds to a sequence of 10 seconds. The video board can be synchronized with an external TTL signal. So a simple electronics system has been developed to send a common synchronization signal to the imaging board, the PDA processing module and the transient recorder on which TTL signals and the signal of gas pressure fluctuations in the bed are directed.

(2) The high frequency acquisition PIV system is based on a 7W argon laser. The synchronization signal pulse generator is used here to generate two signals in TTL format. These signals are used to trigger the control electronic of a Bragg's cells that is used as an optical gate. The Bragg's cell, on the laser beam output, is used to pro-

duce the required two pulses with finite duration and delay. With this system the flashing of the laser sheet has almost no limit in high or low frequency. The camera used here is an M30, from JAI. It enables a FIELD integration mode with frequency up to 180/360 images per second. Unfortunately, in such a case the image resolution is limited to $752 \times 120/66$ pixels.

For both acquisition systems, images are processed on PC with user-friendly windows based software that has been developed under the DELPHI environment. The software provide raw data analysis as well as statistical data and histograms such as those presented in Figure 8.

3. EXPERIMENTAL RESULTS AND DISCUSSIONS

3.1 Flow regime under study

Different ways are use to characterize the global fluidization regime. In Figure 4, the evolution of the pressure fluctuation and mean pressure in the riser is plotted versus the superficial gas velocity. Pressure is measured at a middle position in the riser: $Z/H=0.385$, $X/H=Y/H=0.5$ and for $60 \pm 9 \mu\text{m}$ glass beads. Classically an increase in the pressure fluctuation amplitude with the superficial gas velocity is first observed, it afterwards reaches a plateau and suddenly drops out. Yerushalmi (1986), Kunni et al (1995), characterize this transition in terms of two velocities. u_{c1} at which the pressure fluctuations and the bed heterogeneity are maximum, and, u_{c2} at which the pressure fluctuations level off, and which mark the onset of the turbulent regime. Figure 5 presents the evolution of the global solid mass flux recirculation, G_s , with superficial gas velocity. The sharp increase in the solid mass flux marks the circulating regime, Lounge (1997). In the pres-

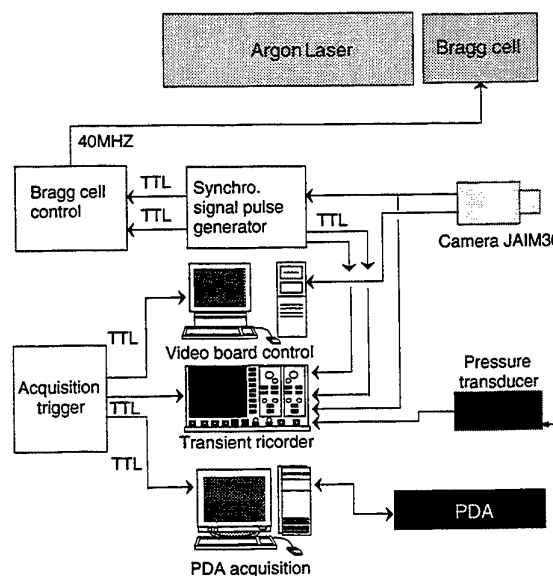


Figure 2 Experimental setup for PIV system working at video frequency and high resolution.

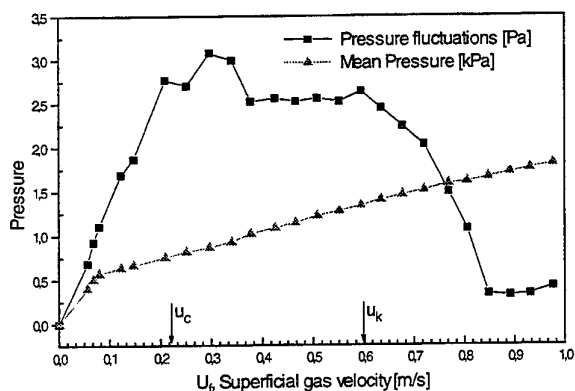


Figure 4 Evolution of the mean pressure and its fluctuations with the superficial gas velocity. Pressure was measured at a middle position in the riser: $Z/H=0.385$, $X/H=Y/H=0.5$ and for $60\ \mu\text{m}$ glass beads. Evolution of the solid flux G_s is also reported.

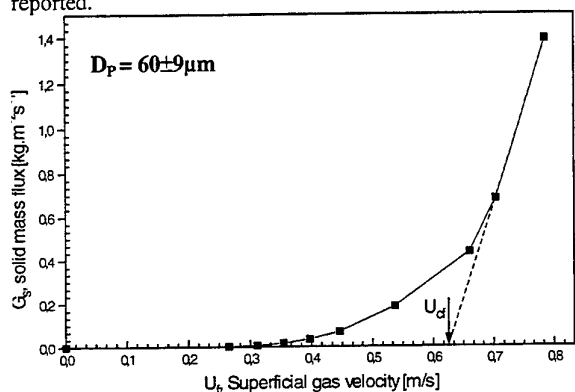


Figure 5 Evolution of the global solids mass flux with the superficial gas velocity.

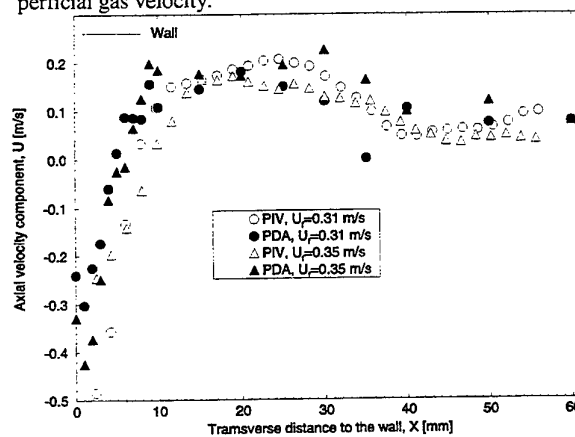


Figure 6 Axial velocity profile obtained with PIV and PDA for fluidized glass beads of $60\ \mu\text{m}$ mean diameter, with $Z/H=0.385$, $Y/H=0.5$, $X/D=0.7..1$.

ent study, for the $60\ \mu\text{m}$ particles and measurement riser center, it has been observed that for a middle height in the riser, PDA and PIV measurements were almost not possible for a superficial gas velocity above 0.35 to 0.45 m/s, due to beam attenuation and multiple scattering effects

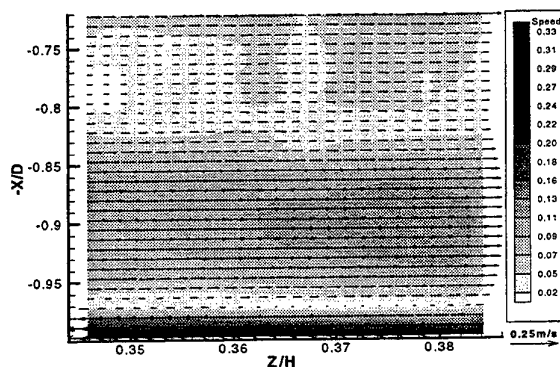


Figure 7 Mean velocity vectors map corresponding to case for $U_g=0.35\ \text{m/s}$ in figure 6.

(which corresponds to an average local mean volume concentration in particles below of 0.1%). Thus our results report here on regimes down to the turbulent off set regime.

3.2 Velocity profiles

Figure 6, shows the evolution of the axial velocity component, U , versus the normalized radial distance X/D , for different superficial gas velocities, according to PDA and PIV. PDA statistics are performed over 5000 validated particles. PIV profiles have been calculated by averaging 250 velocity vectors maps measured every second in order to decrease the sensitivity of the mean velocity profile to a particular temporal structure in the bed. Good agreement is found between PDA and PIV predictions, except near the wall ($X/D=1$). This slight discrepancy may be attributed to the large window size used to perform the image

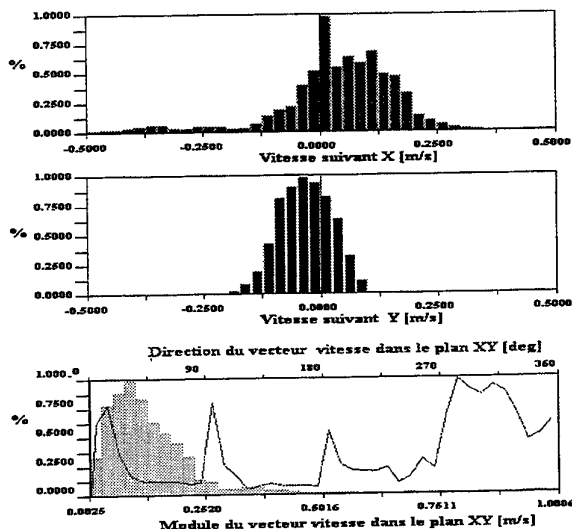


Figure 8 From up to down we found: the number fraction of vectors per class versus the axial and transverse velocity component, vectors angular orientation and speed, for an instantaneous measurement (Figure 9 (c)) and parameters corresponding to Figure 7.

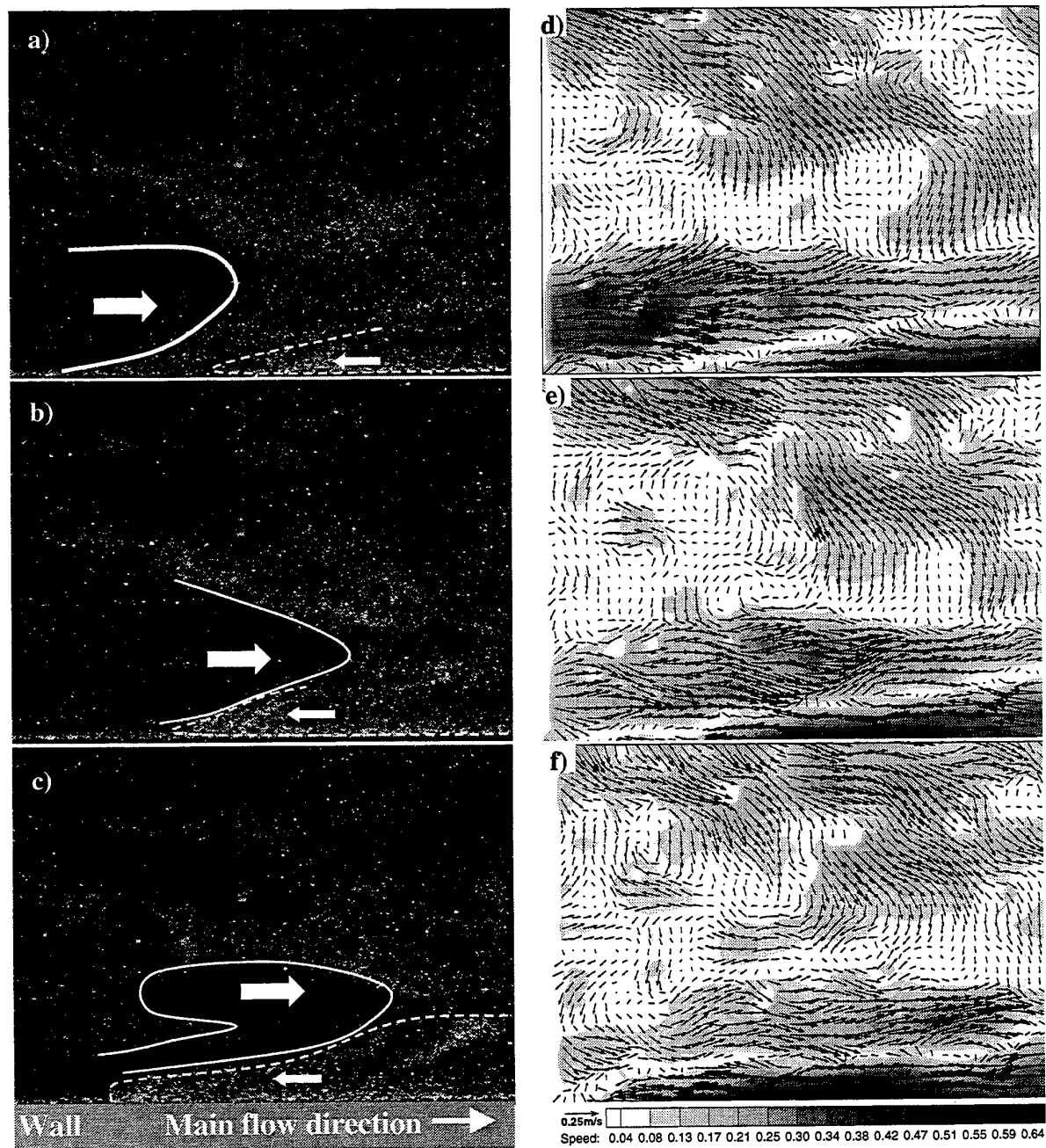


Figure 9 Tomographic sequence of a gas bubbles moving up in the riser and interacting with a cluster of particles moving down at the wall. The corresponding 2D vectors maps obtain with PIV are plotted on the right side. The images are successively delayed in time of 40ms. The fields dimension and location is 83*63 mm and $Z/H=0.385$, $X/L=0.69...1$, $Y/L=0.5$, $U_F=0.35\text{m/s}$.

intercorrelation (32*32 pixels # 3*3mm) which tends to smooth the sharp intensity profile in this region.

From the previous figure one may notice the unusual shape for the velocity profiles, which deviates significantly from the parabolic shape reported for higher superficial gas velocity by Azario et al (1995) that is commonly

reported in the literature for solid velocity profiles in CFB. A maximum in the velocity profiles is observed for typically $X/D=0.9$; it increases with the superficial gas velocity. Van den Moortel (1998) has shown that this behavior is amplified with height in the riser too.

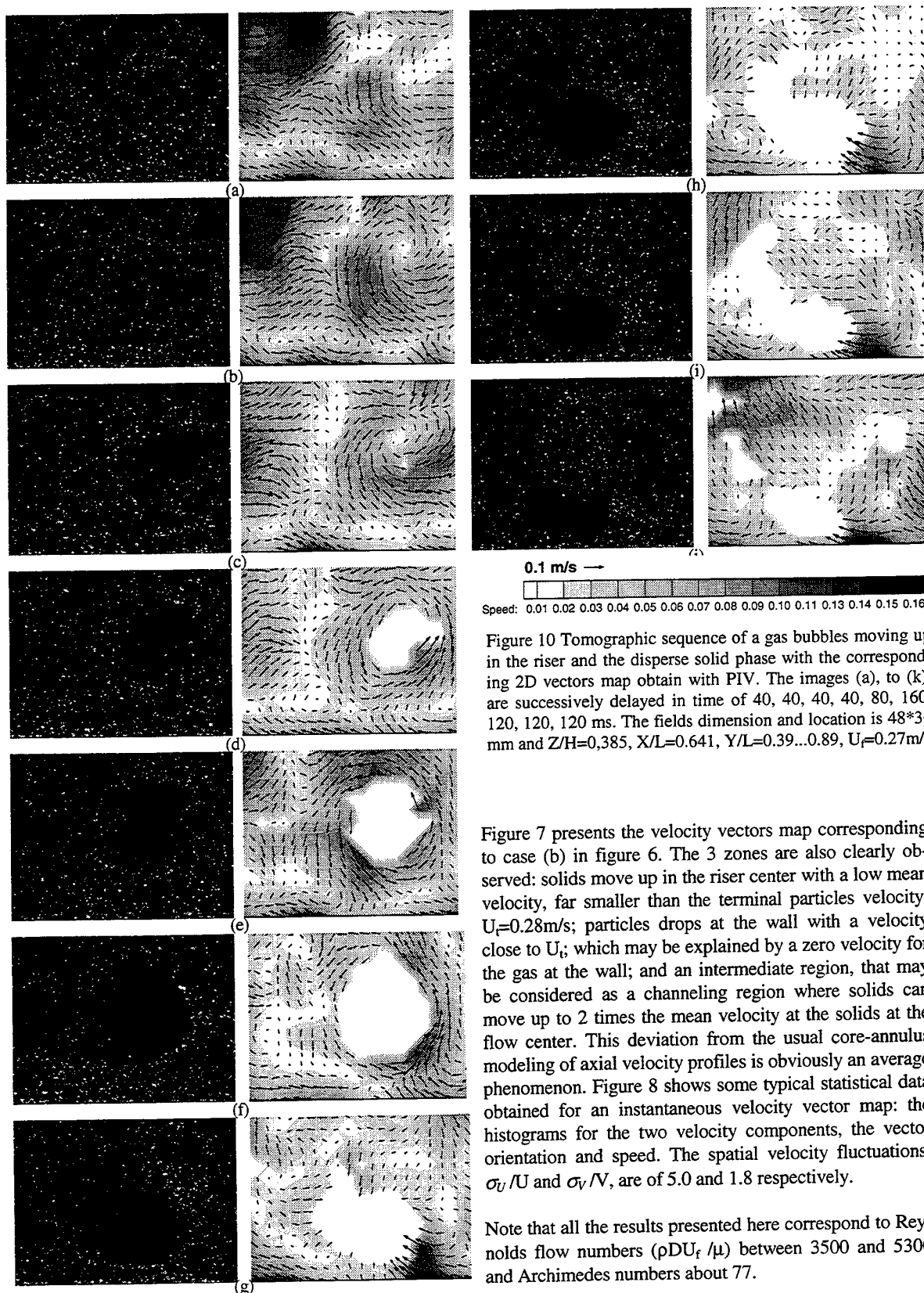


Figure 10 Tomographic sequence of a gas bubbles moving up in the riser and the disperse solid phase with the corresponding 2D vectors map obtain with PIV. The images (a), to (k), are successively delayed in time of 40, 40, 40, 40, 80, 160, 120, 120, 120 ms. The fields dimension and location is 48×36 mm and $Z/H=0,385$, $X/L=0,641$, $Y/L=0,39...0,89$, $U_r=0,27$ m/s

Figure 7 presents the velocity vectors map corresponding to case (b) in figure 6. The 3 zones are also clearly observed: solids move up in the riser center with a low mean velocity, far smaller than the terminal particles velocity, $U_t=0,28$ m/s; particles drops at the wall with a velocity close to U_t ; which may be explained by a zero velocity for the gas at the wall; and an intermediate region, that may be considered as a channeling region where solids can move up to 2 times the mean velocity at the solids at the flow center. This deviation from the usual core-annulus modeling of axial velocity profiles is obviously an average phenomenon. Figure 8 shows some typical statistical data obtained for an instantaneous velocity vector map: the histograms for the two velocity components, the vector orientation and speed. The spatial velocity fluctuations, σ_u/U and σ_v/V , are of 5.0 and 1.8 respectively.

Note that all the results presented here correspond to Reynolds flow numbers ($\rho D U_f / \mu$) between 3500 and 5300 and Archimedes numbers about 77.

3.3 Review of some mechanisms induced by gas bubbles on the solid phase heterogeneity

Figure 9 presents a sequence of 3 tomographic images of the solid phase distribution in the laser sheet with dimensions 83*63 mm and location: $Z/H=0.385$, $X/L=0.81\dots 1$, $Y/L=0.5$. The superficial gas velocity is of $U_f=0.35\text{ m/s}$. In these images and the related 2D velocity fields, two basic phenomena are observed: a gas bubble moving up in the riser near the wall and its interaction with a particle cluster falling at the wall. In these images, bubbles are identified as regions of low concentration in particles (dark regions) and clusters as unlighted regions. Note that the image contrast has slightly increased to obtain a better visual understanding of the flow structure. So, nominally, dark regions contain few particles. We may note several things:

- The few particles inside the bubble have an axial velocity far higher than the superficial gas velocity (about 2 times), and about 10 times higher than the mean solid velocity.

- The cluster at the wall moves in an opposite direction to the gas bubble with a velocity magnitude of the same order.

- The cluster and the bubble flows are separated by a region of zero slip velocity that is clearly shown in (d) for instance.

- Comparisons between the velocity vector map and tomographic images show that the burst of velocity corresponding to the bubble seems to propagate, through the dispersed particles in front of the bubble, and to be channeled (and may be accelerated) by the cluster at the wall and the gas-particle flow coming from the center of the riser.

- The rear of the bubble is not as well defined as its front part. Nevertheless the velocity vector map (f) shows that this region seems to correspond to a region of vortices and afterwards of low velocity.

Figure 10 shows the sequence of horizontal tomographies of a gas bubble moving up in the riser and the disperse solid phase for a lower superficial gas velocity than in figure 9. The total sequence duration is of 0.64 s. The field dimension and location in the riser is defined by: 48*36 mm, $Z/H=0.385$, $X/L=0.64\dots 1$, $Y/L=0.39\dots 0.89$. Note that the camera was fixed at a 60° off-axis angle from the laser sheet plane. The camera objective aperture f/D ratio was set to 16 to increase the depth of view and to limit image distortion. This sequence clearly shows the effect of gas bubbles coming from the dense parts of the bed on solids heterogeneity:

- In figure (a) the solid phase is homogeneously distributed in the laser sheet.

- In figure (b) and (c) the particles flow start to spin before the appearance of the gas bubbles (i.e. an empty zone of particles).

- The bubble centrifuge the particles and thus induce a hole (negligible volume fraction) in the disperse solid phase. From figure (e) the angular rotation velocity of the first ring of particles is estimated to be about 1 and 1.5 Hz.

- In figure (f) to (g) the bubble comes near the wall. Its frontier becomes more blurred. It may be thought that this sequence corresponds to the rear of the bubble, as in figure 9 (d).

Figure 11 focuses on the possible comparison that can be made on time series obtained with the PDA system, a pressure probe and tomographic images of the spatial solids distribution. The PDA time series corresponds to the inter particle time delay and the pressure time series, to pressure fluctuations. PDA measurements were performed 5 mm below the pressure probe orifice. Bubbles are clearly identified from the PDA series by a window of low data acquisition and large inter particle time delays whereas, no obvious correlation has been observed with the pressure signal. The power spectrum of pressure fluctuations, not reported here, shows a maximum with a large frequency bandwidth around 3 Hz, which corresponds to a typical frequency observed for dense bed oscillations. This emphasizes the assumption that the pressure measured here is probably not a local pressure fluctuation induced by bubbles but one which comes from the dense and lower part of the bed and which propagates along the riser.

4. CONCLUSION

Particle Imaging Velocimetry (PIV) has for the first time been applied here to the study of the hydrodynamics of the gas-solid flow in a circulating fluidized bed. It has been shown that PIV gives reliable velocity profiles and spatial velocity fluctuations of the solid phase by comparing results obtained with a one component Phase Doppler Anemometer. PIV appears to be more limited in particle concentrations than PDA, limiting flow regime investigations below the turbulent fluidization regime for intermediate positions in the riser. For the considered flow regimes, a severe deviation of the solid velocity profiles from the core-annulus model has been reported.

Qualitative comparisons of tomographic images with PDA time series have been used to evaluate the possibility of obtaining reliable statistics on bubbles and particle clusters and thus to better understand fundamental mechanisms of the formation of heterogeneity in the disperse solid phase.

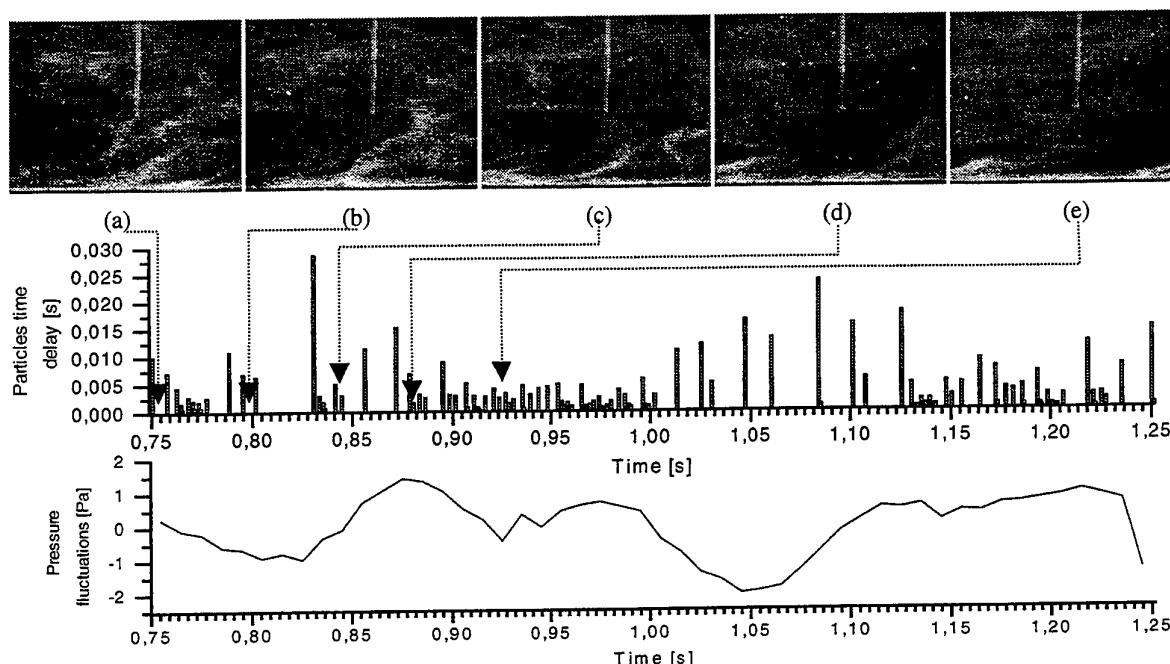


Figure 11 Tomographic sequence on a gas bubble moving up in the riser, the corresponding inter arrival particles time series obtain from the PDA system, and the pressure fluctuations. The images dimension and location are 83×63 mm and $Z/H=0.385$, $X/L=0.81 \dots 1$, $Y/L=0.5$, $U_r=0.35$ m/s.

5. ACKNOWLEDGMENTS

The authors are grateful to the CNIM Co., Environmental Department (La Seyne-sur-Mer, France) and the Région Provence-Alpes-Côtes d'Azur for providing partial financial support for this work and to Roland Faure, for the building of the synchronization box.

6. REFERENCES

- Azario E., Tadrist L., Pantaloni J., Cathieuw P., Velocity analysis of solids phase in circulating fluidized bed using phase Doppler analyser, *Fluidisation XIII*, Tours, France, 1995.
- Cattieuw P., Etude expérimentale des écoulements gaz particules dans un lit fluidisé circulant. PhD thesis. Université de Provence, France, 1992.
- Horio M., *Hydrodynamics, in Circulating Fluidized Beds*, Grace J.R., Avidian A.A. and Knowlton T.M. (Edts), Blackie Academic & professional Press, London 1997, pp21-85.
- Lounge M., *Experimental Techniques, in Circulating Fluidized Beds*, Grace J.R., Avidian A.A. and Knowlton T.M. (Edts), Blackie Academic & professional Press, London 1997, pp312-358.
- Yerushalmi J., *High velocity fluidized beds, in Gas Fluidization technology*, chapter 7, Ed. Geldart D., John & Willey sons, 1986.
- Kunni D. and Levenspiel O., *Fluidization Engineering*, Butterworth-Heinemann (ed.), Stoneham MA, 1991.
- Onofri F., Prise en compte de la dimension finie des faisceaux d'éclairage en granulométrie optique: anémométrie phase Doppler- Diagnostics des écoulements diphasiques, PhD thesis, Université de Rouen, France, Nov. 1995.
- Onofri F., Développement d'une chaîne de Vélométrie par Images de Particules, Applications aux Lits Fluidisés Circulants, Internal report, UMR CNRS 6595-IUSTI, Août 1997.
- Sankar S.V., Inenaga A. and Bachalo W.D., Trajectory dependent scattering in Phase Doppler interferometry: minimizing and eliminating sizing error, *6th Int. Symposium on Application of laser techniques to fluid mechanics*, Lisbon, Portugal, July 20-23, paper 12.2, 1992.
- Van den Moortel, Analyse locale et ponctuelle des écoulements gas-particules dans un lit fluidisé circulant : étude expérimentale et modélisation de la formation des amas, Université de Provence, France, PDA thesis that will be defended in Oct, 1998.

INVESTIGATION OF A PARTICLE LADEN WAKE FLOW BY MEANS OF PARTICLE IMAGE VELOCIMETRY

T.J. Möller and K.A. Bütetfisch

German Aerospace Center - DLR, Institut für Strömungsmechanik, Bunsenstrasse 10, D-37073 Göttingen, Germany

ABSTRACT

The flow of particles in the wake of a bluff body has been studied experimentally by means of particle image velocimetry (PIV) to improve the understanding of complex turbulent particle laden flows. Hence it was possible to obtain the instantaneous velocity field of the dispersed phase. To achieve knowledge of the influence of the Stokes-Number St on the particle flow the particle diameter has been varied. Also different Reynolds-Numbers of the mean flow, i.e. mean velocities have been utilised in this investigation. Since the particle/fluid density ration has been chosen high, possible effects due to gravity should be noticeable in the experiments.

1. INTRODUCTION

The motion of particles in turbulent flows is of interest in many fields of technical applications ranging from combustion and environmental processes to process engineering. Therefore many experimental and theoretical publications have covered the field in the past. A recent survey on the numerical aspects of particle motion in turbulent flows is given by Elghobashi (1994). Snyder and Lumley (1971) and Wells and Stock (1983) studied experimentally the motion of particles in a grid generated simple turbulent flow. In both studies Laser Doppler Velocimetry (LDV) has been used to determine the particle velocity and particle dispersion. Investigations of turbulent wakes generated by the flow of particles past objects in opposite are rarely found in the literature. Tang et al.

(1992) presented a numerical study of particle dispersion the wake flow of a bluff body. Stock (1996) noticed in his survey the need for experimental studies of particles motion in wake flows. An example for the technical significance of this type of particle laden flows in environmental processes is presented by Horlbeck et al. (1995).

The purpose of this paper is to show the influence of particle inertia and velocity on the resulting particle flow, i.e. the effect of Stokes- and Reynolds-number. The present paper demonstrates the application of PIV to particle laden flow. From the PIV data the influence of particle initial velocity and particle diameter on the flow of particles in the wake of a bluff body is determined. Furthermore from the velocity data possible effects of gravity on the particle flow can be observed. First results of the presented investigation are reported by Möller et al. (1997).

2. PARTICLE MOTION

The behaviour of particles in a gas flow is governed by particle inertia and the interaction with the turbulent fluid surrounding it. Consider a small diameter in the range of μm , rigid, spherical particle the inertia of such a particle can be characterised by its aerodynamic particle response time τ_p . It is defined for a particle with radius r_p as:

$$\tau_p = \frac{2}{9} \frac{r_p^2 \rho_p}{\nu \rho_f}$$

Where ρ_p denotes the particle density, the ρ_f fluid density, the r particle radius and ν the fluid viscosity. This expression can be interpreted as the time needed for the particle to react to fluctuations of velocity of the continuous phase. The above definition is based on flow in the Stokes regime. A corresponding fluid time scale τ_f for this problem can be defined by a typical lengthscale L and the fluid mean velocity U_f . This yields to $\tau_f = L / U_f$. The ratio of these time scales then defines the Stokes number St :

$$St = \frac{U_f \tau_p}{L}$$

The particle Reynolds number Re_p is defined as:

$$Re_p = \frac{2r_p |\vec{U}_p|}{\nu}$$

where U_p is the velocity of the particle. In the experiments presented in this paper the Stokes-number has been varied between 0.1 and 19 and the particle Reynolds-number between 0.5 and 10.5.

The influence of gravity on the particle flow can be characterised by the so called drift velocity u_d which is defined as:

$$u_d = g \tau_p$$

here g denotes the acceleration due to gravity.

3. EXPERIMENTAL SET-UP

3.1 Wind tunnel

The present experiments were carried out at a low speed windtunnel of the DLR Göttingen (s. fig. 1). The test section of this wind tunnel has a cross-section of $30 \times 30 \text{ cm}^2$. In the present investigation flow velocities between 2.5 m/s and 4.5 m/s have been employed. The flow can be observed through glass windows which are the side walls of the wind tunnel in the region of the test section.

Different turbulence grids can be installed near the end of the nozzle of the windtunnel in order to generate turbulence. The results presented in this paper have been obtained employing a grid with 23.5 mm mesh

size and a rod diameter of 2.5 mm. The distance between observation area and the grid was 560 rod diameters. Hot wire measurements give a turbulence intensity of 3.5% measured in the area of the PIV plane. These measurements have been performed to make sure the turbulent properties and the absolute value of velocity of the continuous flow is distributed homogeneously within the PIV plane.

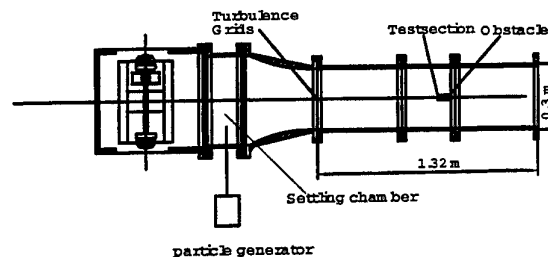


Figure 1 Schematic view of the windtunnel

In the testsection of the windtunnel a rectangular obstacle has been mounted. The dimension of this obstacle are 0.1 m in (x)-direction, 0.3 m in y-direction and 0.01 m in z-direction (D is the body thickness) yielding a blockage of 3.3 percent. Figure 3 shows the set-up and the here used co-ordinate system. The obstacle has been installed 840 mm downstream of the turbulence grids.

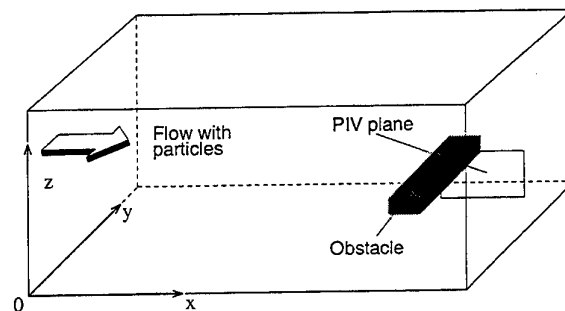


Figure 2 co-ordinate system and sketch of testsection

3.2 Particles

The particles employed in this study are siliciumcarbid (SiC) particles, which density is 3210 kg/m³. This means a ratio of particle density ρ_p to fluid density ρ_f of 2666.

table 1: parameter of the investigated particles

d_p [μm]	τ_p [10^{-3} ms]	u_d [m/s]
3	0.089	$8.7 \cdot 10^{-4}$
8	0.63	$6.2 \cdot 10^{-3}$
30	8.9	$8.7 \cdot 10^{-2}$

Where d_p denotes the particle diameter. The flow was seeded with this particles in the settling chamber upstream of the screens used to reduce the turbulence of the windtunnel. Table 1 shows the important parameters of the particles used in the present paper.

By a numerical calculation it has been estimated the 3 μm particles follow velocity fluctuations of the continuous flow in the investigated flow region comparable to 1 μm particles within the scope of the resolution of the applied measurement system. Hence the flow field of the 3 μm particles represent also the flow field of the continuous phase. Therefore it is possible to make sure, the result for different particle diameters are effected by the particle properties and not influences by the continuous flow. To calculate the trajectory of an individual particle the following instantaneous particle equations have to be solved numerically:

$$\frac{d\vec{U}_p}{dt} = \frac{[\vec{U}_f(y(t), y) - \vec{U}_p]c_d}{\tau} - g\delta_{i3}$$

$$\frac{d\vec{x}}{dt} = \vec{U}_p$$

Where δ denotes the Kronecker symbol and c_d is an empirical non-Stokesian correlation for the drag factor, which is given by:

$$c_d = \frac{24}{\text{Re}_p} (1 + 0.15 \text{Re}_p^{0.687})$$

The necessary data of the flow field has been obtained using the ResCUE code [s. Skalicky (1994)]. The calculation has been performed for particles with 1 μm and 3 μm diameter and yield to the above described results. Details about this calculations is reported by Möller (1996).

3.3. PIV set-up

To determine the velocity of the particles the DLR particle-image-velocimetry (PIV) system has been employed. A detailed description of this system is given by Raffel et al. (1998). Figure 2 shows the optical set-up used in the experiments. The particle flow is illuminated by a Nd:YAG Laser with a pulse length of 20 ns and energy of 70 mJ per pulse. The scattered light is then recorded photographically and Kodak T-MAX film is employed for the presented experiments. The size of the PIV plane was 5 by 7.5 cm. To improve focussing of the PIV image in the film plane a CCD chip is installed in the camera. Details of this technique are reported by Raffel (1993).

Analysis of the PIV images was performed by digitising each film negative with a high-resolution scanner at 2700 dpi. The displacements vectors were computed by local cross-correlation of the two interrogation windows of the PIV recording, as described by Willert (1996). The interrogation window size was 64 x 64 pixel. Hence a 102 x 78 vector field was created for each PIV image.

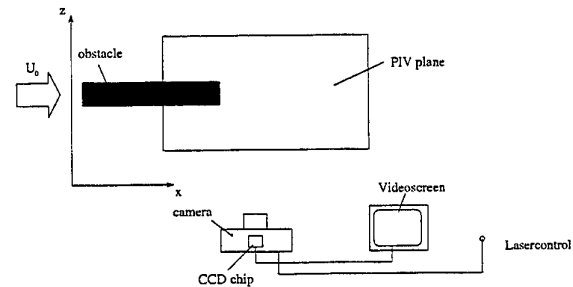


Figure 3 Experimental set-up for piv recording

4. RESULTS

A typical PIV result for an instantaneous flow field is displayed in fig. 4. Here the flow field of a flow

with particles with $3\ \mu\text{m}$ diameter and a mean velocity of $2.5\ \text{m/s}$. In order to enhance the visibility of spatial structures in the flow field the mean flow velocity U_0 has been subtracted from the u -component in fig. 4. Fig. 5 shows a flow field averaged over 20 single PIV results. From such averaged data the following results have been obtained.

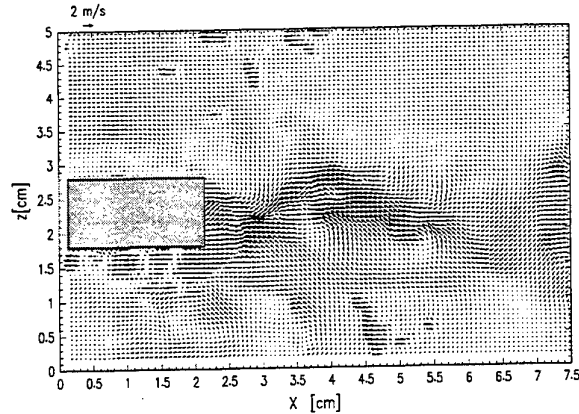


Figure 4: instantaneous flow field for $d_p = 3\ \mu\text{m}$ and $u_0 = 2.5\ \text{m/s}$.

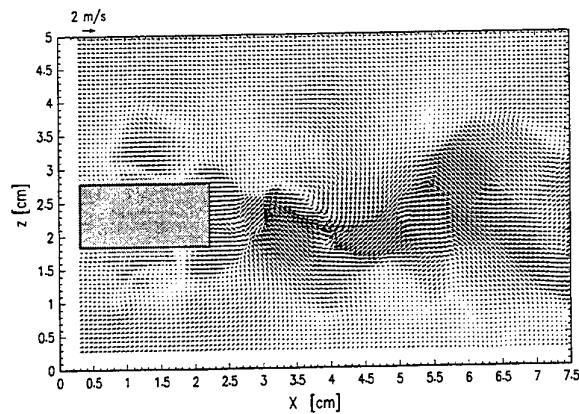


Figure 5: flow field averaged over 20 single PIV results, $d_p = 3\ \mu\text{m}$, $u_0 = 2.5\ \text{m/s}$.

From the PIV data velocity profiles for the position $x/D = 5$ have been determined. Where D is the obstacle thickness, which is 0.01m for all presented results. Fig. 6-8 show the development of the u -

component of the particle velocity across the PIV measuring plane. The black rectangle within the figures symbolises the bluff body.

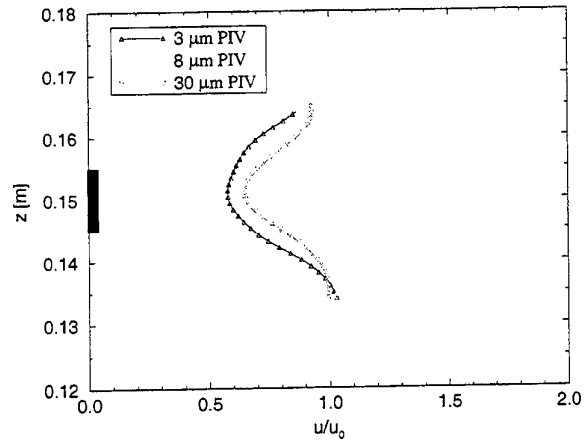


Figure 6: velocity profile for $u_0 = 2.5\ \text{m/s}$ and $x/D = 5$.

In the case of $u_0 = 2.5\ \text{m/s}$ (s. fig. 6) the minimum velocity u_{\min} in the velocity profile differs only slightly for 3 and $8\ \mu\text{m}$ particles. In opposite for $30\ \mu\text{m}$ the velocity decay is significantly smaller. This could be explained by the larger particle response time τ_p of the $30\ \mu\text{m}$ diameter particles.

Fig 7 shows the data for $u_0 = 3.8\ \text{m/s}$. Here for all three investigated particle diameters the value of u_{\min} is clearly different. The obvious asymmetry of the velocity profile of $30\ \mu\text{m}$ particles is maybe due to gravity.

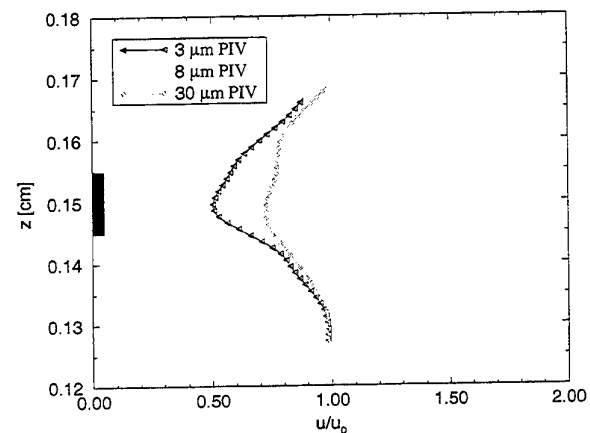


Figure 7: velocity profile for $u_0 = 3.8\ \text{m/s}$ and $x/D = 5$.

In the case $u_0 = 4.5$ m/s which is presented in fig 8 the velocity profiles for the different particle diameters differ clearly. A comparison of u_{\min} for this flow velocity with the values of u_{\min} in the case of $u_0=3.8$ m/s shows the values do not differ significantly.

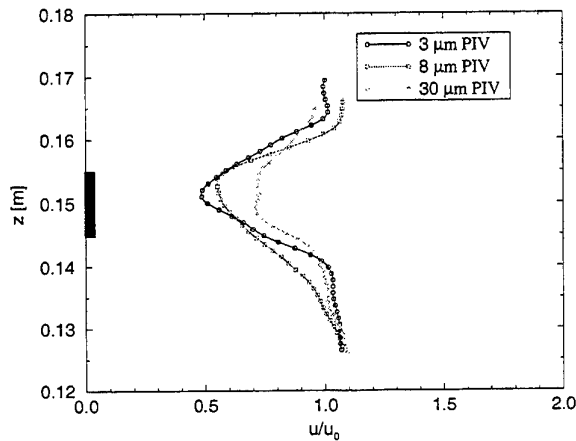


Figure 8: velocity profile for $u_0 = 4.5$ m/s and $x/D = 5$.

It can be seen clearly the particle diameter influences the motion of the particles significantly. The velocity decay in the wake is only influenced by the particle diameter, i.e. the Stokes number. Also the width of the velocity profile is effected by the particle diameter. Here the width decreases with increasing particle diameter. This results supports the finding of Tang et al. (1992) which also report the Stokes number as the import parameter for the nature of this type of flow. The particle initial velocity u_0 in opposite seems not to dominate the flow of the particles around the obstacle. The influence of the particle initial velocity u_0 is present when looking at the geometry of the particle velocity profile. Where a higher particle initial velocity u_0 leads to increasing deformations of the velocity profile. Also the differences between u_{\min} for the different particle diameter for one specific initial velocity are on a small scale increasing with increasing initial velocity.

Furthermore the position of the minimum velocity u_{\min} is influenced by the drift velocity u_d . An increasing drift velocity leads to a decreasing z position of the point of $u = u_{\min}$. This effect could be explained by the influence of gravity, since the particles with 30 μ m diameter have a significant drift velocity which is

10^2 time larger than the drift velocity of 1 μ m diameter particles.

5. CONCLUSIONS

A turbulent particle laden wake flow has been investigated experimentally by means of particle image velocimetry. To determine the influence of particle diameter, i.e. Stokes number, and particle initial velocity, i.e. Reynolds number, these parameters have been varied. The PIV method has been utilised to determine the velocity field of mono-disperse particles with different diameters. It is shown the PIV technique has been adapted successfully to this problem. From the PIV data velocity profiles at the position $x/D=5$ have been established.

The experimental data shows the particle diameter has a strong influence on the behaviour of the particle laden flow. The particle diameter rules the minimum velocity within the wake flow just as the width of the velocity profile. It is found the particle initial velocity in opposite has only little influence on the velocity profiles. The geometry of the velocity profile is slightly effected by the particle initial velocity. Just as the difference of u_{\min} for different particle diameters for one initial velocity. Nevertheless the appearance of the velocity profile is mainly dominated by the particle diameter.

The PIV results were able to show clearly the influence of particle diameter on the velocity defect within the wake is much stronger than the effect of the particle initial velocity. Furthermore an influence of gravity has been determined by the experimental results. The position of the point with u_{\min} in the velocity profile moves downwards in direction of gravity with increasing particle diameter, i.e. drift velocity.

6. ACKNOWLEDGEMENTS

The first author would like to thank Dr. M. Raffel for his introduction to the PIV technique and the DLR PIV system. Furthermore Dr. C.E. Willert for his support in the evaluation of the PIV data.

7. REFERENCES

- Elghobashi, S. 1994, On predicting particle-laden turbulent flow. Appl. Scient. Res., vol. 52, pp. 309-329.
- Horlbeck, B. & Höhler, G. & Möller, T.J. & Bütefisch, K.A. 1995, Strömungstechnische Versuche an einem Modell des Abwetterkanals des geplanten Endlagers Konrad. In: Entsorgung: Wiederwertung - Beseitigung Band II, J. Brauns, GG. Eigenwillig, pp. 628-632.
- Möller, T.J. & Bütefisch, K.A. 1997, Particle dynamics in a turbulent confined gas-particle flow around a rectangular obstacle. ZAMM, vol. 7, pp. 224-225.
- Möller, T.J. 1996, Experimentelle und numerische Untersuchung einer teilchenbeladenen Strömung um einen stumpfen Körper. Deutsches Zentrum für Luft- und Raumfahrt. Research Report DLR-FB 96-24.
- Raffel, M. & Willert, C.E. & Kompenhans, J. 1998, Particle Image Velocimetry - A practical guide. Springer Verlag, Berlin.
- Raffel, M. 1993, PIV-Messungen instationärer Geschwindigkeitsfelder an einem schwingendem Rotorprofil. Deutsche Forschungsanstalt für Luft- und Raumfahrt. Research Report DLR-FB 93-50.
- Skalicky, T. & Rösler, M. 1994, ResCUE V2.16, Kurzbeschreibung. University Dresden. Research Report.
- Snyder, W.H. & Lumley, J.L. 1971, Some measurements of particle velocity autocorrelation functions in a turbulent flow. J. Fluid Mech., vol. 48, pp. 41-71.
- Stock, D.E. 1994, Particle dispersion in flowing gases - 1994 Freeman scholar lecture. ASME J. of Fluids Eng., vol. 118, pp. 4-17.
- Tang, L. & Wen, F. & Yang, Y. & Crowe, C.T. & Chung, J.N. & Troutt, T.R. 1992, Self-organizing particle dispersion mechanism in a plane wake. Physics of Fluids A 4, vol. 10, pp. 2244-2551.
- Wells, L.P. & Stock, D.E. 1983, The effects of crossing trajectories in the dispersion of particles in a turbulent flow, J. Fluid Mech., vol. 136, pp. 31-62.
- Willert, C.E., 1996, The fully digital evaluation of photographic PIV recordings. Appl. Scient. Res., vol. 56, pp. 79-102.

SESSION 25

COMBUSTION 2

EXPERIMENTAL INVESTIGATION OF SPATIO-TEMPORAL CORRELATION BETWEEN AERODYNAMIC AND FLAME FRONT LOCATION IN AN AXISYMETRIC NON PREMIXED BLUFF BODY BURNER FLAME

A. SUSSET[†], M. TRINITE

CORIA - UMR 6614 - CNRS

76821 Mont-Saint-Aignan cedex, France

D. HONORE, D. JAFFRE, M. PERRIN

Gaz de France, Research and Development Divison, CERSTA

BP 33, 93211 La Plaine St Denis Cedex, France

ABSTRACT

Flame front imaging by Spontaneous Emission Spectroscopy technique and instantaneous aerodynamic field by PIV measurements are made simultaneously in a turbulent non-premixed methane/air flame stabilized by the wake effect of a bluff-body. In order to study correlations between aerodynamic and flame front location we have developed post-processing tools for image analysis and velocity fields processing. These tools are put together in a software called PopPIV which allows also to carry out statistics on velocity fields.

Comparison between mean velocity and RMS fields obtained by PIV with previous LDV measurements has clearly shown the bias induced by PIV measurements when large velocity gradients are present in the interrogation window.

Dual imaging techniques experiment and image post-processing tools development, have allowed us to put forward a scenario of the ejection of burning structures from the recirculation zone and their convection downstream of the flow leading the flame stabilization.

1. INTRODUCTION

Experimental study of interaction between chemistry and fluid mechanics in non-premixed turbulent flame is of great interest to characterize complex phenomena governing flame stabilization mechanisms in industrial natural gas flames. For this purpose, simplified industrial-like bluff-body model burners have been the subject of several studies at Gaz de France, see for example Neveu *et al.* (1994), Mokaddem *et al.* (1997), Susset *et al.* (1996). For such a burner, stabilization of the flame is obtained by the wake effect of the obstacle

on the flow, generating a recirculation zone downstream from the burner exit where methane and air are mixed.

Mokaddem *et al.* (1997) in previous experiments of flame front visualizations by Spontaneous Emission Spectroscopy (SES) technique have observed a quasi-periodic ejection of burning gas packets from the recirculation zone. While instantaneous PIV velocity field measurements by Susset *et al.* (1996) have demonstrated the presence of several unstationary coherent structures in the flow.

In the present study, we have carried out simultaneously flame front imaging by SES technique and instantaneous velocity field measurements by PIV in order to study spatio-temporal correlation between instantaneous flow aerodynamic and flame front location.

2. EXPERIMENTAL SETUP

2.1. Burner Description and Case Studied

Several geometries of axisymmetric bluff-body burner have been already the subject of numerous studies, see for example Perrin *et al.* (1990) and Schefer *et al.* (1996).

Figure 1 shows the geometric characteristics of the burner. The studied case corresponds to a bulk flow velocity of 21 m/s in the central methane jet, and 7.5 m/s in the annular jet of air. This case was studied in reactive conditions, without any confinement. The Reynolds Number found in the methane and air jets are 7000 and 3300 respectively.

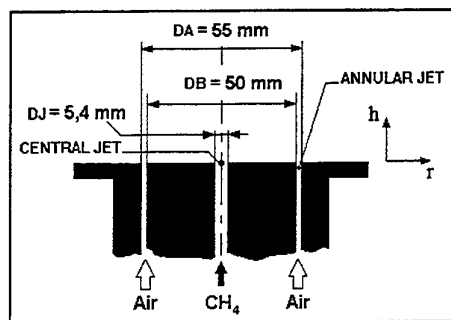


Fig. 1 Geometric characteristics of the burner.

2.2. Experimental set-up and Synchronization

The experimental set-up is presented on figure 2. The intensified CCD camera (Proxitronic Nanocam) is synchronized by the PIV camera video signal. The PIV camera (Lhesa LH510 VI) drives both the multi-cavities Nd-Yag laser and the intensified CCD camera. Each sequence of 250 PIV images are digitized at video rate whereas flame front images are saved on a video tape recorder and digitized later. A photographic flash lamp triggered at the beginning of the sequence is used as a temporal reference signal to rebuild synchronicity of the two images series. The exposure control being limited to the odd field in triggered mode, the CCD sensor of the PIV camera is operated in un-shuttered mode. However, to improve the quality of the recorded signal, an interferential filter is used ($\lambda = 532 \pm 10$ nm), in order to eliminate most of the radiations from the flame and the hot particles. The field of view covered by the PIV camera is 54×54 mm² area, seen through a f:1.2/50 mm lens (Nikkor) set at f:2.

The intensified CCD camera is fitted out with a narrow band filter (1 nm) centered at 516.5 nm to isolate the bandhead of the vibronic transition ($d^3\Pi_g, v'=0 \rightarrow a^3\Pi_u, v''=0$) of the C₂ Swan System. The field of view covered by the intensified CCD camera is 68×68 mm² area, seen through a f:1.2/50 mm lens (Computar) set at f:2.8. In order to avoid image reflections caused by the metallic coating of the interferential filters it is required to place the two cameras on the same side. The intensified camera is placed on the optical axis perpendicular to the laser sheet. Due to the small size of the cameras and their lenses, the angle between the two optical axis is about 3°. This short angle and the thickness of the laser sheet (0.5 mm) reduce the bias for PIV measurements coming from the velocity component perpendicular to the laser sheet.

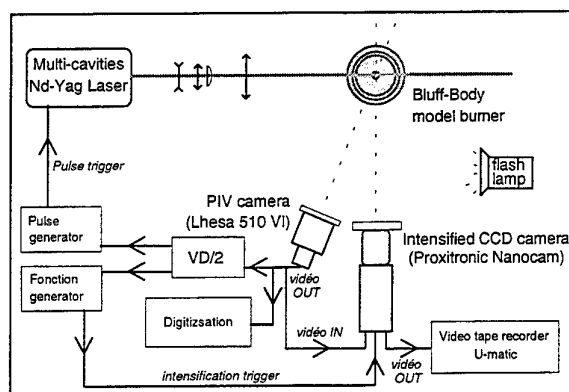


Fig. 2 Simultaneous double imaging experimental set-up.

The synchronization timing diagram is presented on figure 3. The PIV camera drives the multi-cavities Nd-Yag laser shots by the way of a pulse generator (DG 535 - Stanford research) and exposure duration (250 μ s) of the intensified CCD camera by the way of a function generator (DS345 - Stanford Research) triggered by VD/2 field extracted from the PIV camera video signal. This set-up ensures the perfect synchronicity between the acquisition of PIV images and flame front images.

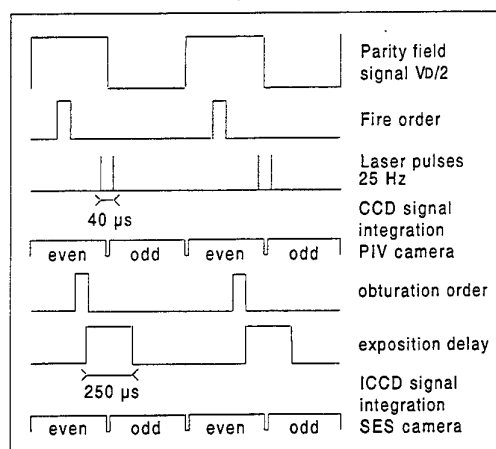


Fig. 3 Synchronization timing diagram.

The digitization rate (25 Hz) enables to acquire a lot of PIV/SES images. In order to perform statistics, we choose to acquire 3000 pairs of PIV/SES images. Figure 4 shows an example of rough data : an image of the flame front obtained by SES on a left side and an instantaneous velocity field measured by intercorrelation of two PIV images on the right side.

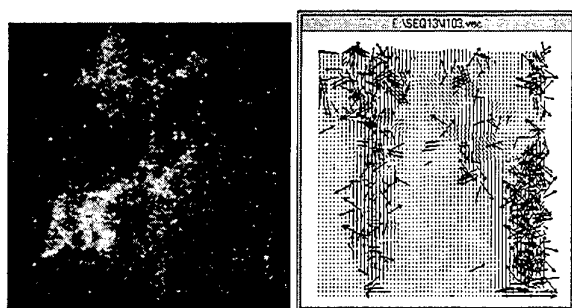


Fig. 4 : SES (left) and PIV (right) rough data before post-processing.

These data need to be post-processed for quantitative study of correlations between flame front position and aerodynamic. The next part presents algorithms and tools developed for the post-processing of rough data presented on figure 4.

3. POST-PROCESSING TOOLS

3.1. Post-Processing of SES Images.

Due to the integration along the optical line of sight of C2 chemiluminescence in the unstationary flame, instantaneous images did not revealed the distribution of the flame front within the laser plane. Then care must be taken when analysing the correlation between planar PIV measurements and integrated flame front images. Moreover the poor quality of SES images recorded (intensification noise, Mie scattering of particles, video recording noise) leads us to extract only qualitative information of the local presence or absence of the flame. For this purpose, four post-processing steps have been defined to obtain finally binary images where 0 corresponds to a non-reactive region and 1 to a reactive one.

Binarization. This first step is currently used in image processing techniques. Its aim is to reduce the dynamic of the image in order to keep only a desired information. Figure 5 shows the result of binarization.



Fig. 5 : Binary image

Erosion. This step is used to filter the noise in the binary image. Each pixel at 1 near a pixel at 0 become nil. Only pixels at 1 without neighbors at 0 stay at 1.

Figure 6 shows the result of erosion.

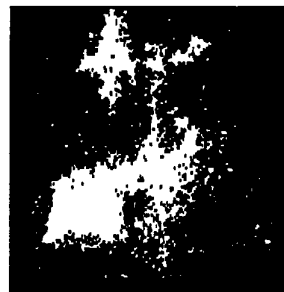


Fig. 6 : Binary image after erosion.

Average 5x5. This step is used to soften the image of Mie scattering particles which have not been filtered by erosion. This operation is a low band spatial filter which consist in assigning at a pixel the average grey level calculated over a 5x5 window of pixels. Figure 7 shows the result of averaging.



Fig. 7 : 8 bit level grey image after average 5x5.

Fillfilter. This step is used in image recognition in order to decrease the disparity of grey level in continuous shapes. In our case it enables to extract the overall shape of the flame front. The fillfilter algorithm contains 3 steps. First the image is binarized. Then only pixels at 1 having a neighbor at 0 remain at 1. This second step is used to determine outlines. Finally all pixels at 0 included in an outline are set to 1. Figure 8 shows the results of Fillfilter.



Fig. 8 : Final image after the Fillfilter operation.

Some steps of the image post-processing require parameters set by the experimenter. It should be remind that due to the integration along the optical line of sight of C2 chemiluminescence and the poor quality of SES images recorded, we only extract qualitative information of burning gases location. Nevertheless our post-processing algorithm has been validated by comparison between the averaged image of 1000 post-processed images and an other averaged image previously obtained by Mokaddem *et al.* (1997) in better recording conditions.

3.2. Post-Processing Tools for PIV.

PIV data post-processing requires to use post-processing parameters such as scaling factors, threshold filters, validations, interpolation, spatial filter grids and so on. The optimization of such parameters and the building of an appropriate post-processing scheme is a key asset for the use of PIV velocity fields as quantitative information. Therefore we developed a software called PopPIV (POst-Processing software for Particle Image Velocimetry) running under Windows 95/NT, with a graphical interface which provides a visual feedback that allows the user to easily and rapidly optimize post-processing parameters.

Standard functions.

- scaling factors : the user loads a reference image, selects couples of pixel/real points for the automatic calculation of scaling factors.
- experimental settings : the user sets pulse separation delay, scaling factors, pixel translation, time and scaling units. When experimental settings are applied to a vector field, the position of the mouse on a velocity field indicates in real time the position and velocity in real units.
- threshold filter : the user sets the validity ranges on each velocity component and on the signal/noise ratio.
- validation filter : the user sets a grid of neighbors (3x3, 3x5, ...) and a percentage of similarity. For each vector of the field man processes a similarity coefficient defined as :

$$k_i^{similarity} = \left(1 - \frac{\Theta}{\pi/2} \right) \left(1 - \frac{|N_i - N_j|}{\max(N_i, N_j)} \right)$$

with i for the considered vector,

j for its neighbors,

Θ = angle between i and j ($0 < \Theta < \pi/2$),

and N the magnitude of the velocity vector

This approach to validation may remove valid as well as invalid vectors if the level of spurious vectors is more than moderate. The solution to this problem is to perform a second pass through the data using only

validated values to compute local trends for comparison. Figure 9 shows the comparison of two averaged field (240 instantaneous velocity fields) of the axial velocity RMS without and with validation filter .

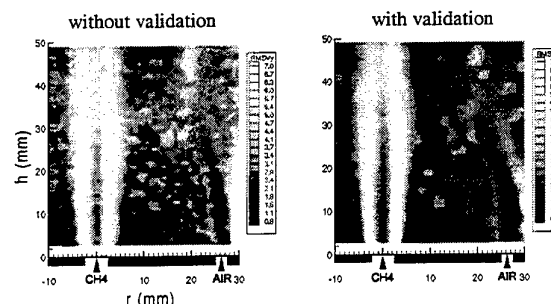


Fig. 9 : Effects of the validation on spurious vectors

It is obvious that the validation filter removes some spurious vectors which can't be erased by standard threshold filters.

- interpolation : the user interpolates filtered velocity vectors. This interpolation is processed from nearest neighbors.
- spatial filtering : the user chooses the size (3x3, 5x3...) and the weight values of the numeric grid. Such spatial filtering can be used as a smoothing operator (linear, gaussian, ...).
- derived quantities : magnitude, vorticity and divergence are calculated for each velocity vector.

All the parameters of these standard functions can be saved and recalled. Each function can be used several times with different parameters during the post-processing. Therefore PopPIV enables to optimize post-processing parameters thanks to the feedback provided by the graphical interface. Moreover this software allows the user to build a personalized post-processing scheme for the use of PIV velocity fields as quantitative information. Figure 10 presents the resulting velocity field after standard post-processing of the rough velocity field shown figure 4.



Fig. 10 : Instantaneous velocity field post-processed with PopPIV

Once the post-processing scheme is defined it can be applied to an unlimited number of velocity fields. We also develop other tools that can be applied to each velocity vector file :

- data extraction : on a point, a line, an area.
- arithmetic operations between velocity fields.
- correlations between images and velocity fields.

The development of hardware performances enables to acquire and process a lot of PIV velocity fields. Today we can and shall perform statistics on such data. PopPIV also integrates statistics tools applied to an unlimited number of velocity vector files :

- Mean velocity field,
 - RMS field,
 - Joint PDF,
 - Spatial correlations between separate points.
- Since the PopPIV code is 32 bit built, the processing speed is very high : about 10000 velocity vectors per second on a standard configuration (PC 200 Mhz).

In order to validate our PIV measurements and processing scheme we compare on figure 11 the mean velocity fields obtained by PIV on the present study with previous LDV measurements performed by Neveu *et al.* (1994).

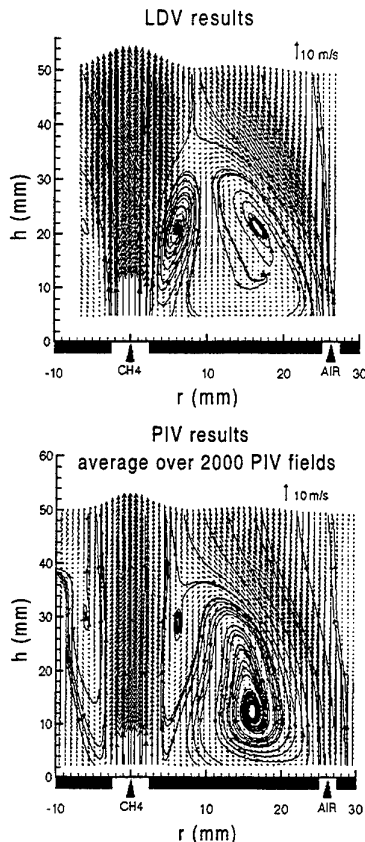


Fig. 11 : Comparison of the mean dynamic fields from LDV and PIV.

The overall structure of the average dynamic field is similar for the two methods. The wake effect of the bluff-body generates a recirculation zone downstream from the burner exit which consists of a centrifugal vortex driven by the methane jet and a centripetal vortex driven by the annular air jet.

Main difference seen in the central fuel jet can be attributed to the lack of spatial resolution of PIV in comparison with the strong velocity gradient. Figure 12 presents the interrogation window size compared to the velocity gradient in the central fuel jet.

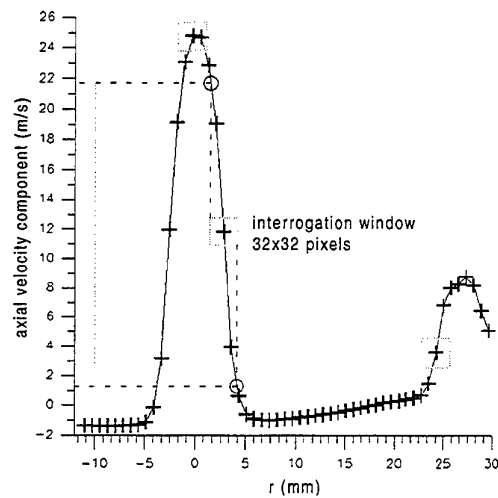


Fig. 12 : Mean radial profile of axial velocities at $z = 5.6$ mm (from 2167 PIV velocity fields).

The range of velocity in an interrogation window reaches very large values in the methane jet boundary (0.4 to 8.8 pixels i.e. 1 to 22m/s). The loss of particle in an interrogation window between the two successive images increases with the displacement of particles. Then the general trend is to favor small displacement measurements rather than large one when gradients are strong. This bias leads to decrease the width of the profile thus explains the difference between LDV and PIV measurements for the central fuel jet shape.

Discrepancy between these two velocimetry techniques can also be observed on the axial velocity RMS fields presented on figure 13. Main difference can be attributed to the combined effect of velocity gradient and particle spatial distribution inhomogeneity.

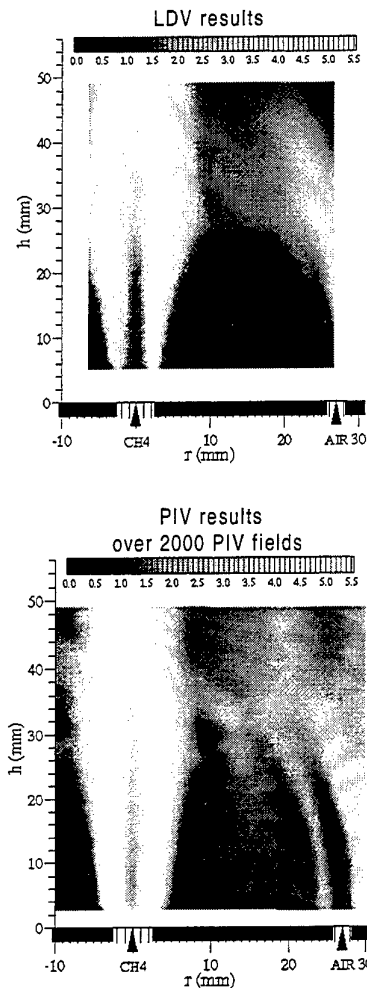


Fig. 13 : Axial velocity RMS fields by LDV and PIV.

Let us consider several successive PIV measurements in a non-fluctuating flow with a large velocity gradient in an interrogation window. As velocity determined by PIV corresponds to the most probable particle displacement in the interrogation window, it depends on particles spatial distribution. Therefore particles distribution inhomogeneities in the interrogation window affect the measured instantaneous velocity. Then even though the local RMS value is theoretically nil, this bias induces a virtual RMS value. This analysis has to be validated by theoretical study of the real dynamic and spatial resolution of the PIV technique.

In the studied flow, the suggested phenomenon involves an overestimation of the RMS value of velocity on the methane jet boundaries downstream from the burner exit up to $h \approx 25$ mm (Figure 13). Above this height, the velocity gradient as well as the particles distribution inhomogeneities are smaller, then this bias no longer appears and the RMS value obtained by PIV is quasi-equal to the LDV one. Similar effect is also present in

the air jet region. These experimental bias induced by large gradients would be eliminated by decreasing the interrogation window size and modifying its shape. This can be realized by the use of direct correlation algorithm and interrogation windows offset, see Lecordier (1997).

4. CORRELATIONS BETWEEN AERODYNAMIC AND FLAME FRONT POSITION.

4.1. Processing Method.

As mentioned above PopPIV includes specific tools for the study of correlations between images and velocity vectors field. In our study velocity fields are re-sized in the corresponding flame front image coordinates. After such processing, each vector is classified to be « reactive » or « non-reactive ». A vector is defined as a « reactive » one if, in the corresponding flame front image, the grey level averaged over the area corresponding to the PIV interrogation area (32x32 pixels) is greater than 50% of pixel at 1. If not, the vector is defined as a « non-reactive » one. Figure 14 illustrates this procedure.

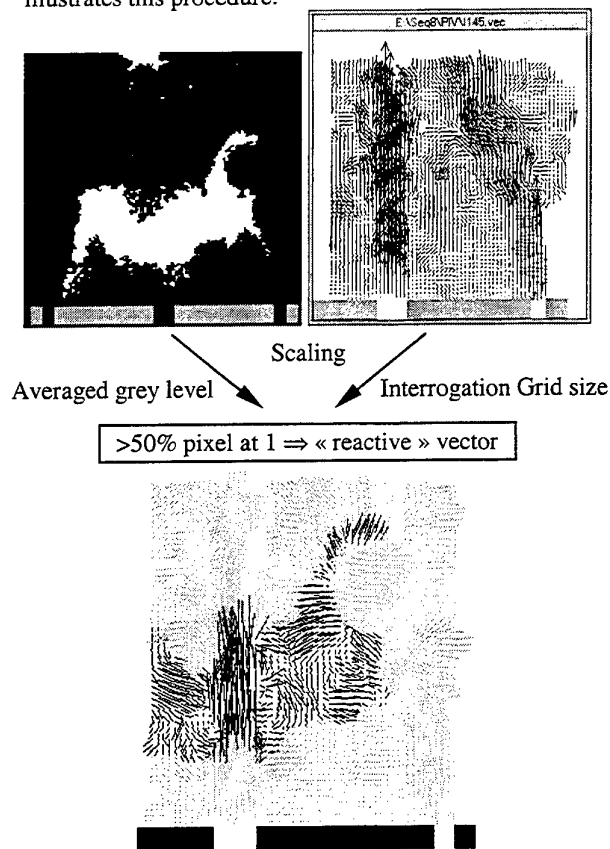


Fig. 14 : SES image and PIV field matching procedure.
(black : reactive vector - grey : non-reactive vector)

4.2. Statistical Study

Figure 15 presents mean velocity fields obtained from « reactive » and « non-reactive » vectors averaged over 480 images.

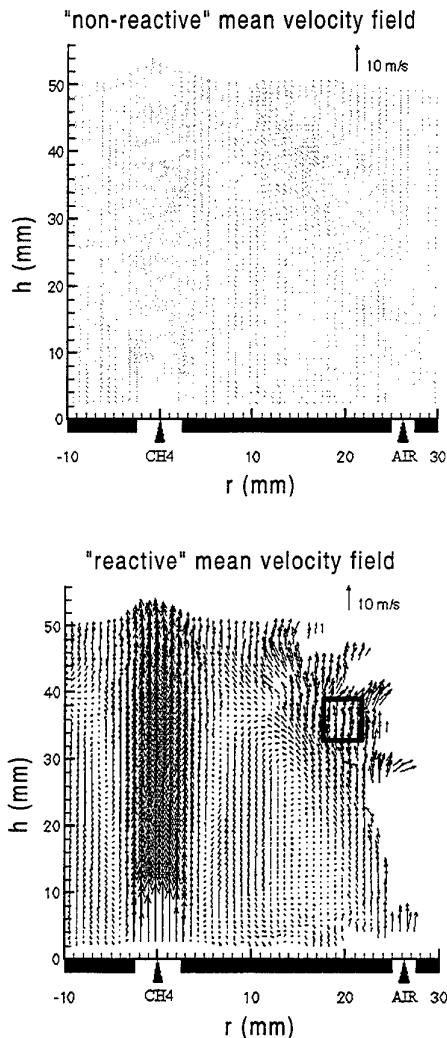


Fig. 15 : Mean « non-reactive » and « reactive » velocity fields averaged over 480 images.

We can notice that the main difference between the « reactive » and « non-reactive » averaged field is located in a region centered at $r = 20$ mm and $z = 35$ mm. Due to the burner axisymmetric geometry even though the C_2 chemiluminescence signal is integrated along the optical line of sight, the probability to observe burning gases located in the laser sheet is greater far from the main axis. Then there is no doubt that « reactive » vectors defined in the region of interest come from the matching of the flame with the tomographic PIV plane.

Simultaneous local measurements of velocity and temperature, previously performed by LDV and FWCT (Fine Wire Compensated Thermocouple), have shown a bimodal distribution of velocity/temperature in the flow on the edge of the recirculation zone Neveu et al. (1994). We also find such a bimodal distribution with a radial « reactive » vector component smaller than the « non-reactive » one. Figure 16 presents local LDV/FWCT measurements at $r = 20$ mm ; $z = 35$ mm in comparison with « reactive » and « non-reactive » velocities obtained from PIV/SES experiment by averaging over a 5×5 mm² area centered on the same location.

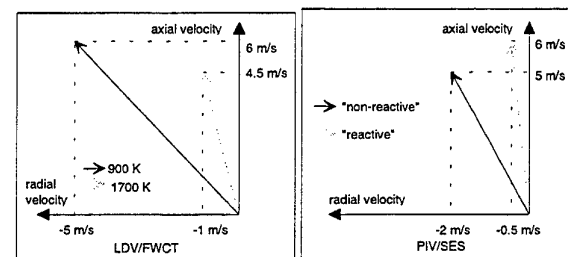


Fig. 16 : Bimodal distribution of velocity/temperature for different simultaneous techniques

The main difference between the absolute velocity components values for the two velocimetry techniques can be attributed to the averaging over the region of interest for PIV measurements. Moreover the velocity bimodal distribution determined from LDV/FWCT measurements depends on temperature (900 K or 1700 K) whereas for PIV/SES measurements only the qualitative gas state (i.e. « reactive » or « non-reactive ») is taken into account. However, PIV/SES results seems to find again such intermittent flame/flow interaction.

Regarding to such velocity distribution we put forward that a burning structure is ejected from the recirculation zone to the air jet and then convected downstream by the air flow. Imaging techniques provide more information on the burning structures than local measurements due to spatial correlation of data. Regarding to instantaneous PIV/flame front image pairs and to illustrate our hypothesis, we can construct a sequence of instantaneous PIV/flame front image pairs. Figure 17 shows a sequence of three instantaneous PIV/flame front pairs. However due to image acquisition rate (25 Hz) compared to flow structures velocity, the present PIV/SES experiment is not time resolved. Then the suggested scenario can not be validated. For this purpose, new post-processing algorithms dedicated to coherent structure study is being developed. Jets and vortices are coherent structures which can be extracted from instantaneous PIV measurements. Their study could lead to determine flow phase construction.

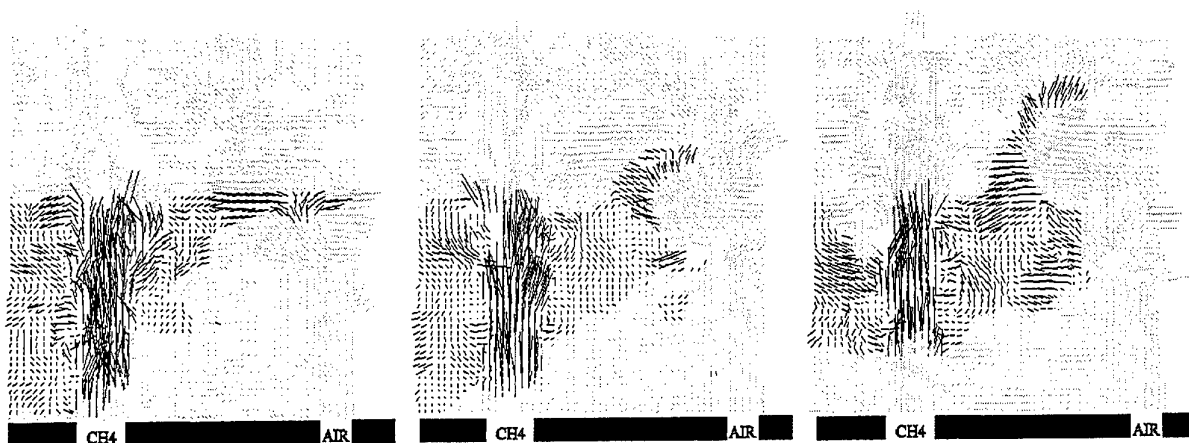


Fig. 17 : Burning structure ejection sequence constructed with 3 instantaneous PIV/flare front image pairs

Moreover a simultaneous time resolved SES imaging and PIV measurements will be realized to validate these new tools.

5. CONCLUSION

We have shown that simultaneous imaging experiment could give precious information on unstationary phenomena of interaction between chemistry and fluid mechanics for the characterization of flame stabilization. Development of specific post-processing tools has been required to extract more quantitative information from PIV measurements. Highlighting of experimental bias in PIV results due to large velocity gradients in the interrogation windows has demonstrated the need of new velocity calculation protocols for the application of PIV technique in complex turbulent flows. However it is obvious that future development of post-processing tools based on instantaneous velocity fields, such as temporal phase construction for pattern determination, would be the next challenge to exploit the fullness of information contained in PIV data.

REFERENCES

- Lecordier, B. 1997, Etude de l'interaction de la propagation d'une flamme prémélangée avec le champ aérodynamique par association de la tomographie laser et de la Vélocimétrie par Images de Particules, Ph.D. thesis, University of Rouen, F.
- Mokaddem, K., Durox, D., Scouflaire, P., Rolon, J.C., Jaffré, D. & Perrin, M. 1997, Experimental investigation of a turbulent non-premixed bluff-body stabilized CH4/AIR flame, 16th International Colloquium on Dynamics of Explosion and Reactive Systems, Krakow.
- Neveu, F., Corbin, F., Perrin, M. & Trinité, M. 1994, Simultaneous velocity and temperature measurements in turbulent flames obtained by coupling LDV and numerically compensated finewire thermocouple signals, Proc. 7th International Symposium on Application of Laser Techniques to Fluid Mechanics, Lisbon.
- Perrin, M., Namazian, M., Kelly, J. & Scheffer, R.W. 1990, Effect of confinement and blocage ratio on non-premixed turbulent bluff-body burner flames, 23th International Symposium on Combustion, Orléans.
- Scheffer, R. W., Namazian, M., Kelly, J. & Perrin, M. 1996, Effects of Confinement and Bluff-body Burner Recirculation Zone and Flame Stability, Combust. Sci. and Tech., vol. 120, pp.185-211.
- Susset, A., Jaffré, D., Perrin, M., Gray, C. & Richon, J.B. 1996, A PIV investigation in an axisymmetric non premixed Bluff Body burner flame, Proc. 8th International Symposium on Application of Laser Techniques to Fluid Mechanics, Lisbon.

SIMULTANEOUS PIV AND PLIF MEASUREMENTS IN NONPREMIXED TRANSVERSE JET FLAMES

E. F. Hasselbrink, D. Han, M. G. Mungal and R. K. Hanson

Mechanical Engineering Department, Stanford University, Stanford CA 94305-3032, USA

ABSTRACT

Particle Image Velocimetry (PIV) and Planar Laser-Induced Fluorescence (PLIF) of the OH radical are performed in a lifted, methane transverse jet flame. The measurements are carried out with the PLIF images acquired in the time between the two PIV laser pulses, so that on the fluid-mechanical timescale, the images are effectively simultaneous. PIV is obtained using twin Nd:YAG lasers and cross-correlated image pairs; OH PLIF is obtained using an excimer-pumped dye laser via excitation of the $Q_1(6)$ line of the $A \leftarrow X(1,0)$ band. OH PLIF images are corrected for background and laser sheet profile. Approximately 100 PIV/OH realizations are acquired at four locations (lee and windward sides of the jet, at the flamebase and at $1/2$ the visible flame length) in a jet flame with jet-to-crossflow blowing ratio of 10. At the flamebase, both instantaneous and average realizations clearly show streamline divergence upstream of the flame base due to heat release, as well as acceleration of the fluid through the flame base. The OH regions at the flamebase are typically quite thick, and are often broken into small islands. Flow and flame interaction are also clear in the instantaneous data at the $1/2$ flamelength position further downstream, where interactions with vortices are clear in the lab frame of reference. OH regions at the $1/2$ flamelength position, are generally thin, sinuous regions but are occasionally diffuse.

1. INTRODUCTION

In recent years, experimental and computational efforts have greatly improved understanding of the dynamics of flames, especially their dependence on, and interaction with, the velocity and scalar fields surrounding them. Studies of the effect of mixture fraction gradients (Ruetsch et al. (1995)), discrete vortex interaction (Mueller et al. (1995), Veynante et al. (1994)), and steady and oscillating strain rates (Egolfopoulos (1994), Im & Chen (1997)) have generally found strong coupling between the

flow and the heat release. That is, not only do the upstream flow and mixture fraction fields influence the flame, but the heat release due to combustion directly influences the flow approaching and departing the flame reaction zone. Ruetsch et al. (1995) found that not only does an upstream mixture fraction gradient cause a laminar flame to take on a triple-flame structure, but that the heat release and curvature of this flame allow the flame to propagate faster than the laminar flame speed. Mueller et. al found that not only does an approaching vortex stretch a flame (possibly to extinction), but that the heat release can generate vorticity of the opposite sign due to baroclinic torque.

It is generally hoped that such findings may improve understanding of turbulent jet flames. Certainly the presence of a flame influences these flows; the work of Becker & Yamazaki (1978), Clemens & Paul (1995) and Rehm & Clemens (1997) show that burning jets have lower entrainment rates and show less quasi-periodic coherency of the large-scale vortices than the non-burning case. However, if an understanding of these effects in terms of laminar flame dynamics is to be gained, both the local fluid flow and the location of reaction zones must be simultaneously measured.

In the present work we describe our technique for simultaneously obtaining images of the OH radical field in a flow and the local velocity field surrounding it. We then present and discuss instantaneous and average velocity and OH fields in several regions of the transverse jet, a flow commonly used in industrial and power utility boilers. We identify clear influences of the effects of the heat release on the flow. We also identify regions of the flame where instantaneous strain rates in the flame are large enough to significantly affect the flame.

2. EXPERIMENTAL TECHNIQUES

2.1 Flow Apparatus

A schematic of the experimental arrangement is shown in Figure 1. The flow facility is a vertical indraft

tunnel operating at 1.65 m/s with a 50 x 50 cm test section and rounded inlet with 2.5:1 contraction ratio. Two honeycombs and a cascade of several screens straightens the flow and reduces the freestream turbulence intensity (measured using a hot-wire) to 0.8% without the use of cross-stream particle seeders, and 1.0% when in use (measured using PIV). The tunnel has a large 50 x 80 x 0.63 cm Pyrex window for viewing the flow on the front side, and a 15 x 15 x 0.95 cm quartz window on the back, mounted in the aluminum walls. The back tunnel wall is comprised of several movable plates so that the viewing area may be easily changed. The interior of the wind tunnel is painted black to reduce reflections.

The 99.0% methane jet is injected normal to the crossflow through a 25 cm long tube (6.35 mm OD, 4.8 mm ID, 316 stainless steel), protruding 7 cm into the wind tunnel. The jet tube is located within an annular tube (9.5 mm OD) which serves as a hydrogen pilot. Without the hydrogen pilot, the flame lifts off from the jet exit about 7 cm. A blowing ratio of $r \equiv [(\rho_j u_j)/(\rho_u u)]^{1/2} = 10.1$ (nominally $r = 10$) is investigated, with jet-exit Reynolds number of 6250.

Both the jet and crossflow are seeded with 0.3 μm (nominal) alumina (Al_2O_3) particles, using fluidized-bed seeders and cyclones for agglomerate removal. The crossflow is seeded upstream of the tunnel inlet using a jet-ejector system. Two heavily seeded air jets (1.8 cm ID) spaced 12 cm apart are directed into a 60 cm long rectangular channel (25 cm x 13 cm) positioned 1m below the tunnel inlet. A small fan near the inlet assists the entrainment of air into the channel and the mixing with the heavily-seeded air. A honeycomb at the channel exit reduces the turbulence of the exiting flow, producing a uniform, yet dense, distribution of particles. The fan and the jet flowrates are set so that the flow at the channel exit is approximately equal to the wind tunnel speed.

2.2 OH Imaging System

Due to the presence of PIV particles, a nonresonant excitation strategy is required; we thus excite a transition in the $A^2\Sigma^+ \leftarrow X^2\Pi$ (1,0) band of OH near 283 nm, and collect fluorescence in the (1,1) and (0,0) bands near 315 nm. Barlow & Collignon (1991) have shown that for the $Q_1(6)$ line of this band, population and quenching effects in equilibrium flames largely offset each other, such that the fluorescence signal is proportional to OH concentration to within $\pm 10\%$.

The elements of the OH imaging system are shown in Fig. 1. A Lambda-Physik EMG-203 XeCl excimer laser pumps a Lambda-Physik FL3002 dye laser using Coumarin 153 (540A) dye, producing light at 566nm which is frequency-doubled to 283 nm using a BBO crystal. At repetition rates of a few Hz, pulse energy of 3 mJ/pulse at 283 nm is obtained, but this falls to about 1.5 mJ/pulse at the 15Hz image acquisition speed due to population depletion in the excimer laser. A spherical lens and cylindrical lens telescope form the beam into a non-expanding sheet, approximately 40mm tall and 300 μm thick at the image

region. Fluorescence is captured on a Princeton Instruments 512 x 512 pixel Pentamax camera with a fiber-coupled MCP intensifier at 14.7 Hz framing rate. The camera is equipped with a Nikkor f/4.5 105 mm UV lens, a Schott UG-5 filter to reject flame emission, and two Schott WG-305 filters (1 mm and 3 mm thick) to reject elastic scattering from the particles. Gating the intensifier for 400 ns, starting 100 ns before the arrival of the laser sheet into the wind tunnel, also rejects flame emission. The viewing region is 35 mm on a side, for a magnification of 0.22. Hereafter this camera and laser will be referred to as the "OH camera" and "OH laser", respectively.

Tuning of the dye laser was performed using the fundamental beam and a Burleigh Instruments pulsed wavemeter (WA-4500), and by using a laminar flame, observing OH signal on the camera while scanning the laser across several transitions. When the laser was tuned off line center, blank images were acquired, ensuring that no soot scattering or broadband fluorescence from other species was observed.

The OH images are corrected for background and mean laser sheet profile, but because the data are used merely to identify reaction zones, shot-to-shot laser sheet corrections are not performed. Although quantitative PLIF is possible in principle (see the discussion section), the PIV particles introduce additional uncertainty due to laser sheet extinction. Signal-to-noise ratio for peak OH levels is approximately 5 without pixel binning. For purposes of presentation with the simultaneous velocity data, the OH data is binned according to the size of the PIV data grid. With 64 x 64 data points in the PIV grid, this results in a 6 x 6 bin, (0.4 mm in physical space), giving an effective signal-to-noise ratio of 30. Smearing caused by binning is not expected to be serious because the narrowest OH structures observed in the original images are > 1mm thick.

2.3 PIV Imaging System and Image Processing

The PIV system in this study, also shown in Fig. 1, consists of a dual-cavity Nd:YAG laser (Spectra Physics PIV-400, 400 mJ pulse at 532 nm formed into a 300 μm thick sheet), a high resolution CCD camera (1008 x 1018 pixel array, Kodak ES-1.0 interline frame transfer camera with 105 mm Nikkor lens at f/5.6), and a PC with frame grabber to acquire and process the images. Hereafter, this laser and camera will be referred to as the "PIV laser", and the "PIV camera" to distinguish them from their OH imaging counterparts. Like the OH system, the two frames are acquired at 14.7 Hz framing rate, the first frame being exposed for 255 μs and the second frame for about 32ms. The interline architecture of the ES-1.0 CCD allows for independent images to be taken as close as 400 ns apart, but typical laser pulse separation is 10 - 40 μs . The first PIV laser pulse arrives two microseconds before the OH laser pulse; the timing is set using a Stanford Research Systems DG-535 digital delay generator.

PIV images are processed using the InsightTM software package (ver. 1.34, TSI Inc.) using the cross-correlated subregions (32 x 32 pixels) of frame-straddled

images. Image magnification is 34.4 pixels/mm, for a total viewed area of 29 mm square. With about 50% subregion overlap, 64×64 vectors are obtained, for about 1/2 mm resolution. This resolution is smaller than typical strained diffusion flame thicknesses (about 1-3 mm), and comparable to the Kolmogorov scale $\eta/\delta \sim 11\text{Re}^{-3/4}$, where δ is the local jet width. Reynolds number is a weakly decreasing function of distance along the trajectory of the transverse jet, but a typical value for the present case is $\eta \sim 0.5\text{mm}$, based on 3 cm local jet width and $\text{Re} = 6250$.

3. DISCUSSION OF EXPERIMENTAL ISSUES

3.1 PIV accuracy

Issues of PIV accuracy in flames have been discussed at length in previous work by Muñiz & Mungal (1996), and Hasselbrink, et. al (1997, 1998). The uncertainty is usually dominated by thermophoresis effects. Thermophoresis is a phenomenon in which a particle experiences a force opposite the direction of the fluid temperature gradient. The effects of thermophoresis on velocity measurements in flames has been studied by Sung et al. (1994), who also give formulae for the thermophoretic velocity (valid for particles smaller than 1 μm diameter). Based on these formulae, worst-case thermophoretic velocities (assuming 2000 K/mm temperature gradient at 1300 K, using air properties) in flames are about 15 cm/sec. It is a tempting possibility for the future that this could be corrected using the simultaneous OH PLIF images.

The other major PIV uncertainty is due to subpixel resolution. Westerweel (1993) finds that subpixel resolution uncertainty is about ± 0.1 pixels, about ± 9 cm/s in the present case. Furthermore, when there are strong velocity gradients, PIV measurements made using fixed interrogation regions are biased towards lower speeds because lower speed particles are more likely to remain in the interrogation region.

PIV accuracy is also affected by the elimination of spurious vectors and the interpolation of "dropouts", which arise when a good correlation is not obtained. Spurious vectors are eliminated using two filters:

- (1) Range filter: Checks that the vectors do not exceed reasonable limits on the u and v displacements.
- (2) Consistency filter: Checks that at least two of the eight nearest neighboring vectors have displacements within a radius of 2 pixels of the vector in question.

Both of these filters are derived from the experimental "rules of thumb" for good PIV set down by Keane & Adrian (1990): (1) that the displacement be less than 1/4 the interrogation region size, and (2) that the displacement vary less than a few percent from vector to vector.

Although average data yield is better than 98% for the measurements presented here, the missing vectors need to be interpolated from their neighbors to provide a complete field. The interpolation scheme used is a 2D linear interpolation method which solves the equations $\nabla^2 u = 0$, $\nabla^2 v = 0$, using valid vectors as Dirichlet boundary

conditions and the edges of the field as Neumann boundary conditions. The solution is obtained using a stable relaxation method. This interpolation method is simple and overdamped (i.e., the maximum and minimum values of the interpolated values are within the range of the valid vectors), but it is preferable to underdamped methods which can generate non-physical fluctuations.

3.2 OH Imaging

A major issue with OH PLIF imaging is interpretation of the images as an indicator of combustion reactions. OH is not always a reliable marker of where fuel is being consumed, because although OH formation reactions are fast ($\sim 20 \mu\text{s}$), the recombination reactions which eliminate OH are slow ($\sim 1\text{-}5$ ms). Hence OH tends to linger in high temperature zones, and cannot be considered to be in chemical equilibrium in most turbulent flows. The extent to which equilibrium is expected is characterized by the Damkohler number, $\text{Da} \equiv \tau_{\text{flow}}/\tau_{\text{chem}}$, a ratio of characteristic flow and chemical timescales. For the present flow $\tau_{\text{flow}} = \delta/U \sim 2\text{ms}$, so that $\text{Da} \sim 1$ based on recombination rates. Thus the presence of OH does not necessarily imply that heat release reactions are occurring.

As shown in the analysis given in Hasselbrink et al. (1997, 1998) it is unlikely that the particles affect the flame reactions or thermal transport in the flow, with the possible exception of radiative losses. Flames in a flow laden with Al_2O_3 particles are significantly brighter and yellower than without, and radiation losses are probably larger.

4. RESULTS

Figure 2 shows the context of the four measurement locations relative to the flame envelope. These are the lee and windward edges of the flame envelope at about 1/2 the distance from the flamebase to the flame tip, (which we call the $L/2$ position), and at the lee- and windward- side flamebases.

Figure 3 is a sampling of one velocity field with superimposed OH signal contours at each of the four locations described in Fig. 2. The OH regions at the $L/2$ position (Figs. 3(a), 3(b)) are typically thin sinuous regions, often with multiple radial layers and with occasional "islands" of OH. These same "islands" exist at the flamebase, but in general the OH regions are much broader there. The OH region in Fig. 3(c), for example, is approximately 7mm thick.

Examples of flame/flow interaction at the flamebase are clear in Figs. 3(c) and 3(d). In both cases, the leading edge of the flame lies in a low velocity region. In Fig. 3(c) the flow is also seen to accelerate through the flamebase, presumably due to dilation from the heat release. The effect is also clear in the average data (ensemble average of 109 fields) in Fig. 4(a) and (c), which compare the average OH contours and average velocity magnitude contours at the lee side flamebase position. The S-curved shape of the mean velocity magnitude contours corresponds to the OH

contours, implying that the heat release from the flame is responsible for the acceleration. A future comparison with a non-burning jet will be necessary to confirm this effect.

The same contour comparison for the windward side flamebase is shown in Figs. 4(b) and 4(d). The effect of the flame on the velocity field is not nearly as dramatic. We suggest that this is because the windward flamebase fluctuates (along the edge of the jet) significantly more than the lee side flamebase; since the flame is present less often at any one area, (as evidenced by the much smaller average OH signal levels), the ensemble-averaged data smears the instantaneous effects more significantly.

5. DISCUSSION

The OH images presented here are not shot-to-shot corrected, and hence cannot be considered quantitative. However, quantitative OH PLIF imaging has been successfully applied previously, and so it is intriguing to consider the possibility of quantitative OH PLIF imaging simultaneous with PIV. The only major new uncertainty is laser sheet extinction due to scattering by the PIV particles. The intensity I of the sheet after traversing a distance L through air seeded with particles is given by $I/I_0 = \exp(-\gamma L)$, where I_0 is the initial intensity and $\gamma = Q_{sc} n_{part} \pi a_p^2$. This formulation does not account for multiple scattering, and is only valid for $\gamma L \ll 1$. Using a typical PIV seeding density of $n_{part} = 100 \text{ mm}^{-3}$, scattering efficiency $Q_{sc} = 2$ and particle radius $a_p = 1 \mu\text{m}$, we estimate $\gamma = 6 \times 10^{-4} \text{ mm}^{-1}$. (Note that this assumed seeding density is about twice that assumed for autocorrelation PIV -- higher seeding densities are possible for cross-correlation PIV, and are desirable for PIV in flames due to the loss of density through the flame). Thus, every 10mm length of seeded air at typical PIV densities extinguishes the laser by about 0.6%. Since the region seeded with particles tends to flap $\pm 3\text{cm}$ in the wind tunnel, the uncertainty in the sheet extinction before the viewing region is about 1.8%. However, this should be confirmed by monitoring the sheet both before and after entering the test section on a shot-to-shot basis.

6. CONCLUSIONS

The application of PIV and OH PLIF techniques simultaneously provides information about flame and flow interaction that cannot be obtained with either technique separately. Streamline divergence upstream of the flamefront, acceleration of the flow through the flame, and the distortion of the flame by vortical motions are clearly visible in the data. Future work will continue to quantify the effects of the flame on the flow by comparing to a non-burning case. Also, measurement of the strain rates in the regions of high OH signal is another priority, in order to determine whether the flame is locally extinguished by high strain rates induced by turbulent motion.

It appears possible to improve on the present technique by implementing quantitative OH PLIF with PIV. However, this is not straightforward in the present flow configuration because this requires shot-to-shot sheet monitoring before and after the test section in order to ensure that laser extinction does not exceed several percent. Under these conditions, the dominant uncertainties would be the signal dependency on population and quenching (10%-20%) and camera and shot noise sources.

REFERENCES

- Barlow, R. S. and Collignon, A. 1991, Linear LIF Measurements of OH in Nonpremixed Methane-Air Flames: When are Quenching Corrections Unnecessary, Twenty-Ninth Aerospace Sciences Meeting, January 7-10, 1991, Reno, NV, Paper No. 91-0179.
- Becker, H. A. and Yamazaki, S. 1978, "Entrainment, Momentum Flux and Temperature in Vertical Free Turbulent Diffusion Flames", *Combustion and Flame* 33, pp. 123-149.
- Clemens, N. T. and Paul, P. H. 1995, "Effects of heat release on the near field flow structure of hydrogen jet diffusion flames", *Combustion and Flame* 102:3, pp. 271-284.
- Egolfopoulos, F. K. 1994, "Dynamics and Structure of Unsteady, Strained, Laminar Premixed Flames", in *Twenty-Fifth Symposium (International) on Combustion*, The Combustion Institute, Pittsburgh, PA, pp. 1365-1373.
- Hasselbrink, E. F., Mungal, M. G., and Hanson, R.K. 1997, "Planar Velocity Measurements and OH Imaging in a Transverse Jet", AIAA 35th Aerospace Sciences Meeting and Exhibit, Reno NV, Paper No. 97-0118.
- Hasselbrink, E. F., Mungal, M. G., and Hanson, R. K. 1998, "Simultaneous Planar Velocity Measurements and OH Imaging in a Transverse Jet Flame", *Journal of Visualization* vol. 1, to appear May 1998.
- Im, H. G. and Chen, J. H. 1997, Chemical Response of Methane/Air Diffusion Flames to Unsteady Strain Rate, Western States Section/The Combustion Institute, Fall Meeting, October 23-24, 1998, South Coast Air Quality Management District, Diamond Bar, CA, Paper No. 97F-111.
- Keane, R. D. and Adrian, R. J. 1990, "Optimization of particle image velocimeters, part I: double-pulsed systems", *Measurement Science and Technology* 1, pp. 1202-1215.
- Mueller, C. J., Driscoll, J. F., Sutkus, D. J., Roberts, W. L., Drake, M. C. and Smooke, M. D. 1995, "Effect of unsteady stretch rate on OH chemistry during a flame-vortex interaction: to assess flamelet models", *Combustion and Flame* 100:1-2, pp. 323-331.
- Muñiz, M., Martinez, R. E., and Mungal, M. G. 1996, "Application of PIV to Turbulent Reacting Flows", in Proceedings of the 8th International Symposium on Application of Laser Techniques to Fluid Mechanics, Lisbon, Portugal.
- Rehm, J. and Clemens, N. T. 1997, A PIV/PLIF Investigation of Turbulent Diffusion Flames, AIAA 35th

Aerospace Sciences Meeting and Exhibit, Jan 6-9, 1997, Reno, NV, Paper No. 97-0250.

Ruetsch, G., Vervisch, L. and Liñan, A. 1995, "Effects of Heat Release on Triple Flames", Physics of Fluids 7:6, p. 1447.

Sung, C. J., Law, C. K. and Axelbaum, R. L. 1994, "Thermophoretic Effects on Seeding Particles in LDV Measurements of Flames", Combustion Science and Technology 99, p. 119.

Westerweel, J. 1993, "Analysis of PIV Interrogation with Low Pixel Resolution", in SPIE-2005 Optical Diagnostics in Fluid and Thermal Flow, SPIE, San Diego, CA.

Veynante, D., Vervisch, L., Poinot, T., Liñan, A. and Ruetsch, G. R. 1994, "Effects of Heat Release on Triple Flames", in Proceedings of the Summer Program, Center for Turbulence Research, pp. 55-73.

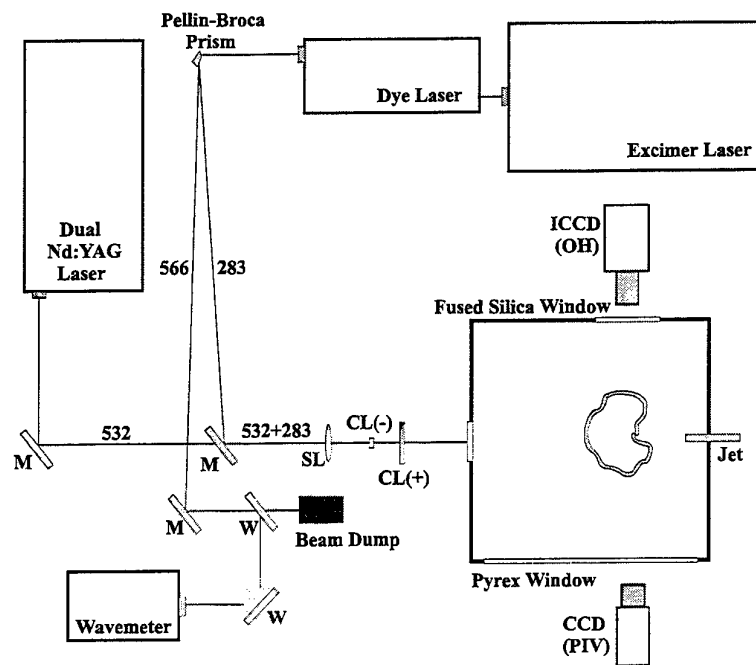


Fig. 1. Schematic for simultaneous OH PLIF and PIV. M denotes mirrors, SL a spherical lens, CL a cylindrical lens, and W denotes a glass optical window. A weak reflection of the fundamental from two windows is used to monitor the fundamental wavelength for the purpose of tuning the laser.

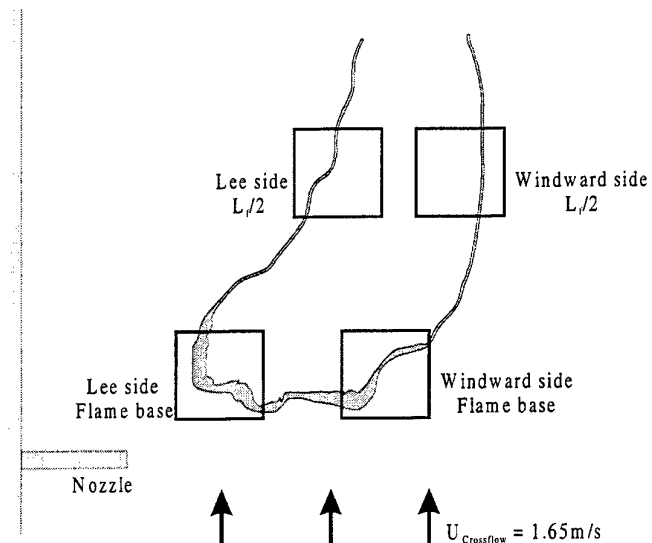
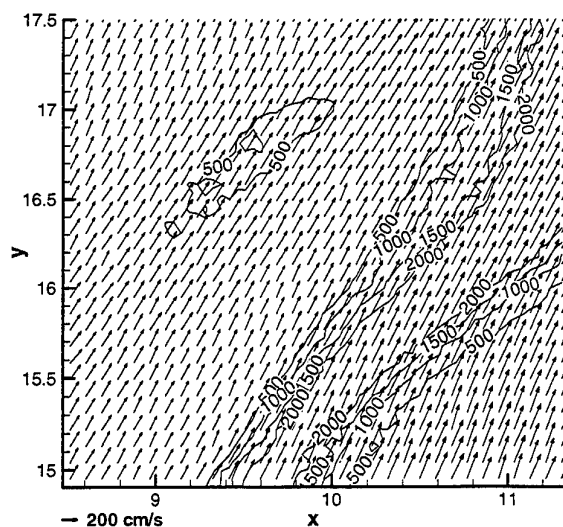
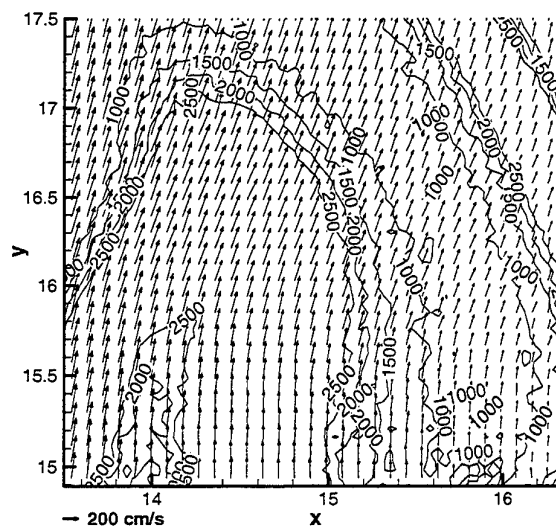


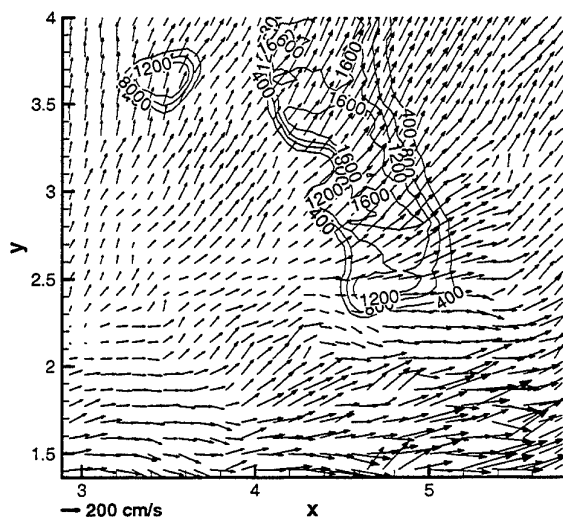
Fig. 2. Context of the four data locations in terms of the transverse jet flame. The visible emission from the lifted flame envelope is shown relative to the nozzle and the crossflow along with squares representing data locations.



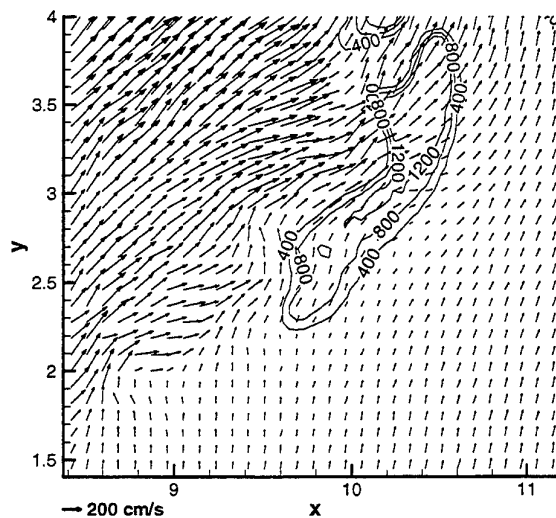
(a) Lee side, $L_t/2$ position



(b) Windward side, $L_t/2$ position

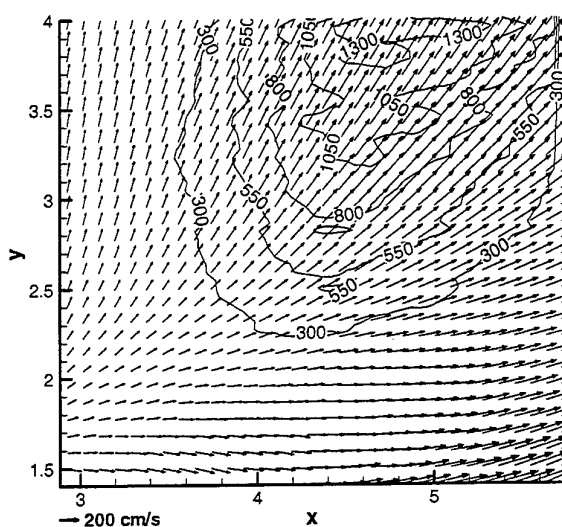


(c) Lee side, flamebase position

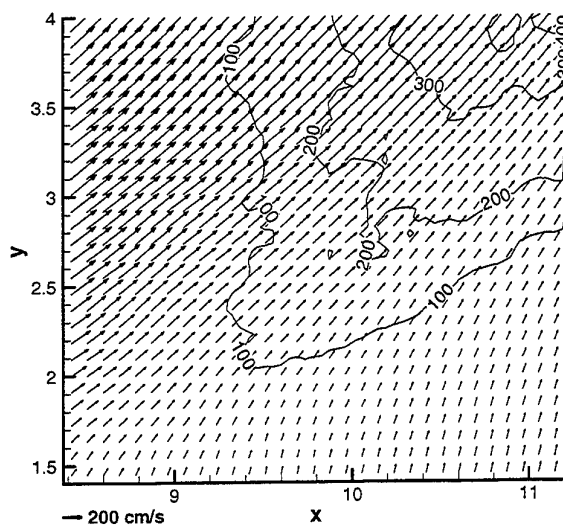


(d) Windward side, flamebase position

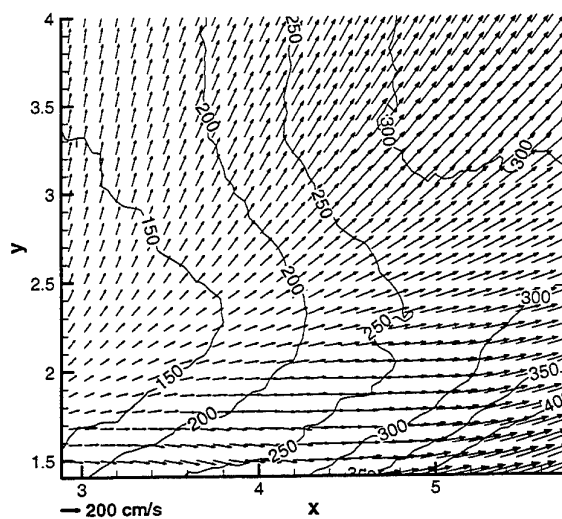
Fig. 3. A sampling of simultaneous OH PLIF/PIV realizations corresponding to each of the four locations depicted in Fig. 2. Axes are distance from the jet nozzle in centimeters. Contours are of OH signal. The higher speeds of the main jet flow are visible in the right edge of (a), the left edge of (b), the right/bottom edge of (c), and the left/upper edge of (d).



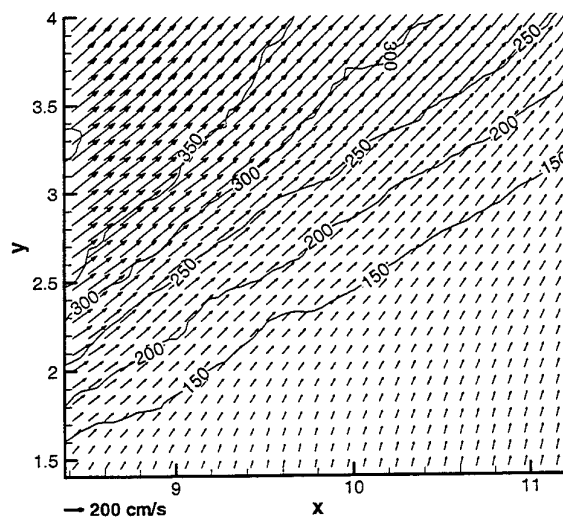
(a) Lee side flamebase, OH contours



(b) Windward side flamebase, OH contours



(c) Lee side flamebase, $|V|$ contours



(d) Windward side flamebase, $|V|$ contours

Fig. 4. Averaged OH (top) and velocity magnitude (bottom) in the lee side (left) and windward side (right) flamebase regions. Higher spatial fluctuations of the flame on the windward side leads to much lower average OH signal and a less noticeable effect on the flow due to the smearing caused by ensemble averaging.

SIMULTANEOUS P.I.V. AND OH PLANAR L.I.F. IN THE STABILIZATION REGION OF A LIFTED TURBULENT JET FLAME

C. Maurey, A. Cessou and D. Stepowski

CORIA UMR6614

CNRS-Université & INSA de Rouen, 76821 Mt St Aignan, France

ABSTRACT

The instantaneous velocity field has been measured in the stabilization region of a non-premixed turbulent jet flame. Particle Image Velocimetry (P.I.V.) and OH Planar Laser Induced Fluorescence (L.I.F.) have been performed simultaneously to study the jet dynamics at the flame lift-off location. The location where the velocity measurement has to be done is discussed. A conditional velocity measurement is performed from the simultaneous P.I.V. and fluorescence images and is compared to measurement at the bottom of the flame as it is done from decrease in particle seeding.

From recent works (Kaplan et al., 1994, Schefer et al., 1994) it appears that the flame stabilizes through turbulent premixed flame propagation. The turbulent propagation allows the flame to return to an upstream lift-off location after its extinction by a vortical structure.

1. INTRODUCTION

Stabilization of jet diffusion flames results from the competition of different physical phenomena : turbulent mixing, chemical reaction, ... As a result the understanding of flame stabilization is complex and numerous theories have been proposed in the past as reviewed by Pitts (1989). Vanquickenborne and Van Tiggelen (1966) proposed that the flame stabilization occurs where the flow velocity balances the turbulent flame speed along the stoichiometric line. From the same assumption Kalghatgi (1984) proposed an approximation law for lift-off height according to the type fuel and jet exit velocity. Peters and Williams (1983) described the flame lift-off phenomenon as the extinction of a non-premixed flamelet submitted to a too high scalar dissipation. Byggstøl and Magnussen (1983) have also proposed an extinction mechanism. The large scale structures of turbulence may also play

a role (Broadwell et al., 1984), (Miake-lye and Hammer, 1988).

Pitts (1989) concluded that the current experimental characterization of flame stabilization was insufficient to determine the actual physical processes that controls flame stabilization. So more recently numerical and experimental works have been carried out. Numerical investigation (Kaplan et al., 1994) shows that the flame stabilizes along the stoichiometric line and on vortical structures. The base of the flame is attached at a vortical structure, moves up with it and quickly jumps down to a new lower vortex. Recent numerical simulation of triple flame (Ruetsch et al., 1995, Veynante et al., 1994) provides also some interesting results to further investigate the behaviors of the flame in concentration gradient. Such behaviors could be expected in turbulent-jet flame. Due to the complex interactions which control the stabilization phenomenon simultaneous measurements are required with spatial and temporal resolutions. The expected role of the large-scale structures and the motion of the flame required at least 2D measurements to get conditional data. Schefer et al. (1994) have performed two-pulse images of the CH/ CH₄ distribution in a lifted CH₄-jet flame. The results show strong flame/vortex interactions which can lead to flame extinction resulting in downstream movement in the lift-off point or premixed flame propagation to upstream location. Due to significant entrainment of air by the fuel jet the fuel and air are premixed at the stabilization point (Schefer et al., 1994) and local stoichiometry and turbulent characteristics are primary factors controlling flame stabilization. Flow velocity field have been performed at the flame base (Muñiz and Mungal, 1997, Schefer and Goix, 1998) using P.I.V. with the use decrease in particle density as a marker for the high temperature region. The most upstream location of the high temperature region is used to define the flame base and perform a conditional velocity measurement.

2. EXPERIMENTAL SET-UP

Under these conditions the flame is lifted-off above the injector and is stabilized without pilot flame. The results for one operating condition alone are presented (Table 1). This condition corresponds to the "lift-off condition", i.e. the condition for which the flame lifts off when the jet velocity is increased. Measurements have been done from lift-off to blow-out and also in the hysteresis range, they are not presented here since the purpose of the paper is the conditional measurement method.

Table 1

U_0 (m/s)	Re	ID (mm)	OD (mm)	U_{coflow} (m/s)
20.37	2700	2	3	0.05

The coflow is seeded with zirconium particles (ZrO_2). Since these particles can survive flame temperatures the P.I.V. measurement can be done in the vicinity of the OH zones. Nominally $1\text{ }\mu\text{m}$ particles are entrained to the jet and seed the region where the flame stabilizes. These particles have the displacement ($\pm 10\%$) relative to the fluid for flow frequency of 4200 Hz . In addition particles experience

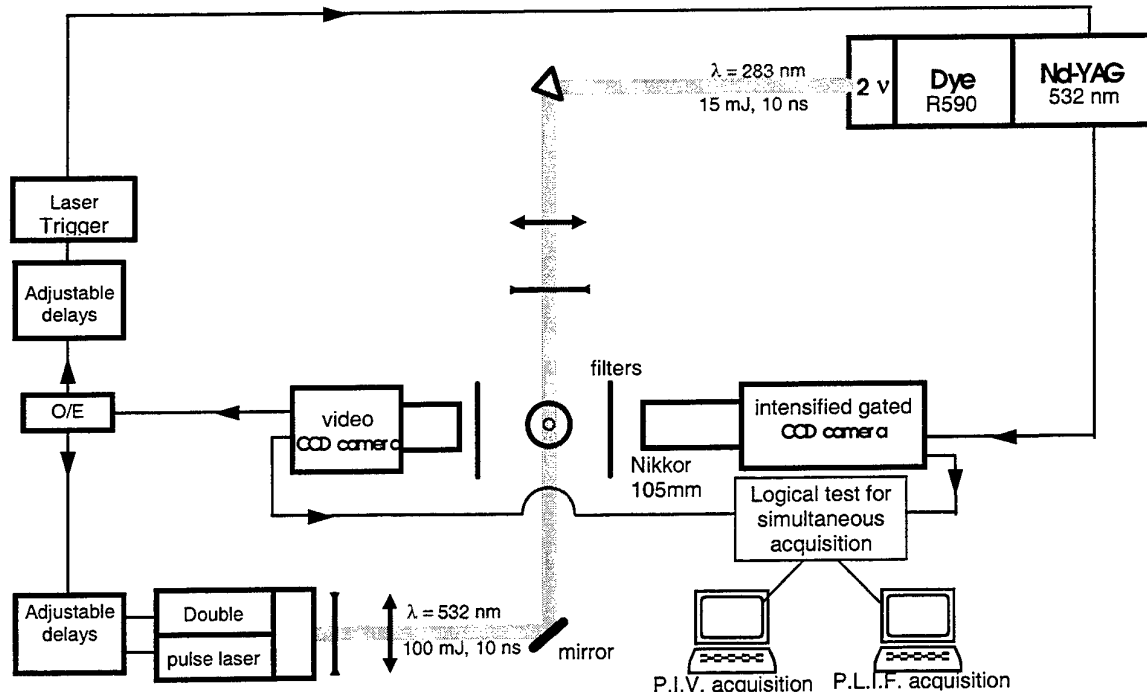


Figure 1: Experimental Set-up

thermophoretic forces in the temperature gradient at flame base. A specific investigation for ZrO_2 particles should be done but an error of few cm/s may be expected (Sung et al., 1994).

The ZrO_2 particles are illuminated by a double-pulsed laser sheet at 532 nm crossing the jet through a plane of symmetry (Figure 1). The laser source is the second harmonic of a Nd:YAG laser, 100 mJ/pulse, containing two independent cavities. A laser sheet (300 μm thick) is focused by a spherical ($f=1000$ mm) and a cylindrical ($f=-25$ mm) lenses. The scattered light is collected onto a CCD array (736 x 576 pixels) through an interferential filter to rejected at once the flame radiation and the scattered UV light from particles. Both successive images are stored on the odd and even CCD fields (Lecordier et al., 1994). Two fields of view have been imaged : the "near field" (3 cm x 2 cm) and the "far field" (7.5 cm x 6 cm). The time delay between pulses is 9 μs for the "near field" and 19 μs for the "far field" condition. The V2IP software package (Gatto et al., 1995) is used to work out the average particle displacement in each sub-region (64 x 64 pixels²) of the image by cross-correlation technique. The overlap between two neighboring sub-regions is 80%, and each vector represents the average velocity in a $6.2 \times 6.2 \times 0.35$ mm³ or $2.5 \times 2.5 \times 0.35$ mm³ for the far and near fields respectively.

The OH ground state is laser probed by pumping the $Q_1(6)$ line of the (0,1) vibrational band of the ($X^2\Pi-A^2\Sigma$) transition. Over the expected temperature range in the reaction zone (1200-1800 K) the relative population of the absorbing rotational level ($J''=6$) is nearly independent of the temperature. The laser bandwidth is about five times that of the absorption line so as to prevent spectral shift or fluctuation of the tunable laser source. The pulsed radiation ($\lambda \sim 283.9$ nm, $\Delta t = 10$ ns, $E \sim 20$ mJ) is provided by the second harmonic of a dye laser pumped by a Nd:YAG laser at 10 Hz. The fluorescence is detected via the (1,1) and (0,0) radiative relaxation bands ($\lambda \sim 315$ nm). The laser sheet (120 mm high x 400 μm thick) is focused in the same plane as P.I.V. measurement by a spherical lens ($f=1000$ mm) and a cylindrical lens ($f=-50$ mm). The fluorescence from the laser sheet is imaged at 90° onto a gated intensified CCD camera (576 x 384 x 14 bits) with a 105 mm, f/4.5 UV lens. The scattering at laser wavelength from the seeded particles is rejected by placing a high pass filter in front of the detector.

Timing of P.I.V. and L.I.F. lasers is monitored by the video clock of the P.I.V. camera which is divided by 5. Delays are adjusted to get the chosen delay between the two green pulses and to place the

UV laser pulse between the green pulses. With such a synchronization and a gate width of 30 ns no green scattered light from the particles are collected on the fluorescence images.

3. CONDITIONAL MEASUREMENT OF VELOCITY

In previous works (Muñiz and Mungal, 1997, Schefer and Goix, 1998) the abrupt drop in seeding due to the decrease in fluid density across the flame allows the thermal boundary of the flame base to be marked. However this method requires a confinement to insure a homogeneous seeding around the flame and it offers a low resolution and a low signal-to-noise ratio. Figure 2 shows the superposition of an instantaneous velocity field and the simultaneous OH L.I.F. image. It appears that the flame structure is quite complex in the flame stabilization region with a very sharp edge in the inner part of the OH zone. The calculation of the stabilization of a triple flame (Veynante et al., 1994) shows that the interaction of the flame with vortices leads to complex structures labeled "leading-edge

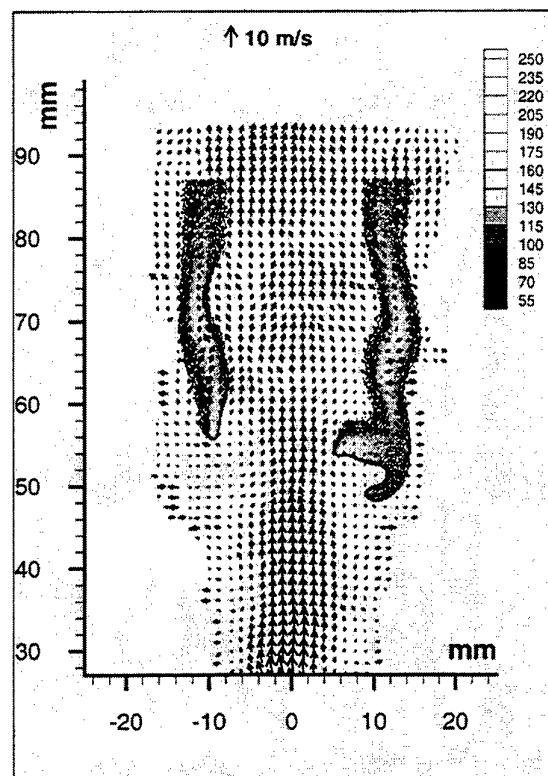


Figure 2 : example instantaneous velocity field and the simultaneous OH L.I.F. image ("far field")

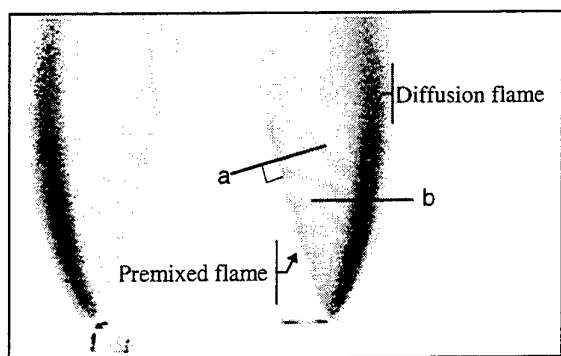


Figure 3: example of instantaneous image of OH P.L.I.F. in a rich premixed flame of CH_4 -air ($\phi=1.25$). (Gray scale is inverted, the stronger the signal is, the darker the image is.)

flame" rather than "triple flame". Thus such structures may be expected in the turbulent jet rather than the two wings of the triple flame.

Experimental results of Schefer et al. (1994) show that the flame can return to upstream locations when it was carried distances downstream by vortical structures, thus a premixed reaction zone must exist in the lower part of the flame. In addition the flame

stabilized in a layer where the mixture is stoichiometric (Kaplan et al., 1994, Schefer et al., 1994). The question is whether a stoichiometric premixed flame can be identified on the OH L.I.F. images?

From OH laser induced fluorescence all the OH radicals present in the laser sheet are observed. OH radical has a long lifetime due to its recombination by three-body reactions, and can be transported through the flow by diffusion and convection (Barlow et al., 1990, Cessou and Stepowski, 1996). At this point, let us compare the OH L.I.F. signal in a premixed flame and a diffusion flame.

OH P.L.I.F. has been performed in laminar Bunsen burner fed with methane-air mixture. The equivalence ratio, ϕ , is 1 or 1.25. Figure 3 shows an instantaneous image of OH P.L.I.F. in a laminar premixed flame of $\phi=1.25$. Two different reaction zones occur: an inner reaction zone which is the rich premixed front flame, surrounded by an outer diffusion flame where excess fuel burns with ambient air. OH radical trails downstream the premixed reaction zone due to its long lifetime leading to a smear in burned gases on the image. In the diffusion flame OH radical diffuses on either side of the reaction zone. Two profiles have been extracted (Figure 4): one

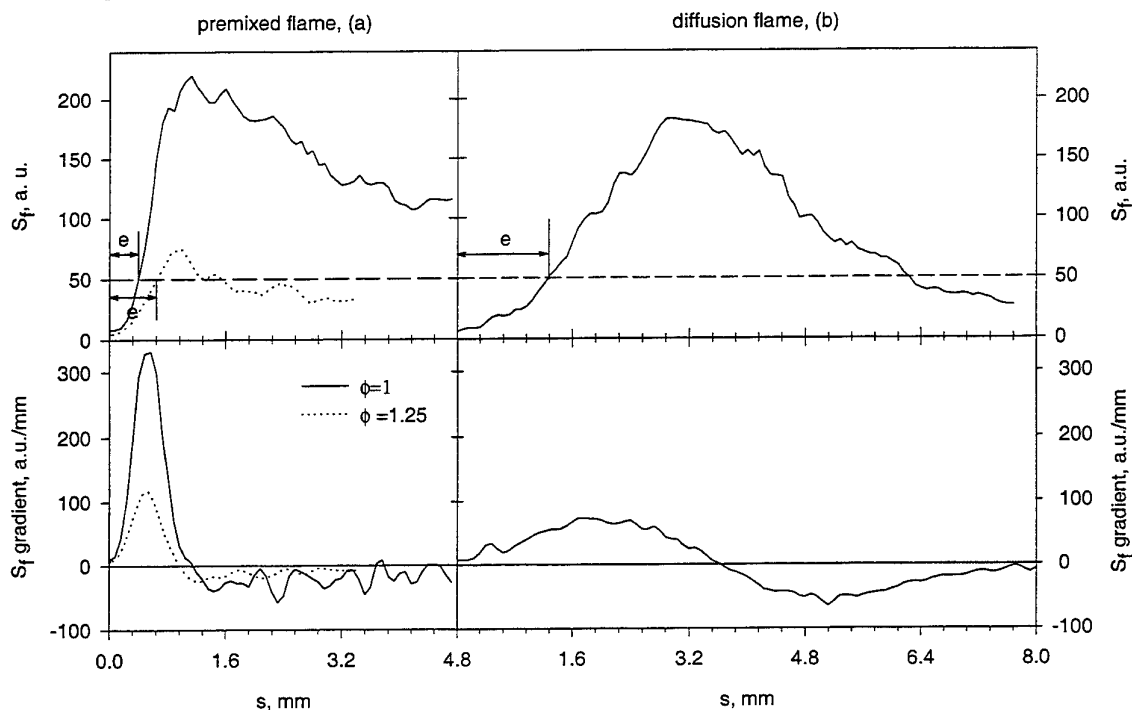


Figure 4 : at the top : example of instantaneous profile extracted through the premixed flames (a) and the diffusion flame (b), at the bottom : mean gradient of fluorescence signal calculated from the instantaneous profiles (a) and (b)

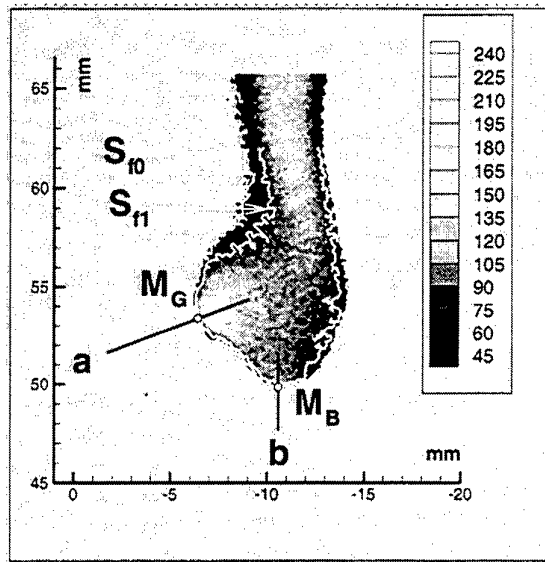


Figure 5 : example of instantaneous OH P.L.I.F. in the stabilization region of the turbulent jet flame, and determination of the points M_G and M_B

perpendicularly through the premixed flame front (Figure 3 a), another through the diffusion flame (Figure 3 b). Profile (a) shows a great dissymmetry, from the fresh gases the profile is very sharp while fluorescence signal decreases slowly in burned gases. Profile (b) is symmetric on both sides of the maximum. From all of the instantaneous profiles the mean gradient of the fluorescence signal is calculated and shown (Figure 4) for two premixed flame ($\phi=1$ and $\phi=1.25$) and the diffusion flame. For the two equivalence ratios the gradients of the fluorescence signal in the premixed flames are greater than this in the diffusion flame. Therefore the thickness, e , between two fluorescence signal levels is smaller in premixed flame than in diffusion flame (Figure 4). It is noteworthy that the gradient of OH fluorescence for stoichiometric premixed flame is much larger than for a diffusion flame.

This result leads one to suppose that the turbulent premixed reaction zone in the lower part of the lifted jet flame can be identified where the gradient of the fluorescence signal is maximum, more especially if the flame is stoichiometric. We have applied this assumption and compared with measurements at the bottom of the flame. In addition, it should be stressed that on OH L.I.F. images the fresh/burned gas interface can be clearly identified in a premixed flame by a sharp signal level gradient, while OH L.I.F. marks the reaction zone in a diffusion flame.

A threshold level, S_{f0} , is worked out to identify the OH fluorescence signal levels on the images. More details about the determination of S_{f0} is available in a paper of Cessou and Stepowski (1996). A second level, S_{f1} , is chosen above S_{f0} . The iso-lines $S_f=S_{f0}$ and $S_f=S_{f1}$ are extracted (Figure 5). Each contour line is then sampled at evenly spaced intervals

$ds_i = \sqrt{dx_i^2 + dy_i^2}$. For removing the digital noise, which is characterized by high frequency structures, the instantaneous contours are smoothed through a gaussian filtering with a width corresponding to the measurement resolution, namely $350 \mu\text{m}$. From the observation of the laminar premixed flame, the point, M_G , of the S_{f0} -line where the distance to the S_{f1} -line is minimum is defined as the lift-off location, namely the location of the turbulent premixed flame which stabilizes the jet flame. The location of this point M_G , i.e. the height and the radius, and the orientation of the S_{f0} -line are stored on each image.

Once the lift-off point is defined, the nearest velocity vector is worked out and the projection onto the normal direction to the contour at M_G is calculated. The normal direction is set positive towards the flame.

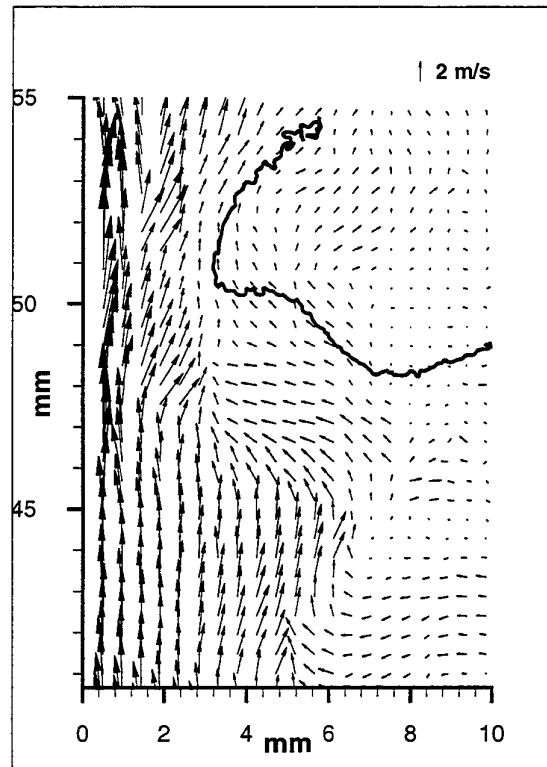


Figure 6 : instantaneous velocity field at the flame lift-off location, the outline of the OH fluorescence has been superimposed

This measurement is compared with the other method which consists in measuring the axial velocity at the bottom, M_B , of the flame (Figure 5), as it is performed in measurement from decrease in particle density (Muñiz and Mungal, 1997, Schefer and Goix, 1998).

4. DISCUSSION

Figure 6 shows an instantaneous velocity field in the region of lift-off location. The figure is a fraction of a "near field" image, the outline S_0 of the simultaneous OH fluorescence image is superimposed. The jet centerline velocity is about 5 m/s, the decrease from the inlet velocity is due to the entrainment of ambient air. With a centerline velocity of 5 m/s the velocity entrained air is of the order of 1 m/s. We can note that the flow field diverges as the flame is encountered and the streamlines upstream the flame have a complex meandering appearance. Thus the velocity vectors along the fluorescence outline in the lower part of the flame have many orientations.

Figure 7 shows the location of the lift-off points M_B and M_G . In this figure the mean location is almost the same for the both methods (black points in the figure), the differences in height and radius are 3.8 mm and 0.15 mm respectively.

The difference between the both measurement methods is more obvious when the instantaneous measurements are compared. Figure 8 shows the distance between the points M_G and M_B for each of the 40 images acquired. The distance is in order of 4 mm with a lot of shot to shot fluctuations, therefore the conditional velocity measurements in M_G and M_B will be different in magnitude and direction.

Figure 9 shows the histograms of conditional velocity V_G and V_B measured at the lift-off locations M_G and M_B respectively. V_G is the velocity component at M_G normally to the flame outline. V_B is the axial velocity at M_B . The histogram accounts only 40 samples but some differences already appear. The histogram of V_B looks like the measurement of Muñiz and Mungal (1997) On these histograms only the velocity of the flow at the flame base is shown thus the flame velocity is unknown and we do not know if the flame sustains instantaneously itself against the flow or not. At the time of the measurement we do not know if the flame is being carried distances downstream or is returning upstream locations. We note that the most probable velocity is about the laminar flame speed value ($S_L = 0.43$ m/s) showing that statistically the flame stabilizes in region where it can balance the flow field velocity. The maximum of the histogram of V_B is about 3 m/s and almost all the values are

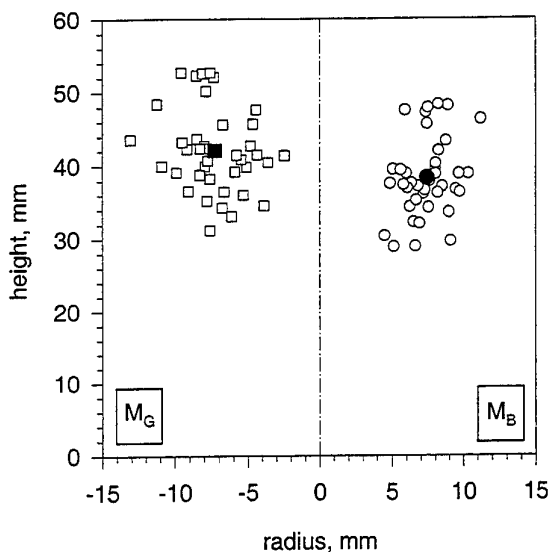


Figure 7 : instantaneous lift-off locations defined as M_G (on the left) or M_B , (on the right). The black points are the mean locations.

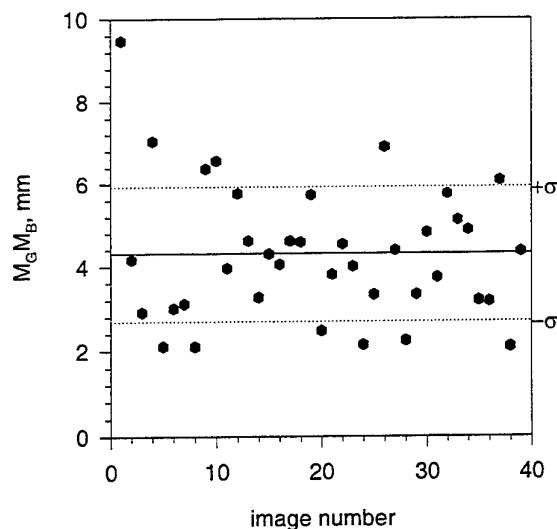


Figure 8: instantaneous distance between M_G and M_B for the 40 images acquired

positive. The maximum of the histogram of V_G is also about 3 m/s and the minimum is about -2 m/s. The occurrence of velocities less than 0 means that the fluid does not flows to the flame, fluid is entrained into the jet by a vortical structure. In this case or when the velocity is much larger than S_L the

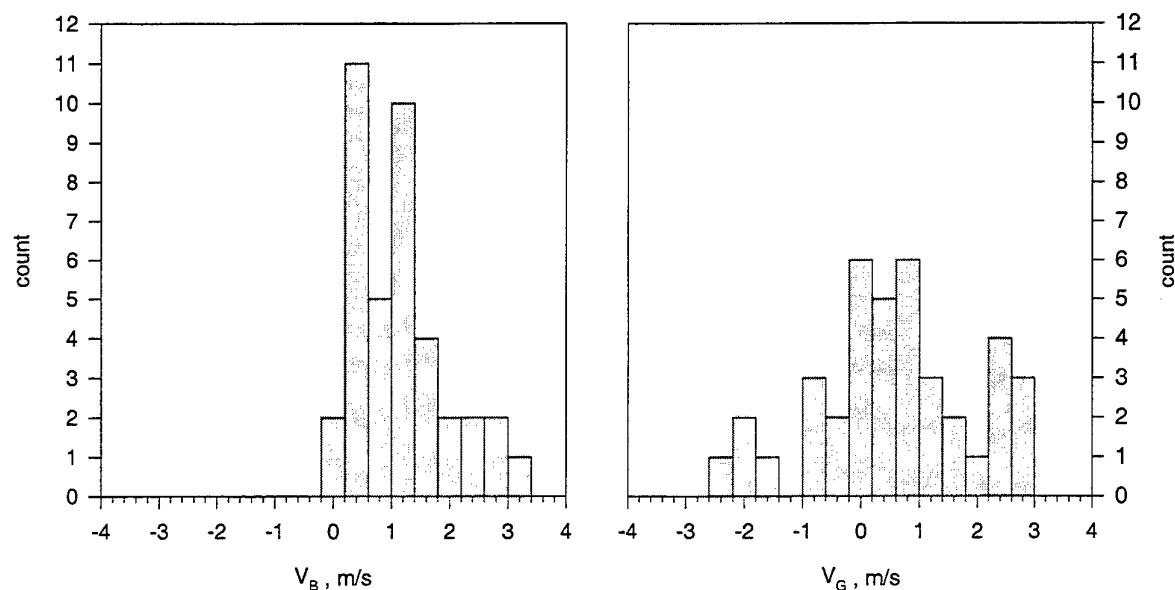


Figure 9 : conditional velocity V_B and V_G measured at M_B and M_G respectively from the 40 images acquired

flame does not sustain itself but propagates upstream or recedes downstream respectively. The histogram of V_B shows some skewness while it is more symmetric for V_G . This result has also been observed for different operating conditions not presented here.

5. CONCLUSION

Simultaneous P.I.V. and OH P.L.I.F. measurements have been performed in a turbulent lifted-jet flame. A method has been proposed to measure the conditional velocity of the flow at the flame base. The location where the reaction is the most intense at the flame base is identified on the OH fluorescence images. The flow velocity component is measured normal to the flame outline at this location. This measurement is compared with this performed at the lowest point of the OH fluorescence zone. Instantaneously the location, the magnitude and the orientation of the velocity at the two points are different. Although this weak sampling of this preliminary results some features of the flow at the flame base already appear.

The most likely flow velocity at the lift-off location is almost the laminar propagation speed S_L , the velocity ranges between $-4S_L$ and $6S_L$. We can expect that for the high velocity values the flame follows a vortical structure to downstream locations. When the flow velocity is less than zero the flame returns to upstream locations. From such measurements

it is difficult to deduce if the flame can be stabilized in an oncoming flow whose velocity is greater than S_L as expected from calculation of triple flame. Even if we note that the flow diverges as the flame is encountered a quantification of the decrease in oncoming velocity is tricky due to the meandering of the streamlines.

This paper presents some preliminary results of simultaneous measurements of velocity field and flame location and a proposition of conditional measurements. Parametric investigation of flame stabilization process requires now an improvement in measurement resolution and statistical sampling.

REFERENCES

- Barlow, R., Dibble, R. W., Chen, J.-Y., Lucht, R. P., 1990, Effect of Damköhler Number on Superequilibrium OH Concentration in Turbulent Nonpremixed Jet Flames, Combustion and Flame, vol. 82, 235
- Broadwell, J.E., Dahm, W.J.A., Mungal, M.G., 1984, Blowout of Turbulent Diffusion Flames, Proc. Twentieth Symposium (International) on Combustion, pp. 303-310, The Combustion Institute, Pittsburgh
- Byggstøl, S., Magnussen, B.F., 1983, A Model for Flame Extinction in Turbulent Flow., Proc. 4th Symposium on Turbulent Shear Flows, Karlsruhe, Germany, 1983
- Cessou, A., Stepowski, D., 1996, Planar Laser Induced Fluorescence Measurement of [OH] in the Stabilization Stage of a Spray Jet Flame, Combustion Science and Technology, vol.118, 4-6, p.361

- Gatto, B., Lecordier, B., Rouland, E., Vottier, S., Trinité, M., 1995, Logiciel de vélocimétrie laser par inter-corrélation d'images de particules (V2IP) , Concession du logiciel à LOT-ORIEL
- Kalghatgi, G.T., 1984, Lift-off Heights and Visible Lengths of Vertical Turbulent Jet Diffusion Flames in Still Air, Combustion Science and Technology, Vol. 41, pp. 17-29
- Kaplan, C.R., Oran, E.S., Baek, 1994, Stabilization Mechanism of lifted Jet Diffusion Flames , Proc. Twenty-Fifth Symposium (International) on Combustion, pp.1183-1189, The Combustion Institute, Pittsburgh
- Lecordier, B., Mouqalid, M., Vottier, S., Rouland, E., Allano, D., Trinité, M., 1994, CCD Recording Method for Cross-Correlation PIV Development in Unstationary High Speed Flow, Experiments in Fluids 17, pp. 205-208
- Miake-lye, R.C., Hammer, J.A., 1988, Lifted Turbulent Jet Flames : A Stability Criterion Based on the Jet Large-Scale Structure, Proc. Twenty-second Symposium (International) on Combustion. The Combustion Institute, Pittsburgh 1988, pp.817-824.
- Muñiz, L., Mungal, M.G., 1997, Instantaneous Flame-Stabilization Velocities in Lifted-Jet Diffusion Flames, Combustion and Flame, vol. 111, pp.16-31
- Peters, N., Williams, F., 1983, Liftoff Characteristics of Turbulent Jet Diffusion Flames, AIAA Jnl, Vol.21, n°3
- Pitts, W.M., 1989, Importance of Isothermal Mixing Processes to the Understanding of Lift-Off and Blowout of Turbulent Jet Diffusion Flames, Combustion and Flame, vol. 76, pp. 197-212
- Schefer, R.W., Goix, P.J., 1998, Mechanism of Flame Stabilization in Turbulent, Lifted-Jet Flames, Combustion and Flame, vol. 112, pp. 559-574
- Schefer, R.W., Namazian, M., Kelly, J., 1994, Stabilization of Lifted Turbulent-Jet Flames, Combustion and Flame, vol. 99, pp. 75-86
- Schefer, R.W., Namazian, M., Filtopoulos, E.E.J., Kelly, J., 1994, Temporal Evolution of Turbulence / Chemistry Interactions in Lifted, Turbulent-Jet Flames, Proc. Twenty-Fifth Symposium (International) on Combustion, pp. 1223-1231, The Combustion Institute, Pittsburgh.
- Sung, C.J., Law, C.K., Aaxelbaum, R.L., 1994, Thermophoretic effects on Seeding Particules in LDV Measurements of Flames, Combust. Sci. and Tech. Vol. 99, pp. 119-132
- Vanquickenborne, I., Van Tiggelen, A., 1966, The Stabilization Mechanism of Lifted Diffusion Flames, Combustion and Flame, vol. 10 , pp. 59-69
- Veynante, D., Vervisch, L., Poinot, T., Liñan, A., Ruetsch, G., 1994, in Studying of turbulence Using numerical Databases, eds. V.P. Moin and W.C. Reynolds, Center of Turbulent Research, Stanford University, pp. 55-73

DETECTION OF 3D TEMPERATURE GRADIENTS IN TURBULENT PREMIXED FLAMES WITH THE DUAL-SHEET LASER RAYLEIGH SCATTERING TECHNIQUE

Armin Soika, Friedrich Dinkelacker and Alfred Leipertz

*Lehrstuhl für Technische Thermodynamik (LTT)
Universität Erlangen-Nürnberg, Am Weichselgarten 8, D-91058 Erlangen, Germany*

ABSTRACT

Two closely separated laser light sheets have been employed to obtain high spatially and temporally resolved images of Rayleigh scattering instantaneously. Combined with appropriate image processing tools, three-dimensional thermal gradients can be evaluated and compared with results of laminar strained flame calculations. Here, good agreement could be found with our experimental investigations on premixed V-shaped flames in a grid generated homogeneous turbulent flow field. In order to study flame-vortex interactions the Karlovitz number $Ka = (\delta_{L,th}/l_K)^2$ was systematically modified by varying the equivalence ratio ϕ while keeping the turbulent Reynolds number Re_t constant at 87 or 134. Because of a nearly Gaussian shaped statistical distribution of the thermal gradients, the 50%-median and the width of the distribution are taken as suitable measures characterising the flame response on turbulent motions in the unburned gas.

It was found, that negatively curved cusps (concave towards the reactants) show a steepening of the flame temperature profile, while positively curved flame elements can be identified by a retardation of the overall reaction process. Regarding the thermal gradient distribution, the growing wrinkling of the flame front with increasing ϕ results in an increase of the width. Instead of thickened turbulent flames, as predicted by theory, we observe a reduction of the flame thickness especially for very lean flames ($\phi < 0.55$) marked with the highest Karlovitz number ($Ka = 4.6$).

Thus, we assume that in our experiments the flame response depends more on flame curvature than on effects caused by modification of Ka , but with the result of a significant reduction of the flame front thickness due to turbulent stretch.

1. INTRODUCTION

One current task of flame investigation is to find a suitable strategy for modelling turbulent flames in a reliable and adequate manner. Because of their complexity, the description of the interaction between the turbulent motion and the reaction in terms of curvature and tangential strain is difficult, but must be solved in regard of the importance of these additional mechanisms for heat and mass transport.

To classify different burning regimes according to the effects of these interactions, different burning diagrams with characteristic turbulence parameters and flame properties have been proposed e.g. by Borghi (1985) and Peters (1986) (Fig.1). Here, the field of premixed turbulent flames was subdivided into different sections, mainly distinguished by the shape of the flame front and its inner structure. Because of discrepancies between theoretical and experimental results, flames characterised by fast chemistry in regard of the time scales for turbulent mixing ($Da > 1$) but with sizes of the smallest eddies similar to the flame front thickness ($Ka \approx 1$) are object of recent investigations [Mansour et al. (1992), O'Young and Bilger (1997), Ferrao and Heitor (1993), Buschmann et al. (1996)]. On the basis of Damköhler's conception, Kolmogorov scaled vortices l_K are expected to penetrate into the flame front $\delta_{L,th}$ if $l_K \ll \delta_{L,th}$, thus enhancing the diffusive transport of heat and species with the result of thickened turbulent flames marked with a widely spread thermal gradient distribution. Nowadays it is assumed, that especially the scalar gradients in the "preheat zone" are affected by small scaled turbulent motions, while the structure of the "inner layer reaction zone" ($T \approx 1200$ K) remains unchanged [Peters (1997)]. Subsequently the thermal gradient distribution of the "inner layer" should be not affected by increasing Karlovitz

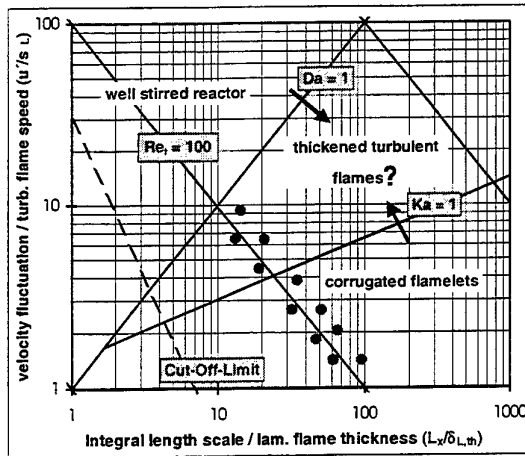


Figure 1: Classification of turbulent premixed flames, including our field of investigation ● and the Cut-Off-Limit [Poinso et al. (1996)] ---

numbers Ka . In contrast to that, recent numerical simulations of flame-vortex interactions showed less influence of small scaled vortices. Therefore Poinso et al. (1996) defined a "Cut-Off-Limit", below which vortex scales do not affect the flame front in a significant way.

To review the ability of small scaled eddies to penetrate into the reaction zone with the consequence of thickened turbulent flames, extensive experimental evidence is required. In the present study, the implication of turbulent motions on the reaction progress is figured by the thermal gradient

distribution. This is approached by visualisation of the instantaneous temperature field of a well defined flame configuration using an instantaneous dual-sheet Rayleigh temperature technique in combination with high spatial resolving detection systems.

2. EXPERIMENTAL ARRANGEMENT

2.1 Burner and Flow Configuration

The two dimensional V-shaped flame is stabilised by a 2 mm rod located 10 mm downstream of the burner exit in a circular coaxial jet with an inner core of premixed methane/air mixture with 40 mm in diameter. The burner is surrounded by an outer annular jet of filtered air with 150 mm in diameter in order to shield the methane/air jet from the mixing layer formed with the room air and to prevent the entrainment of dust particles, which would disturb the laser diagnostic measurements. Using a turbulence grid, nearly homogeneous turbulence conditions can be achieved in the region of the flame. With laser doppler anemometry (LDA) the mean axial velocity U , the rms-value u' of its fluctuation and the turbulent time correlation L_T have been determined at different downstream positions, from which the integral length scale L_x was derived (Table 1). The influence of the wire is only visible in the centre of the core region. In order to vary the turbulent flow field, flames with two different mass flow rates of 10 kg/h ($Re_t = 87$) and 18 kg/h ($Re_t = 134$) are investigated. For both cases,

Table 1: Experimental conditions and relevant parameters at a flow rate of 18 kg/h.

Turbulence intensity	u'	[m/s]	0.36					
Mean axial velocity	U	[m/s]	3.51					
Integral time scale	L_T	[ms]	1.7					
Integral length scale	$L_x = U \cdot L_T$	[mm]	5.96					
Turbulent Reynolds number	$Re_t = L_x \cdot u' / \nu$	[/]	134					
Kolmogorov scale	$l_K = 1.28 \cdot L_x \cdot Re_t^{-0.75}$	[mm]	0.194					
Taylor microscale	$l_T = 6.35 \cdot L_x \cdot Re_t^{-0.5}$	[mm]	3.26					
Turbulent strain rate	$a = u' / l_T$	[1/s]	110					
Equivalence ratio	ϕ	[/]	0.50	0.55	0.60	0.70	0.80	
Lam. flame speed	s_L	[m/s]	0.04	0.06	0.09	0.18	0.26	
Lam. flame thickness	$\delta_{L,th} = \nu / s_L$	[mm]	0.41	0.29	0.17	0.09	0.06	
x-Borghi	$L_x / \delta_{L,th}$	[/]	14	21	35	66	96	
y-Borghi	u' / s_L	[/]	9	6	4	2	1	
Damköhler number	$Da = (L_x / u') / (\delta_{L,th} / s_L)$	[/]	1.5	3.2	9.2	32.3	68.0	
Karlovitz number	$Ka = (\delta_{L,th} / l_K)^2 = 15^{-0.5} \cdot a \cdot \delta_{L,th} / s_L$	[/]	4.6	2.2	0.8	0.2	0.1	

the Karlovitz number, which represents a significant parameter describing the flame-vortex interaction in terms of a length scale relation or a dimensionless stretch number [Peters (1986), Abdel-Gayed et al. (1989)], was modified by altering the stoichiometry of the methane/air mixture between $\phi=0.5$ (very lean mixture) and $\phi=0.8$. Thus, the operating conditions are varied systematically along lines with constant turbulent Reynolds number in the region of the expected "wrinkled flamelets" ($Ka < 1$) and the expected "thickened turbulent flames" ($Ka > 1$) (Fig.1).

2.2 Dual-Sheet Laser Diagnostics

Figure 2 shows a schematic of the laser diagnostic set-up. The second harmonic beam from a Nd:YAG laser (532 nm) of 150 mJ/pulse is expanded with two planar-convex lenses. To enable the separation of the scattered light, we used a tuneable KrF-excimer laser operating at 248 nm (120 mJ/pulse) with ~ 0.001 nm linewidth as the second laser. Both laser beams are steered to pass through cylindrical lenses to be formed into two closely separated laser light sheets in the symmetric axis of the burner nozzle. The laser sheet thickness as well as the spacing of the two laser sheets was measured in the focus with a suitable beam profiler system, finding a $150 \mu\text{m}$ thickness for both laser sheets and a spatial separation of $400 \mu\text{m}$. At the focus, where the flame is situated, the detection area was confined to a 15 mm by 20 mm region with satisfactory beam profiles.

The signal of the dual-sheet Rayleigh scattering technique at incident laser frequency is separated by a

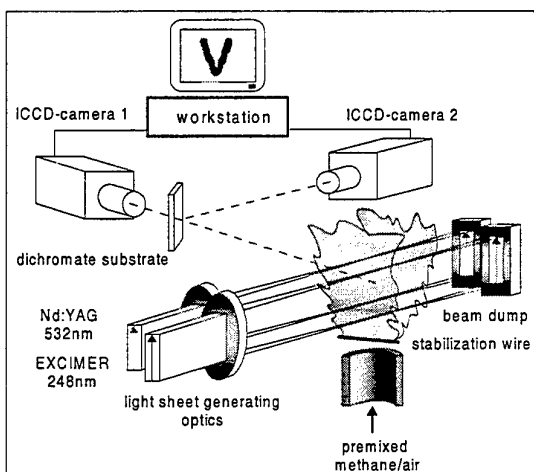


Figure 2: Experimental set-up for imaging of the inner structure of the reaction zone.

dichromate substrate. The scattered light at 532 nm was collected by a macro lens system (1:2.5/90 mm) with a spatial resolution of $75 \mu\text{m}$, while for the scattered light at 248 nm an UV-objective (1:4.5/105) has been used resulting in a spatial resolution of $62 \mu\text{m}$. To prevent emission interference, the two laser beams were temporally shifted by 250 ns, which is extremely small compared to the convection time of the flow. In combination with a temporal resolution of about 10 ns, "frozen structures" are imaged on two intensified charge-coupled device (ICCD) cameras with a dynamic range of 14 bits. Due to different flame speeds in the range of the investigated flame stoichiometries, different flame angles of the V-shaped flame are the consequence. To ensure the detection of the flame front under the same turbulent flow field, the downstream location chosen for scalar imaging correspond to 55 mm for the leanest flames and 25 mm for near stoichiometric flames.

3. DATA REDUCTION

3.1 Rayleigh Scattering Technique

The Rayleigh scattering signal is proportional to the number density of the molecules weighted with their Rayleigh scattering cross sections [Fourgette et al. (1986), Dibble and Hollenbach (1981)]. For the investigated premixed methane/air flames, the effective Rayleigh scattering cross section remains constant within $\pm 2\%$ in the unburned and burned side. Gas pressure variations are negligible with respect to the absolute pressure, so the ideal gas law can be used to relate the field temperature $T(x,y)$ to the number density, yielding for the flame temperature:

$$T_{\text{flame}}(x,y) = \frac{\bar{\sigma}_{\text{flame}}}{\bar{\sigma}_{\text{air}}} \cdot \frac{(I_{\text{air}} - I_{\text{back}})}{(I_{\text{flame}} - I_{\text{back}})} \cdot T_{\text{air}} \quad (1)$$

where I_{flame} and I_{air} represents the Rayleigh scattered light intensity of the flame image at unknown temperature and of a calibration image with air at defined temperature T_{air} . I_{back} is the background light intensity that includes the readout noise of the camera chip, while the relation of $\bar{\sigma}$ represents the weighted Rayleigh cross section of the flame and air sample volume. With respect to shot-to-shot energy fluctuations of the laser beam and systematic errors, the inaccuracy of the temperature measurements is estimated to be better than 15% for this experimental arrangement.

3.2 Image Processing

Based on the measured scalar temperature field the flame front thickness has been evaluated using suitable methods of digital image processing. In a first step, the temperature field was spatially filtered twice by assigning the median value of each 3x3 kernel to the central pixel before the three-dimensional gradients were determined using the following expression.

$$\text{grad}T(x, y, z)_{3D} = \left(\left(\frac{T(x + \Delta x) - T(x - \Delta x)}{2\Delta x} \right)^2 + \left(\frac{T(y + \Delta y) - T(y - \Delta y)}{2\Delta y} \right)^2 + \left(\frac{T(z + \Delta z) - T(z)}{\Delta z} \right)^2 \right)^{0.5} \quad (2)$$

The terms on the right hand side represents the contributions of each dimension to the local thermal gradient, with Δx and Δy as the spacing in the plane of one laser sheet and Δz as the separation distance between both. For the determination of the depth gradient (third term), an accurate point to point relation between the two temperature images is required. Therefore, a mesh target was imaged to define a transformation rule, which allows the attachment of corresponding pixels with an accuracy of 1 pixel, i.e. around 75 μm .

The obtained gradient field $\text{grad}T(x, y, z)_{3D}$ can be used to calculate the turbulent flame front thickness conditioned at specified reaction progress variables $c = (T - T_{\min}) / (T_{\max} - T_{\min})$.

$$\delta_{T,c} = \frac{T_{\max} - T_{\min}}{(\text{grad}T)_{3D}|_c} \quad (3)$$

To account for the measured temperature field, the maximum and minimum temperature level T_{\max} and T_{\min} were determined by taking the average value of a 20x20 pixel kernel in the corresponding temperature region.

3.3 Advantages of the Dual-Light Sheet Technique

To ensure the accurate distinction of the temperature gradients, three-dimensional effects resulting from fluctuating inclination of the flame front relative to the laser have to be excluded [O'Young and Bilger (1997)]. As a test, the extent of different intersection angles on the temperature

gradient distribution was approximated by turning the flame relative to the two parallel light sheets. The flame front thickness of a weak ($\phi = 0.55$) as well as of a strongly corrugated flame ($\phi = 0.7$) was determined under angles of 90° (perpendicular intersection), 60° and 30° using both two and three-dimensional evaluation procedures.

Independent of the intersection angle and stoichiometry, the flame front thickness obtained with the 3D-gradient technique matches within $\pm 100 \mu\text{m}$ with the measured flame thickness for perpendicular crossing. From that the resulting accuracy of the 3D-data is estimated to be about 100 μm . The 2D-thickness, determined from a single laser light sheet, corresponds to the 3D-data for 90°, while for 60° and 30° the temperature slope is decreased, as expected. Since here the flame thickness depends strongly on the intersection angle, we used the double light sheet technique combined with the corresponding data processing for all subsequent experimental investigations.

A typical probability density function (*pdf*) of the measured 3D-gradients conditioned at $c = 0.6$ is shown in Fig. 3 for a flame with $\phi = 0.5$ and $Re_t = 134$. Regarding the shape of the gradient-*pdf*, a nearly Gaussian distribution can be seen. As a characteristic average value, the 50%-median (here nearly equal to the *maximum* and the *mean*) of the function is compared with numerical data. In a test case with artificial flame fronts, the whole image processing procedure was applied revealing good agreement with the pretended values.

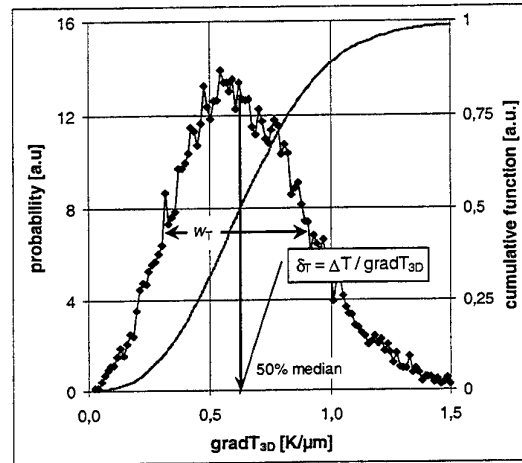


Figure 3: Distribution of the temperature gradients for $\phi = 0.5$, conditioned at $c = 0.6$. Determination of the average gradient (50% median) and the width w_T

As a second parameter, the *width* w_T can be determined as a measure for the fluctuation of the temperature gradient at the specified condition c .

From 30 obtained images per flame type, about $(600 \times 30 =)$ 18000 flame front gradients have been measured each to ensure an appropriate statistical accuracy. This allows a detailed analysis of the turbulent interactions and the corresponding perturbations of the flame front.

4. RESULTS AND DISCUSSION

As a significant flame parameter, the turbulent flame front thickness δ_T computed with the steepest thermal gradients is used to examine the influence of turbulent eddies on the chemical reaction progress. In terms of a pre-evaluation process, the maximum temperature rise was found to be located around $c=0.6$ for all investigated flames, that why the obtained results and conclusions are confined to that reaction progress variable.

4.1 Comparison between 2D and 3D-Data

One of the main attributes of turbulent motion is its three dimensionality and randomness in time and space. From this point of view, it is reasonable to expand the planar detection of the temperature field by one laser light sheet to a quasi-three-dimensional imaging technique. The necessity can easily be derived from Fig. 4, showing two simultaneous mapped planar temperature fields of a strongly wrinkled flame with $\phi=0.8$, which were binarized both at the threshold temperature $T_{c=0.6}$ together with their superposition.

On a first glance, the two closely separated images show the same topology, but only when overlaid, the small differences become obvious. In spite of the nearly planar flame surface of the V-shaped flame, additional thermal gradients due to flame curvature normal to the detection plane are taken into account at the computation of the flame front thickness. Therefore, this new measurement technique gains in necessity the more wrinkled and corrugated the flame front is.

4.2 Observed Temperature Profiles

One of the major interest of our investigations was the comparison between data sets from laminar flame

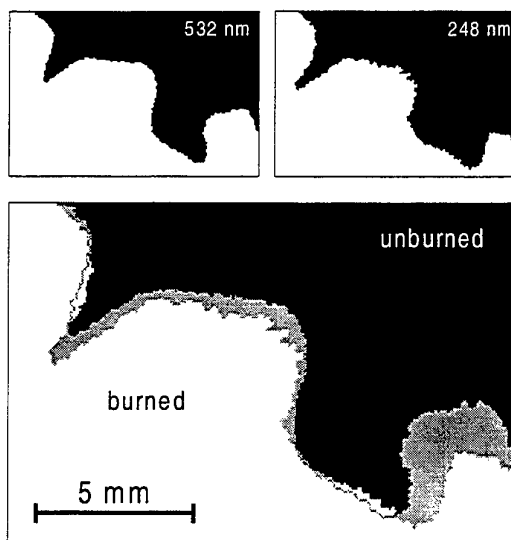


Figure 4: Temperature fields, binarized at $c=0.6$ from two closely separated laser light sheets, and their superposition ($Re_t = 134$, $\phi = 0.8$).

calculations (CHEMKIN) [Kee et al. (1991), Hemm (1997)] with those generated with experimental measurements. Here, the temperature profiles of the investigated flame configurations were object of detailed examinations. As a first result, the maximum temperature level T_{max} was found to be approximately 250 K below the adiabatic flame temperature T_{ad} , while the minimum temperature level T_{min} fits well with the initial set conditions of the numerical simulation ($T_{inlet} = 300$ K). For an explanation, we regard the lack of heat radiation in the laminar flame calculations to be responsible for the discrepancy between the temperature profiles especially at higher temperatures.

Here, two reasons support our line of argumentation. Firstly, the amount of transferred heat increases strongly with temperature (proportional to the fourth power of T) and is therefore linked only with elevated temperatures. Analyses of the gaseous heat radiation revealed, that the emission spectrum lies mainly in the infrared ($>1 \mu m$) with CO_2 and H_2O as the predominant contributors [Hottel et al. (1935)]. Because these species only appear in the hot exhaust gas, the influence of heat radiation is confined to higher reaction progress variables c (e.g. $c=0.8$).

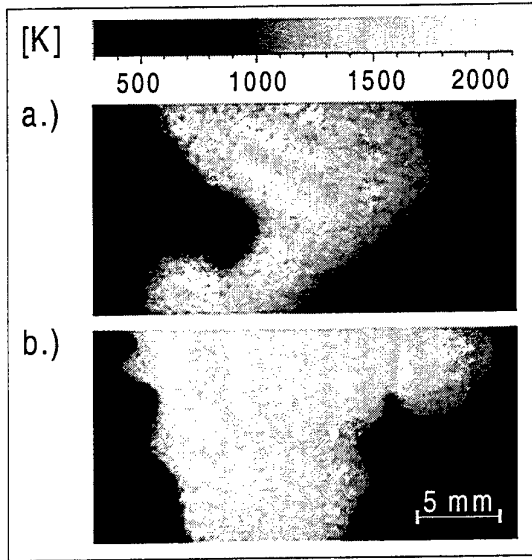


Figure 5: Instantaneous temperature fields of two different flames ($Re_t = 134$). a.) $\phi = 0.5$ b.) $\phi = 0.7$

Concluding, we expect heat radiation with only minor extend in the "preheat zone" and "inner layer" up to $c = 0.7$, while with increasing reaction progress radiation is responsible for reduced upper temperature level. To enable the comparison between measurement and calculation and therefore the validation of consisting combustion models of premixed turbulent flames, the measured thermal gradients subsequently have to be related to the adiabatic temperature level T_{ad} , leading to

$$\left. \text{grad} T_{3D,rel} \right|_c = \left. \text{grad} T_{3D} \right|_c \cdot \frac{T_{ad}}{T_{max}} \quad (4).$$

4.3 Modification of Thermal Gradients due to Curvature

Figure 5 shows two characteristic instantaneous temperature fields for flames with $\phi = 0.5$ and $\phi = 0.7$, both in a turbulent flow with $Re_t = 134$. Obviously one can see differences concerning the curvature radii and the frequency with which the perturbations of the flame front occur. To reveal the influence of this two different flame modes, detailed examinations at different curved flame front elements were made and compared with laminar unstrained calculations.

For $\phi = 0.7$, Fig.6 illustrates the differences of the temperature gradients between positive and negative curved flame fronts as a function of temperature. Both diagrams contain the data of ten selected flame

front areas with individual kernel sizes adapted to the local flame structure.

Flame front elements orientated convex towards the unburned gas (positive curvature) have smaller temperature gradients than laminar unstrained flames. Moreover the maximum temperature level is reached only far behind the flame front, approximately in a distance equal to the curvature radius. This can be explained by a defocusing effect of heat at positively curved flame elements. In case of negative curved regions, the temperature gradients are significantly higher and even partly beyond the calculated gradients. Here, high temperatures can be detected right behind the flame front, while the gradients in the "preheat zone" are smoother. This is due to a focused heat transfer to the fresh and unburned gas, resulting

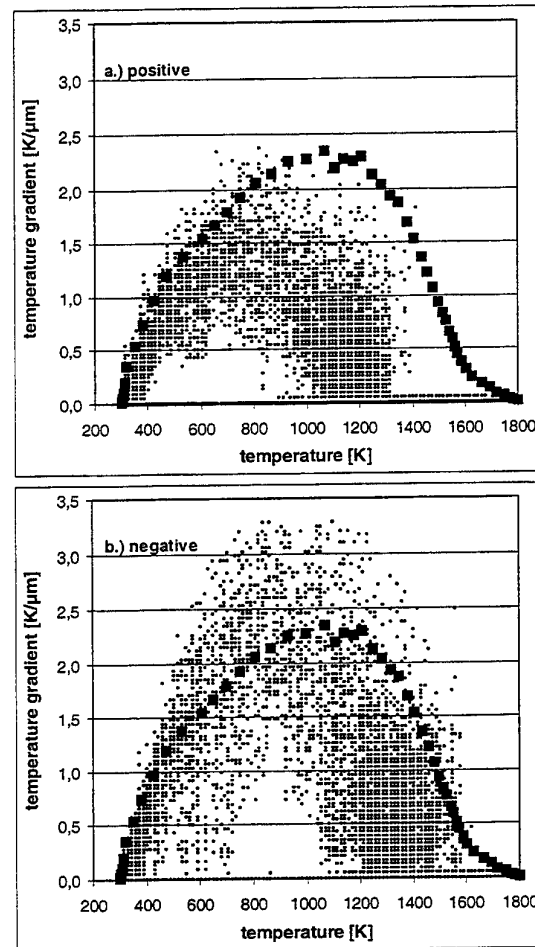


Figure 6: Scatter plot of temperature gradients for a flame with $\phi = 0.7$ at a.) positive b.) negative curved region. Squares represent calculated laminar unstrained temperature gradients (CHEMKIN).

in an elevated temperature level. The mechanism of diffusional transport of heat as well as their importance on flame stability is discussed in detail by Law (1988) and Rutland/Trouvé (1993). Concerning the distribution of the thermal gradients for $c=0.6$, this behaviour is also reflected by slightly increasing widths $w_{T,c=0.6}$ with increasing mixture fractions ϕ (decreasing Ka). This observation was made independent of the investigated turbulent Reynolds number Re_t .

With regard to the consisting flame theories, we can not confirm experimentally the ability of small eddies to penetrate into the flame front, because then molecular mixing would result in a reduction of the thermal gradients and above all to more spread gradient distribution especially for flames with the highest Ka numbers. Instead, our results confirm more the existence of a undisturbed "inner layer" located around a reaction progress variable $c=0.6$ due to the small rate of change of the width $w_{T,c=0.6}$, which obviously is linked to curvature.

Thus we regard the influence of the smallest eddies l_K to be smaller than expected from theory due to damping of turbulent motions by the increase of viscosity with temperature. Moreover, studies of She et al. (1990) have revealed only locally confined turbulent structures like vortex tubes, so that interactions occurs only at some rare flame front elements. This fits quite well with numerical simulation of flame-vortex interactions [Poinsot et al. (1996)] and justify the definition of a "Cut-Off-Limit"

for turbulent scales.

4.4 Modification of the Global Flame Thickness

Regarding the average turbulent flame thickness conditioned at $c=0.6$ (defined here as the "inner layer") in Fig.7, the thickness $\delta_{T,c=0.6}$ is increasing for $Ka < 0.5$, while flames with $Ka > 0.5$ are marked with a significant decrease in comparison with laminar unstrained calculations. These three-dimensional measurements confirm previous results from 2D-measurements [Buschmann et al. (1996)]. Furthermore, good agreement with strained laminar calculations [Pitsch (1996), Sung et al. (1996)] at equal turbulent strain rate could be found. Thus, the flame behaviour in turbulent flows seems to be dominated by stretch, resulting in a reduction of the flame thickness for lean mixtures. The extent depends strongly on the mixture fraction ϕ .

5. CONCLUSION

For premixed turbulent flames it was assumed that for increasing turbulence intensity and especially for Karlovitz numbers above one a regime with thickened flames exist (e.g. Borghi diagram). Since the measurement of the instantaneous local flame structure is very difficult for premixed turbulent flames, it was not possible in the past to measure the detailed flame front in a conclusive way. With the application of laser diagnostic techniques in the dual plane approach instantaneous 3D-temperature gradients of a axisymmetric V-flame with nearly homogeneous turbulence have been determined. In order to modify the Karlovitz number Ka of the reacting flow, the stoichiometry was changed systematically, while holding the turbulent Reynolds number constant at either $Re_t=87$ or 134 . Resulting from frequent highly curved flame elements, near stoichiometric flames are characterised by more wrinkled flames and a broadened distribution of the gradients.

The assumption that for $Ka > 1$ the smallest eddies entrain into the reaction zone and widen could not be verified for the conditions measured here, while our results confirm more the existence of a undisturbed "inner layer" at a reaction progress variable $c=0.6$.

Although the flames were investigated in a moderate turbulent flow field ($Re_t=87$ and 134), large part of the flames especially for $\phi=0.5$ have a flame structure as being close to the "laminar region". It seems, that the theoretically expected limit between laminar and turbulent flames with $Re_t=1$ is an underestimation. Instead of that a "Cut-Off-Limit",

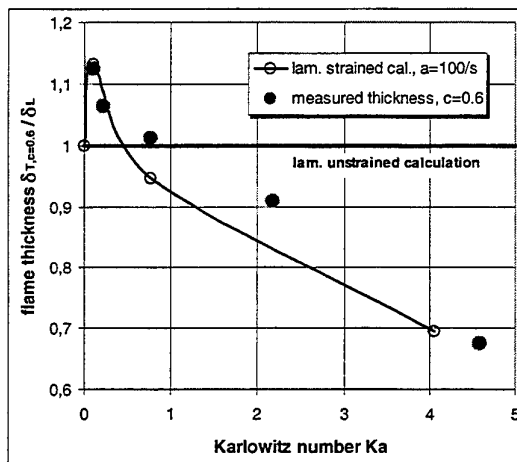


Figure 7: Measured turbulent flame thickness conditioned at $c=0.6$, normalized with the laminar unstrained flame thickness δ_L (CHEMKIN). For comparison the thickness determined from laminar strained calculation ($a=100$ 1/s) is enclosed.

proposed from direct numerical simulations [Poinso et al. (1996)] below with the influence of turbulent eddies on the flame can be neglected, might be more relevant. Note that only the shape of this limit was fixed without exact location in the field of turbulent premixed flames.

Therefore it can be concluded, that in our experiments the spread of the thermal gradient distribution depends more on the flame curvature than on the Karlovitz number. The influence of Kolmogorov scaled eddies seems to be negligible compared to the turbulent strain rate acting in the tangent plane of the flame front, resulting in an overall reduction of the flame front thickness.

ACKNOWLEDGEMENT

The authors gratefully acknowledge financial support of parts of the work by Deutsche Forschungsgemeinschaft (DFG).

REFERENCES:

- Abdel-Gayed, R.G. Bradley, D. & Lung, F.K. 1989, Combustion Regimes and the Straining of Turbulent Premixed Flames, Combustion and Flame, The Combustion Institute, vol. 76, pp. 213-218.
- Borghi, R. 1985, in Recent Advances in Aeronautical Science, ed. Bruno C, Casci C., pp. 117-134, Pergamon, London.
- Buschmann, A., Dinkelacker, F., Schäfer, T., Schäfer, M. & Wolfrum, J. 1996, Measurement of the Instantaneous Detailed Flame Structure in Turbulent Premixed Combustion, 26th Symposium (Int.) on Combustion, The Combustion Institute, Pittsburgh, pp. 437-445.
- Dibble, R.W. & Hollenbach, R.E. 1981, Laser Rayleigh Thermometry in Turbulent Flames, 18th Symposium (Int.) on Combustion, The Combustion Institute, Pittsburgh, pp. 1489-1499.
- Ferrao, P. & Heitor, M.V. 1993, On the Analysis of Turbulent Mixing in Recirculating Flames, Proceedings of the Joint Meeting of the British and German Sections of the Combustion Institute, Queens College, Cambridge, pp. 80-83.
- Fourquette, D.C., Zurn, R.M. & Long, M.B. 1986, Two-Dimensional Rayleigh Thermometry in a Turbulent Nonpremixed Methane-Hydrogen Flame, Combust. Sci. and Tech., vol. 44, pp. 307-317.
- Hemm, A. 1997, Einfluß der Rauchgas-rezirkulation auf die Flammenfrontstruktur von laminaren Vormischflammen, LTT-Rept. LTT97-02.
- Kee, R.J., Grcar, J.F., Smooke, M.D. & Miller, J.A., 1991, CHEMKIN- A Fortran Program for Modelling Steady Laminar One-Dimensional Premixed Flames, Sandia Rept. SAND85-8248.
- Law, C.K. 1988, Dynamics of Stretched Flames, 22th Symposium (International) on Combustion, The Combustion Institute, Pittsburgh, pp. 1381-1402.
- Mansour, M.S., Chen, Y.-C. & Peters, N. 1992, The Reaction Zone Structure of Turbulent Premixed Methane-Helium-Air Flames Near Extinction, 24th Symposium (Int.) on Combustion, The Combustion Institute, Pittsburgh, pp. 461-468.
- O'Young, F. & Bilger, R.W. 1997, Scalar Gradient and Related Quantities in Turbulent Premixed Flames, Combustion and Flame, The Combustion Institute, vol. 109, pp. 682-700.
- Peters, N. 1986, Laminar Flamelet Concepts in Turbulent Combustion, 21th Symposium (International) on Combustion, The Combustion Institute, Pittsburgh, pp. 1231-1250.
- Peters, N. 1997, Turbulent combustion: Introduction and Overview, ERCOFTAC Summer School on Turbulent Combustion: Modelling and Diagnostics, Aachen.
- Pitsch, H. 1996, private communication, RWTH Aachen.
- Poinso, T., Candel, S. & Trouvé, A. 1996, Application of Direct Numerical Simulation to Premixed Turbulent Combustion, Prog. Energy. Combust. Sci., vol. 21, pp. 531-576.
- Rutland, C.J. & Trouvé, A. 1993, Direct Simulations of Premixed Turbulent Flames with Nonunity Lewis Numbers, Combustion and Flame, The Combustion Institute, vol. 100, pp. 485-494.
- She, Z.-S., Jackson, E. & Orszag, S.A. 1990, Intermittent Vortex Structures in Homogeneous Isotropic Turbulence, Nature, vol. 344, pp. 226-228.
- Sung C.J., Liu, J.B. & Law, C.K. 1996, On the Scalar Structure of Nonequidiffusive Premixed Flames in Counterflow, Combustion and Flame, The Combustion Institute, vol. 106, pp.168-183.

THE EFFECT OF ROTATION ON BLUFF-BODY STABILISED FLAMES

D. Duarte and P. Ferrão

INSTITUTO SUPERIOR TÉCNICO

Dept. of Mechanical Engineering

Av. Rovisco Pais

1096 Lisboa Codex

Portugal

ABSTRACT

Measurements in baffle-stabilised flames for $Re = 1.5 \times 10^5$ and different swirl numbers are used in this paper to improve our understanding of the effect of pressure gradients on the conservation of turbulent kinetic energy and of the turbulent flux of the mean reaction progress variable, \tilde{c} , or turbulent heat flux, $\overline{p u_i c}$, for strongly sheared flames. To achieve these objectives, a previously reported LRS/LDV system (Ferrão and Heitor, 1998) was conveniently optimised to provide simultaneous velocity-scalar measurements, which allow for the quantification of detailed heat transfer characteristics.

The physical phenomena responsible for the turbulent diffusion of \tilde{c} were studied using the transport equation for $\overline{p u_i c}$, where the pressure gradients have been obtained by analysis of the transport equation of momentum. The results obtained for the highly sheared turbulent flames studied are consistent with previous DNS calculations for basic flamelet combustion and show that a pressure decrease from unburnt to burnt gases promote counter-gradient transport.

1 INTRODUCTION

Recent direct numerical simulations (DNS) of premixed combustion in isotropic turbulent flows for low Reynolds number, representative of flamelet combustion (Veynante et al, 1997), reveal that the local flow structure near the flame influence the dominant regime for turbulent transport, namely counter-gradient or gradient scalar transport. In addition, DNS calculations reported by Veynante and Poinot (1997) show that the mean pressure gradient across the flame front modifies the turbulent flame structure due to differential buoyancy mechanisms between heavy cold and light hot gases. The result is that pressure decreases from unburnt to burnt gases is found to decrease wrinkling, flame brush thickness,

turbulent flame speed and to promote counter-gradient transport. In this context, this paper extends this analysis to high Reynolds number flames, making use of detailed measurements of velocity and scalar characteristics in baffle-stabilised flames under different pressure fields.

It is well known that previous attempts to extend knowledge on laminar flames and non-reacting fluid mechanics, to turbulent combustion have been limited by the fact that turbulent mixing in flames is altered by the accompanying heat release and can, as consequence, be qualitatively different from that occurring in non-reacting flows. Examples include counter-gradient diffusion, e.g. Libby and Bray (1981), Bray et al. (1985), in either confined non-premixed swirling flames, Takagi et al. (1985), or in unconfined premixed flames, Heitor et al. (1987), Ferrão and Heitor (1995).

Turbulent recirculating premixed flames stabilised downstream of baffles have been shown to be characterised by non-gradient scalar fluxes (e.g. Takagi et al., 1984; Takagi and Okamoto, 1987; Fernandes et al., 1994; Duarte et al., 1996), the extent of which appears to be particularly influenced by the magnitude of the mean pressure gradients associated with the streamline curvature. Experimental evidence is reported in Heitor et al. (1987), Ferrão and Heitor (1995) and Duarte et al. (1996), although it remains to be quantified for different pressure distributions.

Strongly swirled recirculating flames include additional features because of the effects of centrifugal forces and curvature in zones of mean shear, as discussed by Takagi et al. (1984) and Takagi & Okamoto (1987). These authors have provided evidence of the existence of counter-gradient diffusion of heat in confined non-premixed flames at low swirl numbers and found that the radial Reynolds stresses and the variance of temperature fluctuations were reduced in comparison to the unswirled flame.

This paper is intended to analyse the interaction between gradients of mean pressure and density fluctuations for high Reynolds number flames. The effect of swirl on the aerothermochemistry of propane-air recirculating flames is particularly addressed and the results are used to assess the extension of main findings on turbulent scalar transport, obtained by DNS calculations for a single flamelet to a flame of practical interest.

Finally, the Bray-Moss-Libby (Bray, 1980) model for the prediction of turbulent scalar flux, which has been extended to account for pressure gradients by Veynante and Poinot (1997), is shown to be qualitatively in accordance with the experimental results obtained for $\overline{u''c''}$, although the probability density functions of c are not bimodal in the flame studied, and the flow is much more complex than the one modelled by those authors.

The following section describes the experimental techniques used throughout this work. Section 3 presents the experimental results, which are analysed and discussed in section 4. Finally, the main conclusions of the work are presented in the last section of the paper.

2 EXPERIMENTAL METHOD

2.1 The Flames Studied

The experiments reported in this paper were conducted in unconfined swirling and non-swirling premixed flames of air and propane with an equivalence ratio of 0.6, stabilised on a disk with $D = 56$ mm in diameter, which is located at the exit section of a contraction with 80 mm in diameter. The annular bulk velocity is equal to $U_0 = 42.4$ m/s, resulting in a Reynolds number, based on the disk diameter, of 1.5×10^5 . Swirl could be imparted to the premixed reactants by a set of curved blades, located upstream of the contraction, resulting in a swirl number of $S = 0.33$.

2.2 The Experimental Techniques

The instrumentation used throughout this work consists on a combined LDV/LRS system, which was based on a single laser light source (5 W argon-ion laser) as depicted in figure 1. The system has derived from that described by Ferrão and Heitor (1998), as the main data acquisition system includes a 16 bits analogue/digital converter, in place of the 12 bits data acquisition board previously used.

The laser Doppler velocimeter was based on the green light (514.5 nm) of the laser and was operated in the dual-beam, forward scatter mode with sensitivity to

the flow direction provided by a rotating diffraction grating. The calculated dimensions of the measuring volume at e^{-2} were 606 μm and 44 μm . The Rayleigh scattering system was operated from the blue line (488 nm) of the same laser source, which was vertically polarised and made to pass through a 5:1 beam expander. The light converged in a beam waist of 50 μm diameter, and was collected at 90° from the laser beam direction, through a slit of 1 mm. The collected light was filtered by a 1 nm interference filter and passed through a polariser in order to increase the signal-to-noise ratio. A calibration procedure was implemented in order to compensate for number density dependence on the chemical composition. The uncertainty on the average temperature was quantified as 4%.

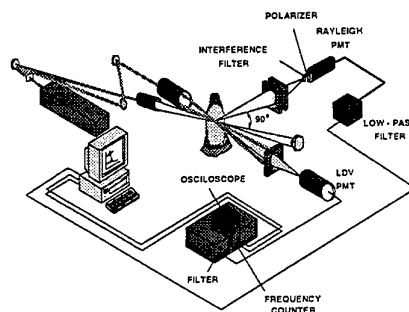


Fig. 1 - Schematic diagram of the combined LDV/Rayleigh scattering system

The signal was amplified and low pass filtered at 10KHz before digitalisation. The temporal resolution of the system depends on the integration time associated with this filter, which is quantified to be 50 μs . This value, associated with the typical flow velocities, give rise to path lengths of about 1mm and, therefore, smaller than the integral length scales in the reaction shear layer. The resolution of the system was confirmed by the measured temperature distributions, which include instantaneous values close to either adiabatic or room temperature, confirming that the system is capable of resolving the temperature fluctuations associated with the premixed flames analysed in this work.

The details associated with the accuracy of the experimental method used, and in particular of the laser Rayleigh scattering, have been discussed by Ferrão and Heitor (1998) and are not reported here.

3 EXPERIMENTAL RESULTS

The most salient features of the mean flow characteristics of the two flames studied can be inferred from the velocity distribution represented in figure 2. For the non-swirling flame ($S = 0$) the results are similar to those found in other baffle-stabilised recirculating flames (e.g. Heitor et al, 1987; Ferrão and Heitor, 1995), in that they exhibit a recirculation region extending up to $x/D = 2.21$, where the fluid has a large and fairly uniform mean temperature, surrounded by annular region of highly sheared fluid where gradients of mean temperature are large.

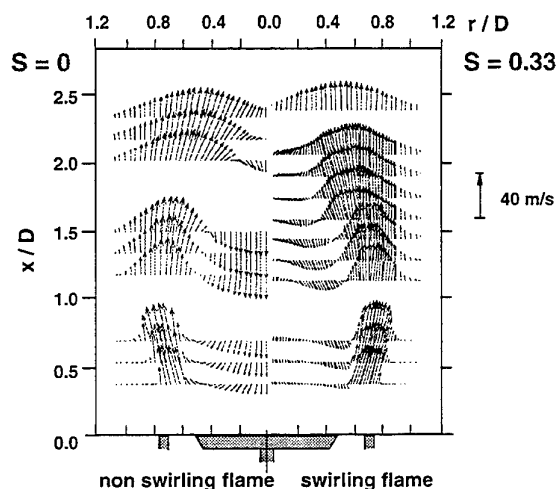


Fig 2 - Mean velocity vectors along a vertical plane of symmetry.

The single recirculation zone of the unswirled flame is to be contrasted to that of the swirling flame ($S = 0.33$), which is shorter, wider and annular in shape, because it includes an inner annular vortex with positive velocities along the centreline. The inner recirculation zone is associated with positive mean velocities along the centreline up to the first stagnation point. This nature of the swirling flame is characterised by a comparatively large inclination of the mean velocity vectors at the exit which, together with the aspects mentioned before, represents a direct consequence of the centrifugal forces associated with the swirl motion. The turbulent characteristics of these flames were presented elsewhere (Caldas et al, 1997) and are not discussed here.

The isotherms, represented in figure 3, are highly curved and reveal non-planar flames oblique to the oncoming reactants. For these conditions, the results of figure 3 show that the turbulent heat transfer rate for the two flames considered is restricted to the reacting shear layers, with absolute values of $\overline{u''c''}$ considerably

higher than those of $\overline{v''c''}$. As a consequence, a large component of the vectors of turbulent heat transfer is directed along the isotherms rather than normal to these, as would be expected from gradient-transport models of the kind used in non-reacting flows.

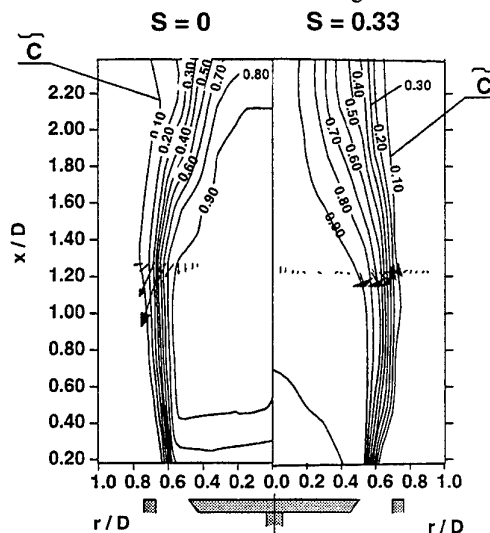


Fig. 3 - Isocontours of mean progress reaction variable, together with the turbulent heat flux vectors.

The analysis of the photography of figure 4 shows that reaction occurs along a thin shear layer, characterised by intense temperature gradients (flame brush), located between the locus of maximum axial velocity and the locus of the mean separation streamline, which is curved along its length. This curvature imposes mean velocity effects on the turbulence field in a way that depends on the level of interaction between the gradients of mean pressure typical of the present flames and the associated density fluctuations.

An instantaneous representation of the flame structure is depicted in the photography of figure 4, where the flame was seeded with alumina particles and illuminated with a ND-YAG laser source, with 9 ns pulse duration. As the colour scheme is inverted, the dark regions are associated with fresh reactants, and the interior grey zone corresponds to the hot products.

Although flame brush is roughly oriented along the isotherms, turbulent motion strongly interacts with the flame and, as a consequence, flame fronts are randomly oriented, resulting in a complex flow pattern when compared to a single isotropic flame analysis, as performed in current DNS studies (e.g. Veynante et al., 1987). This suggests that extension of DNS scalar transport models for flames of practical interest is to

be performed with precaution and require experimental validation.

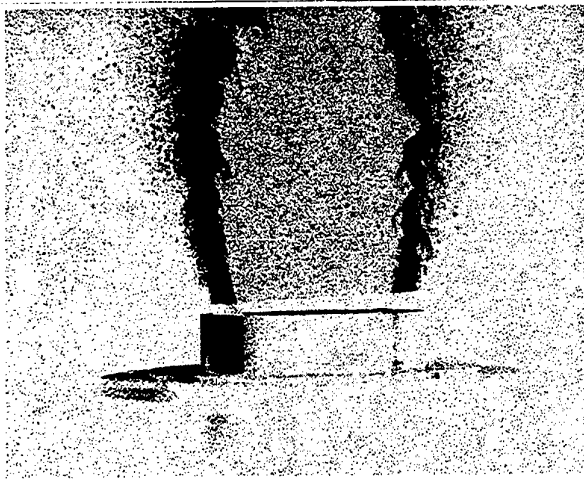


Fig. 4 - Instantaneous flame (B) visualisation during a 9 ns Nd-Yag laser pulse.

The next section discusses this extension for premixed recirculating flames with different swirl numbers.

4 DISCUSSION

The physical phenomena responsible for the conservation of turbulent kinetic energy, k , and for the turbulent diffusion of c are analysed by evaluating the transport equations of k and $\widetilde{u''c''}$ respectively, for an axial location of $x/D \approx 1.21$.

The terms involved in the conservation equations of momentum and turbulent scalar flux are made non-dimensional by $\rho_u \widetilde{u_o''^2}/l_t$, where ρ_u is the mass density of the unburned gases, $\widetilde{u_o''^2}$ is the velocity fluctuation of the unburned gases and l_t is the turbulent length scale. On the other hand, the terms involved in the turbulent kinetic energy budget are made non-dimensional with reference to $\rho_u \widetilde{u_o''^2}^{3/2}/l_t$.

As this discussion is dedicated to the interaction between turbulence and combustion, the analysis is focused on the flame brush, which has been defined by the region limited by $\tilde{c} = 0.02$ and $\tilde{c} = 0.98$.

The mean reaction progress variable, c , will therefore be used to represent the evolution of the different parameters across the flame brush. In addition, it should be noted that for the referential adopted, $r > 0$ denotes outward radial locations and $x > 0$ downstream axial locations.

4.1 Conservation of Momentum

Simultaneous measurements of time-resolved velocity and temperature allow for the experimental quantification of the relative magnitudes of the terms involved in the conservation equation of momentum, which can be written as, Rodi (1970):

Axial component [1]:

$$\underbrace{\bar{\rho} \bar{U} \frac{\partial \bar{U}}{\partial x}}_{\text{I}} + \underbrace{\bar{\rho} \bar{v} \frac{\partial \bar{U}}{\partial r}}_{\text{II}} = - \underbrace{\frac{\partial \bar{p}}{\partial x}}_{\text{III}} + \underbrace{\mu \nabla^2 \bar{U}}_{\text{IV}} - \left(\frac{\partial(\bar{\rho} \widetilde{u''^2})}{\partial x} + \frac{1}{r} \frac{\partial(r \bar{\rho} \widetilde{u''v''})}{\partial r} \right)$$

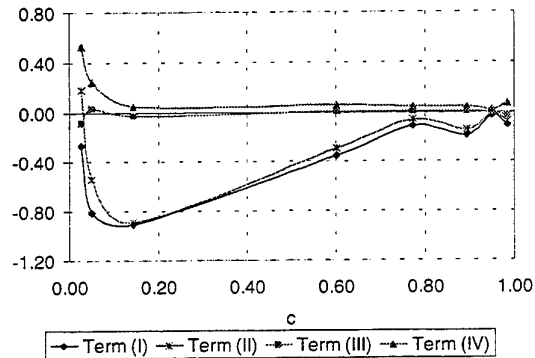
Radial component [2]:

$$\underbrace{\bar{\rho} \bar{U} \frac{\partial \bar{v}}{\partial x}}_{\text{(I)}} + \underbrace{\bar{\rho} \bar{v} \frac{\partial \bar{v}}{\partial r}}_{\text{(II)}} = - \underbrace{\frac{\partial \bar{p}}{\partial r}}_{\text{(III)}} + \underbrace{\mu \left(\nabla^2 \bar{v} - \frac{\bar{v}}{r} \right)}_{\text{(IV)}} - \left(\frac{\partial(\bar{\rho} \widetilde{u''v''})}{\partial x} + \frac{1}{r} \frac{\partial(r \bar{\rho} \widetilde{v''^2})}{\partial r} - \frac{\bar{\rho} \widetilde{v''^2}}{r} \right)$$

Mean pressure gradients have been obtained by difference of the terms in the conservation equation for momentum.

Figures 5 and 6 shows radial profiles of the measured terms involved in the transport equation of momentum for the flames analysed ($S = 0$ and $S = 0.33$), for an axial location of $x/D = 1.21$ which corresponds to the main width of the recirculating flame. The results obtained along the flame brush are represented as a function of the mean progress reaction variable, c .

Fig. 5 a)– Radial profile of the main terms involved in equation [1], for the non swirling flame ($S = 0$) at



$x/D = 1.21$.

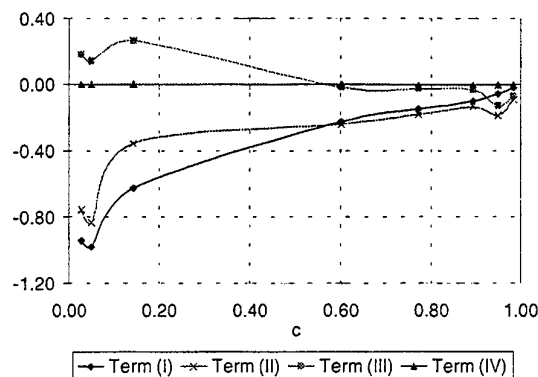


Fig. 5 b)– Radial profile of the main terms involved in equation [2], for the non swirling flame ($S = 0$) at $x/D = 1.21$

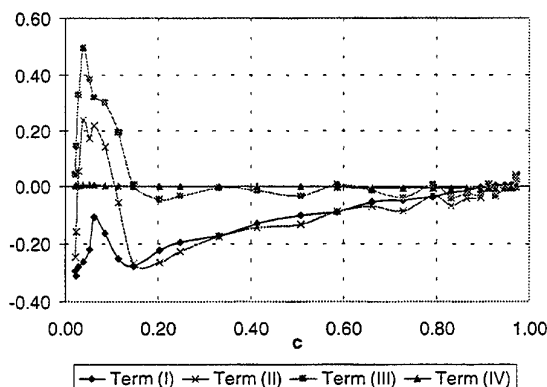


Fig. 6 a)– Radial profile of the main terms involved in equation [1], for the swirling flame ($S = 0.33$) at $x/D = 1.21$

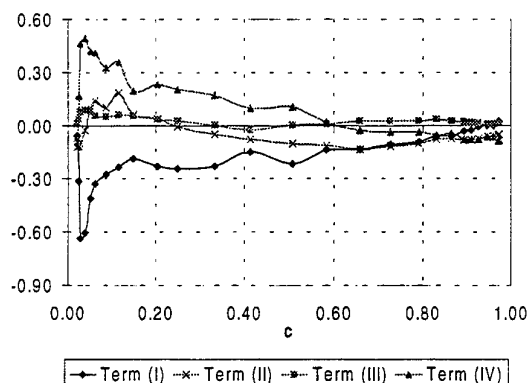


Fig. 6 b)– Radial profile of the main terms involved in equation [2], for the swirling flame ($S = 0.33$) at $x/D = 1.21$.

The analysis of figures 5 and 6 shows that the mean pressure gradients are dominated by the difference between the two components of the convection term (also the diffusion term in the balance of radial momentum).

The evolution of the pressure gradients across the axial location analysed is a consequence of the effect of streamline concentration and curvature and, for the swirling flow, the effect of rotation.

In general, it should be noted that swirl contributes to attenuate pressure gradients, and promote adverse pressure gradients in the leading region of the flame brush ($c < 0.2$). The analysis of the influence of this different pressure distributions in the turbulent characteristics of the flow can be quantified by analysis of the turbulent kinetic energy budget.

4.2 Turbulent Kinetic Energy Budget

The turbulent kinetic energy budget, for high Reynolds number steady flows, can be written as, (Jones, 1980).

$$\begin{aligned} \frac{\partial}{\partial x} (\bar{\rho} \tilde{U} k) + \frac{1}{r} \frac{\partial}{\partial r} (r \bar{\rho} \tilde{V} k) &= -\bar{\rho} \tilde{u}''^2 \frac{\partial \tilde{U}}{\partial x} - \bar{\rho} \tilde{v}''^2 \frac{\partial \tilde{V}}{\partial r} - \bar{\rho} \frac{\tilde{V}}{r} \tilde{w}''^2 - \\ &\quad \text{(I)} \quad \text{(II)} \\ -\bar{\rho} \tilde{u}'' \tilde{v}'' \left(\frac{\partial \tilde{U}}{\partial r} + \frac{\partial \tilde{V}}{\partial x} \right) &- \bar{\rho} \tilde{u}'' \tilde{w}'' \frac{\partial \tilde{W}}{\partial x} - \bar{\rho} \tilde{v}'' \tilde{w}'' \frac{\partial \tilde{W}}{\partial r} - \\ &\quad \text{(III)} \\ -\tilde{u}'' \frac{\partial \bar{p}}{\partial x} - \tilde{v}'' \frac{\partial \bar{p}}{\partial r} &- \text{Diffusion - Dissipation} \\ &\quad \text{(IV)} \end{aligned} \quad [3]$$

Where k is the turbulent kinetic energy, $k = \tilde{u}''^2 + \tilde{v}''^2 + \tilde{w}''^2 / 2$. The four terms identified in the previous expression represent the convection of k by the mean flow field (I), the production of k by the interaction between normal stresses and normal strain (II), the production of k by the interaction between shear stresses and shear strain (III) and the production of k by the mean pressure work (IV).

These terms have been calculated for the two flames studied, making use of the experimental data obtained and considering that:

$$\tilde{u}'' = \frac{\overline{\rho u''}}{\bar{\rho}}$$

as suggested by Meunier et al (1981). The results obtained are represented in figures 7 and 8.

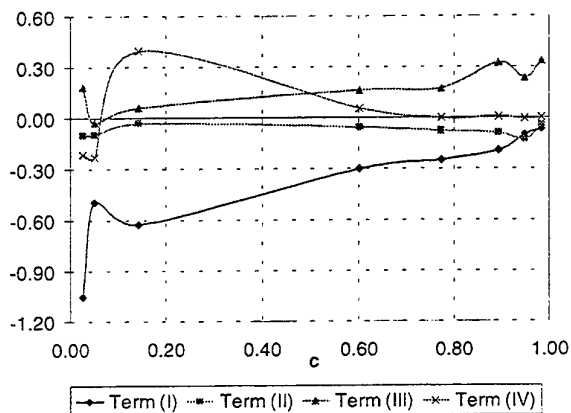


Fig. 7 – Radial profiles of the main terms involved in equation [3], for the non-swirling flame ($S = 0$) at $x/D = 1.21$.

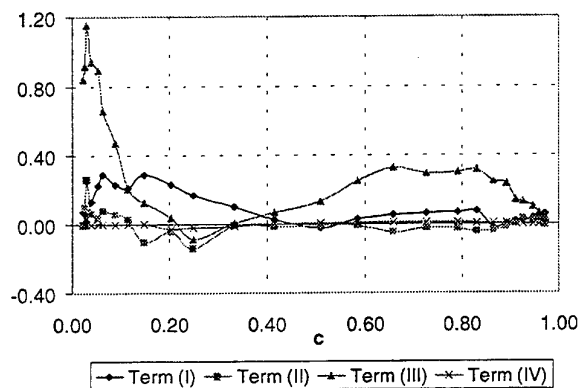


Fig. 8 – Radial profiles of the main terms involved in equation [3], for the swirling flame ($S = 0.33$) at $x/D = 1.21$.

Analysis of figure 7 and 8 shows that the interaction between shear stresses and shear strain is generally the dominant term in the production of turbulent kinetic energy, giving rise to a strongly anisotropic turbulent field with comparatively large axial velocity fluctuations.

It should however be noted that, for the non-swirling flame, where pressure gradients are more intense, figure 7 shows that, for $c < 0.5$, thermal dilatation and associated density variations overcome viscous dissipation and lead to a net flame production of turbulent kinetic energy, as predicted by Bray-Moss-Libby theory, Libby and Bray (1981).

This experimental finding is particularly relevant considering that DNS is limited to low Reynolds number flows and, as a consequence, viscous dissipation is always a dominant factor in the numerical simulations. Consequently, DNS is unable to reproduce the full range of dynamical regimes that occur in a flame of practical interest.

4.3 Conservation Equation For Turbulent Scalar Flux

The conservation equation of turbulent scalar flux for high Reynolds number flow, can be written as:

$$\bar{\rho} \bar{U}_j \frac{\partial \overline{u''_i c''}}{\partial x_j} = - \left[\underbrace{\left(\bar{\rho} \overline{u''_j c''} \frac{\partial \bar{U}_i}{\partial x_j} + \bar{\rho} \overline{u''_i u''_j} \frac{\partial \bar{c}}{\partial x_j} \right)}_{(I)} + \underbrace{\bar{c}'' \frac{\partial \bar{p}}{\partial x_i}}_{(II)} - \underbrace{\left[\bar{c}'' \frac{\partial p'}{\partial x_i} + \frac{\partial}{\partial x_i} (\bar{\rho} \overline{u''_i u''_j c''}) \right]}_{(V)} \chi \right] \quad (4)$$

where (I) represents the convection by the mean flow, (II) and (III) are source terms due to the mean velocity and mean progress variable gradients, (IV) represents the effect of mean pressure gradients and (V) represents the fluctuating pressure term and transport by the turbulent flow field.

The main terms involved in equation [4] are evaluated and presented in figures 9 and 10 for the flames studied.

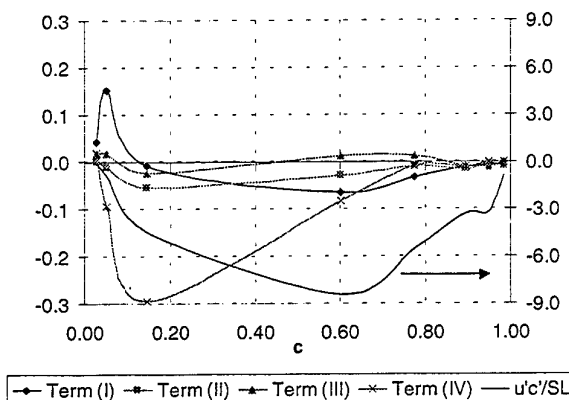


Fig. 9 a)– Radial profile of the main terms of equation [4] in the axial component, together with the corresponding turbulent heat flux, for the non-swirling flame ($S = 0$) at $x/D = 1.21$.

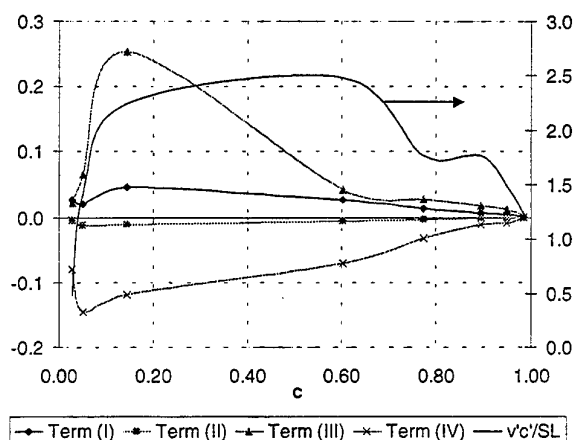


Fig. 9 b)– Radial profile of the main terms of equation [4] in the radial component, together with the corresponding turbulent heat flux, for the non-swirling flame ($S = 0$) at $x/D = 1.21$.

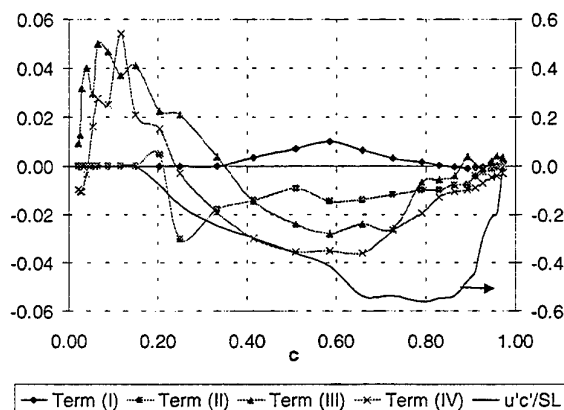


Fig. 10 a)– Radial profile of the main terms of equation [4] in the axial component, together with the corresponding turbulent heat flux, for the non-swirling flame ($S = 0.33$) at $x/D = 1.21$.

The results show that turbulent heat transfer is restricted to the reacting shear layer, where the temperature gradients exists. For the swirling flame, figure 10 a), it is shown that the term due to the interaction between pressure gradients and temperature fluctuations (term IV) is dominant in the production of $u''c''$ and is responsible for the counter-gradient turbulent heat transport. Although this result is similar to that obtained for non-swirling flames, a new feature consists on the important contribution of the term resulting from the interaction between Reynolds stresses and temperature gradients (term III),

which is similar to term IV, and this was not observed for the non-swirling flame.

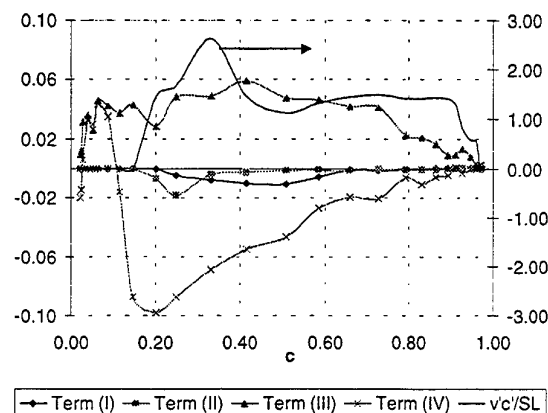


Fig. 10 b)– Radial profile of the main terms of equation [4] in the radial component, together with the corresponding turbulent heat flux, for the swirling flame ($S = 0.33$) at $x/D = 1.21$.

It has been shown in the literature that the process of counter-gradient heat transport can be explained by the preferential deceleration of the products of combustion, relatively to the cold reactants (e.g., Heitor et al., 1987; Hardalupas et al., 1996), and this is experimentally confirmed by this study.

The analysis of the transport equation of the radial component of turbulent heat flux, figure 9 b) and 10 b), shows that $\overline{v''c''}$ is always positive, as predicted by gradient hypothesis. This is mainly because the interaction between Reynolds stresses and temperature gradients (term III) is the dominant term in the region where $\overline{v''c''}$ occurs, although the interaction between pressure gradients and temperature fluctuations (term IV) constitutes an important contribution for the production of counter-gradient $\overline{v''c''}$, and cannot be neglected. For $c < 0.2$, term IV is dominant and is responsible for the attenuation of $\overline{v''c''}$.

In the swirling flame, figure 10 b) shows that for $c < 0.2$, the terms representing the radial component of the turbulent heat flux contribute to produce gradient diffusion, but the value of $\overline{v''c''}$, which was positive for $c > 0.2$, vanishes. A possible explanation for this behaviour is suggested by Veynante et al (1997), based on the DNS of a single flamelet, in that the fluctuating pressure term (which is not measurable with current diagnostic techniques) can be an important source of counter-gradient diffusion and may balance the gradient-diffusion terms measured for $c < 0.2$ and justify the attenuation of $\overline{v''c''}$.

In the theory of turbulent premixed flames, the modelling of the turbulent flux of c , $\overline{u''c''}$, has been first suggested in the Bray-Moss-Libby, Bray (1980), based on the classic flamelet assumption of fresh reactants ($c=0$) and fully burnt products ($c=1$) separated by thin flame sheets.

This model has recently been improved by Veynante et al. (1997) and by Veynante and Poinso (1997), where the later authors suggest the following expression in which the first term models the gradient diffusion, the second accounts for counter-gradient diffusion and the last incorporate pressure gradient effects:

$$\overline{u''c''} = \tilde{c}(1-\tilde{c}) \left[\tau S_L - 2\alpha u' - a \frac{\tau^2 Re_f}{12K} \left(\frac{1}{\delta_t} \right)^2 \nabla p S_L \right]$$

where:

$$Re_f = \frac{\delta_t S_L}{\delta_t}$$

$$\delta_t = \frac{T_b - T_u}{\max \left(\frac{dT}{dx} \right)}$$

$$K = \frac{1}{1 + (\tau + 1)^{-0.76}}$$

$$\nabla p = \left(\frac{\partial p}{\partial x} \right) \frac{\delta_t}{\rho_u \tau S_L^2}$$

S_L is the laminar flame speed, δ_t is the thermal thickness of the flame, K and a are constants of the model.

The comparison of the results obtained with this model against the values of $\overline{u''c''}$ and $\overline{v''c''}$ measured for the swirling flame are represented in figure 11 and 12.

Although the model suggested by Veynante and Poinso (1997) was derived for simple flamelets and thus, for flames characterised by bimodal probability density functions of c , which are not representative of the flames analysed, the results of figures 11 and 12 show that the model presents qualitative agreement with the values measured.

A major feature of this new model consists on the correction for the pressure gradients which is found to be of major relevance in both components of the turbulent heat flux.

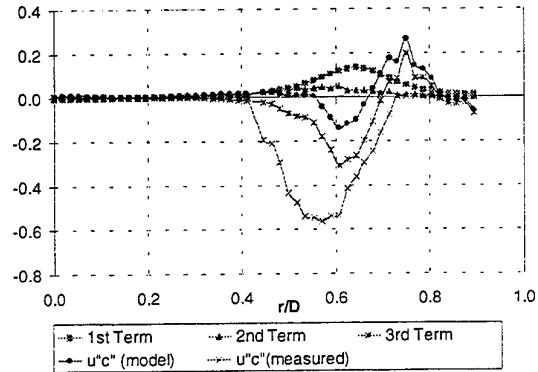


Fig. 11 – Comparison between the modelled and measured axial component of the turbulent heat flux, for the swirling flame.

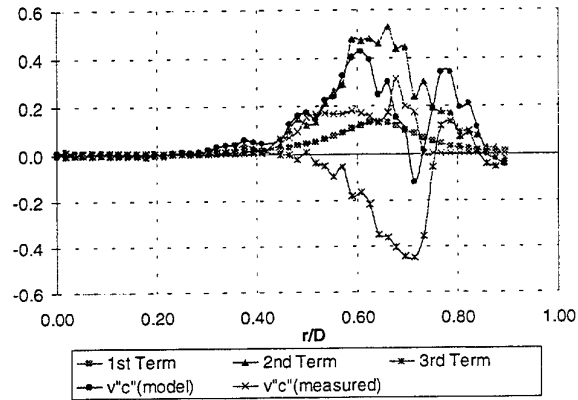


Fig. 12 – Comparison between the modelled and measured radial component of the turbulent heat flux, for the swirling flame.

5 CONCLUSIONS

Simultaneous measurements of time-resolved velocity and temperature obtained by laser-Doppler velocimetry and laser-Rayleigh scattering in the near wake of premixed recirculating flames of propane and air, have improved our understanding of the interaction between pressure gradients and density fluctuations in high Reynolds number flames. The results extend previous knowledge derived from DNS in comparatively low Reynolds number flames and show that:

- Swirl attenuates the rate of turbulent heat transfer due to the decrease of the temperature gradients across the reacting zone, but does not alter the

existence of a large zone of flame characterised by non-gradient scalar fluxes.

- In the production of turbulent kinetic energy for the non-swirling flames, where pressure gradients are more intense, and for $\tilde{c} < 0.5$, thermal dilatation and associated density variations overcome viscous dissipation and lead to a net flame production of turbulent kinetic energy, as predicted by Bray-Moss-Libby theory, Bray and Libby (1981).
- The model recently suggested by Veynante and Poinot (1997) which was derived for simple flamelets characterised by bimodal probability density functions of c , is shown to represent qualitatively the evolution of turbulent flux of the mean reaction progress variable, c , or turbulent heat flux, $\rho u''c''$. A major feature of this new model consists on the correction for the pressure gradients, which is found to be of major relevance in both components of the turbulent heat flux.

ACKNOWLEDGEMENTS

The authors acknowledge financial support by the BRITE/EURAM programme of the DGXII of the Commission of the European Communities, under the contracts CT/95-0106.

REFERENCES

- Bray, K.N.C., Libby, P. and Moss, J.H. 1985. Unified Modelling Approach for Premixed Turbulent Combustion – Part I: General Formulation. Combustion and Flame, 61: 87-102.
- Bray, K.N.C. 1980, Turbulent flows with premixed reactants, in: Turbulent Reacting Flows, ed. P.A. Libby and F. A. Williams. Topics in Applied Physics, vol. 44, pp. 115-183. Springer.
- Caldas, F. D. Duarte, Ferrão, P., Heitor, M.V. and Pope, C. 1997. On the use of laser Rayleigh scattering to study the aerothermochemistry of recirculating premixed flames. In: Developments in Laser Techniques and Fluid Mechanics, eds. Adrian et al., Springer Verlag, pp. 439-455.
- Duarte, D., Ferrão, P. and Heitor, M.V., 1996, Flame structure characterisation based on Rayleigh thermometry and two-point laser Doppler measurements, in: Developments in Laser techniques and application to Fluid Mechanics, Eds. Adrian et al., Springer Verlag, pp. 185-249.
- Fernandes, E.C., Ferrão, P. Heitor, M.V. and Moreira, A.L.N., 1994, Velocity-temperature correlations in recirculating flames with and without swirl. Experimental Thermal and Fluid Science, 9, pp. 241-249.
- Ferrão, P. and Heitor, M.V. 1995. Turbulent mixing and non-gradient diffusion in baffl-stabilised flames. In: Turbulent Shear Flows - 9, Eds. Durst et al., Springer Verlag, pp. 427-437.
- P. Ferrão and M.V. Heitor (1998). Simultaneous velocity and scalar measurements in premixed recirculating flames, Experiments in Fluids, vol. 24, pp. 399-407.
- Hardalupas, Y., Tagawa, M. and Taylor, A.M.K.P., 1996. Characteristics of counter-gradient heat transfer in a non-premixed swirling flame. In: Developments in Laser Techniques and Applications to Fluid mechanics, ed Durst et al., Springer Verlag, pp. 159-184.
- Heitor, M. V., Taylor, A. M. K. and Whitelaw, J. H.: The interaction of turbulence and pressure gradients in baffle-stabilized premixed flames. J. Fluid Mechanics, vol. 181, pp. 387-413, (1987).
- Jones, W.P. 1980, Models for Turbulent Flows With Variable Density and Combustion, Prediction Methods for Turbulent Flows, ed. Wolfgang Kollman, Hemisphere Publishing corporation, New York.
- Libby, P. and Bray, K.N.C. 1981. Counter-Gradient Diffusion in Premixed Turbulent Flames. AIAAJ, 19:205-213
- Meunier, S., Champion, M. and Bellet, J.C. 1981. Premixed combustion in a turbulent boundary layer with injection. In: Proc. of 3rd Turbulent Shear Flows, pp. 3.38-3.43.
- Rodi, W. 1970, Turbulence models for environmental problems, Prediction Methods for Turbulent Flows, ed. Wolfgang Kollman, Hemisphere Publishing corporation, New York.

Takagi, T., Okamoto, T., Taji, M. and Nakasuji, Y., 1984, Retardation of mixing and counter-gradient diffusion in a swirling flame. In: Proc. 20th Symposium (Intl.) on Combustion, pp. 251-258. The Combustion institute, Pittsburgh.

Takagi, T. and Okamoto, T., 1987. Direct measurements of the turbulent transport of momentum and heat in the swirling flame, in Laser diagnostics and modelling of combustion, ed. Iinuma, K. et al., pp 273-280. Springer Verlag, Berlin.

Takagi, T., Okamoto, T. Taji, M. and Nakasuji, Y. (1985). Retardation of mixing and counter-gradient diffusion in a swirling flame. In: Proc. of Twentieth Symp. (Intl.) on Combustion, The Combustion Institute, pp. 251-258.

Veynante, D. and Poinso, T. 1997, Effects of pressure gradients on turbulent premixed flames, J.Fluid. Mech., vol. 353, pp 83-114.

Veynante, D. Trouvé, A. , Bray, K.N.C. and Mantel, T. 1997, Gradient and counter-gradient scalar transport in turbulent premixed flames, J.Fluid. Mech., vol. 332, pp 263-293.

Simultaneous Planar OH and Temperature Measurements for the Detection of Lifted Reaction Zones in Premixed Bluff-body Stabilised Flames

Dieter Most, Volker Höller, Armin Soika, Friedrich Dinkelacker and Alfred Leipertz

Lehrstuhl für Technische Thermodynamik (LTT)

Universität Erlangen-Nürnberg, Am Weichselgarten 8, D-91058 Erlangen, Germany

Abstract

A bluff-body stabilised highly turbulent and premixed lean methane/air flame has been investigated with simultaneous planar laser Rayleigh scattering and planar laser-induced fluorescence of OH, systematically varying exit velocity and equivalence ratio ϕ . From that a conditional thermal flame front thickness is calculated by determining the steepest gradient while the OH-radical concentration is taken as a indicator for zones with or without a burning reaction. Thus the measured thermal fronts were distinguished in non-reacting and reacting flame fronts.

In the case of non-reacting flame fronts the thickness is found to be independent of equivalence ratio and exit velocity. For reacting flame fronts a relative thinning, compared to laminar unstretched flames is measured as a function of the non-dimensional stretch factor K_T , which is an expression for vortex induced local stretch.

Although contact between burnt and fresh gas immediately takes place direct downstream the burner nozzle, from OH images a lifted reaction zone can be found to be at least 11 mm the burner nozzle. This lift-off cannot be recognised with thermometry techniques. Neither a unique local turbulent stretch scale $a_T = u'/l_T$ nor the non-dimensional stretch factor $K_T = a_T/(u'/s_L)$ can be found to predict the flame lift-off. Instead a unique global mean stretch $A_m = \delta U/\delta y$ seems to be a adequate criterion for most of the flame conditions. Only for very lean mixtures this does not match. Here a residential-ignition delay time model seems to fit more to the observed lift-off heights.

1. Introduction

Optimising of combustion processes by increasing efficiency, reducing pollution exhaust and avoiding burner instabilities is of topic interest for designers of burners, gasturbines, motors etc. With detailed knowledge about local combustion processes and heat and mass transport mechanism in combination with flow fields calculation, it would be able to predict the behaviour of flames in advance, it would be able to "design" a flame.

Of special interest are "clean" flames driven with lean premixed mixtures. While for laminar and laminar-like conditions already adequate models are provided, this is not the case for highly turbulent flames. Although for this conditions generally accepted models already exist, e.g. the phase diagram of Peters (1986) which describes a broadening of the flame with increasing turbulence intensities, the prediction of flame behaviour is still not sufficient. Recent experiments using planar

laser imaging techniques under different turbulent premixed flame conditions indicate only partially modified pre-heat zone structures [Mansour et al. (1992); Buschmann et al. (1996)] and detailed flame-vortex investigations show that flames are locally quenched at these high turbulence intensities [Dinkelacker et al. (Pittsburgh 1998), Poinot et al. (1990), Roberts et al. (1992)]. Non of these effects is considered in the model introduce by Peters (1986)

Thus, in order to achieve time and spatial resolved 2-dimensional information about temperature structures of highly turbulent flames a bluff body stabilised flame is investigated in this study. In order to achieve information about reaction the OH-radical concentration is taken as a criterion which can distinguish zones of reacting from those of non-reacting fresh fuel and those of burnt exhaust gas. Therefore it has been measured qualitatively using planar laser-induced

fluorescence (LIF). The combination of planar temperature and planar OH-LIF measurement techniques allows to identify non-reacting temperature fronts and reacting flame fronts as well and to determine from that a thermal thickness distribution conditioned to reaction zones.

2. Experimental Set-up

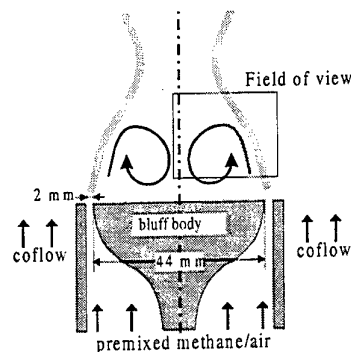


Figure1: Schematic of the bluff-body burner and the field of view

For stabilising a turbulent premixed flame at high exit velocities v_{exit} a bluff-body configuration has been chosen. Here, a circulation zone is produced in its wake through which burnt hot gas flows back, heats the fresh cold gas up and ignites it (Fig 1). This kind of flame stabilisation allows to run the burner with high turbulence intensities resulting from high shear rates. Thus a stable flame can be obtained over a wide parameter field (measurements with v_{exit} up to 29 m/s).

In the experiments reported here the burner is operated with premixed lean methane/air. A bluff body of 44mm diameter is placed concentrically in the burner tube of \varnothing 48mm. The premixed fuel flows through the left ring gap of 2mm width. To get detailed information about interaction of high turbulence with burning reaction the investigated flame conditions have been systematically varied between exit velocities from 5 to 29m/s and equivalence ratios from 0.55 to 1.0.

Mixture fraction is adjusted in an external chamber which is supplied with dried filtered air and methane of high purity (99.995%) by two mass flow controllers which also monitor exit velocity. To prevent entrainment of interfering Mie-scattering from dust particles a coflow of filtered air with a mean velocity

of 0.5m/s coats the flame from the environment. The velocity field is measured with a Laser Doppler Velocimetry (LDV) system, which allows simultaneous point-measurement of two velocity components of the flow field. To cover the whole field of interest measurements in several axial (up to 75mm) and radial (up to 40mm) positions have been performed with a positioning accuracy of ± 0.3 mm. At each measured point at least 3000 samples were taken. Thus the axial, radial and tangential averaged velocities V_a , V_r and V_t , turbulent fluctuations v'_a , v'_r and v'_t and the macro length scale L_x have been determined under isothermal flow conditions. V_t is found to be zero, while v'_r and v'_t are found to be nearly equal. Thus the mean rms velocity fluctuation v'_{rms} can be expressed with the turbulent kinetic energy k from

$$v'_{rms} = (2 \cdot k)^{0.5} \quad (1)$$

$$k = 0.5 \cdot (v_a'^2 + v_r'^2 + v_t'^2) = 0.5 \cdot (v_r'^2 + 2 \cdot v_t'^2) \quad (2)$$

With light sheet techniques 2-dimensional information about the spatial structure of the detailed combustion process can be obtained with high spatial and temporal resolution. Applying planar Laser Rayleigh Scattering (LRS) [Kampmann et al. (1993)] the temperature field has been investigated. For

more extended information simultaneous
qualitative Laser Induced Fluorescence (LIF)

[Krämer et. al. (1995); Roberts et. al. 1992]
of OH-radicals is applied.

2.1 Thermometry -Laser Rayleigh Scattering

To enable simultaneous OH (qualitative) and temperature measurement a KrF excimer laser with wavelength $\lambda=248\text{nm}$ and a pulse length of 15ns has been applied for Rayleigh Scattering forming a light sheet with cylindrical lenses of 20mm height and less than $200\mu\text{m}$ thickness at the place of interest in the flame.

The Rayleigh signal is proportional to the number of molecules in the gas sample weighted with their molecule specific Rayleigh cross section factor $\sigma(\lambda)$. Therefore in isobaric conditions comparing the Rayleigh signal intensity I_{flame} of a measurement with the measured signal intensity I_{air} at known conditions (air with T_{ref}), the molecule density and from that the gas temperature T can be calculated by using the perfect gas law from

$$T(x, y) = T_{\text{ref}} * \frac{I_{\text{air}}(x, y) - I_{\text{back}}(x, y)}{I_{\text{flame}}(x, y) - I_{\text{back}}(x, y)} * \frac{\bar{\sigma}_{\text{flame}}}{\bar{\sigma}_{\text{air}}} \quad (3)$$

Here $\bar{\sigma}$ is the averaged Rayleigh cross section factor of the whole sample volume. The images will be corrected with the background noise (I_{back}) of the camera system.

The investigated images are taken perpendicular to the laser sheet by an intensified 14 bit CCD camera. Flame luminosity is suppressed by setting the exposure time of the image intensifier down to 100ns, sampling only laser-induced signals. For thermometry measurements the maximum error has been estimated to be 11%, taking into account Signal-to-Noise-Ratio (SNR) better than 12:1, variation of Rayleigh cross section in the gas volume of 3% and laser fluctuation of 5%.

2.2 Simultaneous OH-LIF and LRS

Figure2: Schematic set-up for simultaneous T-and OH-measurement

For simultaneous measurement of OH-radicals and temperature the same KrF excimer laser is tuned to excite the $P_1(8)$ line of the (3-0)transition of the A-X band at 248.17nm. [Krämer et al. (1995)]. To separate the Rayleigh and the LIF signal a dichromatic mirror has been installed, which reflects at 248nm but transmits at 308nm (see Fig 2). With this set-up a resolutions of $(58\mu\text{m})^2$ per pixel can be achieved. A bandpass filter (UG11) is installed in front of the LIF-ICCD camera to suppress interfering signals of other wavelengths. Thus a qualitative image of the OH-concentration field can be obtained. Here, the SNR was larger than 8. The reflected Rayleigh signal is measured with a second ICCD-camera with a pixel resolution of $(58\mu\text{m})^2$. The cameras will be operated simultaneously monitored by the pre-trigger signal of the laser which initiates a recording only if both camera systems are ready.

Figure3: Simultaneous taken images of the T- and OH-distribution ($v_{\text{exit}}=10.6 \text{ m/s}$, $\phi=0.6$)

3. Evaluation technique

The local flame front thickness is calculated from the extrapolation of the steepest temperature gradient to measured T_0 and T_{max} . From the received raw temperature images a 2-dimensional gradient field of the flame front is determined using a combination of a horizontal and vertical oriented Sobel filter within a 3×3 matrix [Dinkelacker et. al., (Kyongju1998)]. For examination of the flame front only those gradients are sampled where the temperature has a value of about $(T_{\text{max}}-T_0)/2$. Typically in this temperature range the steepest gradients are found. From simultaneous obtained OH- and temperature images the OH-radical is used to indicate the burning reaction. A point to point assignment between OH- and temperature field is achieved by a transformation rule with an accuracy of 1 pixel. Regions with high OH-signals (*superequilibrium*) and steep OH-concentration gradients indicate local reaction conditions. Therefore only at this locations the flame front thickness is calculated out of the temperature images.

For each investigated flame condition the ensemble from 30 single-shot images, of measured conditional thickness, containing front length of about 150 pixel each, is collected into a probability density distribution. From that the maximum value is taken as flame front thickness for this characteristic burning conditions. A systematic error is produced by occasional non-perpendicular crossing between the three-dimensionally oriented front and the light sheet. A recent systematic comparison between three-dimensional and two-dimensional measurements [Soika et al. (1998)] indicates, that with this light-sheet set-up the three-dimensional flame front thickness can be estimated from the maximum of the two-dimensional thickness distribution. Errors of the thickness measurement are estimated to $\pm 50\mu\text{m}$.

3. Measurements

3.1 Investigated Flames

The thermal flame front structure is measured at the outer flame contour in two different regions above the burner nozzle (pos.1 11 ± 8 mm, pos.2 34 ± 8 mm). As indicated in Fig 4 the investigated flames are well located within the *distributed* or *broadened flames* regime and the *stirred reactor* regime of the phase diagram [Peters (1986)].

Figure4: Phase diagram for turbulent premixed flames [Peters 1986] with exemplary investigated flame conditions. The laminar flame thickness is calculated to $\delta_L = \nu_i / S_L$, where ν_i is the kinematic viscosity inside the flame at $T \approx 1250$ K [Göttgens et al. (1993)]; open (pos.2) and filled (pos.1) symbols indicate two different downstream positions investigated

(v_{exit} ● 5.1m/s, ■ 13.8m/s, ◆ 28.7m/s)

For all operation conditions the temperature images show a sharp partly wrinkled frontier between hot and cold gas. For high exit velocities single vortex structures are visible direct above the burner nozzle, looking similar to Rayleigh instability structures of corresponding flow systems. Further downstream the flame front is much more corrugated, but still a sharp front exists. If thermal flame thickness is determined without OH conditioning results not easy to interpret were produced (see Fig5).

Figure5: Measured front thickness not conditioning with reaction criterion (filled symbols pos.1; open pos.2)

Therefore simultaneous temperature and OH measurement is necessary. The OH-concentration images are used to detect the burning reaction zone in a "tri-modal-way". First case: *fresh fuel* or air. Here no burning takes place and therefore no OH-signal can be detected. Second case: *reaction*. A relatively large OH concentration with a superequilibrium value and steep gradient indicates reaction in the early part of the reaction zone (e.g. upper part of Fig. 6b). Third case: *burnt gas*. Behind the reaction zone the high superequilibrium OH signal reduces gradually to the equilibrium value of the burnt region. Three typical OH-images are shown in Fig6. Note that the burner nozzle is located at the right side ($r = 2.2$ - 2.4 cm). The temperature measurements at these location show a strong temperature gradient immediately above the burner exit. This is caused by the contact of recirculated hot gas with fresh cold fuel. From that the reaction zone would be expected to be direct above the nozzle. In the OH-images no superequilibrium-OH can be found here. Obviously the reaction zone is lifted, which is only revealed in the OH-images. Up to a height of about 11mm the low equilibrium-OH signal, coming from contact of recirculated burnt gas fresh fuel is visible.

This lift-off is different to lift-off phenomena of e.g. realised in a jet, a swirl burner or a fresh-to-back configuration of two jets. In these cases the lift-off is achieved by hydrodynamically stabilising a zone with hot gases somewhere above the burner nozzle enabling there the ignition. Further upstream the flow condition are above the blow out limits thus the flame cannot flashback to the nozzle. The fuel cannot be ignited, since there is not enough heat to start the reaction at the exit. A convective ignition delay happens.

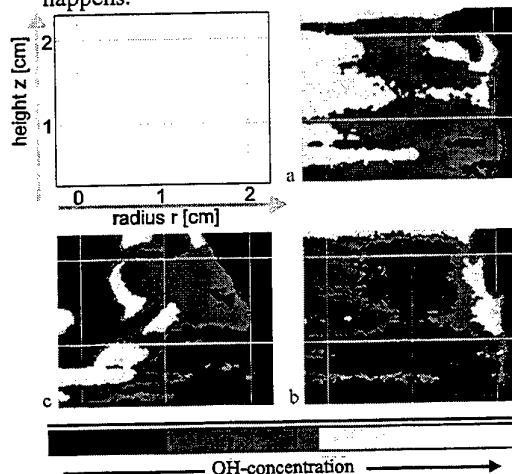


Figure6: Exemplary images of OH-concentration at v_{exit} 21.3m/s; a: $\phi=0,8$; b: $\phi=0,7$; c: $\phi=0,65$ (here burning occurs inside the less turbulent recirculation zone); the burner nozzle is located at $r=2.2-2.4\text{cm}$, $z=0\text{mm}$

Contrary to that in a bluff-body burner, the contact with the hot recirculation zone is managed immediately above burner nozzle. No convective ignition delay should take place. For very lean mixtures ($\phi \leq 0.7$) and high exit velocities ($>21.3\text{m/s}$) burning occurs partially inside the less turbulent core of the recirculation zone, while no ignition occurs at the outer contour of the flame (Fig6c). The location of reaction zone fluctuates between the core and the contour of the flame.

3.2 Flame Front Thickness

In height 2, there is usually a reaction and therefore a real flame front visible, except at exit velocity $\geq 21,3\text{ m/s}$, $\phi=0.65$. Comparing only reacting cases with laminar calculated unstretched flames [Göttgens & Dinkelacker (1997)], a slightly increased flame front thickness for stoichiometric methane/air mixtures and a significant decrease for lean mixtures $\phi \leq 0.7$ can be observed (examples given in Fig7).

Figure7: Measured flame front thickness at height2 in comparison to calculated laminar unstretched flames [Göttgens & Dinkelacker (1992)]

Figure8: Flame front thickness δ normalised by thickness δ_L of a calculated laminar unstretched front plotted against local stretch parameter K_T

Plotting measured flame front thickness, normalised by the thickness of the calculated laminar unstretched flame δ_L versus the local stretch factor [Bradley 1992]

$$K_T = (u'/l_T) / (\delta_{L,2e}/s_L) = a_T \cdot v / s_L^2 \quad (4)$$

an influence of local stretch on the flame front is visible (Fig8). Here

$$a_T = (v_a^2 + v_r^2 + v_t^2)^{0.5} / l_T = (2 \cdot k) / l_T \quad (5)$$

is the turbulent strain rate, calculated with the Taylor length l_T , while v is the kinematic viscosity of cold gas mixture and s_L the laminar burning velocity.

If the thermal flame front thickness is determined for conditions without reaction (missing superequilibrium-OH) it is found to be independent of equivalence ratio and exit velocity (Fig9). The averaged thickness at 8 mm height is $560\text{ }\mu\text{m}$ and at 30mm $650\text{ }\mu\text{m}$. The independence of the thermal thickness from stoichiometry and the increase with height indicates that here diffusional heat transfer without reaction takes place, since for reacting flame fronts the thermal thickness depends strongly on ϕ . This fits to the observation of missing superequilibrium-OH. Basing thermal diffusion as heat transfer mechanism, the profile and thickness of the front should be dependent on time after contact with hot gases and therefore dependent on exit velocity. But no different profiles are visible. On the other hand heat transfer should increase with the turbulent intensity. Obviously both effects compensate each other.

Figure9: Front thickness without reaction (filled pos.1, open pos.2)

3.3 Lifted reaction zone

Lift-off heights for the different flame conditions are shown in Fig 10. The lift-off height is about 11mm for nearly all equivalence ratios and exit velocities. Only for very lean mixtures with exit velocities above 21,3m/s the reaction starts at a higher position.

These behaviour cannot be explained by a unique ignition criterion. Instead it seems that two different conditions have to be fulfilled for ignition

- (a) chemical ignition delay and
- (b) sufficient low turbulent strain rate.

For the chemical delay a strong dependency on temperature is known [Warnatz et al. (1986)]. Since the temperature of the hot gas depends strongly on ϕ , the ignition delay time τ is significantly larger for lean mixtures), leading to a qualitative behaviour as shown in Fig.10 (dottedline).

Figure10: Height of measured (full line) and theoretical ignition derived from chemical ignition delay (dotted line)

While the chemical ignition delay time depends on the flame temperature and thus on the stoichiometry, it is dominant for very lean mixtures with low flame temperatures. Here an ignition height is found, which can be understood from different convection velocities.

On the other hand high turbulent strain rates can also be the reason of quenching, or in this case for the prevention of ignition [Pitts et al. (1989)]. If this effect is independent from the chemical mixture, a constant lift-off height should be found for different ϕ and one exit velocity. A combination of both effects should lead to a lift-off height behaviour as found experimentally (Fig.10 full line).

Assuming a ϕ -dependent ignition delay time the "chemical-dominated" lift-off height is expected to increase with higher convection velocity, which fits to the observation (v_{exit} 28.7m/s, Fig. 10). On the other hand the "chemical" lift-off height is expected to be lower for reduced exit velocities, which in the observed case (v_{exit} 13.8m/s, $\phi \geq 0.7$) obviously is below the "turbulence-dominated" lift-off height. Thus, the combination of a *turbulent dominated criterion*, being independent on stoichiometry, and a *chemical ignition delay criterion* can explain the observed lift-off height behaviour in a remarkable manner.

Furthermore we tried to find a suitable criterion for the *turbulent dominated* lift-off cases (no ϕ -dependency, v_{exit} 13.8m/s, 21.3m/s with $\phi \geq 0.7$). For that we determined four different characteristic quantities from the turbulent flow-field and the flame, measured with LDV and referenced to the corresponding position of the most probable flame front location.

Two quantities describe the turbulent flow field: The mean strain rate $A_m = |dV/dy|$ describes the gradient of the mean flow, while the turbulent strain rate $a_T = v_{rms}/l_T$ is a measure for the small scaled turbulence. For both the corresponding normalisation with thermochemical data of the flame mixture is determined additionally, leading to $K_m = A_m * v / S_{L2}$ and $K_T = a_T * (\delta_{L2el} / S_L)$. Note that K_T corresponds to the "Karlovitz number" used in [Bradley (1992)].

Figure 11: Comparison of different critical local strain parameter for lifted reaction zones

Plotting the local burning or non-burning condition as a function of these four quantities (Fig.11) it can be found that $A_{m,crit} \approx 1800 \text{ s}^{-1}$ is a suitable criterion for ignition in these flames, while all other quantities (including the Bradley Karlovitz number K_T) show overlapping regions of burning or non-burning conditions, thus being not suitable as a distinctive criterion.

4. Conclusion

With the investigated bluff body burner highly turbulent flames can be produced. At this turbulence conditions a burning reaction is not always visible at the border of hot gas towards fresh fuel. Since this effect is not visible in temperature images, in experiments an indicator for reaction intensity, like OH concentration ascent has to be measured, too. Then the measured temperature fronts can be distinguished in non-reacting and reacting flame fronts.

Compared with calculated unstretched laminar flames a thinning of the flame front is visible for the reacting case, which is contrary to the models included in the phase diagram [Peters (1986)]. This thinning is found to be dependent on the local stretch factor K_T .

Directly above the burner nozzle up to a height of 11mm, no burning reaction can be detected. Instead a lifted reaction zone is found. While for $\phi \geq 0.7$ starting point of reaction is found to be not dependent on exit velocity and equivalence ratio, for very lean mixtures a ϕ and v_{exit} dependency is visible.

For an explanation of this finding two different ignition criteria seem to be necessary, taking into account both chemical ignition time and a hydrodynamic strain.

Since the chemical ignition delay time depends on the flame temperature it is dominant for very lean mixtures with low flame temperatures. Only if this effect is shorter than a certain value, the local hydrodynamic strain seems to determine the lift-off height. As a suitable lift-off criterion for the hydrodynamic case the mean strain rate $A_m = |dV/dy| = 1800 \text{ s}^{-1}$ distinguishes between burning and non-burning conditions. The strain rate a_T , representing the strain influence from eddies, and also the non-dimensionalised strain rates – including Bradley's Karlovitz stretch factor K_T – are not suitable. To predict the lift-off height of the flame both, the *turbulent* and the *chemical dominated ignition criterion* have to be considered.

Acknowledgement

The authors gratefully acknowledge financial support of parts of the work by Deutsche Forschungsgemeinschaft.

References:

Buschmann, A., Dinkelacker, F., Schäfer, T., Schäfer, M. and Wolfrum, J., Measurement of the Instantaneous Detailed Flame Structure in Turbulent Premixed Combustion, 26th Symp. (Int.) on Combustion, The Combustion Institute, Pittsburgh, PA, p. 437-445, 1996

Bradley, D., How Fast Can We Burn, 24th Symp. (Int.) on Combustion, The Combustion Institute, Pittsburgh, PA, p. 247-262, 1992

Dinkelacker, F., Soika, A., Most, D., Höller, V. and Leipertz, A., Measurement of Local Temperature Gradients in Turbulent Combustion Systems using Two-Dimensional Laser Diagnostics, Proc. to 11th Int. Heat Transfer Conf., Kyongju, Korea, 1998

Dinkelacker, F., Soika, A., Most, D., Hofmann, D., Leipertz, A., Polifke, W., and Döbbeling, K., Structure of Locally Quenched Highly Turbulent Lean Premixed Flames, 27th Symp. (Int.) on Combustion, The Combustion Institute, Pittsburgh, PA, 1998

Göttgens, J., Mauss, F., Peters, N., Analytic Approximation of Burning Velocities and Flame Thickness of Lean Hydrogen, Methane, Ethylene, Ethane, Acetylene and Propane, 24th Symp. (Int.) on Combustion, The Combustion Institute, Pittsburgh, PA, 1992

Göttgens, J. (data), Dinkelacker, F. (eval.), personal communication, 1997

Kampmann, S., Leipertz, A., Döbbeling, K., Haumann, J. and Sattelmayer, Th., Two-Dimensional Temperature Measurement in a Technical Combustor with Laser Rayleigh Scattering, Applied optics, 32, No 30, p. 6167-6172, 1993

Krämer, H., Kampmann, S., Münch, K.-U. and Leipertz, A., Simultaneous Measurements of Temperature and Concentration Fields inside Technical Combustion Systems, Proc. Air pollution and Visibility Measurements, vol. 2506, pp. 85-93, Munich, 1995

Mansour, M. S., Chen, Y.-C. and Peters, N., The Reaction Zone Structure of Turbulent Premixed Methane-Helium-Air Flames near Extinction, 24th Symp. (Int.) on Combustion, The Combustion Institute, Pittsburgh, PA, p. 461-468, 1992

Peters, N., Laminar Flamelet Concepts in Turbulent Combustion, 21th Symp. (Int.) on Combustion, The Combustion Institute, Pittsburgh, PA, p. 1231-1250, 1986

Pitts, W.M., Assessment of Theories for Behaviour and Blow-out of Lifted Turbulent Jet Diffusion Flames, 22th Symp. (Int.) on Combustion, The Combustion Institute, Pittsburgh, PA, p. 809-816, 1989

Poinsot, T., Veynante, D., Candel, S., Diagrams of Turbulent Combustion based on Direct Simulation, 23th Symp. (Int.) on Combustion, The Combustion Institute, Pittsburgh, PA, p. 613-619, 1990

Roberts, W.L., Driscoll, J.F., Drake, M.C., Ratcliff, J.M., OH Fluorescence Images of the Quenching of a Premixed Flame During an Interaction with a Vortex, 24th Symp. (Int.) on Combustion, The Combustion Institute, Pittsburgh, PA, p. 169-176, 1992

Soika, A., Dinkelacker, F., Most, D. and Leipertz, A., Detection of 3D Temperature Gradients in Turbulent Premixed Flames with the Dual-Sheet Laser Rayleigh Scattering Technique, Proc. to 9th Int. Symp. on Appl. of Laser Tech. to Fluid Mechanics, Lissabon, 1998

Warnatz, J., 24th Symp. (Int.) on Combustion, Resolution of Gas Phase and Surface Combustion Chemistry into Elementary Reactions, The Combustion Institute, Pittsburgh, PA, p. 553-579, 1992

SESSION 26

SCALAR MEASUREMENTS II

Measurement of free surface inclination using specklegram

Koji OKAMOTO, Gentaro TANAKA and Haruki MADARAME

Nuclear Engineering Research Laboratory,
University of Tokyo,
Tokai-mura, Ibaraki, 319-11, Japan

ABSTRACTS

The interaction between the flow and free surface of liquid is very important to evaluate the free surface turbulence. In order to measure the free surface shape variation quantitatively, the specklegram technique is applied to free surface measurement. The laser light through the optical fiber have lots of speckle noises. When the light with speckle is illuminated from the bottom to surface, the speckle pattern refract at the free surface. With measuring the speckle pattern movement, the information of the free surface is obtained. The displacement of the speckle pattern gives the surface inclination. Then, the surface shape was reconstructed using the linear approximation. The experiments of the water and polymer solution jet demonstrate the effectiveness of the present technique.

1 INTRODUCTION

The interaction between the flow and free surface of liquid is very important to evaluate the free surface turbulence. The three-dimensional free surface shapes and the three-dimensional velocity distributions beneath the free surface should be simultaneously measured. Several techniques to measure the free surface shapes had been proposed using the light. Dabiri et al. (1997) proposed the color light reconstruction technique. They illuminated the free surface using the color light. The inclinations were obtained with the function of color (RGB) image, using the geometrical reflection information. However, the color coding for accurate measurement was relatively difficult. Also the setup of the measurement system was complex, since they used the light reflection. Suzuki and Sumino (1995) proposed the photometric stereo technique using twin light source. They also used the reflection at free surface. In these techniques, the light source position and color plate should be precisely set. Because the accuracy of the light source position directly related to the reconstructed wave shape.

Using the refraction at the free surface, many researchers (e.g., Jehne et al. 1994) proposed the optical

technique for the inclination measurement. However, to get the accurate results, the system was relatively complex.

The specklegram is widely used to measure the wall surface variation. The movement of the speckle pattern reflected the wall surface was calculated from the visualized images, then, the variation of the wall could be analyzed. The specklegram measurement needs just the laser source and camera system, showing the very simple system.

In this study, the specklegram was applied to measure the free surface movement. Also, to quantitatively measure the absolute water level variation, the random reconstruction technique was proposed. To reconstruct the surface shape easily, the refraction at the surface was used. With the simple and easy setup, high accurate surface shape could be reconstructed.

2 SPECKLEGRAM FOR INCLINATION MEASUREMENT

2.1 Visualization

The original specklegram was applied to measure the small surface vibrations. The laser light illuminated onto the solid surface might contain lots of small speckles. With tracking the speckle pattern movement, the solid surface vibrations could be easily visualized and quantized. Therefore, the camera settings and image analysis were very simple, showing the high effectiveness of the specklegram technique.

In order to measure the liquid free surface vibration, the similar technique can be applied. However, the reflection at liquid surface is not the same with that at solid surface. Only small portion of the laser light is reflected at the liquid surface. Also the reflected light highly depended on the direction. Therefore, Dabiri and Gharib (1993) used the relatively low angle illumination, causing the system to be complex.

In this study, the refraction at the liquid surface is used in stead of the reflection. The laser light through the optical fiber system contains lots of speckle noises caused by the small defection of the fiber and multi-reflection at the fiber surface. The speckle noises

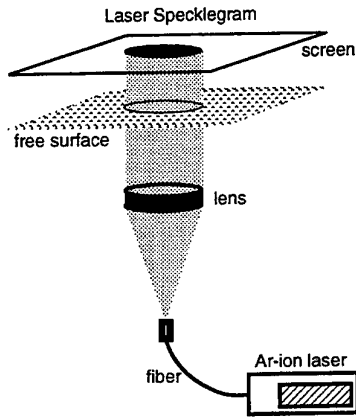


Figure 1: Schematic of the specklegram illumination

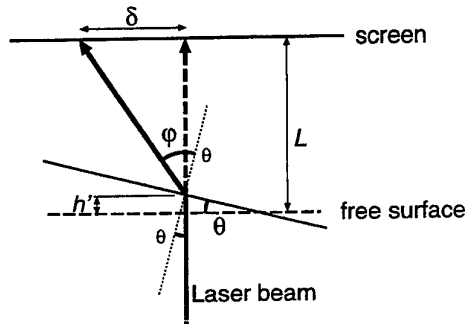


Figure 2: Refraction at free surface

through the optical fiber is applied to the speckle pattern for the surface measurement. The cone beam laser ejected from the optical fiber is converted into parallel beam using the lens. The liquid free surface is illuminated from the bottom of the test tank, i.e., the direction of the laser light is perpendicular to the free surface.

Figure 1 shows the schematic of the inclination measurement. Without the liquid surface disturbance (plane surface), the illuminated parallel laser light is not refracted at the interface (free surface). Then, the speckle pattern projected on the screen is recorded by CCD Video camera (Sony DCR-TRV9). When the water free surface is affected by turbulent jet, the surface shape is distorted. The inclination of the surface causes the laser light refraction at the surface, resulting in the projected speckle pattern to be distorted.

As shown in Fig. 2, the pattern distortion (δ) is directly depended on the surface inclination and location.

$$\delta = (L - h') \tan \theta \quad (1)$$

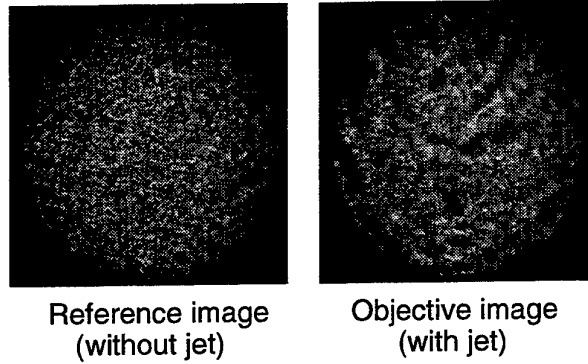


Figure 3: Example of specklegram

$$n \sin \theta = \sin(\theta + \phi) \quad (2)$$

where n denotes the refraction index of the liquid. The vertical variation (h') of surface location also affects on the inclination (θ). Because the variation is usually very smaller than the distance ($h' \ll L$), the variation could be neglected. Also, when the distortion (δ) is small enough, following approximation is applicable.

$$\theta \approx \tan \theta \approx \sin \theta \quad (3)$$

With substituting the equations, the inclination ($\theta = \partial h' / \partial x$) could be expressed as,

$$\theta = \frac{\delta}{(n-1)L} \quad (4)$$

Then, the normal vector at the surface can be easily obtained.

2.2 Image Analysis

Figure 3 shows the example of the speckle images. The left image corresponds to the plane liquid surface and right one does to the turbulent surface. The speckle patterns are distorted by the surface inclinations.

Using the cross-correlation technique, the displacement of the pattern is calculated. In the calculation of the cross-correlation factor, the following equation is applied,

$$R_{(s,t)} = \frac{\sum (f_{(x,y)} - \bar{f})(g_{(x+s,y+t)} - \bar{g})}{\sqrt{\sum (f - \bar{f})^2 \sum (g - \bar{g})^2}} \quad (5)$$

Because of the refraction at the free surface, the projected light intensity varies dramatically. Therefore, the normal cross-correlation technique using FFT may give lots of erroneous data. With substituting the average intensity, the efficiency of the pattern matching is improved.

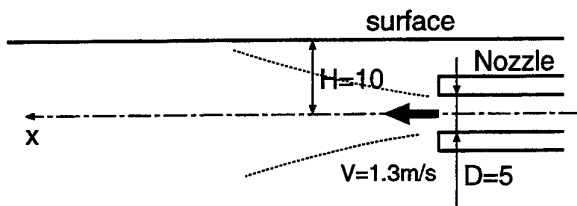


Figure 4: Schematic of experimental setup

Since the image resolution is not so high, the cross-correlation functions are interpolated using the parabolic function for obtaining the sub-pixel resolution. The accuracy for sub-pixel displacement calculation was verified using the PIV Standard Images provided by Visualization Society of Japan (VSJ, 1997). The accuracy was confirmed to be 0.1 pixel resolution using the present cross-correlation program.

The size of the speckle image is 320×240 pixel. The displacement vectors are calculated for the grid point. The interrogation area for the cross-correlation is 20×20 pixel. The surface inclination at the grid point is calculated using Eq.(4).

The surface shapes are reconstructed from the surface inclination information. To reconstruct the shapes, random reconstruction technique is applied. Initially, the surface shapes are assumed to be flat, i.e., $h'(x, y) = 0$. With generating the random number, certain location (x, y) and direction $(x/y\text{-axis})$ is selected randomly. The surface (h') is then modified according to the inclination,

$$\epsilon = \alpha \left(\frac{h'(x + \Delta x, y) - h'(x, y)}{\Delta x} - \theta \right) \quad (6)$$

where α is a relaxation factor ($\alpha < 0.5$), and ϵ is a modified height in one step, ($h' \Rightarrow h' \pm \epsilon$, respectively). This procedure is repeated until the surface shape convergence. Then, the converged surface shape is the reconstructed one. Using the above procedure, the average surface height remains to be zero, ($\sum h' = 0$).

3 EXPERIMENT AND DISCUSSION

3.1 Experimental Setup

The present technique was applied to the experiment of interaction between jet and free surface. Figure 4 shows the schematic of the experimental setup. The test section was a rectangular tank having a free surface. A circular nozzle was set horizontally beneath the free surface to form a jet. The nozzle's inner diameter is 5[mm]. The center of the nozzle was set 10[mm] under the free surface ($H/D = 2$).

The injected jet interacted with the free surface, causing the wavy free surface condition. The head tank was used to supply the constant flow rate.

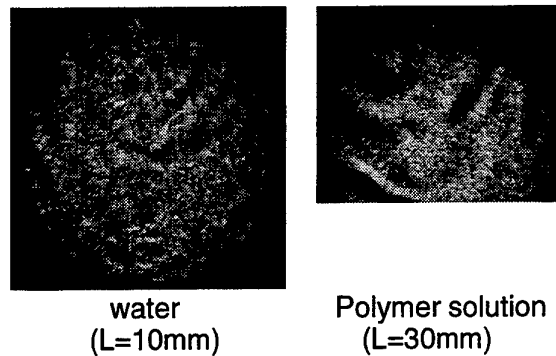


Figure 5: Specklegram of water and polymer solution

The velocity of the injected jet was set to 1.35[m/s] (Reynolds number was about 7500).

In this study, to clarify the surface shape variation, the polymer solution jet was also used. The polymer solution was an aqueous solution of a polyacrylamide(50 wppm), whose average molecular weight was about 10 million. The dry polymer powder was solved into water. The mixed polymer solution were kept for more than 24 hours to hydrate.

With the polymer solution, the turbulence were modified, i.e., Toms Effects (Toms, 1948, Virk, 1975). The injected jet condition will be varied from the pure water condition, although the Reynolds number was almost the same. The surface tension of the polymer solution (polyacrilamide; 50wppm) was confirmed to be the same with that of pure water (Ishizaki et al, 1995). Therefore, the polymer solution only affected on the jet turbulence. The surface response for the polymer solution was not clarified yet. However, the surface shape will be much calm than that of pure water jet.

In this study, the polymer solution jet was injected into polymer solution and water jet was injected into water, respectively. The free surface shape was measured for the water and the polymer solution.

3.2 Visualized Surface

Figure 5 shows the example of visualized free surfaces for pure water and polymer solution. The qualitative wave shape can be recognized with the intensity variation of the surface images. At the top of the wave, the positive curvature shape of the free surface acts as the convex lens, causing the laser intensity to increase. While, at the bottom of the wave, the image intensity is dark. Thus, the wave shape can be qualitatively visualized. In the polymer solution images, the bottom half of the illumination are lacked. From these figures, high frequency waves are visualized for the water surface, while the polymer solution surface is relatively calm. The qualitative information

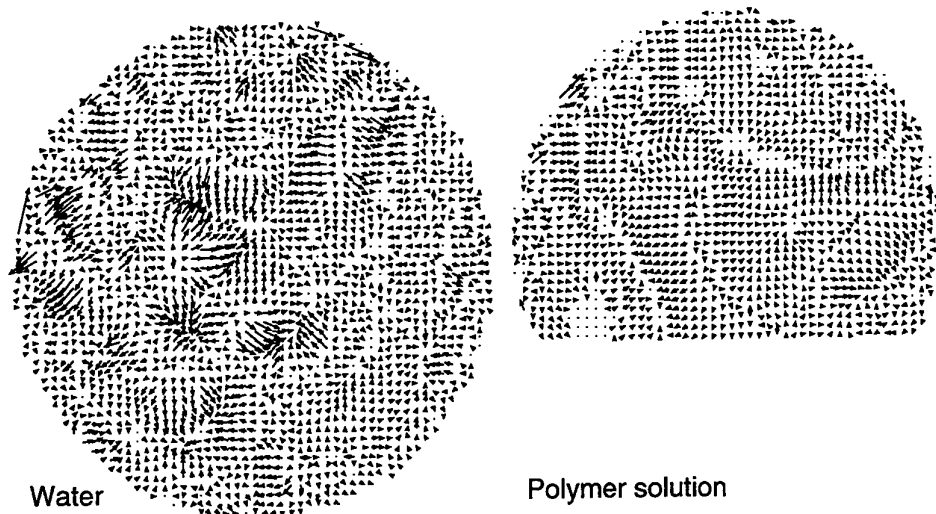


Figure 6: Displacement vector calculated by cross-correlation technique

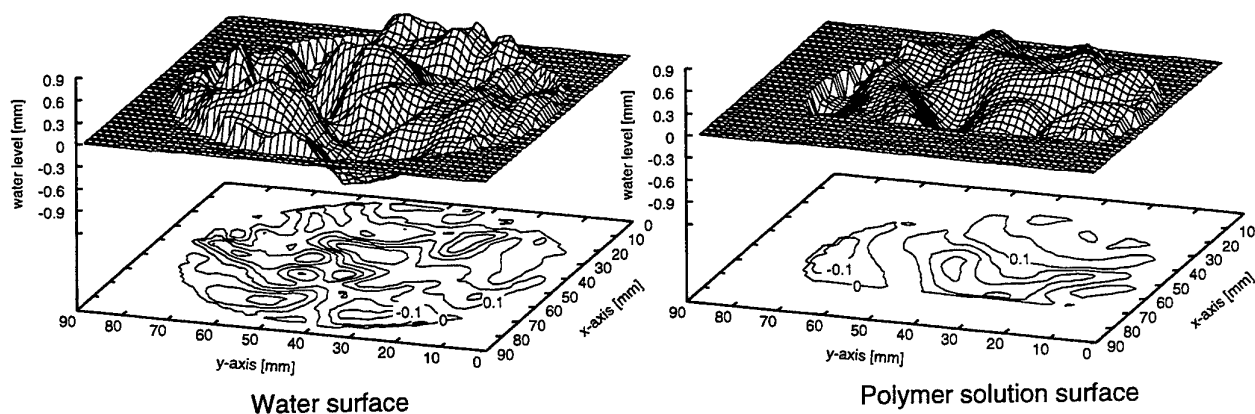


Figure 7: Reconstructed water level

are also obtained from the specklegram images.

In this study, the quantitative information is calculated from the specklegram images using cross-correlation technique. The intensity variation causes the noise of the images Figure 6 shows the example of the calculated displacement vectors calculated by the cross-correlation between the reference and target images. The surface wave is quantitatively captured. From these displacement vectors ($\vec{\delta}$), the inclination and surface height distributions are calculated as shown in Fig. 7. Since the laser light illuminated with circle shape, only the visualized surface heights are captured. The diameter of the visualized surface area is about 10cm. The surface shape is quantitatively reconstructed.

For the water surface, the spatial frequency of the

wave is high and the surface inclinations are steep. For the polymer solution surface, because the polymer modify the turbulence condition, the surface wave is calm. These tendencies are quantitatively obtained. Also, the surface wave information can be quantitatively calculated from the water level height data.

3.3 Surface Movement

The visualized images are recorded onto the Digital Video camera (Sony DCR-TRV9). The image capture interval is 1/30 sec (33.3msec). With analyzing the surface fluctuation, the information of surface disturbance could be obtained. Figure 8 shows the transient free surface height. The wave propagates from top to downstream. The quantitative information can be easily reconstructed.

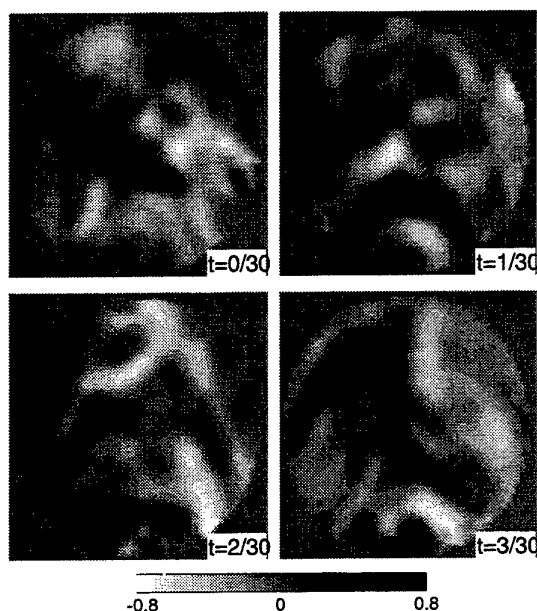


Figure 8: Transient free surface shapes

Because the surface height is reconstructed from the inclination, the relative height (h') is obtained. In the reconstruction process, the surface height is modified randomly. Since the height modifications are always $+\epsilon$ and $-\epsilon$, the average value of h' in the area remains to be zero. Therefore, the relation between relative(h') and absolute height(H) is expressed as,

$$H(x, y, t) = h'(x, y, t) + C(t), \quad (7)$$

where $C(t)$ is the average water level of the target area at $t = t$. The target area is about 10cm in diameter, which is relatively larger than the wave length. Therefore, average water level (C) could be assumed to be almost constant. With the present assumption, the absolute height can be easily determined.

Figure 9 shows the example of the water level fluctuation obtained by the present technique. The selected location is the center of the image, i.e., 50 mm downstream of the jet nozzle. The surface fluctuation can be clearly measured. Figure 9 also shows the water level fluctuation data taken by the condenser type water level meter with 100 Hz sampling. The data of water level meter contains lots of noises. The amplitude of the present measurement technique is relatively smaller than that of water level meter. The water level meter data have errors caused by the surface tension and measurement system. It contains with relatively large noises, showing larger amplitude of the wave fluctuation. The present technique also has the problems. In the cross-correlation calculation, the displacement is obtained for the area averaged value.

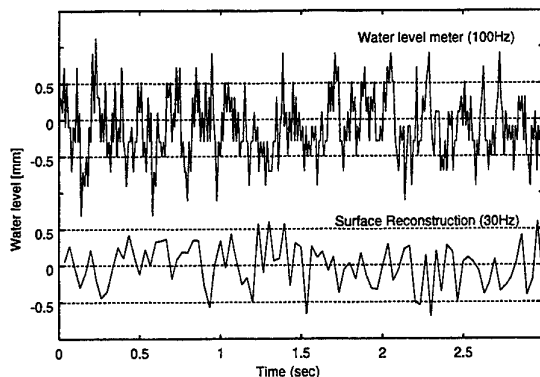


Figure 9: Waterlevel fluctuations

Therefore, the measured inclination might be a little bit smaller than the actual inclination. These small error may cause the smaller fluctuation. The improvement of the surface height measurement technique is the next task. However, the surface fluctuation frequencies in both data are almost similar. The present technique is confirmed to be obtained the quantitative absolute water level data.

3.4 Simultaneous Measurement

In this study, to quantize the free surface location, the free surface is illuminated by the cylindrical laser light. Therefore, the flow field under the free surface was simultaneously visualized. With using the three-dimensional PIV technique, the flow field under the free surface can also be measured. However, there exists several problems to measure the velocity under the free surface.

The visualized area is relatively large, i.e., $\phi 10\text{cm}$ and 10cm height. So, the accurate measurement using the CCD camera is not so easy. The surface reflection may generate the imaginary particle image. Also, the reflection at the screen may destroy the particle image. To establish the three-dimensional simultaneous measurement, these problems should be overcome. However, with restricting the illumination area, the simultaneous measurement will be able to carried out.

4 CONCLUSION

The specklegram technique was applied to measure the free surface shape variation quantitatively. The laser light with speckle noises caused by the optical fiber was illuminated from the bottom to surface. The speckle pattern was refracted at the free surface, resulting in the pattern to be distorted. With measuring the speckle pattern distortion, the information of the free surface is obtained. The surface shape was reconstructed using the linear approximation. The experi-

ments of the water and polymer solution jet demonstrate the effectiveness of the present technique.

REFERENCES

D.Dabiri, X.Zhang, and M.Gharib, 1997, "Quantitative Visualization of Three-Dimensional Free Surface Slopes and Elevations," *Atlas of Visualization III, The Visualization Society of Japan*, pp.1.

Jahne, B., Klinke and J., Waas, S., 1994, "Imaging of short ocean wind-waves - a critical review," *J. Opt. Soc. Am*, Vol.11, No.8, pp.2197

Suzuki T, and Sumino, K., 1995, "A technique of wave measurement using photometric stereo," *J. Vis. Soc. Japan*, Vol.15, No. S-1, pp.351.

P.S.Virk, 1975, "Drag Reduction Fundamentals," *AIChE.J.*, Vol.21, No.4, pp.625

B.A.Toms, 1948, "Proceedings of the First International Congress on Rheology," North-Holland Publishing Co.

Y.Ishizaki, K.Okamoto and H.Madarame, 1996, "Turbulence Reduction at Free Surface with Polymer-Solution," *ASME FED Vol.237*, pp.137.

VSJ, 1997, "PIV Standard Project; Standard Images," <http://www.vsj.or.jp/piv>.

CT-TYPE 2D LASER CONCENTRATION METER WITH NO ROTATING PARTS

—Application of 'Virtual - Load' method to an inverse problem —

Mikio Hino¹⁾ and Yukinari Sato²⁾

1) Faculty of Policy Studies, Chuo University,
Higashi - Nakano, Hachioji, Japan

2) KANOMAX JAPAN INC, 2-1, Suita, Osaka, Japan

ABSTRACT

In a previous paper (Hino, 1997), the well-known technique of double Fourier series expansion has been applied to solve the inverse problem of CT-type 2D laser concentration meter. The method had some defects that the accuracy of solution to the inverse problem is considerably lowered by the measurement errors included incidentally.

In this paper, a new method of 'virtual-load' estimation (Hino, 1975) is applied. A field is considered to be the deflection of a 'virtual elastic plate', deformed by 'virtual loads' (w). The problem reduces to solve a system of simultaneous linear equations ($A \cdot w = R$) in which the matrix A is composed of the Green function of virtual plate deflection and components of the given vector R are the decay rates of laser intensities, which are the integrated information of the field.

The usefulness and effectiveness of the 'virtual-load' method compared to the Fourier expansion method are confirmed by numerical simulation and laboratory experiment.

1. INTRODUCTION

Various methods and principles of the inverse-, and / or invasive or remote sensing estimation of an object and a flow field are developed in recent years. CT(Computer Tomography) used especially in medicine is a well-known technique to detect invasively or remote sensingly the internal structure of non-transparent materials.

1.1 Velocity Measurement :

For invasive or non-invasive measurement of flow velocities, LDV (Laser Doppler Velocimeter) based on the phenomenon of Doppler shift of scattered laser frequency is nowadays widely applied in laboratories for use in water as well as in air. Supersonic anemometers are used in meteorology and recently in lakes, rivers and ocean. Recently, the PIV and PTV have advanced from the qualitative visualization technique of flow field to the quantitative one of flow velocity measurement.

1.2 Concentration Measurement :

On the other hands, the development of measurement technique of concentration seems to be delayed. Concentration measurement of solute or sediment at a point are made by either the electric conductivity of solution or the intensity variation of light from photodiode through narrow spacing.

Two-dimensional concentration distribution of a flow field is usually measured by taking the sliced picture of dye visualized by strong light sheet. However, the applicability of this kind of technique is rather limited. In meteorology, radar technique is applied for 2-D or 3-D measurement of the distributions of cloud / rain droplets and aerosol.

In principle, X-ray CT-scan or supersonic device used in medicine may be applied for 2-D measurement of flow concentration field. However, the former apparatus is too large and heavy to be operated in a laboratory or outdoor real flow (river) and too expensive for purchase by common researchers and

the second one is designed for inspection of a local organ of human body, and difficult to apply directly to flow field.

Aim of this study :

In order to resolve these defects, we developed a handy CT-type 2D laser concentration meter. The design policy we adopted is as follows,

- (1) The apparatus has no moving parts except the control device of laser ray direction,
- (2) The apparatus is as simple as possible, and is designed not to disturb flow fields,
- (3) The scanning period should be shortest to obtain the instantaneous measurement,
- (4) The apparatus should be low cost for common researchers to buy it.

2. APPARATUS and METHOD OF ANALYSIS

Arrangement of Source and Receiver of Laser Ray :

An array of laser sources units are placed on one side and photo-cells (laser ray receivers) on the opposite side of a square frame. A laser ray is emitted from point I_{1i} the coordinate of which is designated as $(x_{1i}, y_{1i}, i=1,2,\dots,i_{\max})$ and without broadening received by a I_{2j} th photocell at $(x_{2j}, y_{2j}, j=1, 2, \dots, j_{\max})$ (Fig. 1). The intensity of ray is denoted as I_i . The extinction

of laser light intensity (I) through a concentration field, $C(x,y)$, is expressed by

$$dI/ds = -\lambda C(x, y) \cdot I \quad (1)$$

where s means a distance along a laser ray path.

$$x = x_1 + s \cdot \cos \theta \quad (2)$$

$$y = y_1 + (x_2 - x_1) \cdot \tan \theta \quad (3)$$

$$\tan \theta = (y_2 - y_1) / (x_2 - x_1) \quad (4)$$

where subscripts i, j are neglected for simplicity, and

Serial number (Π) is given to each ray path which is emitted from (x_{1i}, y_{1i}) and received at (x_{2j}, y_{2j})

$$\Pi = (I_{1i} - 1) \cdot I_{2\max} + I_{2j} \quad (5)$$

Inverse Problem :

Integrating Eq.(1) along the ray path, we obtain the following relation,

$$\begin{aligned} R(y_1, y_2) &= \int C(x, y) ds \\ &= \int C(x, y_1 + x \cdot \tan \theta) dx / \cos \theta \end{aligned} \quad (6)$$

where $R(y_1, y_2)$, the decayed ray intensity, is so-to-speak an integrated information on $C(x,y)$ brought about by a ray,

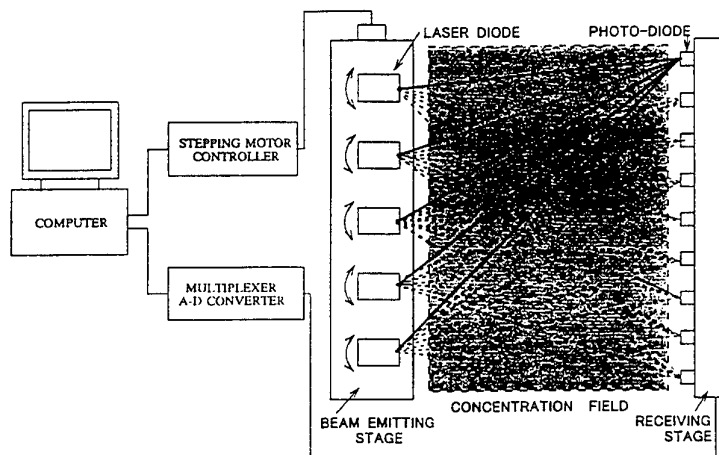


Fig. 1 : Diagram of arrangement of source and receiver, and ray paths of CT-type laser concentration measuring system.

$$R(y_1, y_2) = (\lambda)^{-1} \ln(I/I_0) \quad (7)$$

By some means, we must solve Eq.(6) to find inversely the 2-D concentration field $C(x, y)$.

Contrary to the common belief, the standard method of solving the inverse problem ; i.e. double Fourier expansion has proved to be inappropriate. Measurement error gives rise to singular matrix to fail to solve the inverse problem.

A new technique of 'virtual-plate and load' which was proposed by one of writers (Hino 1975) is applied instead. The method is a kind of 2-dimensional interpolation technique. A two-dimensional concentration field, $f(x, y)$, is considered to correspond to the deflection of an elastic plate by loads acting on various points (ξ, η) of the plate. By use of Green's function $G(x, y; \xi, \eta)$ which means the deflection of a plate at arbitrary point (x, y) by unit load on point (ξ, η) . The formula to be solved is expressed in a matrix form, and discribed in detail in section 4.

3. SOLUTION by DOUBLE FOURIER EXPANSION

Formulation of Inverse Solution :

The mostly favored standard way of solving the inverse problems of this sort is to have recourse to the Double Fourier Expansion of an unknown field.

A concentration field is expressed by Eqs. (8a,b),

$$C(x, y) = \iint f(K_x, K_y) \cdot \exp\{2\pi i(K_x x + K_y y)\} dK_x dK_y \quad (8a)$$

$$= \sum f(k_x, k_y) \cdot \exp\{2\pi i(k_x x/L_x + k_y y/L_y)\} dk_x dk_y \quad (8b)$$

where $\Delta K_x = 1/L_x$ and $\Delta K_y = 1/L_y$, L_x and L_y are the fundamental wave lengths in the direction of x and y , respectively, k_x and k_y mean the wave numbers ($k_x = 0, \pm 1, \dots, \pm k_{x\max}$, $k_y = 0, \pm 1, \dots, \pm k_{y\max}$). Note should be taken the difference in the meanings of upper case letters (K_x, K_y) and the lower case letters (k_x, k_y).

Inverse Solution by Double Fourier Method :

Eq. (8b) is rewritten by a matrix from as ;

$$A_c \cdot f = C \quad (9)$$

where A_c is the matrix composed of $\exp\{2\pi i(k_x x/L_x + k_y y/L_y)\} dk_x dk_y$.

Insertion of Eq.(9) into Eq.(6) yields Eq.(10)

$$A \cdot f = R \quad (10)$$

where A and f are complex valued, the elements of matrix A are represented as follows ,

$$A(k_x, k_y) = \int_0^{x_{2j}} \exp(2\pi i k_x x/L_x) \cdot \exp(2\pi i k_y (y_{1i} + x \tan \theta) L_y) dx / \cos \theta \quad (11)$$

$$= \exp(2\pi i k_y y_{1i}) \{ \exp(2\pi i (k_x + k_y \tan \theta) x_{2j}) - 1 \} / 2\pi i (k_x + k_y \tan \theta) \quad (k_x + k_y \tan \theta \neq 0) \quad (12a)$$

$$= x_{2j} \exp(2\pi i k_y y_{1i}) \quad (k_x + k_y \tan \theta = 0) \quad (12b)$$

and R is the matrix yielded by substitution of Eq.(8) into Eq.(6).

If the following condition is satisfied between the numbers of given information and unknowns,

$$(2k_{x\max} + 1) \times (2k_{y\max} + 1) \leq I1_{\max} \times I2_{\max} \quad (13)$$

the solution of the inverse problem could be obtained by the least-squares method.

Inverse operation of Eq.(10) gives the optimal solution of Eq.(10) as

$$f = [A^T A]^{-1} [A^T R] \quad (14)$$

Failue of Double Fourier Series Method :

When the inversion estimation of a concentration field was performed with regard to a simulated concentration data, that is the values of elements of decayed laser intensity were computed by Eq.(6) for a given concentration field, and the Fourier coefficients were determine by Eq.(14), the inversely estimated concentration field coincided exactly with the given one. However, a small error introduced artificially or incidentally in the measurement matrix R gave rise to

a singular matrix $A^T R$ to fail solving the inverse problem of Eqs.(9) and (10).

Matrices A and R , and coefficient vector f are separated into real and imaginary parts,

$$A = (A_r, iA_i) \quad (15)$$

$$f = (f_r + \varepsilon_{fr}) + i(f_i + \varepsilon_{fi}) \quad (16)$$

$$R = (R_r + \varepsilon_{Rr}) + i(R_i + \varepsilon_{Ri}) \quad (17)$$

Eq.(10) is rewritten as,

$$[A_r, -A_i] \begin{vmatrix} f_r + \varepsilon_{fr} \\ f_i + \varepsilon_{fi} \end{vmatrix} = [R_r + \varepsilon_{Rr}] \quad (18)$$

$$[A_i, A_r] \begin{vmatrix} f_r + \varepsilon_{fr} \\ f_i + \varepsilon_{fi} \end{vmatrix} = [\varepsilon_{Ri}] \quad (19)$$

Since the right-hand side of Eq.(19) cannot be measured, large error will be brought about if we solve the equation by putting $\varepsilon_{Ri} = 0$.

Detailed theoretical discussion and further means have been described in Hino (1998). An advanced method which does not use the imaginary part of R , i. e. Eq. (19) was considered and tried. However, the results were not favorable.

4. INVERSE ESTIMATION by THE 'VIRTUAL - LOAD' METHOD

Idea of 'Virtual-Load' Method :

The 'Virtual-Load' method is a kind of 2-D interpolation technique proposed more than 20 years ago by the first writer (Hino, 1975). A 2-dimensional field $C(x,y)$ is assumed to correspond to the deflection of an elastic (square) plate supported freely on four edges covering a wider region than the 2-D field considered.

Deflection of an elastic plate at point (x,y) by a unit load acting on point (ξ, η) is given by Green's function $G(x,y; \xi, \eta)$,

$$G(x,y;\xi,\eta) = (4/(\pi^4 ab)) \sum \sum \cdot (\sin(m\pi x/a) \cdot \sin(n\pi y/b) \cdot \sin(m\pi \xi/a) \cdot \sin(n\pi \eta/b)) / (m^2/a^2 + n^2/b^2) \quad (20)$$

Since the effect of loads is additive, the total deflection $C(x,y)$ by 'virtual-loads' $w_p (p=1, \dots, p_{max})$ is expressed as

$$C(x, y) = \sum G(x, y; \xi_p, \eta_p) w_p \quad (21)$$

Substitution of Eq.(21) into Eq.(6) yields the following relation, Eq.(22),

$$R_{II} = \sum GG(\Pi, p) w_p \quad (22)$$

, or in matrix form as

$$[GG] [w] = [R] \quad (23)$$

where vector w is

$$w = [w_1, w_2, \dots, w_{p_{max}}]^T \quad (24)$$

and matrix element $GG(\Pi, p)$ is given by

$$GG(\Pi, p) = \int G(x, y_1 + x \tan \theta; \xi_p, \eta_p) dx / \cos \theta \quad (25)$$

where

$$\Pi = (I_1 - 1) \cdot I_{2_{max}} + I_2 \quad (26)$$

and

$$I_1 = 1, 2, \dots, I_{1_{max}}$$

$$I_2 = 1, 2, \dots, I_{2_{max}}$$

$$\Pi_{max} = I_{1_{max}} \cdot I_{2_{max}}$$

If $\Pi_{max} > p_{max}$, applying the inverse matrix $[GG]^T$ on both sides, we obtain Eq.(27)

$$[GG]^T [GG] \cdot [W] = [GG]^T [R] \quad (27)$$

As may be seen, the 'virtual load' method solves for the virtual loads $w_p (p=1, 2, \dots, p_{max})$ instead of coefficients $f(K_x, K_y)$ in the Fourier expansion method.

After inversely solving the virtual loads w_p from Eq. (27) the concentration field is reconstructed by Eq.(21), that is,

$$C = G_c \cdot w \quad (28)$$

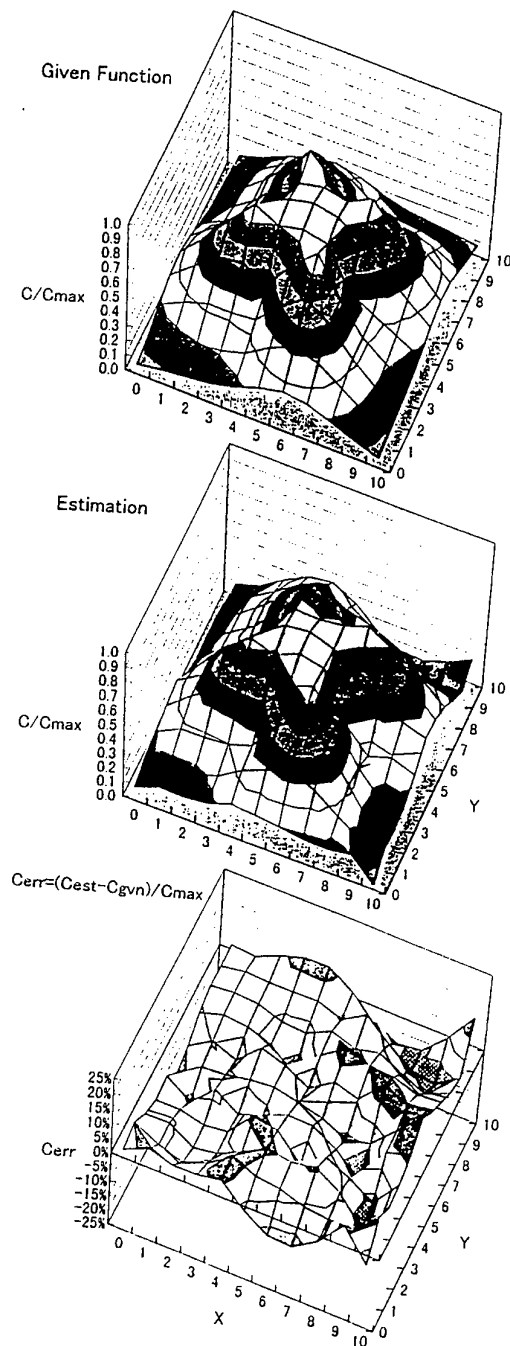


Fig. 2 : Test of the reliability of the inverse estimation by ' virtual-load ' method for a star fish type concentration distribution which is simulated by Eq.(29). Given-(upper) and estimated-(middle) concent-ration distribution, and estimation error (lower).

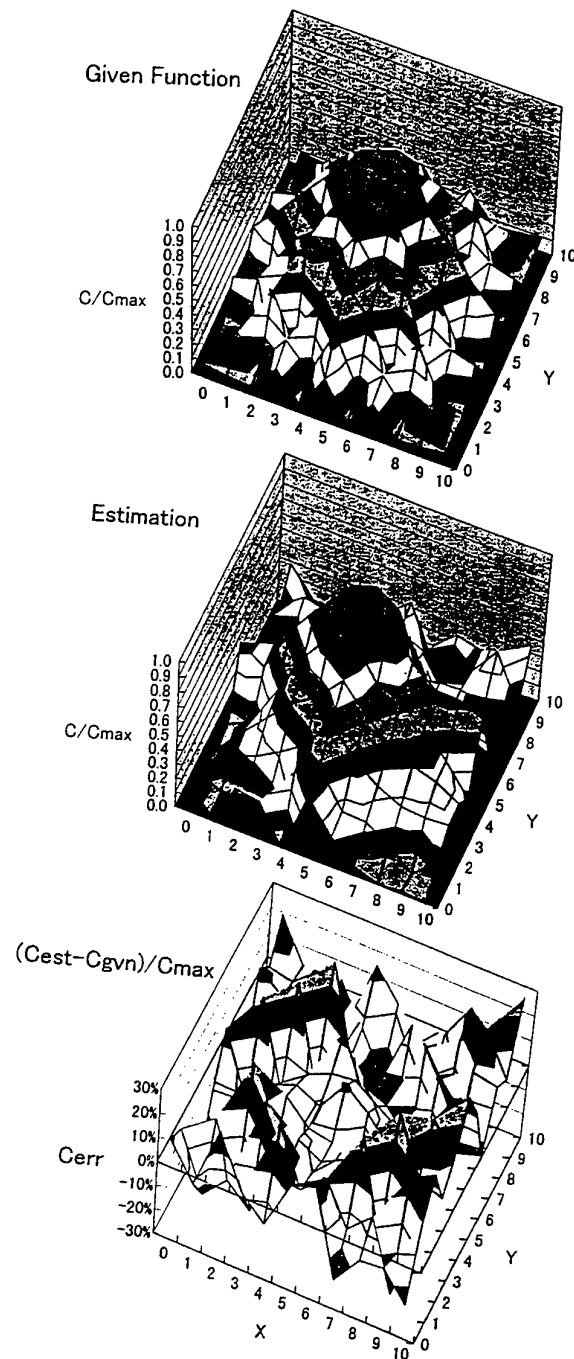


Fig.3 : Test of the reliability of the inverse estimation by ' virtual-load ' method for a more complex concent-ration distribution numerically simulated. Given-(upper) and estimated-(middle) concentration distri-bution and estimation error(lower).

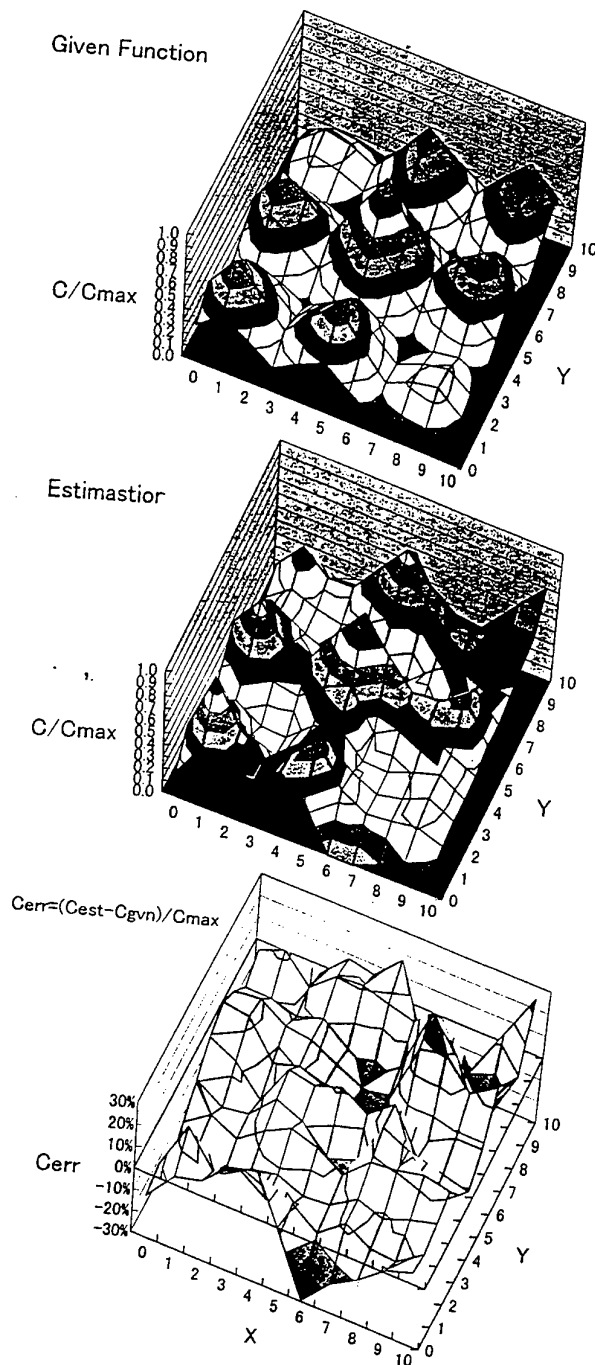


Fig.4 : Test of the reliability of the inverse estimation by 'virtual-load' method for a multi-peak concentration distribution expressed by Eq.(30). Given-(upper), estimated-(middle) concentration distribution and estimation error(lower).

5. EXPERIMENTAL RESULTS

Numerical Experiments by Simulated Data :

Distribution of concentration field by a colored jet is simulated numerical by Eq.(29) or Eq.(30)

$$C(x, y, z) = C_{\max}(z) (1 + \alpha \sin(2\pi m \theta)) \cdot \exp(-(x_2 + y_2)/r_0(\theta, z)) + \varepsilon_r \quad (29)$$

$$C(x, y, z) = C_{\max}(z) (1 + \alpha \sin(2\pi m \theta)) \cdot \exp(-(x_2 + y_2)/r_0(\theta, z)) \cdot \cos(x - x_0) \cdot \cos(y - y_0) + \varepsilon_r \quad (30)$$

where z : distance along a jet axis, x and y : coordinate in a plane perpendicular to the jet axis, θ : angle to x -axis in the (x, y) plane, r_0 : representative radius of the jet, ε_r : measurement errors which are given by rounding off the simulated value at the order of 3 digit (for instance, $C = 1.061 \dots$ is rounded as $C = 1.1$ which contains an error $\varepsilon_r = 0.04$ which amounts to 5% error).

Eq. (29) expresses a star fish shaped distribution and Eq.(30) simulates a multi-peak type one.

Figures 2(a), (b) and (c) show a simulated concentration distribution given by Eq.(29), the inverse estimation by the 'virtual-load' method recomposed from Eq.(21), i. e. Eq.(28) and the absolute error between the given field and the estimated one, respectively.

Figs. 3 (a), (b) and (c) and Figs. 4(a), (b) and (c) also illustrate comparisons between the exact and the simulated more complex concentration field and the error distribution.

As a whole, the estimation errors by the 'virtual-load' method are within about 10~15% for the imposed measurement error of 5%.

Laboratory Experiment of a Jet Concentration :

An experiment as shown in Fig. 5 was performed. A water jet of kaolin solution of concentration 500ppm was discharged from a nozzle of 10mm diameter into water tank at a velocity of 50mm / s.

From one edge, 11 laser source rays were shed and they were received at the opposite side by 11 receiver, the area of scan being 100mm × 100mm.

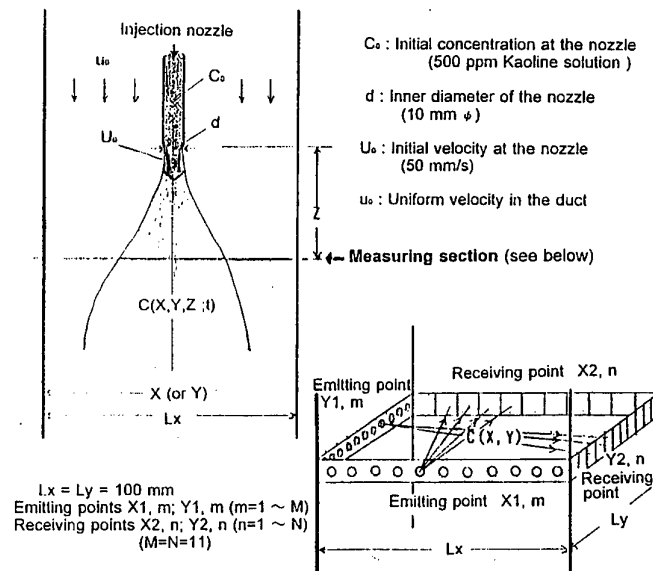


Fig.5 : Experimental apparatus.

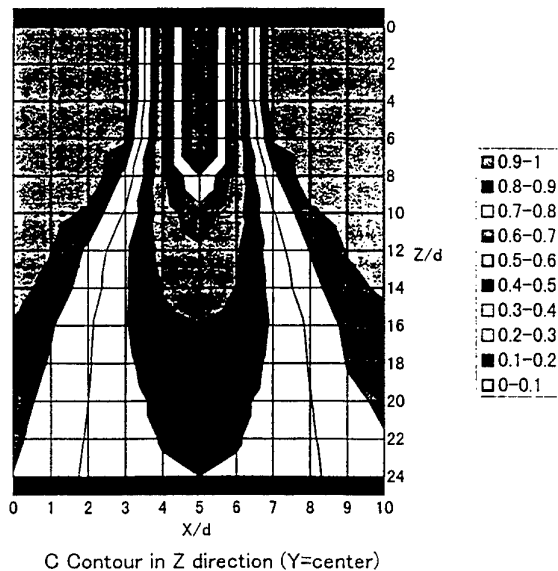


Fig.6 : Concentration distribution of a jet of kaoline solution on the axial plane.

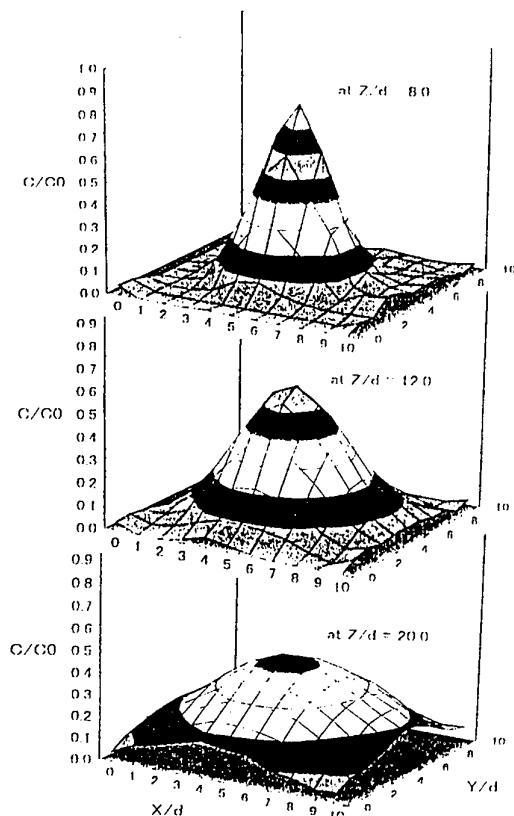


Fig.7:Concentration distribution on planes perpendicular to the axis.

The laser ray scan operation was made at distances of $z/d = 8.0, 12.0$ and 20.0 from the origin. The estimated concentrations by the 'virtual-load' method at the three sections are given in Figs. 6 and 7. The obtained results seem to be reliable.

REFERENCE

Hino, M. 1975, Proposal and explanation of 'Virtual-Load' method, Tech.Report No.18. Dep.of Civil Eng., Tokyo Inst. of Tech.

Hino, M. and Miyanaga, Y. 1975, Computation of wave force and wave diffraction by the Green function

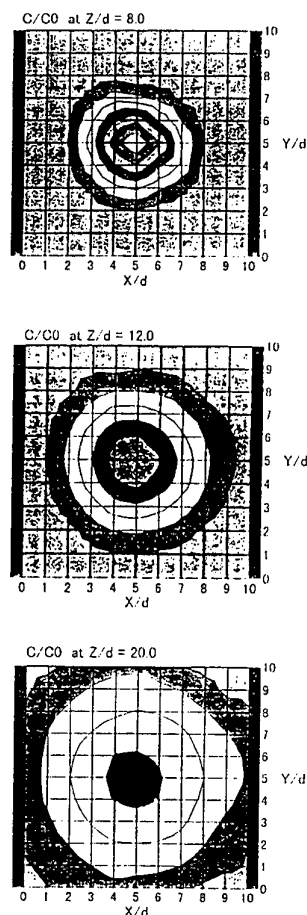


Fig.8 :Contour line representation of concentration distribution on planes perpendicular to the axis.

and the 'virtual-load' method, Proc. JSCE, no. 237, pp. 51-82.

Hino, M. 1997, Development of CT-type laser sediment concentration meter, (Measurement system of 2- and 3-dimensional instantaneous sediment concentration), Report of Research Project, Grant-In-Aid For Scientific Research (B)(2) (1996), Project no. 07455200, supported by the Ministry of Education, Culture and Science.

Hino, M. 1998, CT-type laser concentration meter, Annual Journal of Hydraulic Eng., vol. 42, JSCE, pp. 565-570.

APPLICATIONS OF LASER IN THE STUDY OF THERMODYNAMICAL PROPERTIES OF HEAVY OILS AND PETROLEUM-IN-WATER EMULSIONS

Germán Da Costa

Departamento de Física
Univ. Simón Bolívar, A.P. 89000, Caracas 1080-A, Venezuela

ABSTRACT

A petroleum-in-water emulsion is heated by a CW He-Ne laser beam incident in the liquid free surface. The resulting temperature distribution creates a centripetal thermo-convective flow which drives the petroleum droplets to the central hot point. Coalescence of an increasing number of petroleum droplets gives rise to the formation of a homogeneous petroleum bulk. A centrifugal stress distribution now grows up in the central bulk as a result of temperature dependence of the interfacial tension of the petroleum-water interface. An equilibrium state between centrifugal and centripetal forces is finally attained and the system remains at rest. The whole sequence is visualized by observation of the light beam scattered out from the liquid volume. A theoretical model explains the main features of the thermoconvective flow.

1. INTRODUCTION

Petroleum-in-water emulsions have an increasing technical and economical importance. Their development allows transportation and commercialization of highly viscous heavy oils. A stable emulsion formed by approximately spherical petroleum droplets (diameter about 10 microns) suspended in a continuous phase of water is obtained by mechanical agitation and addition of surfactants. Pumping and stocking of a stable emulsion of this kind is easily performed using engineering means similar to those used to process pure petroleum. On the contrary, when stability of the emulsion is destroyed by any physical reason the petroleum droplets fuse together to form larger droplets, a process known as coalescence. This finally results in

the formation of a solid mass of pure petroleum which plugs the pipelines and settles down forming a highly viscous precipitate. This is obviously to be prevented by any means. Though surfactants generally prevent coalescence of neighbouring droplets, introduction of increasing amounts of petroleum per unit volume, or development of strong temperature and velocity gradients finally provokes destabilization of the emulsion. Investigation of physical situations which destroy emulsion stability has utmost economical importance.

In the present paper we study the effect of thermoconvective currents which provoke coalescence of the Venezuelan product known as Orimulsion. This fuel is a mixture of 70 percent petroleum and 30 percent water plus surfactants, which results in a stable emulsion of petroleum in water at usual working conditions. In our experiments, a thermal gradient is induced in the emulsion by heating with a CW laser beam. The resulting thermoconvective phenomena are analyzed by observation of the backscattered light field. Laser-induced surface phenomena in the interface between two continuum phases of petroleum and water are studied in Section (2) of the present paper. Laser-irradiation of a petroleum-in-water emulsion gives rise to a sequence of events whose visualization and interpretation are presented in Section (3). A theoretical interpretation of phenomena described in Section (3) is given in Section (4). Earlier application of optical techniques to study coalescence of water-in-petroleum emulsions (i.e. droplets of water suspended in petroleum, which is the inverse of the case treated in the present paper) is reported in refs. [1,2].

2. LASER-INDUCED DEFORMATION OF A PETROLEUM / WATER INTERFACE

The behaviour of a liquid interface heated by a Gaussian laser beam (figs.1,2) is determined by the temperature dependence of the density and the interfacial tension [3-6].

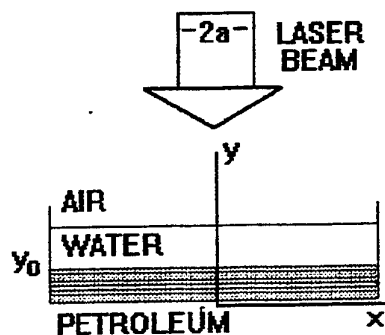


Fig.1: Laser heating of petroleum/water interface



Fig.2: Interferometric records of the petroleum/water interface.

Both quantities are decreasing functions of temperature. As seen in fig.2 in the early heating stage the interface adopts a convex bell-shaped profile, which is due to density decrease. For longer heating times the interfacial tension decrease results in the formation of a pit in the top of the convex profile. The pit depth increases and finally an equilibrium shape is attained. In the final asymptotic

stage the central region acts as an aspherical concave mirror for the incoming laser beam. Fig.(3) shows the light intensity distribution in the reflected laser beam observed in that case. Concentric light intensity maxima and minima are due to interference between light rays coming from different regions of the liquid mirror. The external bright ring is the geometric caustic of reflected light rays. A theoretical interpretation [3-6] of preceding experimental results is given in what follows.

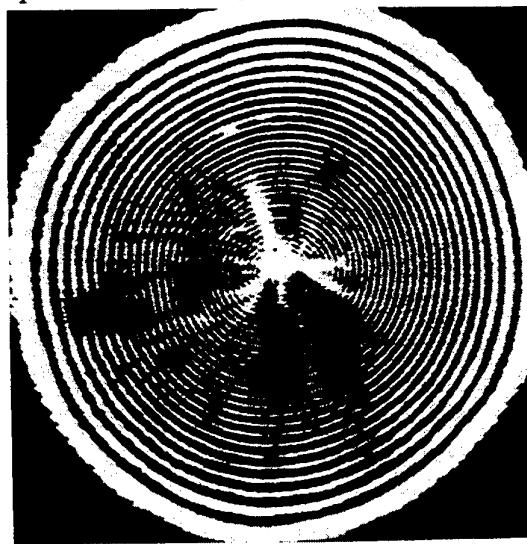


Fig.3: Photograph of the laser beam reflected from the petroleum/water interface

The temperature distribution in a liquid film (initial temperature T_0) heated by a Gaussian laser beam is:

$$T - T_0 = T_c \cdot f(\beta, \gamma) \quad (1a, b)$$

$$f(\beta, \gamma) = \int_{\inf}^{\sup} \frac{d\theta}{\theta \exp \theta}$$

where $\beta = x/a$ ("x" and "a" are defined in fig.1), $\gamma = t/t_0$, (t) is the heating time, $t_0 = a^2/4\kappa$ is the thermal time constant, $\sup = \beta^2$ and $\inf = \beta^2/(1+\gamma)$. The thermal diffusivity and thermal conductivity are (κ, k) respectively. The initial film thickness is (y_0) . The power absorbed by the sample per unit area is $Q(\beta) = Q_0 \cdot \exp(-\beta^2)$ and the characteristic temperature of the liquid is $T_c = Q_0 a^2 / 4ky_0$. This temperature distribution induces in turn density and interfacial tension distributions $\rho(T), \alpha(T)$ which in a first-order approximation are given by:

$$\begin{aligned}\rho(T) &= \rho_0 + \rho_T(T - T_0) \\ \alpha(T) &= \alpha_0 + \alpha_T(T - T_0)\end{aligned}\quad (2a,b)$$

where $\rho_0, \alpha_0, \rho_T, \alpha_T$ are the initial values (at temperature T_0) of ρ, α and their partial derivatives. As a result of simultaneous density and interfacial tension variations the liquid free surface adopts the profile given by:

$$y = \left[y_0^2 \left(\frac{\rho_0}{\rho} \right)^{3/4} + \frac{3}{\rho g} (\alpha - \alpha_0) \right]^{1/2} \quad (3)$$

where (g) is the acceleration of gravity. Substitution of eqs.(1 and 2) into eq.(3) yields:

$$\begin{aligned}u = \frac{y}{y_0} &= \left\{ \left[\frac{1}{1 + Df(\beta, \gamma)} \right]^{3/4} + \frac{3Af(\beta, \gamma)}{1 + Df(\beta, \gamma)} \right\}^{1/2} \\ u &= [w^{3/4} - C(w - 1)]^{1/2}\end{aligned}\quad (4a,b)$$

with the definitions:

$$\begin{aligned}w &= \frac{1}{1 + Df(\beta, \gamma)}, D = \frac{T_c \cdot \rho_T}{\rho_0} \\ A &= \frac{T_c \cdot \alpha_T}{\rho_0 g y_0^2}, C = \frac{3A}{D} = \frac{3\alpha_T}{g y_0^2 \rho_T}\end{aligned}\quad (5)$$

Eqs.(4a,b) give the surface profile $y(x)$ with time (t) as a parameter. The relative importance of density and interfacial tension variations is taken into account by the dimensionless quantities (A, D, C). It is noted that (A, D) are usually negative quantities. In the particular case $A=0$ only dilatation (due to density variation) exists, and the surface adopts a convex bell-shaped profile. In the case $D=0$ there is no dilatation but only a surface contraction due to interfacial tension variation. Therefore, in the general case ($A \neq 0, D \neq 0$) there exists a competition between both effects. Dilatation tends to lift the surface points (which implies $\partial u / \partial \gamma > 0$) while contraction tends to push them down

($\partial u / \partial \gamma < 0$). The sense of the vertical displacement at any surface point is thus determined by the sign of the partial derivative:

$$\begin{aligned}\frac{\partial u}{\partial \gamma} &= \frac{du}{dw} \cdot \frac{\partial w}{\partial \gamma} = \\ &= \frac{3 - 4Cw^{1/4}}{8uw^{1/4}} \left[-Dw^2 \frac{\partial f(\beta, \gamma)}{\partial \gamma} \right]\end{aligned}\quad (6)$$

A straightforward calculation shows that the condition for the displacement to be directed upward is $f(\beta, \gamma) < f_c$, where:

$$f_c = [(4C/3)^4 - 1] / D \quad (7)$$

This conclusion allows us to classify the possible time-evolution of the surface profile, depending on the value of the parameter (C):

a) If $C \geq 3/4$ we have $f_c \leq 0$. Since $f(\beta, \gamma)$ is always positive, the condition $f(\beta, \gamma) < f_c$ can never be fulfilled. All the surface points travel downward at any instant of time.

b) If $C < 3/4$ we have $f_c > 0$. This case is recorded in fig.(2) at different instants of time. In the first stage following $t = 0$ the condition $f(\beta, \gamma) < f_c$ is fulfilled by all the surface points. Dilatation is the predominant phenomenon. At a certain instant of time ($t = t_c$) the function $f(\beta, \gamma)$ attains the value (f_c). For any instant of time $t > t_c$ the function $f(\beta, \gamma)$ intersects the horizontal line with ordinate f_c at two points placed symmetrically with respect to the vertical axis. In the central region between these intersection points the interfacial tension gradient is great enough to overcome the initial dilatation. In this central region the vertical displacement of the surface points is directed downward, while the external region is still in the dilatation stage. The competition between dilatation and contraction observed in fig.(3) proves that $C < 3/4$ for the petroleum samples used in our experiments.

3. VELOCITY DISTRIBUTION IN THE THERMOCAPILLARY LIQUID FLOW

As shown in ref.(4) the horizontal component of the velocity vector is:

$$v = \frac{y_0}{2a\mu} \frac{\alpha T}{\partial \beta} \left[\frac{3H}{2} - 1 \right] H$$

$$\frac{\partial T}{\partial \beta} = \frac{2T_c}{\beta} \left\{ \exp(-\beta^2) - \exp\left(-\frac{\beta^2}{1+\gamma}\right) \right\} \quad (8a,b)$$

where (T) is the temperature at the liquid surface and (H) is the normalized depth of the considered point in the liquid ($H = y / y_0$). Note that as shown in fig. 4 the liquid flow is centrifugal down to a certain depth below the liquid free surface, while for larger depth it is centripetal. Therefore, a continuous circulation of liquid is established as a result of the temperature gradient imposed by the laser beam and to the temperature dependence of interfacial tension. Fig.(5) shows an experimental record of the reflected light beam, where images of bubbles travelling with the fluid allows experimental verification [6] of the theoretical velocity distribution (eq.8a,b).

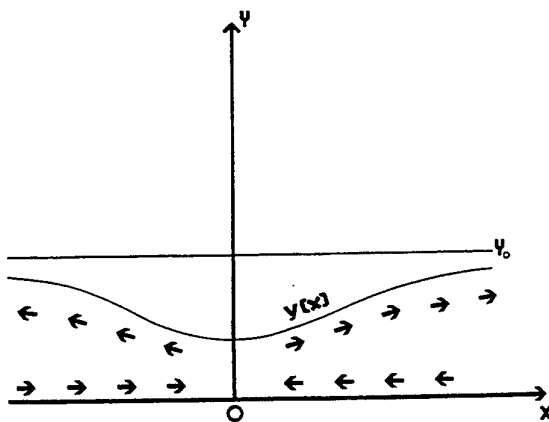


Fig.4: Sketch of the velocity distribution in the petroleum bulk of fig.1.

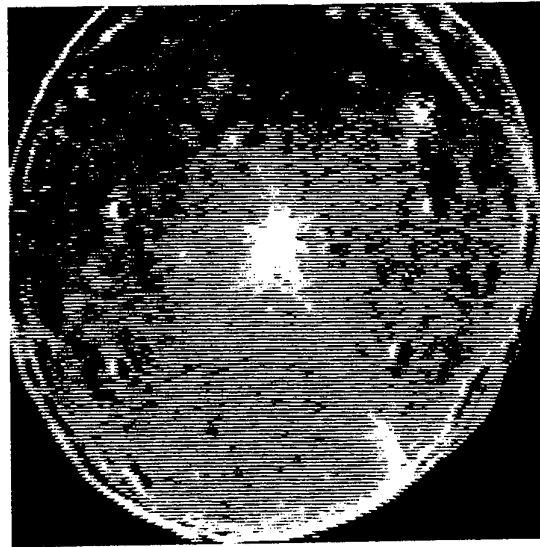


Fig.5: Images of bubbles which serve as tracers of the velocity distribution in the laser-induced thermoconvective flow.

4.LASER-INDUCED CONVECTIVE PHENOMENA IN EMULSIONS OF PETROLEUM IN WATER

4.1 Experimental Results

The behaviour of a laser-heated emulsion of petroleum (70%) in water (30%) studied in the present Section was first reported in ref.[7]. The water phase is continuous, while the petroleum phase is formed by spherical droplets with diameter about 10 microns. The experimental setup is shown in fig.6.

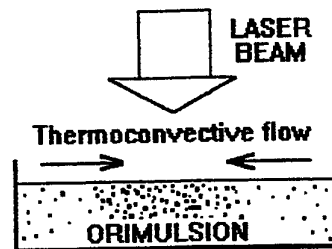


Fig.6: Laser heating of petroleum-in-water emulsion

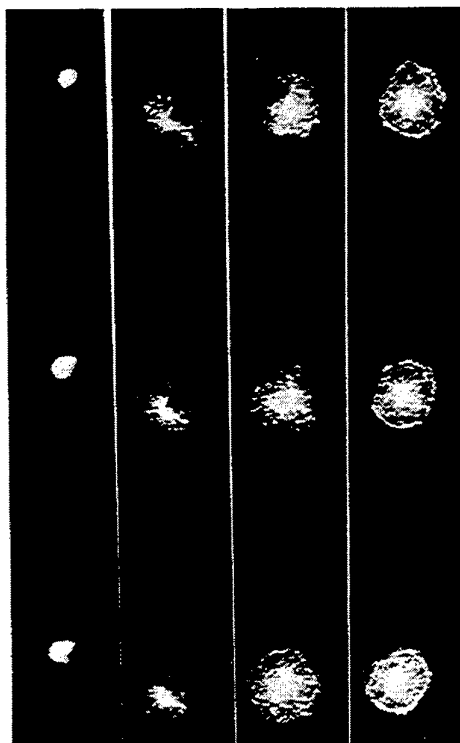


Fig.7: Photographic time-sequence of the light intensity distribution in the laser beam reflected from the petroleum-in-water emulsion

The light-intensity distribution in the reflected light beam is shown in fig.7 at different heating times. Time increases from up to down and then from left to right. The bright spot appearing in the early heating stage (first column in the photographic sequence) corresponds to direct reflection of the laser beam at the water surface covering the emulsion. The intensity of light reflected by the underlying petroleum droplets is still very low. Light is absorbed by the petroleum droplets, thus increasing their temperature which turns progressively higher than the temperature of the surrounding water matrix.

Heat is then transmitted by conduction from the petroleum droplets to surrounding water and the water temperature increases. The resulting water temperature is higher at the central region (where the laser power per unit area is a maximum) than at the periphery. Consequently a centripetal thermo-convective water flow grows up, driving the petroleum droplets from the cold external region up to the hot central region. The concentration of petroleum droplets thus increases around the central hot point, which increases in turn the heat absorption at this region. An avalanche effect takes place. A theoretical model describing this sequence of events is presented in Section (4). The amount of laser light scattered from droplets in the central region rapidly increases too. At a certain instant of time (second column in the photographic sequence) a speckle pattern suddenly appears around the central bright spot. The light speckles travel toward the central hot point. Each individual speckle exists only during a certain lifetime, thus drawing a radial dash in the visual field. This phenomenon is known as "boiling" in Speckle Metrology [8]. It is due to illumination of the radially travelling petroleum droplets with a coherent light beam. An enlarged photograph of the speckle pattern is shown in fig.8.

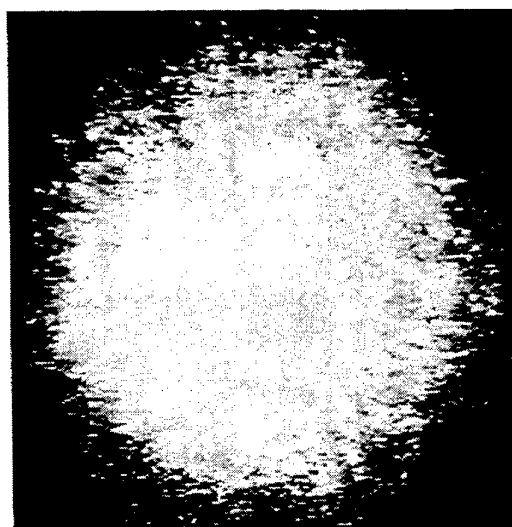


Fig.8: Photograph of the speckle pattern due to scattering of the laser beam by the petroleum particles suspended in the water matrix.

We remind that in this early stage the force field driving the petroleum droplets is centripetal, and that the droplets are still neatly separated from each other. However, accelerated confluence of droplets towards the central point produces collisions, coalescence, and formation of larger droplets. This is made evident in the following stage by the appearance of increasingly larger bright spots in the central region. These light spots are just the geometrical images of increasingly larger droplets. Simultaneously, a bright ring appears around the central region. The bright spots within it move in the centrifugal sense, contrary to the centripetal sense of movement of the surrounding speckle field. These optical phenomena announce coalescence of the emulsion and formation of a more and more definite conglomerate of pure petroleum, resulting from coalescence of an increasing number of petroleum droplets. In this central bulk formed only by petroleum the centrifugal gradient of the interfacial tension studied in Section (2) provokes the formation of a cavity, which gives rise in turn to appearance of bright rings in the reflected light beam. An interference ring system progressively grows up within the bright ring while the diameter of the external speckle pattern diminishes. Now the bright spots in the central region clearly travel in the radial direction outward from the center. Finally the external speckle pattern disappears and only the classical interference pattern corresponding to a homogeneous petroleum sample (fig.3 and last column in fig.7) remains.

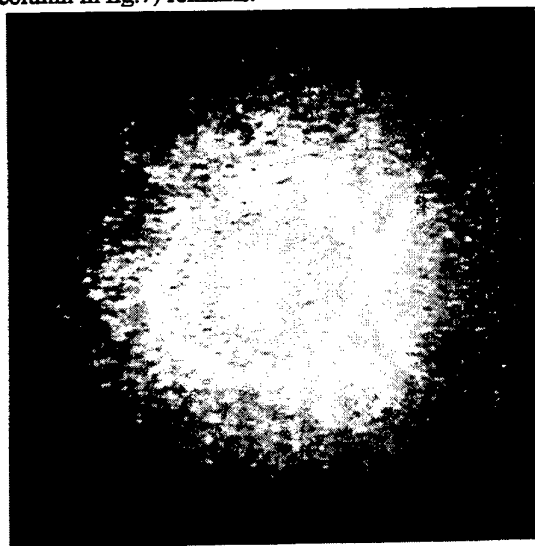


Fig.9: Bright ring reflected from the laser-heated emulsion, when the centripetal thermoconvective flow provokes coalescence of petroleum droplets.

4.2 Theoretical Analysis

Thermoconvective phenomena leading to coalescence of petroleum droplets in the central region are explained by means of the following theoretical model [7]. The present analysis is limited to a one-dimensional flow along an axis (Ox), which corresponds to a radial flow line in the true axisymmetrical experiment. The origin (O) coincides with the intersection of the laser beam axis with the liquid surface. Let $\rho(x,t)$, $v(x,t)$, $T(x,t)$ be the density, velocity and temperature of petroleum droplets respectively. The density $\rho(x,t)$ is defined as petroleum mass per unit volume of the emulsion. These quantities are coupled through the follow system of differential equations:

$$\begin{aligned} \frac{\partial \rho}{\partial t} &= -\frac{\partial (\rho v)}{\partial x} \\ \frac{\partial T}{\partial t} &= \alpha \cdot \rho \cdot \exp[-(x/a)^2] \\ v &= \beta \cdot \frac{\partial T}{\partial x} \end{aligned} \quad (9a-c)$$

Eq.(9a) is just the continuity equation. Eq.(9b) states that the local temperature increase per unit time is proportional to the local density of petroleum droplets (which are the main heat-absorbers) and to the local power of the laser beam, given by the exponential term. The radius of the laser beam is (a). In eq.(9c) the velocity of the droplets is assumed to be proportional to the local temperature gradient, which takes into account the thermoconvective effect. The parameters (α , β) are positive constant quantities which resume the thermal and mechanical properties of the emulsion. Therefore, a global phenomenological characterization of underlying microscopic interactions is made. Due to the explicit expression of the time partial derivatives of density and temperature (eqs.9a,b) the above system is readily discretized in time. Assuming uniform distributions for the density and temperature and null velocity at ($t=0$), the corresponding values of these quantities at successive instants of time ($t=i \cdot \Delta t$, where $i=1,2,3,\dots$ and Δt is a time interval) are calculated. Fig.(10) shows the density distribution at different instants of time ($i=4,5,6,7$) corresponding to a particular choice of parameters ($\alpha=\beta=3, \Delta t=0.05$). The calculated density of petroleum droplets clearly increases around the

origin ($x=0$) for increasing heating time, thus giving rise to coalescence.

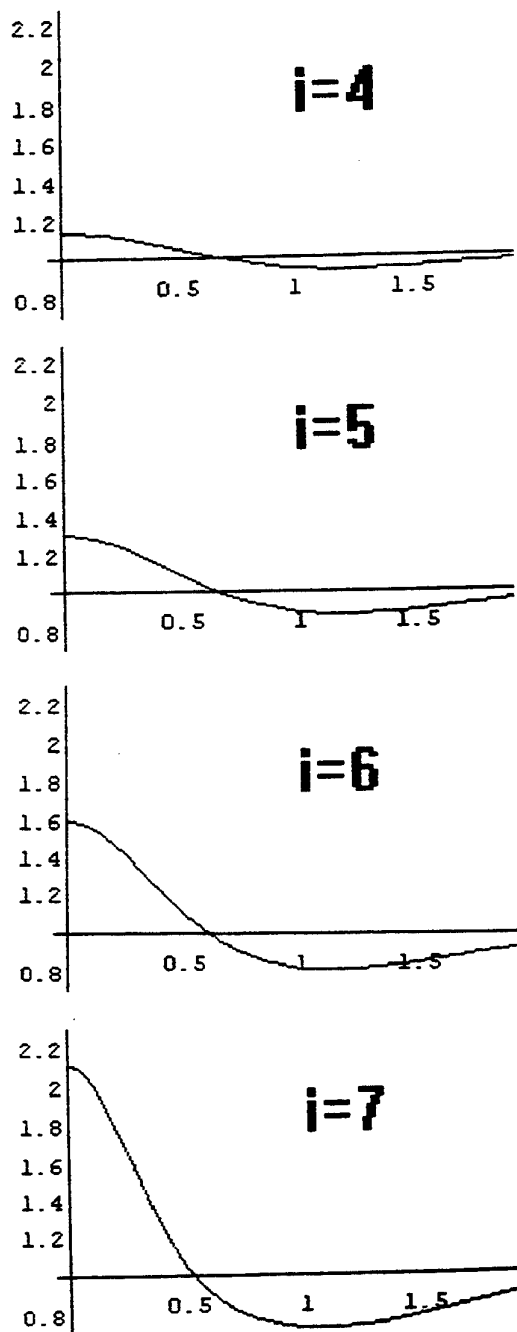


Fig.10: Each graph represents concentration of petroleum particles as a function of distance to central hot point at arbitrary scales and increasing heating time ($t = i \cdot \Delta t$)

5. CONCLUSIONS AND ADDITIONAL REMARKS

Preceding results show that introduction of a strong enough axisymmetric temperature gradient with a maximum at the center provokes coalescence of a petroleum-in-water emulsion. A single laser beam is used to produce the temperature gradient and to provide a vivid visualization of resulting hydrodynamic phenomena. It is thus seen that in the early heating stage the petroleum droplets are driven toward the central hot point by the centripetal thermoconvective water flow. The increasing amount of droplets approaching the central region results in the formation of a homogeneous petroleum bulk, where thermocapillary phenomena are predominant. This experiment was performed at different heating rates. In this aim, the linearly polarized laser beam (25mW) passes through a rotating polarizer. When the power of the laser beam incident in the liquid surface is lower than 20 mW (the diameter of the Gaussian laser beam being about 2mm at the inflection point of the power distribution) optical phenomena shown in fig.(7) (centripetal rush of light speckles) do not take place any more. We conclude that there exists an abrupt threshold of the temperature gradient necessary for initiation of the centripetal thermoconvective phenomenon and resulting emulsion coalescence. Determination of this critical temperature gradient at different concentrations of petroleum per unit volume of the emulsion requires deeper knowledge of the emulsion thermal properties, which is a subject of current research.

The optical procedure described above is therefore an useful experimental tool for real-time monitoring of laser-induced coalescence of petroleum-in-water emulsions. The theoretical model presented in Section (4) yields a description of the thermoconvective flow in terms of macroscopic (thus measurable) variables, in spite of complexity of interactions occurring at the microscopic level.

REFERENCES

- 1) D.J.Miller, "Coalescence in crude oil emulsions investigated by a light transmission method", *Colloid and Polymer Science* 265(1987)342-346
- 2) D.J.Miller and R.Böhm, "Optical studies of coalescence in crude oil emulsions", *Journal of Petroleum Science and Engineering* 9(1993)1-8
- 3) L.Landau and E.Lifschitz, *Fluid Mechanics* (MIR, Moscow,1971) pp.296-297
- 4) V.G.Levich, *Physicochemical Hydrodynamics* (Prentice-Hall, Englewood Cliffs, NJ, 1962) pp.384-390.
- 5) Germán Da Costa and Rafael Escalona, "Time evolution of the caustics of a laser heated liquid film", *Appl.Opt.* 29(1990)1023-1033.
- 6) Germán Da Costa, "Optical visualization of the velocity distribution in a laser-induced thermocapillary liquid flow", *Appl.Opt.* 32 (1993)2143-2151.
- 7) Germán Da Costa, "Laser-induced Coalescence of Petroleum-in-Water Emulsions", *Opt.Commun.* (May 1998)
- 8) J.W. Goodman, "Statistical Properties of Laser Speckle Patterns", chapter 2 in *Laser Speckle and Related Phenomena* (Topics in Applied Physics, vol.9, Springer Verlag 1975, ed. J.C. Dainty).

APPLICATION OF NONLINEAR INFRARED SPECTROGRAPH FOR RESEARCHING OF THE METHANE CONTAINING FLOWS

A.B. Britan, P.V. Kozlov, V.A. Levin, S.Yu. Mitichkin, V.G. Testov

Institute of Mechanics
Lomonosov Moscow State University, Russia

ABSTRACT

Infrared (IR) broadband spectroscopy in shock-tube studies has been limited to short duration of the working process of the unit. In this case, it is difficult to use a frequency scanning of the radiation, and the use of broadband noncoherent sources such as globars leads to a low sensitivity of such systems. After the emergence of diodes lasers the problems of irradiators for the frequency scanning were solved, but a wide proliferation of such systems is hindered owing to a complexity of their operation and an instability of characteristics. In addition, diode lasers are characterized by a rather narrow (1 cm^{-1}) range of tuning and a long scanning period (from 30 to 100 μs , on the scale of shock-tube test time).

In IR spectroscopy problems are posed by detectors and recording devices. In view of these concerns the possibility of non-linear optical conversion of IR radiation into visible radiation (up-conversion) has been examined. As long as the information on the IR radiation is preserved after the conversion, such an approach permits visualization of the IR image or absorption spectrum and detection of short IR radiation pulses. A proper device (a non-linear spectrograph) should include a source of IR radiation, a radiation frequency conversion element (up-converter), a spectral dispersion block, and visible range recording camera.

The nonlinear IR spectrograph (Britan *et al* (1995)) has been used in the present work for registering the absorption spectra of methane within the zone of the Q branch of the ν_3 band behind the shock waves and under normal conditions. The corresponding spectra were calculated (Britan *et al* (1996)) on the basis of the data of the absorption molecular lines HITRAN92 (Rothman *et al* (1992)).

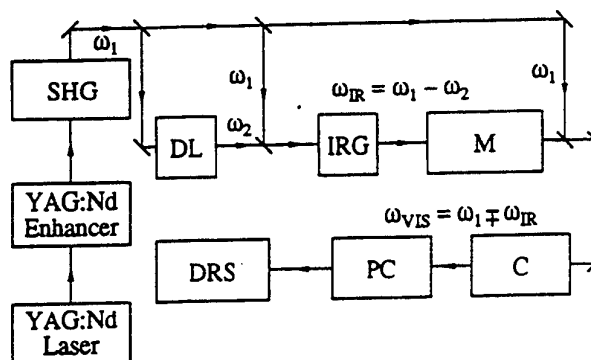


Fig. 1. Schematic diagram of the nonlinear IR laser spectrograph: (SHG) second-harmonic generator; (DL) dye laser; (IRG) infrared generating crystal; (M) medium studied; (C) up-converter; (PC) polychromator; (DRS) detection and record system.

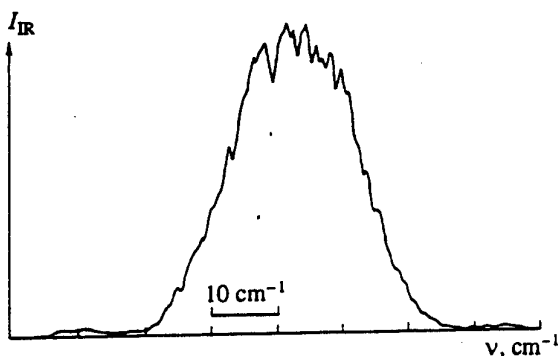


Fig. 2. Intensity of the output IR radiation versus the wave-number for a dye laser with a small generation linewidth.

PRINCIPLES OF OPERATION OF A NONLINEAR
SPECTROGRAPH

Figure 1 shows a schematic diagram of the nonlinear IR spectrograph. The system operation is based on the principle of sequential transformation of a part of laser radiation in nonlinear optical crystals, which are used for obtaining a broadband IR emission and for detection of the IR spectrum.

The broadband IR emission (with the frequencies ω_{IR}) is obtained in the process of difference-frequency generation on mixing the pumping radiations, represented by the second harmonic ($\lambda = 532$ nm, frequency ω_1) of a YAG:Nd master laser ($\omega_1/2$) and a dye laser (ω_2), in a nonlinear optical crystal. In order to provide efficient conversion, the width of the spectrum generated by the dye laser must be close to the bandwidth of the phase matching region of the crystal. The frequency variation of the IR emission performed by tuning the dye laser and changing the phase matching direction in the crystal.

The up-conversion of the IR radiation is performed by using nonlinear optical crystals for obtaining difference or sum frequencies:

$$\omega_{\text{VIZ}} = \omega_1 \mp \omega_{\text{IR}},$$

where ω_{VIZ} is the frequency of the converted (visible) spectrum. The up-converted radiation, expanded into spectrum with the aid of a polychromator, is detected by a optical (visible-range) multichannel analyzer or recorded on photographic film.

The task of obtaining a high spectral resolution poses certain requirements on the bandwidth of the master laser, because the IR frequencies are converted into those of the visible range on adding or subtracting the frequency of pumping radiation. Moreover, we must also ensure a sufficiently high intensity of the master radiation in order to provide a multiple frequency conversion and reliable detection of the spectrum, which requires using an amplifier. Radiation of a double frequency ($\lambda = 532$ nm) is used for the pumping of a dye laser and as one of the interacting waves for the generation of frequency difference and summation frequencies. Let us consider operation of the particular elements of the spectrograph.

Among the currently available nonlinear optical materials, promising properties are offered by a potassium titanyl phosphate (KTP) crystal that is known as one of the most efficient frequency doubler for YAG:Nd lasers. The transparency range of the KTP crystals extends from 0.35 to 4.5 μm . The angular tuning characteristics of KTP in the 0.4 - 4.0 μm wavelength range were studied by Dyakov *et al* (1988), but we have studied the possibility of using KTP crystals in the following nonlinear optical conversion processes:

(i) Obtaining a broadband IR emission in the course of difference frequency generation on mixing a second harmonic radiation of a YAG:Nd laser and a dye laser - a collinear interaction in the XZ plane representing a frequency difference process $o(532 \text{ nm}) + e(\text{DL}) \rightarrow o(\text{IR})$ process.

(ii) Up-conversion of the broadband IR radiation by difference (or sum) harmonic generation on mixing the IR radiation with a second harmonic of the YAG:Nd laser - a collinear interaction in the XZ plane representing a frequency difference process $o(532 \text{ nm}) + o(\text{IR}) \rightarrow e$ or a frequency summation process $o(\text{IR}) + e(532 \text{ nm}) \rightarrow o$.

We must take into account that the spectral width of the region of phase matching is inversely proportional to the crystal thickness d , while the intensity of converted radiation in the plane wave approximation is proportional to d^2 . Therefore, the choice of the thickness of a crystal providing a required width of the region of phase matching for broadband IR generation is limited by the necessity to obtain a sufficiently high intensity at the spectrograph output, so as to match the sensitivity of the existing detector systems.

The spectral width of the region of phase matching calculated in the plane wave approximation for a crystal with $d = 3.5$ mm and an IR wavelength of 3 μm amounts to about 11 cm^{-1} . Figure 2 shows the intensity of the output IR radiation I_{IR} at $\lambda = 3$ μm as a function of the wavenumber ν measured in a crystal mixing a second harmonic of the YAG:Nd laser and the radiation of a tunable dye laser with a narrow generation linewidth (0.1 cm^{-1}). The width of the region of phase matching was about 23 cm^{-1} . One the reasons for the discrepancy between the calculated and measured values is the plane wave approximation used for the calculation.

Taking into account that the angles of phase

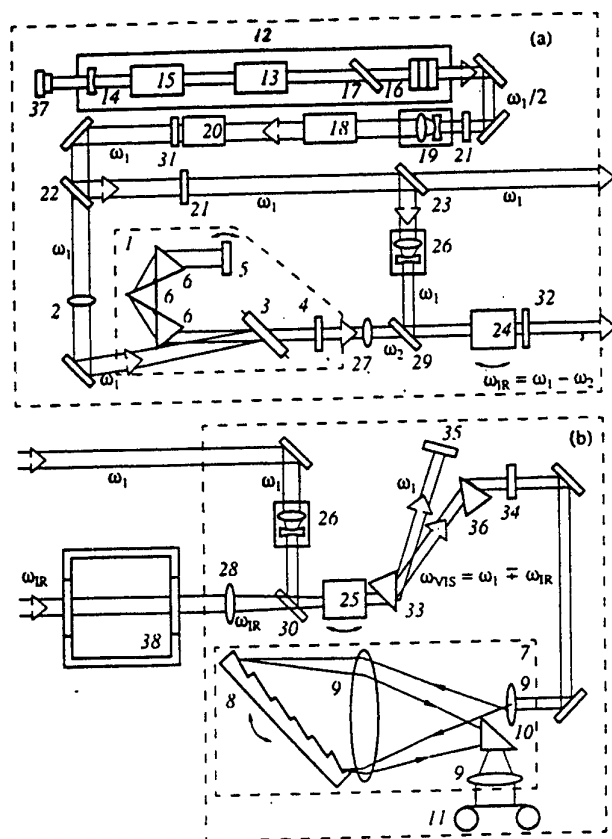


Fig. 3. General schematic diagram of the nonlinear laser IR spectrograph showing (a) transmitting and (b) receiving parts: (1) dye laser; (2, 27, 28) lenses; (3) cell; (4, 5) semitransparent and nontransparent mirrors; (6) equilateral prism; (7) polychromator; (8) grating; (9) lens element of the autocollimator; (10, 33, 36) prisms; (11) optical multichannel analyzer; (12) YAG:Nd laser; (13) active element; (14) concave non-transparent mirror; (15) LiF crystal; (16) interference reflector (stack); (17) glass plate; (18) enhancer; (19, 26) telescopes; (20) KTP crystals; (21) crystal quartz plates; (22, 23) dividing mirrors; (24, 25) KTP crystals; (29, 30) dichroic mirrors; (31, 32, 34) optical filters; (35) shield; (37) photodiode; (38) cell with methane.

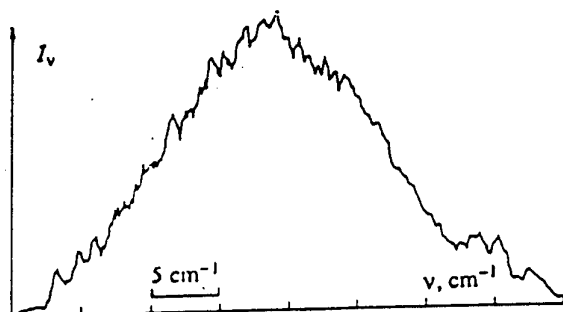


Fig. 4. Spectral distribution of the dye laser radiation.

matching are virtually equal for all the processes under consideration, we may use identical crystals both for the generation of IR emission and for the up-conversion.

BROADBAND DYE LASER

A tunable broadband emission in the visible range for conversion into the IR spectral range was generated by a dye laser 1 (Figure 3). The pumping (using second-harmonic emission from a YAG:Nd laser focused by lens 2) was performed within a quasi-collinear scheme offering certain advantages as compared to the conventional system with transverse pumping. The output radiation has homogeneous radial structure and exhibits a divergence close to that of the diffraction type, which affects the efficiency of the subsequent nonlinear optical conversion. Cell 3 with a cyclic dye pumping, having a 5 mm thick active part, was oriented at the Brewster angle relative to the axis of the resonator formed by semitransparent (4) and nontransparent (5) dielectric mirrors. The output wavelength tuning was performed by rotating the nontransparent mirror.

We tested selective resonators of various types in order to provide generation of a sufficiently broadband spectrum. Using a dispersion element comprising three equilateral prisms 6 (Figure 3), made of a TF-3 glass and mounted in the minimum deflection position, allowed us to obtain the IR emission within a bandwidth approaching the spectral width of the phase matching of the crystal. The IR emission in the wavelength range of about $2.7 \mu\text{m}$ was obtained with a DCM dye, and emission with $\lambda = 3-4 \mu\text{m}$ was obtained using phenalemin-430 and 6-aminophenalenone dyes. The energy of the emitted pulse for the DCM dye was about 2 mJ.

The spectra of output radiations of the nonlinear IR spectrograph and dye laser were obtained with the aid of polychromator 7 (Figure 3b) based on the autocollimation scheme comprising a diffraction grating 8 with 2400 lines/mm, first order of the diffraction spectrum. The radiation expanded into spectrum was either detected on a photographic film or entered an optical multichannel analyzer 11. The densitograms of the films were measured with an IFO-451 microphotometer. Figure 4 shows a spectrum of the emission intensity of the dye laser.

The spectral resolution of the polychromator was evaluated by measuring the transmission spectra of the dye laser emission in the Fabry-Perot etalons and was found to be 0.6 cm^{-1} . The minimum wavenumber interval resolved by the diffraction grating (Demtroder (1982)) 0.08 cm^{-1} was (for $\lambda = 600 \text{ nm}$). The Fabry-Perot etalons were also used for calibration of the frequency scale of the spectra.

OPTICAL SCHEME AND CHARACTERISTICS OF A NONLINEAR IR SPECTROGRAPH

The optical scheme of a nonlinear IR spectrograph is depicted in Figure 3. The YAG:Nd master laser 12 has an active element 13 with a diameter of 3 mm and a length of 65 mm mounted in a resonator with nontransparent mirror 14 (curvature radius, 5 m) compensating the effect of the thermal lens formed in the active element in the course of lasing. The resonator has a length of 92 cm. This ratio of the resonator length to the diameter of the active element eliminates the necessity of introducing a diaphragm separating a single transverse mode in the resonator.

The active element is pumped by a xenon lamp with a pulse energy of about 20 J. The energy stability of the laser is ensured by a passive Q-switching scheme with a LiF crystal 15 containing F_2^- color centers. The passive Q-switching, together with using an interference reflector (stack) 16 as the output mirror, provides the conditions for stable lasing in a single longitudinal mode (Kharchenko and Shuvalov (1988)). The duration of the lasing pulse is about 30 ns and the generation linewidth is below 0.01 cm^{-1} , which is markedly lower as compared to the polychromator resolution.

The stack used in the reflector is composed of three 5-mm-thick glass plates in optical contact. The central plate has a concentric circular hole. Glass plate 17, mounted in the resonator and oriented at the Brewster angle, provided vertical polarization of the output radiation. The pulse power of the master laser was 25 mJ and reached 180 mJ after passing amplifier 18 with an active element having a diameter of 6 mm and a length of 90 mm. A homogeneous illumination of the active element in the amplifier is provided by telescope 19 with a magnification coefficient of 3.

The second harmonic is generated in a KTP crystal 20 having a length of 20 mm. The second harmonic radiation pulse has a power of 60 mJ. Rotation of the radiation polarization vectors, ensuring the synchronous interaction of waves in the

nonlinear crystals, is performed by quartz crystal plates 21 cut perpendicularly to the optical axis.

On exiting from the second harmonic generator, the radiation was divided by mirror 22 into beams of equal intensity, one of which was used for pumping dye laser 1 and the other was employed as one of the interacting waves in the processes of frequency difference and sum generation in the KTP crystals. The beam was split by mirror 23 into two parts with the intensity ratio 2:1, entering different crystals. The beam of greater intensity enters crystal 24 for the IR emission generation, and the beam of smaller intensity is used in crystal 25 for the up-conversion.

In order to increase the radiant power density of waves interacting in the crystals, diameters of the pumping radiation beams are reduced to $1/4$ by telescopes 26, while the dye laser radiation and the IR emission are focused by lenses 27 and 28. The beams are matched within the crystals with the aid of dichroic mirrors 29 and 30.

The noninteracted part of radiation in the crystals is rejected after the frequency doubler and the IR generator by filters 31 (SZS-21) and 32 (IKS-7), respectively. Prism 33 mounted at the output of the up-converter serves to spatially separate the radiations of pumping and converted beams. It was impossible to use filters of the KS type for separating the converted radiation, because this material exhibits a strong luminescence on exposure to pumping radiation. The noninteracted IR radiation was separated from converted radiation by filter 34 (KS-13), and the noninteracted pumping component was absorbed by shield 35. The beam direction was restored by prism 36.

The IR pulse energy was $90 \mu\text{J}$, which was reduced to $4 \mu\text{J}$ after the up-conversion. Attaining the phase matching of the interacting waves was determined by monitoring the amplitude level of the signals of converted radiation, detected by PbS and PbSe photoresistors. Because the resolution of a grating with a fixed number of lines decreases with an increase in the wavelength of the incident radiation, the up-conversion was performed on the basis of the difference-frequency generation process. In addition, this variant simplified adjustment of the optical system. Radiation generated by the up-converter was expanded into spectrum by polychromator 7 and registered with detecting system 11.

The system was designed as two units representing the irradiator (Figure 3a) and receiver

(Figure 3b). By an appropriate modification of the dye laser (and using diffraction gratings as dispersion elements), it is possible to transform the device into an IR spectrometer with a narrow emission linewidth (0.1 cm^{-1}). Moreover, a common element base allows the instrument to be converted into a CARS spectrograph.

Because of the use of a single-frequency YAG:Nd master laser, the spectral resolution of the IR spectrograph is determined by the spectral resolution of the polychromator (0.6 cm^{-1}) and, unlike the case of a system based on the alkali metal vapor presented by Avouris *et al* (1981), can be in principle improved further. The spectral range of the nonlinear IR spectrograph with the same dye (DCM) extends from 2.7 to $3.7 \text{ }\mu\text{m}$ and increases to $4.5 \text{ }\mu\text{m}$ on changing dye.

In order to study the possibility of synchronization of the process studied with operation of the IR spectrograph with passive Q-switching in the master laser, we have measured the time interval between the initiating pulse of the power supply unit of the master laser and the front of the laser pulse. The latter pulse was detected by a nanosecond photodiode 37 (Figure 3a). Measurement of more than one hundred laser pulses gave a scatter of $\pm 2.5 \text{ }\mu\text{s}$, which was the value determining the temporal resolution of the system. Therefore, the IR spectrograph with passive Q-switching of the master laser can be used for investigation of high-rate processes, in particular, those behind shock waves. A further decrease in the time scatter at the expense of some reduction of the energy stability is possible in a system using an active Q-switching of the master laser and a Fabry-Perot etalon in the resonator for frequency stabilization Demtroder (1982).

Because the recording of spectra on photographic media is a rather cumbersome process, the IR absorption spectra of the medium studied were detected with a visible-range optical multichannel analyzer OSV-31 (Special Design Bureau, Academy of Sciences of Estonia) based on a 512-element linear photoelectric converter and an image brightness amplifier (electrooptical converter) connected with an optical-fiber coupler. The absorption spectrum obtained from the OSV-31 analyzer was transmitted via an interface and stored in a computer.

MEASUREMENT OF THE ABSORPTION SPECTRUM OF METHANE

A schematic of the shock tube test section and the

spectroscopic equipment is shown in Figure 5. The operation of the tube and the nonlinear IR spectrograph is synchronized with a piezo-electric transducer. The signal from the transducer sent through a delay generator starts an electronic power-supply unit for pump lamps of pulsed lasers and registering camera. A signal from the transducer clears the buffer of the camera and forms a power-supply high-voltage gate pulse for the image-brightness amplifier of the camera. The moment of the flash of the irradiator of the IR spectrograph is controlled according to readings of the photodiode.

The quantitative characteristic of a radiation absorption at the wavenumber ν is usually an absorption coefficient α_ν , which is defined according to Bouguer-Beer-Lambert law:

$$I_\nu = I_{\nu 0} \exp[-\alpha_\nu \chi l],$$

where I_ν and $I_{\nu 0}$ - are intensities of the incident and passed radiation correspondingly; χ - concentration of absorbing particles; l - length of the absorption zone.

It is known that α_ν depends on the temperature T and pressure P of the medium being studied. Let us assume that the pressure measured in a rather simple way in homogeneous flows is known. If the value of the concentration χ is also known then after measuring the ratio $I_\nu/I_{\nu 0}$ it is possible to obtain the value of T and vice versa, and that is widely used in the studies of gas flows. In order to determine the temperature in such a way, the function $\alpha_\nu(T)$ should be known through preliminary measurements (a calibration). The necessity of determination another parameter of the medium in addition to the pressure is a deficiency of this method: when the temperature is determined the concentration must be known.

The interval between adjacent lines of the P and R branches of the ν_3 band of the methane is approx. 10 cm^{-1} . Taking into consideration spectral width of the probing radiation of the nonlinear IR spectrograph, the section of the spectrum from 3000 to 3020 cm^{-1} is the most informative one. A high density of absorption lines is characteristic for the above-mentioned interval: here there are intensive lines of the Q branch of the ν_3 band and also more weak lines corresponding to other vibration types of the molecule of methane.

The absorption spectrum within the zone of the Q branch of the ν_3 band of the methane under normal conditions (the temperature is $T_0 = 293 \text{ K}$, the pressure is $P_0 = 1 \text{ atm}$) registered with the

nonlinear IR spectrograph is shown in Figure 6. The dots correspond to the readings of individual photodiodes of the registering linear detector of the optical multichannel analyzer. The concentration of methane in the mixture with argon contained in the shock tube channel with $l = 9.8$ cm in width is $\xi = 1.2\%$, the number of superimposed registered spectra is 30. In Figure 6 there is also probing radiation spectrum in the absence of the absorbing medium (I_{v0}) recorded after the absorption spectrum measurement and an evacuation of the tube (curve 1).

Figure 7 is a record of the same spectrum section obtained through a summation of results of the spectrum registration during four experiments in the shock tube $\xi = 15\%$, $M = 2.25$, the initial pressure in the channel is 0.05 atm. M is the Mach number of the incident shock wave. The readings of the pressure transducer in the probing section (10 mm from the channel end) allow the value of the pressure, $P = 1.88$ atm, to determine at the moment of the spectrum registration. The calculation gives the value of the temperature corresponding to this pressure which is equal to 1370 K. Curve 1 in Figure 7 is a record of the probing radiation spectrum I_{v0} averaged according to the above-mentioned four experiments after the evacuation of the tube after every experiment.

The calculation of the absorption spectrum, I_v , when taking a device contour into account under normal conditions and when $\xi = 1.2\%$ and $l = 9.8$ cm, is shown in Figure 6 (curve 2). The calculation of the absorption spectrum, I_v , when the pressure $P = 1.88$ atm, the temperature $T = 1370$ K behind the shock wave and $\xi = 30\%$, is shown in Figure 7 (curve 2). The value of ξ accepted in the calculation was doubled in comparison with that one used in the experiment because the applied calculation model gives a lower value of α_v , when the temperature, T , is rising.

The calculated spectra obtained describe experimental data quite well, and this fact shows a possibility of using spectroscopic data for determination of the temperature of methane-containing mixtures within the studied range of T by the shape of the absorption spectrum.

ACKNOWLEDGEMENTS

The authors are thankful to V.V. Krasnikov, M.S. Pshenichnikov, and V.S. Solomatina for help. This research was supported by the Russian Foundation for Basic Research and the Grant Competition Center for Basic Research in Energetics and Electrical Engineering.

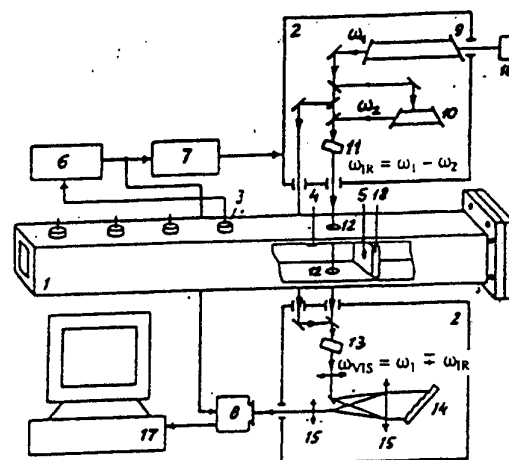


Fig. 5. Measuring section of the shock tube and registration system: (1) the shock tube; (2) the nonlinear IR spectrograph; (3-5) pressure transducers; (6) delay generator; (7) electronic power-supply unit; (8) optical multichannel analyzer; (9) YAG:Nd laser with amplifier and frequency doubler; (10) dye laser; (11) IR generator; (12) optical windows; (13) up-converter; (14) grating; (15) autocollimator; (16) photodiode; (17) computer; (18) end wall.

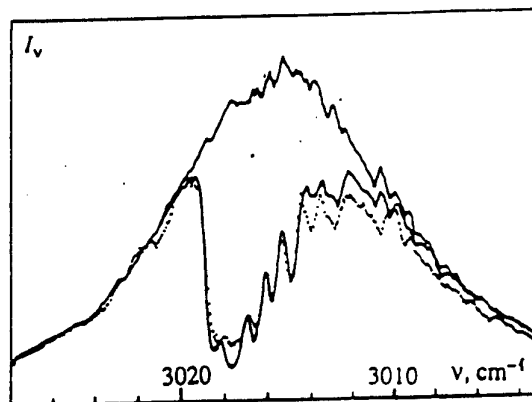


Fig. 6. Absorption spectrum under normal conditions.

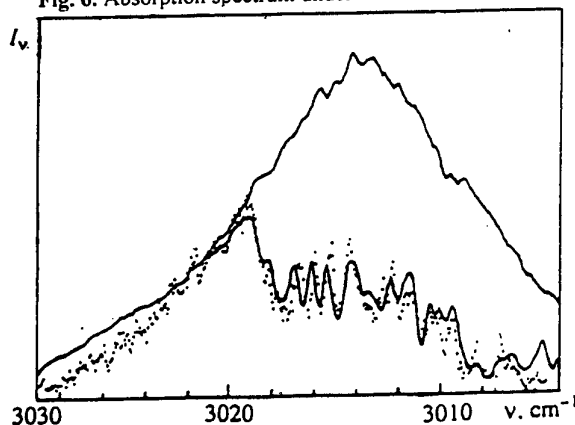


Fig. 7. Absorption spectrum behind a shock wave.

REFERENCES

- Avouris, Ph., Bethune, D.S., Lankard, J.R., Ors, J.A. & Sorokin, P.P. 1981, Time-Resolved Infrared Spectral Photography: Study of Laser-Initiated Explosions in HN_3 , J. Chem. Phys., vol. 74, pp. 2304-2312.
- Britan, A.B., Levin, V.A., Mitichkin, S.Yu. & Testov, V.G. 1995, Broadband Absorption-Coefficient Measurement on Methane Using Shock Tube, J. Quant. Spectrosc. Radiat. Transfer, vol. 54, pp. 589-598.
- Britan, A.B., Kozlov, P.V., Levin, V.A., Mitichkin, S.Yu. & Testov, V.G. 1996, Broadband Spectroscopy on Methane Using Shock Tube and Nonlinear Infrared Spectrograph, J. Quant. Spectrosc. Radiat. Transfer, vol. 56, pp. 933-940.
- Demtroder, W. 1982, Laser Spectroscopy: Basic Concepts and Instrumentation, Springer, Berlin.
- Dyakov, V.A., Krasnikov, V.V., Pryalkin, V.I., Pshenichnikov, M.S., Razumikhina, T.B., Solomatin, V.S. & Kholodnikh, A.I. 1988, The Sellmeier Equation and Tuning Characteristics of KTP-Crystal Frequency Converters in the Range from 0.4 to 4.0 μm , Kvantovaya Elektronika (Moscow), vol. 15, pp. 1703-1704.
- Kharchenko, M.A. & Shuvalov, V.V. 1988, Stable Pulse Lasers for Nonlinear Spectroscopy of High Resolution, Kvantovaya Elektronika (Moscow), vol. 15, pp. 798-804.
- Rothman, L.S., Gamache, R.R., Tipping, R.H., Rinsland, C.P., Smith, M.A.H., Benner, D.C., Malathy Devi, V., Flaud, J.-M., Camy-Peyret, C., Perrin, A., Goldman, A., Massie, S.T., Brown, L.R. & Toth, R.A. 1992, The HITRAN Molecular Database: Editions of 1991 and 1992, J. Quant. Spectrosc. Radiat. Transfer, vol. 48, pp. 469-507.

Concentration Measurement by Molecular Absorption Using Narrow Band Tunable Infra-red Laser

Tatsuya KAWAGUCHI, Koichi HISHIDA, and Masanobu MAEDA

Dept. System Design Engng., Keio University
3-14-1, Hiyoshi, Kohoku-ku, Yokohama 223-8522

ABSTRACT

This paper describes a technique to measure the spatial concentration distribution of substances using the absorption characteristics in the near infra-red light of molecules.

Measurements of concentration, temperature and flow velocity have been performed^{[1],[2]} by LIF technique, i.e. noting the temperature dependence of fluorescence characteristics of Rhodamin-B in water solution as excited by green light in combination with a PIV technique. The flow around a bubble with a moving boundary was investigated by using fluorescent particles and PIV^[3]. An analysis of the turbulent interaction of different phases including liquid-liquid, gas-liquid or gas-gas phases are of interest. In particular the boundary of a liquid-liquid mixture is hard to detect with visible light.

In this work a new measurement technique employing the spectroscopic detection of molecules in the near infra-red region was investigated. Since it can detect the molecule itself, therefore we can observe the mass transfer and diffusion phenomena directly. Additionally we can distinguish a specific substance from many others; thus the concentration of each substances can be measured from a relationship between absorbance and concentration.

INTRODUCTION

Classical shadow-graphy and schlieren photography visualize the concentration or density map of the compressible or high temperature flow field, for example in supersonic or combustive flows. Ad-

ditionally, holographic measurements of velocity^[4], mass transfer^{[5],[6]} and temperature field^{[7],[8]} have been developed in recent years. To analyze mass transfer and diffusion precisely, however a quantitative and time-series based measurements are required.

Recent advances of near infra-red and visible semiconductor laser sources for telecommunication or high speed computer networks have equally inspired a new generation of laser measurements based on an absorption spectroscopy.^[9] Operating at room temperature with wavelength tuning, high spectral purity, and long term stability are attractive characteristics of spectroscopic absorption sensing. The structure of a basic diode laser consists of a short cleaved section of lasing material with ohmic contacts at the top and bottom. The injected current through the gain medium generates an optical gain along the laser axis and the finite reflectance of the cleaved crystal planes is sufficient to create a Fabli-Perot resonator. These are common structures in the visible or near infra-red laser diode; that is, the gain medium tends to oscillate in a single longitudinal mode defined by one order of the resonator.

The wavelength of a general diode laser can be tuned in two ways. By adjusting the temperature of the diode element, the effective optical index of the waveguide is changed; thus adjusting the resonant condition of the laser cavity. Using this approach, each laser diode can typically be tuned from 3 to 5 nm between 275K and 325K. For Fabri-Perot lasers, this tuning range is typically not continuous and exhibits hysteresis and regions of multimode instability. In the continu-

ous tuning range the mode hops may be as small as 100pm. Because of the thermal mass of the diode and heater/cooler element, this type of tuning is usually restricted to a few Hz of maximum bandwidth.

The second mode of wavelength tuning involves the injection of current density into the gain section. At any given temperature, the injection current can be varied to modulate the optical index. Of course, the output power is also modulated, but the laser wavelength may be tuned quickly. In fact the injection current modulation bandwidths on the order of 10GHz are achieved in telecommunications lasers.

Absorption-based sensors have high sensitivity and selectivity when a spectrally narrow source and frequency modulation^[10] are used to probe a spectrally narrow feature. Tuning the wavelength of the light source across the absorption feature distinguishes the isolated feature from background absorption, scattering or excitation effects due to obscuration of the optical path or changes in the total source power coupled onto the receiver. Thus, most applications relevant to gas or fluid dynamics are based on absorption by low molecular weight molecules with a well resolved absorption transition.

Water vapor, droplets or liquid, are the trace in atmospheric air and is the major species of most industrial flows. There are three types of fundamental vibrations as shown in Figure 1. The absorption measurements of overtone and combination vibration absorption bands like in other hydrocarbons are performed. The $\nu_1 + \nu_3$, $2\nu_1$, and $2\nu_3$ absorption bands corresponding the 1.3 μm - 1.4 μm region, include well-resolved lines at the technically important wavelength near 1.31 μm or 1.38 μm .

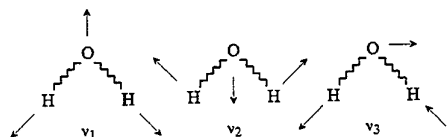


Figure 1: Fundamental vibration of H-O-H bond. $\nu_1 = 3657\text{cm}^{-1}$, $\nu_2 = 1595\text{cm}^{-1}$, $\nu_3 = 3756\text{cm}^{-1}$,

As well frequency modulation spectroscopy has successfully been applied in the various forms to near-IR and visible diode lasers for detection of H_2O ^{[11]-[15]}, CH_4 ^[16], C_2H_2 ^[14], NH_3 ^[17] and O_2 ^{[18],[19]}. In particular as for an absorption spectrum in this region between 6300 and 7900 cm^{-1} of water, H_2O ,

detailed research about the line intensities were conducted by J.-Y.Mandin. et al^[20]. The group reported many absorption bands.

MEASUREMENT TECHNIQUE

The following measurement technique is based on the absorption of liquid water in the near infrared region. The absorbance of the probe beam through an absorbing medium describes the Lambert-Beer relation given by

$$A(\nu) = \frac{I(\nu)}{I_0} = -c_m d \varepsilon(\nu) \quad (1)$$

where $A(\nu)$ is the absorbance at frequency ν . I_0 is the incident intensity of the probe beam and $I(\nu)$ is the intensity after propagation through the length 'd' of the absorbing medium and $\varepsilon(\nu)$ is the spectral molar absorption coefficient. If there exists a spatial concentration distribution, it corresponds to the line integral value of absorbance along the probe beam.

In order to accurately detect absorption, the wavelength of the light source needs to be adjusted to the absorption line. Figure 2 show a diagram of the laser diode power supply that controls the injection current and the temperature to stabilize the output power and the wavelength.

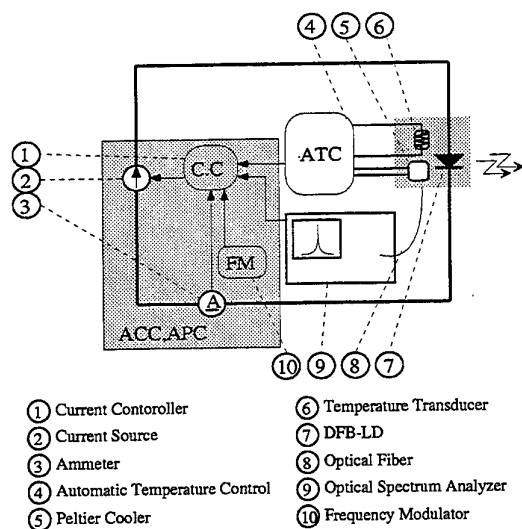


Figure 2: Laser diode power supply with Automatic Temperature Control(ATC) and Automatic Power Control (APC).

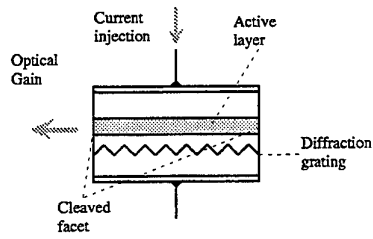


Figure 3: Structure of Distributed Feed-back(DFB) laser diode.

In the present study, we adopted an InGaAsP/InP DFB(Distributed Feedback)[13],[21],[22] laser diode as shown in Figure 3 has a narrow emission spectrum, typically less than 30MHz ($\sim 0.2[\text{pm}]$) in the near infra-red region. The detailed specifications are shown in Table 1. DFB lasers have been developed at wavelength as short as 760nm and are commonly available as InGaAsP/InP devices out to $2\mu\text{m}$. They can also be temperature tuned over 3-5nm about the normal operating wavelength although the injection current tuning rate is typically below $10^{-2}[\text{nm} \cdot \text{mA}^{-1}]$, and $10^{-1}[\text{nm} \cdot \text{K}^{-1}]$

Table 1: Optical and electrical characteristics of Anritsu DFB laser diode module at $T_c = 298[\text{K}]$

item	symbol	value(Typ.)	unit
Forward Voltage	V_F	1.5	V
Threshold Current	I_{th}	35	mA
Optical Output Power	P_0	4	mW
Spectral Half Width	$\delta\lambda$	30	MHz
Side Mode Sup- pression Ratio	SMSR	35	dB
Parallel Beam Divergence	$\theta_{//}$	35	deg
Perpendicular Beam Diver- gence	θ_{\perp}	40	deg
Rise time	t_r	0.5	ns
Fall Time	t_f	0.7	ns

EXPERIMENT AND RESULT

Absorption Spectrum

In the experiments two substances, water and acetone, were used to confirm the efficiency of our absorption sensor. Figure 4 shows the corresponding absorption spectrum between $0.8\mu\text{m}$ and $2.0\mu\text{m}$. It shows that a $1.38\mu\text{m}$ DFB light source can distinguish water from acetone whose absorbance is extremely small in comparison with waters at this wavelength.

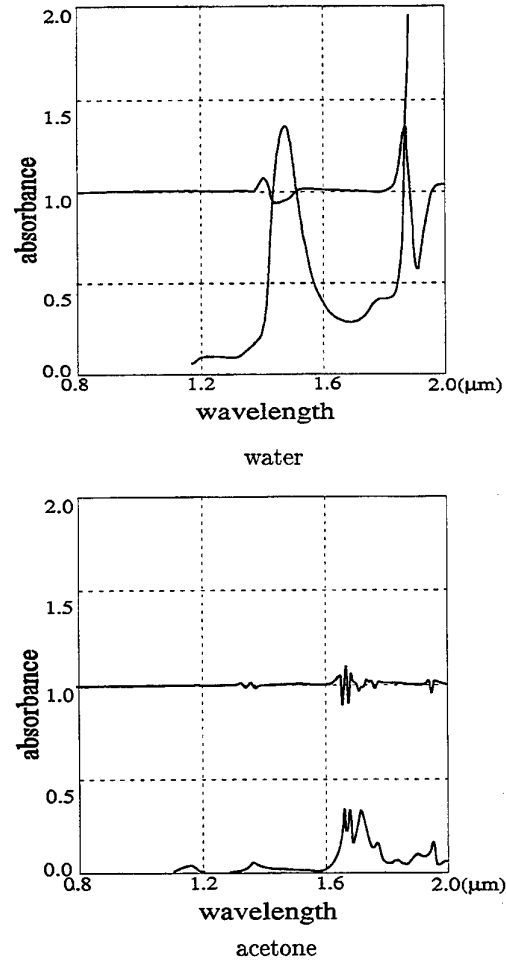


Figure 4: Experimental near infra-red absorption spectrum and the twice differentiated spectrum of liquid water and acetone between $0.8\mu\text{m}$ and $2.0\mu\text{m}$
; temperature = 293[K], pressure = 0.1[MPa],
pass length = 10.0[mm].

Concentration and Absorbance

Initially we checked the relationship between the concentration and the absorbance. The experimental apparatus is shown in Figure 5. The InGaAs photodiode detects the intensity of the laser beam through a sufficiently mixed solution of acetone and water. From the result in Figure 6, we confirmed that the absorbance was directly proportional to the concentration of water. So it is possible to apply the relation described by Equation 1 in this case.

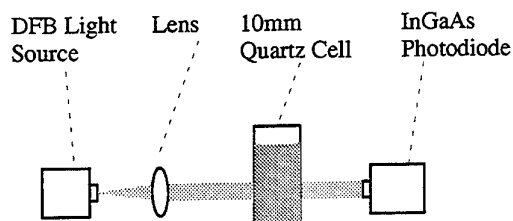


Figure 5: Measurement system to verify the relationship between concentration and absorbance.

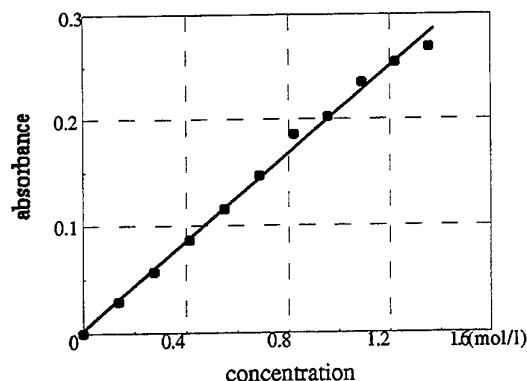


Figure 6: Measured absorbance of water at $1.38\mu\text{m}$ as a function of the concentration

Concentration Distribution Measurements

Secondly, we measured the spatial concentration of water in a acetone pool, as the first step toward extension to multi-dimensional measurements using a Computer Tomography (CT) technique. This system consists of a DFB light source, linear image sensor, signal processor and host computer as shown in Figure 7. When the laser sheet

was directed into the pool, only the water absorbed the light and the absorbance of water was observed by the sensor located on the opposite side of the light source. The InGaAs linear image sensor with Peltier cooling was adopted to observe the distribution of absorbancies which has sensitivity in the near infra-red region. A detailed specification is shown in Table 2. The projected image on the sensor were first converted to analog video signal. The images were logarithmically amplified by a signal processor in order to convert the intensity information to absorbancies and to widen the dynamic range. The information was then transferred into a personal computer through a 60 MSPS, 12bit high speed Analog to Digital converter.

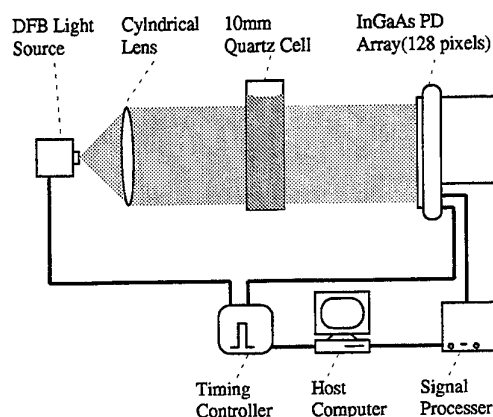


Figure 7: Experimental set-up to measure the spatial distribution of concentration.

Table 2: Optical and electrical characteristics of linear image sensor.

item	symbol	value	unit
Pixel Width	-	50	μm
Pixel high	-	200	μm
A number of pixel	-	128	pixels
pixel rate	f	up to 1	MHz
Sensitive wave-length	λ	0.9 - 1.7	μm
Dark Current	I_D	3	pA/pixel
Cooling Temperature	T_S	263	K

Figure 8 illustrated the experimental results which were obtained in the way described above. This figure shows the one-dimensional time-resolved distribution of a water and acetone mixture droplet (A) in a pure acetone pool (B). The concentration distribution of water spreads according to convection and diffusion. Furthermore, the droplet as a whole is descending in the direction of gravity.

Figure 9 illustrates the sectional concentration distribution of the round jet. This is performed by changing the initial H_2O concentration, the other conditions such as average velocity, temperature, nozzle diameter were fixed. As the initial concentration was changed from 0.1 to 0.01[mol/l], the measured concentration distribution were followed.

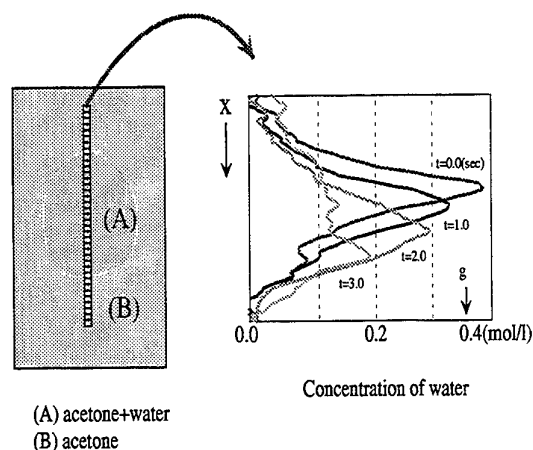


Figure 8: Spatial distribution of concentration : [water]+[acetone] droplet in a [acetone] pool.

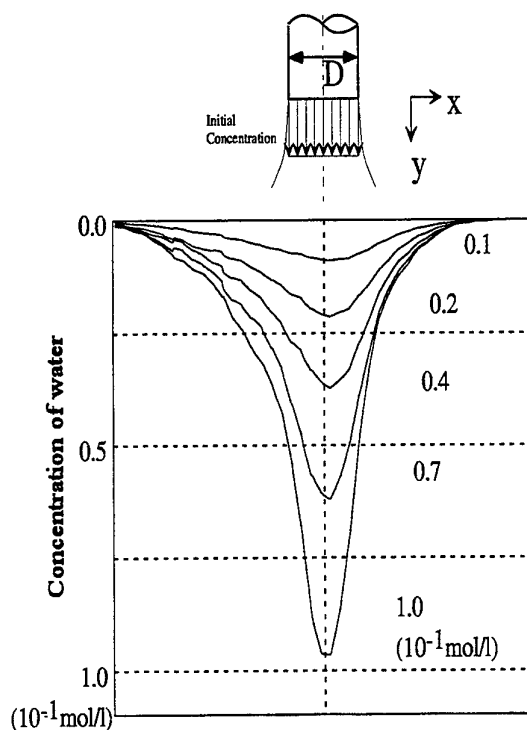


Figure 9: Spatial distribution of concentration; round jet at $x/D=5.0$: initial concentration of $H_2O = 0.01 - 0.1$ [mol/l], nozzle diameter $D = 1.0$ mm, average velocity $U = 3.2 \times 10^{-3}$ m/s

Conclusion

In this work, we accomplished to measure the one-dimensional temporal distribution of concentration which is invisible information, with a pair of near infra-red DFB laser diodes and a linear image sensor. This spectroscopic detection technique has high sensitivity and quantitiveness, that can be utilized in a various media by choosing the absorption band corresponding to the substance under search. Multiple projected images enable us to obtain the sectional image of the concentration in combination with a CT technique. It is easy to extend the method to the three dimensional measurement. As a projected matrix image was observed, we could obtain the time resolved volumetric distribution of concentration using a 3-D CT technique.

ACKNOWLEDGMENTS

The authors would like to thank ANRITSU CO.LTD. for the supply of the DFB laser diodes used in this work. We would like to acknowledge Prof. K. Uehara for his helpful advices during the experiments.

References

- [1] A.Tokuhiro, M.Maekawa, A.Fujiwara, K.Hishida and M.Maeda, "Measurements in the wake of two bubbles in close proximity by combined shadow-image and PIV technique" ASME, FEDSM97-3067, 1997.
- [2] E.Mastorakos, M.Shibasaki and K.Hishida, "Mixing enhancement in axisymmetric turbulent isothermal and buoyant jets", Exp. in Fld., 20, pp.279-90., 1996.
- [3] J.Sakakibara, K.Hishida and M.Maeda, "Measurement of thermally stratified pipe flow using image-processing techniques", Exp. in Fld., 16, pp.82-96., 1993.
- [4] H.Royer, "Holography and particle image velocimetry", Meas. Sci.Technol. Vol.8 No.12, 1997
- [5] H.Grosse-Wilde and J.Uhlenbusch, "Measurement of local mass-transfer coefficients by holographic interferometry", Int.J. Heat Mass Transfer. Vol.21, pp.677-682, 1977
- [6] A.Ito, D.Masuda and K.Saito, "A study of flame spread over alcohols using holographic interferometry", Combustion and Flame, 83, 375-389, 1991
- [7] A.Ito, and T.Kashiwagi, "Measurement technique for determining the temperature distribution in a transparent solid using holographic interferometry", Appl. Opt., Vol.26, No.5, 1987
- [8] S.Kato and N.Maruyama, "Holographic Interferometric Measurements of the Three-Dimensional temperature field with thermally developing flow in the measuring-beam direction", Exp. Thermal and Fluid Sci., 1989, 2, 333 - 340
- [9] A.S.Bonanno, J.M.Olinger and P.R.Griffiths., ed. K.I. Hildrum, T.Isaksson, T.Naes, and A.Tandberg, "Near-Infrared Spectroscopy" Ellis Horwood, Chichester, 1992.
- [10] C.B.Carlsle and D.E.Cooper, "Tunable-diode-laser frequency-modulation spectroscopy using balanced homodyne detection", Opt. Lett., 14, 1306-1308, 1989
- [11] D.E.Cooper and J.P.Watjen, "Two-tone optical heterodyne spectroscopy with a tunable lead-salt diode laser", Opt. Lett., 11, 606-608, 1986
- [12] C.B.Carlsle and D.E.Cooper, "Tunable diode laser frequency modulation spectroscopy through an optical fiber : high-sensitivity detection of water vapor", Appl. Phys. Lett., 56, 805-807, 1990
- [13] B.F.Ventrudo and D.T.Cassidy, "Operating characteristics of a tunable diode laser absorption spectrometer using short-external-cavity and DFB laser diodes", Appl. Opt., 29, 5007-5013, 1990
- [14] R.Grosskloss, P.Kersten and W.Demtroder, "Sensitive amplitude- and phase-modulated absorption spectroscopy with a continuously tunable diode laser", Appl. Phys., B58, 137-142, 1994
- [15] J.A.Silver and D.C.Hovde, "Near-Infrared diode laser airborne hygrometer", Rev. Sci. Instrum., 65, 1691-1694, 1994
- [16] A.Lucchesini, I.Longo, C.Gabbanini, S.Gozzini and L.Moi, "Diode laser spectroscopy of methane overtone transitions", Appl. Opt., 32m 5211-5216, 1993
- [17] M.Feher, P.A.Martin, A.Rohrbacher, A.M.Solva and J.P.Maier, "Inexpensive near-infrared diode-laser-based detection system for ammonia", Appl. Opt., 32, 2028-2030, 1993
- [18] D.M.Bruce and D.T.Cassidy, "Detection of oxygen using short external cavity GaAs semiconductor diode laser", Appl. Opt., 29, 1327-1332, 1990
- [19] L.C.Phillipe and R.K.Hanson, "Laser diode wavelength-modulation spectroscopy for simultaneous measurement of temperature, pressure, and velocity in shock-heated oxygen flows", Appl. Opt., 32, 6090-6103, 1993
- [20] J.-Y.Mandin, J.-P.Chevillard, C.Camy-Peyret and J.-M.Flaud, "Line Intensities in the $\nu_1 + 2\nu_2$, $2\nu_2 + \nu_3$, $2\nu_1$, $\nu_1 + \nu_3$, and $2\nu_1 + \nu_2 + \nu_3 - \nu_2$ Bands of H_2^{16}O , between 6300 and 7900 cm^{-1} ", J.Mol.Spectrosc., 118, 96-102, 1986
- [21] N.A.Morris, J.C.Connolly, R.U.Martinelli, J.H.Abeles and A.L.Cook, "Single-mode distributed-Feedback 761-nm GaAs-AlGaAs quantum-well laser absorption", IEEE Photon., Technol. Lett.7, 455-7, 1995,
- [22] H.Nagai, T.Matsuoka, Y.Noguchi, Y.Suzuki and Y.Yoshikuni, "InGaAsP/InP distributed feedback buried heterostructure lasers with both facets cleaved structure", IEEE J.Quantum Electron., QE-22 No.3, pp450-7, 1986

SESSION 27

TWO-PHASE FLOWS III

THERMOCAPILLARY BUBBLE EXPERIMENTS USING LIQUID CRYSTALS

G. Wozniak

Chair of Experimental Mechanics
Freiberg University of Mining and Technology, Freiberg, Germany

ABSTRACT

The surface tension driven flow in the liquid vicinity of gas bubbles on heated solid walls has been investigated both, in a reduced gravity environment aboard a sounding rocket and in earth-bound experiments, using liquid crystal tracers as flow and temperature indicators. Comparison of single bubble results obtained in microgravity to those measured on Earth reveals that due to the interaction of thermocapillarity and buoyancy a very compact vortex flow results on ground, while in microgravity the influence of the surface tension driven flow penetrates much deeper into the bulk. Also, results of double bubble experiments in a gravitational environment are presented and discussed.

1. INTRODUCTION

In numerous natural and industrial processes the knowledge of the behaviour of liquids due to temperature gradients plays a fundamental role as far as momentum, heat, and mass transfer are concerned. On Earth, temperature gradients cause fluid density variations which, in turn, lead to flows driven by buoyant effects. However, buoyancy vanishes in orbit due to the virtual absence of gravity but the existence of a free fluid interface between a liquid and a gas or two immiscible liquid phases can induce bulk fluid motion. Thus a bubble or

drop will cause convection in the vicinity of its periphery when placed in another liquid and subjected to a temperature gradient. This flow arises as a consequence of the variation of the surface tension with temperature, which in turn causes tangential stresses within the fluids along the interface, and is known as thermocapillary convection.

With the advent of space flight this phenomenon has received increasing impetus because the mechanism is independent of gravity for its action, and will be ubiquitous in the reduced gravity environment aboard orbiting vehicles and outer space probes as gravity is on Earth in causing buoyant convection. Also, the thermocapillary effect is of considerable importance in present activity areas in space processing. Examples are the production of novel two-phase materials using the absence of sedimentation in microgravity, the containerless processing of glass in order to obtain a better product quality, or the growth of larger monocrystals exhibiting higher purities when compared to crystals grown under the disadvantageous influence of buoyancy on Earth.

Bubbles, resulting from solidification, melting and other operations present surfaces being the driver of thermocapillary convection. Furthermore, these bubbles, when not attached to a solid object, will migrate in the direction of warmer liquid areas or container walls (where they usually remain) due to the nature of thermocapillary convection. Attached to a solid wall bubbles are a steady driver of convection of the fluid surrounding them. The topic of the thermocapillary bubble and drop migration is reviewed by Wozniak (1988) and Subramanian (1992) and

will not be discussed here. The objectives of the present study are to investigate the structure of the bulk temperature and velocity fields induced by bubbles attached to solid walls. Therefore, experiments on Earth have been performed on different bubble configurations. Also, an experiment in a reduced gravity environment using a sounding rocket has been conducted in order to study a situation where buoyant convection vanishes. In all these experiments liquid crystal tracers have been used which offer the advantageous feature of simultaneous temperature field and velocity field information.

2. PHYSICAL CONSIDERATIONS OF THERMOCAPILLARY BUBBLE FLOW

The interface of two adjacent fluids will not be in equilibrium if there is a variation of interfacial tension over the interface. Such variation may arise because of the presence of extraneous matter in the interface or because the temperature of the interface is not uniform. An interface gradient of interfacial tension induces motion within the fluids on either side of the interface so that it can be balanced by viscous shearing stresses. The induced fluid motion is due to the fundamental fact that fluids can only sustain shear stresses when being in motion. For the sake of simplicity, we let $z=0$ in Figure 1 be a straight interface between two fluids, with η_1 and η_2 being the dynamic viscosities on either side. Then, if $T(x)$ is the temperature at distance x along the interface,

$$\frac{d\sigma}{dT} \frac{dT}{dx} = \eta_1 \frac{\partial u_1}{\partial z} - \eta_2 \frac{\partial u_2}{\partial z} \quad (1)$$

where σ is the interfacial tension, u_1 and u_2 the x -components of the fluid velocities on either side, and their gradients are evaluated at the interface. The interfacial tension varies weakly with temperature and most fluid systems exhibit a negative $d\sigma/dT$. Consequently, the direction of the thermocapillary flow is towards colder areas of the interface because its tension there is higher.

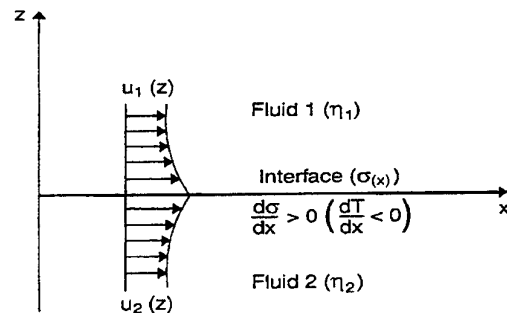


Fig. 1 Mechanism of interfacial tension driven flow due to a temperature variation of the interface

A schematic of the single bubble flow configuration investigated is shown in Figure 2. A gas bubble (air) is positioned in the liquid matrix under a heatable wall. The liquid cavity is cooled from below in order to introduce an upward vertical temperature gradient. This ensures an initially stable stratification and thus reduces buoyant effects in the ground-based experiments. For reasons given above the expected flow direction along the periphery of the bubble is from the heated wall towards the colder bubble pole.

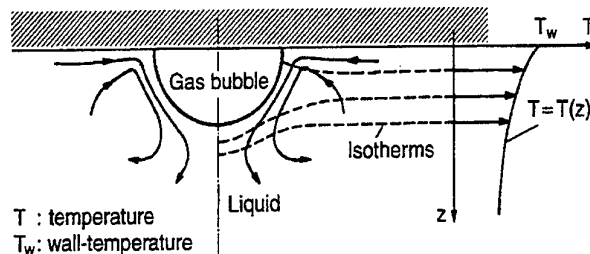


Fig. 2 Schematic of the thermocapillary flow around a bubble under a heated horizontal wall

The properties of the steady temperature and the velocity field surrounding the bubble can be obtained by solving the governing continuity, Navier-Stokes, and energy equations along with the associated boundary conditions. When convective transport effects are important, the problems are nonlinear. The relative importance of convective transport of energy when compared to conduction can be judged from the magnitude of the Péclet number whereas a similar ratio for momentum transport is described by the Reynolds number, Re . When a velocity scale characteristic of thermocapillary migration is used, the Péclet number is known as the Marangoni number, Mg . The

definitions of the Reynolds and Marangoni numbers are given below.

$$Re \equiv \frac{R_c v_0}{\nu} \quad (2)$$

$$Mg \equiv \frac{R_c v_0}{\kappa} \quad (3)$$

Here, R_c is a characteristic radius of the bubble, ν the kinematic viscosity of the continuous phase, and κ its thermal diffusivity. The reference velocity, v_0 , is defined below.

$$v_0 \equiv \frac{|\sigma_T| |\nabla T_\infty| R_c}{\eta} \quad (4)$$

In the above, η is the dynamic viscosity of the continuous phase, σ_T is the rate of change of interfacial tension with temperature, and ∇T_∞ is the temperature gradient imposed in the continuous phase fluid. It is worth noting that

$$Mg = Re \cdot Pr \quad (5)$$

with Pr being the Prandtl number defined as

$$Pr \equiv \frac{\nu}{\kappa} \quad (6)$$

Another dimensionless group characterizing physical features of our problem is the Bond number Bo ,

$$Bo \equiv \frac{\rho \beta g R_c^2}{|\sigma_T|} \quad (7)$$

describing the relative importance of buoyant forces when compared to capillary forces. In definition (7) ρ denotes the density of the continuous phase fluid and β its thermal volume expansion coefficient.

3. EXPERIMENTAL

In the following, after describing the experimental set up and technique, three different experimental configurations will be presented, which are: a single bubble in gravity,

a single bubble in microgravity, and a double bubble in gravity.

3.1 Experimental Set Up and Measuring Technique

Conceptually, the experiments were simple. Within a test cell mounted in the experimental set up and filled with a suitable liquid, a temperature gradient was established, followed by the introduction of the bubble(s). The subsequent motion of the matrix liquid via liquid crystal tracer tracking was recorded for later analysis on photographic colour film using a multiexposure mode.

The heart of the experimental apparatus is the test cell. The interior dimensions were typically 50 mm in each direction. Vertically, the cell was closed by plane copper walls connected with electrical heaters or Peltier elements in order to heat and cool, respectively, for thermal gradient establishment. The other four walls were made of optical quality glass. In order to measure and control the temperature gradient, temperatures were measured at the heating and cooling plates as well as within the liquid layer using calibrated thermistors. The mean temperature of the liquid matrix was kept at ambient temperature in order to minimize lateral heat losses.

The liquid used for the experiments was a silicone oil (AK 10, Wacker Chemie GmbH) of 10 centistokes nominal kinematic viscosity. Table 1 provides its fluid properties.

Kinematic viscosity ν	$10^{-3} \text{ m}^2/\text{s}$
Thermal diffusivity κ	$8.2 \times 10^{-8} \text{ m}^2/\text{s}$
Density ρ	930 kg/m^3
Volume expansion β	10^{-3} K^{-1}
Surface tension σ	$19.9 \times 10^{-3} \text{ N/m}$
Variation of surface tension with temperature $\sigma_T \equiv d\sigma/dT$	$-6.4 \times 10^{-5} \text{ N/Km}$

Table 1 Fluid properties of the test liquid silicone oil (AK 10, Wacker Chemie GmbH) at $T=25^\circ \text{C}$

3.2 Liquid Crystal Tracers

As outlined before, the principle of the method is based on seeding the liquid flow medium with liquid crystal particles which are able to indicate both the velocity- and temperature field. The investigated flow plane (i. e. symmetry plane of corresponding bubble configuration) is illuminated by a white light sheet and recorded on photographic material via multi-exposures. The resulting flow image contains the tracks of the particles and thus the

spatial velocity information within the plane of the light sheet. In addition, the respective colours of the particles indicate the local temperature within the illuminated plane and thus the temperature field.

Chiral nematic liquid crystals behave as multilayered Fabry-Perot interference filters and reflect incident visible radiation selectively. Any disturbance of the forces maintaining the internal structure of the crystals results in a change in the wavelength of the selective reflection. In this respect it should be noted that the shear-stress dependences of the colour reflection behaviour of the liquid crystals are eliminated in the presented experiments as a result of their encapsulation with some resins. If the variation of the distance of the internal interference layers is due to temperature changes, the selectively reflected colour of the crystal is a measure of the temperature. This process is reversible and can therefore be used for temperature measurements provided the crystals are properly calibrated. More details on flow seeding with liquid crystals are published by Wozniak et al. (1996). The general physics of liquid crystals is described by de Gennes and Prost (1993). Since the reflected colour play of the crystals is also depending on the viewing angle, we adjusted the angle between the illumination and the recording axis in the calibration experiments as well as in the flow experiments to 90°.

The liquid crystal tracer type used was an encapsulated one of 12 µm in mean diameter (type TCC 1001, BHD Chemical Ltd.). The concentration of the tracers within the matrix liquid was approximately 0.1 weight percent. The density of the applied liquid crystal material is approximately 1000 kg/m³ and thus fairly close to the density of the matrix liquids used. However, the encapsulation of the tracers reinforces sedimentation processes. We therefore conducted sedimentation tests and found that sedimentation becomes only visible after several days. Consequently, we neglected this effect and assumed that the tracers follow the flow without any slip. Also, an influence on the matrix liquids surface tension due to the introduction of liquid crystals could not be excluded a priori. So we measured the surface tension of the matrix liquids with and without

dispersed tracers but found no significant difference between the corresponding values.

4. RESULTS AND DISCUSSION

4.1 Single Bubble Experiments

Experimental parameters of the single bubble experiments are provided in Table 2. Figure 3a and 3b display the principle results of the earth-bound single bubble experiment. In Figure 3a the liquid flow velocities driven by the bubble are shown in a local velocity vector representation. Local flow directions are indicated by the directions of the vectors and velocity magnitudes by their lengths, where a velocity/length reference scale is given at the bottom of the plot. Figure 3b shows the resulting stream lines and some isotherms. The flow topology consists of a three-dimensional toroidal vortex on top of a secondary one turning in counterdirection. Note that the bubble shape is flattened due to the hydrostatic pressure difference on Earth. The maximum velocities close to the bubble surface evidently indicate that the flow is surface tension driven. The surface carries warm liquid from the heated upper plate to the lower and thus colder region of the fluid matrix until buoyancy and continuity bring the fluid up again resulting in a quite compact vortex. The vortex is active along the entire contour of the bubble.

	m - g	l - g
Pr	122	122
Mg	204	287
Bo	10 ⁻⁴	1.28
$\bar{N}T_v$	4.8 K/cm	3.8 K/cm
D _H	4.5 mm	6 mm
D _V	3.5 mm	2.1 mm
R _c	2.25 mm	3 mm

Table 2 Experimental parameters and dimensionless groups of both experiments with D_H and D_V being the maximum horizontal and vertical bubble dimensions, respectively. In the µ-g data set only the large bubble (see Figure 4) has been considered. The characteristic bubble radius R_c used for estimating the dimensionless groups is defined as half of the horizontal dimension of the respective bubble. Liquid properties are taken at T=25°C (see Table 1).

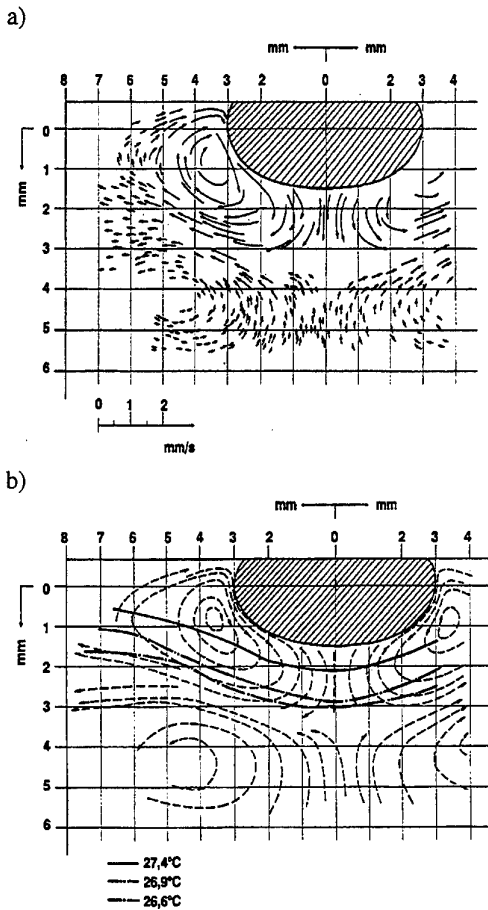


Figure 3 Results of the single bubble experiment on Earth, a) velocity vector field, b) isotherms and reconstructed streamlines

It is evident that the buoyant influence on thermocapillary flows in earth-bound experiments is inevitable. Therefore, we set out to perform a thermocapillary bubble experiment in reduced gravity under otherwise similar physical conditions. This allows to directly compare both results. The sounding rocket experiment was flown in a rocket used in the European TEXUS* programme providing approximately 6 minutes of reduced gravity duration with residual gravity levels of $10^{-4}g_0$, where g_0 is the average acceleration due to gravity on the Earth's surface. General information on microgravity sounding rockets is provided by Minster (1995). Table 2 contains

* Technologische Experimente Unter Schwerelosigkeit

the characteristic experimental data which we were able to keep similar to those of the earth-bound experiment except, of course, the Bond number Bo .

The results of the low gravity experiment are shown in Figure 4a and 4b in a similar way Figure 3 is organised. Unexpected interactions of the wetting and pressure conditions in the bubble injection system during flight lead to an introduction of a few satellite bubbles which do not affect the principal result and thus will not be considered any further. The large bubble is the principle driver of the flow. Due to the absence of the hydrostatic pressure the bubble is spherical in shape. Thermocapillary convection is the only flow mechanism here and leads to a jet-like flow indicated by the reconstructed flow field of Figure 4a and 4b, respectively. Remarkable here is, that the convection penetrates much deeper into the bulk and the symmetrical large vortex is still relatively active in the lower part of the matrix. This tendency, when compared to the gravitational experiment, is supported by the spherical bubble shape in the low gravity environment.

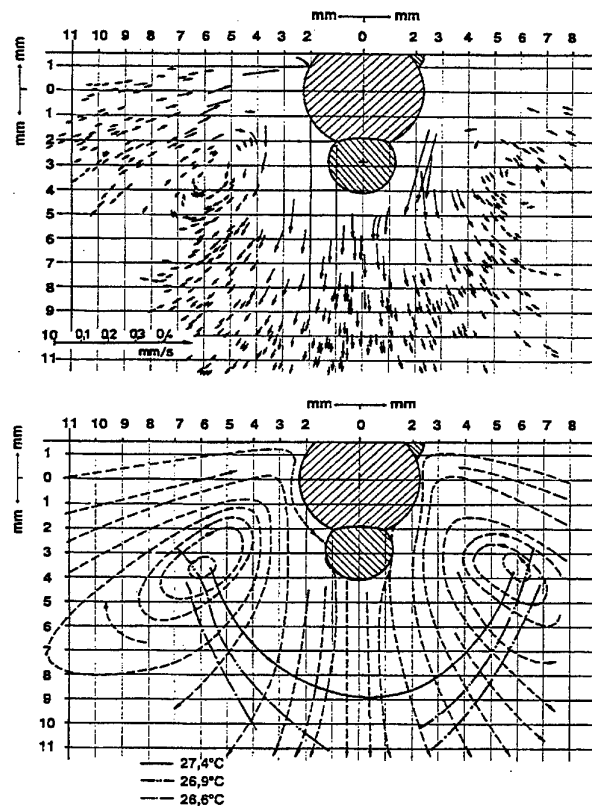
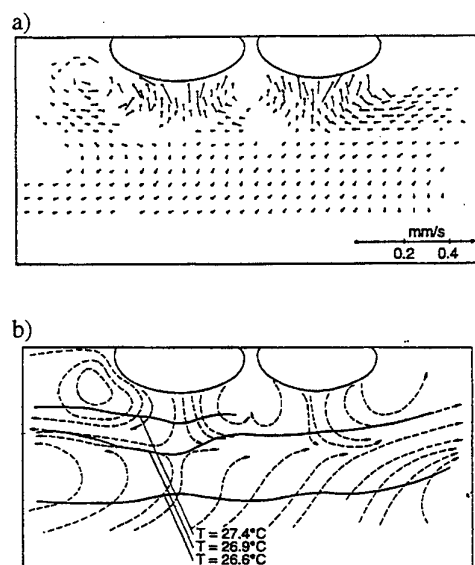


Figure 4 Results of the low gravity experiment, a) velocity vector field, b) reconstructed streamlines and isotherms

4.2 Double Bubble Experiments

The double bubble configuration consists of two bubbles under a heated solid wall placed next to each other. These experiments are the initiation of a study of the thermocapillary interaction of multiple bubble systems on heated walls. For example, one could conjecture that bubbles situated close enough to each other attract or repel each other. Also, the flow topology will be different when compared to single particle configurations, which in turn, has consequences regarding the heat and mass transfer. We investigated two bubbles each of 6 mm horizontal dimension and varied their distance from each other between 5 mm and 1 mm. The result of the 1 mm distance experiment is shown in Figure 5. Two very close vortices are active especially in the tight liquid volume between the bubbles. Nevertheless, the bubbles did not influence each other regarding a change of their position. Furthermore, the experiments showed that with decreasing distance between the bubbles the penetration depth of the thermocapillary convection tends to increase.



5. CONCLUDING REMARKS

Figure 5 Typical results of the double bubble experiments, a) velocity vector field, b) streamlines and some isotherms

In a first experiment the flow characteristics of the surface tension driven flow around a bubble under low gravity conditions could be demonstrated. Comparison with ground based experiments reveals that the penetration of the thermocapillary convection driven by the bubble surface is suppressed by the presence of gravitational acceleration. This result leads to the conclusion that in low gravity materials processing the presence of bubbles is more significant than it is on Earth. First experiments on double bubble configurations did not show effects regarding a change of position of the bubbles. The performance of liquid crystals as tracers showed that this technique is a valuable experimental tool for thermocapillary flow experiments. It is intended to automate the simultaneous flow velocity and temperature (colour) evaluation in the future.

REFERENCES

- De Gennes, P. G. & Prost, J. 1993, The Physics of Liquid Crystals, Oxford University Press
- Minster, O. 1995, Facilities for microgravity investigations in physical sciences supported by ESA. Special publication of the european space agency, ESA SP-1116 (revision 2), pp. 29-33
- Subramanian, R. S. 1992, The motion of bubbles and drops in reduced gravity, in Transport Processes in Bubbles, Drops, and Particles, edited by R. Chhabra and D. De Kee, Hemisphere, New York, pp. 1-41
- Wozniak, G., Siekmann, J. & Srujijes, J. 1988, Thermocapillary bubble and drop dynamics under reduced gravity - survey and prospects. Z. Flugwiss. Weltraumforsch., vol. 12, pp. 137-144
- Wozniak, G., Wozniak, K. & Siekmann, J. 1996, Non-Isothermal Flow Diagnostics Using Microencapsulated Cholesteric Particles, Appl. Sci. Res. vol 56, pp. 145-156

SIMULTANEOUS MEASUREMENTS OF CONTINUOUS AND DISPERSED PHASE IN BUBBLE COLUMNS BY PDA

D. Bröder and M. Sommerfeld

Institut für Mechanische Verfahrenstechnik und Umweltschutztechnik
Martin-Luther-Universität Halle-Wittenberg
06099 Halle (Saale), Germany

ABSTRACT

The hydrodynamics in a bubble column of 140 mm diameter and a height of 800 mm was analysed using a phase-Doppler anemometer (PDA). In order to allow the application of PDA, the bubble column was aerated with relatively fine bubbles with a size spectrum between about 0.3 and 1.5 mm. The gas hold-up was varied in the range between 0.5 and 4 %. For allowing the measurement of the liquid velocities in the bubble swarm seed particles were added. The discrimination between seed particles and bubbles was based on size measurement. Therefore, the performance of the PDA for a simultaneous measurement of liquid phase and bubble velocities was analysed first using Mie theory. These results revealed that a scattering angle of 70° is recommended for sizing both tracer and bubbles. Moreover, the effect of light absorption was studied experimentally. Results are presented for different gas hold-up. The measured properties in the bubble column include local bubble size distributions, bubble and liquid velocities, and the slip velocity between both phases. Moreover, the turbulent kinetic energy and one-dimensional turbulence spectra were determined in order to allow the assessment of bubble-induced turbulence.

INTRODUCTION

Bubbly flows are found in a number of practical and industrial processes, such as sewage water purification, and bubble column reactors. The latter find applications as gas-liquid contactors in chemical and biochemical processes. The hydrodynamics in bubble columns is determined by the bubble rise and hence bubble size distribution and

gas hold-up. Moreover, turbulence will be induced by the bubble rise due to the evolution of large scale flow structures, shear produced in the vicinity of the bubble, and bubble wake structures. Especially mass transfer in bubble columns will be largely affected by turbulence.

A detailed experimental analysis of the hydrodynamics in bubble columns requires the measurement of local bubble size distribution, void fraction, bubble velocities and liquid velocities. Commonly probe techniques, such as split-film probes, fibre optical probes, and electrical probes are used for such measurements. However, measurements with intrusive techniques become very difficult for small bubbles (i.e. for bubble sizes smaller than 2 mm) and may result in considerable errors due to the distortion of the flow.

Detailed experimental studies in bubble columns using optical non-intrusive techniques, such as laser-Doppler anemometry (LDA), phase-Doppler anemometry (PDA) and visualisation techniques are quite rare. One of the first studies of the hydrodynamics in a bubble column by LDA was performed by Franz et al. (1984). Measurements of the liquid phase mean velocity and turbulence are reported for different gas hold-up. Recently, Mudde et al. (1997) applied LDA for the measurement of liquid velocities and turbulence properties, such as Reynolds stresses and turbulence spectra. They succeeded to perform measurements up to a gas hold-up of 25 %.

PDA will additionally allow the measurement of local bubble size distribution in bubble columns, requiring however spherical bubbles. For air bubbles in water this limits the applicability of PDA to bubble diameters up to about 1.2 mm for allowing accurate size measurements. Larger bubbles will have an ellipsoidal shape and the error in size measurement

will increase as reported by Tassin and Nikitopoulos (1995).

With these restrictions in mind Bischof et al. (1994) applied PDA for the analysis of coalescence behaviour and mass transfer in a bubble column aerated with fine bubbles with a size spectrum between 100 and 1000 μm . From the measured bubble size distributions and the resulting mean diameters determined along the column it was found that the bubble size increases considerably within the first 100 mm above the aerator. This was due to bubble coalescence. It was shown that surface active substances can effectively reduce coalescence and thereby enhance mass transfer (Bischof et al. 1994).

The performance of PDA for measurements of bubble size was recently analysed by Hardalupas et al. (1995) using geometrical optics. It was shown that a linear response curve can be obtained only when reflected light dominates, i.e. at collection angles between 70° and 80° . Moreover, the effect of the Gaussian beam was investigated.

The present study is related to the examination of the hydrodynamics in a bubble column aerated by fine bubbles. PDA is applied for a simultaneous measurement of the velocities of both phases and for the determination of the local bubble size distribution.

TEST FACILITY

The bubble column used in the investigations has a diameter of 140 mm and a height of 800 mm (i.e. water level in the column). In order to reduce refraction effects at the curved wall, the bubble column is placed in a square vessel which also is filled with tap water. The aerator is build using a porous membrane with a pore size of 0.7 μm . In order to fix the membrane it is mounted between two perforated plates, which are screwed on top of a small stagnation chamber. The aerator is connected via a flow meter to a pressurised air supply system. Once the aerator is pressurised the membrane bulges and small bubbles are produced at the holes of the perforated plate so that a homogeneous aeration is established over the cross-section of the aerator with a diameter of 100 mm. The gas flow rate was varied by increasing the supply pressure. As a result of the stronger bulging of the membrane at higher pressures also the bubble size was slightly increased with gas flow rate. Measurements were performed up to a gas hold-up of about 4 % and the established bubble size spectrum was in the range between 0.3 and 1.5 mm. In order to reduce bubble coalescence propanol was added to the tap water at a volume concentration of 0.004%.

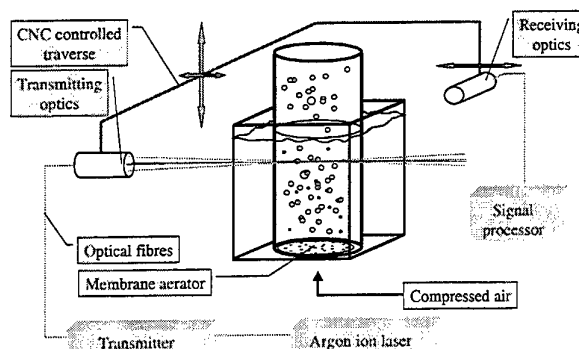


Fig. 1 Schematics of the test facility with bubble column and PDA-System

PDA-SYSTEM

A two-component fibre optics PDA (Dantec, Fiber-PDA) was used to measure bubble size and velocities, but also the continuous phase velocities. The transmitting and receiving optics modules were mounted on a computer controlled 3-d traversing system. This allowed fully automated measurements of cross-sectional profiles at different heights above the aerator. The profiles were measured in the direction of the optical axis of the transmitting optics. As a result, the optical path length of the laser beams in the water changes when scanning a profile. This results in a shift of the beam crossing location and hence the measurement volume. In order to compensate for this effect, the receiving optics was automatically moved in the horizontal direction in order to ensure that the optical axis always intersects with the centre of the measurement volume. The optical path length of the scattered light remains constant since the bubble column is placed in a square vessel.

Bubble size measurements are preferably performed at scattering angles between 70° and 90° since in this range reflected light is dominant and the scattering intensity shows a local maximum for both perpendicular and parallel polarisation (Tassin and Nikitopoulos 1995, Crowe et al. 1998). In the present studies perpendicular polarisation was selected. Mie calculations of the phase size relations for different scattering angles (i.e. 50° , 70° and 90°) show fairly linear curves for all the considered scattering angles (Fig. 2). However, at 50° the Mie result does not agree with geometrical optics (GO) which is the result of the interference between reflection and refraction. Although a linear phase-size relation is found at 90° , this scattering angle is not appropriate for the tracer

measurements as will be demonstrated below. Therefore, a scattering angle of 70° was selected for the present studies. The optical configuration of the PDA system was selected in such a way to allow bubble size measurements up to 2.0 mm by using mask C in the receiver (Table 1).

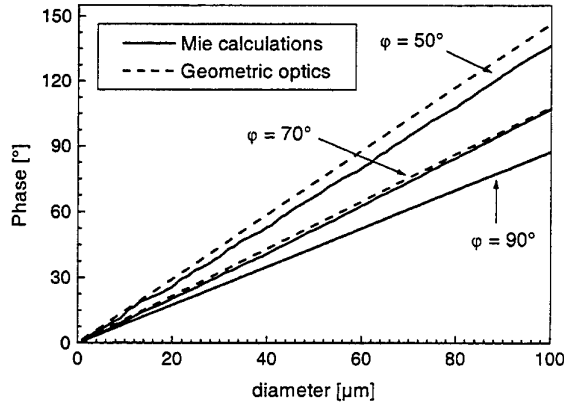


Fig. 2 Mie calculations of phase-size relations for several scattering angles and air bubbles in water (relative refractive index $m = 0.75$)

Focal length transmitting lens	500 mm
Initial beam separation	38 mm
Wavelength for velocity component U	514.5 nm
Wavelength for velocity component V	488 nm
Gaussian beam diameter	1.35 mm
Fringe spacing U-component	6.77 μm
Fringe spacing V-component	6.43 μm
Length of probe volume U-component	8.52 mm
Length of probe volume V-component	8.08 mm
Diameter of probe volume U-component	0.243 mm
Diameter of probe volume V-component	0.230 mm
Receiver orientation	70°
Focal length of receiving lens	400 mm
Polarisation angle	90°
Spatial filter	100 μm
Effective length of imaged probe volume	126 μm

Table 1 Optical parameters of the PDA-system

For allowing simultaneous measurements of bubbles and liquid phase velocities small tracer particles were added to the liquid. The tracer particles need to fulfil the following requirements:

- The particles must be small and light enough to follow the turbulent fluctuations of the liquid phase.

- The scattering intensity should be high enough so that the tracer signals are detected with a sufficiently high data rate.
- The size distribution measured for the tracer particles should be well separated from that of the bubbles in order to allow discrimination of bubble and tracer measurements based on size.

The latter requires that also for the tracer particles reflected light is dominant at a scattering angle of 70° . In preliminary studies several seed particles were examined. The properties of these particles are summarised in Table 2. The metal coated glass beads had relatively low scattering intensities due to their small size and their relatively high density results in sedimentation after some time. More suitable for the considered application were the Polyamid and Vestosint particles which have nominal diameters of around 50 μm and a density close to that of the water. Both kind of particles have a refractive index of around 1.5 which yields a rather low relative refractive index of 1.132.

Seed Particles	Nominal Size [μm]	Measured Size [μm]	Density [g/m^3]
Coated glass beads	4	40	2.5
Polyamid	50	65	1.06
Vestosint	70	55	1.06

Table 2 Properties of seed particles

In order to assess the performance of the PDA in sizing these tracer particles, several Mie calculations were performed. In Fig. 3 the phase is plotted versus scattering angle with the particle size as a parameter. It is obvious that below 55° no accurate size measurements are possible due to interference between refraction and reflection (i.e. the phase changes from negative to positive values with increasing particle size). However, between 60° and 85° reflection seems to be dominant. This is also revealed by plotting the phase as a function of particle size for the selected scattering angle of 70° (Fig. 4). Stronger fluctuations in the phase-size relation are observed up to particle diameters of about 60 μm . For larger particles a fairly linear relation is obtained. Since the seed particles are only used as an indicator for the fluid phase, accurate size measurements are not anticipated and the fluctuations should not cause serious problems.

In order to confirm whether the seed particles are appropriate for the desired application, separate size measurements were performed by dispersing the

particles in water using a small stirred vessel. The measured size distribution is shown in Fig. 5 for the Polyamid and Vestosint particles. The size spectrum of the Polyamid particles ranges up to about 150 μm and the number mean diameter was found to be 65 μm . Although the Vestosint particles are non-spherical the measured size distribution is fairly narrow and a number mean diameter of 55 μm is obtained. Therefore, both seed materials are appropriate for the application in bubbly flows.

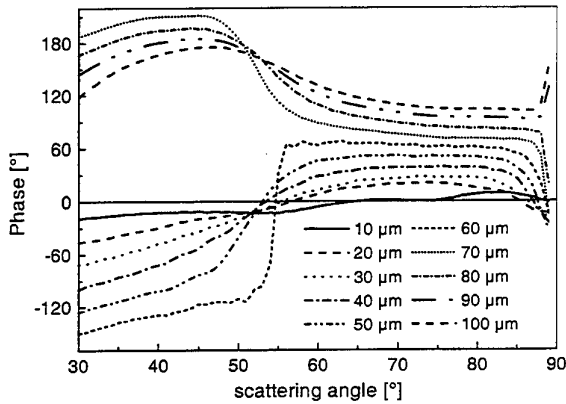


Fig. 3 Variation of phase with scattering angle for several particle sizes, Mie calculation ($m = 1.132$)

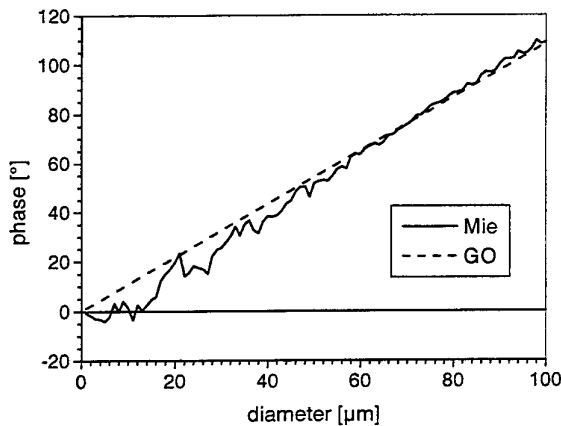


Fig. 4 Phase-size relation for a scattering angle of 70° for solid particles in water ($m = 1.132$), comparison of Mie calculations and geometrical optics

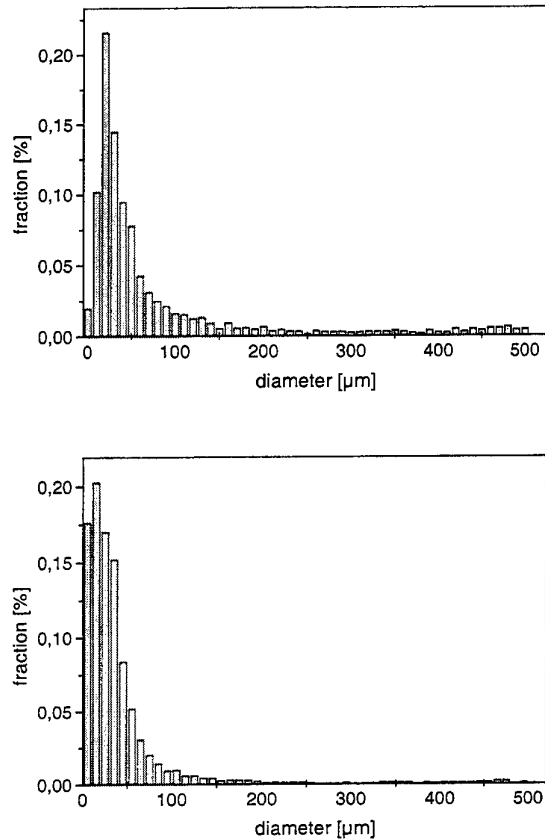


Fig. 5 Particle size distribution measured in water, upper figure: Polyamid particles, lower figure: Vestosint particles

A typical measurement of the combined size distribution of seed particles and bubbles is shown in Fig. 6. Between about 200 and 300 μm a clear gap is observed, so that a separation of tracer and bubble measurements should be possible. In order to obtain the velocities of both phases and to determine bubble mean diameters the collected data had to be re-processed after the measurement. The liquid phase velocities were obtained from all the signals with a diameter less than 150 μm and all signals which give a size above 300 μm were considered as originating from bubbles. By statistical averaging both sets of data the mean velocities and the fluctuating components of both phases were obtained. For velocity bias correction the residence time method was used.

In order to collect more scattered light from the seed particles, the measurements of the fluid phase velocities in the bubbly flow was performed using mask A in the receiving optics which has a larger aperture. The bubble phase properties were obtained

by repeating the measurements using mask C in the receiving optics.

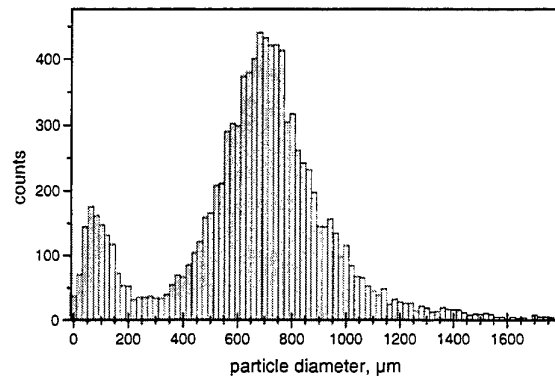


Fig. 6 Typical measurement of the combined size distribution of seed particles (Polyamid) and bubbles.

The turbulent kinetic energy of the continuous phase was obtained from the fluctuating components in the axial and tangential direction in the following way:

$$k = \frac{1}{2} (\overline{u^2} + 2 \overline{w^2})$$

Moreover, the data for the seed particles allowed to obtain time series without any disturbance by bubbles. Hence, it was also possible to calculate one-dimensional spectra of the turbulent kinetic energy. For this purpose the Software Qquick, Version 2.3 developed by Nobach et al. (1997) was used.

MEASUREMENTS IN THE BUBBLE COLUMN

The measurement of bubble and continuous phase properties for the different flow conditions were performed in four cross-sections above the aerator (i.e. at heights of 30, 100, 300 and 480 mm). A summary of the flow conditions considered in the present study is given in Table 3. Especially at higher gas hold-up, it was found that the validation rate decreases with increasing optical path length of the transmitting beams in the bubble column. This is associated with disturbances of the light beams by the bubbles and the absorption of the light in the with seed particles contaminated water. Therefore, the measurements were only performed for half a profile from the centre towards the wall facing the transmitting optics.

Air flow rate [l/h]	Superficial gas velocity [cm/s]	Gas hold-up [%]
40	0.072	0.47
80	0.14	0.68
160	0.29	1.24
320	0.58	2.92

Table 3 Investigated flow conditions

The light absorption mainly affects the data rate for the tracer measurements, since their scattering intensity is much lower compared to that of the bubbles. This effect is illustrated in Fig. 7, where measured size distributions of tracer particles and bubbles are shown. Near the wall (i.e. $r/R = 0.93$) the number of collected and validated tracer signals is much higher than that of the bubbles. When moving into the bubble column the number of tracer signals continuously decreases and on the centre line the number reduces to about 50 %. Profiles of the resulting data rate for the tracer signals are shown in Fig. 8 for different gas hold-up. The data rate decreases from about 4 to 7 Hz near the wall to around 2 Hz on the centre line. With increasing gas hold-up the data rate should be decreasing. Since however the data were collected during different measurement series, the concentration of the seed particles may have varied so that this trend is not obvious from Fig. 8.

The effect of air flow rate and gas hold-up on the hydrodynamics in the bubble column is discussed in the following section by considering the measurements performed 480 mm above the aerator, where an almost developed flow is established. The required higher aeration pressure for producing higher air flow rates causes an increase of the bubble number mean diameter near the centre line of the bubble column from 670 to 930 μm (Fig. 9). Towards the wall the bubble size slightly increases for the low gas hold-up. For the higher gas flow rates the bubble diameter decreases to a minimum at $r/R \approx 0.75$ and then increases again towards the wall. This observation seems to be associated with a transverse migration of bubbles due to lift forces.

The increase of bubble size with flow rate is also associated with an increase in both the absolute bubble rise velocity (Fig. 10) and the liquid velocity in the core region of the bubble column (Fig. 11). The bubble velocity is almost constant up to the wall for the low gas hold-up of 0.47 and 0.68 %. For the higher gas flow rates it decreases slightly from the centre line to the wall. Close to the wall a maximum in the bubble velocity is observed before it drops down at the wall. The vertical component of the liquid mean velocity is much lower than the bubble mean velocity. Except for

the lowest gas flow rate, the liquid velocity shows the highest values in the core region. With increasing air flow rate a stronger upward flow is induced by the bubble rise. Near the wall (i.e. between $r/R = 0.85$ and 1.0) the liquid velocity is close to zero.

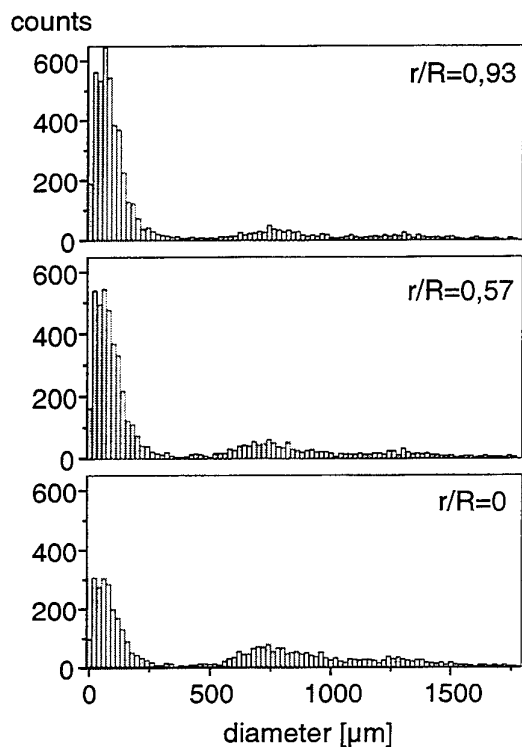


Fig. 7 Combined size distributions of tracer and bubbles collected at different radial positions (gas hold-up 2.95 %)

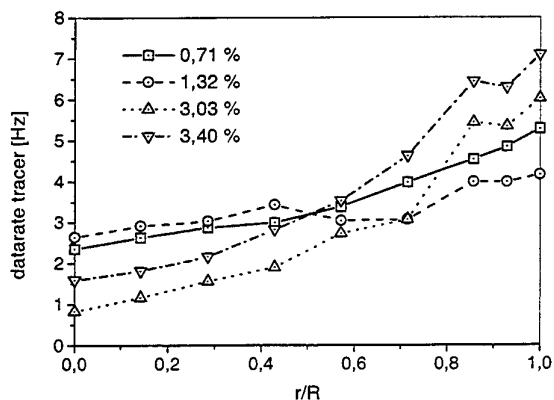


Fig. 8 Profiles of the data rate obtained for tracer particles (Polyamid) for different gas hold-up, 480 mm above the aerator

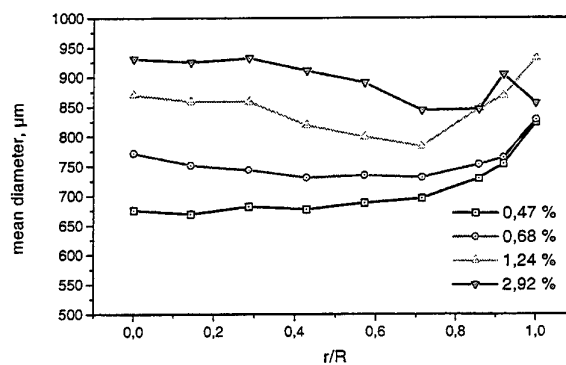


Fig. 9 Profiles of the bubble number mean diameter for different gas hold-up 480 mm above the aerator

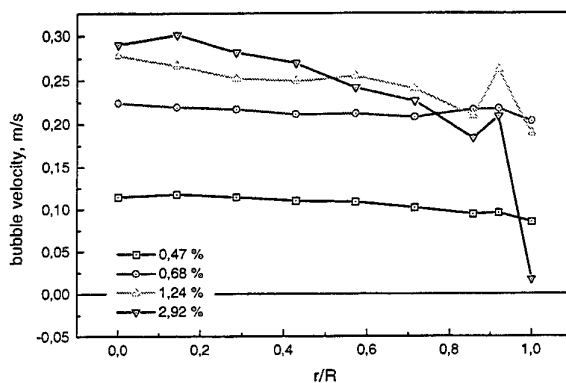


Fig. 10 Profiles of the vertical component of bubble mean velocity for different gas hold-up ($z = 480$ mm)

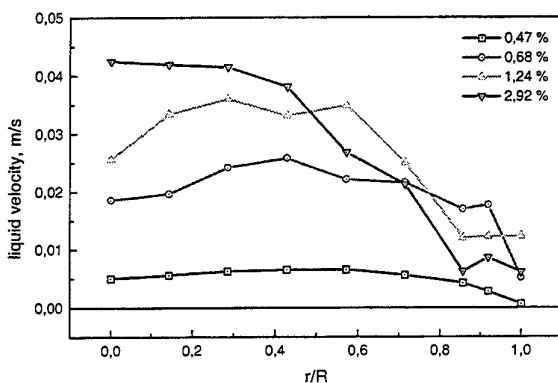


Fig. 11 Profiles of the vertical component of the liquid mean velocity for different gas hold-up ($z = 480$ mm)

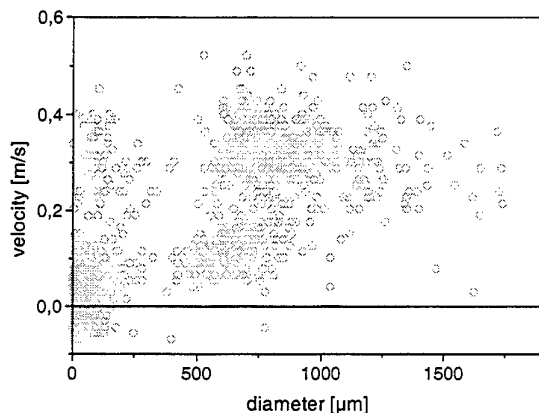


Fig. 12 Size-Velocity correlation for seed particles and bubbles (gas hold-up: 1.24 %, $z = 480$ mm, $r/R = 0.57$)

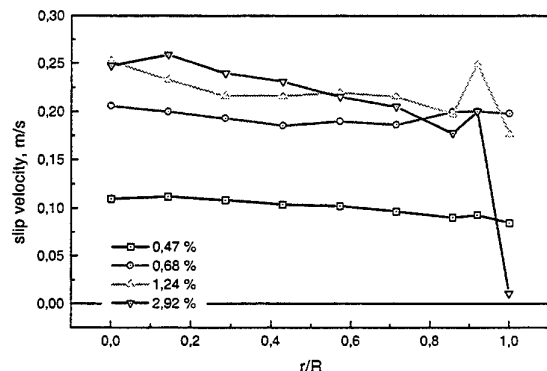


Fig. 13 Vertical component of the slip velocity for different gas hold-up ($z = 480$ mm)

The bubble slip velocity was calculated as the difference of the mean velocities of bubbles and tracers. A typical result for the size-velocity correlation (Fig. 12) shows again a clear separation between seed particles and bubbles. The velocities of the seed particles cover almost the entire range of bubble velocities, i.e. are found between -0.05 and 0.4 m/s, but are mainly clustered between -0.05 and 0.1 m/s. Also the bubbles show two distinct clusters with velocities around 0.1 m/s and 0.3 m/s. This shows clearly the dragging of the fluid by the bubbles.

The shape of the slip velocity profiles is very similar to those of the absolute bubble velocity, since the liquid velocity is very low (Fig. 13). The slip velocity is almost constant over the entire cross-section of the bubble column except for the highest gas flow rates in the near wall region.

The comparison of the measured slip velocity with the terminal rise velocity of single bubbles for contaminated water (see Clift et al. 1978) reveals that the measured values are considerably larger (Fig. 14). Note that the measured slip velocity is an average value over the entire cross-section 480 mm above the aerator. The difference between measured slip velocity and single bubble rise velocity increases with gas hold-up. This effect is associated with swarm effects, i.e. the hydrodynamic interaction between bubbles. It is expected that the bubbles are entrained in the wakes of preceding bubbles causing a dragging effect.

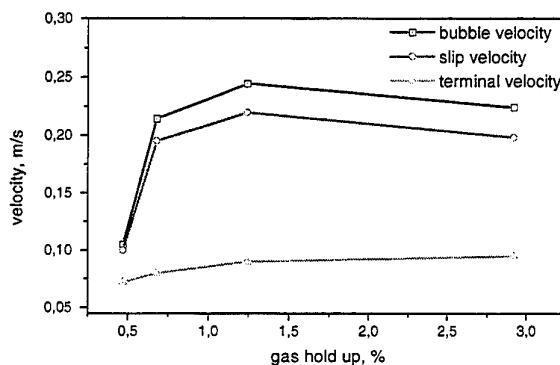


Fig. 14 Variation of measured averaged bubble and slip velocity (480 mm above the aerator) with gas hold-up and comparison with the terminal velocity of single bubbles (Clift et al. 1978).

The turbulent kinetic energy of the liquid phase is increasing with gas hold-up. A drastic increase is observed from the lowest gas hold-up of 0.47% to the next higher value of 0.68% (Fig. 15). For these two cases the bubble Reynolds number based on the average slip velocity increases from 70 to 143 , so that the wake generated turbulence should have a considerable contribution. However, also the liquid velocity and the shear gradients increase considerably from the lowest gas flow rate to the higher values, which also contributes to the production of turbulent kinetic energy.

The turbulence structure in a bubble column was further analysed by considering the one-dimensional spectra of turbulence for different gas hold-up (Fig. 16). For these measurements it was necessary to sample more than $10,000$ tracer signals. The slope in the high frequency range (i.e. between 1 and 100 Hz) corresponds roughly to that in the inertial range of single-phase flows. The increase of gas hold-up results in an increase of the spectral density over the entire frequency range which is not observed in other types of two-phase flows. In grid turbulence for example,

Lance and Bataille (1991) found a decrease of the power spectrum in the low frequency range and an increase in the high frequency range. It is argued that this is the result of wake generated turbulence. Further measurements for different bubble sizes are required to allow a better interpretation of these effects.

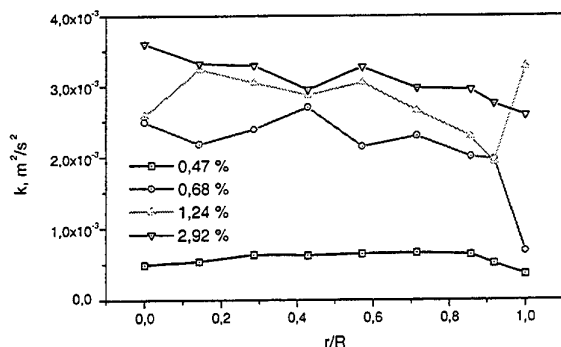


Fig. 15 Turbulent kinetic energy of the liquid phase for different gas hold-up ($z = 480$ mm)

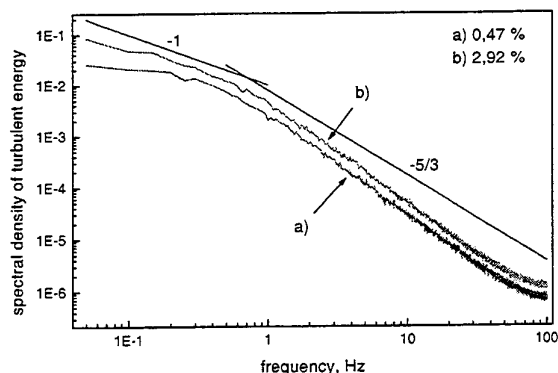


Fig. 16 One-dimensional spectra of turbulence versus frequency of fluctuation for different gas hold-up 480 mm above the aerator

CONCLUSIONS

An experimental study of the hydrodynamics in a bubble column was performed using phase-Doppler anemometry. Mie calculations were performed to select the optimum configuration of the PDA for simultaneous measurements of seed particles and bubbles. At a scattering angle of 70° , reflection was found to be dominant for tracer and bubbles resulting in fairly linear phase-size relations. It was demonstrated that a proper discrimination of tracer and bubble signal based on size measurement was possible. Light absorption in the bubble column

however results in a considerable decrease of the data rate when moving the measurement volume deeper into the bubble column.

Simultaneous measurements of bubble and liquid phase velocities revealed that the slip velocity between the phases is increasing with gas hold-up and is larger than the terminal velocity of single bubbles. Moreover, the continuous phase turbulence is enhanced with increasing gas hold-up and bubble size. The degree to what extent the bubble wakes contribute to the turbulence level needs further analysis.

ACKNOWLEDGEMENT

The financial support of the research project by the Deutsche Forschungsgemeinschaft under contract number So 204/13 is gratefully acknowledged.

REFERENCES

- Bischof, F., Durst, F., Sommerfeld, M. & Shakouchi, T. 1994, Use of phase-Doppler anemometry for characterizing the mass transfer in a fine bubble swarm. Proc. of the German-Japanese Symp. on Multi-Phase Flow, Karlsruhe, Germany, pp. 53-66
- Clift, R., Grace, J.R. & Weber M.E. 1978, Bubbles, Drops, and Particles. Academic Press, New York.
- Crowe, C.T., Sommerfeld, M. & Tsuji, Y. 1998, Multiphase Flows with Droplets and Particles. CRC Press, New York.
- Franz, K., Börner, Th., Kantorek, H.J. & Buchholz, R. 1984, Flow structures in bubble columns. Ger. Chem. Eng., Vol. 7, pp. 365-374.
- Hardalupas, Y., Moreira, A.L.N., Taylor, A.M.K.P. & Whitelaw, J.H. 1995, Evaluation of the phase Doppler technique for the measurement of bubbles. Proc. of The 2nd Int. Conf. on Multiphase Flow, Kyoto, Japan.
- Lance, M. & Bataille, J. 1991, Turbulence in the liquid phase of a uniform bubbly air-water flow. J. Fluid Mech., Vol. 222, 95-118.
- Mudde, R.F., Groen, J.S. & Van Den Akker, H.E.A. 1997, Liquid velocity field in a bubble column: LDA experiments. Chem. Eng. Sci., Vol. 52, pp. 4217-4224.
- Nobach, H., Müller, E. & Tropea, C. 1997, Efficient estimation of power spectral density from laser-Doppler anemometer data. Submitted for publication Journal of Fluid Mechanics.
- Tassin, A.L. & Nikitopoulos, D.E. 1995, Non-intrusive measurements of bubble size and velocity. Experiments in Fluids, Vol. 19, 121-132.

THE DETERMINATION OF THE BUBBLE GROWTH RATE IN BOILING HEAT TRANSFER BY PHASE-DOPPLER ANEMOMETRY.

Thomas I. Nonn

Dantec Measurement Technology
Tonsbakken 16-18
Skovlunde, Denmark DK-2740

ABSTRACT

In this paper the time history of a vapor bubble growing from a cavity on a uniformly heated surface is examined using Phase-Doppler Anemometry (PDA). Advances in light scattering instrumentation have made it possible to record in real-time the evolution of a bubble as a function of time shortly after nucleation. PDA allows for reliable measurements of spherical particles down to the order of the wavelength of the light source used (Saffman et al, 1984). Utilizing a specialized signal processor, bubble growth histories were recorded under atmospheric pressure for water at both saturation and subcooled temperatures. To substantiate the use of PDA and to quantify the contribution of scattering from a conductive surface, light scattering analysis using the Generalized Lorenz-Mie theory was employed.

It was found for a given optical configuration that the dynamic range of the instrumentation allowed for measurements of bubbles from 10 to 540 microns, below that currently possible by photographic techniques. Bubble growth records were recorded for steps of heat flux from 300,000 to 700,000 Watts / m². Measurements were carried out at several locations on the heat source to confirm results. Averaged bubble growth histories compared favorably with earlier bubble growth models utilizing bubble waiting time, which was subsequently determined using PDA.

INTRODUCTION

In boiling heat transfer, the average rate at which a bubble attached to heated surface grows can be used to estimate the overall heat transfer rate from the surface to the surrounding liquid. Having a detailed time history of an individual bubble can also provide insight to the dynamic and complex processes of boiling which have, since the early part of this century, intrigued both scientists and engineers alike.

Boiling itself is a common phenomena found in many aspects of industry where phase transition takes place, such as in nuclear reactors, chemical production facilities and heat exchangers. In today's electronic world boiling heat transfer has become connected with the dissipation of energy from large integrated chips (VLSI's) in super computers. Unfortunately, a comprehensive theory of boiling, one which can model the entire boiling process from the onset of nucleation to detachment, and which can predict the heat transfer rate from a solid interface to a liquid, does not exist. Due to the unusually complex geometrical, thermal, and dynamic character of bubble growth, the possibility that a suitable mathematical model can be developed seems unlikely. During the 1950's and 1960's, a large number of investigations were engaged in identifying and characterizing the principal processes related to boiling heat transfer. While no satisfactory complete theory emerged, a number of investigations cast light on aspects of boiling that were of increasing industrial importance.

As in any other theory of science, a theory on boiling must be substantiated by direct physical evidence. In the case of boiling heat transfer, this was usually accomplished by direct visualization, either by pure high-speed photographic techniques (Vogel et al, 1989) or high-speed film techniques in combination with CCD technology (Harvey et al, 1996). During an experimental run the image history of a bubble is recorded and compiled, detailing the bubble geometry from shortly after nucleation on through to detachment. The number of images captured would depend on the frequency rate of bubbles produced and the maximum frame rate of the camera. The sequence of images stored would then require extensive post-processing to determine the bubble dimensions so as to extract the growth rate. Of great interest to investigators is the period immediately following nucleation, labeled in the literature as the initial growth period. Investigators have come to within 100 microseconds using conventional high-speed photography, and nearly 10

microseconds using streak photography (Sernas and Hooper, 1969).

The typical spatial resolution of photographic techniques is on the order of a few hundred micrometers. The data sampling rate that can be maintained at this resolution is approximately 5,000-6,000 frames/s, though some cameras can operate up to 14,000 frame/s. However, the uncertainty in time is directly related to the maximum frame rate. At 5,000 frame/s, two frames are separated by a time interval of 200 microseconds, at 14,000 frame/s, 70 microseconds.

To make the bubbles large enough to satisfy the resolution of the photographic medium, investigators often lowered the pressure in the test section to 10-20 % of an atmosphere. Reducing the surrounding pressure had the effect of reducing the force of buoyancy and the required superheat to initiate boiling, that is, a bubble will grow to a much larger size and exist longer before detaching, thus making it easier to record. The disadvantage of this technique is that one cannot make accurate measurements on smaller scale bubbles, those often found in experiments running at atmospheric and higher pressures, where bubbles will detach at sizes on the order of 1-2 millimeters. Photographic techniques are used primarily for conveying spatial information and do not have the dynamic temporal response characteristic of point-based measurement systems, such as those found in laser Doppler systems.

The present study aims to present a technique utilizing the special light scattering properties of a bubble illuminated by a laser light source to determine accurately the growth rate of individual bubbles under a variety of conditions. The resolution of PDA is of the order of the wavelength, which implies measurements of bubbles as small as a micron. Though typical cavity sizes are said to range from 20-50 microns, the PDA instrument can be used to measure bubbles reliably that are smaller, perhaps providing insight to little known boiling processes. PDA is a non-intrusive technique that can operate under noisy conditions, permitting measurement of particles immersed in complex flows.

Due to the complicated nature of boiling, the interaction of neighboring bubbles and the convection of fluid in the region of highest activity, the resulting measurements were often obtained by overlapping growth curves from bubbles issuing from the same cavity. If it is assumed that the heat flux is uniform and that bubbles grow with reasonable regularity from cavities on the heat source surface, data from separate bubbles should fall onto predictable curves. Knowing

the average surface temperature and the liquid superheat temperature at the surface, as well as the values of the physical properties of water, the measured average heat flux can be related to the actual measured growth rate and compared against known bubble growth models.

DESCRIPTION OF EXPERIMENT

To facilitate observation and measurement of growing bubbles a test facility was constructed consisting of a small copper heat source embedded within a glass silica insulator, as shown in Figure 1. On the backside of the heat source several layers of ceramic insulation were bonded and then encased in silicon gel to limit heat loss. Insulated thermocouple heating wire was woven into the etched base of the heat source to provide a reasonably uniform temperature distribution along the surface.

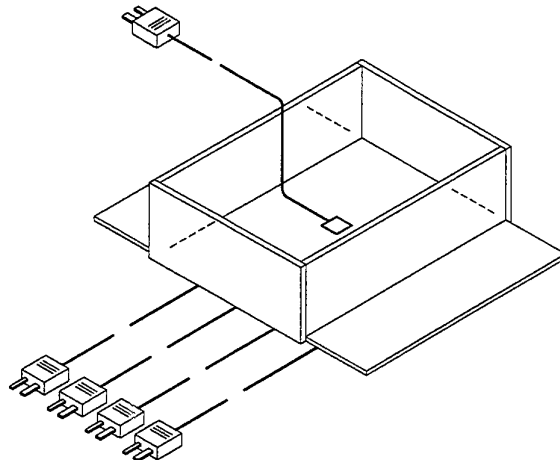


Fig. 1 Perspective of test section and thermocouples. The four thermocouples on the left measure heat source surface temperature, the remaining thermocouple measures the superheat temperature.

Several thermocouples placed at different locations at 0.13 mm beneath the surface were used to monitor temperature gradients. An additional thermocouple was placed on the surface of the insulation plate adjacent to the heat source, to measure the local superheat temperature. To remove impurities and inert gasses from within cavities at the surface of the heat source, the system was degassed for several hours prior to measurement as the test liquids were brought to their saturation temperatures. The entire assembly was placed on a traversing mechanism that allowed movement in x,y and z directions. The movement of the test facility during measurements was governed by micrometers that

permitted accurate displacements of position to within 1 micron. The sides of the assembly were constructed of optical glass to limit distortion, and the top was left open to allow free evaporation of the fluid.

The measurement hardware consisted of a Dantec 57N10 PDA processor utilizing FiberFlow fiber optics components. Due to the presence of the heat source the typical PDA optical bench configuration was tilted upright 90 degrees such that the receiver was mounted vertically above the test facility, as in Figure 2. In this way the plane of intersection of the laser beams was parallel with the heat source surface, reducing the possibility of accumulating additional scattering energy from the heat source. The light source used was a 300 mW Ar-Ion laser coupled to a Dantec transmitter. The transmitter houses a Bragg cell that shifts one of the beams by 40 MHz so as to remove any directional ambiguity. Fiber optics facilitates the manipulation of the measurement volume within the test section. An ordinary lab microscope was used as an aid in identifying boiling sites suitable for measurement. To ensure good signal quality a digital oscilloscope was attached to the Doppler signal-out connector of the processor. After identification of a suitable boiling site the test section micrometers were adjusted to fine tune the signal quality.

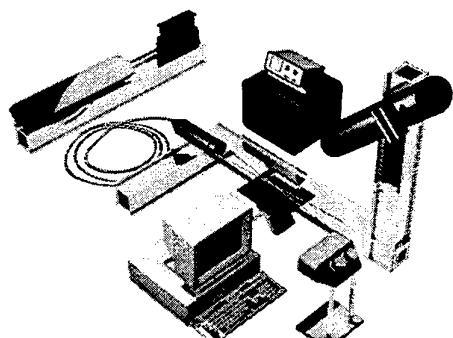


Fig. 2. Layout of experimental setup showing transmitting and receiving optics, microscope, signal processor, test section and PC.

The basic operation of the PDA processor requires the signal from a single particle passing through the LDA probe measurement volume to satisfy certain threshold requirements. A stationary bubble does not create the characteristic Doppler burst signal created by a moving particle, but rather a continuous modulated signal that increases in amplitude. To measure phase as a function of time for an envelope whose amplitude increases the burst

detector needed to be externally triggered. This was accomplished by using an external 50 kHz clock source. The timescales involved with bubble growth from nucleation on to departure are typically on the order of 1-2 milliseconds, therefore for each bubble at least 40-50 measurements are possible.

When distilled water is used at STP conditions the expected bubble departure size is approximately 1 mm. An important factor in considering PDA measurements is the amplitude of the input signal. Scattered light signals are detected by photomultipliers (PMs) whose sensitivity is dependent on the input driving voltage and the intensity of the scattered light. For particles larger than the wavelength of the light, the amplitude of intensity of scattered light varies with the particle diameter squared. This places a limit on the driving current of the photomultiplier, and improper setting of gain will produce clipped signals, retarding the measurement quality. The dynamic range of the instrument is 1:50, that is, if one adjusts the gain to measure at minimum a 1 micron particle, then the maximum particle size that can be accepted by the instrument will be 50 microns before signal clipping occurs.

Another determining factor in the measurement is the dimension of the transmitting and receiving optics. Short focal lengths for both the transmitting and collection optics reduce the probe measurement size and increase the size resolution, but limit the maximum measurable size. Likewise increasing the focal lengths and reducing the half-angle spacing of the transmitting beams increases the maximum bubble size that can be measured. As indicated in the tables below, 500 mm and 310 mm focal lengths were used for the transmitting and receiving optics, respectively. With a beam spacing of 30 mm and a beam diameter of 1.4 mm, this configuration produces an ellipsoidal probe measurement volume that is 10.4 mm long and 0.23 mm in diameter. The maximum measurable particle for this optical configuration is 530 microns.

Gaussian beam diameter	1.4 mm
Beam separation	30 mm
Focal length	500 mm
Fringe spacing	8.6 μ m
Number of fringes	27
Probe volume dimension in X	0.23 mm
Probe volume dimension in Y	0.23 mm
Probe volume dimension in Z	10.4 mm

Table 1. Setup of transmitting optics.

Scattering angle	72 degrees
Focal length	310 mm
Particle/medium refractive index	1.0/1.334
Maximum diameter	530 um

Table 2. Setup of receiving optics.

The selection of the scattering angle for the receiving optics requires careful thought. In the near-forward region both reflection and refraction contribute to the scattering of light. As one moves to the side-scatter region (> 60 degrees) the refracted component of the scattering intensity drops dramatically. With perpendicular polarization there is still a contribution from the second order scattering, therefore, the best results for reflection are obtained with parallel polarization.

To obtain the best possible records of bubble growth the gain of the PDA processor was adjusted so that the optimum size range could be established. Gain is controlled by adjusting the high voltage supplied to the photomultipliers. With the optical configuration giving 530 um as a maximum and taking the dynamic range of the processor into account, the lower bound on measurable particle size would be 10 microns. Although the maximum diameter is less than the expected departure diameter, this range was selected because longer focal lengths would have made bubble measurement difficult due to the resulting increase in the probe measurement volume size.

The setup and control of data acquisition was controlled by a commercially available application software called SIZEware, written by the author and released by Dantec. Though designed specifically for PDA measurements, the software could also acquire data from the processor while externally triggered. SIZEware contains numerous routines for the calibration of the processor, data acquisition, data processing as well as presentation. For the purposes of this paper the software was used to control acquisition and raw data processing. To post-process the raw acquired data and analyze the growth of bubbles an additional software program called BubbleGrowth was created.

MEASUREMENT PROCEDURE

The entire measurement process begins with the polishing and cleaning of the copper heat source surface. This is followed by 1-2 hours of degassing of

the heat source and bulk liquid. Once the thermocouple measuring the liquid temperature at the surface registered a superheat in excess of 4 deg C the surface would begin to populate with slowly growing bubbles. With the superheat raised to 7-8 deg C the bubbles would begin to issue regularly from specific sites. Eventually the surface becomes dense with activity, requiring the use of a microscope to aid in finding a suitable site. The location of a site is accomplished by moving the measurement volume steadily over the surface, adjusting altitude to minimize reflection from the surface, as shown in figure 3. From the eyepiece on the receiving optics unit one begins to focus onto a site by moving the crosshairs onto a bubble. Bubbles are clearly visible in the eyepiece, and appear as blinking images under the intense illumination of the laser beam. Once a site is established the incoming signal can be evaluated and fine-tuned with the oscilloscope and the micrometers beneath the test section.

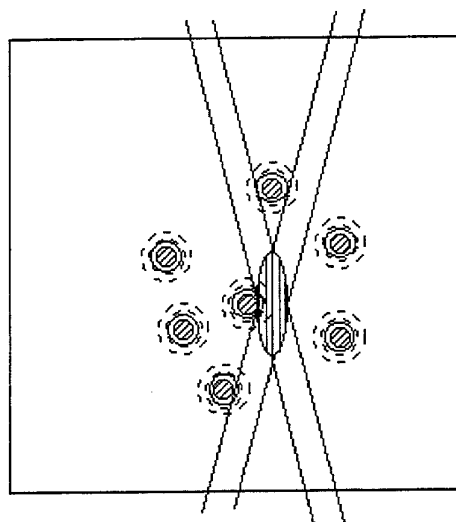


Fig. 3. Alignment of the PDA measurement volume over a suspected nucleation site.

Externally clocked at 50 kHz, the processor is software triggered to begin acquiring data. For each measurement 100,000 validated samples were acquired. This means the processor and software acquire data until 100,000 acceptable samples are stored. 50-60 % of the incoming data is discarded due to forced sampling, however, the remaining validated measurements each represent a point on the growth curve of a bubble.

The processing of measurements requires the careful screening of data. Noisy, poorly resolved samples are rejected in favor of samples showing a high signal-to-noise ratio. Once the phase shifts are validated, they are subjected to the diameter sphericity test.

Due to the intense activity on the heat source surface during boiling the records often acquired are incomplete and usually detail only a portion of the bubble's growth history. Bubble growth is a monotonic process. Data records from different bubbles from the same site can be aligned in

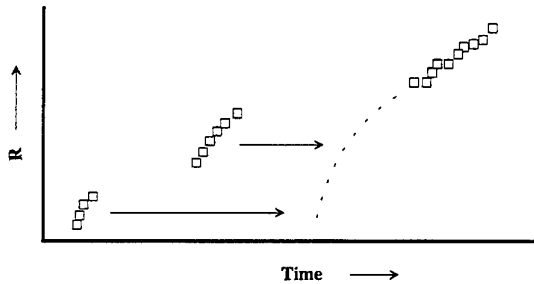


Fig. 4. Independent bubble histories are overlapped to produce a characteristic growth curve.

such a way as to reveal the full growth history of an average bubble. Figure 4 illustrates this process where records are shifted in time so that overlapped with one another produce a single monotonic curve. This resulting curve can then be compared with the observations of other investigators.

The measurements of bubble frequency and concentration were carried at a distance of one millimeter from the surface, so that the built-in burst detector could mark the arrival time and transit time of each bubble as they passed through the probe volume. The transit time can be used to determine the void fraction or burst length of the bubble, if one considers purely, one-dimensional flow. Having the burst length of each bubble allows for the determination of particle density within a cubic centimeter. This particle density can be used to compare the calculated and measured values of the heat flux.

RESULTS

The recording of bubble growth was carried out at different sites on the heat source surface. Due to the intense activity on the heat source surface sites were arbitrarily selected based on clarity of the data. A useful site was one that produced bubbles at regular

intervals and whose results could be averaged over many bubble histories to produce a characteristic growth curve. For the presentation two sites were chosen which best represented the boiling response curve. At each site the heat flux was varied for nine steps beginning with $292,000 \text{ W/m}^2$, as shown in Table 3. The heat flux was increased in steps until the surface superheat reached 15°C , and then the heat flux was decreased in the same steps. Beyond this temperature the heat source began showing signs of burnout, a rapid increase in the backside temperature of the heat source.

For each heat flux step the voltage, current, superheat temperature, and bulk fluid temperature were recorded. Prior to measurement the system was allowed some time to stabilize. Data was sampled at 50 kHz until $100,000$ validated samples were recorded in the buffer. The raw data appears in a time series as a series of vertical lines separated by a seemingly regular interval. This regular interval corresponds to the bubble growth waiting time, which represents the period where cooler liquid, brought closer to the surface due to the wake of a rising bubble, is reheated.

Heat Flux (W/m ²)	T_w °C	$T_w - T_{\text{sat}}$	t_w (sec)
292000	108	8	0.05
326700	109	9	
364000	110	10	0.03
392030	110.5	10.5	
431550	111.2	11.2	0.025
477400	112.2	12.2	0.02
517500	112.6	12.6	0.02
567600	113	13	
616250	113.8	13.8	

Table 3. List of heat flux and wall superheat measured during experiments.

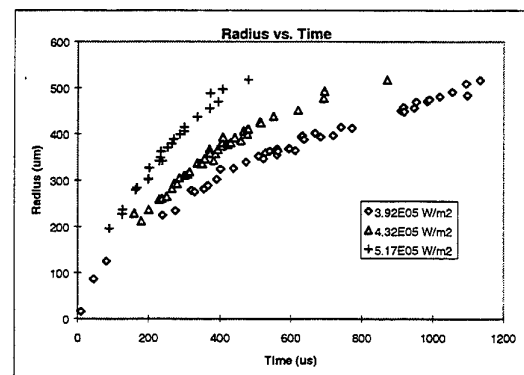


Fig. 5. Averaged growth histories for bubbles at site A for varying heat flux.

Increasing the heat flux reduced the waiting time to the order of 0.01 secs, where it stabilized and did not change upon increasing flux. Applying this waiting time in bubble growth relations produced an estimated cavity size on the order of 50 microns, the same result achieved by Judd (1985) for a smooth copper heat source.

COMPARISON WITH THEORY

The theoretical work outlined by Mikic and Rohsenow (1969) was used for comparing the present results with theory. Because the bulk liquid temperature in the test section hovers near the saturation temperature and differs from the surface superheat, the equation for a non-uniform

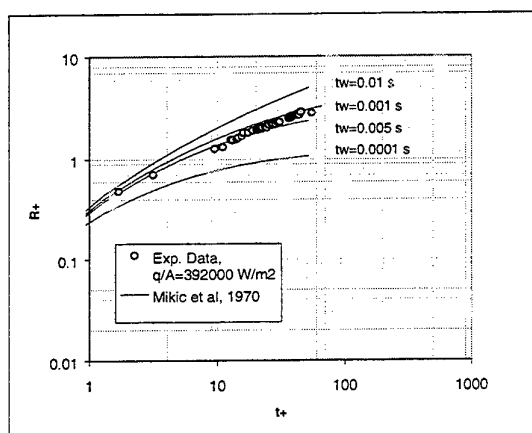


Fig. 6. Bubble growth history for a single flux from site A compared with Mikic et al for different waiting times. R_+ and t_+ represent dimensionless radius and time.

temperature field was used. Using the bubble frequency estimated from experiment, the bubble growth curves were evaluated for different waiting times and then compared with the measured results in the next section. In Figure 6 the measured data is compared against Mikic et al for the waiting times of 0.01, 0.001, 0.0005, and 0.0001 seconds. A waiting time of 0.001 secs was found to agree with all the measured data. This implies a weakness in the models when used for bubble measurements in the small size range. None of the past investigators obtained consistent measurements of bubble growth in the range of 0-200 microns, which is of interest here.

CONCLUSION

In this study PDA was shown to produce bubble growth records comparable to the results of other investigators. Reliable measurements could be made of the bubble growth rate at STP conditions for varying heat flux. Because of the limitations imposed by earlier measurement techniques further investigation of the waiting time is required to verify the stabilization of the waiting time. The PDA instrument was found to be reasonably simple to setup and operate in this application.

Bubble waiting time, growth time and bubble density also play a pivotal role in characterizing the boiling heat transfer process. In addition to measuring the growth rate, the PDA instrument can be used to measure the bubble rise velocity and diameter, from which the bubble frequency can be determined. In addition, PDA can be used to determine the bubble population density over a specific area on the heat source.

From an experimental perspective, boiling nucleation is a vast subject, therefore, the principle aim of this study was to present the technique as a viable alternative to more traditional methods of recording bubble growth.

REFERENCES

- M. Saffman, P. Buchhave, H. Tanger, Simultaneous Measurement of Size, Concentration and Velocity of Spherical Particles by a Laser Doppler Method, Proceedings, *The Second International Symposium on Applications of Laser Anemometry to Fluid Mechanics*, Lisbon, July, 1984.
- Vogel A., Lauterborn W. and Timm R. 1989, Optical and Acoustic Investigations of the Dynamics of Laser-produced Cavitation Bubbles Near a Solid Boundary, *J. Fluid Mechanics*, vol. 206, pp. 299-338.
- Harvey S. B., Best J. P., Soh W. K., 1996, Vapour Bubble Measurement Using Image Analysis, *Measurement Science and Technology*, vol. 7, no. 4, pp. 592-604.
- Sernas V., Hooper F.C., 1969, The Initial Vapor Bubble Growth on a Heated Wall During Nucleate Boiling, *Int. J. Heat Mass Transfer*, vol. 12, pp. 1627-1639.
- Judd R.L., Ibrahim E.A., 1985, An Experimental Investigation of the Effect of Subcooling on Bubble

Growth and Waiting Time in Nucleate Boiling,
Transactions of the ASME, vol. 107, pp. 168-174.

Mikic B.B., Rohsenow W.M. and Griffith P., On
Bubble Growths, *Int. J. Heat Mass Transfer*, vol. 13,
pp. 657-666, 1969.

3-D MEASUREMENTS OF BUBBLE MOTION AND WAKE STRUCTURE IN TWO-PHASE FLOWS USING SCANNING PARTICLE IMAGE VELOCIMETRY (3-D SPIV) AND STEREO-IMAGING

Ch. Brücker

Aerodynamisches Institut der RWTH Aachen
Wüllnerstr zw. 5 u. 7, D-52062 Aachen, Germany

ABSTRACT

Scanning-Particle-Image-Velocimetry is used in combination with a stereoscopic mirror system to record the three-dimensional wake structure and the bubble coordinates simultaneously over time in a bubbly two-phase flow. Pulsed planar swarms of 8-16 bubbles with a mean diameter of 0.8 cm were released simultaneously in a counter water stream where they are captured nearly in the same vertical position during the observed period. The results demonstrate the important role of the wake-capture process in bubble interaction. Only when trailing bubbles are captured within a wake of leading ones, bubble collision and possibly coalescence happens. For the bubble size studied we found a regular shedding of hairpin vortices building a chain of vortex loops in the wake downstream. A video-animation of the temporal evolution of the flow demonstrates this dynamic process which is difficult to express in single pictures.

1. INTRODUCTION

Bubble interaction in swarms is understood as a main factor in amplification of turbulent kinetic energy production in bubbly two-phase flows. The interaction is mainly caused by the individual wake structure, the wake capture process and the interaction of several bubbles in clusters or "chimneys" [1]. Shedding of vortices with ordered structure from the bubble wake plays an important role in these mechanisms.

Most of the knowledge about the wake structure of bubbles has been achieved so far from flow visualization studies of single ascending bubbles [2] or two bubbles in line [3]. However, for a more detailed knowledge of bubble dynamics, three-dimensional and time-recording measurement techniques are required which are able to reconstruct the vortical wake structures generated within the flow. For this reason we utilized a three-dimensional

extension of classical Particle-Image-Velocimetry termed as Scanning-Particle-Image-Velocimetry (SPIV) which is based on tomographic scanning of the flow volume of interest using a scanning light-sheet technique, see [4,5]. The scanning light-sheet samples the flow volume rapidly in depth within a set of staggered planes in each of which the flow field can be analyzed with advanced three-dimensional PIV algorithms. This technique offers a better resolution compared to 3-D Particle-tracking techniques, however it requires high-speed imaging. It already has been successfully applied to the wake of a solid spherical cap as an approximation of a spherical cup bubble [6] and is here utilized to resolve the time-dependent three-dimensional flow field in the wake of a bubble cluster rising in quiescent fluid.

Under the difficult conditions of instantaneous flow measurements in multiphase flows containing swarms of larger bubbles with random location, the multi-planar method of SPIV has the advantage to provide information in the scanned volume at each location. Therefore, important dynamical features driven by the wake structures are not overseen as possibly in case of a stationary sheet used in conventional PIV. Similar important as the three-dimensional aspect is the fact, that the time-history of the flow is recorded with sufficient accuracy. Otherwise, the dynamical behavior of both phases cannot be related to each other within a swarm of bubbles.

This paper presents the results of time-recording measurements of bubble motion and wake structures via SPIV and digital high-speed imaging in a pulsed swarm of relative few bubbles. The major aim of the study is the understanding of bubble interactions in swarms with bubbles corresponding in size to the typical bubble size as used in real chemical reactors (of order of 1 cm and more). For these conditions, the maximum void fraction of the dispersed phase at which PIV measurements could reveal the wake structure is limited to about 5%.

Otherwise strong optical distortion at the phase boundaries prohibit any quantitative correct measurements over larger fields which could help to recognize the structure of the wake flow.

2. EXPERIMENTAL SETUP

2.1 Bubble generator and water channel

In the present study we focus on large bubbles with a diameter of the order of 1 cm as typical for real chemical reactors. A bubble release mechanism similar as that described in [1] was used to generate planar swarms of 8 bubbles. This bubble generator enables the controlled generation of bubbles with near equal volume and a simultaneous planar release. A rotating plate with 8 or 16 holes is used which is placed between two fixed plates from which the top is the release plate and the bottom the filling plate, respectively. In the filling position, each chamber is filled with a defined gas

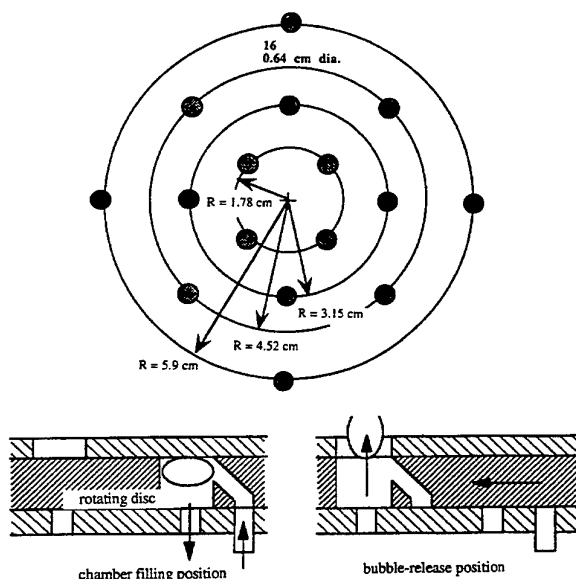


Fig. 1: Bubble generator

volume using a proportioning screw with 8 or 16 syringes in parallel order connected with small tubes to the filling plate. In the release position, the chambers open at the top and bottom and the pressure difference drives the bubbles out of the generator.

In the first version, a plate with 8 holes with a diameter of 6 mm over an area of $4 \times 4 \text{ cm}^2$ was used. The diameter of the thereby generated bubbles was on average 8 mm with a scatter of less than 1 mm. The

resulting Eötvös-number is about 10 and the Reynolds-number is approximately 200, based on the equivalent bubble diameter. Therefore, the bubbles can be expected to be of elliptical shape and to ascend in zig-zag and helical trajectories for a single bubble. Within a cluster of bubbles, the interaction of the bubbles and the wakes lead to more complex behavior.

The described bubble generator is placed at the bottom of a rectangular water column with a cross-section of 10 cm by 10 cm in square. All side walls of the 2 meter long test section are made of transparent acrylic glass to provide optical access from 360° . The test section is fixed to a large water reservoir at the top in which the small tracer particles (Vestosint, $\varnothing \approx 30 \mu\text{m}$) can be mixed to the fluid prior to the experiments. Either experiments with bubbles rising in quiescent fluid or within a counter stream can be realized with the vertical water channel. For the latter case, a single swarm is generated and – after the swarm reaches the mid of the test section – a valve at the bottom left side wall is opened to a certain position such that the swarm of bubbles remains nearly in the same position for observation of longer periods.

2.2 Optical setup with scanning device and stereoscopic mirror system

For application of SPIV in the bubbly flow, we used a digital high-speed video camera (*Speedcam+512*, 512×512 pixel resolution) with a recording rate of 1000 frames/sec and a high-speed rotating drum scanner for synchronized sequential scanning of the flow volume. Fig. 2 depicts a sketch of the optical arrangement for the tomographic recording using the high-speed camera. The scanning light-sheet is oriented in a vertical plane and is scanned in direction parallel to the viewing direction within the flow volume. The total scanning width was 2.4 cm with a number of 5 planes, each 0.6 cm spaced apart. From successive images in each plane (temporal separation $\Delta t = 5 \text{ ms}$), the 2-D velocity field within the light-sheet can be determined by cross-correlation technique.

To obtain also the bubble motion in addition to the flow field, we applied a shadow-method simultaneous to the illumination in a light-sheet and used a stereoscopic viewing arrangement. The simultaneous recording was realized here with a stereoscopic mirror arrangement and the split-screen technique, see fig. 2. The viewing directions have an angle of 90° perpendicular to each other which offers the determination of the 3-D position of the bubbles in the volume of interest. The incoming light from both viewing directions is deflected in the mirror system such that the imaging sensor area of the is illuminated in two equal rectangular segments which

corresponds to both views (split-screen technique). Note, that for this reason the effective horizontal resolution of each view is reduced by a factor of two. Thus, the viewing area is 3cm x 6cm with a resolution of 256x512 pixel (magnification of 1/10).

An alternative arrangement uses the shadow-

technique with background illumination from two sides if only the bubble dynamics is of interest. In other experiments we also used two drum scanners scanning the flow simultaneous in two perpendicular light-sheets to obtain all three velocity components in the scanned volume with the stereoscopic recording system.

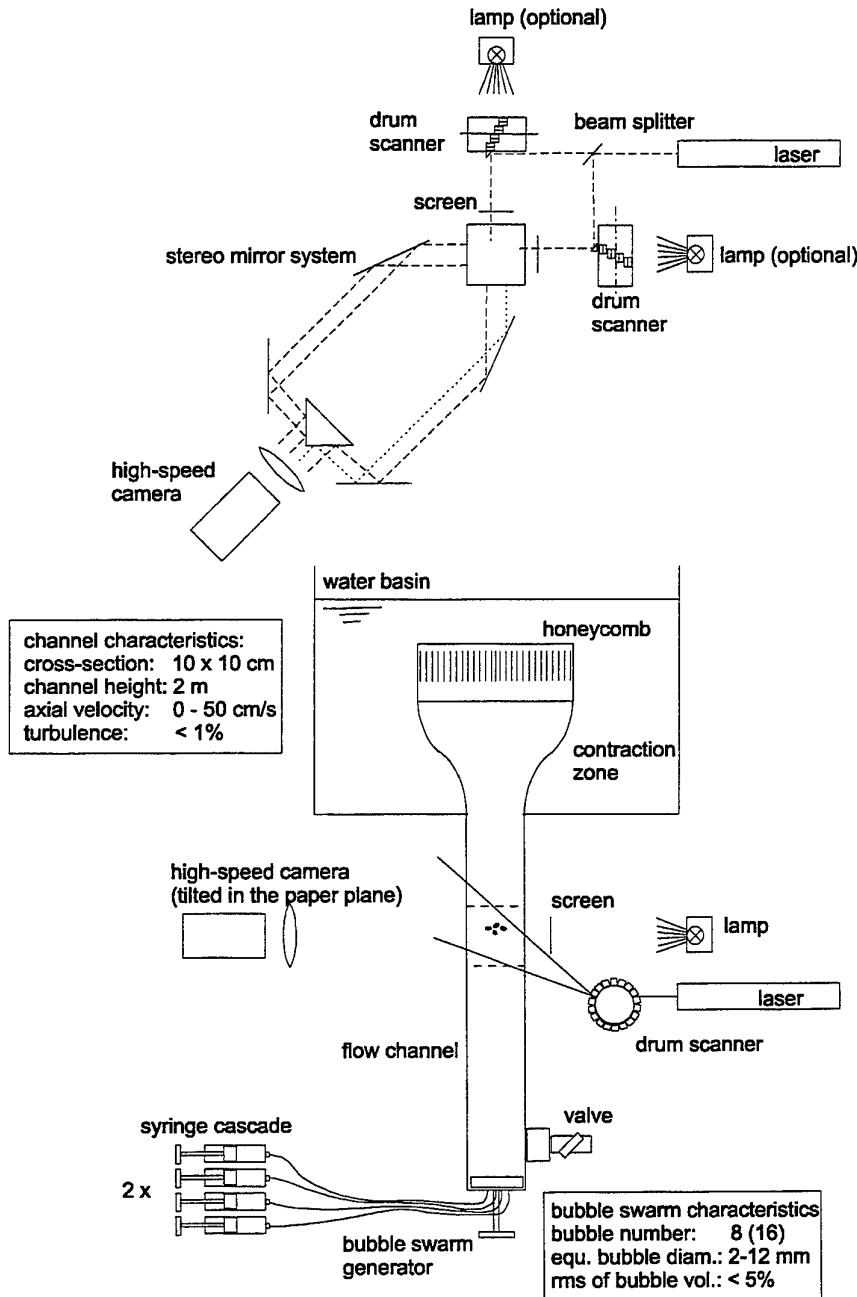


Fig. 2: Sketch of the optical arrangement for Scanning PIV in a vertical bubble column using two simultaneous scanning light-sheets and a stereo mirror system

As we see later, images of the bubbles can be obtained even without any background illumination only by the shadow of the light scattered from the particles in the light-sheet. Though in this case the image quality of the bubbles is bad, it is often still good enough for the three-dimensional reconstruction of the bubble position.

In order to avoid direct light from the scanning laser beam on the video chip, the rotating drum unit was tilted such that the direct beam crosses the flow under a

certain offset angle and passes above the drum unit. If two laser sheets are used simultaneously, we used the both lines of the Ar⁺ laser with 488nm and 514nm separate in the multi-line mode and placed color filters in the path of the non-corresponding viewing direction such that both segments on the chip only receives the scattered light from the corresponding light-sheet.

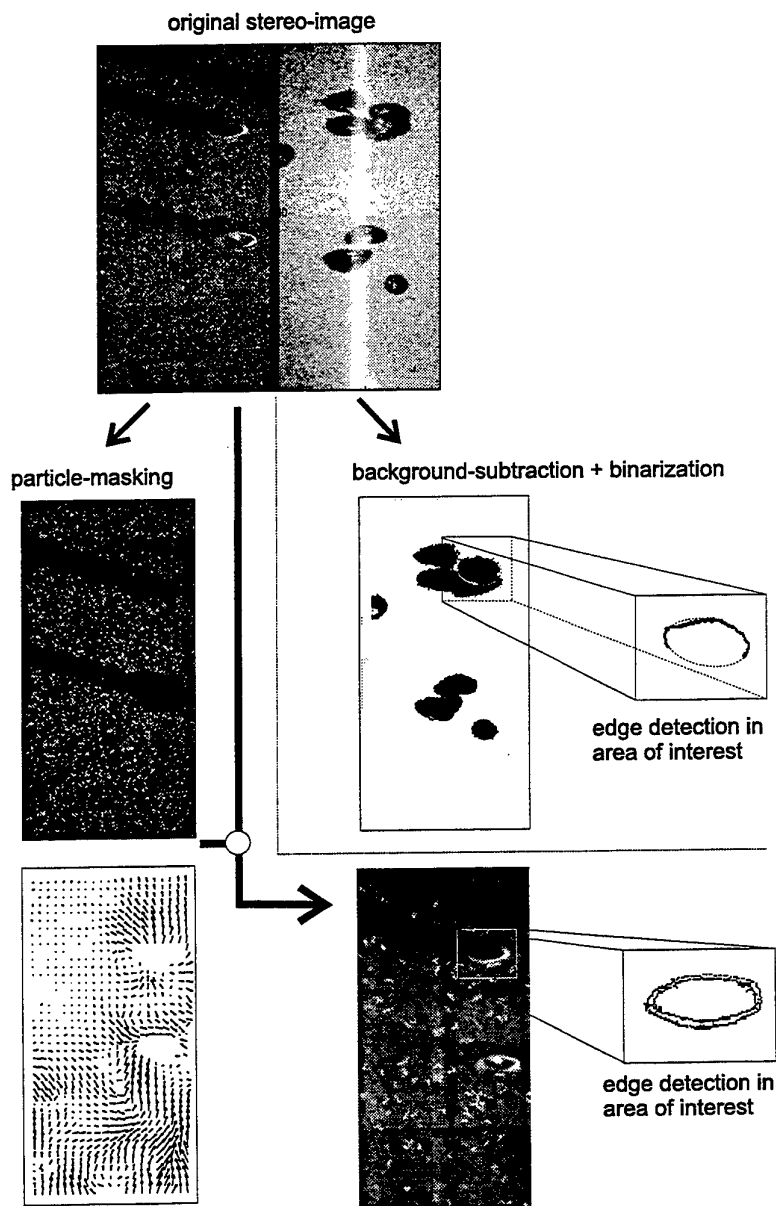


Fig. 3: Processing steps on the left and right image segment for a stereo-image in an experiment with combined light-sheet method and shadow-technique (phase discrimination, bubble contour detection and velocity field determination)

2.3 Image processing

From the images of the bubble in both views the three-dimensional bubble shape and location can be determined via back-projection procedure. In addition, the particle images within the fluid are used to determine the flow field. The necessary initial image processing steps for phase discrimination are shown in the following figure. The left half of the recorded image shows the light scattered by the particles in the light-sheet as typical for PIV. On the right half, one can see the shadow-images of the bubbles within the volume illuminated from the back by a lamp. In this image configuration, the projection direction is parallel to the light-sheet orientation which means, that the bubbles are seen from perpendicular views, one view from the scattered light originating from the light-sheet and one view from the direct projected light of the lamp.

The position of the light-sheet is well seen on the right as a white stripe. By means of the shadow of the laser behind the bubbles one can also find the images of the bubbles on the left and right side which correspond to one bubble in the illuminated volume (those, which are at the same vertical coordinate and which shade the light-sheet). A calibration grid was recorded prior to the experiments to find out the correct relation between object coordinates and image coordinates.

The particle images are separated from the original image by means of a particle masking technique. Therefore, the original image is first binarized (subtraction of a background image and thresholding) and those regions are said to belong to particles, where 2-8 pixels with value 1 are together. This yields after a dilatation procedure finally a binary mask which is used for masking of the original image. With a logical AND and OR procedure of the original image, one obtains the image of solely the bubbles and the image of solely the particles. The bubble contours are determined by edge-detection algorithms.

Out of the bubble contours on both views, the three-dimensional position and orientation of the bubble is estimated. Therefore a rotational symmetric revolution of the bubbles with an elliptical cross-section is assumed as a first approximation. The data of the ellipsoid are obtained by a least-square fitting method from the determined contour coordinates. From the data of the ellipse in both views, we obtain the angle of attack of the bubble against the horizontal axis and the wobbling angle.

The flow field is determined by an improved DPIV method using the method of cross-correlation with adaptive window shifting and iterative window size reduction (see also [7]). This allows - compared to previous methods - a higher spatial resolution and a higher accuracy of the estimated velocity vector. In

addition, the signal to noise ratio increases (the bias error is eliminated due to the shifting method) and due to the window refinement, the cross-correlation can be applied also close to the surface of the bubbles without loss of accuracy. Due to the prior binary masking of the particle images, all image information of the bubbles is removed and no additional falsification due to the dispersed phase exists. The cross-correlation procedure runs over the complete image first. At the end, all vectors are removed at those locations, where the average number of particles is less than 3 in the interrogation window. At these locations, the local fluid vector is estimated by the average of the neighboring vectors. At the blank regions - the area of the dispersed phase - the cross-correlation fails and no information is obtained. This procedure yields at the end the 2-D velocity field within the light-sheet plane. In case of dual-scanning with two perpendicular light-sheets, all three velocity components can be determined in the scanned volume. For the dispersed phase, the temporal information of the center of the ellipsoids gives the trajectories and the velocity vectors of the bubbles.

3. RESULTS OF MEASUREMENTS

With the described bubble generator, first experiments of the bubble wake structures were carried out for bubbles ascending in quiescent fluid. In this study we used a dual-scanning method, scanning two light-sheet perpendicular to each other with two drum scanners through the volume of interest. This has a cross-section of 3.5 x 3.5 cm in square and a vertical extension of 7 cm. In the experiments the bubbles were released and as soon as they enter the observation volume, the camera memory loop is triggered and the next 1000 images are stored. The following result represents an experiment out of numerous others, where the wake capturing process is well seen. Fig. 4 gives the reconstructed bubble trajectories in a perspective view and a view from top together with an indication of the bubble sizes in the lower right corner (the bubble geometry could be determined from the shadows of the light scattered from the particles in the illuminated planes without any additional background illumination). All bubbles have more or less the same diameter of the projected area of order of 1 cm. The Reynolds-number based on this diameter amounts ca. $Re=250$. The figure displays in addition at the right the vertical coordinate of the bubbles over the recording time. A characteristic picture of the induced flow field is shown in a vector plot, where the background color in a rainbow spectrum represents the amount of upwards velocity (red color indicates a region with high upwards motion, blue a

region of low vertical motion). The flow fields in the two perpendicular light-sheet planes are shown together to illuminate the three-dimensional nature of the wake.

In the present experiment, two bubbles enter first the observation volume (no. 2 and no. 3) which are followed by two other bubbles (no. 1 and no. 4), which show a much increased vertical velocity and collide later with

suction effect. The top view demonstrates, that the leading bubbles move more or less in a helical path overlayed with a linear sideways motion, whereas the trailing bubbles have no characteristic trajectory and are mainly driven by the wake of the leading bubbles. To later moments they collide with the leading bubbles and drift laterally away. The colored region shown in the

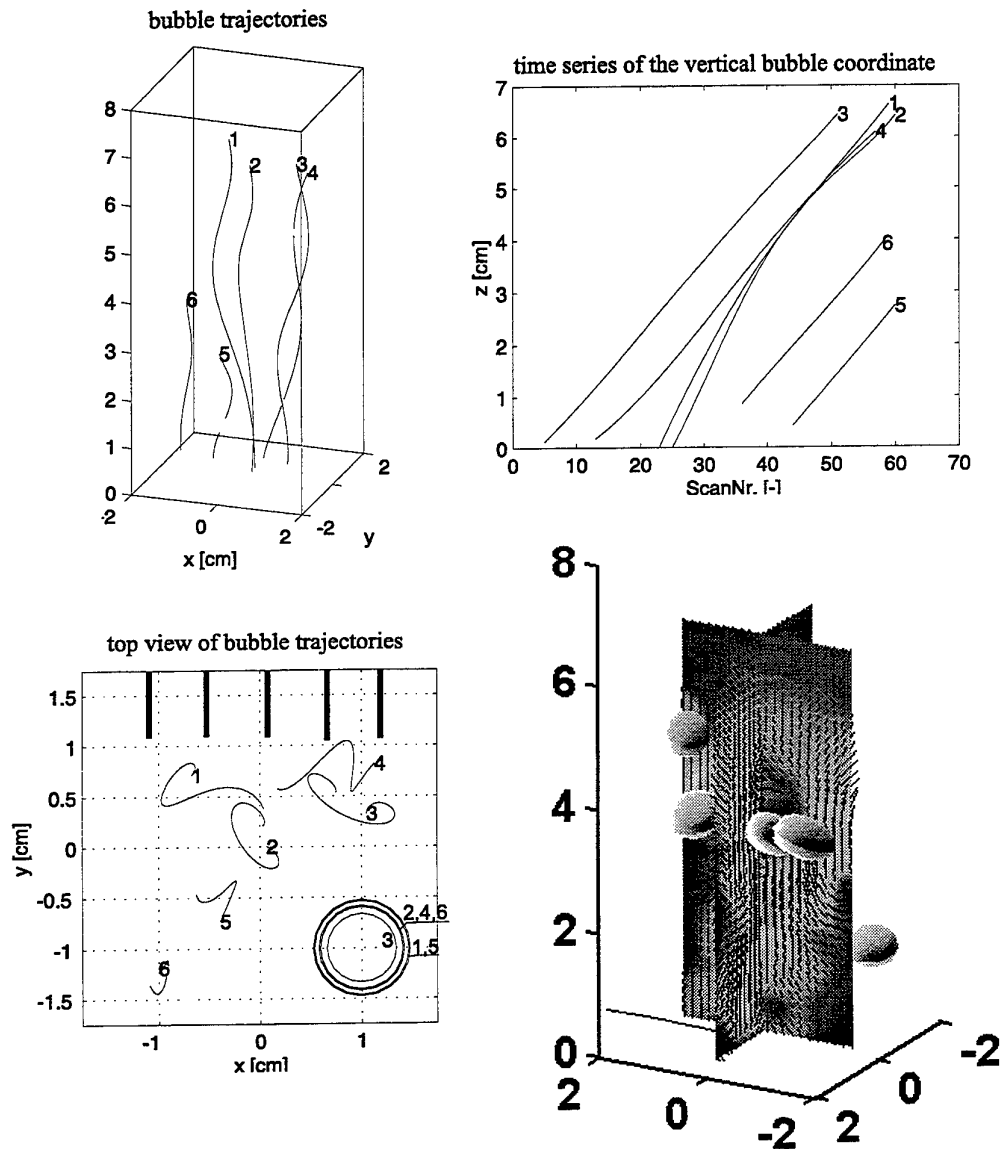


Fig. 4: Three-dimensional trajectories of bubbles in a swarm with 8 bubbles ascending in quiescent flow and corresponding wake structure to a characteristic moment of the bubble cluster ($Re \approx 2500$, the background color in the vector plot indicates the amount of vertical upwards flow)

the leading bubbles. This is well documented in the plot showing the vertical bubble motion where the trailing bubbles show an increased ascending velocity due to the

vector plot indicate that wake fluid with increased vertical velocity is left in a helical structure behind the bubble.

Another experiment demonstrates the interaction of bubbles over longer periods which was carried out in counter flow to keep the bubbles in the observation region. The mean downwards flow velocity was abruptly adjusted from rest to 20cm/s after the bubbles entered

the frame. Here, only a single light-sheet was used for scanning and the other view was used for shadow-imaging of the bubbles. The graphical presentation is equal to that of the last figure. In the vector plot the downwards velocity component by the counter flow is subtracted. Here, the color represents the amount of the

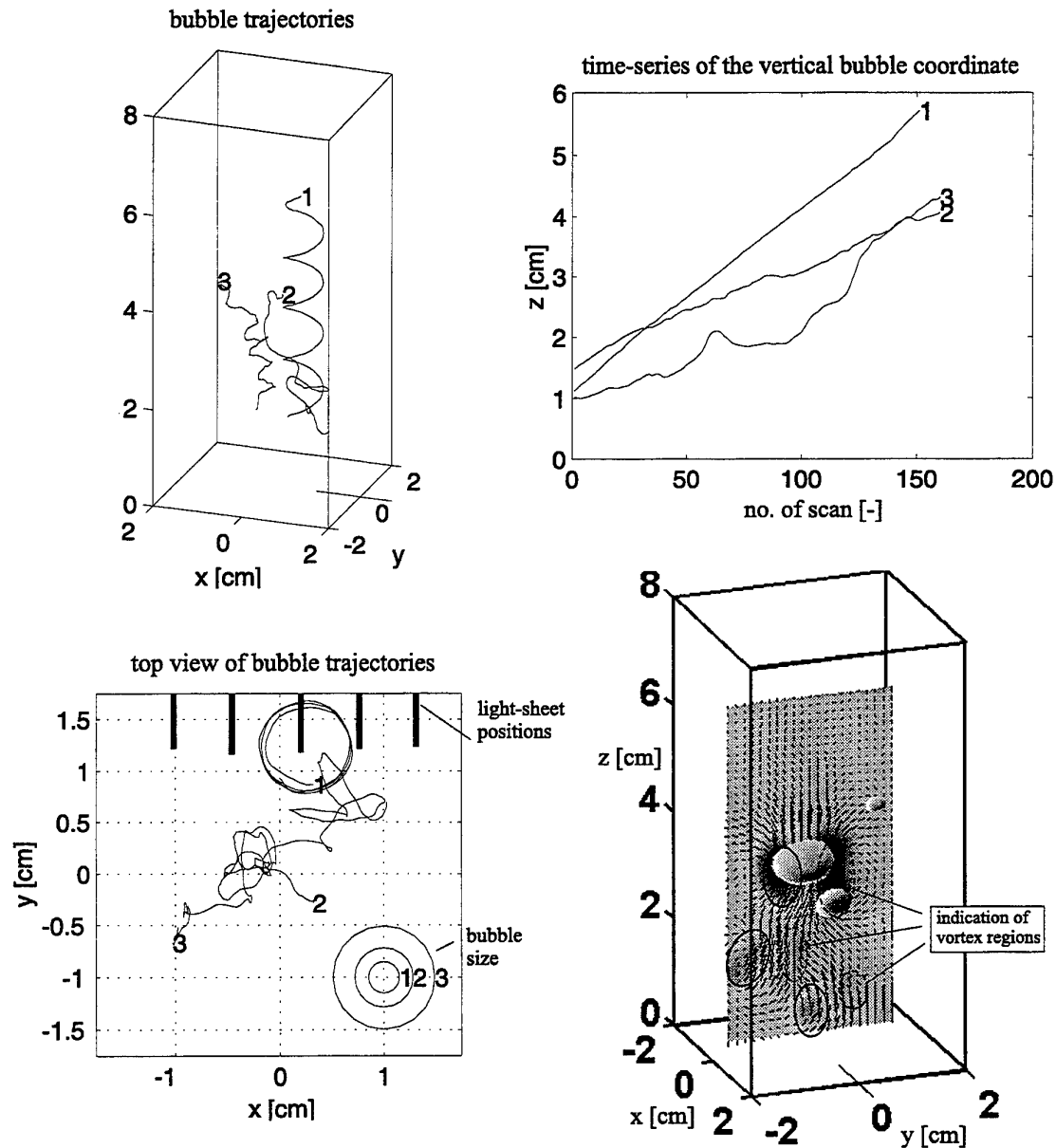


Fig. 5: Three-dimensional trajectories of bubbles in a swarm with 8 bubbles in a counter flow and corresponding vortical structure in the wake to a characteristic moment of the bubble cluster ($Re \approx 2500$, the background color in the vector plot indicates the amount of vorticity)

vorticity component normal to the light-sheet plane. It was calculated by means of central difference schemes from the measured velocity field and was smoothed to remove erroneous small scale regions of high vorticity and to clarify the large-scale vortices.

A two-fold capturing event of a small satellite bubble no. 2 (this bubble was generated with a reduced gas volume in one of the chambers of the bubble generator) into the wake of a larger leading bubble no. 3 could be observed in the recorded period (scan no. 50-70 and scan no. 100-135 in Fig. 5). Note, that in all experiments collisions were observed exclusively after wake capturing (this agrees with the findings from [1,2]) as also seen in the presented results where prior to collision the small bubble is captured by the wake of the larger one. The small bubble first reaches to a certain moment (scan no. 50 in the plot of the vertical bubble coordinates over time in Fig. 5) a critical minimum distance to the large leading bubble and is then trapped into the wake rapidly. It is then accelerated and approaches the large bubble, however, it happens that it is repelled again (scan no. 60 in Fig.5). To a later moment, the small bubble is captured to the second time into the wake of the large bubble (scan no. 120) and then collides with it (scan no. 135).

The vorticity distribution clarifies the ring-like vortical structure in the attached wake of the large bubble. Farther downstream, the remainder of a loop-like vortical structure can be seen. This structure was found to be shed periodically from the larger bubble similar as observed in the wake of a spherical cap [6]. A computer animation of the dynamical process can be downloaded from the WWW www.aia.rwth-aachen.de/public_html/christoph as an avi-file (also published on the CD of the Proc. 3rd Int. Conf. Multiphase Flows, [8]).

A more clarifying presentation of the wake structure is shown in Fig. 6 by means of a spatio-temporal reconstruction of the vorticity field. First, from each scan the plane with the closest location to the center of the leading bubble was chosen (in most cases plane no. 4). From the derived vorticity field in this plane, a horizontally aligned stripe out of the field at a fixed location 2 cm downstream of the centroid of the bubble was taken and the vorticity information there was staggered scan-by-scan in a data array. The resulting data matrix displayed as a contour plot gives the spatio-temporal evolution of the vorticity in this location of the wake of the leading bubble over the complete period of recorded bubble motion. Because the shedding of the vortices was found to be nearly periodic in time with an approximate constant velocity with which the vortices are swept downstream, the vertical coordinate in Fig. 6 can be interpreted either as the time coordinate or alter-

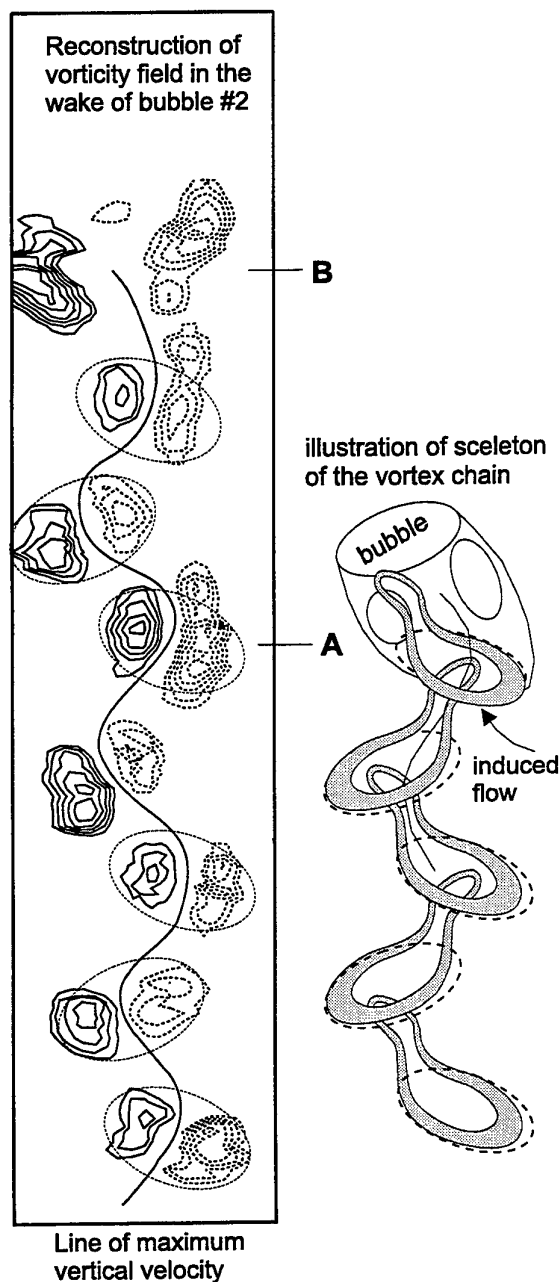


Fig. 6: Spatio-temporal reconstruction of the vorticity field in the wake of the leading bubble no. 2 and the corresponding model of the wake structure. (A: moment of capturing of bubble no. 3 into the wake of bubble # 2. B: moment of collision)

natively as the vertical coordinate in a frozen picture of the wake. Contour lines of constant vorticity are shown where the vorticity exceeds a certain cut-off level.

The spatio-temporal reconstruction demonstrates the nature of the wake as a chain of alternately tilted ring-like vortex structures with a regular zig-zag orientation in this plane. The neighboring positive and negative contour lines represent therein slices through ring-like vortical structures. The orientation of these structures are marked in the graph by ellipses, which also clarify the correspondence of the positive and negative contour lines. From inspection of the instantaneous vorticity field in the other planes of the scans, we could see that these structures do not represent closed vortex rings but the heads of downstream oriented hairpin-like vortices which are arranged in a chain of vortex loops as explained in the sketch on the right-hand side beneath the vorticity reconstruction.

These results clearly demonstrate to the first time quantitatively that the wake of bubbles at this range of Reynolds-number consists of a chain of vortex loops similar as observed in the wake of solid axisymmetric bluff bodies like prolate spheroids, spheres or spherical caps [9,10]. It is also obvious from the measurements that the wake is not a helical vortex structure as quoted in [11]. Our measurements confirm earlier results using qualitative visualizations of the wake of spherical cap bubbles made by Yabe and Kunii (1978) [12] and recent flow visualization studies of the wake of ellipsoidal polystyrol particles rising in water [13].

Further interesting to note is that the capture process of the small bubble into the wake of the leading bubble is triggered by the shedding vortex loops. The moment of wake capturing initiation in the second capturing cycle (see scan no. 100-135 in Fig. 5) is marked in the graph in Fig. 6 at point "A". The smaller bubble at this moment is located at the right-hand side of the large bubble at the region where the arrow is located in the sketch. The arrow marks the direction of the flow field induced by the loop over it to this moment. This induced flow is responsible that the smaller bubble is driven into the wake. Both events, on one hand that the bubbles reach a minimum distance to each other to that moment of their individual paths, and on the other hand that the small bubble is then at the right place with respect to the induced flow field (and to the right time within the shedding cycle) are the conditions for the wake capturing to take place.

It needs a further complete shedding cycle until the captured bubble collides with the leading bubble which is marked in Fig. 6 as "B". During this period the bubble motion is not continuous - see the plot of the vertical bubble coordinate over time in Fig. 5 - but the bubble is alternately accelerated (scan no. 100), decelerated (scan no. 115) and accelerated again (scan no. 120+). Careful inspection of the shedding cycle revealed that the acceleration phase of the small bubble is coupled in time

to the passing by of a loop with the head oriented to the right. Vice versa, the following deceleration phase is coupled by the passing by of the next loop with the head oriented to the left. This is due to the change of the induced flow field at the right-hand side of the vortex chain from where the small bubble approaches the large one. With the period of the alternate loop orientation and zig-zag arrangement the induced velocity at the considered location switches alternately from a positive to a negative vertical component. While in the first wake capture cycle (scan no. 50-70) the deceleration was strong enough for the bubble to be repelled again from the leading large bubble, in the here described second wake capturing cycle the deceleration is not sufficient to reject the bubble again out of the wake so that the bubbles finally collide.

Overall, the results demonstrate that the wake capturing process is strongly coupled to the periodical shedding. Therefore, the shedding of vortices in the wake of bubbles trigger the probability of wake capturing and therefore the probability of collision and coalescence. This could possibly help to develop a more accurate statistical model of bubble interaction in multiphase flows.

Finally, the obtained bubble trajectories are discussed in context with the observed bubble wakes. A first striking results is that the smallest bubble no. 1 with a diameter of 3 mm has the maximum rising velocity and a near perfect helical path (see Fig. 5). It has also the highest angle of attack of about 40° to the horizontal and a large ratio of the helix diameter to the bubble diameter of about 3. An explanation therefore can be found in the theory put forward by Saffman (1956) [14] which is the subject of a following paper. No indications of a periodic shedding could be found from the obtained flow field which gives the hint, that the wake consists of a pair of attached streamwise vortices as also found at lower Reynolds-numbers of order of 200 in the wake of solid axisymmetric bluff bodies [10]. This has to be proven with PIV experiments where the light-sheet is oriented horizontally which is subject of our future work. Bubble no. 2 initially shows a zig-zag-like motion which is coupled with the shedding of vortex structures similar as in case of the large bubble no. 3, see Fig. 6. The angle of attack of the bubble is about 25° - 30° to the horizontal and the ratio of oscillation amplitude to the bubble diameter is about 2 (see Fig. 5). As soon as the bubble is captured in the wake of bubble no. 3, the motion is more or less determined by the pressure field in the wake of the large bubble which can be seen in a large increase of the angle of attack of the bubble. Bubble no. 3 shows initially a rocking motion which persist until short before the collision. It moves in an irregular helical path with a ratio of the oscillation

amplitude to the bubble diameter of less than 0.5. The path oscillation frequency is definitely coupled to the vortex shedding frequency similar as found for bubble 2.

4. CONCLUSION

A scanning PIV method has been developed for application in multiphase flows, where simultaneously the bubble trajectories and shape as well as the flow field can be obtained in the three-dimensional flow volume. A stereoscopic mirror arrangement and the split-screen technique have been used to store two perpendicular views of the flow field on a digital high-speed video-camera. A maximum of 1000 images could be recorded with a frame frequency of 1000 Hz which was sufficient to follow the bubbles motion and flow evolution in detail. Cross-correlation technique was used to reconstruct the velocity field within the light-sheet planes. Using special phase discrimination algorithms we could also detect the bubbles and track their position during time of recording within the scanned volume.

The results demonstrate that the wake of the bubbles at Reynolds-numbers of order of 1000 consists of a regular chain of hairpin-like vortices with their heads oriented downstream and arranged in a zig-zag manner (the heads point alternately to the left and right-hand side). From previous SPIV measurements of the wake structure behind a solid spherical cap [6,10] it can be said that the basic wake structure is the same. In case of the solid spherical cap it was found that the hairpin-like structures result from the instability of the wake against helical waves with a wave number of 1 in azimuthal direction which is similar for all axisymmetric solid bluff bodies and seems to hold also for the wake of spherical or ellipsoidal bubble. The loops are generated by two counter-rotating azimuthal waves of the same amplitude and phase velocity.

The observation of an incomplete and a following complete capturing processes of a smaller bubble into the wake of a leading large bubble during the recorded period could be directly related to the vortex shedding in the wake of the leading one. Hence, the shedding of vortices in the wake of bubbles trigger the probability of wake capturing and therefore the probability of collision and coalescence. This demonstrates that the wake nature is a dominant feature in multiphase flows which has a large influence on bubble-bubble interaction and cluster formation. In addition, it was found that the bubble path oscillations are strongly related to their wake nature. In general, the results demonstrate the necessity of time- and whole-volume measurement techniques to describe the flow in the wake of the bubbles.

ACKNOWLEDGEMENTS

The author thanks the DFG for sponsoring the work in the Focus-Research-Program "Analyse, Modellierung und Berechnung mehrphasiger Strömungen", Kr 387/35

REFERENCES

- [1] Stewart, C.W., 1995, Bubble interaction in low viscosity liquids, *Int. J. Multiphase Flows* **21**(6), pp. 1037-1046.
- [2] Fan, L.S.F., 1990, Gas-Liquid-Solid Fluidization Engineering", *Butterworths Ser. in Chem. Eng.*, Butterworths, Boston, London
- [3] Komazawa, I.; Otake, T. & Kamojima, M., 1980, Wake behavior and its effect on interaction between spherical-cap bubbles, *J. Chem. Eng.* **13**(2), pp. 103-109.
- [4] Brücker, Ch., 1995, Digital-Particle-Image-Velocimetry (DPIV) in a scanning light-sheet: 3-D starting flow around a short cylinder, *Exp. in Fluids* **19**, pp. 255-263
- [5] Brücker, Ch., 1996, 3-D Scanning Particle-Image-Velocimetry (3-D SPIV), *VKI Lecture Series on Particle-Image-Velocimetry LS-1996-03*, Von Karman Institute, Rhode-St-Genese, Belgium
- [6] Brücker, Ch., 1996, 3-D Scanning-Particle-Image-Velocimetry: Technique and Application to a spherical Cap Wake Flow, *Applied Sci. Res.* **56**(2-3), 157-179
- [7] Willert C., 1997, Stereoscopic Digital-Particle-Image-Velocimetry for wind tunnel flows, *Meas. Sci. Techn.* **8**, pp. 1465-1479.
- [8] Brücker, Ch., 1998, Bubble interaction in swarms: a study of the wake structures with tomographic Particle-Image-Velocimetry, *Proc. 3rd Int. Conf. Multiphase Flows*, June 8-12, Lyon, pp.
- [9] Fan L.S., Tsuchiya, K. 1990, Bubble wake dynamics in liquid and liquid-solid suspensions, *Butterworths Ser. in Chem. Eng.*, Butterworths, Boston, London
- [10] Brücker, Ch., 1997, Untersuchung des Nachlaufs einer Kugelschale mit der dreidimensionalen Particle-Image-Velocimetry (in german), *Abhandlungen aus dem Aerodynamischen Institut* **32**, pp. 58-67.
- [11] Lindt, J.T., 1972, On the periodic nature of the drag on a rising bubble, *Chem. Eng. Sci.* **26**, pp. 1776-1777
- [12] Yabe, K. & Kunii, D., 1987, Dispersion of molecules diffusing from a gas bubble into a liquid, *Int. Chem. Eng.* **18**, pp. 666-671
- [13] Lunde K & Perkins, R.J. 1997, Observations on wakes behind spheroidal bubbles and particles. Paper no. FEDSM97-3530, ASME-FED Summer meeting, Vancouver, Canada
- [14] Saffman, P.G., 1956, On the rise of small air bubbles in water, *J. Fluid Mech.* **1**, pp. 2

INVESTIGATION OF THREE-DIMENSIONAL BUBBLY FLOW MEASUREMENT USING DISPLACEMENT PARTICLE IMAGE VELOCIMETRY TECHNIQUE

Javier Ortiz-Villafuerte, Yassin A. Hassan and William D. Schmidl

Department of Nuclear Engineering, Texas A&M University
College Station, TX 77843, USA
Phone: 409-845-7090, Fax: 409-845-6443, e-mail: y-hassan@tamu.edu

ABSTRACT

A three dimensional two phase flow measurement study is performed to obtain a full-field quantitative description of a two-phase bubbly flow. A three-dimensional Displacement Particle Image Velocimetry (DPIV) technique is used for measuring simultaneously the velocity field of the two phases. The scattered light from the particle seed represents the instantaneous positions of particles that lie in the plane/volume of the light. The light pulses is obtained by chopping the light from a continuous wave laser. The points imaged on the frame then need to be tracked, with spacings proportional to the local velocity vector in the plane/volume of illumination. In this study, a developed neural network tracking routine is employed.

The shape of rising air bubbles in a pipe flow is also investigated with the Shadow Displacement Particle Image Velocimetry (SDPIV) flow visualization technique. A test volume of bubbly flow is globally illuminated with a pulsed light from a continuous wave laser with an acoustic-optic beam chopper, and a LED's red light. The viewing volume is observed with four CCD cameras connected to frame grabbers. One of the camera is positioned opposite to the LEDs. A digital image of a rising bubble is acquired and analyzed to identify its shape. A reconstruction method, based on the Dynamic Generalized Hough Transform (DGHT) algorithm that can determine the shape of a bubble from a SDPIV or a DPIV image is employed.

1. INTRODUCTION

The knowledge of bubbly flow behavior is important for optimum design and safe operation of a wide range of industrial systems. One important aspect is the multidimensional effects which occur at different flow regimes. The behavior of bubble moving in a liquid differs from that of solid particle. The bubble shape can change due to the action of hydrodynamic force. Bubble dimensions and shape play an important role in heat and mass transfer. Bubble volume and shape also affect the rise velocity and drag coefficient. The purpose of this study is to present a hybrid technique to simultaneously identify the bubble shape and velocity vectors of the bubbly flow.

Although many flow measurement techniques exist in the chemical, petroleum and nuclear industries, and many of these flows have been studied, there still exists a lack of information and understanding of the physical phenomena. Basic hydrodynamics, mixing, mass and heat transport have not been described based on first principles. Traditionally, design and scale-up of the systems are largely based on models. In these models, the design parameters are largely evaluated by empirical correlations which are applicable to narrow operating ranges. A good knowledge of the structure of the flow, including the behavior and pattern of the phases, is important in areas as safety of the nuclear power plants and efficient design of combustion systems. Many researchers have been interested in the bubbly pipe flow phenomenon, so it has been studied extensively over many years. Several studies have

been performed (Hassan *et al.* 1991; Hassan *et al.* 1992; Kashinsky *et al.* 1991; Nakoryakov *et al.* 1996; Zun 1996; among others). One of the measurement techniques utilized in the study of bubbly flows is the particle image velocimetry (PIV). The PIV technique is a nonintrusive flow measurement technique that has been well developed for acquiring velocity field data (Adrian 1991; Hassan *et al.* 1992; among others).

The purpose of this study is to present a hybrid technique to identify the bubble shapes and velocity vectors of the bubbly flow. This technique is the Shadow Displacement Particle Image Velocimetry (SDPIV) flow visualization technique which utilizes particle image velocimetry to measure the flow-field in conjunction with a red shadow technique to record the full shape of the bubbles. In such way, the velocity vector information of the bubbly flow and bubble identification and distortion are simultaneously extracted.

2. EXPERIMENTAL SETUP

A test facility was constructed to conduct the experiment to identify the bubble shape. The flow setup consisted of a vertical clear glass pipe, a pump and a water filter. The size of the pipe was 1.27 cm inside diameter and 1.59 cm outside diameter. The pipe curvature causes difficulty in ascertaining the laser light location and also decreases the extent of images received by the cameras. To minimize the curvature effect, the test section was enclosed in a rectangular plexiglass box with a refractive index approximately the same as that of the glass tube. The box was filled with water.

The optical setup included an Argon laser, a Bragg cell, mirrors, a beam splitter lens, and a multimode fiber with a fiber coupler as shown in Figure 1. The light source is a 5 watt model 165 ion laser. It produces light at approximately 514 nm (which corresponds to green light). The laser beam passes through a Bragg cell which chops the beam as triggered. After leaving the Bragg cell, the light is directed by a mirror to a beam splitter that separates the beam into two parts. Each part is directed to a separate fiber coupler. The beam then passes into a 400 μm multimode fiber, which transmits the beam to the experimental setup.

The data acquisition system consisted of four digital cameras, each equipped with a telephoto lens, a 2x range extender, a close-up lens, and a light intensifier system with a gain factor of 1:12000. The cameras are model GP MF-702. These cameras have a resolution of 640 x 480 pixels when run in RS-170 frame interlace mode at 30 frames per second. By running the camera in field mode, the resolution is

reduced to 640 x 240; however, the framing rate is increased to 60 frames per second. The cameras were run in field mode to take advantage of the higher framing rate. The facility setup and basic camera arrangement are also illustrated in Figure 1. To measure the bubble's shape, the PIV system is supplemented with a red shadow-image technique. The shadow is produced from LEDs located opposite to one of the CCD cameras. A red filter is placed in front of this camera lens to only produce the bubble shadow.

3. BUBBLE SHAPE IDENTIFICATION AND RECONSTRUCTION FROM PIV IMAGES

The interaction between rising gas bubbles and the surrounding fluid determines the shape of the bubble and the extent of the disturbance to the surrounding flow field. Instantaneous bubble shapes and sizes are important because they reflect the dynamic changes of their pressures inside the bubbles and in the surrounding fluid. Consequently, the velocity field changes of the surrounding fluid are also expressed. Bubble shape and dimensions play an important role in heat and mass transfer between the continuous and dispersed phases, since they determine the interfacial area available for such phenomena. Bubble volume and shape also affect the rise velocity and drag coefficient.

The PIV technique employed in this study is capable of providing the instantaneous bubble shapes. Multiphase flows can be easily studied by PIV, if the image of each phase is easily distinguishable. Several methods were reported to separate the images resulting from different phases. The use of fluorescent tracers is one way of solving this problem. With the aid of optical filters, one may separate the radiation scattered by fluorescent and neutral particles. In this process, one camera captures both phases, and the other camera with the filter only captures the seed particle images. Then, by subtracting the images from both cameras the bubbles can be distinguished. This method of distinguishing phases also has the advantage that the tracer particle images that overlap with the bubble images can also be identified by the camera equipped with the filter. Another method for identifying the phases considers the different image sizes of the seed particles and bubbles. This approach can be employed by applying the mask technique to a digital PIV record such that the images of particles that are either smaller or larger than a predetermined threshold value disappear from the image (Gui *et al.* 1996). Once an image of a bubble is obtained, it needs to be processed to determine the shape and dimensions of the target bubble.

For three-dimensional PIV measurements, the viewing volume is illuminated by a cone of light. In this approach, the bubble images obtained showed only fragments of the bubble, and not the whole two-dimensional projection shape. In addition, the bubble image shape delineated a different shape of the natural bubble shape. This effect is due to the change of scale and also to perspective distortion of the lens action, the lack of adequate illumination, or the intensive light reflection from the bubble. To enhance the bubble image the bubble shadow is recorded by the camera which is located opposite of the LEDs light. The light intensity from the LEDs is low, compared to the laser light, so the camera with the filter acquires only the image of the bubble shadow. A typical SDPIV image of a rising bubble in stagnant liquid is presented in Figure 4d.

Several shape-identification and reconstruction techniques for distorted or incomplete images exist. They go from simply matching the image to a geometrical curve or surface, to the use of parametric curves or surfaces, for example Bezier and spline curves, or to the mapping of the original shape into a parametric space, the Hough transform for example. In the present study, a two-dimensional image reconstruction process has been developed to determine both shapes and dimensions of the bubbles. This reconstruction method is based on the Dynamic Generalized Hough Transform (DGHT) algorithm, which is presented in detail by Leavers (1992). The DGHT algorithm is particularly useful when the object to be recognized and reconstructed is symmetric (e.g., circles, ellipses, etc.). Then, a three-dimensional reconstruction can be achieved by combining two or more images obtained from cameras at different view angles during the PIV setup. In addition to the shape image of LEDs light. The image analysis process is divided into several steps. The main steps of the reconstruction procedure are shown in Figure 5. A more detailed description of the reconstruction steps is given by Hassan *et al* (1998).

The Hough transform decomposes a boundary into its constituent shape primitives. In principle, for any analytically given curve, the DGHT algorithm can be used to compute all parameters associated with the curve (Leavers 1992). In the present case, the DGHT algorithm was applied for detection of ellipsoidal shape. The complete process is illustrated in Figure 6. After each iteration the ellipse parameters are estimated. Although effective stopping criteria to end the calculation cycle for the DGHT algorithm is given, we simply iterate for a number of times. For each parameter, the value with the highest frequency corresponds to the value that best satisfies the ellipse equation. Histograms can be

constructed for each parameter. The width of the histogram is related to the standard deviation, so it is a direct measurement of the uncertainty associated with the determined parameter. A well-defined, isolated peak tells us that the parameter has a good statistical value. When the distribution, the histogram, shows multiple or wide peaks the quantity or quality of the connectivity points is insufficient or bad.

Once the ellipse parameters are known, one can visually overlay the reconstructed ellipse over the original image for a fast comparison of the reconstruction process accuracy. Figure 7 describes the three steps of the reconstruction process applied to the SDPIV image given in Figure 4d. The histograms of the computed semimajor and semiminor axes are also shown in this figure. An overlay of the determined edge-detection operator and the ellipse determined by the computed parameters is shown in Figure 7c. It can be concluded that the computed parameters, through the DGHT algorithm, yield an ellipse that closely matches the bubble shape.

A similar reconstruction process was carried out for the bubble image from the center camera, Figure 4a. By combining the results from these two cameras, orthogonal to each other, the values calculated for the bubble's semiaxes are: $a = 1.068$ mm, $b = 1.265$ mm, and $c = 1.416$ mm. The shape corresponds to an oblate spheroid. The spherical-equivalent radius is 1.241 mm.

The DGHT algorithm offers some advantages over other reconstruction techniques. It yields all five parameters associated with the bubble, so dimensions, shape and the travel path are determined. Other techniques, basically, simply interpolate, and sometimes extrapolate, between the boundary points available for the reconstruction. Although this can give a closer match to the real shape of the bubble, the dimensions and three-dimensional movement will have to be determined by other means. Memory storage and computation time are not much a problem to consider, in the DGHT algorithm. When occlusion of objects exist the DGHT algorithm has also been proven to get good results. The primary disadvantage of this scheme is the need for *a priori* analytical expression for the curve to be detected. Thus, for a very distorted bubble, the best that the DGHT algorithm can achieve is the approximation of the actual shape to a given curve.

4. CONCLUSIONS

The PIV has demonstrated its ability to provide quantitative velocity information in such a manner that several advantages can be realized over

the more traditional methodologies. A reconstruction process based on the Dynamic Generalized Hough Transform algorithm was described. This process can determine the shape of a bubble obtained from SPIV or PIV images. Particle Image Velocimetry is a very promising, powerful tool to study the structure of multiphase, three-dimensional, steady and transient fluid flows.

REFERENCES

- Adrian R.J. 1991, Particle-Imaging Techniques for Experimental Fluid Mechanics, Annual. Rev. Fluid Mech., Vol.. 23, pp. 261-304.
- Gui L. & Merzkirch W. 1996, Phase-Separation of PIV Measurements in Two-Phase Flow by Applying a Digital Mask Technique, ERCOFTAC Bulletin, Vol. 30, pp. 45-48.
- Hassan Y., Schmidl W., & Ortiz-Villafuerte J. 1998, Investigation of Three-Dimensional Two-Phase Flow structure in a Bubbly Pipe Flow, Meas. Sci. and Technol. 9, pp. 309-326.
- Hassan Y., Blanchat T., Seeley Jr. C.H. & Canaan R. E. 1992, Simultaneous Velocity Measurements of Both Components of a Two-Phase Flow using Particle Image Velocimetry, Int. Journal of Multiphase Flow, Vol. 18(3), pp. 371-395.
- Hassan Y.A. & Canaan R. E. 1991, Full-Field Bubbly Flow Velocity Measurements Using a Multiframe Particle Tracking Technique, Experiments in Fluids, Vol. 12, pp. 49-60.
- Kashinsky O.N., Timkin L.S. & Cartellier A., 1993, Experimental Study of Laminar Bubbly Flows in a Vertical Pipe, Experiments in Fluids, Vol. 14, pp. 308-314.
- Leavers V.F. 1992, Shape Detection in Computer Vision Using the Hough Transform, Springer-Verlag, New York.
- Nakoryakov V.E., Kashinsky O.N., Randin V.V. & Timkin L.S. 1996, Gas-Liquid Bubbly Flow in Vertical Pipes, Journal of Fluids Engineering, Vol. 118, pp. 377-382.
- Zun I. 1996, The non-rectilinear Motion of bubbles Rising Through a Stagnant and Distributed Liquid, World Congress III of Chemical Engineering, Tokyo, paper w-0216.

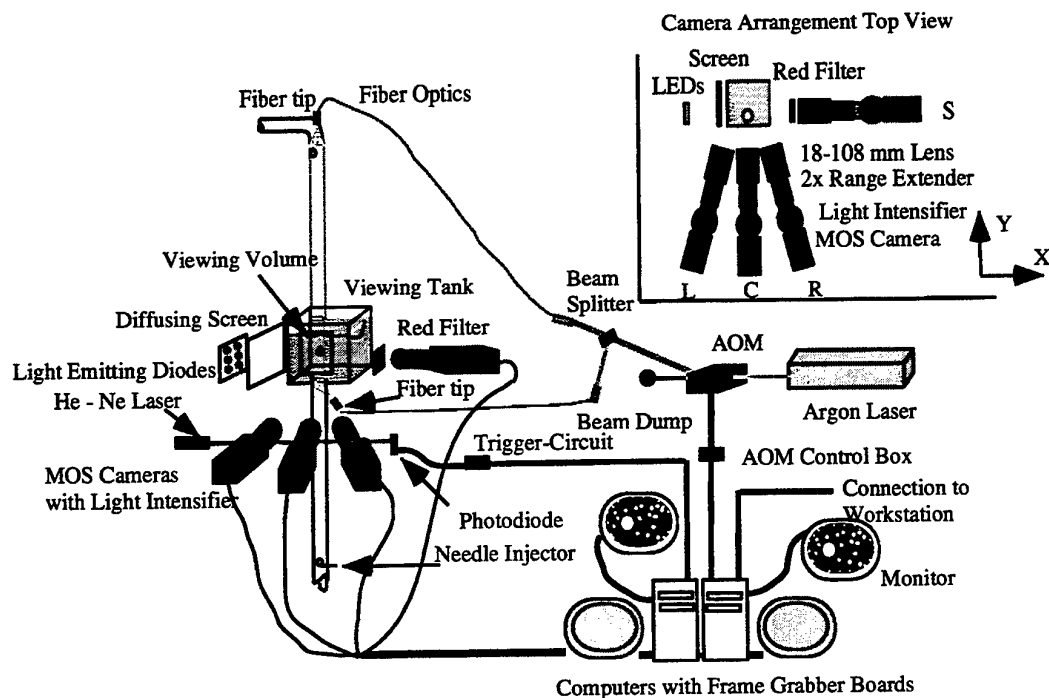


Figure 1. Experimental Setup For Bubbly Flow Pipe Experiment

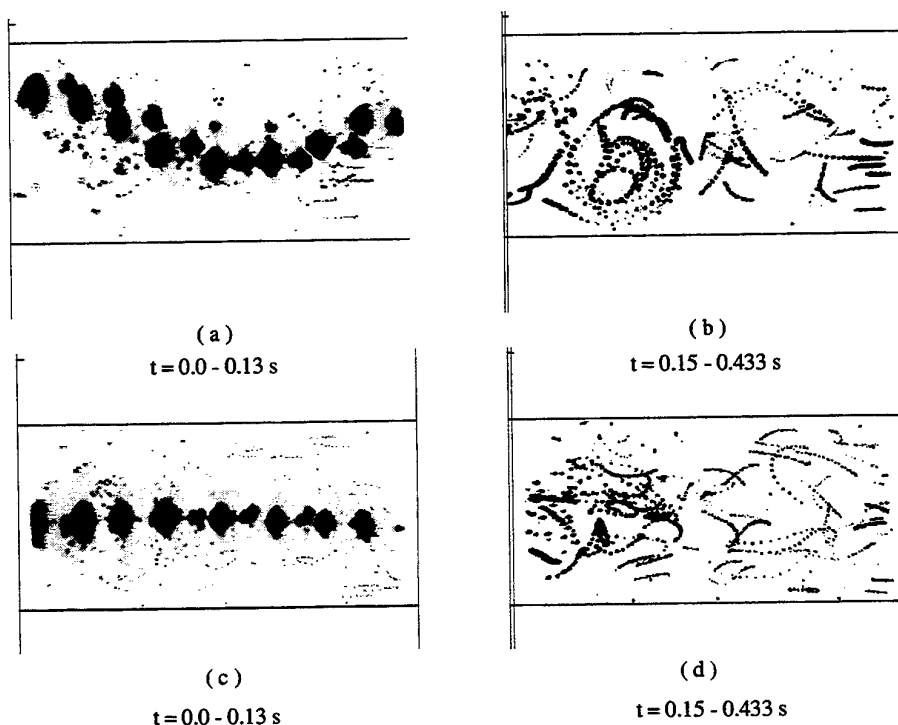


Figure 2. Overlay of PIV images for air bubble injected in stagnant liquid. (a) and (c) during the presence of the bubble in the viewing volume. (b) and (d) after the bubble departure. The images of (a) and (b) are from Z-X plane view. (c) and (d) are from Z-Y plane view.

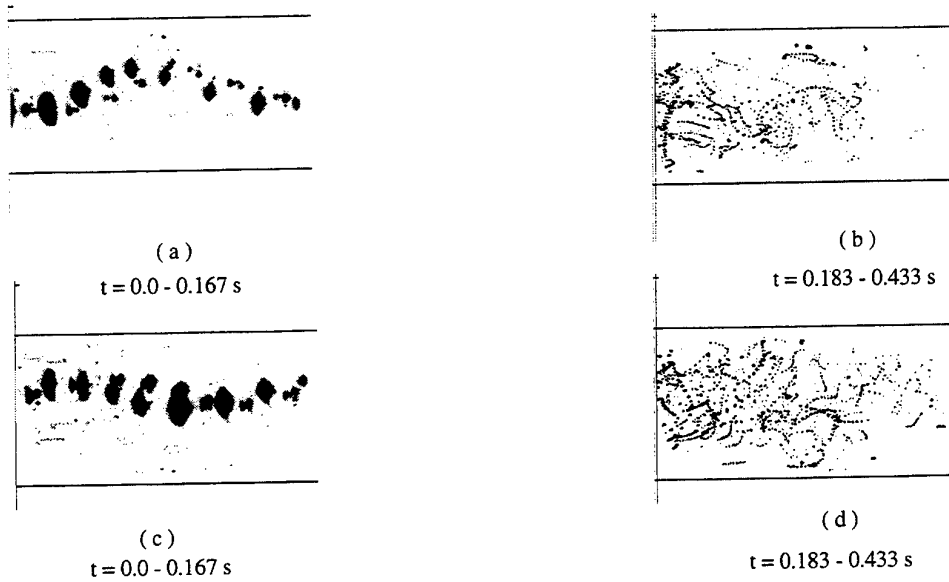


Figure 3. Overlays of PIV images for the co-current flow case. (a) and (c) during the presence of the bubble in the viewing volume. (b) and (d) after the bubble departure. The images of (a) and (b) are from Z-X plane view. (c) and (d) are from Z-Y plane view.

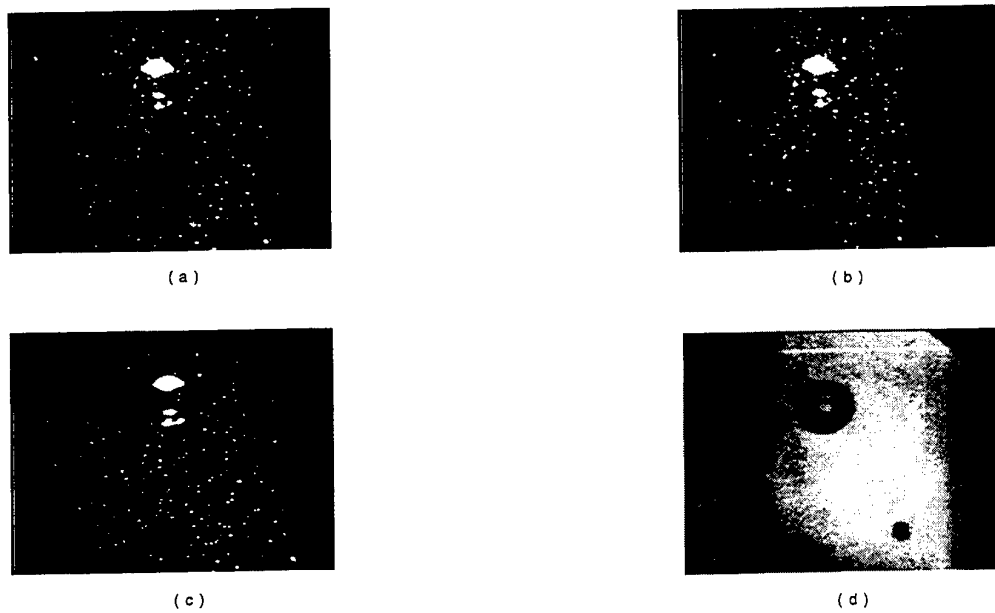


Figure 4. The four simultaneous images of a rising bubble. (a) is the image from the center camera, (b) image from right camera, (c) image from left camera, and (d) the shadow image of the bubble.

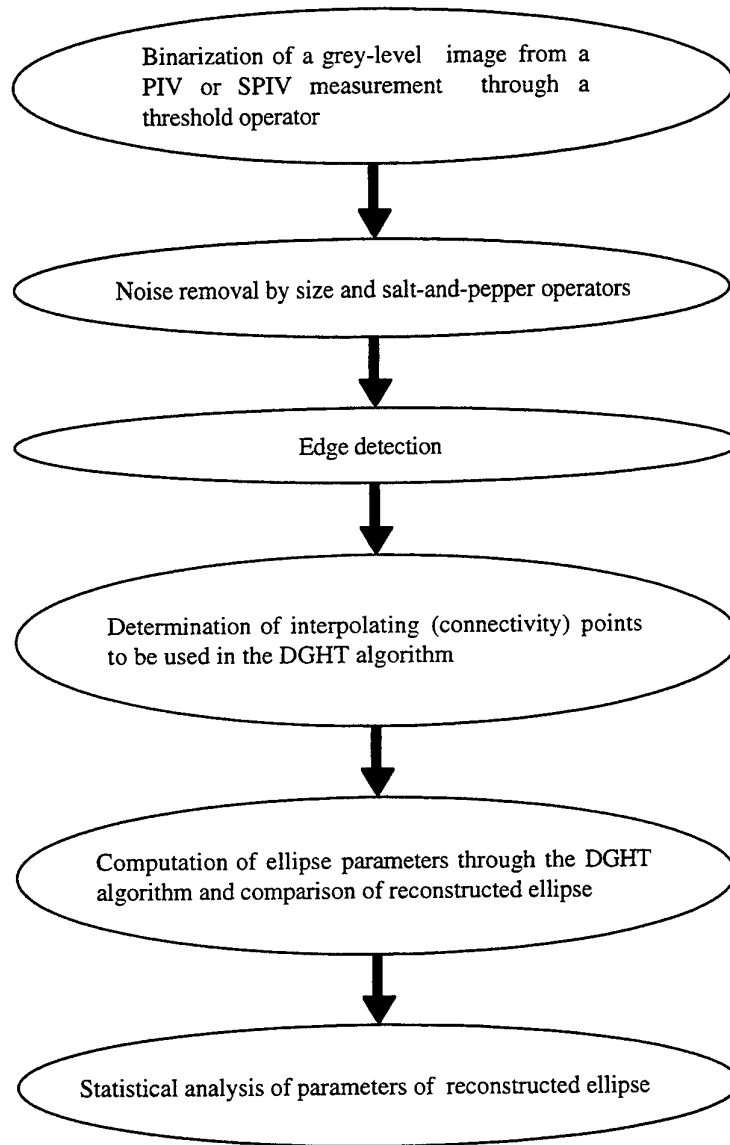


Figure 5. Steps of reconstruction process for a bubble image of PIV or SPIV technique.

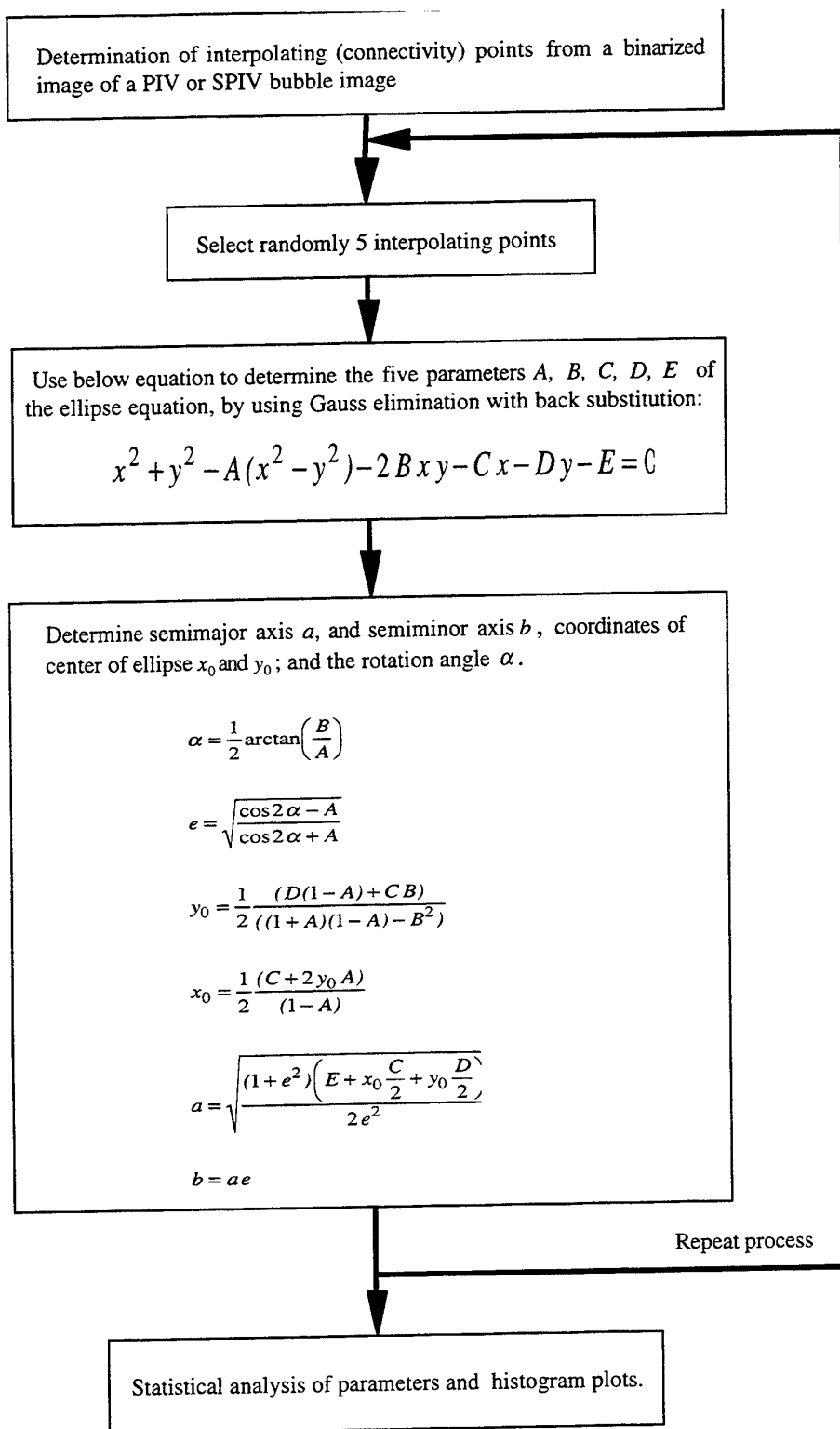
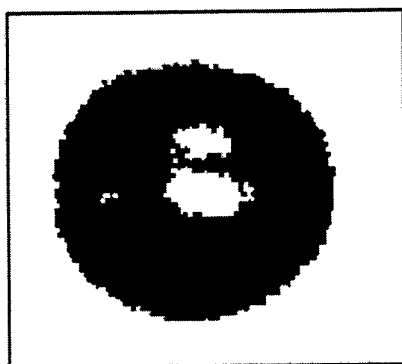
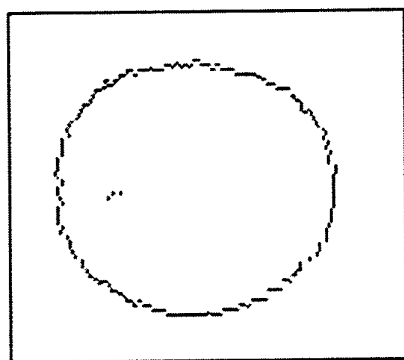


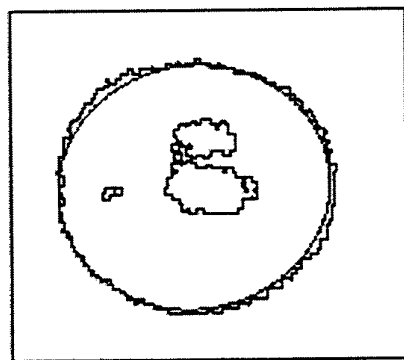
Figure 6. The Dynamic Generalized Hough Transform algorithm procedure.



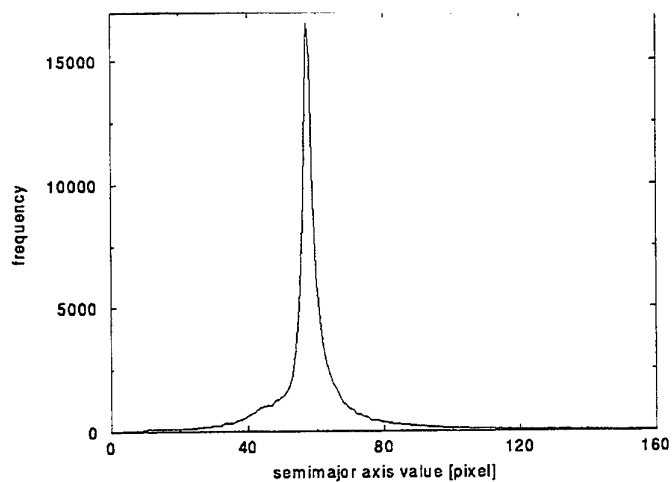
(a)



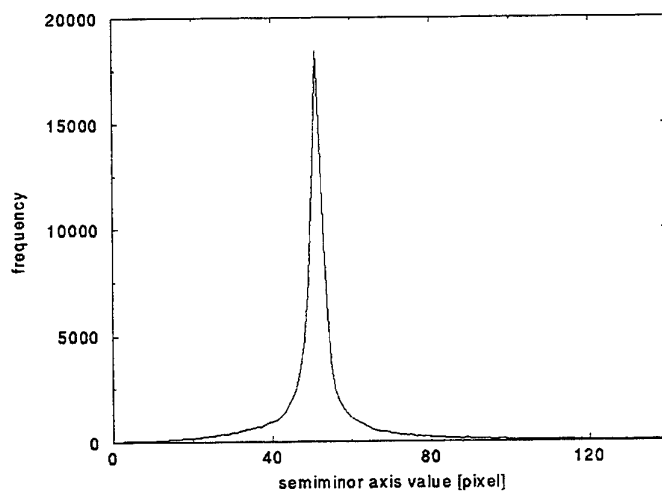
(b)



(c)



(d)



(e)

Figure 7. Reconstruction of the bubble shape: (a) The binary image after applying the threshold, size and noise-removal operators to the SPIV image. (b) The connectivity points to be used in the DGHT algorithm. (c) The overlay of the edge-detection operator and the best ellipse. (d) and (e) histograms of the frequency of the semimajor and semiminor axes, respectively.

SESSION 28

LDV OPTICS II

FIRST BREADBOARD STUDY ABOUT THE OPERATION OF MINIATURIZED LASER DOPPLER ANEMOMETRY (LDA) IN VIEW OF AN APPLICATION ON TEST CONTAINER LEVEL OF THE FUTURE FLUID SCIENCE LABORATORY (FSL)

Jens Immohr, Christoph Egbers and Hans J. Rath

Center of Applied Space Technology and Microgravity (ZARM)
University of Bremen, 28 359 Bremen, Germany

ABSTRACT

We report on a concurrent study of the miniaturization of a Laser Doppler Anemometer measuring system for the integration into the Experiment Test Container of the Fluid Science Laboratory on the International Space Station.

1 INTRODUCTION

The *Microgravity Facilities for Columbus* (MFC) are the most important European contribution to the International Space Station's (ISS) utilization and will continue throughout the station's lifetime.

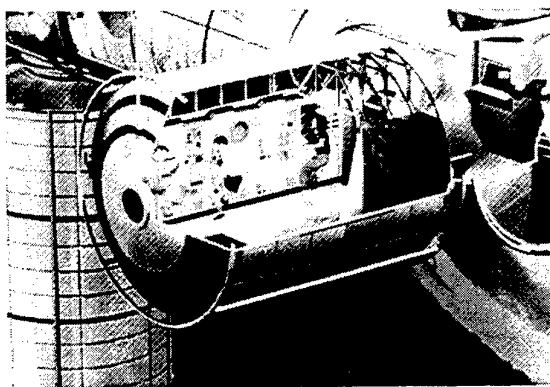


Fig. 1 Inside view of the Columbus Orbital Facility at the International Space Station (Larter and Gonfalone, 1996)

Microgravity research covers a wide range of activities. The first phase of the MFC-Program encloses the years 1997 to 2003 and will operate with

the four disciplines material and fluid science, biology and human physiology. This phase includes the development of the following facilities:

- the Fluid Science Laboratory (FSL),
- the Biolab,
- the European Physiology Modules (EPMs) and
- the Material Science Laboratory (MSL).

These four multi-user facilities will be launched and accommodated in the Columbus Orbital Facility (COF) at the end of the year 2002 (see Fig. 1). All facilities will be high modular in design to allow easy upgrading and maintenance of the science protocols and manually exchanging of the fluid science experiments because of the planned longterm operation period of the future space station (see Larter and Gonfalone, 1996).

2 SCIENTIFIC OBJECTIVES

Fluid science experiments in space are designed to study dynamic phenomena in the absence of gravitational forces. Under the conditions of microgravity the gravitational forces are quasi eliminated. This means all gravity driven effects like convection, fluid static pressure and sedimentation are reduced to zero.

Our main field of interest is focussed on the future Fluid Science Laboratory, results out of our field of research: the Spherical Gap Flow Experiment (see Fig. 2).

The hydrodynamic instabilities of a viscous incompressible fluid flow in the gap between two concentric spherical shells under a central force field represents an important model for astro- and geophysics. Investigations on thermal instabilities

occurring in the spherical gap flow are of basic importance especially for the understanding of symmetry-breaking bifurcations during the transition to turbulence. Furthermore, the practical interest of this research area is based in various engineering applications such as heat exchangers, thermal storage systems and solar energy collectors, etc.

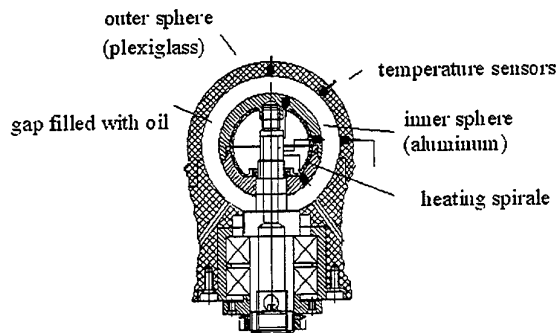


Fig. 2 Sectional view of the Spherical Gap Flow Experiment.

A long term Spherical Gap Flow Experiment application at the future space station is in particular interesting, because the time period for the development of one characteristic fluid flow situation close to the critical point could take some hours or more.

For the application of Laser Doppler Anemometry (LDA) technique in space no common measuring system is acceptable in its dimensions for the integration at the scientific racks of the space station. New miniaturization techniques must be applied to develop applicable measuring systems. The FSL offers many kinds of interferometric measuring systems and visual observation possibilities, but no LDA measuring technique.

3 THE CONCEPT OF THE FLUID SCIENCE LABORATORY

The basic system concept of the FSL comprises the facility with a variety of subsystems required to ensure the anticipated functions and operations (see Fig. 3).

The FSL supports scientific microgravity research in the field of fluid physics by means of specific triggering and observation of phenomena inside of transparent and at the surface of opaque media. It is characterized by a high level of modularity on all experiment and facility (sub-)system

levels. Specific control and data processing modes allow for quasi real time experiment operation.

Research in this space laboratory environment can be conducted hands-on by crew members, from the ground in a telescience mode or using an internal automation. An combination of all three modes is possible.

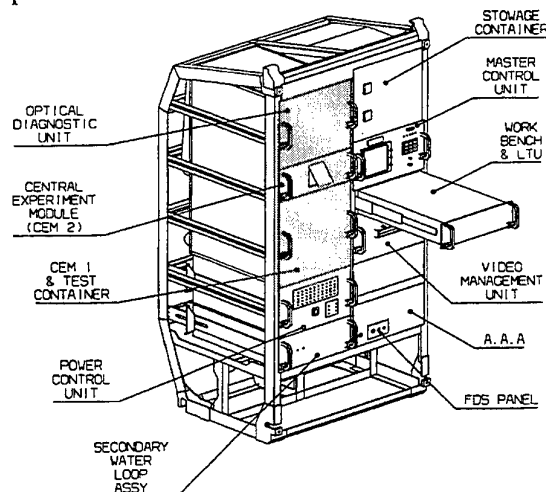


Fig. 3 The Fluid Science Laboratory with its different (Alenia-ESA, Nov. 1997).

The FSL includes a manually accessible operational area called Central Element Module (CEM). The CEM module is designed to house sequentially the modular experiment cells, called Experiment Test Container (ETC), as illustrated in Fig. 4. Above the experimental CEM module the main diagnostics unit of the FSL is placed: the Optical Diagnostic Module (ODM).

Both modules (CEM and ODM see Fig. 5) contain different gas- and diode lasers, white light sources, optical lenses at rotating wheels as well as fixed and moveable mirror units to switch between the different positions of observation and measuring operations possibilities.

The actual scientific fluid experiment is housed inside the fluid Experiment Cell (EC) which is arranged in the very center of the ETC housing in the crossing of the two perpendicular optical axis. The windows are designed to allow a field of view of $A = 80 \times 80 \text{ mm}^2$. The design definition consider a volume aiming at $V = 400 \times 270 \times 280 \text{ mm}^3$ which results out of an optimization process under the given engineering constraints e.g. interfaces, mass, geometry, stowage accommodation, etc. (see Alenia-ESA, Nov. 1997).

Under different and actively alterable stimulations the FSL comprises experimental research at least in the following areas (see Held and Zell, 1996, Immohr *et al.*, 1997):

- hydrodynamic behaviour of fluid systems,
- phase interface behaviour of non-equilibrium fluid systems,
- experiments of crystal growth from vapours, surface deformations and oscillations of fluid bridges,
- nucleation and condensation phenomena in over-saturated and sub-cooled liquids,
- critical point phenomena,
- Bernard-Marangoni problems,
- visualization of cell motion and membrane behaviour,
- Soret-coefficient problems,
- sloshing in vessels and surface tension tanks,
- combustion processes and flame spreadings,
- simulation of heat and mass transfer processes in heat pipes,
- boiling heat transfer and vaporisation processes,
- electrolysis and electrophoretic observation,
- G-jitter induced disturbances in heat and mass transfer processes,
- etc.

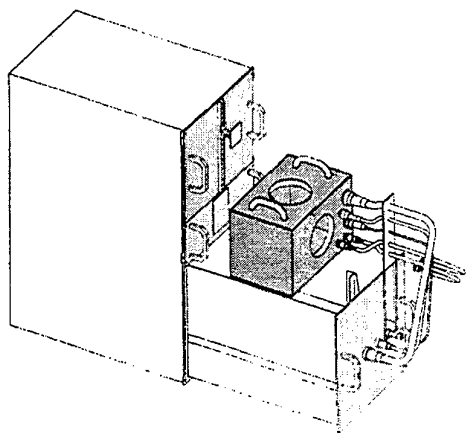


Fig. 4 The Central Element Module with the open drawer for the assimilation of the Experiment Test Container. At the front side of the CEM the electrical/optical interfaces and the water cooling pipes are visible (Alenia-ESA, Nov. 1997).

The ODM includes the following optical diagnostics:

- visual observation in two axis with electronic imaging and photographic back-up, background-

sheet- and volume illumination with white light and laser light sources,

- Particle Image Velocimetry (PIV),
- Photogrammetry,
- thermographic mapping of free liquid surfaces and
- interferometric observation by means of a holographic interferometer [Wollaston/Schlieren mode combined with shearing mode, Electronic Speckle Pattern Interferometry (ESPI)]

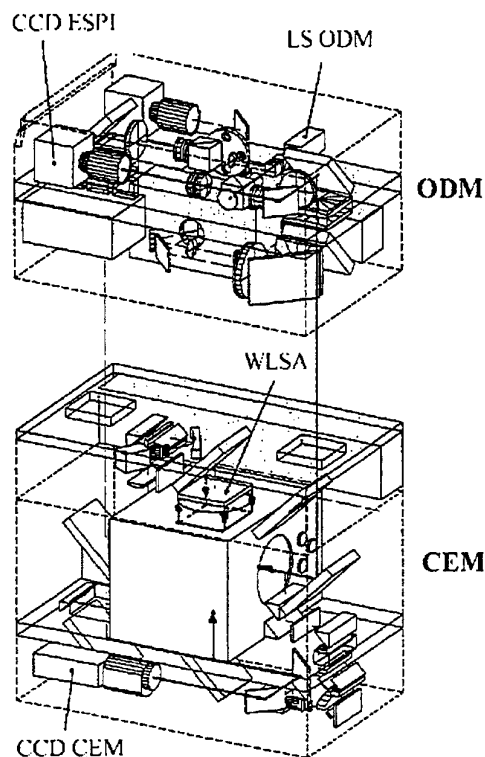


Fig. 5 Schematic view of the diagnostic combination for Wollaston / Schlieren Interferometry. For this case in operation: CCD ESPI camera and the laser of the Optical Diagnostic Unit (LS ODM) along the y-axis + bottom viewing with CEM CCD camera and White Light Source No. A (WLSA). In the middle of the Central Element Module the Experiment Test Container is located. The arrows show the optical ways for the different observation and measuring methods for this special case (Alenia-ESA, Nov. 1997).

An additional Reference Test Container (RTC) gives optional the possibility to calibrate the diagnostics with optical targets and to verify the mechanical, optical and electrical interfaces. The RTC

will be a permanent flight support equipment of the FSL in orbit.

4 THE TASKS

The time varying nature of involving e.g. fully three-dimensional laminar-turbulent transition and convection phenomena means, that for the subject of velocity measurements the LDA technique is a capable and very precise velocity measurement system. It should be installed in addition to the currently planned optical diagnostics of the FSL.

The requirements of the planned measuring system shall comply with actual available measuring specifications of common LDA measuring systems. The fluid flow velocities of experiments inside the FSL are assumed with $u = 0.001 \text{ m/s}$ to $u = 0,1 \text{ m/s}$. This assumption is valid for all future experiments of the FSL. The geometrical dimensions of the optical probe shall not exceed $\varnothing = 40 \text{ mm}$ in diameter and $l = 50 \text{ mm}$ in length.

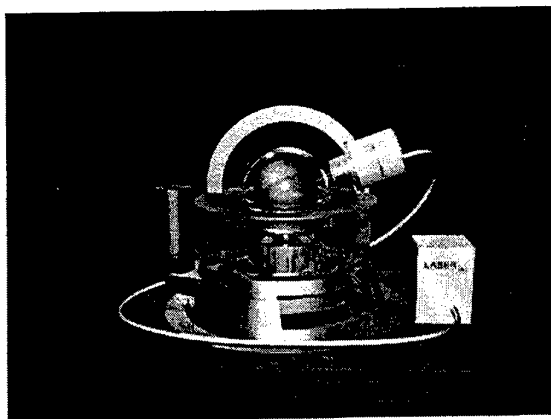


Fig. 6 Principle sketch of the Spherical Couette Flow Experiment integrated with the miniaturized LDA into the Experiment Test Container.

The evaluation of possibilities to divide the LDA system and to separate the laser from the optic probe with fiber connection or a direct beam into the ETC is a main goal for the first step of this investigation (see Fig. 6 and Fig. 7).

This solution has the most modularity in view of using an existing laser light source from the ODM/CEM or to integrate a miniaturized laser diode system into the ETC. This variant offers also a good condition for the operation of a future three dimensional traversing unit, which should operate as a optional multi-user application tool for suitable fluid

flow experiments in the FSL. The first step will include a fluid flow data registration of a one dimensional measuring direction.

The second step of miniaturization will guide the development into the direction of a measuring system, which joined all components of the LDA in one body: laser, optics and the detection tool. With the electric interface integrated in the LDA probe the measuring data will be buffered on a harddisc storage of the FSL, which will be sent via downlink further on to the earth based ground station. At the ground station the raw data processing will be executed with the application of the FFT-technique.

This second step solution has the biggest advantage in view of the operation inside the ETC, because the modularity of the FSL will not be disturbed with additional electrical and optical interfaces. Because of the raw data processing at the ground no further signal processing unit must be installed at the FSL.

In addition to the first and second step of this miniaturized LDA development a furthermore measuring direction is foreseen to receive two dimensional measuring data of the fluid flow experiment.

5 RESULTS

We investigated the feasibility of using existing gas- or diode laser systems, which are foreseen for the ODM in the FSL rack, to build up a LDA measuring system on ETC level (see Immohr and Egbers, 1997; Immohr, 1997).

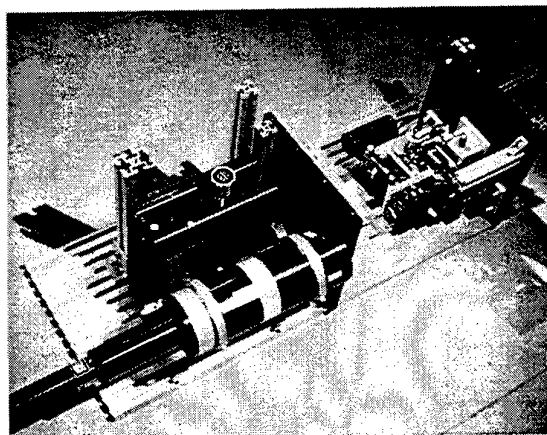


Fig. 7 All over view of the first breadboard prototype of the miniaturized LDA. Between the two black parallel plates the volume of the original

Experiment Test Container in its dimensions of $V = 400 \times 270 \times 280 \text{ mm}^3$ is simulated.

As a result of the technological data scan of available LDA systems or measuring principles from our point of view it is not possible to integrate a common LDA system without modifications or special adaptations on Experiment Test Container level (Immohr *et al.*, 1997).

A first breadboard study shows a possible solution for an ETC based LDA measuring system mounted onto a two dimensional xy-traversing unit (see Fig. 7). An external laser unit initiates two parallel laser beams into the ETC, in which the beams are guided via three mirrors, a beam splitter and a focus lens to the measuring point (see Fig. 8). The backscattered light is focussed in this first study on a photomultiplier tube. In future the backscattered light alignment will operate with a suitable photo diode.

For the application of Laser Doppler Anemometry at the Spherical Couette Flow Experiment a special traversing system has been designed where the optical probe is mounted at a circularly formed guide bar across the experimental shell. The laser is connected via a fiber with the optical probe (see Fig. 6). The fluid experiment cell is placed in the center of the field of view for an additional observation with digital cameras for two directions.

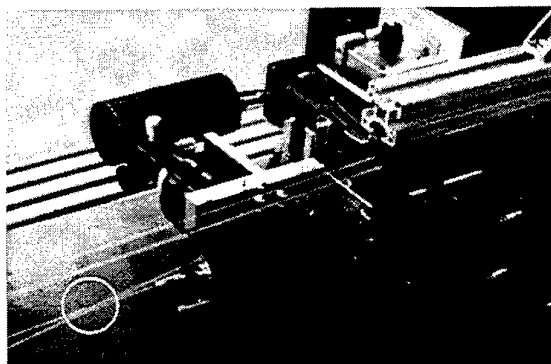


Fig. 8 Close by view of the optical and traversing components of the first breadboard prototype. The circle marked area indicates the measuring volume.

The application of LDA techniques and visual observation on the Spherical Couette Flow Experiment requires an optical correction for the accurate determination of the probe volume locations and for the interference fringe spacing due to refraction effects of the spherical outer surface. Because of the radial adjustment of the optical probe

the optical axis of the front lens passes perpendicular through the surface of the outer spherical shell. As a consequence the correction for the two laser beams, which are in the same plane, could be calculated for a cylindrical surface. However, the fact, that a small probing volume is needed to produce sufficient spatial resolution, which could be obtained only by a large intersection angle, the small-angle approximation cannot be used in this case. The application of the optical correction method for the Spherical Couette Flow Experiment is described in Meiering (1993).

6 ACKNOWLEDGMENTS

The financial support (ESTEC Purchase Order Ref. No. 170397) for this work from the European Space Company (ESA) is gratefully acknowledged. The authors thank Dr. J. Becker, Dr. S. Damp and Prof. Dopheide for fruitful discussions during this work.

7 REFERENCES

Alenia-ESA, 18/19 November 1997, ESA/ESTEC-FSL-Fluid Science Laboratory (FSL) Status Report, Phase B1 Final Presentation, ESTEC Noordwijk, the Netherlands.

Egbers, C., Beyer, W. & Rath, H. J. 1996, LDV measurements on thermal convective instabilities in spherical gap flow. Proceeding of the 8th International Symposium on Application on Laser Techniques to Fluid Mechanics, Lisbon, Portugal.

Held, J. & Zell, M. 1996, Design Report-Description of the Test Container (TC) of the Fluid Science Lab (FSL). Daimler Benz Aerospace Dornier, Friedrichshafen, Germany.

Immohr, J. 1997, Konzeptstudie zur Integration eines miniaturisierten Laser Doppler Anemometers (LDA) in das Fluid Science Laboratory (FSL) der Internationalen Raumstation (ISS/Columbus). Diplomarbeit. Zentrum für angewandte Raumfahrttechnologie und Mikrogravitation ZARM, Universität Bremen, Germany.

Immohr, J. & Egbers, C. 1997, Laser Doppler Anemometry measuring systems in view of an application on Test Container Level of the future Fluid Science Laboratory. Final Report, ESTEC Purchase Order Ref. No. 170397. Center of Applied

Space Technology and Microgravity ZARM,
University of Bremen, Germany.

Immohr, J., Beyer, W., Egbers, C. & Rath, H. J. 1997.
Study on Suited Laser Doppler Anemometry (LDA)
Measuring Systems for Fluid Flow Experiments in the
Fluid Science Lab (FSL). Proceedings of the 7th
International Conference of 'Laser Anemometry
Advances and Applications'. University of Karlsruhe,
Germany.

Larter, N. & Gonfalone, A. 1996. International Space
Station - A Guide for European Users. Early
Opportunities Issue SP-1202. European Space
Agency (ESA) Publications Division, Noordwijk, the
Netherlands.

Meiering, A. 1993. Anwendung der Laser Doppler
Anemometrie für Strömungsuntersuchungen im Spalt
zwischen zwei konzentrisch rotierenden Kugeln.
Diplomarbeit. Zentrum für angewandte
Raumfahrttechnologie und Mikrogravitation ZARM,
Universität Bremen, Germany.

DEVELOPMENT OF FIBER OPTIC LASER DOPPLER VELOCIMETER SENSOR FOR MEASUREMENT OF LOCAL BLOOD VELOCITY

K. Ohba, M. Nishiyama and K. Korenaga

Department of Mechanical & Systems Engineering
Kansai University, Japan

ABSTRACT

In order to measure the local velocity field in opaque fluid flows like blood flow, a new laser Doppler velocimeter has been newly developed. It has a pickup consisting of a small distributed index lens attached at the tips of two fibers which are joined side by side in parallel. The distributed index lens has a tip the shape of an obliquely truncated cone. In order to measure blood velocity of higher blood concentration, it is necessary to improve signal quality from the sensor and to receive stronger scattered light. Therefore we have developed a technique to reduce of reflected light and to increase signal receivable area using higher numerical aperture (NA) optical fiber and distributed index (DI) lens with oblique end.

1. INTRODUCTION

Although knowledge of the detailed local velocity field in blood flow through bifurcation, curved, tapered and small vessels is very important, it is difficult to measure the local velocity field in such flows of opaque fluids like blood accurately and precisely due to lack of an appropriate measurement method. Ultrasound Doppler velocimeter, which is widely used in the medical field, has disadvantage of low spatial resolving power. Tanaka and Benedek (1975) developed a fiber optic catheter for an in vivo measurement of blood velocity. Their catheter was,

however, not capable of local measurement. This was because the pickup of their catheter consisted of a single fiber, and therefore the velocity signal originated from a stagnation region of the flow field around the fiber tip has a dominant contribution to the LDV signal, because light intensity is strongest near the fiber tip and it becomes weaker as the measuring volume becomes farther away from the fiber tip. A special technique for signal processing is required in order to obtain the correct velocity. Kilpatrick *et al.* (1982) and Nishihara *et al.* (1982) developed modified types of the mono-fiber LDV probe. Their systems, however, suffered from the same disadvantage as the above-mentioned one. Whereas, a fringe mode fiber optic LDV developed by Knuhtsen *et al.* (1982) has a different disadvantage in that its large pickup inevitably disturbs flow.

In order to measure the local velocity field in blood flow, a new LDV has been developed to overcome such disadvantages (1982)(1983). In our previous work we developed a dual-fiber optic LDV for blood flow measurement. This LDV had a pickup consisting of a small distributed index (DI) lens attached at the end of two fibers which were joined side by side in parallel. The distributed index lens had a tip of the shape of a truncated cone (1993). It was shown that the LDV was able to measure bovine blood velocity of blood concentration around 20%, which is defined as the volumetric ratio of blood volume to the volume of

mixture of blood and physiological sodium chloride solution (1996). In order to measure blood velocity of higher blood concentration, it was necessary to improve signal quality from the sensor and to receive stronger scattered light. Therefore we have developed a technique to reduce reflected light and to increase signal receivable area.

2. MEASUREMENT PRINCIPLE AND PROCEDURE

A schematic diagram of the present fiber optic LDV is shown in Fig.1. The pickup consists of two graded index silicon optical fibers and a distributed index (DI) lens having the shape of like a truncated cone, which is attached at the end of the two fibers. The two fibers are joined side by side in parallel, one of which is a transmitting fiber and the other is receiving one. Laser beam is emitted into fluid from the DI lens, and is converged to the minimum diameter at a focal point, which is considered to be the measuring (sampling) volume. The scattered light from scattering particles in fluid flow is collected by the receiving fiber via DI lens.

The Doppler frequency f_D is related to the flow velocity u by the following equation.

$$f_D = 2 \frac{n}{\lambda_0} |u| \cos \theta$$

Where θ is the angle between u and the axis of the laser beam emitted from the DI lens, n is the refractive index of fluid, and λ_0 is the wave length of laser light in vacuum.

A schematic diagram of the present LDV system is shown in Fig.2. The system works in the mode of reference beam. A part of the laser beam emitted from the transmitting fiber is reflected at the tip of the DI lens, which is used as a reference beam (local oscillator light). The DI lens is a product of the Japan Sheet Glass Co.Ltd., having 2mm in diameter and 0.46 in pitch. The focal length in water is 0.7mm for the case of He-Ne laser. A multimode G.I. fiber of 50 μ m in core

diameter and 125 μ m in cladding has been used. The Doppler signal is processed by a commercial spectrum analyzer, HP Model 8553B/8552B.

Laser light is emitted from one of the fibers and received by a PIN photo diode through the other. In the present experiment the open channel for fluid flow has been used. An annular channel filled with white pigment (titanium oxide) particles intermixed into water is put on the rotating disc (turn table) which rotates at a constant speed. The LDV pickup was inserted into the fluid flow from the free surface at an inclination angle of 130°.

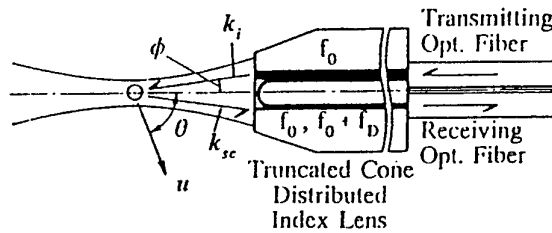


Fig.1 Schematic diagram of the pickup of the present fiber optic laser Doppler velocimeter.

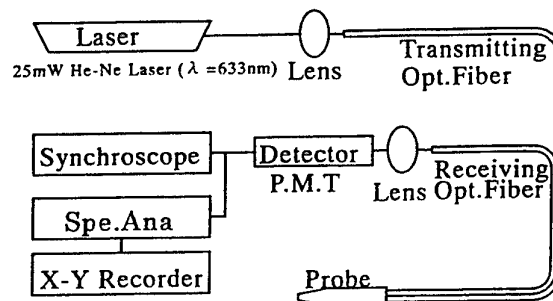


Fig.2 Schematic diagram of the optical and signal processing system

3. EXPERIMENTAL RESULTS AND DISCUSSION

3.1 Measurement of Velocity Using Obliquely Truncated Cone DI Lens

For raising a signal quality it is very important to reduce reflected light. The laser light reflecting from the output end of the DI lens is detected by photomultiplier through receiving optical fiber. The high intensity of the reflected light in the detected light deteriorates the signal quality. Hence in our newly developed DI lens of truncated cone shape, we adopted an oblique end to make the reflected light from the output end divert to outside of the DI lens. A schematic diagram of the obliquely DI lens of truncated cone shape is shown in Fig.3.

The effect of the obliquely truncated cone DI lens on the quality of the laser Doppler signal which is scattered from white pigment (titanium oxide) particles intermixed into water has been examined experimentally. The experimental results are shown in Fig.4. The horizontal axis shows a frequency, the vertical axis shows P.D.F. of LDV signal. The vertical lines of each graph show the frequency which corresponds to the real velocity calculated from the relationship $v_{\theta} = \omega r$. The result shows that it can measure the pigment velocity at a little higher concentration compared with the case of using the truncated cone DI lens.

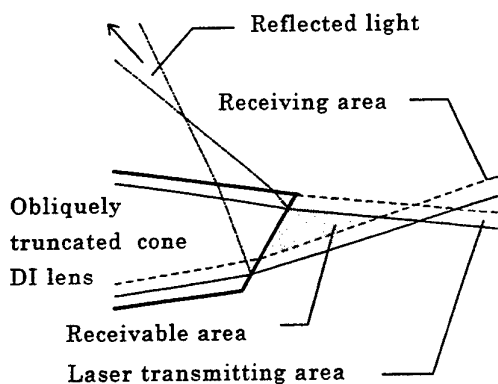
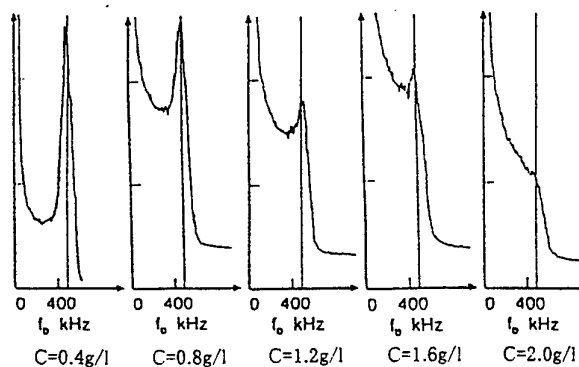


Fig.3 Schematic diagram of obliquely truncated cone DI lens

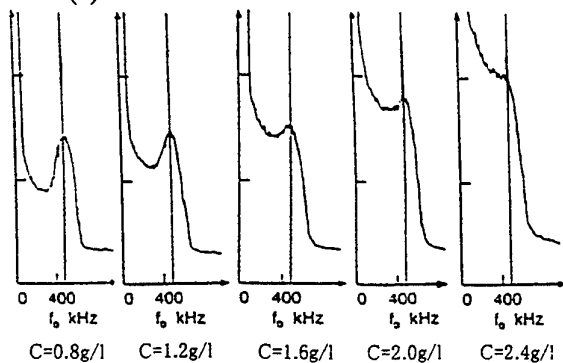
3.2 Measurement of Velocity Using Optical Fiber of Higher Numerical Aperture

In order to receive stronger scattered light, it is necessary to increase the signal receivable area, which is an area overlapped by the laser transmitting area and the receiving area, shown as a hatched area in Fig.3. Only the scattered light from a red blood cell in this area can be received by the sensor. In order to expand the signal receivable area a probe which has a receiving optical fiber of higher numerical aperture (NA) has been examined experimentally.

The results are shown in Fig.5. The results showed that expansion of the receivable angle by using higher N.A. optical fiber did not contribute to receiving stronger scattered light. It is because that this sensor detects only the scattered light on the line which passes through the focal point of the receiving area and within the receivable area.



(a) In the case of truncated cone DI lens



(b) In the case of obliquely truncated cone DI lens
Fig.4 Effect of different type DI lens on LDV signal

3.3 Experiments with a Probe Using Multimode Coupler and Both the Optical Fiber and DI Lens With Oblique End

For receiving stronger scattered light it is necessary to overlap the laser transmitting area and the receiving area completely. Hence, we propose a new probe which consists a coupler for graded index fiber (multimode coupler). A schematic diagram of the LDV system using a multimode fiber is shown in Fig.6. By using the multimode coupler, it is possible to join the transmitting and receiving fibers into a single fiber before connecting to the probe. Therefore transmitting and receiving areas can overlap each other completely. And as a result, the largest receivable area is obtained. However, at the same time it increases the intensity of reflecting light because laser light reflects not only at output end but also at input end of the DI lens. Hence a new method of installation of the DI lens using both the optical fiber and the DI lens with oblique end have been developing. The optical fiber and DI lens are connected at their oblique end. The reflecting light from fiber input end can not transmit in the optical fiber because reflecting angle is higher than the critical angle of transmitting in the optical fiber.

The effect of the new probe using multimode coupler and both the optical coupler and DI lens with oblique end on the quality of the laser Doppler signal has been examined experimentally. In this experiment insertion angle of probe is 110° instead of 130° .

The results are shown in Fig.7. The result shows that it is possible to measure the velocity for the pigment concentration up to 3.6 g/l. But their signals are faster than the real velocity calculated from the relationship $v_\theta = \omega r$.

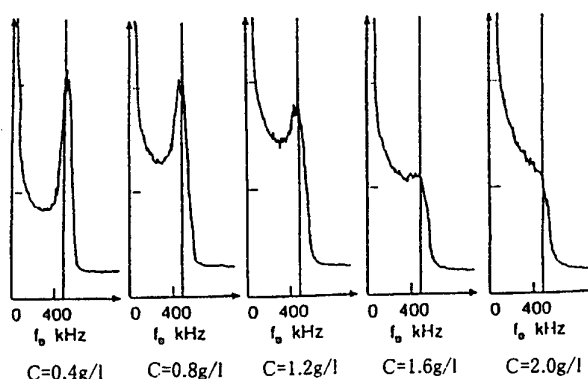


Fig.5 Effect of probe which has a receiving optical fiber of higher NA on LDV signal

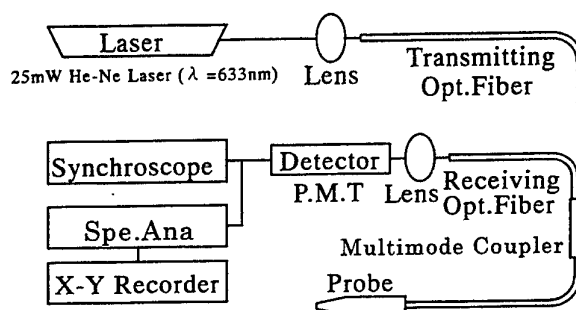


Fig.6 A schematic diagram of the LDV system using a multimode fiber.

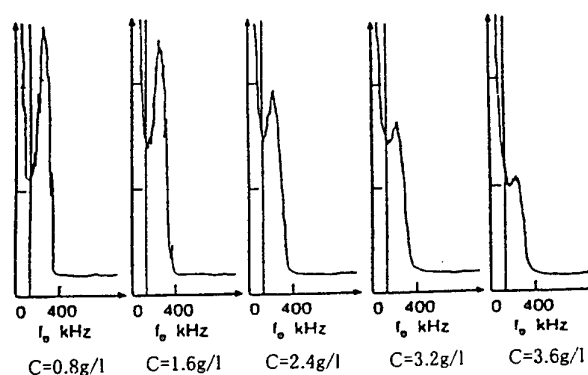


Fig.7 The effect of probe using multimode coupler and both the optical coupler and DI lens with oblique end on LDV signal

CONCLUDING REMARKS

The followings have been elucidated from the above-mentioned experiments

- (1) A fiber optic LDV sensor having an obliquely truncated cone DI lens can measure the pigment velocity at a little higher concentration compared with the case of using truncated cone DI lens.
- (2) The probe which has the receiving optical fiber of higher numerical aperture (N.A.) for expanding the receivable angle does not contribute to receiving stronger scattered light.
- (3) The probe using multimode coupler and both the optical coupler and DI lens with oblique end is possible to measure the velocity for the pigment concentration up to 3.6g/l. But their signals are faster than the real velocity calculated from the relationship $v_{\theta} = \omega r$.

REFERENCES

- Tanaka, T. and Benedek G. B., 1975, Measurement of the Velocity of Blood Flow (in vivo) Using a Fiber Optic Catheter and Optical Mixing Spectroscopy, Applied Optics, vol.14 (1), pp.189-196.
- Kilpatrick, D. *et al.* 1982, Blood Velocity Measurement by Fiber Optic Laser Doppler Anemometry IEEE Trans. BME, vol.29 (2), pp.142-145.
- Nishihara, H. *et al.* 1982, Optical-Fiber Laser Doppler Velocimeter for High-Resolution Measurement of Pulsatile Blood Flows, Applied Optics, vol.21 (10), p.1785.
- Knuhtsen, J. *et al.* 1982, Fiber-optic Laser Doppler Anemometer with Bragg Frequency Shift Utilising Polarisation-Preserving Single-Mode Fiber, J. Phys. E: Sci. Instrum., vol.15, pp.1188-1191.
- Ohba, K. and Matsuno, T. 1982, Local Velocity Measurement of Opaque Fluid Flow Using Laser Doppler Velocimeter with Optical Dual Fiber Pickup, Eng. Appl. Laser Velocimetry, ASME, p.145.
- Ohba, K. and Matsuno, T. 1983, Local Velocity Measurement of Opaque Fluid Flow Using Laser Doppler Velocimeter with Optical Dual Fiber Pickup Trans. JSME, vol.49-447, p.2380 [in Japanese].
- Ohba, K. and Fujiwara, N. 1993, Development of Fiber Optic Laser Doppler Velocimeter for Measurement of Local Blood Velocity Laser Anemometry: Advances and Applications, SPIE, vol.2052, pp.195-201.
- Ohba, K. and Korenaga, K. 1996, Development of Fiber Optic Laser Doppler Velocimeter for Measurement of Local Blood Velocity, Proc. 8th Int'l Symp. On Appl. Of Laser Tech. To Fluid Mech., pp.40.4.1-5.

SESSION 29

BIOLOGICAL FLOWS I

DPIV MEASUREMENTS OF PULSATILE FLOW IN A CONSTRICTED PIPE AT HIGH REYNOLDS NUMBERS

A. Borg, J. Bolinder and L. Fuchs

Department of Heat and Power Engineering, Division of Fluid Mechanics,
Lund Institute of Technology, Box 118, 221 00 Lund, Sweden

ABSTRACT

Pulsatile flow in a constricted pipe with a cross-sectional area reduction of 75 % at $Re_{max}=8600$ is studied by means of DPIV measurements and numerical simulations. Detailed two-dimensional information about the flow field downstream of the constriction is provided. The flow is analysed in terms of phase average and fluctuating velocities. Measured velocities are generally in good agreement with simulations. During early systole the flow resembles a starting jet flow. Growing shear instabilities rapidly makes the jet turbulent. The flow field at peak systole and in the decelerating phase is turbulent with large fluctuations in the jet shear layer. The estimated wall shear stress shows large spatial and temporal variations during early systole. At peak systole and in the decelerating phase, the mean wall shear stress is negative in a region 1.5 pipe diameters downstream of the constriction. The fluctuating wall shear stress values are however as large as the mean values in this region.

1. INTRODUCTION

Pulsatile flow passing through a constriction in a pipe or a channel is found in a large variety of practical realizations. Our interest is mainly in biological flows, and with special emphasis on flow through constricted arteries, i.e. arteries subject to atherosclerotic lesions.

Blood flow in the arteries is pulsatile with a frequency determined by the heart. The flow in the arterial system is generally laminar, but as the peak Reynolds number at rest in the largest arteries is around 3000, transition to turbulence can occur during the high speed part of the cycle. During exercise the peak Reynolds number can reach even higher values, up to as high as six times the value at rest, Ku (1997). Local defects like stenoses can

change this situation, creating intermittently turbulent flow for much lower Reynolds numbers. From one-dimensional, inviscid theory we know that an area increase, and a deceleration of the flow both give rise to an adverse pressure gradient, and hence in the poststenotic area we can expect recirculation zones during the cycle.

In straight vessels, the most important nondimensional fluid mechanical parameters are the Reynolds number, $Re=UD/\nu$, the Strouhal number, $St=\omega D/U$, and the Womersley number, $\alpha=(StRe)^{1/2}=D(\omega/\nu)^{1/2}/2$. The Strouhal number is the ratio of time scale for convection to the time scale for one pulsatile cycle, and the Womersley number is the square root of the ratio of unsteady forces to viscous forces.

In the biomedical field, one of the most important questions is the presumed relation between local hemodynamics and the development and progression of vascular disorders. In the arterial tree, pathological manifestations are found primarily at certain locations: the inner bend of the aortic arch, the carotid sinus, the curved coronary arteries and bifurcations. Ku et al. (1985) showed that plaque formation correlates well with low and oscillating shear stress in the carotid bifurcation. Pritchard et al. (1995) performed experiments that show that the adhesion rate of monocytes is correlated with the magnitude of the shear stress. Adhesion rate increases with decreasing shear stress. In vitro experiments on how vascular endothelium responds to shear stress gradients, performed by De Paola et al. (1992), reveals that regions of enhanced cell division is limited to areas where shear stress gradients are high. In poststenotic flows, in the region just behind the constriction, the wall shear stress is low and of varying sign, which would imply an increased tendency of plaque formation.

Previous studies of pulsatile flow in constricted tubes include the experimental work of Siouffi et al.

(1984) and Ahmed and Giddens (1984). Both of these used LDA velocity measurements together with flow visualization to study the post-stenotic flow pattern. Siouffi et al. investigated a case with a physiological type of inflow corresponding to the parameters $Re_{max}=320$ and $\alpha=6$. Their measurements showed that for a constriction with a cross-sectional area reduction of 75%, the flow remains laminar throughout the cycle, with a recirculation zone that changes length and strength during the pulsatile cycle. The experiments by Ahmed and Giddens showed that for flow with $Re_m=610$ ($Re_{max}=1000$) and $\alpha=7.5$ and a cross-sectional area reduction of 75%, the flow becomes unstable during the cycle with vortex shedding and transition to turbulence. Ojha et al. (1989) observed a similar behavior for a flow with the same reduction in cross-sectional area, and with $Re_m=575$ ($Re_{max}=935$), and $\alpha=7.5$, using a photochromic tracer method. They showed that downstream of the constriction, transition to turbulence was triggered just before peak flow, through the breakdown of waves and streamwise vortices that were shed in the shear layer. During the turbulent generating part of the cycle the poststenotic field could be divided into four different regions: a stable jet region, a transition region, a fully turbulent region, followed by a relaminarization zone.

This study, focusing on high Reynolds numbers, is the first in a planned series of PIV measurements of constricted pipe flows. Physiologically, the high Reynolds number corresponds to exercise conditions. The geometry represents a rather severely constricted straight artery. Previous experimental work on post-stenotic flows lack detailed instantaneous two-dimensional information of the flow field, which may be obtained by PIV. The present work presents phase-averaged and fluctuating velocity information at a few positions of the pulsatile cycle. A detailed picture of the spatial and temporal evolution of the starting structure during early systole is presented. The measured starting structure is also compared to three-dimensional numerical simulations of the same flow.

2. METHODS

2.1 Flow System and Instrumentation

The geometry of the idealized stenosis model and a principal drawing of the experimental setup are shown in Fig. 1. The employed coordinate axes are also indicated. The stenosis model is made by plexi-glass, and has a cross-sectional area reduction factor of 75%. The experimental apparatus consists of a liquid membrane pump, which delivers a pulsatile flow with systolic and diastolic periods of approximately equal duration. During the systolic phase, a

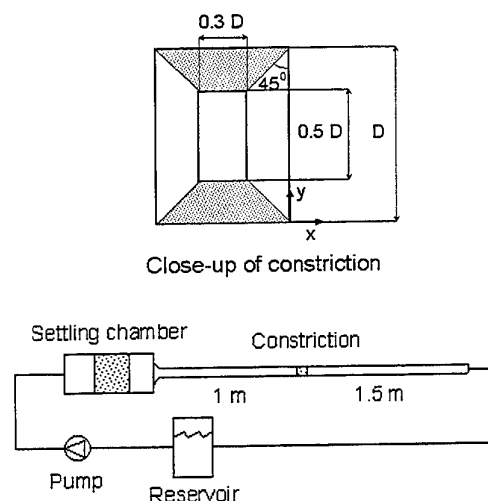


Fig. 1 Schematic drawing of experimental setup

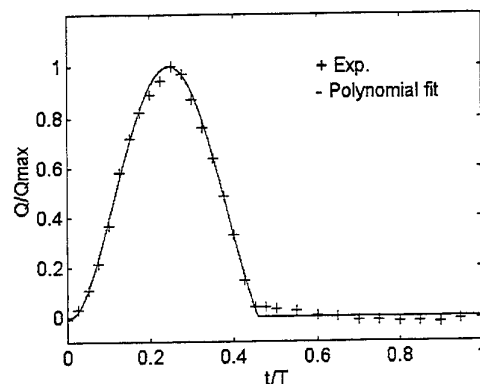


Fig. 2 Nondimensional flow rate versus time. A 4th order polynomial fit is shown for the systolic phase.

volume of 120 ml is delivered from the pump, whereas during the diastolic phase the volume flow is zero. The pump is connected via a settling chamber to a straight glass pipe, with an internal diameter of 21.7 mm. The stenoses model is fitted in the glass pipe 46 diameters downstream of the outlet of the settling chamber. The pipe is immersed in a plexi-glass container filled with water, which reduces refraction effects at the pipe wall. The test fluid is water at room temperature.

All data are made dimensionless using as a reference length scale the pipe diameter $D=21.7$ mm, as a reference time scale the period of the pump $T=3.55$ s, and as a reference velocity scale the maximum mean velocity in the pipe $U_{max}=0.379$ m/s. In terms of nondimensional parameters the flow can be described

by $Re_{max}=8560$, $\alpha=14.7$ and $St=0.101$. The volume flow rate as a function of time is shown in Fig. 2. This was obtained by integrating PIV velocity measurements in the pipe just after the settling chamber.

A commercial system (LaVision) is used for DPIV measurements. It consists of a high-resolution (1280x1024), 12 bit, cross-correlation CCD camera, a double cavity 25 mJ Nd:Yag laser, and software. The camera and laser are triggered by the pump, to get measurements at a specific phase of the cycle. Measurements are performed in the center-plane of the pipe just after the constriction. One pixel corresponds to 35.7 μm , which means that the measurement plane covers 45.7 mm of pipe length, i.e. about two pipe diameters. Measurements were also performed just downstream of the first measurement plane. An interrogation cell size of 32 pixels with 50 % overlap is used. This means that we get 37 vectors across the span of the pipe (though not representing fully independent measurements). The light-sheet thickness is about 1.5 mm, which implies that the interrogation volumes are approx. of cubic shape. This is adequate, since we expect that the out-of-plane motion is of the same order of magnitude as the in-plane motion. With an image magnification, $M=0.188$, and a numerical aperture, $f^\#=16$, the depth of field is estimated to about 2 cm, which is far wider than the light-sheet thickness. The time-separation between the pulses is adjusted according to the one-quarter rule, i.e. the maximum particle displacement is allowed to be about 8 pixels. The flow is seeded with particles named Vestosint (Hüls GmbH), with a size around 15 μm . The particle density is about 12 per interrogation area, computed with a threshold set to three times the background noise level. This ensured that the number of spurious vectors were low enough to be able to sort them out by the post-processing algorithm. The particle image diameter is about 3.5 pixels.

2.2 DPIV Algorithm and Error Estimate

The software provided with the DPIV system performs a cross-correlation analysis to determine the average particle displacement in the interrogation areas. The sub-pixel interpolation is done with a center-of-mass algorithm, where the lowest value in a 3x3 area around the correlation peak first is subtracted from all other correlation values. The most often recommended sub-pixel interpolation method is to fit a Gaussian distribution to the correlation peak, see e.g. Westerweel et al. (1996). Preliminary comparisons of the present center-of-mass estimate and a Gaussian fit showed a maximum difference of about 0.1 pixel. A more complete evaluation is under way.

For the post-processing of the vector fields, an in-house algorithm was developed, which comprises a local median test to remove stray vectors, filling up of empty spaces, and finally a light smoothing filtering to remove high-frequency noise. In the local median test, the median velocity in a 3x3 region around the vector to be tested was first computed. This was done individually for each component. The allowed deviation from the median was fixed for the whole vector field to about ± 2 pixels for both components. If the highest correlation peak did not pass the median test, the next highest peak was tested, and so forth down to the fourth highest peak. Places where no acceptable vector could be found were filled up with the average velocity of the neighboring 8 vectors. The median test was repeated once with a filling-up pass in between. This post-processing algorithm was found very effective. For a complete vector field of more than 2500 vectors, only a few suspicious vectors remained, which could be corrected manually. At last a Gaussian-like 3x3 smoothing filter was applied, with a standard deviation of 0.6 vector spacings, which implies a filter kernel with a center-to-corner ratio of 16. In all stages of the post-processing, no-slip condition at the pipe walls was assumed, which improved the near wall behavior of the algorithm.

The uncertainty in the displacement calculation is estimated to 0.1 pixel, which for a maximum displacement of 8 pixels gives an accuracy of at best 1 % for the velocity estimate. Locally the present flow has very large gradients. In these areas we can expect a gradient bias error towards the smaller velocity in the interrogation areas. The smallest scales that can be resolved are about 1 mm, which is of the order of the Taylor microscale. The Kolmogorov scale for the present flow is estimated to about 30 μm , which is similar to the pixel size. Near the pipe walls, there are small errors in the location and size of the interrogation areas, due to refraction at the curved pipe wall, and due to image distortion by the camera lens. This combined error is of the order of one pixel, and it was not corrected for.

Phase average velocity fields were computed from sets of $N=10$ or $N=30$ instantaneous velocity fields. According to Moffat (1988), the uncertainty in the estimate of the mean is $S/N^{1/2}$, where S is the standard deviation of the N individual measurements. For $N=10$, the true standard deviation σ lies between 0.70 S and 1.75 S , and for $N=30$ between 0.80 S and 1.34 S .

2.3 Numerical Methods

The fluid is an incompressible Newtonian fluid, which is governed by the Navier-Stokes equations. In Cartesian tensorial form they read

$$\frac{\partial u_j}{\partial x_j} = 0, \quad (1)$$

$$\frac{\partial u_i}{\partial t} + \frac{\partial u_j u_i}{\partial x_j} = -\frac{1}{\rho} \frac{\partial p}{\partial x_i} + \nu \frac{\partial}{\partial x_j} \frac{\partial u_i}{\partial x_j}. \quad (2)$$

The spatial discretization is performed on a three-dimensional Cartesian grid, using a third-order upwind scheme for the convective terms. The other terms are discretized by a fourth-order central difference scheme. The time integration is done by a three time-level second-order implicit scheme.

The flow is modeled from the beginning of the constant area in the constriction. At the pipe wall, no-slip conditions are assumed. At the entry section, a uniform velocity profile is assumed with a magnitude equal to the instantaneous volume flow rate in the experiments divided by the cross-sectional area of the constriction. The flow is unforced, i.e. no explicit disturbances are added to the inflow. Only disturbances from numerical round-off errors and internal loop iterations are present. At the outflow section, which is located 12 pipe diameters downstream of the constriction, a Neumann condition is used for the velocity in the direction normal to the outlet plane. The computational domain is covered by a hierarchy of global grids, and one local grid extending from the inlet to 6 diameters downstream. The local grid has a resolution of $120 \times 48 \times 48$ cells in the x , y and z directions, respectively. The nondimensional time step is $0.16 \cdot 10^{-3}$, which means that one complete cycle is covered with 6250 time steps. Due to the high computational demand, only one complete cycle was simulated. The spanwise resolution is slightly better than in the PIV measurements, but still the smallest scales are not resolved. As we do not use an explicit subgrid scale model for the non-resolved scales, energy is drained from the large scales by dissipation provided by the numerical scheme.

3. RESULTS AND DISCUSSION

3.1 Accelerating phase

The flow pattern associated with the early acceleration phase is essentially deterministic, i.e. the difference between ensemble averaged data and instantaneous data is small. Figure 3 shows measured and simulated velocity fields at four instants of the early accelerating phase. Only one half of the flow field is shown. The flow is nearly symmetric. The measured fields are phase averages of 10 measure-

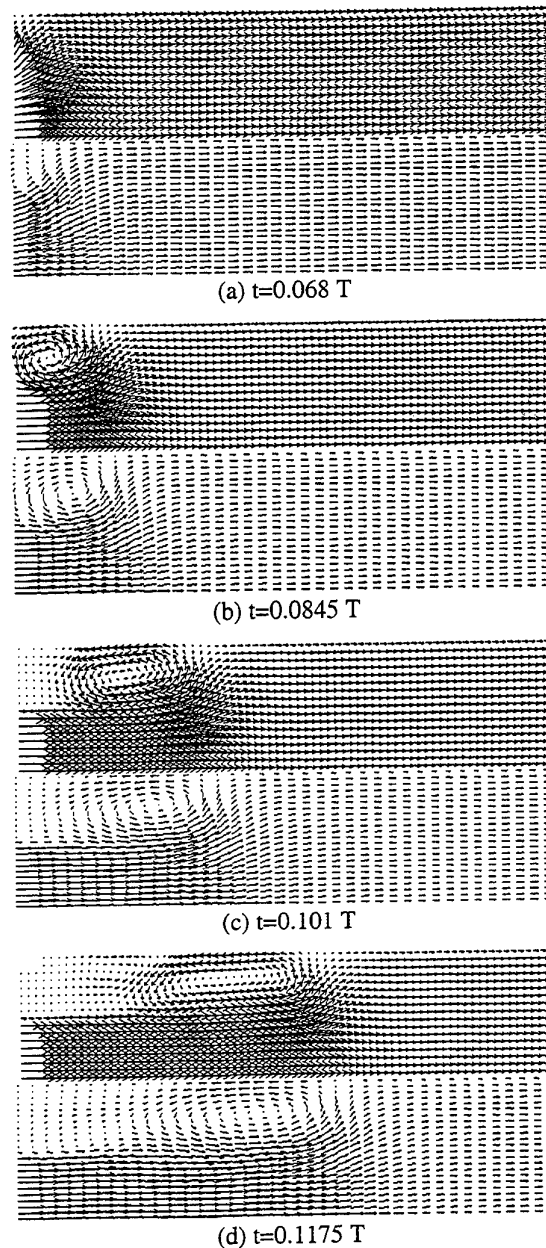


Fig. 3 Measured phase average velocity fields (upper), compared to instantaneous simulated fields (lower), at early accelerating phase.

ments, whereas the simulated fields are instantaneous. Note that the streamwise resolution of the simulated flow is lower. The starting flow is characterized by a uniform flow ahead of a jet flow progressing from the constriction. In Fig. 3b, a vortex has formed in the jet shear layer. This main vortex moves downstream at a similar speed to the jet front. Due to interaction with the pipe wall, the main vortex is stretched while

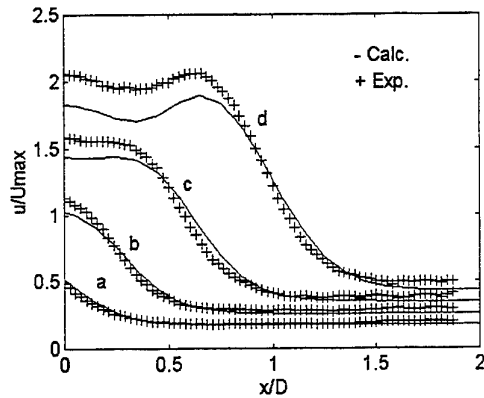


Fig. 4 Streamwise velocity component along center-line for the same cases as in Fig. 3.

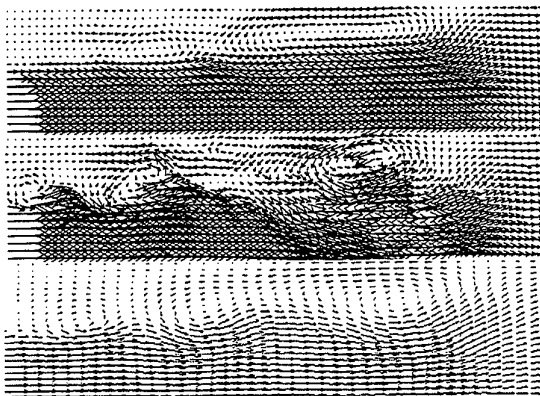
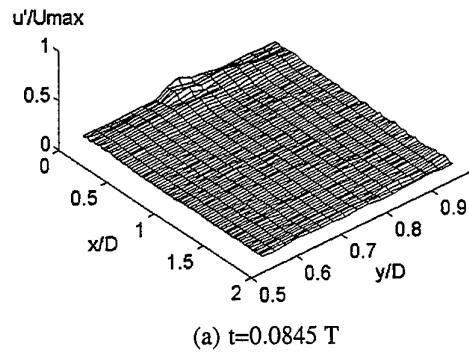


Fig. 5 Velocity field at $t=0.134 T$. Measured phase average (upper), measured instantaneous (middle) and simulated instantaneous (lower).

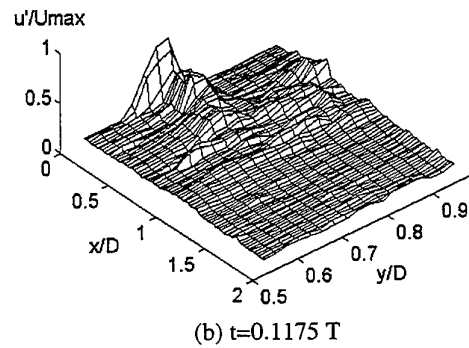
progressing downstream. In Fig. 3d, additional vortices have formed behind the main vortex.

The overall agreement between measurements and computations in Fig. 3 is good. This is further quantified in Fig. 4, where the center-line velocities are shown for the same data as in Fig. 3. The computed values in the jet core are about 10 % lower than the measured. This can be explained by a contraction effect of the real flow in the throat of the constriction. The simulated flow did not show any contraction, as it was started just downstream of the leading edge of the throat. Note that the local increase in the jet core velocity, seen in Fig. 4 around $x=0.7D$ for curve d, is caused by the contraction effect of the main vortex.

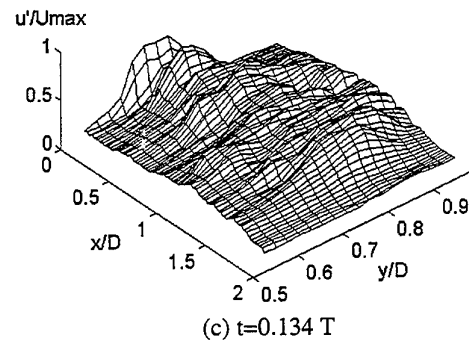
After $t=0.12T$ the difference between instantaneous and phase averaged velocities becomes larger. Figure 5 shows measured phase averaged and instantaneous velocity fields compared to simulated data at



(a) $t=0.0845 T$



(b) $t=0.1175 T$



(c) $t=0.134 T$

Fig. 6 Fluctuating streamwise velocity at three instants of accelerating phase

$t=0.134T$. The mean field was computed from $N=30$ measurements. The real instantaneous flow is more disordered than the simulated, which may be explained by a higher upstream disturbance level in the real flow.

The streamwise velocity fluctuations at three instants up to $t=0.134T$ are shown in Fig. 6. The fluctuations are at first high mainly in the shear layer immediately after the constriction, Figs. 6a and 6b. In part these high fluctuations can be explained by the insufficient PIV resolution of the thin jet shear layer. Depending on the instantaneous tracer particle distribution in an interrogation area in the shear layer, the highest correlation peak may correspond to either a

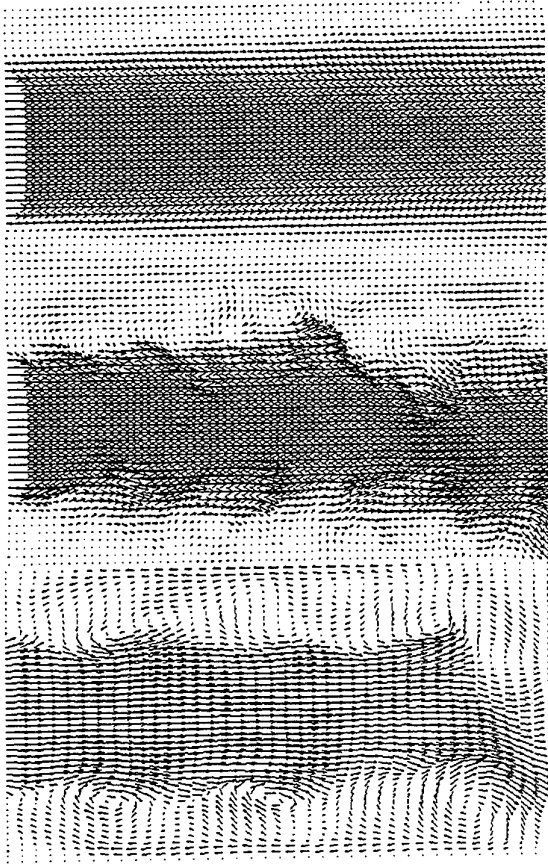


Fig. 7 Velocity field at $t=0.24 T$. Measured phase average (upper), measured instantaneous (middle) and simulated instantaneous (lower).

high or a low velocity, which gives large fluctuations. At $t=0.134T$, Fig 6c, the velocity fluctuations are more evenly spread over the flow field, but still they are small in the jet core.

Transition to turbulence evolves differently in the measured flow field and in the simulated. In the measured field, the breakdown to turbulence is more rapid, most likely due to a higher upstream disturbance level. In the simulations, transition to turbulence occurs close to peak flow by the breakdown of axisymmetric and helical structures. This transition is preceded by a continuous increase of the streamwise vorticity. Cohen and Wygnanski (1987) investigated the evolution of instabilities in a steady axisymmetric jet. They showed that close to the jet inlet, a large range of modes are amplified, which suggests a high sensitivity of the present flow to disturbances from the throat.

3.2 Peak and decelerating phase

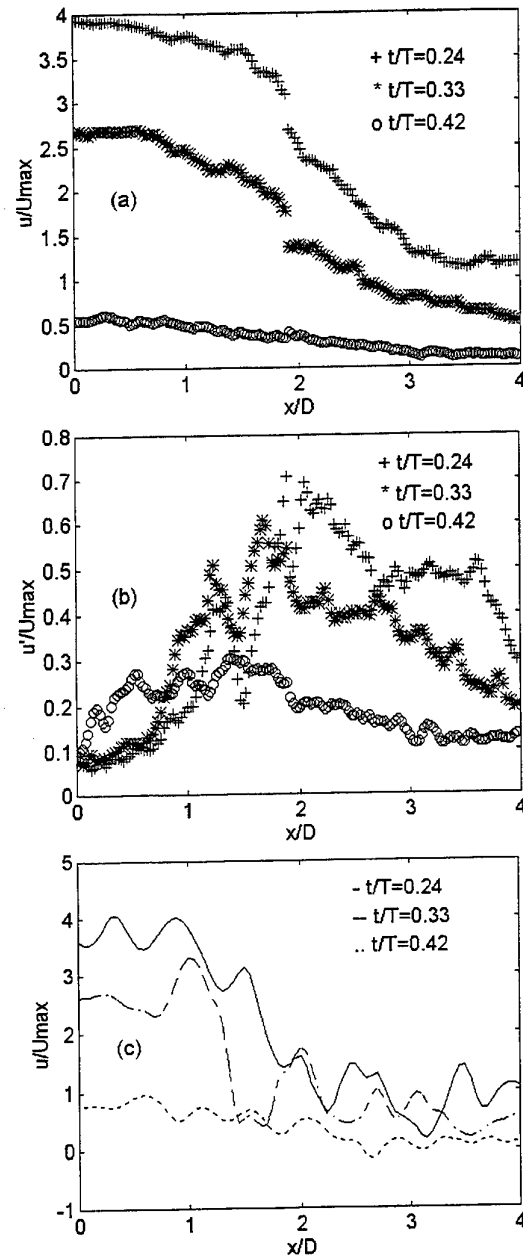


Fig. 8 Data of streamwise velocity component along center-line at three instants of decelerating phase. (a) Measured phase average. (b) Measured rms. (c) Instantaneous data from simulation.

We now turn to the turbulent peak flow and two subsequent instants during the decelerating phase. Figure 7 shows the measured phase-averaged velocity field, obtained from $N=30$ samples, and measured and computed instantaneous fields at peak flow rate. Large scale vortices with similar wave lengths are

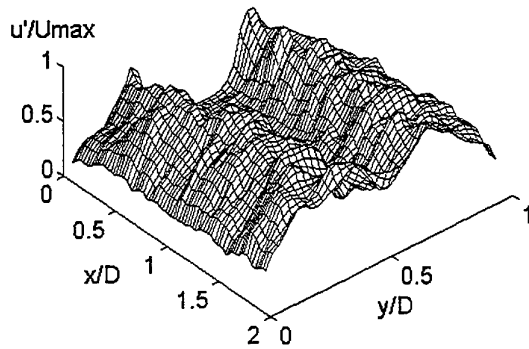


Fig. 9 Fluctuating streamwise velocity at $t=0.24 T$.

present in both the measured and simulated instantaneous velocity fields. Analysing the frequency content of the simulated axial velocity at a point on the center-line, $0.5 D$ downstream of the constriction, reveals two peaks in the frequency spectrum corresponding to the Strouhal numbers 0.22 and 0.44 (based on the frequency $f=1/T$, peak axial velocity and throat diameter). The most amplified frequency in a free circular jet corresponds to a Strouhal number of 0.3 , Crow and Champagne (1970).

Figures 8a and 8b show the measured phase averaged and fluctuating streamwise velocity along the center-line for peak flow and two later instants. The most striking feature is the rapid decay of the streamwise velocity around two diameters downstream of the constriction, for the two highest flow rates. This is also the location where the velocity fluctuations reach a maximum. The discontinuities in Fig. 8a are because the data upstream and downstream of $x=2D$ were acquired at different times, with a camera movement in between, so the phase averages were not computed from the same set of instantaneous data. For $N=30$ measurements the uncertainty in the mean for peak flow at $x=2D$ may be estimated using the rms data to around $0.25U_{\max}$. Additional error is due to misalignment of the two measurement regions. The instantaneous simulated axial velocity component along the center-line is shown in Fig. 8c for comparison. A rapid decay of the axial velocity around $x=2D$ is obtained in the simulations as well. Lieber and Giddens (1990) made similar observations for a flow with $Re_{\max}=1000$, $\alpha=5.3$, and a constriction with a cross-sectional area reduction of 90% . In their measurements the place with rapid decrease of the center-line velocity, and high fluctuation level was located approximately 5 to 6 diameters downstream.

Figure 9 shows the rms data of the velocity at peak systole. The fluctuation level is high in the jet shear layer, and increases somewhat downstream. The

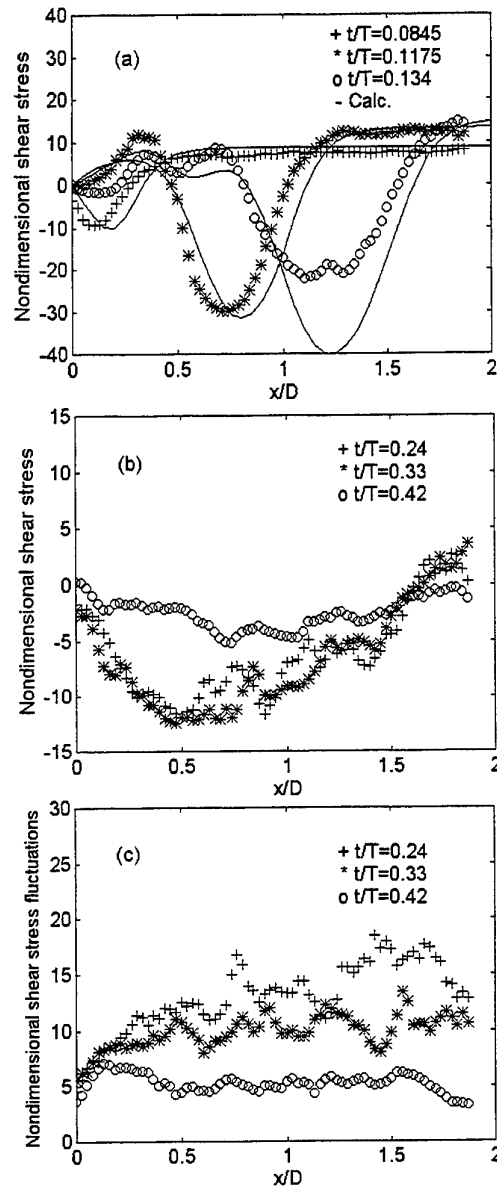


Fig. 10 Phase-averaged first-order estimate of non-dimensional wall shear stress $(D/U_{\max})\partial u/\partial y$.

(a) Three instants at early systole with comparison to instantaneous data from simulation. (b) Three instants at peak and decelerating phase. (c) Rms data for the same cases as in diagram (b).

relatively undisturbed jet core region is clearly visible.

3.3 Wall shear stress estimates

Figure 10a shows the variation of shear stress at three different instants during the starting phase. As a result of the movement of the main vortex, the wall

region experiences large spatial and temporal velocity gradients during this part of the cycle. The simulated wall shear has a similar amplitude as the measured shear, albeit a small shift in phase. Figure 10b shows the phase averaged shear stress at peak flow and two subsequent instants in the decelerating phase. The mean shear stress is negative in a region extending approximately 1.5 D downstream of the constriction. The magnitude of the phase averaged values is lower than the peak values in the starting phase, but as shown in Fig. 10c the fluctuation level is high. Especially around the reattachment point the fluctuations are much higher than the phase averaged values.

According to Lieber and Giddens (1990), arteries of several species, including man, tend to adjust their diameters permanently such that the mean wall shear stress is in the range of 1-2 N/m². They also suggest that intimal thickening in the neighbourhood of a constriction in the aorta requires that the wall shear stress must be low throughout the cycle. Not only in the mean sense, but also for the instantaneous field. Their suggestion is based on an animal study on monkeys where it has been shown that intimal thickening downstream of a constriction in the animal's aorta correlates better with the absolute value of pulsatile shear stress than the mean value. If one scales our results with a blood viscosity of 4·10⁻³ kg/sm, a velocity of 1.52 m/s and a diameter of 21.7 mm, one finds that only in the very immediate region behind the constriction, the shear stress is lower than 1 N/m² throughout the cycle. This implies that intimal thickening will not progress downstream of the constriction for the present flow conditions and geometry.

ACKNOWLEDGEMENTS

Financial support by TFR, the Swedish Research Council for Engineering Sciences, is greatly acknowledged.

REFERENCES

- Ahmed, S.A. & Giddens, D.P. 1984, Pulsatile Post-Stenotic Flow Studies with Laser Doppler Anemometry, J. Biomech., vol. 17, pp. 695-705.
- Cohen, J. & Wygnanski, I. 1987, The Evolution of Instabilities in the Axisymmetric Jet. Part 1. The Linear Growth of Disturbances Near the Nozzle, J. Fluid Mech., vol. 176, pp. 191-219.
- Crow, S.C. & Champagne, F.H. 1970, Orderly Structure in Jet Turbulence, J. Fluid Mech., vol. 48, pp. 547-591.
- De Paola, N., Gimbrone Jr., M.A., Davies, P.F. & Dewey Jr., C.F. 1992, Vascular Endothelium Responds to Fluid Shear Stress Gradients, Arteriosclerosis and Thrombosis, vol. 12, pp. 1254-1257.
- Ku, D.N. 1997, Blood Flow in Arteries, Annu. Rev. Fluid Mech., vol. 29, pp. 399-434.
- Ku, D.N., Giddens, D.P., Zarins, C.K. & Glagov, S. 1985, Pulsatile Flow and Atherosclerosis in the Human Carotid Bifurcation. Positive Correlation Between Plaque Location and Low and Oscillating Shear Stress, Arteriosclerosis, vol. 5, pp. 293-302.
- Lieber, B.P. & Giddens, D.P. 1990, Post-Stenotic Core Flow Behaviour in Pulsatile Flow and its Effects on Wall Shear Stress, J. Biomech., vol. 23, pp. 597-605.
- Moffat, R.J. 1988, Describing the Uncertainties in Experimental Results, Experimental Thermal Fluid Sci., vol. 1, pp. 3-17.
- Pritchard, W.F., Davies, P.F., Derafshi, Z., Polacek, D.P., Tsao, R., Dull, R.O., Jones, S.A. & Giddens, D.P. 1995, Effects of Wall Shear Stress and Fluid Recirculation on the Localization of Circulating Monocytes in a Three-Dimensional Flow Model, J. Biomech., vol. 28, pp. 1459-1469.
- Ojha, M., Cobbold, R.S.C., Johnston, K.W. & Hummel, R.L. 1989, Pulsatile Flow through Constricted Tubes: An Experimental Investigation using Photochromic Tracer Methods, J. Fluid Mech., vol. 203, pp. 173-197.
- Siouffi, M., Pelissier, R., Farahifar, D. & Rieu, R. 1984, The Effect of Unsteadiness on the Flow through Stenoses and Bifurcations, J. Biomech., vol. 17, pp. 299-315.
- Westerweel, J., Draad, A.A., van der Hoeven, J.G.Th. & van Oord, J. 1996, Measurement of Fully-Developed Turbulent Pipe Flow with Digital Particle Image Velocimetry, Experiments in Fluids, vol. 20, pp.165-177.

STEADY AND UNSTEADY LDV AND PIV INVESTIGATIONS OF FLOW WITHIN 2D LUNG BIFURCATIONS MODEL

A. Ramuzat, S. Day & M.L. Riethmuller

Environmental and Applied Fluid Dynamics Department
von Kármán Institute for Fluid Dynamics, Chaussée de Waterloo, 72
1640-B Rhode-St-Genèse, Belgium

ABSTRACT

The behavior of airflow through the lungs is largely affected by the characteristics of the flow field local to each bifurcation. Characterizing this flow field allows understanding, predicting and treating pulmonary diseases. This paper presents a current investigation of this flow through an in vitro model of multiple bifurcations. Steady and unsteady flow conditions have been investigated by means of the LDV and PIV measurement techniques. For the steady case, the comparison between LDV and PIV measurements shows a good agreement between velocity profiles at different stations. To simulate controlled periodic flows, a system of 4 pistons has been designed to control the flow at each outlet of the 4 branches. PIV measurements have been performed to understand the behavior of unsteady bifurcating flows and to evaluate a criterion for the quasi-steadiness of periodic flows. The evolution of the Womersley number α , parameter characterizing the behavior of unsteady flows in relation to the time dependent growth of boundary layers is presented. Moreover, a limit based on measurements of the development time after a suddenly reversed flow is also discussed.

1. INTRODUCTION

Chronic pulmonary illnesses are more and more frequent in our environment due to pollution effects or asthmatic problems. To identify the factors that may be contributing to breathing disturbances and to the contribution of the effect of pollution on the alterations in breath patterns, a better understanding of the human pulmonary system is needed. As a result, fields to be investigated are mostly flows in lungs under high breathing frequency and aerosol deposition in lung bifurcations under unsteady conditions. Moreover, the respiration pattern has to be better understood and investigated to have the possibility to determine the

appropriate therapy as most of the medical treatments are based on aerosol deposition in the bronchial tree.

This task is by no means a simple one since the lung is a complex network of successive bifurcations. The airways, from the trachea to the alveolar zone, divide by dichotomy and become shorter and narrower as they penetrate deeper into the lung. As a result, in vivo investigations of pulmonary flows are not possible, and in vitro experiments have to be performed in models. During the study of Corieri (1994), a complete modeling of the flow in a three dimensional single bifurcation has been made. As a result of this study, it has been shown that the first bifurcation influences the flow in the second and in the third bifurcation when the length of the second bifurcation is not long enough. To extend the investigations to a system of three generations, the choice of the pulmonary zone to be studied is the laminar flow zone. To study the complex flows, a 2D model of multiple bifurcations has been designed. Steady and unsteady flows have been investigated through this model using LDV and PIV techniques. The experimental facility will first be described. Then the measurement techniques will be presented, and results for steady and unsteady flows will be discussed.

2. EXPERIMENTAL MODEL

The experimental model represents two-dimensional multiple symmetrical bifurcations. It has been designed following the description of Weibel (1963) concerning the lung geometry. The characteristic dimension such as the length to width branch ratio is equal to 3.27. The branching width ratio between two successive generations of bifurcations is equal to 0.8 and the angle of branching ($\theta = 70^\circ$) has been chosen following the dimensions of lung geometry described by Hammersley and Olson (1992) and also reported by Pedley (1977). The model has been built using rectangular tubes made of Plexiglas to allow the optical access. The model

therefore has a two dimensional geometry with the dimensions scaled up from the lung characteristics. The angles of the model are sharp.

A sketch of the facility is represented on figure 1. The set-up is composed of the bifurcation model. At the outlet of the four branches, four Venturi tubes allow the determination of the flow rate passing in each tube. Four pistons are placed after the Venturi tubes. The flow in the model is a gravity flow and the velocity can be controlled using four needle valves placed after the four pistons. A system of stagnation tanks and downstream overflow tanks allow the creation of a uniform steady flow. To avoid any unsteadiness caused by the interaction between branches, the un-coupling system of outlet tubes has been installed. A stagnation tank is placed at the top of the bifurcation to create a smoother entrance that leads to better-developed flow at the test section. Furthermore, an overflow tank maintains a uniform and adjustable downstream pressure. Typical dimensions of the facility are the following: the mother branch has a length of 96.0 cm and a width of 3.0 cm. The first daughter branches are 7.86 cm long and 2.4 cm wide. The second daughter branches are 15.36 cm long and 1.92 cm wide. The depth of the channels is constant throughout the entire facility and equal to 9.0 cm.

The piston system, located downstream of the test section but before the outlet tank, allows the creation of an unsteady flow through the bifurcation. In this way, the gravity flow principle will be conserved. In order to keep the four outlets independent of one another, it was necessary to use four separate pistons. The latter are mechanically fixed to one another so that the flow rate in each branch is the same. To adjust the mean and unsteady flows, ball valves are placed between the Venturi tubes and the pistons, and needle valves are also placed between the pistons and the outlet tank. Therefore, if, for example, the needle valves are completely closed, all the water moved by the pistons will be forced through the test section. In contrary, partially opened needle valves enables a steady flow only or a steady flow superimposed with an unsteady flow by adjusting the piston motion controlled by a stepper motor. A picture of the piston system is presented on figure 2.

The characteristic non-dimensional number of this study is the Reynolds number, based on the mean velocity in the parent branch and the width of the parent branch, given as:

$$Re = \frac{VD}{\nu} \quad (1)$$

where V is the average velocity of the 2D velocity profile in the parent branch, D is the branch diameter and ν is the fluid dynamic viscosity.

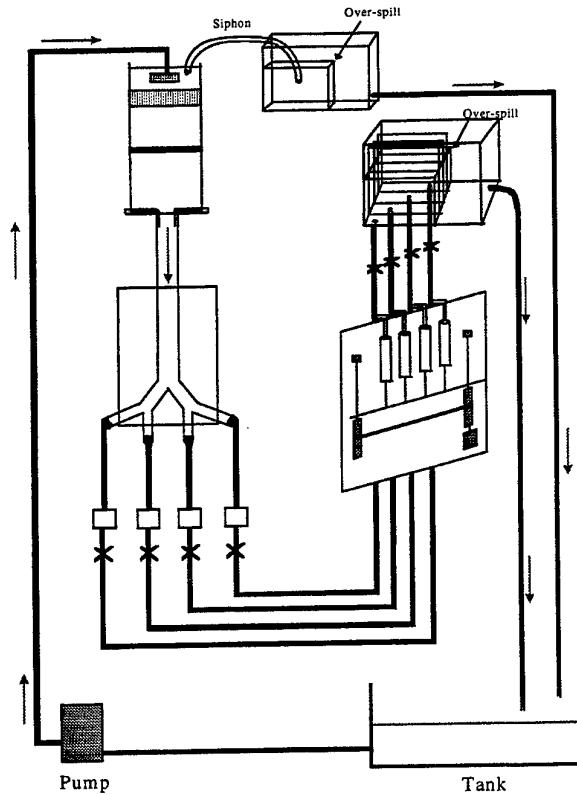


Figure 1: Sketch of the experimental facility

A range of Reynolds numbers from 200 to 800 can be obtained by adjusting the flow rate in the facility.

The Strouhal number is a second important parameter. It characterizes unsteady flows and is given as:

$$St = \frac{\omega L}{V} \quad (2)$$

where (V/ω) is proportional to the amplitude motion of a fluid particle during a sinusoidally varying flow rate at the angular frequency of oscillation ω , and L is a typical geometrical length.

The Womersley number, a quantification of the quasi-steadiness by comparing the thickness of the oscillating boundary layer with the thickness of the fully developed boundary layer ($d/2$ for internal flows), is given as:

$$\alpha = \frac{d}{2} \sqrt{\frac{\omega}{\nu}} \quad (3)$$

where d is the channel internal diameter

In the pulmonary physiology, the flow is considered quasi-steady in the laminar zone of the conductive part of respiratory tract. To consider the quasi-steady flow, the Strouhal and the Womersley numbers should both be less than 1.

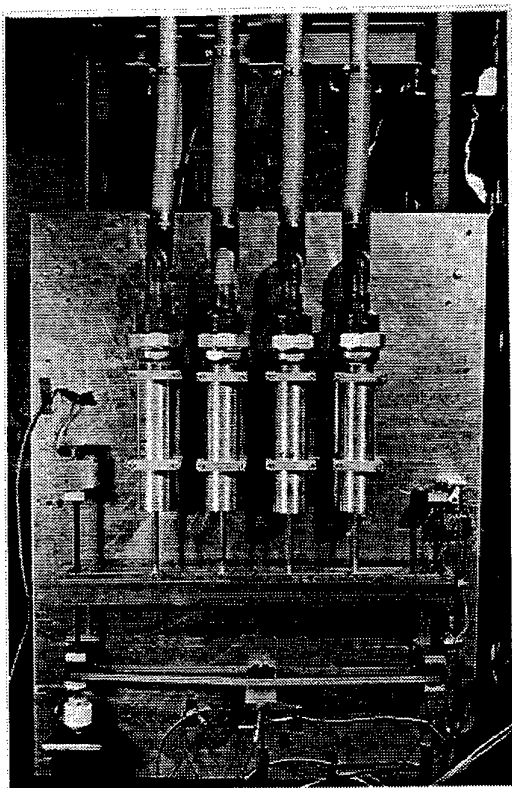


Figure 2: Picture of the piston system

3. EXPERIMENTAL DETAILS

3.1 LDV Measurements

For the steady approach of this investigation, Ramuzat (1996) has studied flows at Reynolds numbers between 300 and 800 with a 2D Laser Doppler Velocimetry technique. The LDV optical system used is a two-dimensional fiber optics TSI Laser Doppler Velocimeter with backscatter mode. The optical probe is of a special type: the beam diameter at input waist of the transmitting lens is 3.52 mm before focusing. The lens selected has a focal length of 360 mm. As a result, the probe diameter is 48.4 μm and the beam angle is 5.49°. The optical probe is mounted on a 3 axis traversing system that allows to automate the acquisition and measurement methods. This system allows programming the traverse as a function of the geometry of the model. Different positions in the model have been investigated.

3.2 PIV Measurements

The steady and unsteady flows within lung bifurcations have been experimentally investigated with the PIV technique by Day (1997). The PIV system used

to perform experiments in the model is sketched in figure 3. The system uses a continuous laser sheet formed by a cylindrical lens placed at the end of the fiber optic cable.

The camera's electronic shutter controls a short exposure of the video images. The video sensor is a Sony Hi-8 camera model type VX1E. This camera allows the adjustment of the aperture, shutter speed, and the gain. The typical settings for the measurements are an aperture of 1.6, shutter speed between 1/100 and 1/250 second and a gain set to the maximum of 18 dB. The particle images at this shutter speed truly appear as round particles instead of the streaks that are created at lower shutter speeds. A 5 W continuous argon (Ar) laser connected to a fiber optic cable attached to a cylindrical lens was used throughout the measurements. The main advantage of this system is that the laser sheet may be very easily located to measure in different planes through the facility.

3.3 Seeding Particles

The particles used for the PIV experiments are neutrally buoyant. These polyamide particles called Vestosint® are manufactured by Hüls GmbH Inc., Germany. Their average diameter is 10 μm and their density is 1.01 g/cm^3 . Figure 4 shows an example of the seeding particles. On this picture, the particles look all similar and spherical.

Since we have a low water speed and since the density of the particles is equal to that of the water, there is no doubt that the particles follow the flow without velocity lag. This was verified by calculating the response of these tracers to a velocity step.

4. RESULTS

4.1 Steady Flow

A comparison between LDV and PIV measurements is presented in figure 5. This comparison has been performed for the study of steady flows for a Reynolds number of about 300. Indeed, for higher Reynolds numbers, it has been shown in a previous study by Ramuzat et al. (1997) that the flow became unsteady and had an oscillatory character. This comparison could therefore only be possible for low Reynolds numbers.

For the acquisition of the LDV data, each point of the velocity profiles has been averaged with a minimum of 512 data points. In contrary, the PIV technique allows to get instantaneous information of the flow field. Comparisons need average velocity fields to be measured. This is done by ensemble averaging 15 PIV fields.

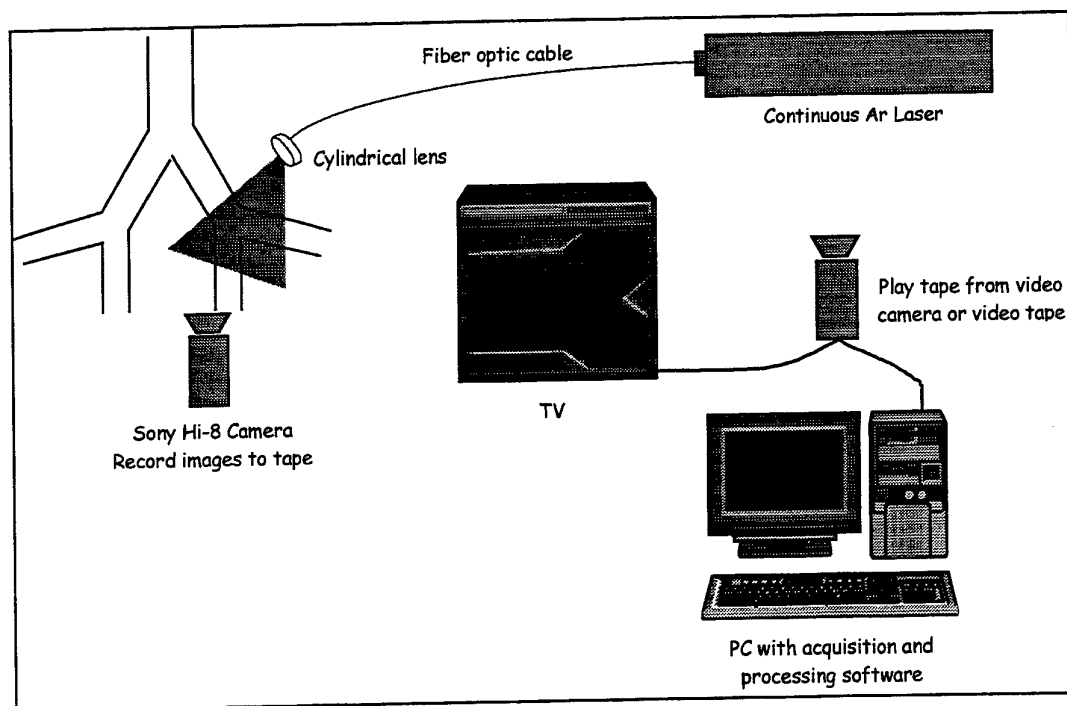


Figure 3: PIV set-up and picture acquisition system

As we are in steady flow condition, the comparison between LDV measurements and the average PIV field shows a good agreement between the 2 different methods for different stations within the bifurcation.

In figure 5, the different graphs present the velocity profiles at different stations. In the parent branch, at station 1 located 50 cm upstream of the first bifurcation, the velocity profile is Poiseuille like. LDV and PIV measurements are in good agreement.

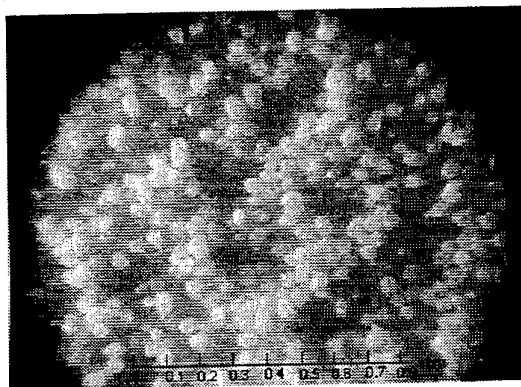


Figure 4: Example of seeding particles (Vestisint®)

Downstream of the first bifurcation, at station 2, the velocity profile shows a small recirculation zone close to the external wall of the bifurcation, and a velocity peak towards the internal wall of the divider. The PIV measurements show a slight discrepancy with the LDV

measurements at the level of the recirculation zone. This is due to the fact that the PIV velocity profile is averaged with a lower number of data than the LDV velocity profile. However, the shape of the two different profiles is very similar. The same remark can be made for stations 3 and 4, downstream of the second bifurcation. For station 3, the location of the maximum velocity is not at the same position on the two velocity profiles. This can be explained by the difficulty to reproduce experiments at the same exact location. At station 4, where acceleration and recirculation zone appear, the flow is more susceptible to unsteadiness.

The different results allow us to validate the LDV measurements already performed and the measurements performed with the PIV technique. The PIV measurements will now be discussed for the study of the unsteady flow within the double bifurcation.

4.2 Unsteady Flow

For unsteady flow, PIV obtains both spatial and temporal information. Unsteady measurements have been performed for two types of imposed unsteadiness. The first flow consists of a sudden flow reversal. A sudden reversal of flow means that the pistons used to create a periodic flow are driven at constant speed with a sudden change of direction. The period of the imposed unsteadiness is of 60 seconds.

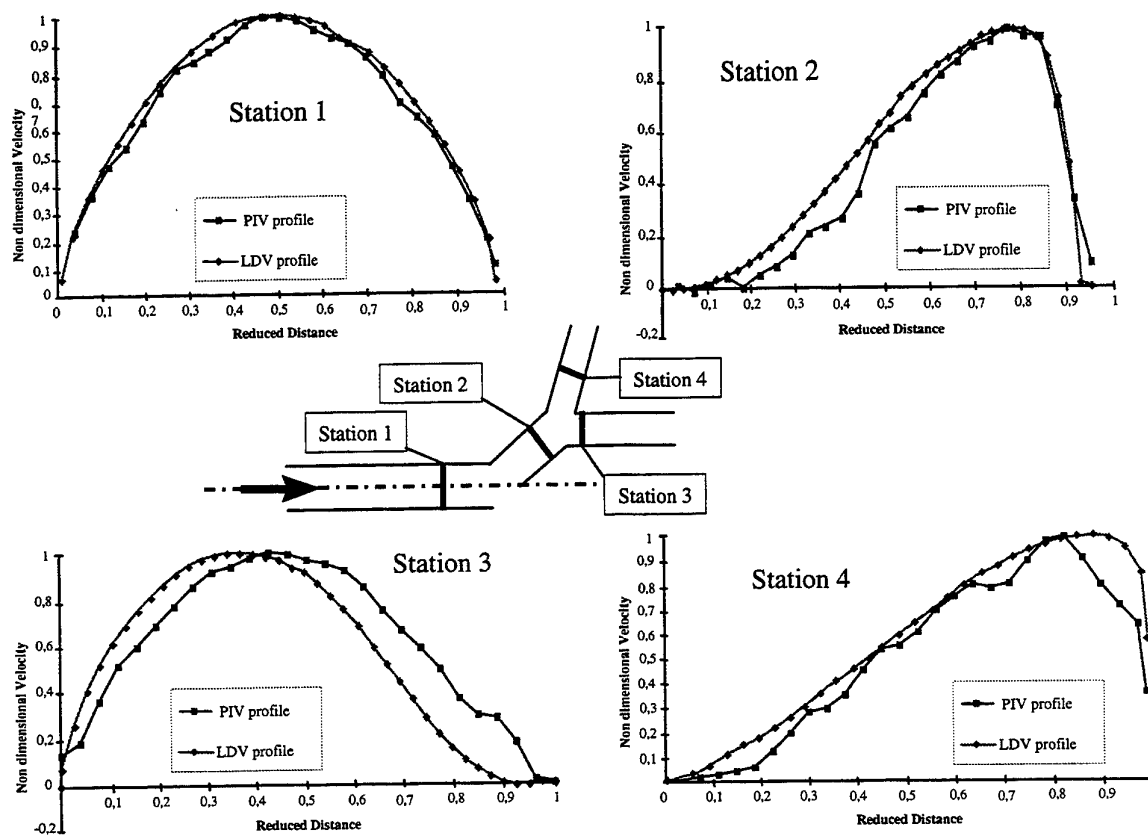


Figure 5: Comparison between LDV and PIV for steady flow

Figure 6 represents the evolution of the flow rate through the bifurcation, at the outlet of the four branches.

PIV measurements have been performed to study the evolution of the velocity flow fields with time. Figures 7 and 8 present the time series of the velocity fields at the level of the first and second bifurcation. The flow rate at the inlet is fixed to 100 l/hr, which corresponds to a Reynolds number of 420 based on the peak velocity of the unsteadiness in the parent branch. In these figures, inspiration is the direction of the flow from the left to the right, and expiration the other flow direction from the right to the left.

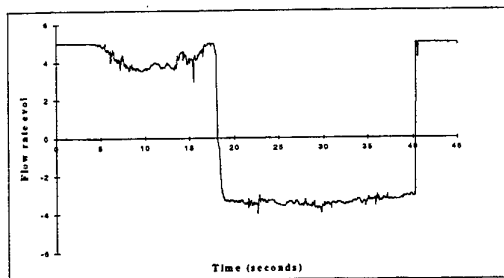


Figure 6: Flow rate :suddenly reversed flow

Figure 7 shows the evolution of the expiratory velocity profile with time, at the level of the first bifurcation just after reversal.

Unlike inspiratory flow, fully developed expiratory flow through symmetrical bifurcations is symmetrical. Three main phases may describe the development of expiratory flow after reversal.

Inspiratory flow (pre-phase to expiratory) in the model is characterized by a Poiseuille profile at the inlet of the bifurcation. The regions near the wall (low velocity prior to flow reversal) respond quickly to the pressure change caused by the sudden reversal of the motion of the pistons. The previously high velocity core requires a longer time to decelerate and then reverse direction due to its large momentum. Because of the conservation of volume, high velocity regions at both walls and a region of near zero velocity in the center of the bifurcation characterize the initial flow field after reversal. This is visible in the image taken 1 second after reversal.

The second stage of development is characterized by a filling of the velocity profile so that the difference of velocity at the walls and the center decreases until the velocity is nearly uniform across the section and similar

to a fully developed turbulent velocity profile. This filling is principally due to viscous interaction between the high velocity regions at the wall and the neighboring low velocity regions that act to increase the core velocity while smoothing the peak of the high velocity regions at the wall. Because the axes of the daughter and parent tubes are not aligned, the fluid entering the parent branch has a component of momentum towards the center of the parent branch. This effect plays a large role in determining the shape of the fully developed flow through a bifurcation as measured further upstream of the first branch. The effects of this momentum force moving fluid towards the center of the section together with the viscous forces in the parent branch and create a nearly flat velocity profile typical of the second stage of development. This stage is shown in the measurements at times near 11 seconds after reversal.

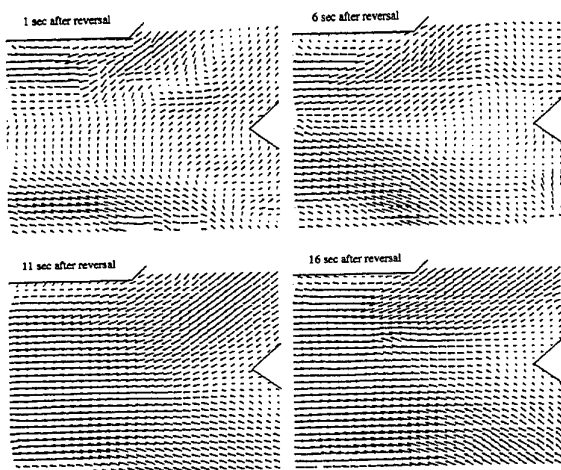


Figure 7: Expiration velocity flow field for $Re = 420$ at the level of the first bifurcation

The third stage of development is related to a boundary layer forming over the divider wall of the bifurcation. Initially after flow reversal, the boundary layer on the divider wall is very thin so that the flow entering the parent branch has a nearly uniform velocity distribution. After a period of time, boundary layers form over the walls of the daughter branch and act to decrease the velocity at both walls. This boundary layer forming over the divider wall joins together at the dividing point of the bifurcation to form a velocity depression in the profile. The velocity profile in stage three is characteristic of fully developed expiratory flow.

Figure 8 presents the time series of the flow at the level of the second bifurcation. The same phenomenon that acted to establish the expiratory flow acts for the inspiratory flow. Again, high velocity regions at the

walls characterize the flow immediately after reversal. Unlike the flow described above, the conditions before flow reversal are asymmetrical. The progression comes from viscous effects, which act to create a smoother profile across the section. At the same time, the pressure force has sufficient time to reverse all parts of the flow field so that the flow seems to be developing towards a Poiseuille profile.

Afterwards, the position of the maximum peak in the Poiseuille profile migrates towards the dividing wall and establishes itself at a distance that is characteristic of fully developed flow at the given Reynolds number. This effect is similar to the effects described for expiratory flows. The momentum of the entering fluid acts to move the fluid towards the dividing wall. In this case, the development of the boundary layer in the upstream section also plays a large role on positioning this high velocity point.

The simultaneous development of the boundary layer on this divider wall acts to keep the point of maximum velocity at a finite distance from the inner wall. In this region, the boundary layer growth and modification of the inlet flow occur in a way that the migration of the high velocity region is always in the same direction. It continually moves from the center towards the divider wall until relaxing in the position for fully developed flow.

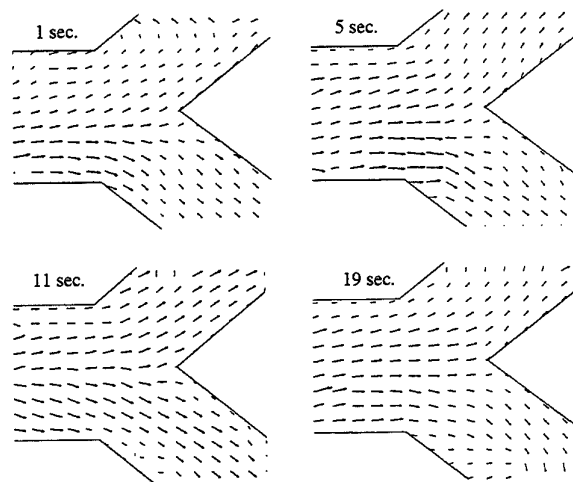


Figure 8: Inspiration velocity flow field for $Re = 420$ at the level of the second bifurcation

Figure 9 presents this evolution of the PIV instantaneous velocity profiles. This figure shows the fully developed PIV velocity profile measured at steady condition and two PIV velocity profiles measured after sudden reversal.

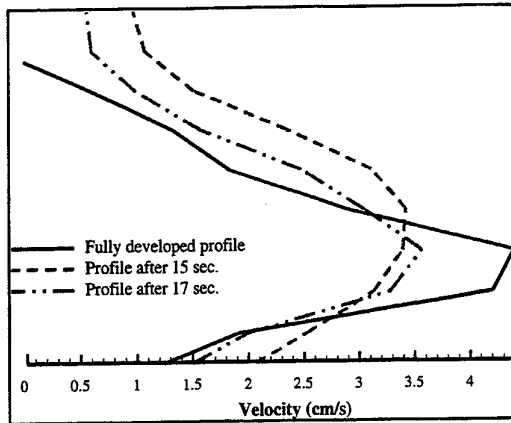


Figure 9: Velocity profiles after sudden reversal at $Re = 750$, upstream of the 2nd bifurcation, at station 2

In all the time series of velocity profiles, there is a clear evolution of the velocity profile that results in an established profile with a maximum velocity located next to the divider wall. The distance between the divider wall and the point of maximum velocity is perhaps the main characteristic of the velocity profile.

Figures 10, 11 and 12 present the comparison for three different locations between the steady LDV measurements and the PIV profiles obtained at different moments after reversal. These three graphs allow the determination of the development time for the velocity after reversal.

To determine the quasi steadiness of the flow, a method based on the time development of the velocity has been developed and used by Day (1997). This method compares the shape of the last velocity profile before reversing to the LDV velocity profile obtained in the steady study. From this comparison, it is possible to determine a Womersley number based on the time development of the flow.

The Womersley criterion that is very often used when justifying the assumption of quasi steadiness is based on the growth of the boundary layer after a fluid is instantaneously put into motion. The frequency term $\sqrt{\frac{v}{\omega}}$ of the Womersley number is derived from the evaluation of boundary layer thickness as a function of time. The boundary layer thickness is given as:

$$\delta \approx \sqrt{\nu t} \approx \sqrt{\frac{\nu}{\omega}} \quad (4)$$

According to (4) the thickness of the boundary layer is not a function of the mean flow velocity. For lack of any better relation between the suddenly reversed and the sinusoidal case, we will use the relation $f = 1/2t$. In this way, the frequency corresponds to a wave with a period equal to exactly two times the development time.

A Womersley number of 1 calculated in this way predicts that a square wave flow will re-establish itself in each flow direction exactly before changing direction again.

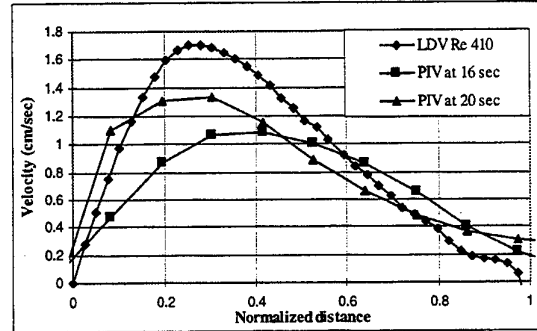


Figure 10: PIV and steady LDV profiles at station 2

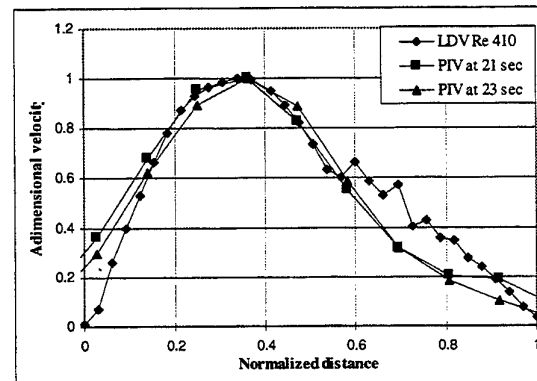


Figure 11: PIV and steady LDV profiles at station 3

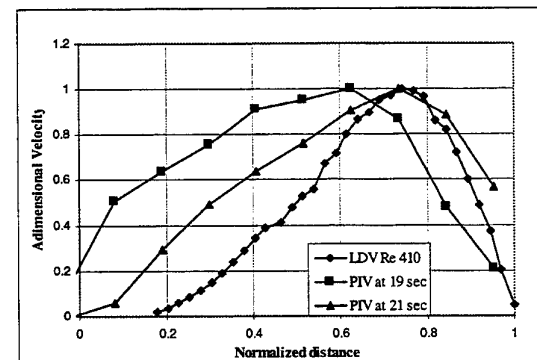


Figure 12: PIV and steady LDV profiles at station 4

As applied to a sinusoidal wave, this implies that the flow will remain quasi-steady as the flow rate changes from positive maximum to negative maximum during a time period equal to that of the development time.

In order to maintain consistency with the traditional Womersley number, the relation $f = 1/2t$ was simply

substituted into the equation for the Wommersley number so that

$$\omega = 2\pi f = \frac{\pi}{t} \quad (5)$$

where t is the development time of the suddenly reversed flow.

Using this approach, the Wommersley number was calculated for sudden reversal unsteadiness of different amplitudes for different Re , at a period of 60 seconds. The data obtained suggest that the time dependent behavior of the unsteady flow is not function of the Reynolds number. This is in agreement with the definition of the Wommersley number (equation (3)). Nevertheless, these results imply that the value of the Wommersley number used as a criterion for the quasi steadiness should be greater than 1. Taking into account the exact solution for the boundary layer development of a suddenly started uniform flow over an infinite plate, the criterion has been estimated to a limit value of 5. In order to neglect the unsteady effects of the flow, the Wommersley number should be significantly less than this limit.

To estimate the applicability of this criterion, a second imposed unsteady flow has been investigated. This second controlled unsteadiness is a sinusoidal variation of the flow rate around a zero mean value.

For a constant period of 60 seconds, and a Reynolds number range from 250 to 600, the Wommersley number was found constant and equal to 3.8.

For the same amplitude signal, i.e. for a Reynolds number around 400, the period has been varied between 30 to 60 seconds. The evolution of the Wommersley number is presented in figure 13 as a function of the period of the sinusoidally varying flow rate.

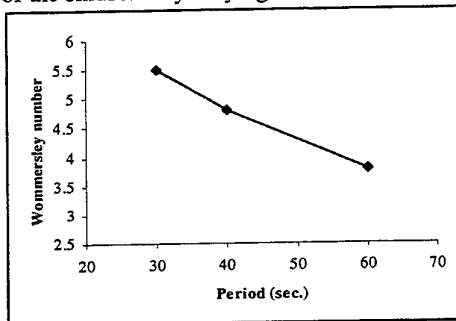


Figure 13: Wommersley number vs. period

Figure 13 shows that when the period is increasing, the Wommersley is decreasing. For α less than 5, the flow has been found quasi-steady over the high forward flow rate part of the cycle, nevertheless it exhibits an unsteady behavior near the reversal forward to reversed flow. This unsteadiness could be due to three-dimensional effects of the flow.

5. CONCLUSIONS

A comparison between LDV and PIV measurement for steady flow shows a good agreement between the different velocity profiles at different stations within the 2D multiple bifurcation.

For the unsteady case, PIV measurements have been performed. The evolution of the flow could now be better investigated and a first study with a "square" unsteadiness allows to conclude about the quasi steadiness of the flow. For a Wommersley number α based on the time development of the flow, it has been shown that the flow is quasi steady for $\alpha < 5$.

Nevertheless, as different types of unsteadiness can be applied to the model, a more complete approach should next be undertaken. Moreover, the natural unsteadiness of the flow that appears for high Reynolds number should also be investigated when an imposed unsteadiness is applied to the model. The problem could be coupled with the forced unsteadiness, or completely eliminated.

We also can conclude that sinusoidally varying flow through the bifurcation behaves differently than the instantaneously reversed flow used above, but its development time is relevant to the quasi-steady assumption for sinusoidally varying flows.

REFERENCES

- Corieri, P. 1994, Experimental and numerical investigation of flows in bifurcations within lungs airways, Ph. D. Thesis, Université Libre de Bruxelles.
- Day, S. 1997, Experimental investigation of the unsteady flow through multiple lung bifurcations, VKI PR 1997-15.
- Hammersley, J. and Olson, D. 1992, Physical models of the smaller pulmonary airways, J. Appl. Physiol., 72 (6), pp. 2402-2414.
- Pedley, T.J. 1977, Pulmonary fluid dynamics, Ann. Rev. Fluid Mech., 9, pp.229-274.
- Ramuzat, A. 1996, Experimental investigation of flows within 2D bifurcations, VKI PR 1996-22.
- Ramuzat, A., Angelucci, L. & Riethmuller, M.L. 1997, Particle Image Velocimetry with a Bragg cell as optical shutter. Proc. 17th ICIASF, Monterey.
- Weibel, E. 1963, Morphometry of the human lung, Academic Press, pp. 110-148, New York.

SPECTRAL AND INSTANTANEOUS FLOW CHARACTERISTICS OF VASCULAR JUNCTIONS USING CONTINUOUS DPIV

Ygael Grad and Shmuel Einav

Department of Biomedical Engineering, Tel-Aviv University, Ramat Aviv, Tel-Aviv 69978, Israel.

ABSTRACT

Continuous Digital Particle Image Velocimetry (CDPIV) was used to map the flow field of vascular junctions and obtain the anastomoses spectral signature. This was done due to the fact that a significant percentage of implanted vascular bypass grafts fail early post surgery. Biofluid factors such as abnormal shear stresses and turbulence have been cited to promote graft failure. Previous studies were based on mean flow properties, while the pulsating flow field is affected by instantaneous and spectral distribution. Laminar to turbulent transition, flow separation, rotation and waves reflected from host artery leave characteristic spectral signature which escapes detection when only mean data is sampled. Our work was aimed into the time and frequency domain characteristics. Our in-vitro model consists of pulsating pump, transparent distensible graft tubes and variable anastomoses angles. Dimensions were based on in-vivo data. Continuous sequences of experimental images, followed by their calculated velocity and vorticity transient fields, are given as animated presentation of distensible anastomoses. High shear stress peaks and vortices were observed at the anastomosis toe. Flow reversal or separation was Womersley parameter dependent. The flow profile and spectra were dependent on graft angle and elasticity. Better host-graft match resulted in less flow disturbances and flatter spectral distribution. This can be translated in Doppler ultrasound or sound frequencies terms and thus potentially assist clinical observations.

1. INTRODUCTION

Hemodynamics has long been cited of being involved in arterial diseases. Atherosclerosis is the most prevalent vascular disease in the human circulatory system. In its advanced stages plaques can completely occlude the vessel, preventing perfusion of tissue distal to the blockage. When treatment modalities such as pharmacological interventions and angioplasty fail, or in other forms of vascular injury, replacing the diseased segment with a vascular graft is a common therapy available today. Even though replacement of large vessels has been reasonably successful, problems with loss of patency within several months after implantation is more acute with medium and small vascular graft replacements (diameters less than 6 mm). Loss of patency due to advanced stages of intimal thickening results in failure of about 40% of the grafts within five years after implantation. Thrombosis is primarily responsible for failures within 30 days after implantation, and intimal hyperplasia for failures within 6 months post surgery. A number of studies indicate that alterations in mechanical stresses due to the implants may be the causative factors in the intimal thickening. These stresses may include alterations in static deformations, static stresses, pulsatile deformations and stresses, as well as altered shear stress at the blood-intimal boundary. These alterations are induced by the changes in material properties between the host artery and vascular graft, the presence of suture at the anastomotic site, as well as the geometry of the anastomosis. For optimal functioning the implanted graft should have the same dynamic response to pulsatile flow as a natural artery.

An important measure of flow characteristics under pulsatile flow is the impedance of the vascular segment, consisting of resistance, inertance or inductance, and compliance. For a replacement graft of the same size as the diseased artery, mismatches in compliance may be the most important factor in the failure of the graft.

End-to-side anastomosis (Fig. 1) is common particularly in vascular reconstruction of occluded coronary vessels. The graft is attached to the host artery distal to the occlusion in order to enable perfusion of the vascular bed downstream from the occlusion (blood flowing from the graft through the host artery). At the proximal end, blood will flow from the host artery to the graft, branching out at the site. Differences can be expected between the proximal and the distal anastomosis. Clinical results with this configuration demonstrate that the preferred locations of intimal hyperplasia are in the toe region of the anastomosis, as well as along the outer wall in the region where the inlet stream from the bypass graft impacts against the vessel wall. In end-to-side anastomoses, the geometry of the anastomosis (in particular the anastomotic angle) may be a more important factor in the flow characteristics, rather than the mismatch in elastic properties between the graft and the host artery.

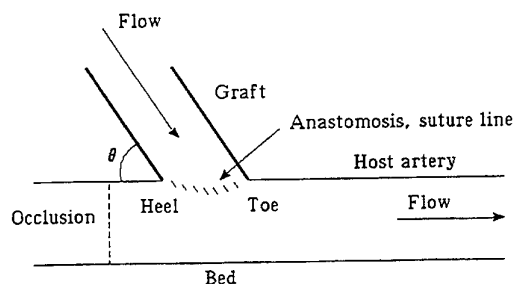


Fig. 1, Distal End-to-side anastomosis

Theoretical and in vitro experimental studies are therefore aimed to investigate the mechanical factors responsible for the failure of these grafts. However, disagreement between results may be attributed to differences in the gross boundary conditions and experimental setup, such as; 2D vs. 3D geometry, steady state vs. pulsating flow waveform, rigid vs. compliant walls, but also to the fine details of each condition.

The anastomosis has a stenotic effect, which depends on the geometry and method of vascular reconstruction. Even the finest suture line alters the original flow field, the new hood line changes the intima's surface, which is seen as an obstacle by the blood flow. This leads to thrombus formation or even

aneurysm in end-to-side and end-to-end anastomoses made of homo or artificial grafts. It is therefore suggested that tools sensitive to the waves reflected from the altered (anastomosed) surface should be introduced. Most of the works done so far lack at least one of the above mentioned criteria. There are no studies which have focused on the instantaneous time domain in such hemodynamic configuration nor provided its detailed spectral analysis. This is mainly due to experimental difficulties with conventional measurement systems. The general objective of the newly introduced CDPIV system is to solve the experimental difficulty. Therefore, special emphasis will be given to obtaining a thorough investigation of the flow field time domain instantaneous characteristics and its spectral analysis. For that purpose, a DPIV system was elaborated to operate continuously in real-time and used to map the fine structures of the boundary layers at the anastomosed area. Unlike most systems, which are based on moving one measurement volume from point to point, the CDPIV enables whole-field time-dependent flow analysis, at any given cross section, at the same instance. The continuous system is based on the DPIV, which is a modified non-intrusive technique that permits the mapping of instantaneous flow-fields. Gharib et al., 1991, has demonstrated the strength of DPIV by capturing, viewing and processing flow images of vortex rings. The seeding density, illumination and the other experimental parameters could be modified. Spatial velocity measurements were successfully compared with data obtained by direct measurement and the velocity data was used to compute the spatial and temporal vorticity and circulation.

Spectral analysis is an excellent mapping tool. If we take, for example, an elastic graft anastomosed to a rigid tube, then the spectral analysis of the velocity time data will reveal the frequencies of the waves reflected back from the bed of the rigid host artery. If we change the elasticity parameters of the host artery, then the typical characteristic frequencies will move along the frequency axis, representing the new material, dependent harmonics. By selectively changing the stiffness parameters of the graft, while keeping the other flow and model parameters unchanged, a relation between the anastomosis compliance match (or mismatch) and the behavior of its typical spectrum will possibly appear. This signature is important, because it can be used vice versa to identify changes, like intimal hyperplasia, in the state of the anastomosis vessels. The spectral analysis can give a better understanding of flow

behavior, energy transfer from larger to smaller scale eddies, and may imply the loci of deposits sites.

2. EXPERIMENTAL APPARATUS AND MEASUREMENT PROCEDURES

The experimental system is schematically described, in Fig. 2. A water-glycerin mixture, seeded with silver coated ($\phi=10\mu$) glass micro spheres, is pumped through a circuit of tubing to the vascular anastomoses model. The mixture satisfies both conditions of viscosity and refraction, index matching. An external reservoir head maintains chamber's pressure and temperature. Valves control the flow ratio between the graft and the host artery. An electronically controlled pulsating pump is used to produce the desired pulsating waveform. The flow direction can be reversed in order to sweep between distal to proximal anastomosis.

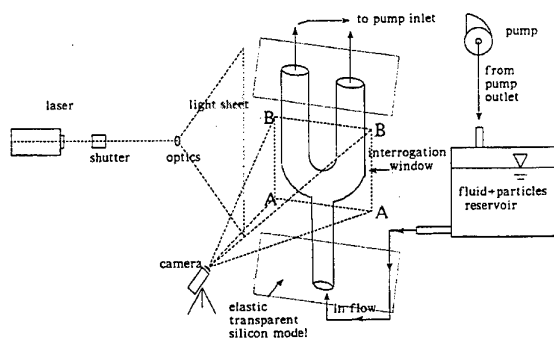


Fig. 2, The experimental setup

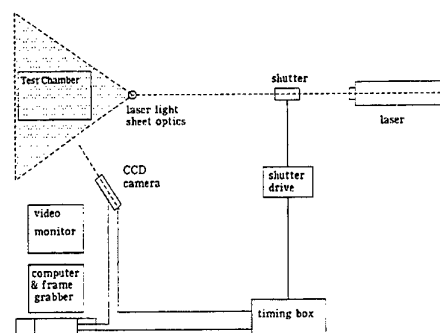


Fig. 3, The CDPIV system

An Argon-Ion, laser light sheet was used to illuminate a thin layer of reflecting particles inside the fluid. By strobing the laser sheet at the video camera's framing rate via a timing device (Fig. 3) and an

electronic shutter, corresponding sections of each two successive images were matched. The camera overlooking the interrogation window A-A-B-B (Fig. 2) at the bifurcation captured the particles' shift in the stream. The actual time step between images could be lower than 0.5ms. The timing values were experimentally selected to achieve optimal images, without smearing of the illuminating particles (the CDPIV is not a "push a button and get the result" system). Each successive image pair was cross-correlated and the velocity field was computed. CDPIV was used to record minutes-long sequences of cardiac cycles consisting of thousands of video frames. The particles were continuously filmed by NTSC (Pulnix TM-9701 29.97fps 8Bit grayscale 480x768) CCD video camera and simultaneously transferred to the computer. Real-time video hardware-compression combined with ultra-fast hard disks as storage device were used to overcome the well known data transfer-rate bottle-neck using conventional PC platform.

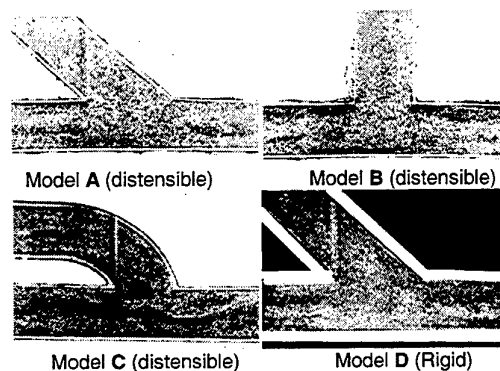


Fig. 4, The models

The models are described in Fig. 4. The vascular grafts were made of transparent elastic silicone models of human artificial anastomosis. Re and α (Womersley) dimensionless numbers were maintained at flow ranges and pulse rates, taken from in-vivo data. The models were scaled up, by a diameter factor of 3 to 15mm, to improve the spatial resolution. The mean velocity was scaled down by a factor of 3 and the pulsation frequency was scaled down by a factor of 9, thus improving the temporal resolution while keeping the Strouhal and Re ratio. The flow division at the bifurcation was always kept 50:50 for later comparison. Model A, shaped at 45 degrees, was used for the basic tests. First, a Reynolds number scan was performed at $Re=100, 200, 300, 400, 500$ while keeping the α number at the equivalent of 80 BPM. Then a "heart-rate" scan was performed by swapping α between (equivalents of) 60 and 100 BPM at

$Re=100, 300, 500$. The geometry effect was later tested, using models B (90-degree bifurcation) and C (curved bifurcation) at α (equivalents of) 60 and 80 BPM at $Re=300$. Finally, the wall stiffness effect was tested using the rigid model D, shaped identically as model A, at the same conditions (60, 80 BPM, $Re=300$) as models B and C.

It is very important to mention the sampling frequency. The CDPIV is capable of delivering 30 images per second, thus 15 flow fields can be sampled per second. However, the fact the Strouhal number dictated an experiment slower by a time factor of 9, enabled a sampling rate equivalent to 135 flow fields per second. This sampling rate covers most of the known hemodynamic phenomena.

The basic calibration test was performed under steady flow conditions. The flow rate, which was computed by integrating the velocity profiles obtained from the CDPIV process, was in close agreement (error $<3\%$) with the known flow rate of the pump.

3. EXPERIMENTAL RESULTS

3.1 The Instantaneous Flow

The velocity vector plot (Figs. 5) describes the particles shift in time, which was calculated between two typical sequential images captured in model A.

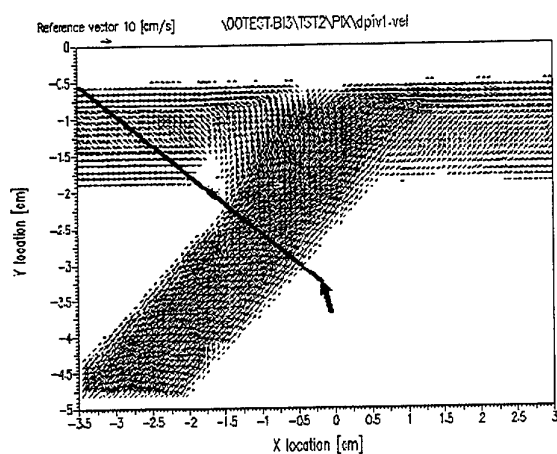


Fig. 5, Velocity vector plot

The axes describe the position and size [cm] of the model. The reference vector on the top left corner is provided to estimate each vector's velocity. The inlet is at the bottom left, where the velocity distribution is parabolic. Then the graft's core flow hits the vascular bed of the host artery, generating a stagnation zone. The right host side exhibits a high velocity narrow jet

near the vascular bed and low velocity near the toe. The left side exhibits flow separation near the heel. The skewed line describes the exact location of the velocity components' profiles cross section presented in the following figures. The good spatial resolution (110 pixels/cm) was achieved by scale up. Thus, each vector was calculated between two sequential rectangular windows of 16×16 pixels with overlapping of 8 pixels.

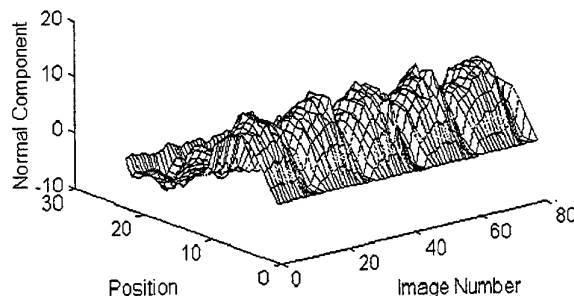


Fig. 6, Spatial-temporal velocity distribution, normal to the cross section in Fig. 5

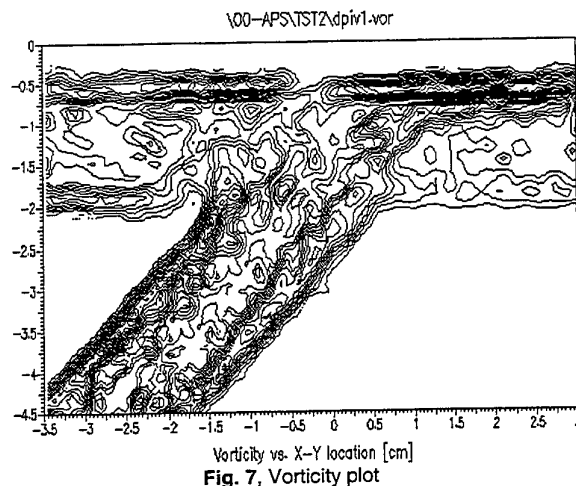


Fig. 7, Vorticity plot

Fig. 6 describes spatial and temporal distribution of the velocity component normal to the location described by the skewed line in Fig. 5. The normal component was calculated out of the velocity vector field. The vertical axis describes the normal velocity component amplitude [cm/sec]. The position axis describes the location described by the skewed line, where the arrow tip in Fig. 5 corresponds with the position axis origin. The time axis is represented by the image-number. It corresponds to the pulsating flow cross-section, as calculated from the DPIV images sampled continuously in time. A typical Poiseuille parabolic profile is exhibited as function of the position and the inclination of the skewed line,

relatively to the vessel diameter. The parabolic profile's velocity amplitude clearly follows the pulsating cycle in the graft, however, its amplitude is smaller in the host vessel.

The spatial-temporal distribution of the tangent velocity component was similar to the normal component in Fig 6. However, the Poiseuille parabolic profile behavior had the same amplitudes both in the graft and in the host vessel due to the inclination of the skewed line relatively to the vessel.

The contours in Fig. 7 describe the vorticity field calculated out of the vector flow field (Fig. 5). The axes describe the position [cm] of the model and its size. High vorticity lines concentration can be seen on the graft walls especially in proximity of the toe and the heel. The vascular bed of the host exhibits two zones of high vorticity lines concentration on its right and left sides. Between them, on the wall center, an abrupt void may be observed. This location coincides with the stagnation zone observed in the CDPIV films. The wall, right to the toe, exhibits a contour line decrease at the same location where flow separation was observed in the experiments. Small vortices may be observed ("moving") between, the high vorticity concentration on the heel and the high vorticity concentration downstream on the wall, left to the heel. (Vortex shedding was observed there in the continuous vorticity films).

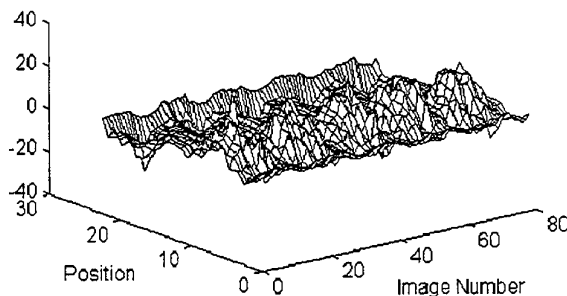


Fig. 8, Reynolds stresses, spatial-temporal distribution

Fig. 8 describes spatial and temporal distribution of the Re stresses at the location described by the skewed line in Fig. 5. The vertical axis describes normalized stress amplitude. The position axis describes the location described by the skewed line, where the arrow tip in Fig. 5 corresponds with the position axis origin. The time axis is represented by the image-number. It corresponds to the pulsating flow cross-section, as calculated from the DPIV images sampled continuously in time. The Reynolds stresses are exhibited as function of the position and the inclination of the skewed line, relatively to the vessel

diameter. High stress peaks are noticed, at the position of the walls of the graft and the host, in the proximity of the heel. The peaks' amplitude, clearly follows the pulsating cycle in the graft, demonstrating the destructive fatigue cycles exerted on the anastomosis.

3.2 The Flow Spectrum

Spectral analysis was performed to characterize the flow field structure in all the models and flow conditions.

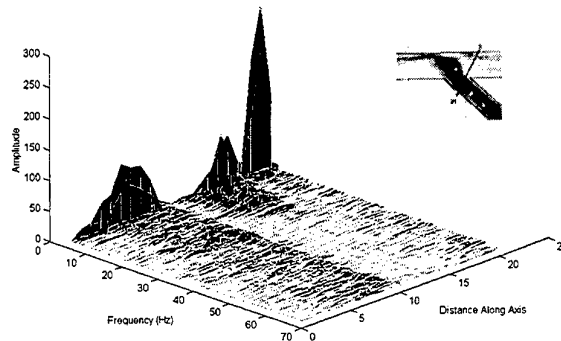


Fig. 9, Spatial spectral distribution, model A

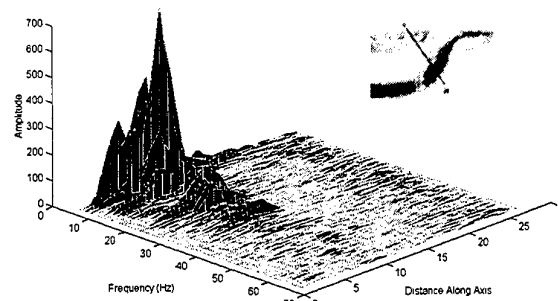


Fig. 10, Spatial spectral distribution, model C

Fig. 9 depicts the spatial frequency distribution of the velocity along the skewed line, which is shown in the small figure of model A. It describes the power spectrum of the tangent velocity component fluctuations. The frequencies were calculated out of the instantaneous velocity vector field. A channel, along all the frequencies range, may be observed at the distances of 10-12 where the skewed line crosses outside the model. This channel borders between the flow fluctuations in the host region (distances of 0-10) and the graft region (distances of 12-21). The graft region starts with frequencies concentrated below 20 Hz and continues with a plateau. The host region seems to be flat except the frequencies concentrated at 25-30Hz. (The high amplitudes below

5Hz, along the entire distance axis, is generated by the high energy of the core of the pulsating flow). The frequency axis reaches a maximum of 67.5 Hz according to the Nyquist criteria and Strouhal frequency factor.

Fig. 10 similarly depict the frequency distribution in model C at the same flow conditions. The main phenomenon is observed in the host as protruding frequencies, accumulated around 15, 25 and 35Hz. Their location along the distance axis corresponds with the location of a large eddy, which was observed in the experiments. The graft region appears to be flat.

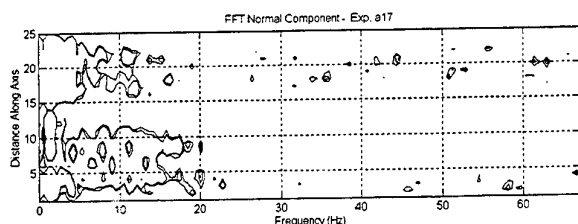


Fig. 11, Normal velocity spectrum, model D, Re=300, 80BMP

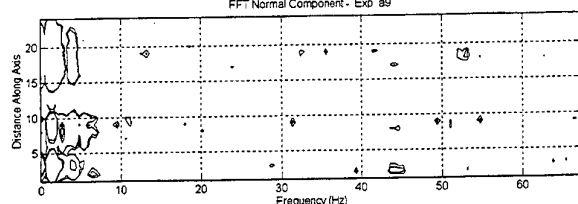


Fig. 12, Normal velocity spectrum, model A, Re=300, 80BMP

Fig. 11 describes the frequency distribution in the stiff model D, while Fig. 12 describes the frequency distribution in the distensible model A. Both figures describe the spectral distribution of the normal velocity component fluctuations along the same skewed line, and at the same flow conditions. The contour lines in the distensible model (Fig. 12) reveal that most of the energy is concentrated below 7Hz along the entire distance axis. A few single frequencies at 32Hz, 45Hz and 54Hz disturb the flat plateau. It is evident that stiff model (Fig. 11) exhibits a much wider energy distribution between 0-20Hz.

Figures 13, 14 and 15 describe the spectral distribution of model A under the same pulse rate (80BMP) while Re increases from 300 to 400 and 500, respectively. The tangent component fluctuations were calculated at the same cross section. The increase in Re from 300, trough 400 to 500 is observed as widening of the energy distribution along the frequency axis, from 0-6Hz through 0-26Hz up to the whole frequency range in Fig. 18B, respectively.

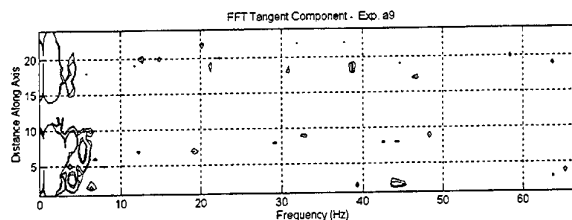


Fig. 13, Tangent velocity spectrum, model A, 80BMP, Re=300

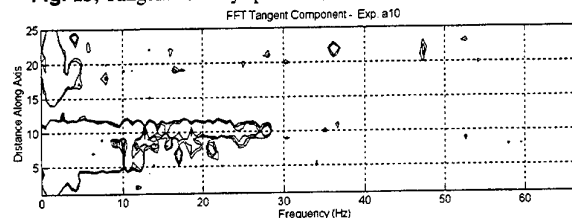


Fig. 14, Tangent velocity spectrum, model A, 80BMP, Re=400

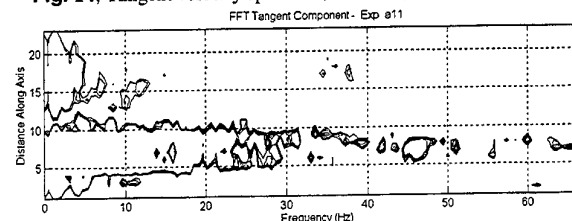


Fig. 15, Tangent velocity spectrum, model A, 80BMP, Re=500

1. CONCLUSIONS AND DISCUSSION

Zones of high shear stress peaks and traveling vortices were observed around sharp non-streamlined anastomosis toe and heel. Flow reversal or separation was Womersley parameter dependent. Vorticity films, presenting the exact susceptible loci, animated the separation and reattachment cycles. The mechanism of energy transfer from larger to smaller scale eddies may imply of preferred deposits locus. The flow profile and spectra was dependent on the anastomosis angle and the graft elasticity. Changes in the Reynolds number left their well-defined signature in the spectra, however, the Womersley parameter did not exhibit a specific tendency. A stiffer model resulted in a much wider spectral distribution. The introduction of a system capable of the PIV spatial resolution combined with the, yet partial, LDV temporal resolution is very important when examining unsteady whole field flows. This system enabled us to take a longer look at the pulsating flow instantaneous characteristics and its derivatives. It is expected that CDPIV temporal resolution will improve as video cameras' speed-resolution-price ratio keeps improving with the drop in capacity-speed-price of storage devices. It is therefore important to find a feasible three component convenient technique for measurement of 3D CDPIV.

NOMENCLATURE

DPIV	Digital Particle Image Velocimetry
CDPIV	Continuous DPIV
α	Womersley Number
Re	Reynolds Number
St	Strouhal Number
BPM	Beats Per Minute

REFERENCES

- Bluestein D., Einav S., 1993, "Spectral Estimation of LDA data in pulsatile flow through heart valves", *Experiments in Fluids* 15,341-353,1993.
- Chandran, K.B.; Kim, Y.-H., 1994, "Mechanical aspects of vascular graft-host artery anastomoses", *IEEE Engineering in Medicine and Bio. Magazine* Vol: 13, Iss 4 p. 517-24
- Chang, K.C., Tseng, Y.Z., Kuo, T.S., Chen, H.I., 1995, "Impedance and wave reflection in arterial system: simulation with geometrically tapered T-tubes", *Medical & Biological Engineering & Computing*, Vol: 33 Iss: 5 p. 652-60 Sept. 1995
- Enden G. and Popel A. S., 1994, "Numerical study of plasma skimming in small vascular bifurcations" *J. Biomechanical Eng. Transactions of the ASME* v.116, p79-88, 1994.
- Fei, Ding Yu; Thomas, James D.; Rittgers, Stanley E., 1994, "Effect of angle and flow rate upon hemodynamics in distal vascular graft anastomoses: A numerical model study", *J BIOMECH ENG TRANS ASME*. 1994 vol. 116, no. 3, pp. 331-336
- Grarib M. and C. E. Willert, 1991, "Digital Partcle Image Velocimetry", *Experiments in Fluids* 10, 181-193, 1991.
- Hughes, P.E.; How, T.V., 1995, "Flow structures at the proximal side-to-end anastomosis. Influence of geometry and flow division", *Transactions of the ASME. Journal of Biomechanical Engineering*, Vol: 117 Iss: 2 p. 224-36
- Keynton, R.S.; Rittgers, S.E.; Shu, M.C.S., 1991, "The effect of angle and flow rate upon hemodynamics in distal vascular graft anastomoses: An in vitro model study.", *TRANS. ASME J. BIOMECH. ENG.* 1991. vol. 113, no. 4, pp. 458-463
- Kim, Y.H.; Chandran (a), K.B., 1993, "Steady flow analysis in the vicinity of an end-to-end anastomosis", *Biorheology*, Vol: 30 Iss: 2 p. 117-30
- Kim, Y.H.; Chandran (b), K.B.; Bower, T.J.; Corson, J.D., 1993, "Flow dynamics across end-to-end vascular bypass graft anastomoses", *Annals of Biomedical Engineering* V. 21 Iss:4 p. 311-20
- Liepsch D., Kaluzynski K., 1995, "The dynamics of pulsatile flow in distensible model arteries", *Technology and Health Care* 3,153-159,1995.
- Liepsch D., Zimmer R., 1995, "The dynamics of pulsatile flow in distensible model arteries", *Technology and Health Care* 3,185-199,1995.
- Ohba K., Kamino H., Urabe T., Ikedo S., 1995, "Pulsatile Flow Through a Tapered U Bend as Simulated Aortic Arch (Flow Characteristics and Velocity Field)", *Bio-Medical Fluids Engineering*, Vol. 212 1995.
- Paz D., Einav S., Elad D., 1991, "Numerical Model of Blood Flow Through a Bifurcation: Interaction Between an Artery and Small Prosthesis", *Med. & Biol. Eng. & Comput.*, 1992, 30, 543-550.
- Sakurai A., Ohba K., Futagami Y, Tsujimoto M., 1996, "The Effect of Longitudinal Tention on flow in Collapsible Tube", *JSME Int. journal.*, vol 39, No 2, 361-367, 1996.
- Steinman, D.A.; Ethier, C. Ross, 1994, "Effect of wall distensibility on flow in a two dimensional end-to-side anastomosis" *J. BIOMECH ENG TRANS ASME*. 1994 vol. 116, no. 3, pp. 294-301
- Steinman, D.A.; Vinh, Bach; Ethier, C. Ross; Ojha, M.; Cobbold, R.S.C.; Johnston, K.W., 1993, "Numerical simulation of flow in a two dimensional end-to-side anastomosis model." *J BIOMECH ENG TRANS ASME*. 1993. vol. 115, no. 1, pp. 112-118
- Stewart,S.F.C.; Lyman, D.J., 1992, "Effects of a vascular graft/natural artery compliance mismatch on pulsatile flow." *J. BIOMECH.* 1992. v. 25, no. 3, pp. 297-310.
- Vagner, E.A.; Sukhanov, S.G.; Aptukov, V.N., 1982, "Mechanical behavior of vascular anastomoses in sclerotic arteries and a model for this behavior." *MECH. COMPOSITE MATER.* 1982. vol. 18, no. 2, pp. 240-245
- W, K.C.; Marble, A.E.; Sarwal, S.N.; Kinley, C.E.; Watton, J.; Mason, M.A. ,1986, "Simulation of coronary artery revascularization.", *J. BIOMECH.* 1986. vol. 19, no. 7, p491-499
- White, S.S.; Zarins, C.K.; Giddens, D.P.; Bassiouny, H.; Loth, F.; Jones, S.A.; Glagov, S., 1993, "Hemodynamic patterns in two models of end-to-side vascular graft anastomoses: Effects of pulsatility, flow division, Reynolds number, and hood length. *J BIOMECH ENG TRANS ASME*. 1993. vol. 115, no. 1, pp. 104-111

LOW COHERENCE INTERFEROMETRY FOR FLOW MEASUREMENT

Adrian Gh. Podoleanu, John A. Rogers and David A. Jackson
Applied Optics Group, School of Physical Sciences, University of Kent,
Canterbury, CT2 7NR, United Kingdom
Fax: +44 1227 827558; e-mail: A.G.H.Podoleanu@ukc.ac.uk

ABSTRACT

We present preliminary results of imaging into milk using a fiberised set-up and Doppler optical tomography method. High signal to noise ratio has been obtained with only 150 μ W power to the flow, penetration range is up to 2 mm.

1. INTRODUCTION

Low coherence reflectometry (LCR) has emerged as a method for absolute surface profile and distance determination with very good axial and transversal accuracy and has been applied to reflectance measurements of different structures. LCR has also been successfully applied to in vitro and in vivo imaging of different biological tissues. Lately, a great deal of attention has been devoted to retinal imaging, Huang D et al (1991) and Podoleanu et al (1998) and in skin imaging Birngruber R et al (1997). For such applications, once the structure is investigated in detail using LCR, the interest is to find more about the local blood flow. Determination of blood flow in retinal vessels and in tiny vessels inside skin tumours may offer relevant information about the tissue and the illness. This technique, termed optical Doppler tomography (ODT) Chen Z et al (1997), combines laser Doppler flowmetry with LCR. ODT has been applied for instance to monitor in vivo blood flow dynamics and vessel structure after a vasoactive drug and photodynamic therapy, Chen (1998). A version of this technique, the color Doppler optical coherence tomography (CDOCT) Izaat et al (1997) uses colour to superpose the velocity mapping over the anatomical image.

In comparison with laser anemometry, where two beams at an angle are used and the interference takes

place between two object beams, ODT has the advantage of interfering the object light from the sensing arm of the OCT with a very powerful beam, from the reference arm of the OCT. However, the immediate disadvantage of ODT lays with the need to tilt the flow object, as the Doppler shift frequency ν is proportional with the cosine of the angle θ' between the ray direction and the flow direction:

$$\nu = 2 v \cos \theta' / \lambda \quad (1)$$

where v is the flow velocity and λ the wavelength in air. LCR has the capability of achieving very good depth accuracies (down to 3.7 μ m, as demonstrated with a Kerr lens mode-locked Ti:Al₂O₃ laser at 830 nm). This has the potential of microflow speed determination. The position of investigation may be chosen using the LCR in imaging mode and after that the instrument operation may be changed to flow measurement. The current focus is on the reduction of acquisition time while maintaining a good signal to noise ratio, which calls for investigations into new, improved, interferometric configurations.

A form of LCR, dynamic low coherence interferometry (DLCI) was reported by Bizheva et al (1998) for noninvasive imaging of Brownian motion within the turbid media. A single axial scan can be used for the determination of both optical as well as dynamic properties of the highly scattering, but low absorbing medium. The transition from the single to multiply scattering can also be characterised using only one axial scan.

All these represent different versions of LCR and prove the usefulness of the method.

2. EXPERIMENTAL SET-UP

Our configuration is based on a spliceless array of two fiberised single mode couplers. Light from either a pigtailed superluminescent diode, SLD or a three electrode laser, 3EL, both working on the same wavelength ($\lambda = 0.85 \mu\text{m}$) is injected via the coupler DC0 into a coupler, DC1, which transmits 25% of the power to the object arm. In this arm, the light propagates through a phase modulator, PM, which consists of 2 turns of fiber wrapped around a piezo-cylinder. Light subsequently travels via a microscope objective, C1, then enters an orthogonal scanning mirror pair, MX and MY, serving the aiming (imaging purposes) and passes through lenses L1 and L2 to the object (which finally should be skin, retina, etc). In our case, a silicone tube, ST, with internal diameter of 4.8 mm is used which can be suitably angled at angles θ between the ray direction and the tube direction and is travelled by milk as a liquid with known properties as measured in Yoon (1993) and in Yaroslavsky (1996). The flow can be set at different speeds between 0 - 3

coherence matching the reference and the object arm. Polarization controllers, FPC1-3 are mounted in the sensing arm and in each of the reference arm ports. Two photodetectors, PD1 and PD2 collect the returned optical signals from the optical coupler receiver outputs. The photodetected signals are applied to the two inputs of a differential amplifier, DA, in a balanced detection configuration. The spectrum of the signal is then analysed on the spectrum analyser SA and mixed with the signal of frequency f in the mixer X to shift the Doppler signal about zero frequency.

The focal length of the lens L2 can be adjusted for different objects. For retina investigations, the lens L2 is the eye lens. For a lens with 2 cm focal length, the transversal resolution on the target is about $20 \mu\text{m}$ and this will be the precision in choosing the area where the flow has subsequently to be determined. The depth resolution is determined as a convolution of the depth confocal profile of the receiving aperture fibre (identical in our set-up with that of the launching fibre)

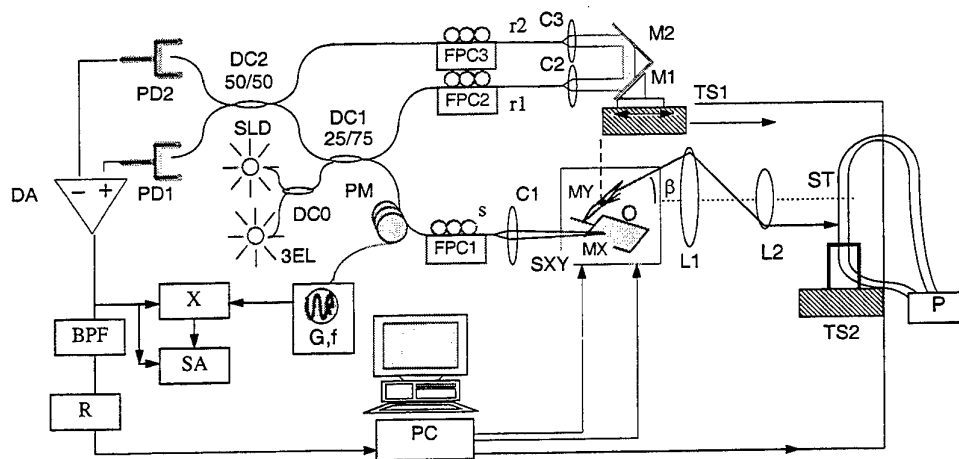


Figure 1. Experimental OCT set-up

cm/s altering the power applied to the pump P.

The transmitted light from the other port of DC1 (the reference beam), which is of much higher power than the signal beam, is directed via the microscope objectives C2, C3 and mirrors M1 and M2 to the second coupler DC2 (receiver). In this way, light from reference mirrors is not sent back to the optical source (both SLD and the 3EL sources are prone to oscillations under optical feedback). All fibre ends are polished at 4° to reduce the noise associated with the backreflected light. The mirrors serving to recirculate the reference beam are mounted on a computer controlled translation stage TS1 to allow for the

with the correlation profile of the source power spectrum (if the dispersion in the set-up is compensated for, otherwise the final correlation profile is enlarged, as shown in Drexler (1998)). The confocal profile width of $\text{FWHM} = 0.8 \text{ mm}$ was measured by scanning a mirror through the focus of the lens L2 and measuring the amplitude of the returned signal. In air, the FWHM of the correlation profile is either $20 \mu\text{m}$ or $120 \mu\text{m}$, determined by half of the coherence length of the SLD or 3EL respectively. Consequently, the depth sampling interval is mainly due to the coherence profile.

3. EXPERIMENTAL RESULTS

The images in Fig. 2 show an XY image of the tube

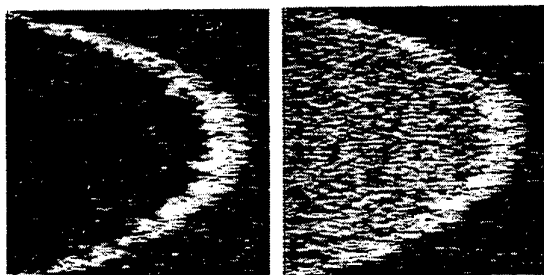


Figure 2. OCT image for the empty tube (left) and for the tube filled with the milk (right). 4 mm x 4 mm

before and after introducing the milk. The images were obtained scanning horizontally at 600 Hz and building a frame at a rate of 2 f/s. The tube was inclined at $\theta = 70^\circ$. In the left hand side of the Fig. 2 right, and in the middle, the light scattered corresponds to a point 0.9 mm inside the milk. The internal wall of the tube appears as an arc, brighter when no liquid is inside (due to the larger variation in the index of refraction between silicone and air in comparison with the variation in the index of refraction between silicone and milk).

Fig. 3 shows the spectrum of the signal when the reference arm matches the wall-liquid interface. In this case the peaks on the frequency modulation $f = 35$ kHz and on the $2f$ of the signal applied to PM are shown. Moving the tube closer to the lens L2 by 200 μ m, the spectrum displays the split of the phase modulation components with the amount $2v$, as shown in Fig. 4. (The spectrum also shows a remnant component on f ,

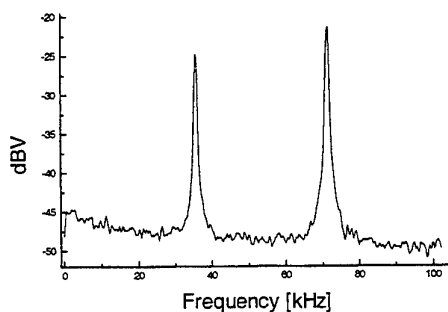


Figure 3. OCT signal spectrum from the interface wall-milk.

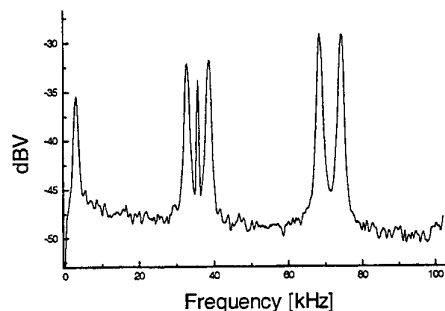


Figure 4. OCT signal spectrum, 0.2 mm depth, $\theta = 70^\circ$.

due to the parasitic intensity modulation introduced by the piezocylinder). A shift of the stage by δ corresponds to a shift of the coherence matched point in the flow by δ/n , where n is the index of refraction of the liquid. However, the waist of the beam moves further away to $n\delta$ from the tube wall. Consequently, in order to keep the waist at coherence, for each δ movement of the translation stage TS2, the translation stage TS1 has to be moved towards increasing the reference path by $\delta(n^2 - 1)$. The procedure is called dynamic focus, as discussed in Fercher et al (1997) and Chen et al (1998).

The graph in Fig. 5 shows the amplitude and the frequency of the signal depending on the depth inside the flow (depth measured in air). The flow was set at 8 mm/s and the dynamic focus method applied. As shown, we could collect signal up to 2 mm inside the tube.

We have determined the Doppler shift as dependence on the depth, with and without dynamic focus. As shown in Fig. 6, the two graphs coincide reasonably well. The values on the horizontal axis in

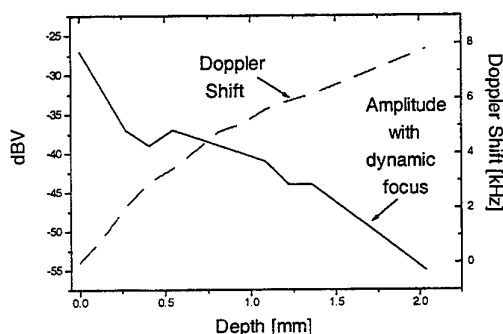


Figure 5. Amplitude of the Doppler shift component and its frequency obtained using dynamic focus for the tube inclined at $\theta = 70^\circ$.

Fig. 6 were obtained for the case without dynamic focus (when only TS2 was moved) by dividing TS2 movement by n and for the dynamic focus case by multiplying the TS2 movement by n . The coincidence of the two graphs proves the value $n = 1.36$ for the milk used in the dynamic focus correction.

The tube is too large to penetrate beyond the middle and register a decrease in the speed and consequently in the Doppler frequency. However, the profiles of the speed in Fig. 5 and 6 retrace the laminar profile of the flow inside.

The maximum frequency 8 kHz in Fig. 5 and 6 corresponds to a speed of 16 mm/s, obtained from equation (1) for $\lambda = 0.85 \mu\text{m}$. For laminar flow we expect for the velocity a peak of twice the mean, which was 8 mm/s, according to Sabersky (1971). In working out the frequency, we have taken into account the final angle between the ray and the flow (due to refraction in the silicone material and then into the milk) as well as the fact that the middle of the tube for $\theta = 70^\circ$ is at 2.55 mm instead of 2.4 mm.

Doppler shifts for 3 different angles are shown in Fig. 7, when the flow was set at 14 mm/s.

Fig. 8 shows the spectrum analyser profile taken with two different sources with two different coherence lengths, 300 μm inside the flow set at 14 mm/s, for the tube inclined at $\theta = 45^\circ$. The spectrum analyser linewidth was 64 Hz and the signal averaged 100 times (acquisition time $15.6 \times 100 = 1.56 \text{ s}$). The profile obtained with the 3EL (coherence length 240 μm , is as expected larger than the profile obtained with the SLD (40 μm coherence length). However, its amplitude is similar with the amplitude obtained with the SLD, although the 3EL power is half of that of the SLD. A possible explanation of this may involve the dispersion effects in the milk which are more important for SLD than for the 3EL according to Drexler (1998). The

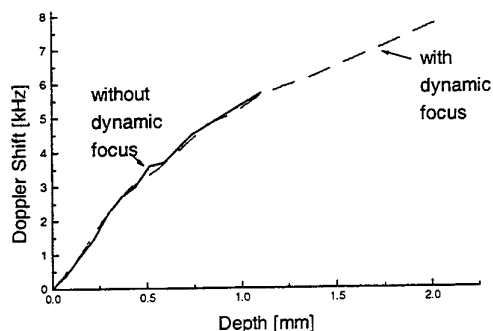


Figure 6. Doppler shift measured with and without dynamic focus versus the depth in the tube (measured in air).

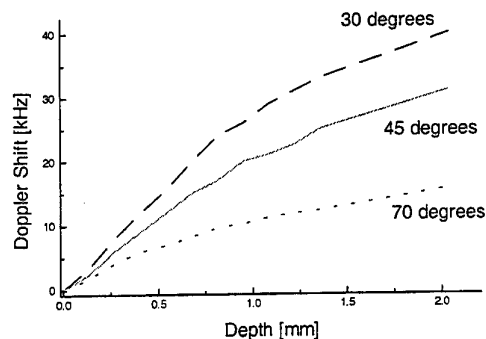


Figure 7. Doppler shift dependence on the depth inside the tube for different angles θ .

FWHM are 0.4 kHz with the SLD and 1 kHz with the 3EL. The peak in the middle represents the coherence signal from the wall, unaffected by the spectrum enlargement due to the flow.

4. CONCLUSIONS

Experiments have shown that the OCT system

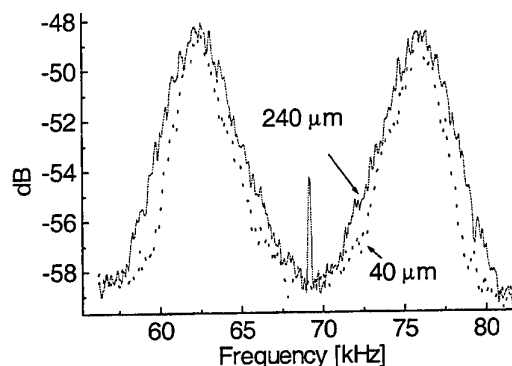


Figure 8. Coherence signal spectra for two low coherence sources with two different coherence lengths.

has sufficient sensitivity to obtain images from within a dense scattering liquid (milk). Using the DOCT method, the flow speed can be accurately determined.

The Doppler shifts were determined by averaging the spectra over time intervals of 1-2 s. This means that for each pixel in the image. When imaging,

the Doppler shift introduced by the galvanomirror, as shown in Podoleanu et al (1996) adds to the Doppler shift produced by the fluid.

In order to eliminate the tilt influence on the value of the speed determined using the DOCT method, the imaging mode of the OCT can be used to find the tilt. This will be especially useful in those cases where the object is inaccessible, as for instance the retina.

Experiments are continuing in order to implement the two operation principles, imaging plus flow characterization in vivo.

5. ACKNOWLEDGEMENTS

The authors acknowledge the support of the UK Engineering and Physical Sciences Research Council and of the University of Kent..

6. REFERENCES

- Bizheva K, Siegel A & Boas D 1998 Dynamic Low Coherence Interferometry as a Tool for Imaging and Quantification of Brownian Motion within Highly Scattering Media, Proc. Advances in Optical Imaging and Photon Migration, OSA, Orlando, Florida, pp. 103-105.
- Birngruber R 1997, Optical coherence tomography of the human skin, J. American Ac. Dermatology, Vol.37, No.6, pp.958-963
- Boas_D. A. et al 1998 Using dynamic low-coherence interferometry to image Brownian Motion Within Highly Scattering Media, Opt. Lett., Vol.23, No.5, pp. 319-321.
- Chen Z et al 1997 Optical Doppler tomographic imaging of fluid flow velocity in highly scattering media, Opt. Lett., vol. 22, No. 1, pp. 64-67.
- Chen Z et al 1998 Optical Doppler Tomography: Imaging in Vivo Blood Flowing Pharmacological Intervention and Photodynamic Therapy, Photoch. and Photob., 67(1), pp. 56-60.
- Chen_ZP et al 1997 Noninvasive Imaging of In Vivo Blood Flow Velocity Using Optical Doppler Tomography, Opt. Lett., Vol.22, No.14, pp.1119-1121
- Fercher A. F. 1996, 'Optical coherence tomography, J. Biomed. Opt., 1(2), , pp. 157-173.
- Huang D.et al 1991 'Optical Coherence tomography', Science 254, pp. 1178-1181.
- Drexler W et al 1998 'Investigation of dispersion effects in ocular media by multiple wavelength partial coherence interferometry', Exp. Eye Res., Vol.66, No.1, pp.25-33
- Izatt J. A et al 1997 In Vivo Bidirectional Color Doppler Flow Imaging of Picoliter Blood Volumes Using Optical Coherence Tomography, Opt. Lett., Vol.22, No.18, pp.1439-1441
- Podoleanu et al (1996) 'Coherence Imaging by Use of a Newton Rings Sampling Function', Opt. Lett. 21, pp. 1789-1791.
- Podoleanu et al 1998 'Transversal and Longitudinal Images from the Retina of the Living Eye Using Low Ccoherence Reflectometry', J. Biomedical Optics, 3(1), pp. 12-20.
- Saberski et al 1971 Fluid Flow. A First Course in Fluid Mechanics, pp. 221-222, The Macmillan Company, New York
- Yoon G et al 1993 Coherent Backscattering In Biological Media - Measurement and Estimation of Optical-Properties, Appl. Opt., Vol.32, No.4, pp.580-585
- Yaroslavsky I V et al 1996 Inverse Hybrid Technique For Determining the Optical-Properties of Turbid Media from Integrating-Sphere Measurements, Appl. Opt., Vol.35, No.34, pp.6797-6809.

SESSION 30

OPEN FORUM

SESSION 31

ENGINES I

INVESTIGATION OF IN-CYLINDER FLOW INSIDE IC ENGINES USING PIV WITH ENDOSCOPIC OPTICS

J. Gindele, U. Spicher
Institut für Kolbenmaschinen, Universität Karlsruhe, Germany

ABSTRACT

The in-cylinder flow of IC-engines has a large effect on mixture preparation and combustion. Especially for future combustion concepts like lean-burn engines, the knowledge of the interaction between the in-cylinder flow and combustion as well as the interdependencies between the global flow structure and the mixing process are becoming essential.

The two dimensional velocity field inside the cylinder of a four stroke SI-engine was investigated by means of digital Particle Image Velocimetry (PIV). For observation of the tracer particles a double frame CCD camera was used with endoscopic optics, due to practical difficulties coupled with the design of an optically accessible cylinder. The use of an endoscope for observation of PIV images provided a simple optical access and a very easy handling, but endoscopic optics lead to a distortion of the recorded images.

Therefore multiple investigations were performed to develop a calculation method for correction of distorted PIV measurements. This report presents two different methods to compensate the distortion by calculation methods, one applied to the PIV raw image, the other applied to incorrect correlated vector plots. Both techniques are capable to rectify the PIV measurements and a comparison between the methods revealed good agreement. The results of the PIV measurements demonstrate the flexibility which can be achieved with the use of an endoscope for flow field observation.

1. INTRODUCTION

Considering new combustion concepts like direct injection engines the tuning of the flow field inside the cylinder of IC-engines became more important.

These engine concepts require controlled gas motion such as tumble or swirl over a wide range of operating conditions. Since new four valve engines use various piston designs and variable swirl and tumble inlet ducts, it is crucial to have a precise knowledge of the structure of the in-cylinder flow

The first steps of the development of new engines are mostly done by using CFD. With new powerful numerical calculation methods, it is possible to obtain good predictions for in-cylinder gas motion. However, experimental flow data are required as boundary conditions and for validation of the multidimensional in-cylinder models. Further on, some phenomena like cyclic variations for example can not be predicted with numerical methods. Therefore the interest in the measurement of the in-cylinder flow field is still very strong. Measuring the in-cylinder flow in IC-engines is a difficult task, due to the unsteady transient flow processes with high velocities and high gas temperatures. Therefore the application of laser techniques is essential. These measurement techniques always require optically accessible cylinders. For that reason most investigations must be done with expensive test rig set-ups and furthermore at low engine speeds because of the limited stability of quartz parts. In order to speed up the development process of new engines, the experiments should be carried out with test engines which are close to the production engine.

Many experimental studies report results on in-cylinder flow using optical measurement systems. Most common techniques are Laser Doppler Anemometry (LDA) and Particle Image Velocimetry (PIV). The PIV technique has become more important because a whole instantaneous flow field can be obtained with one single measurement. Remarkable advances have been made in the last years with the development of digital image recording and processing, so that the PIV technique today is a

powerful tool for flow visualization which can be handled easily (e.g. Reuss et al, 1995, Charoenphonphanich 1996, Rouland 1997). However, especially the PIV technique requires full optical access for illumination and recording of tracer particles. One way to realize a good optical access without expensive quartz cylinders is the use of endoscopic optics (Neußer 1995). But, the application of endoscopes leads to radial symmetric distortion of the images. This distortion is caused by the wide-angle lenses of the optical arrangement which yields incorrect correlation of the particle displacement and thus erroneous vectors. Since the distortion of wide-angle optics is determined, it can be compensated.

This report focuses on the use of endoscopic optics for recording PIV images and different possibilities are shown to compensate distortion. In the present study DPIV measurements were carried out inside the cylinder of a single cylinder four stroke engine. In this engine an endoscopic optics was used due to practical difficulties coupled with the design of an optically accessible cylinder.

2. ENDOSCOPIC OPTICS

Endoscopes are basically very thin periscopes and they are widely used for medical applications. Recently, endoscopes are more and more used for technical applications like for example the visual examination of cavities.

The optical system of a modern endoscope consists of an objective, a various number of relay systems for image transmission and an ocular at the eyepiece, as shown in figure 1. In order to increase the total amount of light that can be transmitted through the optical system Hopkins (1976) developed the rod lens system where due to the short air spaces the light transmitting capacity was doubled.

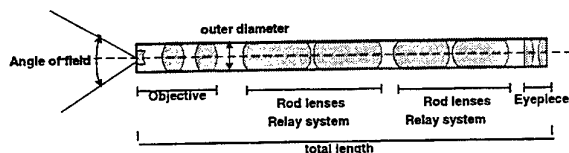


Figure 1: Optical system of an Hopkins endoscope

The magnification of an endoscopic optics is inversely proportional to the working distance. Hence

a plot of magnification versus working distance is a hyperbola as shown in figure 2.

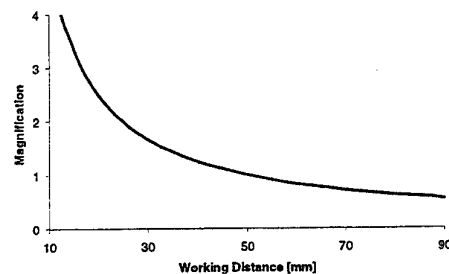
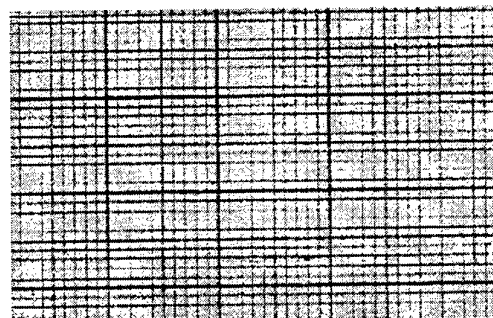
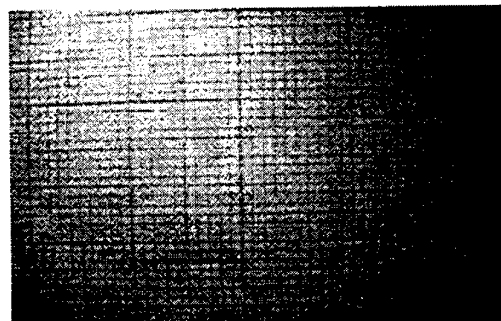


Figure 2: Magnification on the optical axis versus working distance for an endoscope

Moreover, the magnification of an object line segment varies with its distance from the optical axis. This aberration is caused by the special arrangement of lenses and aperture (iris) in endoscopes and is called distortion. As the magnification decreases with the distance from the axis the distortion is negative and a straight line in the object plane is imaged concave toward the axis. Figure 3 shows a distorted and a non-distorted image. The appearance of these images explains the terminology "barrel" distortion occasionally applied to this aberration.



non-distorted



distorted

Fig. 3: distorted and non-distorted image

As the magnification varies with the radial distance of an object point from the optical axis, the distortion is radial symmetric. Distortion is usually measured in terms of the distance of the actual image point from the image point that would result if the magnification throughout the field were equal to that near the axis, relative to the distance of the latter to the axis. When thus measured, distortion is proportional to the square of the image height. On the optical axis the distortion is zero.

Apart from distortion, a further problem results by the application of endoscopes for visual examinations. Due to the small aperture and the large number of optical elements used in endoscopes a much stronger illumination is needed. However, with the use of stronger light sources, this problem can be compensated (Levi 1968, Hett 1969).

3. CORRECTION OF DISTORTION

The distortion of the PIV images, as mentioned above, obviously lead to a incorrect correlation of particle displacement because of the incorrect positions of pixels on the image. As the distortion D is radial symmetric the problem can be described mathematically as follows:

$$D = 1 + A\phi^3 + B\phi^2 \quad D = \frac{R}{r} \quad (1)$$

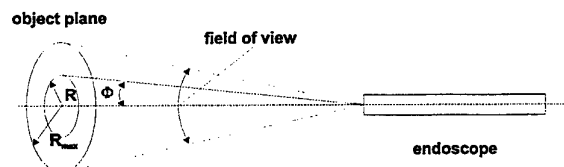


Figure 4: Angle of view and radius on the object plane

According to figure 4, R is the real radial distance of an object point from the optical axis and r is the radial distance of the distorted referring image point from the center of the image. The factors A and B are parameters which have to be found with a calibration procedure.

Due to the complexity of the optical system, the parameters of distortion of an endoscope can not be predicted, as a precise knowledge of all optical components would be indispensable. Therefore empirical and statistical methods must be used to find the parameters which describe the distortion of an image.

Fundamentally there are two different approaches to solve the problem. One way is to rectify the PIV bitmap images before the cross-correlation procedure. The second way is the correction of the erroneous vectors after correlation of the incorrect particle displacement on distorted images. Both techniques have been developed and will be described and compared in the following sections.

Correction of raw bitmaps

To correct the bitmaps, a mapping procedure using a calibration image was utilized. The procedure is very similar to one used by Willert (1997) to rectify stereoscopic PIV images and is also broadly used in the field of Digital Image Processing, Gonzalez et al. (1992). It consists on, creating a mapping:

$$\begin{aligned} X &= a_1x^2 + a_2y^2 + a_3xy + a_4x + a_5y + a_6 \\ Y &= b_1x^2 + b_2y^2 + b_3xy + b_4x + b_5y + b_6 \end{aligned} \quad (2)$$

Where (X,Y) are pixel coordinates in the undistorted field and (x,y) are pixel coordinates from an distorted calibration image. The pairs of corresponding points are calculated through cross-correlating the distorted image with a point, and superimposing an image of the correct calibration.

To obtain the 12 coefficients for each point in the calibration image, 6 neighboring points are needed. The criteria is to select the 6 closest points. Naturally this introduces errors, especially in the borders, where bigger variations in distortion are expected between the points.

After obtaining the coefficients for all points in the distorted calibration image, the inverse mapping of equations (2) is used to determine for the coordinates (X,Y) what point given by (x,y) rounded to the next integer is closest in the distorted image. Then the gray value of this point is attributed to the pixel coordinates (X,Y) .

Correction of vector plot

For the use of this technique it must be assumed that the cross-correlation of the particle displacement is possible in spite of the distortion of the image. This problem could appear when using endoscopes with a wider field of view which provide stronger distortions.

The basic principle of this method is the determination of the error of correlated vectors due to the distortion of the raw bitmaps. For the cross-

correlation the images are divided into interrogation regions. In this sub-areas the particle displacement is assumed to be equal. Accordingly the distortion is assumed to be equal. The correlation of distorted particle images results in a shortening of the absolute value and in a rotation of the vector. Furthermore the vector has a false position. As the distortion of the vectors depends on their radial distance from the optical axis, it can be described with parameters which represent a torsion (α, β) and deformation (a, b) of the local cartesian x,y-coordinate axis of the interrogation area. Figure 5 explains this relation.

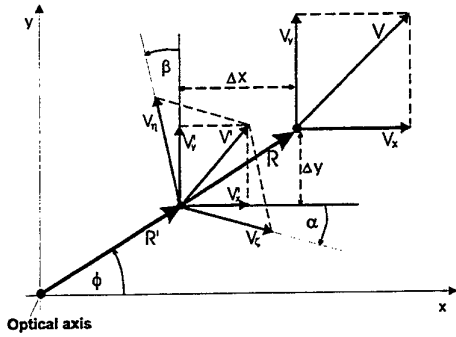


Figure 5: Deformation and torsion of coordinate axis due to distortion of images, distorted vector V' , correct vector V .

The determination of the parameters is performed with two virtual PIV images, one with a known virtual shift in x-direction (X -shift) and one with a known shift in y-direction (Y -shift). The erroneous vectors V' are then normalized with the vector $V_{opt.axis}$ in the center of the image where the distortion is zero. The deformation in x- direction a and in y-direction b are calculated as follows:

$$a = \left[\frac{\left(\sqrt{V_x'^2 + V_y'^2} \right)_{local}}{\left(\sqrt{V_x'^2 + V_y'^2} \right)_{opt.axis}} \right]_{X-shift}$$

$$b = \left[\frac{\left(\sqrt{V_x'^2 + V_y'^2} \right)_{local}}{\left(\sqrt{V_x'^2 + V_y'^2} \right)_{opt.axis}} \right]_{Y-shift} \quad (3)$$

V_x and V_y are the cartesian components of an vector V . The torsion of the local coordinate axis α and β is given by:

$$\alpha = \left[\arctan \left(\frac{V_y'}{V_x'} \right)_{local} - \arctan \left(\frac{V_y'}{V_x'} \right)_{opt.axis} \right]_{X-shift}$$

$$\beta = \left[\arctan \left(\frac{V_x'}{V_y'} \right)_{local} - \arctan \left(\frac{V_x'}{V_y'} \right)_{opt.axis} \right]_{Y-shift} \quad (4)$$

With known parameters a, b, α and β for each interrogation area, the corrected vectors can be calculated as follows. A distorted vector V' is transformed into the distorted coordinate system ζ, η as shown in figure 6. The components of V' in the distorted coordinate system ζ, η are V_ζ and V_η calculated, according to figure 6, with the equations below.

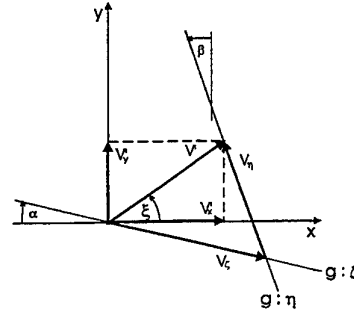


Figure 6: Distorted coordinate axis

$$V_\zeta = \pm \sqrt{\left[\frac{-\sin \beta \cdot (V_x' + \cot \alpha \cdot V_y')}{\sin \beta - \cot \alpha \cdot \cos \beta} + V_x' \right]^2 + \left[\frac{\cos \beta \cdot (V_x' + \cot \alpha \cdot V_y')}{\sin \beta - \cot \alpha \cdot \cos \beta} + V_y' \right]^2}$$

$$V_\eta = \pm \sqrt{\left[\frac{-\sin \beta \cdot (V_x' + \cot \alpha \cdot V_y')}{\sin \beta - \cot \alpha \cdot \cos \beta} \right]^2 + \left[\frac{\cos \beta \cdot (V_x' + \cot \alpha \cdot V_y')}{\sin \beta - \cot \alpha \cdot \cos \beta} \right]^2} \quad (5)$$

Then the rectified vector V can be calculated with the following equations:

$$V_x = \frac{V_\zeta}{a}; \quad V_y = \frac{V_\eta}{b} \quad (6)$$

Finally the position of the vector must be corrected. As mentioned above, the distortion is described by equation (1), with:

$$\phi = \arctan(R/l) \quad (7)$$

Where l is the distance of the object plane from the entrance pupil of the endoscope. The correct position x and y of the vector is determined with Δx and Δy :

$$\Delta x = R'(D-1) \cdot \cos \phi \quad ; \quad \Delta y = R'(D-1) \cdot \sin \phi$$

$$x = x' + \Delta x \quad ; \quad y = y' + \Delta y \quad (8)$$

The factors A and B for determination of the distortion D , can be obtained easily with a calibration image, e.g. like shown in figure 3.

Calibration procedure

With a calibration procedure of the endoscope and camera objective, the parameters of distortion can be determined once and then used to rectify all measurements done with this arrangement. The endoscope used for the investigation was a forward viewing Storz Boroskop, Type 86270 AF with a field of view of 67 degree, an outer diameter of 6.5 mm and a total length of 200 mm. The determination of the parameters needed for the rectification of the PIV measurements, was performed with a virtual image of particles, containing equidistant white dots on black background (Fig. 7). This image was recorded through the endoscope using the same configuration like in the measurements and the parameters for the rectification of the bitmaps were calculated.

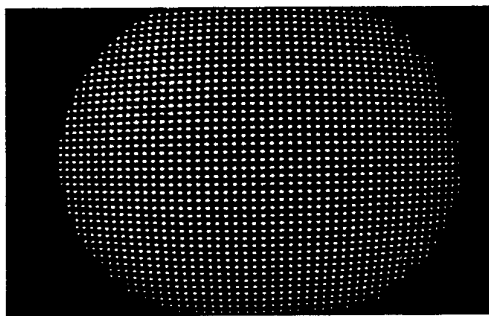


Figure 7: Calibration image

Additional frames were recorded with small displacements to the latter. The cross correlation of these images yielded the vector field with which the rectification parameters for the correction of vector plots were determined

The following plots show the parameters of deformation a and b and the angles of torsion α and β of the coordinate axis.

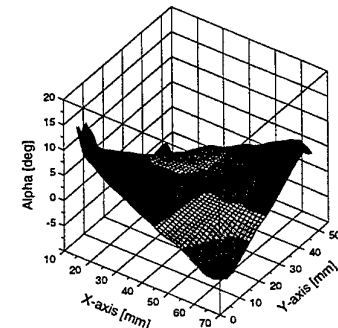
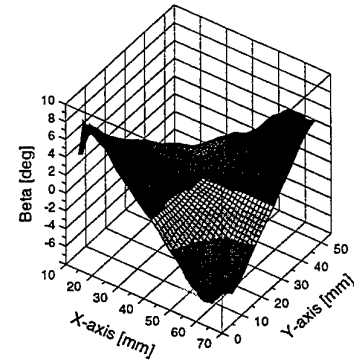
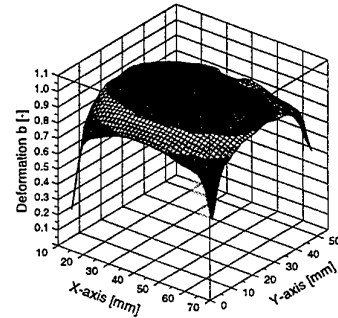
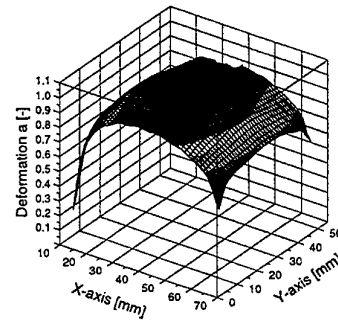


Figure 8: Deformation and Torsion of Vectors

Comparison between the methods

With both methods distorted particle images with a virtual shift between the images were processed. The result of the cross correlation of the distorted images is shown in Figure 9.

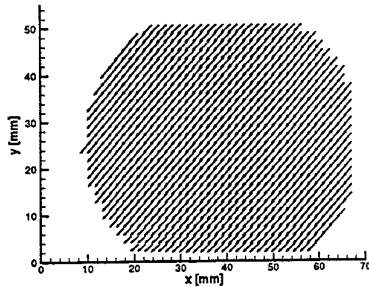


Figure 9: Virtual parallel flow, cross correlation of distorted images

The torsion and deformation of the vectors is shown in Figure 10.

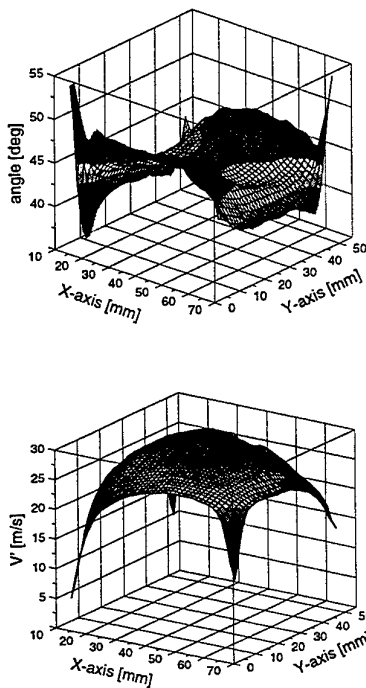


Figure 10: Deformation and torsion of vectors of the test images

As the whole image was linear shifted with an angle of 45 degrees all vectors should have the same absolute velocity and the same angle.

To compare the methods this virtual PIV measurement was rectified using the procedures described above. The corrected bitmap image is shown in figure 11.

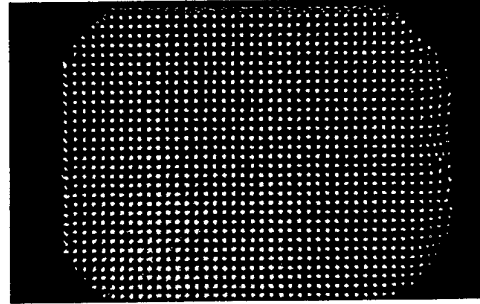


Figure 11: Rectified bitmap

The cross-correlation of the rectified bitmap images leads to the velocities shown in figure 12.

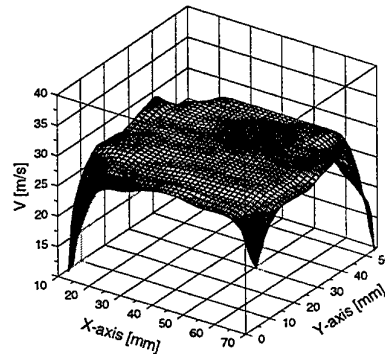


Figure 12: Rectified velocity V of virtual parallel flow, cross correlation of rectified bitmaps

Figure 13 shows the corrected velocities of the erroneous vector plot.

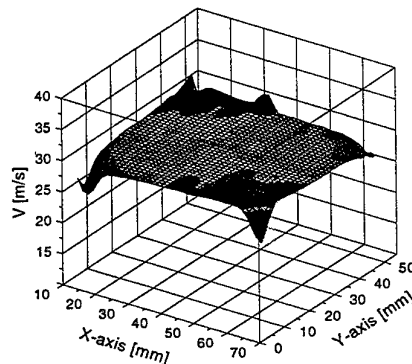


Figure 13: Rectified velocity V of virtual parallel flow, vectors corrected after cross correlation of distorted images

Both techniques yield the same correct vectors. The deviation from the virtual velocity is within 3%. The errors on the edges are caused by incorrect correlation of dark areas at the borders of the image.

4. PIV EXPERIMENTS

The PIV measurements were performed using the experimental configurations shown schematically in Figure 14.

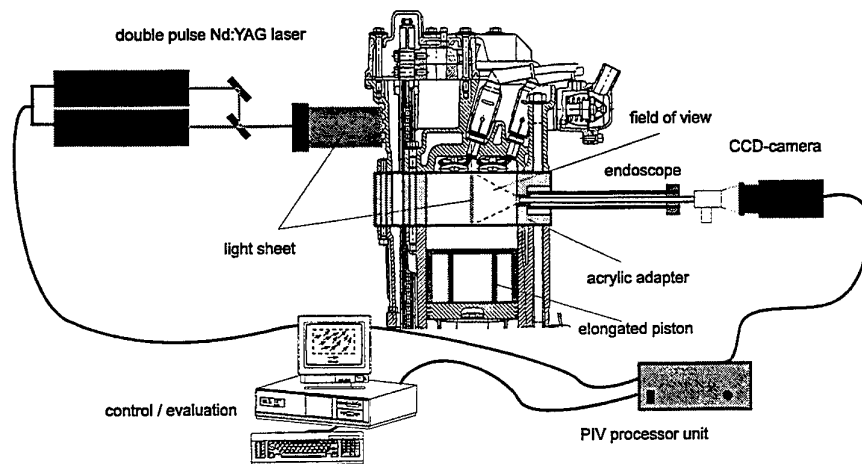


Figure 14: Experimental setup for PIV measurements

The laser beams of two coupled Nd:YAG lasers were formed into a planar laser sheet by passing it through a cylindrical and a spherical lens. The Nd:YAG lasers supply pulses of 532 nm light (second harmonic) with energies up to 320 mJ and with a pulse duration of 5 ns, at a repetition rate of 10 Hz. Using two lasers the pulse separation can be set individually down to 1 μ s. The light sheet passed through the cylinder via a transparent acrylic periphery which was fitted between cylinder head and the cylinder liner. For observation of the light sheet the endoscope was mounted into a sleeve which was fitted in the cylinder liner. For protecting the endoscope and for sealing the combustion chamber a quartz window was glued on the front side of the sleeve. A double frame 8 bit gray scale CCD camera (Dantec DoubleImage 700) was mounted in front of the endoscope to record the PIV images. The CCD chip has a spatial resolution of 768 by 484 pixels and is specifically developed for PIV cross-correlation.

This camera is able to capture two frames with minimum time between successive frames of 2,5 μ s. The camera was equipped with a Storz lens which was especially designed for the use with endoscopes.

The digital PIV image maps are transferred to a processing unit which is able to cross-correlate the two images nearly in real time. For the evaluation process of vector maps a cross-correlation technique was used as described by McCluseky (1995). The size of interrogation area was set to 64x64 pixel with a 75 % overlap between neighboring regions. The vector maps and the bitmap images are finally transferred to a PC where they were stored and post processed. The vector maps were rectified using the methods described above. Using a PIV configuration

with a fast hardware processor, the correction of distorted vector maps is much more convenient, as the cross-correlation can be done nearly on-line without time intensive rectification of the bitmap images.

To measure at defined crank angle positions, the system must run in a triggered mode which allows to activate the laser and the camera with an external trigger event. Nd:YAG lasers are usually pulsed with a fixed

repetition frequency due to thermal effects of the laser cavity. Therefore PIV recordings could be made at fixed time intervals only determined by the laser repetition rate. To overcome this limitation a window triggered mode was used. This mode exploits the fact that for the used lasers, it was possible to advance the subsequent train of pulses a small amount relative to their normal firing time as the thermal time constant within the laser rod is normally much longer than the pulse repetition rate and no immediate deterioration of the beam quality will occur. If the trigger event comes within a pre-defined trigger window before the regular laser firing time, the recording and laser firing sequences will be initiated immediately after the trigger event without waiting for the next regular pulse (FlowMap User Manual 1996).

Using solid particles for seeding can be a problem in engines because they cause abrasion and damage the engine very fast. Therefore for the first experiments olive oil seeding particles were used but the scattered light intensity was too poor. A compromise was found with lycopodium spores (diameter approx. 30 μ m, specific gravity 0.8 g/cm³). The particles were powdered by a cyclone and injected into the air filter box.

The experiments were carried out on a single cylinder 4-stroke SI-engine. The engine has a pentroof cylinder head with two inlet and two exhaust valves. The main geometrical details of the engine were as follows:

Bore:	100 mm
Stroke:	83 mm
Intake valve opening:	17° BTDC
Intake valve closure:	45° ABDC
Exhaust valve opening:	47° BBDC
Exhaust valve closure:	15° ATDC

For the PIV measurements an optically accessed acrylic spacer was fitted between the cylinder head and the cylinder. In order to keep the compression ration constant, the piston was elongated. The spacer was equipped with oil and water ducts, so the engine could be operated under real conditions and no further geometrical changes of the engine had been necessary.

The location of the light sheet and the field of view is shown in Figure 15. The flow was examined in a vertical cross sectional plane through the center of the cylinder between inlet valves and exhaust valves. The spacer was 34 mm in height.

The PIV measurements were made under motored conditions at 2000 rpm. Several crank angle positions were investigated. At each crank angle position at least 50 measurements were made to perform a statistical analysis.

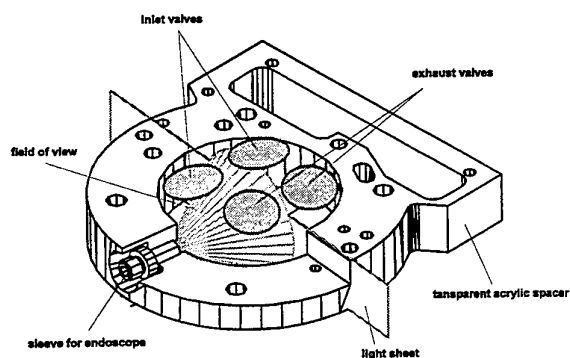


Figure 15: field of view

5. EXAMPLE RESULTS

Finally two results of the PIV measurements are shown to demonstrate the capability of the technique.

Figure 16 and Figure 17 give a rough impression of the entire intake flow situation. The inlet flow was expected to generate a tumble flow which results from a uneven mass flow distribution over the intake valve cross section. As figure 16 shows, a strong non-symmetric inlet jet develops but a strong tumble vortex can not be observed. A second minor mass flow is visible that escapes from the lower part of the valve head and then runs along the right cylinder wall. As an up coming component can not be detected in this plane, and furthermore horizontal components can be observed, a strong swirling component must be assumed.

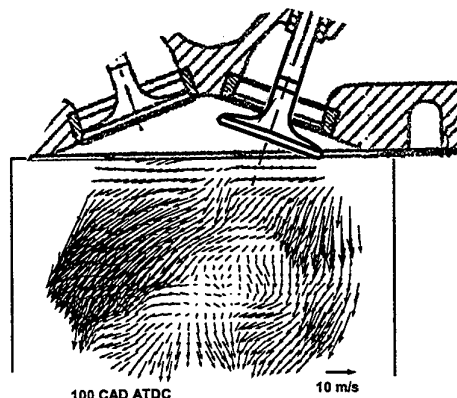


Figure 16: Averaged flow field at 100 CAD ATDC

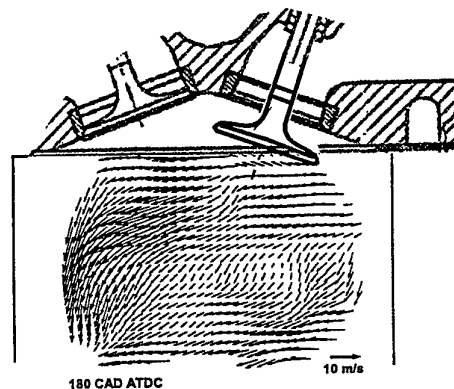


Figure 17: Averaged flow field at 180 CAD ATDC (BDC)

6. SUMMARY AND CONCLUSIONS

The use of an endoscope for observation of PIV images provides a simple optical access and a very easy handling. Hence, this recording technique gives further possibilities to use the PIV technique for difficult accessible fluid flows. Two simple methods have been introduced for compensating the radial

symmetric distortion of images recorded through an endoscope. With this techniques, it is possible to use endoscopic optics for precise PIV measurements and it is therefore feasible to use PIV in engines which are very close to production engines.

The drawbacks of glass ring applications could be avoided completely when using small light sheet optics mounted in the cylinder liner. The development of such optics could increase the flexibility of the PIV technique in the future. A powerful measuring tool like PIV is useless if it is not applicable due to practical difficulties associated with optical access.

ACKNOWLEDGEMENTS

The software for the rectification of the bitmap images was developed by C. Freek, J.M.F. Raposo and F. Puphal of the Volkswagen AG, Germany. The authors would like to thank for this valuable contribution to this work.

REFERENCES

Charoenphonphanich, C. 1996, In-Cylinder Fluid Motion and Mixing of a Dual Intake Valve Spark Ignition Engine, SAE-paper 960266.

Flow Map 2.0 User Manual 1996, Dantec Measurement Technology, Denmark, 1996.

Hett, J. H. 1969, Medical Optical Instruments, in Applied Optics and Optical Engineering, ed. Rudolf Kingslake, 1st ed., vol. 5, pp. 251-280, Academic Press, New York, London.

Hopkins, H. H. 1976, Optical Principles of the Endoscope, in Endoscopy, ed. George Berci, 1st ed., pp. 3-63, Appleton-Century-Crofts, New York.

Gonzalez, R., Woods, R., 1992, Digital Image Processing, pp 268-272, Edison Wesley, New York.

Levi, L. 1968, Applied Optics, pp. 420-423, John Wiley & Sons, New York.

McCluseky, D. R. 1995, Obtaining High-Resolution PIV Vector Maps in Real-Time, International Workshop on PIV- Fukui 95, Fukui, Japan.

Neußer, H. J., Spiegel, L., Ganser, J. 1995, Particle Tracking Velocimetry – A Powerful Tool to Shape

the In-cylinder Flow of Modern Multi-Valve Engine Concepts, SAE-paper 950102.

Reuss, D. L., et a. 1995, Particle Image Velocimetry Measurements in a High-Swirl Engine Used for Evaluation of Computational Fluid Dynamics Calculations, SAE-paper 952381.

Rouland, E. et a. 1997, Particle Image Velocimetry Measurements in a High Tumble Engine for In-Cylinder Flow Structure Analysis, SAE-paper 972831.

Willert, C., 1997, Steroscopic Digital Particle Image Velocimetry for Application in Wind Tunnel Flows in Measurement Science and Technology, Vol. 8, No. 12, pp.1465-1480.

APPLICATION OF CROSS CORRELATION PARTICLE IMAGE VELOCIMETRY TO THE CHARACTERISATION OF UNSTEADY ROTATING FLOW

M. Mouqallid* - A. Belghit** - M. Trinité*

* URA CNRS 230-CORIA - Université-INSA de Rouen - 76821 Mont-Saint-Aignan (France)

** Université Caddi Ayyad - Faculté des Sciences Semlalia - Marrakech (Maroc)

ABSTRACT

Two dimensional velocity distributions measured with cross-correlation particle image velocimetry (PIV) were used to investigate cycle-to-cycle variations of a rotating flow created in a piston cylinder assembly. The PIV technique used here consists in recording successive and separate images of the flow and applying cross correlation to them. Two techniques are used here to achieve this goal : the first is concerns the combination of a double pulsed Yag laser with a special CCD camera. This camera enables two separate images to be obtained a very short time delay between them (5 μ s). The second technique is high speed tomography. The light source is a copper vapour laser capable of producing pulses at a repetition rate up to 10KHz and the laser sheet is recorded with a high speed film camera. The cyclic variations are studied by comparing the instantaneous cycles with each other, by comparing these cycles to the ensemble averaged flow patterns and by examining the distribution and the level of the turbulence. Special attention will be paid to the instabilities accompanying the small vortex in the corner of the chamber.

1. INTRODUCTION

The confined rotating flow is one of the most fundamental and complex flows. It is encountered in several engineering applications, for example in internal combustion engines. In recent years attention has focused in the automotive industry on generating turbulence in spark-ignited engines through large scale vortices to achieve fast and stable combustion. The fluid motions consist of large scale vortices called "swirl" and "tumble". This type of flows are usually sensitive to small initial variations in the flow and are

subject to strong instabilities leading to cycle to cycle variations in engines, Reynolds (1980) , Daily (1988). In order to understand these phenomena, it is necessary to characterise the whole velocity field of

the flow at the same time. The traditional single point measurement probes such as hot wire or LDA provide velocity measurements at a limited number of locations and consequently, are not able to reveal the spatial coherent structures present in the flow. The usual process of ensemble averaging many runs used in LDA cannot represent the structure of the flow field due to the unsteady and non repeatable nature of certain flows. The turbulence intensity is evaluated as the difference between the instantaneous velocity field and the ensemble averaged velocity field. The use of this definition can overestimate the turbulence level in non-stationary rotating flows, since large variations may be included in fluctuation velocity. For these reasons, the study of large variations requires measurements of the instantaneous 2D (3D would be better) velocity field quantitatively at any time of the development of the flow. PIV is revealed as an excellent tool for this analyse. This is confirmed by the experiments that will be discussed here. Measurements of this type have recently been carried out in engines (e.g. Nino *et al* (1993), Reuss *et al* (1995), Rouland *et al* (1997), Marc *et al* (1997)).

The aim of this work is to present firstly some experimental results concerning the velocity fields of a rotating flow created during induction in a piston cylinder assembly with large optical access. It permits a more easy investigation by optical methods. The second objective of this research is to show the ability of PIV to obtain rapidly an appreciation of the cycle-to-cycle variations accompanying the large structure. The third is to examine the possible influence of the corner vortex on the principal flow in this particular

configuration. This secondary vortex is influenced by unsteady initial conditions and can modify the position of the main vortex. Of course the situation in the real internal combustion engine is very complex and different but the counter rotating vortices generated under valve can lead to a similar effect on the main vortex and consequently can be responsible for cycle-to-cycle variations in the aerodynamical point of view. More generally, the large structures initiated at the beginning of the cycle can be responsible of this kind of fluctuations. The recently developed Particle Image Velocimetry technique (Lecordier *et al* (1994a), (1994b), Mouqallid *et al* (1994)) is employed in this research. The experiment is conducted in a single-stroke piston cylinder assembly developed in the framework of the co-ordinated French CNRS ARC Program.

2. EXPERIMENTAL FACILITIES

2.1 Combustion chamber

The combustion device is composed of two main parts : a combustion chamber of 60x60mm square cross section and 100mm length, and an axisymmetrical, pneumatic-driven, single-shot piston mounted in a cylinder. The vortex is created by a slot (3x60mm) located in the corner of the chamber. The chamber is initially filled by air seeded with silicon oil droplets. The piston is then activated and locked on the inlet surface of the flow generator by means of an electronically-controlled compressed air supply on its rear face. The total induction occurs in 90ms giving an equivalent engine speed of 300 revolutions per minute. Optical access is provided with three rectangular quartz windows. A detailed view of the combustion chamber is shown in figure 1. The piston is monitored by an electronic sequencer whose output provided variable trigger pulses to control the timing of the cameras and laser pulses. The piston motion is analysed in real time by means of an opto-electronic position transducer installed on the piston rod in order to control its reproducibility.

2.2 PIV measurements

Two types of images have been taken : recorded video images and high speed movies. The video images are recorded by a special CCD camera (LH510) which enable two successive images to be acquired with a very short time delay. This camera is combined with a double pulsed Yag laser. The time delay between the two laser pulses is set to about 10-40 μ s according to the velocity field and

magnification ratio. The laser beams were focused into sheets across the mid plane of the combustion chamber by one cylindrical and one spherical lens. The laser sheet thicknesses were measured and found to be 250 μ m. The pictures were taken perpendicular to the laser sheet. With this camera, the development of the flow can be observed using various delays between the start of the piston movement and the triggering of the laser pulses. A specific time controller was used for pulsing the lasers and triggering the camera. To capture flow images, an acquisition system (frame grabber) is synchronised with the laser pulses. In the frame grabber memory, the images are digitised in a 756x581 points format with 256 grey levels.

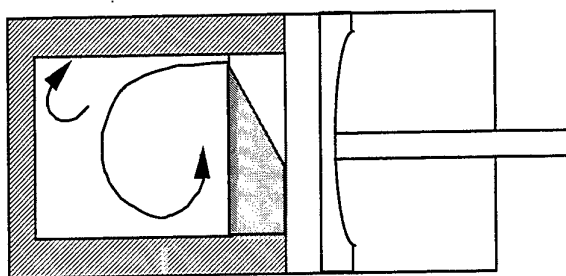


Fig. 1. Schematic of the combustion chamber

The movies were taken with a high speed Cordin camera. With this system we can follow the evolution of the flow with time for each cycle. To extract quantitative information from laser sheet tomography records, a high resolution film acquisition device has been used. A film scanner connected with a Macintosh computer digitises each film picture. This device is able to retain the high photographic film resolution and thus provides a powerful means for image processing. The light source is a copper vapour laser. It delivers pulses at an adjustable repetition rates up to 10KHz. The laser beam is focused with spherical and cylindrical lenses to produce a 600 μ m thick laser light sheet across the mid plane of the combustion chamber.

2.3 Cross-correlation PIV algorithm

An in-house developed algorithm (V2IP) which is based on the cross-correlation function is used to calculate the average displacement of local groups of particles in consecutive images. In this case, the flow exposures are stored on dissociated supports. The images are scanned by moving the same two windows across each field. Contrary to auto-correlation, a single peak, representing the location of the maximum of correlation is distinguished. The maximum location gives the average particle displacement between the

two exposures within the interrogation windows. The correlation peak position is determined by using a Gaussian subpixel analysis. Thus, this technique does not introduce a displacement ambiguity and resolves the very low velocity, including zero displacement. Consequently, the cross-correlation method is very adequate to resolve the structure of high speed flows and for three-dimensional flows such those found in an internal combustion engine. A detailed description of the cross-correlation treatment method used here is given in Rouland *et al* (1994).

3. RESULTS AND DISCUSSION

The intake slot (3mmx60mm) is located on one of the four corners of the chamber as depicted in figure 1. This special inlet configuration was used to obtain a rotating flow. In these experiments, the piston, in compressing the seeded air, generates a jet in the chamber. The structure of the flow is a result of the interaction of the intake jet with the chamber walls. Firstly, the jet flow is directed tangentially to the first wall and then deflected by the other walls of the chamber. The interaction of the jet with the wall produces a complex structured flow including two pairs of counter-rotating vortices shown schematically in figure 1. The first one occupies the entire chamber, and the second is located in the corner of the chamber.

The aspects of flow were examined for two different sizes of observation. First, the experiment was performed with a field of view 60x90mm corresponding to an overview of the flow field in the combustion chamber. A more detailed view on the corner of the chamber 20x30mm reveals the existence of a corner vortex rotating in the opposite direction to the principal vortex. This corner vortex seems to play an important role in the development of the flow in the combustion chamber. PIV is performed at a precise time after the piston departure ($t=100\text{ms}$). It is important to understand the dynamic behaviour of this kind of unsteady flow. The temporal evolution of flow during each cycle will be investigated by means of high speed laser tomography combined with cross correlation PIV. The results are given in section 3.4. The data for these experiments were taken at the later stage (160ms after the piston departure) of the development of the flow because of the magnitude of the velocities in the flow and the limited repetition rate of the laser.

3.1 Cyclic variations of the flow

A series of velocity vectors fields was provided and some typical ones are reported in figures 2a-c.

These figures show three selected examples of the instantaneous velocity vector fields taken at $t=100\text{ms}$. The images corresponding to these results are taken on the symmetry plane of the chamber. The origin of the coordinates is located at the corner of the chamber in the symmetry plane. The sampling window had a size of 32 by 32 pixels (4mmx4mm) and was overlapped by 50% with the next window.

As illustrated in these examples, the dominant feature of the flow field is a strong well defined vortex which is significantly different from cycle to cycle. In particular, the instantaneous centre of rotation, the size and the shape of the vortex change from one experiment to the next. Fig 2-d shows an ensemble averaged velocity field. The ensemble averaged velocity shows a smoother distribution than the instantaneous velocity. By averaging the data, the detailed structure that can be found in the instantaneous flow field such as in figures 2a-c is lost. So, it is not safe to characterise the flow by ensemble averaging velocity, particularly when the nature of the structures in the flow is not repeatable. This further justifies the importance of using the PIV technique in the study of the unsteady flows. It is necessary to analyse engine velocity data on an individual cycle basis, because the pattern in any particular cycle can be responsible for some variations in the time necessary to burn the charge in the combustion chamber.

The cyclic variations can be observed on the locations of the centre of the vortex. We have used an algorithm to find the centre of the vortex. This algorithm is based on a comparison with a pure solid body rotation model. Figure 3 shows that the spatial locations of the vortex centre for the instantaneous velocity fields are highly dispersed.

As an indication of vortex intensity, the total angular momentum of the flow about the centre of rotation is adopted. The vortex intensity was calculated with respect to a reference point which is the centre of the vortex. The vortex intensity was determined as follows :

$$R = \frac{\sum_{i=1}^n \vec{r}_i \times \vec{v}_i}{\sum_{i=1}^n \vec{r}_i \cdot \vec{r}_i}$$

Where \vec{r}_i is the distance between the centre of the vortex and the measurement point, \vec{v}_i is the velocity vector and n is the number of the measurement point in the velocity field. Figure 4 shows the vortex intensity for various cycles. The comparison between the cycles indicates a constant value of the vortex intensity. This

means that variations observed on the vortex centre had a slight effect on the vortex intensity. At the present time, the origin of these variations is difficult to explain and the basic mechanisms that lead to cyclic variations are not well understood. Reynolds (1980) suggested that the recirculating flows of this type are usually sensitive to small variations in the flow and hence there are probably substantial cycle-to-cycle

flow variations. In our experiments, the cyclic variations can be explained by the fact that there are probably small differences at initial conditions and boundary conditions (see section 3.3) between individual cycles and there may be other physical effects that magnify these small differences considerably.

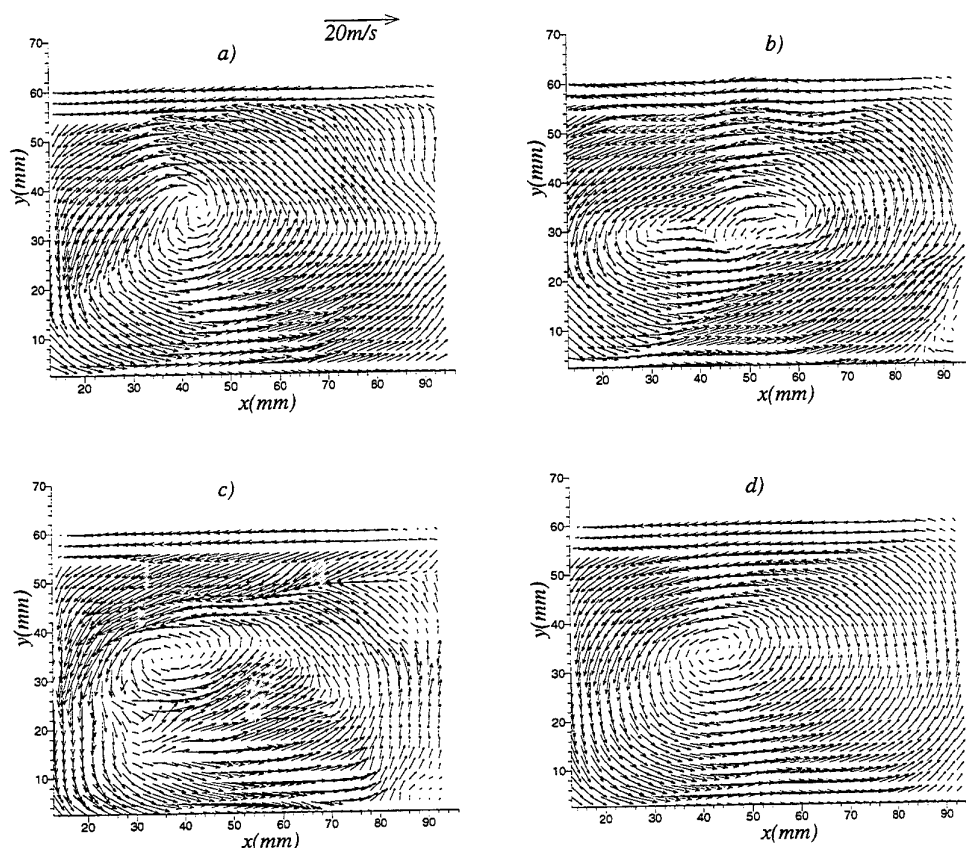


Fig. 2. Examples of instantaneous (a-c) and mean (d) velocity fields, $t=100\text{ms}$

For each velocity map, a single mean and rms velocity representative of the overall flow were calculated and presented in figures 5 and 6. The figure 5 show that the two component of the global mean velocity fluctuates around the value zero. The level of radial fluctuations (figure 6) is lower than of the axial ones. We note the slight variations of these parameters from one cycle to another.

3.2 Turbulence kinetic energy

The rotating flows are characterised by the breaking up of the main vortex (tumble) into smaller structures during the compression stroke. By this process, the rotational energy of the tumble is

transferred into turbulence. In our device, we cannot simulate the compression stroke and consequently, the turbulence in the combustion chamber is generated in the induction process by the shear layers created by the jet and by other regions such as the impingement of the jet on the chamber walls.

In engines the level of the turbulence depends on the turbulence definition. The easiest definition of turbulence is based on simple averaging : the velocity field is measured in various cycles at the same time; the average over many cycles is determined; the turbulence intensity is evaluated as the difference between the cycle-resolved and the mean velocity field. The use of this definition can overestimate the

turbulence level in non-stationary flows, since cyclic variations may be included in velocity fluctuations.

In order to separate cyclic variability and velocity fluctuations associated with turbulence dissipation, it is necessary to separate the high and low frequency components of the velocity field from the single image. The method used here consists of determining a local average over a square window in the spatial domain at each grid point of the instantaneous flowfield. The low-pass filtered velocity distribution was subtracted from the instantaneous velocity distribution, resulting in a high-pass filtered velocity. In this experiment, the effect of changing the size of the window on the flowfield has been examined. The size of the average window is chosen to be 8mm.

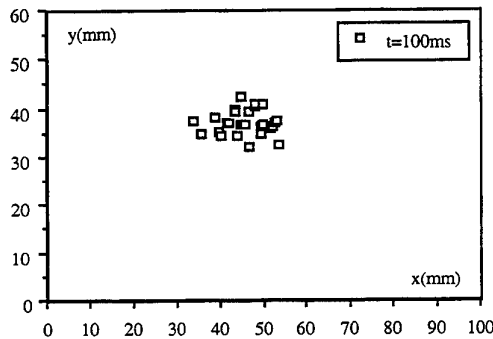


Fig. 3. Locations of the instantaneous vortices centre.

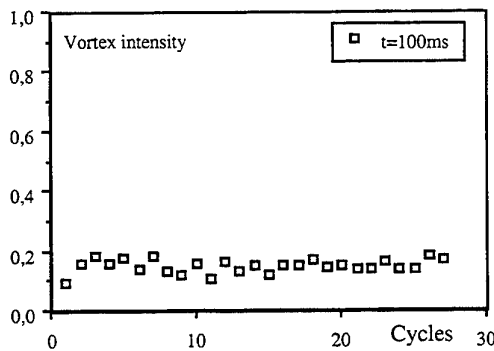


Fig. 4. vortex intensity for different cycles.

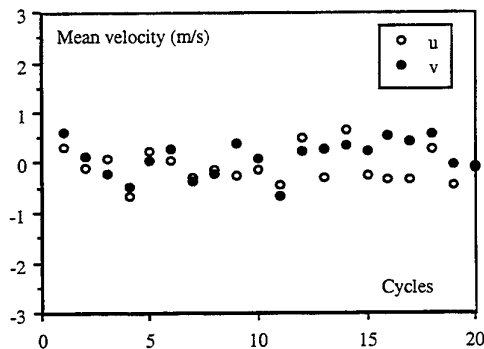


Fig. 5. Global mean velocity for different cycles

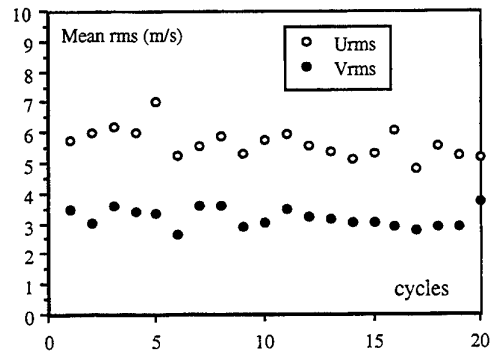


Fig. 6. Global rms for different cycles

Figures 7 and 8 show respectively the distribution of the intensity of turbulence for high and low frequency component of the velocity. The turbulence is defined as :

$$I_t = \frac{\sqrt{u'^2 + v'^2}}{\sqrt{u^2 + v^2}}$$

Where the u and v denote the components of the velocity. The distribution corresponding to low frequency component of the velocity (figure 7) exhibits a zone of "higher turbulence" levels which is located near the centre of vortices where the velocity is small, i.e. in a zone where the cycle-to-cycle variations are important. The figure 8 shows that the intensity of turbulence corresponding to high frequency component of the velocity is "uniformly" distributed within the field.

As for the LDV measurements, the use of filtering technique involves the selection of the filter (size of the averaging window) like the cut-off frequency in the frequency domain. For this reason no attempt is made in this study to extract a so called "true" turbulence and there is no doubt that high resolution PIV measurements will be interesting for extraction of small scales. This can be performed with a high resolution camera (1000x1000 for example).

3.3 Corner vortex

In our experiment, the corner vortex is one of the factors contributing to cycle-to-cycle instabilities with its effect on the principal flow (central vortex). The existence of a corner vortex flow within an engine cylinder was first observed by Tabaczynski *et al* (1970) in water flow, who concluded that the vortex is

generated by the scraping off and rolling up of the boundary layer on the cylinder wall by the piston crown. The study reported here focuses on instabilities accompanying this vortex.

Figure 9 shows three instantaneous velocity fields at $t=100\text{ms}$. The ordinate and abscissa origin is at the corner of the chamber on the symmetry plane. It corresponds to figure 1. The size of the observation field is $20 \times 30\text{mm}$. The sampling window had a size of 32 by 32 pixels ($1.4\text{mm} \times 1.4\text{mm}$) and was overlapped by 50% with the next window.

From these figures, it can be noted that the substantial visual differences between cycles in corner vortex concern the size, shape, and location of vortex centre. In particular, we can observe on fig 9-c that there is no apparent well defined corner vortex flow such as the ones observed for the other two cases. It should be noted that this disappearance of the corner vortex existed in many runs (not shown). Two possible explanations for this behaviour are : First, the corner vortex was not yet formed. Second, the corner vortex flow structure was not always stable and sometimes broke up under certain conditions soon after it had formed. This instability generated a more complex 3D flow structure as can be seen the figure 9-c and seems to greatly affect the centre location, the size and therefore the intensity of the principal flow.

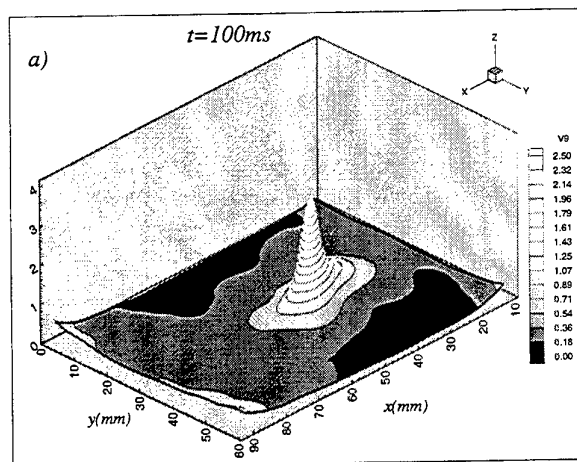


Fig. 7 . Low-pass filtered turbulence intensity

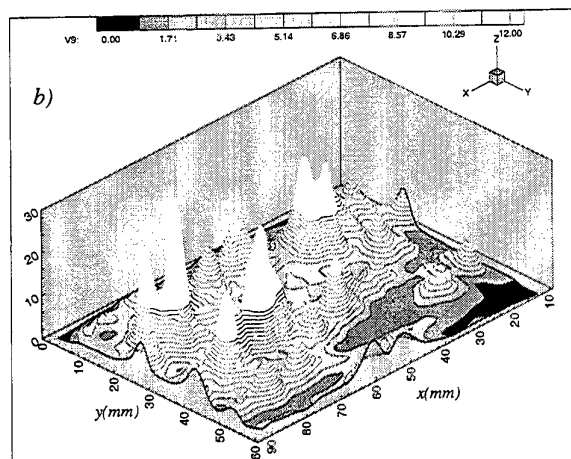


Fig. 8. High-pass filtered turbulence intensity

It is of some importance, of course, to understand the dynamical behaviour of the corner vortex, its interaction with the principal flow and its interaction with the walls of the chamber. A first way to answer this question is through a knowledge of the whole time history of the flow with a good spatial and temporal resolution in order to evaluate information on how the corner vortex motion changes during one complete cycle if possible or during a characteristic time corresponding to the flame duration (5 to 10ms). Unfortunately, the copper vapour laser used in this study does not permit this, due to its limited repetition rate (10KHz). With the arrival of higher repetition rate copper vapour lasers (up to 40KHz), flows of this type can be examined with an excellent temporal resolution. Consequently, the temporal evolution presented in this study concerns only the principal flow (central vortex) at its late stage of development.

3.4 Temporal evolution of the flow

Due to the unsteadiness of this flow in the combustion chamber, it is important to know the whole time history of the flow field. In this case the high speed version of PIV is used. The camera speed used in this experiment resulted in a time of about $125\mu\text{s}$ between consecutive images. Pairs of images on the film are processed to evaluate information on how the flow field is changing. The sampling window had a size of 64 by 64 ($1.8\text{mm} \times 1.8\text{mm}$) and was overlapped by 50% with the next window. This bigger size of correlation window was chosen because of both the higher velocities occurring at this time and the limited time between consecutive images.

As mentioned before, in our experiment the vortex was not compressed, so it continued to rotate until it broke up. These results were obtained to study the

persistence of the vortex set up in the combustion chamber by the intake jet. The results of the flow studies consist of a series of films. For these experiments, the field of view is limited to 40x50mm around the centre of the chamber. We present here a small example of data obtained by this technique. The results reported in this section are excerpts from a film (the film contains 52 images) of the flow field which describe the flowfield in its later stages. Figure 10 presents the temporal evolution of the instantaneous velocity distribution taken at $t=160\text{ms}$ after the piston start movement. At this time, there is no intake jet flow

only the residual angular momentum of the vortex. We can observe on this figure that :

- the angular momentum of the vortex is so high that this large flow structure remains active when the piston is stopped.

- for the same cycle, the evolution of the vortex is low with respect to the scale of the combustion duration. A small precession movement can be observed but for the time range of few milliseconds, it signifies that for each individual cycle the position of the vortex could be considered steady but different from one cycle to another. The corner vortex which is also different could be limited to the steady position of the vortex.

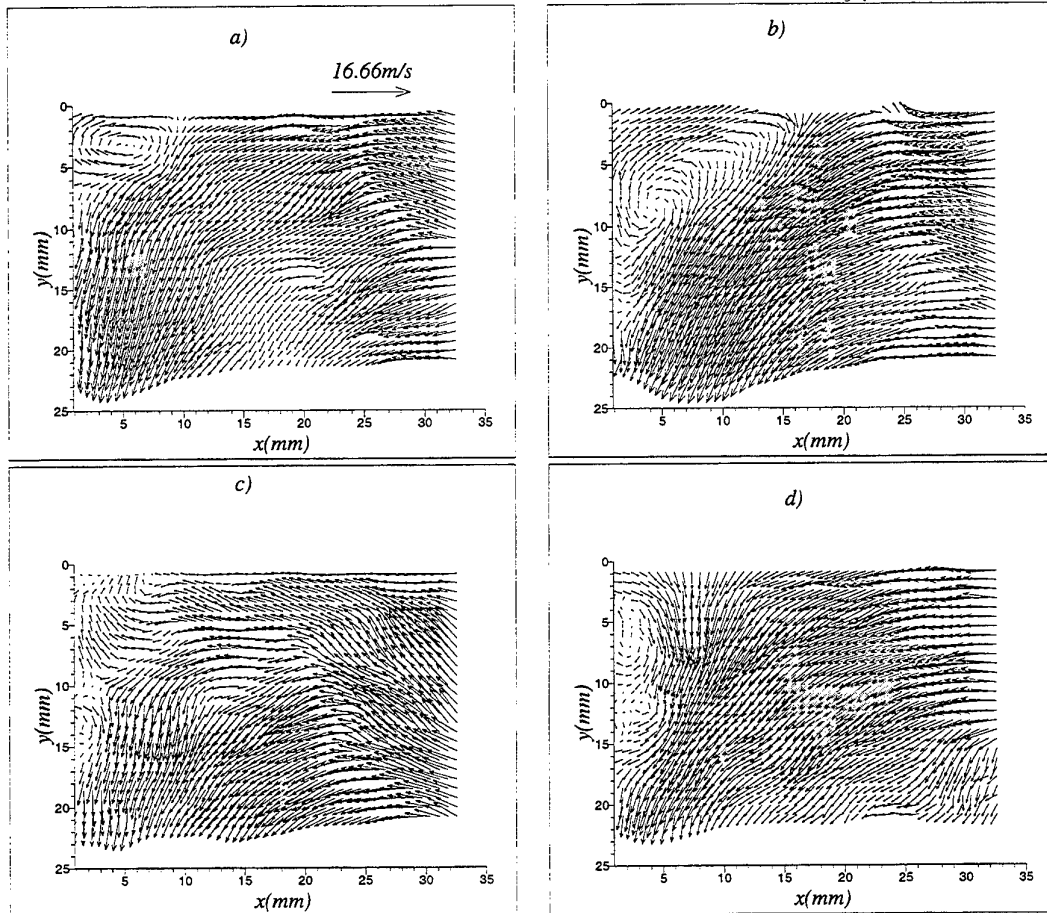


Fig. 9. Instantaneous velocity fields , corner vortex à $t=100\text{ms}$

4. CONCLUSION

This study presents detailed measurements of a rotating flow generated during the induction process in a piston cylinder assembly. The investigation of the flowfield was performed using cross-correlation particle image velocimetry. The main conclusions of this study can be summarised as follows :

- cyclic variations of the rotating flow were examined by comparing several instantaneous distributions from the same experimental conditions.

- the flow motion is dominated by a complex flow including two pairs of counter rotating vortices.

- the comparison between the cycle-resolved and the ensemble averaged flows shows that the use of an ensemble averaging in order to characterise the flow is unsafe, principally when the flow is not repeatable.

-the low-pass filtered intensity of turbulence shows a maximum near the centre while the high-pass filtered intensity of turbulence is uniformly distributed on the flow field.

-the flow structure of the corner vortex is inherently unstable and breaks up under certain conditions. This instability must be analysed through the temporal evolution of the velocity field during each cycle.

-the unsteady and non-repeatable nature of the engine flow studied favours the use of PIV measurements.

Nevertheless, the PIV does not yet offer the required time and spatial resolution necessary for the description of the turbulence field. A better understanding can be obtained with a time-resolved PIV. For this purpose a high frequency repetition rate

laser is needed (100KHz). Such value can be expected with the evolution of the copper vapour laser.

ACKNOWLEDGEMENTS

The authors would like to gratefully acknowledge the financial support provided for this work by ARC CNRS/ECOTECH/GIE PEUGEOT and RENAULT.

REFERENCES

Daily, J.W. 1988, Cycle-to-cycle variations: a chaotic process ?. Combustion science and technology, vol. 57, pp 149-162.

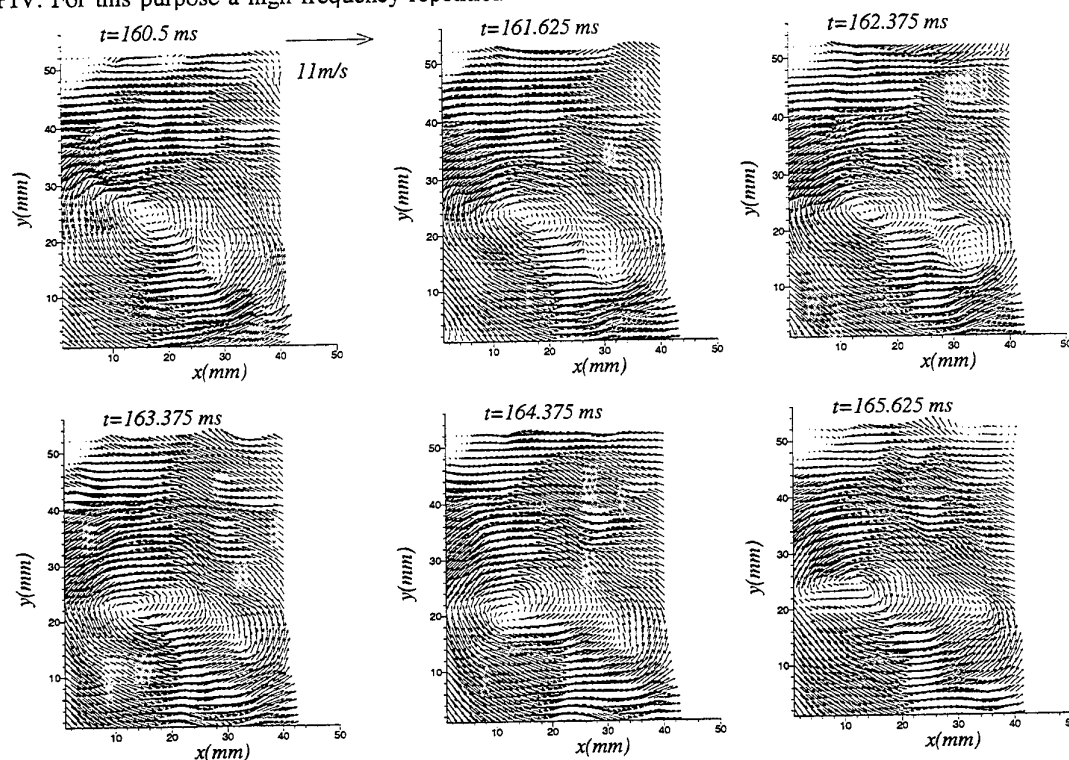


Fig. 10. Temporal evolution of the velocity field

Lecordier, B., Mouqallid, M. & Trinité, M. 1994a Simultaneous 2D measurements of flame front propagation by high speed tomography and velocity field by cross-correlation. 7th International Symposium on Applications Of Laser Techniques to Fluid Mechanics , Volume 1, pp 15.2.1, 15.2.8

Lecordier, B., Mouqallid, M., Vottier, S., Rouland, E., Allano, D. & Trinité, M. 1994b, CCD recording method for cross-correlation PIV development in

unstationary high speed flow. Experiments in Fluids, 17, 205-208.

Marc, D., Boree, J., Bazile, R. & Charnay G. 1997, Tumbling vortex flow in a model square piston compression machine : PIV and LDV measurements. SAE paper n°972834.

Mouqallid, M., Lecordier, B. & Trinité, M. 1994, High speed laser tomography analysis of flame propagation in a simulated internal combustion engine -applications to nonuniform mixture. SAE paper n°941990.

Nino, E., Gajdeczko, B.F. & Felton, P.G. 1993, Two-color Particle Image Velocimetry in an engine with combustion. SAE paper n°930872.

Reuss, D.L., Kuo, T.W., Khalighi, B., Haworth D. & Rosalik, M. 1995. Particle image velocimetry measurements in a high -swirl engine used for evaluation of computational fluid dynamics calculations. SAE paper n°952381.

Reynolds, W.C. 1980, Modelling of fluids motion in engines-An introductory overview. Combustion modelling in reciprocating engines, eds. Mattavi, J.M., and Amann, C.A., Plenum Press, pp. 99-124.

Rouland, E., Vottier, S., Lecordier, B. & Trinité, M. 1994, Cross-correlation PIV development for high speed flow with a standard CCD camera. The institute of Mechanical Engineers city, University of London

Rouland, E., Trinité, M., Dionnet, F., Floch A. & Afif, A. 1997, Particle image velocimetry measurements in a high tumble engine for in-cylinder flow structure analysis. SAE paper n° 972831.

Tabaczynski, R.J., Hoult, D.P. & Keck, J.K. 1970, High Reynolds number flow in a moving corner. J.Fluid Mech., vol 42, pp 249-255.

VISUALISATION AND PIV-MEASUREMENTS INSIDE THE INTAKE PORT OF AN IC-ENGINE

G. Rottenkolber, K. Dullenkopf and S. Wittig

Lehrstuhl und Institut für Thermische Strömungsmaschinen (ITS)
Universität Karlsruhe
Germany

ABSTRACT

Improvements in fuel mixture preparation of modern IC-engines are only possible by a better and more detailed understanding of the basic processes taking place inside the intake port of the engine especially at cold start conditions.

To analyze global spray parameters like spray tip penetration and spray cone angle visualization of the fuel spray was done outside the engine. The evaluation of this parameters was automated by means of a versatile programmable software for image analysis. The influence of different injection angles and air flow velocities on the spray distribution was observed inside the intake manifold and the cylinder. Furthermore, the visualized effects were correlated to unburned hydrocarbon (HC) emission measurements.

To provide more detailed and quantitative information about velocities of the fuel droplets and the intake air flow particle image velocity (PIV) measurements were done. With this technique typical effects like droplet wall interaction or air flow vortices could be detected.

1. INTRODUCTION

From statistics it is well known that about 70% of the journeys for private transport are less than 10 km. Furthermore, in the first 60 to 80 seconds of driving 70% of the whole emission is produced. The requirement of meeting the more stringent emission standards for automotive internal combustion engines under cold start conditions has initiated a comprehensive effort to examine the elements of the engine that contribute to emission

formation. In this respect fuel mixture preparation, as one of the key elements, has gained special interest. As pointed out by numerous authors (e.g. Zhao *et al.* 1995) a further reduction of emissions will only be possible through an enhanced understanding of the basic processes of fuel preparation in the intake port and the cylinder.

The first stage of liquid fuel mixture preparation is the atomization of the fuel into a spray. Typical modern instruments widely used for spray analysis are diffraction instruments, laser light sheet techniques (LLS, PLIF) (Wensing *et al.*, 1997 and Wensing *et al.*, 1998), phase doppler instruments (PDA) (Kirwan *et al.*, 1989 and Amer *et al.*, 1995) and more recently particle image velocimetry (PIV) (Brand and Merzkirch, 1994). Great efforts had been made to reduce droplet sizes by using for example air-assisted, heated vaporizing, piezoelectric or ultrasonic vibration injectors (Namiyama *et al.*, 1989), Harada *et al.*, 1992 and Saito *et al.*, 1993). Although the engine performance is influenced by the spray characteristics, precise correlations between spray parameters and e.g. transient response or HC emissions do not exist. One reason is, that injection parameters including mean drop size, spray momentum, spray cone angle and pulse-to-pulse variability, do not give sufficient information to describe the complex phenomena inside the intake port. Furthermore, the intake manifold geometry needs to be well matched to the injection timing, the injector position and the injection angle. The whole process is an unsteady and very complex combination of spray, geometry and aerodynamic parameters.

In general the amount of HC emissions increases if the fuel is injected when the intake valves are open. On the other hand the

transient operating performance is improved in some cases. With increasing drop sizes higher amounts of HC emission occur during open-valve injection, while during closed-valve injection the drop sizes do not affect emissions and performance. In both cases, open- and closed-valve injection, wall wetting and built up of wall films deteriorates transient operating performance and increases HC emissions (Yang *et al.*, 1993, Alkidas, 1994 and Daniels and Evers, 1994).

In the present paper the effects of injection timing and spray angle on the fuel distribution inside the intake port and the cylinder is shown by means of LLS and PIV. Comparisons are drawn between the visualized effects, HC emissions and in-cylinder pressure measurements (*Institut für Kolbenmaschinen, Universität Karlsruhe*).

2. EXPERIMENTAL EQUIPMENT

In continuing our effort to study injection concepts for IC-engines, previously published by Wittig *et al.* (1996), Samenfink *et al.* (1996) and Elsässer *et al.* (1997), the intake port of a real engine was modified to study the fuel system at various engine conditions including cold start. In order to achieve good optical access the cylinder head of a four cylinder engine was cut off in a plane through the middle of the intake port of the outer cylinder. Based on original CAD data the inner contour of the missing part was then machined from acrylic glass and fitted to the cylinder head, as can be seen in Fig. 1.

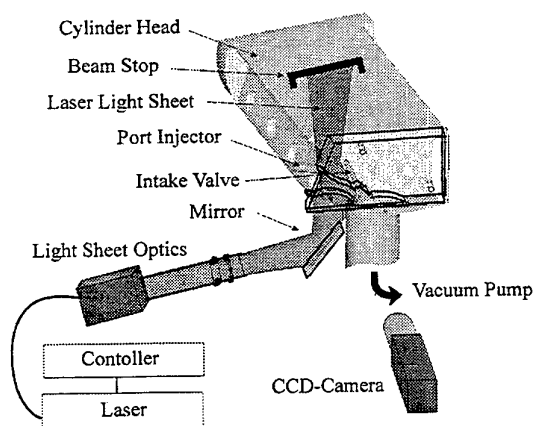


Figure 1: Experimental setup for visualization and PIV measurements

Fig. 1 also shows the setup of the optics for visualization and PIV measurements. To generate the light sheet a Copper Vapor Laser CVL (Oxford) was used. The CVL is a pulsed laser with a pulse frequency up to 40 kHz and a pulse duration between 10 and 40 ns. As detector a DoubleShutter CCD-camera (PCO) with high resolution (1280x1024) and 12bit dynamic range was used for both type of measurements. Coupled trigger and phase shifter units allowed independent and flexible control of injection, laser, and camera timing in order to synchronize the exposure with the injection.

3. VISUALISATION

The high temporarily and spatially resolved results from the visualization yield global information on the propagation characteristics of the fuel spray. Because of the strong cycle to cycle variation (see Fig. 2 right side) 100 single exposures had to be analyzed statistically to obtain a more general impression of the spray. The analysis of the images was automated by means of the programmable software OPTIMAS. First of all reflections originating from scattered light at the walls were reduced by subtracting a background image. By means of setting a certain threshold, calculated from a part of the image without any droplet information, the background noise was separated from the light scattered by fuel droplets. The probability density distribution was then calculated by adding 100 binary images. Fig. 2 shows two single shot exposures and the resulting probability density distribution of an injection in still air outside the intake port.

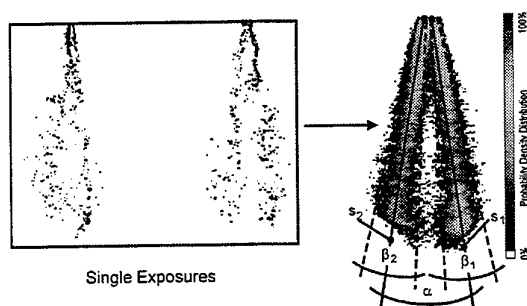


Figure 2: Probability density distribution of the spray in still air outside the intake port

With the density distribution spray parameters like spray tip penetration s , spray cone angle β and the angle between the two spray axis α could be calculated automatically. Before starting the calculation the points of injection had to be fixed. The automated process began with determining the edge of the spray and the intensities of the density distribution. The program stored these values in a three dimensional array. By means of straight lines of regression distances and angles could be calculated.

The results of the time resolved measurements are shown in Figure 3.

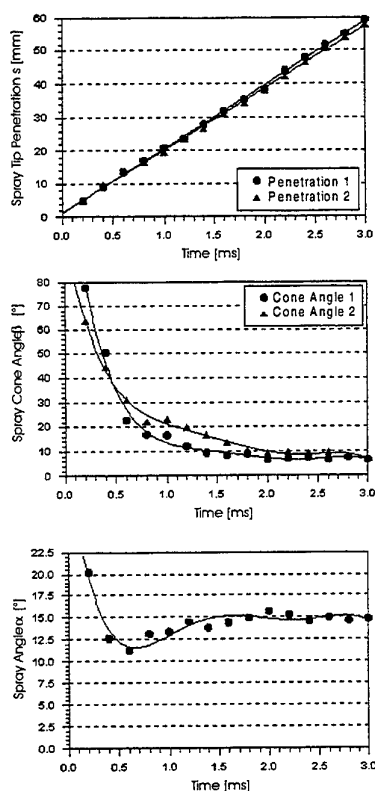


Figure 3: Spray characteristics

The three spray characteristics mentioned above are shown with the time after the beginning of injection. The spray tip penetration increases linearly with the injection time. Thus, because of the high initial momentum of the drops, the velocity of the spray tip is constant throughout the observed time span. The two spray angles remain constant after a setting time of about one millisecond after injection start. This kind of basic tests performed on a separate test bench in still air provided important information for a

first evaluation of the mixture formation process inside the intake port of a real engine.

In a second step the spray distribution was investigated inside the intake manifold and consequentially inside the cylinder, too. The evaluation of the probability density distributions was carried out automatically in the same way as described above. It is remarkable that the amount of reflections inside the intake port was very high. Therefore removing of the reflections by subtracting a background image was of great importance. Figure 4 shows an exemplary result for closed-valve injection at three different angular positions of the injection nozzle.

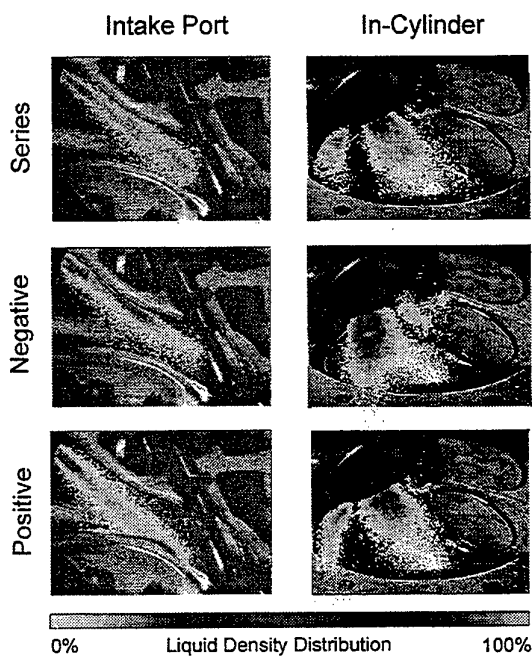


Figure 4: Closed-valve injection

The top images show the liquid density distribution of the spray in the series production engine. The fuel is accurately sprayed to the intake valves. Even minimal deviations of the angular position with respect to the series angle are leading to massive droplet impact on the intake manifold walls. Under conditions as shown in the lower images more than 40% of the fuel mass is stored in the liquid films (Samenfink *et al.*, 1998). This results in a longer fuel transport time and therefore a decreasing transient response (Alkidas, 1994). The effect on the fuel distribution inside the cylinder is evident as well. For the series angle the fuel penetrates into the cylinder centrally without wetting the spark plug or the cylinder walls extensively.

For the „positive“ and the „negative“ angle wall wetting takes place, but the amount of fuel in liquid films is moderate.

The situation changes completely, if the fuel is injected when the intake valves are opened. The image series in Figure 5 shows the probability density distributions of the spray during open-valve injection. Again the angular position of the injection nozzle was varied in the same way as shown in Figure 4.

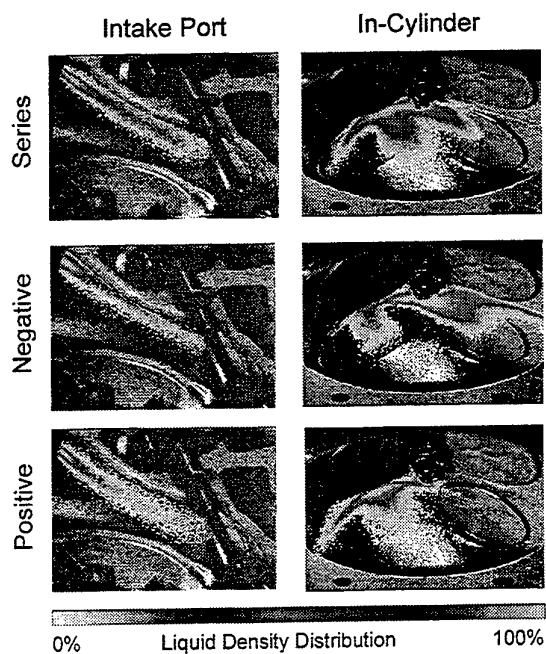


Figure 5: Open-valve injection

The fuel is pushed towards the upper manifold wall. Especially for the negative injection angle most of the droplets impact on the upper wall. Furthermore, inside the cylinder the intake air flow drags the droplets towards the spark plug and the outlet valves. In regards to wall wetting inside the port as well as inside the cylinder the positive injection angle is the most favourable.

In the following comparisons between the visualized effects, HC emissions and in-cylinder pressures (Figure 6) are drawn. The measurements were done at engine operating conditions of 2000 rpm and 4 bar average in-cylinder pressure. The values are demonstrated relative to the series angular position of the injector and closed-valve injection.

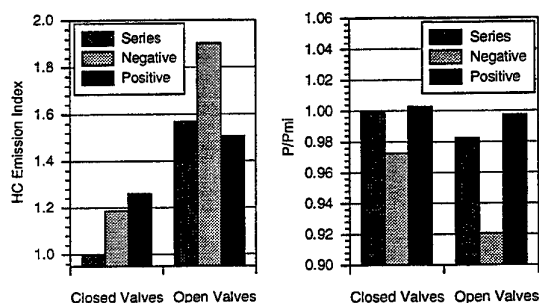


Figure 6: HC emission and in-cylinder pressure

During closed-valve injection HC emissions increase for any deviation from the standard injection angle. For the negative angle the HC emissions are higher and the in-cylinder pressure is lower than for the positive angle, because wall wetting in the area of the spark plug and the outlet valves is worse than liquid films in the intake valve region. If the fuel is injected when the intake valves are opened, again the negative angle shows dramatically high emissions and low pressures. The effects of wall wetting described above become stronger, because the intake air flow drags the fuel droplets to the upper manifold wall and inside the cylinder to the spark plug and the outlet valves. Therefore the HC emissions are generally higher during open-valve injection than during closed-valve injection.

4. PARTICLE IMAGE VELOCIMETRY

In order to gain more detailed and quantitative information on the flow and the velocity of individual droplets particle image velocimetry (PIV) measurements were performed with the same setup. PIV is a suitable technique to measure under highly unsteady conditions, because it records a 2D flow situation at one instance of time.

The double shutter camera allowed to get two consequential images with a short time gap of about 200 ns. Because the maximum pulse frequency of the laser (30 kHz) limited the image acquisition, the exposure timing had to be fitted to the laser frequency. Therefore, the dynamic range for the presented setup was about 40 m/s. The maximum detectable velocity depends on the offset controlled by the software. The spatial resolution depends on the size of the correlation spot, which had to

be 64 pixel to obtain a satisfactory correlation intensity. Due to the double shutter option, data acquisition and processing was possible using the cross correlation technique, that can handle lower quality images. For the evaluation of the measurements the PIV analysis software package VISIFLOW (AEA) was used. The post-processing of the vector plots was carried out by means of the programmable data base software ACCESS. To reduce cycle to cycle variations and to provide a more general result a statistical data reduction had to be done with the PIV vector plots. Therefore, the automation of the evaluation process with VISIFLOW and ACCESS was inevitable. Figure 7 demonstrates a phase averaged vector field from 100 individual exposures (top image) together with a single exposure of the droplet impact area at the lower wall.

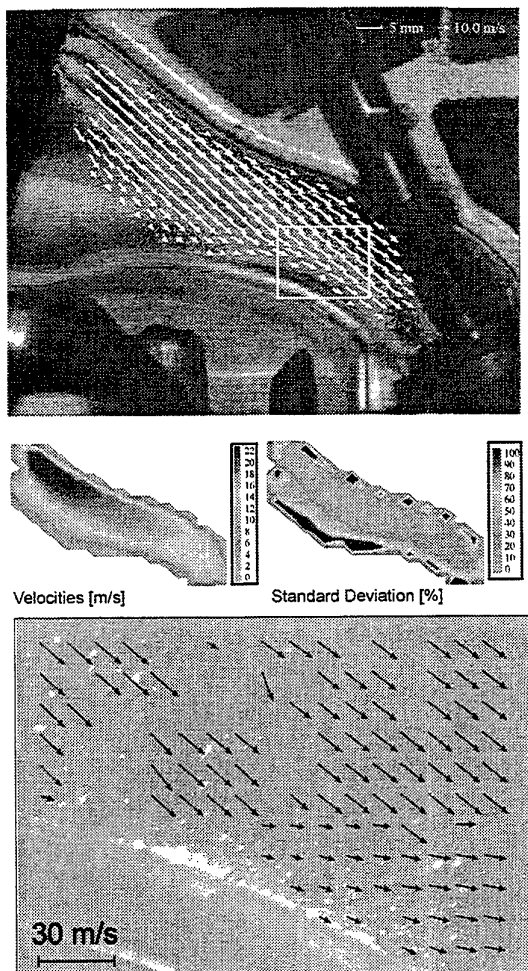


Figure 7: Averaged and individual droplet velocity distributions inside the intake port from PIV measurements

During fuel injection the intake valve was closed and the fuel nozzle was oriented at a positive angle. The droplets start off the injector at velocities of about 24 m/s. They are decelerated to about 20 m/s at the spray tip. Obviously, the droplets at the edge of the spray have lower absolute velocities with a higher standard deviation compared to the droplets on the middle axis. The direction of the vectors shows, that many droplets hit the wall on the bottom of the manifold. The area of impact was zoomed out (lower image of Fig. 7) to demonstrate droplet wall interaction. Under the presented conditions the momentum of the droplets was relatively high. Therefore, the droplets impacting the wall were destroyed and secondary droplets of smaller size and different trajectories were ejected (droplet destruction or splashing, see Samenfink *et al.*, 1998). The impact velocity was about 20 m/s and the average impact angle 35° , whereas the ejected droplets had velocities of about 13 m/s and an angle of 30° . From measurements of the primary spray the mean droplet diameter was known to be about $150 \mu\text{m}$. Velocities and angles measured with PIV did exactly match the values calculated with correlations from Samenfink (1998).

Especially during open-valve injection the influence of the air flow on the spray distribution was of particular interest. Therefore the intake air flow was seeded with small DES particles ($\text{SMD} < 5 \mu\text{m}$, Palas PIV-generator). Figure 8 shows a phase averaged vector plot of the air flow field from 100 individual exposures and a single exposure of the injector tip region.

The averaged vector plot on the right side demonstrates, that the air flow at the entry into the intake port was directed towards the upper wall, which corresponded to the measurements of the liquid phase. A conspicuous area was discovered in the region of the injector tip, where slow velocities had been detected. The single exposure vector plot on the left side of figure 8 shows a strong vortex because of a flow separation at the flange of the cylinder head. In the vortex and at the walls fuel could be accumulated, which affects the transient response of the engine.

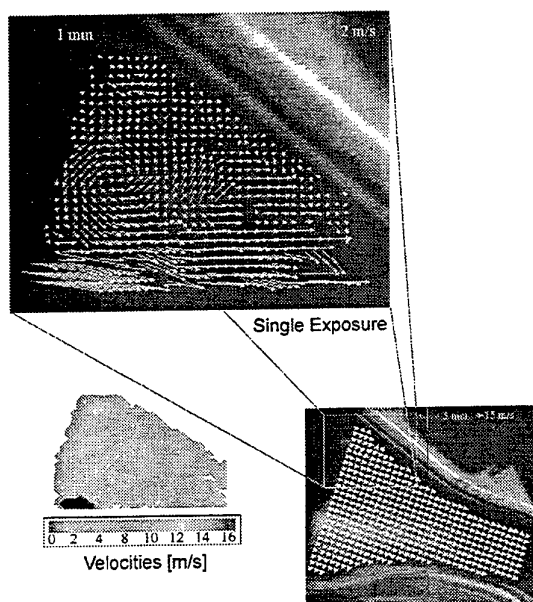


Figure 8: PIV measurements of the intake air flow

5. CONCLUSIONS

A further reduction of emissions especially at cold start conditions will only be possible through an enhanced understanding of the basic processes of fuel mixture preparation inside the intake port and the cylinder. Therefore visualisation and, to get more detailed information about droplet trajectories, PIV measurements were carried out under realistic engine like conditions.

By means of a laser light sheet technique and CCD-camera based image processing the two phase flow was investigated. The evaluation of fuel density distributions and spray parameters was automated by means of a programmable image analysis software. The post-processing of the PIV vector plots was improved and automated, too.

The influence of different injection angles and air flow velocities on the spray distribution and hydrocarbon emissions was observed inside the intake manifold and the cylinder. If the injection angle deviates from the series position and the fuel is injected when the intake valves were opened, intense interaction and of the spray with the wall and built up of wall films could be observed. Especially for the open-valve injection the fuel wets the inner cylinder walls at the critical area close to the outlet valves. Therefore the

HC emissions were always higher for open-valve injection compared to closed-valve injection. By means of phase resolved and phase averaged PIV measurements detailed and quantitative information about the trajectories of the fuel droplets and the intake air flow could be provided. Important phenomena like droplet wall interaction could be studied. The results from experimental investigations corresponded well with recently published correlations from Samenfink (1998). In the area of the injector a strong vortex was found. This vortex could lead to increased wall wetting near the injector and therefore to impaired transient response of the engine.

By means of these results together with some additional PDA measurements planned in the future analytical and numerical models and simulations will be evaluated and improved. In a joint project at the University of Karlsruhe together with the Institut für Kolbenmaschinen and sponsored by the Forschungsvereinigung Verbrennungskraftmaschinen e.V. (FVV) complementary investigations with a fired engine are under way to complete the study with combustion and emission measurements.

ACKNOWLEDGEMENTS

The assistance and the support of the *Forschungsvereinigung Verbrennungskraftmaschinen (FVV)* and the *Institut für Kolbenmaschinen, Universität Karlsruhe* are gratefully acknowledged.

REFERENCES

- Alkidas A. C., 1994, The Effect of Fuel Preparation on Hydrocarbon Emissions of a S.I Engine Operating Under Steady-State Conditions, SAE Technical Paper, No. 941959.
- Amer A. A. and Lai M.-C., 1995, Time-Resolved Measurements of a Transient Gasoline Spray, SAE Technical Paper, No. 950509.
- Brand A., and Merzkirch W., 1994, PIV applied to a Spray Jet, Part. Part. Syst. Charact., Vol. 11, pp. 156-158.

Daniels C. H. and Evers L.W., 1994, The Influence of Mixture Preparation on a Warm 1.9L Ford Engine, SAE Technical Paper, No. 940444.

Elsäßer A., Samenfink W., Ebner J., Dullenkopf K. and Wittig S., 1997, Dynamic of Shear-Driven Liquid Films, 7th international Conference Laser Anemometry Advances and Applications, Karlsruhe, Germany.

Harada K., Shmizu R., Kurita K., Muramatsu M., Makimura T., and Ohashi M., 1992, Development of Air-Assisted Injector System, SAE Technical Paper, No. 920249.

Kirwan J. E., Drallmeier J. A., Coverdill R. E., Crawford R. R., Peters J. E., 1989, Spray Characteristics of Throttle Body Fuel Injection, SAE Technical Paper, No. 890318.

Namiyama K., Nakamura H., Kokubo K., and Hosogai D., 1989, Development of ultrasonic Atomizer and its Application to S.I. Engines, SAE Technical Paper, No. 890430.

Saito A., Kawamura A., Tani T., Ogiwara Y., 1993, Analysis of spray Characteristics of Heated Nozzle for Gasoline Injection (1st Report, Observation of Nozzle Inside and Spray Shape), Proceeding of the 2nd ILASS-Japan Symposium, pp. 157-162.

Samenfink W., Elsäßer A., Wittig S. and Dullenkopf K., 1996, Internal Transport Mechanism in Shear-Driven Liquid Films, In: 8th international Symposium on Applications of Laser Techniques to Fluid Mechanics, Lisbon, Portugal.

Samenfink W., Elsäßer A., Dullenkopf K. and Wittig S., 1998, Droplet Interaction with shear-driven liquid films: Analysis of the Secondary Droplet characteristics, ILASS-EUROPE 98, Manchester.

Wensing M., Münch K.-U., Leipertz L., 1997, Characteristics and Application of Gasoline Injectors to SI Engines by Means of Measured Liquid Fuel Distributions, SAE Technical Papers, No. 972947.

Wensing M., Krämer H., Münch K.-U., Leipertz L., 1998, Mixture Formation and

Combustion of a Four-Valve SI Engine Investigated by Advanced Two-Dimensional Laser Measurement Techniques, COMMEDIA 98, Japan.

Wittig S., Elsäßer, Samenfink W., Ebner J. and Dullenkopf K., 1996, Velocity Profiles in Shear-Driven Liquid Films: LDV Measurements, In: 8th international Symposium on Applications of Laser Techniques to Fluid Mechanics, Lisbon, Portugal.

Yang J., Kaiser E., Seigl W. O., Anderson R. W., 1993, Effects of Port-Injection Timing and Fuel Droplet size on total and Specited Exhaust Hydrocarbon Emissions, SAE Technical Paper, No. 930711.

Zhao F.-Q., Lai M.-C., and Harrington D., 1995, The Spray Characteristics of Automotive Port Fuel Injection - A Critical Review, SAE Technical Paper, No. 950506.

Influence of Axial Compression on a Strongly Swirling Cylinder Flow

J. Keller[†], J. Volkert[†] and C. Tropea[‡]

[†] *Lehrstuhl für Strömungsmechanik, University of Erlangen-Nürnberg,
Cauerstr. 4, 91058 Erlangen, Germany*

[‡] *Fachgebiet Strömungslehre und Aerodynamik, TU Darmstadt,
Petersenstr. 30, 64287 Darmstadt*

Abstract

The behaviour of axially compressed in-cylinder swirling flow has been investigated in a rapid compression machine. The experiment represents an idealization of the flow field found in internal combustion engines. Laser Doppler measurements of all three velocity components were carried out for a variety of swirl numbers and compression rates. Results for two geometries, a flat cylinder head and a bowl-in-head geometry, will be presented. The experimental data serve as a reference for numerical simulations including direct numerical simulations (DNS) and numerical predictions utilizing Reynolds stress modeling (RSM).

1. Introduction

The importance of swirl effects upon the performance of I.C. engines has been documented by numerous investigations ([1],[2]). Especially in the field of D.I. engine development (both high-speed Diesel and D.I. gasoline engines), the properties of intake-generated swirl, its break down and interaction with squish effects and thereby its ability to generate or sustain turbulence during the compression stroke are of great interest. Without attempting to review all of the relevant literature a general distinction between experiments including the combustion process (fired engine studies) and those concentrating on fluid mechanical aspects (motored engines) can be made. While some qualitative conclusions about the effects of global flow patterns upon the combustion performance can be drawn from combustion experiments ([3]), detailed measurements of fluid flow in motored engines or more simplified test rigs contribute to understanding the basic aerodynamic effects, that is the evolution of large scale flow behaviour and turbulence, both of which directly influence mixture formation and combustion.

A considerable number of researchers have investigated swirl under idealized conditions ([1],[2],[4]). While the necessity of this type of investigation is

evident, a closer examination of past studies indicates that most have been performed with very specific and unique geometries (initial and boundary conditions) and are thus not very universal in their conclusions. Furthermore contradictory answers have been given to basic questions such as "Is turbulence enhanced or damped in the presence of swirl?", or "does swirl survive until top dead center of compression?" In light of these contradictory statements derived from previous experiments, a further simplification of the geometry and swirl process has been undertaken in this work in an effort to allow more general conclusions to be drawn - well-knowing that their pertinence to real engine geometries may be reduced.

This paper presents a simplified experiment looking at an idealized in-cylinder swirling flow generated by a rotating cylinder. After a period of constant rotational speed the cylinder is abruptly stopped and the decaying swirling flow is compressed by means of a hydraulically driven flat piston. The evolution of the flow field during the compression phase is observed by Laser Doppler Anemometry to describe the global flow behaviour and the turbulence field for a variety of swirl rates and piston velocities. Beside the experimental work being presented here, the long-term goal of the overall project focuses on the development and improvement of a numerical program based on Reynolds stress turbulence modeling capable of capturing the effects of rotation and compression. Once validated, this program can be applied to extended parametric studies and simulations of more complex geometries in the future. Thus, in addition to helping to understand the physical phenomena under consideration, the experimental data presented here can be considered as a reference data base supporting the development of turbulence models. This data is complemented by direct numerical simulation (DNS), representing an additional reference data base.

2. Experimental Apparatus

The rapid compression machine used to investigate the time-dependant behaviour of in-cylinder swirling flow under the influence of an axial compression has been described in detail in [5] and [6]. A brief summary of the experimental apparatus and its operation is given here to emphasize the most important features of the test rig. In order to avoid any influence of non-controllable inlet conditions (one could think of cyclic variability of valve motion) or pre-cyclic flow history (previous periods in periodically running machines) on the initial flow field, a one-shot experiment capable of generating an exactly reproducible inlet swirling flow was built. The initially axisymmetric in-cylinder swirl is produced by externally rotating the cylinder around its axis (spin-up phase). Thus the apparatus allows a well-defined adjustment of the initial swirl intensity through the rotation rate. Moreover, the initial flow structure does not depend on the swirl rate and can be considered as non-stratified in the axial direction, at least in the cylinder head ([6]).

Every experiment (or shot) consists primarily of two phases. The first is related to the generation of swirl in the cylinder; the second phase is a compression stroke performed by an axially driven piston after stopping the cylinder rotation.

As shown in Figure 2.1, the cylinder head (clearance volume, z_c) can easily be interchanged to allow the use of different head geometries. In the present study a flat cylinder head (FZK) and a bowl-in cylinder geometry (SZK) were used.

Although the major goal of the overall project was to study the influence of compression upon the in-cylinder flow, experiments were also carried out without compression as a reference (free decaying swirl, hereafter denoted as "spin-down"). The range of operating parameters for the swirl mode is characterized by the rotation rate of the cylinder (N_W). The motor used to drive the cylinder is capable of rotation rates up to $N_W = 3000 \text{ min}^{-1}$, with experiments being performed in the range $N_W \leq 1800 \text{ min}^{-1}$. The compression mode is characterized by two parameters, compression ratio and compression rate. The compression ratio, while adjustable through the clearance height, z_c , was fixed to a value of $\epsilon_c = 5.0$. The compression (or strain) rate S is defined as the instantaneous piston speed, v_p , versus the length of the current volume to be compressed (z):

$$S = \frac{1}{z} \frac{dz_p}{dt} = \frac{v_p}{z} \quad (1)$$

The hydraulic system allows experiments to be performed at constant S in the range of $0.0 \leq S \leq$

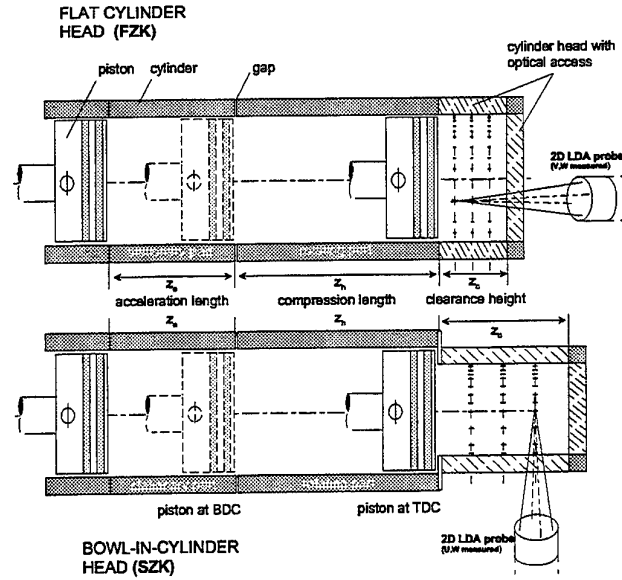


Figure 2.1: Experimental setup - geometry and LDA measurement configurations

11.5 Hz and measurements were carried out at $S = 0.5 \text{ Hz}$ and $S = 11.5 \text{ Hz}$. Note that a constant strain rate corresponds to an exponentially decaying piston velocity.

3. Measurement Equipment

The **Laser Doppler Anemometer** employed in the present study has already been presented in [5]. The essential specifications of the four-beam, two-component backscatter LDA are given in table 1.

2-COMPONENT-LDA PROBE			
BEAM SEPARATION:	$D = 22 \text{ mm}$		
NUMBER OF FRINGES :	$N_f = 9.96$		
FOCAL LENGTH f	120 mm		
	$\lambda = 488 \text{ nm} \quad \lambda = 514 \text{ nm}$		
INTERS. HALF ANGLE ϕ	5.237°	5.237°	
MCV DIAMETER d_{mcv}	$25.82 \mu\text{m}$	$27.22 \mu\text{m}$	
LENGTH OF MCV l_{mcv}	$281.65 \mu\text{m}$	$296.9 \mu\text{m}$	
FRINGE SPACING Δx	$2.67 \mu\text{m}$	$2.82 \mu\text{m}$	
MCV : MEASUREMENT CONTROL VOLUME			

Table 1: Specifications of the LDA probe

Oil droplets, produced in a pressure atomizer and injected through the gap (Fig. 2.1), with diameters of $d_p \leq 1 \mu\text{m}$, were used for seeding during the spin-up phase. The scattered light collected in backscatter mode is focused onto a graded index fiber and directed to color separation optics. Two photomultipliers are used to detect the signals. After passing the signals through a two-channel down-mixer and bandpass filters, counter processors (TSI 1980/1990) are used for signal processing.

4. Data Processing

In contrast to the processing of stationary data, the analysis of of instationary velocity time series cannot be reduced to a well-defined, generally applicable procedure. As discussed in the following, in many cases it rather depends, at least to a certain extent, on the physical process being investigated and sometimes requires a more or less arbitrary definition of turbulence. The procedure becomes even more complex if single-shot experiments or quasi-periodic flows, are considered.

In the present work, both aspects, instationarity and one-shot character have to be taken into account and therefore are discussed in the following.

Instationarity: Since a constant mean velocity does not exist, the separation of mean flow (\bar{U}) and turbulent fluctuations (u') in the sense of Reynold's decomposition $U(t) = \bar{U} + u'$ is not possible. A time-dependent mean (bulk) velocity $\bar{U}(t)$ must be derived by separating large scale motion from small scale turbulent velocity fluctuations. This process of **energy partitioning** implicitly requires a decision as to which part of the spectrum of the instantaneous velocity signal represents turbulence. It is easily understandable that any kind of separation of scales that cannot be related explicitly to some physical phenomenon (e.g. combustion related classification of turbulent scales) suffers from a lack of physical justification - the definition of turbulence becomes in a way arbitrary.

One-shot character: In order to build statistics around the mean velocity at a certain point in time (regardless of how the mean velocity is defined) the experiment has to be repeated several times with the data acquisition synchronized to the experimental program. Phase-synchronized ensemble averaging of all cycles can be used for statistical analysis, assuming that the mean flow behaviour is exactly reproduced from one shot to the next. If this assumption is not fulfilled, so-called cycle-to-cycle variations of the global flow structure cause an over-estimation of the turbulence intensities, even if they are not considered to represent turbulence in a physical sense. In such cases, cycle-resolved analysis is recommended if the in-cycle data rate enables the estimation of a bulk velocity evolution (within every single cycle). Without defining too precisely what is meant by turbulence, several researchers have tried to define and recognize which flow motions are to be attributed to turbulence and which to mean convection and/or cyclic variations. As mentioned before, the choice of an appropriate method should, whenever possible, be based on an underlying physical process which determines a "useful" separation of scales according

to their influence upon the phenomena investigated. However, in many cases such a physical justification of the separation of scales is not available - no generally applicable approach can be expected.

Restricting the discussion to one-point velocity time series, energy partitioning is mostly realized by filtering techniques applied in the time ([7],[8]) or frequency domain ([9],[10]), even if more elaborate decomposition schemes have also been developed ([11-13]).

The present work utilizes filtering techniques in both time and frequency space, including the application of different filters. Ensemble averaging and cycle resolved analysis were compared to quantify the effect of cyclic variability on the turbulence statistics. In the following a brief summary of the applied techniques is given.

ENSEMBLE AVERAGING (EA): A phase-coincident average over all cycles of the LDA velocity samples falling into a defined time interval Δt is computed. The mean velocity, denoted as W_{EA} , is considered as constant within the interval Δt resulting in a stair type curve $W_{EA}(t)$ as shown in Figure 4.1.

SMOOTHED ENSEMBLE AVERAGING (SEA): An important shortcoming of simple time window averaging as applied in EA appears as soon as steep gradients of the mean velocity occur within Δt . The assumption of constant mean velocity results in an overestimation of the turbulence intensity through summation of the velocity differences between the instationary velocity samples $W(t_i)$ and the constant value W_{EA} (Fig. 4.2). In order to avoid such false turbulence, smoothing of the mean velocity is applied, corresponding to the approach presented by Rask ([8]). The time window average W_{EA} is assigned to the center of the bin Δt and a spline interpolation is computed between successive center points to approximate the continuous behaviour of the bulk flow. In contrast to EA, an individual mean velocity W_{SEA} is now available at every point t_i .

CYCLE-RESOLVED SMOOTHED ENSEMBLE AVERAGING (CRSEA): The SEA procedure applied to individual cycles is denoted as CRSEA. Averaging the results from all cycles then gives the global mean and turbulence parameters. In contrast to SEA, cycle-by-cycle fluctuations do not contribute to the derived turbulence intensities.

CYCLE-RESOLVED FREQUENCY FILTERING (CRFF-i): While CRSEA presents a cycle-resolved time-filtering approach, CRFF-i stands for cycle-resolved analysis including filtering of the individual time series in spectral space. After reconstruction of the velocity signal by sample & hold interpolation and Fourier transformation of the velocity

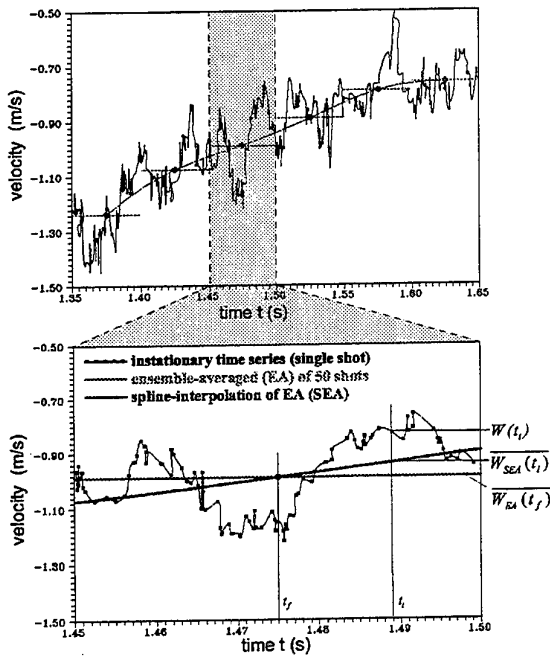


Figure 4.1: Typical velocity time series outlining different data reduction schemes

series, a filter function $H(f)$ is applied in the frequency domain. Inverse transformation of the filtered spectrum gives the bulk velocity evolution and the turbulence intensity is then derived in physical space corresponding to the procedure described above. Depending on what kind of filter is applied, the parameter "i" stands for one of the following: R (rectangular or top-hat filter), F (Fermi-Dirac type filter), G (Gaussian filter) or N (Nuttall-filter, series of weighted cosines)).

Before choosing a particular technique for further processing, the performance and characteristics of the different approaches will briefly be examined using data from the rapid compression machine.

Fig. 4.2 shows the mean swirl velocity with time for an initial rotation rate of $N_W = 1200 \text{ min}^{-1}$ and a compression rate of $S = 11.5 \text{ Hz}$ (FZK). Clearly all processing methods yield basically the same result. An exploded view of the same data, shown in Fig. 4.3 indicates that the top hat filter (CRFF-R) leads to signal oscillations in time domain, which in fact are artifacts of the specific filter.

The turbulent component of the swirl velocity is shown in Fig 4.4, evaluated using the various techniques. Clearly the non-cycle resolved techniques (EA, SEA) lead to much higher turbulence estimates due to cyclic variability of the large flow patterns as explained before.

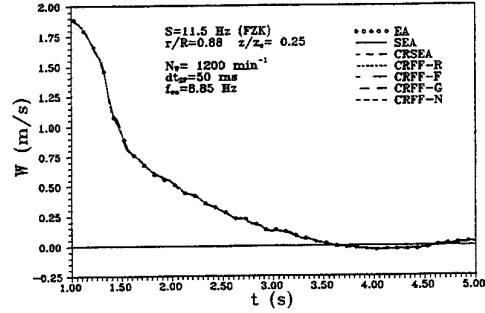


Figure 4.2: Swirl velocity evolution: results from different processing methods

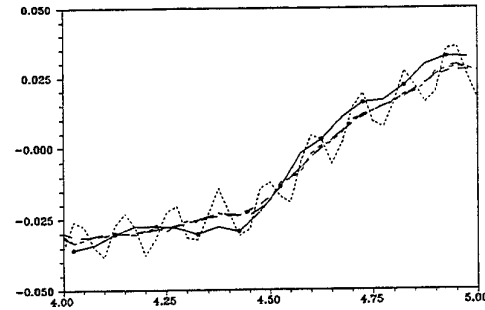


Figure 4.3: Exploded view of Fig. 4.2 showing oscillations in W when filtered in spectral space using a top-hat filter

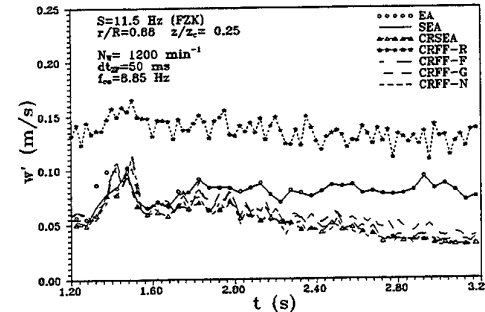


Figure 4.4: Fluctuating component of swirl velocity derived by different methods

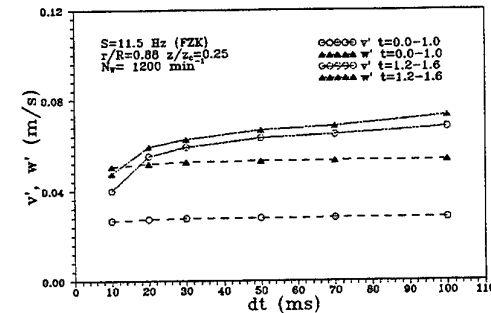


Figure 4.5: Time averaged velocity fluctuations as a function of the cut-off frequency

The cycle-resolved methods yield similar results with exception of the CRFF-R using a top hat filter, which shows unrealistically high RMS values due to the problem of oscillation in the mean velocity as seen before.

For further analysis the CRSEA approach is chosen, because of the following reasons:

1. Sudden changes" (sharp edges) in the bulk flow evolution, i.e. the sudden drop of W after stopping the cylinder rotation, are not well handled with frequency domain filters. Inevitably the sharp changes will be smoothed out. The time domain analysis allows such cases to be considered by aligning the time windows with the instant of change, e.g. the stopping instant of the cylinder rotation ([8]).
2. There are no significant differences in v' , w' compared with the other cycle-resolved methods.
3. It is computational easier to implement.

The effect of the cut-off frequency (expressed as time window size $\Delta t = 1/f_{co}$) on the turbulence levels v' and w' is shown in Fig. 4.5. As expected, the energy designated as turbulence decreases as the cut-off frequency increases. A sharp drop at $\Delta t = 20$ ms suggests that this might be an appropriate choice for subsequent processing, simply because it is a distinct and recognizable point in the curve.

5. Results and Discussion

To aid the interpretation of subsequent results, the (stationary) flowfield immediately prior to stopping the rotating cylinder is briefly described. The mean normalized tangential velocity is shown in Fig. 5.1 for three rotational speeds with comparison to computed profiles using the Reynolds Stress turbulence model. The deviation from solid body rotation is due to the stationary part of the cylinder and the stationary piston (Fig. 2.1). The computed flow field in the axial/radial plane is illustrated in Fig. 5.2 for the entire cylinder and Fig. 5.3 again demonstrates good agreement between measurements and computations for the axial velocity component at three axial stations accessible to LDA measurements.

5.1 Decaying Swirl during Spin-Down

As a reference, the time-dependent swirl during spin-down is examined in Fig. 5.4. The swirl decay is similar for all initial rotation speeds, except for $N_W = 300 \text{ min}^{-1}$. In this case the boundary layer of the tangential component reacts slower to the new wall condition, but more distinctive is the apparent development of stronger secondary flows. This is corroborated by both DNS ([14]) and RSM ([6]) computations. The data presented in Fig. 5.4 ap-

pears in the following figures denoted by SD (spin-down).

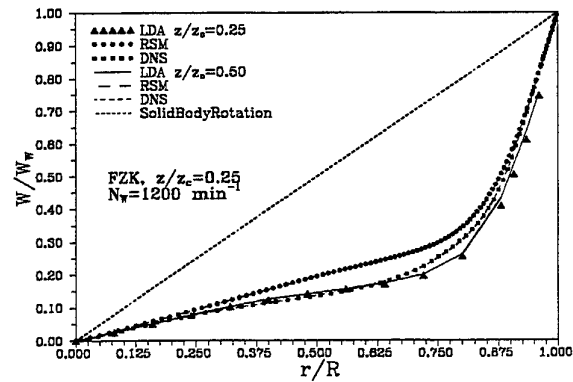


Figure 5.1: Swirl velocity profiles for different rotation rates - comparison of LDA, RSM and DNS results

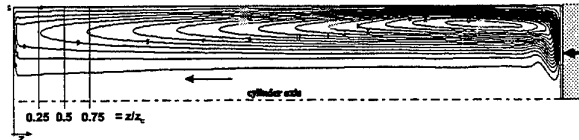


Figure 5.2: Streamlines documenting the secondary flow in the axial/radial plane of the cylinder

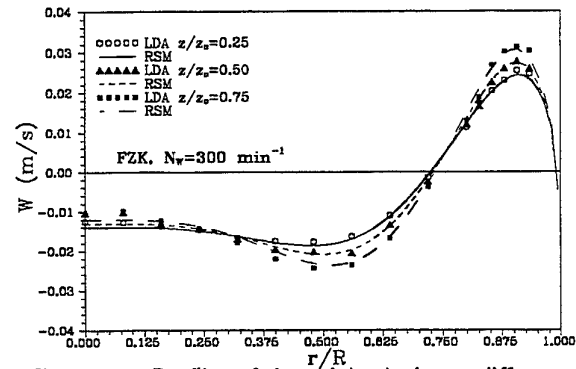


Figure 5.3: Profiles of the axial velocity at different axial positions

5.2 Influence of Compression upon the decaying Swirl

The swirl decay under compression is summarized in Fig. 5.5. In this figure the tangential velocity has not been normalized, to allow the three results for different initial rotation rates to be better distinguished from one another. More instructive than the absolute swirl velocities is the difference to the spin-down case. Note that the cylinder begins to stop rotating at $t = 1.00$ s and comes to a full stop at $t = 1.30$ s.

The piston begins compression at $t = 1.36$ s (UT, bottom dead center) and ends the stroke at $t = 1.59$ s (OT, top dead center).

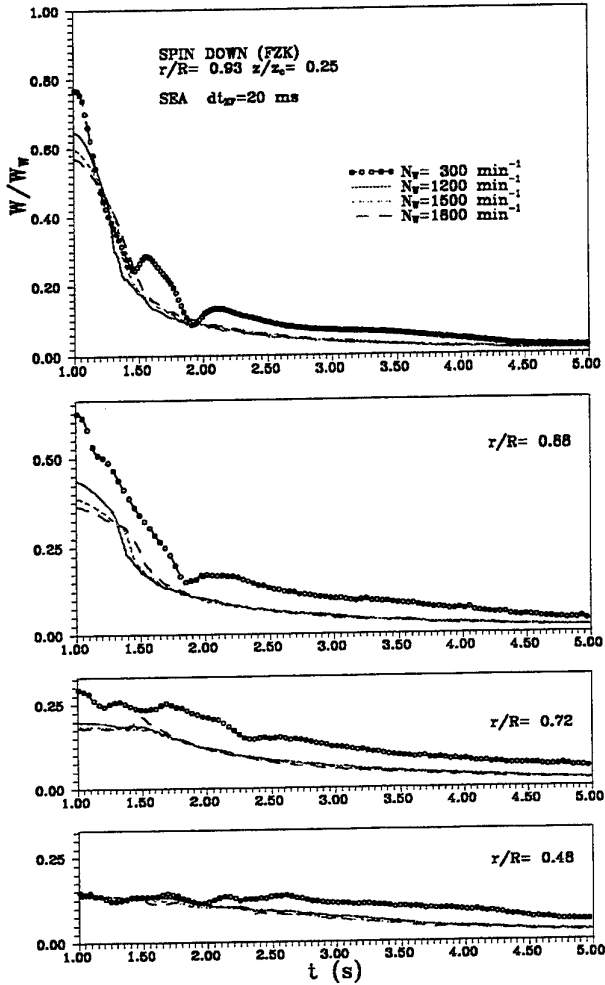


Figure 5.4: Spin-down behaviour for different initial swirl numbers

Except for the case $N_0 = 300 \text{ min}^{-1}$, very little deviation in swirl behaviour is noticed until half way through the compression stroke.

The swirl velocity with compression shows now also for the higher initial swirl rates signs of secondary flow, especially at the radial positions $r/R = 0.72$ and 0.48 . The deviations from the spin-down case are significantly larger with increasing distance from the cylinder wall.

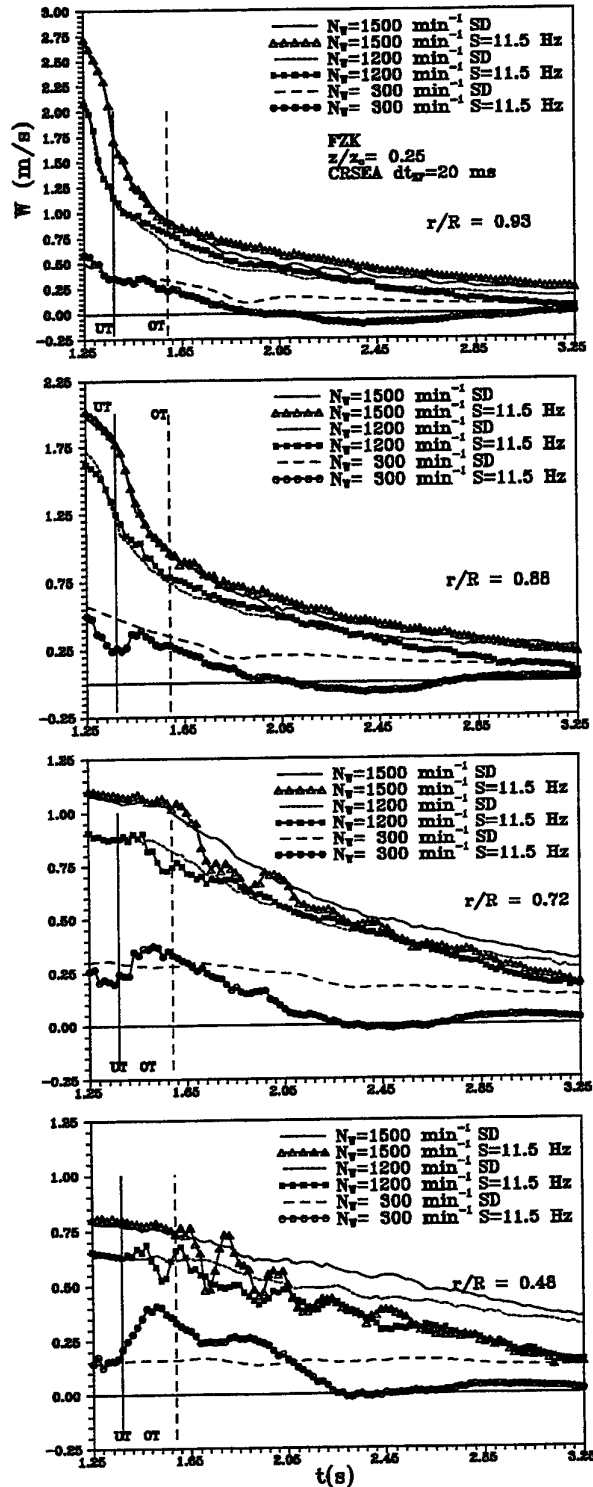


Figure 5.5: Swirl velocity evolution for different initial swirl rates showing the influence of compression on the swirl decay

In any case, the swirl velocity decays much faster with compression than without, however in the period following top dead center. This is understandable since the piston and cylinder head are close together and their boundary layers act to suppress the swirl. In fact at high time delays ($t > 4s$) a reverse swirl develops ([7]). For the time period during compression, the measured swirl velocity is only marginally less than the spin-down case. In Fig. 5.6 the swirl behaviour with compression is shown for the bowl-in-head geometry, i.e. with squish at the end of the compression stroke.

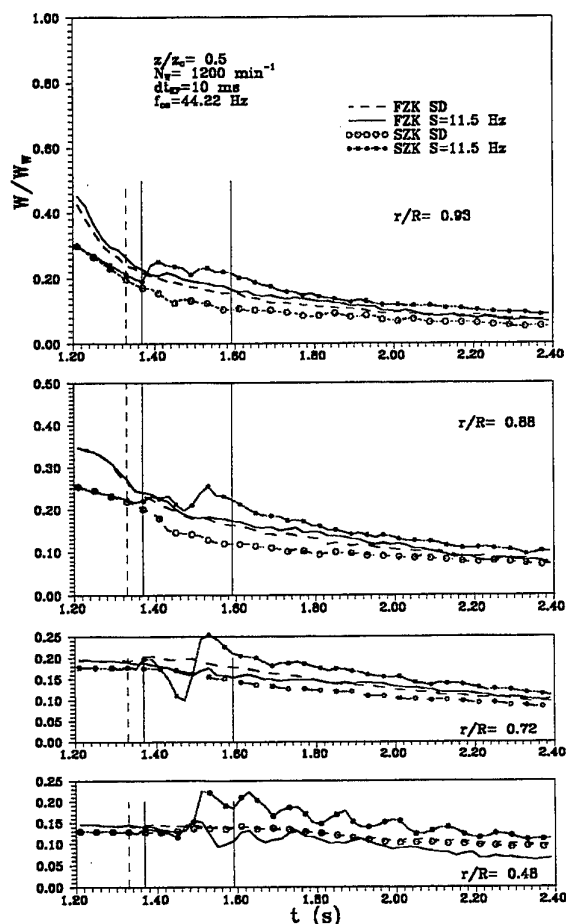


Figure 5.6: Swirl velocity evolution - comparison of swirl behaviour in the different cylinder heads

The data for the flat cylinder head is included in this figure for comparison. The normalized swirl velocity is lower for the SZK geometry due to the slightly different structure of the initial profile in comparison to those presented in Fig. 5.1. With compression, the tangential velocity rises sharply throughout the bowl.

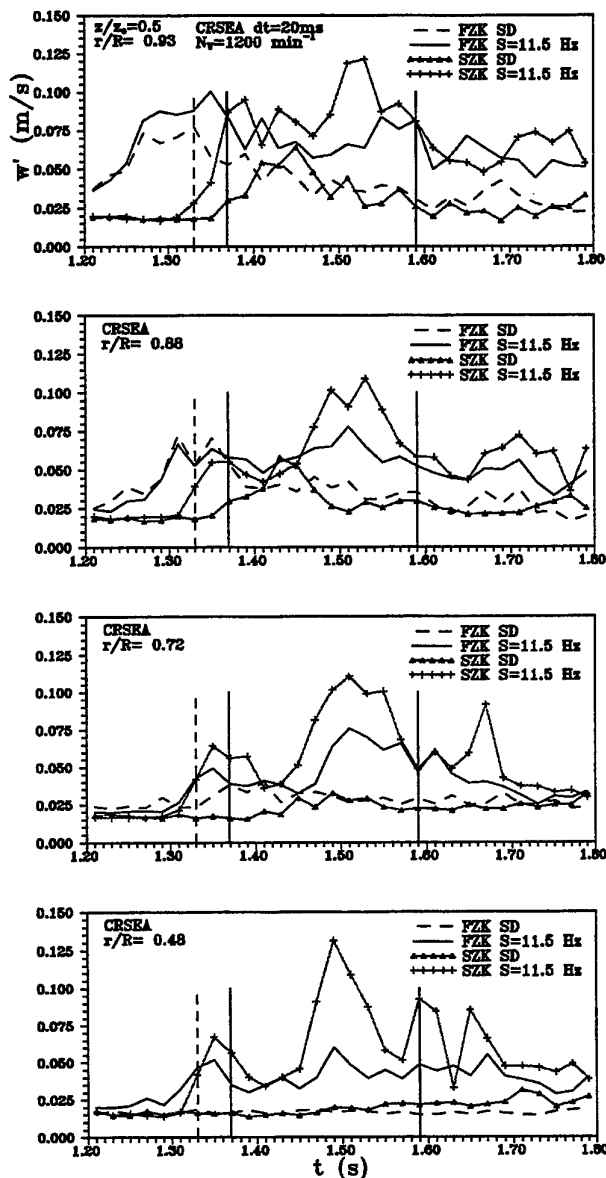


Figure 5.7: Evolution of the fluctuating tangential velocity in both the flat and the squish cylinder - comparison of spin-down and compression cases

Conservation of angular momentum dictates that the swirl velocity must increase when the fluid is forced into a smaller diameter. For the axial plane shown in Fig. 5.6 ($z/z_c = 0.5$) this increase occurs already at the beginning of the compression stroke, at least for the higher radii. Only in the center of the cylinder a delay of about half of the compression stroke duration is observable.

For comparison purposes, the necessary increase of tangential velocity to conserve angular momentum, given a linear velocity profile over the radius and neglecting all losses, is proportional to $(R_{cyl}/R_{bowl})^3$, where R_{cyl} and R_{bowl} are the cylinder and bowl radius respectively. In the present case this geometric factor is 1.36, resulting in a theoretical increase of W by a factor of 2.53. From Fig. 5.6 an increase of the measured swirl velocity in the range of 1.15 – 1.73 depending on radial position can be observed.

In Fig. 5.7 the fluctuating tangential velocity is shown, evaluated as described in section 4, using the CRSEA method.

Results for both cylinder heads and for spin-down and compression are shown. Some general trends can be noted. In all cases the turbulent velocity fluctuations increase during compression and remain higher beyond top dead center. The degree of increase depends on the exact location and the cylinder head geometry. Especially at high radii a rise of w' can be registered already before compression starts. This is related to the developing boundary layer after stopping the cylinder rotation. Also for spin-down, an increase of w' near the wall can be registered, however it is not as large as for the case with compression. Finally it can be seen that due to squish-generated shear flow effects in the bowl-in-cylinder geometry, the velocity fluctuations during and after the compression stroke are larger for the squish cylinder than for the flat cylinder head. A general conclusion from this study is therefore, that the compression promotes velocity fluctuations.

6. Summary and Conclusions

This paper presents LDA measurements of the flow-field in an idealized swirling flow geometry, with and without compression. The purpose is to investigate the influence of compression on the swirl velocity and its fluctuations. The results show that the swirl decays faster with compression, starting about half way through the compression stroke. The influence is larger at smaller radii, suggesting that at larger radii the wall boundary layer is exerting a strong influence on the velocity profile. Secondary flows arise during compression, more apparent at lower initial swirl numbers. Finally, the tangential velocity fluctuations rise significantly during compression, more so for the bowl-in-head geometry than for the flat head.

Acknowledgements

The authors would like to acknowledge support by the Deutsche Forschungsgemeinschaft through grant

Tr 194/7 and by the EEC Joule III program.

References

- [1] HEYWOOD, J.B. (1987) *Fluid Motion within the Cylinder of Internal Combustion Engines - The 1986 Freeman Scholar Lecture*, Journal of Fluids Engineering, Vol. 109, 3-35
- [2] ARCOUMANIS, C. AND WHITELAW, J.H. (1987) *Fluid Mechanics of Internal Combustion Engines - a Review*, Proc. Instn. Engrs, vol. 201, 57-74
- [3] WITZE, P.O. AND MENDES-LOPES, J.M.C. (1986) *Direct Measurement of the Turbulent Burning Velocity in a Homogeneous-Charge Engine*, SAE 861531
- [4] ARCOUMANIS, C., TANABE, S. (1989) *Swirl generation by helical ports*, SAE 890790
- [5] VOLKERT, J., TROPEA, C., DOMANN, R. AND HÜBNER, W. (1996), *Combined Application of PIV and LDA to Swirling Flows under Compression*, 8th Int. Symp. on the Appl. of Laser Techniques to Fluid Mechanics, Lisbon, Portugal
- [6] HANJALIC, K., JAKIRLIC, S., KELLER, J., TROPEA, C. AND VOLKERT, J. (1997), *Evolution of In-Cylinder Spin-Down Turbulence subjected to a single-stroke compression: Experiments and Modelling*, 11th Symp. on Turbulent Shear Flows, Grenoble, France
- [7] BOPP, S., DURST, F. AND TROPEA, C. (1990), *In-Cylinder Velocity Measurements with a Mobile Fiber Optic LDA System*, SAE 900055
- [8] RASK, R.B. (1981) *Comparison of Window, Smoothed-Ensemble and Cycle-to-Cycle Data Reduction Techniques for Laser Doppler Anemometer Measurements of in-Cylinder Velocity*, *Fluid Mechanics of Combustion Systems*, ed. Morel, T., Lohmann, R.P. and Rackley, J.M., 11-20, ASME
- [9] FANSLER, T.D. AND FRENCH, D.T. (1988) *Cycle-Resolved Laser-Velocimetry Measurements in a Reentrant-Bowl-in-Piston Engine*, SAE 880377
- [10] BRERETON, G.J. AND KODAL, A. (1991) *A Frequency-Domain Filtering Technique for Triple Decomposition of Unsteady Turbulent Flow*, ASME, vol. 114, 45-51
- [11] HILTON, A.D.M., ROBERTS, J.B. AND HADDED, O. (1991) *Autocorrelation Based Analysis of Ensemble Averaged LDA Engine Data for bias-free Turbulence Estimates: A Unified Approach*, SAE 910479
- [12] DAW, C.S. AND KAHL, W.K. (1990) *Interpretation of Engine Cycle-to-Cycle Variation by Chaotic Time Series Analysis*, SAE 902103
- [13] GLOVER, A.R., HUNDLEBY, G.E. AND HADDED, O. (1988) *An Investigation into Turbulence in Engines using Scanning LDA*, SAE 880378
- [14] GÜNTSCH, E. (1996) *Kompression isotroper Turbulenz im Zylinder - Eine numerische Studie* - Ph.D. Thesis, Technical University of Munich, Germany

SESSION 32

LDV SIGNAL PROCESSING

CORRELATION ESTIMATOR FOR TWO-CHANNEL, NON-COINCIDENCE LASER-DOPPLER-ANEMOMETER

H. Nobach¹, E. Müller², C. Tropea³

¹Dantec Measurement Technology
Tonsbakken 16-18, 2740 Skovlunde, Denmark

²Universität Rostock, Fachbereich Elektrotechnik und Informationstechnik
Institut für Nachrichtentechnik und Informationselektronik
Richard-Wagner-Straße 31, 18119 Rostock, Germany

³FG Strömungslehre und Aerodynamik (SLA), Technische Universität Darmstadt
Petersenstr. 30, 64287 Darmstadt, Germany

ABSTRACT

Two new estimators are introduced for correlation functions between two or more channels of a laser Doppler anemometer (LDA). The first estimator is based on a slotting technique and the second on a sample-and-hold reconstruction with a refinement of the correlation estimate. In both cases the coincidence requirement between channels is eliminated. The estimators are applicable to two-component or three-component LDA, but is more interesting for two-point or multi-point LDA, where coincidence is practically non-existent or where the effective separation distance goes to zero for overlapping volumes, thus biasing the spatial correlation function at low separations.

1. INTRODUCTION

Two or multi-channel laser Doppler anemometry (LDA) is used when correlations between velocity fluctuations are required. In a two velocity component LDA, the two measurement volumes are at the same location in the flow and the correlations between components represent components of the Reynolds shear stress tensor. If a two-point or multi-point LDA is considered, the correlations then represent spatial correlations. Most commonly, these correlations between velocity fluctuations are evaluated at time lag zero (covariance or after normalization correlation coefficient), however in principle all time lags can be considered, in which case the correlation function or space-time correlation function between velocity fluctuations can be obtained.

There are three basic deficiencies in present LDA systems which can be eliminated using the new estimators for cross-correlations. The first concerns the need for coincidence. Conventional estimators of the cross-correlation function work directly from the definition

$$R_{AB}(\tau) = \frac{1}{N} \sum_{i=1}^N u_A(t_i) u_B(t_i + \tau) \quad (1)$$

whereby it is understood that the mean has been removed

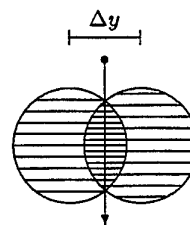


Figure 1: Two-point configuration leading to spatial bias of the cross-correlation function.

from the input signals u_A and u_B . Thus a product $u_A u_B$ can only be contribute to the sum if velocity information from the two channels come with a time lag of exactly τ . Practically an acceptance window in time (coincidence window) is tolerated, however in many applications this window must be chosen very narrow to avoid a loss of correlation, hence a biased estimator. Physically, the required window width will be dictated by the time correlation function itself, and must often be chosen empirically and/or iteratively.

In any case, given a narrow coincidence window, the data rate of coincident velocity pairs may become very low, especially for spatially separated measurement volumes, which will be the focus of this paper. Thus, the duration of the measurement to achieve a statistically satisfactory number of samples N may become intolerably long. Accepting a lower value of N simply increases the variance of the estimate.

A second deficiency concerns the coincidence window implementation, which is available at the hardware level only for $\tau = 0$. In this case only data pairs which occur simultaneous in time are actively acquired, minimizing the amount of collected data. For other time lags ($\tau \neq 0$) no hardware coincidence is forseen. If the function $R_{AB}(\tau)$ is to be evaluated at many τ values, then all data must be acquired from both channels and coincidence must be implemented at the software level. In this case, again, due to the generally lower 'hit' rate of coincidence, large amounts of data must be acquired and recorded to yield statistically secure estimates.

A final difficulty with present estimators has been pointed out by Benedict and Gould [2] in their discussion of two-point correlation estimates when the separation distance becomes very small. Such measurements are necessary if direct measurements of dissipation are to be attempted. Once the two LDA measurement volumes begin to overlap any *g*-type correlation will become biased because coincidence will be triggered when a single particle passes through the overlapping region, as illustrated in figure 1. However velocity data from the two channels is not originating with the surmised spatial separation of Δy , but with an effective spatial separation of zero. Thus the estimator using coincidence will lead to a spatial bias in the near-field region. This bias is very significant, since the number of such single particle, two channel signals is much more frequent than two particle, two channel coincident signals.

All of the above difficulties will be alleviated using the new estimators. The next section describes briefly the simulation techniques used to produce test signals. The two new estimators for non-coincidence, cross-correlation are introduced in section 3. The performance of the estimators applied to two-point LDA is studied in section 4 and a discussion and conclusion are given in section 5.

2. SIGNAL SIMULATION

The results presented in this paper have been achieved using simulated signals, which allow systematic variation of influencing parameters and also evaluation of absolute errors, i.e. estimator biases. The techniques for generating a time-dependent, three-dimensional velocity field of given statistical characteristics have been introduced previously in [3]. Since in the present case a two-point LDA system is being examined, a spatial dependence must be added, with a given spatial correlation function. Details of how this was achieved can be found in [5].

The two situations which were examined are shown pictorially in figure 2 and correspond to a *f*-type and *g*-type correlation respectively. The main flow direction is along the *x*-axis and the mean velocity in both the *y* and *z* directions is zero. A cosine function was chosen to describe the spatial correlation with an integral length scale (first zero crossing) of $57 \mu\text{m}$ in the direction of the measurement volume separation and 1 m in the other two directions, the latter case making its influence negligible. The measurement volumes had dimensions of $40 \mu\text{m}$ (*x*) \times $40 \mu\text{m}$ (*y*) \times $40 \mu\text{m}$ (*z*). Although unrealistic at $40 \mu\text{m}$, the length (*z*) has no particular consequence since there is no *z* velocity component and thus, together with the particle concentration, only the data rate is effected by this dimension.

An uncorrelated noise component could be added to the simulated velocity values. The simulation was then repeated for various values of measurement volume separation, either in *x* or *y*, for an *f* or *g* type correlation respectively. Two cases for each correlation type were investigated. The first case had a mean velocity of 10 m/s and a variance of $1 \text{ m}^2/\text{s}^2$, in which case 100 repetitions of the simulations were used to enable the statistical certainty of the results to be established. The second case had a mean velocity of only 1 m/s , thus representing a much higher turbulence level.

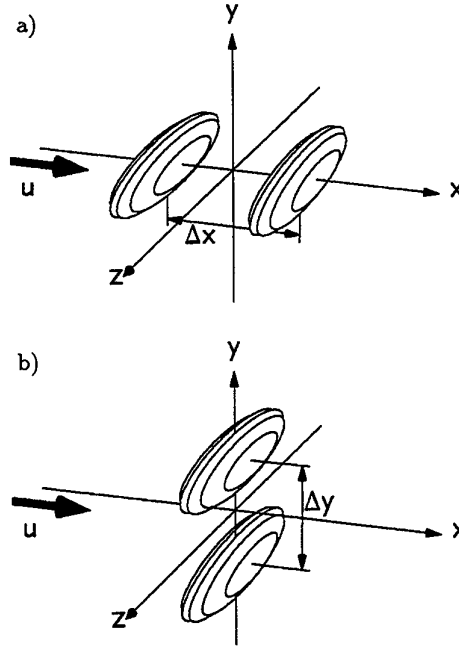


Figure 2: Measurement volume positions for signal simulation: a) *f*-type and b) *g*-type correlations.

The conditions of the four simulation cases are summarized in table 1.

3. DESCRIPTION OF ESTIMATORS

3.1 Coincidence based Estimator

For comparison purposes a software implementation of the conventional hardware coincidence was used to evaluate the coincidence based correlation given by

$$R_{AB}^{(c)}(0) = \frac{1}{N_c} \sum_{h=1}^{N_c} u_A(t_{Ah}) u_B(t_{Bh}) \quad (2)$$

where N_c is the number of coincidence events and the arrival times satisfy the relation

$$|t_{Ah} - t_{Bh}| < \tau_c. \quad (3)$$

The data rate of coincident events is denoted by \dot{n}_c .

3.2 Slot Correlation Estimator

The slot correlation estimator is given by

$$R_{AB}^{(s)}(k\Delta\tau) = \frac{\sum_{i=1}^{N_A} \sum_{j=1}^{N_B} u_{Ai} u_{Bj} b_k(t_{Bj} - t_{Ai})}{\sum_{i=1}^{N_A} \sum_{j=1}^{N_B} b_k(t_{Bj} - t_{Ai})} \quad (4)$$

where the weighting function b_k is given by

$$b_k(\Delta t) = \begin{cases} 1 - \left| \frac{\Delta t}{\Delta\tau} - k \right| & \text{for } \left| \frac{\Delta t}{\Delta\tau} - k \right| < 1 \\ 0 & \text{otherwise} \end{cases} \quad (5)$$

Correlation Case		f-type		g-type	
		1	2	3	4
Mean velocity [m/s]	m_u	10	1	10	1
Velocity variance [m ² /s ²]	σ_u^2	0	0	0	0
Reynolds stresses [m ² /s ²]	c_{uv}	0	0	0	0
Integral time scale [ms]	I_u	40	400	40	400
Integral length scale	L_x	57.3 μ m	57.3 μ m	1 m	1 m
Record length [s]	T	100	1000	100	1000
MV dimensions [μm]	2a	40	40	40	40
	2b	40	40	40	40
	2c	40	40	40	40
Coincidence time [μs]	τ_c	5	50	500	5000
Lag time interval [ms]	$\Delta\tau$	10	100	10	100
Particle conc. [m ⁻³]	c_p	3×10^9	3×10^9	3×10^9	3×10^9
Noise Level [m ² /s ²]	σ_N^2	0.1	0.001	0.1	0.001

Table 1: Summary of simulation parameters for data sets 1–4.

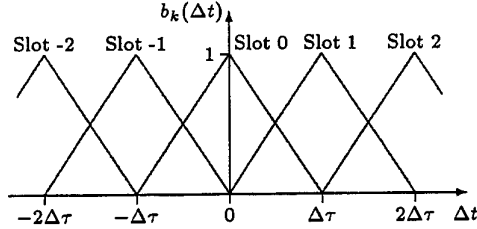


Figure 3: Illustration of weighting function $b_k(\Delta t)$.

and $\Delta t = t_{Bj} - t_{Ai}$. This weighting function is illustrated in figure 3 and represents a modification to conventional slot correlation estimates. Physically the slots are no longer sharply defined and this results in a lower variance of the correlation estimate, since slot quantisation noise is reduced.

The data rate, or *slot* rate, is denoted by $\dot{n}_s(k\Delta\tau)$.

3.3 Reconstruction based Estimator

Details of the estimator based on signal reconstruction can be found in [4]. A sample-and-hold (S+H) reconstruction has been employed with a re-sampling at the time intervals of $\Delta\tau$. The S+H can be represented by

$$\begin{aligned} u_A(t) &= u_{Ai} & \forall & t_{Ai} \leq t < t_{Ai+1} \\ u_B(t) &= u_{Bj} & \forall & t_{Bj} \leq t < t_{Bj+1} \end{aligned} \quad (6)$$

and the resulting cross-correlation estimator by

$$R_{AB}^{(n)}(k\Delta\tau) = \begin{cases} \frac{1}{N_r - k} \sum_{i=1}^{N_r - k} u_A(i\Delta\tau) u_B((i+k)\Delta\tau) & \text{for } k \geq 0 \\ \frac{1}{N_r - |k|} \sum_{i=1+|k|}^{N_r} u_A(i\Delta\tau) u_B((i-|k|)\Delta\tau) & \text{for } k < 0 \end{cases} \quad (7)$$

where N_r is the total number of resampled data points.

The low-pass filter associated with this reconstruction and re-sampling (eg. [1]) is compensated for by recognizing that the filter F can be inverted, i.e.

$$R_{AB}^{(r)} = F^{-1} R_{AB}^{(n)} \quad (8)$$

to yield an improved estimate of the cross-correlation function $R_{AB}^{(r)}$. This stage of the estimation has been termed refinement and has been initially formulated for autocorrelation function to improve frequency spectrum estimation from LDA data [6].

4. RESULTS

4.1 f-type Correlation

The results for case 1 (low velocity bias) are summarized in figure 4, showing the expectation and the data rates for the f-type correlation. In figure 4a the three estimates are compared to the theoretical spatial correlation (cosine). Also the reconstruction estimate without refinement has been added to this figure. The reconstruction technique exhibits a very low systematic error, with or without refinement. The refinement is not really necessary since almost all particles producing a signal in the first measurement volume also result in a signal in the second measurement volume (low turbulence).

The slot correlation lies consistently below the reconstruction estimate, due to multiple particle measurement in the slots. This can be seen by examining the data rates, as shown in figure 4b. The mean expected data rate at zero time lag is estimated from the particle concentration, the mean velocity and the projected measurement volume to be approximately 38 s^{-1} . Whereas the coincident estimator achieves about this value, the slot correlation lies significantly above. Thus cross-correlation contributions from different particles within a slot are being considered, which lowers the estimate marginally. Physically this means a small influence of the time correlation function is entering into the spatial correlation estimate.

The coincidence estimate performs very well up to a spatial separation corresponding to the overlapping of the measurement volumes. Due to the short coincidence time chosen (5 μ s), the data falls off abruptly beyond this point. Only the fastest particles still fulfil the coincidence requirement, thus strongly biasing the correlation estimate.

The empirically determined variance of the reconstruction estimate was found to be the lowest (not shown).

Results for case 2 (high turbulence level) are shown in figure 5, in which all estimators are seen to be biased. This is an error associated with the classical velocity bias. As in the previous case, the coincident estimator undergoes a negative bias at larger separation, due to the selection of only fast particles through the coincidence window.

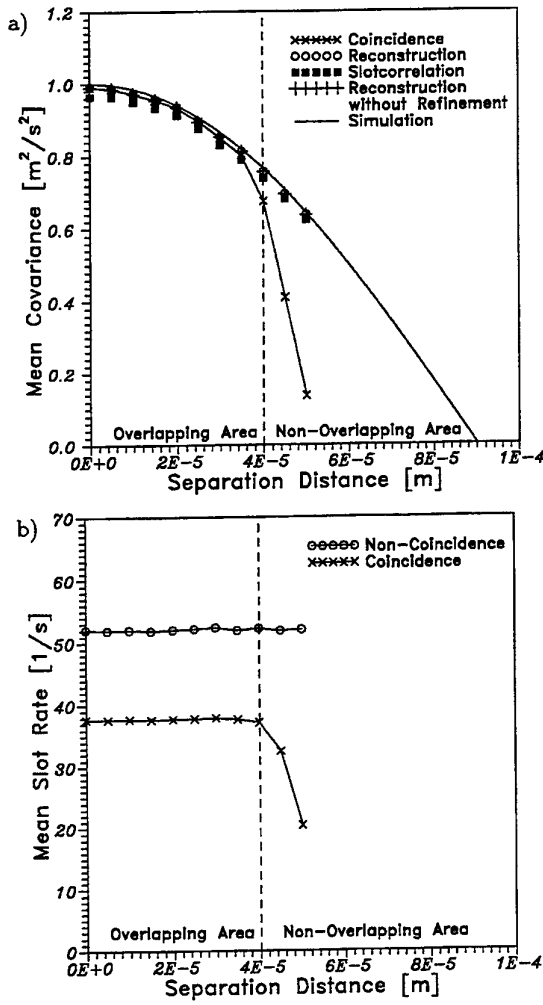


Figure 4: Results for case 1: low turbulence, f -type correlation.

The effect is not as abrupt in this case, only because the turbulence level is higher and the effect becomes 'smeared' out.

Again the variance of the reconstruction estimator is the lowest.

4.2 g -type Correlation

The results for the g -type correlation at low turbulence are summarized in the three diagrams of figure 6. In the diagram of the mean covariance (figure 6a), also the reconstruction estimate without refinement is shown and agrees well with results presented in [4].

The coincidence estimator exhibits a strong systematic error for spatial separations in which the measurement volumes still overlap. This corresponds to the problem outlined in conjunction with figure 1. Since the effective spatial separation remains effectively zero for overlapping volumes, the mean covariance maintains a value close to 1. For non-overlapping volumes, this estimate follows the

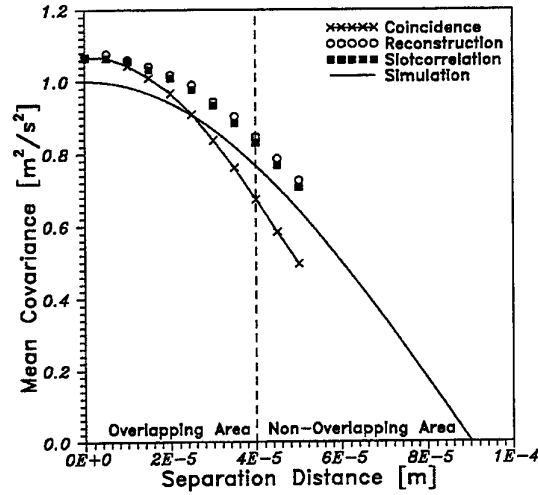


Figure 5: Mean covariance estimated for case 2: f -type correlation at high turbulence.

reconstruction estimate, however the data rate decreases dramatically, as seen in figure 6c. Consequently, the estimator variance is also very high (figure 6b).

The reconstruction estimate is very close to the prescribed correlation at small separations but lies below at high separation values. This is related to the spatial averaging over the finite size of the two measurement volumes, an effect which is not present in the f -type correlation. This effect can be evaluated as a spatial integral

$$c_{AB}^{(m)} = \int_{\Delta y - 2c}^{\Delta y + 2c} \sigma_u^2 \cos \frac{y}{L_y} p(y) dy \quad (9)$$

where $\sigma_u^2 \cos \frac{y}{L_y}$ is the prescribed spatial correlation and where the probability of the y value of the particle passage is uniform across the volume

$$p(y) = \frac{1 - \left| \frac{y - \Delta y}{2c} \right|}{\int_{\Delta y - 2c}^{\Delta y + 2c} \left(1 - \left| \frac{y - \Delta y}{2c} \right| \right) dy} \quad (10)$$

The value of $c_{AB}^{(m)}$ has been added to figure 6a and describes the reconstruction estimator well at larger lag times. At very small lag times single particle, two channel signals dominate and the true zero correlation is estimated.

The slot correlation exhibits both the spatial averaging mentioned above and the temporal averaging over the slot width and lies therefore below the reconstruction estimate.

As in previous cases, the reconstruction also exhibits the lowest variance, as seen in figure 6b.

Finally results for the g -type correlation at high turbulence levels is shown in figure 7. As in case 2, a systematic error of the covariance is apparent for the reconstruction and slot estimates. The lower variance of the reconstruction estimate is even more pronounced. The data rate behavior is similar to that in case 3. (figure 6c).

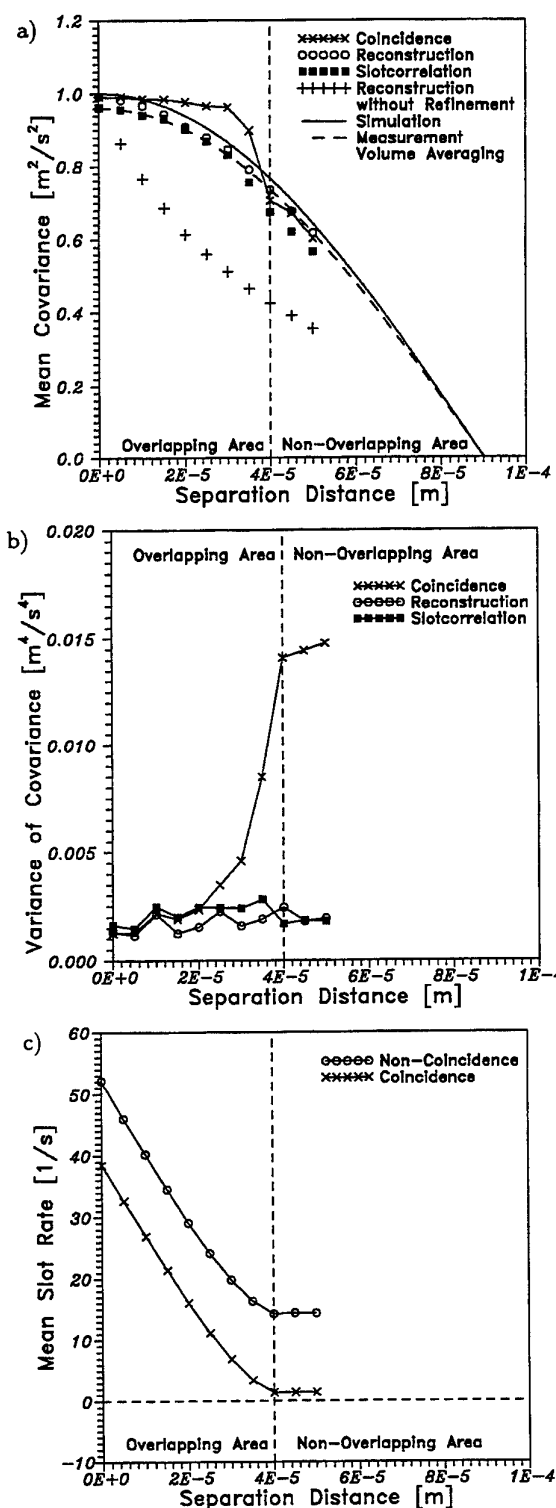


Figure 6: Results for case 3: low turbulence, g -type correlation.

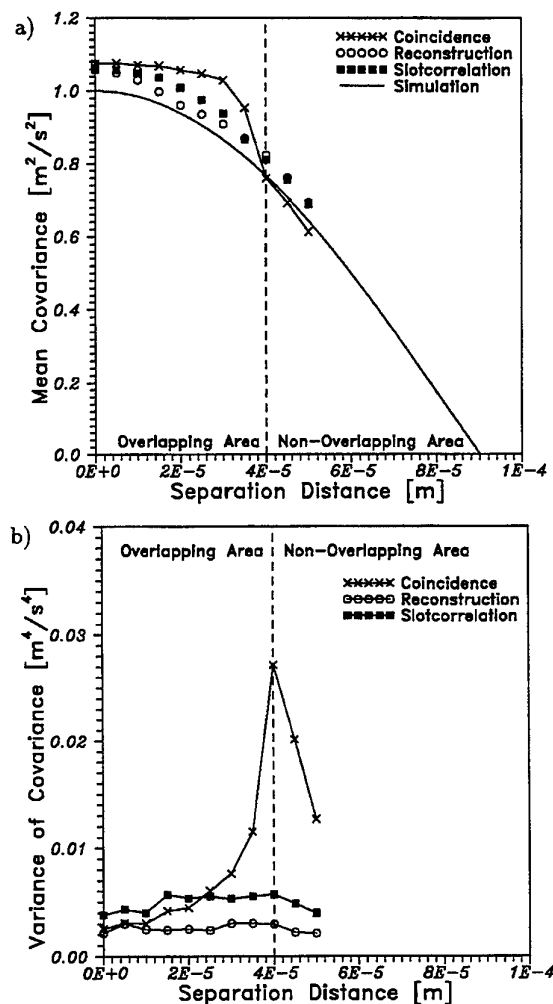


Figure 7: Results for case 4: high turbulence, g -type correlation.

Practically, the lower variance exhibited by the slot correlation and reconstruction estimate should allow shorter measurement times to achieve a given uncertainty. This has been more explicitly investigated by computing the estimators' variances as a function of particle concentration and also measurement time. The results are presented in figures 8a and b respectively, using the flow parameters of case 3.

Included in these figures are results using 3 coincidence window widths, between 1 ms and 10 ms. The 10 ms window corresponds to the slot width employed, however already leads to a reduced (biased) correlation. The 1 ms window is more realistic. For a given variance, the slot correlation or reconstruction estimate leads to measurement times of a factor 5 less than with the coincidence estimate. Similarly, the slot correlation and reconstruction estimate achieve a given variance at much lower particle concentrations, for a fixed measurement time. Indeed, at very low particle concentrations the slot correlation outperforms the reconstruction estimate. This lies presam-

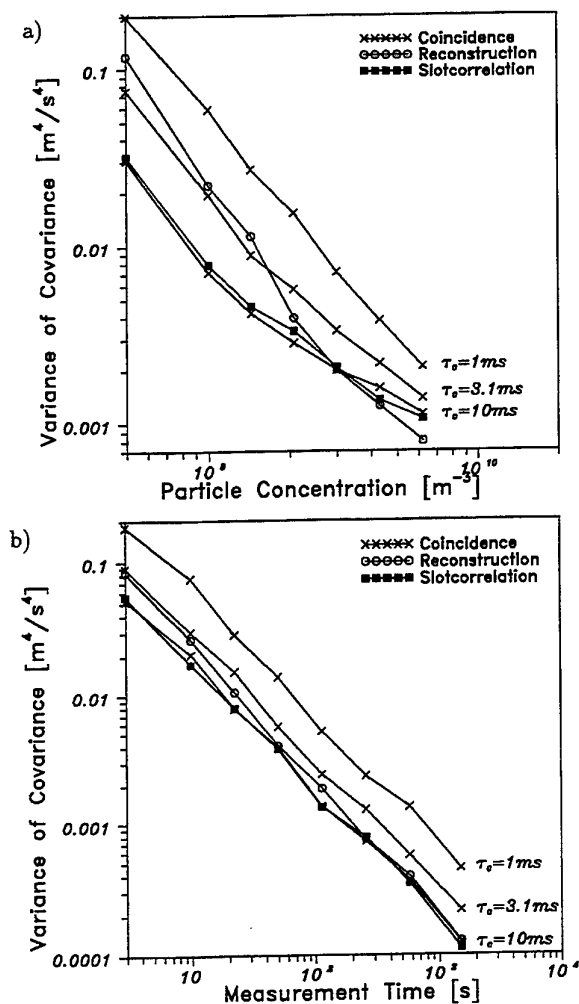


Figure 8: Estimators' variance for case 3: low turbulence, g -type correlation.

ably in the fact that at very low particle concentrations, the particle rate \dot{n} , required for the refinement step, is poorly estimated. In either case however, the improvement factor is much less than for the measurement time.

Note that figure 8a and b are both plotted in a double logarithmic scale, indicating the power law behavior of the variance as a function of particle concentration and measurement time.

5. CONCLUSIONS

The present results indicate clearly the advantages of the slot correlation and the reconstruction estimate over a coincidence estimate for the cross-correlation of velocity data from a two-point LDA. For the user the main advantage lies in a significantly shorter measurement duration to achieve a given variance, typically a factor of 5 or larger. Furthermore the spatial bias for overlapping measurement volumes is completely avoided.

The reconstruction technique shows less systematic error than the slot correlation and furthermore has a lower variance. On the other hand the slot correlation is significantly easier to implement, requires less computational time and is also robust when the particle concentration varies significantly. The main disadvantage of the slot correlation is the inherent time averaging over each slot width.

6. ACKNOWLEDGEMENTS

Funding from the Deutsche Forschungsgemeinschaft under grants Tr 194/9 and Mu 1117/1 is gratefully acknowledged.

REFERENCES

- [1] Adrian, R. J.; Yao, C. S.: *Power Spectra of Fluid Velocities Measured by Laser Doppler Velocimetry*. Exp. in Fluids 5 (1987), 17–28.
- [2] Benedict, L. H.; Gould, R. D.: *Understanding biases in the near-field region of LDA two-point correlation measurements*. Proc. 8th Int. Symp. of Appl. of Laser Techn. to Fluid Mechanics, Lisbon, Portugal (1996), paper 36.6.
- [3] Fuchs, W.; Albrecht, H.; Nobach, H.; Tropea, C.; Graham, L. J. W.: *Simulation and Experimental Verification of Statistical Bias in Laser Doppler Anemometry including Non-Homogeneous Particle Density*. Proc. 8th Int. Symp. on Appl. of Laser Techn. to Fluid Mechanics, Lisbon, Portugal (1992), paper 36.2.
- [4] Müller, E.; Nobach, H.; Tropea, C.: *A Refined Reconstruction-based Correlation Estimator for Two-channel, Non-coincidence Laser Doppler Anemometer*. Measurement Science and Technology, vol. 9 (1998), no. 3, pp. 442–451.
- [5] Nobach H.: *Verarbeitung stochastisch abgetasteter Signale — Anwendung in der Laser-Doppler-Anemometrie*. Shaker Verlag Aachen, 1998 (Berichte aus der Lasertechnik), also Rostock, Univ., Diss., 1997, ISBN 3-8265-3332-1.
- [6] Nobach, H.; Müller, E.; Tropea, C.: *Efficient estimation of power spectral density from laser Doppler anemometer data*. Experiments in Fluids, vol. 24 (1998), no. 5/6, pp. 499–509.

IMPROVED RECONSTRUCTION OF TURBULENT VELOCITY FLUCTUATIONS FROM LASER-DOPPLER ANEMOMETRY DATA

by

Hans R.E. van Maanen (S.I.E.P.-R.T.S., dept. EPT-DF)
(P.O. Box 60, 2280 AB Rijswijk, Netherlands)
(email: H.R.E.vanMaanen@siep.shell.com)

and

Frank J. Nijenboer (University of Twente)
(Currently at TNO-FEL, dept. 4-2, P.O. Box 96864, 2509 JG The Hague, Netherlands)
(e-mail: nijenboer@fel.tno.nl)

Abstract

Velocity signal reconstruction for LDA data is an attractive approach for turbulence research. The reduction of the noise level is essential as the noise obscures the small eddies. Previous work has shown that first-order Kalman reconstruction improves the signal quality. In this paper we will describe a further development of this approach in which we can avoid assumptions about the flow properties as these are derived from the raw data themselves. From the cross-power spectrum an extended reconstruction filter can be derived which forces the statistical properties of the flow onto the reconstructed signal and gives this a low Mean Squared Error value in time domain.

1. Introduction.

Laser-Doppler Anemometry (LDA) is the only measurement technique which is able to measure turbulent velocity fluctuations in highly turbulent flows (turb. int. > 30 %) with a high spatial and temporal resolution (ref. 1). The major disadvantage of LDA measurements is the combination of randomly time-sampled velocity estimates and an unfavourable Signal-to-Noise Ratio (SNR) of the individual velocity estimates (ref. 2). This hampers the interpretation of the data and obscures the small eddies of the turbulent velocity fluctuations. In previous work we have used first-order Kalman reconstruction in order to improve the reconstructed signal (ref. 3). Although this gives a significant improvement in both the temporal and spectral estimates of the turbulent fluctuations, the simple turbulence model used for this first-order reconstruction is a limiting factor. Especially the assumption that the turbulence

generating accelerations can be approximated by a Gaussian distributed white noise signal neglects the decrease in accelerations for the smaller scales due to viscous forces. We have therefore extended the technique to improve the reconstruction of the turbulent fluctuations, using an improved spectral estimation, based on the cross-covariance technique or the curve-fitting to the slotted Auto Correlation Function (ref. 5 and 7).

2. Spectral estimates.

Application of first-order Kalman reconstruction to LDA data results in a continuous velocity trace which can be regarded as the sum of the actual velocity fluctuations and a residual noise contribution (ref. 3). Although improvement of the input signal for the Kalman reconstruction reduces this noise significantly (ref. 6), it has not been

eliminated. Yet, by using either the curve-fit spectral estimator (ref. 5) or the cross-covariance technique (ref. 7), the turbulence power spectrum can be retrieved, without making assumptions about the flow, to below the noise level (In the remainder of this paper we will use the spectral estimator based on the cross-covariance technique, but except for one aspect, the procedure is identical when the curve-fit approach is used). Because the properties of the turbulence are unknown, the development of this data-processing technique is based on simulations, which have been described in previous work (ref. 2 - 6 and 8). Using such simulations it has been shown that the power spectrum obtained by the cross-covariance technique is the correct estimator. This was likely, but it could not be proven then (ref. 7), but fig. 1 clearly shows it. The whole chain of data-generation and processing to obtain the cross-power spectrum is presented in "Data-Processing I"

3. Signal quality determination.

A suitable criterion for the characterisation and optimization of the reconstruction performance is the Mean Squared Error (MSE):

$$MSE = \frac{1}{T} \int_0^T \theta^2(t) dt ; \quad \theta(t) = v(t) - \hat{v}(t)$$

in which:

$v(t)$ = actual velocity fluctuations

$\hat{v}(t)$ = reconstructed velocity fluctuations

The MSE is thus a measure for the difference between the reconstructed and actual velocities and the lower the value, the better. The power spectrum of the reconstructed signal and the distribution of the accelerations will also be used to study the results of the reconstruction scheme.

4. The extended reconstruction filter.

The two first-order Kalman reconstructed velocity signals can be averaged in order to increase the SNR with a factor of $\sqrt{2}$, and this

signal will be denoted by $v_n(t)$. The power spectrum of $v_n(t)$ can be found (fig. 2) and the difference of this spectrum and the cross-power spectrum represents the residual noise contribution. The ratio of the cross-power spectrum and the spectrum of $v_n(t)$ can be used as an extended reconstruction filter, which would force the correct spectral characteristics on $v_n(t)$. (Note that it is required to take the square root because we need the *amplitude* and the spectra represent *power*). Because of the variance in the cross-power spectrum for high frequencies, a parameter description of such a filter has been used, similar as in ref. 5 and 11:

$$G(f) = \left(\frac{1 + \left(\frac{f}{f_1}\right)^m}{\left[1 + \left(\frac{f}{f_2}\right)^m\right] \cdot \left[1 + \left(\frac{f}{f_3}\right)^6\right]} \right)^{\frac{1}{2}}$$

in which f_1 , f_2 and f_3 are characteristic frequencies and m is an exponent. The four parameters can be fitted to the experimental result, see fig. 3. The actual reconstruction is done by convolving $v_n(t)$ with the impulse response of the extended filter. To include the correction for the random sampling (ref. 2 and 3), the transfer function of the extended filter is:

$$G(f) = \left(\frac{\left[1 + \left(\frac{f}{f_1}\right)^m\right] \cdot [1 + (2\pi f t_0)^2]}{\left[1 + \left(\frac{f}{f_2}\right)^m\right] \cdot \left[1 + \left(\frac{f}{f_3}\right)^6\right]} \right)^{\frac{1}{2}}$$

in which t_0 is the average time between two successive Doppler signals. After convolving $v_n(t)$ with the impulse response (see fig. 4) the reconstructed signal has the correct spectral properties without any further assumptions about the properties of the flow **and** it is corrected for the low-pass properties of the random sampling. It can therefore be regarded as a close to optimum estimation of the turbulent velocity fluctuations at any instant in time. The complete data-processing procedure is shown in "Data-Processing II".

5. Results.

The output signal of the data-processing procedure has been analyzed and compared with the expected values. As a first step, the output signal is, together with the simulated turbulence it was to reconstruct, shown in fig. 5. Only some small deviations can be seen.

Secondly, the MSE Values have been calculated and are presented in table 1. The improvement is obvious.

Thirdly, the power spectrum has been calculated and it is presented in fig. 6, showing it is correct over 5.5 decades with a small residual noise contribution, due to the residual noise in the cross-power spectrum.

Furthermore, the distributions of the *accelerations*, which is more sensitive to noise than that of the *velocities*, have been calculated after the various steps and are shown in fig. 7 - 12, starting at the simulated turbulence and ending at the reconstructed turbulence.

All these analyses shown that the reconstruction has been successful.

6. Discussion.

The reconstruction of the velocity produces a signal that has a close resemblance to the input signal. However, there will always be some residual noise present as is clear from table 1. This is inherent to the LDA measurement process and cannot be avoided. However, it can be optimized as has been discussed previously (ref. 2 - 6 and 9). As the cross-covariance technique reduces the noise because the noise contributions are not correlated, the approach works best when the SNR of the input signal is already as high as possible. Advantageous is, however, that it allows to use larger values of the Kalman filter gain and thus a less-critical setting of the parameters. Yet, again the results of this work emphasize the importance of the data-rate which determines the high-frequency resolution of the spectrum (ref. 10) and the residual noise contribution (see table 1). Still, the technique described in this paper enables us to obtain signals which have, in all aspects, properties which are in agreement with the statistics of the turbulence and are thus very similar to HWA signals. These statistical properties of the turbulence have been derived from the data itself,

so there is no need for assumptions which could easily lead to "self-fulfilling prophecies". The only exception is the assumption that the accelerations are limited in order to apply the first-order Kalman reconstruction. Such a limitation is realistic as the forces are limited.

The major disadvantage of this approach is that it is rather (computer) time consuming. However, computing power still increases at an incredibly fast rate and it is also cheap in comparison to an LDA system: the price ratio of LDA/PC is roughly 100. In our view it is better to spend more on PC's in order to enable data-processing algorithms like these than to leave important information unused. On top of that we think that experiments that improve our knowledge of and insight into the mechanisms of turbulence are worth a couple of PC's. And apart from the investment: don't forget the amount of time (which is money too!) involved in getting the experiments done. In our view is the quality of the results more important than the required processing time.

On-line use of this approach can be done if the Kalman and extended filter properties have been derived from a previous measurement. This requires a stationary flow and stationary measurement conditions, but in many (laboratory) cases this is feasible. It would, however, require specialized hardware (DSP chips).

Although the technique has been developed for LDA signals, it can be used for similar signals, obtained from e.g. HWA, as well. With low turbulence intensity, such signals can become noisy too.

The use of the cross-covariance is only possible when two independent measurement chains are available. The curve-fitting approach (ref. 5) allows to do the same on a single measurement chain, but one loses the 3 dB gain in the SNR due to the averaging of the signals, meaning a higher residual noise level in the output signal. Note that the curve-fit approach, which has been developed for "low" data-rate conditions, can be applied to high data-rate conditions as well, but the reconstruction still requires the high data-rate.

7. Conclusions and future work.

- Estimation of the Power Spectral Density of the turbulent velocity fluctuations using the cross

covariance technique leads to a correct estimator of the PSD.

- Processing the first-order Kalman reconstructed velocity signal with an extended reconstruction filter results in reconstructed turbulence which has spectral properties with the correct statistics and low MSE values in time domain.
- Optimisation of the total LDA system remains essential. The important parameters are the SNR of the individual velocity estimates and the data-rate.
- Application of the curve-fit technique enables a similar data-processing for single chain measurements.
- Automatic "design" of the extended reconstruction filter by determining the parameters is possible.

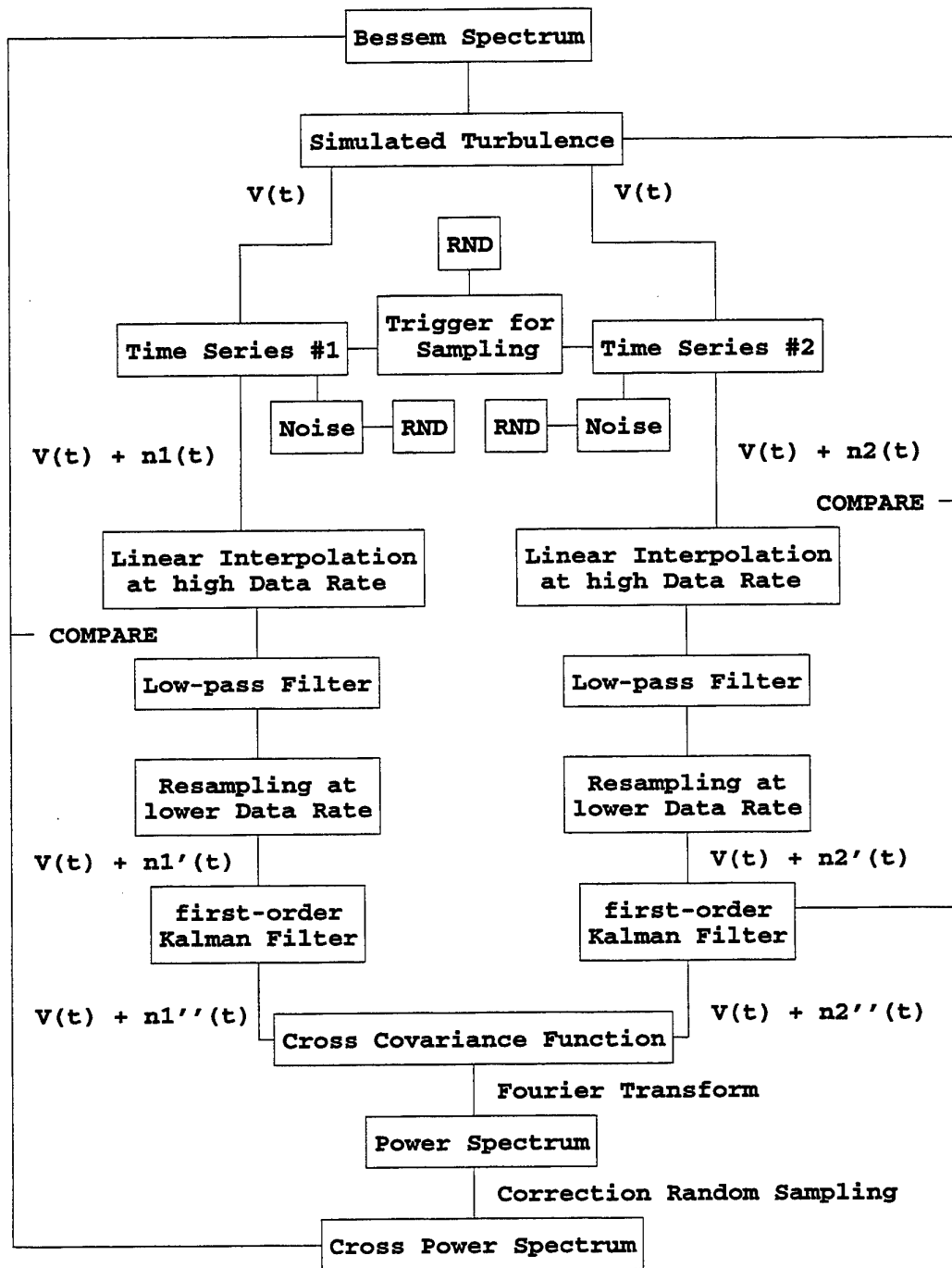
References

1. F. Durst, A. Melling and J.H. Whitelaw, "Principles and Practice of Laser-Doppler Anemometry", Academic Press, 1976.
2. R. Booij and J.M. Bessem (ed.), Report on Workshop "User's Needs for Laser Doppler Anemometry", Supplement to the Proc. 5th Int. Conf. on Laser-Doppler Anemometry, August 1993, Veldhoven (Netherlands).
3. H.R.E. van Maanen and H.J.A.F. Tulleken, "Application of Kalman reconstruction to Laser-Doppler Anemometry data for estimation of turbulent velocity fluctuations", Proc. 7th Int. Symp. on Appl. of Laser Techniques to Fluid Mech., July 1994, Lisbon (Portugal), paper 23.1
4. H.R.E. van Maanen and M. Tummers, "Estimation of the Auto Correlation Function of Turbulent Velocity Fluctuations using the Slotting Technique with Local Normalisation", Proc. 8th Int. Symp. on Appl. of Laser Techniques to Fluid Mech., July 1996, Lisbon (Portugal), paper 36.4
5. H.R.E. van Maanen and A. Oldenziel, "Estimation of Turbulence Power Spectra from Randomly Sampled Data by Curve-Fit to the Auto Correlation Function, Applied to Laser-Doppler Anemometry", Measurement Science and Technology 9 (March 1998), pp. 458 - 467.
6. H.R.E. van Maanen, "A Novel Re-Sampling Technique for Randomly Sampled LDA Data", Proc. 7th Int. Conf. "Laser Anemometry: Advances and Applications", Sept. 1997, Karlsruhe (Germany), paper 12.3
7. H.R.E. van Maanen, K. van der Molen and J. Blom, "Reduction of Ambiguity Noise in Laser-Doppler Velocimeter by a Crosscorrelation Technique", Proc. LDA-Symposium, August 1975 Copenhagen (Denmark), pp. 81-89.
8. J.M. Bessem and H.R.E. van Maanen, "Optimization of digital storage of random analogue data", Meas. Sci. Technol. 5 (1994), pp. 1331 - 1338.
9. H.R.E. van Maanen and F.J. Nijenboer, "Application of the Wavelet Transform to Laser-Doppler Signal Processors", Proc. 8th Int. Symp. on Appl. of Laser Techniques to Fluid Mech., July 1996, Lisbon (Portugal), paper 31.4
10. A. Høst-Madsen and Chr. Caspersen, "The Limitations in High Frequency Turbulence Spectrum Estimation using the Laser Doppler Anemometer", Proc. 7th Int. Symp. on Appl. of Laser Techniques to Fluid Mech., July 1994, Lisbon (Portugal), paper 11.2
11. E. Müller, H. Nobach and C. Tropea, "Model Parameter Estimation from LDA Data at Low Particle Rates", Proc. Laser Anemometry 1995 (Hilton Head Island, SC, U.S.A.) FED-Vol. 229 Laser Anemometry ASME 1995 pp. 417 - 424.

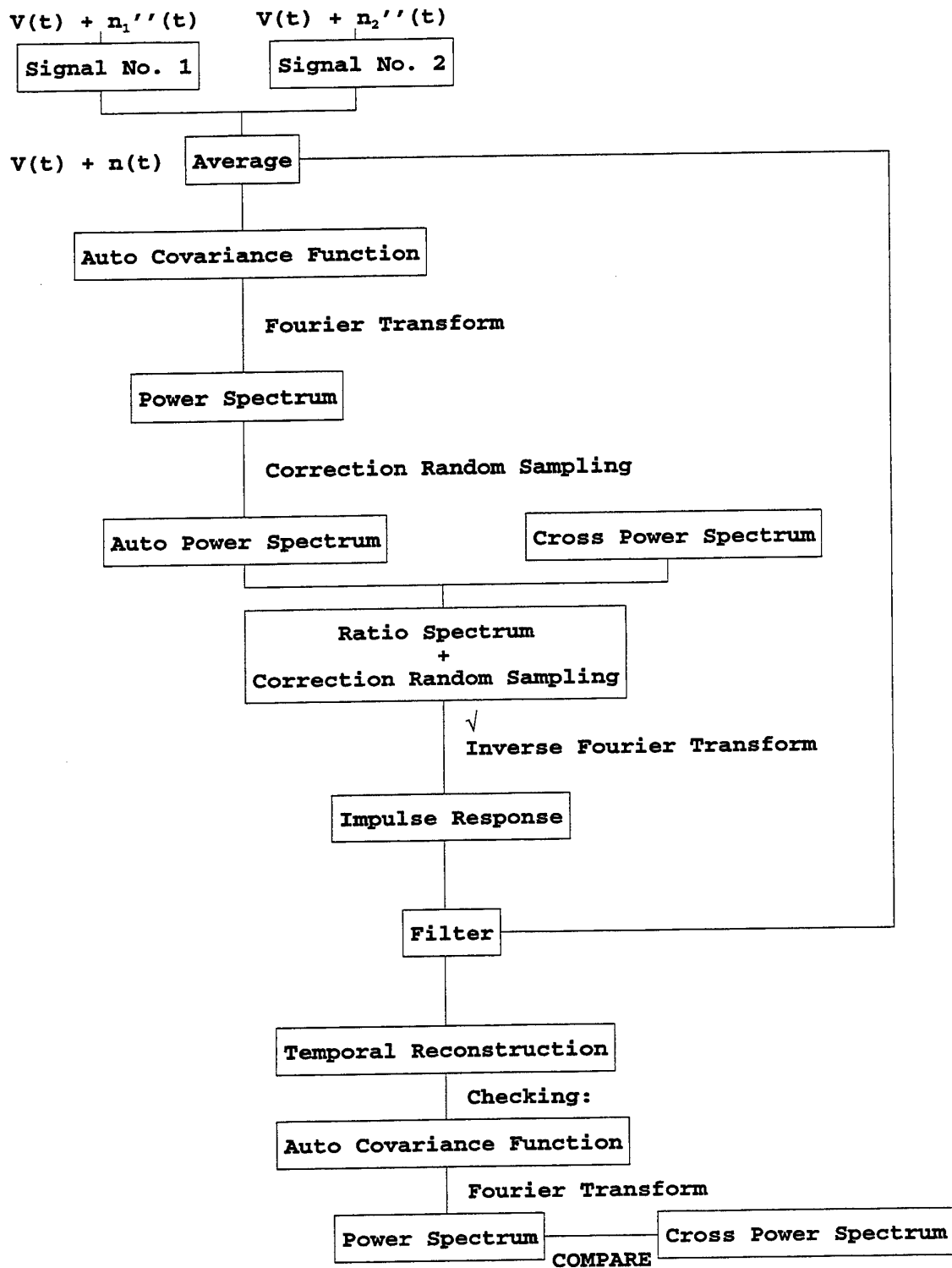
Table 1: Mean Squared Error Values.

<u>Condition</u>	<u>MSE (x 10⁻⁵), arb. units</u>
1. Low (1 kHz) rate linear. interpol.	15.9292
2. High (10 kHz) rate linear. interpol.	10.4186
3. As 2. with Gaussian filter.	9.1148
4. 1 st -order Kalman rec. (DR 500 Hz).	7.0037
5. As 4. + extended. reconstr.	3.6940
6. As 5. (DR 1000 Hz)	2.0195

Data Processing I



Data Processing II



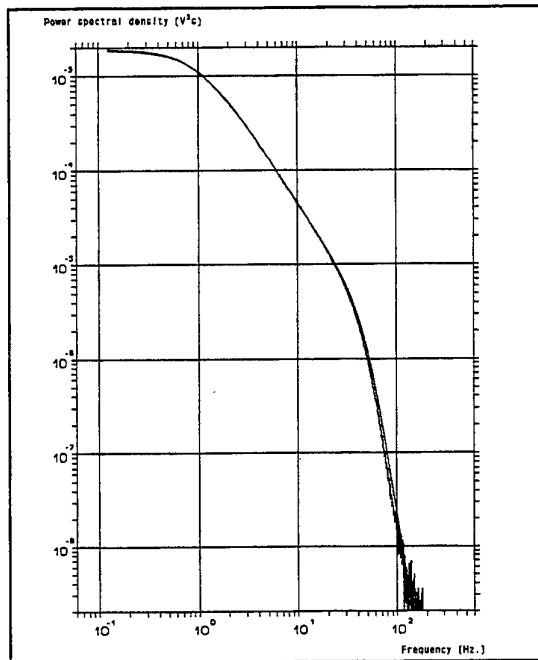


Figure 1: Cross power spectrum derived from the cross covariance function of two Kalman reconstructed velocity traces (data rate = 1 kHz) and the spectrum of the simulated turbulence.

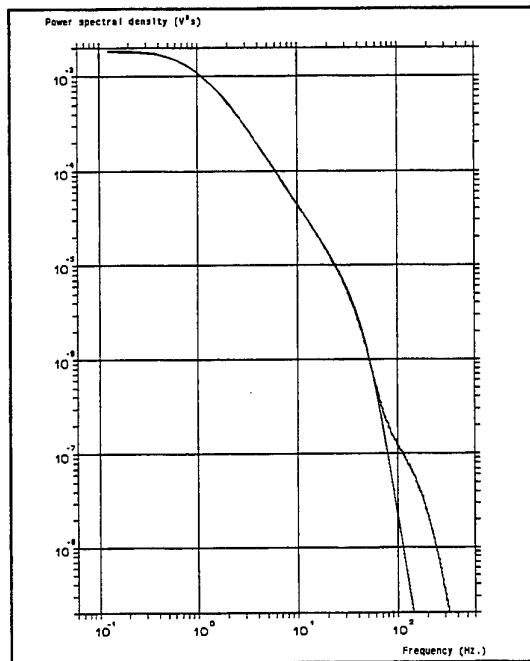


Figure 2: Auto power spectrum derived from the auto covariance function of the average of two Kalman reconstructed velocity traces (data rate = 1 kHz).

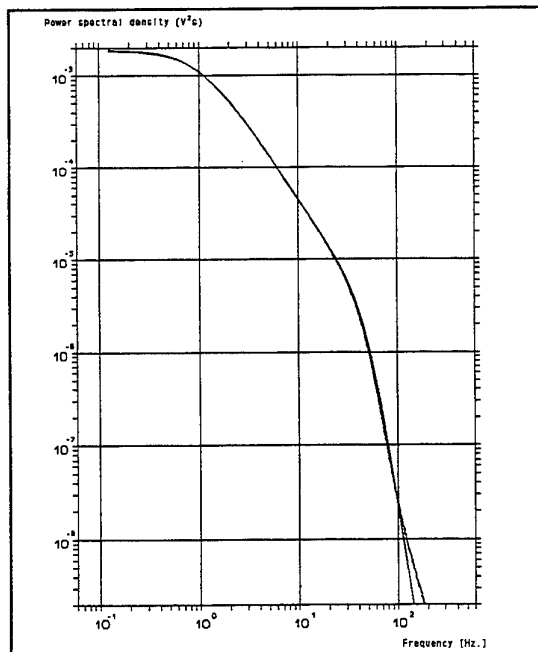


Figure 6: Auto power spectrum derived from the auto covariance function of the extended filtered version of $v_n(t)$ (average sampling rate = 1 kHz).

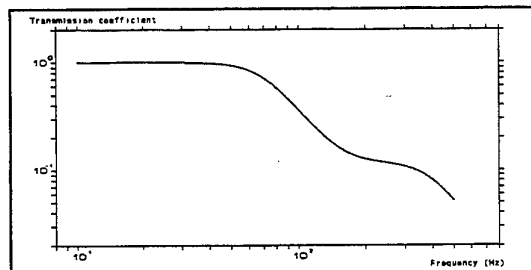


Figure 3: Characteristic of the extended reconstruction filter. $f_1 = 151$ Hz, $f_2 = 70$ Hz, $f_3 = 395$ Hz and $m = 5.6$

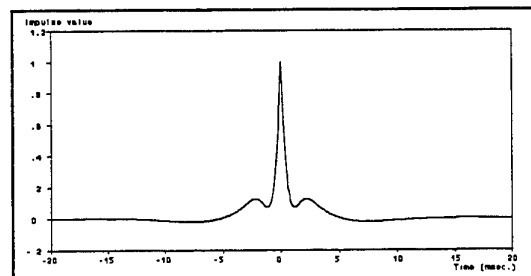


Figure 4: The impulse response of the filter of the extended reconstruction filter, including a correction for the random sampling.

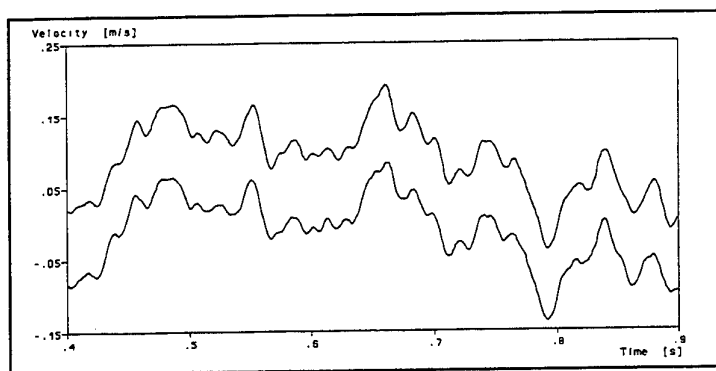


Figure 5: Simulated turbulence (upper curve) and reconstructed turbulence (lower curve); average data rate of 1 kHz.

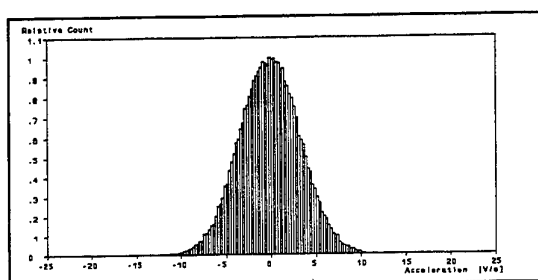


Figure 7: Histogram of the accelerations derived from the simulated turbulence.

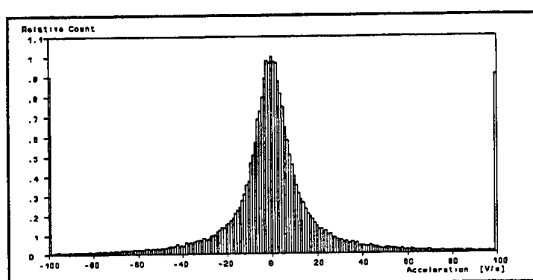


Figure 8: Histogram of the accelerations derived from the randomly sampled turbulence. Note the scale!

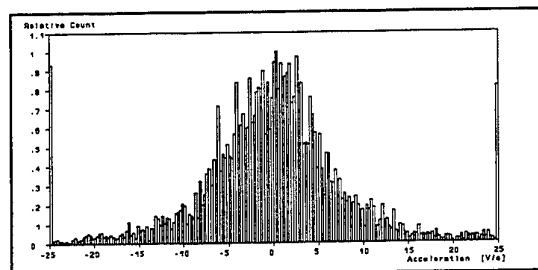


Figure 9: Histogram of the accelerations derived from the interpolated signal.

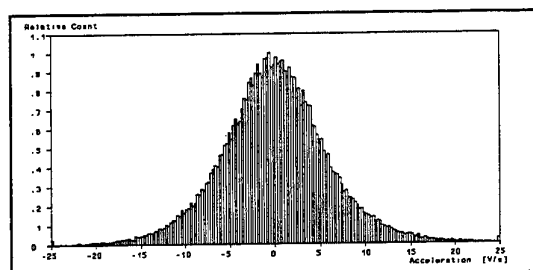


Figure 10: Histogram of the accelerations derived from the first-order reconstructed turbulence.

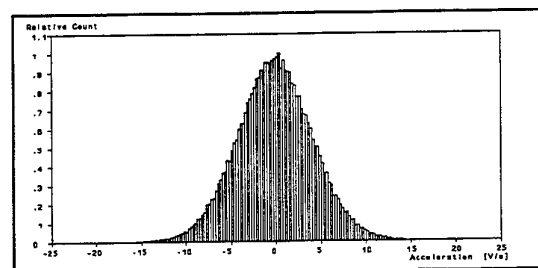


Figure 11: Histogram of the accelerations derived from the first-order Kalman reconstructed turbulence.

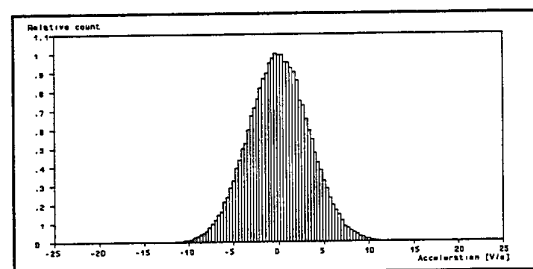


Figure 12: Histogram of the accelerations derived from the first-order Kalman reconstructed turbulence and extended reconstruction filtering.

DETERMINATION OF DOPPLER FREQUENCIES AND CHARACTERISTIC FREQUENCY MODULATION PHENOMENA IN LASER DOPPLER SIGNALS

Peter Lehmann

Meß- und Regelungstechnik, FB Produktionstechnik
University of Bremen, Germany

ABSTRACT

The prime task of laser Doppler signal processing is the determination of the Doppler frequency of a measured burst signal. In the first part of this paper digital algorithms for this purpose are examined by Monte Carlo simulations. Especially those algorithms that are based on the fast Fourier transform (FFT) (either in combination with a spectral peak interpolation procedure or as a realization of the discrete Hilbert transform) represent a good choice in this context. However, in practical applications of LDA the Doppler frequency is not always exactly stationary. For example, particle accelerations or droplet oscillations give rise to characteristic frequency modulation phenomena of the Doppler signals. These can be observed, when time-frequency analysis is applied. Therefore, several approaches in this field have been studied in order to obtain maximum information from a measured Doppler burst. Two of these methods are also based on the analytic signal calculated via Hilbert transform. These are the 'direct time-frequency estimation' and the 'Wigner-Ville distribution'. As an alternative an algorithm based on the 'short time Fourier transform (STFT)' will be introduced, which provides realtime capabilities by use of a recursive computation of the Fourier coefficients corresponding to the time-frequency representation of the signal. All algorithms have been first investigated using simulated frequency modulated signals and have been applied also to measured Doppler signals obtained under different experimental conditions.

1. INTRODUCTION

Signal processing in laser Doppler anemometry generally deals with an accurate determination of the Doppler frequency of a measured burst signal in the

presence of noise. The most common digital algorithms for this purpose are based on spectral analysis using the fast Fourier transform (FFT) (e.g. Matovic and Tropea 1991) or autoregressive (AR) parameter identification (e.g. Kay and Marple 1981) or use the noise reduction properties of the autocorrelation function (ACF-methods) (e.g. Matovic and Tropea 1989). In the following, the practical applicability of these different approaches will be assessed by the computational load and the frequency estimation error obtained from Monte-Carlo simulations. In general, it is assumed that the parameters of the signals, which are to be analysed, are stationary. This means that the Doppler frequency does not change within the sampling period.

However, on experimental investigation characteristic frequency modulation phenomena could be observed in laser Doppler signals (Lehmann et al. 1997). Such effects appear when the particles under investigation are accelerated within the LDA measurement volume or in the case of drops or bubbles, which show temporal changes of their shape (e.g. droplet oscillations). A constant acceleration of a spherical particle results in a linear frequency modulation of the Doppler signal. In addition, an oscillating particle shape leads to a periodic modulation of the Doppler frequency. Of course, a periodic frequency modulation occurs if Doppler signals are produced by particles in an acoustic field (Herzog et al. 1996).

2. DETERMINATION OF DOPPLER FREQUENCIES

Since the early applications of the laser Doppler technique a broad variety of digital signal processing approaches has been proposed. Some of the most used algorithms showing a high accuracy and an acceptable computational burden will be discussed in this section.

With respect to that what follows not only the dependence on the signal-to-noise ratio will be taken into account but also the shape of the burst amplitude and the

number of cycles of the signal under investigation will be varied.

The most wide-spread method, however, may be the computation of the power spectral density (PSD) via FFT combined with an interpolation between the maximum spectral lines of the PSD in order to reduce errors resulting from the finite spectral resolution of the FFT. Due to the intensity distribution of a Gaussian laser beam it is generally assumed that the shape of the burst envelope is also Gaussian, so that the Gaussian spectral peak interpolation can be applied successfully (Matovic and Tropea 1991).

Otherwise, if only a small section of a complete Doppler signal is evaluated, one can assume that the burst amplitude shows an approximately exponential change (either an exponential increase or an exponential decrease). In these cases the so-called Rajaona spectral peak interpolation (Rajaona and Sulmont 1985, Lehmann 1997) should be preferred, which assumes that the signal $s(t)$ in the time domain may be described by

$$s(t) \sim \text{Re}(\exp(i\omega_0 t + \phi_0)), \quad (1)$$

where $\text{Re}(\dots)$ denotes the real part of the embraced complex number. Exponential changes of the amplitude are taken into account since the angular frequency ω_0 may be complex. In contrast to the Gaussian spectral peak interpolation the Rajaona algorithm is based on the complex-valued Fourier coefficients instead of the real PSD.

The Hilbert transform of a signal $s(t)$ results in the analytic signal $a(t)$ with the real part $\text{Re}(a(t)) = s(t)$ and a 90° phase-shifted signal as the imaginary part. The discrete Hilbert transform (DHT) is realized as follows: The discrete signal $s_n = s(n \Delta t)$ ($n \in \{0, \dots, N-1\}$, where N is the number of sample points) is first transformed by FFT to the frequency domain. Then the spectral coefficients A_k are chosen such that $A_k = 2S_k$ for $k \in \{0, \dots, N/2-1\}$ and $A_k = 0$ for $k \in \{N/2, \dots, N-1\}$. Finally, an inverse FFT of the coefficients A_k yields the discrete analytic signal. An alternative technique to produce the analytic signal is the quadrature demodulation technique (QDT), which was widely applied in the context of LDA over the last years (e.g. Czarske et al. 1993, Strunk et al. 1996).

The time-dependent phase $\phi(t)$ is determined from the analytic signal by use of the relationship

$$\phi(t) = \arctan(\text{Im}(a(t)) / \text{Re}(a(t))) + m 2\pi, \quad (2)$$

where m is an integer which can be obtained by an unwrapping procedure. The Doppler frequency f_D results from the gradient of $\phi(t)$ if a linear relationship

$$\phi(t) = 2\pi f_D t + \phi_0$$

is assumed (i.e. a stationary Doppler frequency) and can be obtained by linear regression (Czarske et al. 1993, Lehmann and Schombacher 1997). However, due to the sampling process in the frequency domain, the imaginary part of the analytic signal is periodically continued. This results in the curves shown in Fig. 1. If the number of sampled signal cycles is not an integer this leads to discrepancies between the 90° phase-shifted signal and the imaginary part of the DHT at the beginning and at the end of the sampling period (see Fig. 1b). In order to avoid systematic errors in the frequency estimation only the discrete phase values ϕ_n with $n \in \{10, \dots, N-11\}$ have been used for frequency estimation by linear regression.

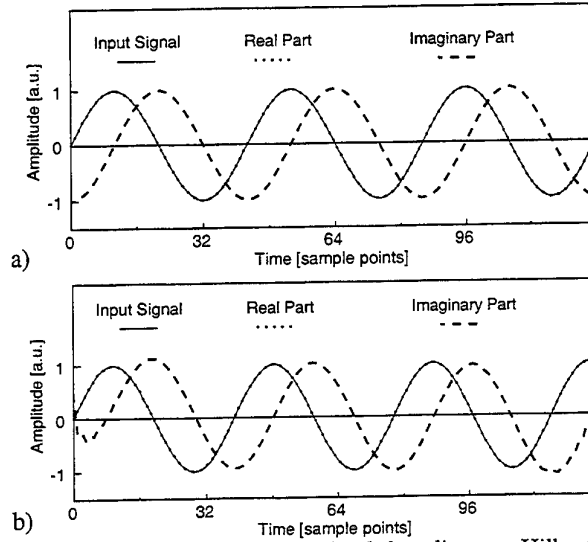


Fig. 1: Analytic signals obtained by discrete Hilbert transform corresponding to a sinusoidal input signal of a) 3.0 cycles per sampling period and b) 3.3 cycles per sampling period ($N=128$).

A completely different approach to the spectral analysis of Doppler signals is the maximum entropy method (MEM) realized by the Burg-algorithm (Kay and Marple 1981, Kammeyer and Kroschel 1992, Press et al. 1989). This autoregressive method is based on the autocorrelation function (ACF) of the signal. The signal under evaluation is approximated by a recursive filtering of a white noise generation process. The power spectral density $P(z)$ in the z -domain is approximated by

$$P(z) \approx a_0 / |1 + \sum_{k=1}^M a_k z^k|^2, \quad (3)$$

where M is the number of poles of the PSD estimation. By use of the Burg-algorithm the unknown coefficients a_1, a_2, \dots, a_M are estimated. For details it is referred to the relevant literature.

Another LDA signal processing method based on the ACF has been studied but was rejected due to a lack of accuracy (Matovic and Tropea 1989).

In order to compare the performance of the signal processing approaches under investigation Monte Carlo simulations have been carried out. Laser Doppler signals of well known signal-to-noise ratio (SNR) were produced by the addition of Gaussian white noise to Gaussian weighted or pure sinusoidal functions. The frequency estimation errors have been calculated for 100 realizations of the stochastic noise process assuming a constant SNR value. The SNR was defined according to the commonly used SNR definition (e.g. Shingpaugh et al. 1992). Final results of the frequency estimation error given as the standard deviation (related to the assumed Doppler frequency) are depicted in Fig. 2 assuming a sinusoidal signal with 3.3 cycles within the sampling period as it is shown in Fig. 1b. Due to the occurrence of leakage this may be interpreted as the 'worst case' (see Lehmann and Schöne 1997). When the SNR is greater than 8 dB the Hilbert transform method exhibits the best results. However, also the FFT in combination with the Rajaona interpolation yields satisfying results and should be preferred especially when the signal quality is low. For comparison, in Fig. 2 also the Cramer-Rao lower bound is plotted (Rife and Boorstyn 1974).

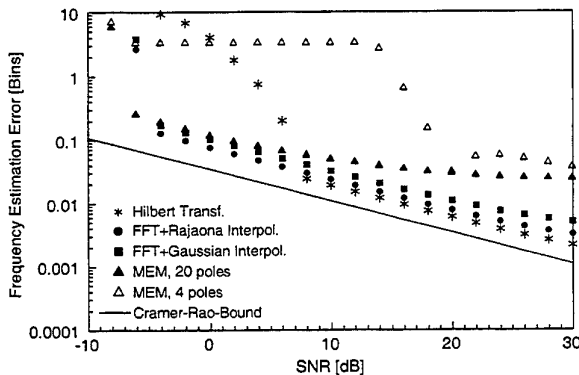


Fig. 2: Frequency estimation errors of different signal processing algorithms obtained from Monte Carlo simulations assuming the sinusoidal signal according to Fig. 1b.

The situation is different if we assume a Gaussian weighted sinusoidal signal symmetrically within the sampling period. Due to the Gaussian envelope the Rajaona interpolation shows rather large errors as it was to be expected. For high SNR values (>14 dB) the results of the Hilbert transform method, the MEM results assuming four poles, and the Gaussian windowed FFT with Gaussian spectral peak interpolation show the smallest errors. For lower signal quality only the FFT combined with a Gaussian spectral peak interpolation

should be used. Note, that although information of the signal is lost by use of the Gaussian window, there is only less influence on the frequency estimation for low SNR but because of the leakage reduction the estimation error shrinks significantly for higher SNR. The maximum entropy method (assuming 4 poles) is a promising alternative in comparison with FFT signal processing, when the signal quality is sufficient and the number of cycles within the sampling period is high enough.

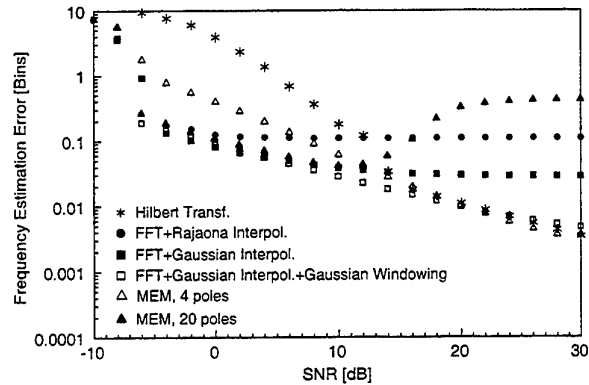


Fig. 3: Frequency estimation errors of different signal processing algorithms obtained from Monte Carlo simulations assuming a Gaussian weighted sinusoidal signal with 33.3 cycles within the sampling period (the maximum amplitude is reduced by $1/e^2$ at the beginning and at the end of the record period).

Finally, Tab. 1 gives the computational load of the different numerical algorithms introduced above in relation to common FFT signal processing.

Tab. 1: Computational load for different algorithms

FFT+ spectral peak interpolation (Gaussian or Rajaona)	100 %
Hilbert transform method	360 %
MEM method, 4 poles	144 %
MEM method, 20 poles	565 %

3. TIME-RESOLVED LDA SIGNAL PROCESSING

Frequency modulation phenomena can be determined by use of time-frequency analysis. Several approaches that allow a time-resolved determination of spectral characteristics have been published over the last years. For LDA applications a high resolution of the frequency estimation procedure must be required in order to avoid that the occurring frequency variation will be overwhelmed by uncertainties of the estimation algorithm. This chapter is intended to examine and to

compare different methods with respect to the demands of LDA and PDA. Three algorithms seeming convenient have been chosen. These are the 'direct time-frequency estimation' based on the analytic signal, the 'Wigner-Ville spectral distribution (WVD)' followed by a Gaussian spectral peak interpolation, and the 'short time Fourier transform (STFT)' in combination with the spectral peak interpolation introduced by Rajaona (Rajaona and Sulmont 1985), which takes an exponential change of the signal amplitude into account. The direct time-frequency estimation and the WVD are based again on the analytic signal obtained either by DHT (discrete Hilbert transform) or by the quadrature demodulation technique (QDT) (Czarske et al. 1993). The results presented here are based on the DHT as described in the previous chapter. Instantaneous frequency values f_n of a signal result from the discrete phase values φ_n , $n \in \{0, \dots, N-1\}$ by use of the rectangular numerical differentiation formula:

$$f_n = (\varphi_n - \varphi_{n-1}) / (2\pi \Delta t). \quad (4)$$

The Wigner Ville distribution is generally defined by (Skerl et al. 1994, Lehmann 1997):

$$WV(t, f) = \int_{-\infty}^{\infty} w(\tau/2) a(t + \tau/2) \times w^*(-\tau/2) a^*(t - \tau/2) \exp(-i2\pi f\tau) d\tau. \quad (5)$$

The numerical computation of the WVD can be achieved by a discrete Fourier Transform:

$$WV_{m,k} = \frac{1}{M} \sum_{n=0}^{M-1} w_n^2 a_{m+n} a_{m-n}^* \exp(-i\pi kn/M), \quad (6)$$

where the Wigner Ville spectrum is related to the m -th sample point on the time scale using $2M$ of all N sample points of the analytic signal. For the window function w_n we choose again the Gaussian function in order to apply the Gaussian spectral peak interpolation in the frequency domain.

Alternatively the STFT can be used for time-frequency estimation. The formula

$$S_{m,k} = \frac{1}{M} \sum_{n=0}^{M-1} s_{m+n-M/2} \exp(-i2\pi kn/M) \quad (7)$$

yields the spectral coefficients S_k related to the m -th sample point in the time domain. Note, that no window function is used in this formula. This allows to calculate the spectral coefficients related to the $(m+1)$ -th sample point by recursion:

$$S_{m+1,k} = (S_{m,k} + (s_{m+M/2} - s_{m-M/2})/M) \times \exp(i2\pi k/M). \quad (8)$$

By this recursive computation of the spectral coefficients a greatly reduced computational burden could be achieved (Lehmann 1997). To improve the frequency resolution of the STFT the Rajaona spectral peak interpolation is applied to estimate the instantaneous Doppler frequency using the spectral coefficients $S_{m,k}$, $S_{m,(k-1)}$ and $S_{m,(k+1)}$, where it is assumed that the k -th DFT spectral line corresponds to the maximum spectral peak in the local PSD.

The performance of these different methods could be further improved by FIR-filtering. The time-frequency signal f_n is convoluted by the filter function

$$g_n = \exp(-(n - n_0)^2 / (n_0 - 1)^2), \quad (9)$$

where $n \in \{0, \dots, 40\}$ and $n_0 = 20$. In the following the different methods are compared on the basis of a measured Doppler signal obtained from a rising butylacetate drop in water (Schombacher 1997). The Doppler signal is shown in Fig. 4. In the time-domain one can not observe any changes of the Doppler frequency. However, the results of time-frequency estimation exhibit the characteristic behaviour as it is shown in Fig. 5 and Fig. 6: The Doppler frequency shows a nearly linear increase and a superimposed periodic modulation. These effects result from the acceleration of the droplet within the measurement volume and a periodic oscillation of the droplet shape.

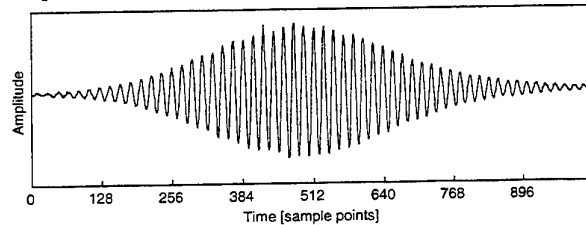


Fig. 4: Laser Doppler signal obtained from a rising butylacetate droplet of 1.1 mm diameter in water (distance between measurement volume and droplet detachment: 10 mm).

Fig. 5 was obtained by use of the direct time-frequency estimation method. The fine line shows rather large fluctuations resulting from the noise dependence of the numerical differentiation procedure. This curve can hardly be utilized to identify frequency modulation phenomena. Although the signal quality is high, only the bold line, which represents the time-frequency curve after FIR filtering, shows the main characteristics of the signal. The corresponding results of the WVD and STFT technique are depicted in Fig. 6. In these two cases the time-frequency curve is less influenced by noise.

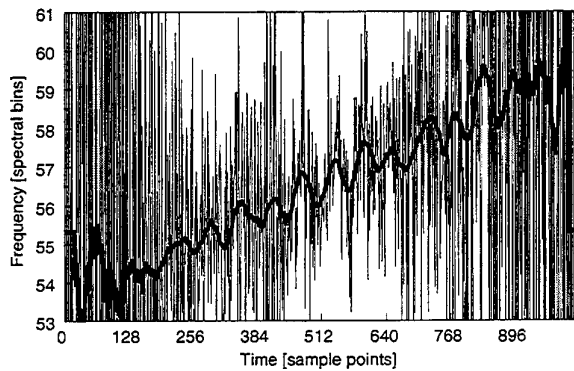


Fig. 5: Result of the direct time-frequency estimation for the Doppler burst according to Fig. 4: fine line: result without filtering, bold line: result after FIR filtering.

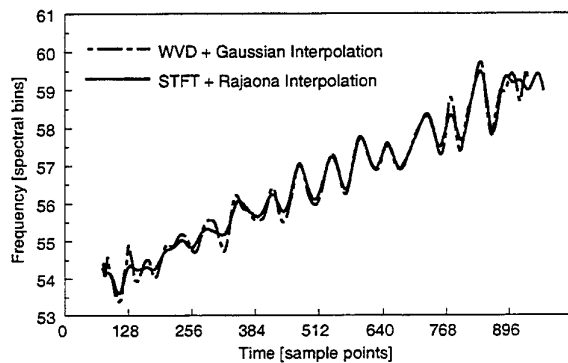


Fig. 6: Time-frequency curves for the Doppler burst according to Fig. 4 obtained by WVD and STFT ($M=64$).

To study the dependence of the different approaches on the signal-to-noise ratio (SNR) more quantitatively, Monte-Carlo simulations have been performed. Gaussian white noise has been added to a test signal given by

$$s_n = \sin(2\pi(50 + 2.5 \frac{n}{N}) \frac{n}{N} + 0.5 \sin(10\pi \frac{n}{N})), \quad (10)$$

which shows a linear and a superimposed sinusoidal frequency modulation (see Fig. 7d).

Some results of time-frequency analysis are shown in Fig. 7. The diagrams in Fig. 7a and 7b were obtained under the assumption of SNR=10 dB. In the case of the direct time-frequency estimation the frequency modulation can only be established if FIR-filtering is applied (bold line in Fig. 7a). The Wigner-Ville and the STFT based methods can be used both in the case of the 10 dB signal (see Fig. 7b). However, if the SNR is reduced to 0 dB the direct time-frequency estimation (followed by FIR-filtering) and the WVD fail as it can be seen in Fig. 7c. From the STFT result shown in Fig. 7d

the principal time-frequency behaviour can be established even in this case.

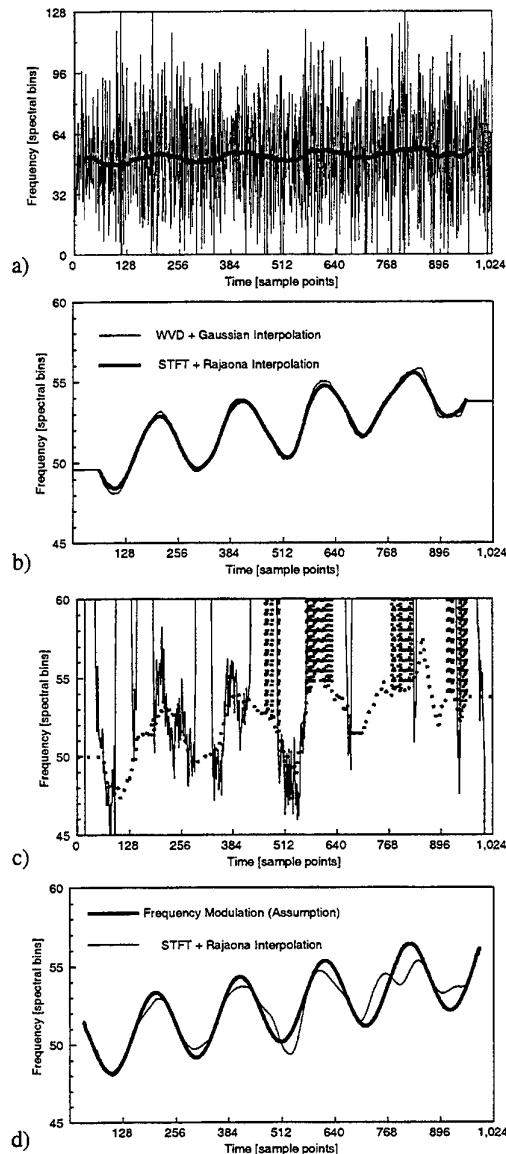


Fig. 7: Comparison of methods for time-frequency analysis assuming a linear and a superimposed periodic frequency modulation and SNR values of 10 dB (Fig. 7a and 7b) and 0 dB (Fig. 7c and 7d). Fig. 7a: results of the direct time-frequency estimation (fine line), same result after FIR filtering (bold line); Fig. 7b: results of WVD and STFT ($M=128$); Fig. 7c: results of the direct time-frequency estimation after FIR-filtering (solid line) and WVD results (dotted line); Fig. 7d: STFT result (fine line), bold line: frequency modulation acc. to eq.(10).

If the computational efficiency is also taken into account, the modified STFT should be preferred for practical applications, since this method allows a time-frequency analysis in realtime. Due to the recursive computation of spectral coefficients according to eq. (8) the computational burden of the STFT method in comparison with the WVD is less than 5 % (Lehmann 1997).

4. APPLICATIONS OF TIME-RESOLVED SIGNAL PROCESSING

In the following only the recursive STFT method in combination with the Rajaona spectral peak interpolation is used to analyse Doppler signals measured under different experimental situations. The results shown in Fig. 8 exhibit the frequency modulation of Doppler signals produced by water droplets of 50 μm diameter, which were generated by a piezoelectrical droplet generator.

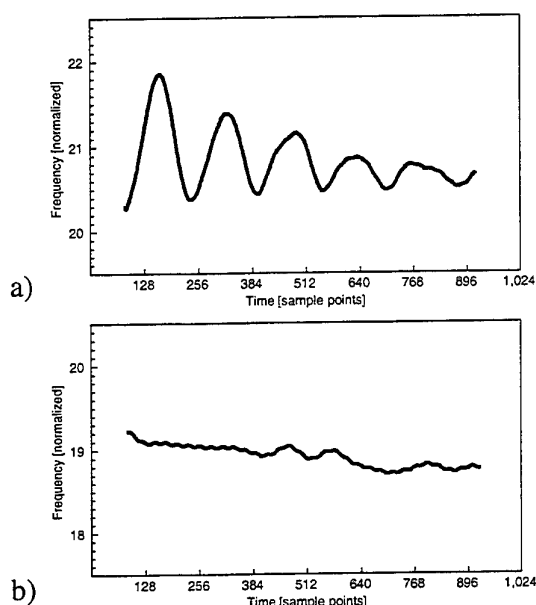


Fig. 8: Time-frequency curves calculated for Doppler signals produced by water droplets (a) soon after detachment from the droplet generator, (b) for a larger distance between droplet generator and measurement volume.

In the case of Fig. 8a the measurement volume was positioned close to the orifice of the droplet generator. The periodic frequency modulation which can be explained by an oscillating droplet shape stimulated by the detachment of the droplet is damped within the measurement volume. For Fig. 8b the distance between droplet generator and measurement volume was about 20

mm. At this distance the droplet oscillation has been damped down, so that the Doppler signal shows no periodic frequency modulation. Nevertheless, a nearly linear decrease of the Doppler frequency can be observed in Fig. 8b, which is attributed to the deceleration of the droplet due to a convective air stream that was directed against the motion of the droplet.

Besides the computational efficiency with respect to time-frequency estimation another advantage of the STFT technique in comparison with the WVD is its applicability to phase Doppler signals (i.e. a time-resolved PDA phase difference curve can be determined) as it is shown in Fig. 9. The experimental results according to Fig. 9 were taken from a rising toluene drop in water. An oscillation of the droplet shape was achieved by the rather large drop size (diameter ≈ 2.5 mm) and by measuring only a short time after the droplet's detachment from the capillary. The Doppler signal shows a strong periodic frequency modulation. In Fig. 11 the corresponding simulation results which were obtained from the mathematical modeling of the oscillating droplet shape according to Fig. 10 in combination with ray tracing computations based on geometrical optics are presented.

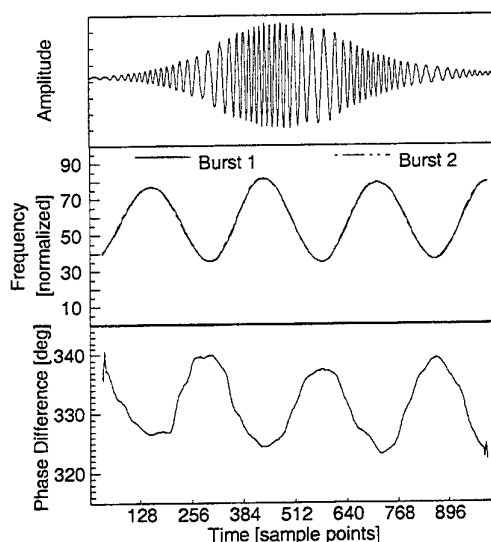


Fig. 9: Burst signal produced by a rising toluene drop in water and results of time-resolved signal processing.

A satisfying agreement between theoretical and experimental results can only be reached by a combination of the two basic types of oscillation according to Fig. 10, where the amplitude of the type B oscillation is chosen six times larger than the amplitude of the type A oscillation

and the volume $V = \pi d_e^3/6$ ($d_e = 2.5$ mm) is constant (Lehmann et al. 1998):

$$\begin{aligned} d_v/2 &= 1250 \mu\text{m} + 10 \mu\text{m} \cos(8\pi z / L_m), \\ b_2 &= d_v/2 + 60 \mu\text{m} \cos(8\pi z / L_m), \\ b_1 &= d_v - b_2. \end{aligned}$$

The variable 'z' represents the position of the droplet which moves with constant velocity along the vertical axis (z-axis) and L_m is the length which is covered by the droplet during the sampling period.

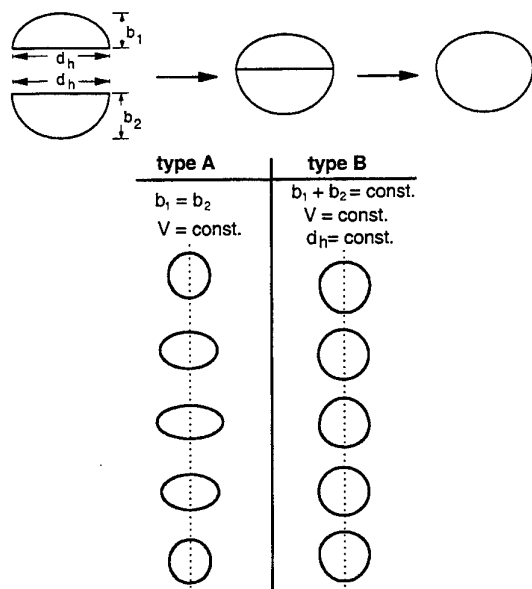


Fig. 10: The double semi-ellipsoid shape (Clift et al. 1978) and basic types of droplet oscillation.

If a pure centre of gravity oscillation (type B) is assumed the Doppler signal in the time domain and the frequency modulation are in agreement with the experimental observation, but the PDA-phase difference does not show any significant temporal changes. Furthermore, if an oblate / prolate oscillation (type A) is assumed, an opposite time-frequency behaviour can be observed and a rather large periodic phase difference modulation results.

In Fig. 9 and 11 both, the experimental and the simulated signals show the same sinusoidal frequency modulation. In addition, the phase difference modulation in Fig. 9 is in accordance with the ray tracing result denoted as 'Theoret. Result' in Fig. 11. The ray tracing result agrees also with the result of signal processing obtained from the simulated Doppler signals.

With this background the results of time-frequency analysis presented in Fig. 5, 6, 8, and 9 allow to determine characteristic parameters describing particle deformation and acceleration. The sampling frequencies

for the experimental situations corresponding to Fig. 4-6, Fig. 8 and Fig. 9 are given in Tab. 2.

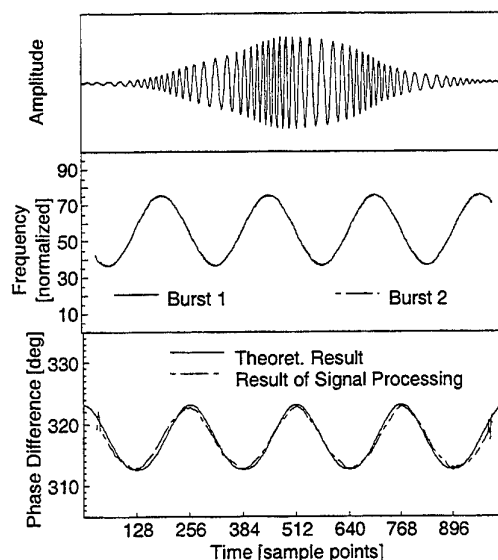


Fig. 11: Simulation results obtained from mathematical modeling of an oscillating toluene drop in water (combination of oscillation types A and B) and ray tracing computations to simulate PDA bursts.

Tab. 2: Sampling frequencies corresponding to different experimental situations.

	Fig. 4-6	Fig. 8	Fig. 9
Sampling Frequency [MHz]	0.012	3.75	0.054

5. DISCUSSION

In the previous sections frequency estimation procedures and several methods for a time-resolved LDA signal analysis have been investigated. The results have shown that FFT-based methods provide a high accuracy in both cases, the determination of a unique Doppler frequency of a stationary signal, and the determination of instantaneous frequencies in cases of non-stationary Doppler signals, which appear when particles are accelerated or droplets change their shape.

The recursive STFT algorithm presented in the latter context offers considerable benefits:

- a satisfying accuracy even in the presence of noise,
- a reduced computational effort and thus realtime capabilities,
- the computation of time-resolved PDA phase differences when required.

With respect to future applications of LDA and PDA these features may be utilized

- to obtain more information from LDA signals and, as a consequence, to increase the accuracy of flow measurements without instrumental modifications
- to check the sphericity assumption of the PDA principle and to extend the range of application of the PDA technique since the quantitative analysis of droplet oscillations finally leads to the viscoelastic properties of the particle system under investigation.

REFERENCES

- Czarske, J.W., Hock, F., Müller, H. 1993, Einsatz der Drehzeigersignalverarbeitung in der Laser-Doppler-Anemometrie, Technisches Messen, vol. 60, no. 3, pp. 99-105.
- Clift, R., Grace, J.R., Weber, M.E. 1978, Bubbles, Drops and Particles, Academic Press, New York.
- Herzog, P., Valière, J.C., Valeau, V., Tourniois, G. 1996, Acoustic Velocity Measurements by Means of Laser Doppler Velocimetry, Proc. 8th Int. Symp. on Applications of Laser Anemometry to Fluid Mechanics, pp. 36.4.1-36.4.8.
- Kay, S.M. & Marple, S.L. 1981, Spectrum Analysis - A Modern Perspective, Proc. of the IEEE, vol. 69, no. 11, pp. 1380-1419.
- Kammeyer, K.D. & Kroschel, K. 1992, Digitale Signalverarbeitung, B.G. Teubner, Stuttgart.
- Lehmann, P., Schombacher, E.H., Wriedt, T. 1997, Determination of Droplet Accelerations, Oscillations, and Non-Sphericities by Phase Doppler Anemometry, Proceedings 7th International Conference on Laser Anemometry - Advances and Applications, pp. 671-678.
- Lehmann, P. & Schöne, A. 1997, Estimation of the Signal-to-Noise Ratio of Laser Doppler Signals, Proceedings 7th International Conference on Laser Anemometry - Advances and Applications, pp. 99-106.
- Lehmann, P. & Schombacher, E.H. 1997, Features of a Combined FFT and Hilbert Transform for Phase Doppler Signal Processing, Meas. Sci. Technol., vol. 8, pp. 409-421.
- Lehmann, P. 1997, Schnelle Zeit-Frequenz-Analyse auf der Grundlage der Kurzzeit-Fourier-Transformation, Technisches Messen, vol. 64, no. 6, pp. 247-258.
- Lehmann, P., Schombacher, E. H., Lohner, H., Bauckhage, K. 1998, Characterization of Nonspherical and Oscillating Droplets by Phase Doppler Anemometry and Rainbow Refractometry, Preprints 7th European Symposium Particle Characterization, pp. 109-118.
- Matovic, D. & Tropea, C. 1989, Estimation of LDA Signal Frequency Using the Autocovariance Lag Ratio Method, J. Phys. E: Sci. Instrum., vol. 22, pp. 631-637.
- Matovic, D. & Tropea, C. 1991, Spectral Peak Interpolation with Application to LDA Signal Processing, Meas. Sci. Technol., vol. 2, pp. 1100-1106.
- Press, W. H., Flannery, B.P., Teukolsky, S.A., Vetterling, W.T. 1989, Numerical Recipes in Pascal, Cambridge University Press, Cambridge
- Rajaona, R.D. & Sulmont, P. 1985, A Method of Spectral Analysis Applied to Periodic and Pseudoperiodic Signals, J. Comp. Physics, vol. 6, pp. 186-193.
- Rife, D.C. & Boorstyn, R.R. 1974, Single-Tone Parameter Estimation from Discrete-Time Observations, IEEE Trans. on Information Theory, vol. 20, no. 5, pp. 591-598.
- Schombacher, E. H. 1997, Laseroptische Meßtechniken zur Bestimmung prozessrelevanter Größen in der Flüssig/Flüssig-Extraktion, Diss. thesis, University of Bremen, VDI-Fortschrittberichte, Reihe 8, Nr. 648.
- Shinpaugh, K.A., Simpson, R.L., Wicks, A.L., Ha, S.M., Fleming, J.L. 1992, Signal Processing Techniques for Low Signal-to-Noise Ratio Laser Doppler Velocimetry Signals, Experiments in Fluids, vol.12, pp. 319-328.
- Skerl, O., Schmidt, W., Specht, O. 1994, Wigner-Verteilung als Werkzeug zur Zeit-Frequenz-Analyse nichtstationärer Signale, Technisches Messen, vol. 61, no. 1, pp. 7-15.
- Strunck, V., Müller, H., Dopheide, D. 1996, Time Domain Single Tone Analysis Using Quadrature Algorithm, Proc. 8th Int. Symp. on Applications of Laser Anemometry to Fluid Mechanics, pp. 6.6.1-6.6.4.

QUADRATURE DEMODULATION AS ADVANTAGEOUS DOPPLER SIGNAL PROCESSING TECHNIQUE

J. Czarske and O. Dölle

Laser Zentrum Hannover e.V., Development Department,
Hollerithallee 8, D-30419 Hannover, Germany, email cz@lzh.de

ABSTRACT

We present the application of the quadrature demodulation technique (QDT) for advantageously Doppler frequency determination. The QDT allows to measure low frequency burst signals, having also less than one signal period. Therefore small velocities can be time-resolved measured in the base band. This contribution presents a detailed investigation of the QDT properties like the frequency measuring error in dependence of e.g. the signal-to-noise-ratio and the signal frequency. In order to achieve a high data rate of the QDT, digital signal processors can be employed.

1. INTRODUCTION

Several signal processing techniques, like Fourier processors or zero crossing counters, are to date available for the laser Doppler velocimetry (LDV), see e.g. Shinpaugh et al. (1992), Tropea (1995). However, one challenge is still the time-resolved measurement of low Doppler frequencies. Using for example zero crossing counters, a precision frequency determination requires a great number of signal periods, since the occurring periods within the measuring time interval directly determine the possible number of measuring values. The measuring error of the fast Fourier transformation (FFT) signal processing technique is also dependent on the signal period number. The reason is mainly the leakage effect of the FFT, which results in a high systematic frequency error. In consequence, both signal processing techniques did not allow a time-resolved measurement of low signal frequencies. One method, used to solve these problems is adding of a auxiliary carrier frequency f_c to the Doppler signal frequency f_D , so that the resulting LDV signal has a sufficient period number $n=(f_c+f_D)\Delta t$ in the observed signal time interval Δt . This method is known as fringe biasing, referred to the enhancement of the resulting fringe number, crossed by the scattering particle. The fringe biasing can be realized e.g. by using of two Bragg cells, having a slightly different frequency shift or by a down-mixing of the frequency-shift LDV measuring signal with a reference oscillator signal, having a small offset of e.g. 1 kHz compared to the high carrier frequency. However, these techniques need two very stable oscillators, having neglect short time jitter and frequency drift, since also a small change of the carrier frequency can result in a great

measuring error of a low Doppler frequency. Furthermore, the adaptation of the carrier frequency for Doppler signals, having a frequency change is problematically.

In this contribution we demonstrate that the recently developed quadrature demodulation signal processing technique (QDT), Czarske et al. (1993), can overcome these drawbacks. The QDT allows real-time directional Doppler frequency measurements nearly independent on the signal period number, so that also small velocities can be determined in the base band. The operation of the QDT in the base band eliminates the mentioned problems of the fringe biasing, like the need of a stabile carrier frequency. Hence, the QDT enables the realization of novel directional LDV schemes, using advantageous laser sources, see e.g. Müller et al. (1994), Czarske (1996). The QDT is based on the determination of the phase time function of the generated quadrature signal pair. Hence it anticipates the interferometrical principle of LDV systems, meaning that the phase is directly proportional to the position of the scattering particle in the measuring volume. Therefore the QDT allows a direct access to complex particle movements, caused e.g. by turbulent flows or sound waves. An alternative method for the frequency-time analysis is the Wigner-Ville transformation (WVT), which is based on an iteration formalism. However, the WVT does not allow real-time measurements, requires a high memory effort and has systematic frequency errors caused by the iteration procedure, see Strunck et al. (1996).

The advantages of the QDT should be briefly addressed as follows: (i) An on-line Doppler frequency measurement is possible, since the QDT does not need an iteration procedure. (ii) The QDT is a maximum-likelihood estimator, reaching the Cramer-Rao (CR) lower uncertainty bound in contrast to zero crossing counters. In comparison with the FFT the need of window functions is not necessary. Additionally, the complicated center frequency interpolation between the discrete frequency values of FFT spectrum can be saved. (iii) Directional discrimination in the base band, so that the effort for the generation of a stabilized carrier frequency can be saved. Thus, novel optical schemes for LDV systems can be realized, e.g. the use of novel laser sources for a direct carrier frequency generation without having to use any additional frequency shift elements, see e.g. Czarske et al. (1997). (iv) Measurement of low velocities in the base band. The access to the position time function of the scattering particle enables accurate measurements of slow motions, e.g. the velocity zero can be measured by the QDT as a constant

phase time function. (v) Accurate frequency determination of LDV burst signals, having only a few periods or a fraction of one period, which was first demonstrated by Müller et al. (1995). The signal phase can be determined in principle independently of signal period numbers. In consequence, also scattering particles moving nearly parallel to the fringe system can be measured, which occurs e.g. in complex multiple-dimensional fluid flows. (vi) Time resolved measurement of frequency modulated LDV signals, occurring e.g. due to velocity gradients in the measuring volume. The QDT allows to determine the momentary Doppler frequency as derivative of the signal phase, so that the time frequency distribution is directly available.

These referred features of the QDT should be illuminated in this paper. One aim is to investigate the Doppler frequency measuring error in dependence on different signal parameters like SNR and period number. Furthermore we will present a technical realization of the QDT, which is based on a digital signal processor (DSP).

2. INVESTIGATIONS ON THE QUADRATURE DEMODULATION TECHNIQUE (QDT)

2.1 Principle of the QDT

The quadrature demodulation technique (QDT) consists of three stages by Czarske et al. (1993): (1) The generation of a quadrature signal pair, i.e. a sine signal and a cosine signal (2) the time-resolved determination of the phase angle of the signal pair and (3) the evaluation of the determined phase-time function, e.g. in order to calculate the momentary Doppler frequency.

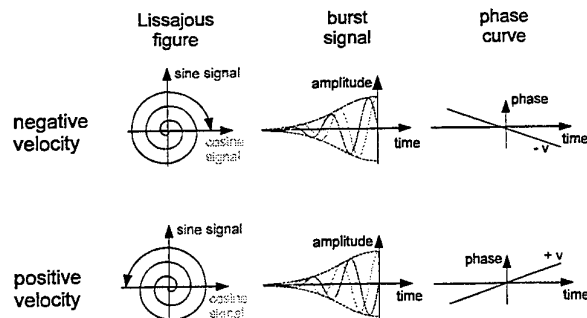


Fig. 1 Quadrature signal pairs, given for opposite moving directions of the scattering particle.

- (1) Signal generation: The quadrature signal pair is given by two signals $a_1(t)$, $a_2(t)$ having the same amplitude $A(t)$ and a phase difference of $\phi_2(t) - \phi_1(t) = \pm 90^\circ$, so that one can say the signals are in quadrature. They can be described as a complex signal in Cartesian coordinates as well as in polar coordinates: $a(t) = a_1(t) + i a_2(t) = A(t) [\cos \phi_1(t) + i \cos \phi_2(t)] = A(t) [\cos \phi(t) \pm i \sin \phi(t)] = A(t) \exp [i \phi(t)]$, where the common phase angle $\phi(t)$ is set to $\phi_1(t)$ and is given by $\phi(t) = 2\pi f_D t$. In Fig. 1 the quadrature signal pair is shown for opposite velocity directions. As can be seen, the direction of

the fluid flow corresponds to the sign of the phase difference. The quadrature signal pair can be generated by different phase shift methods according to Czarske (1996): (i) Mathematical calculation of the phase shift, e.g. by using the Hilbert transformation. (ii) Using an optical phase shift between two generated fringe systems. (iii) Electrical phase shift generation: Directional heterodyne LDV systems generally have a constant carrier frequency, which easily allows the realization of a constant quadrature phase shift, e.g. by using a simple delay line, a LC circuit or a PLL oscillator. Down mixing of the in-line and the quadrature carrier signals with the carrier frequency Doppler signal results in a quadrature signal pair, laying in the base band, see Fig. 2. The necessary components like mixers and low pass filters are commercially available at low cost, e.g. from the company mini-circuits.

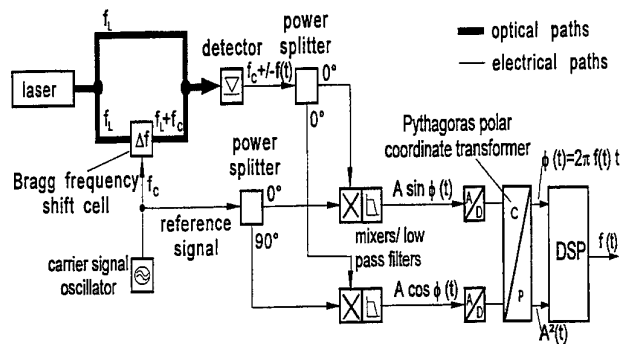


Fig. 2 Heterodyne LDV system, used for the generation and demodulation of the quadrature signal pair

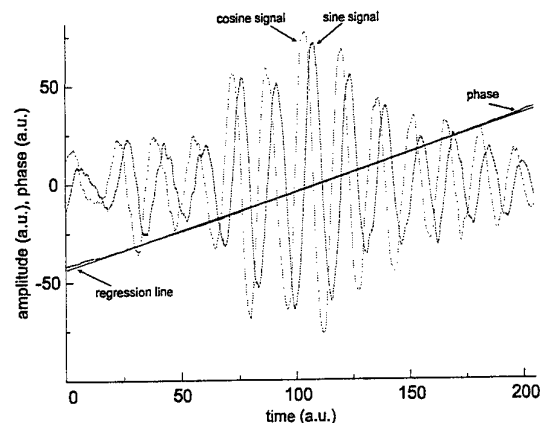


Fig. 3 Measured quadrature signal pair. A straight regression line was fitted to the phase time curve.

- (2) Phase measurement: The phasor $a(t)$ of the quadrature signal pair is running on a spiral Lissajous figure (see Fig. 1), where the phase angle is given by the following expression:

$$\phi(t) = \arctan \{ \text{Im}[a(t)] / \text{Re}[a(t)] \} = \arctan \{ [A(t) \sin \phi(t)] / [A(t) \cos \phi(t)] \}. \quad (1)$$

This formula can be implemented by e.g. digital polar coordinate transformers, see Fig. 2. Since the phase is a relative value, the incremental counting of the period number of the LDV signal is necessary. The resulting unwrapped signal phase $\phi(t)$ is directly proportional to the position $x(t)$ of the scattering particle:

$$\phi(t) = 2\pi x(t)/d \quad (2)$$

where d is the fringe spacing of the fringe system in the measuring volume.

- (3) Phase evaluation: The determined phase time function can be evaluated by different methods, given e.g. in Boashash (1992). Using e.g. a simple differentiation of the phase, the momentary Doppler frequency is directly achieved. The occurring fluctuations of the frequency can be reduced by a smoothing of the phase differences or the fitting of a regression curve to the phase time function (see Fig. 3). The resulting coefficients of the regression curve correspond to the spectral moments of the burst signal like center Doppler frequency and mean Doppler frequency change, which are proportional to the mean velocity and mean acceleration, respectively, of the scattering particle movement through the measuring volume.

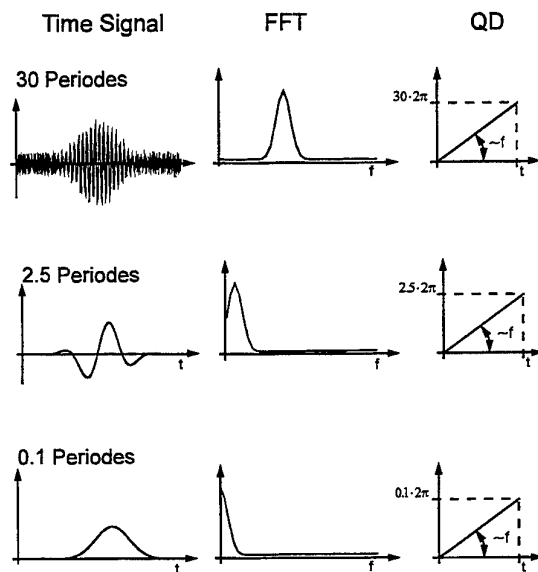


Fig. 4 Comparison between the real FFT and the QDT for low period burst signals. The different bursts can be generated according to Müller et al. (1995) by a tilted flow direction with respect to the fringe system in the measuring volume.

2.2 Determination of the frequency measuring error

We have investigated the systematic and statistical measuring error of the QDT and the FFT signal processing technique. First the systematic measuring error in dependence on the available period number will be discussed. In Fig. 4 the FFT spectrum and the QDT phase curve are shown for burst signals, having different period numbers. As can be seen, burst signals with low period number have a FFT spectrum with an asymmetrical line and a DC offset. In consequence, the center frequency determination exhibits a systematic deviation. In Fig. 5 the measuring error is shown in dependence on the signal period number. Using the FFT without time signal windowing (rectangular window) the leakage effect results in a high systematic measuring error for a not whole and small period number. This measuring error can be significantly reduced by a signal windowing, e.g. by the Hanning window, see Fig. 5. However, at least two signal periods are necessary for a precise FFT frequency estimation. In contrast to this familiar result, the measuring error of the QDT is in principle independent on the period number, since the QDT is based on the determination of a phase time curve and the phase value uncertainty is not influenced by the period number, see equation (2) and Fig. 4. However, a technical realization of the QDT has only a limited phase resolution due to the quantization process. This influences the frequency measuring accuracy, since the phase regression line flips between the available quantization steps. In Fig. 5 the systematic measuring error in dependence on the periods with the amplitude quantization bit number as parameter is outlined. Assuming a typical 8 bit resolution of the two digitized quadrature signals, the signal frequency can be accurately determined also for time intervals with only 1/100 periods. Consequently, low fluid velocities can be time-resolved measured in the base band, e.g. velocities down to $v = d \cdot f = 50 \mu\text{m/s}$ can be measured in short time intervals of 1ms, assuming a fringe spacing of $d = 5 \mu\text{m}$ in the measuring volume of the differential LDV system.

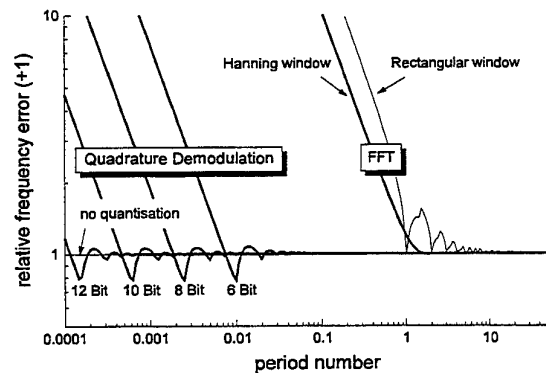


Fig. 5 Center frequency systematic measuring error against period number. (LabVIEW simulation: 512 samples, 1s time interval duration, real FFT with interpolation by seven point arithmetic mean calculation).

Hence, fluid flows with small velocity fluctuations at short time scales can be measured by QDT. Furthermore burst signals, having small period numbers due to a fluid flowing almost perpendicular to the LDV sensitivity vector can be evaluated as shown by Müller et al. (1997). This could allow a higher data rate for multiple dimensional LDV systems.

Next the statistical measuring error of the QDT and the FFT signal processing technique should be compared. Generally, the statistical error Δf of a maximum-likelihood estimator is given by the well-known Cramer-Rao (CR) bound according to Czarske (1996):

$\Delta f = \sqrt{6/(2\pi T \sqrt{\text{SNR}} \sqrt{N})}$, for $N \gg 1$, where T is the measuring i.e. averaging time of a quadrature signal pair with rectangular shape, SNR is the signal-to-noise ratio and N is the measuring value number. In Fig. 6 this formula is compared with the simulation results of the FFT and QDT. The FFT does not reach the CR bound. The reasons are mainly the reduction of the available signal power due to the used window and interpolation deviations between the discrete frequency values of the FFT. The QDT reaches the CR bound, but shows a phase demodulation threshold around a SNR of 9 dB. This threshold results mainly from the impossibility of an unwrapped phase measurement when the noise causes failures of the period counting. The threshold can be reduced by a smaller noise bandwidth or also by averaging procedures for the phase measurement according to Boashash (1992). This is currently under investigation.

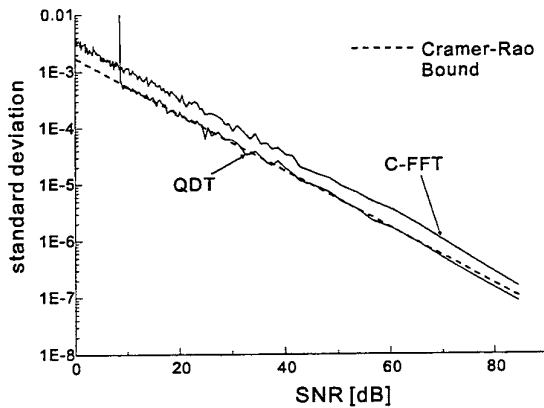


Fig. 6 Center frequency statistical measuring error against SNR, where quantization noise is not considered (LabVIEW simulation: 512 samples, 1s time interval duration, complex FFT: average of the center frequency amounts, calculated by seven point arithmetic mean).

2.3 Investigations on the burst signal processing

In contrast to the investigation of continuous signals in the former section, the SNR of burst signals is time dependent and for long measuring/averaging times there is a significant reduction of the SNR. Hence, the optimum averaging time of the burst signal, which corresponds to the minimum frequency error, needs to be determined. Fig. 7 shows that at first the error is reduced with averaging time, since the number of measuring values is increased. Then the error worsens due the reduction in SNR for long averaging times. The optimum averaging time is given approximately by the $+/-1/e^2$ Gaussian signal duration, assuming a shot noise limited measuring process, which occurs e.g. in APDs. Furthermore, it was assumed that the SNR is only dependent on the averaged power of the quadrature signal pair. Hence, the change of the SNR within one signal period is neglected. It should be noticed

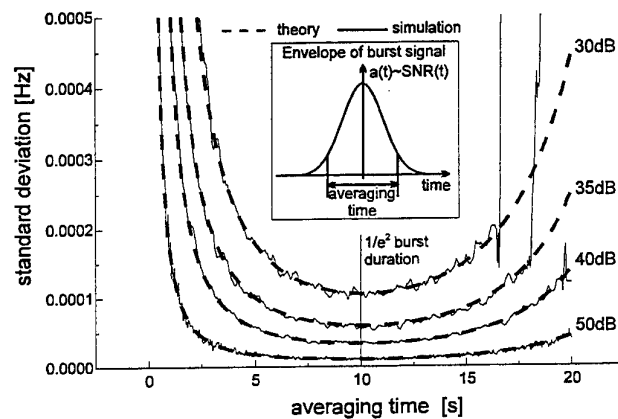


Fig. 7 Center frequency statistical measuring error of Gaussian burst signal against measuring time, assuming shot noise (LabVIEW simulation: $1/e^2$ duration is 10s, 512 samples, 50 averages, smoothing of the resulting curves). SNR values given for burst amplitude maximum.

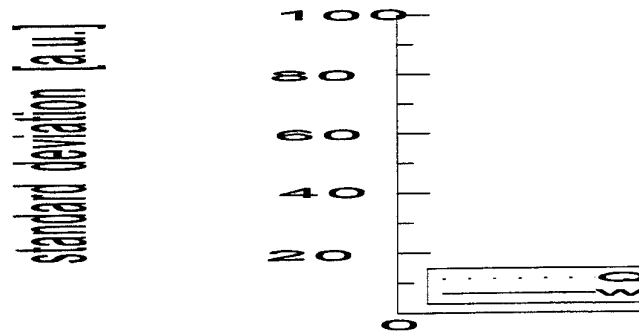
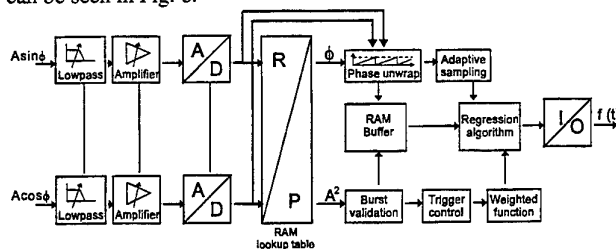


Fig. 8 Center frequency statistical measuring error of Gaussian burst signal against measuring time, assuming shot noise (LabVIEW simulation: $1/e^2$ duration at 5 a.u., 512 samples, 30 dB SNR at

In Fig. 8 the dependence of the FFT measuring error on the averaging time is shown. In contrast to the conventional QDT (where a regression of not weighted phase values is accomplished) the measuring error of the FFT converges for great measuring times asymptotically to a straight line of fixed value. These different behaviors results from the time domain and frequency domain signal processing of the QDT and FFT, respectively. Uncertain measuring values could have a strong influence on the measuring result of the time domain signal processor. Besides the QDT these could be observed also at counters, see Ruck et al. (1995). In consequence, the measuring time interval has to be limited, e.g. to the $\pm 1/e^2$ burst duration. Alternatively, a weighted linear regression can be accomplished, where the phase values are weighted inversely to their variance, according to Czarske (1996). Hence, then uncertain measuring values have a reduced influence on the center frequency determination, so that the measuring error is reduced, as can be seen in Fig. 8.



3. IMPLEMENTATION OF THE QUADRATURE DEMODULATION TECHNIQUE (QDT)

In Fig. 9 the scheme for a realization of the QDT is shown. The incremental phase values can be generated by different methods, e.g. by using a RAM table. Together with a detection of signal periods, e.g. by determining the 2π phase jumps, the unwrapped phase is achieved. The determined phase is the primary information about the movement of the scattering particle. These information can be extracted from the phase time series by different methods, see e.g. Boashash (1992). One possibility is the calculation of spectral moments on the LDV burst signal, like center frequency, average chirp frequency change, etc., which corresponds to the averaged velocity, acceleration, etc. of the scattering particle in the measuring volume. Based on a polynomial regression of the phase the spectral moments can be accurately determined. However, a multiple-parameter regression requires a high computational effort. The use of digital signal processors

The diagram illustrates the architecture of the DSP-Set-C50. At the top center is the main component, the **DSP TMS320C50**, which includes **-16Bit fixed Point**, **-80MHz**, and **-20KB RAM**. Surrounding this central unit are several peripheral components: **Flash-ROM**, **SRAM**, **Watch-Dog**, and **Timer** are positioned at the top; **PLD** is on the left; and **A/D-U** and **D/A-U** are on the right. All these components are interconnected with the central DSP unit. Below the main components is a section titled **Application Interfaces**, which includes **RS232**, **ITAG**, **Digital I/O**, and **Analogue I/O**.

```

graph TD
    DSP[DSP TMS320C50  
-16Bit fixed Point  
-80MHz  
-20KB RAM]
    Flash[Flash-ROM]
    SRAM[SRAM]
    Watch[Watch-Dog]
    Timer[Timer]
    PLD[PLD]
    ADU[A/D-U]
    DAU[D/A-U]
    RS232[RS232]
    ITAG[ITAG]
    DigitalIO[Digital I/O]
    AnalogueIO[Analogue I/O]

    DSP --- Flash
    DSP --- SRAM
    DSP --- Watch
    DSP --- Timer
    DSP --- PLD
    DSP --- ADU
    DSP --- DAU
    DSP --- RS232
    DSP --- ITAG
    DSP --- DigitalIO
    DSP --- AnalogueIO
  
```

Fig. 10 80MHz DSP card with two synchron ADU (12bit, 600kS/s), two synchron DAU (12bit, >150kS/s), one 128kWords RAM/Flash-ROM, one universal timer and on-board programmable PLD.

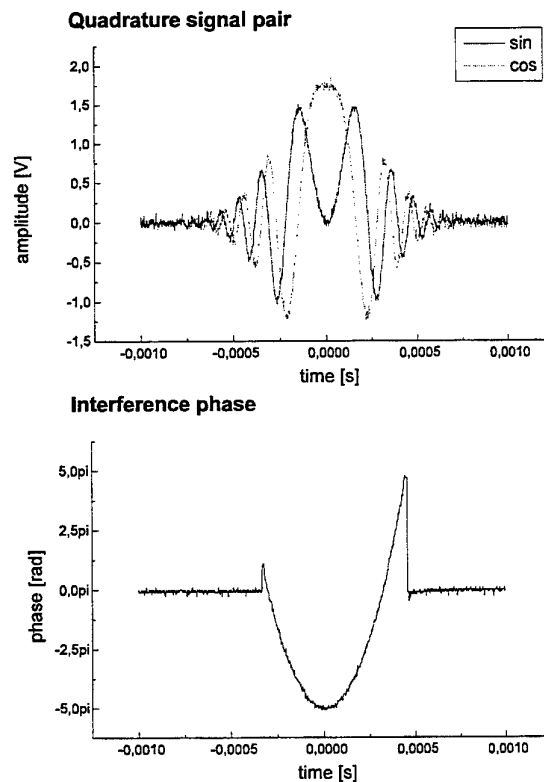


Fig. 11 Measuring result of the DSP-QDT. The quadrature signal pair was generated by an arbitrary signal generator (LeCroy LW420). The generated chirp frequency modulation of the burst signal results in a

quadratic phase curve, which can be evaluated e.g. by a second-order regression.

Although this low-cost DSP-QDT processor (card prize about \$500) was originally planned only for a first concept study, it reaches data rates around 100Hz for complex regression procedures. Fig. 11 shows a first experimental result of this DSP-QDT.

4. CONCLUSIONS

We have presented investigations into the QDT, that verify the in chapter I listed potential advantages of the QDT for the processing of LDV signals. (i) High data rate signal processing possible: A miniaturized QDT processors, using a digital signal processor (DSP) was realized. This DSP-QDT allows the calculation of e.g. quadratic regression curves for the determination of the center frequency and the chirp frequency change. A high data rate should be achieved by floating-point DSPs in the future. On-line measurements of high Doppler momentary frequencies are possible by a QDT, employing gate arrays or ASIC circuits, see Strunck et al. (1996). (ii) Low frequency measuring uncertainty: The measuring error of the QDT reaches the CR bound for a SNR above the demodulation threshold. Hence, the QDT is well suitable for the processing of high quality burst signals. The application of the QDT for LDV systems, having low laser and scattering light powers, respectively, requires the reduction of the demodulation threshold. This is under work. (iii) Directional discrimination in the base band: Generating the quadrature signal pair by optical or electrical methods, see section 2.1, the sign of quadrature phase shift and therefore the sign of the phase slope depends on the flow direction. In contrast to these methods, the use of the Hilbert transformation for quadrature signal pair generation did not allow a directional discrimination, since the phase shift sign is fixed. Hence, the optical or electrical phase shift generation should be preferred. (iv) Low velocity measurement in the base band: The QDT allows frequency measurements of LDV signals, having only a fraction of one signal period. As was shown in section 2.2, velocity down to e.g. 50µm/s can be measured in the base band, i.e. without the technical efforts of the conventionally used fringe biasing. Hence, slow processes like crystal growing, see Jones et al. (1991), could be an application field of the QDT. (v) Measurement of bursts, having low period numbers: In complex fluid flows, scattering particles can pass the measuring volume nearly parallel to their fringe system. The resulting low period number bursts can be accurately processed by the QDT. (vi) Measurement of frequency modulated bursts: As shown e.g. by Lehmann (1997) LDV bursts with characteristic frequency changes occurs at certain acceleration processes in fluid flows. Furthermore, the

LDV signal frequency is defined modulated by sound field measurements, see e.g. Hann et al. (1997). The QDT allows a determination of the momentary Doppler frequency, so that it is well suited for these application fields. Compared to the short-time FFT, the processing by QDT is nearly independent on the available period number, so that a high time resolution can be achieved.

In the future, the signal processing by the QDT should be investigated in certain LDV applications. Furthermore, a miniature QDT processor with high data rate of several kHz should be realized by a powerful DSP.

ACKNOWLEDGMENTS

The authors thank the BMBF (16N6689) for partially funding. Mr. B. Kösters is acknowledged for his encouragement at the implementation of the QDT on the digital signal processor.

REFERENCES

- Boashash B 1992, Estimating and interpreting the instantaneous frequency of a signal - part 2: algorithms and applications, Proc. o. IEEE, Vol. 80 pp.540-568
- Czarske J Hock F Müller H 1993, Quadrature demodulation - a new LDV-burst signal frequency estimator Proc. 5th int. conf. on laser anemometry - advances and applications, Veldhoven, 23-27 August 1993 ed. J Bessem et al. (Bellingham, WA, SPIE)
- Czarske J 1996, Verfahren zur Messung und Auswertung der Interferenzphase in der Laser-Doppler-Velocimetrie', VDI-Fortschritt-Berichte 1996, 8, 530, VDI, Düsseldorf, Germany.
- Czarske J Dölle O Freitag I Welling H Müller H 1997, Optimized two-component directional laser Doppler velocimeter using a chirp frequency modulated powerful Nd:YAG miniature ring laser Proc. 7th int. conf. on laser anemometry - advances and applications, Karlsruhe, 8-11 September 1997, ed. B Ruck, A Leder D Dopheide, pp.73-80
- Hann D, Jack S, Greated C, Rinkevichius B, Grechikhin V, Tolkachev A, Stephanov A, 1997 Laser Doppler measurement in complex sound fields Proc. 7th Int. Conf. Laser Anemometry Advances and Applications, Karlsruhe, pp.107-114
- Jones O, Glicksman M, Lin J, Kim G, Singh, 1991 Development of a laser Doppler system for measurement of velocity fields in PVT crystal growth systems Proc. Crystal Growth in Space and Related Optical Diagnostics, Proc. SPIE 1557 pp.202-208

Lehmann P 1997, Schnelle Zeit-Frequenz-Analyse auf der Grundlage der Kurzzeit-Fourier-Transformation Technisches Messen 6, pp.247-258

Müller H Czarske J Kramer R Többen H Dopheide D Arndt V Wang H 1994, Heterodyning and quadrature signal generation: advantageous techniques for applying new frequency shift mechanisms in the laser Doppler velocimetry. Proc. 7th Int. Symp. on Applications of Laser Techniques to Fluid Mechanics, Lisbon, paper 23.3 (1994).

Müller H Többen H Strunck V Arndt V Dopheide D 1995, Quadrature demodulation in novel frequency shift LDV systems as an alternative to fringe biasing, Proc. 6th EALA/ASME/JSME Laser anemometry conference, Hilton Head, SC, USA, 1995, FED-Vol. 229, pp.455-458

Müller H Strunck V Dopheide D 1997, The application of quadrature demodulation techniques for investigation of flows, Flow Meas. Instrum. Vol.7, pp.237-245

Ruck B Pavlovski B 1995, Grenze der Genauigkeit bei der LDA-Turbulenzmessung, Lasermethoden in der Strömungsmeßtechnik, 4. Fachtagung, Rostock, 12.-14.09.1995, paper 5.

Shinpaugh K, Simpson R, Wicks A, Ha S, Fleming J 1992, Signal-processing techniques for low signal-to-noise ratio laser Doppler velocimetry signals, Experiments in Fluids 12 pp.319-328

Strunck V Müller H Dopheide D 1996, Time domain single-tone analysis using quadrature algorithm. Proc. 8th Int. Symp. on Applications of Laser Techniques to Fluid Mechanics, Lisbon, paper 6.6.

Tropea C 1995, Laser Doppler anemometry: recent developments and future challenges, Meas. Sci & Tech., 6 pp.605-619

THE MEASUREMENT OF STRUCTURE FUNCTIONS WITH LASER DOPPLER ANEMOMETRY

G.P. Romano

Dept. Mechanics and Aeronautics
University "La Sapienza", Via Eudossiana 18, 00184 Roma, Italy

ABSTRACT

The measurements of velocity differences by Laser Doppler Anemometry is highly contaminated by noise and by the non-uniform distribution of data in time. The aim of this paper is to emphasize on which flow scales the distortions caused by these effects are sensed and how it is possible to correct the data. Several reconstruction schemes are considered: hold and sampling, Kalman and slotting technique. The comparison with theoretical predictions and data from Hot Wire in a channel flow allows to assess unambiguously the validity of the different reconstruction schemes for the present evaluation.

1. INTRODUCTION

The Laser Doppler Anemometry (LDA) is now a very well established technique for the measurement of flow velocity. However, the problem of reducing the noise contribution at the high frequencies is still open. The major contributions to this noise derive from the measurement volume size: it can be minimized, but not completely eliminated (George and Lumley (1973)). The analysis of the Doppler signal, detected by the photomultiplier, is also complicated by the random time arrival of the tracer particles in the measurement volume. Therefore, the statistics of LDA data is biased from both noise and non-equispaced samples contributions.

In the past, several methods have been suggested to account for these effects (George and Lumley 1973, Gaster and Roberts 1977, Buchave *et al* 1979, Edwards 1987). More recently the problem is addressed towards the use of conventional algorithms for noise reduction after interpolation between data. The latter is performed using the zero-order ("hold and

sampling") (Adrian and Yao (1986)) and higher-order polynomial or even exponential interpolators (Edwards (1987), Benak *et al* (1993), Host-Madsen (1994)). In particular the first is frequently used because it is simple and avoids bias errors on the derived statistical quantities (Benak *et al* (1993)). Interpolation and resampling algorithms more sophisticated than the hold and sample, show limited improvements and interpolation effects can give spectral slopes which can be erroneously interpreted as deriving from turbulence (Muller *et al* (1994)).

Another point to be considered is that, in order to avoid any contamination from the interpolation algorithm, the resampling frequency must be not larger than the 1/5 of the original mean sampling frequency (Adrian and Yao (1986)). Considering the Poisson arrival times statistics of tracer particles, the mean sampling frequency could be much lower than the maximum "instantaneous" particle arrival rate. This means that the high frequency behaviour is lost when doing equispaced data resampling. This is the reason for demanding direct "data reconstruction" algorithms. Among them, the most promising is the Kalman reconstruction, which basically is a filter self-arranging on the local signal variations (Benedict and Gould (1995), van Maanen and Tulleken (1996)). The implementation of the method requires the specifications of three parameters (basically the *rms* of the noise and of the signal acceleration and the resampling frequency): the choice of such parameters is crucial for the statistics of the resulting resampled equispaced signal. The two *rms* can be determined from considerations on the flow time scales and on the noise contribution. For the selection of the resampling frequency, it should be considered that usually the best results are obtained when it is as high as the maximum particle arrival rate of the non-equispaced data (Benedict and Gould (1995)).

The objective of this paper is to point out how the different interpolation and reconstruction schemes affect the results derived from the LDA data. In particular, together with the evaluation of statistical moments as correlation and spectral functions, the attention is focused on the moments of the velocity difference between two points separated by a distance r (the so called structure functions). This choice depends not only on the fundamental role of these invariant quantities in the study of turbulence, but also on the fact that well known theoretical predictions over a broad range of flow scales have been given for structure functions (Monin and Yaglom (1971)). In particular predictions derived from Kolmogorov theory can be compared to data in the dissipative range ($r \sim h$, where h is the Kolmogorov microscale) and in the inertial range ($h \ll r \ll L$, where L is the integral scale). Departures from the Kolmogorov theory have been observed in the inertial range due to intermittency effects (Frisch (1995)). For this reason, also experimental results from Hot Wire Anemometry (HWA) by Antonia *et al* (1997) are compared to data. For HWA the noise contamination is felt at very small scales and the non-equispaced data effect is not introduced. The investigated flow is a fully developed turbulent channel at low Reynolds numbers for which a large amount of information is available.

2. EXPERIMENTAL SET-UP

The flow field under consideration is a fully developed turbulent channel flow filled with water. Details of the experimental set-up are given by Romano (1995). The coordinates x, y, z refer to the streamwise, wall-normal and transverse directions respectively. Measurements are made in the test section (extending along $y = 2$ cm and $z = 20$ cm) at about 160 cm downstream of the inlet ($x/h \gg 80$, where h is the channel half-height). The flow is seeded with metal coated particles (particle size equal to 4 μm , that is 0.04 h). The Kolmogorov length scale h and the corresponding time scale h/U_1 (where U_1 is the local mean velocity) are derived from the DNS results by Antonia *et al* (1991) at nearly the same Reynolds number. An asterisk will indicate normalization by such Kolmogorov scales.

Data are taken at different distances from the wall (from $y^+ = 10$ to $y^+ = 200$, where $+$ denotes normalization by friction velocity u^* (equal to 2.1 cm/s at $y^+ = 200$) and kinematic viscosity) and at different Reynolds number (from 1500 to 5000 based on the half channel height and bulk velocity). The LDA

system works in forward scatter using a BSA for signal analysis (mean data rate $f_0 = 3$ kHz). About $1.5 \cdot 10^6$ samples are collected at each point (velocity and arrival time). For the present system, the estimated lower bound for the variance of the frequency estimator is less than 0.05 Hz, corresponding to a relative error on the smaller measured frequency of $\pm 0.05\%$ (Tropea (1993)). These severe requirements are necessary for the present investigations. Results are compared to equispaced HWA data in a similar channel (Reynolds number $\gg 3300$) by Antonia *et al* (1997).

3. DATA ANALYSIS

The quality of the LDA measurements can be obtained by considering the mean data density N_D , defined as the ratio between the integral time scale and the mean valid data interarrival time (inverse of valid data rate): $N_D = T_E / \Delta t$ (sometimes this data density is defined using Taylor microscale rather than integral time scale). A general criterion to avoid velocity bias errors is to maintain the parameter N_D as high as possible (say larger than 5 using Taylor microscale) (Edwards (1987)). Benak *et al* (1993) reported that N_D must be greater than 15–20 to avoid errors due to bias towards positive time lags in correlation functions. In the present measurements, N_D is always larger than 70 (using integral time scale) and larger than 20 (using Taylor microscale): velocity and correlation bias errors are avoided by this selection.

At first, acquired velocity and arrival time data are resampled at the mean data rate ($f_0 = 3$ kHz) to obtain equispaced set of data by using zero-order interpolation (hold and sampling method). Adrian and Yao (1987) have shown that a "step" noise is introduced by such interpolation. Nevertheless, given the high data rate of the present measurements, this source of noise is less than the noise from Doppler broadening, and it is sensed at frequencies hundreds of Hz over the maximum detected frequency (Romano (1995)). Conventional algorithms are applied to the equispaced data to compute time-correlation coefficients and auto-spectral power density functions.

The second resampling algorithm is the Kalman reconstruction (examples from hold and sampling and Kalman reconstructions are given in Figure 1). The selection of the *rms* of the noise is based on the evaluation of the spike in the auto-correlation function (determined by the hold and sampling procedure).

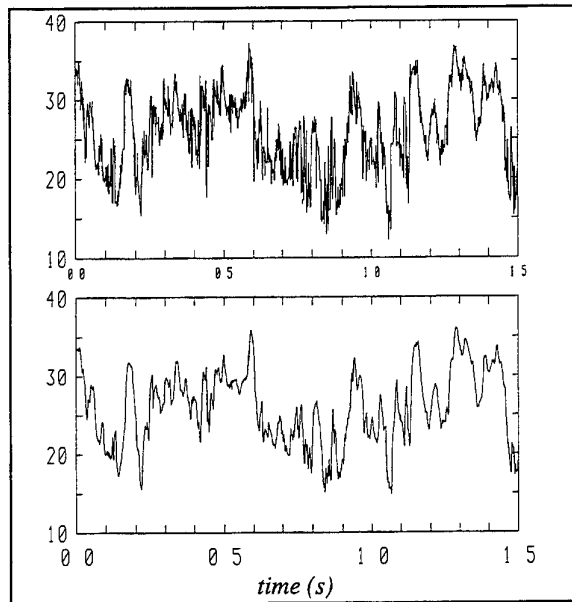


Fig 1. Time history of velocity (in cm/s) from hold and sampling (top) and from Kalman reconstruction (bottom): $Re=4500$, $y^+=20$.

The separation of the noise and signal contributions is obtained by plotting the auto-correlation function vs the square time delay and by fitting this plot with a line (Romano *et al* (1997)). Recalling that, for a stationary flow, a second-order Taylor series expansion about $t = 0$ leads to:

$$\overline{u(t)u(t+\tau)} \approx \overline{u^2(t)} - \frac{\overline{\partial u}}{\partial t} \frac{\tau^2}{2}$$

Therefore, the extrapolated linear fit to the measured data vs τ^2 intercepts the vertical axis at a point which represents the true or correct value of the signal mean square value. The correction procedure is shown on Figure 2, for the data at $y^+ = 20$: the noise spike close to the origin is evident. The mean-square noise term is about 1.5% of the total mean-square value. Similarly, proceeds the evaluation of the *rms* of the acceleration, s . It is basically given by (Benedict and Gould (1995)):

$$\sigma = \sigma' = \overline{a^2} / \tau_E^2 h^{1/2}$$

where $\overline{u'^2}$ is the variance of the velocity signal (determined before) and τ_E is the Taylor microscale. The resampling frequency is selected from the mean data rate, f_0 , up to $3f_0$.

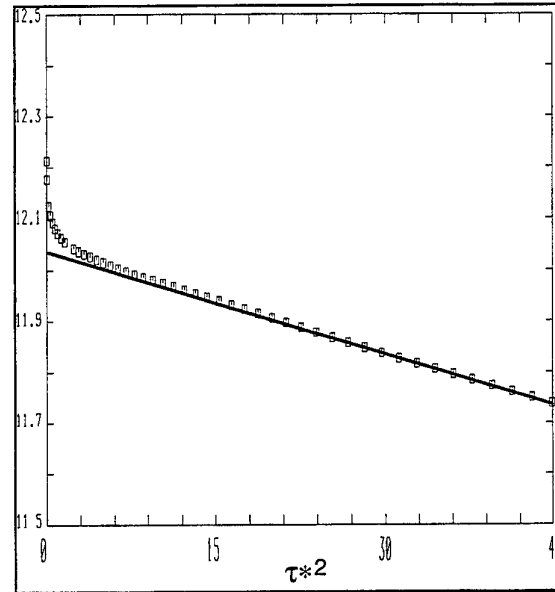


Fig 2. Velocity auto-correlation function as a function of time delay τ^2 (normalized by Kolmogorov scale) at $y^+=20$ and $Re = 3500$. The straight line fit to the data is used to evaluate signal and noise contributions.

From the reconstructed signals, for stationary conditions, the n^{th} -order temporal structure functions are evaluated as the moments of the difference between the velocity at time t and $t+\tau$:

$$\overline{\delta u^n(\tau)} = \overline{[u(t) - u(t+\tau)]^n}$$

Wherever Taylor's hypothesis is verified (at least down to $y^+=15$) this relation can be interpreted as equivalent to that in space.

4. EXPERIMENTAL RESULTS

When considering statistical moments, the comparison between data obtained from the hold and sampling and from the Kalman reconstruction gives the following results:

- the first four moments of the velocity are very similar (there is a slight decrease in second and fourth moment from hold and sampling to Kalman data as can be noticed in Table 1);
- the first four moments of the velocity derivative are strongly different (the variance of the Kalman reconstruction is more than 10 times lower than that from hold and sampling as given in Table 1); the value obtained for the variance of the velocity

derivative gives $\overline{(\partial u^+/\partial x^+)^2} \approx 7 \cdot 10^{-4}$, using Taylor's hypothesis, which is close to the corresponding DNS ($\overline{(\partial u^+/\partial x^+)^2} \approx 1.7 \cdot 10^{-3}$) and HWA values ($\overline{(\partial u^+/\partial x^+)^2} \approx 1.5 \cdot 10^{-3}$). The evaluation of the same quantity from the hold and sampling data gives $\overline{(\partial u^+/\partial x^+)^2} \approx 9 \cdot 10^{-2}$, a value which is clearly in error due to noise;

- correlation and spectral functions from Kalman reconstruction do not show the same noise at small delay and large frequencies noticed from the data from hold and sampling (as in Figure 2). In Figure 3 an example of auto-correlation function is given: when the data are plotted vs t^2 (as in the second figure), some deviation from the linear trend is still observed near zero delay.

These results slightly depend on the resampling frequency (there is a 3% difference between the variances obtained by resampling at $2f_0$ and at $3f_0$) and much more on the choice of the *rms* of the acceleration s (there is a 50% difference from $s=2s^\circ$ to $s=s^\circ/2$). The variances obtained with $s=2s^\circ$ are very similar to those obtained from HWA. Results on the variance of the normalized velocity derivative are summarized in Table 2.

	mean	rms	skewness	flatness
velocity (HS)	8.31	2.48	0.42	1.91
velocity (K)	8.27	2.38	0.41	1.84
vel. deriv. (HS)	3.14	520	0.068	22.1
vel. deriv. (K)	2.89	42.2	0.526	4.43

Table1. Velocity and velocity derivative statistical moments (mean and rms in cm/s) from hold and sampling (HS) and Kalman reconstruction (K) (resampling frequency $2f_0$, noise rms 0.4cm/s and acceleration rms $s \gg s^\circ = 184 \text{ cm/s}^2$): $y^+ = 20$, $Re = 3500$.

	$\overline{(\partial u^+/\partial x^+)^2}$
DNS	$3 \cdot 10^{-4}$
hold and sampling	$1.1 \cdot 10^{-3}$
Kalman $s=s^\circ$, $f=2f_0$	$1.3 \cdot 10^{-4}$
Kalman $s=s^\circ/2$, $f=2f_0$	$6.1 \cdot 10^{-5}$
Kalman $s=s^\circ$, $f=3f_0$	$1.3 \cdot 10^{-4}$
Kalman $s=2s^\circ$, $f=3f_0$	$2.9 \cdot 10^{-4}$
Kalman $s=2s^\circ$, $f=2f_0$	$2.8 \cdot 10^{-4}$

Table2. Variance of velocity derivative from Kalman reconstruction using different resampling frequency f and acceleration rms (noise rms = 0.32 cm/s): $y^+ = 200$, $Re = 3500$.

To emphasize the effect of such parameters, in Figure 4 the probability distributions of the velocity differences for the same data given in table 2 are shown. The strongly non-gaussian behaviour of such velocity differences is clearly observed. In comparison to the data from hold and sampling, the Kalman reconstruction is able to avoid the noise contribution that gives overestimation of the width of the probability distribution (related to $\overline{(\partial u^+/\partial x^+)^2}$). However, the result is strictly dependent on the selection of the parameters: when the rms of the acceleration is too low ($s=s^\circ/2$) the width of the distribution is even underestimated (see also Table 2).

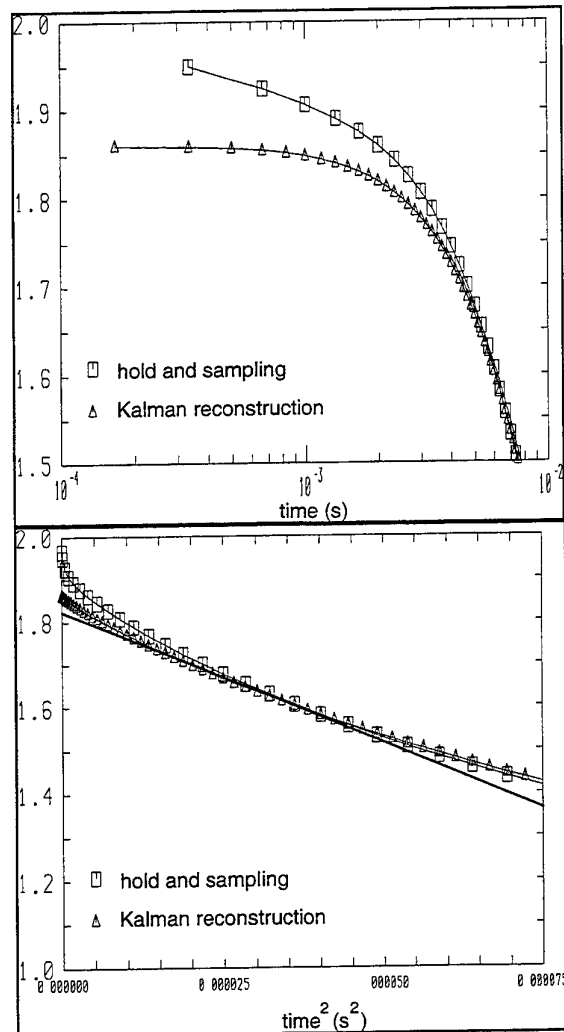


Fig 3: Auto-correlation function from hold and sampling and from Kalman reconstruction (resampling frequency $2f_0$, noise rms $\gg 0.3 \text{ cm/s}$ and acceleration rms $s \gg s^\circ = 306 \text{ cm/s}^2$): $Re = 3500$, $y^+ = 200$.

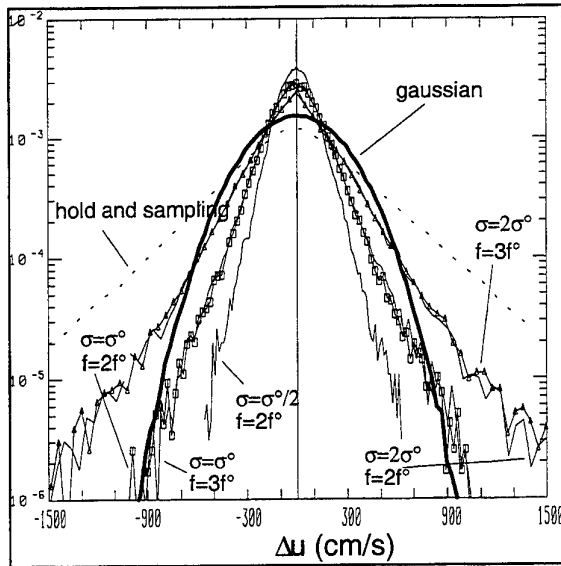


Fig. 4. Probability density distributions of velocity differences: hold and sampling and Kalman method using different parameters. $y^+=200$, $Re=3500$.

The results on the velocity derivative mostly concern with the small scale behaviour. To investigate the effect on the whole range of scales, the comparison involves the velocity differences and structure functions. In Figure 5 the second and third order structure functions, for the data taken at $y^+=20$ and $Re=3500$, are given together with HWA data and with theoretical results for the dissipative range ($\overline{\delta u^n(\tau)} \approx \tau^n$) and for the inertial range ($\overline{\delta u^n(\tau)} \approx \tau^{n/3}$) derived from Kolmogorov theory (Monin and Yaglom (1971)). In this case, the Kalman reconstruction is performed using a resampling frequency equal to $2f_0$ and a variance of the acceleration $s=s^\circ$. Similar plots are obtained at different distances from the wall. It is possible to notice that the data obtained from Kalman reconstruction very well reproduce theoretical and HWA behaviours in the dissipative range. On the other hand, the deviation from hold and sampling data is observed even in the inertial range. This deviation is dependent on the parameters of Kalman reconstruction and in particular on the acceleration *rms*: in Figure 6 the results obtained with different selection are shown. The effect is emphasized when structure functions are divided by $(r/h)^n$: such plots are given in Figure 7. From these figures it is observed that when the small scales are well reproduced (as for $s=s^\circ/2$), the inertial range behaviour is lost.

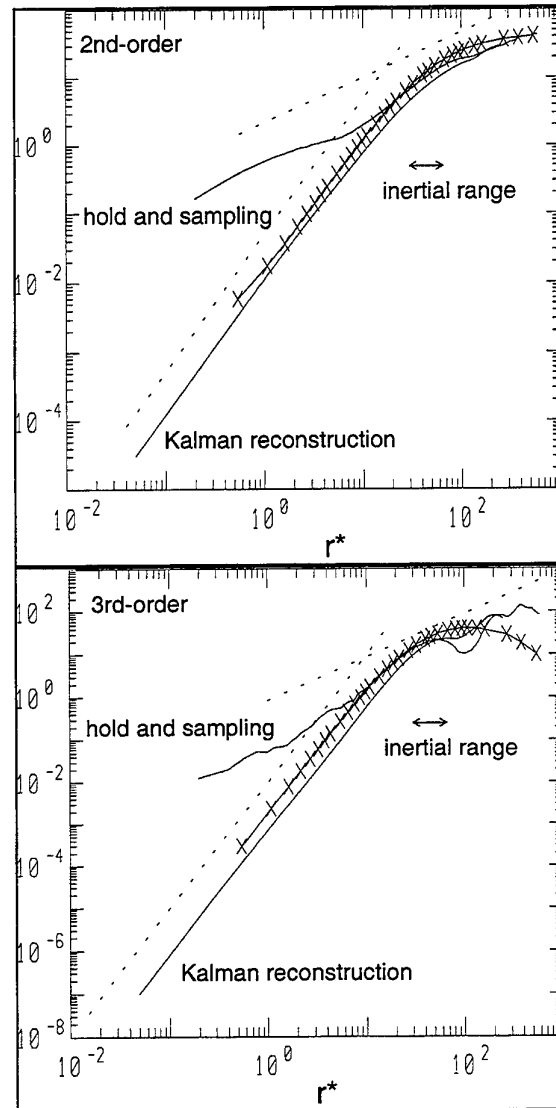


Fig. 5. Second and third order structure functions as a function of non-dimensional distance for hold and sampling and Kalman reconstruction (resampling $2f_0$, acceleration *rms* $s \gg s^\circ$): $y^+=20$, $Re=3500$. Comparison with HWA data (x) and Kolmogorov relations (dotted lines).

On the other hand, when the small scale results are not completely satisfactory (as for $s=2s^\circ$), the inertial range is captured much more better. This is noticed in second-order and even more in third-order structure function. Therefore, although the Kalman reconstruction is a very promising technique for noise reduction in LDA, the effect on the whole range of scales depends critically on the selection of the parameters required by the scheme.

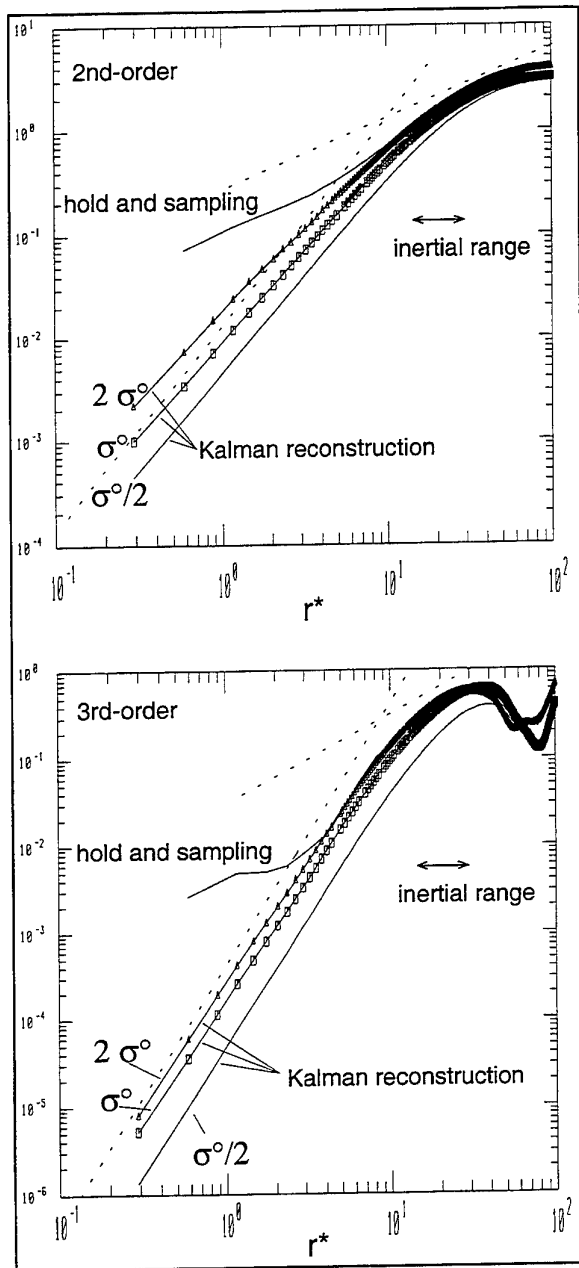


Fig 6. Second and third order structure functions as a function of non-dimensional distance for "hold and sampling" and Kalman reconstruction: $y^+=200$, $Re=3500$. The three curves for Kalman reconstruction correspond to different choices of the variance of the signal acceleration compared to $\sigma^\circ = \overline{a_u'^2} / \tau_E^2 h^{1/2}$. The resampling frequency is always equal to $2f_0$. Comparison with theoretical Kolmogorov relations (dotted lines).

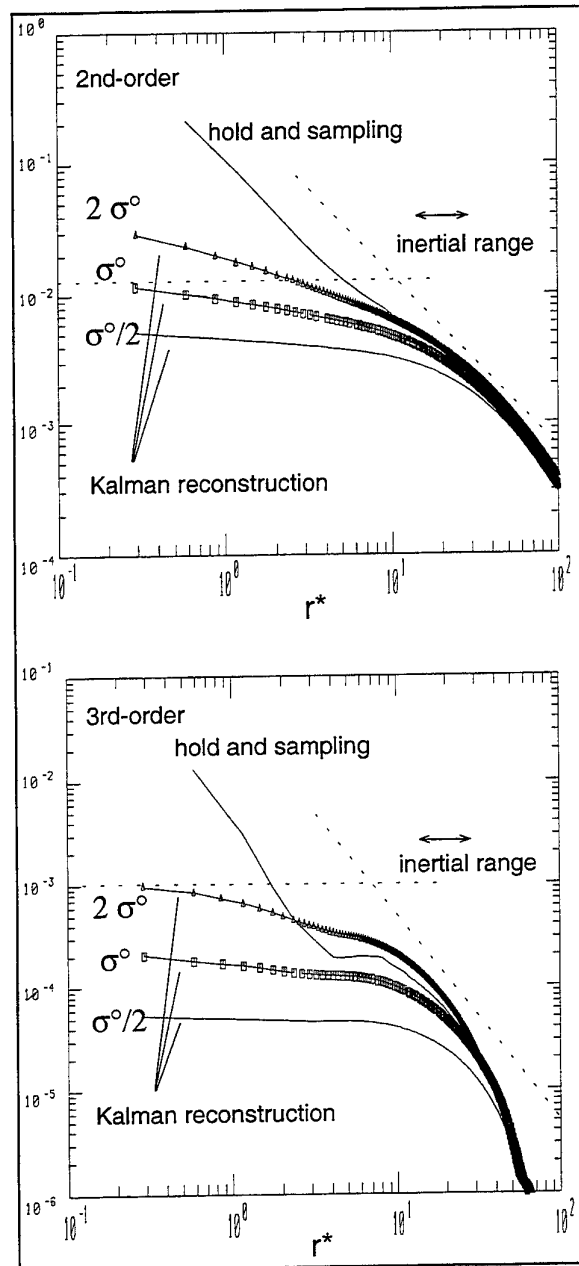


Fig 7. Second and third order structure functions divided respectively by $(r/h)^2$ and by $(r/h)^3$ as a function of non-dimensional distance for "hold and sampling" and Kalman reconstruction: $y^+=200$, $Re=3500$. The three curves for Kalman reconstruction correspond to different choices of the variance of the signal acceleration compared to $\sigma^\circ = \overline{a_u'^2} / \tau_E^2 h^{1/2}$. The resampling frequency is always equal to $2f_0$. Comparison with theoretical Kolmogorov relations (dotted lines).

Moreover, for the present data, it was not possible to reproduce the theoretical behaviour in both the dissipative and inertial ranges with a given choice of such parameters. The self-arranging filter used in the Kalman reconstruction reproduce a behaviour that is not the same expected for the flow over the entire range of scales. From this point of view, it could be questionable to derive information on the structure function properties from such a reconstruction.

Finally, a few comments should be made on the evaluation of structure functions using another promising algorithm: the modified slotting technique (Tummers and Passchier (1996)), which is derived from the slotting technique described by Mayo (1974) and used by Gaster and Roberts (1977) for spectral estimation. It operates on the original non-equispaced samples by subdividing the time axis into "slots" and directly computing the contribution to the auto-correlation function of each pair of data points whose time separation falls within the slot. Its major advantage is that it does not require any preliminary interpolation or filter. On the other hand, due to the reduced size of the slot, the statistical variability is increased so that in the "classical" version the improvement at small scales is not remarkable. The modification of Tummers and Passchier (1996) consists of normalizing the auto-correlation function in each slot by the variance of the velocity computed only in that slot. The result for the auto-correlation coefficient attains a high quality and resolution at very small scales (up to 1/100 of the Taylor microscale). However, for the computations of structure functions, the determination of the correlation coefficient is not sufficient because correlation functions are required. The latter can be derived from the former provided a noise-free variance can be evaluated from the data. This is possible only if the procedure for the separation of noise and signal contributions previously described is employed (Romano *et al* (1997)): this fact limits the usefulness of the slotting technique for the evaluation of structure functions. On the other hand, the results obtained without the noise contribution evaluation are very similar to those obtained with the simpler hold and sampling technique.

5. CONCLUDING REMARKS

The possible procedures for evaluating structure functions from noisy LDA data are. Velocity increments are much more difficult to estimate than correlation functions due to noise contamination. The effect over a wide range of scale can be evaluated in

comparison to theoretical results in the dissipative (small scales) and inertial (intermediate scales) range.

The hold and sampling reconstruction method displays a large contamination in the dissipative range. Almost independently on the distance from the wall, the effect of noise is sensed up to $r^+ \gg 30$ for temporal increments. Hence, it largely obscures the scaling behaviour in the small to intermediate scale interval. This problem is particularly important when performing scaling investigations at small Reynolds numbers where the useful scaling region is restricted.

On the other hand, the Kalman reconstruction scheme suffer from drawbacks (selection of parameters and noise removal) that limit their use for structure function evaluation. In particular it is not possible to select a single value of the free parameters of the scheme able to reproduce the expected theoretical behaviour over the entire range of scales.

ACKNOWLEDGEMENTS

The author wish to thank R.A. Antonia for providing very useful discussions and the HWA data. The support of MURST is also acknowledged.

REFERENCES

- Adrian R.J. & Yao C.S., 1987, Power spectra of fluid velocities measured by laser Doppler velocimetry, Expts. in Fluids, vol.5, pp.17-28.
- Antonia R.A., Kim J. & Browne L.W.B., 1991, Some characteristics of small-scale turbulence in a turbulent duct flow, J. Fluid Mech., Vol.233, pp.369-388.
- Antonia R.A., Zhou T. & Romano G.P., 1997, Second- and third-order longitudinal velocity structure functions in a fully developed turbulent channel flow, Physics of Fluids, vol.9 (11), pp.3465-3471.
- Benak M., Sturm M. & Tropea C.D., 1993, Correlation estimators for two-point laser Doppler anemometry, Proceedings of Laser Anemometry: advances and applications, Veldhoven (the Netherlands) SPIE vol.2052, pp.613-622.
- Benedict L. & Gould R.D., 1995, Experiences using Kalman reconstruction for enhanced power spectrum estimates, Proceedings of Laser Anemometry: advances and applications, Hilton Head (USA) FED vol.229, pp.1-7.

- Bucchave P., George W.K. & Lumley J.L., 1979, The measurement of turbulence with the laser Doppler anemometry, Ann. Rev. Fluid Mech., vol.11, pp.443-503.
- Edwards R.V., 1987, Report of the special panel on statistical particle bias problems in laser anemometry, J. Fluid Eng., vol.109, pp.89-93.
- Frisch U., 1995, Turbulence The legacy of A.N. Kolmogorov, Cambridge University Press, UK.
- Gaster M. & Roberts J.B., 1977, The spectral analysis of randomly sampled records by a direct transform, Proc. R. Soc., vol.354, pp.27-58.
- George W.K. & Lumley J.L., 1973, The laser Doppler velocimeter and its application to the measurement of turbulence, J. Fluid Mech., vol.60, pp.321-362.
- Host-Madsen A., 1994, A new method for estimation of turbulence spectra for laser Doppler anemometry, Proceedings of applications of Laser Anemometry to Fluid Mechanics, Lisbon (Portugal), pp.11.1.1-11.1.8.
- Mayo W.T., 1974, A discussion of limitations and extensions of power spectrum estimation with burst counter LDV systems, Proceedings IInd Int. Workshop on Laser Velocimetry, Purdue University, pp.90-104.
- Monin A.S. & Yaglom A.M., 1971, Statistical Fluid Mechanics : Mechanics of Turbulence, Cambridge, Mass., MIT Press.
- Muller E., Nobach H. & Tropea C.D., 1994, LDA signal reconstruction: application to moment and spectral estimation, Proceedings of applications of Laser Anemometry to Fluid Mechanics, Lisbon (Portugal), pp.23.2.1-23.2.8.
- Romano G.P., 1995, Analysis of two-point velocity measurements in near-wall flows, Expts. in Fluids, vol.20, pp.63-83.
- Romano G.P., Antonia R.A. & Zhou T., 1997, Evaluation of temporal and spatial velocity structure functions obtained with LDA, Submitted to Expts. in Fluids.
- Tropea C.D., 1993, Refined turbulence measurements using laser Doppler anemometry. Proceedings of Refined Flow Modelling and Turbulence Measurements, Presses de l'Ecole Nationale des Ponts et Chaussees, Paris, pp.257-268.
- Tummers M.J. & Passchier D.M., 1996, Spectral estimation using a variable window and the slotting technique with local normalization, Meas. Sci. Technol., vol.7, pp.1541-1546.
- Van Maanen H.R.E. & Tulleken H.J.A.F., 1994, Application of Kalman reconstruction to laser Doppler anemometry data for estimation of turbulent velocity fluctuations, Proceedings of applications of Laser Anemometry to Fluid Mechanics, Lisbon (Portugal), pp.23.1.1-23.1.8.

BENCHMARK TESTS FOR THE ESTIMATION OF POWER SPECTRA FROM LDA SIGNALS

L. H. Benedict

Lehrstuhl für Strömungsmechanik, University of Erlangen-Nürnberg
Cauerstr. 4, 91058 Erlangen, Germany

H. Nobach

Dantec Measurement Technology
Tonsbakken 16-18, 2740 Skovlunde, Denmark

C. Tropea

FG Strömungslehre und Aerodynamik (SLA), Technische Universität Darmstadt
Petersenstr. 30, 64287 Darmstadt, Germany

ABSTRACT

A set of 34 simulated data sets for the testing of power spectrum algorithms for LDA data has been created and made available at the internet address <http://www-nt.e-technik.uni-rostock.de/~nobach/benchm.html>. In this paper the characteristics and diagnostic intent of the data sets are described, as are initial results from 7 research groups who have tested 10 algorithms using these data sets. The results have highlighted strengths and weaknesses of the algorithms as well as the test cases. The initial results indicate that two modified versions of the slotting technique, a refinement for sample-and-hold reconstruction, as well as two parametric methods all offer significant improvement over the traditional slotting, direct, and reconstruction estimators. Modifications to the test cases will be discussed with the participants during the conference in preparation for further testing.

1. INTRODUCTION

Despite the relative complexity involved with estimating power spectra from data sampled randomly in time, the development of statistical estimators and computational algorithms for calculating power spectra from laser Doppler anemometer (LDA) data began in the early seventies, when the LDA was still in a stage of infancy. This pioneering work resulted in two estimators, the so-called "slotting technique," described by Mayo et al. (1974), Shay (1976), Scott (1974, 1976), and Gaster and Roberts (1975); and a direct transform presented by Gaster and Roberts (1977). Coincidentally, most of these researchers discontinued their activity in this area shortly after this series of publications. Additionally, the problem of velocity bias, identified by McLaughlin and Tiederman (1973), focused attention on simpler velocity statistics, so that the topic of power spectrum estimation for LDA data was of low priority for the LDA community for roughly a decade.

In the mid to late eighties, a gradual rekindling of interest took place as investigators tried to use the power spectrum as

a means to study the small scales of turbulence. Comparative studies such as Srikantiah and Coleman (1985) and Tropea (1986), however, indicated that the early estimators possessed a high degree of variance and a susceptibility to velocity bias. Adrian and Yao (1987) also showed that the age old sample-and-hold reconstruction of LDA data led to a filtered noise effect, which obscures the high frequency portion of the spectrum.

At Veldhoven in 1993, the rekindling of interest quickly turned to heated debate as the modern generation of time and frequency domain processors were shown not to improve the quality of power spectrum estimates. Attention thus returned to algorithmic development. Since then, a number of power spectrum estimators have been proposed, ranging from the modifications of the slotting technique to noise filtering reconstruction schemes and parametric methods, such that a comparative overview is necessary. Such comparative tests were recently attempted by Benedict and Gould (1995), Tummers and Passchier (1996a) and Britz and Antonia (1996), but it has become evident that a single research group can no longer implement and thoroughly test all of the estimators which have been proposed. Furthermore, the most useful standards for comparison and necessary range of testing conditions has not been clear.

With this in mind, the present authors are developing a set of simulated and real benchmark LDA data sets to be used by the authors of power spectrum algorithms in assessing the relative performance of their method. As a first attempt at evaluating the effectiveness of this approach, a large number of authors (>30) were invited to participate in computing power spectra from a wide variety of simulated data sets. Results from 7 of these authors have been received and will be presented below. Note that no authors (with the exception of H. Nobach) were aware of the true underlying spectrum before commencing.

The final purpose of the paper is therefore to establish a standard with which new or improved LDA spectral estimators can be compared in the future. Readers interested in obtaining details of the benchmark test or the data sets are

invited to access the data generation program at [http://www-nt.e-technik.uni-rostock.de/~nobach/benchm.html](http://www.nt.e-technik.uni-rostock.de/~nobach/benchm.html).

2. DEFINITIONS AND NOMENCLATURE

To this point we have spoken generally of the power spectrum as the quantity of interest. Here, however, we establish terminology and mathematical definitions of the quantities of interest. Participants were asked to estimate the one-sided, autospectral density function (ASDF) defined as

$$G_{uu}(f) = 4 \int_0^{\infty} C_{uu}(\tau) \cos(2\pi f\tau) d\tau \quad \text{or} \quad (1)$$

$$G_{uu}(f) = \frac{2}{T} \left| \int_{-\infty}^{\infty} u(t) \exp(i2\pi ft) dt \right|^2$$

for the autocorrelation with cosine transform or direct Fourier transform approaches respectively. Here $C_{uu}(\tau)$ is the autocovariance function (ACF) given by

$$C_{uu}(\tau) = \overline{u(t)u(t+\tau)} = \int_0^{\infty} G_{uu}(f) \cos(2\pi f\tau) df \quad (2)$$

where $u(t)$ is the fluctuating velocity, $u(t) = U(t) - \bar{U}$ and τ is the lag-time.

To aid in evaluating results, participants were also asked to provide the autocorrelation coefficient function (ACCF) defined as

$$\rho_{uu}(\tau) = \frac{1}{u^2} \int_0^{\infty} G_{uu}(f) \cos(2\pi f\tau) df \quad \text{or} \quad (3)$$

$$\rho_{uu}(\tau) = \frac{C_{uu}(\tau)}{C_{uu}(0)} = \frac{u(t)u(t+\tau)}{u^2}$$

corresponding to their ASDF estimates. Also, quantities such as the integral time scale, T_u , and the Taylor time scale, λ_u , were used as figures of merit in the analysis. Their definitions are given below.

$$T_u = \int_0^{\infty} \rho_{uu}(\tau) d\tau = \frac{1}{u^2} \int_0^{\infty} C_{uu}(\tau) d\tau = \frac{G_{uu}(0)}{4u^2} \quad (4)$$

$$\frac{1}{\lambda_u^2} = \left. \frac{-1}{2} \frac{d^2 \rho_{uu}(\tau)}{d\tau^2} \right|_{\tau=0} = \frac{2\pi^2}{u^2} \int_0^{\infty} f^2 G_{uu}(f) df \quad (5)$$

3. DESCRIPTION OF BENCHMARK DATA SETS

Simulated data sets have been used exclusively for this first round of benchmark testing since, for simulated signals, the true spectrum is known and thus systematic errors (biases) can be evaluated. The techniques used for simulation are well established and tested and are based on a conveyor belt

model, as described in detail by Fuchs et al. (1992). With this method, a primary time series of evenly spaced samples with extremely high sample rate is first generated. The desired spectral content is obtained by applying the true spectrum as a filter to a Gaussian distributed random noise sequence.

Particles are numerically seeded randomly in space and convected through the LDA measurement volume with the prescribed velocity series to yield a data set consisting of arrival time and velocity (one component). The data validation rate (DVR), \dot{N} , is the particles per second and the mean data density is given by

$$\dot{N}_D = \dot{N} T_u = T_u / \tau_m \quad (6)$$

where τ_m denotes the mean time between validated bursts, i.e. $1/\dot{N}$.

Ultimately the Nyquist frequency of the primary time series determines the maximum frequency which any algorithm can hope to resolve, and round-off errors in the double precision velocity estimates limit the number of decades in amplitude which can be calculated. It is imperative that the Nyquist frequency of the primary time series be set high enough so as not to artificially limit the performance of the estimators. Results returned by the participants indicate that the resolution of the primary series was unfortunately insufficient for certain cases in these first benchmarking tests, although, in general, it was possible to make a useful comparison. Modifications to the simulated data sets will thus be made before testing continues.

Simulated data are described by number of samples, N , and data density, \dot{N}_D . They are divided into *groups* (of which there are 3) and *cases* (34 in all). For each case, there are 10 data sets. Participants were asked to provide ASDF estimates for each of the ten data sets as well as the average ASDF and average ACCF. The ASDFs for each case were used to calculate the statistical variance of the participants' spectral estimators.

General Characteristics: $\bar{U} = 0$, $\overline{u^2} = 1 \text{ m}^2/\text{s}^2$, $N = 250000$

Group S-1 (one case)

Band-limited random noise with Gaussian amplitude distribution and a very steep roll-off at 2000 Hz. This flat spectrum makes filtering effects immediately obvious. (primary series DVR: 10 kHz; Poisson sampled DVR: 1 kHz)

Group S-2 (24 cases)

This group exhibits a Pao-like spectrum, which decreases exponentially (in log coordinates) with increasing frequency, and is given by

$$G_{uu}(f) = \frac{C_1 \exp \left[-15 \alpha (f/f_d)^{\frac{4}{3}} \right]}{1 + \frac{1}{\alpha \pi} \left(\frac{f}{f_d} \right)^{\frac{5}{3}}} \quad (7)$$

where $\alpha=0.1$. There are 6 basic cases for this group as specified in Table 1. Further cases were then created by adding Gaussian noise, one-dimensional velocity bias, or both.

Table 1 Parameters for Group S-2

Case	f_d (Hz)	C_I (m ² /s ²)	T_u (s)	DVR (Hz) Prim.	\dot{N}_D Pois.	DVR (Hz) Poisson
2-1	3	0.46	0.115	100	0.5	4.35
2-2	30	0.046	0.0115	1000	0.5	43.5
2-3	300	0.0046	0.00115	10000	0.5	435
2-4	3	0.46	0.115	100	10	87
2-5	30	0.046	0.0115	1000	10	870
2-6	300	0.0046	0.00115	10000	10	8700

Cases S-2-1 to S-2-6

3 different integral time scales at 2 different data densities, no noise or velocity bias.

Cases S-2-7 to S-2-12

Same as Cases S-2-1 to S-2-6 but with added Gaussian noise.

By maintaining a constant \bar{u}^2 but changing the integral scale, the signal to noise ratio (SNR) is varied and therefore tests an estimator's ability to resolve multiple decades in the presence of noise

Cases S-2-13 to S-2-18

Same as Cases S-2-1 to S-2-6 but with one-dimensional velocity bias (i.e. correlation between instantaneous velocity and particle rate), no noise

Cases S-2-19 to S-2-24

Same as Cases S-2-1 to S-2-6 but with noise and velocity bias

Group S-3 (9 cases)

The spectrum of this data group exhibits a distinct peak at $f_p = 100$ Hz and is described by

$$G_{uu}(f) = 0.256 \exp_{10} \left\{ -\frac{5}{3} m_0 \left(\lg \frac{f}{1 \text{ Hz}} \right) - \frac{2}{3} m_0 \left(\lg \frac{f}{100 \text{ Hz}} \right) \right. \\ \left. + 2.004 \exp \left[-50 \left(\lg \frac{f}{100 \text{ Hz}} \right)^2 \right] \right\} \quad (8)$$

Cases S-3-1 to S-3-3

$\dot{N} > 2\pi f_p$, $\dot{N} \approx f_p$, $\dot{N} \approx f_p/5$ without noise

Cases S-3-4 to S-3-6

As above but with a low noise level

Cases S-3-7 to S-3-9

As above but with a high noise level

4. DESCRIPTION OF PARTICIPANTS' ESTIMATORS

A total number of seven participants submitted results as summarized in Table 2. Before giving further details regarding the algorithm used by each participant, a general classification will be introduced, as represented schematically in Fig.1. Most techniques can be classified into one of the following:

- slotting technique and cosine transform
- direct transform
- reconstruction with equi-distant resampling and FFT

In each of the algorithmic routes, additional steps (shown as dashed boxes) can be found, representing various enhancements made by the participants to these basic algorithms. In the following, the three major algorithmic procedures are introduced, and variations implemented by the participants are highlighted.

Table 2 Summary of participants and methods

Participant	Method	References
Ihalainen et al. I	slotting technique	Mayo et al. (1974)
Ihalainen et al. II	S&H reconstruction	Adrian & Yao (1987)
Ihalainen et al. III	linear reconstruction	Saarenrinne et al. (1997)
Ihalainen et al. IV	DQSE method	Marquadt and Acuff (1983), Saarenrinne et al. (1997)
Nobach I	refined S&H recon. with noise suppression	Nobach et al. (1998)
Nobach II	fuzzy slotting technique	
Nobach III	model parameter est.	Müller et al. (1998)
Rajpal	Lomb Scargle method	Rajpal (1995)
Romano	S&H reconstruction	Adrian & Yao (1987)
Sree	slotting technique	Mayo et al. (1974), Sree (1985)
Tummers & Passchier	slotting technique with local normalization and variable window	Tummers & Passchier (1996a, 1996b)
van Maanen	Parametric	van Maanen & Oldenziel (1998)

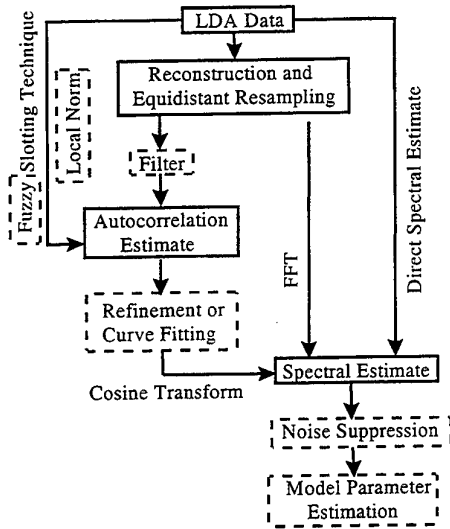


Fig. 1 Schematic for spectrum algorithms

4.1 The Slotting Technique

The slotting technique, generally credited to Mayo et al. (1974), consists of the following algorithm for estimating the discrete autocovariance function,

$$C_{uu}(k\Delta\tau) = \frac{\text{sum}\{u_i u_j\}(k\Delta\tau)}{H(k\Delta\tau)} \quad k = 0, 1, \dots, M-1 \quad (9)$$

where $\text{sum}\{u_i u_j\}(k\Delta\tau)$ represents the sum of all cross products with lag times falling in the time interval (i.e. slot) $(k - 0.5)\Delta\tau < (t_j - t_i) < (k + 0.5)\Delta\tau$, $H(k\Delta\tau)$ is the number of cross products falling within this slot, and $\Delta\tau$ is the slot width. The parameter M is the number of slots and is chosen by the user.

A one-sided ASDF estimator is formed for the slotting technique by taking its discrete cosine transform as follows.

$$G_{uu}(f) = 4\Delta\tau \left[\frac{1}{2} C_{uu}(0) + \sum_{k=1}^{M-1} C_{uu}(k\Delta\tau) w(k\Delta\tau) \cos(2\pi f k\Delta\tau) \right] \quad (10)$$

where $w(k\Delta\tau)$ represents a discrete lag window.

Sree. Note that the first slot ($k = 0$) in the slotting technique is treated separately in Eq. (10) because its width is $\Delta\tau/2$. Normally, the lag products falling within this first slot are ignored (with regard to biases arising from processor dead times and probe volume effects) and the sum of autoproduts is used in place of the sum of cross products. A drawback of using the autoproduts is that they include a noise contribution which biases the autocovariance and ASDF to higher values. Sree thus using only the cross products for the first slot. Otherwise his approach is the standard slotting technique and, referring to the schematic of Fig. 1, follows the

path of slotting technique, autocorrelation estimate, cosine transform.

Ihalainen et al. I. The strategy of this group was to include both autoproduts and cross products in the first slot.

Nobach II. A severe limitation of the standard slotting technique is its high variance (roughly constant at high frequency), which leads to poor estimates of turbulence spectra at frequencies well below the mean sampling rate. In order to reduce the variance of the slotting technique, Nobach employs a lag products weighting scheme called the *fuzzy slotting technique* and defined as

$$b_k(\tau) = \begin{cases} 1 - \left| \frac{\tau}{\Delta\tau} - k \right| & \text{for } \left| \frac{\tau}{\Delta\tau} - k \right| < 1 \\ 0 & \text{otherwise} \end{cases} \quad (11)$$

This scheme allows lag products to contribute to two slots simultaneously and weights lag products that lie close to the slot centers more heavily as seen in Fig. 2.

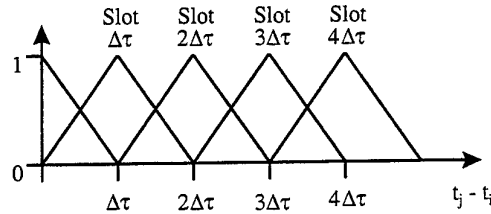


Fig. 2 Fuzzy slotting technique schematic

Tummers & Passchier. Another method for reducing variance in the slotting technique has been dubbed *local normalization* by Tummers and Passchier (1996a, 1996b) and van Maanen and Tummers (1996). In this case, an ACCF normalized by a variance estimate particular to each slot is used as the basis for the cosine transform. This results in the following slotting algorithm

$$\rho_{uu}(k\Delta\tau) = \frac{\text{sum}\{u_i u_j\}(k\Delta\tau)}{\sqrt{\text{sum}\{u_i^2\}(k\Delta\tau) \text{sum}\{u_j^2\}(k\Delta\tau)}} \quad (12)$$

and corresponding one-sided ASDF estimator

$$G_{uu}(f) = 4C_{uu}(0)\Delta\tau \left[\frac{1}{2} + \sum_{k=1}^{M-1} \rho_{uu}(k\Delta\tau) w(k\Delta\tau) \cos(2\pi f k\Delta\tau) \right] \quad (13)$$

While Eq. 12 has been shown to have significantly lower variance for small lag times than Eq. 9 normalized by $C_{uu}(0)$, the variance at large lag times is unchanged; therefore, the use of local normalization alone does not lead to an improved ASDF. Tummers and Passchier indicate, however, that combining a variable lag window whose lag width decreases with increasing frequency with the local normalization does produce a much improved ASDF.

van Maanen. Here the starting point is also the slotting technique with local normalization, but instead of attacking the variance problem with creative windowing schemes, van Maanen and Oldenziel (1998) recommend curve-fitting the

locally normalized ACCF in order to remove variability in the ASDF estimates almost completely. To this end, they have developed an eight-parameter autocorrelation model which is extremely flexible and can be analytically Fourier transformed.

4.2 Direct Transform

Direct transform methods of ASDF estimation are based on the adaptation of the periodogram approach for equispaced data to the case of random sampling. The standard estimator in this regard is that of Gaster and Roberts (1977) given by

$$G_{uu}(f) = \frac{2}{N^2 T} \left\{ \left| \sum_{j=0}^N u(t_j) d(t_j) \exp(i2\pi f t_j) \right|^2 - \sum_{j=0}^N u^2(t_j) d^2(t_j) \right\} \quad (14)$$

where $d(t_j)$ is a data window. This estimator has yet to be represented in these benchmarking tests; however, Tummers and Passchier (1996a) have shown that its variability, even with block averaging, is no better than the slotting algorithm. Benedict and Gould (1995) have also shown that uncorrelated noise results in a negative bias in ASDF estimates using this method. Its advantage is speed in its blockaveraged form.

Rajpal. Scargle (1982) modified the periodogram to make it equivalent to a least squares fitting of sine curves to a data set. His scheme has been applied by Rajpal (1995) and Saarenrinne et al. (1997) to simulated data and turbulent flows.

Ihalainen et al. IV. Another modification to the periodogram is described by Marquardt and Acuff (1983). In this approach, a data spacing factor is incorporated into the periodogram. For Poisson sampling, the factor becomes the inverse of the sampling rate squared.

4.3 Reconstruction with FFT

Reconstruction approaches create equi-spaced time series by resampling according to various interpolation schemes, thereby allowing that an FFT be used in making ASDF estimates. The most common scheme by far is *sample-and-hold* (zero-order). This is the simplest of the polynomial class of reconstruction algorithms.

Adrian and Yao (1987) were the first to call attention to the filter characteristics of reconstruction algorithms. Since then it has been well documented by van Maanen and Tulleken (1994), among others, that the filter effect becomes significant at frequencies under $\dot{N}/2\pi$ in the case of Poisson sampling. If noise is present in the signal, the ASDF estimates can break down well before this filter cut-off. In such a case, additional filtering (see Fig. 1) can be implemented prior to calculating the autocorrelation function. The application of Kalman filtering, for instance, has been investigated by van Maanen and Tulleken (1994) and Benedict and Gould (1995), but has not yet been applied to the benchmarking data.

Ihalainen II and III. implemented the standard sample-and-hold and linear reconstruction schemes respectively.

Romano also implemented the standard sample and hold algorithm.

Nobach I. Recently, Nobach et al. (1998) developed a *refinement* that cancels the filter effect associated with sample-and-hold reconstruction. The approach is to derive an expression for the resampled autocorrelation function in terms of the true autocorrelation function. The relation is then inverted to estimate the true autocorrelation. The ASDF follows from a cosine transform. Referring to Fig. 1, the procedure follows the steps reconstruction, autocorrelation estimate, refinement, spectral estimate. A step for noise suppression can be added when necessary. In principle, a refinement can be derived for any reconstruction algorithm, but it is not always possible to invert the resulting expression.

5 DISCUSSION OF PARTICIPANTS' RESULTS

The flat spectrum (up to a cut-off) data set of Group1 was intended as a prerequisite diagnostic case to ascertain whether a participant's estimator exhibited a filtering effect above a particular cut-off frequency. Only the reconstruction techniques without refinement displayed such filtering. Fig. 3 shows the results for sample-and-hold and linear reconstruction submitted by Ihalainen et al. One may notice that these reconstruction techniques not only filter above a cut-off frequency, but also indicate a positive bias error. This error is reflected in the integral scale errors presented in Table 3 (at the end of the paper). Note that the severity of this bias error is determined by the energy content of the signal at frequencies greater than approximately $\dot{N}/2\pi$. Thus for the spectra presented in Fig. 4, the bias is only significant for the low data rate case. Also note in Fig. 1 that the linear reconstruction has a slightly lower bias error, but that the filter cut-off frequency (visually perceived at $\dot{N}/10$ or 100 Hz) is the same. Thus one should not be fooled by Fig. 4 into thinking that the sample-and-hold scheme has performed better at high data rate than the linear estimator. It is merely coincidence that the sample-and-hold filtering effect better matches the spectrum over this frequency range.

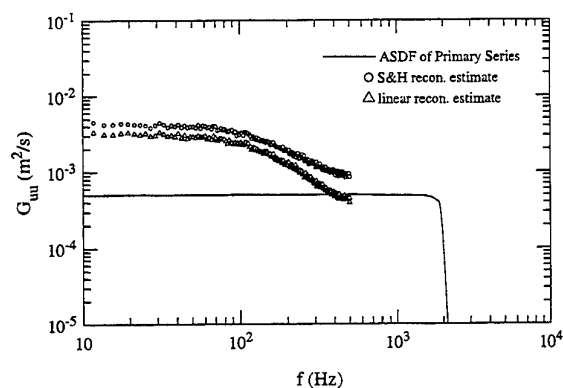


Fig.3 Reconstruction estimators applied to Case S-1

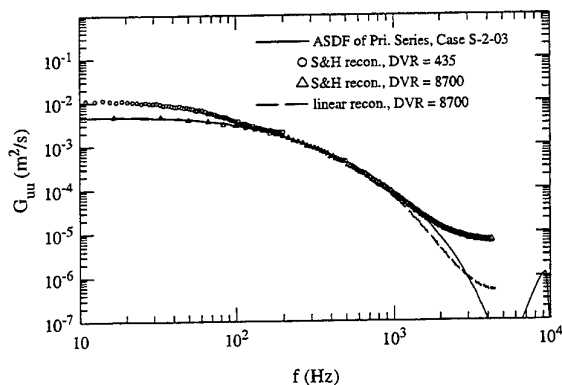


Fig. 4 Results of Romano (low DVR) and Ihalainen et al. for Case S-2-03

Group three was also a set of mainly qualitative diagnostic devices designed to check whether the methods were capable of ascertaining a spectral peak in a wide-band spectrum as various noise levels and data densities. These results require further analysis; however, it appears that all methods with the exception of the reconstruction methods, which functioned only for the highest data density, were able to determine the peak of 100 Hz. The reconstruction and direct methods were also strongly influenced by noise; although the peak was still recognizable. Finally, the variable window approach of Tummers and Passchier resulted in a significant frequency broadening of the peak, but this was deemed to be a tolerable result.

The Group 2 cases were designed to be indicative of actual turbulence spectra and to allow for some quantitative comparisons of the different methods. It must be admitted that an error in communication between the present authors led to the creation of data sets with relatively low resolution in the primary series. This lessened the value of the comparison to some extent, as a maximum of roughly 5 decades in amplitude could be recovered from the primary time series, but was discovered to late to be corrected in time for the present analysis. Fig. 5 presents a comparison of the true theoretical spectrum and the actual spectrum of the primary time series for Case S2-1. The spectrum of the primary time series is matched well if the exponent in Eq. (7) is considered to be 4.11/3 instead of 4/3.

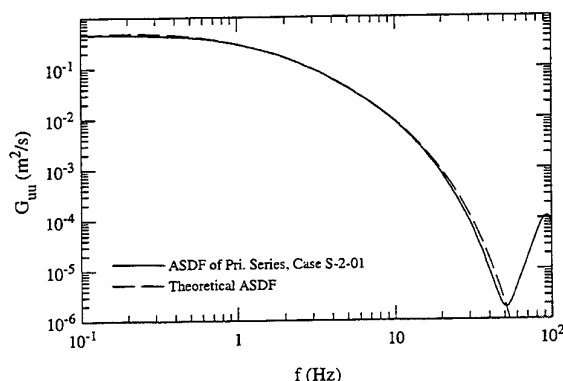


Fig. 5 Comparison of theoretical Group 2 spectra to those obtained from primary time series

Two standards of comparison were estimates of integral scales and microscales, calculated by the present authors from results submitted by the participants (recall that participants were not aware of the exact values during their work). The errors in these time scale estimates are presented in Tables 3 and 4. Some caution should be used in interpreting the microscale results as sometimes biases in different parts of the spectrum canceled in the integration, leading to tolerable microscale estimates. This was the case for the linear reconstruction results of Ihalainen et al. III for example.

Generally speaking, the reconstruction without refinement and direct methods did not perform well for these tests. The reconstruction methods were able to estimate the integral scale only under high data density conditions and the microscale not at all. Noise tended to make both estimates worse. The refinement of Nobach I led to much better results. This is not fully reflected in the table as all the cases for this method have not yet been submitted but are reported to be equivalent to Nobach II. It must be mentioned, however, that the noise suppression scheme employed by Nobach I is not fully convincing. A combination of noise and velocity bias also seems to pose problems.

A surprising result of the comparisons thus far has been the performance of the parametric approaches. The results of Nobach III are excellent in general with problems only occurring for the cases in which velocity bias appears at low data density. The method of van Maanen also appears to be very reliable as the limited results submitted thus far were somewhat unfairly influenced by the resolution of the primary time series. It should be noted that this scheme is designed to most accurately predict the high frequency portion of the spectrum so it is not surprising the integral scale results leave something to be desired. This does not represent a drawback as a better estimate of the integral scale would be available from the locally normalized ACCF when using this method.

As was expected, the standard slotting technique showed a high variance and an inability to cope with noise or bias. Noise problems could be circumvented by using the lag products in the first "half-slot" in place of the autoproductions, however this would rarely be a useful solution under real measurement conditions where processor dead time or the probe transit time limit the minimum inter-arrival time which can be obtained.

The fuzzy slotting technique of Nobach III and the locally normalized slotting technique with variable window implemented by Tummers and Passchier both produced excellent overall results. The method of Tummers and Passchier would appear to be the best of all methods; however, the results presented here can only be considered preliminary. Fig. 6 presents the normalized standard deviation of their ASDF estimates for Case S-2-1 as compared to those of Ihalainen et al. I, achieved with the standard slotting technique at similar frequency resolution. The improvement is obvious.

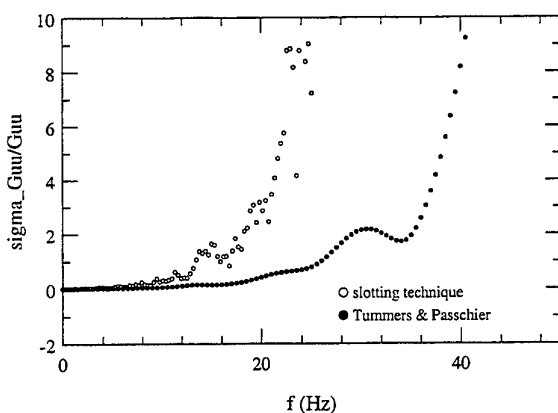


Fig. 6 Comparison of variance of two slotting algorithms

6. CONCLUSIONS

A set of 34 simulated data sets for the testing of power spectrum algorithms for LDA data has been created and made available at the internet address <http://www-nt.e-technik.uni-rostock.de/~nobach/benchm.html>. Initial results from 7 research groups who have tested 10 algorithms using these data sets have indicated strengths and weaknesses of the algorithms as well as the test cases. Of the algorithms tested, modifications to the slotting technique, known as *local normalization* and the *fuzzy slotting technique* as well as two parametric methods and a refined reconstruction algorithm appear to offer significant advantages over traditional slotting, direct, and reconstruction estimators. Modifications to the test cases will be discussed with the participants during the conference in preparation for further comparative tests. Real LDA data sets will also be considered in the future.

ACKNOWLEDGMENT

The first author wishes to acknowledge the financial support of the Alexander von Humboldt Foundation and National Science Foundation during the course of this work.

REFERENCES

- Adrian, R.J. & Yao, C.S. 1987, Power Spectra of Fluid Velocities Measured by Laser Doppler Velocimetry, *Exp. Fluids*, 5, 17-28.
- Benedict, L.H. & Gould, R.D. 1995, Experiences Using Kalman Reconstruction for Enhanced Spectrum Estimates, *ASME/JSME Fluids Eng. and Laser Anem. Conf.*, Hilton Head, SC, Aug. 13-18, FED-Vol. 229, 347-354.
- Booij, R. & Bessem, J.M. (Eds.) 1993, Report on Workshop, User's Needs for LDA, Supplement to *Proc. 5th Int. Conf. on Laser Anemometry - Advances and Applications*, Veldhoven, Netherlands, Aug. 23-27.
- Britz, D. & Antonia, R.A. 1996, A Comparison of Methods of Computing Power Spectra of LDA Signals, *Meas. Sci. Technol.*, 7, 1042-1053.
- Fuchs, W. Albrecht, H. Nobach, H. Tropea, C. & Graham, L.J.W. 1992, Simulation and Experimental Verification of Statistical Bias in Laser Doppler Anemometry Including Non-Homogeneous Particle Density, *Proc. 6th Int. Symp. on Applications of Laser Techniques to Fluid Mech.*, Lisbon, Portugal, July 20-23, paper 8.2.
- Gaster, M. & Roberts, J.B. 1975, Spectral Analysis of Randomly Sampled Signals, *J. Inst. Maths. Applics.*, 15, 195-216.
- Gaster, M. & Roberts, J.B. 1977, The Spectral Analysis of Randomly Sampled Records by a Direct Transform, *Proc. R. Soc. Lond. A.*, 354, 27-58.
- Marquardt, D.W. & Acuff, S.K. 1983, Direct Quadratic Spectrum Estimation with Irregularly Spaced Data, in *Time Series Analysis of Irregularly Observed Data*, ed. Emanuel Parzen, 211-223, Springer Verlag, Berlin.
- Mayo, W.T. Jr. Shay, M.T. & Riter, S. 1974, The Development of New Digital Data Processing Techniques for Turbulence Measurements with a Laser Velocimeter, *AEDC-TR-74-53*.
- Müller, E. Nobach, H. & Tropea, C. 1998, Model Parameter Estimation from Non-equidistant Sample Data Sets at Low Data Rates, *Meas. Sci. Technol.*, 9, 435-441.
- Nobach, H., Müller E. & Tropea, C. 1998, Efficient Estimation of Power Spectral Density from Laser Doppler Anemometer Data, *Exp Fluids*, 24, 489-498.
- Rajpal, A.K.P. 1995, Power Spectrum Estimates of LDA Measurements Using Scargle Periodogram Analysis, *ASME/JSME Fluids Eng. and Laser Anem. Conf.*, Hilton Head, SC, Aug. 13-18, FED-Vol. 229, 411-415.
- Saarenrinne, P. Soini, S. Ihalainen, H. & Kaleva, O. 1997, Turbulence Spectral Power Density Estimation for Laser Doppler Anemometer Measurements in a Mixing Tank Flowfield, to *Proc. 7th Int. Conf. on Laser Anemometry - Advances and Applications*, Karlsruhe, Germany, Sept 8-11.
- Scott, P.F. 1974, Random Sampling Theory and its Application to Laser Velocimeter Turbulent Spectral Measurements, *Report No. 74CRD216*, Tech. Info Series, General Electric Co., Corporate Res. and Development.
- Scott, P.F. 1976, Distortion and Estimation of the Autocorrelation Function and Spectrum of a Randomly Sampled Signal, Ph.D. thesis, Rensselaer Polytechnic Institute, Troy, NY.
- Shay, M.T. 1976, Digital Estimation of Autocovariance Functions and Power Spectra from Randomly Sampled Data Using a Lag Product Technique, Ph.D. thesis, Texas A&M University, College Station, TX.
- Srikantiah, D.V. & Coleman, H.W. 1985, Turbulence Spectra from Individual Realization Laser Velocimetry Data, *Exp. Fluids*, 3, 35-44.

Tropea, C. 1986, Turbulence-induced Spectral Bias in Laser Anemometry, *AIAA Journal*, 29, no. 3, 306-309.

Tummers, M.J. & Passchier, D.M. 1996a, Spectral Analysis of Individual Realization LDA Data, *Report LR 808*, Faculty of Aerospace Engineering, Delft University of Technology, Delft, The Netherlands.

Tummers, M.J. & Passchier, D.M. 1996b, Spectral Estimation Using a Variable Window and the Slotting Technique with Local Normalization, *Meas. Sci. Technol.*, 7, 1541-1546.

van Maanen, H.R.E. & Oldenziel, 1998, Estimation of Turbulence Power Spectra from Randomly Sampled Data by Curve-Fit to the Autocorrelation Function Applied to Laser Doppler Anemometry, *Meas. Sci. Technol.*, 9, 458-467.

van Maanen, H.R.E. & Tulleken, H.J.A.F. 1994, Application of Kalman Reconstruction to Laser-Doppler Anemometry Data for Estimation of Turbulent Velocity Fluctuations, *Proc. 7th Int. Symp. on Applications of Laser Techniques to Fluid Mech.*, Lisbon, Portugal, July 11-14.

Table 3 Integral scale (T_u) errors for Group 2 (in percent)

Case	Iha I	Iha II	Iha III	Iha IV	Noba I	Noba II	Nob III	Rajpal	Roman	Sree	Tumm	Maanen
S2-01	0.49					1.6	1.3		160	-1.0	-7.5	
S2-02	1.7			-74		1.6	1.3		160		-7.5	
S2-03	1.1					1.6	1.3		160		-7.5	
S2-04	2.0				0.57		2.5	-95	1.5		-6.1	
S2-05	-1.0				0.57		2.4	-50	1.5		-6.1	
S2-06	-15	4.0	3.5		0.57		2.4	400	1.5		-6.1	
S2-07	0.44					1.5	1.1		150	-1.1	-7.6	
S2-08	1.7					1.5	1.1		150		-7.6	
S2-09	0.15					1.5	1.1		150		-7.6	
S2-10	1.9				0.64		2.4	-95	-6.4		-6.2	-16
S2-11	-0.66				0.64		2.2		-6.4		-6.2	
S2-12	-15	4.7			-0.64		2.3		-6.4		-6.2	-22
S2-13	270					-0.12	1.5			260	-6.2	
S2-14	260			7.8		-0.12	1.4				-6.2	
S2-15	270					-0.12	1.4				-6.2	
S2-16	260					3.7	2.4				-6.6	
S2-17	260					3.7	2.4				-6.6	
S2-18	270	24	20			3.7	2.5				-6.6	
S2-19	270				160		160		160	260	-0.26	
S2-20	260				160		160		160		-0.26	
S2-21	270				160		160		160		-0.26	
S2-22	260				18		17		-1.4		-1.5	
S2-23	260				18		17		-1.4		-1.5	
S2-24	260				18		17		-1.4		-1.5	

Table 4 Taylor microscale (λ_u) errors for Group 2 (in percent)

Case	Iha I	Iha II	Iha III	Iha IV	Noba I	Noba II	Nob III	Rajpal	Roman	Sree	Tumm	Maanen
S2-01	-1.7					-16	1.1		-9.1	5.1	-6.3	
S2-02	-1.6			120		-16	1.1		-9.1		-6.3	
S2-03	-16					-16	1.1		-9.1		-6.3	
S2-04	-1.8				-13		-11	-18	-28		-5.5	
S2-05	-2.5				-13		-6.6	-74	-28		-5.5	
S2-06	-10	-28	11		-13		-6.6	-92	-28		-5.5	
S2-07	0.63					8.6	3.1		-9.7	6.4	-4.3	
S2-08	-12					8.6	3.1		-9.7		-4.3	
S2-09	-54					8.6	3.1		-9.7		-4.3	
S2-10	-2.0				27		-5.5	-18	-49		-5.3	-5.4
S2-11	-14				27		-2.7		-49		-5.3	
S2-12	-47	-51			27		-2.7		-49		-5.3	-7.6
S2-13	0.47					-32	-29			-18	-3.9	
S2-14	-----			-14		-32	-26				-3.9	

S2-15	----					-32	-27				-3.9	
S2-16	-3.0					-1.1	-2.4				-4.6	
S2-17	----					-1.1	-2.4				-4.6	
S2-18	----	-31	19			-1.1	-2.4				-4.6	
S2-19	1.9				-52		-38		-4.6	-18	3.4	
S2-20	----				-52		-28		-4.6		3.4	
S2-21	----				-52		-36		-4.6		3.4	
S2-22	-5.0				20		6.5		-46		1.5	
S2-23	----				20		6.5		-46		1.5	
S2-24	----				20		6.5		-46		1.5	

SESSION 33

COMPLEX FLOWS III

DPIV - MEASUREMENTS FOR EXAMINATION OF TRANSIENT FLOW PHENOMENA

J. Reuber and J. Köngeter

Institute of Hydraulic Engineering and Water Resources Management, Aachen University of Technology, Germany
e-mail: reuber@iww.rwth-aachen.de
http://www.iww.rwth-aachen.de

ABSTRACT

Combined system intercepting sewers are facilities to buffer the gauging water at storm water events to prevent water pollution. This paper deals with the physical simulation of a special type of a combined system intercepting sewer called Combined Sewer Detention Tank, which has to be optimised due to its frequent malfunction in practice. A physical model of such a detention tank is installed, where different flow phenomena and transport mechanisms can be simulated. The transient flow field is recorded using the Digital Particle Image Velocimetry (DPIV). Velocity profiles are detected as well as complex flow structures during a simulated transient precipitation event. The results of the measurements are of an acceptable accuracy to calibrate and validate the numerical model.

1. INTRODUCTION

The treatment of gauging water is an actual problem for townships and communities in Germany and other countries in the European community. One area of this wide field of investigation is the construction and redevelopment of combined system intercepting sewers. The function of these facilities is to buffer the waste in the gauging water at storm water events to prevent water pollution and afterwards, during dry weather, drain it away to a wastewater treatment plant.

A special type of a combined system intercepting sewer is a so called Combined Sewer Detention Tank (CSDT). The overall performance of a CSDT concerning the sedimentation capacity is subject of current research projects. The high hydraulic load factor can lead to an increasing risk of erosion of already settled material. Subject of this investigation is to examine the flow field in selected areas in a physical model of a circular CSDT.

The measured data serves to calibrate and verify a numerical model, which is able to calculate the flow-field and the transport mechanisms in a CSDT. This will lead to proposals for an effective construction.

The DPIV is used to examine the flow field in different areas in the center line of the physical model of the CSDT. LDA-measurements are not able to represent the transient flow phenomena which result from permanently changing discharges according to the simulated hydrograph. Furthermore, LDA-measurements in the whole flow field would exceed the available time frame of the project.

In the following the physical model of the CSDT is presented followed by the experimental conditions and a detailed description of the measurements. The results of the DPIV measurements under transient flow conditions are presented and discussed.

2. PHYSICAL MODEL OF CSDT

The physical model of the CSDT consists of 6 smooth circular plexi-glass modules with a total length of 9.30 m and an inner diameter of 0.441 m. On the inlet-side (Figure 1, left) water is pumped through a circular intake (0.15 m diameter) with a centrifugal pump (maximum capacity: 50 l/s). A controller is installed to enable a stepwise or continuous change of inflow.

The other side of the tube (Figure 1, right) consists of a circular overflow with a diameter of 0.15 m and a throttle pipe of 0.05 m diameter. The entire model is placed on top of a channel with a height and a width of 1.0 m to provide visual access to the bottom of the tube. Fig. 1 shows a photograph of the CSDT-model placed on top of the channel.

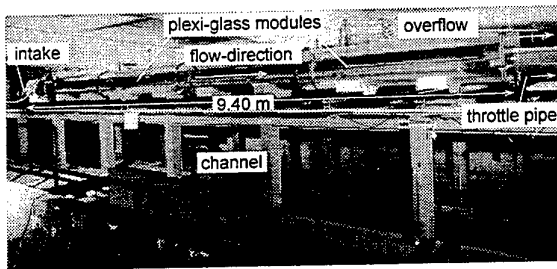


Fig. 1: Physical Model of CSDT

3. EXPERIMENTAL CONDITIONS AND MEASUREMENTS

The flow measurement in the physical model is performed using the Digital Particle Image Velocimetry (DPIV) which is the only technique to detect transient phenomena in a reasonable span of time.

3.1 Set-up of DPIV Devices and Data Processing

To visualise the flow the liquid is seeded with small tracer particles (polyamide) with a nominal diameter of $28 \mu\text{m}$. For illumination a laser lightsheet is generated in combination with a rotating polygon mirror and a parabolic mirror for parallelisation of the laser beam. The thickness of the light sheet is approximately 3.0 mm . The DPIV devices are placed under the CSDT-model to generate the lightsheet from the bottom of the tube. This is to avoid reflections and distraction of the laser beam caused by the free water-surface.

The laser lightsection (44.2 cm by 57 cm) is registered by a CCD-camera. The camera is placed in a defined angle under the pipe because of distortions due to the circular shape of the CSDT (Feldhaus, 1993). The field of view of the camera is 44.0 cm by 26.0 cm after correction of the distortion mentioned above. The DPIV devices can be moved along the axis of the CSDT so that arbitrary cross-sections can be analysed. The images are digitised and saved with an overlay frame grabber. The digital images are corrected and afterwards interrogated in 64×64 -pixel sub-images (this corresponds to areas of $2.16 \times 4.92 \text{ cm}$) with a spacing of 16 pixels (i.e. a 75% overlap; corresponding to 0.54 cm in x - and 1.23 cm in z -direction). The velocity field is obtained by cross-correlation and Fast Fourier Transformation. Fig. 2 shows the setup of the DPIV devices. All velocity fields are checked for inaccurate velocity measurements with a special type of dynamic filter algorithm. It works sequentially for every measured velocity vector:

A certain area around each vector representing the velocity is defined, for which the surrounding vectors are analysed to judge its quality.

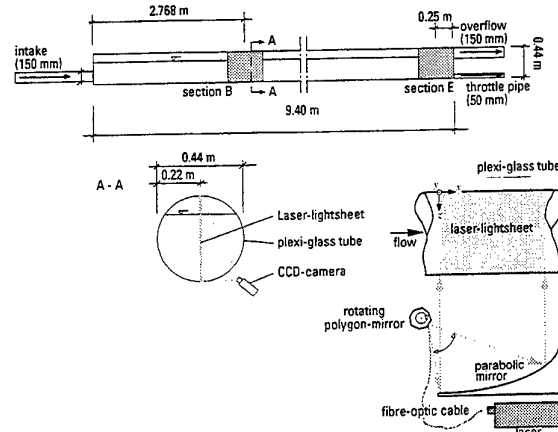


Fig. 2: Sketch of CSDT with marked investigated areas and set-up of DPIV devices

The mean velocity and standard deviation of the horizontal and vertical components as well as of the absolute values are calculated from all vectors in that area. Afterwards the algorithm checks if the deviation lies within tolerable limits. If not, it will be marked unusable.

The tolerated deviation is calculated from a static and a dynamic contribution. The static part mirrors the fact that the continuous grey values in the original image have to be converted to discrete positions in the digitised image. It has to be chosen according to the real size of a pixel. The dynamic contribution takes the fluctuations of the vectors in the area into account and is calculated as a multiple of the standard deviation. The main advantage of this technique is, that no correct vectors are filtered out as it could happen by using only a static contribution. In areas with many inaccurate vectors the mean velocity would shift in the wrong way. The effect of using a dynamic part is that the whole velocity field has to be filtered for several times, because the allowed limits will be reduced with the reduction of the standard deviation. This algorithm is repeated until no inaccurate vectors can be detected (Leucker 1995, Raffel & Kompenhans 1992). The maximum filtered vectors are about 5 %.

A simple smoothing algorithm is used afterwards to interpolate the filtered velocities to get a better visual access to the flow structures.

3.2 Accuracy of the used DPIV- system

The accuracy of the DPIV-measurements is strongly dependant on the resolution of the system components. The DPIV-system presented here uses a frame grabber with a x-resolution of $n_x = 768$ pixel ($x = 26$ cm) and y-resolution of $n_y = 572$ pixel ($y = 44$ cm). The dimensions of one pixel can be calculated to

$$\Delta x = \frac{x}{n_x} = \frac{26}{768} = 0.0339[\text{cm}] \quad (1)$$

$$\Delta y = \frac{y}{n_y} = \frac{44}{572} = 0.0769[\text{cm}] \quad (2)$$

The maximum difference between the real and the measured position of the center of area is one pixel (Leucker 1995). This results in maximum differences Δu and Δv between the real and the measured flow velocity, using a sampling rate of 25 Hz, of

$$\Delta u = \frac{x}{n_x \cdot \Delta t} = \frac{26}{768 \cdot 0.04} = 0.85[\text{cm/s}] \quad (3)$$

$$\Delta v = \frac{y}{n_y \cdot \Delta t} = \frac{44}{572 \cdot 0.04} = 1.92[\text{cm/s}] \quad (4)$$

The maximum detectable flow velocity is limited by the sampling rate and the dimensions of the observed area. To get a clear cross-correlation peak, Keane & Adrian (1990) remark, that the covered distance of a particle within a time step Δt must be shorter than a quarter of the side-length of a sub-image. Using 64x64-pixel sub-images, the maximum flow velocities $u_{\max 64}$ and $v_{\max 64}$ are

$$u_{\max 64} = \frac{1}{4} \cdot \frac{x_A \cdot \Delta x}{\Delta t} = \frac{1}{4} \cdot \frac{64 \cdot 0.0339}{0.04} = 13.6[\text{cm/s}] \quad (5)$$

$$v_{\max 64} = \frac{1}{4} \cdot \frac{y_A \cdot \Delta y}{\Delta t} = \frac{1}{4} \cdot \frac{64 \cdot 0.0769}{0.04} = 30.8[\text{cm/s}] \quad (6)$$

As a result the theoretical accuracy of the installed DPIV-system can be calculated to

$$\frac{\Delta u}{u_{\max 64}} = \frac{\Delta v}{v_{\max 64}} = \pm 6.3\% \quad (7)$$

if maximum velocities are detected. For lower flow velocities the accuracy decreases proportionately.

To verify the DPIV-system mean velocities in the main flow direction are measured in a vertical slice near the outlet (section E) of the CSDT (Fig. 2). The LDA-system used is a 10 mW He-Ne 1D-backscatter laser using the FFT to calculate flow velocities. Measurements are carried out for constant discharges of 2 l/s and 4 l/s. Fig. 3 shows the position of the LDA-profile and the DPIV-area in the CSDT.

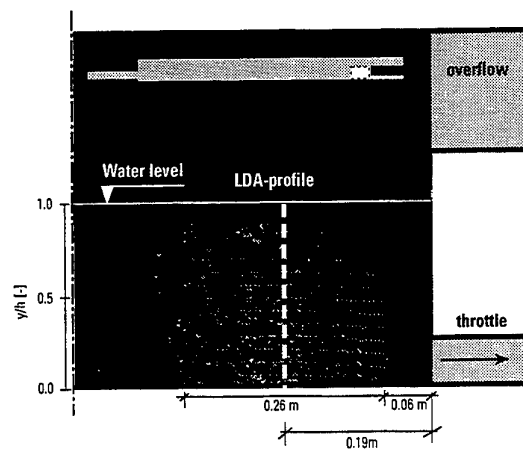


Fig. 3: Position of LDA-profile and detected DPIV-area at section E

The results are presented in Fig. 4. The velocities measured using DPIV are represented by a rhomb, while the LDA-profile is marked with a thick line. The area around the DPIV-values represents the calculated accuracy of $\pm 6.3\%$. It is obvious, that the accuracy of the measured velocities is in the range of the calculation.

At a height of 3 cm above the pipe invert the flow velocities differ for a discharge of 4 l/s. The reason is a velocity gradient above $dv/dz = 0.25$ cm/s/cm, which can not be detected by the dimensions of the sub-images used here.

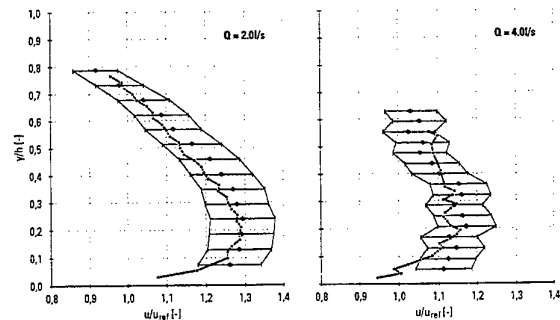


Fig. 4: Results of LDA and DPIV-measurements

3.3 Simulated Flow

To simulate a precipitation event taking place in a combined sewer system, different hydrographs following natural events (BROMBACH 1991) are taken and transferred to model-conditions by using Froude's law. An example for a continuously changing discharge is

shown in Fig. 5, where the Inflow- and throttle-hydrograph as well as the water level and the actual storage are represented.

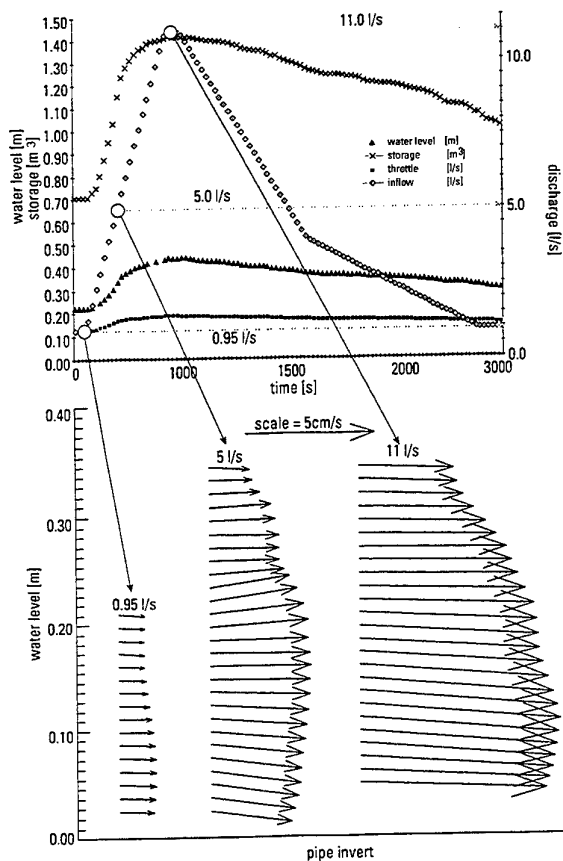


Fig. 5. Simulated Unit Hydrograph with CSDT response and velocity profiles at discharges of 0.95, 5.0 and 11.0 l/s in section B

The duration of one experiment is 3000 seconds. The inflow starts with 0.95 l/s and increases to 11 l/s with a gradient of 1.07 l/min. After a constant discharge for a period of 100 seconds it decreases with two different gradients of 0.47 l/min and 0.15 l/min. To examine the development of the flow field during the experiment in 5 different positions in the physical model of the combined sewer overflow, 25 images are taken 20 times during one experiment with a sampling rate of 25 Hz. This leads to a total of 3000 images, which have to be evaluated. The Reynolds-numbers range between 800 for a discharge of 0.95 l/s and 32000 for 11.0 l/s (based on the hydraulic radius and the mean velocity).

4. RESULTS

The results of the DPIV- measurements in the physical model of CSDT are divided into the observation of velocity profiles during the filling and emptying of the CSDT and the evaluation of flow structures.

4.1 Velocity Profiles

To assess the flow during the simulated precipitation event velocity profiles in section B and E are calculated out of the DPIV measurements. This is managed by projecting the area information onto a profile as demonstrated in Fig. 6. This is only possible, because the mean velocity differences in x-direction are small compared to the absolute velocities.

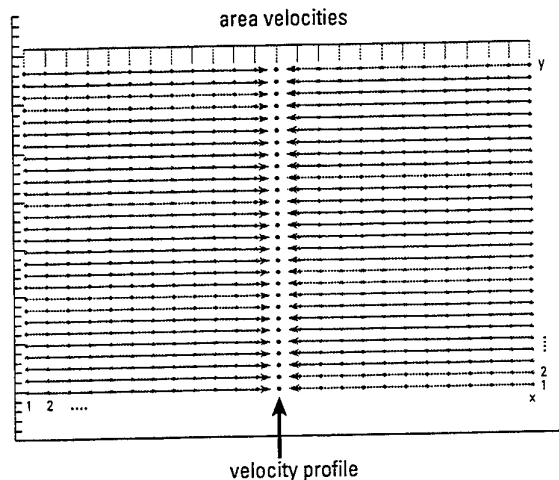


Fig. 6: Transfer of area velocities to velocity profiles

In Fig. 5 different velocity profiles in section B for discharges of 0.95, 5.0 and 11.0 l/s are presented. The influence of the intake can be observed for 0.95 and 11.0 l/s resulting in higher velocities due to the pipe invert. For a discharge of 5.0 l/s highest velocities are in the middle of the profile due to the water level in the CSDT increasing quickly at this point of time.

The velocity profiles in the outflow section E (Fig. 7) demonstrate the influence of throttle and overflow on the flow field. For low discharges (0.95 l/s to 4.0 l/s) the flow is orientated towards the throttle. When the overflow is working the flow is divided and orientated towards the overflow for a discharge of 11.0 l/s. For a decreasing discharge the velocity profile has two maxima in the height of the overflow as well as the throttle (4.0 l/s). At the end of the precipitation event, the maximum flow velocities are in front of the throttle again.

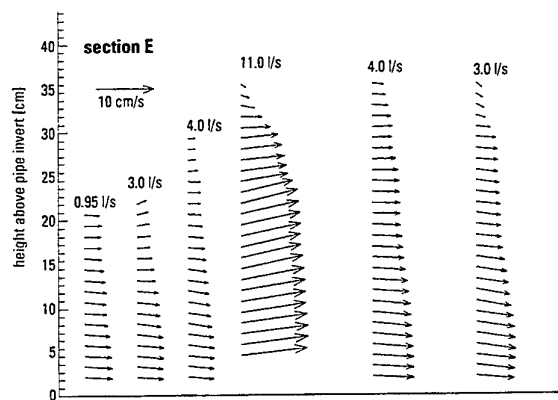


Fig. 7: Velocity profiles in section E

4.2 Flow structures

One example for a time dependent motion analysis is presented in Fig 8. It shows a vector plot of fluctuating velocities u' , v' during a discharge of 5.3 l/s in section B within a time span of 1.8 seconds. Large eddies can be observed "walking" within the flow. The vector plots are calculated by a moving average over 30 images with a stepwidth of 5 images. Fig. 8 shows the corresponding contours of the z-component of vorticity for the same time span in section B as well. Note that the concentrations of vorticity correspond well with the position of large eddies.

The velocity fields corresponding to the velocity profiles in section E during the transient precipitation event are visualised in Fig. 9. It subscribes the interpretation of the flow field from above. To emphasize the flow for decreasing discharge the velocity in x-direction is contour-visualised for 4.0 l/s and 3.0 l/s. While for 4.0 l/s a main flow at the bottom can be observed, for a discharge decreasing further the flow field becomes irregular.

5. CONCLUSIONS

The results show, that the DPIV-technique was able to record the flow-structures in the physical model of CSDT. The accuracy of about 6 % was sufficient for the calibration of a 3D mathematical-numerical simulation model. Velocity profiles and flow structures could be measured for any discharge in the frame of the simulated hydrograph. Only in a section immediately behind the intake, velocity and velocity gradients exceeded the limits of the DPIV system. It could have been observed, that large eddies were extended across half of the

water level, which will have a strong effect on transport mechanisms within the CSDT.

The velocity profiles detected in different points of time allowed insights into the development of the flow. It was obvious that the inflow geometry has an influence on the flow along 2/3 of the CSDT-length, while the outflow geometry influences only immediately in front of the outflow.

The flow velocities at the inflow region were greater for increasing than for decreasing discharge due to the increased water-filled cross-section. At the outflow the flow-velocities behaved vice versa, because the flow through throttle and overflow increased with water level.

ACKNOWLEDGEMENTS

This study was supported by the *Deutsche Forschungsgemeinschaft* (DFG), reference number KO 1573/1-4, research project *Stauraumkanäle mit unten liegender Entlastung*

REFERENCES

- Brombach, H.; Michelbach, S.; Wöhrle, C. 1991, Sedimentations- und Remobilisierungsvorgänge im Abwasserkanal- Teilprojekt 3, Schlußbericht des BMFT-Verbundprojektes Niederschlagsbedingte Schmutzbelastung der Gewässer aus städtischen befestigten Flächen, Umwelt- und Fluidtechnik GmbH, Bad Mergentheim
- Feldhaus, R. 1993, Zur hydrodynamisch-numerischen Simulation von Mischwasserspeichern, Mitteilungen des Instituts für Wasserbau und Wasserwirtschaft, Heft 91, Academia Verlag, St. Augustin
- Keane, R.D.; Adrian, R.J. 1990, Optimisation of particle image velocimeters. Part 1: Double pulsed systems, Meas. Sci. Technol. Vol. 1, pp. 1202-1215
- Leucker, R. 1995, Analyse instationärer Strömungsphänomene zur Vorhersage des Kavitationsbeginns, Mitteilungen des Instituts für Wasserbau und Wasserwirtschaft, Heft 101, Academia Verlag, St. Augustin
- Raffel, M.; Kompenhans, J. 1992, Post Processing: Data Validation, Proceedings of the 6th International Symposium on Applications of Laser techniques to Fluid Mechanics, Lisbon, Portugal, July 20-23, 1992

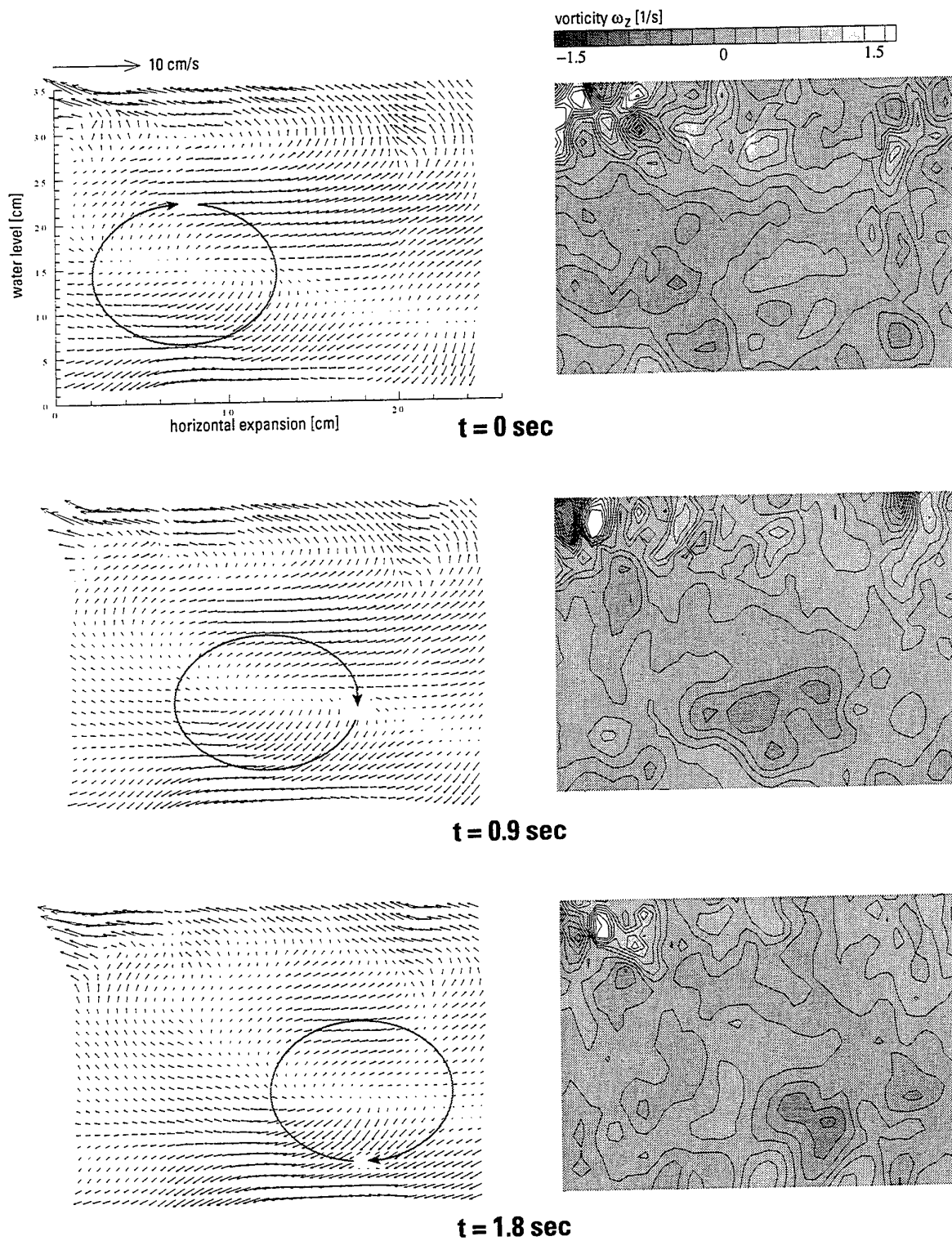


Fig. 8: Vector Plot of Fluctuating Velocities u' , v' during a Discharge of 5.3 l/s in Section B

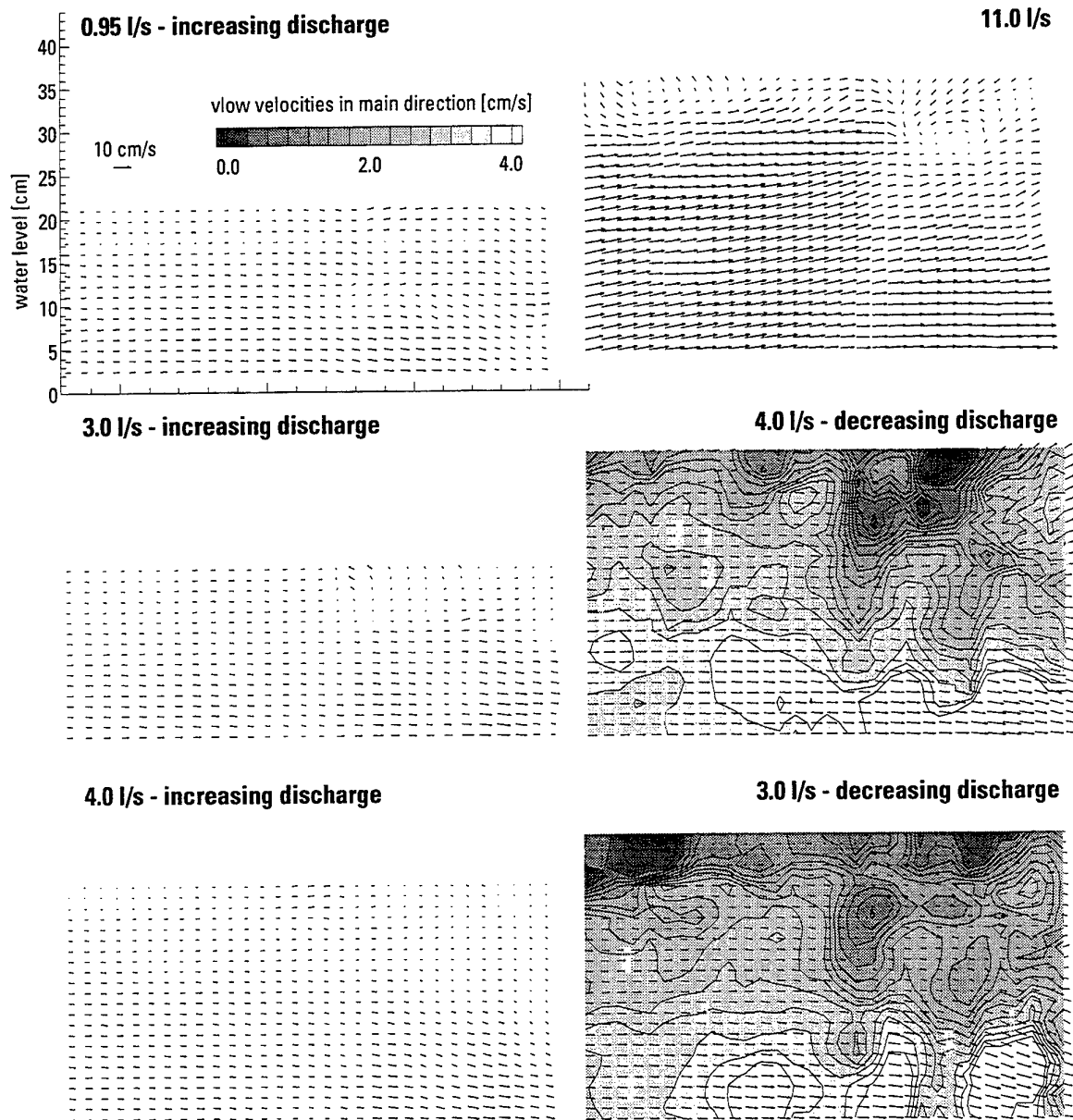


Fig. 9: Velocity Fields in Section E during the Transient Precipitation Event

A Comparison of Velocity-Field Data behind a Double-Swirl Nozzle Measured by Means of Doppler-Global and Conventional Three-Component LDA Techniques

B. Lehmann¹⁾, I. Roehle²⁾

Deutsches Zentrum für Luft- und Raumfahrt

Institut für Antriebstechnik

¹⁾Abt. Turbulenzforschung, Berlin

²⁾Abt. Strömungsmeßtechnik, Köln

Germany

ABSTRACT

The velocity data sets measured by means of a three-dimensional Doppler Global (DGV) technique and of a three-component Laser-Doppler technique are shown, discussed and compared. The measurement object was the same for both measurements and consisted of a dual-flow, dual-swirl atomisation nozzle with a pipe-like flow chamber working as a model combustion chamber. The flow conditions were isothermal and atmospheric.

In spite of a visually good agreement of the global-field velocity plots the velocity components show characteristic and obviously systematic deviations between the results of both measurement techniques. The relative deviations can be of a considerable amount and have suffered up to now from the lack of a reliable physical explanation.

In this sense the features of both techniques demonstrate their special advantages which are the fast whole-field overlook of DGV and the more consistent individual data sets of LDA.

1. INTRODUCTION

Due to their special features the different measurement techniques based on the principle of Doppler-shifted laser light do less compete than supply each other in their results. Conventional LDA data deliver local velocity-field information the acquisition of which needs a rather time-consuming measurement process. The resolution and the accuracy of the statistical data are, however, at least of an order of magnitude higher than the data measured by means of DGV and other well-known whole-field techniques.

On the other hand the global flow measurement techniques aim at the rapid acquisition of the flow data of a complete velocity field in order to give the experimenter a quick overview on a flow-field situation. Up to the present it has to be tolerated that the

flow-field data are commonly less accurate. But the global impression of the instantaneous or of a time-integrated flow-field does not suffer from it.

The represented paper compares the results of a conventional laser-Doppler (LDA) and of a Doppler global technique (DGV) measured in the same flow field behind a dual-stream, dual-swirl air-blast atomisation nozzle. It shall give an impression of the comparability of the different technique's data.

2. MEASUREMENT OBJECT AND OPTICAL DEVICES

2.1 NOZZLE AND FLOW CHAMBERS

The flow field behind the fuel atomisation nozzle was investigated. Such nozzles are an important component of combustion chambers of jet engines. In Fig.1 two circular air flows pass two swirl generators and are combined in the exit of the nozzle. In this way a recirculating flow with strong shear stresses is generated. These shear stresses atomise the fuel film tearing off the atomisation lip of the nozzle. The fuel injector is placed in the center of the nozzle but is not used in the experiment.

The atomisation nozzle has a outlet diameter of 11 mm. It was operated under atmospheric pressure with a pressure drop of 30 mbar and was inserted in a tube with a diameter of 54 mm. The 3D-flow field in the pipe downstream the nozzle was investigated.

2.2 DOPPLER GLOBAL OPTICAL DEVICE

Fig. 1 shows the experimental DGV arrangement. A slit in the tube at the light sheet location avoids measurement disturbances, caused by reflections. Therefore the windows, which are needed to avoid flow leakage, are recessed from the inner wall. The light sheet and camera location was fixed. The nozzle

was moved to change the axial position of the measurement.

The direction of the velocity component v_{xr} measured with the set-up is also indicated in Fig. 1. The other two velocity components needed to determine the 3D-vector could be measured by two further DGV-pictures taken with two other light sheets overlapping at the same location, with the light sheet direction rotated 120° and 240° around the pipe axis. However these two additional measurements are unnecessary, because of the cylindrical symmetry of the flow. Of course this simplified method may only be applied to measure mean values. The instantaneous flow distribution never shows any symmetry because of turbulent fluctuations.

The presented experiment has a cylindrical symmetry and only the time averaged flow field is of interest. Therefore the DGV-system optimised for the measurement of mean flow velocities was used to analyse the flow field.

The light sheet illuminated the whole cross section. The Laser power was 300 mW. The air was seeded with glycerine particles with an average diameter of $0.2\ \mu\text{m}$. The particle density was so low that, with the flow switched on, the scattered light could hardly be seen by the eye. To achieve sufficient image quality, an exposure time from 1 to 5 seconds was needed. This time is sufficient to integrate the turbulent velocity fluctuations.

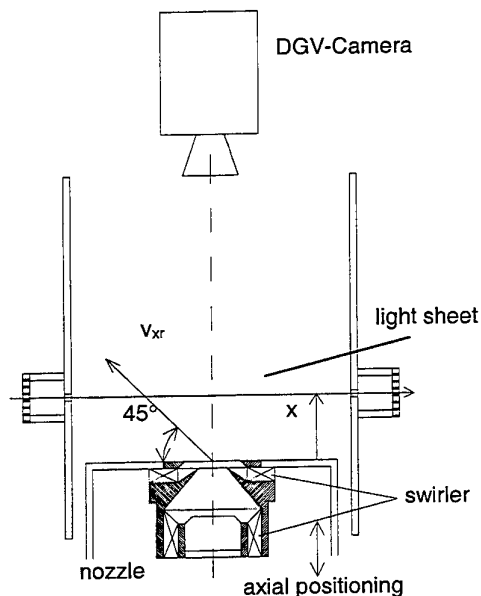


Fig. 1: Set-up of the nozzle and the model-flow chamber for DGV measurements

2.3 THREE-COMPONENT LDA TECHNIQUE

For the conventional LDA measurements an orthogonally arranged three-component LDA optics was used, consisting of a dual- and a single-component device. Two components worked with the green argon-laser line and the scatter-light signals were separated by means of intensity discrimination. The system was the same as described in [5] except that now the x direction had the down-flow orientation of the nozzle axis and y was the traverse coordinate across the flow.

The optical access of the six measuring light beams into the flow chamber was enabled by forming the model chamber from about 0.1 mm thick overhead foil. It was rolled and pasted as a 300 mm long cylinder with the already mentioned diameter of 54 mm. The foil distorted the optical beams especially of the radial-component system insignificantly enough to permit a traverse along more than 80 % of the chamber diameter without any necessary optical readjustment. Even triple-coincidence measurements could be made in this way.

As seeding particles an almost monodisperse SiO_2 -powder was applied with particle diameters of nearly $0.8\ \mu\text{m}$. It was introduced into the settling chamber of the nozzle and thus seeded both partial-air flows.

3. MEASUREMENT RESULTS

3.1 RESULTS OF DGV MEASUREMENTS

The result of a DGV-measurement at a certain axial position x is shown in Fig. 2. The upper part shows the image of the camera behind the iodine cell and the lower part the picture of the reference camera. First the background light is subtracted, then the pictures are divided and the divided picture is corrected in accordance with the pixel specific sensitivity differences. Then, by the use of a calibration function $T(v)$ and with regards to the geometry of the optical arrangement, the distribution of the velocity component v_{xr} is obtained (Fig. 3).

In the next step the user marks the symmetry centre of the picture and the computer calculates the two other velocity pictures by turning the resultant picture 120° and 240° around the symmetry centre. These three pictures are combined to a 3D-vector field which is shown in Figure 4.

The components in the light sheet are represented by a vector plot and the axial component is represented by a so called „luminescence plot“.

This result is obtained after about 30 seconds, the measurement takes 5 seconds, the post processing requires 25 seconds.

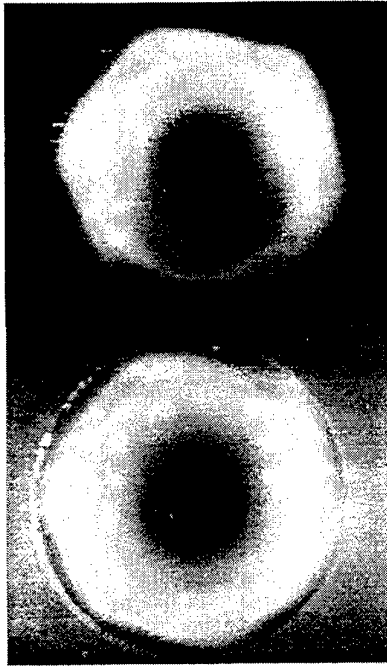


Fig.2: Signal and reference DGV picture

The full volumetric flow field can be acquired within a few minutes by stepwise changing the axial position of the light sheet. As an example, Fig. 5 shows the vector field in the plane along the tube axis. Fig. 10 shows the distribution of the circumferential velocity.

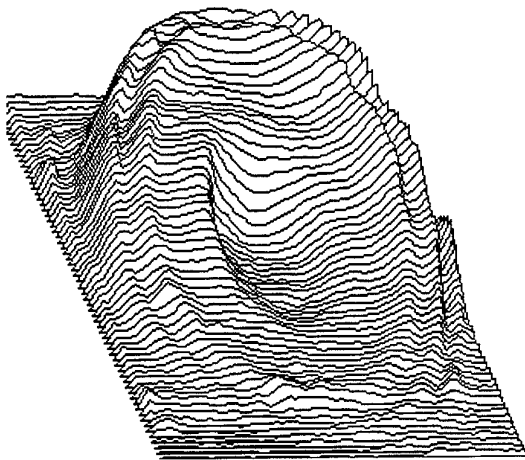


Fig. 3: Result of a DGV-measurement. The distribution of one velocity component.

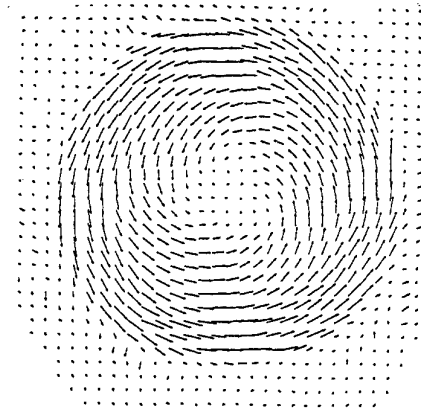


Fig.4: 3D-velocity distribution of the flow 2 mm above the swirl nozzle.

The pictures indicate quite clearly how fast the swirl flow in the tube is smoothed. Secondary flow structures can be observed, especially the recirculation torus in the corners at the bottom of the tube and the axial recirculation. Both effects are very important for the combustion because they are needed to stabilise the flame.

These results show, that this method is an excellent tool for fast analysis of complex flow fields. The resolution is between 1 and 2 m/s, since the smallest vectors which still make sense have a length of 1.5 m/s.

Reliable statements concerning the accuracy of DGV are not yet possible. Among many other potential error sources, we assume that reflections of the laser, reflections of the scattered light and multi-scattering may affect the accuracy as well as high

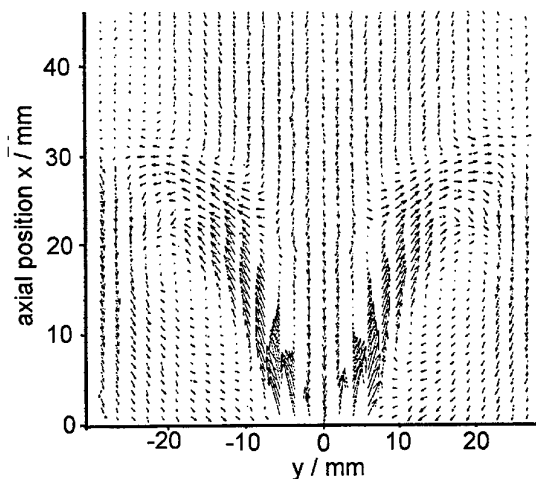


Fig.5: DGV vector plot of the axial-radial velocity vectors in the vicinity of the nozzle

turbulence in combination with non linearity of the iodine line and inhomogeneous seeding causing non-linear averaging.

If such error sources can be avoided, the absolute accuracy can be estimated to be at least smaller than 5m/s.

The vector plot shows, that the DGV measurements near the nozzle ($x=3$ mm) are influenced by the surface representing the burner head plate. This plate was coated with soot. Never the less parts of the scattered light was reflected by this surface and disturbed the measurement resulting in vectors which point slightly too much towards the burner head plate. At this point an enhancement of the DGV system is required.

3.2 RESULTS OF LDA MEASUREMENTS

The results of the laser-Doppler measurements consist of the profiles of all three velocity component's mean velocities U, V and W , their mean fluctuations (rms) u', v' and w' and of the double and triple cross-correlations of the velocity components. Locally measured frequency spectra of the fluctuation were helpful for a deeper insight into the dynamics of the flow field.

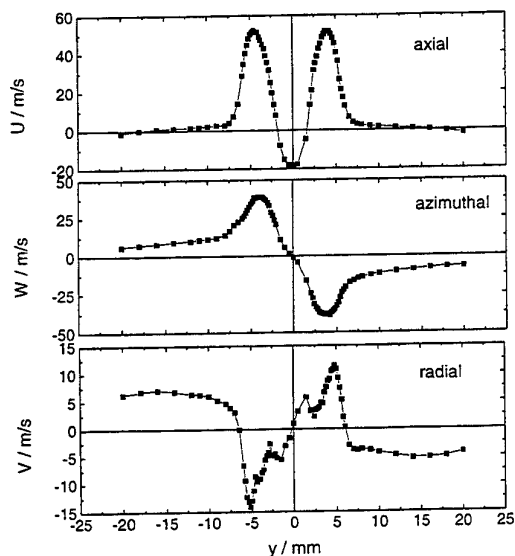


Fig. 6: Mean velocity components at $x=3$ mm

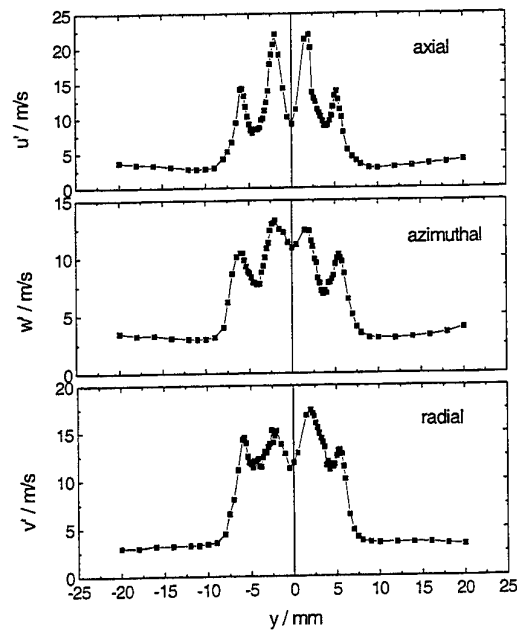


Fig. 7: rms-values of turbulent fluctuations at $x=3$ mm

Fig. 6 shows the velocity profiles at $x=3$ mm behind the nozzle exit. The axial component attains a reversed speed of nearly $U=-20$ m/s on the axis, which means, that in the inner part of the centre nozzle the air flows into the nozzle instead of leaving it. The azimuthal component W attains nearly 80 % of the maximum axial velocity and the radial one V nearly 20 %.

The fluctuation rms-values in Fig. 7 show, that, compared with the maximum mean velocities, the turbulence degree does not exceed the order of 40%.

The cross-correlations in Fig. 8 are normalised with the products of the components' rms values.

The maximum values of 0.6 for the double correlations indicate the activity of highly-coherent large structures in the flow.

The coherent fluctuations imply periodical movements in the flow which were analysed by means of spectral analysis of the LDA data. Fig. 9 is a frequency spectrum of the radial fluctuations measured at $x=6$ mm and $y=10$ mm off-axis. The frequency $f=2.65$ KHz describes an absolute instability effect which is due to the special type of axial and radial velocity profiles of swirl flows.

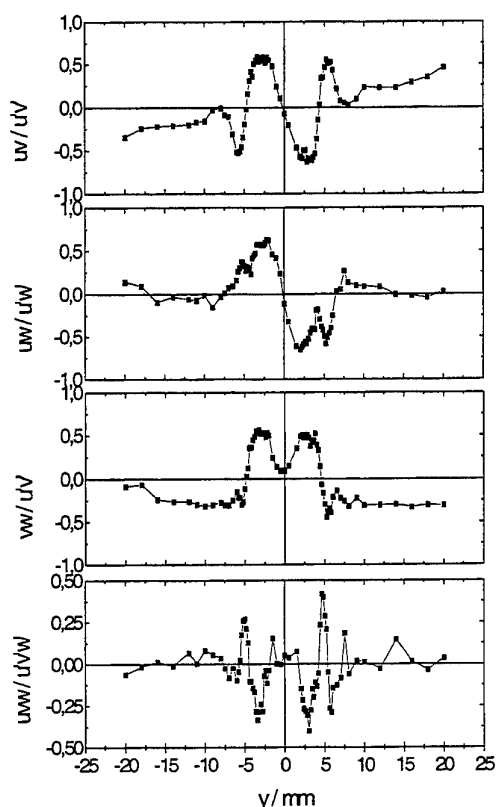


Fig. 8: Normalised double and triple cross-correlation profiles at $x=3$ mm

Such fluctuations are connected with a helically structured fluctuation mode and can also be found in the flow of other similar nozzles. The lower frequency must be due to another instability mechanism which has not upto now been identified. Nevertheless the spectrum shows that the flow field must be highly unsteady.

Such kind of necessarily coincident laser-Doppler measurements were done over several cross-sections of the flow-chamber at different distances x away from the nozzle exit. The results can be combined to form spatial or plane vector fields and thus be compared with the Doppler-global measurements.

4. COMPARISON OF DGV AND LDA RESULTS

In Fig 10 two plots of the u - v vectors are shown, as deduced from the DGV and from the LDA data. For a comparison the results are extracted from the data tables for the same distances x away from the nozzle exit. At the first glance the vector fields seem

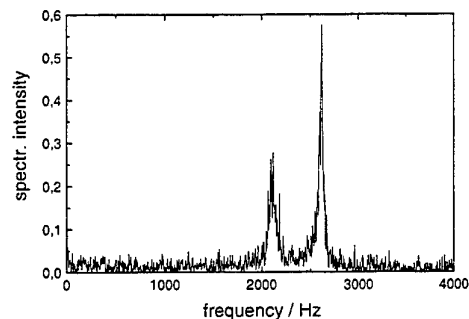


Fig. 9: Frequency spectrum of the radial fluctuations at $x=6$ mm and $y=10$ mm

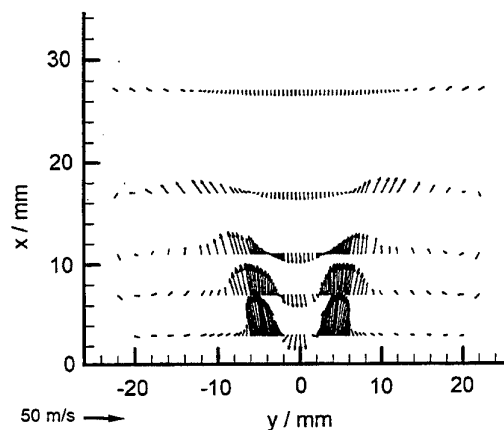
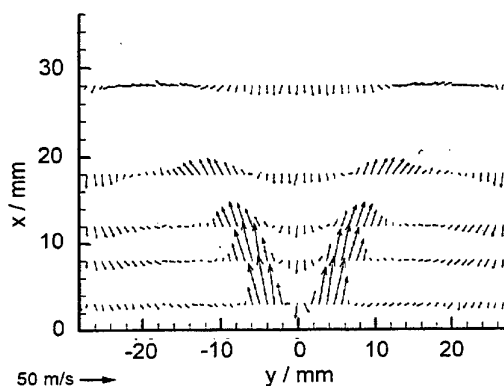


Fig. 10: u - v vector plots of DGV (upper field) and LDA (lower field) measurement results

to be rather identical. But a more accurate look shows that there are, partly, considerable differences between both measurements' data.

In order to have a more realistic impression of the differences between the two differently measured result sets a comparative plot of the velocity components' values instead of the vectors seems to be rec-

ommendable. This has been done in the figures no. 11 to 13 for three different distances x away from the nozzle, each figure containing the plots of the three evaluated velocity components.

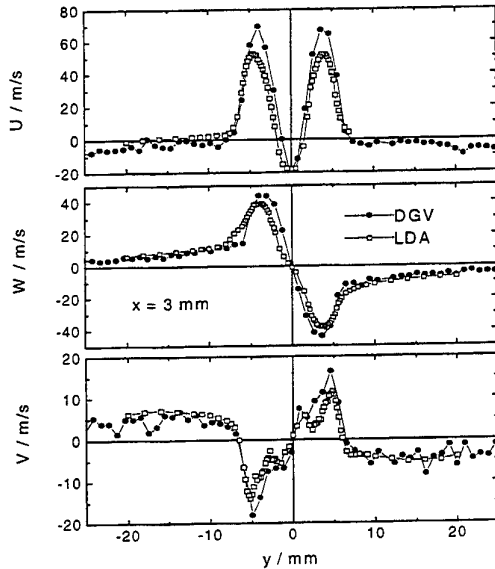


Fig. 11: Mean velocity plots of DGV and LDA data, measured at $x=3$ mm

Close to the nozzle exit at $x=3$ mm (Fig. 11) the axial component U shows an overestimation of the velocity maxima by the DGV technique and a tendency to negative values close by the wall where the LDA data tend to be zero. The circumferential component W behaves similarly for both types of results.

This holds also for the radial component V where the tendency can be observed, that also fine details of the profiles in the near-axis region can be reproduced by means of both kinds of techniques. In the vicinity of the wall, where the velocity values are low, the DGV data show much more scatter than the LDA ones which expresses the restricted resolution features of DGV.

Fundamentally the same interpretations hold for results of the other axial positions $x=11$ mm (Fig. 12) and $x=27$ mm (Fig. 13). The tendency, however, can be recognised that

- the deviations and the scatter of the different data sets arise with decreasing velocities,
- maxima and minima of the velocity profiles seem to be systematically overestimated by the DGV technique compared with the LDA data.

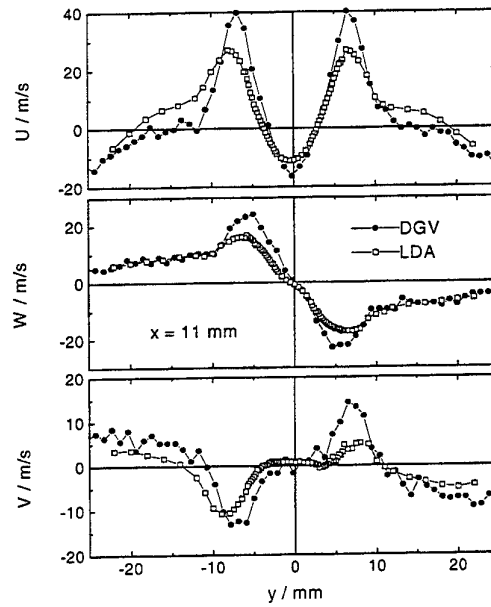


Fig. 12: Mean velocity plots of DGV and LDA data, measured at $x=11$ mm

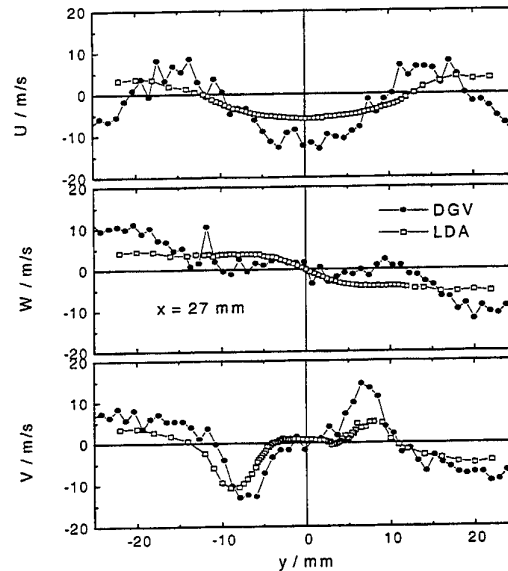


Fig. 13: Mean velocity plots of DGV and LDA data, measured at $x=27$ mm

The order of overestimation attains values of about 30% to 50 % for the axial velocity maxima and holds also for the other components. Nevertheless profile regions with strong and with almost zero velocity

gradients show better agreement of the differently measured results.

The different gradients of the circumferential W profile, especially at $x=11$ mm, makes suppose that there might be an influence of the slit in the chamber wall to the flow field which was applied during the DGV measurements for an undisturbed optical access to the chamber. Such a slit influences more the profile's shape than the extreme values of the velocity.

5. CONCLUSIONS

In spite of a first-glance equality of the velocity-vector fields the comparison of DGV and LDA velocity-component data shows partly considerable differences between the different data sets. The deviations increase with decreasing velocity values and tend to be maximum nearby extreme-value situations of the velocity profiles.

The physical reasons for the deviations are not yet clear but it can be deduced from theory and from the discussed results that the LDA data are more accurate than those measured by DGV. This fact is confirmed when well-known correction techniques are applied to the LDA data which does not introduce a considerable change to the LDA results. The lower scatter of the results and the more localised measurement of LDA give more consistent LDA data and reliability to be compared with numerical model results. Smaller localised measurement volumes are possible, because secondary light scatter effects do not play a role for the LDA technique.

On the other hand the DGV data deliver a quick and complete overview of the flow field and fulfils in this way other kind of important demands than LDA.

Finally it should be remarked that all this agreement of measured results could be obtained in spite of the obvious existence of the already mentioned highly coherent structures in the flow field and the fluctuation dynamics which is necessarily introduced by it.

6. REFERENCES

1. H. Komine: System for Measuring Velocity Field of Fluid Flow utilising a Laser-Doppler Spectral Image Converter. US Patent 4 919 536, 1990.
2. I. Röhle, R. Schodl: Laser-Doppler-Velocimetry auf der Basis frequenzselektiver Absorption. diploma thesis, DLR internal report no. IB-325-8-93, 1993.
3. I. Röhle, R. Schodl: Evaluation of the Accuracy of the Doppler Global Technique. Proc. of Optical Methods and Data Processing in Heat and Fluid Flow, London 14./15. April, pp 155-161, 1994.
4. J.F. Meyers: Evolution of Doppler Global Velocimetry Data Processing. Proc. of Eighth International Symposium on Applications of Laser Techniques to Fluid Mechanics. Lisbon, 8-11 July, 1996.
5. B. Lehmann, C. Hassa, J. Helbig: Three-Component Laser-Doppler-Measurements of the Confined Model Flow behind a Swirl Nozzle. Eighth International Symposium on Applications of Laser Techniques to Fluid Mechanics, 8.-11. Juli, 1996, Lissabon, Portugal.
6. M. Hoffmeister, K. Hertwig, K.-J. Kreul, H. Kretschmar, K. Erler: Modellierung von turbulenten Drallstrahlen für Brennkammern von Flugtriebwerken. VDI-Fortschritt_Bericht, Reihe 7, Strömungstechnik, Nr. 291, 1996, VDI-Verlag GmbH, Düsseldorf.
7. I. Röhle: Three Dimensional Doppler Global Velocimetry in the Flow of a Fuel Spray Nozzle and in the Wake Region of a Car. Flow Measurement and Instrumentation, Elsevier Science Ltd., 1997, Oxford.
8. I. Roehle, C. Willert, R. Schodl: Recent Applications of Three Component Doppler Global Velocimetry in Turbo-Machinery. Proc. of International Symposium on Applications of Laser Techniques to Fluid Mechanics, Lisbon, 13-16 July, 1998.

CHARACTERISTICS OF TRANSVERSE DISPERSION AND FLUID FLOW AT THE EXIT OF SHORT CERAMIC FOAMS INSIDE A PIPE

J.C.F. Pereira and J. Raposo

Instituto Superior Técnico
Mechanical Engineering Department
Av. Rovisco Pais, 1096 Lisboa Codex - Portugal

ABSTRACT

This paper reports experimental measurements of transverse dispersion coefficients in porous ceramic foams for three different pore sizes (10, 20 and 60 pores per inch) and pore Reynolds number $20 \leq \text{Rep} \leq 400$. Two flow configurations were studied corresponding to a short ceramic foam block ($X/D = 0.8$) located in a pipe flow or in a sudden pipe expansion (1:4). The transverse dispersion was evaluated from digital images of smoke dispersion patterns and LDA was used to characterise the axial and radial velocity components at the entrance and exiting the ceramic block and to investigate if separated flow exists in the vicinity of the sudden pipe expansion. The results have allowed to correlate the scalar transverse dispersion in ceramic foams and to interpret their dependence with pore Reynolds number.

INTRODUCTION

Flow in porous media is an interdisciplinary subject that traditionally is of special relevance in hydrology and petroleum engineering. Recently the use of porous ceramic foams or other highly porous materials ($> 85\%$) such as metal wires, metal foils, etc., have received applications in combustors, catalytic exhausters, filters, heat exchangers, etc., see e.g. Trimis and Durst (1997), Msaiorov et al. (1984) and Doltsimis (1996). As a consequence there is a new interest in flow in porous media and related with materials that have a porosity higher than spheres packing ($\cong 40\%$).

The main problem associated with fluid flow in ceramic foams is the relationship between the pore scale flow characteristics and macroscopic flow behaviour. The very limited optical and physical access inside the

porous matrix prevents a direct quantification of the phenomenae at pore level and numerical calculations of the 3D pore flow are still impracticable for engineering calculations. The alternative way to solve the problem is to describe the flow in a macroscopic point a view in which governing equations are obtained by volume average of the microscopic 3D flow and solid structures. Several additional problems are created with the averaging procedure and basic fluid flow questions like how to model the dispersivity tensor or the existence of effective flow separation inside porous media are still not fully answered questions. The complex pore geometry influences the evolution of the flow process, questions arise about the adequability of the existing scalar dispersion models or heat and mass transfer modelling assumptions, derived from packed beds of spheres, to study the flow at high pore Reynolds numbers in ceramic foams, see e.g. Pereira et al. (1998).

Experimental work conducted on velocity distribution in packed beds has shown that the flow is not uniform across the bed, see e.g. Morales et al. (1951), Schwartz and Smith (1953) showing an oscillating profile with the maximum of the peak values at one or two particle diameters from the wall. This is attributed to the oscillation pattern of voidage up to four or five diameters from the wall (over a cross section of the bed of monosized spheres). The flow dependence with pore Reynolds number in packed beds of monosized spheres has been investigated by many researchers, see e.g. Bear (1972), Dybbs and Edwards (1984) and Durst et al. (1987). After the Darcy regime ($\text{Rep} < 1$) there is a steady laminar flow regime in which the streamlines are fixed. Inbetween $150 < \text{Rep} < 300$ unsteady effects play a role but the onset of flow bifurcation, transitional or turbulent regimes are a controversial issue, see e.g. Mickleley (1965), Takatsu and Masuoka (1996) and Nield (1997).

Some of the authors attributed a critical Reynolds number inbetween 110 and 150 see Jolls and Hanratty (1989) and others a value of $Re_p = 300$ Dybbs and Edwards (1989). For sufficient high pore Reynolds number $o(10^3)$ there are experimental evidence that the turbulent flow regime exists within a porous medium - see Kaviany (1991) and their signature is attributed to a post-Forchheimen flow regime in a curve of macroscopic pressure gradient versus Reynolds number, see e.g. Fand et al. (1986).

Experiments of scalar dispersion conducted in ceramic foams have been reported by Hackert et al. (1996) using digital images taken of resulting smoke dispersion patterns. They have concluded that the nondimensionalised transverse dispersion coefficient, D_T/ud , gradually increases with Reynolds number up to a Reynolds number of about 300 or 400 depending on the number of pores per inch and then assumes a constant value in the range 0.11 - 0.16. Benz et al. (1993) have previously reported also for ceramic foams that the constancy of D_T/ud , was attributed to turbulent mixing within each pore. LDV measurements conducted by Hiatt (1994) and Hall and Hiatt (1994), using a perforated foam (to have optical access) show that normalised rms of velocity fluctuation divided by local mean velocity increases and inbetween $300 \leq Re_p \leq 400$ becomes approximately constant with further increase in Re_p . Other applications of LDA to flow in porous media are related with refractive index matched oils though a porous bed Johnston and Dybbs (1975) and this technique has been used also by Yarlagadda and Yoganathan (1989) in a bed of 3 mm diameter glass spheres but at a very low Reynolds numbers.

The task to be tackled is the dispersion of a tracer in isothermal flow in porous ceramic foams, made from Al_2O_3 with 10, 20 or 60 pores per inch (ppi).

In this work the experimental technique based on digital images of the resulting dispersion of a point smoke tracer proposed by Hackert et al. (1996) has been used together with LDA measurements at the entrance and exit of the ceramic foam sample allowing to characterise the multijet like flow structure exiting from the foam. Two flow configurations were used: a straight pipe flow with a foam sample and a sudden pipe expansion with the ceramic foam sample located in the larger pipe. The first flow configuration was used to characterised the transverse dispersion coefficient when the effective velocity in the porous media is one dimensional and the second configuration to investigate the scalar dispersion and presence/absence of flow recirculation when the effective velocity is two-dimensional.

Test Section and Experimental Technique

A schematic of the experimental arrangement is shown in Figure 1a). Compressed air enters in a perspex pipe with 84 mm diameter which serves as a mount for the test section pipe. Air is guided into the test section pipe with 200 mm long by a ceramic foam with 20 ppi which holds a smoke source incense stick. The ceramic sample with 84 mm diameter and 50 mm long is placed in the top of the test section pipe. A laser light sheet, 5 W Ion-Ar, illuminates the exit smoke pattern. Figure 1b) shows the second pipe test

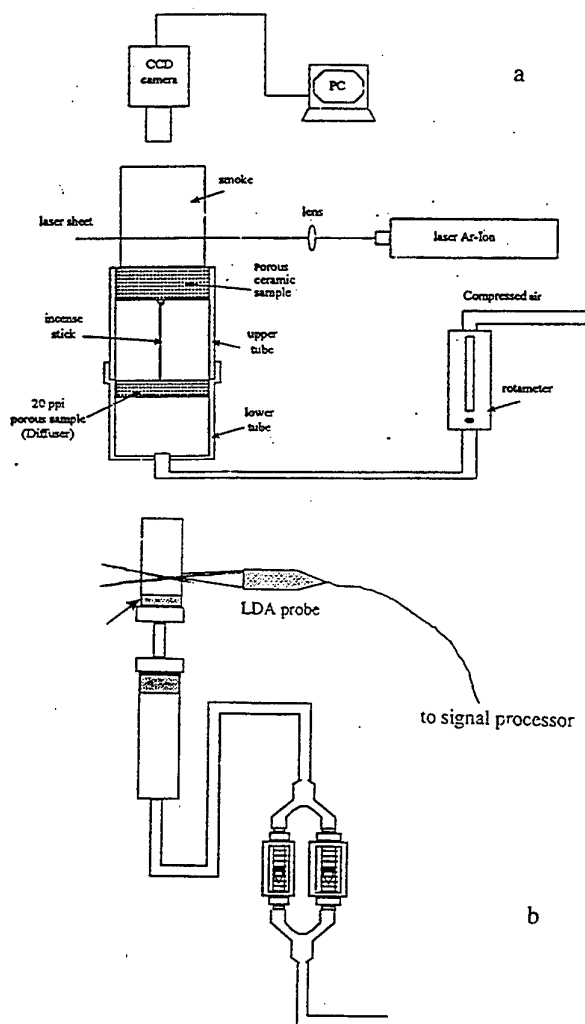


Fig. 1 Test section, a) Foam inside a pipe; b) Foam inside a pipe sudden expansion

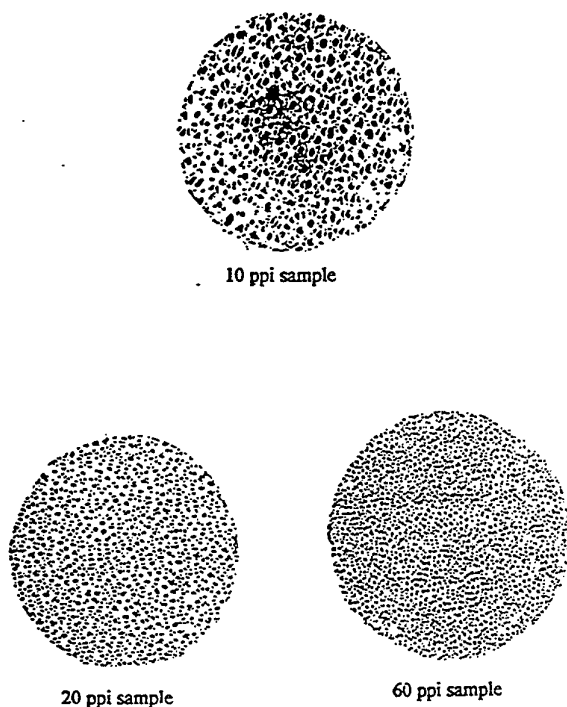


Fig. 1c) Ceramic foams

section used which includes a pipe sudden expansion from 20 mm to 84 mm pipe diameters. The ceramic foam sample could be mounted at different distances from the sudden pipe expansion. Three ceramic foams made from Al_2O_3 with 10, 20 or 60 ppi were used with average pore diameters of 5.1, 2.6, 0.85 mm respectively. Figure 1c) shows the three porosities considered in this work.

Digitised images were taken of the resulting smoke dispersion inside the porous ceramic sample using a CCD (Sony SSC-M370CE) camera linked to a framed grabber video card with 640 x 480 pixel resolution that processes and stores in a PC the digitised images with 256 gray levels. The approximate transverse dispersion coefficient was evaluated from the digitised images using the procedure outlined by Hackert et al. (1996). The main assumption is that the tracer intensity at each pixel is correlated with the tracer concentration and that the dispersion of individual tracer particles approaches a Gaussian distribution in the continuum limit with dispersion coefficients $D_i = \tau_i^2/2t$, $i \equiv x, y \text{ or } z$, for a point source at time $t = 0$. The volume occupied by the tracer is described by $\tau_i^2 = 2 D_i t$ and the average transverse dispersion coefficient between two times, $\Delta\tau^2 = \tau_2^2 - \tau_1^2 = 2D_T(t_2 - t_1)$.

For steady flow time can be replaced with downstream distance $t = x/U$:

$$D_T = \frac{\overline{U} \Delta\tau^2}{2 \Delta x} \quad (1)$$

The procedure to calculate $\Delta\tau^2 = \tau_2^2 - \tau_1^2$, consists on the evolution of the variances of the images intensity at the inlet and outlet of the ceramic foam. The variance is calculated as the mean value of the variances along the two orthogonal co-ordinate directions located at the image mass center and evaluated from five stored images. The accuracy of the variance values is dependent on the image signal to noise ratio and using the same point smoke source depends of the flow pore Reynolds number. The variance was measured only up to the pore Reynolds number that produce an image amplitude intensity, at least one order of magnitude higher than the background intensity.

A two component fiber optics LDA system, DANTEC, operating in backward scattering mode was used to measure the two velocity components at the entrance and exiting the porous ceramic foam specimen. The dimensions of the measuring control volume are 1.07 x 0.07 mm (blue) and smaller than the pore dimensions for 10 and 20 ppi ceramic foams. The Doppler signals were processed by two Burst Signal Analysers. Error sources due to optical alignment (non-uniform grid fringe location) or electronic noise were considered negligible. Errors due to signal processing are low, 0.25% with a frequency shift of 40 MHz. Error source due to velocity variation across the measuring volume are up to five orders of magnitude smaller than the measured rms and can be neglected. The velocity difference between the fluid and the smoke particles is estimated to be smaller than 0.5%. Finally the errors due to the sample size using a confidence level of 99% and 10000 samples are 1% for the mean velocity and 1.2% for the rms values. This brief analysis shows that the estimated errors in the mean and rms velocities are lower than 1.5% and 2% respectively.

RESULTS

Foam Inside a Straight Pipe

Figure 2a) shows an example of the smoke images captured to evaluate the transverse dispersion, D_T , based on the analogy between smoke concentration and the image intensity was made to calculate the transverse variance, see Figure 2b) and c). Figure 3a) shows the transverse dispersion coefficient versus pore

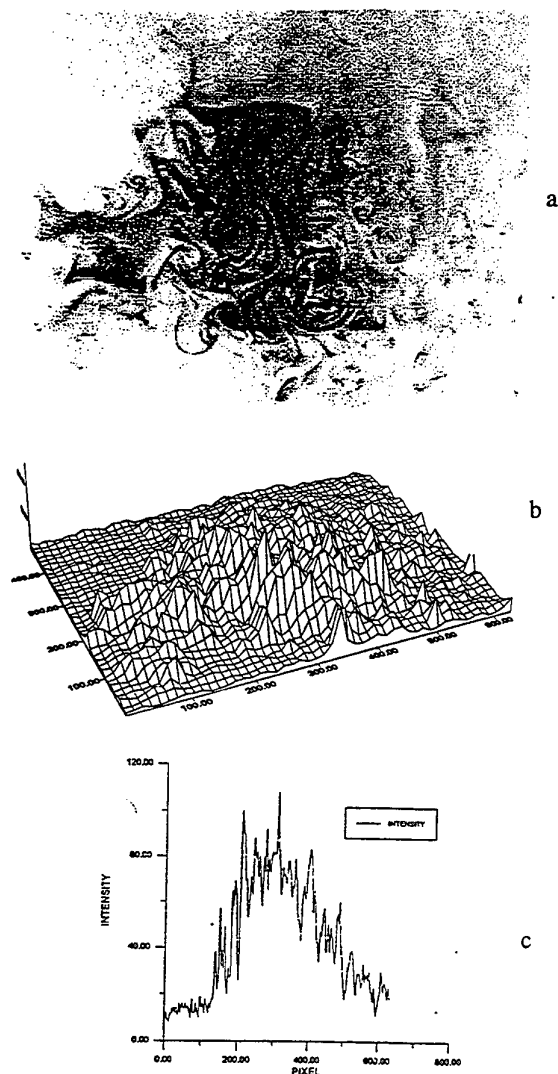


Fig.2a) Image of smoke pattern exiting the foam, $Re_p = 40$; b) Digital image; c) Transversal concentration profile

Reynolds number for three foams (10, 20 and 60 ppi). Obviously for 20 and 60 ppi the Reynolds number limit is lower than for 10 ppi to avoid errors due to image signal to noise ratio.

The first question that one may face related with 3a) is to know if transverse dispersion coefficient is dependent on the foam sample length. Figure 3b) shows clearly that it is, but can be very well correlated see Figure 3c) if one multiplies D_T by the length ratio

relative to 50 mm sample, L_{50}/L_i where L_i stands for the sample length.

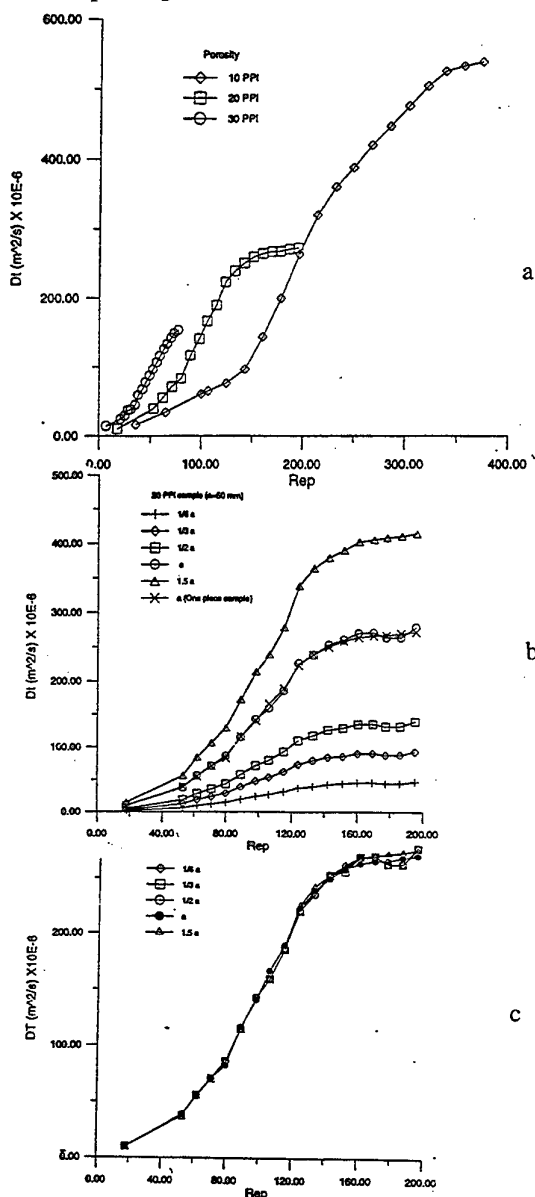


Fig.3a) Transverse dispersion coefficient versus pore Reynolds number for three ppi values; b) Transverse dispersion versus pore Reynolds number for different sample lengths; c) Correlated values with L_{50}/L_i

The second question than one may faces related with Figure 3a) is to know if the distinct curves can be correlated in a family as a function of pore Reynolds

number. Each curve shows a typical dependence with pore Reynolds number that can be approximated by a linear variation in the lower Re_p range and also the upper Re_p range and non linear variation inbetween. This dependence of D_T with Re_p can be better illustrated if the results of Figure 3a) are represented in normalised effective transverse diffusion coefficient, D_T/ud , shown in Figure 4a) in a smi-log plot. It is important to mention that no previous analysis of the individuality of each curve was made and the present results add additional information to the data previously reported by Hackert et al. (1996). The present results clear show that each curve displays a critical upper and lower Re_p and each of these values is well correlated with $Re_{pc1} = Re_{pc10} \times \frac{d_i}{d_{10}}$, being Re_{pc10} the critical upper or lower Reynolds values for 10 ppi. The dependence of D_T/ud with Re_p can be evaluated according to the following expression:

$$\frac{D_T}{ud} = \begin{cases} 0.03, & \text{if } Re_{pc}^L \leq Re_{pc10}^L \times \frac{d_i}{d_{10}} \\ 0.03 + 0.0878 \ln \left[\left(Re_p / Re_{pc10}^L \right) \frac{d_{10}}{d} \right], & \text{if } Re_{pc}^L < Re_p < Re_{pc}^U \\ 0.11, & \text{if } Re_{pc}^U \geq Re_{pc10}^U \frac{d_i}{d_{10}} \end{cases} \quad (2)$$

Expression (2) is valid for the porosity $\psi = 0.87$ and Al_3O_2 foams in the $10 \leq Re_p \leq 400$. However, Benz et al. (1993) report that $D_T \equiv Re_p$ for $Re_p > 400$. Expression (2) is presented in Figures 4b) and also as a function of $(Re_p - Re_p^L) / (Re_p^U - Re_p^L)$ in Figure 4c).

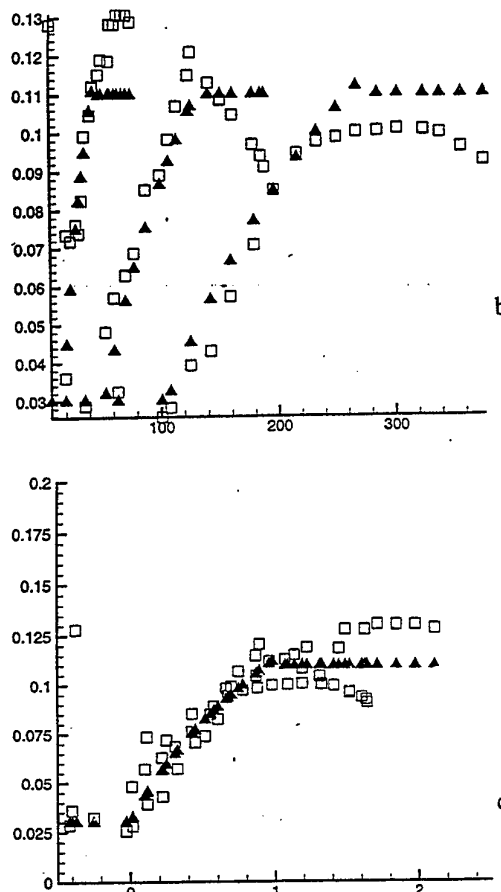
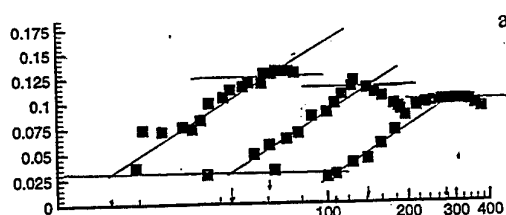
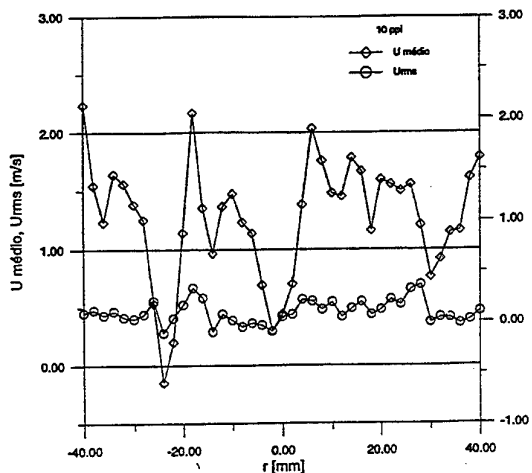
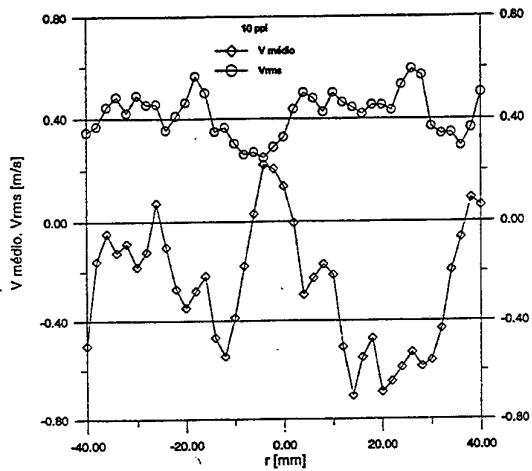


Figure 4a) Normalised effective transverse diffusion coefficient, D_T/ud ; b) Comparison of equation (2) with the measurements as function of pore Reynolds number; c) Transverse diffusion coefficient as a function of normalised pore Reynolds number

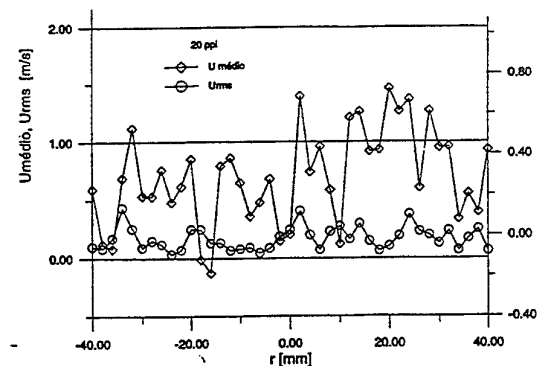
Velocity measurements taken at 5 mm from the exit of the foam and transversing the pipe across a line crossing the symmetry axys, confirm the microjet flow like structure, see Figure 5a) and b) for $Re_p = 226$, 10 ppi and 20 ppi respectively. The flow at the exit of the foam displays a highly 3D flow field with similar axial and radial values of rms velocities but with a dominant mean axial velocity component. The most relevant conclusions derived from the analysis, of many data sets, is that the flow at the exit is a jet flow that expands to a free atmosphere and can not be directly related with the flow inside the porous media.



a



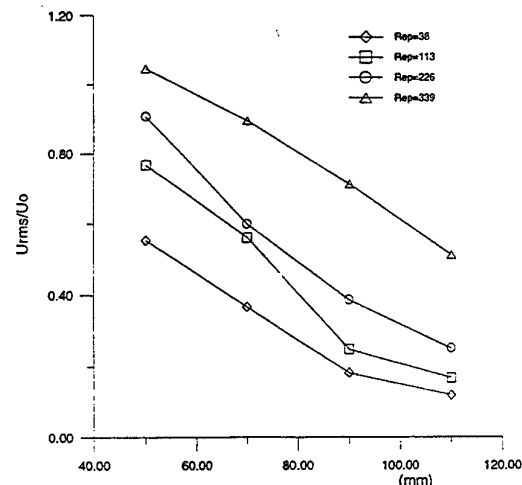
b



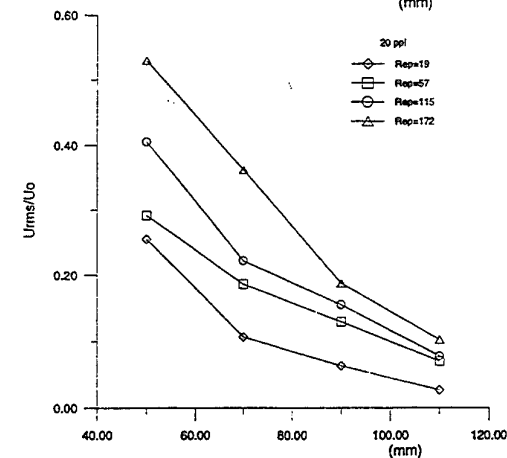
c

Fig. 5 Velocity and rms profiles 5 mm from the exit, along a line crossing the pipe axis, a) Axial velocity 10 ppi; b) Tangential velocity 10 ppi, c) Axial velocity 20 ppi

The higher velocities observed for the 10 ppi relative to 20 ppi are due to the larger potential core jets. The decay of the velocity perturbations, generated by the multijets, along the pipe centreline is shown in Figure 6a) and b) for 10 and 20 ppi (50 mm foam sample). The measurements show that for 10 ppi the axial rms decays even from pipe Reynolds number of ≈ 650 , ($Re_p = 38$) denoting the strong perturbation induced in the flow. For all samples investigated the radial fluctuation decays much faster than the axial rms.



a



b

Fig. 6 Rms decay along the pipe axis, a) 10 ppi; b) 20 ppi

Finally the influence of the length of the foam sample on the exit velocity field is shown in Figure 6c) and for a foam with 12.5 mm there is dominant flow directions associated with holes that could be seen in the foam.

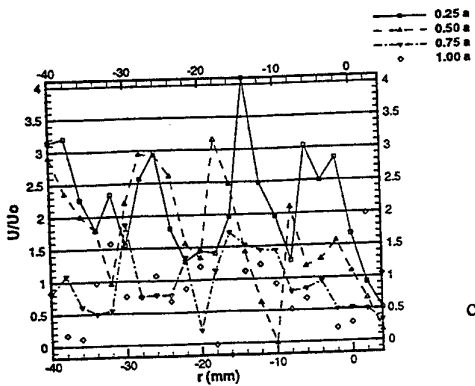


Fig. 6c) Axial velocity for different foam lengths samples

Sudden Pipe Expansion

The results obtained with the 50 mm foam inserted inside the pipe expansion (1:4) see, Figure 7a) are intended to investigate if flow separation occurs at the exit of the foam. The results show in Figure 7b) along a radial direction, for different foam sample lengths and when the foam is located at the sudden pipe expansion ($a = 0$), show that only for a very short sample (12.5 mm) a recirculation region was formed on the pipe wall. These results correspond to $Re = 226$, (10 ppi) for other number of pores per inch no recirculation could be detected. The pressure drop (that was also measured) increases typically four times relative to the same sample located in a straight pipe and the dependence of the pressure drop (divided by the effective velocity) with pore Reynolds number loses its linearity to become a quadratic function of pore Reynolds number denoting that Ergun or Forchheimer correlations to not apply.

In order to investigate the scalar dispersion characteristics in the presence of the sudden expansion the same procedure presented in the previous section was applied. However, it was impossible to obtain any accurate measurement of smoke transversal dispersion due to the signal to noise ratio value. The smoke completely disperses in all the pipe section even for very low pore Reynolds numbers denoting the almost potential like velocity field inside the foam (without separated flow region).

Flow visualisation and LDV measurements were conducted to investigate if it was possible to detect any flow separation inside the foam when the foam sample is not attached to the sudden pipe expansion ($a \neq 0$, see Figure 7a)). The flow in the axisymmetric cavity

formed inbetween the sudden pipe expansion and the

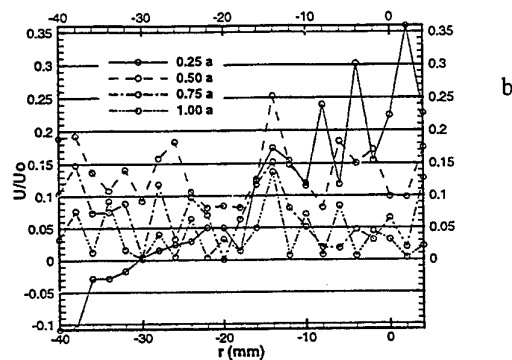
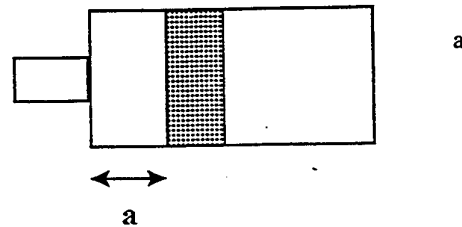


Fig. 7a) Pipe sudden expansion; b) Axial velocity at 5 mm from the foam exit

foam displays the velocity characteristics of a typical cavity and it was impossible to detect if recirculating flow was present close to the pipe wall inside the foam. The mean axial and radial velocities for a $Re_p = 115$ to which corresponds an inlet pipe flow Reynolds number of 16400 and for three relative foam locations to the sudden pipe expansion $a = 40, 60$ and 80 mm, are shown in Figure 8a), b) and c) respectively. The radial velocity profile was taken at 10 mm behind the foam flow entrance, and the results are also plotted in Figure 8d). The results show the formation of a typical cavity flow (in the cavity space) but the measurements taken closer to the foam are not conclusive about the separated flow penetration in the foam.

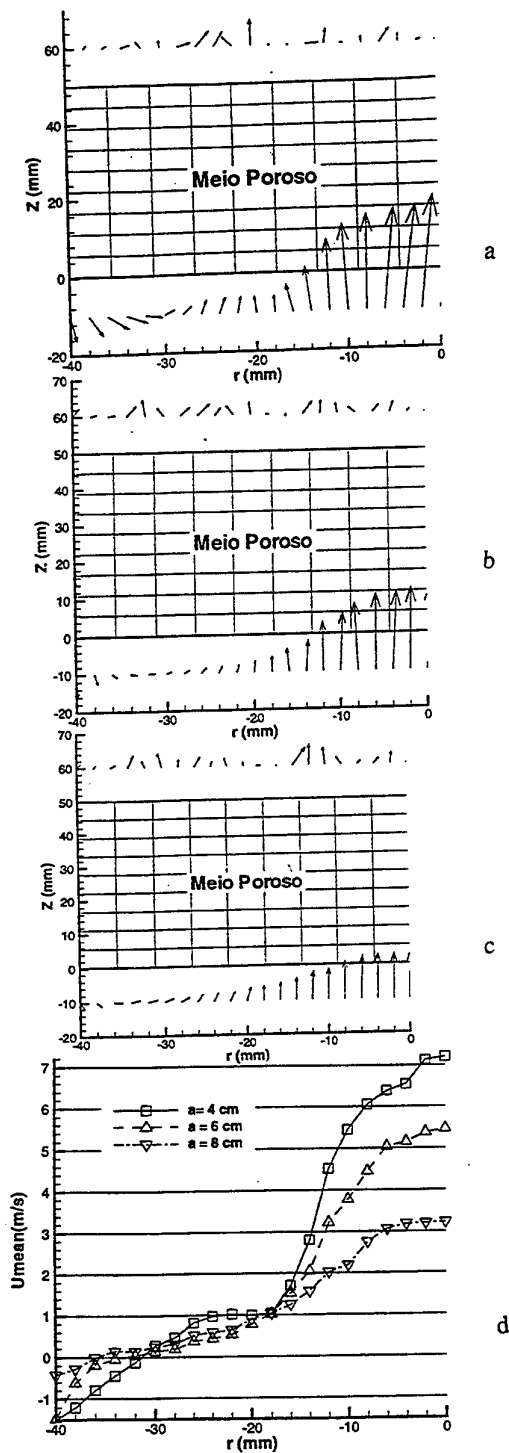


Fig. 7 Radial velocity profile in the cavity before the foam, a) $a = 40$ mm; b) $a = 60$ mm; c) $a = 80$ mm

CONCLUSIONS

Experimental measurements of transverse dispersion coefficients in ceramic foams for three different pore sizes (10, 20 and 60 pores per inch) and porosity equal to 0.87 and for pore Reynolds number $20 \leq Re_p \leq 400$ combined with LDA velocities at the foam exit in two flow configurations: straight pipe and sudden pipe expansion allow to report the following conclusions:

- i) The non-dimensionalised transverse dispersion coefficient D_T/ud changes with pore Reynolds number inbetween two values, denoting a linear variation of D_T below the lower critical value and above the upper critical pore Reynolds number value. Inbetween the cubic variation of D_T with Re_p can be well approximated by a logarithmic function.
- ii) LDA measurements at the exit of the foam reveal the already known threedimensionality of the flow characterised by microjets. However, these jet flows can not be related with flow inside the foam (due to the free flow expansion at the exit) neither it makes sense to attribute conventional flow regimes (transitional or turbulent) to the flow inside porous media.
- iii) The flow inside porous media should be characterised by laminar dispersivity and not by the conventional unsteady, transitional or turbulent regimes. Details of the new modelling assumptions on the nature of the flow in ceramic foams are in preparation, Pereira and Raposo (1998).
- iv) When the foam is inserted in a pipe flow expansion (1:4) the presence of negative velocities at the exit of the foam were only detected for very short samples ($X/D = 0.14$). Otherwise, the strong pressure losses deviate the flow (like potential flow) and no recirculating flow could be detected.
- v) When there is a gap, inbetween the foam and the sudden pipe expansion step wall, a cavity flow is formed and the flow visualisation and LDA measurements in the cavity were not conclusive about the penetration of the recirculating cavity flow inside the foam.

ACKNOWLEDGMENTS

The work was partially supported by PRAXIS No. 3/3.1/CTAE/1915/95 and by EC project THERMIE No. BU-220-97.

REFERENCES

- Hackert, C.L. Ellzey, J.L., Ezekoye, O.A. and Hall, M.J., "Transverse dispersion at high Peclet numbers in short porous media", Experiments in Fluids, 21, 286-290, 1996.
- Durst, F. and Trimis, D., "Combustion by free flames versus combustion reactors", Proc. 4th Int. Conf. on Tech. and Comb. for a Clean Environment, Lisbon, 7-10 July, 1997.
- Maierov, V.A., Vasil'Ev, L.L. and Polyaev, V.M., "Porous heat exchangers-classification, construction, application", J. Engng. Phys., Vol. 47, 1110-1123, 1984.
- Pereira, J.C.F., Costa, M. and Malico, I., "Experimental and numerical investigation of a porous counterflow heat exchanger model", Int. Conf. on Heat Exchangers for Sustainable Development, 15-18 June, 1998.
- Pereira, J.C.F. and Raposo, J., "Modelling assumptions of the nature of the flow in ceramic foams", to be submitted to Journal of Porous Media.
- Morales, M., Spinn, C.W. and Smith, J.M., "Velocities and effective thermal conductivities in packed beds", Ind. Engng. Chem., 43, 225-232, 1951.
- Schwartz, C.E. and Smith, J.M., "Flow distribution in packed beds", Ind. Engng. Chem., 45, 1205-1218, 1953.
- Dybbs, A. and Edwards, R.V., "A new look at porous media fluid mechanics - Darcy to turbulent", Fundamentals of Transport Phenomena in Porous Media, edited by Bear and Corapcioglu, Martinus-Nighoff, New York, 199-254, 1984.
- Mickeley, H.S., Smith, K.A. and Korchak, E.I., "Fluid flow in packed beds", Chem. Engng. Sci., Vol. 23, 273-246, 1965.
- Masuoka, T. and Takatsu, Y., "Turbulent model for flow through porous media", Int. J. of Heat and Mass Transfer, 39, 2803-2809, 1996.
- Fand, R.M., Steinberger, T.E. and Cheng, P., "Natural convection heat transfer from a horizontal cylinder embedded in a porous medium", Int. J. Heat Mass Transfer, Vol. 29, 119-133, 1986.
- Kaviany, M., "Principles of heat transfer in porous media", Springer-Verlag, New York, 1991.
- Johnston, W. and Dybbs, A., "Measurements of fluid velocity inside porous media with a laser anemometry", Phys. Fluids, 18, 7, 1975.
- Hall, M.J. and Hiatt, J.P., "Exit flows from highly porous media", Phys. Fluids, 6, 2:469-479.
- Hall, M.J. and Hiatt, J.P., "Measurements of pore scale flows within and existing ceramic foams", Experiments in Fluids, 20, 433-440, 1996.
- Bear, J., "Dynamics of fluid in porous media", American Elsevier, New York, 1972.
- Nield, A., "Comments on turbulence model for flow through porous media", Int. J. Heat Mass Transfer, 40, No. 10, 2499, 1997.
- Benz, P., Hutter, P. and Schlegel, A., "Radiale stoffdispersionskoeffizienten in durchstromten keramischen schäumen", Wärme-und Stoffübertragung, 29:125-127, 1993.
- Durst, F., Haas, R. and Interthal, W., "The nature of flows through porous media", Journal of Non-Newtonian Fluid Mechanics, 22, 169-189, 1987.

LDA MEASUREMENTS IN A FLASH SMELTING FURNACE MODEL

B. Chiné^(1, 2) and A. Barrientos⁽²⁾

(1) Faculty of Engineering
Catholic University of S.C.
Paicaví 3000, Concepción, Chile

(2) Department of Metallurgical Engineering
University of Concepción
Casilla 53-C, Correo 3, Concepción, Chile

ABSTRACT

We present the results of an experimental research based on laser Doppler anemometry measurements, developed to investigate the fluid dynamics in a cold air model of a flash smelting furnace. By using a complete tenth scale model installed in an experimental rig, velocity and turbulence data were collected inside this metallurgical reactor. Three series of measurements were carried out to investigate respectively the flow inside the shaft, settler and up-take. The experimental results obtained during this study show basically an axisymmetric flow in the shaft, the presence in the settler of flow channelling and reverse flow and finally some recirculation areas in the up-take.

1. INTRODUCTION

The flash smelting process, developed in the late 1940s, is a metallurgical process to treat copper, nickel, copper-nickel, lead and lead-zinc sulphide flotation concentrates. In this process the concentration and conversion of metalliferous ores is obtained by fusion and by thermochemical reaction, which are carried out in a furnace.

In Figure 1 we present a simple picture of the flash smelting furnace, which can be divided in three basic components: a) the reaction shaft with the concentrate burner, where the combustion of the mineral particles occurs; b) the settler, where the resulting upper slag and downer matte phases separate; c) the up-take, through the which the off-gases leave the furnace. In the top of the reaction shaft, the concentrate burner mix the dry particulate

concentrates with the preheated oxygen enriched air (process air) and the distribution air. Then the mineral sulphides oxidize and the resulting metal rich matte phase and slag phase settled and they are tapped separately from the furnace. The reaction gases, produced in the flash smelting process, flow through the settler and finally leave the furnace through the up-take.

The interactions of heat, momentum and mass transfer, which take place in the furnace simultaneously with chemical reactions, originate a complex picture hard to understand well. Despite being in vogue for many years, the design of flash smelting furnace has not been optimized and only a limited amount of researches, both experimental measurements and mathematical modelling of burners and shafts, are been carried out. By using laser Doppler anemometry (LDA) Tanemura *et al* (1989) measured the axial velocity of particles exiting from a nozzle and compared them with their simple mathematical model predictions. Smith (1991) studied the flow regimes in the reaction shaft and the settler of a one twentieth scale water model by using streak photography and a video camera and concentrating principally his investigations on the burners. Other measurements were made by Nguyen *et al* (1992) in a scaled model of a furnace. The authors used their experimental results to validate successively a more complete three-dimensional model. Important researches were developed by Sitalo *et al* (1994) who studied the flow patterns of reaction gas beneath a distributor burner in a 1:14 scale water model. Using the Fluent Computational Fluid Dynamics (CFD) software they simulated the flow through the burner and the flash furnace shaft and compared their numerical results with experimental measurements. These experiments carried out by joining the Digital Particle Image

Velocimetry technique with a high speed video camera showed a temporal instability in the jet exiting from the burner. Jorgensen *et al* (1995), combining streak photographs with video images, provided velocity measurements and flow patterns of several burner configurations in a fourteenth scale perspex model of a flash smelting furnace. Then using the CFD Phoenix package they obtained numerical results which confirmed the presence of strong recirculation regimes within the shaft and showed that the fluid flow and the heat transfer were greatly affected by the combustion process.

The assessment of the quality of a flash smelting process requires a detailed knowledge of the flow characteristics within the furnace. Limitations on access to the flash furnace and the aggressive environment require investigating the physical phenomena in a model. In order to achieve more a detailed indication of the turbulent fluid flow and a better understanding of the process, it was decided to take measurements of air velocities with a laser Doppler anemometry. Thus a complete no-intrusive mapping of the flow field in a cold air model of the furnace was performed, providing valuable data on velocity and turbulence.

2. EXPERIMENTAL RIG

This section describes briefly the experimental arrangement used during the investigation and which is shown in Figure 1. Figure 2 illustrates the coordinate system and the position of all the measurement planes considered here.

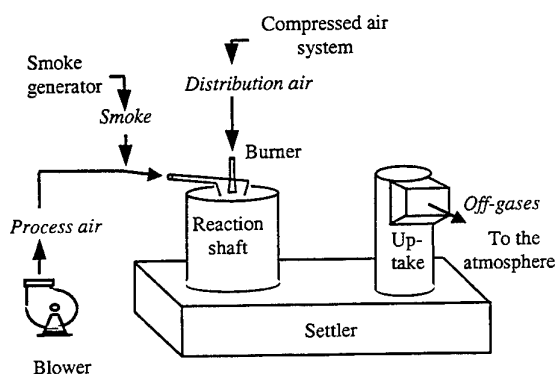


Fig. 1 The flash smelting furnace and the experimental rig.

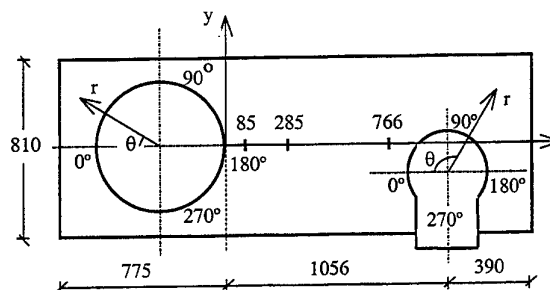


Fig. 2 The coordinate systems and the measurements planes (dimensions in mm).

2.1 Flow Configuration

A tenth scale perspex model of a complete flash smelting furnace was used in the LDA experiments. The reaction shaft has both a diameter and a height of 600 mm, the settler is 810 mm wide, 2221 mm long and 343 mm deep, while the up-take is a 750 mm high cylinder with a diameter of 380 mm. The bottom of the model represented the free surface of the upper slag phase. To permit the intersection of the laser beams, flat windows were inserted both in the reaction shaft and in the up-take. To do this, four symmetrical vertical positions were chosen on the curved walls at $\theta = 0^\circ, 90^\circ, 180^\circ, 270^\circ$. Finally the exact geometry of the burner was also accurately scaled and built.

Cold air at room temperature was utilized in the experimental test, where a 5.6 kW centrifugal blower injected $0.20 \text{ Nm}^3/\text{s}$ of this air (process air) in the burner. The burner exit region, situated at 60 mm from the roof of the shaft, has a 5.9 mm wide annular gap and thus the Re of the main flow at the throat is approximately 3.0×10^5 . The main stream gauge fed pressure measured ahead of the burner inlet was 10 kPa. To generate tracer particles for the LDA measurements a SPT smoke generator was used. Paraffin oil produced the smoke that regulated by a needle valve was injected through a nozzle in the process air current. Also a very low flow of distribution air was taken from a 30kPa compressed air system and brought into the burner distribution plate. Finally the two flows mixed in the shaft and they left the settler by discharging to the atmosphere.

2.2 Measurements Techniques

The velocity measurements inside the flash smelting furnace were carried out using a laser-Doppler velocimeter. The velocimeter is a Dantec

two component fibre optic system with Burst Spectrum Analysers (BSA) and an automatic computer controlled three component traverse systems.

Coherent light with wavelength in the range 457–514.5 nm from a 300 mW Argon-Ion laser was directed to a transmitter box where frequency shifting, to remove the direction ambiguity of the velocities (Durst *et al.*, 1981), and colour separation were performed. A Bragg cell splits the light beam in two beams with a 40 MHz frequency shifting. These beams then pass through a dispersion prism, which provides two green (514.5 nm), and two blue (488 nm) light beams. The shifted and direct beams are led to output aperture, where fibre manipulators are used to focus the beams into fibre optic cables. Then a probe with a 400 mm focal length lens and a measuring volume diameter of 116 μm causes the four beams to intersect. Finally the collected back-scattered light is separated into green and blue components and is directed onto two photomultipliers.

The Doppler signals were processed in two Burst Spectrum Analysers with fast Fourier transform in order to extract the Doppler frequencies. The BSA master for measuring the main component of the velocity and the BSA slave for the other component were set to run in a continuous data collection mode. The experimental data were transferred to a computer for processing via an IEEE-488 interface.

In order to measure the velocity distribution in the shaft, settler and up-take the probe was moved using a highly accurate three component (x - y - z) traverse system, which was controlled by a computer via an RS-232 interface.

The BurstWare 2.0 software package was used to collect all the data, move the traverse, process the data and to present the results.

By means of this facility three series of measurements were performed. First of all the laser beams were focused on four median vertical r , z planes crossing the reaction shaft to study the vertical airflow pattern, its asymmetry and the recirculation region. The radial axis was subdivided in twenty non-equally spaced sections, while in the axial direction a constant $\Delta z = 30$ mm measurement step was applied. Then the measurement volume was positioned on transversal y , z planes in the settler to investigate the velocity of the air stream directed to the up-take. Here a $\Delta y = 38.5$ mm \times $\Delta z = 31$ mm experimental grid with 231 nodes was used for each transversal plane. Finally, it was considered the flow regime in exit region and the laser beams intersection was placed on four median vertical r , z planes crossing the up-take. Velocity data were collected employing

incremental steps of 20 mm for the radial and 36 mm for the axial direction.

In all the experimental work a sample of typically around 1000 Doppler bursts was taken for each measurement point.

3. RESULTS AND DISCUSSION

3.1 Reaction shaft

The axial v_z and tangential v_θ components of velocity for two depths in the vertical r , z plane at 0° , 180° are shown respectively in Figure 3 and 4. As is expected, for an assigned depth below $z = 60$ mm (burner exit) the downwards values of v_z are high in the central core of the jet and decrease towards the peripheral walls, revealing a large recirculation zone in the left side of the shaft ($\theta = 0^\circ$). This agrees with

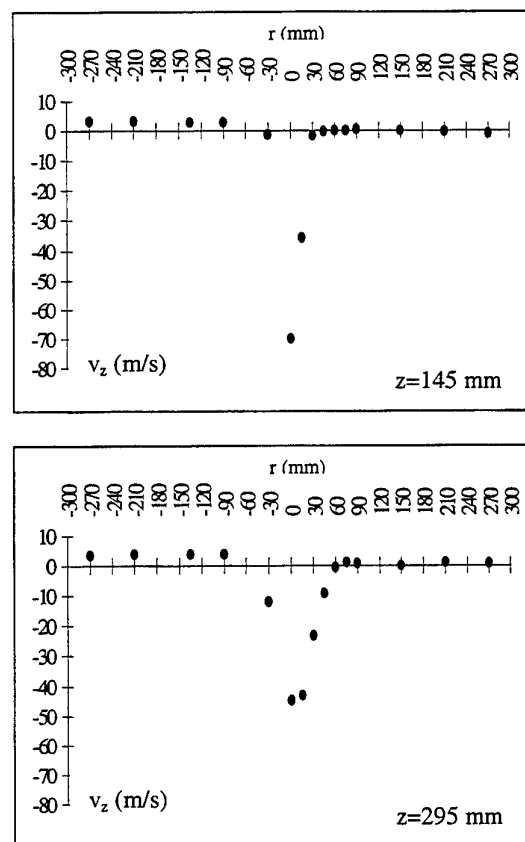


Fig. 3 Axial velocities in the reaction shaft for the depth $z = 145$ mm and $z = 295$ mm. ($r < 0$ means vertical plane $\theta = 0^\circ$, $r > 0^\circ$ means vertical plane $\theta = 180^\circ$).

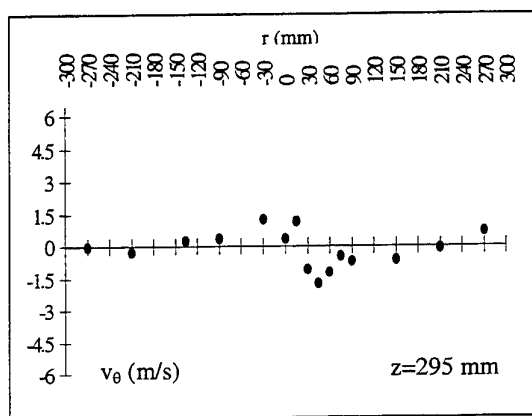
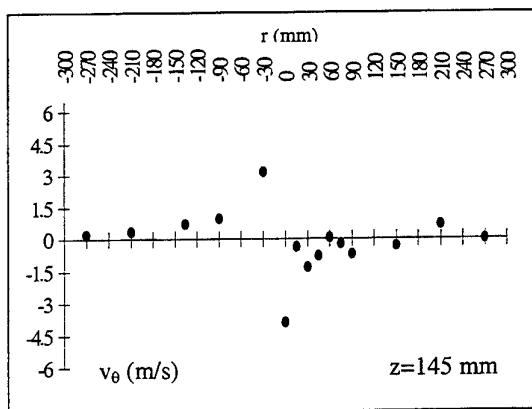


Fig. 4 Tangential velocities in the reaction shaft for the depth $z = 145$ mm and $z = 295$ mm. ($r < 0$ means vertical plane $\theta = 0^\circ$, $r > 0^\circ$ means vertical plane $\theta = 180^\circ$).

the experimental results reported by Jorgensen *et al* (1995) who noticed recirculating flows on both the edges. We can identify in the thin jet less, than $30 \div 40$ mm wide, a maximum velocity value of 70 m/s, measured on the centerline for $z = 145$ mm. Below the roof and above the burner exit the axial velocities are lower. The tangential velocity data depicted in Figure 4 reveals a clockwise rotation of the fluid near the centre of the cylinder, probably owing also to that the inlet is at an angle to the shaft. In order to assess the axisymmetry of the vertical flow pattern, we can compare the prior values of axial velocity with the data presented in Figure 5 and plotted for the same depths on the plane r, z at $90^\circ, 270^\circ$. We observe a weaker upward flow only at $\theta = 90^\circ$ and it is viewed that the jet deviates forward. Then it is possible to assert that the jet moves forward and to the right side (angular sector between 180° and 270°), being thus able to enter the settler. Jorgensen *et al* (1995) and

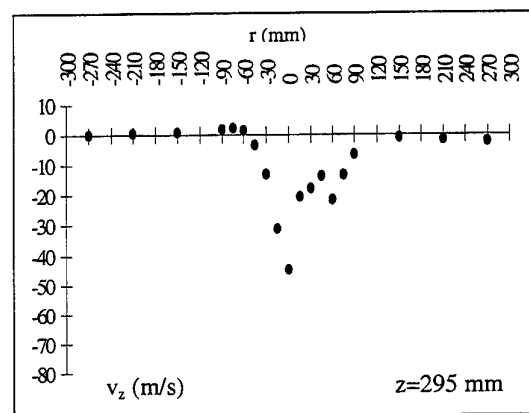
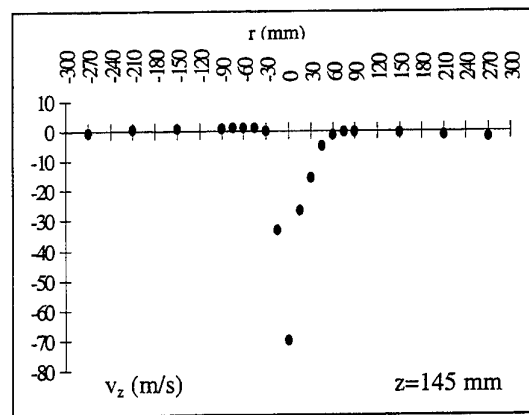


Fig. 5 Axial velocities in the reaction shaft for the depth $z = 145$ mm and $z = 295$ mm. ($r < 0$ means vertical plane $\theta = 90^\circ$, $r > 0^\circ$ means vertical plane $\theta = 270^\circ$).

Sutalo *et al* (1994) observed principally a jet that pointed away from the burner to the left side of the shaft ($\theta = 0^\circ$). As they used an opposite inlet configuration we could attribute to it the difference of the results. Then we could affirm that the flow regime inside the shaft depends on the location of the air gas exit and the position of the inlet. These phenomena have a clear effect on the air distribution, the particle combustion and the drop drag. Finally, an examination of the intensity turbulence, defined here as the ratio of standard deviation to mean velocity, indicates that the turbulence is lower at the centre of the shaft and it is also not symmetric.

3.2 Settler

Other important results were obtained when the air flow regime inside the settler was studied. Figure 6 shows contours of the component of velocity

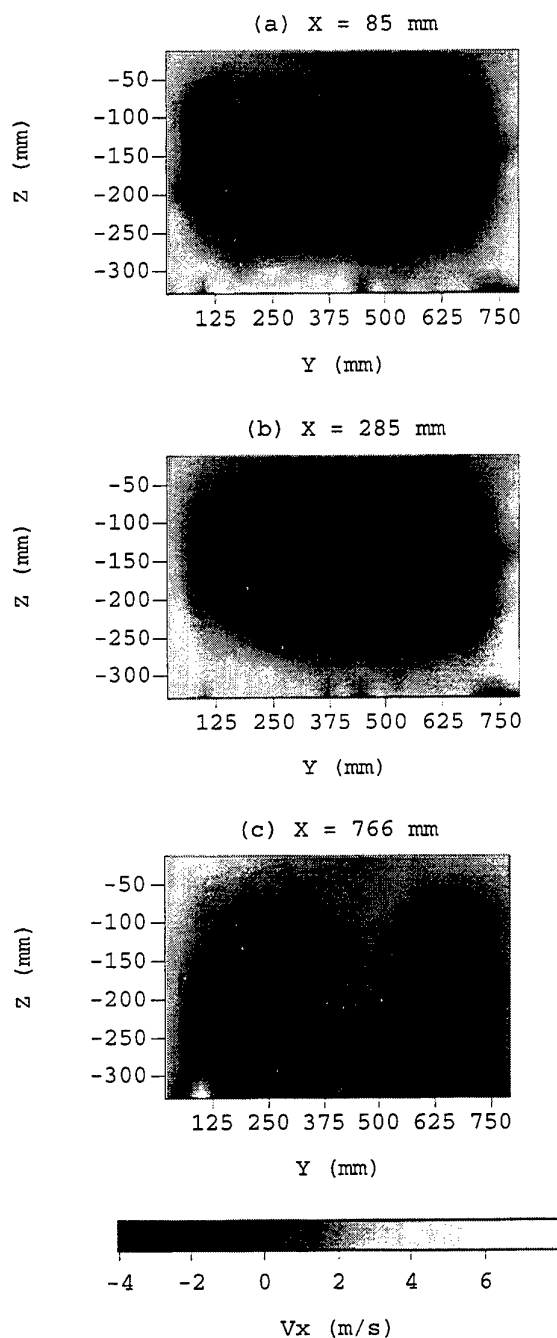


Fig. 6 Contours of velocity in x direction inside the settler for: (a) $x = 85$ mm; (b) $x = 285$ mm; (c) $x = 766$ mm.

parallel to the longitudinal axis of the settler, i.e. in the x direction. The LDA data depict a channelling of the flow towards the walls of the settler. A strong reverse flow is recognized in the inner area of the

furnace and at the bottom the maximum mean velocity is higher than 5 m/s. The existence of flow channelling inside the settler may be associated with the drop drag characteristic of flash smelting processes. The previous v_x values do not permit the totality of smelted drop to settle down, thus explaining some lost of process efficiency. Furthermore, the velocity contours for the plane at $x = 766$ consider the fluid flowing to the exit region, since that new higher velocity data were collected just below the roof of the settler and near the up-take. Finally, for the planes considered here we noted a peripheral annular distribution of the highest values of turbulence intensity.

3.3 Up-take

The velocity field measured inside the up-take demonstrates the existence of recirculating flows. Our experimental work determines that the v_z component is directed upwards on the plane $\theta = 90^\circ$, also it increases linearly with the radius and has a maximum mean value of 1.6 m/s near the wall. The same pattern is observed for the plane $\theta = 180^\circ$. On the other hand, for $\theta = 0^\circ$, 270° v_z is lower leading to downwards velocities around the walls. It is interesting to note that the highest v_θ components and the v_z , v_θ fluctuations are measured close to the circular intersection of the cylinder with the downer side of the off-gas exit duct.

4. CONCLUSIONS

Two components of velocity were measured in a scale model of a flash smelting furnace by laser Doppler anemometry. This experimental technique proved to be a useful tool in characterising quantitatively the fluid dynamics in the furnace. The obtained knowledge on the flow pattern is summarized as follows:

- (1) In the reaction shaft the flow is axisymmetric with an external recirculation region near the left side ($\theta = 0^\circ$). The axial components of velocity show that the trajectory of the jet exiting the burner depends on the location of the air gas exit.
- (2) Flow channelling and a central reverse flow are observed inside the settler, where the maximum velocity values are measured close to the bottom. On a plane perpendicular to the flow direction the LDA data display an annular turbulence intensity distribution.
- (3) The velocity field in the up-take is characterized by the presence of recirculating flows.

REFERENCES

- Durst, F., Melling, A. & Whitelaw J.H. 1981, Principles and Practice of Laser Doppler Anemometry, pp. 342-346, Academic Press, London.
- Jorgensen, F.R.A., Elliott, B.J., Koh, P.T.L. & Nguyen T.V. 1995, Modelling the Burners and Reaction Shaft of a Flash Smelting Furnace 1995, in Flash Reaction Processes, ed. T.W. Davies, Kluwer Academic Publishers, Dordrecht, The Netherlands.
- Nguyen, T.V., Taylor, R.N. & Hall, T.P. 1992, Fluid Flow in a Nickel Flash Smelter, Proc. Aus. IMM Extractive Metallurgy of Gold and Base Metal Conference, Melbourne, pp. 401-406.
- Smith, T.N. 1991, Model Study of Gas Flow in Kalgoorlie Nickel Smelter, Proc. Fifth Aus. IMM Extractive Metallurgy Conference, pp. 245-250.
- Sutalo I.D., Harris J.A., Jorgensen F.R.A. & Gray, N.B. 1994, Model Studies of Transient Flow Through a Flash Smelting Burner and Shaft, in Metallurgical Processes for Early Twenty-First Century, ed. H.J. Sohn, pp. 823-839, The Minerals, Metals & Materials Society, Warrendale, USA.
- Tanemura, H., Fukunaka, Y., Shimada T., Nishihara T. & Kondo, Y. 1989, Transient Motion of Solid Particles Injected from a Nozzle, Scandinavian Journal of Metallurgy, vol. 18, pp. 99-104.

FLOW IN A SCALE MODEL OF THE FLIXBOURGH "BY-PASS" PIPE

R. Teng-yang, K.F. Sollows and J.E.S. Venart

Department of Mechanical Engineering and Fire Science Centre
University of New Brunswick, Fredericton, NB, Canada

ABSTRACT

The flow in a one-sixth scale model of the 'dog-leg' 'by-pass' pipe assembly of the Flixborough chemical plant is examined using laser Doppler velocimeter (LDV), video and proximeter displacement transducers.

The Flixborough works in the United Kingdom was destroyed by a powerful explosion twenty-four years ago (June 1, 1974). The cause of the explosion was determined to be the failure of a temporary pipe bridge (the 'dog-leg' pipe), installed between two reactors. The installation had been only in operation for two months prior to the explosion. The failure of this pipe resulted in the massive release of hot (150-155 °C) cyclohexane at a pressure of 0.96 MPa.

The subsequent ignition of the escaped and vaporized fluid resulted in the explosion. The failure mechanism of the dog-leg pipe has been the subject of extensive research and controversy. To date, no failure mechanism, that did not require excessive over pressure, has been accepted.

The present work investigates the one possibility that appears to have received little consideration - that of a partial circumferential fatigue crack in one of the bellows supporting the ends of the pipe. In this analysis, the approximate axial, lateral and angular (rocking) natural frequencies of the pipe and bellows assembly were determined. These, scaled to the one-sixth flow model used, were compared to flow frequencies measured by video analysis, LDV, and proximeter displacement measurements.

The results indicate that both axial and lateral near resonance conditions could have occurred. Such conditions may have been responsible for a fatigue initiated two-step failure process that is better supported by the physical facts and eyewitness accounts and does not require the over pressure necessary for the single step simultaneous failure of both bellows accepted, albeit reluctantly, by the Court of Inquiry.

1. INTRODUCTION

On June 1, 1974 there was a fire and explosion at the Nypro (UK) Ltd. works near Flixborough, Humberside (formerly North Lincolnshire). An accidental release of cyclohexane at 8.6 barg. and between 150 to 155 °C resulted in an unconfined vapour cloud explosion which caused 28 fatalities and the destruction of the plant as well as severe damage to many buildings in the surrounding countryside.

The catastrophe was initiated in section 25A of the process stream during start-up while cyclohexane feedstock, inerted with nitrogen, was under hot recycle, through the reactor train, R1-R6.

Part of the site plan is shown in Fig. 1 (Dept. Of Employment (1975)).

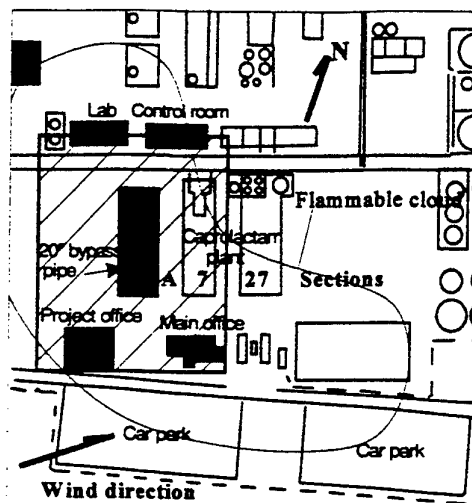


Fig. 1. Site plan of Nypro works showing Section 25A; (CFD simulation area (Venart *et al* (1998(a)) indicated by cross hatch with the estimated envelope of the flammable cloud, Sadee *et al* (1976/77))

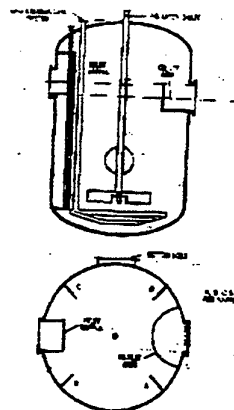


Fig. 2. Internal construction details of the reactor vessels, Artingstall (1974).

In the oxidation sequence the fifth reactor, R5, had been removed and a temporary 0.5 m diameter pipe-bridge, which used the two original 0.7 m diameter bellows and stub

pipe assemblies, had been installed between R4 and R6.

The reactors were fitted with interior overflow weirs and interior baffle plates to ensure level control and bottom feed, proper oxidation and mixing times respectively (Fig. 2).

The original interconnecting pipes and their bellows had permitted the hot pressurized feedstock to communicate by open channel flow over the outlet weir in the upstream reactors, through the bellows connections, into the downstream reactors with a fixed difference in elevation of 0.178 m.

The adaptation, however, doubled the head between R4 and R6 to 0.356 m and additionally resulted in two hydraulic jumps in the very complex flow structure observed (Fig. 3).

The plant had operated for two months, nearly continuously, since the modification and before the explosion.

An official Court of Inquiry was appointed to hold a formal investigation so "to establish the causes and circumstances of the disaster and to point out any lessons . . . to be learned therefrom" (Dept. Of Employment 1975). The essential problem faced by the Court was "to determine what had caused the rupture of the by-pass."

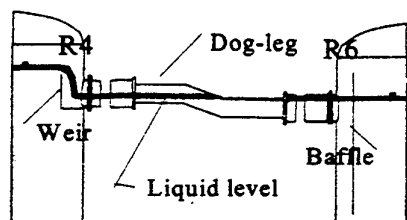


Fig. 3 Reactor train, vessels R4-R6, showing temporary by-pass pipe (Teng-yang, (1997))

The possibilities investigated were: "i) rupture of the by-pass assembly through internal pressure; ii) rupture of the assembly in two stages; a small tear in the (*upstream*, i.e., R4) bellows leading to an escape and a minor (*but external*) explosion causing final rupture; and iii) rupture of the '8 inch' line at the 50-inch split leading also to a minor explosion causing rupture of the by-pass assembly".

Processes ii) and iii), as stated, required an external minor explosion to trigger events; no physical evidence for such an occurrence could be determined thus effectively limiting the possibilities to a consideration of i) only. Despite physical evidence of an internal, and perhaps prior, tear in bellows B4 (i.e., process ii)) and compelling eyewitness evidence only three paragraphs in the final report were devoted to the consideration of the two-stage rupture possibility ii).

On the basis of expert evidence by Newland (1976), based on a dynamic analysis and assessment of energy requirements for both bellows to squirm and the by-pass pipe to buckle as one event, the Court concluded, albeit with low probability, "that the disaster resulted from a one stage failure of the 20-inch assembly" . . . as a result "of conditions of pressure and temperature more severe than any which had previously prevailed but no higher than careful and

conscientious plant operators could be expected to permit." The Court did however state that this conclusion "would be readily displaced if some (*other event of*) greater probability to account for the rupture could be found".

Extensive full scale experiments, which did not involve flow, however, were undertaken in attempts to reproduce the failure. These employed a similar pipe assembly as well as other bellows tests evaluated at the same and more severe operating conditions. These experiments were unable to reproduce the failure process accepted by the Court.

In view of its hesitant conclusion the cause of the accident has been the subject of considerable controversy especially as to the actual failure process; the amount of cyclohexane released, and whether the UVCE formed from its release detonated, Guban (1978).

In this paper we examine the flow conditions prevailing in the pipe and perhaps necessary for the failure to be initiated by fatigue. In this case flow induced vibration causes a crack (known to have been formed in the R4 bellows) to initiate a release scenario that is perhaps more probable than that accepted, although reluctantly, by the Court.

The mechanism proposed requires first a significant tear in the upstream, B4, bellows. This would be followed by a local vapour-gas depressurization and the subsequent boil-up of the now superheated and supersaturated cyclohexane (the cyclohexane's vapour pressure is only 0.51 MPa at the operating temperature). The impact of this rapidly swelling two-phase fluid would result in a head-space impact and dynamic over pressurisation (Gromles (1984), Venart and Ramier (1998)) immediately causing both the compression of the downstream, B6, bellows and the upwards 'squirm' of the B4 bellows.

The compression of B6, by this local over pressure, constrains the dog-leg pipe at its R6 connection and causes the process of B4 squirm to act over the full 356 mm eccentricity. This results in the collapse, by buckling, of the 0.5 m pipe as the B4 bellows bursts at its normal operating pressure.

This failure process has twice the eccentricity over that assumed by Newland and accepted by the Court; it therefore only requires normal operating pressures and not the necessary over-pressure required by the Court with its acceptance of a 178 mm eccentricity.

The p-V work of the expanding two-phase cyclohexane in the B4 bellows and the constraint of the compressed B6 bellows results in the formation of a pinched and collapsed 0.5 m pipe at its lower miter bend; the B6 bellows can, however, still be intact at this point though some discharge could occur through the 0.5 m pipe "pinch" at the buckled lower miter joint.

Because of this sequence of events only one discharge, the R4 outlet, is available to permit the discharge of up to 370 kg/s of cyclohexane for some 30 s. This discharge of some 10-15 tonnes is much less than the 30-60 tonne estimates previously estimated (Sadec *et al* (1976/1977), Roberts and Pritchard (1982)).

This paper examines the flow within the by-pass pipe assembly using a one-sixth scale model of the pipe and its connections. LDV, video and proximeter displacement measurements are combined with estimates of the natural

frequencies of the bellows supported assembly to suggest that the crack found in a piece of the upstream, R4, bellows may have been formed due to fatigue caused by flow induced vibration.

2. THE 'DOG-LEG' PIPE

The design of the 'dog-leg' pipe was certainly inadequate. According to the Court, calculations were only made to determine if the pipe was large enough to carry the required flow and safely contain the pressure. The pressure capability of the assembly as an eccentrically and internally loaded vessel was not assessed, nor were the effects of the changed flow and its influence on the spring-mass system created by the bellows, pipe and fluid.

2.1 The bellows

The two bellows had a mean diameter of 149 mm and were about 230 mm long with 12 convolutions. They were constructed by a cold rolling process from sheet 316L stainless steel originally about 1.2 mm thick; the process of forming reduced the material thickness to about 1 mm. As formed each unit had axial, lateral and angular stiffness in the range of 2770-3300, and 43208-51475 lbf/in as well as 5226-6225 lbf-in/deg, Warner 1975. Each bellows was welded to 304L stainless steel stub pipes, which in turn were bolted up to heavy flanged connections with the reactors and the 'dog-leg' pipe.

2.2 The dog-leg pipe assembly

This dog-leg pipe was fabricated from 304L stainless steel pipe 508 mm in diameter some 4.8 mm thick with two miter bends and 3.91 m long (Fig. 3).

The complete empty assembly, including the stub pipes with their flanges and bolts weighed just over one tonne (1,112 kg). Interior fluid mass, taking into account fluid distribution, increased the total weight to over one and one half tonnes (1625 kg). The assembly was supported, while cold, with spans of standard scaffolding; with the thermal expansion of the reactors to operating conditions, support to the assembly was lost. The natural frequency for such a spring-mass system is in the range of 3-5 Hz axial, 13-16 Hz transverse and 25-30 Hz for the rocking mode and so fluid-structure excitation, particularly in the axial direction, becomes a possibility.

3. EXPERIMENTAL FACILITY

The flow in the dog-leg pipe assembly was determined using a one sixth scale model and Froude number scaling. LDV, video and proximeter measurements and analysis were utilized.

3.1 Froude number scaling

When a flow is governed by inertia and gravity forces, such as in open-channel flow, the applicable Dimensionless parameter used to characterize the flow is the Froude number. This is expressed as the ratio of the inertia to gravity forces. Of course in all flows there will be other forces acting such that there is more often more than one characteristic number that can be utilized to characterize the

flow, e.g. the Reynolds and Strouhal numbers. The conditions necessary to satisfy any two parameters are, however, usually conflicting or require the use of unattainable modeling fluids. The accepted experimental approach is to select the dominant number, in this case the Froude number. Although the conditions for say the Reynolds are violated, provided the flow is turbulent, reliable experimental results may still be obtained from the model, Bakhmeteev *et al* 1982.

Table 1 illustrates the Froude number model scales employed for the one-sixth model employed. Table 2 shows the calculated dynamic characteristics of the model and prototype.

Characteristic & Symbol	Froude Scaling		Comments
	Term	Ratio	
Length (L)	L_r	0.167	-
Time (T)	$L_r^{0.5}$	0.409	-
Velocity (V)	$L_r^{0.5}$	0.409	-
Density (ρ)	ρ_r	1.55	-
Mass (m)	$L_r^3 P_r$	7.21×10^{-3}	-
Frequency (f)	$L_r^{-0.5}$	2.45	-
Discharge (vol/sec) (Q)	$L_r^{2.5}$	0.011	exp. ratio: 0.014
Kinematic viscosity (ν)	$L_r^{1.5}$	0.068	exp. ratio: 3.04
Force (F)	$L_r^3 P_r$	7.21×10^{-3}	-
Pressure (P)	$L_r P_r$	0.258	-

Table 1. Froude number model scales

Parameter & Symbol	Prototype	Model	Scale Ratio (M/P)
Velocity (V) (m/s)	8.3	3.8	0.458
Froude number (F_r)	12.45	12.26	1 : 1
Reynolds number (R_e)	1.1×10^6	3.7×10^4	1 : 31

Table 2. Dynamic characteristics of model and prototype

3.2 The model

The scale model of the by-pass assembly and its connections was fabricated in acrylic. The model consisted of two open rectangular channels, representing the up and down stream reactors, connected together by the model dog-leg pipe. The pipe was connected to the stub-pipes of the channels by surgical rubber cuffs, representing the bellows,

and suspended from a bracket arrangement. The three sections of the apparatus are shown in Fig. 4.

The components all formed part of a closed loop hydraulic system through which water was circulated by means of a centrifugal pump.

The inlet channel (R4) consisted of a rectangular open-top chamber constructed to represent reactor No.4. The size of this chamber was 500 mm long x 250 mm wide x 400 mm deep. The discharge of the circulating pump was led into a honey-comb screen installed in the inlet channel. The honey-comb screen was installed to promote a uniform and reasonably still inlet flow conditions into the overflow baffle and then into the dog-leg pipe.

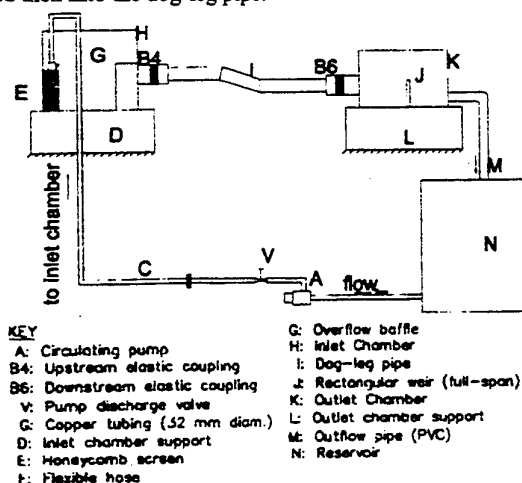


Fig.4 Schematic of experimental facility

The experimental objective was to make LDV measurements in the dog-leg pipe section. Since the LDV instrumentation required optical access, this section was also constructed from acrylic. The pipe was fabricated from three sections of tube, 4-mm wall thickness. The inside diameter of the pipe was 83 mm. The three sections were glued together to form two mitered joints. The slope of the inclined section of the pipe was about 21.5° with the centre line of the horizontal section.

This pipe was installed between the inlet and outlet channels at each end by means of elastic couplings made from cuffs of surgical rubber. These elastic bands were clamped to the pipe and the stub pipe on each end. The couplings were used to represent the bellows in the prototype system.

The outlet channel was physically similar to the inlet channel except that the height of the former was about 70 mm less than that of the latter. The dimensions of the downstream channel were 500 mm long x 250 mm wide x 320 mm deep. A full-span rectangular weir was used to set the flow height in the chamber and also used to determine its discharge.

Tap water was used to model the process fluid. The physical properties of water and cyclohexane are compared in Table 3. The mean temperature of the water was 20°C (room temperature).

3.3 LDV system

The unit used was a Dantec two-component, four

beam, 4 watt argon-ion laser system. The instrument was operated in back scatter mode. The data size varied from 3000 to 4000 samples at each measurement point.

A dedicated computer was used for data manipulation and analysis. Special data manipulation software (Dantec SRE LDA2D version 3.0a) was utilized. The software determined the ensemble mean velocity from the time history of the particles activities. The local mean flow velocity and other flow velocity statistics such as the standard deviations were also computed.

The number of data samples used generally varied from one measurement location to another. Each sample size, however, was large enough to give reliable statistics to describe the flow. At the same time, the size of the sample was small enough to reduce the LDV data acquisition time. This latter consideration was important, particularly in locations, such as on measurement plane 1, where the local mean velocities were relatively low. Between 3000 and 4000 samples were taken at each measurement point. The sampling time was manually determined with a stop-watch, as the system did not have the necessary hardware to measure these times.

Parameter & Symbol	Prototype (Cyclohexane)	Model (Water)	Scale Ratio (M/P)
Density ¹ (ρ) (kg/m ³)	6.45	998	1.55
Kinematic ¹ viscosity (ν) (m ² /s) $\times 10^{-7}$	3.306	10.05	3.04
Discharge ² (Q) (m ³ /s) $\times 10^{-3}$	108	1.53	0.014

Table 3 Dynamic and flow properties of the model and prototype.

3.4 Pipe displacement measuring device

In order to determine the fluid structure interaction a displacement type Proximitor (Brently Nevada Proximitor, 7200 series) was installed at two locations, at one point to determine axial displacements, the other location to record transverse movement in the vertical plane.

Full details of the model, its instrumentation and operation are given in Teng-yang (1997).

4. MEASUREMENTS

The measurement sections are shown in Fig. 5. To obtain representative velocity distributions along the assembly the measurement planes were located at or close to the following sections/components: elastic couplings (B4 and B6), sudden contraction and enlargements, and the mitered joints. A total of thirty-three measurements locations were investigated since at each location LDV measurements were made at three elevations in the flow; one near the surface, another near the bottom of the channel and the third at a point midway between the other two.

Three flow cases were examined, one for the scaled prototype full flow, another for flows greater and smaller than the scaled design flow. The discharge at design conditions was estimated to be 1.53 l/s of water corresponding to 108 l/s of cyclohexane at about 150 °C and 0.96 MPa.

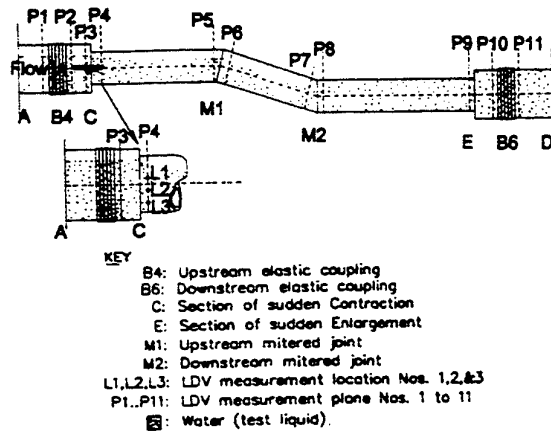


Fig. 5 Location of the LDV measurement planes

The bellows were simulated by elastic rubber cuffs that did not scale in stiffness to those on the prototype. To a first order approximation, however, the pipe could be considered to oscillate, in the axial direction, freely and its natural frequency determined. The natural axial and transverse frequencies of the pipe assembly, as estimated from the proximeter displacement waveforms obtained with the pipe empty, were 5 and 7 Hz respectively.

4.1 Qualitative description of the flow

The flow from the Inlet chamber passes over the overflow baffle in the form of a 'waterfall' into the entrance region of the pipe. Here the flow accelerates and plunges into the pool formed at its base. The flow then travels past the upstream stub pipe and its adjacent junction piece between the pipe bridge into Plane 3 (Fig. 5). The reduction in pipe diameter at this section results in a flow restriction, level increase and fluctuations of the free surface of the flow. Beyond this point within the now smaller diameter pipe there is flow acceleration as it approaches the upstream miter joint, where it attains its greatest velocity, with little variation in its free surface. A hydraulic jump is next formed at the base of the incline at the lower miter joint. This jump is characterized by a rise in the depth of flow, and significant oscillations, both axial and vertically, in the flow. Downstream of the jump, the flow decelerates and fills the pipe flowing into the lower stub end pipe into the outlet reservoir. Like its upstream counterpart, this end of the pipe was observed to oscillate both axially and laterally with the flow.

The entrance region of the pipe (P1) was located about 57 mm below overflow baffle. Here, very high recirculation and mixing was observed. The rapid mixing was characterized by both axial and transverse oscillations in the flow, the effect of which appeared to cause the pipe to oscillate.

Vertical flow fluctuations were also evident at the change of section after the simulated bellows. The

fluctuations in the free surface at this location (plane 3) was determined from the video analysis to be about 12 to 14% of a pipe diameter, relative to the larger pipe of 114 mm diameter. The frequency of these vertical oscillations was about 3.75 Hz, as determined from frame by frame video analysis.

Beyond plane 3, the flow accelerates from a subcritical to supercritical state as it enters the inclined section. Under the design conditions, the pipe here was flowing about half full. This flow next plunges into the lower section of the pipe after the lower miter bend, decelerates and forms a hydraulic jump. The fluctuations of the free surface that accompanied the jump were estimated (again from video analysis) to be between 35 and 65 percent pipe diameters based upon the smaller pipe diameter. The frequency of oscillation was estimated to range from 2.7 to 6.0 Hz in the vertical direction and 3.0 to 3.8 Hz in the axial direction..

Although the pipe flowed full downstream of the jump most of the time, occasionally a "long" bubble was observed to form. This bubble was observed to axially slug and oscillate in the pipe as it proceeded to the outlet chamber.

The interaction of these fluctuations with the pipe resulted in considerable pipe oscillation due to fluid-structure interaction.

4.2 Velocity measurements

The raw flow velocity data obtained from the LDV measurements were stored on disk. Due to hardware limitations, the system could not measure the exact sampling time intervals between Doppler bursts. Since this information was needed to estimate the frequency response of the instrument, it was estimated by measuring the total time for data collection at a measuring point using a stop watch and dividing this time by the number of samples obtained. A uniform temporal sample rate was thus assumed.

4.2.1 Velocity statistics

The summary statistics of the measured velocities are presented in Fig. 6 to 10 for only the design flow case. The detailed measurements and their treatment is to be found in Teng-yang 1997. The statistics were determined by the LDV data analysis unit from the probability distribution functions (pdf) of the sample data. The summary results use the four statistical measures of the measurement: the mean, standard deviation, skewness and kurtosis. Turbulent intensities were estimated by dividing the velocity fluctuation (rms values) by the corresponding mean velocity at a given point.

The mean velocity from the summary results are plotted in Fig. 6. In this figure, the velocity is plotted as a function of the measurement plane. The three bars represent the velocity measurements at the first, second and third measurement points for the respective plane. The dashed lines represent the arithmetic average of the mean velocities. These lines approximately define the envelope of the velocities at the measurement points. In some cases only restricted numbers of measurement planes could be accessed. No measurements were made at P11.

The root mean square (rms) values are indicated in

Fig. 7.

The skewness of the velocity distribution in the summary statistics were also plotted (Fig. 8). The last statistical moment plotted from the summary results was the kurtosis (Fig.9).

In order to enhance considerations of the flows, the degree of turbulence was also plotted. The turbulence intensities were obtained by dividing the velocity fluctuation (rms values) by the corresponding mean velocity at the given point (Fig.10).

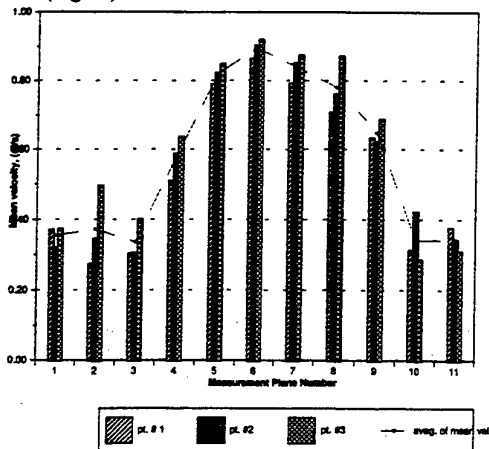


Fig. 6 Mean velocity, design flow

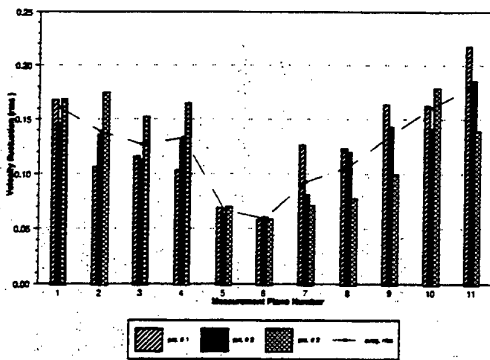


Fig. 7 Velocity fluctuations, design flow
4.3 Pipe displacements

Information about the frequency constituents of the pipe displacements were also obtained from analysis of the raw proximeter data. This information was obtained by processing the raw data in VU-POINT (1992). The data was imported into VU-POINT and fast Fourier transformed (FFT).

The dominant frequency components obtained by the fast Fourier analysis represent the induced excitations imposed on the pipe assembly by the flow; these are indicated in Table 4 for the design flow case only. It can be seen that significant amplitude deflections occur in both the axial and lateral vibrational modes for the pipe at 2.4, 5.4 and 7.3 Hz. These values correspond to prototype frequencies of 1, 2.2 and 3 Hz and are thus close to some of the natural frequencies of the assembly.

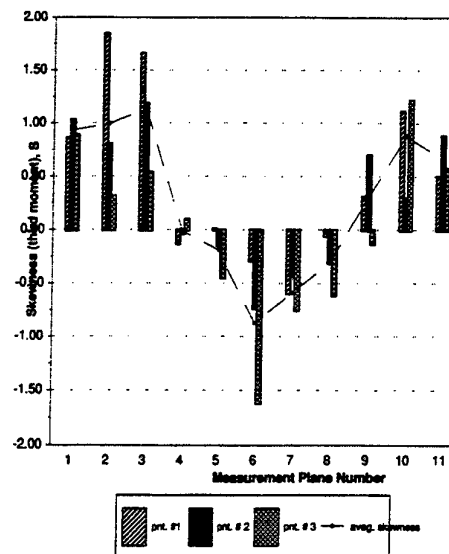


Fig. 8 Skewness, design flow

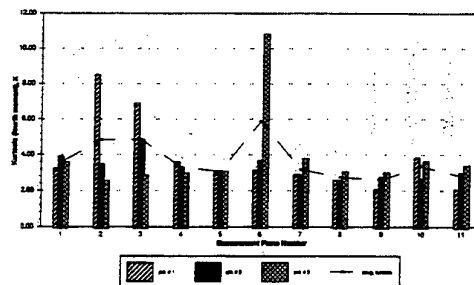


Fig. 9 Kurtosis, design flow

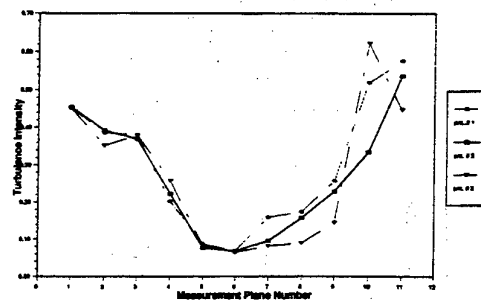


Fig. 10 Turbulent intensity, design flow

5. DISCUSSION

The measurement data was presented in the preceding section. Here, the data are analyzed and discussed. First a discussion of the velocity data will point out how these may be used in an examination of the fatigue life of the prototype bellows. The results of the frequency

analysis are also discussed in order to identify possible resonance frequencies.

Flow Configuration	Axial		Lateral	
	Freq. (Hz)	Amp. (mm)	Freq. (Hz)	Amp. (mm)
Design Flow (1.53 liter/s)	2.4	0.243	2.4	1.34
	5.4	0.310	5.4	1.15
	7.3	1.16	18.1	0.251
	10.3	0.603	21.0	0.171
	17.6	0.209	-	-
	35.2	0.241	-	-

Table 4 Frequency components of pipe displacement, design flow

5.1 Velocity data

Since the summary data are similar for all the three flow cases considered, we shall limit our analysis to the design flow condition. The velocity measurements for this case, are illustrated in Figs. 6 to 10. For convenience the measurement planes are divided into three sections: Sections 1 to 3. Section 1 consists of Planes 1 to 3, Section 2: from Planes 4 to 9, and Section 3 of Planes 10 and 11.

The measurements indicate subcritical flow in Section 1; the maximum mean velocity measured there was about 0.49 m/s for the model, about 0.1 m/s less than the critical velocity of 0.59 m/s. The flow turned supercritical in Section 2, where the velocity was 0.90 m/s; the maximum in the measurements (Plane 6). The range of the mean velocities at Plane 4 was between 0.50 and 0.63 m/s, which suggests critical conditions around this location. The flow turned subcritical again in Section 3 after the hydraulic jump. The lowest velocity measured in this section was about 0.28 m/s. The mean velocity distribution for Case 1 is graphically depicted in Fig.6.

The distribution of the velocity is reflected in the velocity fluctuation (rms values) plot (Fig.7). Comparing Figs.6 and 7, it can be seen that the 'peaks' and 'valleys' of one are reversed on the other. Physically, this means that in the subcritical regions of the flow, velocity fluctuations are high. In contrast, the high velocity region (Planes 4 to 6) is characterized by low velocity fluctuations. Thus, in the subcritical regions of the flow (Sections 1 and 3), relatively high velocity fluctuations (about 0.11 to 0.17 m/s about the mean velocity) were observed. On the other hand, the velocity fluctuations in the supercritical region (Section 2) were between 0.06 and 0.07 m/s of the mean velocity.

5.1.1 Discussion

The analysis of the mean velocity and velocity fluctuations are consistent with the visual observations made during the measurements. Based on the analysis of the flow presented above, a possible origin of the excitation force may be attributed to velocity fluctuations in the flow.

The type of distribution of the data can be inferred from values of the skewness and kurtosis for the velocity

measurements. Graphs of the skewness and kurtosis for the measurements are shown in Figs.8 and 9 respectively. The kurtosis profile (Fig. 9) generally indicates an average kurtosis of about three. This implies that, for most of the measurements, the velocity distribution was approximately normal. The tendency of the velocities towards a normal distribution profile was correlated fairly well by the skewness values.

Assuming a confidence limit of 95 percent (two standard deviations), the maximum the velocity fluctuation would be about ± 0.84 m/s about the mean velocity at location 2 on measurement plane 1. The fluctuating pressure corresponding to this velocity was estimated from equation (1.1) to be about 1.4 kPa for the prototype. The fluctuating stresses associated with this pressure fluctuation were also determined. The stress range due to the pressure, and would have been about 1.3 MPA for the meridional membrane stress, and about 1.2 MPA for the meridional bending stress in the bellows.

Other factors can also contribute to pipe oscillation. Oscillations can be amplified by flow level variations generated by the drop at the entrance region of the pipe. The entrance region of this pipe was located at the base of the overflow baffle in the inlet chamber, only 0.46 pipe diameters downstream of the bellows.

The base of drops are characterized by high flow oscillations. Energy losses associated with drops have been experimentally investigated by Rajaratnam and Chamani (1995). They found that the loss at a drop was mainly due to intense mixing of the jet with the pool behind it. In the mixing zone, the flow was found to be highly fluctuating, with flow recirculation. An important observation by Chamani et al was that, the falling jet was oscillating, the degree of oscillation being dependent on the ratio of the drop height to the critical depth of the flow approaching flow. Chamani et al found the frequency of oscillation of the flow to be 7.5 Hz, for a critical depth to drop height ratio of between 0.06 to 0.35. For our experimental model, this ratio was determined to be about 0.13, well within the range of the ratios considered. Consequently, we can expect flow oscillations in the neighborhood of 7.5 Hz at Plane 1 due to the drop. The effect of this induced frequency can only be to accentuate the pipe oscillations since it is close to the natural axial frequency of the assembly.

The hydraulic jump formed at the foot of the incline pipe section could also act as another source of excitation for the pipe. The formation of a jump is accompanied by high turbulence and flow oscillations. The frequency of the oscillating flow was determined from video analysis to be in the range 2.73 to 6.0 Hz in the vertical direction, and 3.0 to 3.75 Hz in the transverse direction. This frequency range was significant in contributing to the pipe movement. The effect of change of the pipe section was similar to the hydraulic jump. The continuous impact of the water on the annulus between the large and small pipes, due to the fluctuating water level, would further induce pipe oscillation.

6.3 Analysis of the Flow-induced Oscillations

A substantial fraction of the flow variation occurs at the low end of the frequency spectrum. The power

spectrum exhibits a decline with high frequencies. These local peaks are visible at 1.6, 5.7, and 6.8 Hz respectively.

Frequency analysis of the pipe displacement indicated that greater energies were also associated with oscillations also at the low region of the frequency spectrum. This region of high energy components was located approximately between 0 and 25 Hz with most of the energy concentrated at frequencies about 2.5, 7.5, and 10 Hz.

The natural frequencies of the model pipe assembly were measured in this experiment. The axial and lateral frequencies were found to be about 5 and 7 Hz respectively. The fact that these frequencies are low indicates these modes are excitable by the flow whose fluctuating frequency is also low.

The natural frequencies of the full-scale dog-leg assembly were estimated to be between 3-5, 16, and 28 Hz for the axial, lateral, and rocking frequencies. These calculated frequencies are based on a very much simplified model of the dog-leg pipe in which it is replaced by a single section of equal weight. For this reason, the calculated natural frequencies should be considered only as a guide to the order of values expected.

The flow frequencies identified above can be scaled to the full-size dog-leg pipe assembly. The full-scale excitation frequencies corresponding to the observed local peaks in the model test are approximately 0.6, 2.3, and 2.8 Hz. These are sufficiently close to the estimated natural frequencies of the dog-leg pipe assembly to suggest that flow induced vibration of the assembly may have been significant.

6. CONCLUSION

In this work, a one-sixth scale model was used to study the flow in the Flixborough dog-leg pipe assembly. The flow model was based on Froude number scaling, using water as the test fluid. LDV measurements of the streamwise flow velocities were made at key locations along the pipe. The velocity and velocity fluctuations were determined from the statistical measures of the flow. The nature of the velocity distribution of the flow was examined from plots of the measured velocity data.

Proximitor measurements of the displacement of the pipe were also made to determine the frequency of the system with flow in the pipe. Significant frequencies of the proximitor data were compared with determined natural frequencies (axial, lateral, and angular) of the bellows scaled for the model. A comparison was made to determine if any of the system frequencies (with flow) was close to the natural frequency of the bellows to create resonance conditions.

ACKNOWLEDGEMENTS

Many individuals have contributed to the preparation of this work.

The staff at the Health and Safety Laboratory Library in Sheffield, and in particular Mrs. Linda Heritage, are thanked for their help in making the Minutes of Proceedings of the Court of Inquiry and many other documents and reports dealing with the disaster available over an extended period of time.

Dr. Dong-Ming Tan assisted in the preparation of

the figures and animations of the discharge sequences. As well, many graduate students have contributed through background and other studies.

REFERENCES

- Artingstall, G., 1974, Appraisal of the damage in the reactor vessels in Section 25A, Report No. 4, Part 1, Safety in Mines Research Establishment (SMRE), Sept. 11..
- Bakhtmetef, B.A., *et al*, 1982, The hydraulic jump in terms of dynamic similarity, *Classical Papers in Hydraulics*, ASCE, NY, pp. 1-18.
- Dept. of Employment, 1975, *The Flixborough Disaster*, HMSO, London, UK.
- Gromles, M.A., 1984, A simple approach to transient two-phase level swell, *Multi-phase Flow and Heat Transfer III*, Miami Beach, Vol. 1, pp 527-538.
- Gugan, K., 1978, *Unconfined vapour cloud explosions*, IChemE, Rugby.
- Newland, D.E., 1976, Buckling and rupture of the double bellows expansion joint assembly at Flixborough, *Proc. R. Soc. Lond.*, A 351, pp 525-549.
- NIST, 1990, *Standard Reference Database 4: thermophysical properties of hydrocarbon mixtures*, Program Suptrapp, Ver. 1.07, National Institute Standards and Technology, Gaithersburg, MD.
- Rajaratnam, N., and Chamani, M.R., 1995, Energy losses at drops, *J. Hydraulic Research*, 33, pp.373-384.
- Roberts, A.F. and Pritchard, D.K., 1982, Blast effect from unconfined vapour cloud explosions, *J. Occupational Accidents*, 3, pp 231-247.
- Sadee, C., Samuels, D.E. and O'Brien, T.P., 1976/1977, The characteristics of the explosion at the Nypro (UK) Flixborough plant on 1st June 1974, *J. Occupational Accidents*, 1, pp 203-235.
- Teng-yang, R., 1997, *Measurements of Flow Induced Vibration and Flow Velocities in a Scale Model of the Flixborough "Dog-Leg" Pipe*, MscE Thesis, Department of Mechanical Engineering, Univ. Of New Brunswick.
- Venart, J.E.S. and Ramier, S., 1998(b), Boiling liquid expanding vapour explosions (BLEVE): the influence of dynamic re-pressurization and two-phase discharge, ASME Pressure Vessels and Piping Conf., San Diego, July (in press).
- Warner, F. 1975, The Flixborough, *Chem. Engineering Progress*, 71, pp. 77-84.

SESSION 34

MULTI-POINT METHODS

QUANTITATIVE UNSEEDED MOLECULAR VELOCIMETRY IMAGING

Peter A. DeBarber
MetroLaser, Inc.

Lubomir A. Ribarov, Joseph A. Wehrmeyer, Farrokh Batliwala, and Robert W. Pitz
Vanderbilt University

ABSTRACT

A method is established for performing instantaneous quantitative unseeded molecular velocimetry imaging and profiling in airflows. The method is called Ozone Tagging Velocimetry or OTV. OTV has several advantages over other laser-based velocimetry techniques. Major advantages include the abilities to: perform the measurement without the addition of any foreign seed particles or chemicals, probe flows of variable relative humidity, quantitatively and simultaneously visualize small and large scale flow structures, affect the measurements in real time, and cover a large dynamic range of velocities.

The OTV method is a time-of-flight velocimetry technique. OTV measurements are initiated by photochemically marking an airflow with an ozone (O_3) tracer generated by a pulse of light from a narrowband ultraviolet (UV) laser. The relatively stable ozone marker is displaced by convection with the flow. At a later time, a second narrowband UV laser photodissociates the ozone markers. The displacement is readily observed from the laser-induced fluorescence (LIF) of the molecular oxygen photoproducts. The velocity is calculated from the observed displacement of the marked volume over the time interval between the two laser pulses.

1. INTRODUCTION

Although laser diagnostic technology exists for the measurement of flow field parameters such as temperature and concentration, methods for obtaining routine nonintrusive, unseeded quantitative velocimetry profiles and images have been elusive. In general, single point and multiple point, planar, velocity measurements using seeding techniques are now commonly employed (Drain, 1980; Adrian, 1991; McKenzie, 1995), however, the drawbacks associated with seeding flows with foreign materials cause several concerns. These problems include: the additional cost and complexity associated with uniformly seeding large area high volumetric flow

rates, the toxic environmental issues of some seed chemicals, the corrosive nature of specific seed species on flow facility components, and the inability of seed particles to accurately track flows across steep gradients. These reasons have provided ample motivation for investigating unseeded molecular velocimetry methods.

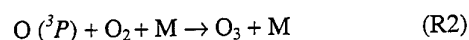
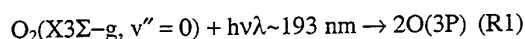
Several molecular-based methods using ambient flow constituents have been developed to alleviate the problems associated with seeding flows. In practice, many of these methods exhibit a new set of drawbacks. For example, Doppler-based methods suffer from poor dynamic range and yield large measurement errors in the lower velocity limits. Certain molecular flow tags are susceptible to chemical depletion, as is the case for O_2 RELIEF (Miles and Lempert, 1997) and OH (Boedeker, 1989) flow tagging. Furthermore, the non-linear laser techniques used to implement some of these alternative methods preclude their use in quantitative imaging applications.

The new method of OTV addresses several of the problems stated above (Pitz et al., 1996). This paper outlines the current state-of-the-art in OTV measurements. The majority of this work has been an ongoing collaboration between MetroLaser, Inc. and Vanderbilt University. The work has proceeded on two parallel courses: theoretical and experimental. We first discuss the OTV conceptual approach. We then cover specific experimental details. Theoretical and experimental results are then presented. The results are followed by a discussion concerning measurement resolution.

2. APPROACH

The OTV concept is divided into two simple to understand steps: "writing" and "reading." The two step concept is shown in Figure 1. The goal of the initial step is to mark the airflow with a long-lived molecular tag. For OTV flow tagging, the tag is a volume of ozone molecules. This is the "writing" step and the general mechanism is summarized in the

following sequence of photochemical reactions:



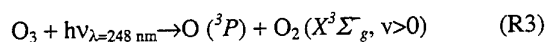
where $\text{M} = \text{N}_2$ or O_2 . The photodissociation of molecular oxygen is initiated by the absorption of a 193 nm photon. Ozone is produced as a result of the three body reaction between one of the atomic oxygen photoproducts, molecular oxygen, and a non-reacting collision partner, either N_2 or O_2 .

The initial position of the marker may be observed from the LIF signal originating from the $\text{O}_2(4-0)$ Schumann-Runge (SR) band excitation or from Rayleigh scattering at ~ 193 nm. The predissociation rate of reaction R1 is approximately 10^{11} s^{-1} (Laufer et al., 1990), and, therefore, the production of the ozone marker is dictated by the relatively slow three body reaction rate of reaction R2 which is $5.7 \times 10^{-46} \text{ m}^6/\text{s}$ at room temperature (Freisinger et al., 1989). For $T = 300 \text{ K}$ and $P = 1 \text{ atm}$, the ozone induction time is estimated to be:

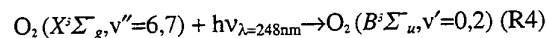
$$\tau_{\text{O}_2} \equiv 1/(k_2 n_{\text{O}_2} n_{\text{N}_2}) \cong 20 \mu\text{s}, \quad (1)$$

where n_i is the i th species number density.

The goal of the "reading" step in the OTV method is to interrogate the displacement of the flow marked by ozone. The reading step is summarized as follows:



After a set time delay, the ozone marker is photodissociated by illumination with a 248 nm laser. The minimum recommended time delay of $20 \mu\text{s}$ is a function of the ozone induction time. The resultant photoproducts are atomic oxygen and vibrationally excited molecular oxygen. An appreciable population of the "hot" O_2 resides in the $v'' = 6$ and 7 vibrational levels. The displacement of the marker is observed by LIF of the vibrationally excited molecular oxygen.



The LIF emission is collected with a filtered intensified CCD camera. The choice of which band to excite and which filters to use depends on equipment availability, measurement geometry, and degree of scattered light interference.

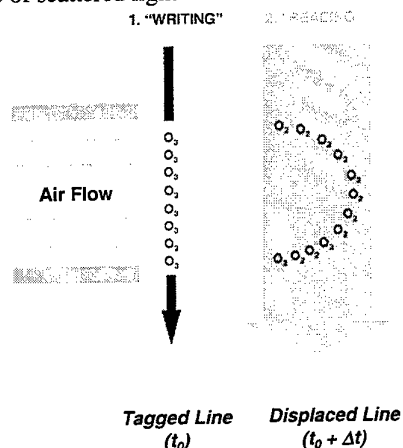


Figure 1. OTV two step concept.

3. EXPERIMENT

For optimum velocity measurement accuracy, two separately tunable narrowband excimer lasers are used. The apparatus is depicted in Figure 2. In a typical configuration, the beam from the writing laser is split and redirected to form a cross in the flow field. The beam from the reading laser is expanded into a thick sheet and illuminates the flow in the vicinity of or slightly downstream of the initial marker. The writing laser is a Lambda-Physik COMPex-150T ($\sim 0.003 \text{ nm}$ linewidth tunable from 192.5 to 193.5 nm) configured for narrowband ArF operation. The reading laser is a Lambda-Physik EMG-160T MSC ($\sim 0.001 \text{ nm}$ linewidth tunable from 248 to 249 nm) configured for narrowband KrF operation. The detector system is a single Princeton Instruments 576 x 384 intensified CCD camera coupled with a Nikon UV camera lens. A third velocity component may be observed with the addition of a second camera.

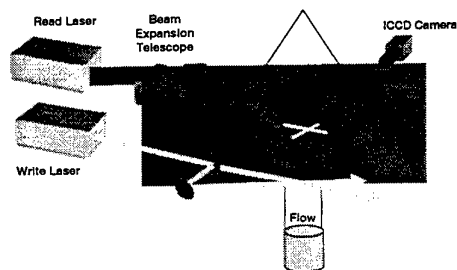


Figure 2. OTV experimental apparatus.

A 0.5% acetone in water liquid filter (McKenzie, 1993) in series with an interference notch filter (Laseroptik GmbH, 0° incidence notch filter) greatly attenuates the 248 nm scatter from the KrF read laser, yet allows observation of the initial write position. For situations where either scattered light at 193 nm is a problem, or where the initial position can be reliably measured from the beam geometry, a single carbon tetrachloride (CCl_4) liquid filter performs well. Figures 3, 4, and 5 show the transmission spectra for the acetone/water, interference notch, and carbon tetrachloride filters, respectively.

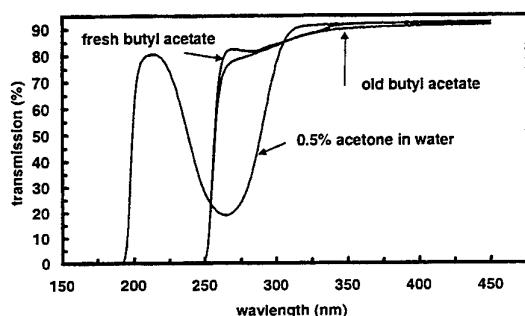


Figure 3. Transmission spectrum for various liquid filters. 10 mm path length.

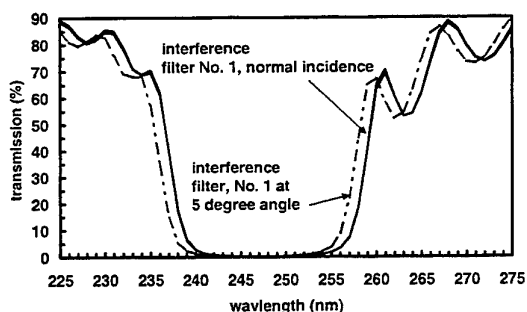


Figure 4. Transmission spectrum for the notch interference filter centered at 248 nm.

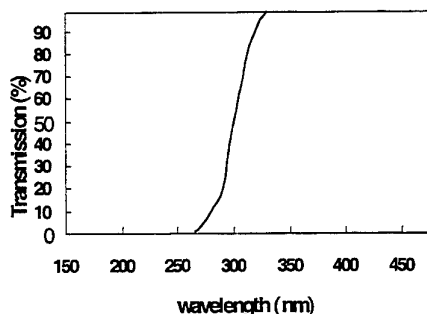


Figure 5. Transmission spectrum for carbon tetrachloride filter. 10 mm path length.

4. RESULTS

The development of the OTV method progressed on two fronts: theoretical and experimental. Modeling of the ozone kinetics is important for defining the operating envelope of the OTV method. To predict O_3 concentration as a function of time, we used the Chemkin-II thermodynamic database and the Senkin chemical kinetics solver (Lutz et al., 1988). These calculations employed a set of 116 reversible reactions.

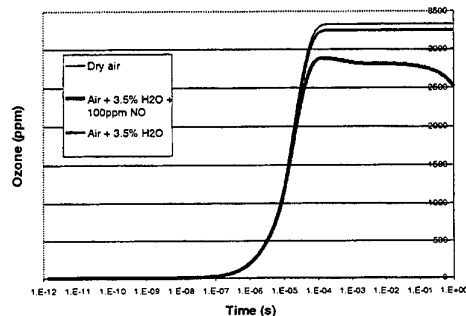


Figure 6. Steady state ozone concentrations calculated for dry, humid, and polluted initial air conditions.

The Senkin code is used to predict the amount of ozone formed under a given set of initial conditions. Figure 6 shows the results for three specific conditions corresponding to dry air (79% N_2 and 21% O_2), humid air (3.5% H_2O), and polluted air (3.5% H_2O and 100 ppm NO) each at $T = 300 \text{ K}$ and $P = 1 \text{ atm}$. We assume that 1% of the O_2 is photodissociated into oxygen (O) atoms.

The results show that the steady state concentrations of the ozone markers are only slightly reduced under humid or polluted conditions, and therefore, ozone molecules provide a very stable, long-lived flow tag. Additionally, Figure 6 shows that for a delay of 20 μs , the ozone concentration is above 50% of its peak steady state concentration. This result is in agreement with our first order estimates based solely on reaction R2.

For ambient conditions consisting of dry air at standard temperature and pressure (STP) and an estimated initial atomic oxygen concentration of 4200 ppm corresponding to 1% O_2 photo-dissociation, a steady state O_3 concentration of $\sim 3300 \text{ ppm}$ is predicted to occur at $\sim 1 \text{ msec}$. This O_3 level is expected to persist for at least 100 msec. Both these predictions attest to the rapid induction and relatively long chemical lifetime of the ozone markers.

As the temperature of the ambient conditions

increases, a decrease in the estimated steady state concentrations and lifetimes of O_3 is observed. Figure 7 shows these effects for four different temperature/pressure conditions.

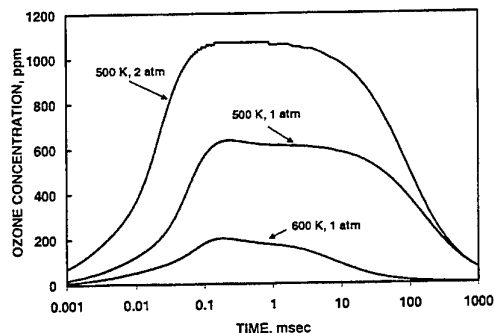


Figure 7. Ozone concentration calculated for various temperatures and pressures for dry, clean air.

At 500 K and 1 atm, the peak concentration has dropped to ~ 600 ppm, thus providing only 16% of the OTV signal expected under STP conditions. This decrease is in addition to that expected from the decrease in total density with temperature. The expected signal loss and lifetime decrease are even more severe at a temperature of 600 K and a pressure of 1 atm, thus precluding OTV from measurements in high temperature combusting flows.

Although it appears that high temperatures are detrimental to O_3 production, it is clear that increased pressures benefit O_3 production by increasing the probability for termolecular ozone producing collisions during the writing step. At 2 atm and 500 K, the steady state O_3 concentration exceeds 1000 ppm, therefore, under certain conditions, the detrimental effects of high temperature may be offset by the benefits of elevated pressures.

While calculations lend confidence in defining the range of applicability for the OTV method, experiments demonstrate the high quality and utility of single-shot OTV imaging. Single shot imaging capabilities are evident in OTV measurements taken in air flows exhibiting simultaneous regions of planar and vortical velocity structure. A 27 mm diameter nozzle was attached to a loudspeaker. The loudspeaker was driven with a 1 Hz square wave. The piston action of the loudspeaker against the nozzle produced a cylindrically-symmetric flow bounded by mushroom-shaped vortices. The cross formed by the two write beams provides an unambiguous reference point. As shown in Figure 8,

the 8 mm displacement of the cross center during the 4 msec delay yields a velocity of 2 m/sec. The position of the marker at zero time delay is determined by removing the butyl acetate filter and recording the O_2 fluorescence excited at ~ 193 nm.

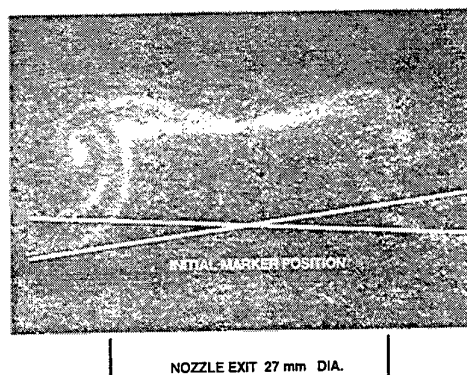


Figure 8. Single shot OTV image of an air flow exhibiting vortex structure.

5. DISCUSSION

We perform an uncertainty analysis with a 1% target uncertainty in the velocity measurement. Molecular diffusion can broaden the ozone tagged line. We begin by noting that diffusional spread of a tag line, assuming a Gaussian profile writing beam, can be expressed as (Miles et al., 1991):

$$fwhm(t) = (8tD\ln 2 + fwhm_0^2)^{1/2}, \quad (2)$$

where $fwhm(t)$ denotes the full width at half maximum of the tagged line, and $fwhm_0$ is that line's initial width. The molecular diffusivity, D , of ozone amounts to $\sim 0.2 \text{ cm}^2\text{s}^{-1}$ at ambient conditions.

The numerical significance of $fwhm(t)$ becomes clear if we first express the uncertainty in the tag displacement measurement using established procedures (Bevington and Robinson, 1992). The mean laminar flow velocity, v , is related to the displacement, d , and delay time, t as follows:

$$v = d/t. \quad (3)$$

The uncertainty associated with the velocity measurement is expressed as:

$$\Delta v^2 = \Delta d^2(\partial v/\partial d)^2 + \Delta t^2(\partial v/\partial t)^2. \quad (4)$$

We substitute in the partial derivatives and divide by v^2 to find:

$$(\Delta v/v)^2 = (\Delta d/d)^2 + (\Delta t/t)^2. \quad (5)$$

For OTV measurements, $\Delta d/d$ will be much larger than $\Delta t/t$. A priori, we know that Δt will be determined by the relative laser jitter and can easily be measured to a precision of $\Delta t \leq 10$ ns. Since $t > 20$ μ sec for sufficient O_3 to form, one finds $\Delta t/t < 0.05\%$. Thus, the timing uncertainty is always negligible. Since we specified a target value of $\Delta v/v = 0.01$, we invert Equation (5) to determine our experimentally required value of Δd to satisfy the target velocity measurement accuracy.

We find that for $t > 20$ μ sec (O_3 growth time), the uncertainty in measuring displacement is:

$$\Delta d = \Delta vt, \quad (6)$$

and for $\Delta t = 10$ ns, $t > 20$ μ s, and $\Delta v = 0.01 \times v$, we find that the uncertainty in measuring displacement is:

$$\Delta d = 0.01tv = 0.01d. \quad (7)$$

Note that the required measurement accuracy, Δd , scales as t , while the diffusional width of the tagged line, $\text{fwhm}(t)$, scales as $t^{1/2}$. Diffusion broadening has been estimated previously (Ribarov et al., 1998). Referring to Eq. 2, for a typical laser line of 0.5 mm diameter, it takes 5 msec for the line to double in size. Thus, diffusion broadening is not important for read/write times of less than 1 msec.

6. CONCLUSIONS

A new method for performing quantitative unseeded molecular imaging and profiling in air flows has been developed. The OTV method uses a stable velocity marker without the addition of any foreign seed materials. The tagged line of ozone molecules is produced at ~ 193 nm with currently available excimer laser technology. The original position of the tagged line is observed by ~ 248 nm KrF excimer LIF. The time-of-flight displacement of the tagged volume of air yields accurate velocities down to a few cm/sec. Evidence from theory and experiment show the OTV method to be applicable over a wide range of velocities, temperatures, and pressures. With two cameras, three orthogonal velocity components may be realized.

7. ACKNOWLEDGMENTS

The authors wish to thank Dr. Ronald H. Kohl, SBIR Phase II Technical Monitor, for his many

helpful discussions. This work received partial support under a U.S. Department of Defense (DOD) Phase II SBIR program sponsored by Arnold Engineering Development Center (AEDC), Air Force Materiel Command, USAF, Contract Number F40600-96-C-0002. In addition, this research was also funded by a grant from NASA-Lewis Research Center, Cleveland, OH (NAG3-1984, Dr. Richard G. Seasholtz, Technical Monitor). We also thank M. S. Smith and B. J. McLure at AEDC, for their technical assistance, and S. P. Nandula and R. J. Osborne, at Vanderbilt, for their help with the kinetics simulations and the computer software. The authors thank M. S. Brown at MetroLaser, Inc. for his help with the manuscript.

8. REFERENCES

- Adrian, R.J., 1991, Particle-Imaging Techniques for Experimental Fluid Mechanics, Annu. Rev. Fluid Mech., vol. 23, p. 261.
- Bevington, P.R. and Robinson, D.K., 1992, Data Reduction and Error Analysis for the Physical Sciences, (McGraw-Hill, Inc., NY).
- Boedeker, L.R., 1989, Velocity Measurement by H_2O Photolysis and Laser-Induced Fluorescence of OH, Opt. Lett., vol. 14, p. 473.
- Drain, L. E., The Laser Doppler Technique, 1980, J. Wiley, New York.
- Freisinger, B.U., Kogelschatz, J.H., Schäfer, J., Uhlenbusch, J. and Viol, W., 1989, Ozone Production in Oxygen by Means of F_2 - Laser Irradiation at $\lambda = 157.6$ nm, Appl. Phys. B, vol. 49, p. 121.
- Laufer, G., McKenzie, R.L., and Fletcher, D.G., 1990, Method for Measuring Temperatures and Densities in Hypersonic Wind Tunnel Air Flows Using Laser-Induced O_2 Fluorescence, Appl. Opt. vol. 29, p. 4873.
- Lutz, A.E., Kee, R.J., and Miller, J.A., 1988, SENKIN: a Fortran Program for Predicting Homogeneous Gas-Phase Chemical Kinetics with Sensitivity Analysis, Sandia National Laboratories, Report No. SAND87-8248.
- McKenzie, R.L., 1993, Rayleigh Rejection Filters for 193-nm ArF laser, Raman Spectroscopy, Opt. Lett., vol. 18, p. 995.
- McKenzie, R.L., 1995, Measurement Capabilities of

Planar Doppler Velocimetry Using Pulsed Lasers, 1995, 33rd Aerospace Sciences Meeting, AIAA Paper No. 95-0297, Reno, NV.

Miles, R. B. and Lempert, W.R., 1997, Quantitative Flow Visualization in Unseeded Flows, Ann. Rev. Fluid Mech., vol. 29, p. 285.

Miles, R.B., Lempert, W.R., and Zhang, B., 1991, Turbulent Structure Measurements by RELIEF Flow Tagging, Fluids Dynamics Res., vol. 8, p. 9.

Pitz, R.W., Brown, T.M., Nandula, S.P., Skaggs, P.A., DeBarber, P. A., Brown, M.S., and Segall, J., 1996, Unseeded Velocity Measurement by Ozone Tagging Velocimetry, Opt. Lett., vol. 21, p. 755.

Ribarov, L. A., Wehrmeyer, J. A., Batliwala, F., Pitz, R.W., and DeBarber, P.A., Ozone Tagging Velocimetry (OTV) Measurements Using Narrowband Excimer Lasers, 1998, 36th Aerospace Sciences Meeting & Exhibit, AIAA Paper No. 98-0513, Reno, NV.

RECENT APPLICATIONS OF THREE-DIMENSIONAL DOPPLER GLOBAL VELOCIMETRY IN TURBO-MACHINERY

I. Roehle, C. Willert and R. Schodl

German Aerospace Center (DLR)
Institute of Propulsion Technology, Linder Höhe, D-51170 Köln, Germany

ABSTRACT

A Doppler global velocimetry (DGV) system optimised for time-averaged three component velocity measurements has been applied in two situations. The system uses a single viewing direction in conjunction with three different illumination directions. A frequency-stabilised Ar⁺-laser ($\sigma_v < 1$ MHz) and a pair of Peltier-cooled CCD's with 12-bit dynamic range allow a measurement resolution better than 1 m/s. A modified version of the hardware was used to map the cross-section of an engine inlet within a 1:10 scale aircraft model. In order to meet spatial constraints within the model, miniature light sheet devices and a flexible endoscope were necessary to obtain the data.

In another application time-average volumetric, three-component velocity data was obtained in a double-staged, 'cold' combustion chamber by translating the light sheet plane at 2 mm increments.

More recent efforts directed toward obtaining phase-averaged DGV data are also presented.

1. INTRODUCTION

Since its invention a few years ago Doppler global velocimetry, also referred to as planar Doppler velocimetry, has undergone a rapid pace of development. In principle the technique is simple: the frequency shift of light scattered by particles suspended in the flow is measured by means of a frequency-to-intensity converter, typically a iodine-vapour absorption cell (Komine 1990, 1991). However, on the background of achieving high quality planar velocity fields, similar to those provided by particle image velocimetry (PIV), the technique is more difficult to apply than PIV due to a number of intrinsic demands placed on the required equipment: 1) The laser has to operate at a known and stable frequency with a bandwidth in the 1 MHz range to yield a measurement resolution better than 1 m/s. 2) The characteristics of the absorption cell (temperature, transmission curves, etc.) have to be very well known. 3) The recording camera pair needs to exhibit a high dynamic range, because the ratio of their signals defines the transmission ratio from which the Doppler

shift is determined. Further, a number of error sources (reflection, multiple scattering, etc.) have to be carefully observed.

Nevertheless DGV offers a number of advantages not found in other planar measurement techniques. For instance, unlike PIV and PTV, there is no need to resolve discrete particles, much less their displacement over short time intervals. DGV only needs to record the light scattered by the illuminated particles and inherently allows the size of the field of view to be chosen arbitrarily. Image resolution is not vital for DGV which makes the technique attractive in situations with poor optical access or varying refractive indices, such as. internal flows or combusting media. Whereas the measurement error in the particle displacement approaches scales relative to the image/object magnification and sensor resolution, the measurement resolution of the DGV system is of absolute nature, independent of the object size. Currently this resolution is on the order of 1m/s, which makes the use of DGV most attractive in flows with higher flow velocities.

With regard to the technical realisation of the DGV concept a number of researchers are focusing their efforts on the development of single-pulse Doppler global velocimeters based on frequency stabilised Nd:YAG lasers. By recording the Doppler-shifted pulsed light from three different observation directions simultaneously using three DGV receivers (cameras), the aim is to obtain instantaneous three-component planar velocity data (McKenzie 1996, Smith et al. 1996, Arnette et al. 1998, Clancy et al 1998). The other efforts in DGV implementation are directed toward the development of time-averaging velocimeters (Meyers 1995, 1996, Roehle 1996, Roehle & Schodl 1997, Roehle 1998]. Such a system will be described next.

2 DGV MEASUREMENT APARATUS AT DLR

The DGV system developed at the DLR-Cologne turbo-machinery instrumentation division is optimised for the recovery of time-averaged, three-component, planar velocity fields. Rather than using three camera systems

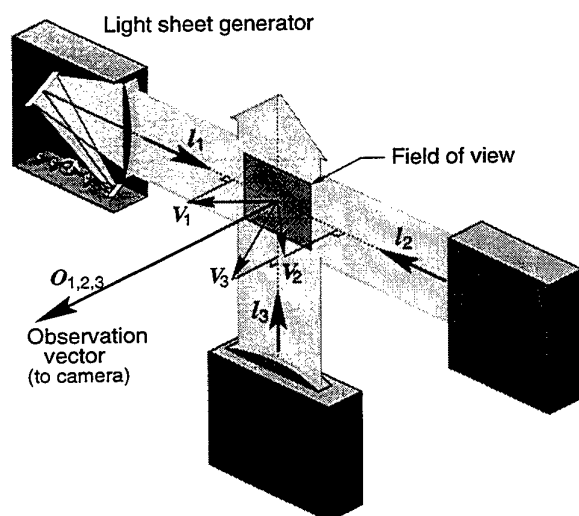


Figure 1. Light sheet arrangement used for time-averaging DGV

for the observation of the illuminated plane, the laser light sheet is introduced into the plane of interest from three different, preferably orthogonal, directions (Figure 1). There are a number of advantages in this approach which make it the method of choice in flow fields that exhibit a steady-state behaviour: Aside from the reduced cost, the single camera set-up allows much easier calibration, both in terms of viewing geometry and intensity-to-frequency conversion. In general, the viewing axis is normal to the illuminated plane such that no de-warping of the images is necessary. This also means that the recovered velocity component images do not need to be explicitly merged because the data fields already coincide.

The DGV system consists of three main pieces of equipment: a) a frequency stabilised CW-laser, b) three light sheet generators, and c) a DGV image acquisition system (i.e. DGV camera). The stabilised laser system consists of a modified Ar^+ -laser operating in the single frequency mode at 514.5 nm and 1-2 Watts. Frequency stabilisation is achieved by directing a portion of the emitted light through a reference iodine cell (Figure 2). In full analogy to the concept of DGV, the beam intensity before and after the iodine absorption cell is used to obtain an intensity fraction. A PID controller is used to maintain this fraction at a fixed value and thereby stabilises the laser frequency. The remaining frequency jitter is on the order of $\sigma_\nu = 1$ MHz. The laser can be continuously tuned over a frequency range of 2 GHz without mode-hops which makes it possible to obtain the transmission curve of the iodine cell. In cases requiring a high reproducibility and knowledge of the absolute frequency, such as for calibrating the iodine cells, a more sophisticated stabilisation based on

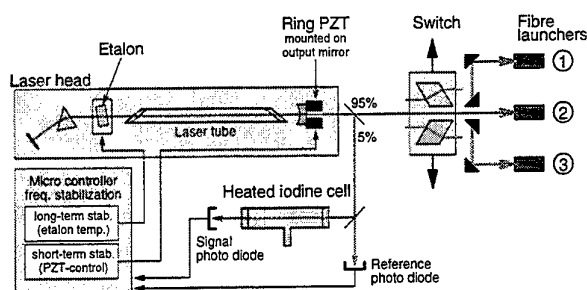


Figure 2. Laser stabilization system and opto-mechanical switch for coupling into transmission fibres

the detection of the hyperfine structure of iodine is used (Roehle 1998).

As indicated in figure 2, an opto-mechanical switch, based on obliquely mounted glass plates and mirrors, directs the frequency-stabilised laser light into one of three fibre launchers which are connected to the light sheet generators via 10 m long multi-mode fibres (10 μm core \varnothing). The light sheet generation employs a sweeping beam approach based on magnifying the linear translation of the laser beam as it passes through a rotating slab of glass (Figure 1). Contrary to the non-uniform, typically Gaussian, light sheet intensity profile obtained with stationary optics (i.e. cylindrical lenses), the sweeping beam light sheet exhibits an essentially top-hat intensity profile. This aspect minimises the intensity dynamics in the measured image with positive influence on the overall signal-to-noise ratio (SNR). The modulation frequency can be varied between 0 and 400 Hz.

The third component of the DGV hardware, the camera system, is diagrammed in figure 3. Whereas the common approach is to use a separate objective lens for each CCD sensor, this receiver employs a single collecting lens in conjunction with a relay lens and a non-polarising beam-splitter to transmit the intermediate image onto the two CCD sensors, one of which views the image through an iodine absorption cell (50mm length, 40mm \varnothing). This optical arrangement is much easier to align and also permits the use of an endoscope which would be located in place of the objective lens. A pair of Peltier-cooled, 12-bit, slow scan CCD cameras with linear sensitivity and high SNR (exceeding 500:1) provide the digital images from which the DGV data is computed. By cooling the CCD down to -15°C , long integration times of tens of seconds are possible because the dark current and associated dark current noise are significantly reduced. For comparison, standard 8-bit video cameras can usually only provide SNR levels of about 40:1. Although micro-positioning is used for alignment of

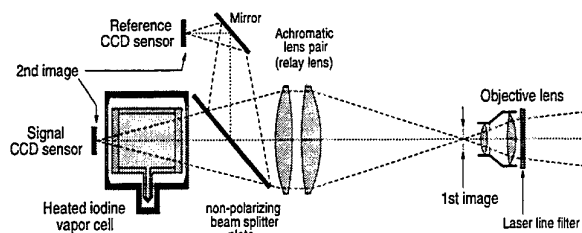


Figure 3. DGV receiving camera optics

the sensors, the residual misalignment is accounted for in software using polynomial image warping.

The iodine cell placed in front of the signal CCD sensor is made from fused quartz glass and contains a small amount of pure iodine. Since the cell's transmission profile strongly depends on the temperature and vapour pressure in the cell, a cell temperature is chosen such that all of the solid iodine is evaporated (in our case 57°C). This fixes the iodine vapour density within the cell. Beyond this temperature significant pressure changes and associated changes in the transmission profile are only possible by much greater temperature changes. As a consequence the precision of the control maintaining a constant temperature within the cell is not as critical as in cells containing both solid iodine and vapour. The control of the vapour pressure using a separately heated cold finger as is common in many other DGV system is not necessary (Chan et al. 1995). However, the final cell transmission curve cannot be pre-determined during the evacuation and filling procedure of the cell and depends to a large extent on the experience of the person filling the cell.

3. DATA PROCESSING AND VALIDATION

A number of processing steps and additional input data are required to reconstruct the three-component velocity data from the three image pairs each of which consist of a signal (viewed through the iodine cell) and a reference image. Ambient light effects and laser reflections are accounted for by subtracting a set of background images which are recorded in the absence of seeding. Another image pair, recorded with uniform illumination, is used to correct for pixel-specific sensitivity.

Since the CCD sensors are not in perfect alignment with each other, an image mapping accomplishes this at this point. Additional de-warping may be used to account for an oblique viewing axis and/or geometrical distortions. Now a quotient image is computed from the spatially coincident image pair – the desired transmission ratio image is formed. The iodine cell transmission profile is applied to the image in the form of a look-up table resulting in an image

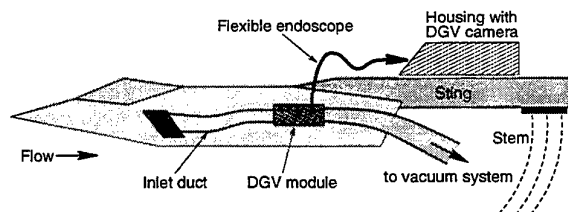


Figure 4. Placement of the DGV-module within a 1:10 scale wind tunnel model. In this unique experiment a flexible endoscope transmitted the image to the external camera

containing Doppler-shifted data which in turn can be readily converted to velocity.

The three distinct, but non-orthogonal, velocity component images are combined by applying a co-ordinate transformation based on the local observation vector and light sheet direction. The observation vector is obtained from the position of the camera collecting optics in relation to the position within the observation plane, while the local illumination vector is either determined interactively from image data or defined directly if the position of the light sheet devices are known.

With current PC-based computing all of the described processing steps take only a few seconds to complete. High-level scripting languages such as IDL are used to make the software both platform-independent as well as open to future modifications.

3.1 Error Sources and Data Validation

Whereas the primary source of error in single pulse is speckle noise (Smith et al. 1996, McKenzie 1997), this does not arise in time-averaging DGV, especially when the light sheet is generated by a scanning beam. The long integration times (up to several seconds) smooth out the moving speckle patterns.

A significant source of error in both single-shot and time-averaged DGV arises due to multiple scattering. It arises when light scattered from particles illuminates other particles. In the presence of moving particles, this scattered light already has a Doppler shift imposed on it. As a consequence the collected light no longer represents the correct Doppler shift. Although this error is known to increase with increased seeding density (Voigt 1998), it has not been fully quantified.

Similar to the multiple scattering error source, the light scattered from dense seeding may illuminate the surrounding areas, such as surfaces and vessel walls. Background images recorded in the absence of seeding do not capture this phenomenon. In this case fluorescent paints or blackened (non-scattering) surfaces can essentially alleviate the problem. Another error source arises in the presence of reflecting surfaces, such as glass windows, which may re-

introduce a portion of the light sheet from a different direction and hence produce an undesired Doppler-shifted signal component. Turbo-machinery applications and other internal flows are mainly affected by this problem such that care must be taken in the optical design of the light sheet access (anti-reflection coatings, beam dumps, etc.).

Data validation in the recovered velocity images is frequently necessary especially near flow bounding walls and other scattering surfaces. Whereas validation schemes typically applied to PIV data assume the sporadic (isolated) occurrence of erroneous data, this is generally not the case in DGV. Frequently non-uniformities in the light sheet, caused by deposits or obstructions on facility windows, introduce a banded disturbance pattern in the velocity component data, that is, a velocity bias aligned with the light sheet disturbance. This lessens the effectiveness of standard neighbourhood-based validation. Rather, validation schemes which are sensitive to the respective light sheet directions have to be applied. This validation has to take place on each individual velocity component image prior to their transform-based merging. This method of validation can be enhanced if volumetric DGV, such as described in the next section, is available.

4. DGV MEASUREMENT APPLICATIONS

The described DGV system has already been applied in a variety of applications including a swirl flow atomiser nozzle and the flow in the wake of a model car (Roehle 1996, Roehle & Schodl 1997). Two more recent applications are described next.

4.1 DGV Measurements in the Model of an DASA-Engine Inlet

The flow field inside a model of an aircraft engine inlet provided by DASA was mapped with DGV. After ground testing the model was mounted in the $3 \times 3 \text{ m}^2$ wind tunnel section of DNW-NWB at DLR-Braunschweig. One of the aims of this investigation was to evaluate the potential use of DGV results in engine development. Contrary to civil transport aircraft the air intake of fighter aircraft are relatively long and curved and thus can exhibit pipe flow phenomena such as pressure losses and flow inhomogeneities. A constant and uniform flow upstream of the engine is required to ensure proper engine operation over the entire flight envelope. Velocity inhomogeneities (vorticity) and the loss of total pressure have to be measured as a function of the mass flux and the aircraft's angle of attack.

The initial stationary set-up of the intake model allowed the DGV measurement accuracy to be

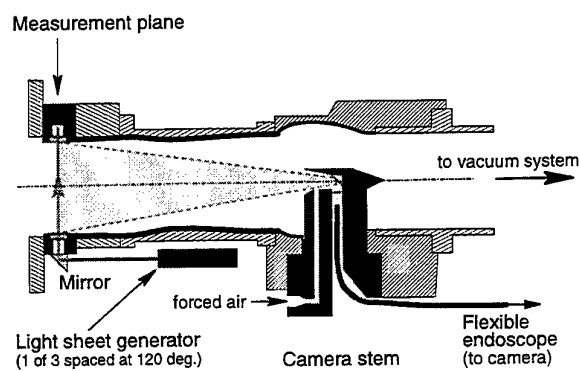


Figure 5. Optical module used for DGV measurements of engine inlet flow

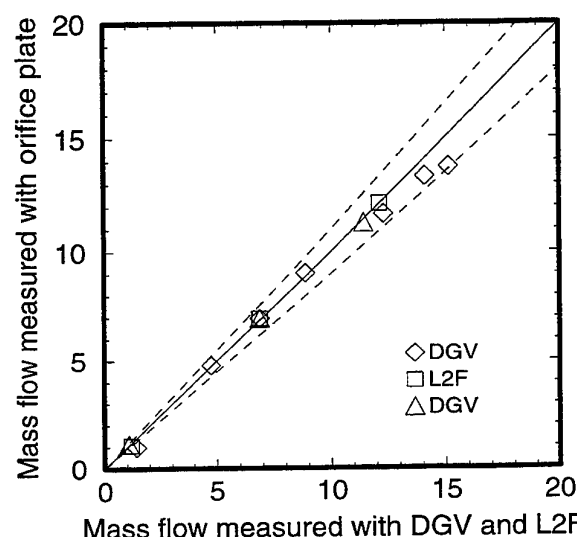


Figure 6. Reduced mass flow rate measured with DGV versus the mass flow rate measured with an orifice flow meter

quantified by comparing the data with laser-2-focus velocimetry data and pressure probe data. In the second step the intake was mounted within a 1:10 scale wind tunnel model such that the effects of aircraft angle of attack, yaw and air speed could be investigated (Figure 4). This DGV application within an aircraft model posed a number of engineering challenges: For one, the light sheets have to remain stationary with respect to the intake duct as the angle of attack is varied, and secondly, due to its size the camera system had to be located externally from the aircraft model. Three miniature scanning light sheet devices (size $50 \times 50 \times 15 \text{ mm}^3$), supplied with laser light via $10 \mu\text{m}$ fibres, along with 90° folding mirrors were mounted on the exterior of the duct such that the cross section of the duct was illuminated by three sheets intersecting at 120° with respect to each other (Figure 5). The gap required for the access of the light sheets was sealed by a cylindrical

glass ring whose diameter was slightly larger than the duct to reduce both light scattering effects near the circumference as well as reduce the build-up of the liquid seeding material (1-5 μ m ethylene glycol droplets) on the glass surface.

The cross section spanned by the three light sheets was imaged from a downstream position via an flexible endoscope which was mounted into a stem such as shown in figure 5. The endoscope transferred the image to the camera system which was mounted on the sting supporting the aircraft model. Although the limited number of fibres in the endoscope ($\approx 40,000$) is far less than the number of pixels on typical CCD sensors, this did not pose a direct problem in the application of DGV other than reducing the spatial resolution to some degree. Techniques requiring the direct imaging of particles, such as PIV, would not have been able of tolerating this loss in spatial resolution. This aspect makes the DGV method especially suitable in situations with poor optical access.

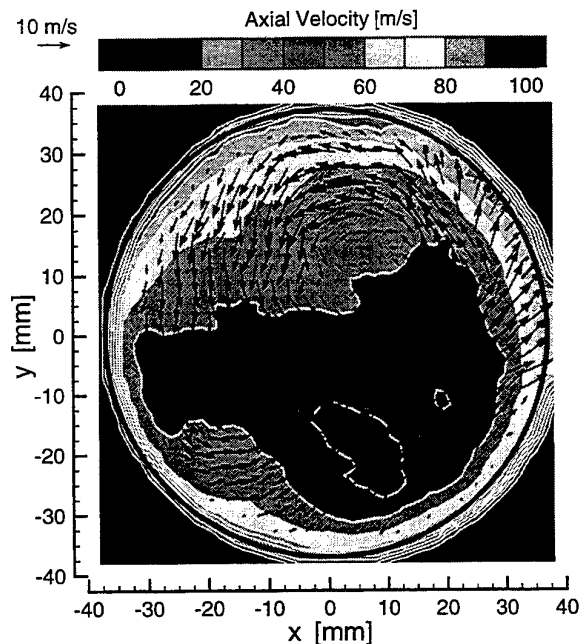


Figure 7. Flow field in the cross-section of an engine intake of an aircraft model placed in the $3 \times 3 \text{ m}^2$ wind tunnel of DNW-NWB at DLR-Braunschweig

During the ground testing phase of the investigation the inlet along with the optical module was tested in a stationary set-up. To achieve a homogeneous seeding distribution in the measurement

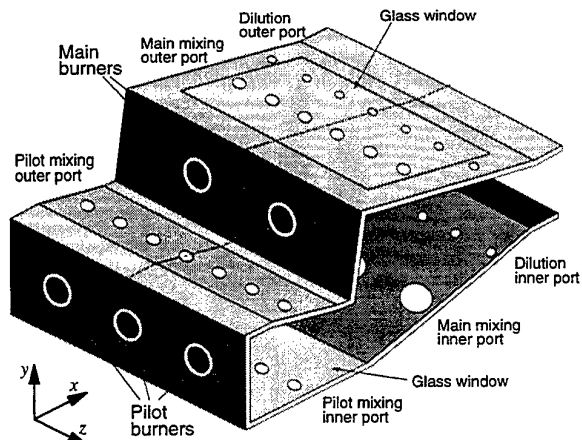


Figure 8. Double-staged combustion chamber with glass windows used in DGV investigation

plane, a seeding box comprised of a fog generator, a fan and screens was placed in front of the inlet. A vacuum system attached downstream of the intake and optical module simulated the engine air supply at flow speeds up to 210 m/s. Figure 6 shows the reduced mass flow rate measured with DGV versus the mass flow rate measured with an orifice meter. The correlation is quite good except for high flow rates. Interestingly enough the deviations occurred past the point where the flow in the smallest cross-section became sonic (choked). The DGV results also compared well with laser-2-focus measurements and pressure probe data.

One of the reconstructed time-averaged flow fields obtained during the wind tunnel phase of the project is shown in figure 7. A strong vortical structure along with an unbalanced axial flow profile can be observed. Important design parameters could be derived from this data such as the total pressure loss and total pressure distortion.

4.2 DGV Measurements in a Combustion Chamber

This application was performed in a double-staged combustion chamber consisting of two main and three pilot burners (figure 8) with optical access from at least three sides at a time. The chamber itself represents a segment of an annular combustion chamber for use in the engine of a transport aircraft. One of the principle aims here was to obtain a data base to validate CFD codes. Since the flow structure inside a combustion chamber is very complex it is desirable to acquire the entire three-dimensional volume data set – a task very tedious to accomplish with single point measurement techniques (e.g. LDA).

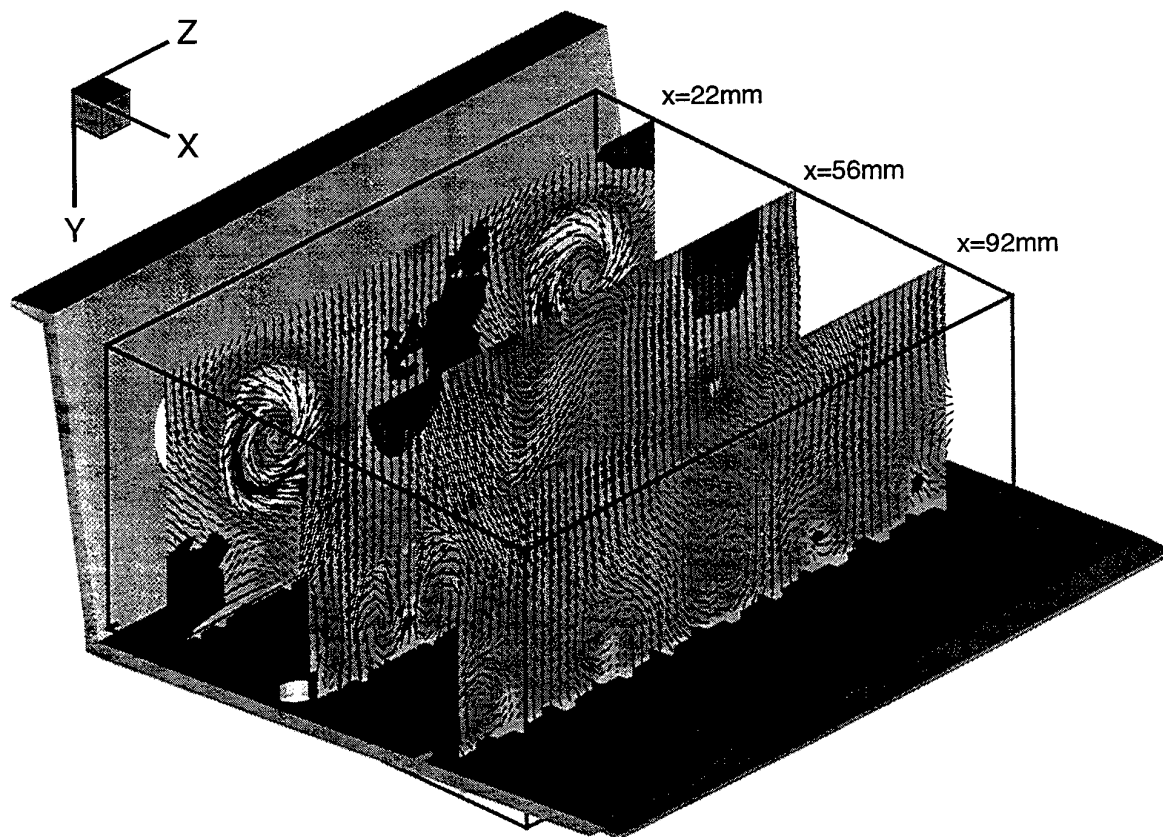


Figure 9. Selected YZ cross-sections through the volumetric three-component velocity data obtained for the main zone (upper zone) of the combustion chamber. The contours indicate the out-of-plane velocity component, v_x .

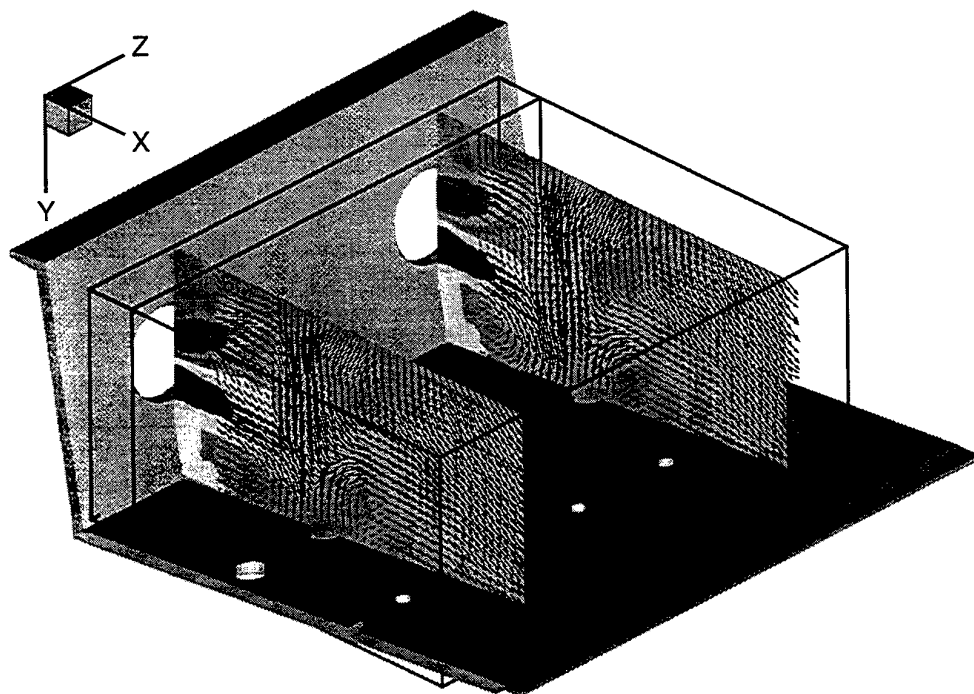


Figure 10. Selected XY cross-sections through the volumetric three-component velocity data obtained for the main zone (upper zone) of the combustion chamber. The contours indicate the out-of-plane velocity component, v_y .

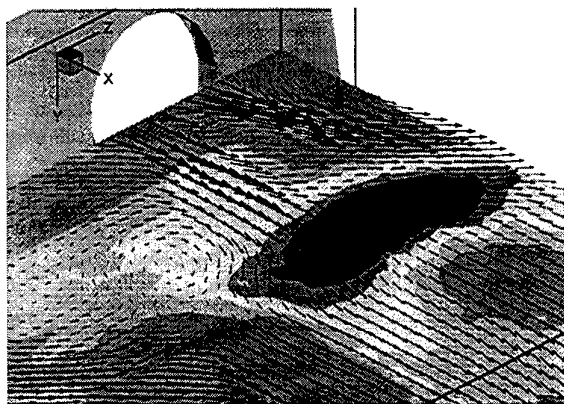


Figure 10. Detail from the XZ-plane intersecting with the centerline of the main burners. The contours indicate the out-of-plane velocity component, v_y .

For the measurement the light sheets were introduced from either side as well as from the top or bottom of the chamber. A mirror was placed downstream of the combustion chamber exit such that the camera was not directly exposed to the flow. The entire DGV equipment, camera and light sheet devices, were mounted on a common translation stage, such that the interior flow field could be mapped in a tomographic manner at increments of $\Delta x = 2$ mm. Up to 50 adjacent planes were recorded in this manner resulting in volumetric data sets containing up to $120 \times 60 \times 50$ distinct data points at a spacing of $1 \times 1 \times 2$ mm³.

The DGV measurements were restricted to the 'cold' (unfired) flow under atmospheric conditions. Measurements in the hot, burning flame were not possible due to the self-luminosity of the seeding particles as well as glowing soot which requires the use of intensifier-gated CCD cameras and pulsed, frequency-stabilised lasers, both of which were not available at the time.

Figures 9,10,11 and 12 give an impression of the quality of the recovered data by showing various cross-sections through the flow. The interaction between the swirling burner flows and the and mixing jets of the secondary air can be easily recognised. Swirls within the mixing jets are also visible and are surprisingly similar to the CFD results (data not presented in this context). A comparison between DGV data and LDA data obtained for the swirler nozzle flow is presented in (Lehmann 1998).

5 CURRENT AND FUTURE EFFORTS

More recent research efforts have been directed toward obtaining phase-averaged DGV measurements, which is of special interest in rotating turbo-machinery. Phase-averaged DGV images can be obtained in two

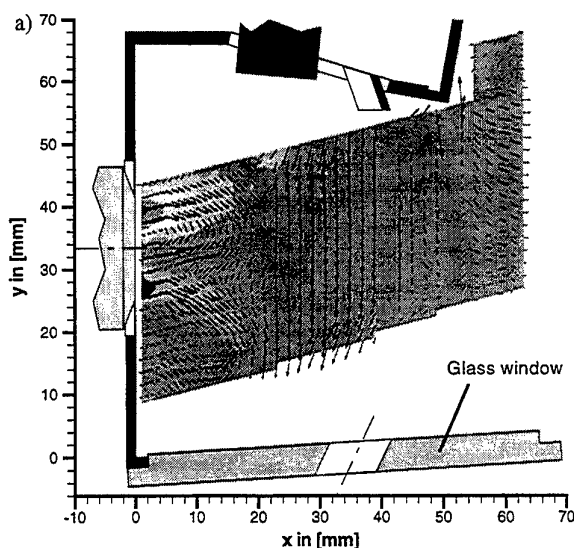


Figure 11. XY-plane extracted from the pilot zone velocity data set, intersection with one of the pilot burners

ways: either through the use of an electronic image shutter or through the modulation of the illumination source (i.e. laser). Electronic shuttering can be achieved through on-chip charge integration using state-of-the-art interline transfer CCD sensors or with the aid of multiply-gated image intensifiers which is rather expensive. Recent tests with a modified, 12-bit, interline transfer CCD camera have demonstrated two major drawbacks to this approach: First, with increasing residency time of the collected charge within the on-chip storage register, a fixed pattern noise arises along with a significant reduction of the SNR. Surprisingly the number of shutter events has little influence which could be easily demonstrated by increasing the duty cycle of the exposures and reducing the total number of exposures such that the total integration time remains constant. Secondly, the storage wells used for on-chip charge integration have a finite extinction ratio on the order of 2000:1 which may be insufficient when imaging luminous flows or using a CW-laser without modulation.

The other approach toward phase-averaged DGV based on laser modulation can be readily implemented on the existing hardware by adding an acousto-optic modulator (i.e. Bragg cell) in the laser beam. The first-order, frequency shifted beam which can achieve 100 percent extinction is used for the illumination of the flow. Since the CCD sensors stay sensitive during the entire acquisition time care must be taken that only little residual light is acquired. This configuration will be used in mapping the cyclic flow field within an engine exhaust system downstream of a turbo-

charger/waste-gate arrangement and upstream of a catalytic converter.

Other research efforts are aimed recovering DGV data from luminous flows such as fired combustion chambers. For this purpose a long-pulse, tuneable, frequency-doubled Nd:YAG laser was developed in collaboration with the Laser Zentrum Hannover (Matthias 1998). The laser operates at a repetition rate of 1 kHz with 2 mJ per pulse at 532 nm and a pulse duration of 400 ns. The injection-seeded design employs a rather long pulse which reduces the Fourier-limited bandwidth to the order of 1 MHz.

6 SUMMARY

With the aim of primarily recovering time-averaged three-component DGV data the recently developed measurement hardware already was successfully applied in a number of different situations and is suited for both confined flows and exterior flows. A variety of sources of measurement uncertainty have yet to be fully understood and treated. On the whole the DGV method is to be understood as an important addition to the established velocimetry techniques such as PIV and LDA.

Further development of the DGV hardware, especially on the laser side, is still possible. In the future narrow-bandwidth, tuneable solid state CW-lasers (typically frequency-doubled Nd:YAG lasers) will become available in small packages which improves the handling and portability of the entire DGV system.

ACKNOWLEDGEMENTS

This work was funded by the German Ministry of Education and Research (BMBF). The authors like to thank DASA for making the inlet DGV data available for publication. Further, BMW-Rolls Royce is acknowledged for allowing the partial publication of the combustion chamber data.

REFERENCES

- Arnette S A, Elliot G S, Mosedale A D & Carter C D 1998, A two-color approach to planar Doppler velocimetry. Proc. 36th Aerospace Sciences Mtg., Reno, Nevada, paper AIAA-98-0507.
- Chan V S S, Heyes A L, Robinson D I & Turner J T 1995, Iodine absorption filters for Doppler global velocimetry. Meas. Sci. Technology, vol. 6, pp. 783-794.
- Clancy P S, Samimy M & Erkin W R. 1998, Planar Doppler velocimetry: three-component velocimetry in supersonic jets. Proc. 36th Aerospace Sciences Mtg., Reno, Nevada, paper AIAA-98-0506.
- Komine H. 1990, System for measuring velocity field of fluid flow utilising a laser-Doppler spectral image converter. US Patent, No. 4 919 536.
- Komine H, Brosnan S J, Litton A B & Stappaerts E A. 1991, Real-time Doppler global velocimetry. Proc. AIAA 29th Aerospace Sciences Mtg. Reno, Nevada, paper 91-0337.
- Lehmann B. & Roehle I. 1998, A comparison of velocity-field data behind a double-swirl nozzle measured by means of Doppler-global and conventional three-component LDA techniques. Proc. 9th Intl. Symp. on Appl. of Laser Techniques to Fluid Mechanics, Lisbon, Portugal, paper 33-2.
- Matthias K. 1998, Ph.D. thesis, University of Hannover (in preparation).
- McKenzie R L. 1996, Measurement capabilities of planar Doppler velocimetry using pulsed lasers. Applied Optics, vol. 35, no. 6, pp. 948-964.
- McKenzie R L. 1997, Planar Doppler velocimetry for large-scale wind tunnel applications. Proc. AGARD Fluid Dynamics Panel 81st Mtg. and Symp. on Advanced Aerodynamic Measurement Technology, Seattle, Washington.
- Meyers J F. 1995, Development of Doppler global velocimetry as a flow diagnostics tool. Measurement Science & Technology, vol. 6, pp. 769-783.
- Meyers J F. 1996, Evolution of Doppler global velocimetry data processing. Proc. 8th Intl. Symp. on Appl. of Laser Techniques to Fluid Mechanics, Lisbon, Portugal, paper 11-1.
- Roehle I. 1996, Three-dimensional Doppler Global velocimetry in the flow of a fuel spray nozzle and in the wake region of a car. Flow Measurement & Instrumentation, vol. 7, no. 3/4, pp. 287-294.
- Roehle I. 1998, Doppler Global Velocimetry. in Advanced Measurement Techniques, von Karman Institute of Fluid Dynamics Lecture Series, Brussels, Belgium.
- Roehle I & Schodl R. 1997, Applications of three dimensional Doppler global velocimetry to turbo machinery and wind tunnel flows. Proc. 90th Symp. of AGARD-PEP on Advanced non-intrusive Instrumentation for Propulsion Engines, Brussels, Belgium.
- Roehle I & Schodl R. 1997, Applications of three dimensional Doppler global velocimetry to turbo machinery and wind tunnel flows. Proc. 7th Intl. Conf. on Laser Anemometry Advances and Applications, Karlsruhe, Germany, pp. 387-395.
- Smith M W, Northam B & Drummond J P. 1996, Application of absorption filter planar Doppler velocimetry to sonic and supersonic jets. AIAA Journal, vol. 34, no. 3, pp. 434-441.
- Voigt P. 1998, Non-linear effects in planar scattering techniques: proofs of existence, simulations and numerical corrections of extinction and multiple scattering. Proc. 9th Intl. Symp. on Appl. of Laser Techniques to Fluid Mechanics, Lisbon, Portugal, paper 26-2.

MEASUREMENT OF INSTANTANEOUS VELOCITY IN A TURBULENT PIPE FLOW USING INDIVIDUAL REALIZATION DIODE ARRAY VELOCIMETRY

E. Huckle, I. Catton
Mechanical and Aerospace Engineering Department
University of California, Los Angeles

and

M. Azzazy
Azzazy Technologies
Aliso Viejo, California

ABSTRACT

Diode Array Velocimetry (DAV) has been used to measure the streamwise fluctuating velocity component of turbulent pipe flow. A steady, turbulent flow of air in a pipe was generated in a laboratory wind tunnel, and three data sets ($Re = 3.6 \times 10^4$, 1.0×10^5 , and 2.0×10^5) were recorded. For each data set, a large number of samples ($\sim 10^5$) were recorded at a constant blower speed, yielding a velocity versus time record. The DAV time sample records demonstrated excellent agreement with the expected Poisson distribution for random sampling.

A PDF of the velocity fluctuations gave mean velocities (5.51, 16.0, and 32.2 m/s, respectively) with turbulence intensities slightly higher than expected. Possible explanations for the high turbulence intensities are given. The flow skewness factors and kurtosis factors (flatness factors) were calculated. The kurtosis value was in excellent agreement with the "near Gaussian" result expected.

The temporal autocorrelation was used to calculate the integral length scales, resulting in lengths 5.7, 2.0, and 1.7 cm, respectively - close to the expected pipe radius of 5.0 cm. The power spectral density was calculated and compared to values found in the literature. The study demonstrates that DAV is a simple, robust laser velocimetry method. Additionally, the results presented here illustrate that DAV is capable of measuring instantaneous velocity in order to measure turbulence characteristics.

INTRODUCTION

There are many aspects of a turbulent flow of which quantization is desirable. Knowledge of the turbulence intensity levels and characteristic scales allows valuable information and insight regarding turbulent mixing and transport.

Fluctuating turbulent velocity is difficult to measure because of several aspects. Using a physical probe to measure fluid velocity is undesirable because the probe itself effects the flow, rendering any measurements less valid. The frequency of the velocity fluctuations is high, meaning that some methods are unable to match response time. Optical methods are desirable because they do not disturb the flow, need no calibration, and give instantaneous velocity component information. With a turbulent velocity versus time signal, such quantities as the moments (mean, standard deviation, skewness, and kurtosis), the temporal autocorrelation (with integral time scale and microscale), and energy spectra may all be calculated.

Much work has been done to measure turbulent velocity with laser Doppler velocimetry (LDV), laser transit anemometry (LTA), and other methods. A new laser velocimetry technique, called diode array velocimetry (DAV), has been proposed in the past (Azzazy, M., Potts, R. L., Zhou, L., Rosow, B., 1997), and was used for this study. DAV is similar to LTA in that the probe volume consists of laser spots, therefore requiring no laser beam coherence. Because the laser spots used in DAV are much brighter than LDV fringes, excellent signal to noise ratios are achievable. DAV is similar to LDV in that Fourier transform methods are employed to calculate velocity from the burst signal. This is different from the "time of flight" measurement principle which LTA is based on. The main advantage of DAV is that probe volume generation is based on imaging a fixed laser diode array, making the optical arrangement simple, inexpensive, and robust.

This paper has several sections. The formulation of diode array velocimetry is described in detail giving mathematical descriptions of the laser diode and DAV signal. The signal processing involved is described next. The experimental optical and flow apparatuses are

then described. A review of relevant turbulence quantities and definitions follows. Experimental results are then presented and conclusions are drawn.

NOMENCLATURE

U	velocity
δ	spot spacing
x	sampling record
S	power spectrum
f	frequency
T_s	integral time scale
t	time
Sk	skewness factor
Kr	kurtosis factor
k	wave number, counting variable
R	autocorrelation
λ_m	microscale
Δt	time between bursts
τ	time lag
ρ	correlation coefficient
P	probability
v	average burst rate
f_l	focal length
I	Intensity
N	total number of samples
d	diameter
f_c	Nyquist frequency
T	total record time

PRINCIPLE OF DIODE ARRAY VELOCIMETRY

The light source used for DAV is a diode laser, which consists of an array of several laser spots. The intensity distribution of a laser diode is generally described by an elliptic Gaussian function (Yariv, 1975) such that

$$I(x, y) = I_0 e^{-2 \left[\frac{x^2}{w_x^2} + \frac{y^2}{w_y^2} \right]} \quad (1)$$

where w_x and w_y are the $1/e^2$ half widths of the Gaussian distribution. However, in most practical applications, the beam divergence in the direction normal to the diode junction (perpendicular to the array) is larger than the divergence along the diode junction (parallel to the array). Therefore, when a collimating lens is used to parallelize the laser light the collimated beam is often truncated in the y-direction (Bopp et al., 1989). Then, the intensity distribution can be described as the product of Gaussian function in the x-direction and a truncated Lorentz function in the y-direction. For a single laser this is,

$$I_s(x, y) = I_x(x) \cdot I_y(y) \quad (2)$$

with

$$I_x(x) = I_{x0} e^{-2 \left[\frac{x}{w_x} \right]} \quad (3)$$

and

$$I_y(y) = I_{y0} \begin{cases} \frac{w_y^2}{w_y^2 + y^2} & |y| \leq R_L \\ 0 & \text{otherwise} \end{cases} \quad (4)$$

where R_L is the radius of the collimating lens.

The optical pattern, generated by an array of laser diodes, is described by summing the output of a single laser diode over the array. Since the array extends in the x-direction, only I_x will be considered in the following analysis. Therefore, the optical pattern at the probe volume is expressed by the relationship,

$$I(x) = \sum_{k=1}^{N_L} I_x[x - (k-1)\delta] \quad (5)$$

where N_L is number of lasers. A high numerical aperture lens collimates the laser beams. A second lens, called the transmitter lens, then focuses these collimated beams into the probe volume. When an entrained particle passes through the probe volume the intensity of the light scattered will be that of several Gaussian shaped peaks corresponding to the particle passing through each laser spot. Substituting $x = ut$ into the above equations, the time dependent signal is then,

$$S(t) = AI_{x0} \sum_{k=1}^{N_L} \exp \left(-2 \left[\frac{ut - (k-1)\delta}{w_x} \right]^2 \right) \quad (6)$$

where A is a parameter which depends on particle size. The DAV signal characteristics described by Equation 6 resemble certain fringe LDV signal characteristics. Both signals have a Gaussian exponential term, and both have a periodic component along the x-direction, i.e., direction of the velocity component to be measured.

DAV OPTICAL EXPERIMENTAL APPARATUS

A laser diode array with five laser spots (100 mW per laser, $\lambda = 826$ nm) was used for the laser source, and is illustrated in Figure 1.

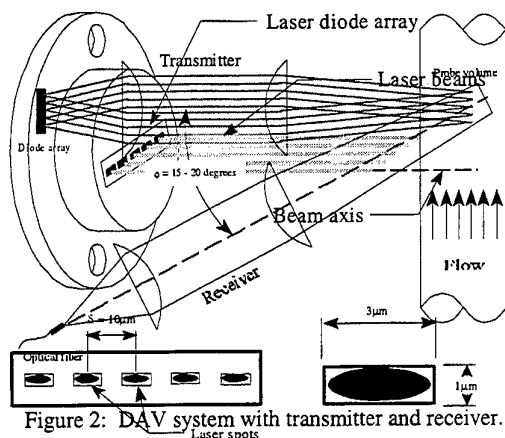


Figure 2: DAV system with transmitter and receiver.

Figure 1: Laser diode with array face dimensions.

Illustrated in Figure 1, the spot dimensions at the array face were $3 \mu\text{m}$ wide and $1 \mu\text{m}$ tall, and the spacing between laser spots was $10 \mu\text{m}$. The spot spacing at the array was verified by the use of a USAF resolution target ($2.2 \mu\text{m}$ between lines).

A 0.25 numerical aperture, $f_1 = 12 \text{ mm}$ lens collimated the diode array output, while a $f_1 = 100 \text{ mm}$, $d = 32 \text{ mm}$ transmitter lens focused the light into the probe volume. This corresponded to a probe volume spot separation of $83.3 \mu\text{m}$ between each of the five spots. The receiver consisted of a $f_1 = 300 \text{ mm}$, $d = 40 \text{ mm}$, and a $f_1 = 60 \text{ mm}$, $d = 32 \text{ mm}$ two lens system used to image a $100 \mu\text{m}$ pinhole at the probe volume, giving an overfill ratio of 1.5 . The receiver was situated in a side-scatter position, with the angle between the receiver and transmitter being approximately 15 - 20 degrees. Both the DAV transmitter and receiver fit on a breadboard mounted onto a translation stage allowing movement of the DAV probe volume across the entire pipe diameter. Figure 2 illustrates the DAV system showing the transmitter and receiver.

As can be seen in Figure 2, the probe volume is imaged into the flow, and, therefore, will be an image of the laser diode face. Thus, it will physically consist of several (5 in this case) focused laser spots, illustrated in Figure 3.

A $100 \mu\text{m}$ core multi-mode optical fiber transferred the light to an APD. From there, the signal was bandpass filtered and sent to the signal processing hardware and software. The digital signal processor used was a QSP model Q340 run on a 486-33 computer, and used a 40 MHz A/D board. The signal analysis software would perform real time frequency calculation

of each burst, convert to velocity, and write a velocity versus time record to the hard drive.

The alignment of the optics and the ability of the burst processor was verified by the using a $10 \mu\text{m}$ wire mounted to the wheel of an optical chopper (Stanford Research Systems model SR540). This simulated a single particle crossing the probe volume, and the RPM could be adjusted to simulate a wide range of velocities.

DAV SIGNAL PROCESSING

The primary function of the DAV signal processor is to acquire the burst signal, calculate the burst

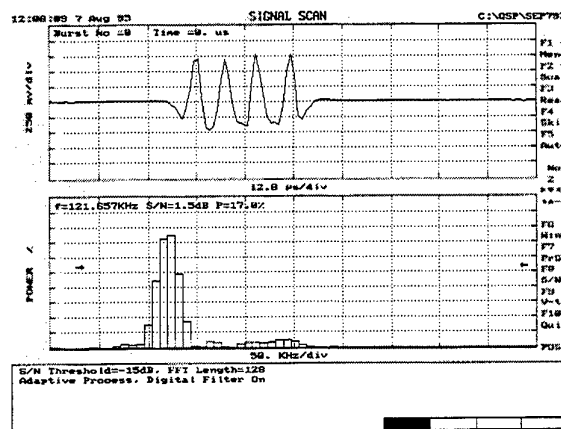


Figure 4: Filtered DAV signal and signal power spectrum.

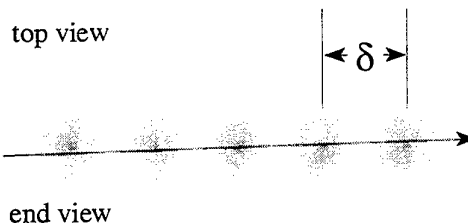


Figure 3: Close up of DAV probe volume with particle trajectory.

frequency in real time, apply the acceptance/rejection criteria, and save the accepted burst frequency. This is achieved through a series of operations. The signal passes through a high-pass filter to remove the zero lobe frequency (pedestal). The signal processing system digitizes the filtered signal and performs a discrete Fourier transform. It then calculates the power spectrum and determines the approximate burst frequency, i.e., the frequency bin at which the power spectrum is a maximum. Bin interpolation around the approximate frequency determines the exact burst frequency.

The signal processing system calculates the burst signal to noise ratio and accepts the burst data only if it

passes an accept/reject criteria that is designed to eliminate false signals. These include those signals generated by simultaneous multiple particles simultaneously in the probe volume. For turbulent flow measurements, the signal processing system builds a histogram of the accepted burst frequencies (realizations) and then computes the average velocity and the root mean square fluctuations.

The power spectrum of the signal from Equation 6 has a dominant zero lobe frequency which masks the desired frequency. Figure 4 shows the voltage vs. time signal and corresponding power spectrum of an unfiltered DAV burst.

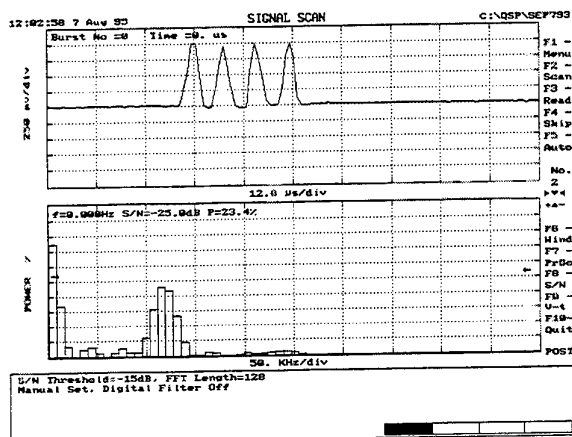


Figure 5: Unfiltered DAV signal and signal power spectrum.

A high-pass filter is used to remove this zero lobe frequency which is analogous to pedestal removal in the LDV technique. The high-pass filter acts as a time-derivative operator in the lower frequency regime. This produces a "sign alternating" characteristic in the signal and consequently removes the DC component and the strong lowest-nonzero-frequency lobe in the signal's power spectrum. Figure 5 shows the filtered DAV signal.

Figures 4 and 5 are actual bursts recorded with a 4 spot DAV system. The top part of the figures shows laboratory measurements of the time trace of the unfiltered and filtered signals respectively. Notice the "sign alternating" character of the filtered signal, in Figure 5. The bottom part of the figure shows the burst power spectrum. Also, notice the increase in the signal to noise ratio due to pedestal removal.

EXPERIMENTAL FLOW APPARATUS

A low speed (up to 35 m/s centerline velocity) wind tunnel was used to generate the flow. The wind tunnel consisted of an inlet section and flow straightener followed by twenty feet of 4 inch diameter smooth pipe. The optical probe was placed 60 diameters downstream

from the inlet. Optical access to the flow was provided by quartz windows shaped to the pipe. Seven more feet of pipe led into the blower, which was a 3 HP Dayton model 4c131 powered by an adjustable speed drive electric motor. The blower's shaft rpm had a range of 300 - 2300 RPM corresponding to air centerline velocities of 4 to 34 m/s (Reynolds numbers 2.5×10^4 - 2.2×10^5). The inlet to the tunnel was free and the blower sucked the air through the tunnel creating a steady turbulent pipe flow. The seeding particles used were micron scale aluminum oxide particles, and were introduced into the flow 20 diameters upstream.

ANALYSIS OF TURBULENT SIGNALS

For DAV, as well as other laser velocimetry techniques, bursts occur at random times, with the time between bursts following a Poisson distribution (Roberts, J. B., Downie, J., Gaster, M., 1980). The PDF of the burst inter-arrival times is known to obey

$$P(\Delta t) = v e^{-v\Delta t} \quad (7)$$

where v is the average burst rate. The Poisson distribution described in Equation 7 has a mean of $1/v$ and a variance of $1/v^2$.

The first moment of a random signal is the mean velocity while the second moment is the variance. The third moment, called the skewness factor, is found from the velocity fluctuation PDF, and is given by,

$$Sk = \frac{\int_{-\infty}^{\infty} (u(t) - \bar{u})^3 P(u') du'}{\left(\sqrt{\langle (u')^2 \rangle} \right)^3} \quad (8)$$

The skewness factor is an indication of how symmetric the velocity fluctuations are. The fourth moment, or kurtosis factor (often called the flatness factor) is similarly defined by,

$$Kr = \frac{\int_{-\infty}^{\infty} (u(t) - \bar{u})^4 P(u') du'}{\left(\sqrt{\langle (u')^2 \rangle} \right)^4} \quad (9)$$

There are many definitions for the autocorrelation and power spectrum of a random signal. However, most of these definitions are not applicable to randomly sampled random signals, and therefore, special algorithms must be used. The "slot" method of autocorrelation (Mayo, 1978, Srikantaiah, Coleman, 1985) is given by

$$R_k(\tau) = R(k\Delta\tau) = \frac{\sum [x(t_i)x(t_j)]_{k\Delta\tau}}{H(k\Delta\tau)} \quad (10)$$

$$k = 1, 2, 3, \dots, m$$

where $[x(t_i)x(t_j)]_{k\Delta\tau}$ is the sum of all of the products $x(t_i)x(t_j)$, and the difference $(t_i - t_j)$ falls in the slot $k\Delta\tau$. Slot $k\Delta\tau$ is the k^{th} slot, and has a width $k\Delta\tau$. $H(k\Delta\tau)$ is the total number of $x(t_i)x(t_j)$ products in the k^{th} slot. For the zero lag term, $k = 0$, the autocorrelation is

$$R_0(\tau = 0) = R(0) = \frac{1}{N} \sum_{i=1}^N x(t_i)^2 \quad (11)$$

with N being the total number of samples. The errors in the time domain for the autocorrelation estimation are $O(\Delta\tau/2)$, therefore, it is desirable to keep $\Delta\tau$ much smaller than $\Delta\tau_{\text{mean}}$.

From the autocorrelation, the integral time scale, T_s , may be calculated, and is given by

$$T_s = \int_0^{\infty} \rho(\tau) d\tau \quad (12)$$

where $\rho(\tau)$ is the correlation coefficient (the autocorrelation divided by its zero lag value). The integral time/length scale gives an indication of the largest eddies in the flow, which, for pipe flow should be the boundary layer, i.e. the pipe radius. The microscale, λ_m , which indicates the smallest "dissipation" scales in the flow is found from the relation

$$\left. \frac{d^2 \rho}{d\tau^2} \right|_{\tau=0} = \frac{-2}{\lambda_m^2} \quad (13)$$

The microscale can be found by fitting a parabola at the vertex of $\rho(\tau)$, given by

$$\rho(\tau) = 1 - \frac{\tau^2}{\lambda_m^2} \quad (14)$$

The one sided power spectrum, calculated using the results from the slot autocorrelation, is given by

$$S_k(f) = S\left(\frac{kf_c}{m}\right) = 2\Delta\tau \left[R_0 + 2 \sum_{r=1}^{m-1} R_r \cos\left(\frac{\pi rk}{m}\right) + (-1)^k R_m \right] \quad (15)$$

where

$$f = \frac{kf_c}{m}; \quad k = 0, 1, 2, \dots, m; \quad f_c = \frac{1}{2\Delta T} \quad (16)$$

with f_c being the Nyquist cutoff frequency.

EXPERIMENTAL RESULTS

The data for this study was obtained by generating a steady, turbulent pipe flow in the wind tunnel, and using DAV to record velocity vs. time. The focus was on obtaining data sets consisting of many samples at a high data rate in order to resolve the turbulence fluctuations in terms of moments, time correlations, and

spectral energy density. Three groups of data were recorded. In each group, the wind tunnel was held at a steady blower RPM value, and many data sets (40 - 50 data sets with ~ 4000 data points each set) were recorded at average sampling rates ranging from 100 to 900 Hz. The resulting data sets corresponded to statistically stationary turbulent centerline pipe flow.

Data Group	Blower RPM	Data Files	Samples	Ave Velocity (m/s)	STD (m/s)	Intensity (%)
1	500	50	3.0E+05	5.5	0.57	10.4
2	1200	50	2.0E+05	16.0	1.39	8.7
3	2100	40	1.6E+05	32.2	2.41	7.5

Table 1: Data recorded.

As can be seen in Table 1, the turbulence intensities are higher than expected. Turbulence intensities on the order of 5% have been recorded in the past (Hinze, 1975). Two possible explanations can be thought of. First, the most likely reason is that, although there were 60 diameters of smooth pipe before the measurement location, the inlet hose for particle introduction was located ~20 diameters upstream. The flow from this hose, which was spraying perpendicular to the flow direction, probably stirred up the pipe flow, generating some added large scale turbulence. A second possible explanation is that the settings on burst signal processor were too lenient with regard to signal to noise threshold. This would have allowed some erroneous data points, corresponding to poor S/N ratio signals, to be recorded.

A FORTRAN program was written to create a PDF of burst inter-arrival times for a DAV data file, comparing the measured burst time lags versus the theoretical PDF predicted by Equation 7.

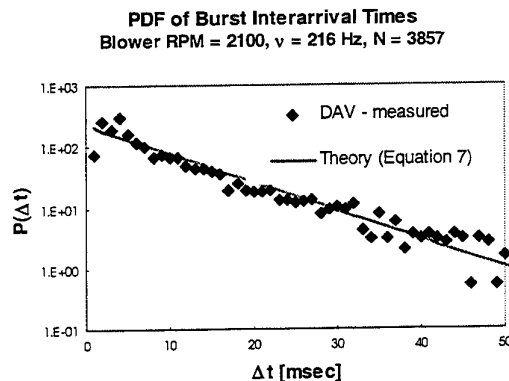


Figure 6 : Graph of burst inter-arrival times.

As can be seen in Figure 6, there is excellent agreement between the measured and theoretical $P(\Delta t)$ for most values of Δt . At very small values of Δt the measured

Data Group	Blower RPM	Integral Time Scale (ms)	Integral Length Scale (cm)
1	500	10.30	5.7
2	1200	1.29	2.1
3	2100	0.53	1.7

Table 3: Calculated integral time and length scales.

vs. theoretical begin to diverge. This is because real burst processors have limitations. The burst processor used in this study processes each burst in "pseudo real time". When a burst occurs, the trigger voltage threshold is exceeded and a specified number of data points (equal to the FFT length) are written to the SRAM on the A/D card. This burst packet of samples is then written to the hard drive of the computer where the signal is digitally processed. However, the SRAM on the A/D card is not bi-directional, meaning that it can only be reading or writing at one time, but not both. Therefore, after each burst is taken into the SRAM, the

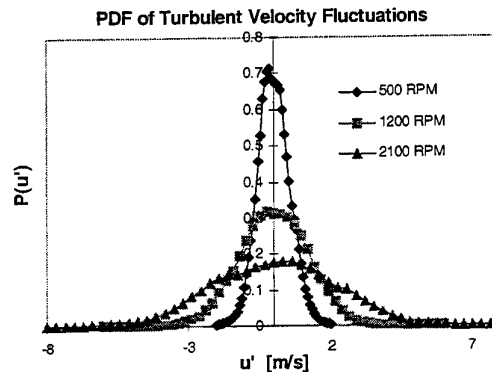


Figure 7: PDF's of turbulent velocity fluctuations.

A/D card is not ready for another burst until the present burst has been written to the hard drive. Unfortunately, although SRAM is very fast, the ISA-bus dictates how fast the burst information is written to the hard drive. This means that there will be a certain range of small Δt 's where there will be few or no burst pairs. For the data taken in this study the minimum time lag was about 4×10^{-4} seconds.

The PDF of the u-component velocity fluctuations, $P(u')$, was recorded and is shown in Figure 7. Equations 8 and 9 were used to calculate the skewness factor and the kurtosis factor, and the results are presented in Table 2.

Data Group	Blower RPM	Skewness Factor	Kurtosis Factor
1	500	0.11	2.94
2	1200	-0.35	2.67
3	2100	-0.21	2.21

Table 2 : Calculated skewness and kurtosis factors.

As can be seen from Table 2, the kurtosis factor is close to the near Gaussian value of 3, which is expected of turbulent pipe flow. The skewness factor results above show that the flow are slightly non-symmetric, and no explanation is given for this.

For the autocorrelation, the "slot" method was used, and the high number of samples ensured that an accurate autocorrelation was constructed. Another FORTRAN program was used to calculate the autocorrelation from Equations 10 and 11. The correlation coefficient was calculated from the autocorrelation. Following Equation 12, $\rho(\tau)$ was integrated, yielding the integral time scales for each data group. When multiplied by the mean velocity the result is the integral length scale. These results are summarized in Table 3.

Physically, the integral length scale corresponds to the size of the largest eddies in the flow. The expected

result is that of the boundary layer, or pipe radius - 5 cm. As can be seen above the integral length scale calculated from group 1 was 5.7 cm and agreed well with the expected. For groups 2 & 3 slightly smaller integral length scales were calculated, but were within a reasonable centimeter scale range. Because of the minimum time lag of the burst processor the $\rho(\tau)$ bin size was too large to have the necessary resolution needed to calculate the microscale.

The power spectrum was calculated from Equations 15 & 16. To quantitatively compare the power spectrum results with the literature (Hinze, 1975, Laufer, 1952) it was necessary to nondimensionalize the data. Frequency was converted to a nondimensional wave number, $(D/2)k$, using the following relations.

$$k = \frac{2\pi}{r_0} \quad r_0 = Ut = \frac{U}{f} \quad (17)$$

Then,

$$\frac{D}{2}k = \frac{D}{2} \frac{2\pi}{U} f = \frac{D\pi}{U} f \quad (18)$$

The power spectral density was normalized by $1/u^2$ as well. The previous data used (Figure 4-9 of Hinze, 1975) corresponded to pipe flow at a Reynolds number of 5×10^5 , which was slightly higher than the present experiment. However, little variation is expected in the power spectrum with differing Reynolds number (Figure 8 of Lawn, 1971). The results are shown in Figure 8.

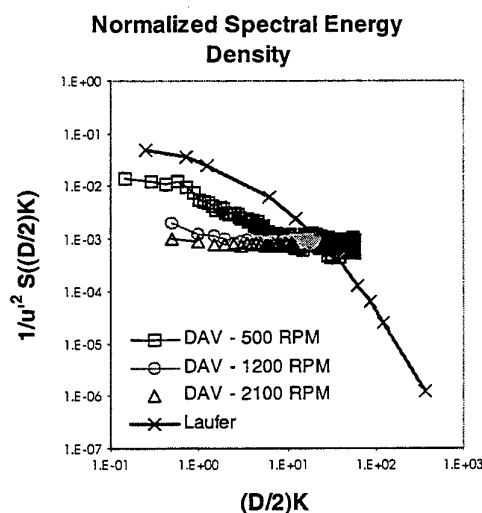


Figure 8: Normalized power spectrum of DAV data.

As can be seen in Figure 8, the measured power spectrum doesn't compare very well with Laufer. Of the 3 data sets, only set 1 (500 RPM) follows the same trend at small values of $(D/2)k$. For values of $(D/2)k$ over 10

the measured values should drop away but do not. It is suspected that errors in the small time lag portion of the autocorrelation are responsible for the errors in the high $(D/2)k$ range (high frequency range). The main problem was that there was not a sufficient amount of data at very high frequencies. As stated before, it is believed that the restricted throughput of the burst processor is to blame, and not DAV itself. If a faster signal processor was used then better high frequency information would be expected.

CONCLUSIONS

It has been shown (Azzazy, M., Potts, R. L., Zhou, L., Rosow, B., 1997) that DAV is comparable to LDV for measuring mean velocity. However, because little work has been done to make DAV directionally sensitive, only flows whose flow direction is known are appropriate. In the present study, advantage was taken of knowing the direction of the x-component of velocity for pipe flow. Also, because the ability of DAV to be extended to multi-component instantaneous velocity measurement has not been investigated, the experimenter is limited to one-component measurements. Therefore, there are many turbulent flows where DAV, at its current level of development, cannot be used for accurate turbulence measurements.

It is suspected that, because DAV has much fewer spots than LDV has fringes, some problems are likely. First, this means that the pedestal frequency for DAV will be much closer to the burst frequency, making filtering more difficult. Additionally, because of the small number of laser spots in DAV, it is suspected that there will be a higher burst rejection rate, resulting in a higher dropout rate (lower duty cycle). Indeed, when DAV and LDV were used for similar flows, under similar seeding conditions, the DAV results had a higher dropout rate. In this study it was suspected that the sparseness of the sampling could be due to this. However, since signal acceptance or rejection depends on many settings it would require further study to quantify this for certain.

This study does show that, for appropriate flows, DAV is capable of adequately measuring instantaneous velocity versus time records. Given the appropriate treatment of these records, turbulence quantities such as moments, correlations, and the power spectrum may be calculated yielding useful qualitative and quantitative information about a turbulent flow.

ACKNOWLEDGMENTS

This work was performed under U.S. Department of Energy, Office of Basic Energy Sciences grant #DE-FG03-89ER14033 A002. Additionally, support was

provided by Grant #NCC 2-374 of NASA Dryden Flight Research Center, Edwards AFB, California.

REFERENCES

Azzazy, M., Potts, R. L., Zhou, L., Rosow, B., (1997) "Flow Velocity Measurements Using Laser Diode Array", *Journal of Applied Optics*.

Bopp, S., Durst, F., Meller, R., Naqwi, A., Tropea, C., and Weber, H., (1989) "Small Laser Doppler Anemometers Using Semiconductor Lasers and Avalanche Photodiodes", *Applications of Laser Anemometry to Fluid Mechanics*, R. J. Adrian, T. Asanuma, D.F.G. Durão, F. Durst, and J.H. Whitelaw (Eds.), pp. 315-337.

Durst, F., Melling, A., Whitelaw, J. H., (1981) *Principles and Practices of Laser Doppler Anemometry*, Second Edition, Academic Press.

Hinze, J. O., (1975) *Turbulence*, McGraw Hill, Inc. Second Edition.

Huckle, E., (1997) "Measurement of Turbulent Pipe Flow with Diode Array Velocimetry", *Masters Thesis*, University of California, Los Angeles.

Laufer, J., (1952) "Structure of Turbulence in Fully Developed Pipe Flow", NACA Rep. 1174.

Lawn, C. J., (1971) "The Determination of the Rate of Dissipation in Turbulent Pipe Flow", *Journal of Fluid Mechanics*, v.48, part 3, pp.477-505.

Mayo, W. T. Jr., (1978) "Spectrum Measurements with Laser Velocimeters", *Proceedings of the Dynamic Flow Conference*, pp.851-868.

Roberts, J. B., Downie, J., Gaster, M., (1980) "Spectral Analysis of Signals from a Laser Doppler Anemometer Operating in the Burst Mode", *Journal of Physics - E: Sci. Instrum.*, v.13, pp.977-981.

Srikantaiah, D. V., Coleman, H. W., (1985) "Turbulence Spectra from Individual Realization Laser Velocimetry Data", *Experiments in Fluids*, v.3, pp.35-44.

Yariv, A., (1975) *Quantum Electronics*, pp 123-126, John Wiley.

APPLICATION OF DIGITAL HOLOGRAPHIC INTERFEROMETRY TO VISUALIZE BUOYANCY CONVECTION

B. Skarman*, K. Wozniak+ and J. Becker #

* Saab Dynamics AB, 58188 Linköping, Sweden

+ University-Essen, Chair of mechanics, D-45127 Essen, Germany

ESA/ESTEC, 2200 Noordwijk zh, Netherlands

ABSTRACT

Microgravity research in the field of fluid physics asks for non-invasive optical diagnostic tools to perform measurements on the geometry of fluid bodies, velocities of particle motion and temperature distributions. Real simultaneous measurements on all parameters involved are necessary for the understanding of the phenomena. The real phenomena are mostly dynamic and three-dimensional. The space application requires robust and reliable instruments, which can be easily operated from ground. Concerning the imaging tools that means, the use of electronic media is the preferred solution. On that background some developments try to improve the interferometer techniques used to perform e.g. measurements on temperature fields. Here in this study the maturity of a fully electronic version of a substitute for a double exposure holographic interferometer is demonstrated. The new method has the additional advantage, to provide truly simultaneously the velocity distribution of the particle flow throughout the whole experimental volume. To come to a realistic quantitative comparison, a well understood experiment studying Bénard Convection was repeated and the measurements were successfully performed with the new tool.

1. INTRODUCTION/BACKGROUND

This development started some years ago triggered by the question:

how can interferometers, to be used for microgravity research in the field of Fluid Physics, be improved? This question concerned the reflight of existing facilities (e.g. HOLOP, BDPU) and the new Fluid Science Laboratory (FSL), planned to be flown on the International Space Station (ISS) within the European Module, the Columbus Orbital Facility (COF) (Figure 1).

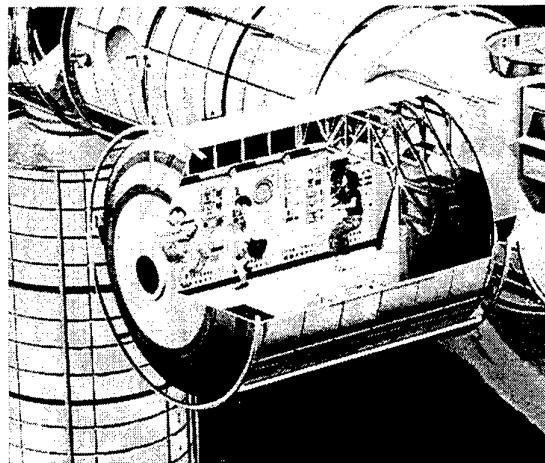


Figure 1: Columbus Orbital Facility

The Fluid Science Laboratory is currently in Phase C/D, and its launch is planned together with the COF module end of 2002. The Fluid Science Laboratory will be a multi-user research facility dedicated to the study of Fluid Physics in its widest sense. This will include 'classical' Marangoni – Bénard Convection as well as new areas getting more and more interest like

crystal growth in solution, plasma crystals and colloid physics. (Figure.2)

there are competing media to store holograms :

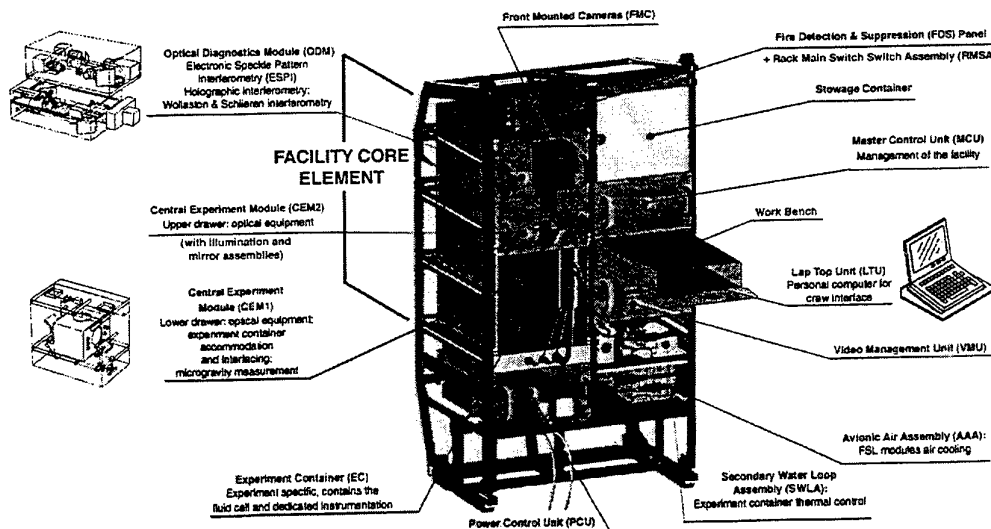


Figure 2: Fluid Science Laboratory

Compared to the old facilities, the new one became highly modular, to provide the flexibility for future upgrades. This concerns the diagnostic modules as well as the whole core element itself. As in the past, the experiments themselves will find their place in Experiment Containers (EC's) to be sequentially inserted and operated.

The Fluid Science Laboratory will offer among other diagnostic tools more than one type of interferometric measurement technique, i.e.:

- Holographic double exposure interferometer
- Differential (Wollaston) interferometer
- Electronic Speckle Pattern Interferometer (ESPI) with a reflective and transparent mode

What concerns holographic interferometry, during FSL project Phase B the concept was to use again the holographic thermoplast film camera. In the meantime

- Larger photorefractive crystals and
- CCD/C-MOS arrays with ever increasing resolution.

This study demonstrates the benefits of the last medium respectively technique.

A method has been developed to record digital holograms with a CCD-camera. A digital hologram is here regarded as a pixel image, where each pixel is complexly valued and contains the amplitude and the phase of the optical wave front in the plane of the CCD-element.

The phase information is comparable with the information in an interferogram and can be used to calculate an interferogram. The amplitude information can be used to calculate an image of an object.

The complete description of the optical wave front makes it possible to use the methods of wave optics to calculate the wave front in an arbitrary plane. This then is equivalent to calculating a focused image of an object in a selected plane. The refocusing is based on an algorithm, which is easily implemented on a computer. The refocusing is illustrated on a hologram of a

slide in figure 3, where the upper image shows the actual focusing on the CCD and the lower the result of digital refocusing.

A wide range of applications can be found for this method. The method can be even applied to microscopic images, where the depth-of-field in general is very limited. The method offers the possibility to record images and then to refocus off-line. Much larger ranges in depth can be covered. In a field-of-view of 0.5×0.5 mm one can refocus within a range of ± 0.5 mm.

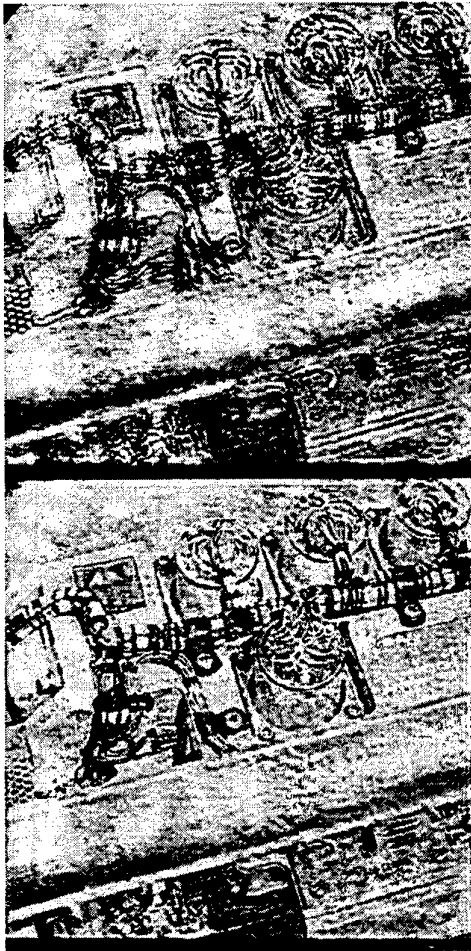


Figure 3: Digital refocusing

These principle features make this technique an interesting candidate for a diagnostic tool for experiments in the field of Fluid Science. Here interferometric images were used in the past to perform

measurements on temperature fields and visual images of light sheets provided the necessary information about the velocities of convection flow within the fluid matrix marked by small tracer particles.

Two diagnostic instruments had to be used real simultaneously to collect these data.

The situation improved with the 'liquid crystal tracer technique', that allows for the first time a real simultaneous measurement of velocities and temperature distributions (Figure 9).

But in cases of higher flow velocities, the limited scanning speed of the light sheet across the fluid cell prevents the real simultaneous observation across the whole fluid volume.

Earlier studies (Skarman et al (1996)) demonstrate that the new holographic technique has the potential to perform both measurements really simultaneously throughout the whole fluid volume, provided that the density and size of the tracer particles are adapted accordingly.

Here in the latest development study the new method has been further improved and compared quantitatively with the old methods on the basis of a repetition of a typical experiment related to Bénard convection. The results will show, that the new method is mature to be applied to similar experiments.

2. OVERVIEW OF THE METHOD FOR RECORDING HOLOGRAMS

2.1 OPTICAL SET-UP

An optical set-up as shown in the right part of figure 4 is used.

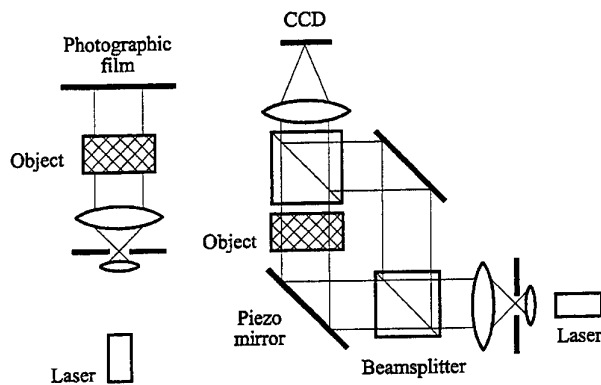


Figure 4: Optical set-up

The object is backlit with a laser, in this case a HeNe laser. A reference beam is also derived from the laser. The object and reference beams are parallel after a combiner in front of the CCD camera. A phase shift can be introduced in the object beam by moving a mirror with a piezo-electric element. The motions are fractions of a light wavelength. The optical system is focused so that a plane within or close to the object volume is in focus.

Through the use of phase-shifting the drawbacks of conventional in-line holographic methods as shown in the left part of figure 4 and described in Vikram (1990) can be avoided.

2.2 ALGORITHMS

Basic for the method of recording digital holograms is the phase-shifting method see for example Creath (1985). The fundamental relation for interferometry and holography is as follows. The intensity $I(x,y)$ recorded on photographic film or on a CCD-sensor is

$$I(x,y) = |O(x,y) + R(x,y)|^2 = |R(x,y) \cdot \gamma(x,y) \cdot \exp(j\phi(x,y)) + R(x,y)|^2 = |R(x,y)|^2 \cdot (\gamma(x,y)^2 + 1 + 2\gamma(x,y) \cdot \cos \phi(x,y))$$

(1)

where

x,y are coordinates in the CCD (or film) plane.

$R(x,y)$ is complex valued and describes the amplitude and phase of the reference wave

$O(x,y)$ is complex valued and describes the amplitude and phase of the object wave

$\gamma(x,y)$ is real and is the transmission or reflection coefficient of the object

$\phi(x,y)$ is real and is the phase shift caused by the object plus phase shifts caused by the interferometer.

$|R(x,y)|^2 \cdot \gamma(x,y) \cdot \cos \phi(x,y)$ is the term that forms an interferogram.

In interferometry $\phi(x,y)$ is the interesting quantity, which is observed through the transformation $\cos \phi(x,y)$. Note that $\cos \phi(x,y) = \cos(\phi(x,y) + k \cdot 2\pi)$ so that only $\phi(x,y)$ modulo 2π appears. If the transmission/ reflection coefficient $\gamma(x,y)$ is not constant or the laser beam is inhomogeneous the phase information is distorted, if no further processing is done. The interferogram does not immediately permit the evaluation of the phase as a numerical quantity, but is a kind of contour plot, that in itself is illustrative. With so called phase-shift methods other presentation forms are possible. (Another method to record digital holograms is described in Schnars et al (1994). This method, however, does not allow the same spatial resolution.)

2.2.1 PHASE-SHIFT METHODS

If one can record a number ($i \geq 3$) digitised images $I_i(x,y)$ of the object and introduces known phase-shifts $\Delta\phi_i$ in the object beam, solutions for every image pixel of $R(x,y)$, $\gamma(x,y)$ and $\phi(x,y)$ are obtainable. The result is a numerical, undistorted value for $\phi(x,y)$. $\phi(x,y)$ is still known modulo 2π .

The phase-shift algorithm works as follows (for simplicity of notation the arguments x and y have been left out). Represent I as

$$I = a \cdot (1 + m \cos \phi) \quad (2)$$

Then a , m and ϕ can be calculated from the phase-shifted images. (Three unknowns and at least three equations pro pixel.) By identification of coefficients in (1) one can solve for physical parameters.

Calculate

$$E(x, y) = \exp[j \cdot \phi(x, y)]$$

$E(x, y)$, which is a complex image, may be regarded as a digital hologram of an object with a constant transmission coefficient $\gamma(x, y)$. The distortion of the phase information due to $\gamma(x, y)$ mentioned above is thus eliminated. $\text{Re}(E(x, y))$ can be interpreted as an interferogram. $\phi(x, y)$ is the modulo 2π phase angle.

Differential holographic interferometry can also be implemented by the recording of two states $E_1(x, y)$ and $E_2(x, y)$.

$$E_1 = \exp(j\phi_1) \text{ and } E_2 = \exp(j\phi_2)$$

The difference can be visualised with

$\Delta\phi = \arg E_1(x, y) - \arg E_2(x, y)$, where $\Delta\phi$ is adjusted to fall in the range $[-\pi, \pi]$.

2.2.2 PHASE UNWRAPPING

As stated above the phase is observed modulo 2π . It is, however, desirable to know the phase ϕ without this limitation. Then the evaluation of e.g. density- or temperature fields in a fluid is possible. $\phi(x, y)$ is assumed to be continuous in x and y . Fig 5a shows the phase modulo 2π . Following the curve from

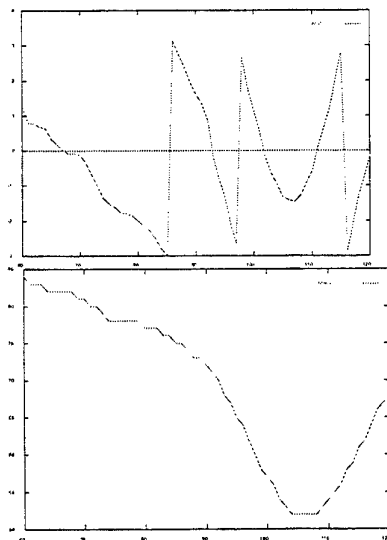


Figure 5a and 5b: "Wrapped" phase and "Unwrapped" phase

left to right one adds 2π to all values to the right of a jump in the curve, if the slope is positive before the jump. If the slope is negative one subtracts. In this study we applied a more advanced method which works in two dimensions.

2.2.3 IMAGING HOLOGRAPHY

The optical set up and appropriate numerical algorithms permit imaging of objects in a backlit volume. This is valid for objects with transmission coefficients in the range $[0.0, 1.0]$. The digital hologram is the complex valued field $H(x, y) = \gamma(x, y) \cdot \exp(j\phi(x, y))$. An expression for $\gamma(x, y)$ can be calculated by identifying coefficients in (1) and (2).

The intensity of this field is $I_H(x, y) = H(x, y) H(x, y)^* = \gamma(x, y)^2$ which is a real valued field and is an image of the object. It is interesting to note, that it is also possible to numerically refocus images recorded in this way.

The procedure is as follows

- 1: Calculate H_{ij} , which is $H(x, y)$ in discrete, equidistant points
- 2: Calculate the two-dimensional discrete Fourier transform F_{kl} of H_{ij} with the Fast Fourier transformation algorithm.
- 3: Apply the following transformation

$$\exp[j \cdot \pi \cdot \lambda \cdot \frac{\delta}{s^2} \cdot (k^2 + l^2)] \cdot F_{kl}$$

where

s the linear size of the object

δ the refocusing distance

λ the light wave length

i, j and k, l pixel indices (j is also used as the imaginary unit)

F the discrete Fourier transform of the recorded image

4: Calculate the inverse Fourier transform

E_{ij}

5: Calculate $I_{ij} = E_{ij} E_{ij}^*$, which is the refocused image intensity.

Recording of a sequence of digital holograms enables the tracking of particles. The holograms contain information about all tracer particles within a volume. By determining the point of best focus for individual particles their position in the depth dimension can be calculated. Comparison of positions in a sequence of images gives the flow directions.

2.3 HARDWARE EQUIPMENT

The digital holography equipment consists of an interferometer with a HeNe-laser, a piezo-electrically controlled mirror for phase shifting, a black-and-white video camera, a video digitiser that digitises 512×512 pixels with 8 bit resolution. For control of recording and image processing a PC with a Pentium processor is used. Piezo control and video digitisation are realised with standard PC boards. The motion of the piezo driven mirror is linear during the recording of the four images, which are used for the application of the phase-shift algorithm.

MEASUREMENT OF THE VELOCITY DISTRIBUTION OF TURBULENT FLOW BY THE LASER PHOTOTHERMAL EFFECT WITH A CCD-LD-INTERFEROMETER

Noboru Nakatani

Department of Industrial Engineering, Ashiya University
13-22, Rokurokuso-cho, Ashiya, Hyogo 659-8511, Japan

ABSTRACT

This paper describes the tagging velocimetry system for measuring the velocity distribution of turbulent flow using the photothermal effect. We use a differential interferometer with a little influence of external disturbance for detecting photothermal effect. For reducing influence of phase fluctuation due to turbulent flow in detecting the photothermal effect, we use a CCD camera synchronization in association with double pulses of a laser diode for recording images of the differential interferometer. And the obtained images before and after pumpings are differentiated by an image processor. The velocity is measured by the time flight of the tagged line induced by photothermal effect. Using jets of a gas mixture of nitrogen and ethylene, we confirm that this measurement system is useful to measure flow velocity distribution in turbulent flow.

1. INTRODUCTION

Particle Image Velocimetry (PIV) [Adrian(1991)] and Doppler Particle Global Velocimetry (DGV) [Meyers (1995)] have been developed for the measurements of flow velocity distributions. However, these methods need to seed scattering particles in a flow; this is not desirable in many

testing environments. For example, the seed particles do not faithfully reproduce the gas flow in high speeds. Gas-phase Doppler-shift velocimetry methods that do not require seeding have been developed by use of laser-induced fluorescence (LIF) [Klavuhn et al(1994)] and Rayleigh scattering [Miles et al (1990)]. At low velocities these Doppler shift methods are inaccurate. Recently, to be freed from these problems, velocimeters using a photothermal effect have been investigated [Nie et al (1986)], [Nakatani et al(1994)]. In the velocimeters velocity distribution was measured point by point.

In our previous study [Nakatani (1997)] we developed the tagging velocimetry system for measuring the velocity distribution of gas flow using the photothermal effect in laminar state. Photothermal velocimeter was proposed by Nie et al (1986). The medium is heated by absorbing the optical energy from a pump-pulse beam and the refractive index of the medium decreases. The change of refractive index was detected by a beam deflection method. In our study, in order to increase the sensitivity, to detect the fast change in refractive index of gas flow and to decrease the influence of external disturbances, we used a differential interferometer of a homodyne type. For reducing influence of optical distortions and

noises, interference patterns were processed by an image processor. The velocity was measured by the time flight of the tagged line induced by photothermal effect.

In this study we make possible to measure flow velocity distribution in turbulent state by reducing the influence of phase fluctuation due to turbulent flow on the interferometer. We use a CCD camera synchronization in association with double pulses of a laser diode for recording images of the differential interferometer, and the obtained interference images before and after pumpings are differentiated by an image processor. Using jets of a gas mixtures of nitrogen and ethylene, we confirm that this measurement system is useful to measure the flow velocity distribution in turbulent flow.

2. MEASURING SYSTEM

The method and the schematic diagram of the tagging velocimetry system are shown in Figs. 1 and 2 respectively. A jet of a gas mixture of nitrogen and ethylene is used as a flow. A pump beam is irradiated to flow for producing a photothermal tagged line. The photothermal tagged line is convected downstream and is observed by the differential interferometer at the time-of-flight delay. The difference in the phase between the measuring points is measured for obtaining the velocity distribution.

The differential interferometer developed by Smith(1955) is used for detecting phase change by photothermal effect. A circular laser diode of 635 nm in wavelength and of 15 mW in power is used as a light source of double pulses. Because the laser diode is suitable to make short pulse light in high frequency and the circular laser diode makes possible to utilize the output power of the

diode effectively. An integrated, internal, beam correcting micro-lens is used for making the circular beam from the elliptical beam. The laser beam is expanded to 40 mm diameter with lenses L1, L2 and L3 for illuminating uniformly flow field in post optical path. The polarisation direction of the laser beam is rotated at angle of 45 degree to the optic axis of a Wollaston prism with a half-wavelength plate between the lenses L1 and L3. After the laser beam passes through a flow field, the beam is focused into a Wollaston prism in dividing angle 2.5 mrad with a lens L3 in focal length 200 mm for dividing two beams. The pair beams are passed through an analyzer and are interfered on an image plane. The phase difference at two points of objects separated by the distance 0.5 mm between the pair beams is detected as shown by the dashed lines in Fig. 2. The operating point of the interferometer at a detector output signal is set at the maximum inclination point of a fringe intensity curve by displacement of the Wollaston prism. We use a CCD camera synchronization in association with double pulses of the laser diode for recording images of the differential interferometer. Owing to wide availability and low cost, we use an interlaced interline CCD camera for recording images of the differential interferometer.

The interference images before and after pumpings are recorded, as shown in Fig. 3 at the location of the pulses of the laser diode on odd and even fields in the CCD camera. As the laser diode is pulsed twice during the time when odd-line and even-line fields are integrating light respectively, the interference images are separately recorded on the frame memory. Each one of the recorded images of the two fields is output as 2:1 interlaced and NTS video signal from the frame memory separately. So the interference images without the interlacing affect

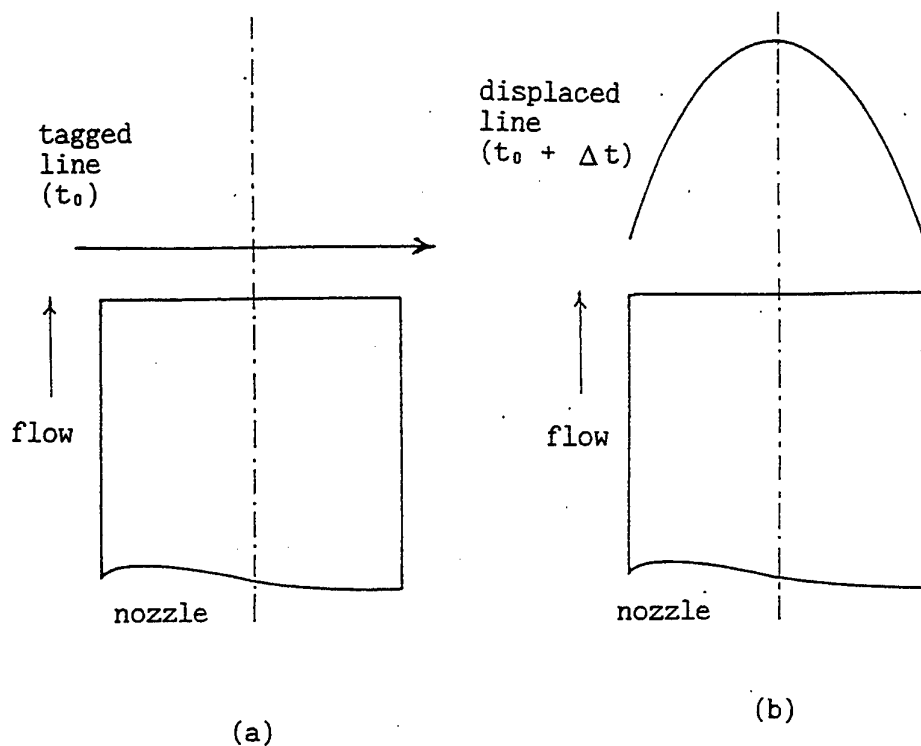


Fig. 1 Tagging method using photothermal effect for the measurement of flow velocity distribution. (a): Pumping at t_0 . (b): Observation at $t_0 + \Delta t$.

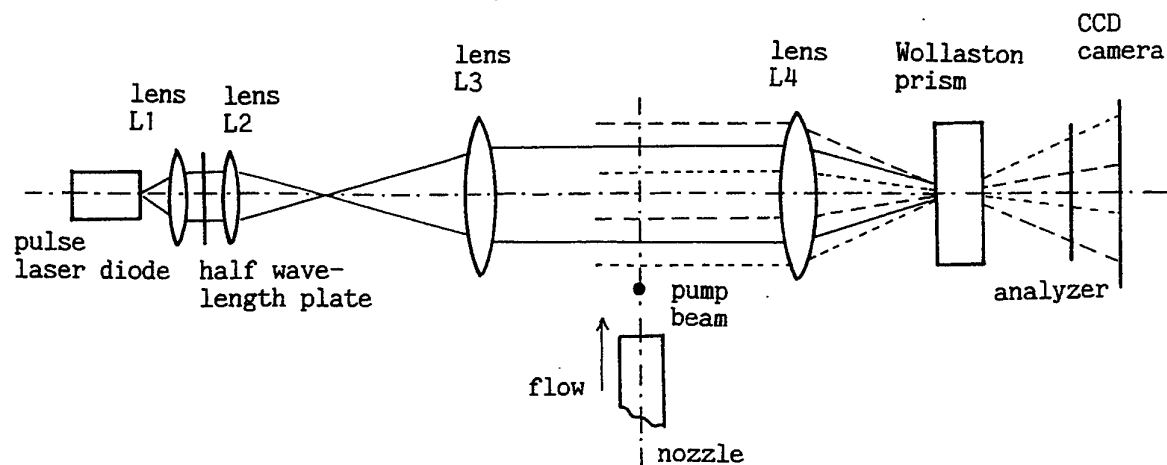


Fig. 2 The measurement system of flow velocity distribution using a differential interferometer.

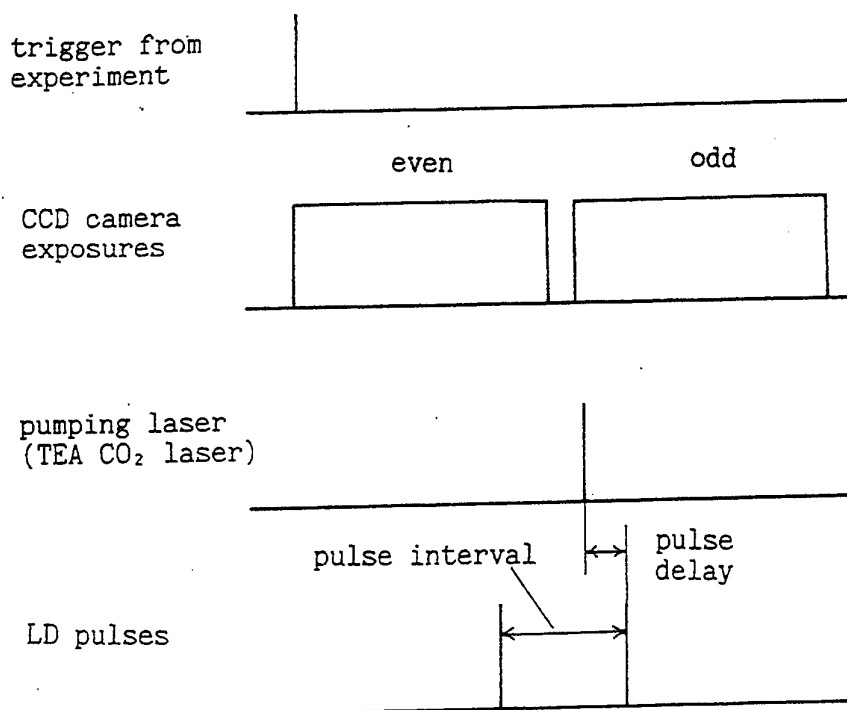


Fig. 3 The external synchronization of the CCD camera cycle with the pulses of a laser diode and the pumping pulse laser.

are produced. To reduce the fluctuation of the phase difference due to turbulence, optical distortion and noise, the images before and after pumpings are differentiated by the image processor as described in next section. We investigate on influence of phase fluctuation on the differential interferometer shown in Fig. 2 in turbulent flow. The nozzle of 4.8 mm in diameter is used. Mixture of nitrogen and ethylene of a 9 : 1 in volume ratio is used as a fluid. Reynolds number is 3500. The phase variation arises from large scale air entrainment by the jet and turbulent mixing. The intensity of the differential interferometer is measured by a photomultiplier. The detected phase difference is shown in Fig. 4, and the power spectrum density of the phase difference, in Fig. 5. This phase fluctuation makes the

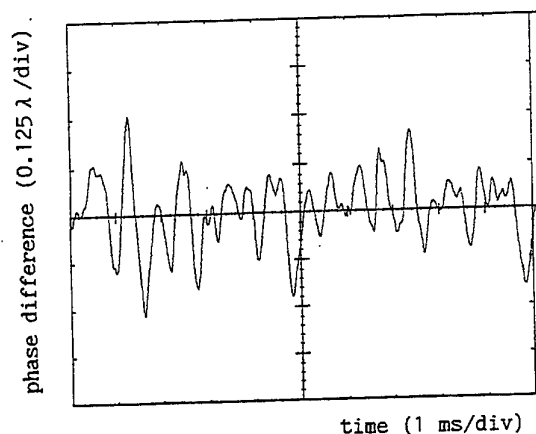


Fig. 4 Typical oscilloscope trace of variation of phase difference in turbulent flow. Reynolds number is 3500. Wavelength λ is 635 nm.

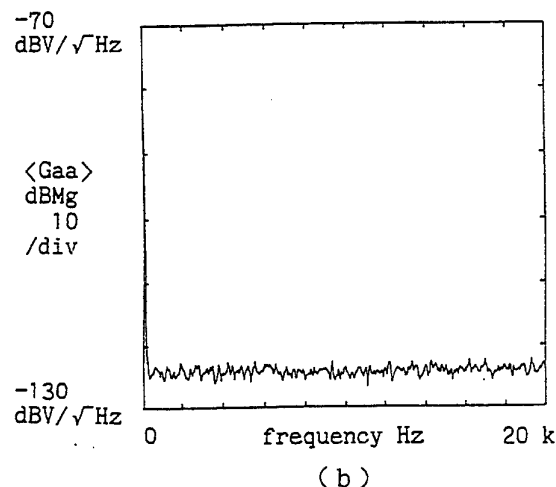
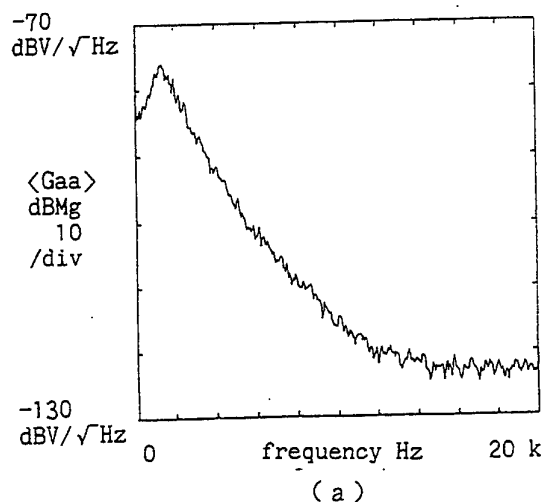


Fig. 5 Typical power spectrum densities of fluctuation of phase difference, $0 \text{ dBV} = 12.5 \lambda$ (λ : 635 nm). (a): In turbulent state. (b): Laminar state.

image quality of the differential interferometer worse.

The analytical model of photothermal image is shown in Fig. 6. Figure (a) shows the relation between the moving puff of phase variation caused by the photothermal effect and the pair probe beams, and figure (b) shows the intensity distributions measured along axis in moving direc-

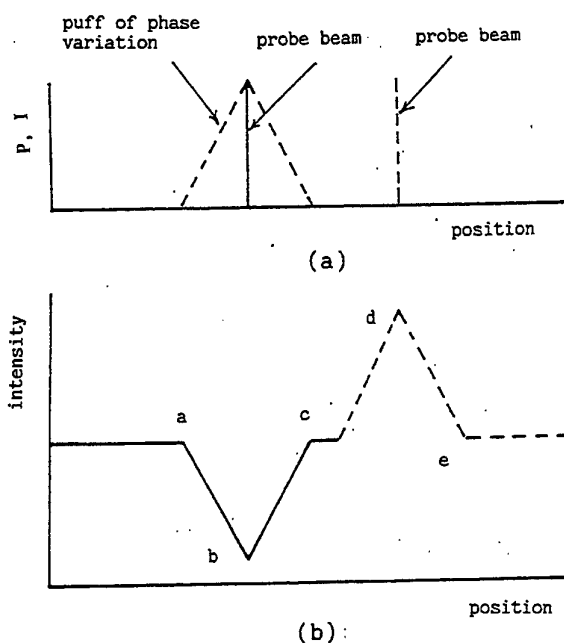


Fig. 6 Analytical model of an observed photothermal signal. (a): Relation between the puff of phase variation and the probe beams. P is phase variation and I is the intensity of a probe beam. (b): Observed intensity distribution.

tion of the puff of phase variation. The Gaussian distribution of the phase variation is simplified by a triangular shape. The phase differences at each two observing points separated by the distance (0.5 mm) between the pair beams are detected. The width of the puff is smaller than the distance between the pair beams. The image points a, b, c, d and e can be used to measure the displacements of puff.

3. MEASUREMENT OF FLOW VELOCITY DISTRIBUTION

Using a jet of a 9:1 in volume

mixture of nitrogen and ethylene, it is demonstrated that this technique is useful to measure flow velocity distribution in turbulent state. The nozzle of the inner diameter in 4.8

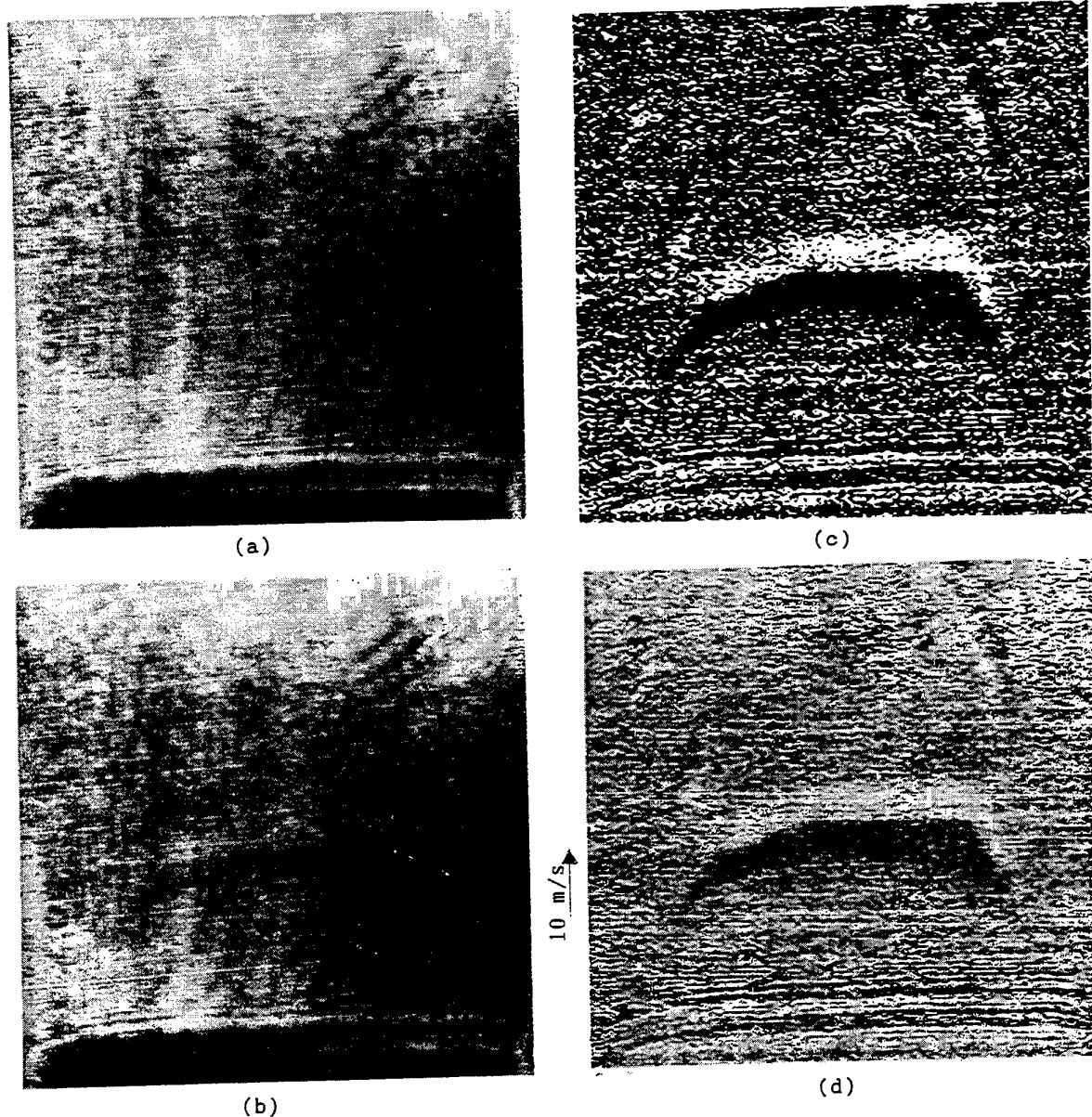


Fig. 7 Patterns of observed with the system shown in Fig. 2 for measuring flow velocity distribution. (a): Image before the pumping. (b): Image at 100 μ s after the pumping. (c): Image obtained by processing of images (a) and (b) (subtracting and multiplying constant). (d): Image obtained by processing of images (a) and (b) (adding constant, subtracting, and multiplying constant).

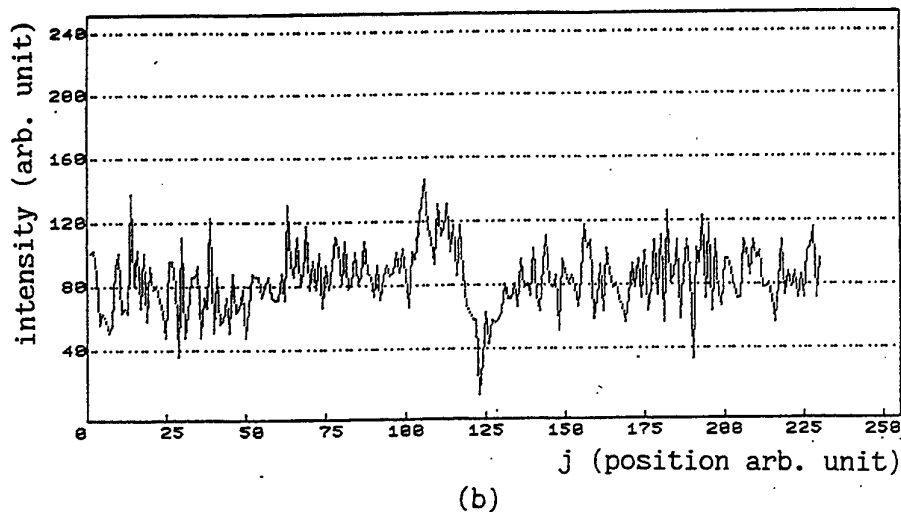
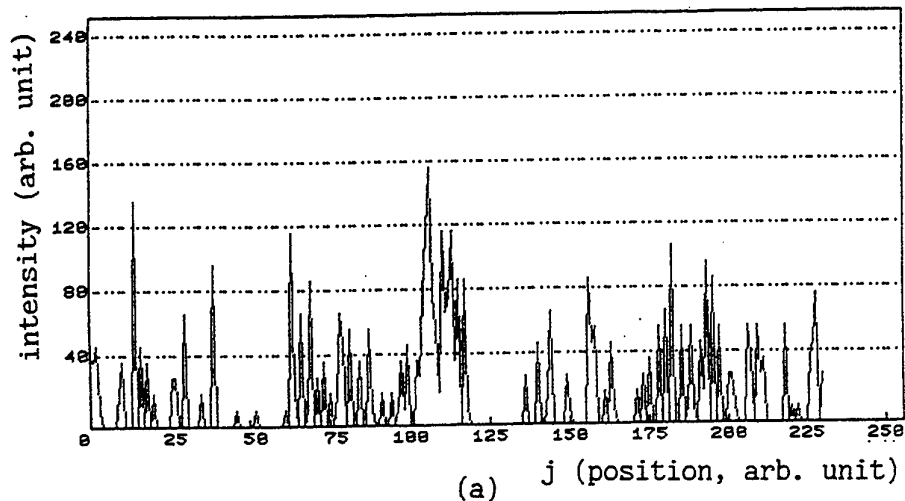


Fig. 8 Intensity distributions of images on centerline of jet.
 (a): Image (c) shown in Fig. 7. (b): Image (d).

mm is used. A TEA CO₂ laser of a short pulse width (50 ns) is used as a pump beam. The typical images before and after the pumpings recorded on the frame memories are shown in Fig. 7. To reduce the influence of the fluctuation of the differential phase due to turbulence, optical distortions and noises, the digital images before and after the pumpings

are differentiated by the use of the image processor. The pulse width of the laser diode is 4 μ s. The pulse interval of the laser diode shown in Fig. 3 is 110 μ s. In Fig. 5 the difference between the power spectrum densities at 10 kHz and at 1 kHz is about 40 dBV. So by the differentiation of the images before and after the pumpings, we can reduce in-

fluence of phase fluctuation to about one hundredth. Fig. 7 (a) shows image (odd-line field) recorded at 100 μ s after the pumping of the TEA CO₂ laser. Fig. 7 (b) shows image (even-line field) recorded at 10 μ s before the pumping. The image of (a) is subtracted from the image of (b) and the obtained image is multiplied by constant 25. The result is shown in Fig. 7 (c). Constant 120 is added to the digital image of (b) and from the obtained image the image of (a) is subtracted. The obtained image is multiplied by 2, subtracted by 120, multiplied by 2.5 and subtracted by 60. The result is shown in figure (d). Along the jet centerline the intensity distributions of the images (c), and (d) are shown in Fig. 8. $J = 210$ is at the exit of the nozzle. The intensity distribution of Fig. 8 (b) shows clearly plus peak and minus peak as those shown in Fig. 6 (b). So we can measure flow velocity from plus peak position at each point. To increasing contrast, from the image (a) in Fig. 7 the image (b) in Fig. 7 is subtracted. In the intensity distribution of Fig. 8 (a) the part of minus sign is cut. We can measure flow velocity from plus peak position or from the front edge of a luminous image. These results show that this technique makes possible to measure flow velocity distribution in turbulent state without influence of the phase fluctuation due to turbulent flow.

ACKNOWLEDGEMENTS

The present research was performed under the supervision of President Shinjou Okuda of Ashiya University.

REFERENCES

- Adrian, R. J., 1991, Particle-Imaging Technique for Experimental Fluid Mechanics, Ann. Rev. Fluid Mech. vol. 23. pp.261-304.
- Klavuhn, K. G., Gauba, G. and McDaniel J. C., J. Popul., OH Laser-Induced Fluorescence Velocimetry Technique for Steady, High-Speed, Reacting Flows, 1994, J. of Propulsion and Power vol. 10, pp.787-797.
- Lecordier, B, Mouqallid, M., Vottier, S., Rouland, E., Allano, D., and Trinite, M., 1992, CCD Recording for Cross-Correlation PIV Development in Unstationary High Speed Flow, Experiments in Fluids Vol.17, No. 3, pp.205-208.
- Meyers, J. F., 1995, Development of Doppler Global Velocimetry as a Flow Diagnostics Tool, Meas. Sci. Technol. vol.6, pp.769-783.
- Miles, R. and Lempert, W., 1990, Two-Dimensional Measurement of Density, Velocity, and Temperature in Turbulent High-Speed Air Flows by UV Rayleigh Scattering, Appl. Phys. vol.B51, pp. 1-7.
- Nie, Y. X., Hane, K. and Gupta, R., 1986 Measurements of Very Low Gas Flow Velocities by Photothermal Deflection Spectroscopy, Appl. Opt. vol.25, pp. 3247-3252.
- Nakatani, N., Oshio, 1994, Measurements of Gas Flow Velocity and Temperature Using Laser Photothermal Effect with a Differential Interferometer, Proc. of the 7th Int. Symp. on Applications of Laser Techniques to Fluid Mechanics, Institute Superior Tecnico, pp.32-5-1-32-5-8.
- Nakatani, N., 1997, Measurement of the Flow Velocity Distribution by the Laser Photothermal Effect with a Differential Interferometer, Proc. of the 7th Int. Conf. on Laser Anemometry Advances and Application, GALA e. V., pp. 27-34.
- Smith, F. H., 1955, Microscopic Interferometry, Research vol. 8, pp. 385-395.

FLUID IMAGE VELOCIMETRY FOR UNSEEDED FLOW.

Y. Levy¹, B. Golovanevsky¹ and T. A. Kowalewski²

¹ Faculty of Aerospace Engineering Technion - Israel Institute of Technology
Haifa 32000, Israel

² Centre of Mechanics, IPPT PAN, Polish Academy of Sciences,
Swietokrzyska 21, PL 00-049 Warszawa.

Abstract

In flows with large velocity gradients, seeding particles tend to spread unevenly with non uniform concentration. These characteristic are emphasized in vortical flows. Conventional Particle Image Velocimetry (PIV) technique has a limited dynamic range and is dependent on the uniform distribution of the seeding particles. A new diagnostic method was developed, which enable to bypass some of these difficulties. The technique proposed as Fluid Image Velocimetry (FIV), is based on the Dynamic Programming (DP) algorithm for Optical Flow (OF) detection from a pair of images. OF detection is typically used in long range photography of large scale moving objects. A similar approach can be used for fluid velocimetry. However conventional OF can not be directly used for fluid measurements mainly due to the contour deformation of the detected object and due to variations in the illumination intensity of the sequential images. It seems that, the condition for identical intensities in the sequential images is compulsory. OF computation enables to extract a dense velocity field from a sequence of images, assuming that intensity is conserved during displacement. The DP OF computation can be considered as an intensity correlation based technique. The principle is to minimize the sum of square differences (SSD) between a pair of images. The originality of the approach is that an optimal matching is searched for entire image strips rather than for pixel neighborhoods. A unique approach is adopted to overcome the practical difference in the recorded intensities using the histogram matching procedure. The technique was calibrated for linear and rotational motions and indicated accuracy of better than 94.7% and 97.64% respectively. The application of FIV was tested in periodic and in reactive flows and demonstrated its definite superiority over the conventional PIV.

Introduction

Particle Image Velocimetry (PIV) analysis of reactive vortical flows and flows with large velocity gradients such as in gas turbine combustors, is a difficult task (see Ref.

[1]). This is mainly due to seeding problem and the difficulties in optimizing of the interrogation area due to the large dynamic range required. In general, PIV requires uniform and highly concentrated seeding by micron size particles. These particles should be inert and capable to withstand the high temperature environment. However in flows with large velocity gradients, the particles tends to spread unevenly, causing non uniform concentration. This problem is emphasized in vortical flow where particles rarely exist at the vortex core and do not always follow the stream lines.

A new method was developed which enable to overcome some of these difficulties. The technique proposed for the fluid flow analysis is the Fluid Image Velocimetry (FIV). It is based on the Dynamic Programming (DP) intensity correlation algorithm for Optical Flow (OF) detection from a pair of images. OF algorithms are typically used in long range photography of large scale moving objects. A similar approach can be used for fluid velocimetry. Colored tracing materials such as paints or smoke, which are mixed in the flow, "paint" unevenly the whole volume of the fluid. The flow, being laminar or turbulent, causes shifting of the colored fluid elements, enabling the detection of the flow movement between sequential images. However conventional OF can not be directly used for fluid velocity measurements mainly due to the deformation of the contours of the detected objects and due to typical variations in the recorded intensities of the sequential images.

OF computation enables to extract a dense velocity field from a sequence of images, assuming that intensity is conserved during displacement. The DP OF computation, can be considered as a correlation based technique. The principle is to minimize a sum of square differences (SSD) between a pair of images. The originality of the present approach is that an optimal matching is searched for entire image strips rather than for pixel neighborhoods. DP is used to provide a very robust strip alignment and pyramidal iterative process is used to compute the flow field. DP algorithm transforms the search problem for a two-dimensional matching (global image matching) into a carefully selected sequence of simpler search problem for mono-dimensional matching (strip matching).

Being based on information from sequential images, the algorithm implementation for PIV is limited to flow of low velocity field or, alternatively, requires a very expensive high speed CCD camera. In the present work while using conventional CCD cameras, this difficulty was overcome by the fact that such cameras are interlaced. We use only one field per frame, i.e. the first fields in the both, the first and the second frames. The two frames are exposed by two sequential laser pulses with a minimal time delay in the order of 5 μ s. Obviously, the use of only one field per frame has the drawback of lower spatial resolution. Like all methods based on image intensity correlation, DP OF algorithm is very sensitive to the illumination and the condition for identical intensities in the sequential images is compulsory. In the presented study, a special image intensity correction is performed before the DP OF algorithm is applied.

In addition to the velocity fluid measurement, the DP OF method can be applied for measurements of alternative flow parameters. It may be used to detect the 2D gradient vector field of the fluid density out of CCD recorded sequential Shadowgraphs (or Schlierens, or Interferograms), heat release pattern out of CH* emission images, ect..

The main limitation for DP algorithm is that it works well only for relative small displacements (typically from 5 to 10% of the image size). However this drawback is somehow compensated by subpixel resolution of the processing routine.

Principle of FIV.

The main principle of the FIV method is based on the DP algorithm for spoken word recognition [5, 6]. One of the central problems in the spoken word recognition research was the elimination (or time normalization) of nonlinear fluctuation in the speech pattern time axis, caused by speaking rate variation. The DP-searching was used for the pattern matching algorithm with nonlinear time normalization effect. In this algorithm, the time fluctuation was approximately modeled with a nonlinear warping function of some carefully specified properties. Timing differences between two speech patterns were eliminated by warping the time axis of one so that the maximum coincidence was attained with the other. Then, the time normalized distance was calculated as the minimized residual distance between them. This minimization process was very efficiently carried out by use of the DP technique.

DP-Matching Principle.

The method adopted for FIV was suggested by Quenot [3, 4], who based his algorithm on the technique used for speech recognition. The main idea of the proposed algorithm for OF detection from a pair of images, was to transform the search problem for bidimensional displacement into sequence of search problems for monodimensional displacements. Two sequential images are identically sliced into parallel and overlapping strips (see Fig. 1 and 2). The strips of images 1 and 2 are seen as sequence of pixel vectors: $a_{i,p}$ and $b_{j,p}$, where $0 \leq i, j \leq I$, and $I+1$ is the number of pixels in slicing direction and p depicts the pixels in each vector, with $-W/2 \leq p \leq W/2$, where $W/34$.

the width of the strip in pixels. The matching process is repeated for every pair of strips, than the slicing is performed in the orthogonal direction. Finally, the whole process has to be reiterated in pyramidal fashion by reducing the strips width and spacing (see Fig. 1). The algorithm is based on search of a transformation that brings the second image over the first one and minimizes the distance $d(i,j)$ between them. This distance defined as:

$$d(i,j) = \sum_{p=-W/2}^{p=W/2} \alpha(p) \cdot |a_{i,p} - b_{j,p}|,$$

Where $\alpha(p)$ is a coefficient used to limit the window effect in the orthogonal (to the slicing) direction.

A matching path between two strips is searched within an adjustment window (see Fig. 2) corresponding to the maximum absolute displacement m . The path should begin on the $i+j=m$ line and end on the $i+j=2I-m$ line. It must be continuous and increasing (Fig. 2).

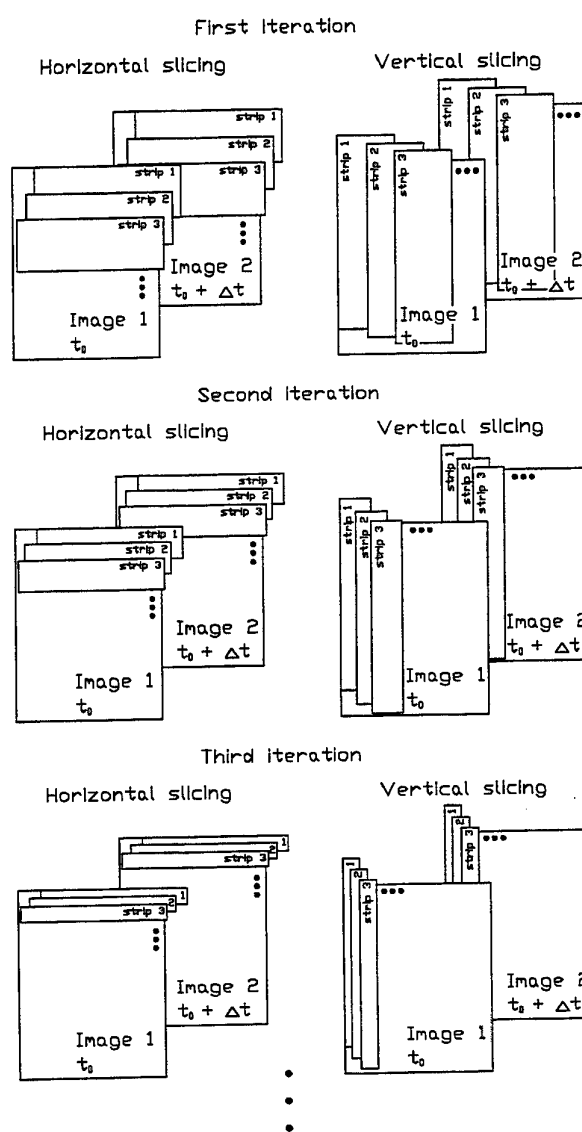


Fig. 1. Image slicing with pyramidal reducing the strips width and spacing.

As in speech recognition algorithm, the global distance $D(i,j)$ is defined for each matching path as the sum of the local distance $d(i,j)$ along the warping function. The minimum of the global distance $D(i,j)$ is defined as an optimal matching. It may not be unique. $D(i,j)$ is calculated using the following recurrent DP equation:

$$D(i,j) = \min \begin{cases} D(i,j-1) + d(i,j-1) + d(i,j) \\ D(i-1,j-1) + 2 \cdot (d(i-1,j-1) + d(i,j)) \\ D(i-1,j) + d(i-1,j) + d(i,j) \end{cases}$$

The initial and adjustment window conditions are:

$$D(i,j)=0, \text{ if } i=j=m, D(i,j)=\infty, \text{ for } |i-j|>m, \text{ or } i+j<m,$$

The end of the optimal path is obtained from the minimum of $D(i,j)$ on the $i+j=2 \cdot I-m$ line. Backtracking from this node along the minimal path provides the optimal path. This path is extrapolated continuously outside of the beginning and the end lines. The m parameter is also decreased along the iteration as are the strip width and spacing.

After each two passes (in the two orthogonal slicing directions), the velocity field is updated for the whole image by interpolation and smoothing, using the relative velocity value calculated for the strip central lines. This iterative process is performed in pyramidal fashion, as mentioned above (see again Fig. 1). The width of the adjustment window around the diagonal $i=j$ is also reduced during iterative process. At each iteration, the matching is searched between the original image 1 and the modified image 2 and not between two original images. Image 2 is transformed, using the velocity field evaluated from previous iterations, to the pattern of the image 1.

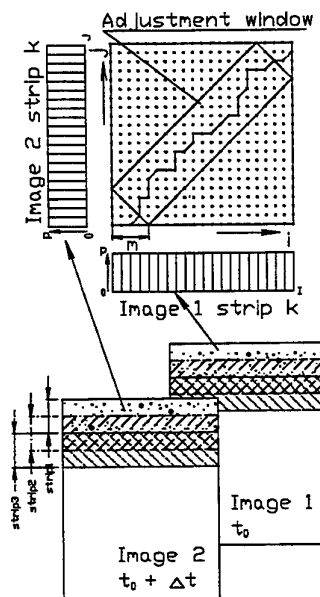


Fig. 2. Images slicing and strips matching.

The main limitation for this algorithm is that it works well only for relative small displacements (typically from 5 to 10% of the image size). This fact limits the algorithm implementation for FIV to flows of low velocity fields or requires very expensive high speed CCD camera. In the present work this difficulty is overcome by the fact that regular CCD cameras are interlaced. We use only one field per frame, i.e. the first field in first frame (second field is double exposed) and the first field in second frame. An additional problem was encountered which initially limited the use of the technique in practical fluid flow. The problem arise from the illuminated technique. The use of two laser pulses from two Nd:YAG lasers for the flow illumination causing difference in the intensity of the two images. It is impossible to receive two completely identical pulses from two different lasers. Obviously, the algorithm, based on intensity correlation must be very sensitive to intensity variation from image to image in the same pair. The FIV algorithm does not work in this conditions. In order to overcome this problem, image intensity correction is performed before the FIV algorithm is applied. Image intensity correction is based on histogram matching algorithm.

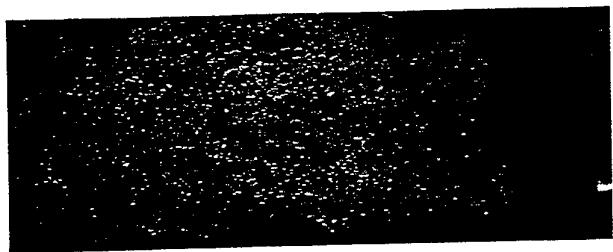
Histogram Matching Algorithm.

This algorithm allows to modify the intensity of the pixel elements of an image so that the normalized intensity histogram of the image matches a specified intensity histogram (i.e. the intensity histogram of the other one). The procedure have the following main steps:

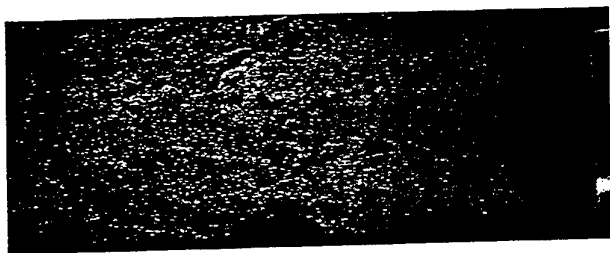
- Calculate the intensity histograms of both images;
- Calculate from the histograms the cumulative sum of the number of the pixel counts for each gray level value of each image in order to get a monotonic function.
- Normalize each of cumulative sum by the total sum.
- Construct the inverse function of normalized cumulative sum of the number of the pixel counts Vs. corresponding gray level bin location (from the histogram) for each image.
- Find by the linear interpolation of the normalized cumulative sum of the highest intensity image, the new gray level bin location corresponding to the normalized cumulative sum of the lowest intensity image.
- Construct the function of the old gray level bin location Vs the new gray level bin location for the image of the lowest intensity.

Apply this function on each pixel in the image of the lowest intensity.

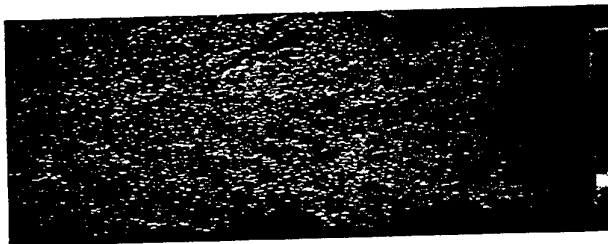
The Figure 3. a-c shows the result of intensity correlation by histogram matching. The procedure was applied on pair of pulsating jets images. The results of PIV and FIV evaluation for this pair of images presents in Figure 15. a, b.



a.



b.



c.

Fig. 3. a.: Low intensity image of pulsating jets;
b.: high intensity image of pulsating jets;
c.: modified low intensity image of pulsating jets.

Experimental Investigation System.

The experimental system includes three parts:

- A. A calibration system for linear and rotation movements.
- B. Periodic pulsation of air jets using our spray combustion instability rig.
- C. Laminar spray combustion system.

A. Calibration of FIV system.

The calibration was performed in three ways. The first part of the calibration was done in order to find conditions for minimum optical aberration. Three objectives and various distances were tested. A millimetric squared paper was chosen as a object of imaging.

The second part of calibration checked the accuracy of uniform linear (rectilinear) displacement measurement. In order to simulate an image of a seeded flow, a picture with randomly placed black spots of different size and location was used (see Fig. 4). This picture, moved by a step motor driven one-directional vertical traverse with a constant velocity, was chosen as a target of imaging. The velocity was controlled via PC. Alternatively, this velocity was measured by recording the time and displacement of the traverse (using linear potentiometer) via Data Acquisition software VIEWDAC.

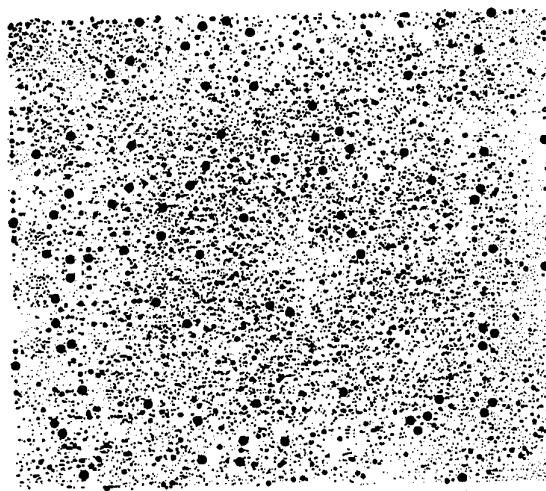


Fig. 4. Simulation of an image of flow with particles.

The third part of calibration included the measurement of two-dimensional components of the velocity vectors. The same picture (see again Fig. 4) was rotated by DC motor with a constant angular velocity. The picture was illuminated by stroboscope lamp (see Fig. 5) with external trigger control (via PC). The angular velocity of DC motor was measured by analog tachometer assembled on axle of the motor (max. voltage ripple 1.5% peak-to-peak).

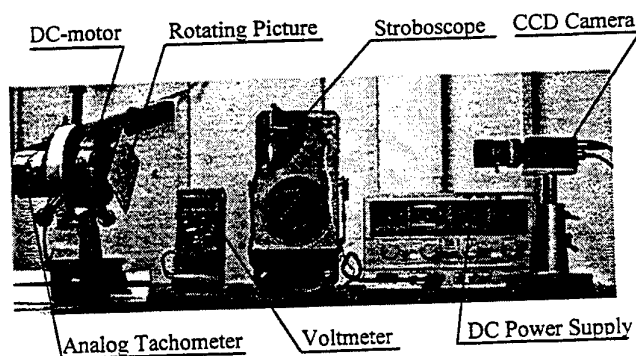


Fig. 5. Rotating velocity measurement calibration test system.

In order to evaluate the accuracy of the technique, two type of data processing are performed. The first is to define the border offset, namely to define the inner region where the data is not affected by the edges of the image. The second type relates to variation of the recorded velocity values (by the FIV system) relative to an alternative ("absolute") measurement technique.

B. Pulsating jets.

The general experimental investigation system (see Fig. 6) consist of combustion chamber, flow system, optical measurement system, data acquisition and processing system. The primary oscillating stream is produced by an ordinary atomizer and pulsating ambient air which enters the chamber through two entrance holes. Through the first entrance hole steady air flow enters and heat up by an

electrical heater, the oscillating air enters from the second one.

The optical measurement system consist of:

- Two Nd:YAG pulse lasers, Quanta-Ray, GCR -16 Series,
- Digital pulse/delay generator, Stanford Research System, Inc., model DG 535,
- Seeder,
- Set of lens and optical components,
- CCD camera, Sony Corp., model XC-75-CE,
- Frame Grabber, Data Translation, model DT 3155,
- Computer, Intel, Pentium 75/32Mb,
- Data acquisition program, Data Translation, SDK,
- FIV program.

The data acquisition and processing system include flowmeters, pressure sensors, air pressure regulators, thermocouples, tachometers, CH-detectors, photodiode, digital oscilloscope, PDPA data acquisition system with computer Pentium 100/16Mb, A/D converter and computer COMPAQ 486/33/8Mb with VIEWDAC data acquisition program.

C. Laminar spray combustion system.

Laminar spray flame (see Fig. 16 a, b). This experimental facility was explained in details in ref. [2]. Images of flow structures are obtained from the region close to the nozzle, where the flame commence.

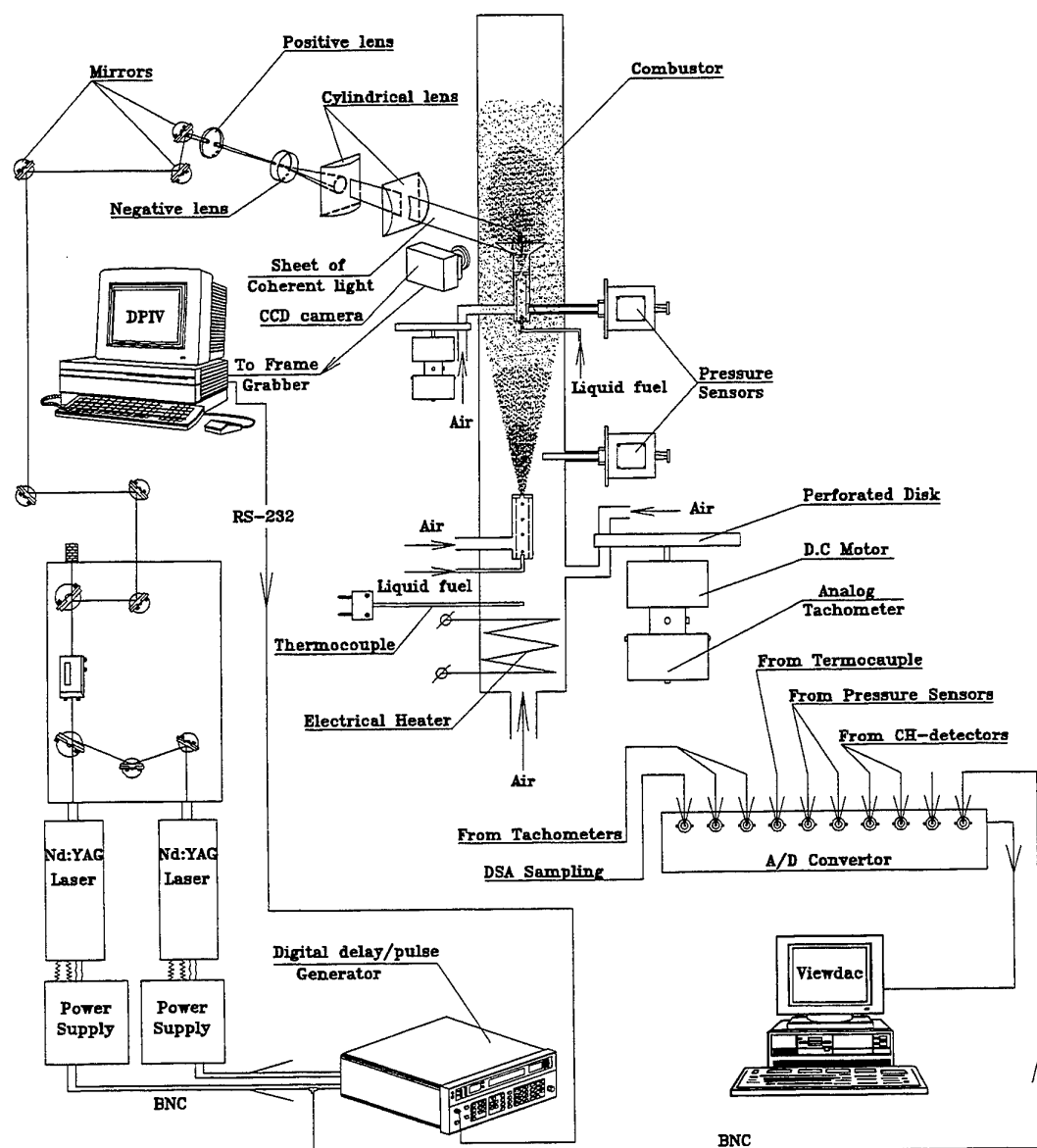


Fig. 6. Experimental Optical System: DPIV and Data Acquisition.

Calibration Tests.

In general, FIV method (as the conventional PIV) may reveal representative velocity result only in an area, which is slightly remote inwards from the original image borders. It may be looked as border offset, where the offset is equal to the value

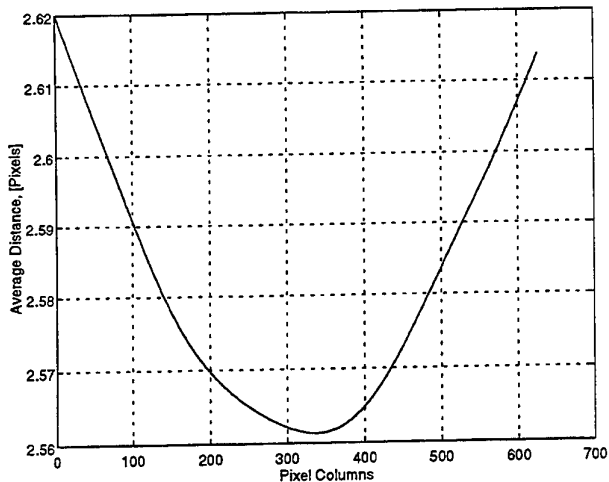


Fig. 7. Variation of distance between two neighbouring lines along the image length (curve fitted).

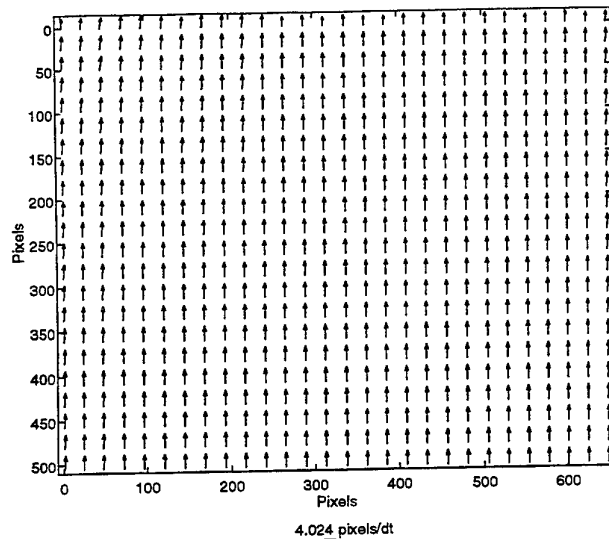


Fig. 8. Rectilinear velocity measurement accuracy test, FIV result.

of maximal displacement in corresponding direction. However, due to optical (spherical) aberration, this offset could be much larger than the maximal displacement. Calibration tests of rectilinear displacement shows that the offset could reach up to 20% of whole image area. In spite of the fact, that for the experimental setup (objective f 2.8, distance 1.12 m) one can not visually recognize significant optical aberration, and indeed it is only about of 2.3% (see Fig. 7), however, calibration tests of rectilinear displacement shows a decrease in the region of representative results by 60 pixels offset in the direction of the displacement. The Figs. 8-10 clearly shows that there are a strong edge effect which have to be taken into consideration. This effect

is also recognizable in the images of the rotating picture (see Figs. 11-13).

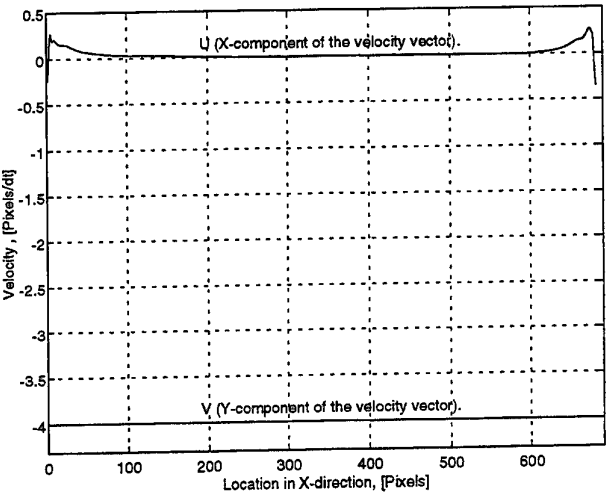


Fig. 9. Variation of the velocity vector components along X-axis. Result displayed are from the middle row of the velocity vectors matrix.

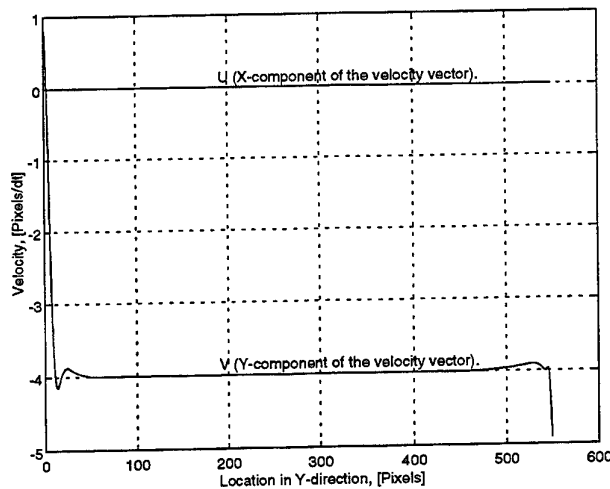


Fig. 10. Variation of the velocity vector components along Y-axis. Result displayed are from the middle column of the velocity vectors matrix.

In addition, images of rotating picture were processed with conventional PIV algorithm. In the conventional PIV processing, the images were tested with several interrogation windows (24x24, 32x32, 48 x48 and 64x64 pixels). Figs 11 and 14 are typical demonstration for the advantage of FIV over PIV. The central part of the figure 14 is blank. In this area even the smallest interrogation window (of the mentioned above) was too large to calculate the average displacement. On the other side, in the periphery of the velocity map (see again Fig. 14), one can see the erroneous velocity vectors. In these area the interrogation window was too small to cover the large tests displacement.

The calibration test indicated that representative velocity values can be obtained only at the inner area which is remote from the border by about three times the maximum velocity value in the displacement direction. The minimal (theoretical) error is

in the order of maximum displacement value in the direction, perpendicular to the slicing direction. However the strip width effect and the spherical aberration increase this value to about three. The velocity value within the inner area were found to follow the reference values with an accuracy of better than 94.7% for linear and 97.64% for rotating velocity tests, which incorporates again the effect of spherical aberration and the inaccuracy of the calibration setup itself.

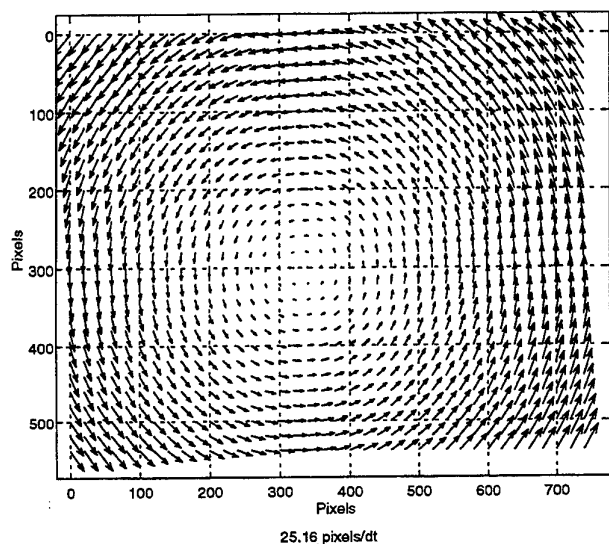


Fig. 11. Rotating velocity measurement accuracy test. FIV calculation result.

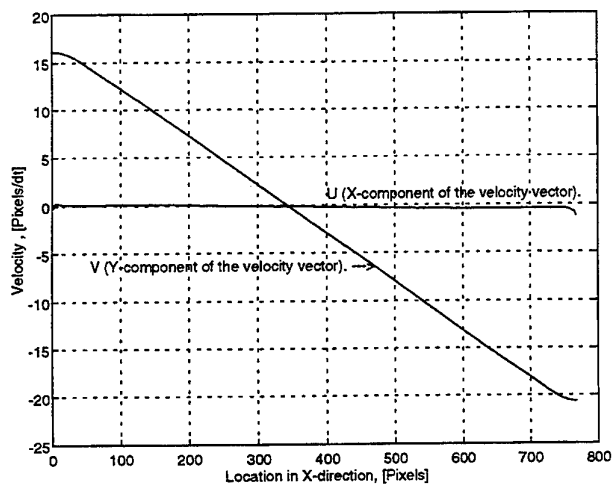


Fig. 12. Variation of the velocity vector components along X-axis. Result displayed are from the middle row of the velocity vectors matrix.

Results and Discussion.

A comparison of FIV method with conventional PIV is provided for experiments of two concentric streams interaction and oscillating laminar diffusion flame. In the first set of experiments, the flow configuration was that of confined concentric air streams, where the inner one was pulsating. The

streams were seeded with Aluminum Oxide particle of 5 μm mean diameter. The flow was illuminated by two Nd:YAG pulse lasers of 8 ns duration fired at 40 μs interval, aligned and focused to a common lightsheet of 0.3 mm thick. The physical dimensions of the field of view was 8 x 6 cm and the image size was 768 x 576 pixels. The raw images were recorded using Sony camera XC-73CE. Conventional PIV processing of the images using

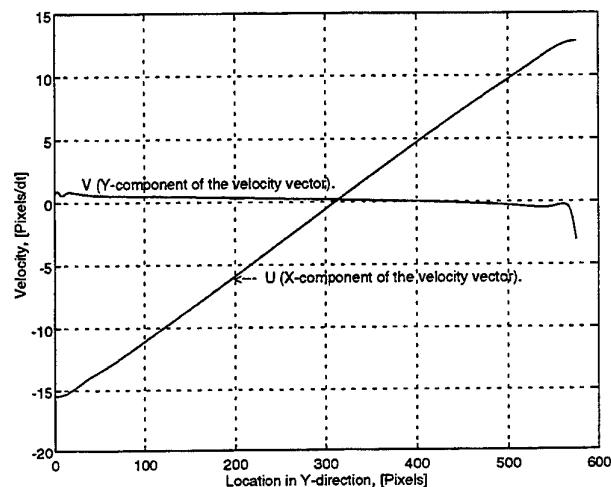


Fig. 13. Variation of the velocity vector components along Y-axis. Result displayed are from the middle column of the velocity vectors matrix.

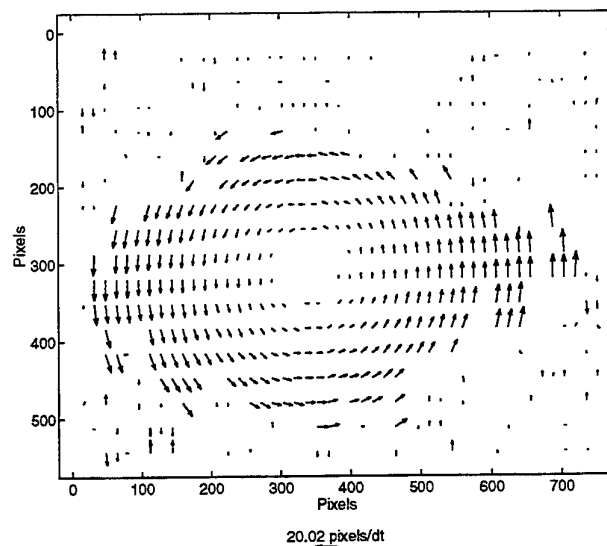
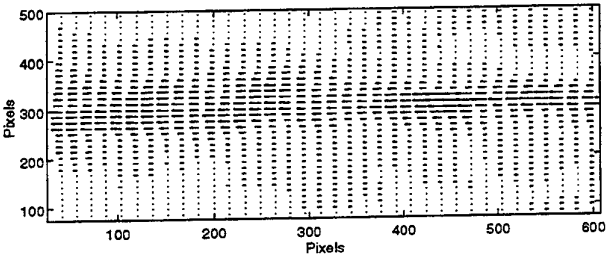


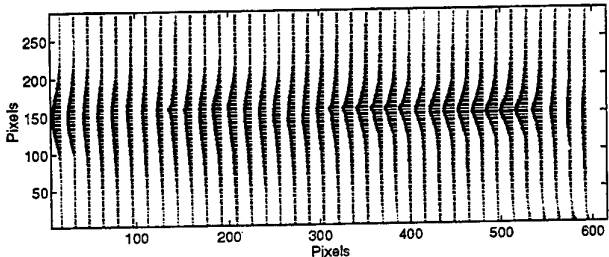
Fig. 14. Rotating velocity measurement accuracy test. PIV calculation result.

interrogation area of 48 x 32 pixels revealed part "a" of the Fig. 15. Velocity profiles are displayed at different axial position relative to the nozzle. The vectors clearly demonstrate the velocity field. However a significant part of the figure 15 is marked with dots. In these area the information within interrogation window was not sufficient to process an accurate velocity value. Part "b" of the figure 15 was obtained using the FIV procedure of the same raw images. It reveals the same flow field but at a much higher accuracy and details. The flow is clearly visualized and the fine

details enable to see the pulsation of flow where an air “pocket” is moving from about pixel raw 600 to pixel raw 300 in a wave motion. It should be noted, that FIV seems to have half the number of rows (288), however in PIV, every second line is obtained from linear interpolation only.



a.



b.

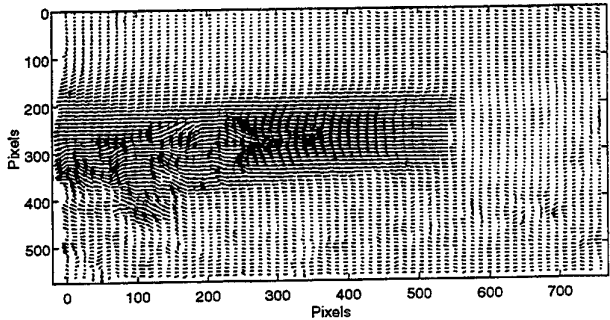
Fig. 15. a.: Cold oscillating stream with coaxial outer steady stream. Typical PIV evaluated vectors for pair of images taken at 40 μ s interval. Scale: 8.6 pixels/mm.

b.: same as above, but for FIV evaluations.

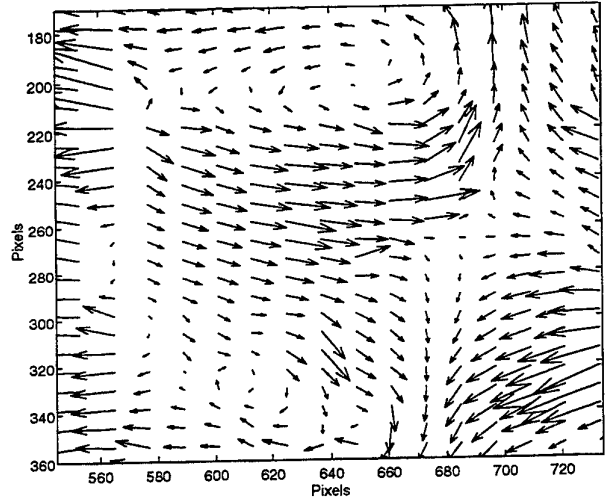
It seems that the additional information obtained in the FIV originates from scattered illumination of small particle. As mentioned before, the size distribution of the Aluminum Oxide had an average value of 5 μ m, however significant portion of the particles extended to the submicron range. These small particles served as the air tracers with much more uniform distribution, practically covering all of the observed volume.

The advantage of FIV method is also seen from analyzing sequential oscillating laminar flame images. The flow and hardware configuration was similar to previously described system. Two sequential images of seeded flow were recorded at 2 ms interval. The flow configuration was as described in details in Ref. [2]. It is of a confined concentric laminar streams, where the inner one included Heptane fuel in form of liquid droplets, vapors and Nitrogen as carrier gas for the droplets. Air flow was the outer stream. The spray combustor, with low flow velocity, exhibits a unique operating mode in which large amplitude, self induced oscillations of flame shape occur. The phenomenon, was analyzed with PIV and FIV. The PIV analysis were not able to recognize small vortex structure in the flame recirculation zone, mainly due to area averaging over the interrogation window. The FIV method recognized the small toroidal vortex structure in spite of the very small displacement (about 0.5-2 pixels). In this case, the ratio of the number of velocity vectors to the number of pixels

is 1 for FIV and about 0.006 for PIV. This is mainly due to the fact that in PIV, every velocity vector is a result of displacement



a.



b.

Fig. 16. a.: Laminar diffusion flame. Typical FIV evaluated vectors for pair of images taken at 2 ms interval. Scale: 13.4 pixels/mm.

b.: same as above: zoom of flame recirculation zone.

averaging over interrogation area (48 x 32 pixels). Using the FIV a dense velocity field for every pixel of the image is obtained, see figure 16. a. In the figure 16. a., b., the orientation is such that the nozzle is shown horizontally (gravity is towards the right direction) and the flow is from right to left. It allows to zoom into the region of interest (the center at the right side of image) and to see the vortices (see Fig. 16 b.).

In addition, the FIV method can be applied for measurements of alternative flow parameters. It may be used to detect the 2D gradient vector field of the fluid density out of CCD recorded sequential Shadowgraphs (or Schlierens, or Interferograms), heat release pattern out of CH* emission images, ect..

References.

1. Adrian, R. J., Multi-point optical measurements of simultaneous vectors in unsteady flow - a review., *Int. J. Heat Fluid Flow*, vol. 7, pp. 127-145, 1986.
2. Levy, Y., Bulzan D. L., On the Oscillation of Combustion of a Laminar Spray, *Combustion and Flame*, V. 100, pp. 543-549, 1995.
3. Quenot, G. M., The "Orthogonal Algorithm" for Optical Flow using Dynamic Programming, *Proc. IEEE ICASSP-92*, V. 3, pp. 249-252, San-Francisco, 23-26 March, 1992.
4. Quenot, G. M., Pakleza, J., Kowalewski, T. A., Particle Image Velocimetry with Optical Flow, Submitted to *J. Experiments in Fluids*, July 13, 1997.
5. Sakoe, H., Chiba, S., A dynamic programming approach to continuous speech recognition., 1971 *Proc. 7th ICA*, Paper 20 C13., Aug. 1971.
6. Sakoe, H., Chiba, S., Dynamic Programming Algorithm Optimization for Spoken Word Recognition., *IEEE Transactions on Acoustics, Speech, and Signal Processing*, V. ASSP-26, N. 1, 1978.

SESSION 35

COMBUSTION III

PIV AND OH LIF IMAGING OF FLAME-VORTEX INTERACTIONS IN AN OPPOSED-JET BURNER

James R. Gord,¹ Jeffrey M. Donbar,¹ Gregory J. Fiechtner,² Campbell D. Carter,² and J. C. Rolon³

¹Propulsion Directorate, Air Force Research Laboratory, Wright-Patterson Air Force Base, OH 45433-7103, USA.

²Innovative Scientific Solutions, Inc., 2786 Indian Ripple Road, Dayton, OH 45440-3638, USA.

³Laboratoire d'Énergétique Moléculaire et Macroscopique, Combustion, École Centrale Paris, Grande Voie des Vignes, 92295 Châtenay-Malabry Cedex, France.

ABSTRACT

The dynamic interaction between a laminar flame and a vortex is examined. The hydroxyl (OH) layer produced by the flame is imaged using planar laser-induced fluorescence (PLIF), and preliminary vortex-characterization data are acquired using acetone PLIF and digital, two-color particle-image velocimetry (PIV). The hydrogen-air flame is supported in a nonpremixed opposed-jet burner. The apparatus is found to produce highly repeatable events, making it ideal for studying the interaction between a flame and an isolated vortex. A distinct annular extinction of the OH layer is observed, in good agreement with previous computational modeling predictions of the apparatus. In cases with no extinction of the OH layer, enhanced burning is observed during the flame-vortex interaction.

1. INTRODUCTION

Recent results in numerical modeling combined with experimental measurements have led to important advances in the understanding of combustion. Numerous investigations have contributed to these advances, including a particular type of study in which the interaction between a laminar nonpremixed flame and a vortex is examined. These experiments involve repeatable, carefully controlled conditions that are highly amenable to experimental study.

In recent computational calculations, Katta (1998) predicted that, during the interaction of a nonpremixed hydrogen-air flame and an isolated vortex, the extinction of the OH layer would occur in an annular pattern. The experiments detailed in this paper are carried out to examine, in part, the validity of this prediction. Experimental results obtained with planar laser-induced fluorescence (PLIF) of OH are used to determine regimes in which the annular, Katta-type extinction occurs. The nonpremixed flame is supported by air and fuel in an opposed-jet burner. The fuel consists of hydrogen diluted with nitrogen. The amount of

hydrogen in nitrogen is varied, along with the strength of the vortex. The temporal evolution of flame-vortex interactions is imaged with the PLIF system.

Recently, additional measurements have been initiated for characterization of vortices. First, acetone is seeded into the vortex and its laser-excited fluorescence is detected. Second, particles are seeded into the flowfield, and the scattering is used for digital, two-color particle-image velocimetry (PIV) measurements. Preliminary results from the use of both techniques are discussed in this paper.

2. BACKGROUND

Numerous experimental studies of the interaction dynamics of vortices and flames have been conducted, and many of these investigations employed two-dimensional imaging to study the interaction. For premixed flame fronts, most measurements have been made using two types of flames. Hertzberg et al. (1984) and Escudie (1988) conducted an experiment in which a Karman vortex street was produced using a cylindrical rod in a cross flow of premixed gases. A V-flame was supported behind a wire positioned downstream of the rod that produced the vortex street. Planar tomographic imaging was used to study the interaction of the vortex street with the flame. A similar interaction between a Karman vortex street and a flame was investigated by Lee et al. (1993) using PLIF imaging of OH and by Nye et al. (1996) using both OH PLIF and PIV. A disadvantage of the vortex street is the difficulty in isolating a single vortex. Nguyen and Paul (1996) studied a more isolated interaction by replacing the Karman vortex street with a vortex that was directed into one side of a V-flame. The vortex-injection process was found to be highly repeatable.

In a second type of study involving premixed combustion, Jarosinski et al. (1988) studied a flame that was ignited at one end of a tube of premixed gases. A vortex was injected at the other end of the tube. The

interaction dynamics were then photographed using a mercury-xenon arc lamp and a rotating-drum streak camera with a rotating-disc shutter. Recently, Driscoll et al. (1994) produced an impressive series of papers concerning a similar flame-vortex apparatus in which either PIV or OH PLIF (or a combination of these imaging techniques) was applied.

Nonpremixed flames have also been the subject of experimental investigation. Rolon et al. (1995) recently developed an apparatus in which a vortex is injected into a flame supported between the nozzles of an opposed-jet burner. This geometry has numerous advantages. First, a stationary flame can easily be produced and isolated. Second, the flame thickness can be varied by changing either the nozzle velocities or the spacing between the upper and lower burner nozzles. More recently, Chen and Dahm (1997) developed a facility for generating a non-premixed burning layer that wraps into a vortex ring. The resulting combustion is studied under conditions of normal gravity and microgravity.

The experiments described in this paper are based on the counterflow geometry of Rolon et al. (1995), and the observations described below rely heavily on the progress outlined in their papers. A fuel mixture of hydrogen and nitrogen allows the use of laser diagnostics in the absence of hydrocarbon interferences, and the reaction zone of these nonpremixed flames is generally much thicker than that for premixed flames. The comparatively simple hydrogen-chemistry mechanisms simplify numerical calculations that are the subject of comparison with experimental results.

3. APPARATUS AND PROCEDURE

3.1 Burner Facility

A picture (a) and diagram (b) of the burner are shown in Figure 1. The configuration is based on the design of Rolon et al. (1995). The flame is supported between upper and lower nozzles separated by 40 mm, each with an exit diameter of 25 mm. The fuel consists of hydrogen diluted with nitrogen and flows from the upper nozzle. Air flows from the lower nozzle. Unique to this type of apparatus is a tube with 5-mm inner diameter that is installed concentrically within the lower nozzle. This tube is attached to a cylinder that contains a piston, which is, in turn, attached to an actuator. Feeding an appropriate current to the actuator causes a solenoid to force the piston upward abruptly, resulting in the emergence of a vortex from the tube. The vortex travels upward within the surrounding oxidizer flow. A flow of air is supplied to the vortex tube such that, in the absence of a vortex, the exit velocity matches the velocity of the surrounding nozzle. To minimize the

impact of room-air disturbances, upper and lower guard flows of nitrogen are supported through outer nozzles.

The hydrogen, nitrogen diluent, and oxidizer air flows are provided by mass-flow controllers with full-scale ranges of 20 l/min, 20 l/min, and 30 l/min, respectively. A continuous flow of air is provided to the vortex tube by a 5-l/min controller, while the guard flow from the upper and lower guard nozzles is provided by two 50-l/min mass flow controllers. The flow rates of each controller are good to $\pm 1\%$ of the full-scale range. The experiments have been repeated for several different flame conditions, as summarized in Table I.

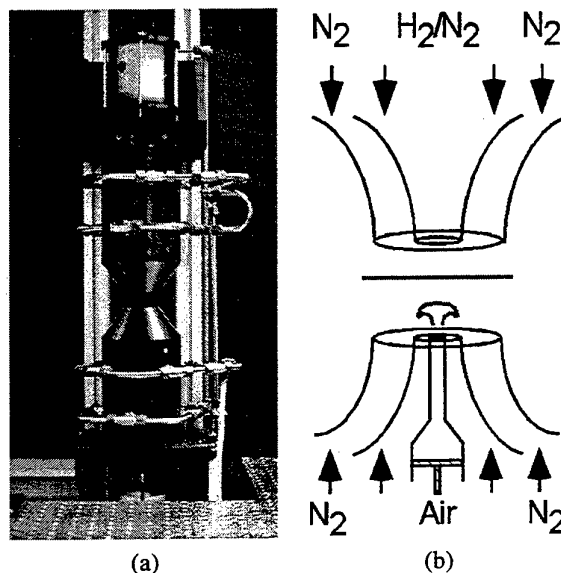


Figure 1. (a) Digital photograph of the opposed-jet burner. (b) Cross-sectional diagram of the burner nozzles and piston.

Table I. Flow rates (l/min) at 21.5°C and 724 mm Hg for five flame conditions. X_{H_2} is the volume fraction of hydrogen in nitrogen diluent.

Gas	Flame					
	A	B	C	D	E	F
H ₂	2.76	3.40	4.04	4.67	5.31	5.94
N ₂ Diluent	17.1	17.1	17.1	17.0	17.0	16.9
X_{H_2}	0.14	0.17	0.19	0.22	0.24	0.26
Air	11.2	11.2	11.2	11.2	11.2	11.2

The vortex properties can be varied by changing the magnitude and the rise time of the current that is fed to the actuator. The impedance of the actuator is in the range from 1 Ω to 1.5 Ω , depending on the frequency content of the current. At full displacement, a current of up to 6 A is provided to the solenoid by a specially

designed, high-speed power amplifier. This can result in considerable power consumption by the actuator if the full displacement condition is maintained for long periods of time. Consequently, an AC waveform is supplied by the initial application of a negative potential, causing the piston to be withdrawn away from the flame. The negative potential is applied for about 0.5 s to allow the flame to recover from this initial disturbance, which is verified by digital, two-color PIV. The potential is then quickly changed to a positive value of the same magnitude with a precisely controlled rise time, τ_r . The strength of the vortex can be increased by increasing the current magnitude, which results in a larger displaced fluid volume through the exit of the tube. Eventually, the maximum displacement of the solenoid is reached. In this case, the vortex strength can also be increased using a smaller value of τ_r . The relationship among volume displacement, τ_r , and the vortex characteristics has been discussed in numerous papers, including those by Rolon et al. (1995), Roberts (1992), and Chen and Dahm (1997). The drive current for the solenoid is obtained by power amplifying the output of a digital arbitrary-waveform generator. This generator is operated at its maximum number of 10 000 quantized steps, resulting in a minimum stepsize of 0.1 ms. For all measurements discussed in this paper, τ_r is set at 10 ms.

Visualization of the vortex formation and propagation via acetone PLIF is accomplished using a vaporizer that is installed between the vortex tube and the mass-flow controller. A bypass valve allows the choice of acetone seeding level. Because the acetone changes the flame characteristics, these visualization studies are limited to non-reacting flows. When the acetone studies are not required, the acetone vaporizer is removed from the apparatus.

Seed particles are introduced into the burner flows when digital PIV measurements of the velocity of the vortex are performed. Three particle seeders are installed: One seeder is placed after the oxidizer-air mass-flow controller and another after the vortex-air mass-flow controller. The third seeder is installed after the junction where the hydrogen and nitrogen gases are mixed. With the use of three seeders, each flow can be seeded with particles individually, or combinations of the different flow fields can be seeded. Each seeder contains hollow spherical ceramic particles with an approximate mean diameter of 2.4 μm . When PIV studies are not required, the seeders are removed from the apparatus.

3.2 Laser Diagnostics

The PLIF system contains a frequency doubled, Q-switched Nd:YAG laser that is used to pump a fre-

quency-doubled dye laser. The light is directed through a telescope that is adjusted to produce a light sheet with a height that matches as nearly as possible the 40-mm burner separation. The resulting beam thickness is $\sim 300 \mu\text{m}$, which corresponds to the full width at 25% of the peak of the intensity profile, and $\sim 15 \text{ mJ/pulse}$ is available at the test section.

Hydroxyl radicals absorb the laser radiation at 281.3414 nm via the $R_1(8)$ transition of the (1,0) band in the A-X system. Fluorescence from the A-X (1,1) and (0,0) bands is detected at right angles through WG-295 and UG-11 colored-glass filters, followed by a 105-mm focal length, $f/4.5$ UV lens. The resulting light reaches an intensified CCD camera with an intensifier gate width of 100 ns. CCD pixels are binned in groups of 2×2 . Data are stored on a personal computer. A color table is used with a maximum value set to 95% of the maximum signal for all images taken at a given flame condition. The low-signal color is assigned by calculating the background noise and selecting a minimum value that is two standard deviations above this level. Therefore, in cases where "extinction" of the OH layer is observed, "extinction" refers to signal levels that fall below this minimum value and are, therefore, assigned the last color in the table. All images represent the signal collected during a single laser shot, and no smoothing of the resulting images is attempted.

In studies of flame-vortex interactions by Najm et al. (1998), LIF was applied as a marker of some other quantity such as heat release or burning rate. In the present experiments, the OH image is obtained for direct comparison with numerical computations of the OH distribution; therefore, no attempt is made to correlate the images with any other quantities.

Acetone PLIF imaging is accomplished using the OH PLIF imaging system. Here, the UG-11 colored-glass filter is removed to permit collection of the acetone fluorescence.

Recent measurements of the velocity field have been implemented using digital, two-color PIV. Here, the ICCD camera is replaced with a color digital CCD. This type of CCD has a mask with green-transmissive filters for 50% of the pixels, red-transmissive filters for 25% of the pixels, and blue-transmissive filters for the remaining 25% of the pixels. Two lasers are used, with one sheet being produced by directly doubling the output of a Q-switched Nd:YAG laser (30 mJ/pulse at the test section). The second light sheet is produced by pumping a dye laser (employing DCM laser dye) with a second frequency-doubled, Q-switched Nd:YAG laser, resulting in laser radiation at 640 nm (40 mJ/pulse at the test section). The thickness of both the red and green sheets is set to $\sim 700 \mu\text{m}$. A digital delay generator is used to drive the timing of the two lasers such that the

red pulses are delayed by a precisely controlled amount of time with respect to the green pulses. In the absence of a vortex, the underlying counterflow velocity field is probed with red pulses that are delayed by up to 1 ms with respect to the corresponding green pulses. For the fastest vortices studied, the delay between red and green pulses is reduced to 10 μ s. The camera shutter is set to be open for 1/15 s to permit both laser pulses to be detected by the color CCD. Most of the flame emission and light emitted by other devices (monitors, etc.) in the laboratory is greatly attenuated by the shutter. Velocity vectors are calculated using the correlation software of Gogenini et al. (1998).

3.3 Synchronization and Timing

Precise synchronization of several experimental events, including vortex generation and propagation, production of laser pulses, and activation of the camera shutter or intensifier, is required. A block diagram of the synchronization scheme is shown in Figure 2.

Because the Nd:YAG lasers are designed to operate at a nominal repetition rate of 10 Hz, the experimental sequence must be synchronized to a 10-Hz master clock that drives the flash lamps and the Pockels cells of the lasers. To trigger the laser(s), the clock sends two signals, one of which travels to a 50- Ω power combiner and then the laser digital delay generator

(DDG). The 10-Hz clock also provides a TTL signal to one of two inputs of a coincidence unit. The second input of the coincidence unit is driven by a TTL pulse from the PLIF camera controller. The coincidence unit outputs a pulse only when pulses from both the 10-Hz clock and the PLIF camera controller are present. When a flame-vortex event is initiated using a personal computer, the PLIF camera controller outputs a pulse \sim 1.3 s in duration. The corresponding output of the coincidence unit is a 1.3-s envelope of TTL pulses spaced by 100 ms. The first pulse in this envelope triggers a master DDG, synchronizing it with the 10-Hz clock and the laser pulse train. This DDG triggers an arbitrary-waveform generator (AWG) that outputs a 1-s waveform, which is amplified and fed to the piston actuator to generate a vortex. Approximately 0.5 s after the AWG waveform is initiated, the vortex is fired; therefore, five laser pulses are generated during the time between computer initiation and the flame-vortex interaction.

When the DDG is externally triggered, the jitter between the trigger and a DDG output pulse is 60 ps plus the output delay divided by 10^8 . Over the 0.5-s period between the first and fifth laser pulses, this corresponds to a jitter of 5.06 ns. The DDG clock jitter specifications are not nearly so good. The jitter between clock outputs is 1 part in 10 000, corresponding to a

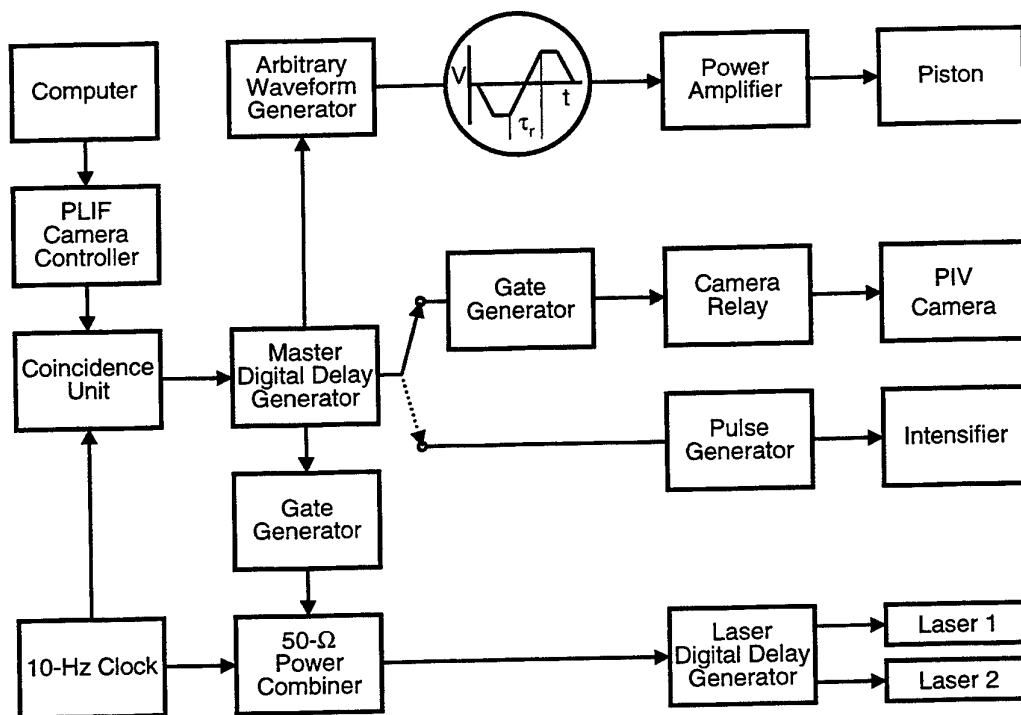


Figure 2. Diagram of electronic timing connections.

jitter of 50 μ s over the same 0.5-s period. Attempting to synchronize the piston with the clock severely limits the temporal resolution available to “freeze” flame-vortex events in time and requires an intensifier gate width significantly larger than 50 μ s. The master DDG is therefore configured to trigger the fifth laser pulse preemptively. A delayed pulse from the master DDG arrives at the 50- Ω power combiner just before the fifth pulse in the clock pulse train, preemptively triggering the laser(s). If no initiation pulse is output from the computer, the laser(s) are triggered by the 10-Hz clock as usual. This approach reduces the jitter in the timing of the fifth laser pulse from 50 μ s to \sim 5 ns while maintaining the nominal 10-Hz repetition rate required by the lasers.

Another output of the master DDG is suitably delayed and directed to the image detector. For PIV experiments, the width of this TTL pulse is adjusted using a gate generator, which closes a relay to trigger the digital PIV camera system. For PLIF experiments, this master DDG output triggers a pulse generator, which, in turn, activates the intensifier of an ICCD camera.

The scheme depicted in Figure 2 provides precise control of the relative timing between the laser diagnostics and the flame-vortex event. To explore the temporal evolution of the event, data are captured utilizing this phase-locked timing sequence: 1) an image is recorded, 2) the delay between vortex production and the laser/camera events is adjusted, and 3) another vortex is initiated and a second image is recorded. This process is repeated to acquire numerous images, each obtained at increasing delay. An animation is then created by assembling the individual images in temporal order. Effective temporal separation between images is selected between 10 μ s and 200 μ s, depending on the time scale of the event under study. The resulting animations are a testament to the high degree of repeatability achievable with this apparatus.

4. RESULTS AND DISCUSSION

4.1 Vortex Characterization

The sequence of acetone images in Figure 3 is typical of the sequential images used to measure the vortex-propagation velocity for a given amplitude and rise time of the solenoid drive current. The six images in the figure are selections from a sequence of 50 images, each delayed by 100 μ s relative to the previous image. If the location of the flame front in the absence of a vortex is known, the acetone PLIF image sequence can be used to estimate the velocity of the vortex at this location. In this case, the propagation velocity is \sim 5 m/s.

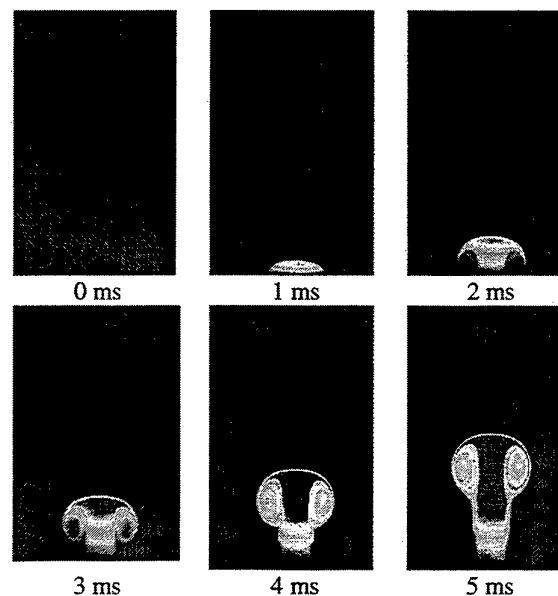


Figure 3. Acetone PLIF images of vortex.

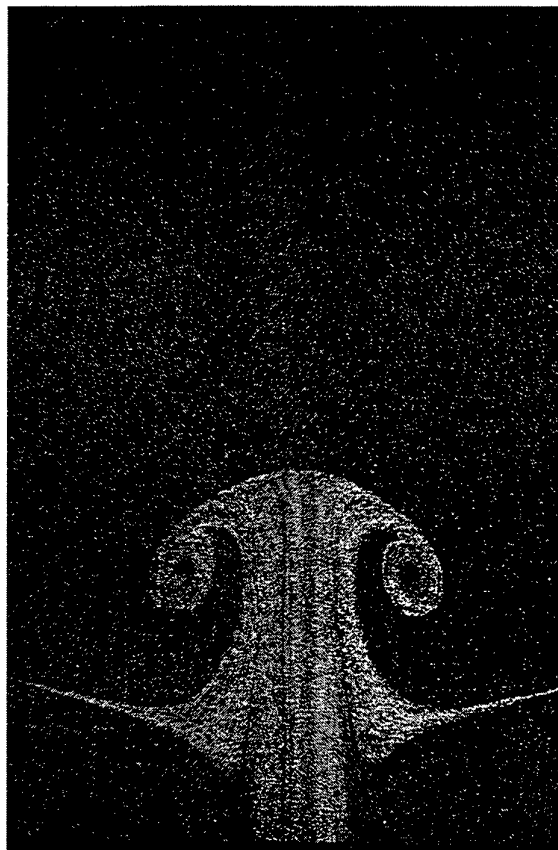


Figure 4. Scattering from particles in vortex flow.

Recently, characterization of vortex properties has been initiated using PIV. For example, Figure 4 contains the scattering signal obtained when seeding the vortex tube flow with a slightly higher particle density than that produced by the upper and lower burner seed levels. The corresponding set of vectors is shown in Figure 5. The maximum vector length in the forward direction yields a propagation velocity of 0.77 m/s. Digital, two-color PIV measurements are readily made when the flame is burning, offering a significant advantage over the acetone PLIF measurements of the vortex-propagation velocity.

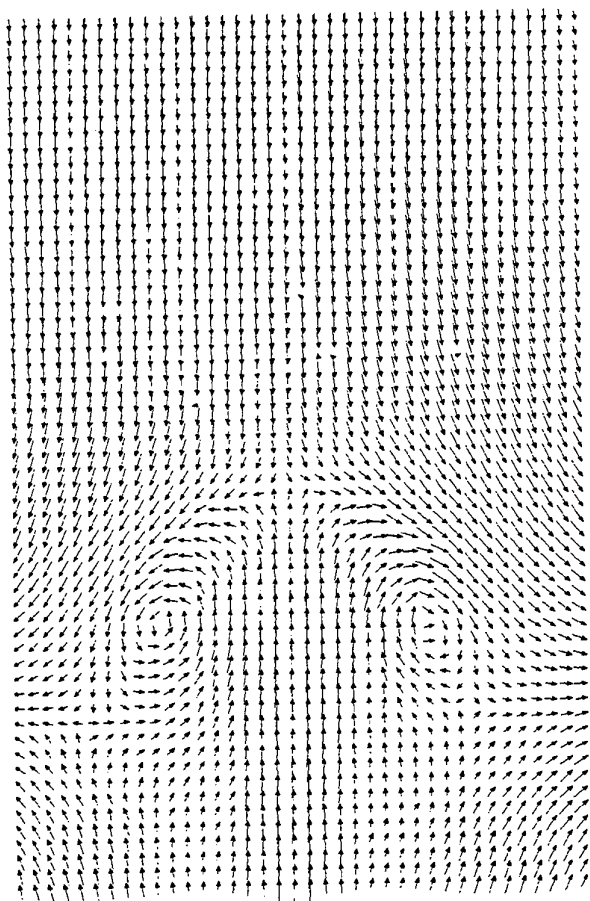


Figure 5. Vectors calculated using the PIV image of Figure 4.

4.2 Regimes of Flame-Vortex Interaction

The PLIF images of OH shown in Figure 6 correspond to a flame-vortex interaction in which extinction of the OH layer is absent. Initially, the vortex creates a small dent in the flame, and this dent then grows. Eventually the flame nearly surrounds the advancing vortex as it approaches the upper nozzle. In the later

interaction stages, the OH PLIF signal level is observed to increase by up to a factor of five over the levels observed without a vortex. The increased signal level is

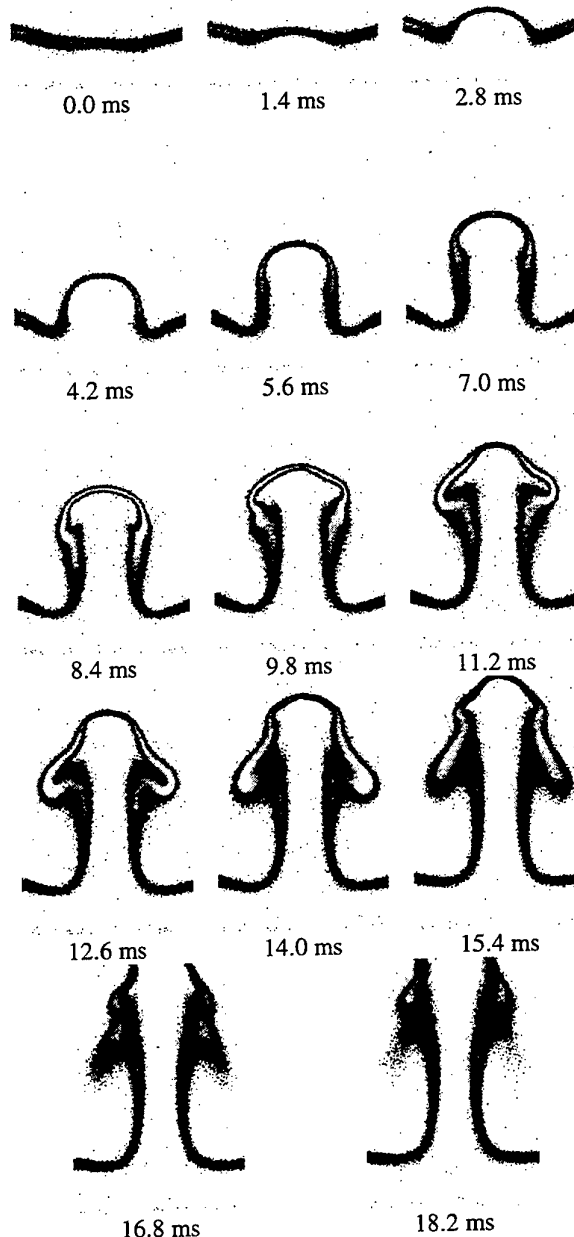


Figure 6. OH PLIF images when OH layer remains intact.

indicated by the light regions of the OH layer in the frames of Figure 6. This change in OH signal level is thought to indicate enhanced burning. For this particular example, the flow rates of Flame D of Table I are

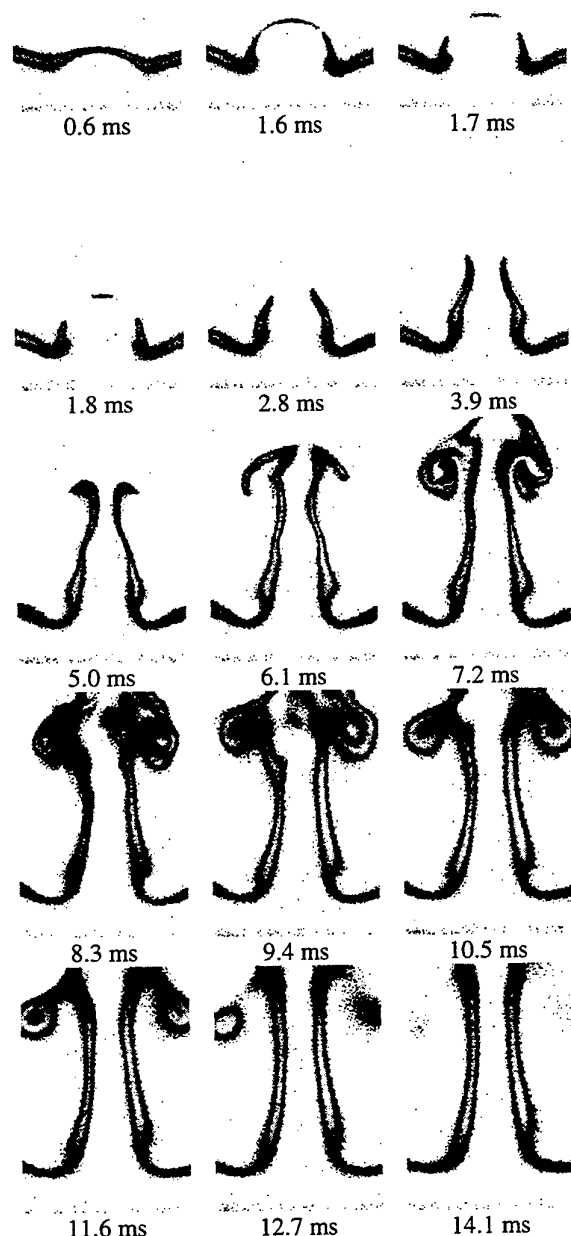


Figure 7. Sequence of images before and after extinction of the OH layer.

used. The images of Figure 7 are obtained with flow conditions corresponding to Flame E of Table I. Extinction of the OH layer takes place in an annular pattern around the sides of the vortex, leaving a burning layer at its leading edge. This behavior was first predicted numerically by Katta [1], well before these experiments were initiated, attesting to the utility of his code. After extinction, the isolated island of flame burns away, and the vortex travels upward toward the other nozzle. The flame follows the vortex, traveling up the stem. As the flame overtakes the vortex, it wraps up and turns in on itself.

To test the temporal resolution of the instrument, a series of sequential images was taken with a delay of 10 μ s. The region of study consisted of frames about 1.8-ms delay shown in Figure 7. This delay regime was chosen to focus on the so-called Katta effect. The repeatability of the apparatus of Rolon et al. (1995) is observed to be exceptional.

5. CONCLUSIONS AND FUTURE RESEARCH

The apparatus of Rolon et al. (1995) has been implemented for the study of the interaction of a flame with a vortex. PLIF measurements of acetone and digital, two-color PIV have been applied to characterize the vortices injected into the opposed-jet flow. PLIF images of OH have been used to observe the dynamics of the interaction of the flame with the vortex. These combined measurements show that this burner can provide effective temporal resolution to at least the 10- μ s level. An annular break in the OH layer has been observed, in excellent agreement with the numerical computations of Katta (1998).

Future work will be directed toward understanding phenomena such as the Katta-type extinction. A variety of parameters can be studied, such as extended ranges of nitrogen dilution in hydrogen, different flame-thickness regimes, and different fuels. To aid in these studies, simultaneous OH PLIF and digital, two-color PIV are presently being implemented, along with measurements of the temperature field.

ACKNOWLEDGEMENTS

The authors are grateful to Mr. K. D. Grinstead, Jr., for assistance in synchronization of the experiment and construction of the solenoid power amplifier. In addition, the authors wish to acknowledge the advice of Dr. L. P. Goss concerning the reduction of two-color PIV data. The authors wish to thank Dr. R. D. Hancock for assistance in assembly and construction of the burner. The authors also acknowledge Drs. R. D. Hancock, W. M. Roquemore, V. R. Katta, and K.-Y.

Hsu for the stimulating discussions of flame-vortex dynamics. Finally, the authors gratefully acknowledge Ms. M. M. Whitaker for her thorough editorial review of this manuscript. This work was supported by Air Force Contracts F33615-95-C-2507 and F33615-97-C-2702.

REFERENCES

- Chen, S.-J. & Dahm, W. J. A. 1997, Vortex Ring/Diffusion Flame Interactions in Microgravity Conditions, Fourth International Microgravity Combustion Workshop, Cleveland, OH, pp. 191-196. NASA Conference Publication No. 10191.
- Driscoll, J. F., Sutkus, D. J., Roberts, W. L., Post, M. E., & Goss, L. P. 1994, The Strain Exerted by a Vortex on a Flame—Determined from Velocity Field Images, Combust. Sci. Technol., Vol. 96, No. 4/6, pp. 213-229. See also: Roberts, W. L., & Driscoll, J. F. 1991, A Laminar Vortex Interacting with a Premixed Flame: Measured Formation of Pockets of Reactants, Combust. Flame, Vol. 87, No. 3/4, pp. 245-256; Roberts, W. L., Driscoll, J. F., Drake, M. C., & Ratcliffe, J. W. 1992, OH Fluorescence Images of the Quenching of a Premixed Flame During an Interaction with a Vortex, Twenty-Fourth Symposium (International) on Combustion, The Combustion Institute, Pittsburgh, PA, pp. 169-176; Roberts, W. L., Driscoll, J. F., Drake, M. C., & Goss, L. P. 1993, Images of the Quenching of a Flame by a Vortex—To Quantify Regimes of Turbulent Combustion, Combust. Flame, Vol. 94, No. 1/2, pp. 58-69; Mueller, C. J., Driscoll, J. F., Ruess, D. L., & Drake, M. C. 1996, Effects of Unsteady Stretch on the Strength of a Freely-Propagating Flame Wrinkled by a Vortex, Twenty-Sixth Symposium (International) on Combustion, The Combustion Institute, Pittsburgh, PA, pp. 347-355; Mueller, C. J., Driscoll, J. F., Ruess, D. L., Drake, M. C., & Rosalik, M. E. 1998, Vorticity Generation and Attenuation as Vortices Convect Through a Premixed Flame, Combust. Flame, Vol. 112, No. 3, pp. 342-358.
- Escudie, D. 1988, Stability of a Premixed Laminar V-Shaped Flame, Prog. Astronaut. Aeronaut., Vol. 113, pp. 215-239.
- Gogineni, S., Goss, L., Pestian, D., & Rivir, R. 1998, Two-Color Digital PIV Employing a Single CCD Camera, Exp. Fluids, in press.
- Hertzberg, J. R., Namazian, M., & Talbot, L. 1984, A Laser Tomographic Study of a Laminar Flame in a Karman Vortex Street, Combust. Sci. Technol., Vol. 38, No. 3/4, pp. 205-216.
- Jarosinski, J., Lee, J. H. S., & Knystautas, R. 1988, Interaction of a Vortex Ring and a Laminar Flame, Twenty-Second Symposium (International) on Combustion, Pittsburgh, PA, pp. 505-514.
- Katta, V. R., Carter, C. D., Fiechtner, G. J., Roquemore, W. M., Gord, J. R., & Rolon, J. C. 1998, Interaction of a Vortex With a Flat Flame Formed Between Opposing Jets of Hydrogen and Air, accepted for publication in Twenty-Seventh Symposium (International) on Combustion The Combustion Institute, Pittsburgh, PA.
- Lee, T.-W., Lee, J. G., Nye, D. A., & Santavicca, D. A. 1993, Local Response and Surface Properties of Premixed Flames During Interactions with Karman Vortex Streets, Combust. Flame, Vol. 94, No. 1/2, pp. 146-160.
- Najm, H. N., Paul, P. H., Mueller, C. J., & Wyckoff, P. S. 1998, On the Adequacy of Certain Experimental Observables as Measurements of Flame Burning Rate, Combust. Flame, Vol. 113, No. 3, pp. 312-332.
- Nguyen, Q.-V. & Paul, P. H. 1996, The Time Evolution of a Flame-Vortex Interaction Observed via Planar Imaging of CH and OH, Twenty-Sixth Symposium (International) on Combustion, The Combustion Institute, Pittsburgh, PA, pp. 357-364.
- Nye, D. A., Lee, J. G., Lee, T.-W., & Santavicca, D. A. 1996, Flame Stretch Measurements During the Interaction of Premixed Flames and Karman Vortex Streets Using PIV, Combust. Flame, Vol. 94, No. 1/2, pp. 167-176.
- Roberts, W. L. 1992, A Premixed Laminar Flame Interacting With a Vortex Resulting in Flame Stretch and Quenching, Ph.D. Dissertation, University of Michigan, Ann Arbor, MI.
- Rolon, J. C., Aguerre, F., & Candel, S. 1995, Experiments on the Interaction Between a Vortex and a Strained Diffusion Flame, Combust. Flame, Vol. 100, No. 3, pp. 422-429. See also: Thevenin, D., Rolon, J. C., Renard, P. H., Kendrick, D. W., Veynante, D., & Candel, S. 1996, Structure of a Non-Premixed Flame Interacting with Counterrotating Vortices, Twentieth Symposium (International) on Combustion, The Combustion Institute, Pittsburgh, PA, pp. 1079-1086.

THREE DIMENSIONAL MAPPING OF TURBULENT FLAME FRONTS.

M. Lawes, C.G.W Sheppard, and R. Woolley

School of Mechanical Engineering, The University of Leeds,
Leeds, LS2 9JT

1. INTRODUCTION

Spark ignited flame kernels in a turbulence field do not immediately experience the full spectrum of turbulence scales present; initially they are wrinkled only by scales of smaller dimensions than the kernel, larger scales merely convecting them. Under nominally identical mean turbulence conditions, successive flame kernels behave differently; dependent upon the nature of the 3-D eddies adjacent to the ignition source from event to event. Not until the kernel becomes large enough to encompass the bulk of scales available in the turbulent field does the burn rate become consistent from shot to shot (Abdel-Gayed *et al.*, 1987). This is the cause of cyclic variation in spark ignition (SI) engines and ignition variability in gas turbines. Slow burning mixtures are particularly affected and the phenomenon is an obstacle to the development of low emissions lean burn and high exhaust gas recirculation (EGR) engines.

The burning rate of such flames is often expressed in terms of a turbulent burning velocity (u_t), a parameter used in many thermodynamic cycle models of engine combustion and in explosion hazard assessment. Turbulent cycle models of engine combustion and in explosion assessment. Turbulent burning velocities are also derived in some newer flame surface area CFD models of turbulent burning (for example Wirth *et al.*, (1993) and Weller *et al.*, (1990)) and can hence be used to validate them. However, measurement of u_t is problematic; particularly for flame kernels in their early stages of development, where it is necessary to quantify the turbulent scales affecting the flame at any instant and where these scales vary in 3-D and from explosion to explosion. The experiments reported here were designed to address these problems using multiple sheet mie-scattered light techniques to capture developing turbulent flame kernels in 3-D.

Combustion systems are routinely observed using 2 dimensional sheet imaging techniques, this is

especially effective in turbulent systems where it is possible to characterise the flame wrinkling (Hicks *et al.*, 1994) , flame curvature (Lee *et al.*, 1993) and reaction progress variables (Chew *et al.*, 1990). However laser sheet measurements do have their disadvantages, inherent in the technique, is that nothing is known of the flame in planes in front or behind the sheet. Experimental apparatus can be designed to overcome this problem so that there is minimal variation in the displacement of the flame just normal to the laser sheet, e.g. V burners in where a turbulent flame is stabilised on a length of wire (Bradley *et al.*, 1992). However this approach often constrains the range of variables that can be studied, such as the turbulence intensity or the initial pressure.

Measurements of non-stabilised outwardly propagating flame fronts are further complicated by flame development. Movement of the flame kernel in the early stages of flame growth can result in a flame displacement well away from the laser sheet. With a single illuminating laser sheet it is often impossible to determine whether the sheet is "slicing" through the centre of the flame kernel. If it is not, the measured flame speed will be higher than actuality as a result of the expansion of the flame normal to the sheet, this may be neglected if the sheet bisects the flame through its centre.

Smaller scales can give the appearance of islands of flame in front of the main reaction that have apparently been ripped away from the main flame, likewise pockets of unburned products can appear behind the main reaction front. Unless very high turbulent levels have been achieved these islands and pockets are usually connected to the rest of the flame front, this has been demonstrated with the use of 3-D imaging techniques (Hicks *et al.*, 1994).

An understanding of these problems has existed since laser sheet measurements were first used within combustion systems and various solutions have been proposed to overcome the limitations of using single sheets. In the first of these a laser beam was rapidly traversed through an aerosol seeded gas jet with the

use of a rotating mirror (Yip *et al.*, 1987). The resulting images were moved across a CCD chip using a second rotating mirror. However, since the images are successive rather than instantaneous, it is necessary that the traverse speed is very high relative to the flow movement between images. A further limit on the system is the number of consecutive images that may be measured at these very high framing rates.

Instantaneous multiple sheet imaging has been achieved using typically 4 sheets of different wavelengths simultaneously generated (using a Nd:YAG laser and Raman shifter) which pass through the flame as parallel light sheets a small distance apart (Mantzarras *et al.*, 1988). The flame is imaged using by Mie scattering, where a seed is selected that whose light scattering properties are destroyed in the flame front so particles scatter light only in the unburned gas mixture. The images are captured onto different parts of a CCD chip. However, 4 sheets would appear to be the limit on the number of sheets that may be simultaneously generated using a single laser and captured with CCD of currently available size.

In this work the number of consecutive imaged sheets has been increased over previous techniques in order to successfully characterise a non-stabilised expanding turbulent flame kernel. The method used is an extension of that used by Yip *et al.*, 1987, therefore, very fast laser repetition and data capture rates were necessary. The technique is devoted to the application of 3-D mapping to developing turbulent flames, the analysis of the imaged flames will be covered elsewhere.

2. EXPERIMENTAL

A 380 mm diameter spherical stainless steel vessel with extensive optical access through 3 pairs of orthogonal windows of 150 mm diameter, was employed. It could be operated at initial pressures and temperatures of up to 15 bar and 600 K, respectively. The chamber was equipped with four fans driven by electric motors, that were run throughout the experiment to generate the turbulent flow field.

The turbulent flow field was calibrated using laser doppler velocimetry (LDV). A single velocity component argon-ion laser LDV system was used with signal processing being performed with a Dantec 57N20 Enhanced Burst Spectrum Analyser (BSA). Directional ambiguity in the velocity measurements was removed by adoption of a 40 MHz frequency shift to one of the beams. Alumina (Al_2O_3) particles,

with a nominal diameter of 0.3 μm , were used to seed the airflow. Measurements indicated that, within the optically accessed central region (150 mm diameter), the turbulent velocity flow field was essentially isotropic with very low mean velocities. The rms turbulent velocity was found to vary linearly with fan speed and, for the fan speed used in this study (500 rpm), was measured to be 0.56 m/s.

The turbulent integral length scale, L , was found directly from a spatial correlation. For these measurements, a second LDV system and BSA processor were obtained on loan from Dantec Measurement Technology. Simultaneous velocities were measured at two points within the combustion vessel. The centre of the vessel was taken as one fixed measurement point whilst the second point was at variable horizontal distances away from the centre. The longitudinal integral length scale, was then calculated from the two point correlation function. The length scale, L , was found to be 20 mm and independent of fan speed. The Taylor scale of the turbulent flows used here was calculated to be approximately 3 mm.

Lean ($\phi = 0.6$) turbulent methane-air flames were ignited in the centre of the vessel. The initial pressure and temperature were 1 bar and 300 K respectively. Two types of flow seeding were tried: cigarette tobacco smoke and solid particles of titanium dioxide (particle size typical 0.22 μm). Both types of seeding were rapidly consumed (or changed scattering characteristics) in the flame, yielding excellent flame definition. However the titanium particles scattered light better and were more pleasant to work with than tobacco. Neither seed proved as effective in the combustion vessel as they had in engine experiments (Hicks *et al.*, 1994). The fans proved remarkably efficient in depositing seed onto the vessel walls and windows; also, the large timescales of bomb combustion events allowed for more time for the seed to be dispersed. Tobacco smoke remained suspended longer, but was less efficient in scattering light and led to tar deposits on the windows with extended use.

Laser sheet images were generated by an Oxford Lasers copper vapour laser (CU15) capable of repetition rates from 2 KHz to 30 kHz. The pulse length was of the order of 20 ns, the pulse energy at 18 kHz was typically 0.5 mJ. The laser beam was focused using a plano-convex lens and a sheet generated with a plano-convex cylindrical lens. The experiment is shown diagrammatically in Fig. 1. The laser sheet was moved using a rotating octagonal mirror, the speed of rotation determining the sheet spacing. The speed of rotation was measured with the use of a helium neon laser pointed towards the

octagon mirror, a photo-diode was then positioned so that it detected the helium neon beam but not the copper vapour laser. There was a slight divergence between adjacent sheets this was calculated to be in the worst case mm.

The flame sheets were imaged with a Kodak Ektapro HS 4540 Motion Analyzer which was used at rates of 4,500 fps full frame (256 x 256 pixels) to 18,000 fps quarter frame (255 x 64 pixels). Once captured the images were downloaded onto video tape. It was possible to record up to 1064 images for each event. A signal from the camera was used to synchronise the camera and laser. The chip had an effective film speed of 1600 ASA and was used in conjunction with a c-mount television lens used with an aperture setting of f 1.1. The large aperture resulted in some image blurring in the sheets furthest from the spark gap where the camera was focused, however, this was preferable to the reduction in contrast between burned and unburned gas if a smaller aperture was used. A 510 nm interference filter was placed between the laser sheet and camera lens to filter out background light from the combustion event, this is unusually intense as a result of the emission of light from the seed as it is heated.

Two alternative methods were used to image flames:

(a) The laser was fired at a high repetition rate (18 kHz) and the mirror was rotated relatively slowly. Each face of the mirror generated one sweep of the through the combustion space with multiple laser firings (and images) per sweep. For a given laser repetition rate the mirror speed determined both the sheet spacing and the number of sweeps through the combustion event. The lower the mirror speed the closer the sheets but the lower the number of sheets that could be recorded of the flame.

(b) The mirror was rotated much faster and the laser fired at each face only once per revolution, with a slight delay in firing from face to face such that the sheet was displaced from shot to shot. With the octagonal mirror used here, this allowed 8 slices per sweep through the combustion event at any instant (assuming minimal flame growth during the sweep). With this method it was possible to obtain very close sheet spacing, but tight control of the rotating mirror and the laser firing was critical to maintaining fixed sheet spacing.

Results for Method (a) are presented here, as it was made the most effective use of the large capacity of the camera. In this work the laser and camera were run at 18 kHz. A sheet height of approximately 50 mm was used. No attempt was made to synchronise the rotation of the mirror with the time of ignition in

order to control the size of flame to be imaged. This was because the initial flame trajectory was found to be highly unpredictable, a result of the low laminar burning velocity of the flame making it prone to convection by large turbulent scales (Hicks *et al.*, 1996).

Method (b) was successfully implemented using a Cordin rotating drum camera and Kodak TMAX 1600 film forced processed to 3200 ASA. The overall image quality was not as good as Method (a) with the video camera, this is thought to be a result of poor seeding density. Method (b) would be better suited on to a mirror with more facets. Method (a) was also tried with the rotating drum camera in order to obtain better spatial resolution of the sheets. However the camera optics had an effective aperture setting of f 4.5 and it is thought this rendered the seeding difficulties more critical, as no sheet images were captured on film.

3. RESULTS

Shown in Figure 3 is a set of 25 laser sheet images, separated by 0.7 mm in the third dimensions, through a flame kernel at an "instant". The flame edge has been enhanced by a hand tracing technique resulting in the addition of a bright line so that the flame edge can be clearly identified. An equivalent sequence of single sheet images at a single plane (for a stationary sheet) are shown in Fig. 2, for a similar mixture. It can be seen that very little flame growth occurs in the time interval (1.4 ms) covering the 25 images shown in Fig. 3. A spark plug is visible in the bottom left hand corner of the pictures and, in this combustion event, the kernel centroid can be seen to have migrated approximately "north north east". This migration is a function of the larger scales of turbulence at the spark gap at the instant of ignition and is random from one combustion event to another (Hicks *et al.*, 1996). Sheets 1 and 25 cut through the flame kernel close to its outer edges, Sheets 12-14 relate approximately to the centroid of the kernel, the spark gap is centred on sheet 13.

Viewed using schlieren photography, such kernels appear almost spherical; these sheet images reveal considerable structure, even at this earlier stage of turbulent flame development. An apparent island of flame can be observed in Frames 17, 18 and 19; however, this can be seen to interconnect with the main kernel in Frame 16. Similarly a pocket of mixture appears inside the flame in Frame 9 and 10; which is seen connected with the outside unburned gas in Frame 8. Although the resolution (≈ 0.7 mm) is poor in absolute terms, relative to the large integral

length scale of the combustion vessel (20 mm) it is possible to determine small scales of turbulence; its adequate to resolve the Taylor scale (3 mm) if not the Kolmogorov scale (0.15 mm). The resolution in the third dimension is similar to that in each 2-D slice.

Shown in Fig. 4 are four successive sets of 6 laser sheet images recorded at successive "instants" through a developing flame kernel. The laser/camera speed was again 18 kHz, but the mirror speed was increased by about 4 times in order to have a greater number sweeps, here the sheet spacing was 3 mm (equivalent to the Taylor scale). The scale is the same, the vertical dimension corresponds to 45 mm in the combustion vessel. In the case of the fourth sweep the sheet quality is poor and the flame edge can only be seen using high contrast. The edge has been added by a hand tracing technique and is identified as a light line. As discussed earlier, there is a compromise between sheet spacing and number of sweeps for a given rotating mirror. The developing 3-dimensional nature of the flame is clear. In this case the pictures do not show the complete kernel; this could be done only at the expense of spatial resolution, as only 64 pixels were available in the vertical direction.

4. CONCLUSIONS

Flames have been successfully mapped in 3 dimensions using Mie scattering images. The spatial resolution was 0.7 mm in both the images and in the third dimension separating adjacent sheets, this was adequate to resolve turbulent features to the Taylor scale for the experiment. A single turbulent flame kernel was "sliced" by 25 laser sheets. Apparent islands and pockets of flame can be seen to be connected to the main flame kernel at the relatively low level of turbulence adopted in this experiment.

REFERENCES

Abdel-Gayed, R.G., Bradley, D. and Lawes, M. 1987, Turbulent burning velocities: a general correlation in terms of straining rate, Proc. R. Soc. Lond., A414, p. 389.

Bradley, D., Lawes, M., Scott, M.J., Sheppard, C.G.W., Greenhalgh, D.A. and Porter, F.M., 1992, Measurement of temperature pdfs in turbulent flames by the CARS technique, 24th Symp. (Int.) on Comb., the Comb. Inst.

Chew, T.C., Bray, K.N.C., and Britter, R.E., 1990, Spatially resolved flamelet statics for reaction rate modelling, Combust. and Flame, vol. 80, pp. 65-82.

Hicks, R.A., Lawes, M., Sheppard, C.G.W. and Whitaker, B.J. 1994, Multiple laser sheet imaging investigation of turbulent flame structure in a spark ignition engine, SAE paper 941992.

Hicks, R.A., Lawes, M., Sheppard, C.G.W., and Woolley, R. 1996, The development of spark ignited turbulent flames, Eighth International Symposium on the Application of Laser Techniques to Fluid Mechanics.

Lee, T.-W., North, G. L. and Santavica, D. A. 1993, Surface Properties of Turbulent Premixed Propane / Air Flames at Various Lewis Numbers Combust. and Flame, vol. 93, pp. 445-456.

Mantzarras, J., Felton, P.G. and Bracco, F.V. 1988, Three-dimensional visualization of premixed-charge engine flames: islands of reactants and products; fractal dimensions; and homogeneity, SAE paper 881635.

Yip, B., Lam, J. K., Winter, M., and Long, M. B. 1987, Time resolved Three dimensional concentration measurements in a gas jet, Science, vol. 235, pp. 1209-1211.

Weller, H.G., Marooney, C.J. and Gosman, A.D. 1990, A new spectral method for calculation of the time-varying area of a laminar flame in homogenous turbulence, 23rd Symp. (Int.) on Comb., the Comb. Inst., pp. 629-636.

Wirth, M., Keller, P. and Peters, N. 1993, A flamelet model for premixed turbulent combustion in S.I. engines, SAE paper 932646.

ACKNOWLEDGMENTS

The authors would like to thank EPSRC for providing financial assistance to conduct these experiments through the ROPA scheme. The Kodak camera was available courtesy of the EPSRC loan pool. The assistance of Dantec Measurement Technology in the loan of the LDV equipment for the spatial correlation experiment is gratefully acknowledged.

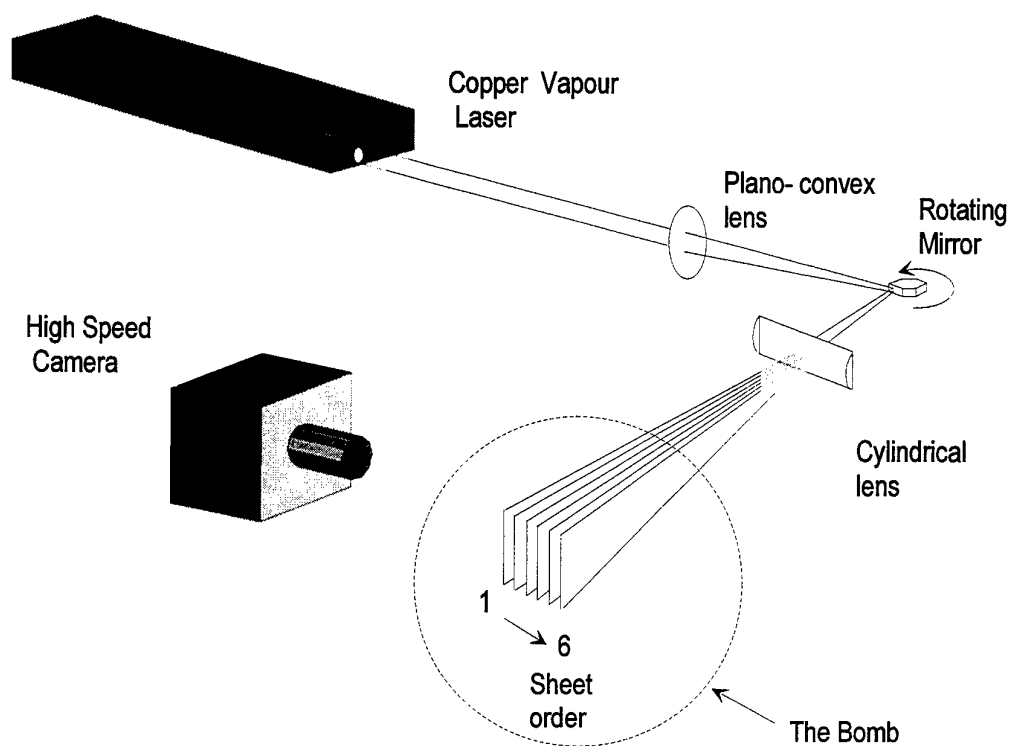


Fig. 1. Schematic diagram of the experiment.



Image 1
32.2 ms from
ignition



Image 2
6 frames later
0.33 ms from
image 1



Image 3
25 frames later
1.41 ms from
image 1

Fig. 2. Successive sheet images of a methane air flame, $\phi = 0.6$, 1 bar, 300 K, $u' = 0.56 \text{ ms}^{-1}$. In these images the sheet is stationary.



Fig.3. Twenty five "slices" through a methane air flame at "one instant", $\phi = 0.6$, 1 bar, 300 K, $u' = 0.56 \text{ ms}^{-1}$ and 28.9 ms from ignition. 0.7 mm between images.

SWEEP 1
32 ms from ignition

SWEEP 2
41.6 ms from ignition

SWEEP 3
50.5 ms from ignition

SWEEP 4
59.4 ms from ignition

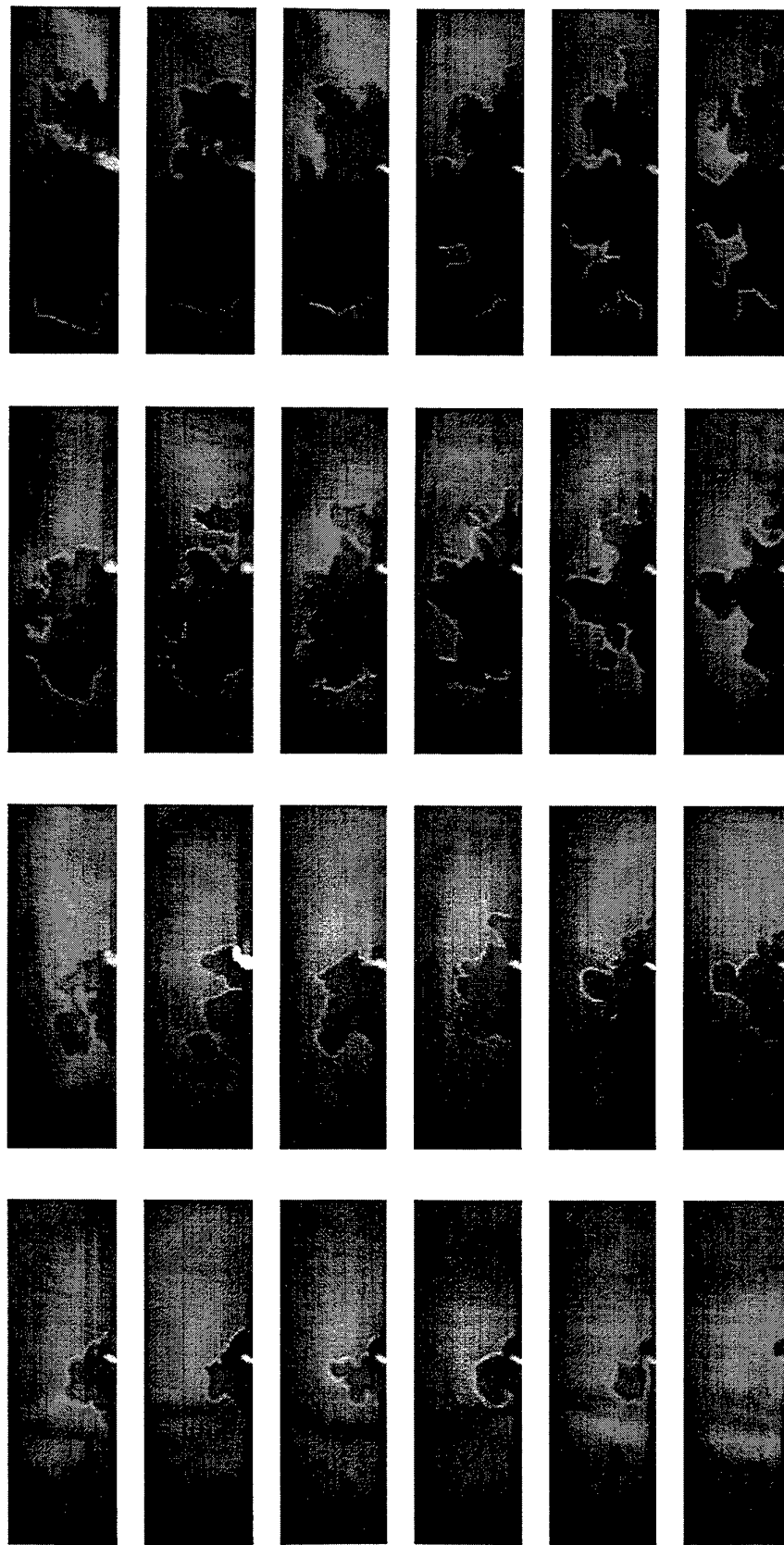


Fig. 3. Six "slices" through a developing flame kernel at four successive times for a methane air flame $\phi = 0.6$, 1 bar, 300 K and $u' = 0.56 \text{ ms}^{-1}$.

Application of new light collecting probe with high spatial resolution to spark-ignited spherical flames

Shohji TSUSHIMA, Fumiteru AKAMATSU and Masashi KATSUKI,

Department of Mechanical Engineering, Osaka University

ABSTRACT

A newly developed light collecting probe named the Multi-colored Integrated Cassegrain Receiving Optics (MICRO) is applied to spark-ignited spherical spray flames to obtain the flame propagation speed in freely falling droplet suspension produced by an ultrasonic atomizer. Two MICRO probes are used to monitor time-series signals of OH chemiluminescence from two different locations in the flame. By detecting the arrival time difference of the propagating flame front, the flame propagation speed is calculated with a two-point delay-time method. In addition, time-series images of OH chemiluminescence are simultaneously obtained by a high-speed digital CCD camera to ensure the validity of the two-point delay-time method by the MICRO system. Furthermore, relationship between the spray properties measured by phase-Doppler technique and the flame propagation speed are discussed with three different experimental conditions by changing the fuel injection rate. It is confirmed that the two-point delay-time method with two MICRO probes is very useful and convenient to obtain the flame propagation speed and that the flame propagation speed is different depending on the spray properties.

1. INTRODUCTION

Since liquid fuel spray flames are heterogeneous turbulent reacting two-phase flows, they have inherently complicated transient structures. Inhomogeneity of spray properties, such as number density, droplet size and velocity, is further complicated as the result of turbulent interactions, which produce various combustion phenomena in the same flow. It was reported that not only diffusion-like phenomena but also premixed-like behaviour were observed in spray flames by Continillo and Sirignano (1990), Cessou *et al.* (1996), Greenberg *et al.* (1996), Li and Williams (1996), Chiu and Lin (1996), Gutheil and Sirignano (1998), and so on. Tsushima *et al.* (1998) concluded that some

portions of the fuel spray disappear rapidly in a premixed-combustion-mode due to preferential flame propagation through easy-to-burn regions, whereas the nonflammable spray regions consist of droplet clusters surrounded by diffusion flames. The results suggest that spray flames do not behave as a conglomeration of single droplets but as a group or cluster of droplets with premixed and diffusion characteristics. Furthermore, to resolve the premixed-combustion-like behaviour in spray flames, clarification of the flame propagation mechanism and quantitative measurement of the flame propagation speed are strongly needed.

Akamatsu *et al.* (1994) observed a spark-ignited spherical flame propagating through a droplet suspension, which is freely falling and entraining surrounding air, in order to observe the flame propagation mechanism and the detailed flame structure in sprays under the minimal influences of atomization and fluid motion. In the study, a pair of short-exposure images of OH-radical chemiluminescence and either of flame luminosity in C₂-radical band or of Mie-scattering from droplet clusters were taken simultaneously to clarify the spatial relation between the nonluminous and luminous flames and unburned droplet clusters. Furthermore, this observation was compared with local continuous measurements, in which OH chemiluminescence, CH bands emission and droplet Mie scattering were simultaneously monitored together with the droplet sizes and velocities by phase-Doppler technique. It was found that a nonluminous flame first propagated continuously through coexisting regions of small droplets and gas-phase mixture and that a number of small-scaled droplet clusters burned randomly associated with discontinuous luminous flames behind the nonluminous flame front.

In the present study, a pair of newly developed light collecting probe named the Multi-color Integrated Cassegrain Receiving Optics (MICRO) is applied to the spark-ignited spherical spray flame for monitoring the time-series signals of OH chemiluminescence from two different locations separated at 6 mm in the vertical direction. The flame propagation speed is calculated by a two-point delay-

time method, in which the time difference between onsets of two chemiluminescence signals detected by each MICRO probe can be measured. In addition, time-series images of OH chemiluminescence are simultaneously obtained by a high-speed digital CCD camera to ensure the validity of the two-point delay-time method with two MICRO probes. Furthermore, the relationship between the spray properties measured by phase-Doppler technique and the flame propagation speed is investigated using three different fuel injection rates. It is confirmed that the two-point delay-time method using the two MICRO probes is very useful and accurate to obtain the flame propagation speed, and that the flame propagation speed are different depending on the spray properties.

2. EXPERIMENTAL APPARATUS

Figure 1 shows the experimental apparatus. An magnetostriction type ultrasonic atomizer (resonance frequency 18.5 kHz) located at 400 mm above a spark gap (4.0 mm) produces kerosene spray. The fuel injection rate is adjusted by an electrically-controlled microsyringe pump. A vertical square duct (280×280×1325 mm) is used to cover the whole test section in order to shield the droplet suspension from surrounding disturbances. The atomized droplets freely fall entraining surrounding air and are ignited by intermittent electric sparks at the gap. After the ignition, a spherical flame emerges near the spark gap and kept on growing with spherical shape for several tens of millisecond. Finally, the spherical flame deforms flowing upward due to the buoyancy effect, and is extinguished by CO₂ injection just below the ultrasonic atomizer. Therefore, the observations are concentrated in the period of the spherical flame propagation. The experiments are conducted at three different fuel injection rates, 4.4, 6.3, and 11.0 cm³/min. The ignition discharge duration time is 20 ms.

To detect OH radical chemiluminescence locally in the flame, two sets of newly developed light collecting probes named Multi-colored Integrated Cassegrain Receiving Optics (MICRO) are used. Kauranen *et al.* (1990) and Nguyen and Paul (1996) have previously applied Cassegrain-type optics to combustion flows to monitor multi-colour images. Figure 2 shows the MICRO probe system used in this investigation, which consists of an optimized pair of concave and convex mirrors combined with an optical fiber cable (Mitsubishi Densen Co. Ltd., ST-U200D-SY, NA = 0.2, core diameter = 200 μm). The MICRO probe system has no chromatic aberration and minimized spherical aberration. In addition, the measurement volume center can be easily visualized using visible laser light guided into an optical fiber through a collimating lens (see Fig. 3) in the reverse direction. This

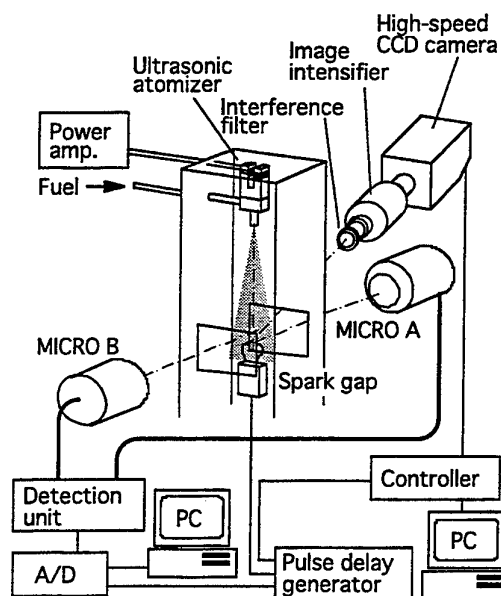


Fig. 1 Experimental apparatus

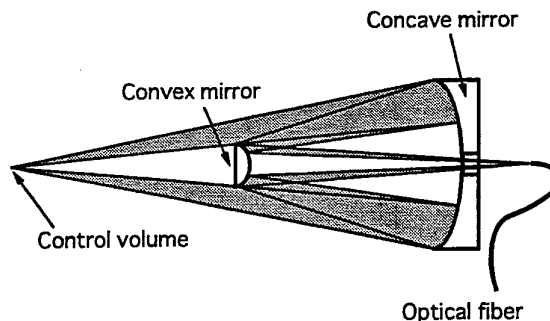


Fig. 2 Configuration of the Multi-colored Integrated Cassegrain Receiving Optics (MICRO)

feature enables precise optical alignment, which is necessary when dealing with UV signals, such as OH chemiluminescence. The light collection efficiency distribution of the system is evaluated using a ray-tracing method by Wakabayashi *et al.* (1998), and the effective control volume size is estimated at 1.6 mm long and 200 μm in diameter.

The light collected by each MICRO probe is directed to a detection unit through the optical fiber cable, as shown in Fig. 3. The light emitted from the other end surface of the optical fiber cable expands according to the numerical aperture (NA). To collimate the expanding light, a collimating lens is attached at the end surface. The OH chemiluminescence signal in the collimated light is detected by photomultiplier tubes (Hamamatsu, R106UH) after passing through a narrow-band optical interference filter

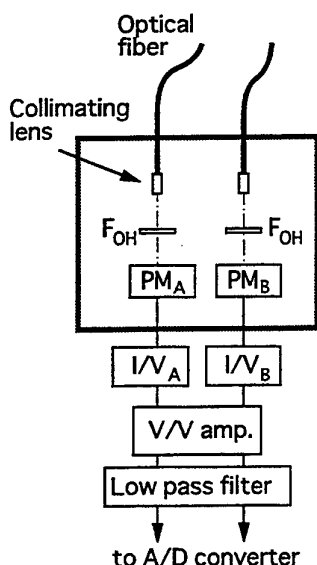


Fig. 3 Configuration of detection unit of the MICRO system

(peak wavelength = 308.5 nm, half-value width = 18 nm) to reject background noise. The current signals from the individual photomultiplier tubes (PMTs) are converted to voltage signals by I-V converters (NF Electronic Instrument, Model LI-76), amplified, and then filtered by an electrical low-pass frequency filter (NF Electronic, FV-665, cut-off-frequency = 5 kHz). The time-series signals are digitized into 12 bits, i.e. 0 to 4096, by an A/D converter (Elmec, EC-2390) and recorded by a computer with digital sampling time of 10 μ s (100 kHz).

Figure 4 shows the measurement location of two MICRO probes (MICRO A and MICRO B) and the spark gap. The MICRO A and B probes are aligned at 4 and 10 mm above the spark gap, respectively. The distance between the two measurement locations is 6 mm.

As shown in Fig. 3, to observe the evolving processes of the spherical spray flame, time-series images of OH chemiluminescence are recorded by a high-speed digital CCD camera (Kodak, EKTAPRO HS4540) simultaneously with the measurement of the two MICRO probes. The OH chemiluminescence from the flame is imaged onto a CCD array of 256 \times 256 pixels in the high speed camera through an optical interference filter (peak wavelength = 308.5 nm, half-value width = 18 nm) and an image intensifier (Hamamatsu, C4273). Images are recorded in the transient memory of the image processing system and digitized into 8 bit, i.e. intensities between 0 and 255. The frame rate is 4,500 frames/s and the maximum number of frames obtained continuously in one run is limited to 1,024, which corresponds to the actual time of 228 ms due to the memory capacity of the image processor. A pulse-delay-generator (Stanford Research Systems, WC Model DG535) is used to control the triggering timing of the spark discharge and each measurement device.

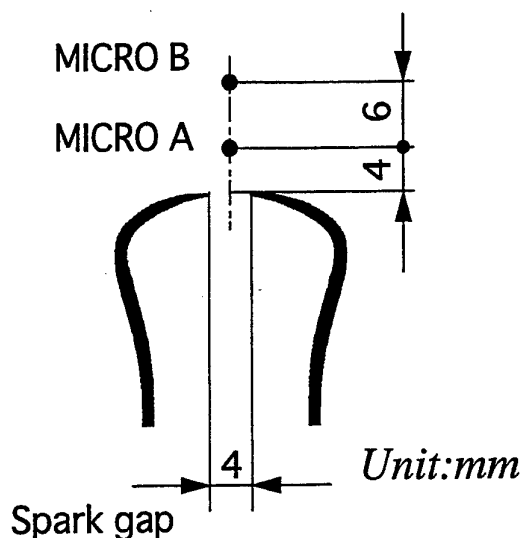


Fig. 4 Arrangement of measurement locations of two MICRO probes and the spark gap

3. RESULTS AND DISCUSSION

3.1 Performance Evaluation of the MICRO Probe System

Before the MICRO probe system could be applied to the spherical spray flame, experimental verification of the MICRO system was conducted. Although the effective control volume size of the MICRO system was estimated at 1.6 mm long and 200 μ m in diameter using the ray-tracing method, a fraction of the light emitted from outside the effective control volume does reach the detectors since chemiluminescence is spatially dispersed in flames and the MICRO system is designed for high sensitivity inside the effective control volume and not for completely blocking external signals. Therefore, simultaneous measurements of OH-radical chemiluminescence by the MICRO probe system

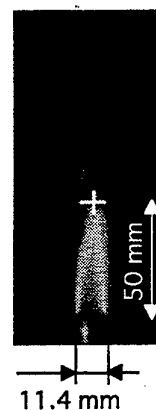


Fig. 5 A direct photograph of the premixed Bunsen flame with the measurement point of both the MICRO system and the electro-static probe

and the ion current by an electro-static probe (Langmuir-probe), whose sensor tip is a Pt-Pt13%Rh thin wire of 100 μ m in diameter and 1 mm long, were conducted in a premixed natural gas Bunsen flame. The inner diameter of the burner port is 11.4 mm. The flame appearance and the measurement point, which was 50 mm above from the burner port, are shown in Fig. 5. The measurement point is located at the fluctuating flame tip on the central axis of the flame. Figure 6 shows the simultaneous time-series signals of the ion current captured by the electro-static and OH radical chemiluminescence obtained by the MICRO system. The OH signals obtained by the MICRO probe show highly spatially resolved features equivalent to the ion current signals detected by the thin tip of the Langmuir probe. These results confirmed that the fraction of light collected from outside the effective control volume is negligible compared to the light collected inside the effective control volume. The MICRO probe system thus exhibited sufficiently high spatial resolution to observe local combustion phenomena without perturbing the flow.

3.2 Observation of Growing Processes of the Spherical Flame

Figure 7 shows time-series signals of OH-chemiluminescence, I_{OH} , obtained by the two MICRO probes together with the corresponding images of OH-chemiluminescence observed by the high-speed digital CCD camera. In image A at $t = 0$ ms, when the spark ignition is initiated, the spark gap is superimposed. The white cross in each image shows measurement locations of each MICRO

probe (see Fig. 4 for the detailed arrangement). As seen in these images, after ignition, the flame front with low brightness is first propagating through the droplet cloud, and thereafter bright luminous lumps appear randomly inside the flame ball. The abrupt increase in time-series signal intensities of the MICRO A probe implies that the flame front passes through measurement location A at $t = 10.4$ ms, while the MICRO B probe, focused at 6 mm above location A, detects the flame front at $t = 47.7$ ms. Local chemiluminescence signals detected by the two MICRO probes are in good agreement with time-series OH chemiluminescence images observed by the high-speed digital CCD camera. Hence, the two-point delay-time method is adopted to deduce the flame propagation speed, V , which is defined as

$$V = L / \Delta t \quad (1),$$

where L denotes the distance between the two measurement locations, which corresponds to 6 mm in this experiment, and Δt is the time difference between the onset of the chemiluminescence signal detected by each MICRO probe. In the case shown in Fig. 5, the Δt is 37.3 ms. The flame propagation speed in this case is calculated at 0.16 m/s.

As reported by numerous researchers, such as Edwards and Marx (1992), sprays have very inhomogeneous spatial and temporal structures such that statistical analysis is required for understanding spray flame behavior. In this study, ignition tests were conducted approximately 100 times at three different fuel injection rates, 4.4, 6.3, and 11.0 cm^3/min . Figure 8 shows the probability distribution of flame propagation speed obtained in each experimental condition. The average flame propagation speed, \bar{V} ,

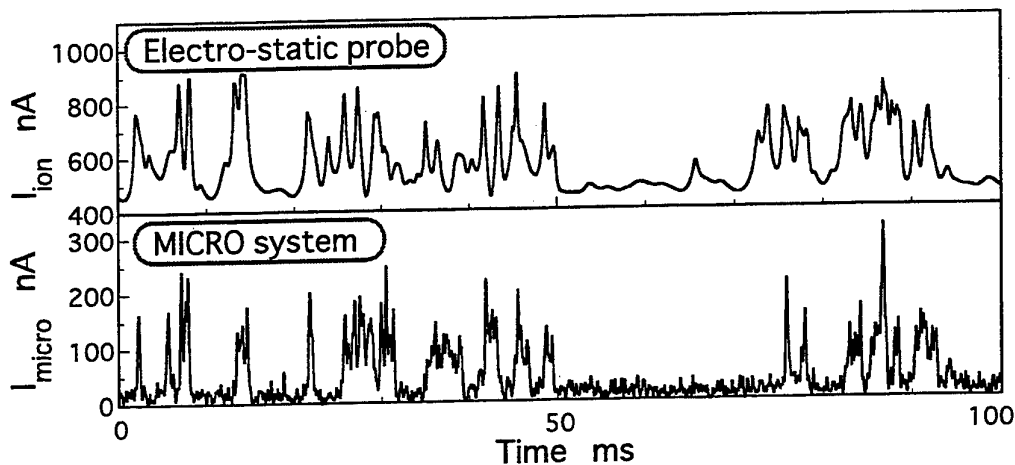


Fig. 6 Time-series signals of OH chemiluminescence obtained by MICRO probe system and ion current detected by the electro-static probe

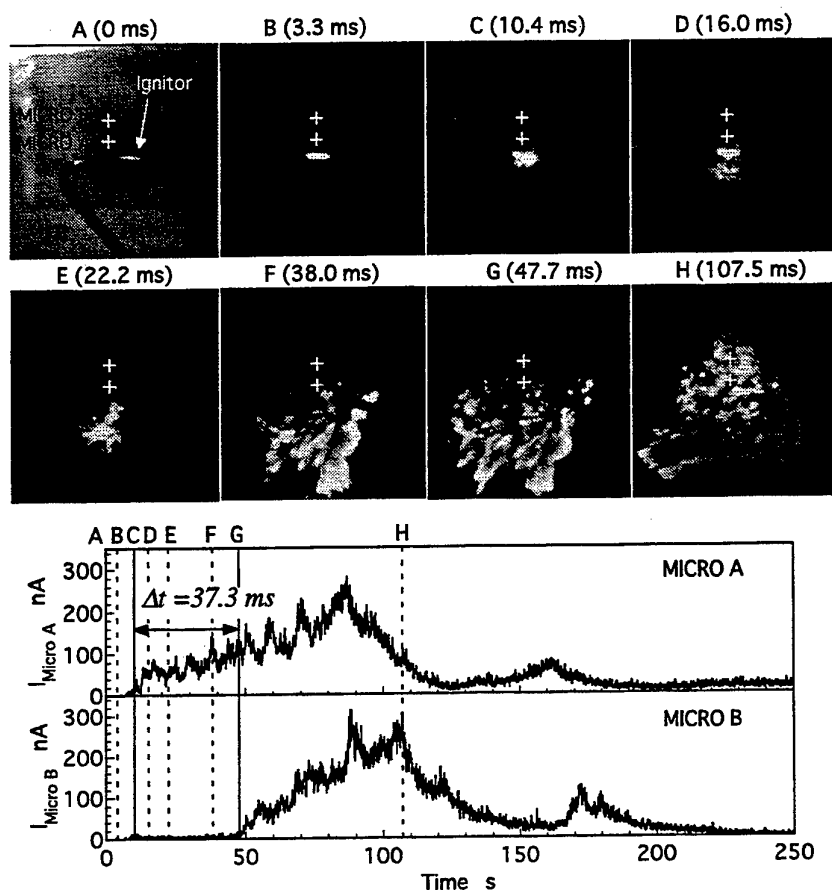


Fig. 7 Time-series data of OH chemiluminescence images recorded by the high speed CCD camera and local OH chemiluminescence monitored by the two MICRO probe systems

measured in the three different conditions is almost the same, ranging from 0.26 m/s to 0.29 m/s, while the RMS value, V' , increases slightly with the fuel injection rate. This is explained by the increase in spray inhomogeneity with increased fuel injection rate, resulting in increased, non-

uniform spatial and temporal flame propagation.

Since the droplets are freely falling with some velocity, the actual corrected flame propagation speed, V_c , in which downward droplet velocity is taken into account, should be deduced. Furthermore, spray characteristics are directly

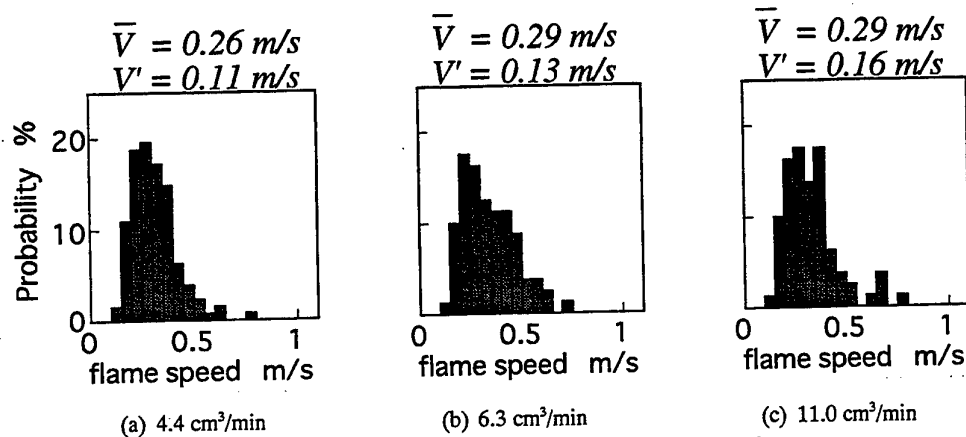


Fig. 8 Probability distribution of the flame propagation speed

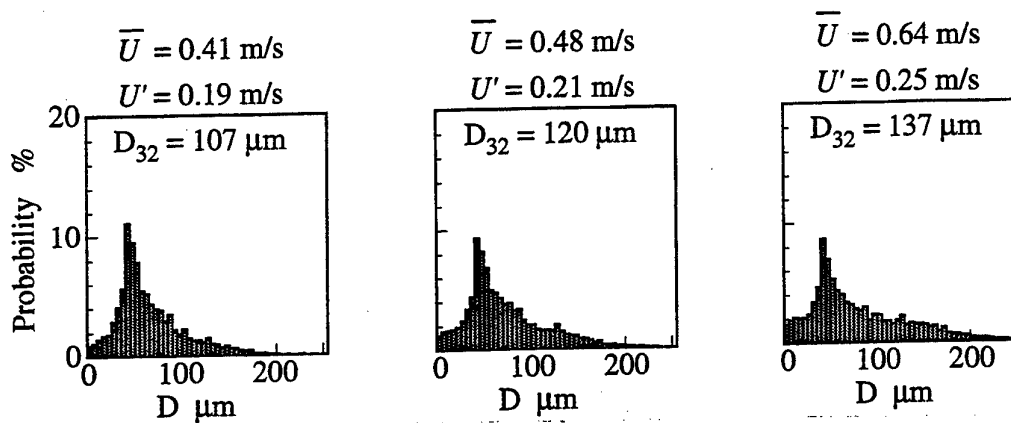


Fig. 9 Size distribution of the droplet suspension at the three different fuel injection rate

connected with flame structure. Hence, it is necessary to know spray properties such as mean diameter, size distribution, number density, slip velocities between gaseous phase and liquid phase and so on. In this study, phase-Doppler technique is applied to the freely falling droplets under isothermal conditions. The control volume of the phase-Doppler system is located in the middle between the two measurement locations of the MICRO probes (7 mm above the spark gap). The droplet size distribution for the three different fuel injection rates are shown in Fig. 9, together with the Sauter mean diameter, D_{32} , mean velocity, \bar{U} , and RMS velocity, U' , of the freely falling droplets. It is shown that the Sauter mean diameter, the mean and RMS velocities increase with the fuel injection rate. The corrected actual flame propagation speed, V_c is defined as follows,

$$V_c = V + U \quad (2)$$

Figure 10 shows the variation of the corrected flame propagation speed, \bar{V}_c , in the three different fuel injection rates, together with the nominal flame propagation speed, \bar{V} , shown in Fig. 7, and the mean downward velocity of the freely falling droplets, \bar{U} , shown in Fig. 8. The solid circle, ●, indicates the average value, and the length of a line segment corresponds to the RMS value. It is shown that the actual corrected flame propagation speed, \bar{V}_c , gradually increases with the fuel injection rate. Increasing the fuel injection rate increases the mass of small droplets, which plays important role in flame propagation due to the increased evaporation rate of small droplets compared to larger droplets. Mizutani and Nakajima (1973) reported that flame propagation speed in their spray flame was enhanced by adding gaseous fuel at the optimized condition. Future work for this experiment will identify the optimized fuel injection rate to enhance the flame propagation speed by conducting a number of experiments in various conditions.

4. CONCLUSIONS

In order to measure flame propagation speed in combustng spray systems, a pair of newly developed light collecting probes named the Multi-color Integrated Receiving Optics (MICRO) was applied to a spark-ignited spherical spray flame, propagation in a droplet suspension to monitor the time-series signals of OH chemiluminescence from two different locations. Firstly, the performance of the MICRO probe was experimentally investigated in comparison with an electro-static probe (Langmuir-probe), with thin sensor tip. The results showed the MICRO probe has sufficiently high spatial resolution to observe local combustion reaction in flames without perturbing the flow. The flame propagation speed was calculated by a two-point

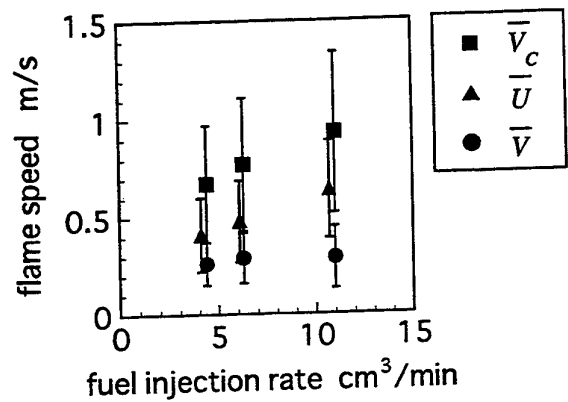


Fig. 10 Variation of actual flame propagation speed at the three different fuel injection rate

delay-time method, in which the time difference between onsets of two chemiluminescence signals detected by each MICRO system was measured. In addition, time-series images of OH chemiluminescence were simultaneously obtained by a high-speed digital CCD camera to ensure the validity of the two-point delay-time method with two MICRO probes. It was demonstrated that the newly developed MICRO probe system was useful to observe time dependent phenomena such as flame propagation. Furthermore, the relationship between the spray properties measured by phase-Doppler technique and the flame propagation speed was investigated for three different fuel injection rates. As a result, the flame propagation speed was different depending on the spray properties.

ACKNOWLEDGMENTS

This research was partially supported by the Grant-in-Aid for Scientific Research, the Ministry of Education, Science and Culture, Japan. The authors wish to express their gratitude to Mr. Yasuhide Okazaki of the Hitachi Zosen Corporation for the courtesy of special arrangement on the measurement equipment.

REFERENCE

- Akamatsu, F., Nakabe, K., Katsuki, M., Mizutani, Y. and Tabata, T., 1994, Structure of Spark-Ignited Spherical Flames Propagating in a Droplet Cloud, in Developments in Laser Techniques and Applications to Fluid Mechanics, Ed. R. J. Adrian, D. F. G. Durao, F. Durst, M. V. Heitor, M. Maeda, J. H. Whitelaw, pp. 212-223, Springer-Verlag.
- Cessou, A. and Stepowski, D., 1996, Planar Laser Induced Fluorescence Measurement of [OH] in the Stabilization Stage of a Spray Jet Flame, Combust. Sci. and Tech., Vol. 118, pp. 361-381.
- Chiu, H. H. and Lin, C. L., 1996, Anomalous Group Combustion of Premixed Clusters, Proc. 26th Symp. (Int.) on Combust., The Combustion Institute, Pittsburgh, pp. 1653-1661.
- Continillo, G. and Sirignano, W. A., 1990, Counterflow Spray Combustion Modeling, Combust. Flame, Vol. 81, pp. 325-340.
- Edwards, C. F. and Marx, K. D., 1992, Analysis of the Ideal Phase-Doppler System: Limitations Imposed by the Single-Particle Constraint, Atomization and Sprays, Vol. 2, pp. 319-366.
- Greenberg, J. B., Silverman, I. and Tambour, Y., 1996, A New Heterogeneous Burning Velocity Formula for the Propagation of a Laminar Flame Front Through a Polydisperse Spray of Droplets, Combust. Flame, Vol. 104, pp. 358-368.
- Gutheil, E. and Sirignano, W. A., 1998, Counterflow Spray Combustion Modeling with Detailed Transport and Detailed Chemistry, Combust. Flame, Vol. 113, pp. 92-105.
- Kauranen, P. Andersson-Engles, S. and Svanberg, S., 1990, Spatial Mapping of Flame Radical Emission Using a Spectroscopic Multi-Colour Imaging System, Appl. Phys., B53: pp. 260-264.
- Li, S. C. and Williams, F. A., 1996, Experimental and Numerical Studies of Two-Stage Methanol Flames, Proc. 26th Symp. (Int.) on Combust., The Combustion Institute, Pittsburgh, pp. 1017-1024.
- Mizutani, Y. and Nakajima, A., 1973, Combustion of fuel vapor-drop-air systems, Combust. Flame, Vol. 21, pp. 343-357.
- Nguyen, Q. V. and Paul, P. H., 1996, The Time Evolution of a Vortex-Flame Interaction Observed via Planar Imaging of CH and OH, Proc. 26th Symposium (International) on Combust., The Combustion Institute, Pittsburgh, PA, pp. 357-364.
- Tsushima, S., Saitoh, H., Akamatsu, F. and Katsuki, M., 1998, Observation of Combustion Characteristics of Droplet Clusters in a Premixed-Spray Flame by Simultaneous Monitoring of Planar Spray Images and Local Chemiluminescence, Proc. 27th Symp. (Int.) on Combust., The Combustion Institute, Pittsburgh, (in Press).
- Wakabayashi, T., Akamatsu, F., Katsuki, M., Mizutani, Y., Ikeda, Y., Kawahara, N. and Nakajima, T., 1998, Development of a Multi-Color Light Collection Probe with High Spatial Resolution; Part 1 Evaluation of Spatial Resolution by Ray-Tracing Method, Transactions of JSME, Vol. 64, No. 619B, pp. 277-282 (in Japanese).

SIZE, SHAPE, VELOCITY AND TEMPERATURE MEASUREMENT OF BURNING COAL PARTICLES WITH A NEWLY DESIGNED OPTICAL MEASUREMENT TECHNIQUE - TOSCA

G. Hackert, S. Wirtz, H. Kremer

Department of Energy Plant Technology (LEAT), Ruhr University Bochum
Universitätsstr. 150, D-44780 Bochum, Germany

1 ABSTRACT

DMT (institute for research and testing, in Essen, Germany) constructed and operates a newly designed high temperature, high pressure drop tube furnace (KOALA). In co-operation with Department of Energy Plant Technology at the Ruhr-University Bochum (LEAT), drop tube investigations of coal particle combustion were performed at various temperatures up to 1500 °C and pressures up to 20 bar. At the same time an atmospheric flat flame burner developed by LEAT is used to observe homogenous and heterogenous ignition processes and the pyrolysis phase during coal particle combustion.

In addition to conventional gas and ash analysis, LEAT employs new methods of insitu particle observation based on Phase shift Doppler Anemometry (PDA) and high-resolution video techniques (TOSCA-system). With this new insitu technique, velocity, size, shape, and surface temperature of the burning particles may be extracted from one particle image only.

It is the aim of TOSCA, both, to produce data for the mathematical modelling and combustion simulation of full scale pressurised applications, and improve the understanding of the elementary reactions involved in pulverised coal combustion at the given conditions.

2 EXPERIMENTAL FACILITIES

The testing facility is characterised as a high temperature, high pressure drop tube furnace as shown in figure 1. In conjunction cold coal particles are dosed into the tube within the centre of the reaction zone with the preheated reaction gas. The tube has a diameter of 70 mm and is 1800 mm high. The coal particle input may be varied from 10 till 100 g/h with the gas flow-through 0 to 60 m³/h. Different residence times of the coal within the reaction tube are realised by variation of the distance between the fixed dosage system and the relocatable collector. A maximum gas and reactor wall temperature of 1600 °C and a maximum pressure of 20 bar are adjustable. To observe different reaction stadiums, the KOALA furnace is equipped with several viewports at three different levels of height.

The second apparatus on a laboratory scale is a small flat flame burner FFB (figure 2). In the center of the flat flame a special coal particle injector supplies particles into the hot gas flow. A quartz glass tube separates the hot atmosphere from the surroundings, to prevent the temperature distribution from being influenced through an increasing air ratio. The tube's material allows the observation of the particles from the initiation of heating /Hackert 1997/.

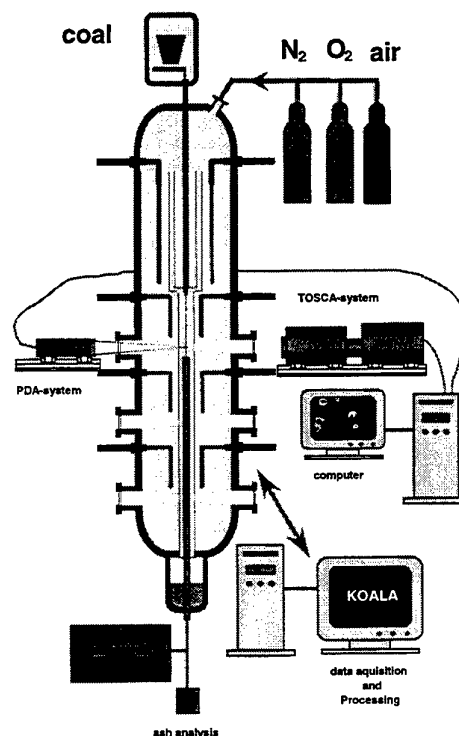


Figure 1: KOALA-furnace equipped with view ports and the PDA and TOSCA-systems

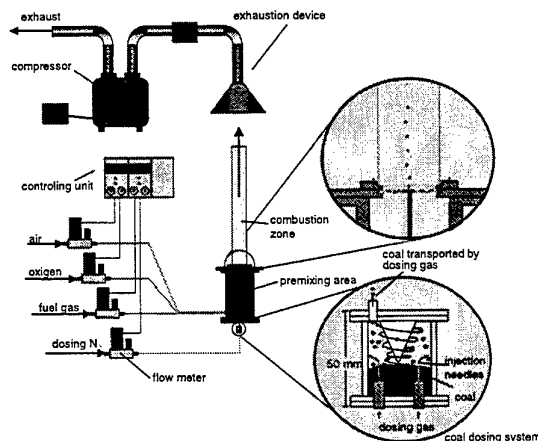


Figure 2: Flat flame burner (FFB) with injected coal particles

3 HIGH RESOLUTION HIGH SPEED CAMERA SYSTEM TOSCA

In addition to conventional gas and ash analysis, the impact of an elevated pressure level to coal combustion is being investigated applying optical measurement methods due to the insitu observation. It is possible to determine the condition of individual coal particles during the different stages of combustion. The measurement system had to be configured to determine velocity, size, shape, and surface temperature of the burning particles. For this purpose, LEAT developed the new measurement system TOSCA /Hackert 1997; Scherello 1996/.

The measurement techniques both at requires high resolution, an extremely short exposure time, next to a high spectrum resolution and measurement accuracy. These requirements are met through the combination of a telemicroscope with two picture amplified CCD-camera systems, fundamentally forming the TOSCA system (Temperature Measurement with Electro Optical High Speed Cameras).

As shown in Figure 3, the individual components of the system can be specified as follows: the telemicroscope is a photosensitive parabolic telemicroscope which works on the basis of the Maksutow principle. A maximum resolution of $2.7 \mu\text{m}/\text{Pixel}$ over a distance of 550 mm are established by using additional lenses. In order to achieve a high picture quality and a high luminous efficiency, an amplified CCD-camera with 12 bit colourscale is used. The camera control system provided by *LaVision, Göttingen Germany*, allows moving particles to be sharply recorded in a small section of a picture ($2 \times 4 \text{ mm}$) without additional illumination. These recordings are done applying extremely short exposure time on the scale of nanoseconds.

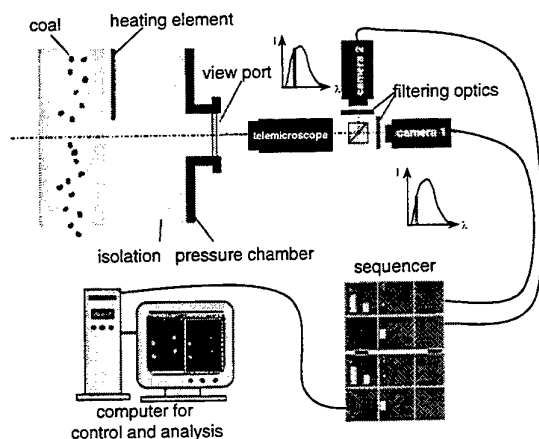


Figure 3: TOSCA-system fixed to one KOALA view port

3.1 Size and Velocity Determination

The size measurement of burning particles within the KOALA furnace provides information about the swelling and bursting of the burning particles and in combination

with the sequence of the burn off. The analysis of the particle shape gives insightprovides information about the aggregate state (solid or liquid) of the coal. Furthermore, the pyrolysis flame and it's influence on coal particle ignition and combustion may be analysed.

In the FFB the pyrolysis flame and the residence time until the ignition takes place may also be determined. The swelling behaviour of different coals and their particle distribution is visible from the injection point up to the coke burn off.

To make a quantitative statement about the size and the velocity of the particle, the resolution of the system (in $\mu\text{m}/\text{Pixel}$) was calibrated with an edged grid. To identify shape and diameter of the particles, an algorithm was developed to sort out the rough data from the size measurement. Figure 4 shows a original picture next to it's processed picture. As shown in Figure 4, the data are extracted form the third picture. To determine the size distribution of the coal, picture series are to be automatically evaluated. As shown in Figure 5 exemplary, results may be graphed as a frequency distribution.

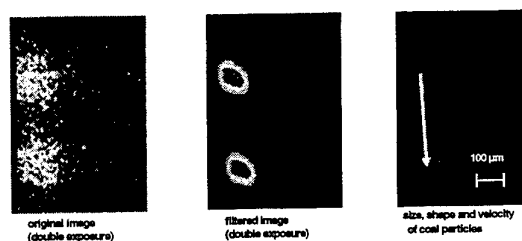


Figure 4: evaluation of double exposed images – from the original image to the size, shape and velocity evaluation

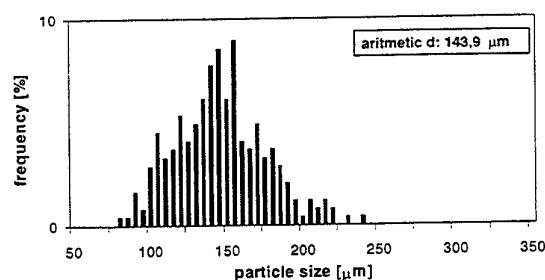


Figure 5: particle size distribution of Westerholt coal ($100 \mu\text{m} - 125 \mu\text{m}$, $T_{\text{gas}} = 1200^\circ\text{C}$, atmospheric, pure nitrogen)

Frequency distributions at different residence times give information about the swelling behaviour of the employed coal, influenced by heating rate and initial size distribution (figure 6).

The particle velocity takes into consideration through multiple exposure and the known time gap between them. The pictures, shown in Figure 4, were taken by using double exposure with a defined delay time.

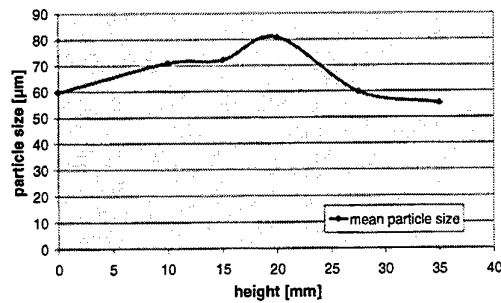


Figure 6: swelling behaviour of Ens Dorf coal (50 µm – 63 µm, $T_{gas} = 1200^\circ\text{C}$, air ratio = 1,15)

As for the size evaluation, the filtered, double exposed pictures are analysed by using the Particle - Tracking - Velocimetry - Algorithm (PTV). Because the direction of the velocity is pre-set, a double exposure is sufficient to clearly determine the direction of the moving particle. For other applications, i.e. swirling flow, the direction of the moving particle may be determined by triple exposure and varying the time gaps between the first and second and the second and third exposure. By automatically evaluating series of pictures, the velocity may be graphed similarly to the size distributions shown in Figure 5.

3.2 Temperature Determination

Any material owning a temperature above zero Kelvin emits thermal radiation. According to Wiens law the product of the object temperature and the wavelength of the maximal spectral radiation is constant ($\lambda_{max} T = 2.8978 \cdot 10^3$ [mK]). Therefore, the maximum of the specific radiation moves towards shorter wavelengths with an increasing temperature into the visible spectral region. For this reason, the human eye perceives the first coloured effect when the object obtains a temperature of 550°C . As the temperature continues to rise, the coloured effect changes from red to white. The specific radiation and the temperature of an ideal object (black emitter, $\epsilon = \alpha = 1$) can be easily related by using the Plancks law of radiation.

$$M_{s\lambda} = \frac{c_1}{\lambda^5 \left[e^{\frac{c_2}{\lambda T}} - 1 \right]} \quad (1)$$

$$\begin{aligned} c_1 &= 3,74184 \cdot 10^{-16} \quad [\text{Wm}^2] \\ c_2 &= 1,438786 \cdot 10^{-2} \quad [\text{mK}] \end{aligned}$$

In contrast to the given relation (1) of an ideal object, the emission and absorption coefficients of real ones depend on the wavelength. Only when a thermal equilibrium is reached are the coefficients equal in value but smaller than one.

$$M_\lambda = \epsilon_\lambda M_{s\lambda} = \epsilon_\lambda \frac{c_1}{\lambda^5 \left[e^{\frac{c_2}{\lambda T}} - 1 \right]} \quad (2)$$

In order to extract the temperature of an object from the thermal radiation, it is necessary important to know the emission coefficient as well as the characteristics of the environment (i.e. reflection) and the transmission geometric. Therefore, the main uncertainty lies in finding the emission coefficient. Two colour pyrometry is a method, which is used to by pass this problem. By applying this method the ration from two adjacent spectral regions are build which the temperature can be determined.

$$I(\lambda, T) = \frac{\epsilon_{\lambda,1}}{\epsilon_{\lambda,2}} \frac{M_{s\lambda,1}}{M_{s\lambda,2}} = \frac{I_1}{I_2} \quad (3)$$

As previously mentioned, the emission coefficient of a black object equals one ($\epsilon_\lambda = 1$). Observing a real object in two different wave length arias, and accepting, that the emission coefficient in both arias are roughly the same, the object can be indicated as a grey emitter. In that case the ϵ -ratio vanishes.

The abovely mentioned technique is used by the TOSCA system in order to point out the particle temperatures. To use this method for determining the temperature on the basis of two colour pyrometry, the radiation of a particle are to be recorded at two different spectral wave length at the same time. To achieve this, a beam splitter is erected in the beam path of camera 1 which reflects the information to camera 2. Camera 2 is placed at a 90° angle from camera 1 to capture the exact inverse. Due to the µm accurate mechanical setup and the exact synchronisation of the cameras, the same section of a picture is simultaneously recorded by both cameras. By using spectral filters in the beam paths of both cameras, a synchron measurement in two spectral regions is achieved (Figure 3). In contrast to other two colour systems working with fibre glass probes /Joutsenoja 1996/, this layout has the advantage that the surface temperature may directly be visualised and interpreted in respect to the particle size, shape and velocity.

In order to measure temperatures quantitatively, the system has to be calibrated by distinguished temperatures. To achieve this, a tungsten strip lamp, which temperatures can be measured using a conventional pyrometer, was used at the LEAT institute. The intensity ratio of two filtered particle recordings from different spectral regions can be related by an exact temperature. Figure 7 shows sections of filtered pictures of particles recorded by camera 1 (λ_1) and camera 2 (λ_2). The pictures are related to each other and the temperature is assigned via a profile given through the calibration function. At the same time, information about the particle form and size is received. The particle velocity may just be pointed out by using double exposure. A graph of the temperature evaluation may also be plotted as a frequency distribution.

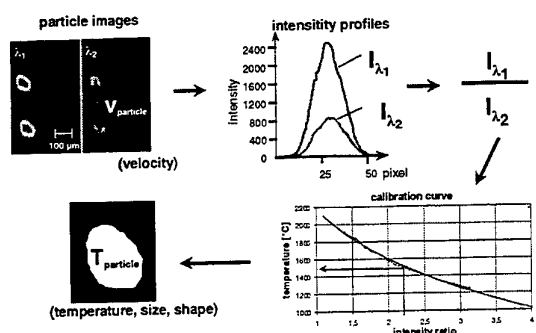


Figure 7: determination of temperature size, shape and velocity using two colour pyrometry

4 RESULTS

Since the measuring system has just been configured recently, a limited series of measurements have been performed and results cannot be extrapolated at this time. Figure 8 shows, one of the clearest results in which the different phases of coal particle combustion are visible qualitatively. Phase 1 shows a pyrolysis flame that has just been ignited. The actual particle is only visible as a shadow behind the pyrolysis flame. In Phase 2 the flame remotes form the particle because of the different velocity of gas and particle. Phase 3 shows an ignited particle with deeply indented, detached pyrolysis flame. The last phase shows the burning coke particle itself.

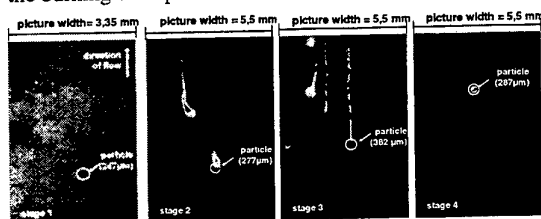


Figure 8: four phases of the coal burn off visualised with the TOSCA-System

Because a clear gas flame would not be seen using this system, the consistency of the pyrolysis flame is left to be determined. It could be liquid tar or small dust or soot particles. Examinations at the FFB shows the swelling effect in dependence to the used coal fraction. Figure 9 shows the swelling of two different coals at the same conditions.

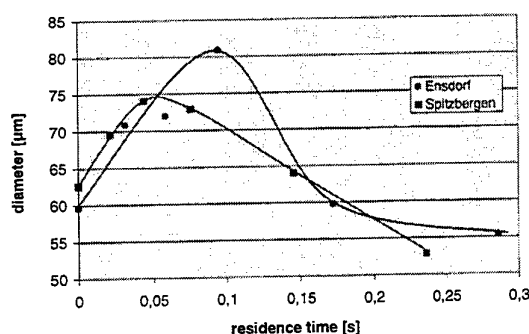


Figure 9: Size modification during the burn off from Ensford and Spitzbergen coal

5 CONCLUSION

With the existing system, a contact free measuring instrument is available for research of hot particles. The main advantage of this system over other systems is that the velocity, size and temperature of a particle can be simultaneously measured. Therefore, a correlation between the particular sizes may be established faster and more precisely than by systems using different measuring devices for each value.

6 REFERENCES

- Christmann, W. 1995: Temperaturmessung mit einem Quotientenpyrometer in einem Heißgaskanal einer Druckkohlenstaubfeuerung, Dissertation, Universität-Gesamthochschule-Essen, Germany.
- Hackert G., Kremer H., Scherello A., Walter M., Wirtz S. 1997: Simultane Erfassung der Temperatur, Größe und Geschwindigkeit von Kohlepartikeln in einem Kohlenstaubdruckreaktor. VDI-Report of the 18th Deutsch-Niederländischen Flammentag, Delft, Netherlands.
- Hackert G., Kremer H., Scherello A., Wirtz S., Bonn B., Seewald H. 1997: Fallrohr-Untersuchungen zur Verbrennung von Kohle bei hohen Temperaturen und Drücken. VDI-Report of the 18th Deutsch-Niederländischen Flammentag, Delft, Netherlands.
- Hackert G., Scherello A., Wirtz S., Bonn B., Seewald H. 1997: Drop tube investigations into coal particle combustion at elevated temperatures and pressures. 9th international conference on coal science (ICCS), Essen, Germany.
- Joutsenoja T., Stenberg J., Hernberg R. 1996: Pyrometric particle temperature measurement in a pressurized fluidized bed gasification reactor. Combustion Science and Technik, Vol. 121, pp. 123-132.
- Scherello, A. 1996: Experimentelle und theoretische Untersuchung des Einflusses von Aufheizgeschwindigkeit und Druck auf die Umsetzung von Kohlenstaubpartikeln; Dissertation. Ruhr-Universität Bochum, Germany.

Laser ignition of single magnesium particles

J.F. Zevenbergen, A.E. Dahoe, A.A. Pekalski, B.R. de Ruiter and B. Scarlett

Delft University of Technology, Division of Particle Technology, Explosion Group,
Julianalaan 136, 2628 BL Delft, The Netherlands

Abstract

By means of laser ignition, the Minimum Ignition Temperature and Minimum Ignition Energy of ultrasonically levitated single magnesium particles are determined simultaneously as a function of particle diameter. The temperature transient of the particles, while being heated by the laser is captured, using a fast optical fiber thermometer. It is shown that the Minimum Ignition Temperature and the, with respect to particle volume normalized, Minimum Ignition Energy are material constants of magnesium and independent of particle size.

(Keywords: laser ignition, ignition energy/temperature, optical fiber thermometry)

1 Introduction

The minimum ignition energy (MIE) and the minimum ignition temperature (MIT) are two key parameters in the assessment of the ignitability of combustible mixtures, like dust clouds. The MIE of a powder is determined with standardized equipment and involves a capacitive electric spark. By gradually lowering the voltage of the capacitor and hence the energy content of the spark, a minimum will be reached at which ignition fails to occur in ten successive attempts. This value is taken as the MIE. However, since each spark generated has a different duration, energy intensity and shape, its application as a means for determining the MIE requires control and quantification of these effects. Thusfar this has proven to be impossible.

The MIT of a powder is determined by means of a furnace [1], which is maintained at a variable but uniform temperature. It consists of a tube 23 cm in length and with a diameter of 3.9 cm. The dust/air mixture is introduced into the furnace by an

air blast from one end of tube. Such an air blast generates a non-uniform turbulent flow field within the oven. Turbulence is known to make a combustible mixture more difficult to ignite, hereby overestimating the MIT. Effects of fouling and residence time of the particles in the furnace also play a significant role in the determination of the MIT. It is therefore generally accepted that a furnace will not give reliable values of the MIT, although being an internationally recognized standard.

Currently a new method is being developed to determine the MIE and MIT of a dust/air mixture simultaneously by means of laser ignition. A laser offers, in comparison by spark and furnace, a far better control over the heating process of the particles. In order to be able to determine these parameters of a dust cloud, it is necessary to perform experiments with single particles. A particle in a dust cloud must reach its MIT in order to ignite. The intensity received by each successive layer within the irradiated volume decreases exponentially with distance. Thus there may be a point beyond which the intensity is too low to contribute to the ignition, e.g. particles beyond this point absorb radiation, but do not contribute to the ignition process. This is exactly the point where measurements of single particle ignition are needed.

Lasers have been previously applied in ignition research. Zhang et al [2, 3] used a continuous Nd:YAG laser with a wavelength of 1.06 μm and a variable output power to heat single particles of coal placed on the end of an optical fibre. The minimum power required to ignite a coal particle was determined and related to the type of coal and the particle size. Depending on the volatile content of the particles, three different ignition mechanisms were identified: homogeneous (gas-phase), heterogeneous and hybrid. The higher the volatile content the more homogeneous the ignition.

Wong et al [4] studied the temperature history before ignition of a char particle suspended in an electrodynamic balance and heated by a CO₂ laser. The temperature history was measured with an optical pyrometer. The effect of oxygen concentration and of the ignition delay time on the probability of ignition were studied.

Qu et al [5] determined the temperature history of graphite and several types of coal particles heated and ignited on a silica plate by a CO₂ laser. The influence of the volatile matter, particle diameter, oxygen content and laser intensity on each type of carbon particle was studied. Increasing the laser intensity shortened the heating time, while an increase in oxygen concentration gave rise to a higher combustion temperature.

2 Experimental

The experimental setup for igniting single particles is shown in Figure 1. A CO₂-laser (Synrad) with a wavelength of 10.59 μm and a nominal output of 60 W is used as the heating source. The laser can be operated in a continuous mode as well as in a pulse mode with a variable pulse duration. The emitted laser beam (4 mm diameter) is split into two equal parts by means of a ZnSe beamsplitter. This to achieve symmetrical irradiation of the particle. Next, with a gold plated, fused silica mirror, each of the two beams is led through a plano-convex ZnSe focussing lens with a focal length of 150 mm. The particle which is to be ignited is held at the focal point of the laser beams by means of an ultrasonic levitator. The temperature of the particle is recorded by means of an optical fiber thermometer (OFT), which can capture temperatures ranging from 200 °C to 2000 °C at a rate of 10.000 measurements per second.

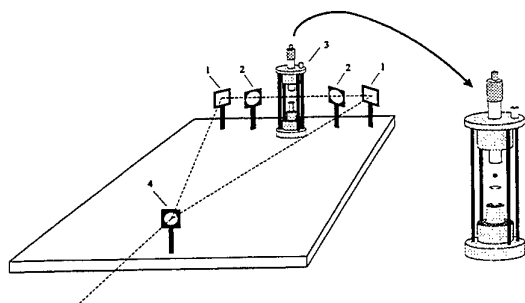


Figure 1. Schematic diagram of the setup used for single particle ignition. (1) Mirror (2) Lens (3) Ultrasonic levitator (4) Beamsplitter.

Spherical magnesium particles with diameters between 250 and 1000 μm were used for the ignition experiments. The particles used for the experiments were not pretreated, like for instance removing the oxide layer. From experience it is known that the naturally formed oxide layer has no traceable effect on the value of the measured MIT. Furthermore, the untreated particles allow for a realistic representation of the material, as used in the process industries.

3 Theory

The temperature distribution within a spherical particle during laser heating is described by the heat conduction equation [6] in spherical coordinates:

$$\frac{\partial(\rho_s C_{p,s} T)}{\partial t} = \frac{1}{r^2} \frac{\partial}{\partial r} \left(r^2 \frac{\partial(\lambda_s T)}{\partial r} \right) \quad (1)$$

Equation (1) is solved subject to the following conditions:

(i) The initial condition.

$$\forall r, \quad t = 0, \quad T = T_\infty \quad (2)$$

(ii) The symmetry condition at the center.

$$\forall t, \quad r = 0, \quad \frac{\partial T}{\partial r} = 0 \quad (3)$$

(iii) The energy delivered to the surface of the sphere.

$$\forall t, \quad r = R, \quad \frac{\partial(\lambda_s T)}{\partial r} = \frac{Q_a I_0}{4 \cdot 2} - h(T - T_\infty) - \epsilon_m \sigma (T^4 - T_\infty^4) \quad (4)$$

For the heat transfer coefficient, h , the Nusselt number for free convection is used.

$$\frac{hd}{\lambda_g} = 2 + 0.59 \left(\frac{d^3 \rho_g^2 g (T_{jR} - T_\infty)}{\eta_g^2 T_\infty} \right)^{\frac{1}{4}} \left(\frac{C_{p,g} \eta_g}{\lambda_g} \right)^{\frac{1}{4}} \quad (5)$$

where the subscript "g" denotes the properties of the surrounding gas. Equations (1) to (5) are solved numerically using an implicit Crank-Nicholson scheme. It should be noticed that the particle is assumed to be irradiated from two sides (factor 2) and that the absorption efficiency, Q_a , is cross-sectional based (factor 4).

The absorption efficiency can be determined by considering a plane, monochromatic wave incident upon the particle with a given size and optical constants. Based on the Maxwell equations [7] Gustav Mie developed his theory, resulting in the most important exactly solvable problem in the theory of absorption and scattering by a spherical particle of arbitrary diameter and complex index of refraction. Mie's solution of the Maxwell equations goes beyond the scope of this article and the reader is referred to the textbooks of Van de Hulst [8] and Bohren and Huffman [9].

A schematic representation of the evolution of the particle temperature is shown in Figure 2. Two regions may be distinguished, namely, a first part in which the particle is slowly heated by irradiation followed by a second part in which the temperature increases rapidly due to combustion. Ignition is defined [10] as the transition from a non-reactive to a reactive state in which external stimuli lead to thermochemical runaway followed by a rapid transition to self-sustained combustion. Hence Figure 2 indeed allows the determination of the MIE and MIT simultaneously of the single particle.

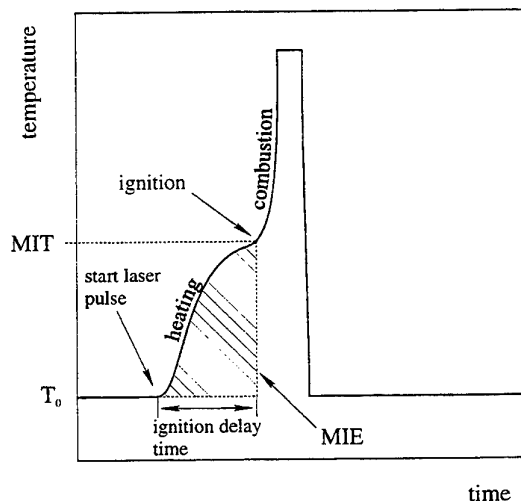


Figure 2. Determination of the MIT and MIE (T_0 denotes the initial temperature of the particle).

4 Results and Discussion

Figures 3 to 5 show the successful irradiation to ignition of magnesium particles with increasing particle size.

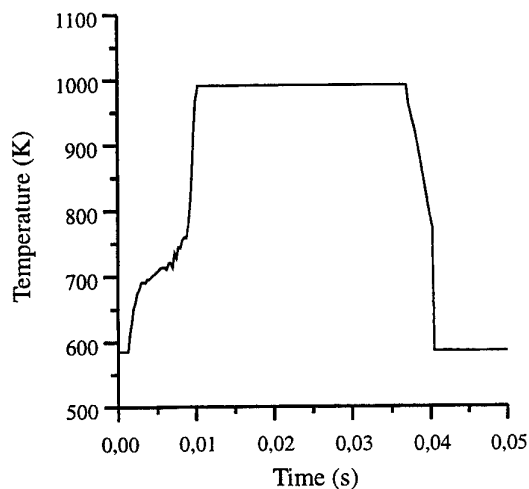


Figure 3. Temperature trace of an ignited magnesium particle ($d = 380\mu\text{m}$).

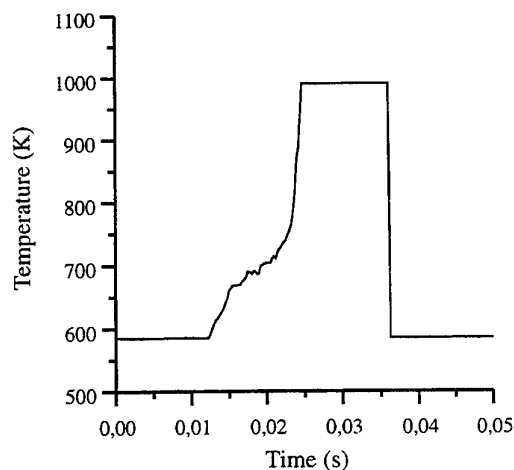


Figure 4. Temperature trace of an ignited magnesium particle ($d = 580\mu\text{m}$).

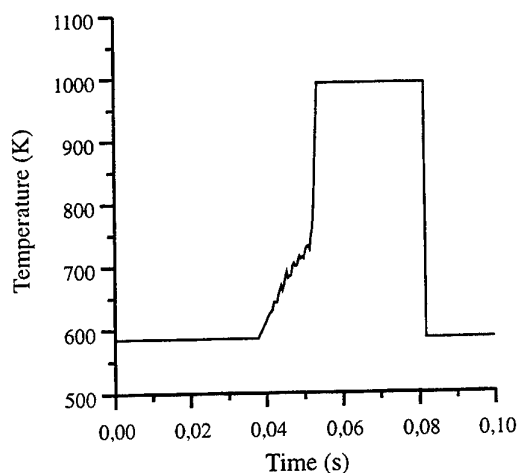


Figure 5. Temperature trace of an ignited magnesium particle ($d = 800 \mu\text{m}$),

The melting point and boiling point of magnesium are 922 K and 1363 K [11] respectively. This indicates that these particles undergo heterogeneous combustion when irradiated to ignition, since for homogeneous combustion the particles must first enter the vapour phase. As can be noticed in the figures, the upper limit of the OFT was set at 1000 K, since the part of the temperature trace beyond this temperature is irrelevant for the determination of the MIE and MIT. In a few separate experiments it was found that the temperature of the particles reaches values well above ($> 2000^\circ\text{C}$, out of scale of the OFT) the boiling point shortly after ignition. This is in agreement with data from literature on the adiabatic flame temperature which varies between 3250 and 3500 K, depending on the equivalence ratio [12]. Note that sometimes, during the heating process, the particle vibrates with small amplitude, causing the "wiggles" in the temperature trace, see Figure 5. Secondly, during the period that the particles combust, they do not always remain in the pressure well in the levitator, but jump out before the combustion process is completed, explaining the differences in combustion time.

In Figure 6 the MIT as a function of particle size is given.

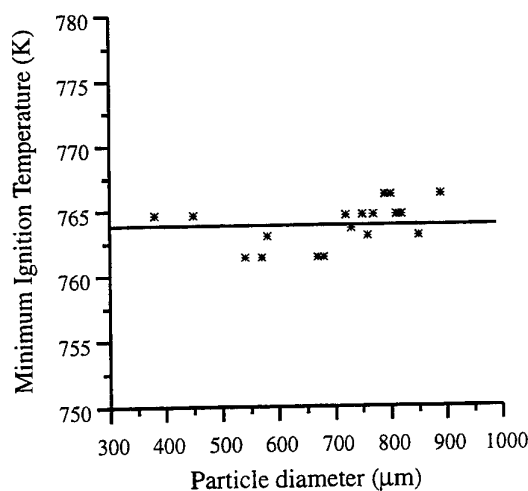


Figure 6. Minimum Ignition Temperature of magnesium particles as function of particle size.

As can clearly be seen from this figure, the MIT is a material constant of magnesium. The MIT of the magnesium particles is 763.83 ± 1.65 K. According to the standard procedure, using a furnace, the MIT of magnesium is 1033 K [1] for a cloud of magnesium particles with a median particle size of $240 \mu\text{m}$, and 833 K for a cloud of magnesium particles with a median particle size of $28 \mu\text{m}$ [13]. As stated before, a particle must reach its MIT, in order to ignite. The MIT of a cloud of magnesium particles should therefore be the same as the MIT of a single magnesium particle. This discrepancy is primarily due to the residence time of the particles in the furnace, which, in turn, is directly related to the settling velocity and hence particle size. The smaller the particles, the lower the settling velocity, the longer the residence time for heating the particles to their MIT. Thus smaller particles require a lower furnace temperature in order to still ignite when reaching the end of the furnace. From a physical point of view one could also reason that the MIT should be a material property and not, as suggested by the results of the furnace method, a function of particle size. This would mean that the activation energy of the combustion (oxidation) reaction is a function of particle size, contradicting the definition of activation energy as suggested by Eyring [14].

In Figure 7 the MIE as a function of particle size is depicted.

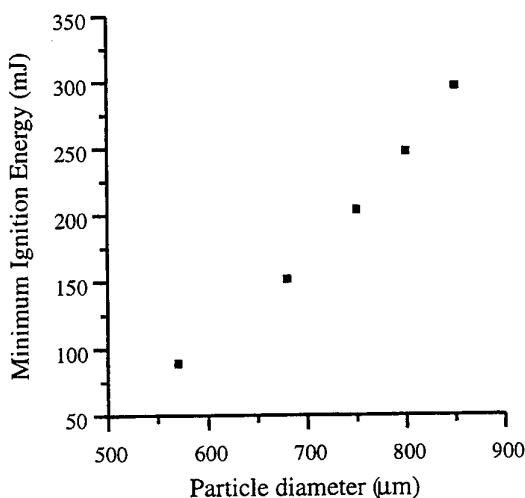


Figure 7. Minimum Ignition Energy of magnesium particles as function of particle size.

The MIE is here taken as the amount of energy accumulated by the particle upon ignition, by integration of Equation 1. This contrary to the electric spark, where the MIE is taken as the amount of energy stored in the capacitor that just fails to ignite the cloud. Figure 8 shows an overlay of the measured temperature trace and the model, confirming the validity of the procedure for determining the MIE.

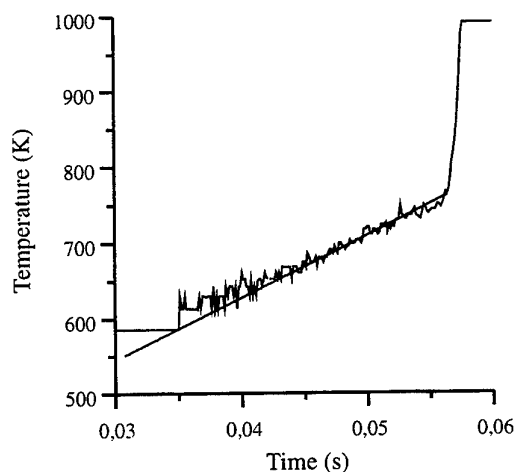


Figure 8. Overlay of the model (Equation 1 on an experimentally measured temperature trace ($d = 850\mu\text{m}$).

As expected the MIE increases with the third power with particle size, since the amount of energy accumulated scales linearly with particle volume (d^3).

Under the condition that the intensity is sufficiently large to heat the particles to their MIT, the MIE (as well as the MIT) is independent of the duration of the laser pulse, as long as it is greater than the ignition delay time, otherwise the particle is not irradiated to ignition.

When normalizing the MIE with respect to particle volume, again a constant value is obtained. This can be explained as follows. For calculating the MIE the left hand side of Equation 1 should be integrated and multiplied with particle volume. Since the MIT is constant and density and heat capacity for each particle follow the same temperature trajectory from room temperature up to the MIT, only the particle volume will change the actual value of the MIE. Therefore, when normalizing with respect to particle size, a constant value will be obtained, see Figure 9. The particle volume normalized MIE of magnesium is $9.20396 \pm 0.02096 \cdot 10^8 \text{ J/m}^3$.

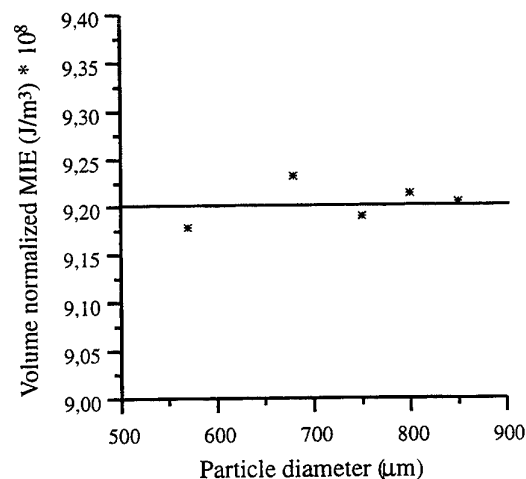


Figure 9. Particle volume normalized Minimum Ignition Energy as function of particle size.

Similar to the dependence of the MIE on the particle size, the ignition delay time shows the same feature of an increasing delay time with particle size, see Figure 10. However, the ignition delay time is, for the same material, not only dependent on particle size, but to a large extent also on the laser intensity received by the particle, under the condition that it will always be sufficiently large to ignite the particle. Although not shown, the ignition delay time can also be normalized with respect to particle volume and (absorbed) laser intensity. When normalized, the ignition delay time will give a strong indication of the validity of the experimental proce-

ture applied for the determination of the MIT in the standardized furnace, since it can be directly related to the residence time of the particles in the furnace.

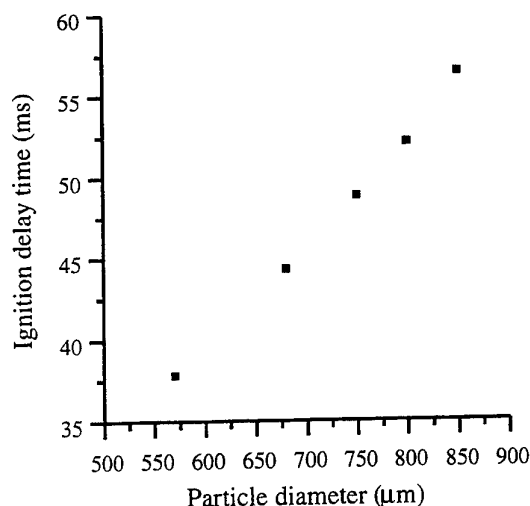


Figure 10. Ignition Delay time as function of particle size.

5 Conclusions

The Minimum Ignition Temperature of magnesium is a material constant and equals 763.83 ± 1.65 K. For all heterogeneously igniting materials, the MIT will be a constant. In principle, for homogeneously or hybridly igniting materials, the MIT will not exhibit a constant MIT as function of particle size, since the heating time will determine the formation of gaseous products that can subsequently ignite and dictate the determination of the MIT. However, when the heating time is small compared to the relaxation time of the devolatilization process, again a constant value should be obtained.

The international recognized standard on the determination of the MIT, using a furnace, lacks a fundamental basis. Measurements performed according to the standard show a particle size dependence of the MIT. However, this effect is not directly related to particle size, but to the residence time of the particles in the furnace, which in turn is related to the settling velocity. The concept of determining the MIT by laser heating is more basic. The key question now to be answered is "how many particles much achieve the MIT before the ignition of an explosion can be considered to become the propagation of an explosion".

The Minimum Ignition Energy of heterogeneously igniting particles is, due to the constant MIT, a function of particle size only. When normalizing the MIE with respect to particle volume a constant value is obtained. The MIE, determined by laser heating, will give the absolute minimum amount of energy that is needed to heat the particles to their MIT, by integration of the accumulation term in the well-known heat conduction equation. This contrary to the spark, where a part of the energy stored in the capacitor will be dissipated in energy forms, other than the energy used for heating the particles. The ignition energy determined with a spark will therefore not be, contrary to what the name suggests, the minimum amount of energy. Only in case of gases, the spark can be used with reasonable accuracy for the determination of the actual minimum ignition energy of these gases, since all parameters involved can be accurately quantified. For dust/air mixtures the spark should be replaced by another technique, for instance a laser.

References

- [1] Eckhoff R.K. *Dust Explosions in the Process Industries*. Butterworth, 1997.
- [2] Zhang D.K., Wall T.F., and Hills P.C. The ignition of single pulverized coal particles: minimum laser power required. *Fuel*, 73:647-655, 1994.
- [3] Zhang D.K. Laser-induced ignition of pulverized fuel particles. *Combustion and Flame*, 90:134-142, 1992.
- [4] Wong B.A., Gavalas G.R., and Flagan R.C. Laser ignition of levitated char particles. *Energy and Fuels*, 9:484-492, 1995.
- [5] Qu M., Ishigaki M., and Tokuda M. Ignition and combustion of laser-heated pulverized coal. *Fuel*, 75:1155-1160, 1996.
- [6] Bird R.B., Stewart W.E., and Lightfoot E.N. *Transport Phenomena*. John Wiley & Sons, Inc., 1960.
- [7] Maxwell J.C. *A Treatise on Electricity and Magnetism*. Dover Publications, Inc., 1954.
- [8] van de Hulst H.C. *Light Scattering by Small Particles*. Dover Publications, Inc., 1981.

- [9] Bohren C.F. and Huffman D.R. *Absorption and Scattering of Light by Small Particles*. Wiley-Interscience, Inc., 1983.
- [10] Kuo K.K. *Principles of Combustion*. John Wiley & Sons, Singapore, 1986.
- [11] Lide D.R. *CRC Handbook of Chemistry and Physics*. CRC Press, Boston, 1992.
- [12] Glassman I. *Combustion*. Academic Press, Inc., third edition, 1996.
- [13] Palmer K.N. *Dust Explosions and Fires*. Chapman and Hall Ltd, 1973.
- [14] Eyring H. The activated complex in chemical reactions. *Journal of Chemical Physics*, 3:107-115, 1935.

PIV IN SPHERICALLY EXPANDING LAMINAR CELLULAR FLAMES

M. Lawes, C.G.W Sheppard, and R. Woolley

School of Mechanical Engineering
The University of Leeds, Leeds, LS2 9JT

1. INTRODUCTION

The use of spherically expanding flames is becoming increasingly common as a method of studying flames under laminar conditions (Dowdy *et al.*, 1990, Bradley *et al.*, 1996). A quiescent gas mixture is ignited and the resultant spherical flame is easily imaged and filmed. The simplicity of the flame geometry means that the effect of stretch is well understood and may be accounted for (Clavin, 1985).

Under certain conditions the flame does not propagate as a smooth laminar flame front, but 'cracks' appear in the surface which ultimately break-up into a number of individual cells. One of the mechanisms responsible for this behavior is thermo-diffusive instability (Markstein, 1964). Here the diffusion of reactive species across the flame dominates over thermal diffusion. Under these conditions the burn rate is enhanced in areas that are convex to the unburned mixture. However, where the flame is concave to the unburned mixture the reaction is starved of the deficient reactant (either fuel or oxidant) and ultimately the flame is quenched. A LIF image of OH is shown in Fig. 1 for a fuel rich ($\phi = 1.4$) iso-octane-air flame. Complete breaks in the flame front are clearly visible. Thermo-diffusive instabilities are observed in lean hydrogen-air or fuel rich heavy hydrocarbon fuel-air mixtures.

Spherical flames can be used to determine values for unstretched laminar burning velocity. These are usually derived from shadowgraph or schlieren flame image. Zhou and Garner (1995) adopted an alternative method to determine the stretched laminar burning velocity, u_n , of spherically expanding propane-air flames by measuring the gas velocity ahead of the flame, u_g , using Particle Image Velocimetry (PIV) then:

$$u_n = S_n - u_g \quad (1)$$

where S_n is the flame propagation speed which was simultaneously measured using ionisation probes.

In the currently reported study PIV measurements for spherically expanding iso-octane - air flames have been made for fuel rich ($\phi = 1.4$) mixtures. This equivalence ratio was chosen in order to investigate the effect of thermo-diffusive cell formation on the gas velocity in front of spherically expanding flames.

The PIV velocities have then been compared with gas velocities predicted from schlieren measurements of similar flames. In this work the flame speed, S_n , was measured directly and u_g is calculated based on an assumption of the laminar flame thickness (Bradley *et al.*, 1994). The transition of the flame to a cellular structure was clearly observed on the schlieren image, there was an associated rise in the flame speed a result of the increased surface area of the flame. Shown in Fig. 2 is an example of this for a iso-octane - air flame at 2 bar. In the early stages the flame speed can be seen to drop with time, this is indicative of a highly unstable flame as the flame speed increases with stretch (Bradley *et al.*, 1994). At 9 ms the flame speed is seen to increase rapidly, at this point the flame surface was observed to have a "pebbled" appearance.

2. EXPERIMENTAL

Flames were ignited in a stainless steel spherical bomb of 380 mm diameter. Three pairs of orthogonal windows of 150 mm diameter provided extensive optical access. Fuel rich iso-octane - air mixtures ($\phi = 1.4$) were burned at 1 and 2 bar, the unburned gas temperature was 358 K. Reactant mixtures were made up within the vessel, fans were run on the inside of the vessel were used to ensure the air and fuel were completely mixed. The vessel was then left for at least 1 minute to ensure the mixture has become quiescent.

The illuminating sheet required for the PIV technique was generated by an Oxford lasers copper

vapour laser (model CU15), the beam was formed into a sheet using plano-convex and plano-convex cylindrical lenses. The laser sheet was positioned directly above the spark plug, eliminating any flow normal to the sheet, only a portion of the flame was imaged; the laser sheet typically being 50 mm high and 0.6 mm thick. The laser repetition rate was nominally 5 kHz. Light from the laser beam was scattered by zirconia seed in the unburned mixture; this was blown in to the bomb during mixing by placing a small charge of compressed air behind a measured quantity of seed.

A high speed Cordin rotating drum camera was used to record the images. Kodak 35 mm TMAX film was used and developed to an effective film speed of 3200 ASA. An interference filter (of approximately 50 % transmission) was placed in front of the camera lens to remove light of wavelengths other than that of the laser beam. The PIV images were digitised using a Nikon LS-1000 film scanner at a resolution of 100 pixels/mm. Particle positions were cross-correlated for successive images using Visiflow, commercial software developed by AEA, Harwell. High accuracy in alignment of the successive images was essential, this was achieved by "bleeding" two laser beams from the main beam into the camera with the use of fibre optic cables. Two reference points were generated on the 2-D image which could be recognised by the software and the images aligned automatically.

3. RESULTS AND DISCUSSION

Shown in Figs. 3 and 4 are two images and their corresponding PIV velocity fields of flames at pressures of 1 and 2 bar, for flame radii of 26 mm. In both cases the flame front is clearly defined by the sudden reduction in seed density associated with the change in gas density in moving from unburned to burned gas in the images; the seeding density is higher in the 2 bar flame. The PIV images were generated using an interrogation area of 128 x 128 pixels, which corresponded to a 1.7 x 1.7 mm section in the vessel. Processing was performed with 50 % overlap. It can be seen that the gas is pushed ahead of the flame having a maximum velocity just in front of the flame (u_g). At 1 bar the flame surface is observed to be smooth and the flame spherical; it has yet to break up into cells, although this does occur as the flame grows to larger radii. At 2 bar (at the same 26 mm flame radius) the presence of cells can be seen across the flame front where the seed has survived in the cracks within the flame front. The seed has not survived very far into the cracks, numerical

computations of thermo-diffusive flames show that despite the quenching of reaction within the cracks the temperature remains very high, this may be sufficient to produce the density drop seen here (Patnaik *et al.*, 1988).

Shown in Fig. 5 is the fall in the gas velocity with distance from the flame front for a flame at 1 bar. The gas velocity quickly decays and reaches zero at above 30 mm ahead of the flame front. The decline in u_g is greatest closest to the flame; thus the measurement of u_g at the flame front may result in errors, as in the PIV technique a single velocity is assigned to an interrogation area. Further investigation of the velocity very close to the flame would be useful.

From Fig. 4 it can be seen that the breaks in the flame front appear to have little influence on the velocity field ahead of the flame. To confirm this, further processing was performed close to the flame front using a smaller interrogation area (64 x 64 pixels, 0.8 x 0.8 mm, 75 % overlap) with the object of observing a diverging velocity field in front of the cracks, a typical example is given in Fig. 6 for a 1 bar flame. The flow field is remarkably uniform along the flame front just ahead of the flame, there appears to be no marked change in the velocity as a result of the presence of cells or any divergence within the flow. Visualisation techniques, e.g. such as subtracting the mean flow and generating streamlines, revealed no divergence in the flow field as a result of the cracks in the flame front.

The gas velocities ahead of the flame measured using PIV are compared to those derived from schlieren experiments, the results are shown in Fig. 7 for a 1 bar flame. In the schlieren measurements the gas velocity was not determined directly but can be calculated based on assumptions of the flame thickness, further details of this method are available elsewhere, Bradley *et al.*, 1998. At smaller radii the PIV measurements give lower velocities than those derived from schlieren images, this is thought to be a result changes in the behavior of the ignition kernel associated with the seed material; however, further work is necessary to confirm this. Nevertheless, later in the flame growth there is reasonable agreement between the gas velocity values derived via the two separate techniques despite the potential inaccuracies identified earlier.

4. SUMMARY

A PIV technique has been used to measure the gas velocity ahead of fuel rich ($\phi = 1.4$) iso-octane - air flames. A certain radii the flame spontaneously broke up into cells as a result of thermo-diffusive instability. Gas velocity ahead of the flame was unaffected by the presence of cells on the flame front. Good agreement was found between the gas velocities ahead of the flame measured with PIV and those derived from schlieren images of flames at the same conditions.

REFERENCES

- Bradley, D., Gaskell, P. H. and Gu, X. J. 1996, Burning velocities, Markstein lengths, and flame quenching for spherical methane-air flames: a computational study, Combust. Flame, vol. 104, p. 176.
- Bradley, D., Hicks, R. A., Lawes, M., Sheppard, C. G. W., and Woolley, R. 1998, The measurement of laminar burning velocities and Markstein numbers for iso-octane - air, and iso-octane - n-heptane - air mixtures at elevated temperatures and pressures in an explosion bomb Combust. Flame, vol. 115, pp. 126-144.
- Bradley, D. and Harper, C. M., 1994, The development of instabilities in laminar explosion flames, Combust. Flame, vol. 99, p. 562.
- Clavin, P., 1985, The development of premixed flame fronts in laminar and turbulent flows. Prog. Ener. Combust. Sci. vol. 11, p. 1.
- Dowdy, D. R., Smith, D. B., and Taylor, S. C. 1990, The use of expanding spherical flames to determine burning velocities and stretch effects in hydrogen/air mixtures, Twenty-Third Symposium (International) on Combustion, The Combustion Institute, Pittsburgh, p. 325.
- Markstein, G.H. 1964, Non-steady flame propagation, Macmillan, New York.
- Patnaik, G., Kailasanath, K., Oran, E.S. and Laskey, K. 1988, Twenty-Second Symposium (International) on Combustion, The Combustion Institute, Pittsburgh, p. 1517.
- Zhou, M., and Garner, C.P. 1996, Direct measurements of burning velocity of propane-air using particle image velocimetry, Combust. and Flame, vol. 106, pp. 363-367.

ACKNOWLEDGMENTS

The authors would like to thank Oxford lasers for providing the alignment mask. The LIF image was taken as part of a collaborative project with Dr. Russell Lockett and Prof. Douglas Greenhalgh of Cranfield University. Experiments were performed on these flames as a result of the inspiration of Prof. Derek Bradley. The work was performed as a part of an EPSRC Grant. Some of the original analysis for this work was performed by Rune Kvale at Leeds as part of his Diploma work for the Norwegian University of Science and Technology.

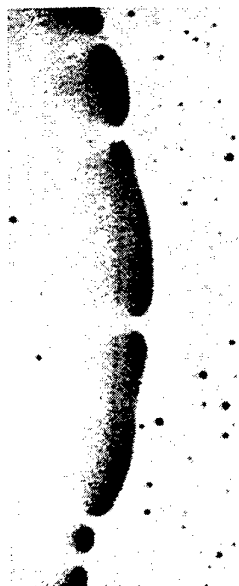


Figure 1. A LIF image of OH for a laminar fuel rich ($\phi = 1.4$) iso-octane - air flame.

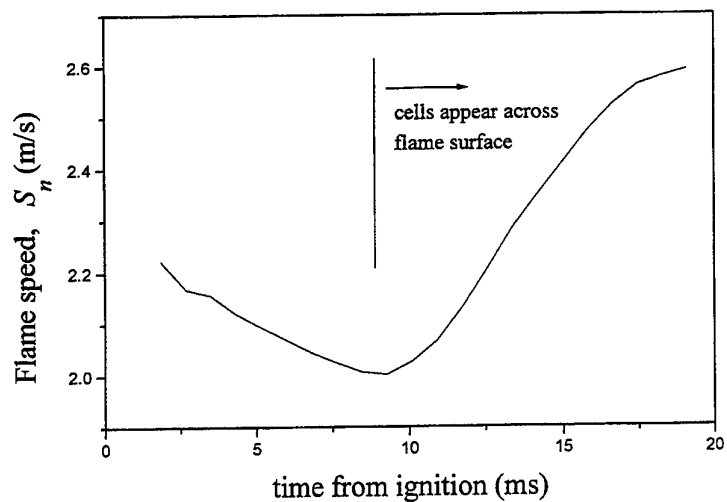


Fig. 2. Flame speed against radius for an iso-octane - air ($\phi = 1.4$) flame at 2 bar. These measurements were derived from high speed schlieren images.

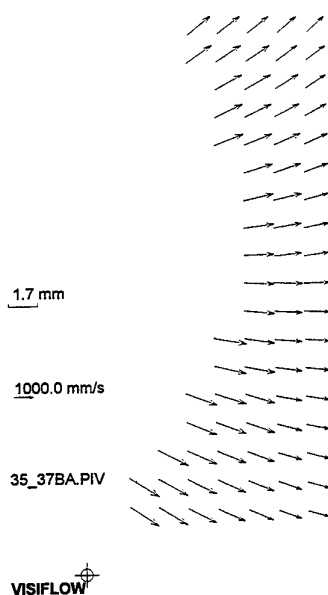
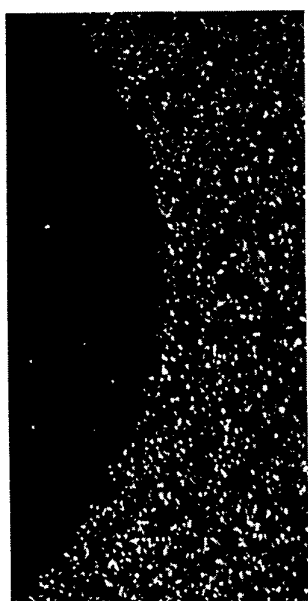


Fig. 3. A sheet image of a $\phi = 1.4$ iso-octane - air flame at 1 bar and the corresponding velocity field. The vertical distance corresponds to approximately 20 mm in the combustion vessel.

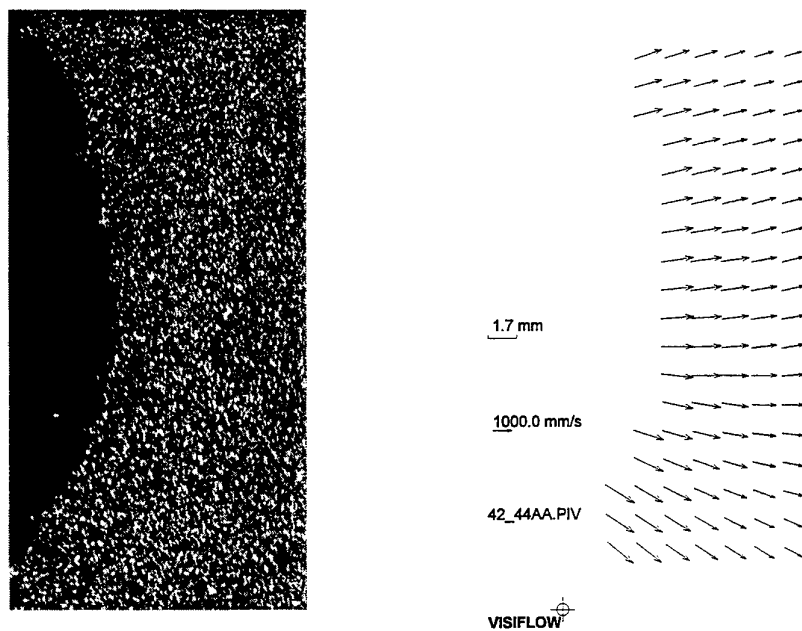


Fig. 4. A sheet image of a $\phi = 1.4$ iso-octane - air flame at 2 bar and the corresponding velocity field. . The vertical distance corresponds to approximately 20 mm in the combustion vessel.

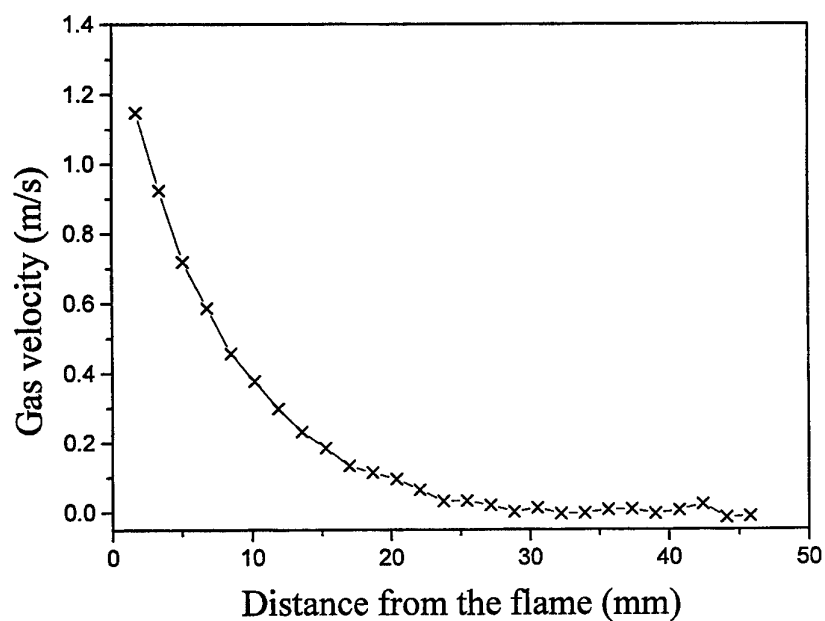


Fig. 5. The gas velocity for a streamline directly vertical from a flame at 1 bar.

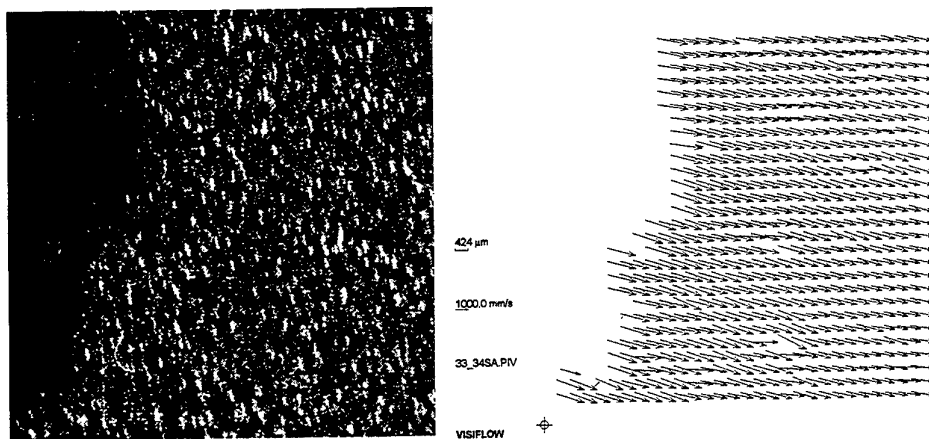


Fig. 6. A sheet image of a $\phi = 1.4$ iso-octane - air flame at 1 bar and the corresponding velocity field. Interrogation area 0.7×0.7 mm, 75 % overlap.

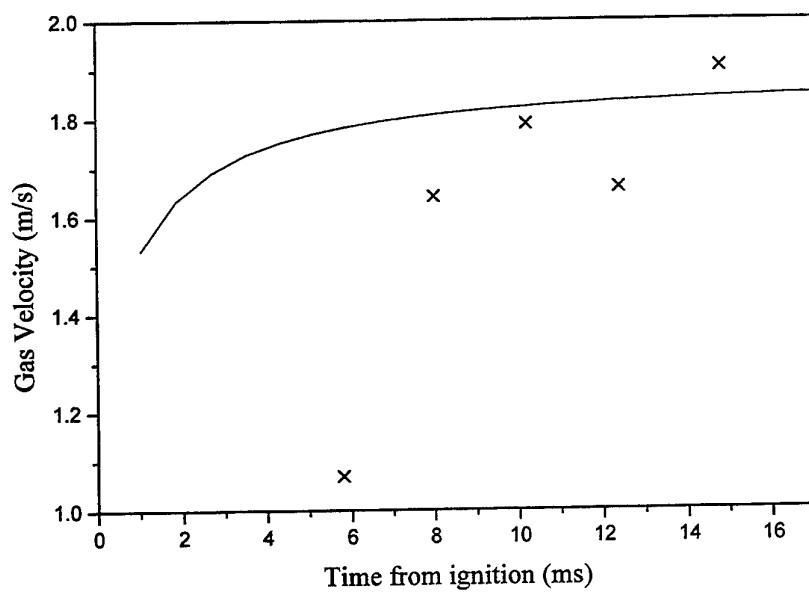


Fig. 7. A comparison between the gas velocity measured directly by PIV and that derived from schlieren images for a fuel rich iso-octane - air mixture at 1 bar.

SESSION 36

TURBO MACHINERY

Measurements of rotating machinery flows under steady and transient operating conditions using LDV and PIV

Rajan K. Menon, Wing T. Lai, Steve D. Hoff and Tim P. Mahon
Fluid Mechanics Instrument Division
TSI Incorporated, P. O. Box 64394
St. Paul, MN 55164, USA

Abstract

The flow field associated with a rotating fan under steady and transient operating conditions was investigated using LDV and PIV. Starting with steady state operation, spatial and temporal evolution of the flow field down stream of the rotor plane was obtained using a PIV system. Measurements in the cross-sectional and stream wise planes were obtained using a high resolution, high frame rate PIV system. At selected locations in a cross-sectional plane downstream of the rotor exit, simultaneous measurements using LDV and PIV were also carried out. Under transient operating conditions, the rotor passage flow was measured using the LDV system. With the fan under constant acceleration, flow fields in the interblade region were measured using LDV while the flow field down stream of the rotor exit plane were measured using the PIV system. Data analysis techniques used involve the ability to study cycle-to-cycle variation, the influence of asymmetries and differences in blade geometry. Issues relating to spatial resolution of PIV and LDV in making measurements in rotating machinery flows were also looked at.

1. Introduction

The dynamics of the flow field associated with compressors, turbines, fans, helicopter rotors and other rotating machinery are of interest in areas relating to operational efficiency improvement and noise reduction. Extracting detailed flow properties with high spatial resolution would allow insight into the nature of the flow, and provide methods to control or manipulate the desired system parameters. However, these type of measurements have demanded unique capabilities from diagnostic systems. Non-invasive techniques offer the greatest promise in meeting these challenging measuring situations.

In the present study, two powerful diagnostic tools - PIV and LDV - were used to investigate the flow field. Phase-averaged measurements using a two component LDV system were carried out to explore the flow in the interblade region of the rotor. Under steady operating conditions, phase-averaged measurements using an LDV system has been carried out to examine the flow properties within the interblade region. In order to examine the rotor passage flow properties under special or off-design conditions, a variety of new approaches have been developed. These include the ability to examine cycle-to-cycle variations, unsymmetric flow patterns in the interblade regions, and focus on special regions in the rotor plane by using unsymmetric and/or multiple data windows.

The desire to obtain instantaneous vorticity fields and information about turbulence structures has highlighted the need for a technique that can measure velocity fields and their spatial derivatives at many points with high accuracy. PIV provides the ability to obtain velocities at thousands of points, simultaneously, in a plane and extract vorticity and strain rates fields, and other spatial variation of flow properties.

The flow field downstream of the rotor exit plane was studied using a PIV system. The diagnostic capability was significantly enhanced by extending the technique to study both the temporal and spatial evolution of the flow fields. Velocity measurements in cross sectional planes parallel to the exit plane were obtained using a high frame rate high resolution PIV system. Using the once-per-revolution signal from the rotor, particle image fields were captured in the phase-locked mode. Vorticity, strain rate fields and other associated properties have also been calculated. In the flow downstream of the rotor, PIV measurements were carried out in the streamwise direction also. The combination of the velocity measurements in the cross-sectional and longitudinal

planes provide a detailed picture of the three dimensional nature of the flow field.

At one of the streamwise locations downstream of the rotor exit, simultaneous LDV and PIV measurements were made to map the flow field in the cross-sectional plane. In this case, the PIV measurements were carried out over a smaller region of the flow field. This allowed the interrogation region for the PIV system to be significantly smaller in size. Results from these and other measurements were used to examine the relative merits of the two measurement techniques in studying the flows associated with rotating machinery.

2. Experimental Arrangement

The periodic swirling flow field generated by the rotational motion of a five-bladed rotor was investigated using LDV and PIV systems. The rotor rpm could be varied from 200 to over 5000. A thin walled diffuser was attached at the exit of the rotor.

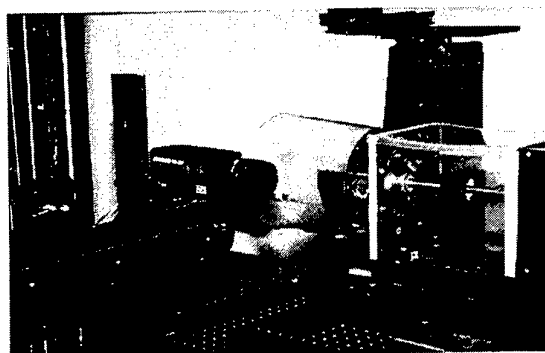


Fig. 1a LDV and PIV measurements in the fan flow
Experimental arrangement

The diffuser was made out of a thin walled plastic sheet so that the effect of the wall thickness on the PIV imaging is minimized. In order to make LDV measurements in the interblade region of the rotor a small window was put on the casing of the rotor.

A once-per-revolution signal from the rotor was used to synchronize the measurements with the position of the rotor blades. This allows the field measurements to be obtained at a fixed position of the blades and hence provides the ability to do phase-averaging. The rotor also was fitted with a shaft encoder so that the angular position of the rotor could be directly read. This is needed for operating situations where the rotor is undergoing deceleration or acceleration. The shaft encoder output was used as

input to the LDV system for the tests when the rotor was operated at constant angular acceleration.

A PIV system with on-line and batch-mode in image analysis and display was used to measure the flow field downstream of the rotor exit plane. The system used a compact dual laser configuration (twin mini-YAG lasers) with integrated beam combination optics. The time between laser pulses can be selected from fraction of a microsecond to milliseconds. The 50 mJ/pulse lasers with 5 nanoseconds pulse duration were operated to have 30 pulses (15 double pulses) per second. The combined beam from the two mini-YAG lasers was delivered to the measuring region using the TSI LASERPULSE light arm. The optical components at the end of the light arm provides a laser sheet, whose thickness and angle of divergence could be controlled. The flow field in a cross-sectional plane (x-y) normal to the downstream direction (z-axis) was illuminated using the light

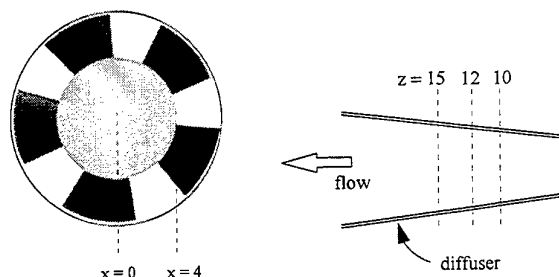


Fig. 1b Streamwise (z) and longitudinal (x)
measurement locations

sheet. In order to capture the image field with high resolution, a TSI PIVCAM 10-30 camera with 1024 X 1024 pixels resolution was used. The system has the unique ability to capture these high resolution images at the rate of 30 frames/sec. The frame-straddling technique used for image capture allows the two images (corresponding to the two laser pulses) to be recorded as separate frames even for very high speed flows. Frame-straddling times of less than 400 nanoseconds could be achieved with the PIVCAM 10-30 camera. Precise control of the laser pulses, camera and capture of the high resolution images was provided by the TSI LASERPULSE Synchronizer system operating under computer control.

The once-per-revolution (OPR) signal from the rotor (from the shaft encoder system attached to the rotor) was used as the input to the Synchronizer system so that phase-locked image capture could be accomplished. The set up and control of the PIV system, and data acquisition, analysis were provided by the TSI INSIGHT-NT software package. This analysis package exploits the benefits of the 32-bit environment utilizing the WINDOWS-NT platform. Real-time image capture was used to optimize seeding, image quality and phase-locked data acquisition. Overlaying the calculated vector field on the raw image field provided a quick verification of system optimization. The camera and the laser light arm were mounted on to the same fixture so that they could be moved together to get the velocity field in the x-y plane at various z-axis (downstream) locations.

Measurements in the interblade region of the fan rotor were carried out using a TSI two component fiberoptic LDV system using COLORBURST, COLORLINK Plus, DATA LINK and IFA 755 signal processor. The scattered light collected by the fiberoptic probe, operating in the backscatter mode, was input to a COLORLINK Plus system. The output of the COLORLINK Plus was analyzed using the IFA 755 Digital Burst Autocorrelator processor. A shaft encoder system was used to track as well as obtain phase information of the rotor. Angular position information of the rotor generated by DATA LINK, using the shaft encoder signal, is multiplexed with each velocity measurement and transferred to computer in the DMA mode. The TSI Windows based data analysis package, PACE, was used to control the LDV system. The software package also collected, analyzed data and displayed the results. The ability of the PACE data analysis package to keep data from each revolution(cycle) separate, compute flow statistics over a selected number of revolutions and estimate cycle-to-cycle variation was used to collect and analyze LDV data during the transient operating conditions of the rotor.

Phase-averaging techniques are used to extract the flow properties in the case of a periodic flow. For a periodic flow, the velocity $u(t)$ at the measuring point can be written as the time averaged value (\bar{u}), the phase-averaged contribution ($\langle u \rangle$) and the fluctuation contribution (u').

$$u(t) = \bar{u} + \langle u \rangle + u'(t)$$

For steady state operation, the phase-averaged mean velocity is given by $\bar{u} + \langle u \rangle$.

To simulate transient operating conditions such as start-up, associated with a rotating machinery, the angular velocity of the rotor was continually varied. Controlled variation of the rotor speed was achieved using a programmable ramp signal generator. This

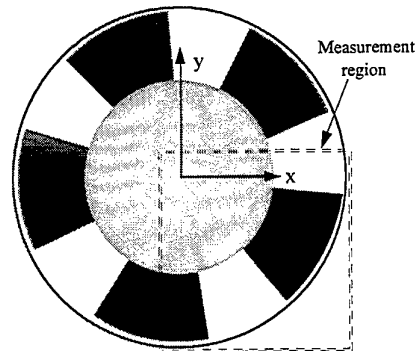


Fig. 2 Rotor and the measurement region

allows the angular velocity (rpm) to be varied based on the selected value of the angular acceleration, b . The angular velocity of the rotor, ω , at any time t could be written as

$$\begin{aligned} \omega(t) &= \omega_0 & \text{for } t \leq t_0 ; \\ \omega(t) &= \omega_0 + b(t-t_0) & \text{for } t_0 < t < t_1 ; \\ \omega(t) &= \omega_1 & \text{for } t \geq t_1 \end{aligned}$$

The value of the angular acceleration, b was obtained experimentally by measuring the angular velocity of the rotor shaft using a separate single channel LDV system.

Water droplets used as seed particles were introduced at the intake to the rotor. In the experiments with angular acceleration, the rotor rpm varied typically from 780 to 2600. The angular acceleration, b , was selected to be a constant in these experiments. The shaft encoder system used with the rotor divides one revolution (360 degrees) into 1000 encoder positions.

3. Experimental Results

3.1 Steady state operation

PIV Measurements in the cross-sectional planes

A region of 9 cm x 9 cm of the flow field downstream of the rotor exit plane was imaged using

the PIVCAM camera operating in the frame-straddling mode. The region imaged by the camera is shown in Figure. 2. It can be seen that the region of measurement covered more than 25% of the flow field in the rotor exit plane. In this arrangement, the light sheet was introduced from the top in the

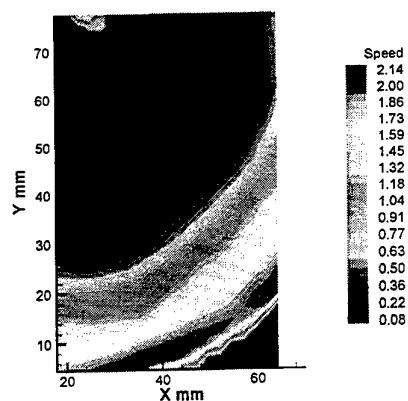


Fig. 3 Contours of velocity magnitude $z = 1$ cm
Phase-averaged statistics

vertical plane and the PIVCAM camera was positioned normal to it. Thus, the camera was placed downstream of the exit plane of the rotor looking into the flow.

In the frame-straddling mode of operation, a pair of images is recorded as two consecutive frames. The

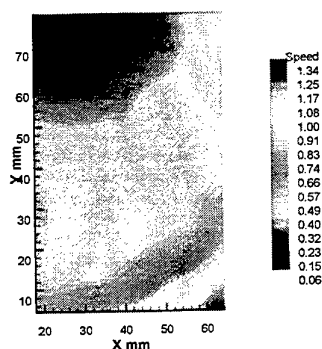


Fig. 4 Contours of velocity magnitude $z = 10$ cm.
Phase-averaged statistics

instantaneous velocity vector field is obtained from the spatial cross-correlation of the image intensity fields in the two frames. At each of the downstream locations 1000 image fields were collected in the

phase-locked mode. Phase-averaged statistics were obtained by capturing these images in batch-mode and averaging the instantaneous velocity fields. PIV measurements were obtained at four downstream locations.

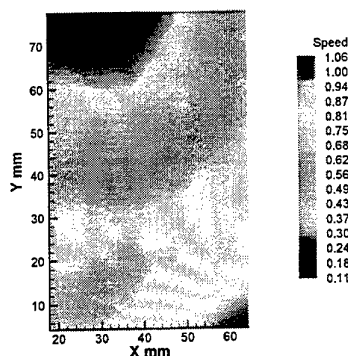


Fig. 5 Contours of velocity magnitude $z = 15$ cm
Phase-averaged statistics

Some of the results from the PIV measurements are given in the Figures 3 to 6. These give the contours

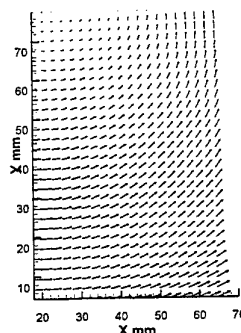


Fig. 6 Velocity vector field $z = 15$ cm.
Phase-averaged statistics

of the mean velocity magnitude, in the x - y plane, obtained by phase-averaging. The region shown in the figures contain 600 vectors. Figure 3 shows the velocity contours for the streamwise location closest to the rotor exit plane ($z = 1$ cm). The effect of the presence of the rotor hub is exhibited by the low velocity region. The center of the low velocity region very nearly corresponds to the center of the rotor hub.

Downstream of the rotor exit plane, the interaction of the different flow regions results in a more uniform

velocity field. The velocity contours in Figures 4 and 5 show the flow development and the gradual reduction in size of the low velocity region.

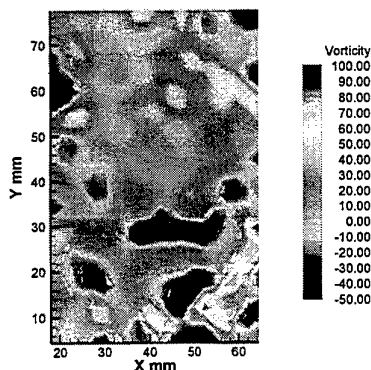


Fig. 7 Vorticity contours at $z = 15$ cm

Figure 6 shows the phase-averaged vector field at $z=15$ cm. The flow pattern clearly exhibits the presence of the swirl component in the x-y plane.

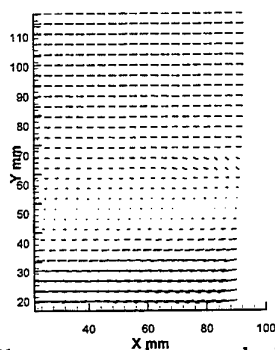


Fig. 8 Phase-averaged mean velocity field in a streamwise diametral plane, $x = 0$

It should be noted the velocity component normal to this (x-y) plane is non-zero and is in general more than the maximum value of the velocity in x-y plane. The flow properties extracted from the instantaneous vector fields include vorticity and strain rate. Figure 7 shows the vorticity contours at $z = 15$. The instantaneous velocity vectors are also superimposed on the vorticity contours.

PIV Measurements in the longitudinal planes

In order to examine the nature of the flow in the streamwise direction, the light sheet was introduced from the top illuminating a longitudinal (streamwise)

plane in the flow.

The PIVCAM camera was focused onto the light sheet through the window of the diffuser. Since the thickness of the diffuser wall was small (0.5 mm), the effect of the wall curvature on the image field captured was neglected.

Phase-locked data capture and analysis provided statistical properties of the flow field in a plane along the longitudinal direction. Figures 8 and 9 show the phase-averaged mean velocity distribution in the streamwise direction. The regions of high

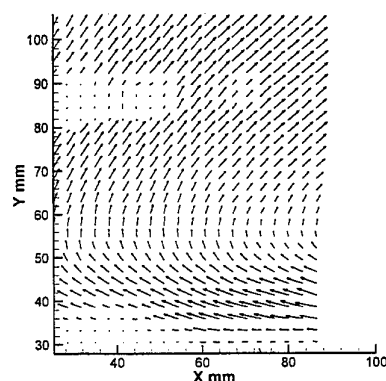


Fig. 9 Phase-averaged mean velocity field in a streamwise plane, $x = 4$ cm.

velocity near the blades and the low velocity near the hub and the associated flow pattern can be clearly seen from the phase-averaged mean velocity field

Combined LDV-PIV measurements

The flow field at the streamwise location $z = 12$ cm was measured using LDV and PIV. These measurements were carried out in a cross-sectional plane at the streamwise location. The purpose of these measurements was to examine some of the practical issues in using LDV and PIV measurement approaches in rotating machinery flows.

As a first step, the size of the LDV measuring volume and the PIV interrogation region was made to be of the same order of magnitude. To accomplish this, the PIV camera was zoomed in to image a smaller region in the flow field. The nature of the experimental set up and access problems limited the PIV image capture region to be about 17×17 mm.

The limitation in lowering the interrogation size to the desired value was image density in the captured images. For these measurements, the seeding density combined with the nature of the flow field placed a

lower limit on the size of the interrogation region to get reliable measurements. The resulting interrogation region size for the PIV measurements was larger (two times) than the measuring volume size for the LDV system. Comparison of the phase-averaged LDV and phase-averaged PIV measurements at selected locations in the flow field showed the velocity values to agree well within the experimental uncertainty.

LDV Measurements in the interblade region

Using the real-time displays of the PACE data analysis package, the seeding distribution as well as other operational parameters of the LDV system were optimized to obtain large and uniform number of measurements for all rotor angular positions. As the data was being collected, real-time display of a selected phase-averaged statistics was also used for system optimization. While the data is being collected, the variation of the flow property selected (e.g., mean, standard deviation), across the data window, reaches a steady distribution (for steady state operation), indicating the collection of adequate number of data points.

Sample results from the measurements in the interblade region of the rotor, under steady state operating conditions, for mid-span location of the LDV measuring volume are shown in Figure 10. The phase-averaged mean velocity values for axial and circumferential components plotted as a

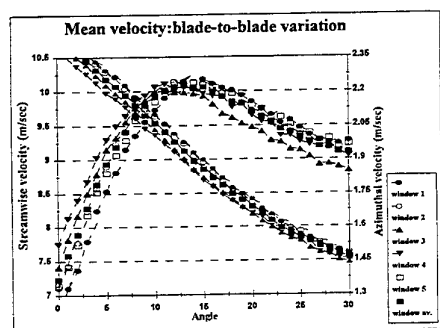


Figure 10 Blade-to-blade variation of flow properties (steady state)

function of the azimuthal angle show the variation of

the flow properties from one interblade gap to the next.

These variations caused by small differences in the blade geometry would be lost if the ability to keep the data from different blade gaps to be separate is not provided. In other words, overlaying the data from the different data windows into a single window (window averaging) would smooth out the flow variations in the individual blade gaps.

3.2 Transient operating conditions

Constant acceleration - LDV measurements

To study the rotor passage flow during non-steady operating conditions, the ability of the PACE analysis package to do cycle-resolved data acquisition and analysis was utilized. The approach was to obtain the flow statistics by averaging the measurements over a selected number of cycles ΔN . The value for ΔN was arrived at by imposing the condition that the change in angular velocity over ΔN cycles is less than $\delta\omega$ where δ is small. For the case of constant angular acceleration, the value of ΔN can be shown to be proportional to ω^2 . Selecting δ to be 0.05, the resulting values of ΔN , angular frequency M ($\omega = 2\pi M$) and other parameters are given in Table 1.

Table 1 Parameters for data analysis

	M	ΔN	Averaged over revolution numbers	Legend
0	13	130	1 to 130	S00
const.	20	160	1000 to 1160	S20
const.	30	360	2420 to 2800	S30
const.	35	500	4170 to 4670	S35
const.	40	630	5600 to 6230	S40

The data collected during each revolution was tagged and stored along with the revolution number so that phase-averaging could be done on a cycle-resolved basis. The PACE data analysis package has the ability to compute phase-averaged statistics over a selected number of revolutions. In the present study, phase-averaged statistics are computed ΔN cycles, where the value of ΔN is given in Table 1 for various angular frequencies (M).

The rotor was run at constant acceleration and the

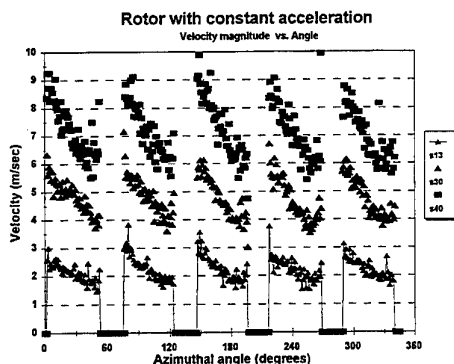


Fig. 11 Velocity magnitude as a function of azimuthal angle

two components of velocity measured in the interblade region was collected and stored. Phase-averaged statistics were computed to get the behavior of the flow for the case when the rotor acceleration was constant. Some of the results from the cycle-resolved analysis are given in Figures 11 through 13. Figure 11 shows the variation of the magnitude of

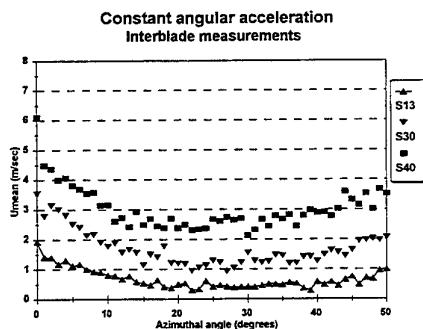


Fig. 12 Window -averaged results; Streamwise velocity vs angle

the velocity vector in the streamwise-azimuthal plane. It can be seen that the interblade velocity profiles vary from one interblade gap to the next. As was pointed out earlier, this was indicative of the possible unsymmetries in the blade geometry.

For the case of a rotor with constant acceleration, the value of the number of cycles (ΔN) over which phase-averaging is proportional to ω^2 . This results in the averaging being done over fewer number of cycles at lower ω . Since phase-averaging is

performed over a limited number of cycles, the computed statistics would show large variance.

In order to increase the number of samples in the averaging process, the window-averaging approach was used. This will typically increase the number of data points by a factor of 5 (the number of interblade gaps). However, this approach would smooth out the variations in the flow properties from one interblade gap to the next.

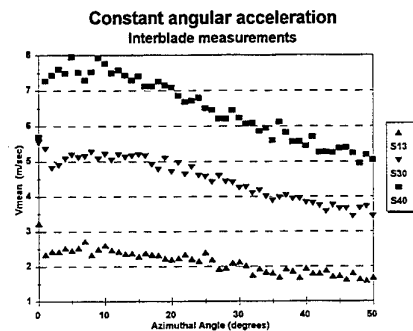


Fig. 13 Window-averaged results Azimuthal velocity vs. angle

Some of the results from the window-averaged analysis are given in Figures 12 and 13. These figures show the variation of the azimuthal and streamwise velocities in the interblade gap, as the rotor rpm increases.

In addition to the LDV measurements, PIV measurements, during the rotor acceleration, were performed at a downstream location ($z = 12$ cm). As before, the measurements were done in a cross-sectional plane parallel to the exit plane. The PIV data analysis package INSIGHT-NT time stamps the

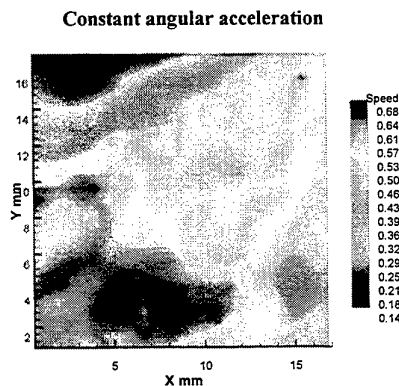


Fig. 14 PIV measurements at $z = 12$ cm (conditions corresponding to S20)

captured PIV images. This information was used to compute the phase-averaged statistics.

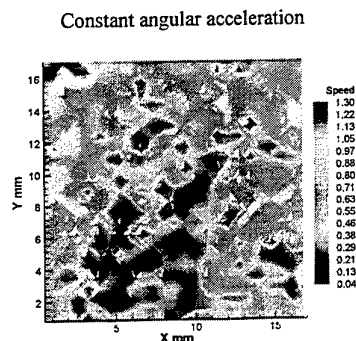


Fig. 15 PIV Measurements at $z = 12$
(conditions corresponding to S40)

Since the maximum speed of the camera is 30 frames/sec, the system captures one vector field per revolution in the current application. Hence, the problem of having few samples in the averaging process is more acute for these measurements when computing statistics over the limited number of cycles ΔN (see Table 1). Some the phase averaged results (magnitude of mean velocity) are shown in Figures 14 and 15.

These figures generally show a larger velocity dynamic range in the region of measurement. This seems to be indicative of the higher speed flow near the rotor blades as the rotor speed is increasing and the velocity in the low speed region increasing slowly.

4. Comments and conclusions

Comparison of LDV data with PIV measurements at selected locations indicated the results to be within the experimental uncertainty. For comparison purposes, the parameters (e.g., number of data points collected, size of the measuring region) for LDV and PIV approaches were chosen to be of the same order of magnitude. The results point out some of the relative merits of the two approaches.

Because of the experimental setup and access limitations, the size of the PIV image capture region was approximately 17×17 mm. The resulting interrogation region was larger than that for the LDV system. If the spatial measurement resolution for LDV and PIV were made to be the same, the PIV measurement region would become approximately 8×8 mm! It can be seen that the region of

measurement (using PIV) reduces significantly in size when the spatial resolution for PIV velocity measurements need to be comparable to that for LDV.

A possible approach to extend the resolution of the PIV would be to have a second analysis to extract the more velocity vectors within the interrogation region. This is generally referred to as super-resolution PIV [Keane, 1995]. This would retain the ability to examine a reasonably large area within the flow while pursuing the ability to obtain high spatial resolution.

The high resolution cameras used in the present experiment can take up to 30 frames/sec. For the present measurements this translates to measuring one vector field for about one per every revolution (or less). Hence, the phase-locked data can be collected for only one rotor position. In comparison, LDV is able to collect data over the entire duration of a revolution providing the ability to obtain velocity measurements for different rotor positions within a single revolution.

Based on these and the current state of the PIV technology, detailed diagnostics and obtaining flow statistics may make LDV attractive for rotating machinery applications especially for studying the interblade gap flows. This is more apt when one is examining aspects such as blade-to-blade variation or cycle-resolved statistics. The ability to obtain information about the overall nature of the flow in a region of interest, still makes PIV more attractive than any other technique. For example, the relative interdependence of various regions in the flow can be easily and quickly perceived from the PIV measurements. With the availability of faster and higher resolution camera technology in the future, PIV will become a stronger diagnostic tool for rotating machinery measurements.

References

- Lakshminarayana, B., 1996, *Fluid Dynamics and Heat Transfer of Turbomachinery*, Wiley.
- Keane, R. D. and Adrian, R. J., Super resolution particle image velocimetry, *Meas. Sci. technol.* 6, 1995.
- Lai, W. T., Bjorkquist, D. C., Abbott, M. P., Naqwi, A. A., Video systems for PIV recording, *Meas. Sci. & Technology*, 9 (3), 1998.

DETAILED MEASUREMENTS OF THE INTERNAL FLOW OF A BACKSWEEP CENTRIFUGAL IMPELLER

EL HAJEM M., MOREL R., CHAMPAGNE J. Y., SPETTEL F.

Equipe Hydraulique INSA Lyon
Laboratoire de Mécanique des Fluides et d'Acoustique, E.C.L. UMR CNRS 5509
Bât 302, 20 av. A. Einstein
69621 Villeurbanne Cedex

ABSTRACT

The performances of a centrifugal pump equipped with a vaned diffuser can be affected by the rotor and the diffuser interaction. Moreover, owing to the distortion of the flow conditions at the interface, the internal flow of the impeller can be altered which results in extra flow unsteadiness and instabilities and thus to further reduction of machine efficiency. The improvement of machine performances can only be achieved if there is a progress in the comprehension of the nature of the complex flow that develops at the gap between the rotor and the diffuser. This paper reports the results of LDA investigation of the internal flow of a backswep centrifugal pump impeller. Data obtained at two sections relative to the diffuser vanes showed a limited extension of the impeller-diffuser interaction on the impeller internal flow.

1. INTRODUCTION

Several studies have been concerned with the interaction of the impeller and its surrounding. Lorett (1986), Miner (1989), Dong (1992) and Liu (1994) studied the action of the volute on the impeller flow, while Inoue (1984), Sideris (1987) and Arndt (1989, 1991) have been concerned with the action of the diffuser. For internal flow studies, a large number of the experimental investigations that revealed the presence of a jet-wake structure at the discharge of centrifugal rotors was concerned with compressors or pumps tested in air as done by Eckardt (1975, 1976), Johnston (1976), Johnson (1978), and more recently Rohne (1991) and Ubaldi (1993). However, Krain (1988) found a velocity profile that differed widely from the jet-wake type flow. For pumps, not only previous studies are fewer; but also little investigations have observed such flow structure (Howard 1975, Adler 1979).

This paper presents the results of LDA measurements obtained at three radial distances upstream the trailing edge of a backswep centrifugal pump impeller. Traverses were made for two distances from the leading edge of the diffuser vanes. The flow structure was found to change as it approaches the impeller exit. This study revealed the presence of a jet-wake flow pattern that develops at the impeller outlet. It was present for both traverses. The available data show that the location and the extension of the wake seem to be unaffected by the proximity by the diffuser vanes.

2. EXPERIMENTAL FACILITY

Experiments were performed on the centrifugal pump test facility of the LMF described earlier by Bois (1990, 1992). It is a closed rig equipped for overall performance characterization of the machine. Water enters the impeller through a straight suction pipe one meter in length.

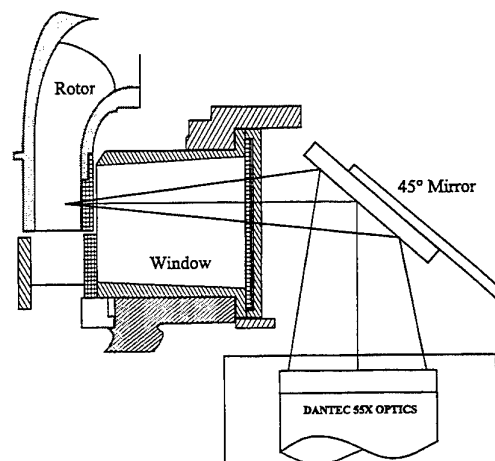


Figure 1 Optic access for internal flow investigation

Table 1 Impeller characteristics

impeller parameter	description	
$R_1 = 98.3$	mm	inlet blade radius at the shroud
$R_2 = 177.3$	mm	impeller exit radius
$b = 26.7$	mm	blade height
$Z = 7$		blade number
$\beta_2 = 22.5$	deg	blade angle
$Q_n = 0.0782$	m ³ /s	design flowrate
$N = 1200$	rpm	rotational speed
$\phi = 0.118$		design flow coefficient
$\psi = 0.481$		design head coefficient
$\omega = 0.577$		specific speed

Table 2 Diffuser characteristics

diffuser parameter	description	
$R_3 = 182$	mm	diffuser inlet radius
$R_4 = 199.3$	mm	Leading edge radius
$R_5 = 199.3$	mm	diffuser exit radius
$b_3 = 28.1$	mm	Diffuser width
$Z = 6$		Vane number
$\alpha_3 = 12$	deg	Vane angle

2.1 Test Impeller

The test rotor is a low specific speed shrouded impeller having seven backswept blades with an exit angle of 22.5 degrees. For LDA measurements, the shroud was made out of plexiglas (Figure 1) and a clear window was realized on the casing.

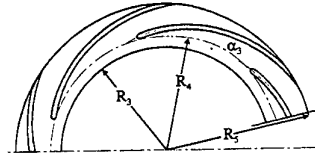
The main geometric data of the impeller and its operating conditions are summarized in table 1. The rotor is driven by a variable speed DC motor with a maximum power input of 45 kW at 1500 rpm. During measurements, a straight wall constant width diffuser with six vanes was used. The geometry of the diffuser is shown on figure 2 and its principle dimensions are given on table 2. The flow is discharged in a spiral casing of industrial type.

2.2 INSTRUMENTATION

A 5 W argon-ion Laser source and a three beam LDA system were used. The optics consists of a 55X Dantec modular optics with a front lens of 310 mm focal length and was used in a backscatter mode. A mirror placed in front of the optics deflected the laser beams so that the measurement volume was positioned in the impeller passage as shown on figure 1. A Bragg cell with a 40 MHz frequency shift is used for flow reversal detection. The entire optical system is mounted on a mill bed, thus it could be traversed in two directions and the measuring volume

Table 3 Measurement location inside the impeller

Measurement radial location	r/R_2
r_1	0.808
r_2	0.909
r_3	0.978

**Figure 2 Diffuser geometry**

set at the desired radii and axial depths. Two counter processors connected to a multiplexer unit that assures a coincidence test checking achieve electronic analysis of the photomultipliers signals. Only signals occurring simultaneously were transmitted together with the corresponding reading of the shaft encoder to a HP controller for further statistical treatment.

Velocity measurements were taken in three radial locations inside the impeller channels just upstream of the trailing edge and designated by r_1 , r_2 and r_3 in table 3. For each radial position, measurements were made at 15 axial points between the shroud and the hub. Rotation of the diffuser permitted to study the influence of the presence of its vanes at the proximity of the traversing section. The two configurations of the diffuser are shown on figure 3.

3. RESULTS AND DISCUSSION

In this paper, the results are presented for the design flow rate of 0.078 m³/s at a rotational speed of 1200 rpm. For each measuring point, 2000 values of the instantaneous velocities and angular position are recorded. The measured velocities together with the peripheral velocity allow the calculation of the absolute and the relative velocity and flow angle.

Figures 4 and 5 show the relative velocities obtained at r_1 and r_3 with the diffuser in its first configuration. The data are presented as a function of the angular position. The same velocity distribution repeated over several periods corresponds to the flow in the seven impeller channels; it illustrates the periodic nature of the relative flow. First, one should notice the strong dependency of the velocity profiles on the measuring location. At $r_1 = 0.818$ and near the

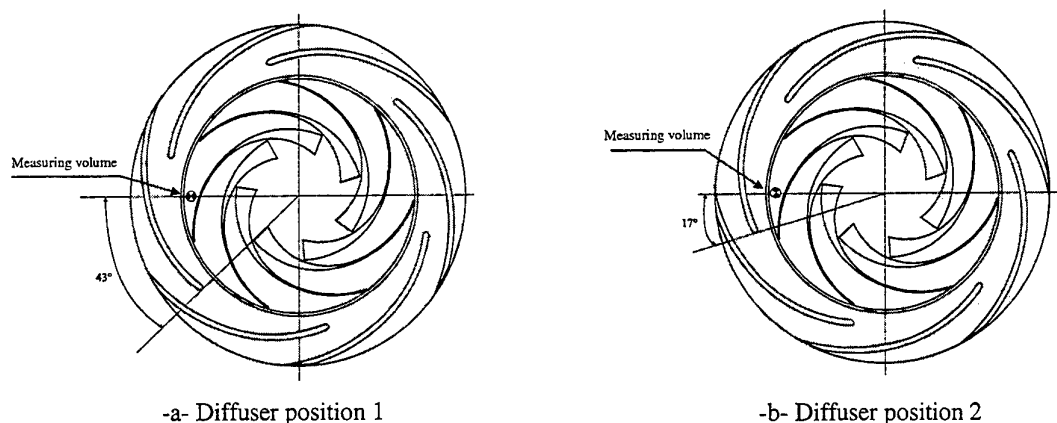
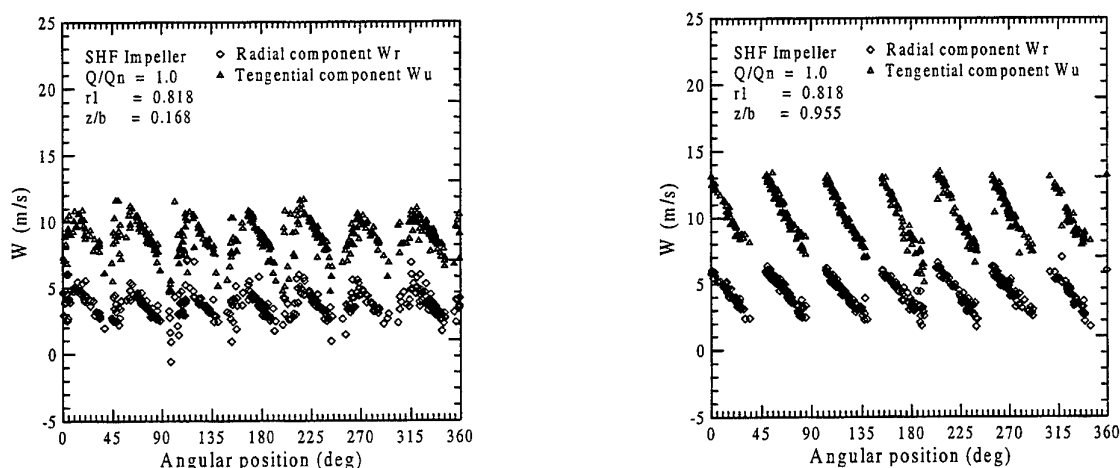


Figure 3 Diffuser dispositions relative to the measuring section



hub ($z/b = 0.955$), the flow structure is the same as expected for a potential flow with high relative velocities near the suction side. This is not the case near the shroud wall where the flow pattern starts to deviate from the theoretical model. This is particularly observed near the suction side where the velocity gradient is inverted. Both components of the velocity reach a maximum at the passage center, beyond this point the potential flow character is still prevailing. One should also notice the important velocity fluctuations registered in the proximity of the suction side.

When the flow moves towards the impeller discharge ($r_3 = 0.978$), the flow pattern is deeply changed. The gradient of the tangential velocity is

now completely inverted near the shroud wall (figure 5a); the velocity increases from the suction to the pressure side where uniform values are registered over a small area. At the hub wall this component of the velocity is uniform but high fluctuations are observed (figure 5b). The radial velocity reaches a minimum near the suction surface at the shroud wall, this minimum moves towards the passage center at the proximity of the hub. The periodic character of the flow is altered which is possibly caused by differences of the impeller channels.

For a global view of the flow structure at the measuring sections, the data obtained for the seven impeller passages is assemble-averaged and presented for a mean passage divided into 17

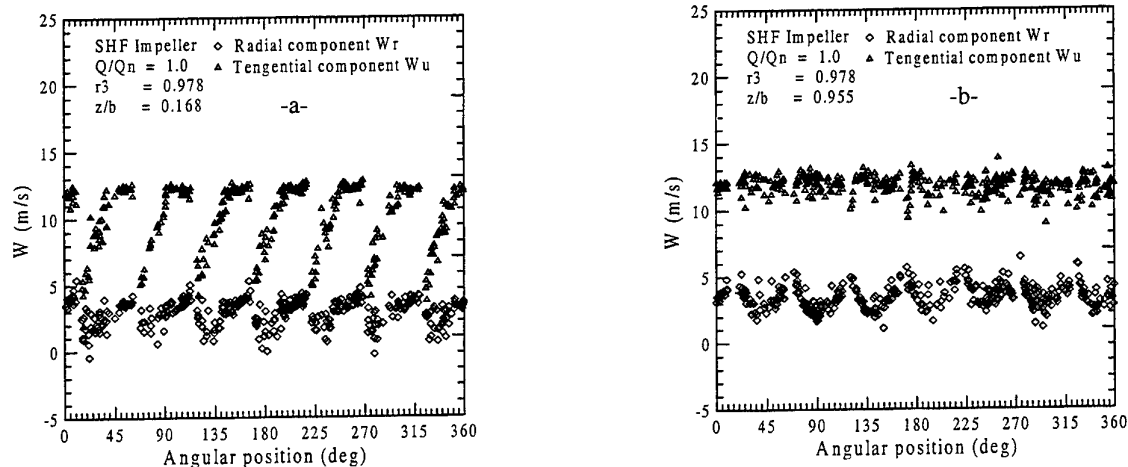


Figure 5 Instantaneous velocity components at r_3 and Q_n

segments of 3 deg angular width. For each segment a mean velocity and a rms coefficient were computed. The results are presented as constant velocity contours normalized by U_2 the impeller tip speed. In these diagrams the measuring points are referred to by the relative axial depth z/b with the shroud wall lying at $z/b = 0$ and the hub at $z/b = 1$. In the circumferential direction the coordinate is y/t , where $t = 2\pi/Z$ is the local passage pitch and Z is the blade number. In this notation $y/t = 0$ corresponds to the suction side and $y/t = 1$ corresponds to the pressure side.

Figures 6, 7 and 8 show an important evolution of the flow structure as approaching the trailing edge. In the first measuring section (figure 6), one can recognize the potential flow character prevailing over a large area of the passage. The velocity has an almost linearly distributed profile from the suction side to the pressure side and it is uniform in the axial direction. Only a small region confined to the suction side/shroud wall corner shows a deviation from the theoretical model. The main feature of the flow in this region is an accumulation of low momentum fluid and steep velocity gradients.

At the next station (figure 7), the previous organization is disrupted and the most striking fact is the appearance of an important velocity gradient near the front wall. The region of low energy fluid has extended and moved towards the suction side of the blade. In fact the flow is starting to be organized in a jet-wake structure as it was reported by other investigators, the wake corresponding to the low energy fluid.

The wake is actually fed with low momentum fluid brought there by the secondary flows that peel

off the boundary layers of the passage walls as reported by Eckardt (19976).

The wake core position is conditioned by the competing centrifugal forces acting on the fluid. As suggested by Ubaldi (1993) and Johnson (1983), this trend can be explained considering the secondary flow development in terms of the Rossby number $Ro = W/\omega R_n$ that measures the relative effect of the centrifugal force due to the meridional streamline curvature and the Coriolis force due to system rotation. R_n is the local radius of curvature of the streamlines.

At the measuring planes of the tested impeller the passages develop mainly in the radial direction as their are located far away from the meridional bend. As a consequence, the Rossby number is less than unity, the rotation effect dominates and stabilizes the wake on the suction side at $z/b = 0.4$ as observed on figure 8. This flow region corresponds to a flow separation as clearly indicated by the contour plot of the relative flow angle β_2 presented on figure 9. The low values correspond to a maximum deviation from the blade surface. Meanwhile, the flow direction of the fluid in the jet is more uniform.

The flow detachment observed in the wake has its origin in the suppression of turbulence exchange between the wake and the jet. This is illustrated by the deep velocity gradient at the shear layers between both phases (figure 8). As turbulence is stabilized in the wake, the boundary layers are more subject to separation.

The relative velocities obtained with the second configuration of the diffuser are given on figure 10. The contours of both components do not reveal any significant change of the flow structure when the

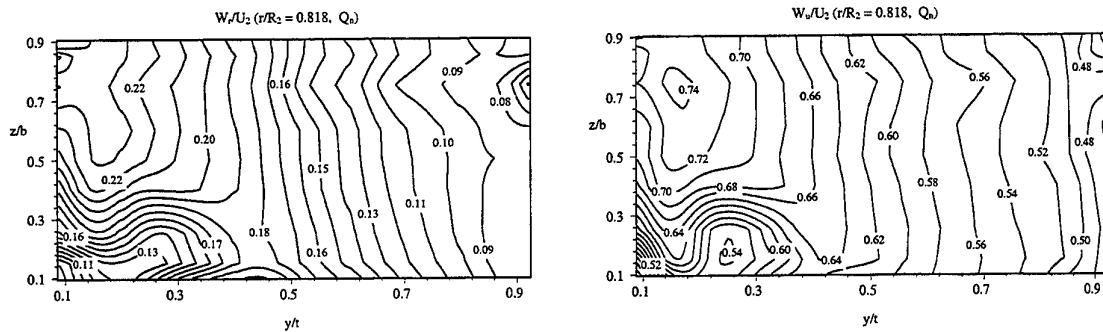


Figure 6 Assemble-averaged velocities at r_1

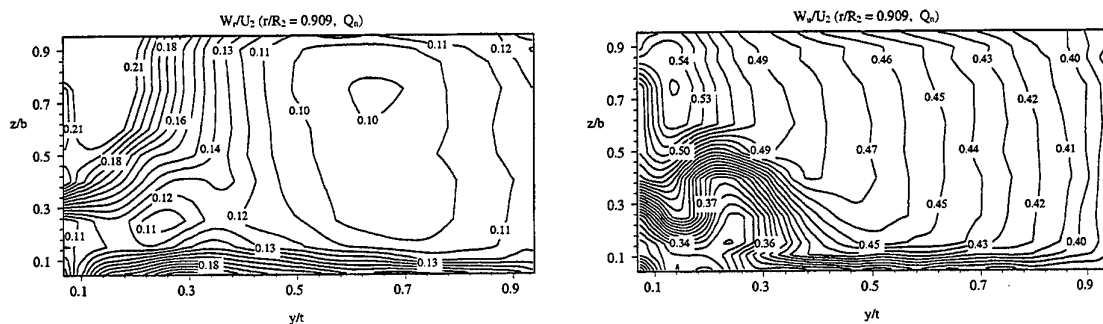


Figure 7 Assemble-averaged velocities at r_2

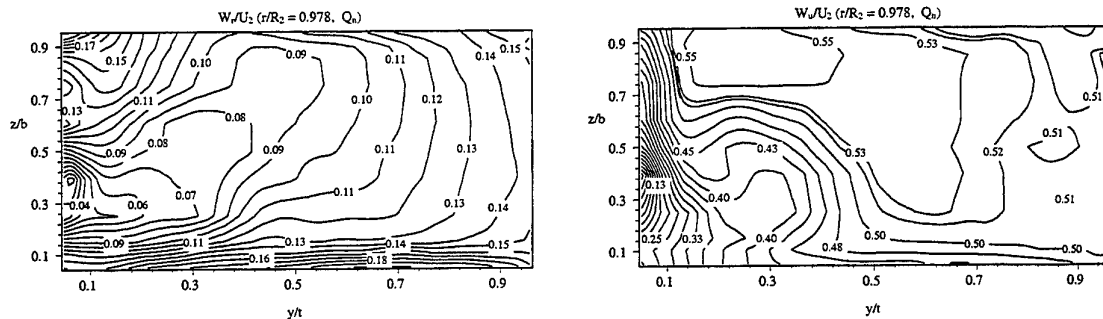


Figure 8 Assemble-averaged velocities at r_3

diffuser vane is closer to the measuring plane. This is not conform to a previous study during which the authors investigated the mean flow using a directional probe at $r/R_2=1.045$ (El Hajem 1996) and found a strong impeller-diffuser interaction. The actual study reveals therefore a limited extension of this interaction to the impeller internal flow. But one should be careful as local phenomena might be present and only measurements covering the entire impeller-diffuser interface will permit a final conclusion.

CONCLUSION

The internal flow of a centrifugal impeller was investigated with an LDA technique. Measurements obtained at three stations show that the flow structure changes as the approaching the impeller discharge. The flow present at the first station is organized as a potential flow model. While in the last station, a jet-wake structure has developed. The measurements obtained at a different distance from diffuser vane leading edge did not reveal any important change in

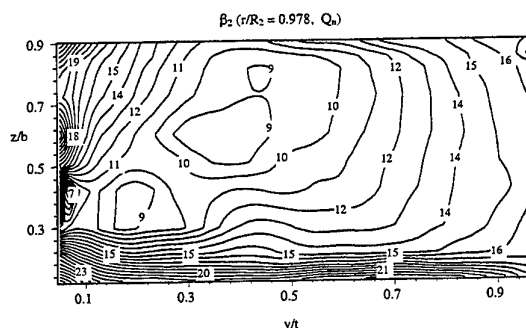


Figure 9 Relative flow angle at r_3

the impeller internal flow. The study is continuing and measurements at complementary distances from the diffuser vanes and at different operating points should be able to give a more complete view of the nature of the flow at the impeller discharge.

REFERENCES

- Adler D., Levy Y. 1979, A Laser Doppler Investigation of The Flow Inside a Backswept, Closed, Closed Impeller, *Journal of Mechanical Engineering Science*, Vol. 21.
- Bois G., Rieutord E. 1990, Etude de l'écoulement en sortie de pompe centrifuge depuis le débit nominal jusqu'au débit critique de recirculation, Action Mécanique M.R.T., Compte-rendu de fin d'étude MRT n°88-H-0636, October.
- Bois G., Combes J.F., Rieutord E. 1992, An Analysis of flow characteristics of the rotor of an hydraulic centrifugal pump using several CFD methods with different levels of approximation, *Proceedings of ISROMAC 4, Honolulu*.
- Eckardt D. 1975, Instantaneous Measurements in the Jet-Wake Discharge Flow of a Centrifugal Compressor Impeller, *Journal of Engineering for Power*, pp. 337-345.
- Eckardt D. 1976, Detailed Flow Investigations within a High-Speed Centrifugal Compressor Impeller, *Journal of Fluids Engineering*, pp. 390-401.
- El Hajem M. 1996, "The study of the flow within a centrifugal impeller running at partial flow rate", Phd thesis, Institut National des Sciences Appliquées de Lyon, France.
- Howard J. H. G., Kittmer C. W. 1975, Measured Passage Velocities in a Radial Impeller With shrouded and Unshrouded Configurations, *Journal of Engineering for Power*, pp. 207-213.
- Johnston J. P., Eide S. A. 1976, Turbulent Boundary Layers on Centrifugal Compressor Blades: Prediction of the Effects of Surface Curvature and Rotation, *Journal of Fluids Engineering*, pp. 374-381.
- Johnson M. W. 1978, Secondary Flow in Rotating Bends, *Journal of Engineering for Power*, Vol. 100, pp. 553-560.
- Johnson M. W., Moore J. 1983, Secondary Flow Mixing Losses in a Centrifugal Impeller, *Journal of Engineering for Power*, Vol. 105, pp. 25-39.
- Krain H. 1988, Swirling Impeller Flow, *Journal of Turbomachinery*, Vol. 110, pp. 122-128.
- Rohne K.H., Banzhaf M. 1991, Investigation of the Flow at the exit of Unshrouded Centrifugal Impeller and Comparison With the classical Jet-Wake Theory, *Journal of Turbomachinery*, Vol. 113, pp. 654-659.
- Ubaldi M., Zunino P., Cattanei A. 1993, Relative Flow and Turbulence Measurements Downstream of a Backward Centrifugal Impeller, *Journal of Turbomachinery*, Vol. 115, pp. 543-551.

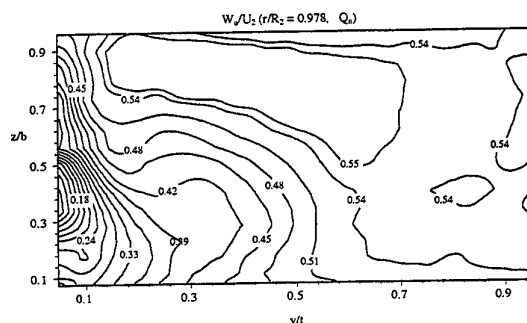
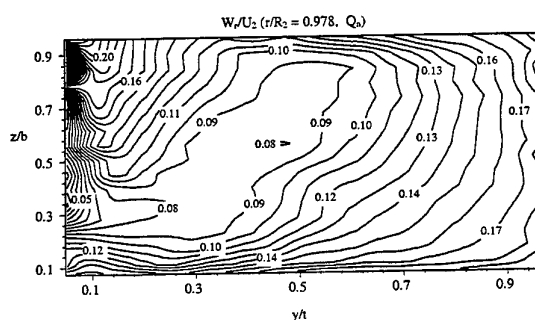


Figure 10 Relative flow velocity at r_3 (configuration 2 of the diffuser)

UNSTEADY BOUNDARY LAYERS ON THE DIFFUSER BLADES OF A CENTRIFUGAL STAGE DUE TO ROTOR BLADE WAKE INTERACTION

A. Cattanei, D. Ottolia, M. Ubaldi, P. Zunino

Istituto di Macchine e Sistemi Energetici
Università di Genova, Italy

ABSTRACT

Boundary layers on turbomachinery blades develop in a flow that is periodically perturbed by the wakes generated by the upstream blade row. Periodic variations of the incident flow have significant effects on the boundary layer development, transition and separation.

To investigate these effects on centrifugal turbomachines, detailed laser Doppler velocity measurements have been performed within the pressure and suction side boundary layers of the diffuser vane of a low-speed large scale centrifugal stage. Instantaneous velocity data have been acquired in phase with the rotor blade passage and have been processed in ensemble average form, in order to separate periodic and random velocity fluctuations.

Features of the unsteady processes within the boundary layer are analysed using time-distance contour plots of the ensemble averaged velocity and turbulence and boundary layer profiles evaluated at the most significant instants within a wake passage period.

1. INTRODUCTION

Flow in turbomachines is unsteady due to rotor-stator aerodynamic interaction. Among the interaction mechanisms of particular importance is the unsteadiness generated by the wakes of the upstream blade row on the flow in the downstream cascade. The wakes carried downstream make the incident flow unsteady in both mean values and turbulence levels. This unsteady condition has a great influence on the blade surface boundary layer development and hence on the associated energy losses and flow stability. Whilst a general model of interpretation of the phenomenon is still not available, at least for axial flow turbomachines knowledge of the unsteady blade boundary layer behaviour has been formed thanks to the intense experimental research carried out whether on large scale models (e.g. Addison and Hodson, 1990) or cascades (e.g. Cumpsty et al., 1995) and isolated airfoils (e.g. Liu and Rodi, 1991).

Experiments on rotor-stator aerodynamic interaction in centrifugal turbomachines are less frequent (e.g. Inoue and

Cumpsty, 1984) and experimental data concerning the boundary layer development on radial diffuser vanes perturbed by the rotor wakes are not available at all in literature. Whilst the general principles of the interaction mechanisms are common for both geometries, large differences between the two cases are expected in practice because of the lower spacing between the interacting rows and the much stronger mixing out of the wakes observed in centrifugal machines (Dean and Senoo, 1960). Therefore the findings coming out for axial machines need to be verified before they could be applied to centrifugal machines.

The present paper reports results of an experimental investigation into the effects of the rotor wake generated unsteadiness on the profile boundary layer developing on the diffuser vanes of a centrifugal stage.

2. EXPERIMENTAL DETAILS

2.1 Centrifugal Stage

The experiment has been carried out on a low-speed large-scale centrifugal stage operating in air in an open circuit. The facility has been described in detail by Ubaldi et al. (1996).

Relevant geometrical data of the stage and operating conditions are summarised in Table 1. The unshrouded impeller of diameter 420 mm has 7 single curvature backswept blades. The radial diffuser has 12 circular arc blades. Coordinates of impeller blade and diffuser vane profiles are given by Ubaldi et al. (1996). The blade height is constant and equal to 40 mm for both rotor and stator. The radial spacing of 6 per cent between impeller outlet and diffuser inlet is typical of modern centrifugal stages.

2.2 Laser Doppler Velocimeter

Velocity measurements into the diffuser vane boundary layer perturbed by the rotor blade wakes were performed by means of a two-colour four beam laser Doppler velocimeter. The system consists of a 300 mW Argon-Ion laser, tuned to 488 (blue) and 514.5 (green) wavelengths, and

fiber transmitting and receiving optics (Dantec fiber flow 60X), operating in backscatter on-axis collection mode. The front lens focal length of 150 mm yields for a 38 mm beam separation a probe volume of 47 μm diameter and 0.40 mm length. A Bragg cell is used to apply a frequency shift (40 MHz) to one of each pair of beams, allowing resolution of directional ambiguity and reduction of angle bias.

The optical access is provided through a flat removable borosilicate glass window inserted in the casing of the model.

The probe volume was oriented with the larger dimension along the spanwise direction in order to have better resolution in the direction normal to the blade surface. The probe was traversed using a computer controlled three-axis mechanism. The motion is transmitted to the carriages by stepping motors through pre-loaded ball-screw assembly with a minimum translation step of 8 μm . The origin for the velocity profile was estimated by visual inspection of the intersection of the laser beams approaching the blade surface and by survey of the analogue signal of the photomultiplier on a digital oscilloscope. Repeatability in establishing the origin was estimated to be ± 0.03 mm.

The flow was seeded with a 0.5-2 μm atomised spray of mineral oil injected in the flow at the suction pipe inlet of the model.

2.3 Measuring Procedure

Boundary layers have been investigated on the forward part of suction and pressure sides of the diffuser vanes by means of 23 measuring traverses normal to the blade surface, located from the leading edge up to a distance of 80 mm measured along the blade. Each boundary layer traverse is made of 24 points with a distance between two adjacent points of 0.05 mm in the region closer to the wall.

An one per revolution signal obtained from the rotor shaft by means of an optical encoder was used to trigger the processors in order to assign to each instantaneous velocity datum the proper time instant within a rotor period.

At each survey point approximately 200000 data for each velocity component were acquired and ensemble

Table 1. Geometric data and operating conditions

Impeller	
inlet blade diameter	$D_1 = 240$ mm
outlet diameter	$D_2 = 420$ mm
blade span	$b = 40$ mm
number of blades	$z_i = 7$
inlet blade angle	$\beta_1' = -65$ deg
outlet blade angle	$\beta_2' = -70$ deg
Diffuser	
inlet vane diameter	$D_3 = 444$ mm
outlet vane diameter	$D_4 = 664$ mm
vane span	$b = 40$ mm
number of vanes	$z_d = 12$
inlet vane angle	$\alpha_3' = -74$ deg
outlet vane angle	$\alpha_4' = -68$ deg
Operating conditions	
rotational speed	$n = 2000$ rpm
flow rate coefficient	$\phi = 0.048$
total pressure coefficient	$\psi = 0.65$

averaged to separate the periodic component of the signal at the impeller frequency from the random component due to turbulence and flow fluctuations not correlated with this frequency.

The decomposition of the signal has been accomplished by dividing each period between two triggering signals in time windows or bins to be filled with the appropriate data. In this way the arrival time for each LDV velocity realisation has been associated with a particular phase of the blade wake cycle. For a wake passing period of 4.29 ms (the impeller revolution period is 30 ms) 50 phase bins imply a bin width of 86 μs and a mean number of samples for each bin of 571.

The following equations define the ensemble averaged velocity and the ensemble averaged rms of the fluctuations not correlated with the rotor passage.

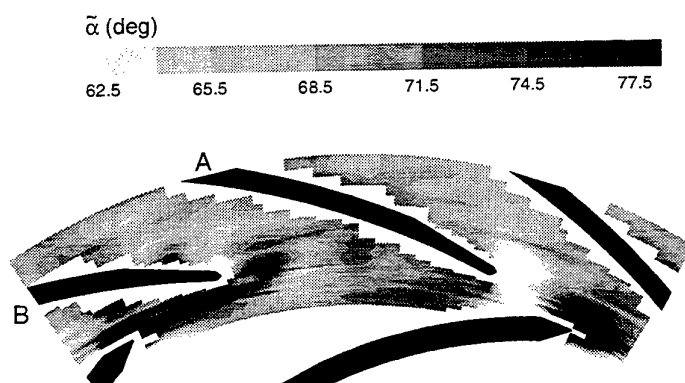


Fig. 1 Instantaneous distribution of the absolute flow angle at the diffuser inlet.

$$\bar{c}(j) = \frac{1}{N} \sum_{n=1}^N c(j, n)$$

$$\sqrt{\bar{c}^2(j)} = \sqrt{\frac{1}{N} \sum_{n=1}^N [c(j, n) - \bar{c}(j)]^2}$$

where $c(j, n)$ is the instantaneous velocity measured during the phase window j , at the cycle n . N is the total number of velocity data stored in the phase window j .

3. EXPERIMENTAL RESULTS

3.1 Overall Flow

At the nominal point $\phi = 0.048$, $\psi = 0.65$, $n = 2000$ rpm, the Reynolds number Re_L based on the diffuser inlet velocity and blade chord is 4×10^5 , which is in the range of turbine and compressor cascade tests with incident wakes (e. g. Schobeiri et al., 1995, Cumpsty et al., 1995).

A detailed analysis of the flow at the impeller outlet and in the vaned diffuser has been recently reported by Ubaldi et al. (1997). From those results the following description of the overall flow can be drawn.

The flow at the impeller outlet is periodic with clearly discernible blade wakes characterised by relative velocity defect and large turbulence level. Due to the moderate impeller blade loading, the impeller blade boundary layer is not separated and a jet and wake flow has not been formed. On the pressure side a region of high relative velocity precedes the wake velocity defect. Due to the geometry of the stage, the deficit in relative velocity of the wake is seen by the absolute observer as an increase of the circumferential absolute velocity and absolute flow angle. Similarly the relative velocity rise which precedes the wake tends to decrease the absolute flow angle.

The absolute flow angle distribution at the diffuser inlet is shown in Fig. 1. The rotor passing blades induce negative incidence on the preceding diffuser vanes (vane A) and positive incidence on the vanes which follow the impeller blades (vane B). That imposes at the diffuser vane inlet cyclic incidence conditions with angular excursions of more than 15 deg, capable of inducing boundary layer dynamic separations which alternate on the two sides of the vane.

3.2 Boundary Layer Development

Figures 2, 3 and 4 show for both pressure and suction sides the time-varying distributions of the ensemble averaged mean and turbulent velocities obtained at different distances from the blade surfaces. In these plots characteristic instants within a wake cycle period can be identified.

Line W passing through the maximum of the turbulent velocity at the boundary layer edge identifies the wake position. The wake passage is always characterised also by an increase of the external mean velocity.

Line S passing through the minimum of the velocity near the wall is indicative of the state of separation of the boundary layer during the cycle. This condition is always accompanied by a steep rise of the turbulence level in the

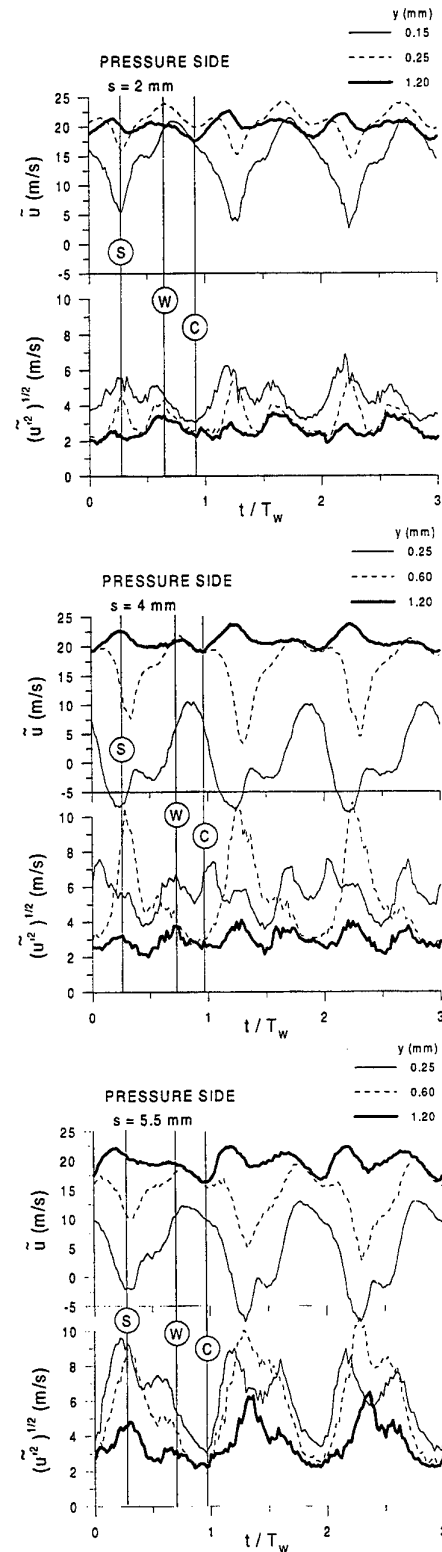


Fig. 2 Ensemble averaged velocity and turbulence time traces from the pressure side of the diffuser vane.

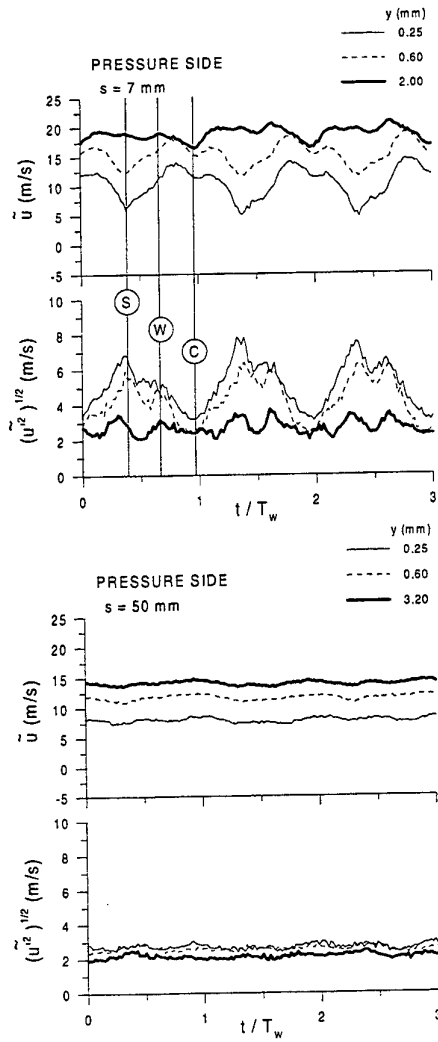


Fig. 3 Ensemble averaged velocity and turbulence time traces from the pressure side of the diffuser vane.

boundary layer region above the separated zone and by an increase in the external velocity due to the flow blockage effect near the surface.

A third line C is drawn passing through the minimum in the external velocity distribution. This position corresponds to "calm" conditions characterised by the lowest rms values all through the boundary layer and in the free-stream and by high velocities near the wall.

Using the cycle-resolved mean and rms velocity distributions, boundary layer profiles for the time instants W, S, and C can be determined and plotted in sequence to show the development along the blade surfaces of the time-dependent boundary layers (Figs. 5 and 6). Plots of the velocity profiles in inner variables u^+ , y^+ help to interpret the boundary layer state at the different streamwise locations (Figs. 7 and 8).

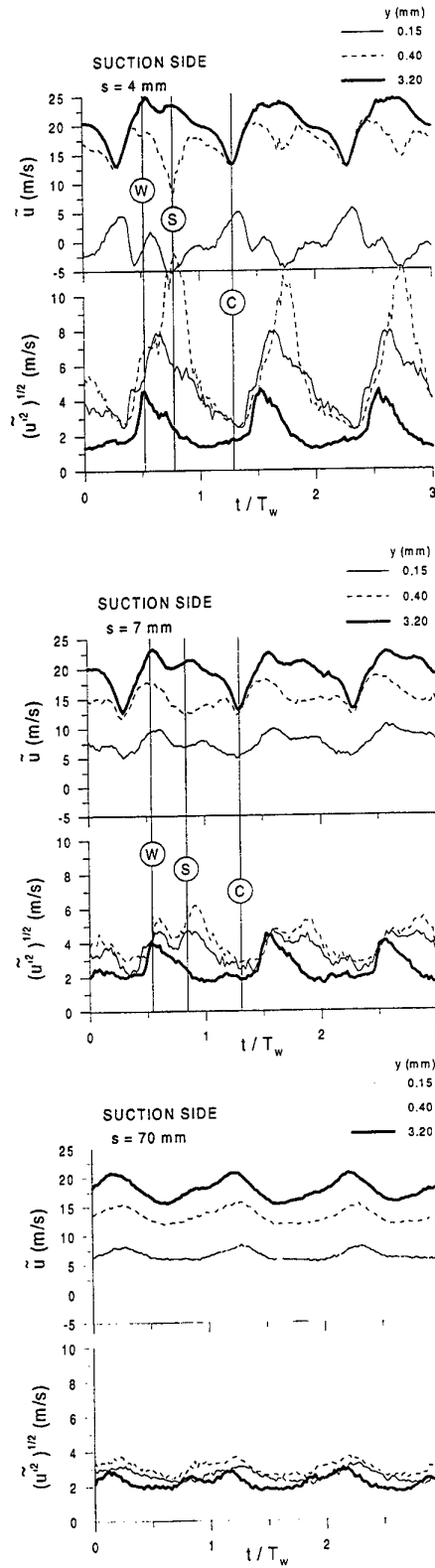


Fig. 4 Ensemble averaged velocity and turbulence time traces from the suction side of the diffuser vane.

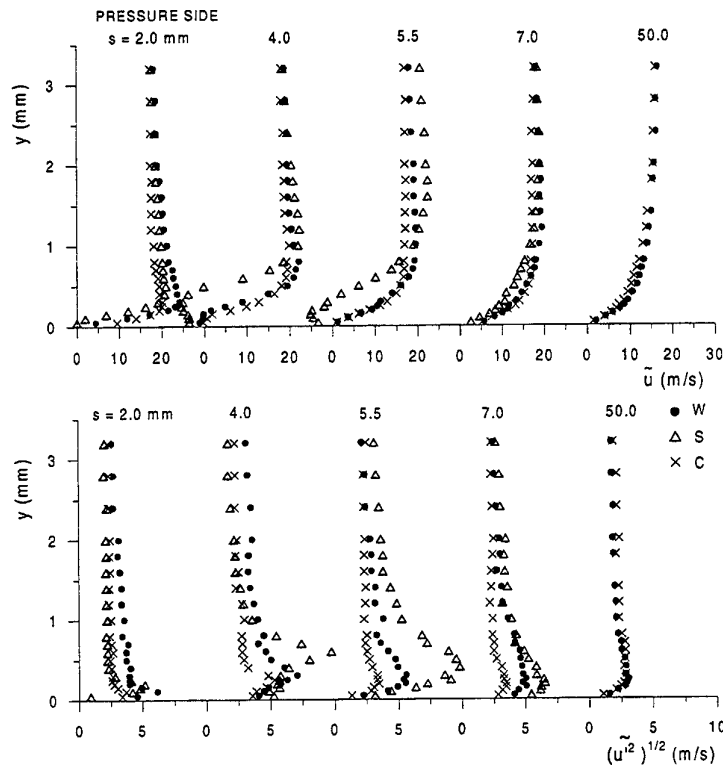


Fig. 5 Ensemble averaged velocity and turbulence profiles at different instants, pressure side.

Pressure side. On the pressure side (convex surface of the diffuser vane), at the beginning the boundary layer is very thin and laminar (Figs. 2 and 5, $s = 2$ mm). However the wake turbulence penetrates within the boundary layer, as shown by the presence of a peak of turbulence at $y = 0.15$ mm in phase with the wake passage *W*. A second peak of turbulence rises within the boundary layer in correspondence of the dip of velocity *S*, associated with the boundary layer separation occurring at the following stations (Fig. 2).

At $s = 4$ mm line *S* on the pressure side (Fig. 2, 5) identifies the instant of more intense flow separation induced by the flow negative incidence preceding the wake passage. At this condition a dramatic increase of the rms velocity appears in the shear layer at $y = 0.60$ mm. The wake passage *W*, which follows the *S* condition of about one half of the cycle period and induces positive flow incidence, tends to remove the separation. The calm condition *C* standing immediately after the wake passage *W*, presents relatively high velocity near the surface and the less severe flow separation within the cycle.

At $s = 5.5$ mm (Figs. 2, 5) the boundary layer is still separated at the instant *S*, but the separation has been suppressed at the instants *W* and *C* (Fig. 5).

At $s = 7$ mm (Fig. 3, 5) reattachment has been completed for all time instants and also the turbulence peak formed in the free shear layer at the preceding stations has here approached the wall. Due to the very high unresolved unsteadiness in the separated shear layer, the length of the periodic separation bubble is short. Even if the worst

condition *S* is considered, the length does not reach twice the leading edge thickness. The effect of the turbulence level on leading edge separated bubbles has been investigated by Walraevens and Cumpsty (1993). Their results show that the leading edge separated bubbles formed on airfoils in steady flow with low turbulence level are larger even at moderate incidence conditions. One important conclusion coming out from their experiment is the important effect of the free-stream turbulence: an increase of turbulence shortens or eliminates the separation bubble.

Velocity profiles of the reattached flow ($s = 7$ mm, Fig. 7) show that the linear sublayer has been redeveloped at this station, while at larger values of y^+ the velocity profiles cannot follow the logarithmic law because of the exceedingly high values of the ratio u_t / u_c . Large values of u_t / u_c and turbulent shear stress found in the present experiment are justified by the extremely high free-stream turbulence level which exceeds the 10 per cent. In practice a boundary layer has been formed after the reattachment which does not follow the logarithmic law of turbulent boundary layers, but is capable to resist large adverse pressure gradients, thank to its high turbulence content.

At $s = 50$ mm the periodicity induced by the passing blades has completely decayed (Fig. 3), the free-stream turbulence and the ratio u_t / u_c remain still very high (Fig. 7) keeping the boundary layer far from separation.

Suction side. The analysis of the boundary layer on the suction side (concave surface of the diffuser vane) follows

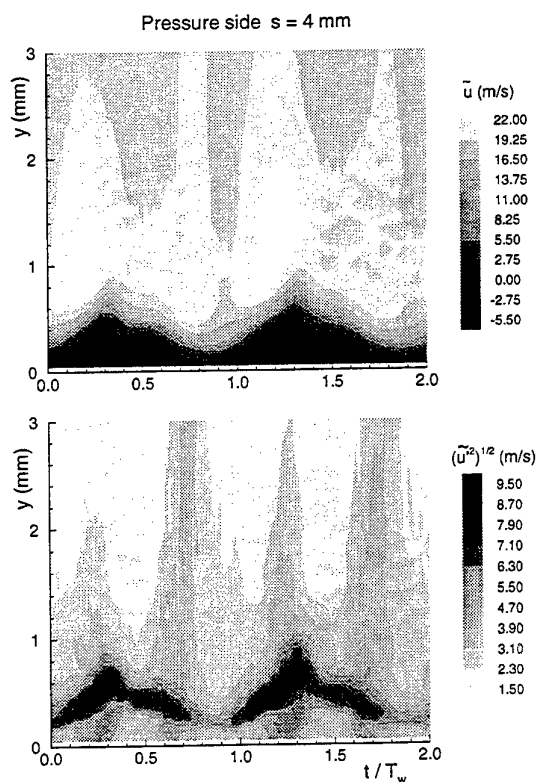


Fig. 9 Time-distance contour plots of the ensemble averaged velocity and turbulence in the boundary layer at $s = 4$ mm, pressure side.

the same guidelines, though some significant differences respect to the pressure side need to be considered.

The periodic unsteadiness induced by the rotor passing blades persists on the suction side for a longer distance, since this side of the vane extends in the semivaneless region which precedes the diffuser inlet throat.

A second important difference is the fact that here is the positive flow incidence, which accompanies the wake passage, that induces separation. It follows that the conditions S and W are now closer and W precedes S . The calm condition C which coincides with the removal of the positive incidence precedes the wake passage (Fig. 4). This pattern results in a more differentiated distribution in time of the mean and rms velocities at the boundary layer edge, with an alternating of zones of higher and lower velocity and turbulence levels (Fig. 4). At station $s = 3$ mm and $s = 4$ mm on the suction side the profiles C (Fig. 6) do not present any zones of negative velocity. Accordingly in Fig. 4 the point C near the wall ($y = 0.15$) shows the highest velocities and lowest turbulence of the cycle.

As regards the separation S which is induced by the positive incidence associated with the wake it seems that the turbulence, conveyed by the wake, entering into the boundary layer plays a positive role.

At station $s = 7$ mm (Fig. 6) the mean flow is reattached all over the time. Because of the very high turbulence level (which is of the order of 20 % within the boundary layer even at the calm condition) the boundary layer velocity profiles present unconventional shapes in u^+ , y^+ coordinates (Fig. 8), which are similar to those observed on the pressure side. On the suction side the periodic effect is more marked and the profiles W and S originated by the reattached shear layer differ considerably from that relative to the calm condition C which presents the highest value of u_t / u_c .

At $s = 70$ mm (Fig. 6) the difference between the two states is still evident but the two velocity profiles tend to more conventional turbulent shapes (Fig. 8).

Differences in the time-varying behaviour of the boundary layer on the two sides of the diffuser vane can be observed by plotting mean and rms ensemble averaged velocities in time-distance contour plots. Figures 9 and 10 give an immediate impression of the boundary layer state at $s = 4$ mm on pressure and suction side. Ensemble averaged mean and rms velocities show that the separated zones alternate with phase opposition on the two sides of the vane and that the separation is more extended on the pressure than on the suction side.

The wake passage is marked by vertical bands of increased turbulence and ensemble averaged velocity extending beyond the boundary layer edge. Turbulence contours confirm that turbulence associated to the wake penetrate in depth into the boundary layer and that the shear layer formed above the separated zone is highly turbulent.

On the pressure side the wake passage W follows of about one half of the passing period the instant of maximum separation S .

On the suction side the wake passage precedes closely the separation condition and its high turbulence content attenuates the separation. The two instants are close and give rise to a single vertical band of increased turbulence and mean velocity. On this side the calm region that follows is clearly discernible as a vertical band of localised reduced mean velocity.

CONCLUSIONS

Results of a LDV investigation of the unsteady boundary layer on the diffuser vane of a centrifugal turbomachine have been presented.

Due to the small radial spacing between rotor and stator rows, the rotor blades imposes on the diffuser strong cyclic variations of the incident flow. Positive and negative incidence variations occur on the diffuser vane as a consequence of the alternating passage of blade wakes and free-stream flow.

Periodic incidence conditions cause boundary layer dynamic separations near the vane leading edge which alternate with opposition of phase on the two sides of the diffuser vane. Due to the high turbulence energy conveyed by the wakes within the diffuser which penetrates into the boundary layers, the periodic separation bubbles remain very short and the separated shear layers reattach early, giving rise to boundary layers which exhibit high turbulence levels and large skin friction coefficients. Thanks to these characteristics the boundary layers are capable of withstanding the adverse pressure gradients imposed by the diffuser.

On the suction side, where the positive incidence conditions inducing separation and the higher levels of turbulence conveyed by the wake are in phase, the periodic separation bubble is less extended both in space and time.

This feature suggests that the diffuser vane may be capable to sustain larger positive incidences without massive separations, thank to the turbulence energy supplied by the wake. In other words it seems that the aerodynamic loading on the forward part of the vane may be increased respect to the non interacting condition because the wake is capable of concentrating turbulence energy during the phase of incidence increasing.

NOMENCLATURE

p_t	total pressure
Q	flow rate
R_2	impeller outlet radius
s	streamwise coordinate

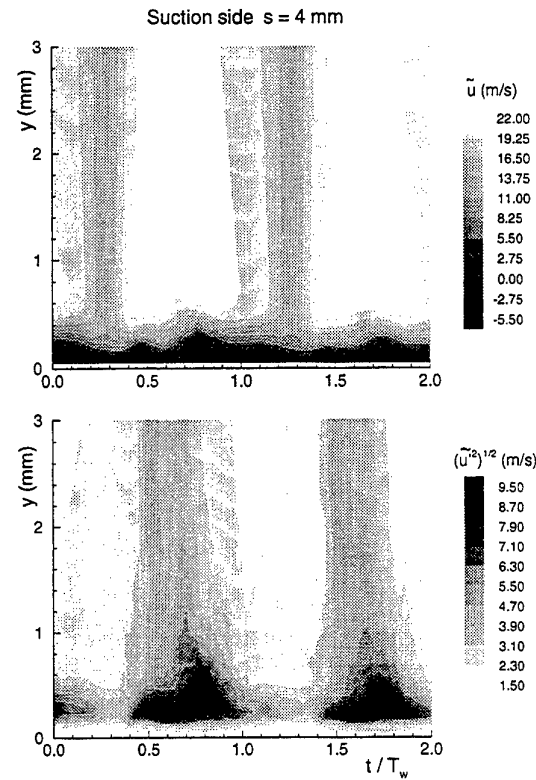


Fig. 10 Time-distance contour plots of the ensemble averaged velocity and turbulence in the boundary layer at $s = 4$ mm, suction side.

t	time
T_w	wake passing period
u	streamwise velocity component
u_τ	friction velocity $= \sqrt{\tau_w / \rho}$
u^+	non dimensional boundary layer inner variable $= u / u_\tau$
U_2	peripheral velocity at the impeller outlet
y	distance from the wall
y^+	non dimensional boundary layer inner variable $= y u_\tau / \nu$
α	absolute flow angle with the radial direction
ν	kinematic viscosity
ρ	fluid density
τ_w	wall shear stress
ϕ	flow rate coefficient $= Q / (U_2 \pi R_2^2)$
ψ	total pressure rise coefficient $= 2(p_{t4} - p_{t0}) / (\rho U_2^2)$
Subscripts	
e	at the boundary layer edge
0	in the suction pipe
4	at the diffuser outlet
Superscripts	
$'$	unsteady quantity

~ ensemble average

REFERENCES

- Addison, J.S. & Hodson, H.P. 1990, Unsteady Transition in an Axial-Flow Turbine: Part 1 - Measurements on the Turbine Rotor, ASME J. Turbomachinery, vol. 112, pp.206-214.
- Cumpsty, N.A., Dong, Y. & Li, Y.S. 1995, Compressor Blade Boundary Layers in the Presence of Wakes, ASME Paper No. 95-GT-443.
- Dean, R.C. & Senoo, Y. 1960, Rotating Wakes in Vaneless Diffusers", ASME J. Basic Eng., vol. 82, pp. 563-574.
- Liu, X. & Rodi, W. 1991, Experiments on transitional boundary layers with wake-induced unsteadiness, J. Fluid Mech., vol.231, pp.229-256.
- Schobeiri, M.T., Pappu, K. & Wright, L. 1995, Experimental Study of the Unsteady Boundary Layer behavior on a Turbine Cascade, ASME Paper No. 95-GT-435.
- Ubaldi, M., Zunino, P., Barigozzi, G. & Cattanei, A. 1996, An Experimental Investigation of Stator Induced Unsteadiness on Centrifugal Impeller Outflow, ASME J. Turbomachinery, vol. 118, pp. 41-54.
- Ubaldi, M., Zunino, P. & Cattanei, A. 1997, Étude expérimentale de l'écoulement instationnaire dans le diffuseur aubé d'une turbomachine centrifuge, Proc. Colloque S.H.F "Le comportement dynamique des pompes et turbines Hydrauliques", Chatou, pp.37-48.
- Walraevens, R.E. & Cumpsty, N.A. 1993, Leading Edge Separation Bubbles on Turbomachine Blades, ASME Paper No. 93-GT-91.

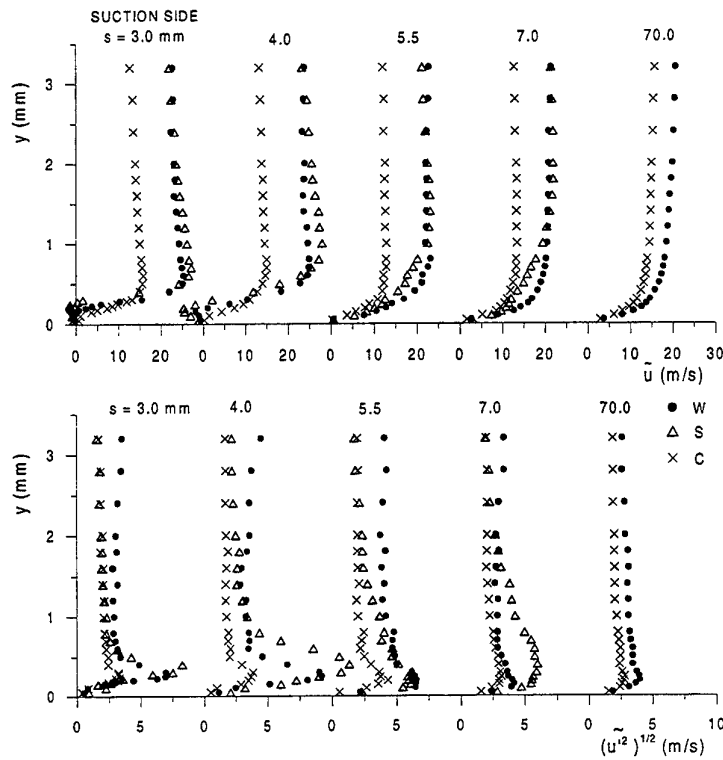


Fig. 6 Ensemble averaged velocity and turbulence profiles at different instants, suction side.

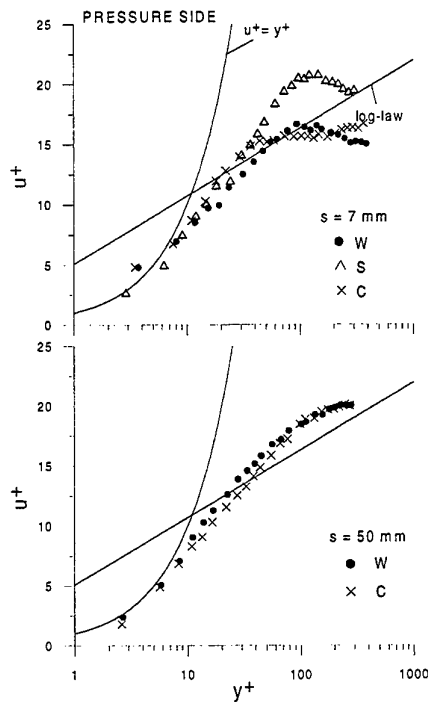


Fig. 7 Ensemble averaged velocity profiles in inner variables, pressure side

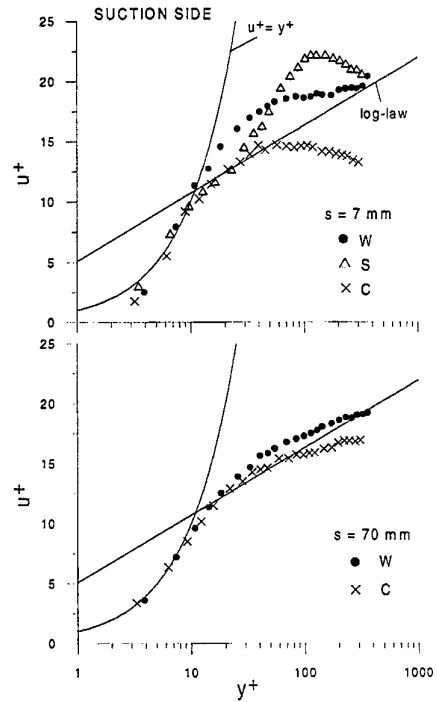


Fig. 8 Ensemble averaged velocity profiles in inner variables, suction side.

EXPERIMENTAL AND NUMERICAL INVESTIGATION OF THE UNSTEADY FLOW IN AN AXIAL TURBINE AT DIFFERENT POINTS OF OPERATION

Ch. Gentner, G. Lein, E. Göde

Institute of Fluid Mechanics and Hydraulic Machinery (IHS), University of Stuttgart, Germany

ABSTRACT

Progress in Computational Fluid Mechanics makes it possible to simulate flow effects hitherto not taken into account when modeling hydraulic machines, like unsteady feedback between runner and guide vanes. For the evaluation of the abilities and limitations of such novel methods of computation laser techniques are an important tool to provide experimental data.

The periodically unsteady flow field in a small axial hydraulic turbine is examined numerically and by means of laser-Doppler velocimetry for three different points of operation. The results of a two-dimensional unsteady calculation carried out with a code based on the Reynolds-averaged Navier-Stokes equations are compared with measurements at midspan of the turbine using a single channel laser-Doppler velocimeter. Significant unsteady periodical variations of axial and circumferential velocity are determined in both measurement and calculation.

1 INTRODUCTION

Commonly used methods for layout and optimization of hydraulic turbines with the aid of numerical methods usually are based on assumed steady state flow and neglect the unsteady interaction between guide vanes and the runner of the machine as presented by Welzel (1998). If the gap between the rotating and the stationary parts of the machine is small, effects of the flow's reciprocal influence can affect the efficiency and performance of the turbine. Recent progress in Computational Fluid Dynamics makes it possible to calculate the flow field in hydraulic machines taking these dynamic effects into account. Laser techniques play an important role in verifying the results of such numerical calculations,

especially for evaluation of novel methods of computation.

At the Institute of Fluid Mechanics and Hydraulic Machinery of the University of Stuttgart the code FENFLOSS for numerical flow calculation based on the Navier-Stokes equations has been developed. This program has been extended to time-dependent and coupled calculation of the flow in the guide vanes and the rotating runner of hydraulic turbomachines.

A small axial turbine for energy recuperation in piping systems is used to compare measured and calculated flow velocities in guide vanes and runner. Results of a two-dimensional instationary calculation carried out with FENFLOSS are compared with velocities measured using a single channel laser-Doppler Velocimeter.

The turbine consists of a ring of 12 guide vanes of 50 mm axial length and a height of 20 mm



Figure 1. Guide vanes (left) and runner of the axial turbine with the plane of measurement

and a runner with 15 blades of the same dimensions. The diameter of the hub is 140 mm and the outer diameter of the runner is 180 mm. The axial gap between guide vanes and runner is 6 mm, so considerable interaction between the two parts has to be expected. The shape of the runner is unusual for a hydraulic turbine, so the assumptions for the initial design should be verified before an optimization of the profile. Figure 1 depicts the hydraulic profile of the investigated geometry and the plane for the measurements. Welzel (1994) gives a detailed description of the studied turbine.

2 THE NUMERICAL METHOD

For hydraulic turbomachines one can assume a three-dimensional unsteady viscous incompressible flow. Since the Reynolds number is usually rather high ($Re > 10^5$) a fully turbulent flow is supposed. At the University of Stuttgart, Germany Ruprecht (1989) developed the finite-element code FENFLOSS, which has been used for the calculations presented in this paper. FENFLOSS is based on the Reynolds-averaged Navier-Stokes equations. The turbulence of the flow is taken into account using the k- ϵ model. Bauer et al (1998) introduced an algorithm which

allows the calculation of several non-matching grids in parallel. The flow quantities of the nodes in the interface region are exchanged downstream and upstream during each global iteration. This method is applied to simulate the unsteady flow caused by the rotor-stator interaction. The unsteady simulation has been carried out with 360 time steps, each corresponding to a rotational movement of the runner of one degree. For each time step the grid of the runner is moved numerically according to the rotational speed for the given point of operation and the flow quantities of the adjoining nodes of both grids are then exchanged.

The flow far from the end walls (hub or casing) in an axial turbomachine may be considered two dimensional, or nearly so. Calculations have been carried out for a plane at midspan of the turbine. Figure 2 shows the grid for the computation. To match the periodic nature of the machine four channels of the guide vane ring and five channels of the runner are simulated. The grid for the guide vanes consists of 17950 nodes, the grid for the runner of 27770 nodes. Measured values of velocity for midspan were applied as boundary condition at the inflow of the guide vanes. At the upper and lower boundaries a periodic boundary condition was applied, thus simulating two infinite linear cascades with relative movement to each other. At the outflow constant and uniform pressure is assumed.

3 EXPERIMENTAL SETUP

The turbine is installed in the closed test circuit at the IHS. Two pumps (each with $H_{\max}=50$ m, $Q_{\max}=0.25$ m³/s) deliver the necessary head for the operation of the test turbine and two tanks on the pressure and the suction side provide for stable operating pressure. The values for flow rate, head and speed, which were applied during the tests, are realistic for a practical application of the turbine.

Measurements and calculations have been carried out for three different points of operation as described in Table 1.

Table 1: Examined points of operation

Rotational speed/min ⁻¹	Head/m	Discharge m ³ /s	Efficiency of turbine/%
1386 (Nominal point)	21.28	0.0846	75
573	21.28	0.0902	50
2107	21.28	0.0831	50

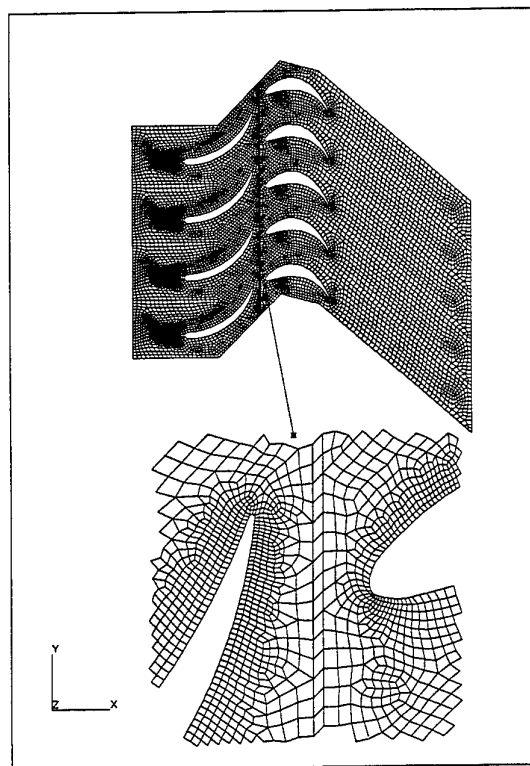


Figure 2: Computational grid of guide vanes (left) and runner with interface region

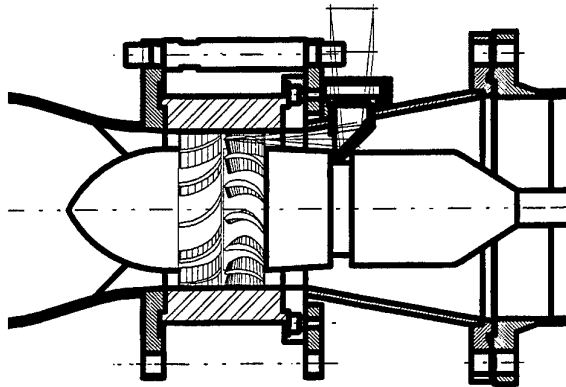


Figure 3: Workshop drawing of the test turbine

For the measurements the turbine was housed in a cylindrical casing made of acrylic glass as seen in Figure 3. For both axial and circumferential components of the velocity a grid with spacings of 5 mm axially and angles of 5° circumferentially was recorded as shown in Figure 4. Measurements were carried out in a cylindrical plane at midspan, diameter 160 mm, which can be seen in Figure 1.

The radial component of the velocity was measured using a mirror which was mounted downstream 100 mm after the runner outlet in the draft tube (see Figure 3). This component has been examined at significant locations in both runner and guide vanes.

The measurements were carried out using a resolver for rotating machinery and a reset was triggered at each revolution of the runner. For a head

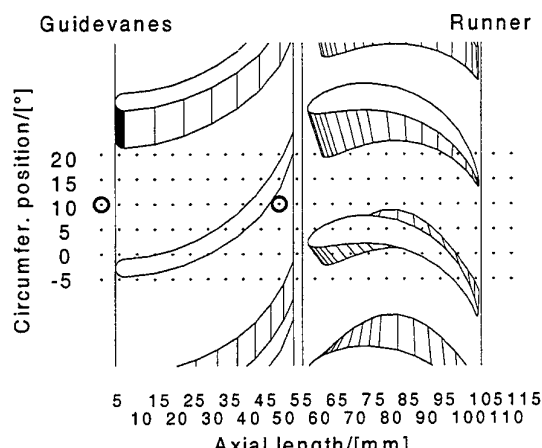


Figure 4: Grid of the positions of measurements

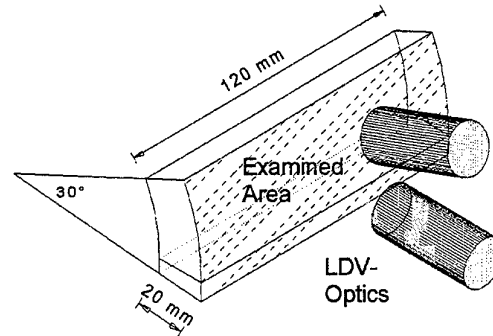


Figure 5: Sketch of the studied flow domain with swivel-mounted LDV optics

of 20 m the nominal speed of the turbine is 1386 min^{-1} . This equals 43.29 ms per revolution. For the analysis the measured velocities were averaged with a resolution in time of 0.1203 ms equivalent to one degree of rotation and thus follow 360 values of velocity per revolution of the runner, which correspond to the time steps of the numerical calculation. For overspeed and sub-nominal speed the resolution in time is 0.0791ms and 0.2909 ms accordingly.

The laser optics were mounted on a three axis traversing table while the light from the laser was transmitted via a monomode optic fiber. To avoid the tracing of the refracted beams through the curved walls of the housing the LDV optics are swivel-mounted. For each angular position of measurement the optics can be tilted such that the optic axis is perpendicular to the surface of the acrylic glass. This simplifies determining the position of the measuring volume in the flow domain. Figure 5 illustrates this setup.

Processing of the LDV data was carried out by means of a digital burst correlator.

The water was seeded with micro-glass bubbles with a mean diameter of $30 \mu\text{m}$. For each position of the measuring volume 100,000 bursts have been recorded. This corresponds to 278 measurements per angular position of the runner. Due to background flare and reflection from the hub and blades the number of data fell short of this limit at some positions. As an exception a few points with less than 30 valid measurements have been included in the results. During the measurement the data rate varied between 10 Hz and 1000 Hz.

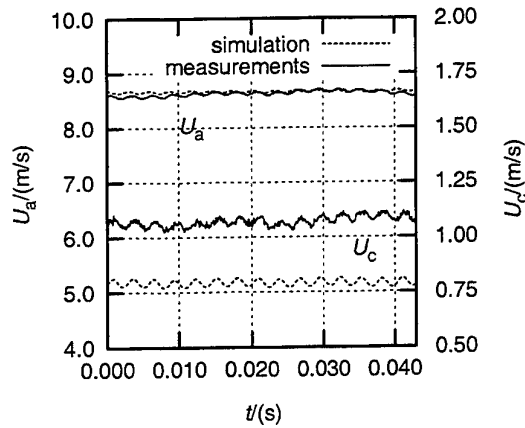


Figure 6: Nominal speed: Velocity at the inflow of the guide vanes (Note the different scales for u_a and u_c)

4 RESULTS

4.1 Time history of velocity

Both measurement and calculation show strong interference between runner and guide vanes. The upstream influence of the passing blades of the runner cascade can be detected up to the inflow of the guide vanes. In Figure 6 time-dependent velocities measured at the inflow of the guide vanes (Point 10°/0 mm in Figure 4) are compared with the results of the numerical calculation. Velocity versus rotational angle show variations according to the rotational speed of the runner. A fluctuation of ± 0.03 m/s around a mean velocity of 8.62 m/s for the

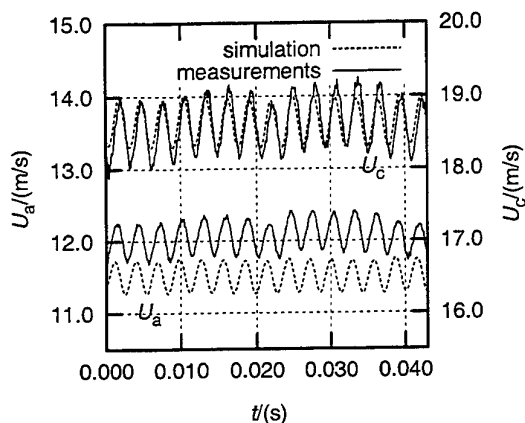


Figure 7: Nominal speed: Velocity at the exit of the guide vanes (Note the different scales for u_a and u_c)

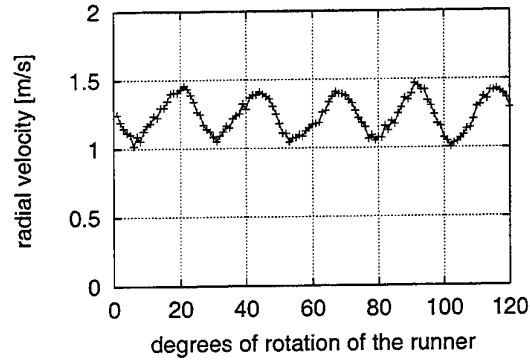


Figure 8: Radial velocity at the exit of the runner, measurement

axial velocity u_a and of ± 0.02 m/s around a mean velocity of 1.07 m/s for the circumferential component u_c have been measured at the nominal point of operation.

In this case the calculation yields a fluctuation of 8.66 ± 0.02 m/s for the axial and of 0.79 ± 0.018 m/s for the circumferential velocity. The calculated velocities match very well with the measurements in respect to the frequency and the magnitude of the oscillation.

Figure 7 shows calculated and measured time slopes of the two velocity components u_a and u_c at the location 10°/50 mm for the nominal point of operation. Frequency and amplitude of the calculated oscillation agree well with the measurements.

Although the height of the blades is comparatively small, even at the nominal point of operation a component in radial direction can be measured. At midspan at the runner outlet

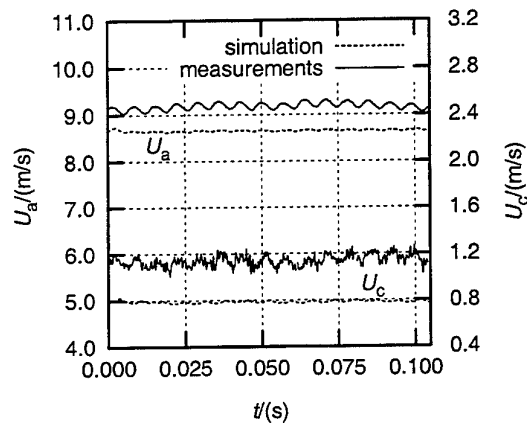


Figure 9: Reduced speed: Velocity at the inflow of the guide vanes (Note the different scales for u_a and u_c)

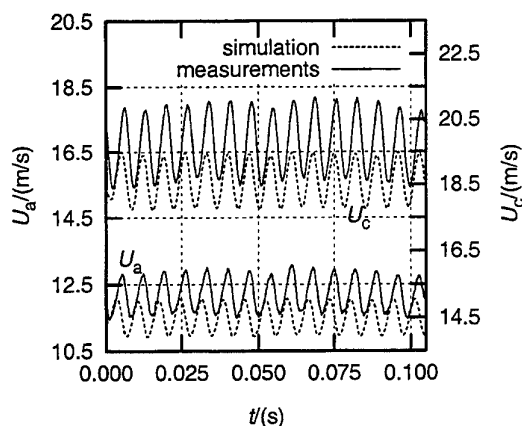


Figure 10: Reduced speed: Velocity at the exit of the guide vanes (Note the different scales for u_a and u_c)

(Point 10°/115 mm in Figure 4) a mean radial velocity of 1.2 m/s is observed. It varies by ± 0.25 m/s as shown in Figure 8. At this location the mean velocity projected on the plane at midspan is 9.38 m/s. If one considers the radial component, the absolute velocity changes by 0.74 percent to 9.45 m/s. Taking this into account, the use of a two-dimensional numerical model for the investigation at nominal operating conditions appears to be justified.

The comparison of the measured and calculated velocities for the sub-nominal point of operation reveals some differences not registered at nominal speed. Figure 9 shows u_a and u_c at the point 10°/0 mm. The time-resolved velocities u_a and u_c at the exit of the guide vane ring (point 10°/55 mm) are compared in Figure 10.

While for the point of reference at the inflow

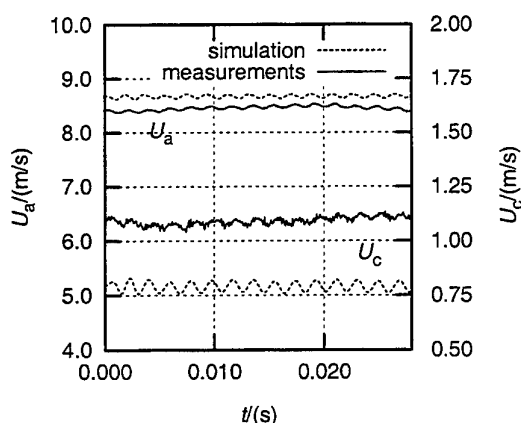


Figure 11: Overspeed: Velocity at the inflow of the guide vanes (Note the different scales for u_a and u_c)

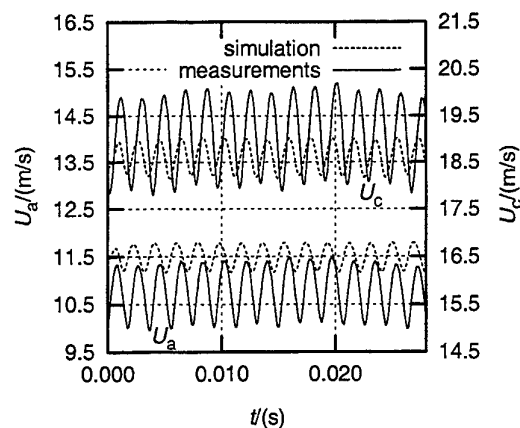


Figure 12: Overspeed: Velocity at the exit of the guide vanes (Note the different scales for u_a and u_c)

of the guide vanes the results are similar to the nominal point, at the exit of the guide vanes greater differences in the time history between measurement and calculation are detected. The calculation does not reflect the greater amplitudes of the oscillation of both u_a and u_c that are found in the measurement. However, the frequency is detected with reasonable accuracy also for this mode of operation.

For the case with greater rotational speed the time history of the velocities at the two points of reference is shown in Figure 11 and Figure 12. Looking at velocity versus time the basic observations are the same for both off-design modes. The main phenomena of the time slope are simulated well in both cases, while there are greater discrepancies for the absolute magnitude of measured and calculated quantities. For the operation at design conditions the initial presumption of nearly two-dimensional flow at midspan is correct. For the operation of the turbine at off-design, where the secondary flow in the runner is more significant, the limitations of a two-dimensional numerical model can be seen. It has to be noted that this isn't a shortcoming of the algorithm for the numerical coupling of the two grids but is particular to the two-dimensional calculation.

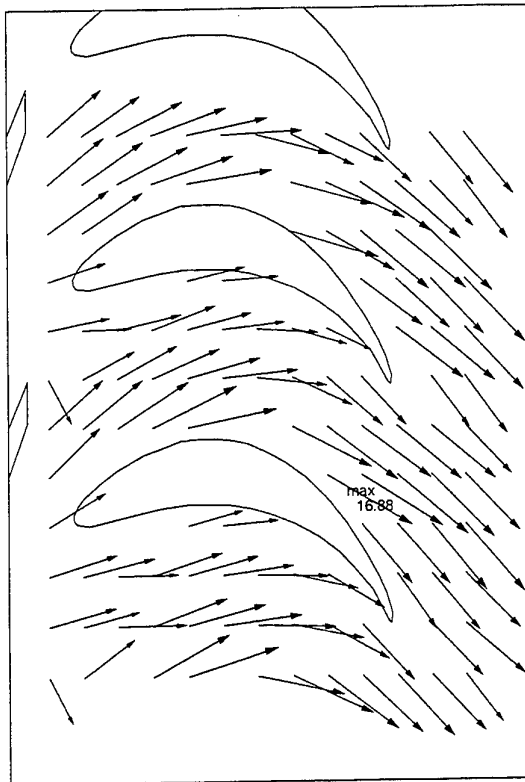


Figure 13: Measured flow field in the relative frame of the runner at nominal speed at $t=0$ s.

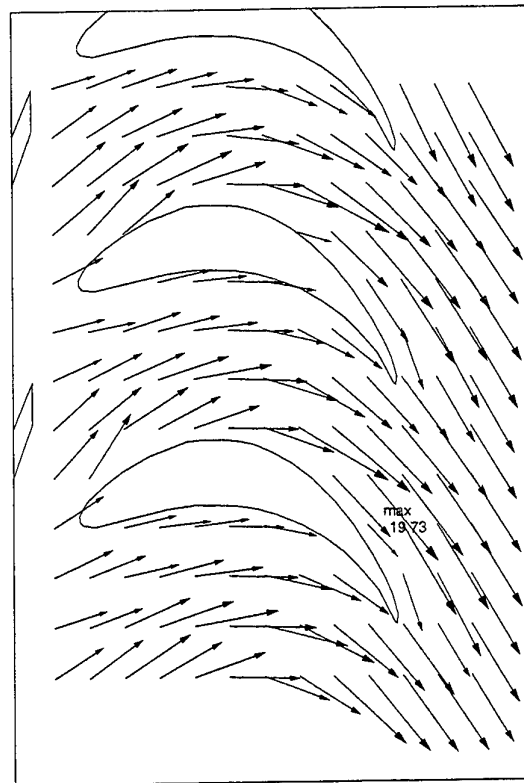


Figure 14: Calculated flow field in the relative frame of the runner at nominal speed at $t=0$ s.

4.2 Instationary flow field in the runner

Measured and calculated flow field in the runner at the nominal speed for the point of time $t=0$ s are compared in Figure 13 and Figure 14. Shown are the resultants of u_a and u_c in the relative frame of the runner. In either case the location of the maximum velocity is found on the suction side at the outflow of the runner. The main features of the non-uniform outflow of the guide vanes are present in both results.

Some difference can be noted in the angles of flow at the exit of the runner. The angle between axial direction and the flow is greater and much more uniform in the calculated flow field. It is a known feature of CFD codes utilizing the k- ϵ model in combination with logarithmic wall functions for turbulence modeling to predict flow separation later than it occurs in reality. In the calculation the flow follows the curvature of the blades better than it does in real flow. It is not possible to give a general order of magnitude for this characteristic but it has to be considered when CFD is used as a tool for the design of hydraulic machines.

The effective angle of flow at the exit of a cascade differs from the angle of the profile. For the design of hydraulic profiles this is generally taken into account using empirical correction factors. The presented measurements allow the verification of the applied factors for the given case and give support for an improved design of the turbine.

Figure 15 and Figure 16 show the flow field in the runner for the sub-nominal point of operation. The location and the order of the maximum velocity agree well for both results.

5 CONCLUSIONS

The unsteady flow field at midspan of a small axial hydraulic turbine has been investigated numerically and with a single channel LDV. Measurements and calculations have been performed for three points of operation.

The measurements show a three-dimensional flow field with strong influence of the runner on the flow in the guide vanes. To achieve the best possible modeling of the flow, a numerical method has to be applied that includes the exchange of information

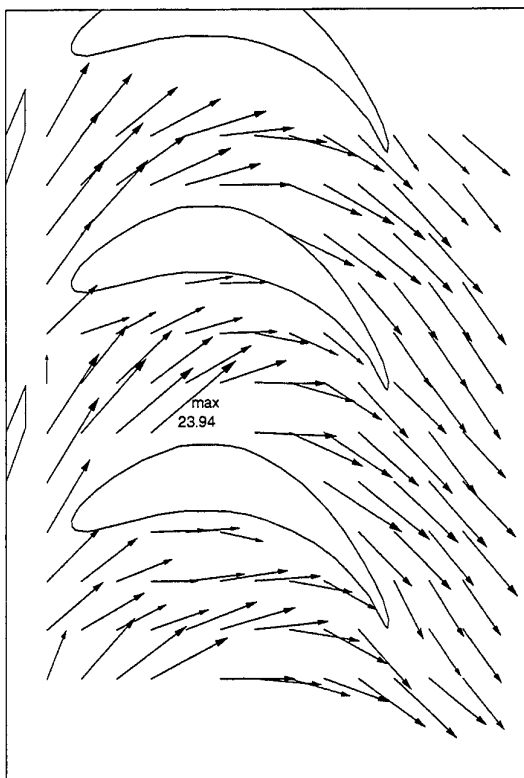


Figure 15: Measured flow field in the relative frame of the runner for reduced speed at $t=0$ s.

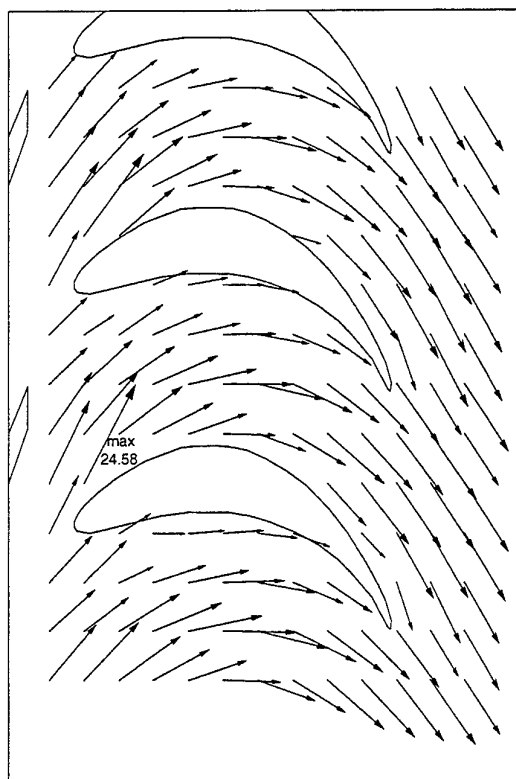


Figure 16: Calculated flow field in the relative frame of the runner for reduced speed at $t=0$ s.

between the two flow domains as well upstream and downstream.

Numerical calculations have been carried out using two-dimensional grids of Finite Elements, one for the fixed guide vanes and one for the rotor. By coupling these two domains and exchanging values for velocity and pressure at the boundaries, the periodic instationary interaction was taken into account.

The comparison of measured and calculated flow field shows the ability of the numerical method to simulate the main features of the unsteady flow field in both runner and stator. For the off-design points of operation with stronger secondary flow certain limitations with respect of the quantitative accuracy of the two-dimensional model are observed.

On the basis of measured and calculated velocity fields further variations of shape for the blades can be examined numerically. The interpretation of these findings will result in an improved design for the turbine leading to higher efficiency and reduced cavitation.

REFERENCES

- Welzel, B. 1998, Optimierung einer Axialturbine, Ph.D. thesis, Institut für Strömungsmechanik und Hydraulische Strömungsmaschinen, University of Stuttgart, Germany
- Welzel, B. 1994, Stand der Entwicklung einer einfach regelbaren Axial-Wasserturbine zum Einsatz als Entspannungsturbine in Rohrleitungssystemen, Proc. VDI-Tagung Energierückgewinnung aus Erdgas und Wasser durch Einsatz von Entspannungsmaschinen, Köln, Germany, pp.49-60
- Ruprecht, A. 1989, Finite Elemente zur Berechnung dreidimensionaler, turbulenter Strömungen in komplexen Geometrien, Ph.D. thesis, Institut für Strömungsmechanik und Hydraulische Strömungsmaschinen, University of Stuttgart, Germany
- Bauer, C., Maihöfer, M., Ruprecht, A., Lein, G. 1998, Simulation of Flow in Hydraulic Turbines Using a Multi Block Algorithm, ECCOMAS 98, Fourth Computational Fluid Dynamics Conference, Athens

SECONDARY FLOW FIELD MEASUREMENTS WITH A LDV IN THE VANED DIFFUSER OF A HIGH-SUBSONIC CENTRIFUGAL COMPRESSOR

D. Stahlecker, E. Casartelli, G. Gyarmathy
Turbomachinery Laboratory
ETH Swiss Federal Institute of Technology, Zurich
Switzerland
Email: stahlecker@lsm.iet.mavt.ethz.ch

ABSTRACT

A three component LDV system has successfully been implemented within a one stage high-subsonic closed loop centrifugal compressor. The crucial features enabling close-to-wall LDV measurements in the narrow width diffuser passage are described. Extensive 3D measurements have been made in the vaned diffuser. Results are shown for the throat cross section and the semi vaneless space. The measurements have been made at best-point and near-surge at a circumferential Mach number of $M_u = 0.75$. The time-averaged velocity results clearly reveal the development of a single large channel vortex in each channel and its change with flow rate. CFD calculations performed in parallel with the TASCflow Navier Stokes Code show remarkable agreement with the experimental results.

NOMENCLATURE

Abbreviations

CFD	Computational Fluid Dynamics
LDV	Laser Doppler Velocimetry
L2F	Laser-2-Focus
PIV	Particle Image Velocimetry
PTV	Particle Tracking Velocimetry
FRAP	Fast Response Aerodynamic Probe

Symbols

b	[mm]	axial diffuser width (=16.8mm)
C	[-]	non-dimensional velocity (c/u_2)
c	[m/s]	flow velocity
\bar{c}	[m/s]	phase-averaged velocity
$\bar{\bar{c}}$	[m/s]	time-averaged velocity
D_2	[mm]	impeller rim diameter
M_u	[-]	impeller tip speed Mach number ($= \frac{u_2}{\sqrt{\gamma R T_1}}$)
N	[-]	number of impeller revolutions during Δt
n_k	[-]	number of LDV bursts within class k
n_t	[-]	total number of LDV bursts collected
r	[mm]	Radius

R	[$\frac{J}{kgK}$]	specific gas constant
T°	[°K]	stagnation temperature
t	[s]	time
Δt	[s]	LDV data acquisition time at a traverse position
u_2	[m/s]	impeller rim speed
x	[m]	pitchwise coordinate in cross sections (positive to pressure side)
y	[m]	axial coordinate (positive to casing)
γ	[-]	isentropic exponent
φ	[-]	flow coefficient ($= \frac{\dot{m}}{\rho_1 D_2^2 u_2}$)
λ	[nm]	wavelength of light
ρ	[kg/m ³]	density
$\bar{\sigma}$	[m/s]	phase-averaged fluctuation
$\bar{\bar{\sigma}}$	[m/s]	time-averaged fluctuation
Θ	[°]	phase-averaging angular window

Subscripts

I	at stage inlet
i	index of velocity doublet
k	phase-averaging class index

INTRODUCTION

Today, the polytropic best-point efficiency of centrifugal compressors with vaned diffusers rarely reaches levels beyond 85%. The low efficiency is a result of the curvilinear flow in the impeller channels causing separation and the undesirable jet/wake structure at impeller exit. Vaned diffusers in centrifugal compressors advantageously increase the stage pressure ratio but unfortunately decrease the stable operating range in the compressor map. A better understanding of the 3D unsteady flow in the impeller and the vaned diffuser should allow centrifugal compressors with higher efficiency, higher pressure ratio and broader operating range to be designed.

At the ETH Turbomachinery Laboratory centrifugal compressor research is currently performed with two test rigs, a high subsonic centrifugal compressor

with vaned diffuser, called 'Rigi', and its 1:1 scale water model counterpart 'Kander'. The latter is specially designed for the visualisation of large-scale flow phenomena such as the impeller inlet recirculation or rotating stall (Gyarmathy (1996), File et al. (1997)). Furthermore CFD calculations are performed with the TASCflow code (Casartelli et al. (1997, 1998)). Of special interest for experiments and CFD calculations is the flow field in the diffuser, because this component is mainly responsible for limiting the stable operating range (Hunziker and Gyarmathy (1993) and Hunziker (1993)).

Because of limited space in the vaned diffuser region, probe measurement techniques can lead to severe blockage effects and thus to biased measurement results. Early centrifugal compressor studies published in literature have mostly been carried out with hot wire anemometers. Disadvantages arose due to calibration, dirt and the impossibility to distinguish negative velocities. Thus recirculation areas were difficult to detect. Nonintrusive optical velocity measurement techniques are therefore an interesting corollary to intrusive measurements using hot wires or in-house developed Fast Response Aerodynamic Probes (FRAP) at impeller exit (Roduner et al. (1998)). An in-house feasibility study of different pointwise (L2F and LDV) and field techniques (PIV and PTV) resulted in the selection of the LDV method (Stahlecker et al. (1997)). Non intrusive field methods like PIV or PTV cannot be applied until now in this high-speed compressor rig.

Extensive LDV measurements in high-speed centrifugal compressors seem not to have been reported yet. In high-speed applications mostly L2F or hot wire measurements were made. Pioneering work was done by Eckhardt (1975) reporting about the jet/wake phenomena measured with a hot wire anemometer at impeller exit, later completed with L2F measurements within an impeller (Eckhardt (1976)). Whereas Eckhardt's measurements have been made in a rig with a vaneless diffuser, Krain (1981) reports L2F measurements in a high pressure ratio vaned centrifugal compressor with radial ended impeller blades. The main focus of these early endeavours made with the non intrusive L2F method was the mixing-out process. Ahmed and Elder (1990) report measurements made with a micro LDV within the impeller. Runstadler and Dolan (1975) report about an optimized LDV system for measurements in a high speed impeller, but only little data is shown.

Precise and extensive LDV measurements were done in low velocity, large scale airflow models i.e. by Chriss et al. (1994), Hathaway et al. (1992, 1993) at NASA Lewis and by Fagan and Fleeter (1991). Measurements in low speed 1:1 scale centrifugal compressor models operated with water or air are reported by Abramian and Howard (1994a,b) and Ubaldi et al. (1996).

A recent general review about laser anemometer applications in turbomachinery is provided by Strazisar

(1993).

Although LDV and L2F measurements were performed in all kinds of turbomachinery facilities from low-speed to high-speed, LDV measurements in narrow width high-speed centrifugal compressors were rarely performed. Even with today's state of the art LDV signal processors it still remains a challenge to make LDV measurements with reasonable data rates in high-speed compressors with small diffuser width. The crucial optical, mechanical & electronic adaptations necessary for making LDV measurements in the high-subsonic centrifugal compressor are presented.

The objective of the present study is to get more insight into the development of secondary flow in the vaned diffuser and, by comparisons to achieve more confidence in CFD based calculations of the diffuser flow. Extensive experimental data are necessary for advanced CFD code validation since decelerated diffuser flows are difficult to predict with the CFD codes and their $k-\epsilon$ models presently available. The 3D LDV velocity field measurements have been made in the semi vaneless space and in the diffuser throat. Diffuser channel vortices could be measured, we believe for the first time in a high-speed centrifugal compressor.

TEST RIG

The high-subsonic centrifugal compressor used during the investigations has a single stage with a vaned diffuser and is operated in a closed loop with air as working fluid (Fig. 1). The unshrouded impeller of $D_2 = 280\text{mm}$ exit diameter has 11 full and 11 splitter blades with a backsweep of 30° to the radial. The 24 circular-arc diffuser vanes begin at 116% exit radius, their camberline stagger angle is set to 25° (Fig. 2). The diffuser has plane parallel side walls and its width is $b = 16.8\text{mm}$. The compressor is driven by a 440 kW DC motor. Since the maximum rotational speed is limited by the shaft seal to 22000 rpm, the rig is operated up to a rim Mach number of $M_u = 0.9$ resulting in a circumferential velocity at impeller exit of $u_2 = 311\frac{\text{m}}{\text{s}}$. For a more complete description of the test compressor refer also to details in Hunziker and Gyarmathy (1993).

During the following investigations the test rig was operated at $M_u = 0.75$ and the measurements were taken at best-point and near surge. At the best-point (averaged zero incidence conditions to the 25° diffuser vanes) the flow coefficient was $\varphi = 0.0747$ ($\dot{m} = 1.7\text{kg/s}$) and the total-to-total pressure ratio was 1.54. For near-surge the flow coefficient was $\varphi = 0.0555$ ($\dot{m} = 1.26\text{kg/s}$) and the total-to-total pressure ratio was 1.57.

LDV SYSTEM AND SETUP

LDV System

The LDV system used is commercially available from TSI and comprises a 3 channel TSI autocorrelator-based IFA 755, a ColorLink, two 25 mm diameter Laser Probes, an External Data Interface with a Rotating Machinery Encoder for tagging LDV bursts with the an-

gular impeller position, a three axis traversing system with control unit, a 120 MHz Pentium PC and a SGI Indigo2 Workstation for data acquisition, reduction and visualisation. The light source is a Coherent Innova 308 ArIon Laser. The LDV unit is remotely placed and connected by long (15m) optical fibres to the compressor rig. In Fig. 4 the compressor stage front view can be seen together with the 3D traversing rails and two LDV probes.

The focal length of both LDV probes is 140mm producing a beam intersection diameter of about 100 μm and an intersection length of about 1.8mm. Due to the off-axis straylight reception at an angle of 34.5° the effective axial flow resolution is improved from 1.8mm to about 0.5mm. The fringe spacings are 4.81 μm ($\lambda = 514.5\text{nm}$), 4.56 μm ($\lambda = 488\text{nm}$) and 4.45 μm ($\lambda = 476.5\text{nm}$).

The rotating machinery encoder labels the validated burst with the angular impeller position relative to a once-per-revolution TTL-level signal from the impeller. The encoder is phase-locked-loop based and has an angular resolution of 0.1°. The impeller position tags allow time-resolved analysis of the unsteady flow to be made over each rotor revolution.

Figure 3 shows the whole 3D LDV system setup which permits semi-automatic data acquisition to be made and quasi "online" visualisation of the raw data. The PC transmits LDV measurement parameters and traversing coordinates via RS232 to the LDV electronic devices. The raw data, transferred from the IFA 755 via Direct Memory Access (DMA) to the PC, is forwarded via NFS to the Unix Workstation where they are stored. The whole data processing takes place on the Workstation with the MATLAB software environment. The quasi "online" raw data visualisation with MATLAB allows the plotting of time and angular histograms only seconds after the completion of a measurement permitting a first appreciation of the acquired data. To enable the data processing with MATLAB a special routine (mex function) was written in C which allows MATLAB to read the TSI binary raw data format. In an "offline" part the whole data reduction and visualisation is performed.

Special Measures for LDV Enhancement

In high-speed centrifugal compressors severe LDV measurement problems arise due to:

1. Lack of adequate seeding concentration in some parts of the diffuser flow channel.
2. Low light scattering power due to the required small particle size and the impossibility of using forward scattering.
3. High flow speed and high velocity fluctuations.
4. Narrow channels, and the abundance of wall reflections.

The following crucial adaptations of the test rig and the LDV system have been made for enabling high-quality

measurements to be performed:

Absorption Filter. Laser Light reflections from narrow walls cause straylight leading to increased LDV burst noise and thereby to a reduced data rate. A damping of the stray light is necessary, otherwise near-wall LDV measurements are not possible. With a 8 mm thick, black, antireflex-coated, absorption filter glass (grey filter, Schott NG 11) used at the hub side of the diffuser (Fig. 5) this straylight intensity was significantly reduced. More than 87% of the incident laser light power is absorbed by the filter.

Off-axis light reception. The scattered light of the particles is collected under an off-axis angle of 34.5°. This combination of the absorption filter glass and the off-axis scattered-light reception arrangement gives the best results with respect to close to wall measurements. Measurements up to approx. 0.7mm wall proximity are possible, even through a moist window and a moist absorption glass. The off-axis arrangement also improves the spatial resolution of the measurements in axial direction from about 1.8mm to 0.5mm.

Probe Holders. Scattered light reception in off-axis arrangement and coincident 2D or 3D measurements are only possible with accurate alignment of the laser beam measurement volumes. Special new probe holders (Fig. 6) have been developed to guarantee a precise probe adjustment and a long term stable intersection of the laser beams.

Seeding. The use of a particle generator (Palas AGF 10.0) for paraffin oil with a high production rate (up to 10⁹1/s) and the closed loop compressor system increases the particle concentration in the piping system and leads to higher data-rates. The mean diameter of the droplet distribution is near to 0.4 μm and the number fraction with diameters beyond 1 μm is negligible. Thus adequate flow following properties of the particles in the high subsonic flow are guaranteed. Agglomeration effects are negligible, but some oil accumulation in the circuit cooler has been experienced.

Despite of the important improvements obtained genuine 3D coincident LDV measurements were still not practicable because of low coincident data rates (less than 70Hz) and the resulting long measurement times. The problem has been circumvented by a sequential 2D + 2D procedure described below. More details of the mentioned measures are also discussed in Stahlecker et al. (1997).

NUMERICAL PROCEDURE AND GEOMETRY

Steady 3D flow field computations have been performed with a commercial Navier-Stokes code, TASCflow, V2.4, ASC Ltd. (1995). Reynolds-Stress averaging is applied to the governing equations in strong conservation form for the turbulent flow. A standard

$k - \epsilon$ model is used. A constant 5% turbulence intensity was assumed at diffuser inlet. The discretisation procedure is based on a Finite-Volume method. The computational grid is a block structured H-type mesh with 102138 active nodes (see Fig. 7). The periodic boundary condition is surface based, i.e. the number of nodes and their distribution on periodic surfaces can vary. The diffuser blade has been placed in the middle of the computational domain to improve the cell shapes at the leading edge. The blade region is a block-off domain in the grid. The flow coefficient for the best-point calculation is $\varphi_{CFD} = 0.0767$, slightly higher than the corresponding flow coefficient of the measurements ($\varphi_{LDA} = 0.0747$). The near surge calculation has been performed at the identical flow rate $\varphi_{LDA} = \varphi_{CFD} = 0.0555$. More details about performed CFD calculations for this centrifugal compressor can be found in Casartelli et al. (1997).

MEASUREMENTS

The 3D field measurements for the two operating points (best-point and near surge) at a rim Mach Number of $Mu=0.75$ have been made in the throat cross section and in the semi vaneless space of the vaned diffuser (Fig. 8). In the throat cross section LDV data were taken at approx. 240 measurement locations. The measurement grid consists of 17 locations from hub to casing and 14 in the pitchwise direction from the pressure side to the suction side (Fig. 9). In the semi vaneless space cross sectional measurements were taken at a comparable amount of positions.

Because of the already mentioned low data rates genuine coincident 3D LDV velocity measurements have not been possible. Instead, the 3D velocity information was set together out of two independent sets of coincident 2D measurements made with different orientation of the two probes (see also Stahlecker et al. (1997). Since the green light (indicating approximately radial velocity) was measured on both occasions, it was checked if the difference between the two measurements was small. This has been confirmed. Thus the conditionally averaged axial velocity component derived from this measurement could be used to complete the first 2D in-plane measurement.

At each measurement position, an amount of about $n_t=25.000$ coincident 2D measurements were taken first, measuring the velocity components in planes parallel to the diffuser casing. The second 2D measurement was made to acquire the third (axial) flow component. The optical axis of the two probes were arranged under an angle of 34.5° . During this second measurement, about $n_t = 12.000$ coincident 2D bursts have been collected at each point. The coincident time-window width was set for all measurements to $4\mu s$. With the good alignment possibilities of the probe holders the time delay of the bursts (which could be observed on an oscilloscope) was typically less than $0.5\mu s$.

DATA REDUCTION

During the LDV data acquisition each validated coincident burst pair was tagged with the angular impeller position for later time-resolved data analysis. One impeller revolution is subdivided into 3600 bins, resulting in a peripheral resolution of 0.1° . After the necessary coordinate transformation of each of the n_t raw coincident velocity doublets collected an impeller twin-channel based phase-averaging procedure is performed with a constant angular window width of $\Theta = 1^\circ$. This 1° step is used only for the calculation of time resolved, over-the-pitch velocity data and is a good compromise between channel resolution and statistical uncertainty. In contrast to hot wire anemometry or FRAP probes the average LDV data rate is low. To achieve an adequate sample size for statistical reasons, data overlay and phase averaging is a common procedure.

This phase-averaging process comprises three steps as seen in Fig.10:

1. classified overlay of all data taken at all N impeller revolutions (up to 24'000), using the 0.1° resolution
2. projection of the 22 impeller channels (11 full and 11 splitter blades) to one representative "Twin-Blade Channel" domain of 32.7° width comprising one splitter and one full blade channel
3. Calculation of 33 phase-averaged mean velocities \bar{c}_k and standard deviations $\bar{\sigma}_k$ with a 1° angular window width.

The 33 phase-averaged velocities and standard deviations per twin-blade channel for time-resolved plots are calculated as follows:

$$\bar{c}_k = \frac{1}{n_k} \sum_{i=1}^{n_k} c_{i,k}, \quad k = 1 \dots 33 \quad (1)$$

$$\bar{\sigma}_k^2 = \frac{1}{n_k - 1} \sum_{i=1}^{n_k} (c_{i,k} - \bar{c}_k)^2, \quad k = 1 \dots 33 \quad (2)$$

Time averaged velocity data, specially calculated for CFD comparisons, is calculated in a refined way. The raw data is phase averaged a second time, as indicated in Fig.10, but this time the phase averaging resolution is set to 0.1° leading to 327 classes within the twin blade channel. New phase averaged local mean and standard deviation values \bar{c}_k and $\bar{\sigma}_k$ are calculated with Eq.(1) and (2) with k running now from 1 to 327. The 327 data groups are then arithmetically averaged to give a single time-averaged value over the twin-passage as:

$$\bar{\bar{c}} = \frac{1}{327} \sum_{k=1}^{327} \bar{c}_k \quad (3)$$

The analogous turbulent fluctuation intensity may be calculated as follows:

$$\bar{\bar{\sigma}} = \frac{1}{327} \sum_{k=1}^{327} \bar{\sigma}_k \quad (4)$$

The averaging over 0.1° classes reduces the influence of velocity bias. In order to obtain mass-averaged mean velocities, the 327 classes must be suitably weighted. This problem is not discussed in the present paper. Phase and time-averaging was done for each axial (y) and pitchwise (x) measurement position. All data sets are made non-dimensional with the impeller rim speed of $u_2 = 260\text{ m/s}$. In the present study only the averaged mean velocity components shall be presented.

ACCURACY

LDV measurement error sources have been widely discussed in literature see for example Boutier (1993), Durst et al. (1987) or Ruck (1987). Errors due to long-term drift and irreproducibility of the compressor operating point is less than 2% of impeller rim speed even in regions of the highest velocity gradients. The positioning of the probes was realized with a three axis traversing unit. For all three axes a 5-phase stepper motor was used and operated in half-step mode permitting 1000 steps per spindle revolution. In half-step mode the bi-directional repeatability for all axes is in the range of $\pm 3\mu\text{m}$. The absolute position error of the probe measurement volumes with respect to the origin of the compressor coordinate system is less than $\pm 0.02\text{ mm}$ in each direction.

The velocity accuracy of a single coincident 2D measurement is a result of:

- the uncertainty of velocity measurement by each beam pair
- the accuracy of the velocity transformation into the orthogonal velocity components of the compressor coordinate system.

The accuracy of each beam pair velocity measurement is mainly influenced by the accuracy and resolution of the TSI IFA755. Experiments with artificial noisy bursts at typical IFA settings revealed an average frequency uncertainty of 0.5%.

The accuracy of the orthogonal velocity components in the compressor coordinate system depends upon the measurement accuracy of the transformation angles required. The transformed in-plane measurements were found to have an accuracy of 2% and the accuracy of the axial velocity is about 3% of impeller rim speed. Up to this point only the maximum relative error of the unbiased single 2D coincident measurements has been estimated. Time-averaged LDV velocity bias of the in-plane velocity components is estimated to be less than 4%, of the axial component less than 2%. This results in a maximum mean and rms velocity error of less than 7% for each of the three components.

RESULTS AND DISCUSSION

The time averaged velocity vector plots of the LDV and the CFD predictions are shown and compared in figures 11 and 12. All velocity vector plots have the same common scale permitting direct comparisons. Vectors shown are transformed into the planes of the

measurement cross sections and do not comprise the normal-to-plane component which is in the order of 200 m/s .

Best-Point

In Fig. 11 the LDV measurement results at best-point are shown for the semi-vaneless space cross section and the throat cross section.

The velocity vector field of the diffuser throat measurements (Fig. 11(b)) clearly reveals the existence of a single large streamwise secondary flow vortex centered near the pressure side/casing corner. At the suction side the velocities have only very small transverse (horizontal) velocity components, and the axial flow is directed from the hub to the casing side. At the lower left corner very low velocities have been measured. (The high, mostly horizontal velocities at the pressure side of the vanes seen in Fig. 11(b) are a result of the inclination (non-perpendicularity) of the measuring cross section to the vane surface at the circular nose contour (see Fig. 8)).

The vector plots of the semi vaneless space cross section (Fig. 11(a)) reveals the initial development of the vortex. Due to the missing pressure side 'guide' vane the vortex is not fully closed. The predominant feature is the existence of a suction-to-pressure-side shear flow near the casing caused by the structure of the impeller exit flow as explored by Roduner et al. (1998). As soon as the right hand side vane traps the flow, there necessarily develops a closed vortex instantaneously. The velocity vectors heading near the suction side have, like the ones in the throat, little transverse component and are oriented from hub to casing.

In Fig. 11(d) and 11(c) the corresponding vector plots of the CFD calculations are shown. Comparing the measured and calculated throat vector plots (Fig. 11(b) and 11(d)) a high degree of similarity of the large scale secondary flow structures is obvious. The CFD calculations predict a single large vortex shifted to the casing pressure side corner as measured by LDV. An overall good agreement of the transverse velocities is seen, whereas the low axial flow velocities in the core region are calculated too low. This is in line with the inlet boundary conditions used for the CFD calculations. These assumed zero axial component and no circumferential variation of the impeller exit flow. Thus all axial components of the CFD calculations must be developed from zero level at the inlet circle (105% radius).

The LDV-CFD vector field comparison of the global flow structures in the semi vaneless space cross section, (Fig. 11(a) and 11(c)), reveals good agreement too. Both show the u-turned flow at mid right. The CFD predicted horse shoe vortex at the suction side hub corner was not measurable with the LDV. Due to the 2D CFD boundary conditions with zero axial component mentioned above, the calculated axial velocities are significantly lower than the measured ones.

Near Surge

For this operating point the measurements show in the throat cross section clear secondary flow (Fig. 12(b)), but in contrast to the higher flow rate at best point, no distinct flow vortex is seen to be developed. The lower left side horse shoe vortex at the vane suction side is indicated by the velocities heading for the pressure side. On the casing, very near to the suction side, a local stagnation point is formed which deflects part of the flow into the upper left suction side corner. This is best seen in Fig. 12(b). Due to the flat diffuser inflow angles at near surge, acceleration effects around the nose are not as significant as at best point, compare Fig. 11(b) and 12(b) near the pressure side.

Also at near surge operating point CFD (Fig. 12(d)) predicts in comparison to the measurements pretty well the secondary flow structure of the throat cross section. Whereas the LDV does not show any closed vortex, a tiny one is predicted by the calculations at the lower left side. The horseshoe vortex is visible. The stagnation point seen in the LDV measurements is also reflected by the CFD calculations, but it is a very small region close to the upper left corner, which is not resolved in the presented CFD vector plots. The differences concerning the axial velocity component are mainly due to the unrealistic CFD boundary condition used.

The near-surge comparison of measurements and calculations in the semi vaneless space (Fig. 12(a) and 12(c)) cross section show good agreement for the suction side vertical flow from hub to casing. This flow turns to the right and is parallel to the casing wall. Differences are obvious for the lower right section. The measurements reveal almost vertical flow towards the casing whereas the CFD calculations predict almost horizontal flow oriented to the right. It will merit to be checked how far the missing axial velocity component of the CFD boundary conditions influences this calculated result.

Unsteady Effects

Time resolved (impeller position dependent) vector flowfields of the LDV measurements, not presented here, have shown that the secondary flow vortex structure at best-point in the throat is virtually stationary. The time resolved streamwise velocity component overlaid on the vector field shows the influence of the unsteady (already highly damped out) jet/wake flow.

CONCLUSIONS

- LDV measurements in a small width ($\leq 20\text{mm}$) high-subsonic centrifugal compressor were shown to be possible if some crucial improvements to the rig and the LDV set-up are made. These comprise:
 1. Black absorption filter glass in conjunction with off-axis scattered light reception.
 2. Special probe holders for accurate laser

measurement volume alignment.

3. Closed loop facility and high production rate particle generator.

- Secondary flow produces a single large stream-wise channel vortex in the throat at best point.
- The global large flow structures (i.e. single channel vortex, horse shoe vortex, stagnation point) of the LDV measurements are well reflected in the CFD calculations. This is the case for both, best-point and near-surge operating point.
- The CFD predicted axial velocities are lower than those measured, which is a consequence of setting zero axial velocity component in the velocity inlet boundary conditions.
- Time resolved data analysis of the throat vector field at best point reveals that the vortex structure is virtually stationary.

ACKNOWLEDGEMENTS

The acquisition of the 3D LDV system was granted by the ETH research fund. The radial compressor research project is funded by the Swiss Commission for the Promotion of Applied Research (KTI) together with ABB Turbo Systems and Sulzer Turbo.

REFERENCES

- Abramian, M. and Howard, J. H. G., 1994a, "A Rotating Laser-Doppler Anemometry System for Unsteady Relative Flow Measurements in Model Centrifugal Impeller", *ASME Journal of Turbomachinery*, 116 pages 260-268.
- Abramian, M. and Howard, J. H. G., 1994b, "Experimental Investigation of the Steady and Unsteady Relative Flow in a Model Centrifugal Impeller Passage", *ASME Journal of Turbomachinery*, 116 pages 269-279.
- Ahmed, N. A. and Elder, R. L., 1990, "Flow Investigation in a Small High Speed Impeller Passage using Laser Anemometry", *ASME Paper 90-GT-233*.
- Boutier, A., 1993, "Accuracy of Laser Velocimetry Measurements", *VKI Lecture Series*, Brussels.
- Casartelli, E., Saxer, A. P., and Gyarmathy, G., 1997, "Numerical Flow Analysis in a Subsonic Vaned Radial Diffuser with Leading Edge Redesign", *ASME 97-GT-185*.
- Casartelli, E., Saxer, A. P., and Gyarmathy, G., 1998, "Performance Analysis in a Subsonic Radial Compressor", *ASME Paper 98-GT-153*.
- Chriss, R. M., Hathaway, M. D., and Wood, J. R., 1994, "Experimental and Computational Results From the NASA Lewis Low-Speed Centrifugal Impeller at Design and Part Flow Conditions", *ASME Paper 94-GT-213*.
- Durst, F., Melling, A., and Whitelaw, J. H., 1987, "Theorie und Praxis der Laser-Doppler-Anemometrie", G. Braun.

- Eckhardt, D., 1975, "Instantaneous Measurements in the Jet-Wake Discharge Flow of a Centrifugal Compressor Impeller", ASME Journal of Engineering for Power, pp. 337-346.
- Eckhardt, D., 1976, "Detailed Flow Investigations within a High-Speed Centrifugal Compressor Impeller", ASME Paper 76-FE-13.
- Fagan, J. R. and Fleeter, S., 1991, "Impeller Flow Field Measurement and Analysis", ASME Journal of Turbomachinery, 113 pages 670-679.
- File, G., Gyarmathy, G., and Staubli, T., 1997, "Water Model of a Single-Stage Centrifugal Compressor for studying Rotating Stall", in *2nd European Conference on Turbomachinery-Fluid Dynamics and Thermodynamics, Antwerpen*, edited by G. Dibelius and R. Decuyper, pp. 317-327.
- Gyarmathy, G., 1996, "Impeller-Diffuser Momentum Exchange During Rotating Stall", ASME Paper 96-WA/PID-6.
- Hathaway, M. D., Chriss, R. M., Wood, J. R., and Strazisar, A. J., 1993, "Experimental and Computational Investigation of the NASA Low-Speed Centrifugal Compressor", ASME Journal of Turbomachinery, 115 pages 527-542.
- Hathaway, M. D., Wood, J. R., and Wasserbauer, C. A., 1992, "NASA Low Speed Centrifugal Compressor for Three-Dimensional Viscous Code Assessment and Fundamental Flow Physics Research", ASME Journal of Turbomachinery, 114 pages 295-303.
- Hunziker, R., 1993, "Einfluss der Diffusorgeometrie auf die Instabilitätsgrenze des Radialverdichters", Ph.D. thesis, ETH Zürich, Switzerland.
- Hunziker, R. and Gyarmathy, G., 1993, "The Operational Stability of a Centrifugal Compressor and its Dependence on the Characteristics of the Subcomponents", ASME Paper 93-GT-284.
- Krain, H., 1981, "A Study on Centrifugal Impeller and Diffuser Flow", ASME Journal of Engineering for Power, pp. 688-697.
- Roduner, C., Köppel, P., Kupferschmied, P., and Gyarmathy, G., 1998, "Comparison of Measured Integral Averages at the Impeller Exit of a Centrifugal Compressor Measured with both Pneumatic and Fast Response Probes", ASME Paper 98-GT-241.
- Ruck, B., 1987, "Laser-Doppler-Anemometrie", AT-Fachverlag, Stuttgart.
- Runstadler, P. W. and Dolan, F. X., 1975, "Design, Development, and Test of a Laser Velocimeter for High Speed Turbomachinery", in *The accuracy of Flow Measurements by Laser-Doppler Methods*, edited by P. Buchhave, pp. 523-552, Proceedings of the LDA-Symposium Copenhagen.
- Stahlecker, D., Csikos, G., and Gyarmathy, G., 1997, "An evaluation strategy of laser doppler velocimetry systems for high subsonic radial compressors.", Proceedings of the 7th International Conference of Laser Anemometry Advances and Applications, pp. 289-298.
- Strazisar, A. J., 1993, "Laser Anemometer Applications in Turbomachinery", in *2. International Symposium on Experimental and Computational Aerothermodynamics of Internal Flows*, edited by R. Dvořák and Kvapilová, volume 1, pp. 77-99, Institute of Thermomechanics, Academy of Sciences, Prague.
- Ubaldi, M., Zunino, P., Barigozzi, G., and Ghiglione, A., 1996, "LDV Investigation of the Rotor-Stator Aerodynamic Interaction in a Centrifugal Turbomachine", 8th International Symposium on Applications of Laser Techniques to Fluid Mechanics, Lisbon, pp. 28.3.1-28.3.8.

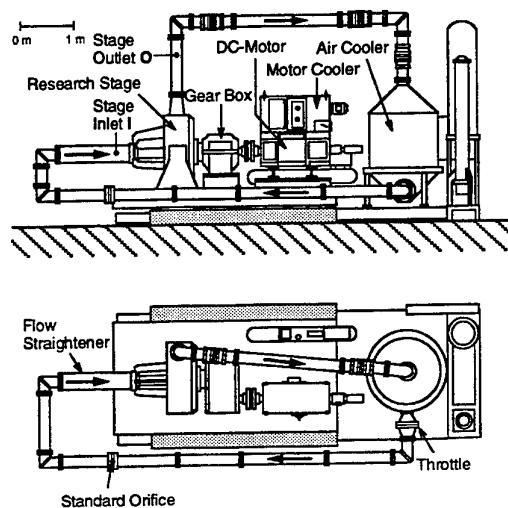


Figure 1: General sketch of the centrifugal compressor test rig.

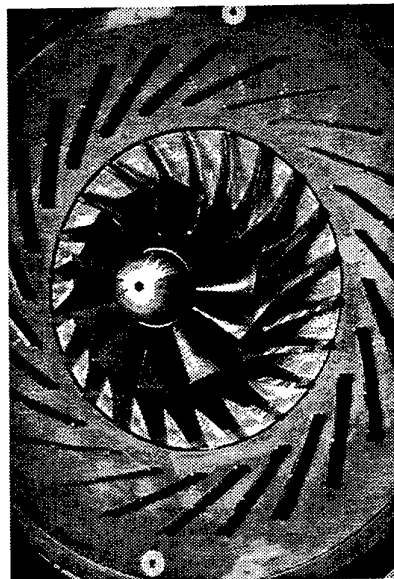


Figure 2: View towards the unshrouded impeller and diffuser (Configuration: 24 vanes, 25° stagger angle).

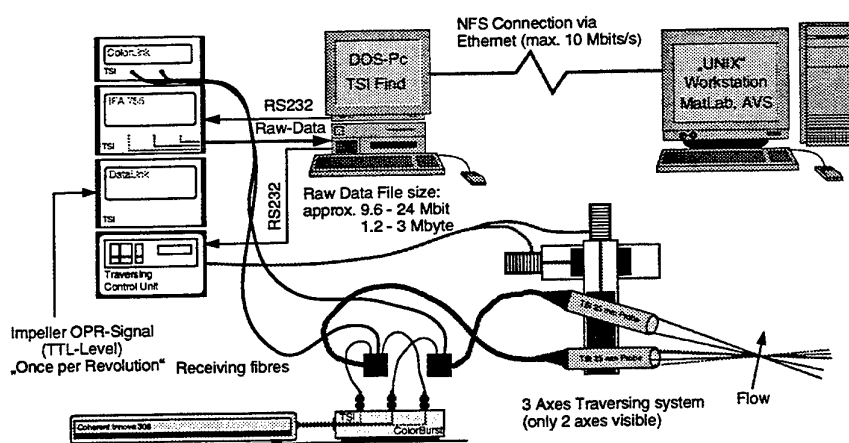


Figure 3: LDV System Setup.

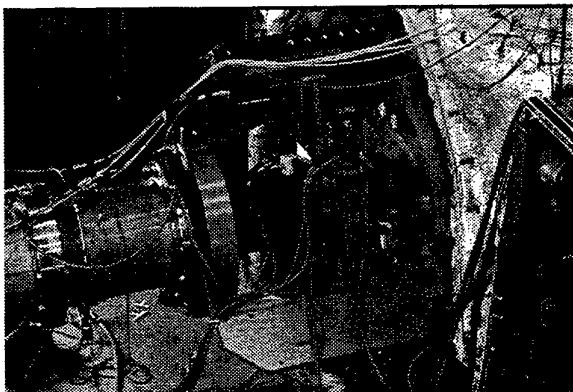


Figure 4: Test compressor with LDV setup. Optical probe traverse mechanism at center, diffuser window access at mid right.

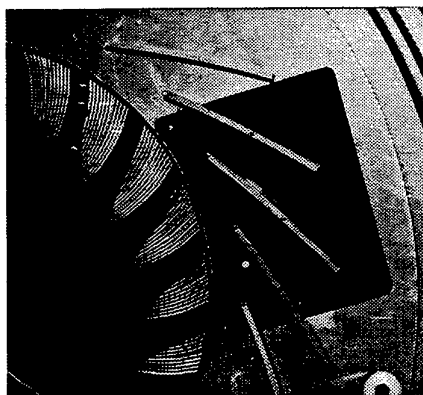
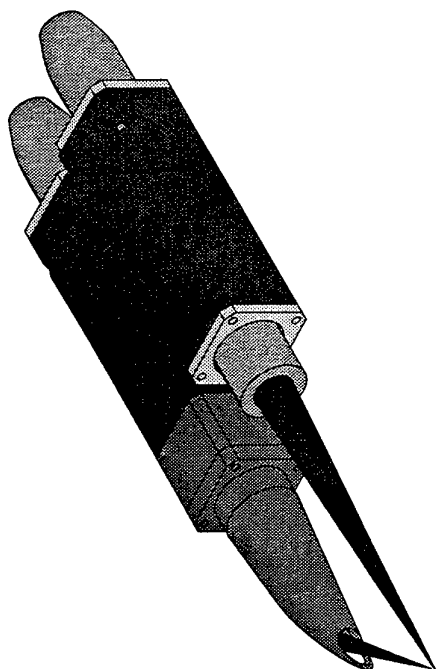
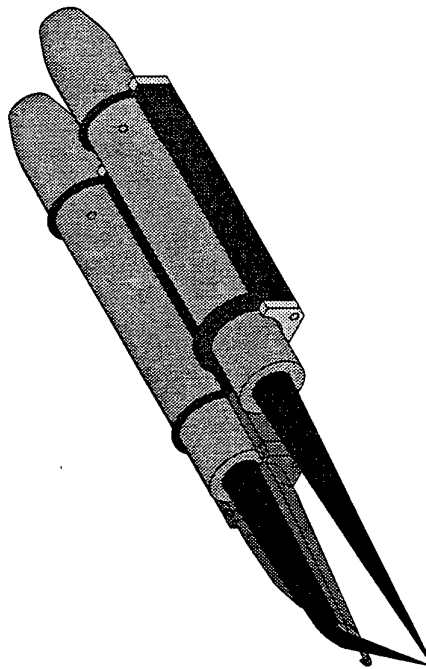


Figure 5: Part of impeller with black absorption filter glass in the diffuser rear wall.



(a) Probe holders with probes and light path.



(b) Uncovered view with three O-rings and flat rubber ring for probe alignment.

Figure 6: New developed special probe holders.

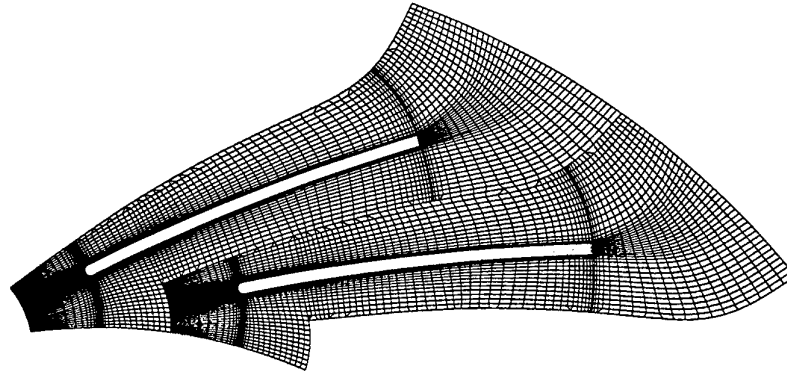


Figure 7: Computational grid with block structured H-type mesh consisting of 102138 active nodes.

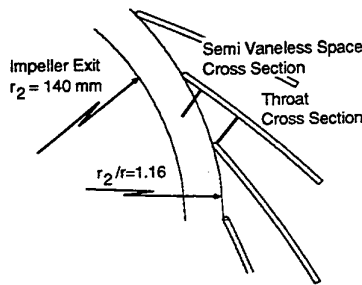


Figure 8: LDV measurement traverses in the semi vaneless space and in the diffuser throat.

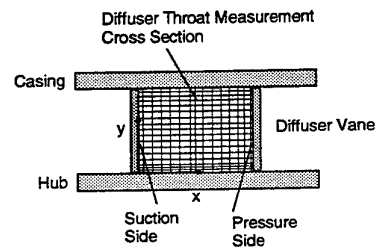


Figure 9: LDV measurement grid of throat cross section consisting of 17x14 unevenly spaced locations.

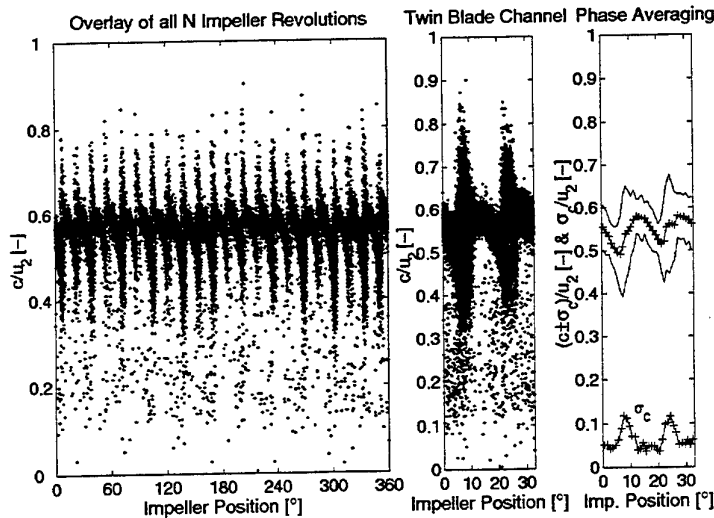
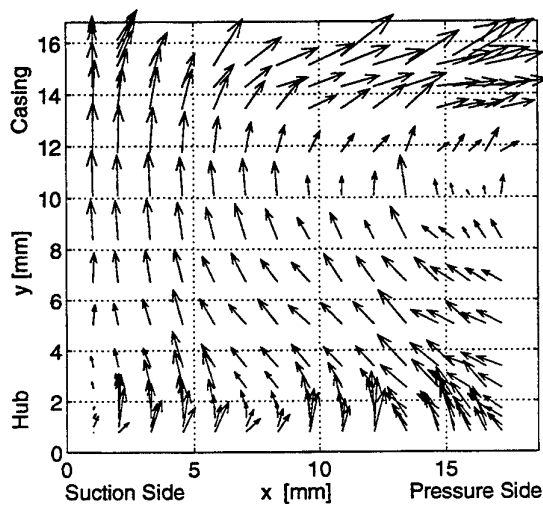
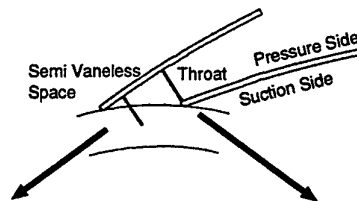
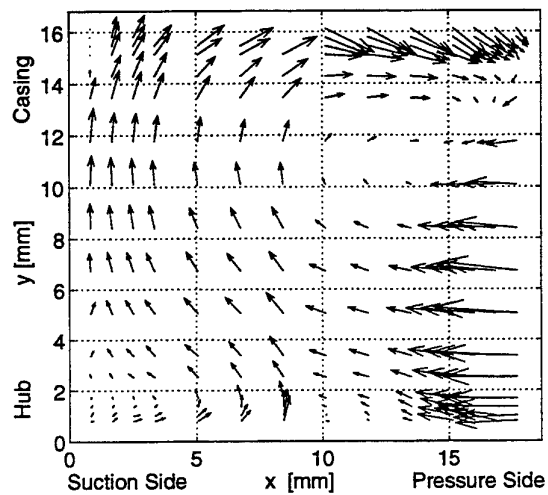


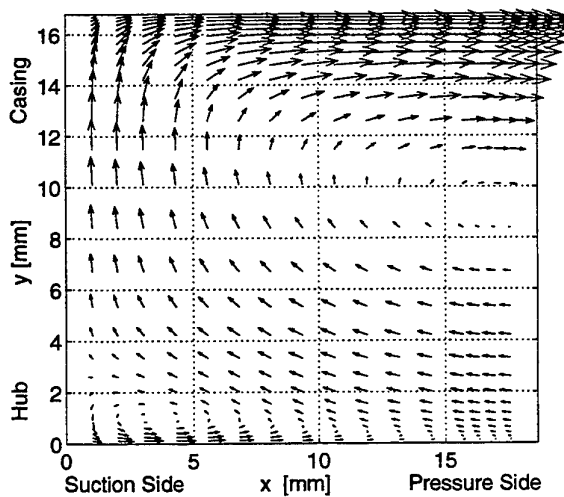
Figure 10: Phase averaging procedure. Left: Data overlay of all N (≈ 6000 -24000) impeller revolutions. Middle: Reduction to one "Twin Blade Channel" (one splitter and one full blade). Right: Calculated 33 phase averaged mean and standard deviation values (1° classes assumed). Sample: streamwise velocity c_s at 105% radius, $y/b=0.2$, $M_u = 0.75$, Best Point.



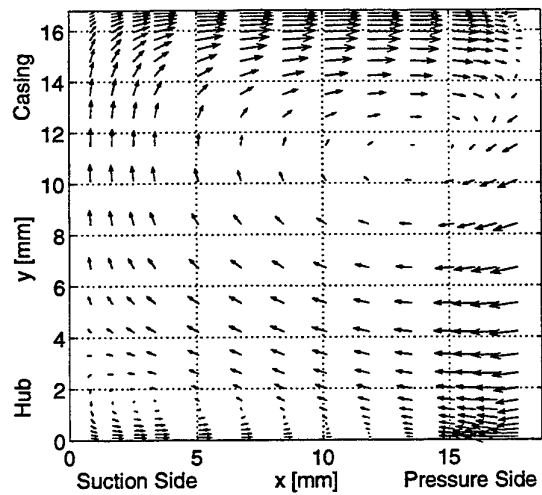
(a) LDA, Semi vaneless space cross section.



(b) LDA, Throat cross section.



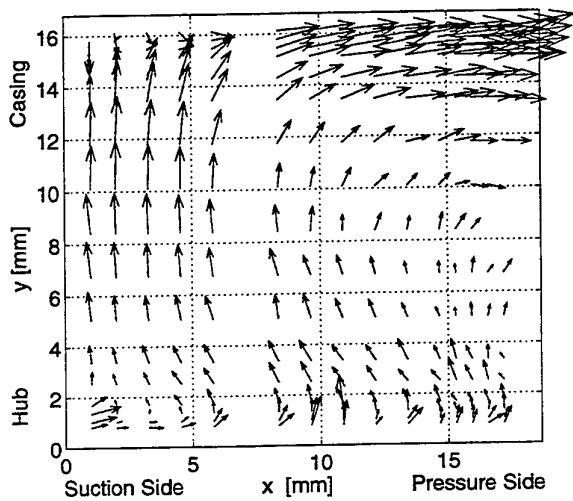
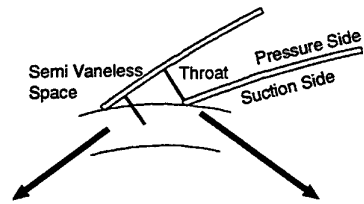
(c) CFD, Semi vaneless space cross section.



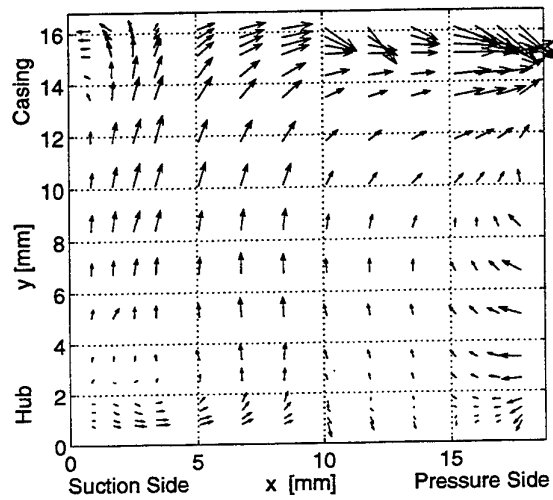
(d) CFD, Throat cross section.

→ : 50 m/s

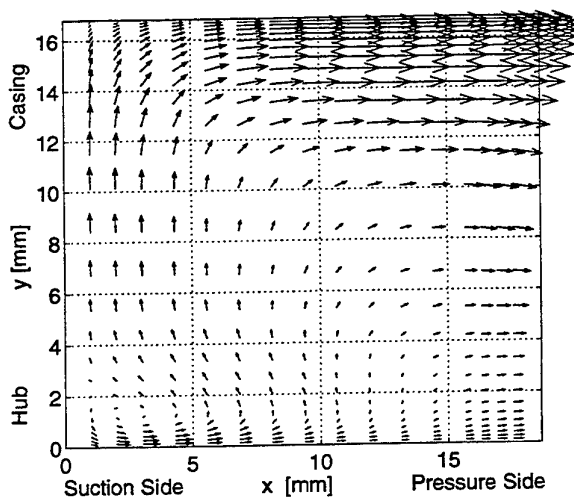
Figure 11: Best-point secondary flow vectors at the semi-vaneless space (left) and at the throat (right); LDV at top, CFD at bottom.



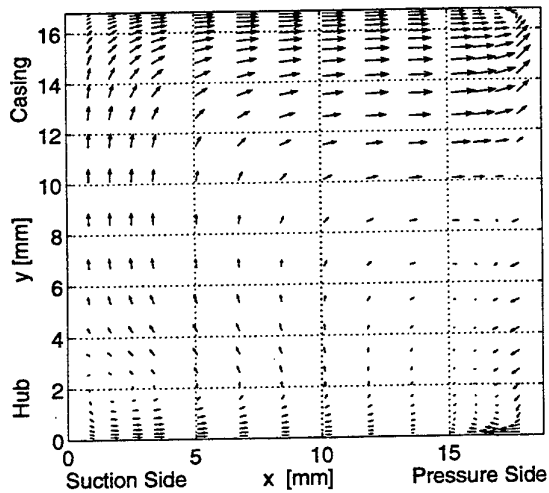
(a) LDA, Semi vaneless space cross section.



(b) LDA, Throat cross section.



(c) CFD, Semi vaneless space cross section.



(d) CFD, Throat cross section.

→ : 50 m/s

Figure 12: Near-surge secondary flow vectors at the semi-vaneless space (left) and at the throat (right); LDV at top, CFD at bottom.

VELOCITY MEASUREMENT DOWNSTREAM AN AXIAL BLADE WHEEL USING LDV-PIV

L. Girardot*, F. Lanzetta**, J.P. Prenel**, J. Stefanini***, R. Menon***

(*) Centre de Recherches des Turbines à Vapeur, GEC-Alsthom, Belfort, France

(**) Institut de Génie Energétique, Belfort, France

(***) TSI Incorporated, St Paul, MN, USA

ABSTRACT

This paper describes the experimental study of the flow downstream an axial blade wheel using non-intrusive measurement techniques. First a Laser Doppler Velocimeter synchronized on the wheel angular position provides temporal representations of the velocity in the blade-to-blade plane. Second a Particle Image Velocimeter is used to give a complementary approach of the flow in the same plane. PIV will allow in one hand to achieve velocity vector field obtained downstream the blade wheel and between the blades on the other hand (blade-to-blade spacing).

1. INTRODUCTION

Due to computer, numerical study is become now the first research and development tool used in all physical domain like turbomachinery. However experimental data are necessary to validate the different numerical models and to verify reached performances by designed machine. In industrial world, the Steam Turbine Research Center (C.R.T.V.) of G.E.C.-Alsthom Company is responsible for the study of different flows and for the determination of element turbine performances.

The efficiency of a steam turbine for electricity production is determined by the performance of each blade wheel that sets the different stages of the turbine. Turbine manufacturers generally use pressure probes (like 3 or 5 holes clinometric probe) to measure the pressure and velocity distribution downstream a blade row. However, the uses of intrusive measurement techniques in turbulent flow generate bias, which are difficult to estimate. More, the use of these measurement techniques, like for example hot wire is physically impossible, due to the fragility of the sensor.

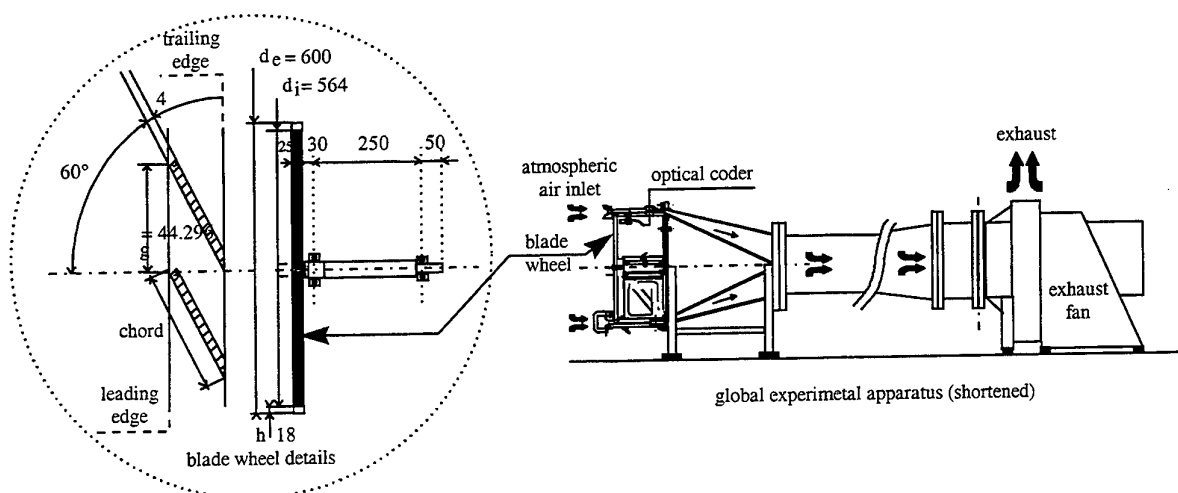
Worried about result accuracy, the industrial center wished to confront these measurement techniques with LDV and PIV through a typical test rig.

The aim of the global study (Girardot 1997) is to determine the velocity distributions and profiles as a function of the wheel angular position in order to obtain a good comprehension of this complex flow, which will allow the confrontation with other industrial measurement systems.

In this work, the flow downstream a blade wheel was examined by using a 2D Laser Doppler Velocimeter. More, Particle Image Velocimetry measurements were done in order to achieve complex flow structures. However in this paper we will present only a part of the many results obtained with the two optical techniques (LDV and PIV).

2. EXPERIMENTAL SETUP

In order to compare and evaluate different measurement techniques, the test rig doesn't need to be necessary sophisticated but must especially respect several characteristics (compressibility, blade frequency, and blade wake...). The global experimental apparatus as shown in Figure 1 was setup to achieve velocity that is similar to flow behavior found in turbomachinery application. The axial mean velocity is about 85 m/s (compressibility limit) and the instantaneous flow is composed of a wake part and a healthy part. The designed rotor consists of 40 blades with a tip diameter of 600 mm, a height of 18 mm and a hornline angle of 60°. So the pitch between two successive blades correspond to 9° of azimuth (blade-to-blade spacing). More, blades have plane constant section with blunt leading edge and sharpened trailing edge.



The wheel is fixed on a dead shaft running freely into two ball bearings. An exhaust fan draws up the air, which means the rotation of the free running axial wheel until a rotation speed of 4,800 RPM. Thus, the blade passage frequency is 3.2 kHz.

3. LASER DOPPLER VELOCIMETRY

3.1 Experimental Setup

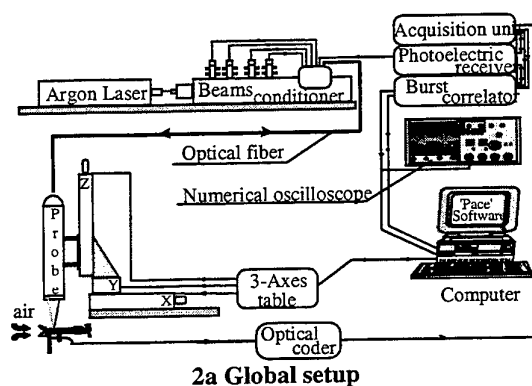
The LDV system as shown in Figure 2a consists of T.S.I two-dimensional Argon based system. The optical probe (transmitting and receiving optics) is mounted on automatic 3 axes traverse system. The optical axis is vertical and proceeds by the upper generative test rig casing as shown in Figure 2b and the fringe networks are positioned at 45° from the axial direction in order to balance the signals. Thus the two measured velocity components are in the blade-to-blade plane (the axial and the tangential components of velocity).

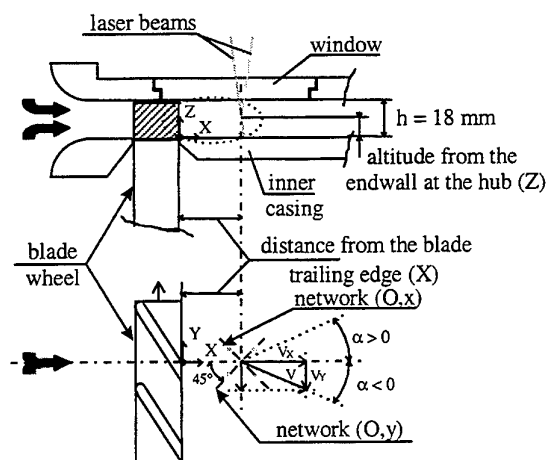
The optical configuration used allows achieving 90 μm diameter and 1.3 mm length measuring volume.

The beams pass through a 2 mm thickness flat window. Due to the small facility test size (reflection), it was impossible to realize any measurements under 3.6 mm from the endwall at the hub and very difficult to obtain some of them at this altitude (radial direction). So the valid results begin at the altitude of 5.4 mm. The flow has been

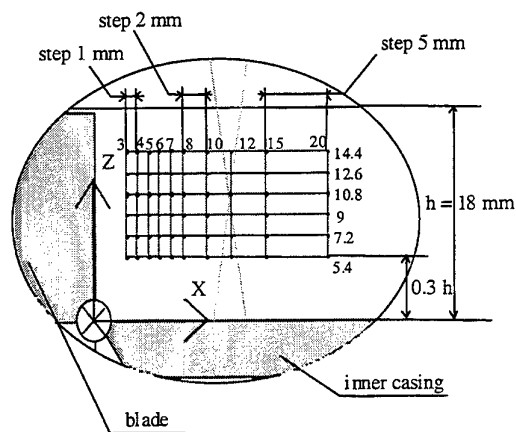
investigated at a distance of 3 mm from the blade trailing edge and at steps of 1mm, 2 mm and 5 mm (axial direction).

Doppler signal is processed by a digital burst correlator (IFA 755), associated to a rotating machinery resolver (RMR). Associated to an optical coder (one pulse / wheel revolution), RMR allows to phase average the data according to the wheel angular position with a resolution of 3600 bins / revolution (0.1°) ; thus each validated particle (coincidence mode) is tagged by the instantaneous blade wheel position. Using an adapted windows based program (PACE) data will be classified for each blade pitch into 30 bins. This configuration will give us a 0.3° resolution.





2 b Coordinate system and laser beams



2 c Flow map

Figure 2 Laser Doppler velocimetry

In order to build a flow map as shown in Figure 2c a radial investigation was done by 1.8 mm steps (so 10 % of height) from the altitude of 5.4 mm.

3.2 Seeding

Seeding ability to accurately follow the flow and to give a representative glittering depends on the dimension and the density of the particles. A smoke/aerosol generator using Shell Ondina oil and nitrogen have been selected to produce the aerosol. The smoke obtained by thermodynamic phase change is a harmless mixture of a pure cosmetic oil and nitrogen (inert gas). The nitrogen passes through an atomizing head and entrains the oil in the gas flow in

order to produce a correct mixture. Then the aerosol enter in a heat exchanger where oil is vaporized to produce particles which the sizes are about $0.3 \mu\text{m}$. This smoke is introduced in the test section farther as possible upstream the blade wheel throughout an inox capilar vertically positioned. The location of the injection point is optimizing for each point investigated in the flow map.

3.3 Results and Discussion

Periodicity. The first step of our study was to investigate the flow periodicity in order to allow data acquisition on the complete revolution and by the same time reducing the acquisition time. Figure 3 shows the velocity distribution (half revolution) as function of the angular position of the wheel at one position in the test rig. We can see from this diagram that the flow is quite reproductive from one blade to the next. We can affirm that this work hypothesis is verified for all positions. By acquiring data on the complete cycle the acquisition time was reduced and phase averaged data between successive blade pitches (and not investigated only for one particular pitch) was done (9° azimuth result from the full revolution).

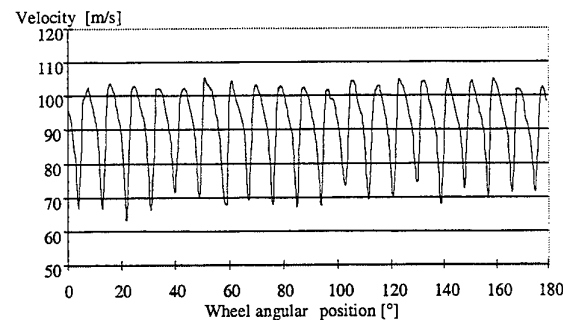


Figure 2 Velocity distribution on the half-cycle

One of the main problems in rotating machinery flow is to control the seeding in order to have one homogenous distribution of particle between each blade and especially in the blade wake. In order to have a good estimation of the mean flow velocity; we collected 30,000 particles for each position in the test rig, which corresponds in the wake part of the flow to a minimum of 250 particles per bin.

Axial evolution. At the altitude of 9 mm from the endwall at the hub Figure 4 and 5 show respectively the global axial evolution of the velocity and angle distribution as the function of the wheel angular position (phase averaged on one blade pitch).

It can be seen from these curves that the wake position is shifted with the axial evolution and moreover that the amplitude of this wake decreases by a factor of 2 when we go away of 20 mm from 5 mm but this reduction is associated to a wake expansion. More, the analysis of the angle distribution shows that this wake is shifted on the opposite way of the wheel rotation because the mean flow angle has a negative value.

Figure 6 corresponds to the mean velocities field obtained at the same altitude $Z = 9$ mm (vectorial representation figures 4 and 5).

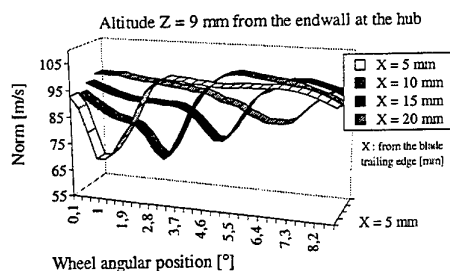


Figure 4 Velocity distribution in a blade-to-blade plane

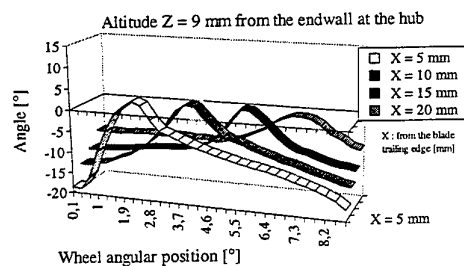


Figure 5 Angle distribution in a blade to blade plane

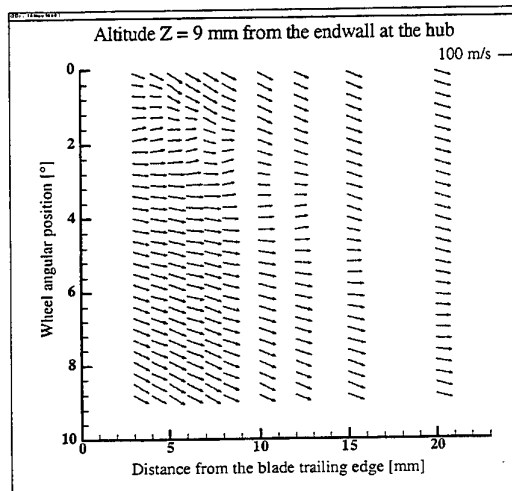


Figure 6 Mean velocities field

Radial evolution. Figures 7 and 8 represent the velocity and angle distribution as a function of the wheel angular position for a fixed blade trailing edge distance ($X = 5$ mm) and for different altitudes (Z).

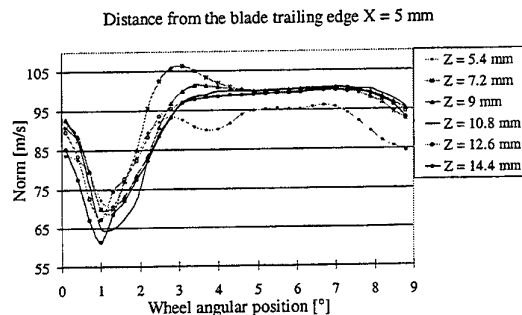


Figure 7 Radial velocity distribution at $X = 5$ mm

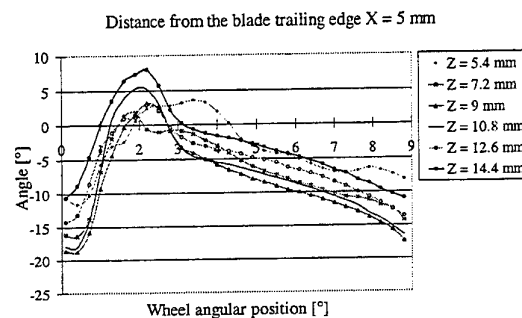


Figure 8 Radial angle distribution at $X = 5$ mm

We can see from these curves that there is a strong velocity gradient near the hub casing ($Z = 5.4$ and 7.2 mm). For altitudes higher than $Z = 7.2$ mm we can see that the velocity distribution is more homogeneous with a slight shift of the wake center position. In fact the flow can be divided into two separate areas, one with a high velocity gradient close to the hub casing and a second one with a quasi-constant velocity.

4. PARTICLE IMAGE VELOCIMETRY

4.1 Experimental Setup

The Particle Image Velocimetry (Figure 9) system is based upon a TSI PowerView system, including 25 mJ dual mini Yag laser (continuum), high resolution cross correlation camera (1K x 1K resolution), synchronizer and "Insight" windows NT based software for acquisition, processing and post processing. As for LDV measurement, PIV

acquisition was phase lock with a TTL external trigger in order to phase average data.

Due to the windows size (15 mm which corresponds to 3°), it was impossible to capture a complete blade pitch. Thus to reconstruct the blade-to-blade flow field, we did 3 separate image sequences each of them shifted of $100 \mu\text{s}$ (3° rotation).

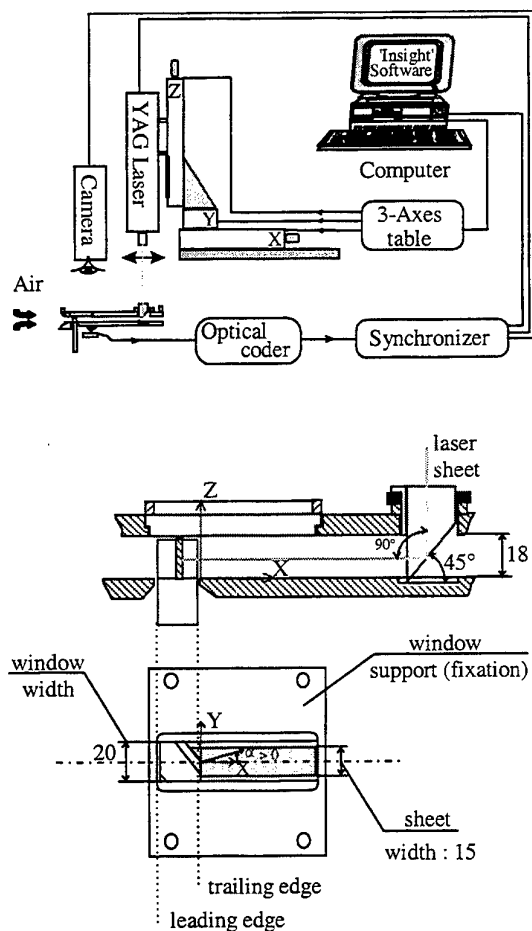


Figure 9 Particle Image Velocimetry

The light sheet is created through cylindrical and spherical lenses and introduces into the test section with a prism mounted in flow downstream the test section. Because of the size of the measuring plane and to avoid blade reflection, the energy used was about 40 % of the full scale, so 10 mJ/pulse.

4.2 Flow Seeding and Data Processing

Like in LDV, seeding is the most critical point for PIV measurement in turbomachinery (Wernet 1997). More, in opposition to LDV, a uniform and

high concentration seeding is necessary for PIV measurement. In our case, we decided to use $1\text{--}2 \mu\text{m}$ water droplet to perform this experiment.

Because of the velocity (100 m/s) and the measuring plane size ($20 \times 20 \text{ mm}$), it was important to achieve a small time between pulses to keep a good spatial resolution. We used a $2 \mu\text{s}$ pulse delay associated to a 32×32 pixels ($1.5 \times 1.5 \text{ mm}$) of resolution with 50% of overlap and a cross correlation technique. We can see from this point that our PIV spatial resolution is 10 times higher than the LDV one.

4.3 PIV Results

Figures 10, 11 and 12 show the PIV results obtained downstream the wheel (wake area) and into the blade-to-blade space.

Figure 10 is a direct comparison with LDV data including stream traces (mean velocities field as function of wheel angular position). We can see from this figure that the velocities field is very similar to those obtained by using Laser Doppler Velocimetry technique (wake position and velocity amplitude). However, we can see that flow angle (wake area) seems to be higher on the PIV velocities field. This can be due to the fact that the response of the particles used for PIV measurement are bigger than the seeding used in LDV or to the fact that the camera was not exactly parallel to the main direction of the flow (angular error).

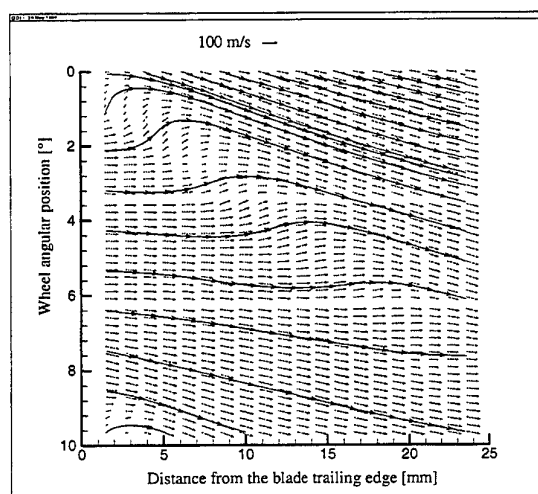


Figure 10 Mean velocities field

Figure 11 shows the mean velocities field obtained into the wake part of the flow, associated to the iso velocity gradients (du/dx). As we can expect, we can see a high velocity gradient upstream and downstream the wake position (wake crossing). More, we can see from this curve that the velocity gradients are symmetrical to the wake center.

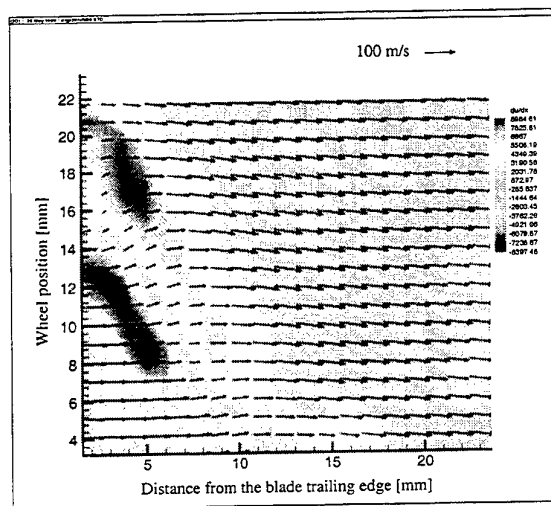


Figure 11 Mean velocities field (wake area)

Figure 12 shows the mean velocities field obtained into the blade to blade spacing. These measurements have been performed in order to control the flow distribution between blades. The velocities field is not display in a fixed reference but in a mobile coordinates system (wheel reference). To perform that, we subtracted to the mean velocities field the wheel velocity (148 m/s). We can see from this figure that the flow is well parallel to the blades.

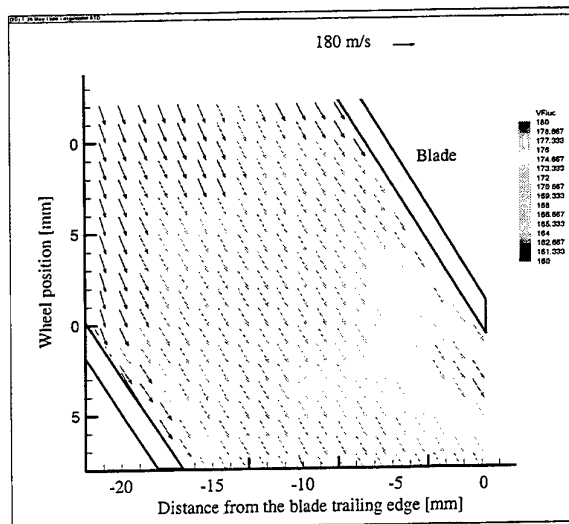


Figure 12 Mean velocities field (inter blades area)

5. CONCLUSION

This work demonstrated the ability of LDV and PIV to investigate an enclosed flow downstream a blade wheel. The knowledge of this complex flow will allow calibrating the industrial probes in order to optimize the efficiency of such turbomachinery by a methodical study of the different stages of a turbine and principally the wake evolution for different blades configuration. More the use of PIV allows investigating unsteady structures that have direct influence on the turbomachinery efficiency.

ACKNOWLEDGEMENTS

This work has been supported by the Steam Turbine Research Center of the G.E.C. - Alstom Company.

REFERENCES

- Girardot, L. 1997, Pressure and Velocity Aerodynamic Measurements Downstream a Blade Wheel, Ph. D. thesis, University of Franche-Comte, France.
- Wernet, M.P., 1997, PIV for Turbomachinery Applications, Conference on Proceedings on Optical technology in Fluid Thermal and Combustion Flow III, SPIE vol. 3172, San Diego, USA

SESSION 37

ENGINES II

PIV MEASUREMENTS DURING COMBUSTION IN A RECIPROCATING INTERNAL COMBUSTION ENGINE

David L. Reuss and Martin E. Rosalik

Engine Research Department
General Motors Global R&D Operations, Warren, MI, USA

Abstract

Two-dimensional particle image velocimetry (PIV) measurements were made in the burned and unburned gas of a firing, reciprocating internal-combustion engine. Cross correlation was used to analyze the double-exposure photographs using a 1.25 mm interrogation spot on a 0.5 mm grid. Electro-optical image shifting was used to resolve the directional ambiguity. The particle properties and the seeding density are the two key features enabling simultaneous measurements in the burned- and unburned-gas regions. The flame coordinates were identified as the interface between the low and high seeding density regions on the PIV photographs. Those coordinates were used to identify the burned and unburned regions of the velocity distributions. High-pass spatial filtering is used to visualize coherent structures of spatial scales L , where $1.25 \text{ mm} < L < 10 \text{ mm}$. Vorticity and strain-rate distributions are computed from the instantaneous velocity. PDFs of these distributions were computed, conditionally sampled on the burned gas, unburned gas and proximity to the flame front. For this paper, analysis of only one realization is presented in detail in order to maintain a manageable number of illustrations yet demonstrate flow properties observed in fifteen recorded realizations.

The high-pass filtering reveals coherent flow structures that appear to correlate with the flame wrinkling, but are otherwise not apparent in the instantaneous velocity distributions. The vorticity in the burned gas regions appears higher than that in the unburned gas regions. The normal strain-rates appear to be large and predominately positive adjacent to the flame and in the burned gas. The shear strain-rate distributions show no obvious variations ahead, behind, or adjacent to the flame. These observations

were apparent both by inspection of the plotted distributions and in the conditionally sampled PDFs.

1. INTRODUCTION

The turbulent flow in reciprocating internal combustion (RIC) engines controls fuel mixing, residual mixing, heat-transfer, and the rate of combustion; consequently, it is a major factor in the engine's efficiency and emissions. Most knowledge of the in-cylinder turbulence has been acquired through single-point time-resolved measurements of motored or precombustion gases using either hot-wire anemometry (HWA) or laser-Doppler anemometry (LDA), Rask (1984), Arcoumanis and Whitelaw (1987) and Valentino et al (1997). These measurements provide the ensemble mean velocity (U) fluctuating velocity (u_i') Reynolds stresses, spatial-correlations, and temporal correlations. Turbulence characterization using these parameters is consistent with current computational fluid dynamics (CFD) codes that solve the time-averaged turbulent flow equations for in-cylinder flow. Few measurements of in-cylinder turbulence have been made in the burned gas regions. This is because HWA measurements are not feasible and LDA measurements in fired engines are even more difficult than in motored engines. Notwithstanding, LDA measurements in research engines have shown that there is little change in the burned-gas turbulence fluctuations between 600 and 1200 RPM, Foster and Witze (1988), but is substantially changed between 1500 and 2000 RPM, Lorenz and Prescher (1990).

One of the most important effects of turbulence is its effect on combustion. Advanced models of turbulent, premixed combustion include local flame-surface generation, local burning rates, and local extinction. Laboratory experiments, Mueller et al.

(1996, 1998), and flame models, Candel and Poinso (1990), have demonstrated that these phenomena are dependent on the local fluid strain; further, baroclinic torque in the flame attenuates small eddies and generates new vorticity in the burned gas that counters the incident vorticity. One consequence of the advances in flame modeling is that the turbulence fluctuation about the mean, u' , is a poor metric for characterizing the turbulence. Whereas u' provides only a random sampling of the coherent velocity structures (cf. Hussain (1986)), strain rate (e_{ij}) and vorticity (w_i) are direct measures of the fluid deformation caused by the coherent structures. Further, e_{ij} and w_i are the fluid properties that control the flame's response to the fluid. Particle Image Velocimetry, PIV, provides the ability to measure the 2-D, instantaneous velocity, out of plane vorticity (w_z) and in-plane strain rates (e_{11} , e_{22} , and e_{12}) over an extended area in a RIC engine. However, PIV measurements in RIC engines have been limited to either motored flow (Reuss et al (1989), Nino et al (1992), Valentino et al (1993), Guibert et al (1993), Sweetland and Reitz (1994) and Reeves et al (1996)) or flow in the unburned gas ahead of the flame (Reuss et al (1990), Nino et al (1993) and Reeves (1995)). The work reported here demonstrates a PIV technique for measuring the velocity, vorticity and strain-rates simultaneously in the burned and unburned gas regions of a firing RIC engine.

The ultimate goal of the work described here is to reveal the physical processes in the flame-flow interaction. With this goal in mind, the engine used in this study was configured to produce a high-swirl in-cylinder flow for three reasons. First, the instantaneous velocity from each realization is well directed and the cyclic variability of the large-scale swirl structure is small; thus, the large-scale flow during each cycle is reasonably repeatable at ignition and any changes in the flow caused by the flame are readily apparent. Second, the flame will pass through a reasonably homogeneous region of turbulence during the early part of the burn. Third, with the well-directed large-scale swirl there is a visually apparent separation between large-scale swirl and the turbulence in the intermediate scales. This property provides a conceptual link between the in-cylinder RIC-engine flow and simple flows traditionally used as starting points for understanding the principles of turbulence.

This paper describes the first step towards the study of flame-flow interaction and has three purposes. One is to describe the technique for making PIV measurements in the burned gas. Because the particle properties and the seeding density are the two key features enabling successful measurements, details

of the seeding technique are provided. A second purpose is to provide a qualitative look at the PIV measurements of turbulence in the unburned and burned gases. A synopsis of the motored flow in this engine is provided as a basis of comparison. Because of the abundance of new information, the scope will be restricted to one realization (i.e. one instant of the combustion event in one cycle). The point of this focus is to demonstrate the new information that can be provided in preparation for a more comprehensive treatment. The third purpose is to demonstrate the use of conditionally sampled probability density functions (PDFs) as a means for quantitative analysis in a subsequent study. In particular, PDFs are used to quantify observations made in the distributions of the vorticity and strain rates.

2. EXPERIMENTAL HARDWARE AND METHODS

Sec. 2.1 provides a brief description of the engine and a synopsis of the motored in-cylinder flow from Reuss et al (1995), which is used for comparison with the fired results in Sec. 3. Details of the particle seeding are discussed in Sec. 2.2. In Sec. 2.3 a brief description of the PIV methodology is repeated from Reuss et al (1989, 1990, 1993), with details added where they are unique to the implementation here. In Section 2.4 the method is described for identifying the flame position on the velocity distributions and for generating the conditionally sampled PDF's.

2.1 The Engine and In-Cylinder Flow

The transparent-combustion-chamber engine used for this study is illustrated in Fig. 1. It is a research, four-stroke-cycle engine with 30 mm intake and exhaust valves (one each), a pancake-shaped combustion chamber and a centrally located spark plug. It has a 92 mm bore, 86 mm stroke, and 12.5 mm clearance at top dead center (TDC), resulting in an 8:1 compression ratio. Optical access to the combustion chamber is provided through a quartz ring, which forms the top 25 mm of the cylinder, and a 70 mm diameter quartz window in the top of the extended piston. More details of the engine are given in Reuss et al (1995). The engine was operated at 1200 rev/min, 40 kPa MAP and fueled with premixed propane at an equivalence ratio of 0.95. Fuel mixing was attained using the method described for seed mixing in Sec. 2.2. The engine was skip fired (five motored cycles and one fired cycle, repetitively) with ignition timing set at 14 ca BTDC (crank-angle degrees before top dead center) compression. Skip firing was employed so that the initial condition for combustion is nearly the same as motored cycles. The

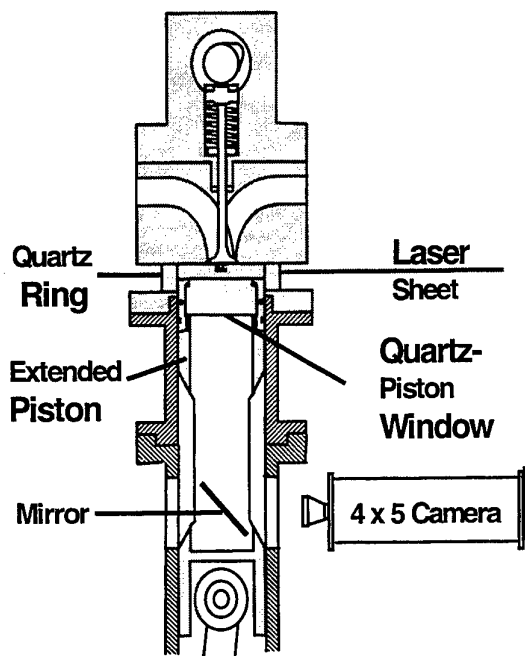


Figure 1 Illustration of the two-valve optical engine, laser sheet, and PIV camera.

PIV photographs were taken 2 BTDC compression, which captured burned and unburned regions of approximately equal areas in the field of view studied

here. MAP and exhaust back pressure were controlled to within ± 1 kPa and engine speed to ± 5 rev/min. The air, cooling water, and oil were controlled to 40 ± 1 C.

To create a repeatable in-cylinder engine flow, an intake valve with a 120 deg shroud was directed tangentially as illustrated in Fig. 2. The resulting high-swirl flow has been measured and computed previously by Kuo and Reuss (1995) and Reuss et al (1995) under motored conditions. Those studies have demonstrated that the largest-scale flow (on the order of the cylinder bore) is a combination of swirl and tumble with a swirl ratio of 6 and tumble ratio of 2 at intake-valve closing. The motored-engine ensemble-mean velocity distribution at the TDC, combustion-chamber mid plane (where the fired-engine measurements were made in this study) is nearly solid body rotation (see Reuss et al (1995)). At TDC the swirl ratio is less than 5 and what remains of the tumble structure is weak and relegated to the center region of the bore. The instantaneous velocity distributions, $u(x,y)$, in Figs. 3a and b demonstrate that the shrouded valve produces large-scale-swirl flow each cycle that is nearly the same as the ensemble-average velocity, but with swirl centers that move from cycle to cycle. The instantaneous velocity distributions in Fig. 3a and b also show cyclic variability in the large swirl structure toward the cylinder wall, which manifests itself as waviness in the vector alignment compared to a nearly circular vector alignment in the ensemble-mean distribution.

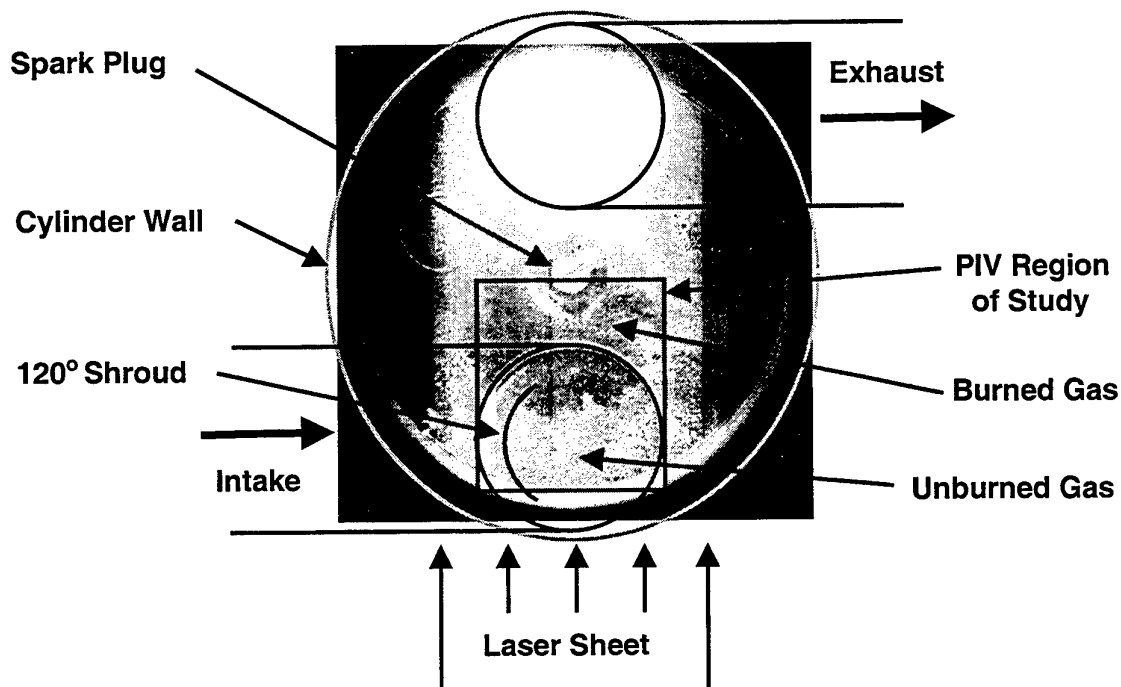


Figure 2 PIV photograph as viewed from the top, front of the engine. The overlaid illustration shows the region of study, shrouded intake valve and ports.

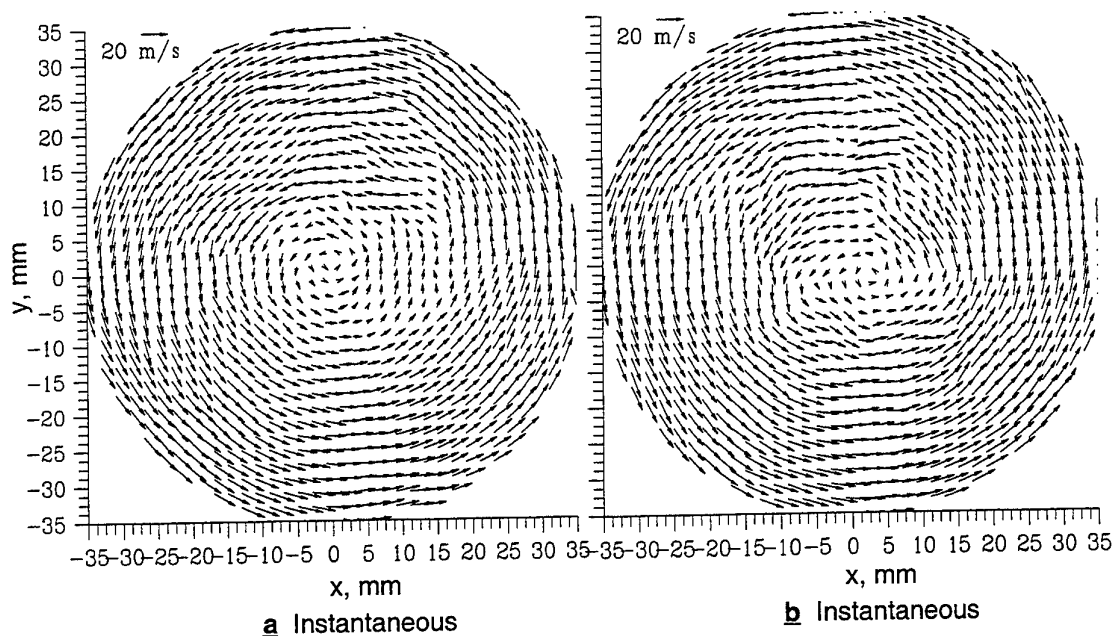


Figure 3 Instantaneous velocity distributions of two different motored cycles showing cyclic variability of the swirl center. Every fourth vector is shown.

This waviness is caused by the superposition of intermediate scale structures ($1\text{ mm} < L < 10\text{ mm}$) associated with the integral scales of the turbulence. These intermediate-scale structures are revealed by high-pass filtering as described in Reuss et al (1989, 1990), and will be shown in the results here. Smaller-scale structures ($< 1\text{ mm}$) are expected to be present in the flow, but are not resolved due to the 1.25 mm resolution of the PIV measurements.

Images of a single flame kernel 8 ca deg after ignition (6 ca BTDC) are shown in Fig. 4. These images are of the visible-light emissions taken simultaneously with two gated, image-intensified, CCD cameras, one viewing through the piston and one viewing through the quartz ring. Fig. 4 shows that the kernel is convected toward the intake valve, which was typical of all images recorded. This bias of the flame kernel is consistent with tumble causing a directed flow at the spark plug that would not otherwise exist in a pure swirling flow. The laser-sheet position shown in Fig. 4 is a reminder that the sheet shows a slice of a complex three-dimensional flame, and one must be mindful of this when interpreting the results.

2.2 Seeding

The particle seeding technique used in this study was the key to making successful measurements in the

burned gas. Optimum seed density cannot be achieved simultaneously in the burned and unburned gas because there is a volumetric expansion across the flame that is greater than five. As a compromise, the

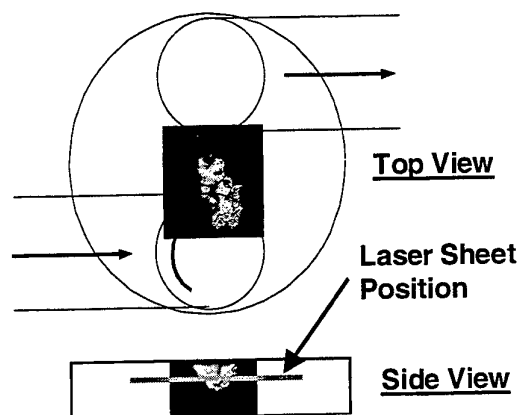


Figure 4 Bottom and side view images of the visible-light emissions recorded simultaneously 6 CA BTDC from a single flame kernel. The laser sheet position (not present for these photographs) is a reminder that the velocity measurements are a two-dimensional sample of a three-dimensional flame.

unburned gas was over seeded to achieve particle density in the burned gas that is sufficient for successful PIV interrogation. In addition, cross-correlation analysis was needed to achieve acceptable analysis of the PIV photographs in the burned-gas region.

The seeding criteria for successful measurements are as follows.

- 1) The particles must follow the flow.
- 2) The particles must scatter enough light to be visible over the background scattering and to be recorded on film.
- 3) The particle concentration must be high enough to yield at least 10 particles per interrogation spot in the burned gas.
- 4) The particle material must survive the high combustion temperatures.
- 5) The particle-scattered light must maintain the polarization of the illuminating laser light as required for electrooptical image shifting (to be discussed in Sec. 2.3).

The refractory particles used here were added to the engine-air flow employing a seeding technique used by Witze and Baritaud (1986) for LDV. Four disposable medical nebulizers (designed for humidifying respirators) were used to atomize a slurry of particles and water. The particle concentration in the slurry is adjusted with the expectation that each droplet will contain one particle and thus the droplet will evaporate leaving one particle rather than an agglomerate. In this study the occurrence of agglomeration was detected empirically by increasing the particle concentration in the slurry until either the photograph contained large particle images or the onset of depolarization of scattered light was observed. As will be described in Sec. 2.3, the use of a birefringent crystal for electrooptical image shifting allows depolarization to be observed as particle pairing while illuminating the particles with a single linearly-polarized laser sheet. The slurry particle concentration used for the tests here is 55 parts unpacked-dry-particle volume to 45 parts water volume.

To assure homogeneous mixing prior to entering the intake plenum, the metered engine intake air was split into two streams, recombined at the base of a "T" (thus impinging), exited through the third leg of the "T", and into a tube with fully developed turbulent flow. The seeded flow from the nebulizers (and propane) was injected through a small hole added to the centroid of the "T" fitting where mixing is expected to be high. The engine-air flow was desiccated to a dew point of less than 0°C prior to seeding in order to assure the evaporation of the particle laden droplets. The nebulizer-air flow was not

metered. Rather, the metered engine air was decreased to maintain the 40 kPa in the intake plenum. The engine-air flow was 83 l/s without the seed and 45 l/s with the seed, suggesting the total seed gas flow (air and water) was 38 l/s. Based on the number of particle images in the photographs, we estimate that the seeding density was 75 and 15 particles/mm³ in the unburned and burned gas, respectively.

Three different polishing were tried for seeding material: boron nitride, titanium dioxide, and zirconium oxide. Nipsil SS-50 White Carbon (Sanbayashi et al (1991)) was tried as well. In spite of the small particle size (all advertised to be less than 1 µm) and attempts with very low concentration slurries, all four powders are unusable because the scattered light was depolarized. It is presumed that the significant depolarization is a result of the irregular (multifaceted) shape inherent in polishing particles. Hollow, spherical particles are used here to minimize the depolarization. These particles are an undisclosed silica-alumina alloy advertised to have a softening temperature of 1500K and a specific gravity of 2.2. The particles were classified and the size distribution analyzed with a Coulter counter. The mean and standard deviation of the number percent and volume percent are 1.6 ± 0.13 µm and 2.0 ± 0.12 µm, respectively, with 99.5 percent of the particles less than 4 µm by volume and weight.

The response of the particles to the fluid motion was estimated using the data of Haghgoie et al (1986). In that study it was shown that 2 µm alumina particles (at a specific gravity of 4) respond to 2 kHz fluctuations in air at STP. The lower specific gravity of the particles used in this study (2.2) and higher gas density that exist in the engine will improve (increase) the particle frequency response compared to the calculations in Haghgoie et al (1986). Further, since the spatial resolution here is on the order of 1 mm, only large-spatial-scale (low temporal frequency) fluctuations are resolved. Consequently, the better than 2 kHz particle response is considered adequate. Finally, the particles are assumed to have a negligible effect on combustion since the ratio of the particle heat capacity to gas heat capacity (assuming no particle-phase change) is estimated to be less than 10^{-5} for the 75 particles/mm³ particle density used here.

2.3 The PIV Measurements

The particles were illuminated with a laser sheet that was formed by superimposing two 532 nm, 100 mJ, cross-polarized, 6 ns duration, Nd:YAG laser beams. The 50 mm wide sheet was made narrower than the possible 70 mm-diameter field-of-view to increase the laser power density and thereby increase the particle-scattered light intensity. The lasers used

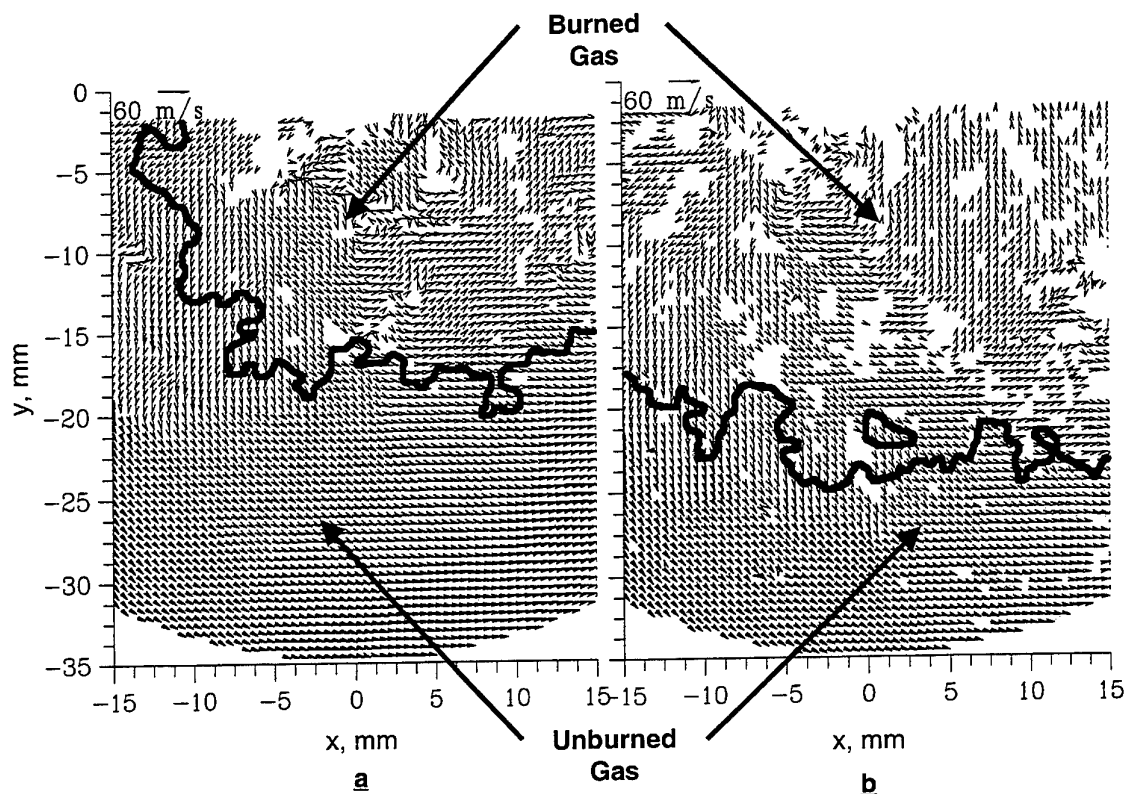


Figure 5 Instantaneous velocity distributions showing the highest (a) and lowest (b) data rates. No vectors are shown at the grid nodes where the interrogations were unsuccessful.

in this study focus near the test section but at slightly different longitudinal positions. Thus, the coincident laser sheets were approximately 0.3 mm and 0.4 mm in the test section based on Polaroid-film burns. Operating with one beam being thicker than the other improves the signal-to-noise ratio during the PIV analysis by decreasing out-of-plane pairing losses caused by (1) out-of-plane fluid velocity and (2) shot-to-shot variability in the out-of-plane beam positions. The two lasers were Q-switched 5 ± 0.01 ns apart. The laser sheets were parallel to the piston top and 6.3 mm from the head, which is the mid plane of the TDC clearance.

To avoid the directional ambiguity inherent in PIV with correlation analysis, the electrooptical image shifting technique developed by Landreth and Adrian (1988) was used and implemented as described in Reuss (1993). As implemented, the technique imparts an image displacement of approximately 0.22 mm displacement for particles with zero velocity. Consequently, positive and negative velocities add and subtract from the shift displacement and thus the

direction of the particle displacement (and therefore velocity) was known.

A large-format (100 mm by 125 mm) film camera with a 210 mm focal length Nikon APO Macor lens at 1:1 magnification is used to photograph the particle images. The photographs were recorded on Kodak 2415 Technical Pan film pushed to approximately 200 ASA for increased sensitivity and contrast. A laser-line optical filter with a 10 nm band width was used to block the flames visible-light emissions and particle incandescence. Particle-image sizes between 10 and 30 μm were observed. The particle image size is larger than the particle size due to the finite diffraction limit of the lens and aberrations caused by the filter and birefringent crystal. The PIV photograph studied here was taken at 2 ca BTDC with the ignition timing at 14 ca BTDC.

An example photograph is shown in Fig. 2, which shows laser light scattered by the cylinder head (background noise) and the particles. The background scattering reveals the valves, intake valve shroud, and spark plug. The photograph in Fig. 2 also shows that the region studied here was a subregion of the

photograph near the entrance side of the laser sheet. The photograph could not be analyzed near the side of the cylinder where the laser exits due to high background light. This was caused by back-reflections (specular) off of the exit-side cylindrical surfaces of the quartz ring.

Image processing is used to analyze the photographic negatives to determine the particle displacement (and thus the fluid velocity) at each point on the 0.5 mm-spaced grid. A TSI Model 6000 interrogation system with a cross-correlation technique is used (see Keane and Adrian (1992)). The cross correlation is between a 1.25 mm square spot centered on each node and a 1.86 mm square spot centered at the position equal to the image-shift distance from the node. The larger second area significantly reduces pair losses due to in-plane displacement since almost all pairs from the first spot are captured. Thus, the signal-to-noise ratio in the correlation plane is improved.

After the interrogation of the entire region, velocity vectors were validated using the post-interrogation refinement procedure described in Reuss et al (1989). The refinement rejects those vectors whose velocity magnitude is greater than ten percent different from the nearest neighbors and thus, if retained, would indicate velocity gradients that are larger than could be reasonable. In the 15 photographs taken here, there were 85 to 96 percent valid vectors. Fig. 5a and b are instantaneous velocity distributions from two different fired-engine cycles showing only the validated vectors. These distributions have the highest and lowest data rates, respectively (4% and 14% rejection rates). It can be observed that the regions of invalid vectors occurred predominantly in the burned gas. Inspection of the correlation space (not shown here) corresponding to the invalid vectors revealed that the invalid vectors are caused by poor signal to noise. The depolarization problem identified by Reuss (1993) was present but not dominant. Inspection into the corresponding image regions indicated low particle-image number density, on the order of twenty particle images per interrogation spot. Although this is a lower number density than achieved in the consistently more successful motored PIV images in Reuss et al (1995), it is not quantifiably different from neighboring image-regions where valid vectors were present. However, at this low number density it is easy to identify the number of particle images but hard to identify image pairs. We hypothesize that regions of low data rates are caused by poor correlation due to insufficient particle pairing. This is consistent with the fact that the use of cross correlation analysis reduced the number of invalid vectors. We further speculate that, having gone to

cross-correlation, out-of-plane motion is the dominant cause of unpaired particles. This hypothesis is consistent with the fact that the 0.3 to 0.4 mm laser sheet thickness is small compared to the 1.25 mm interrogation spot thickness required to capture the in-plane motion. Decreased laser-pulse separation did improve data rates, but at the expense of velocity resolution. Attempts to further test this hypothesis by using a region of the laser sheet that is significantly thicker failed due to insufficient laser energy and due to poor laser-beam transformation. A thicker higher-energy laser pulse would have two effects. First, it would decrease the out-of-plane pair losses. Second, it would increase the total number of image pairs in an interrogation spot (due to the larger illuminated volume) without having to further increase the seeding density in the gas.

2.4 Flame Position Identification and Conditional Sampling

To identify the burned- and unburned-gas regions, it is necessary to identify and mark the flame position in each velocity distribution. It is natural to return to the corresponding PIV photographs and determine the flame-position coordinates by marking the position of the change in light scattering as was done in zur Loye and Bracco (1987). In that work, the large seeding density (many particles per imaging pixel) produced a nearly binary light-intensity distribution with a uniformly high scattered-light intensity in the unburned region and a uniformly low intensity in the burned gas. As a result, the flame position was marked unambiguously.

In this study the flame position in the photographic images is less apparent because the seeding density is optimized for PIV analysis rather than for flame imaging as in zur Loye and Bracco (1987). As a result, the PIV photograph consists of spatially separated individual "bright" particle images in a relatively dark field both in the burned and unburned regions. Thus, the image intensity in the burned and unburned regions is not uniform, but rather it differs by the relative number density of individual particles. The result is that the image contrast between the burned and unburned regions is poor compared to that in zur Loye and Bracco (1987). This can be observed in Fig. 6a, which shows an enlargement of the region of study. To acquire this image, the PIV photographic negative (at 1:1 magnification image of the object space in the engine) was scanned with a resolution of 12 pixels per mm. Also, the brightness and contrast of the scanned image were adjusted with image processing to make the flame boundary between the burned gas (low seeding density) and unburned gas (high seeding density)

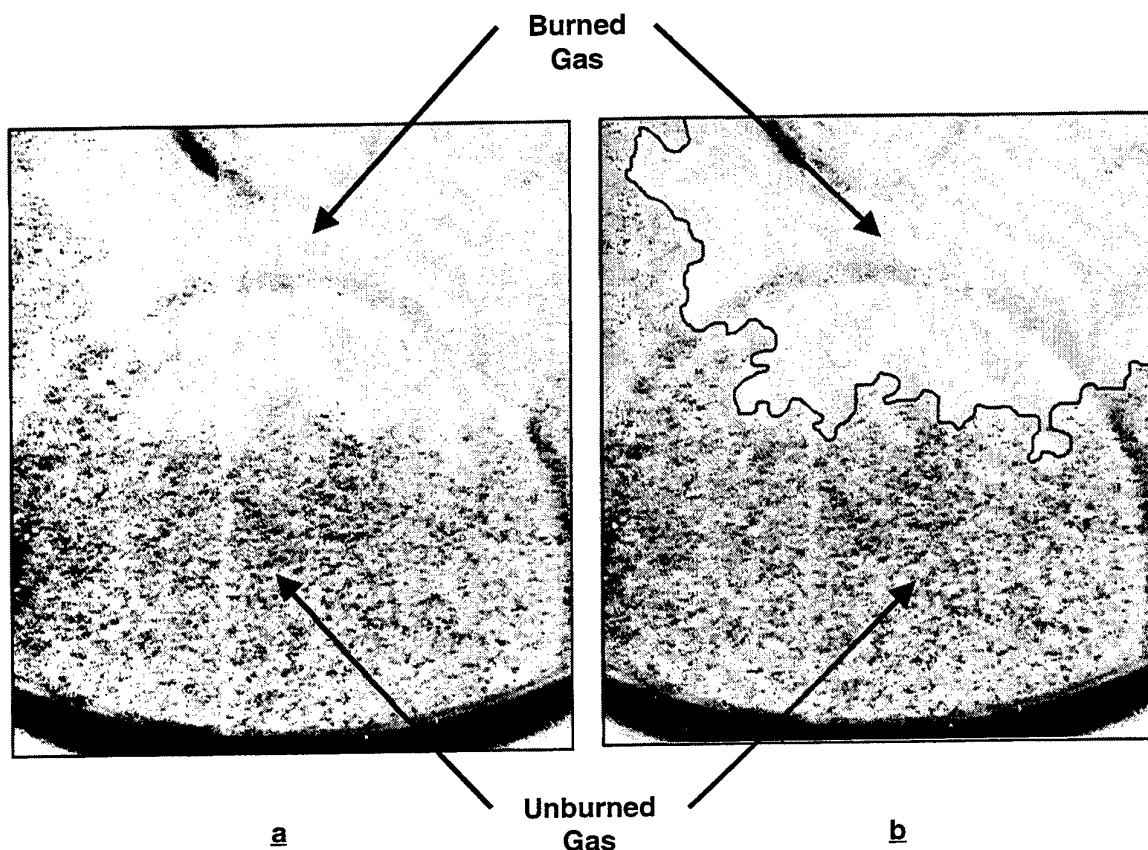


Figure 6 Image enhanced PIV photograph (a) without and (b) with manually drawn flame position.

more apparent to the eye as well as more suitable for publication. After this image processing, it is possible to discern the burned gas region on the largest scales. However, careful inspection of the boundary between the burned and unburned regions reveals that it is still difficult to clearly identify a well-defined position or "edge" between the two regions. An attempt to find an automatic image-processing algorithm to define the boundary between the unburned and burned regions was abandoned.

In lieu of an automatic image-processing algorithm, the flame position was traced manually using the Microsoft Powerpoint drawing tool on a bit map of the scanned negative. An overlay of a hand-drawn flame is shown in Fig. 6b. The image coordinates were carefully registered and converted to the $[x,y]$ coordinates of the PIV interrogation grid and the flame position overlaid on the velocity-distributions as shown in Fig. 7b. The error in the flame position based on boundary ambiguity is estimated to be about 0.2 mm in most regions with occasional position errors as large as 0.5 mm. This is

considered adequate for the 1.25 mm resolution of the velocity scales and 0.5 mm grid used in this study.

In addition to marking the flame position in the velocity distributions, the image processing is used here to identify subregions of the vorticity and strain-rate distributions for conditional sampling. In particular, a flag (zero or one) is assigned to each PIV grid node to indicate if it is in the burned or unburned region. As a third condition, nodes within 1 mm of the flame are identified. PDF's are then computed from these subsamples and used to quantify visual observations.

3. RESULTS

This section presents several hypotheses concerning flame/flow interaction. The suppositions were formulated after observing the distributions of instantaneous velocity, high-pass filtered velocity, vorticity and strain-rates for all fifteen of the realizations recorded in this study. The hypotheses are presented here using distributions from a single

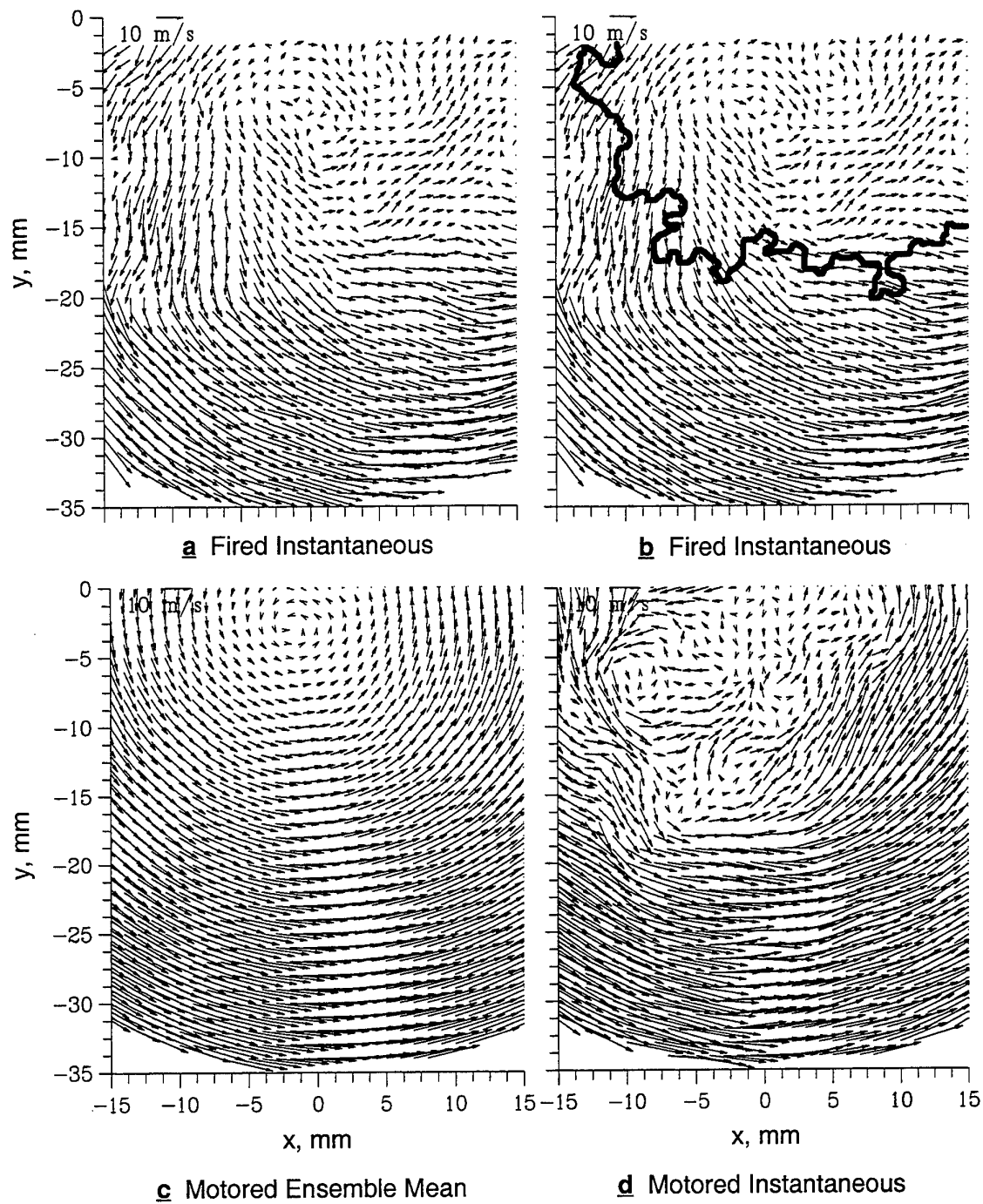


Figure 7 Instantaneous velocity measurements from photograph in Figure 6, (a) with and (b) without flame position. 7c and d show the mean and an instantaneous distribution for the same region of study from the motored tests in Reuss et al (1995). Every second vector is shown.

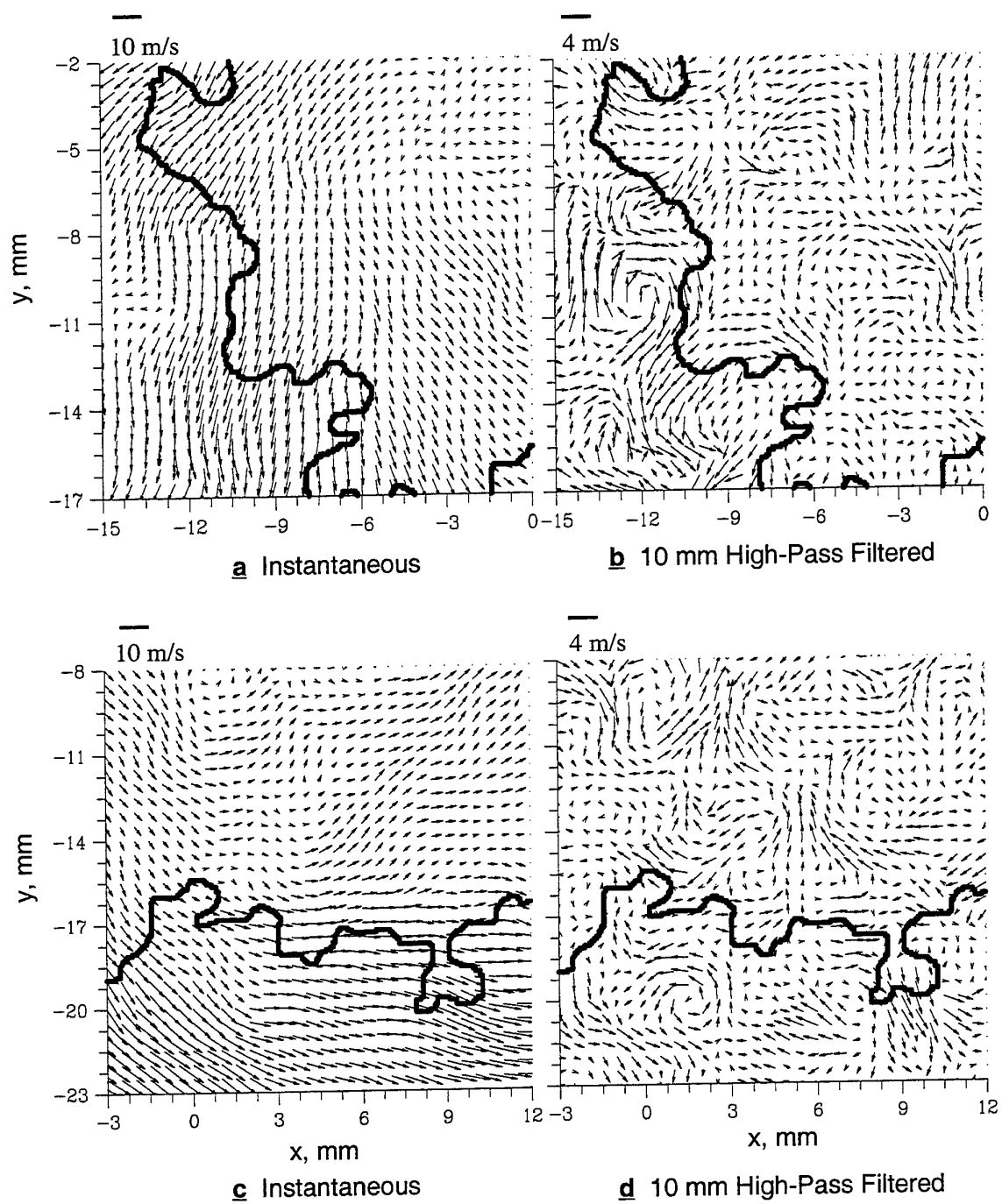


Figure 8 The instantaneous velocity (a & c) and high-pass filtered (10 mm) velocity (b & d) of two subregions in Figure 7b. All vectors are shown.

realization to avoid an unreasonably large number of figures. The hypotheses are based on qualitative observations and conditionally sampled PDF's.

3.1 Instantaneous Velocity Measurements

It is natural to first look at the instantaneous velocity ahead and behind the flame (unburned and burned gas, respectively). The instantaneous velocity distribution corresponding to the PIV photograph in Fig. 6 is given with and without the flame image in Figs. 7a and b, respectively; only every second vector is plotted for clarity. This comparison with and without the flame image is shown to demonstrate that there are no obvious flow features in the instantaneous velocity distribution to mark the flame position. However, it can be observed that the velocity magnitude in the burned gas is generally smaller than in the unburned gas. To assess if this is an effect of combustion or a feature of the motored flow, the instantaneous velocity in the burned gas can be compared with the motored ensemble-mean velocity (100 cycle mean) and randomly chosen motored, instantaneous-velocity distributions shown in Figs. 7c and d, respectively. Note that all four distributions in Fig. 7 have the same velocity scaling. As might be expected, the ensemble- and instantaneous-velocity magnitude is smaller near the center of the swirl, which is coincident with the geometric center of the cylinder ($[x,y] = [0,0]$). However, the velocity magnitude in the burned gases (Fig. 7b) near the upper right hand corner of the region ($[x,y] = [5,-20]$ to $[15,0]$) has decreased considerably. This is expected since the gas expansion across the flame opposes the forced-convective (motored) flow in this region. Notwithstanding, there are remnants of the original swirling flow in the burned gas as indicated by the direction of the flow.

3.2 Turbulence Visualization

The intermediate length-scale turbulence ($1.25 \text{ mm} < L < 10 \text{ mm}$) in the instantaneous-vector distributions reveals itself as waviness in the vector alignment compared to the nearly circular vector alignment in the ensemble-mean distribution (cf. Figs. 7a and c). This turbulence is the superposition of the intermediate length-scale coherent structures with the large-scale swirl structure. It is possible to visualize the coherent structures of the turbulence using the high-pass spatial-filtering technique employed by Reuss et al (1990). This is shown in Fig. 8 for two expanded regions (every vector plotted) of Fig. 7b. Figs. 8a and c show the instantaneous velocity distributions, and Figs. 8b and d show the high-pass filtered velocity distributions. The high-pass filtered velocity distributions are attained through a two step

operation. First, the local average of the instantaneous velocity centered at each grid node is computed by convolution of the instantaneous velocity distribution with a Gaussian-weighting function. Here the Gaussian weighting is 10 mm at the $1/e^2$ point. Second, this local-average velocity (low-pass filtered velocity, u_{lp}) is subtracted from the instantaneous velocity, u , leaving the high-pass filtered velocity, $u_{hp} = u - u_{lp}$. Thus, the high-pass filtered velocity is the velocity observed from a Lagrangian frame of reference where the observer is moving at the local spatial-average instantaneous velocity of the large-scale swirl flow.

Inspection of the velocity distributions in Fig. 8 reveals that the high-pass filtered distributions show coherent structures at this length scale. Using the labels of Hunt et al (1988), it is possible to identify eddies (e. g., rotational structures at $[x,y] = [-4,-10]$, $[-12,-10]$, and $[2,-20]$) and streaming flows at $[x,y] = [-12,-4]$, $[-11,-14]$, and $[10,-21]$. Note that the coherent structures are visible in both the burned- and unburned-gas regions. As noted in Reuss et al (1989), the spatial scale of these structures is consistent with the turbulence integral-length scale measured with LDA in engines of similar geometry. The appearance of these coherent structures has two implications. First, experience has demonstrated that PIV experiments configured with insufficient velocity dynamic range result in high-pass filtered velocity distributions with random vectors rather than coherent structures as observed here. Thus, the appearance of the coherent structures in the burned gas is taken as evidence that the accuracy of the measurements in the burned gas is sufficient to resolve the intermediate scale structures with approximately the same accuracy as measurements in motored and unburned flows. The second implication is that it is possible to measure and visualize the flow structures that affect the flame wrinkling. For example, in comparison to the instantaneous velocity, observations along the flame in the high-pass velocity distribution reveal streaming structures that correlate with the wrinkling. The most obvious correlation is for the streaming structures at $[x,y] = [-13,-4]$, $[-11,-14]$ and $[10,-21]$. It is not obvious that eddies directly affect the flame wrinkling since the flame wraps around but does not appear to propagate through the vortex structures. Speculating, the three dimensional vortex tubes producing the eddies observed in these two-dimensional measurements act to create the streaming flows in between the vortex tubes; the flame is then convected by the streaming flows between the eddies rather than burning through the eddies. This is supported by the streaming flow at $[-11,-14]$ that appears to be formed between the three eddies centered at $[-8,-15]$, $[-12,-11]$

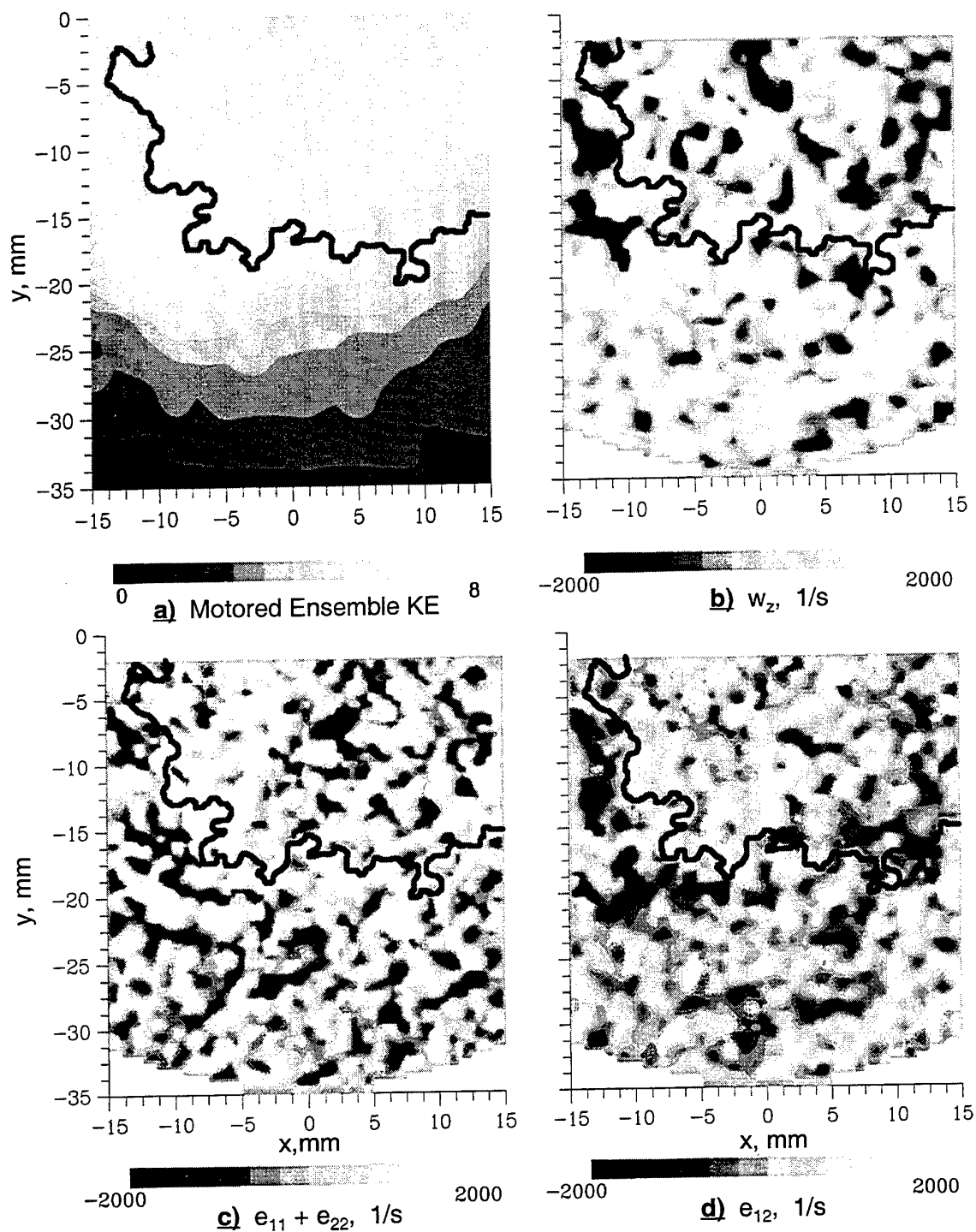


Figure 9 (a) The two-dimensional kinetic energy ($\frac{1}{2}u'^2 + \frac{1}{2}v'^2$) based on fluctuations about the ensemble average of 100 motored cycles. The flame studied here is superimposed to show relative position. Figures b, c, and d are the vorticity, normal-strain rate, and shear-strain rate computed from the instantaneous-velocity distribution in Figure 7a.

and [-4,-11] and, in turn, appears to be stretching the flame to be convex with respect to the unburned gas. This supposition cannot be considered universally true since it is based on observations of only 15 realizations and only one operating condition. Nonetheless, observations of the high-pass filtered distributions make two points. First, u' , the traditional turbulence measure, is a random sampling of coherent structures in the burned gas as suggested in the introduction. Second, the flow-direction and spatial scale of the coherent structures appears to correspond to the flame wrinkling.

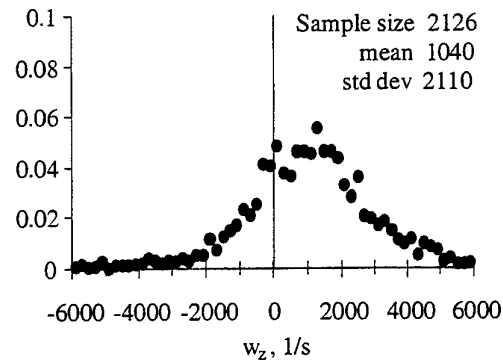
3.3 Turbulence Characterization

To determine the effect of the flame on the in-cylinder turbulence, it is of interest to compare distributions of turbulence kinetic energy, KE, vorticity, w_i , and strain-rate, e_{ij} , from both motored and fired conditions. However, at this time KE from the motored flow and w_i and e_{ij} from fired condition are all that are available for comparison. Thus, we proceed with a qualitative comparison recognizing that KE is based on u' , the random sample of velocity fluctuations about the ensemble mean, while w_i and e_{ij} are direct measures of the fluid deformation due to turbulence from single realizations. For this comparison, the motored-engine KE distribution from Reuss et al (1995) is repeated in Fig. 9a for the region of the cylinder studied in these fired tests with the flame position superimposed. Fig. 9a shows that in the absence of combustion the turbulence is very high in the cylinder center ($[x,y] = [0,0]$), low near the wall, and has a relatively steep gradient between the high- and low-turbulence regions (at a radius between 20 and 25 mm). Fig. 9a shows that the flame at 2 ca BTDC has propagated just to the edge of the high turbulence KE region.

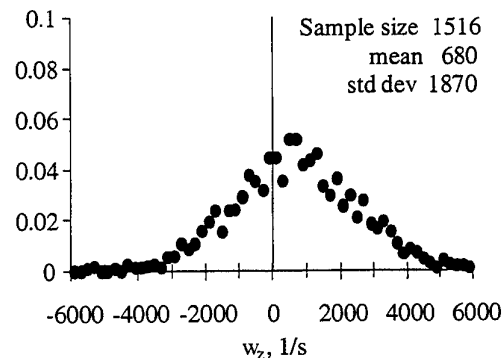
The vorticity, w_z , ahead and behind the flame is shown in Fig. 9b. It can be observed that the unburned gas has predominately positive vorticity as indicated by the predominately light regions. This trend is consistent with the dissipation of large-scale gradients in the large scale swirl structure, which has positive circulation. By comparison, the burned gas vorticity has a more equal balance of positive (light regions) and negative vorticity (dark regions) and the magnitude of the negative vorticity is much greater than that in the unburned gas. This trend was observed in all 15 realizations captured in this study. This observation provided the motivation for measuring the conditionally sampled PDF's shown in Figs. 10a and b for the unburned- and burned-gas regions, respectively. Comparison of Figs. 10a and b at $w_z \approx -2000$ 1/s demonstrates that indeed there is more negative vorticity in the burned gas. Further, the

vorticity distributions are approximately symmetric with the peak of the burned-gas PDF shifted towards zero (also compare the mean values) indicating a more equal distribution of positive and negative vorticity in the burned gas. In the absence of any knowledge about the motored flow, one might assume that the flame has indeed affected the vorticity behind the flame. However, the flame position in Fig. 9a shows that the burned gas is in the high KE region of the motored flow and the unburned gas is predominately in the low KE region. Thus, one might speculate that the flame is behaving as a passive scalar and the differences in the burned and unburned gas vorticity may be the result of the vorticity in the forced-convective motored flow. This supposition is weakly supported by the coincidence of high negative vorticity in the fired cycle and high motored KE in the region $[x,y] = [-15,-20]$ to $[-8,2]$ (upper left hand corner), which is in the unburned gas region.

Figures 9c and d show the distributions of the



a) Unburned gas.



b) Burned gas.

Figure 10 Conditionally sampled PDF's of the vorticity in Fig. 9b.

sum of the normal-strain rates ($e_{11} + e_{22}$) and the shear-strain rate (e_{12}). The spatial scale of the structures are approaching the spatial resolution of the measurements, and thus serve as a reminder that measurements with smaller spatial resolution are desired. Unlike the vorticity distribution, visual

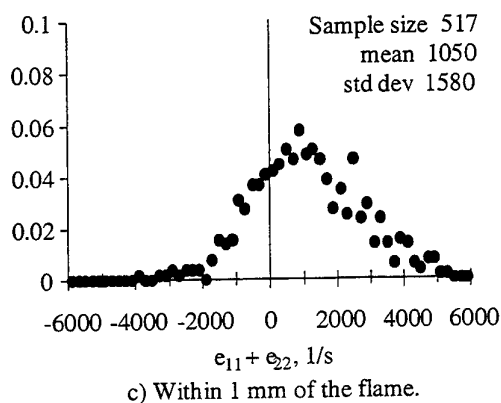
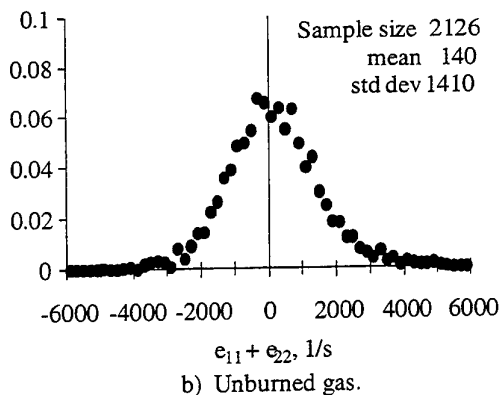
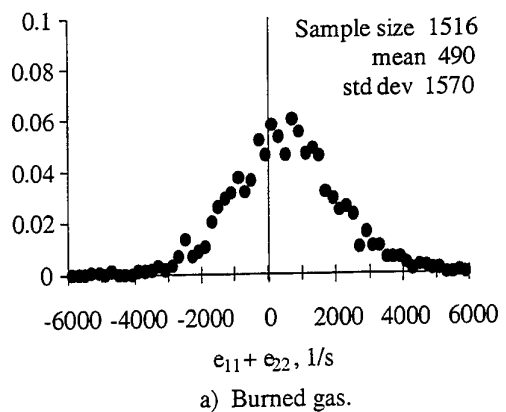


Figure 11 Conditionally sampled PDF's of the normal strain in Fig. 9c

inspection of the normal- and shear-strain-rate distributions does not reveal that the structures are obviously different ahead and behind the flame. However, careful observation while following along the flame reveals that the normal-strain rates are predominately positive adjacent to the flame. The later observation is physically consistent with the high rates of heat release in the flame. In fact, normal-strain was found to be a useful flame marker for the two-dimensional, wrinkled, laminar flames studied by Mueller, et al (1996, 1998). To test the validity of these observations, PDF's sampled in the burned-gas, the unburned-gas and the region within ± 1 mm of the flame are shown in Figs. 11a through c, respectively. Looking first at the unburned-gas PDF (Fig. 11b), it appears nearly symmetric with a mean of 140. By comparison, the burned-gas PDF (Fig. 11a) has shifted towards positive values with a mean of 490 apparently caused by the larger number of occurrences of positive strain rate between 0 and 4000 1/s. Thus, the PDF has shown regional differences not readily apparent from observations of the plotted distribution. The normal-strain-rate PDF sampled within a 1 mm of the flame (Fig. 11c) shows a more dramatic affect. Clearly the peak has shifted in the positive direction compared to the general population in the unburned gas. Further, the distribution has skewed significantly towards positive values with a significant increase in the number of occurrences between 1000 and 5000 1/s.

In the case of the shear strain there are no obvious differences between the unburned- and burned-gas regions, either observed in the distributions or in the PDF's. The PDF for the entire region (burned and unburned gases) in Fig. 12. However, the distribution does show a considerably narrower distribution when compared with the vorticity or normal-strain rates. (compare the standard deviations in Figs. 10 through 12).

The observations described here are insightful as a first step and raise interesting questions concerning the nature of flow and combustion in this high-swirl in-cylinder RIC engine. In particular, what is the link between u' , the traditional measure of turbulence, and the direct measures of the turbulence fluid deformation (it is interesting that the highly-directed swirling flow has large-scale inhomogeneity in the vorticity and normal strains while the shear strain is relatively homogeneous)? Two more questions arise concerning the physics of the flame/flow interaction. In particular, is the flame behaving as a passive scalar leaving the turbulence relatively unaffected, and does the flame propagate preferentially around rather than through the vorticity? Investigation of these questions requires analysis and comparisons of much larger samples under a larger variety of operating conditions.

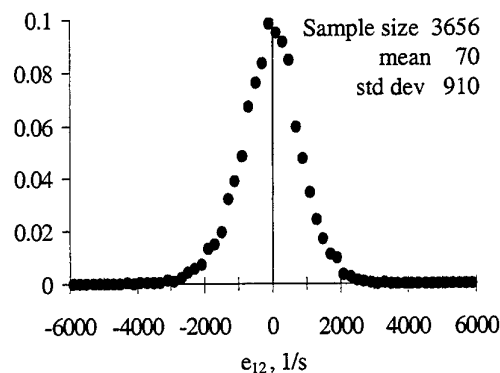


Figure 12 PDF of shear strain in the unburned and burned gas of Fig. 9d.

Even then, analysis is particularly difficult both because these PIV measurements provide only two-dimensional samples of three-dimensional structures, and because no two realizations are the same, which renders it impossible to compare motored and fired cycles directly. However, the conditionally sampled PDFs do provide a tool for comparative analysis.

4. SUMMARY

Particle image velocimetry has been used for simultaneously measuring the velocity ahead and behind a flame in a RIC engine. Electro-optical image shifting was employed to remove the directional ambiguity and a spatial resolution of 1.25 mm was achieved. The techniques required to make these measurements successful are described. We deduce that the data rates in the burned gas could be improved by using thicker higher-energy laser sheets.

Fifteen realizations of the in-cylinder turbulence were recorded at either 2 or 4 ca BTDC. However, the results from only one realization are shown in order to maintain a manageable amount of information. Visual observations of the instantaneous velocity, filtered velocity, vorticity and strain-rate distributions provide insight into the interaction of the flame and the flow. First, the high-pass filter distributions show that u' , the traditional turbulence measure, is a random sampling of coherent structures in the burned gas. This is an expected result, but none the less an affirmation of what was known to be true in non-engine flows, motored-engine flows, and the unburned gas of a fired engine. Second, the gas expansion caused by the flame decreased the magnitude of the swirling-flow velocity in the burned gas region as one might expect. Third, the flow direction of coherent structures revealed in the high-pass-filtered velocity

distribution show a strong correspondence with the flame wrinkling, although the flame appears to propagate around rather than through eddy structures. Fourth, the length scales of the vorticity appear to be the same size as the length-scales of the flame wrinkling.

Observations and conditionally sampled PDFs of the vorticity and strain-rate distributions showed large-scale inhomogeneity. In particular, the vorticity ahead of the flame had a positive bias compared to the burned gas region. The normal-strain rates show a positive bias behind and especially near the flame, which is consistent with the thermal expansion of heat release. Finally, the shear-strain rate appeared to be homogeneous, with a symmetric and considerably narrower PDF when compared to the vorticity and normal shear.

The restricted focus of this paper has been to demonstrate the new information that can be provided in preparation for a more comprehensive treatment. We caution that the observations can not be considered universal since they are made for only fifteen realizations at one operating condition in one engine geometry. In fact, no more than fifteen realizations were recorded due to the difficulty producing PIV photographs with acceptable data rates in the burned gas. We believe we have sufficient evidence to indicate this difficulty occurred because the laser sheets were too thin. Thus, there is a danger of bias since we might have recorded only realizations with small out-of-plane motion. None the less, this work demonstrates a technique for recording two-dimensional velocity distributions in RIC engines, suggests methods for improved experiments, and provides direction for future studies.

5. REFERENCES

- Arcoumanis, C. and Whitelaw, J. H., 1987, "Fluid Mechanics of Internal Combustion Engines - A Review", Proc. I. Mech. E., 201C.
- Candel, S. M., and Poinso, T. J., 1990, "Flame Stretch and the Balance Equation for the Flame Area," Combustion, Science, and Technology, 70.
- Foster, D. E. and Witze, 1988, P. O., "Two-Component Laser Velocimetry Measurements in a Spark Ignited Engine," Comb. Sci. & Tech., Vol. 59.
- Guibert, P., Murat, M., Hauet, B., and Keribin, P., 1993, "Particle Image Velocimetry Measurements: Application to In-Cylinder Flow for a Two Stroke Engine", SAE Paper 932647.

- Haghgooeie, M., Kent, J. C., and Tabaczynski, R. J., 1986, "Verification of LDA and Seed Generator Performance", *Experiments in Fluids*, 4.
- Hunt, J. C. R., Wray, A. A., and Moin, P., 1988, "Eddies, Streams and Convergence Zones in Turbulent Flows", In Report CTR-S88, Proceedings of the 1988 Summer Program, Center for Turbulence Research, Stanford University.
- Hussain, A. K. M. F., 1986, "Coherent Structures and Turbulence," *Journal Of Fluid Mechanics*, 173.
- Keane, R. D., and Adrian, R. J., 1992, "Theory of Cross-Correlation Analysis of PIV Images", *Applied Sci. Res.*, 49.
- Kuo, Tang-Wei, and Reuss, D. L., 1995, "Multidimensional Port and Cylinder Flow Calculations for the Transparent-Combustion-Chamber Engine," *ASME, IVE-Vol. 23, Engine Modeling*.
- Landreth, C. C., and Adrian, R. J., 1988, "Electrooptical Image Shifting for Particle Image Velocimetry," *Applied Optics*, Vol. 27, No. 20.
- Lorenz, M. and Prescher, K., 1990, "Cycle Resolved Measurements on a Fired SI-Engine at High Data Rates Using a Conventional Modular LDV-System," *SAE Paper 900054*.
- Mueller, C. J., Discroll, J. F., Reuss, D. L., and Drake, M. C., 1996, Twenty-Sixth Symposium (International) on Combustion, The Combustion Institute, Pittsburgh.
- Mueller, C. J., Discroll, J. F., Reuss, D. L., Drake, M. C., and Rosalik, M. E., 1998, *Combustion and Flame*, Vol. 112, No. 3.
- Nino, E., Gajdeczko, B. F., and Felton, P. G., 1992, "Two Color Particle Image Velocimetry Applied to a Single Cylinder Two Stroke Engine", *SAE Paper 922309*.
- Nino, E., Gajdeczko, B. F., and Felton, P. G., 1993, "Two Color Particle Image Velocimetry in an Engine With Combustion", *SAE Paper 930872*.
- R. B. Rask, 1984, "Laser Doppler Anemometry Measurements of Mean Velocity and Turbulence In Internal Combustion Engines," in Int. Conf. on Applications of Lasers and Electro-Optics, Boston.
- Reeves, M., 1995, "Particle Image Velocimetry Applied to Internal Combustion Engine In-Cylinder Flows", Ph. D. Thesis, Loughborough University of Technology, England, September.
- Reeves, M., Garner, C. P., Dent, J. C., and Haliwell, N. A., 1996, "Particle Image Velocimetry Measurements of In-Cylinder Flow in a Multi-Valve Internal Combustion Engine", Proc. Inst. Mech. Engrs., Vol. 210.
- Reuss, D. L., Adrian, R. J., Landreth, C. C., French, D. T., and Fansler, T. D., 1989, "Instantaneous Planar Measurements of Velocity and Large-Scale Vorticity and Strain Rate in an Engine Using Particle Image Velocimetry," *SAE Paper 890616*.
- Reuss, D. L., Bardsley, M., Felton, P. G., Landreth, C. C., and Adrian, R. J., 1990, "Velocity, Vorticity, and Strain-Rate Ahead of a Flame Measured in an Engine Using Particle Image Velocimetry," *SAE Paper 900053*.
- Reuss, D. L., 1993, "Two-Dimensional Particle-Image Velocimetry with Electrooptical Image Shifting in an Internal Combustion Engine," in the Proceedings of the International Society for Optical Engineering, Optical Diagnostics in Fluids and Flows, Vol. 2005.
- Reuss, D. L., Kuo, T-W, Khalighi, B., Haworth, D., and Rosalik, M., 1995, "Particle Image Velocimetry Measurements in a High-Swirl Engine Used for Evaluation of Computational Fluid Dynamics Calculations," *SAE Paper 952181*.
- Sanbayashi, D., Ando, H., and Kumagai, H., 1991, "Feasibility of Using Several Powder Materials as the Seeding Particle for LDV Measurement", *JSAE Review*, Vol. 12, No. 2.
- Sweetland, P., and Reitz, R. D., 1994, "Particle Image Velocimetry Measurements in the Piston Bowl of a DI Diesel Engine", *SAE Paper 940283*.
- Witze, P.O., and Baritaud, T. A., 1986, "Particle Seeding for Mie-Scattering Experiments in Combusting Flows", ed. Proceedings of the Third International Symposium on Laser Techniques and Applications, Lisbon Portugal (ed.), Springer-Verlag.
- Valentino, G., Kaufman, D., and Farrell, P., 1993, "Intake Valve Flow Measurements Using PIV", *SAE Paper 932700*.
- Valentino, Gerardo, Corcione, F. E., and Seccia, G., 1997, "Integral and Micro Time Scales Estimated in a DI Diesel Engine," *SAE Paper 971678*.

zur Loye, A. O. and Bracco, F. V., 1987, "Two Dimensional Visualization of Premixed-Charge Flame Structure in an IC Engine, SAE Paper 870454.

In-cylinder Measurements of Mixture Composition for Investigation of Residual Gas Scavenging

P. Miles

ABSTRACT

Laser Raman scattering with broadband signal detection is employed to simultaneously measure the mole fractions of CO_2 , O_2 , N_2 , C_3H_8 , and H_2O under conditions simulating a cold start. The engine is operated with well-premixed fuel and air, such that each of the measured species can be used to independently estimate the mole fraction of burnt residual gases. The residual gas mole fraction estimates are subsequently examined for consistency and for evidence of poor scavenging of H_2O due to condensation on the cold combustion chamber walls. The data indicate that if this mechanism inhibiting H_2O scavenging is operative, it results in H_2O number densities which are only 10-15% higher than expected. It is suggested that these higher than expected levels of H_2O may be associated with Raman scattered light from condensate films on the windows. Raman scattering techniques using backscatter collection geometries are expected to be more sensitive to light scattered from condensate films, which may explain previously measured high H_2O mole fractions.

1. INTRODUCTION

A number of studies have shown that a significant fraction of the unburned hydrocarbon (UHC) emissions from spark ignition engines occur during the warm-up period following a cold-start (e.g. Takeda, *et al.*, 1995). Directly or indirectly, the majority of these disproportionate emissions can be traced to a single common factor: cold surfaces in the combustion chamber and intake ports. Cold combustion chamber surfaces result in increased flame quenching within the combustion chamber, while cold surfaces in the intake port and valve region lead to slow or insufficient fuel vaporization. Poor fuel vaporization, in turn, results in gas phase air/fuel ratios above the flammability limit (with subsequent misfire) and in partial burning associated with mixture inhomogeneities. Dilution of the charge with burnt residuals can exacerbate each of these factors; a dilute mixture is more susceptible to flame quench and has a narrower range of inflammable air/fuel ratios.

Recently, Grünefeld, *et al.* (1995) suggested another mechanism by which cold surfaces might affect cold-start engine operation and emissions. In

their study, which employed laser Raman scattering to measure the in-cylinder gas composition during a cold start simulation, high instantaneous values of residual water content were observed (between 5 and 6%), which correspond to a residual gas content of roughly 40%. Based on the simultaneously measured O_2 gas densities, a residual gas content of only half that corresponding to the water content was deemed more probable. The suggestion was made, therefore, that the residual water content may not be a reasonable marker of the total residual gas content, due to the possibility of preferential scavenging of the different residual gas species. In this preferential scavenging scenario, water vapor condenses on the cold combustion chamber walls during the expansion and exhaust stroke (while N_2 and CO_2 do not), and re-enters the gas phase through vaporization during the subsequent compression stroke. Corroborating this idea of a preferential scavenging mechanism was the observation that the scavenging of the residual water vapor when misfires occurred was 5-10 times slower than expected. It was concluded that charge dilution by residual gases, particularly the slowly scavenged H_2O , was a major cause of misfire and of increased UHC emissions during cold-start and warm-up.

The experimental system used in the above-referenced study, however, may be susceptible to interferences caused by the back-scatter collection geometry employed. The cause of this potential interference can be understood by recognizing that the incident laser beam will scatter Raman-shifted light from any films of fuel or combustion products which condense on the beam entrance or exit windows. A film thickness on the beam entrance and exit windows of roughly $1.3 \mu\text{m}$ would be sufficient to double the measured H_2O content. Furthermore, the energy required to vaporize these films can be shown to be greater than the laser pulse energy, such that window 'cleaning' by the laser pulse is not possible. Thus, in a backscatter geometry, condensate films not only attenuate the scattered light from the gas phase mixture, but may also contribute sufficient signal to invalidate measurements of the gas phase species.

In this paper the in-cylinder residual gas content under simulated cold-start conditions is revisited using a similar Raman scattering technique. An alternate

incident beam. With this geometry, light scattered from films on the beam entrance and exit windows is not in the direct view of the collection optics, and does not contribute directly to the measured signal. Furthermore, in this work the engine is fueled with gaseous propane, which is well pre-mixed with the combustion air. Under these circumstances, each of the measured (non-Nitrogen) major species, CO_2 , O_2 , C_3H_8 , and H_2O , can be used to estimate the residual gas content. The various residual gas estimates can be examined for consistency and thus for evidence of the existence of preferential scavenging of the different residual gas components.

2. FUNDAMENTAL PHYSICS

Vibrational Raman scattering is an inelastic scattering process in which there is a net exchange of energy between the incident light and the scattering molecule. In this exchange, the change in vibrational energy of the participating molecule equals the change in energy of the scattered light. Because the quantized vibrational energy states available to each molecule are unique, the change in energy of the molecule (and, thus, the change in energy, or wavelength, of the scattered light) can be used to identify the scattering molecular species. By collecting scattered light over a broad band of wavelengths, and subsequently dispersing this light onto a multi-channel detector, multiple species can be monitored simultaneously.

The energy of the scattered light from species i , $E_{\text{scat } i}$, is given by (Eckbreth, 1996)

$$E_{\text{scat } i} = E_{\text{laser}} \left(\frac{\partial \sigma}{\partial \Omega} \right)_i N_i \Omega \ell \eta_i \quad (1)$$

where E_{laser} denotes the laser pulse energy, $(\partial \sigma / \partial \Omega)_i$ the differential scattering cross-section of the i^{th} species, N_i the molecular number density, Ω the solid angle subtended by the collection optics, ℓ the length of the beam from which scattered light is collected, and η_i the efficiency of the optical system. From Eq. 1, it is seen that the signal is directly proportional to N_i , provided the differential scattering cross-section is constant. In practice, $(\partial \sigma / \partial \Omega)_i$ is a function of temperature; however, for the limited temperature range considered here this temperature dependence is small and is neglected.

By forming a ratio of the signals collected from each species i to the weighted sum of the signals from the major species, it is possible to determine the species mole fraction independent of such parameters as instantaneous laser power or η_i (which may be affected by such factors as window fouling). The

weighting factors, which represent the signal obtained per molecule of species i relative to the signal obtained per N_2 molecule, are obtained by calibration.

3. EXPERIMENTAL APPARATUS

Measurements reported here are obtained in the Sandia side-valve engine, which is pictured in Fig. 1. The side-wall location of the valves in this engine allows unimpeded optical access to the combustion chamber through a large window in the head. The intake valve can be fitted with a shroud, which allows the introduction of various degrees of swirl to the in-cylinder flow. With an unshrouded valve, mixing of the fresh charge with the residual gases is quite rapid, while with the shrouded valve significant mixture stratification persists throughout the compression stroke (Miles and Hinze, 1998). The incident laser beam enters and exits the cylinder through two small, diametrically opposed windows, and follows a path through the cylinder which approximately bisects the clearance height of the combustion chamber. The engine geometry is summarized in Table 1.

Raman scattered light is collected from a 10.9 mm length of the beam ($\lambda=532$ nm) in the central portion of the combustion chamber. The focused beam diameter within the engine, 0.49 mm as defined by the $1/e^2$ intensity contour, defines the spatial resolution in the plane normal to the beam. After passage through the engine, the beam energy is measured on an instantaneous, shot-by-shot basis. Typical pulse energies of 120 mJ were employed. The collected light is subsequently refocused to form an image of the laser beam at the entrance slit of an imaging spectrograph. As depicted in Fig. 1, the spectrograph disperses the image in the entrance slit spectrally, such that at the exit plane a two-dimensional image is formed, consisting of multiple images of the beam at the entrance slit. Each beam image at the detector plane corresponds to Raman scattered light from a particular molecular species. Thus, at each spatial location, the number density of each species can be determined from the intensity of the appropriate beam image integrated over the appropriate spatial and spectral regions. The size of the detector, and the

Table 1:

Engine geometry and Operating Conditions

Bore	7.64	[cm]
Stroke	8.27	[cm]
Clearance Volume	99.0	[cm ³]
Compression Ratio	4.82	
Speed	600	[rpm]
Manifold Pressure	47.5	[kPa]

dispersion of the spectrograph, are selected such that scattered light from all major species of combustion is imaged onto the array, from CO_2 at 571 nm to H_2O at approximately 660 nm.

The detector employed is an unintensified, cryogenically-cooled, 1024×1024 back-illuminated CCD array, with a (typical specification) quantum efficiency that exceeds 85% over the wavelength range of interest. Due to the lack of an image intensifier, the camera cannot be gated quickly and interference from combustion luminosity necessitates a skip-fired mode of engine operation. This additional complication is outweighed by the high quantum efficiency; typical intensified cameras are characterized by an effective quantum efficiency (accounting for the intensifier noise factor) of approximately 5% (Paul, *et al.*, 1990) in this wavelength range. Because of the limited height of the spectrograph entrance slit, only 75% of the vertical extent of the array is used. Data are obtained in two formats: high-resolution 512×384 images obtained using 2×2 charge binning on the CCD array; and low-resolution 16×12 images obtained binning the charge into 64×64 pixel "superpixels". This massive charge binning is required for instantaneous measurements, where the spatial and spectral signal integration is performed on-chip to minimize the contributions from measurement noise. Employing 64×64 superpixels, the combined contribution from thermally generated dark-noise, spurious charge generation, and electronic read-noise can be characterized by a normally-distributed, random noise source with a standard deviation of $11 e^-$ (Miles, 1998). Thus, for signals greater than approximately $120 e^-$, the measurement is expected to be limited by photoelectron shot-noise. Approximately 600 signal photoelectrons are expected from each superpixel from both CO_2 and H_2O under the measurement conditions employed. Signals from the remaining species are considerably higher.

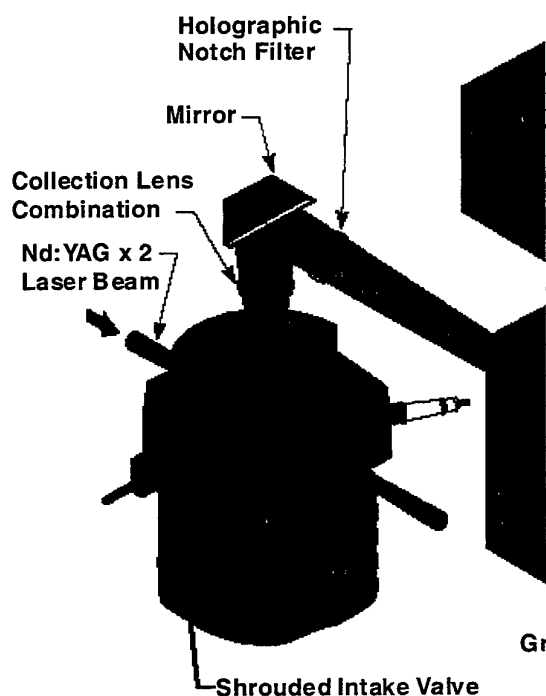


Figure 1: The side-valve research engine and layout of the optical diagnostic system

4. EXPERIMENTAL PROCEDURE

The engine is run slightly lean with premixed propane fuel at an equivalence ratio of 0.96. As mentioned above, a skip-fired mode of operation is employed, wherein the engine is fired three consecutive times and the ignition disabled on the fourth cycle, during which the data are obtained at top dead center (TDC) firing. It was demonstrated that, had it been fired, the combustion performance of the fourth cycle would have been equivalent to that of steady-state operation. To investigate scavenging efficiency after a misfire, an additional motored cycle is added, and data are also obtained at TDC firing of

this fifth cycle.

To simulate cold-start conditions, the engine cooling water is maintained at 21°C . The engine is brought to speed (600 rpm) under motored operation, the ignition enabled, and data acquisition commences after speed stabilization. This start-up procedure required 33 seconds; $2/3$ of which represents motored operation. Data acquisition thus began approximately 11 seconds after first-fire, or, roughly, after 55 engine cycles ($3/4$ of which are fired). 200 single-cycle, low-resolution images are acquired over the next 800 engine cycles, followed immediately by a high-resolution image, cycle-averaged over an additional 400 cycles (100 measurements). During this data acquisition sequence, films of condensate were observed to form on the large cylinder head window. High levels of scattered light also implied the presence of films on the beam entrance and exit windows. These films persisted through the end of the sequence, by which time the cooling water leaving the head had risen in temperature to approximately 24°C . Finally, with the engine stopped and positioned at TDC overlap, air reference spectra for background determination were acquired while flowing air through the engine. During acquisition of the reference

spectra, the films on the windows were observed to shrink but not to disappear.

After allowing the engine to cool, this procedure was repeated with data obtained every fifth cycle, as described above. To investigate the effect of the in-cylinder flow field on the scavenging performance, data were obtained both in the nominally quiescent flow generated by an unshrouded intake valve and in the highly swirling flow ($R_i \approx 10$) created by the shrouded intake valve.

5. SAMPLE DATA AND DATA REDUCTION

A sample high-resolution image, obtained in the quiescent engine flow, is shown in Fig. 2. In contrast to equivalent images obtained under fully-warmed up conditions (Miles and Hinze, 1998), the levels of background light are considerably higher. The elevated background is attributed to the formation of condensate films on the combustion chamber windows and increased elastically scattered light from these films which is insufficiently rejected. Note from the spectrum shown at the bottom of Fig. 2, generated by summing the columns of the image above, that the (spatially) integrated signals remain well defined on a variable background level. The background level can be fit quite accurately in the vicinity of the H_2O and C_3H_8 signals. In the CO_2 and O_2 region, however, the background determination is more ambiguous. To assist with background fitting in this region, the air reference spectra described above are used. Due to the variable film size during acquisition of these spectra, however, uncertainties in the appropriate form of the background are introduced. Thus, the mole fractions of CO_2 and O_2 deduced from the cycle-averaged images are less reliable than the mole fractions of C_3H_8 and H_2O .

Superposed on the image in Fig. 2 is a light-colored grid which depicts the spatial and spectral integration regions defined by the superpixels employed while acquiring the single-cycle images. Due to the extent of the spectral binning, and to the single-cycle shot-noise on the background light, it is even more difficult to fit background spectra accurately to the single-cycle spectra. In previous work, under fully-warmed up conditions, the constancy of the background was used to deduce the appropriate background level in the single-cycle images from the background levels measured in a cycle-averaged image. This strategy is not appropriate here, however, due to the development of films on the combustion chamber surfaces during these cold start simulations, and the subsequent evolution of the

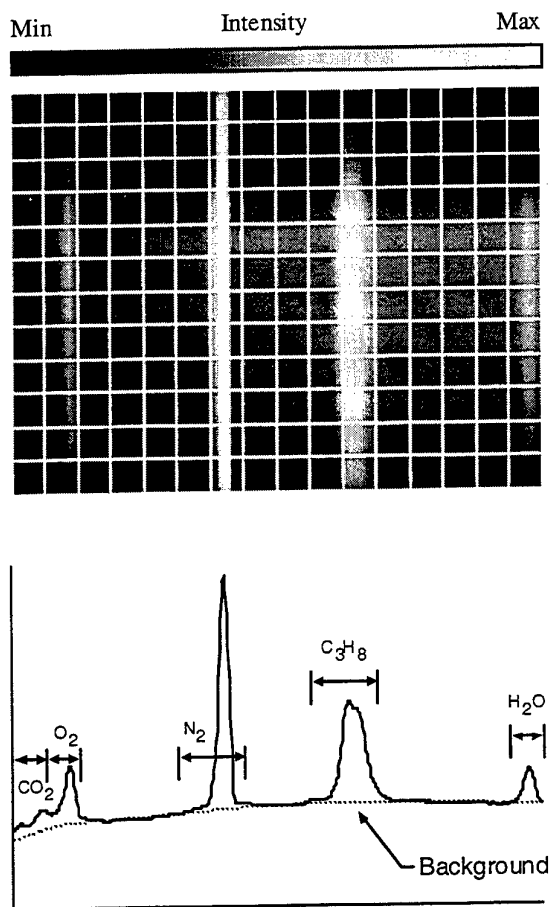


Figure 2: Cycle-averaged image and corresponding spectrum obtained in the quiescent flow.

background level. Quantitative species mole fractions are therefore not easily determined from this single-cycle data. Nevertheless, evidence for preferential scavenging of the combustion by-products can be obtained from the trends observed in the data. The remaining discussion of the data reduction methodology focuses on the identification of these trends within the larger trend associated with film formation and background drift.

From each single-cycle image, a spatially and spectrally integrated "signal" for each species is obtained by summing the appropriate column(s) of the image. These signal values are proportional to the molecular number density of each species, averaged over the 10.9 mm beam length, plus an offset associated with the background light. From consecutive single-cycle images (with images obtained every fourth engine cycle), data sequences are constructed for each species. To separate the background drift from the underlying trends in the

data, a drift sequence $d_j = d_1 + d_2 + \dots + d_{n-1} + d_n$ is defined from the measured N_2 sequence N_j by subtracting the mean signal value:

$$d_j = N_j - \langle N \rangle \quad (2)$$

The projection of any data sequence S_j onto this drift sequence can then be subtracted from the original data sequence to give a drift corrected sequence \hat{S}_j :

$$\hat{S}_j = S_j - \frac{(S, d)}{(d, d)} d_j \quad (3)$$

where (a, b) denotes the standard inner product between sequences a and b .

This technique for background drift removal assumes that the temporal evolution of the background is self-similar for each signal, and can be determined from the temporal evolution of the N_2 signal. Implicit here is the expectation that the true N_2 signal does not change with time. Because the fresh charge is provided to the engine at a constant mass flow rate, metered through critical orifices, the amount of fresh N_2 inducted in each cycle is expected to be approximately constant. Any changes in the charging process associated with engine warm-up will be compensated for automatically by a rising or falling manifold pressure, such that the inducted mass per cycle remains constant. There are, however, at least two mechanisms by which the N_2 signal can be envisioned to change with time: first, by changes in the residual gas mole fraction, and second, via preferential H_2O scavenging.

The first mechanism will be associated with either an increase or decrease in the trapped mass within the cylinder, with a corresponding increase or decrease in the N_2 signal levels. The drift sequence will thus have components associated with both background drift and temporal changes in the N_2 number density. The component associated with the N_2 number density changes may mask changes in the true signal levels associated with H_2O and CO_2 , making changes in the trapped residual mass difficult to detect. This same component, however, would introduce variations in the O_2 and C_3H_8 signals, which are expected to remain constant. By examining the corrected sequences from these fresh charge species, then, it is expected that significant temporal changes in the residual mass can be detected.

Poor scavenging of H_2O , the second mechanism, can increase the trapped mass of N_2 by effectively enriching the N_2 mole fraction in the recycled exhaust gases (because H_2O has been removed). Thus, for the same volume of trapped, gas-phase residual gas, a greater amount of N_2 is present when the proposed preferential scavenging mechanism is operative. It can be shown, however, that this effect is minimal. For sufficient H_2O condensation to double the trapped mass of H_2O , the mass of trapped N_2 is expected to increase by only 0.6%. After applying the above drift correction, this increase in N_2 signal could only mask an increase in the H_2O signal on the order of 2%.

5. RESULTS AND DISCUSSION

Single-cycle, temporal sequences of the signals from superpixels identified with N_2 , C_3H_8 , and H_2O , obtained in the quiescent engine flow, are shown in Fig. 3. The equivalent sequences obtained in the swirling engine flow are shown in Fig. 4. Also shown for reference are sequences corresponding to N_2 obtained under fully-warmed up conditions, in which scattering from condensate films does not occur. Note that in both engine flows a significant temporal variation in the data sequences is observed. Furthermore, based on the N_2 sequence, it is apparent that a large portion of this trend is associated with background drift.

Focusing on Fig. 3, it can be seen that the fluctuations in each sequence are very well correlated from species-to-species. Data obtained under warmed up conditions indicate that in this nominally quiescent engine flow the in-cylinder fluid is well-mixed by TDC, and cycle-to-cycle variations in residual gas mole fraction are approximately 0.005 (Miles and Hinze, 1998). Similarly, it has been shown that under these conditions (no films on the combustion chamber windows), the fluctuations in the background levels from cycle-to-cycle are determined by the statistical shot-noise on the background (Miles, 1998). The large, correlated fluctuations seen in Fig. 3 are thus indicative of cycle-to-cycle fluctuations in scattering from films. In Fig. 4 no such clear correlation in the fluctuations is observed. This is due to two factors: the lower overall magnitude of scattering from films which occurs with this engine flow (implying smaller films); and the higher fluctuations in residual gas mole-fraction, as inferred from the data obtained under fully warmed up conditions.

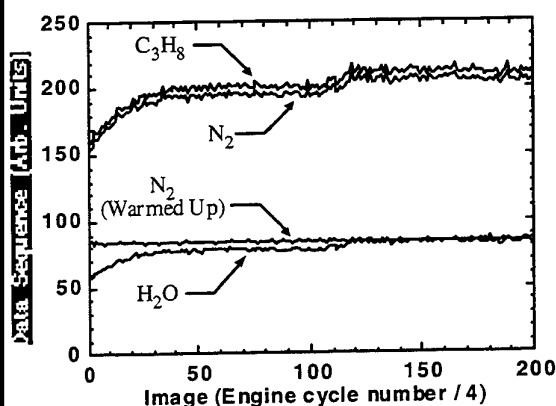


Figure 3: Single-cycle data sequences measured in the quiescent engine flow.

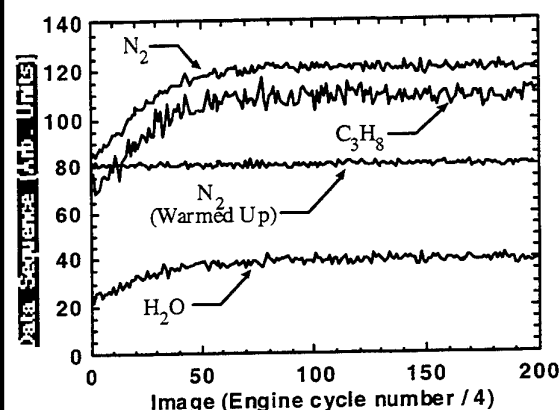


Figure 4: Single-cycle data sequences measured in the swirling engine flow.

Another feature apparent from Figs. 3 and 4 is the relatively steady state of the data sequences near the end of the set of single-cycle images. The asymptotic levels are very close to the levels obtained from the cycle-averaged images obtained immediately afterward*. For example, in the quiescent flow, the cycle-averaged signal levels in units corresponding to Fig. 3 are 210 and 80 for C_3H_8 and H_2O , respectively. In the swirling flow the respective cycle-averaged signal levels are 98 and 35 (cf. Fig. 4). This implies that neither the films nor the mean species number densities are evolving significantly beyond

Table 3
Residual Gas Mole Fraction Determined from Each Major Species Scavenging Cycle

Species	Quiescent Flow	Swirling Flow
CO_2	0.203	0.185
O_2	0.248	0.266
C_3H_8	0.268	0.262
H_2O	0.291	0.295

approximately image 50 in the sequences shown** or roughly 250 engine cycles (50 sec) after first-fire. Thus, the residual gas mole fraction, as determined from the measured species mole fractions obtained from the cycle-averaged images, is likely representative of the residual gas mole fraction fairly early in the cold-start simulation. These residual gas mole fractions, determined by assuming complete combustion of the fuel-air mixture, are presented in Table 2 for both engine flows investigated.

In Table 2, no evidence of significant levels of preferential scavenging is observed, as the residual gas mole fractions derived from the H_2O mole fractions are generally consistent in magnitude with the residual gas mole fractions derived from the remaining species. Nevertheless, residual mole fractions derived from H_2O are typically 10-15% higher than those derived from the other species. These differences, particularly the difference between the estimates from H_2O and C_3H_8 , may be due in part to the precision of the cycle-averaged measurements (about 5%, at worst, under warmed-up conditions) and in part to inaccuracies in the system calibration. Temperature variation in the scattering cross-sections is insufficient to result in differences of this magnitude. The higher than expected measured H_2O content may also be due to two physical factors: a small level of H_2O condensation resulting in poor scavenging, or a small contribution due to Raman scattering from films on the windows.

To help illuminate the cause of the higher than expected water content, the residual gas mole fractions determined from the individual species after a non-fired scavenging cycle are presented in Table 3. There, it is observed that while the mole fractions estimated from the individual species are again generally consistent in magnitude, the residual mole fraction estimated from H_2O is no longer significantly larger than the estimates from the other species, particularly the (most reliable) C_3H_8 estimate. This

* This comparison is possible because both the single-cycle and the cycle-averaged data have been normalized by the measured laser energy delivered during the acquisition of each image.

** Excepting the rather anomalous change in background level observed in Fig. 3 between image 100 and image 120.

behavior is consistent with *more* efficient scavenging of H_2O than the other residual gas species.

Comparing the reduction in residual H_2O after one scavenging cycle between the quiescent and the swirling flow, it is observed that the reduction is greatest for the swirling flow. This is consistent with the hypothesis that the (smaller) films formed in the swirling engine flow are more rapidly vaporized by the in-cylinder flow, leading to a reduction in the apparent H_2O mole fraction after an additional scavenging cycle. Both the apparent better scavenging of H_2O in the swirling flow, and the apparent more efficient scavenging of H_2O discussed above, suggest that the higher than expected H_2O content is likely due to Raman scattering from window films.

Comparison of Tables 2 and 3 also reveals slow scavenging of residual gases, as compared to the intuitively expected $(1 - \eta_{\text{scav}})^n$ dependency of the residual gas mole fraction on the number of scavenging cycles n and the scavenging efficiency η_{scav} . Slow scavenging of H_2O was also observed by Grünefeld, *et al.* (1995), who attribute it to a preferential scavenging mechanism. Here, however, slow scavenging is evidenced by all the major species. Similar slow scavenging has been reported by Galliot, *et al.* (1990).

Finally, it is interesting to note that the cycle-averaged residual gas mole fractions measured in these cold-start simulations are somewhat higher than those measured under warmed up conditions: 0.24 and 0.34 in the quiescent and swirling flow, respectively.

Following the drift correction procedure outlined above, the data sequences corresponding to Figs. 3 and 4 have been corrected for background drift. The drift corrected sequences for the quiescent flow are shown in Fig. 5; corrected sequences obtained in the swirling flow are similar and are not shown here. The single notable observation from Fig. 5 is that the drift correction procedure has removed all obvious secular trends in the data sequences. The only data sequence which demonstrates a possible remaining trend in the data is the H_2O sequence obtained in the quiescent engine flow. This sequence is shown in expanded form by the dotted line in Fig. 6. Smoothing by convolution with an 11-point rectangular window serves to highlight the remaining trends in the data; the smoothed sequence is shown by the solid, heavy line. Although some trends remain, comparison with the scale* in the lower left corner of the figure

* The scale is derived from the following cycle-averaged image

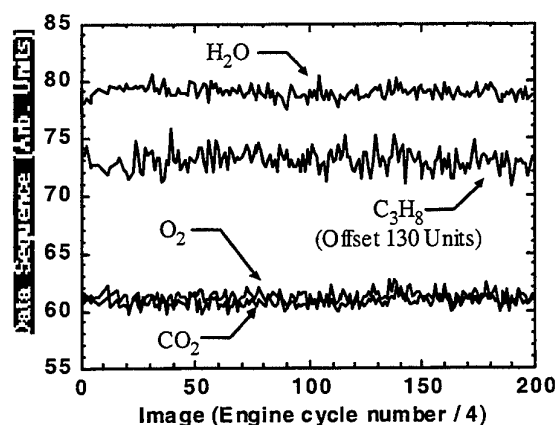


Figure 5: Drift corrected data sequences obtained in the quiescent engine flow.

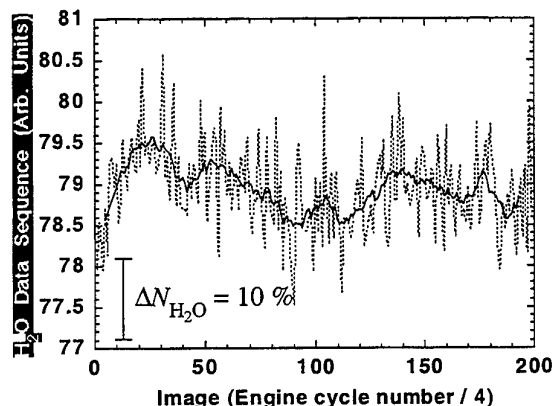


Figure 6: Smoothed and expanded representation of the H_2O data sequence in Fig. 5.

indicates that these trends correspond to a rather small (about 10%) change in the H_2O number density. As noted above, the correction procedure is unlikely to mask a change in H_2O mole fraction associated with poor scavenging of H_2O . The implication from Fig. 6 is that if a mechanism resulting in poor H_2O scavenging is operative, it reaches a relatively steady-state after approximately 11 seconds of engine operation, which corresponds to the beginning of the data sequence shown in Fig. 5. Because the cycle-averaged data discussed above suggest that any preferential scavenging effects at later times are small (if they exist at all), it is reasonable to conclude that the data presented here show no strong evidence for the existence of a preferential scavenging mechanism. If such a mechanism exists, it is significant only in the first few seconds of engine operation.

It should be noted, however, that this conclusion is subject to a few implicit assumptions:

- 1) The low compression ratio engine used here does not inhibit a preferential scavenging mechanism due to insufficient residual gas cooling during expansion.
- 2) The mixture composition obtained from a fairly small volume in the center of the cylinder is representative of (or scales with) the global cylinder composition. Note that H_2O vapor which evaporates from films on the combustion chamber walls may not have time to mix in to the center of the clearance volume by the time the data is acquired, even if data obtained in a warm engine indicate that the fresh charge is well mixed with the residual gases (*i.e.* in the quiescent engine flow).
- 3) The temporal evolution of the background light scattered from films is self-similar for each species, and can be determined from the temporal evolution of the N_2 signal.

Summary and Conclusions

Simultaneous, in-cylinder measurements of the major species of combustion are made using Laser Raman scattering with broadband signal detection under conditions simulating a cold start. Mean, cycle-averaged mole fractions of CO_2 , O_2 , N_2 , C_3H_8 , and H_2O are determined and compared for consistency. This comparison indicates that measured H_2O mole fractions are 10-15% higher than expected. Comparison with species mole fractions obtained after an extra scavenging cycle, as well as differences between the quiescent and swirling engine flow fields, suggest that these higher H_2O concentrations may be due to scattering from films on the window surfaces, rather than poor scavenging of H_2O due to condensation on the cold cylinder walls or other mechanisms.

Due to growth of films on the optical windows during the simulations, a time-varying signal background associated with film scattered light complicates determination of quantitative single-cycle species mole fractions. However, the temporal evolution of the signals, after correction for the varying background, can be examined for evidence of poor H_2O scavenging. Between approximately 11 sec (55 cycles) after the first fired cycle and 170 sec (855 cycles), the time period during which data was acquired, no evidence of significant variation in H_2O scavenging was observed.

References

Eckbreth, A.C. 1996, Laser Diagnostics for Combustion Temperature and Species, 2nd ed., Gordon and Breach, Amsterdam.

Galliot, F., Cheng, W.K., Cheng, C-O, Sztenderowicz, M., Heywood, J.B., and Collings, N. 1990, In-Cylinder Measurements of Residual Gas Concentration in a Spark Ignition Engine, SAE Paper No. 900485.

Grünefeld, G., Knapp, M., Beushausen, V., Andresen, P., Hentschel, W., and Manz, P. 1995, In-Cylinder Measurements and Analysis on Fundamental Cold Start and Warm-up Phenomena of SI Engines, SAE Paper No. 952394.

Miles, P.C. 1998, Raman Line-imaging for Spatially- and Temporally-Resolved, Multi-point, Multi-species Mole Fraction Measurements in an Internal Combustion Engine, Submitted to Appl. Optics.

Miles, P.C. and Hinze, P.C. 1998, Characterization of the Mixing of Fresh Charge with Combustion Residuals Using Laser Raman Scattering with Broadband Detection, SAE Paper No. 981428.

Paul, P.H., van Cruyningen, I., Hanson, R.K., and Kychakoff, G. 1990, High Resolution Digital Flow-field Imaging of Jets, Exp. in Fluids, **9**, pp. 241-251.

Takeda, K., Yaegashi, T., Sekiguchi, K., & Saito, K. 1995, Mixture Preparation and HC Emissions of a 4-Valve Engine with Port Fuel Injection During Cold Starting and Warm-Up, SAE paper No. 950074.

LASER DIAGNOSTICS OF NITRIC OXIDE INSIDE A TWO-STROKE DI DIESEL ENGINE

Genie G.M. Stoffels, Erik-Jan van den Boom, Charles M.I. Spaanjaars, Nico Dam, W.L. Meerts
and J.J. ter Meulen

Applied Physics, University of Nijmegen, the Netherlands

ABSTRACT

The Nitric oxide (NO) content and distribution within the combustion chamber of an optically accessible one-cylinder two-stroke direct-injection Diesel engine have been studied by means of Laser Induced Fluorescence. Using 193 nm excitation of NO, detection of the ensuing fluorescence at 208 nm and 216 nm allows determination of the in-cylinder NO content throughout the whole combustion cycle. Images of the two-dimensional NO distribution in a plane perpendicular to the cylinder axis have been recorded for crank angles larger than 31° after Top Dead Center. The measured NO fluorescence is transformed into an in-cylinder NO content taking into account the changing in-cylinder conditions and the spectroscopic interference of Oxygen fluorescence. It is concluded that, in this engine, the bulk of the NO formation takes place relatively late in the stroke, indicating that most of the NO is formed during the diffusion burning phase.

1. INTRODUCTION

Strategies for the reduction of toxic emissions from Diesel engines focus on particulates (soot) and oxides of Nitrogen (NO_x). Although both of these components are formed during combustion, legislation is concerned only with the exhaust products. Emission control therefore aims at either catalytic exhaust gas after-treatment or at combustion optimisation, where optimisation is taken to imply reduced toxic compound formation while (at least) maintaining combustion efficiency. Combustion optimisation, arguably the more fundamental way of tackling the emission problem, poses a huge challenge both to experimental data acquisition and interpretation, and to theoretical combustion modelling. This paper intends to contribute to the former aspect. We have used non-intrusive optical diagnostics, based on Laser Induced Fluorescence, to monitor the amount as well as the distribution of

Nitric oxide (NO) inside the combustion chamber of a Diesel engine.

Laser based optical diagnostics of combustion processes are appreciated for their ability to combine non-intrusiveness with selectivity for specific chemical species. As such, they have been applied both to open flames and to internal combustion engines. A review can be found in e.g. Eckbreth (1988) and Rhoté and Andresen (1997). Among the manifold of optical techniques available, only Laser Induced Fluorescence (LIF) has the sensitivity to provide instantaneous, two-dimensional (2D) information on minority species distributions in combustion processes. The measurement principle of this planar LIF (PLIF) technique involves electronic excitation of the molecules of interest by a thin sheet of laser radiation, and detection of the subsequent fluorescence in a direction perpendicular to the sheet by an intensified CCD camera. PLIF has been used to demonstrate the presence of a large number of specific small molecules in a variety of combustion environment, but in general the observed data are very hard to quantify. Although in principle the LIF intensity is linearly proportional to the local number density of laser-excited molecules, the proportionality constant depends on the local physico-chemical environment, involving local temperature, density, chemical composition and possibly spectroscopic interference by other molecules. Since these parameters are usually difficult to assess simultaneously with the (P)LIF measurements, one must have recourse to model assumptions.

The present paper reports LIF and PLIF measurements of the NO density within the combustion chamber of a small, two-stroke direct-injection (DI) Diesel engine, running on standard Diesel fuel. NO fluorescence distributions and dispersed fluorescence spectra are presented as a function of crank angle throughout the whole stroke, and ways towards their semi-quantitative interpretation are discussed.

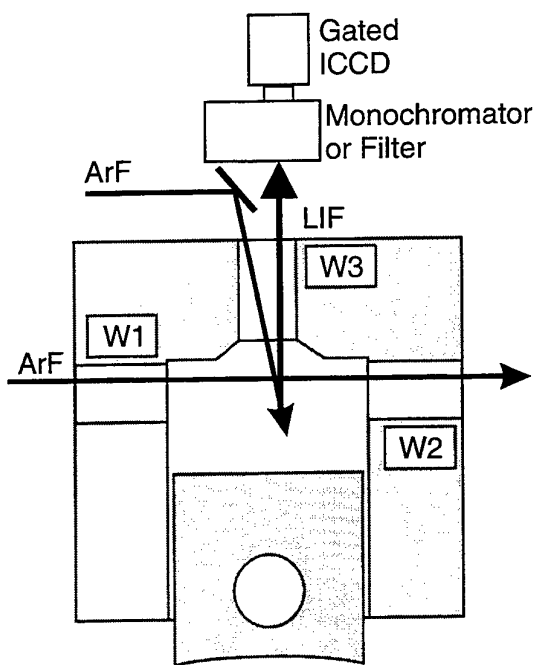


Figure 1: Schematic view of the optically accessible Diesel engine and the optical setup. The excimer laser beam (ArF) either traverses the combustion chamber (as a thin sheet parallel to the piston upper surface) through the two side windows (W1 and W2), or it is used unfocused to illuminate the combustion through the top window (W3). Fluorescence (or natural flame emission) is observed through the top window by an intensified CCD camera (ICCD) positioned behind either a narrow-band reflection filter (used for imaging) or a monochromator (used for fluorescence dispersion).

2. ENGINE AND OPTICAL SETUP

All measurements are performed on a one-cylinder, two-stroke, DI Diesel engine (Sachs; bore 81 mm, stroke 80 mm, swept volume 412 cc) that has been made optically accessible by mounting quartz (Suprasil I) windows in the cylinder wall as well as centrally in the cylinder head (see fig. 1; W1-3). A flat piston with a shallow slot (0.5 mm depth) in its upper surface was used to provide optical access through the side windows throughout the whole engine cycle. The engine is operated steadily running (1200 rpm) on standard Diesel fuel, obtained from a local retailer, and was loaded by a water-cooled electric brake with up to 3.5 Nm (0.44 kW). Fuel is injected through a three-hole nozzle, located 6 mm above the piston surface at Top Dead Center (TDC). Fuel injection starts at 27° before Top Dead Center (bTDC). The exhaust port opens at 105° after Top Dead Center (aTDC), the inlet ports at 121° aTDC. Inlet air is supplied under an over-

pressure of typically 0.2 bar to improve scavenging. With a compression ratio of 13, the pressure P , in the engine follows the curve shown in fig. 2a reaching a peak pressure of 75 bar slightly after TDC. The pressure curve is used together with the volume to calculate the mean temperature of the gas content inside the cylinder (see Heywood (1988)). This, so-called, mean gas temperature is given in fig. 2a (solid line) and reaches a maximum of 1470 K a few degrees after TDC. Combustion is seen to start at 15° bTDC, and natural flame emission can be observed up to about 60° aTDC. Its spectrum shows no additional structure at any crank angle, indicating that it is mainly due to light emission by glowing soot particles. The natural emission spectrum can be well fitted to a Planck black body radiation curve, and can be used to derive a so-called soot temperature from the glowing soot particles as a function of crank angle (Θ). These data, showing a temperature of about 2300 K at TDC have been, included in fig. 2b (■); details will be published elsewhere by Stoffels et al. (1998). In the figure, the dashed line represents the estimated gas temperature based on adiabatic expansion ($PV^\gamma = \text{constant}$, $\gamma = 1.36$) of an ideal gas during the later part of the stroke. It is matched to the experimental data at intermediate crank angles.

All (P)LIF measurements on NO employed a pulsed, tunable ArF excimer laser (Λ Physik Compex 350T; $\lambda = 192.9 - 193.9$ nm, bandwidth ≈ 0.7 cm⁻¹, 20 nsec pulse duration) to excite NO on the $R_1(26.5)$ transition of the $D^2\Sigma^+(v' = 0) \leftarrow X^2\Pi(v'' = 1)$ band at 193.337 nm as determined by Versluis et al. (1991). The laser is synchronised to the engine cycle with a precision of $< 0.6^\circ$ crank angle. It emits a beam with rectangular cross section, which, for the purpose of recording NO fluorescence distributions, is focussed down to a sheet of about 0.1 mm thickness and coupled into the engine through a side window (W1,2). The beam traverses the combustion chamber in a plane perpendicular to the cylinder axis (see fig. 1), and is located within the slot in the piston upper surface when the piston is at TDC. The laser illuminates the whole area beneath the top window, resulting in a measurement volume of 25×0.1 mm (diameter \times thickness). Fluorescence of NO is recorded through a 4-plate reflection filter, tuned to 208 nm center wavelength with a bandwidth of 5 nm (FWHM), through the top window (25 mm diameter; fig. 1) by a 576×384 pixels CCD camera (14 bits dynamic range) equipped with an image intensifier (Princeton Instr. ICCD-576G/RB-E) and a quartz $f/4.5$ 105 mm objective (Nikon). At this setting, the filter is centered on the

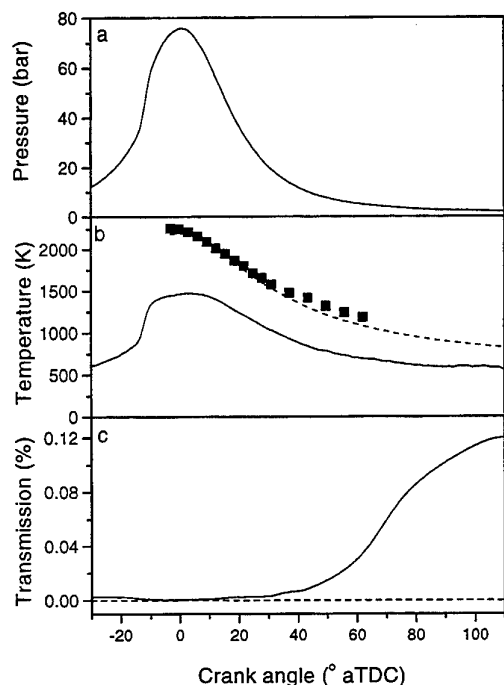


Figure 2: Parameters of the engine running steadily on standard Diesel fuel. a) The in-cylinder pressure b) Mean gas temperature derived from the in-cylinder pressure curve (solid line). Soot temperature derived from the flame emission spectrum (black body radiation; see text) (■). The dashed curve is based on calculations assuming adiabatic expansion of an ideal gas during the later part of the stroke. c) Transmission of the excimer laser beam (193 nm) through the firing engine.

NO $D(v' = 0) \rightarrow X(v'' = 3)$ fluorescence band. Mie scattering images were obtained in the same setup, but with the filter mirrors replaced by broad-band aluminium mirrors.

Alternatively, the unfocused laser beam can be coupled into the combustion chamber through the top window (W1). The advantage of this setup is that the laser beam enters the observation area immediately avoiding attenuation of the laser radiation in the first part of the combustion chamber. (Note, that the laser beam coupled in through the side window has to travel about 25 mm before entering the observation area.) In this case NO fluorescence is detected through the top window by the camera mounted behind an imaging monochromator (Chromex 250IS) with a 1200 gr/mm holographic grating blazed at 250 nm, as part of an Optical

Multichannel Analyser (OMA) setup, to spectrally disperse the fluorescence. For all fluorescence measurements the image intensifier was used with a gate width of 50 nsec, which was sufficient to collect all LIF (no signal increase for longer gate times) while keeping the contribution of the natural flame emission down to a manageable (and usually negligible) level. The latter was, however, always measured separately and subtracted from the LIF data.

3. DATA EVALUATION

Even though qualitative data on chemical species distributions within a combustion environment are of interest in themselves, one of the goals of our present research is to quantify the LIF data as much as possible. This will allow them to be compared throughout the stroke and for different engine operating conditions, different fuels and fuel injection systems, and so on. The LIF yield will be described using a model in which the energy level structure of NO is simplified to a 3-level system coupled to a 'bath' of all other levels by collisional energy transfer processes. Rotational energy transfer in the ground state will be neglected, because of the low laser intensity within the engine. In general the fluorescence yield $S_{LIF}(x, y)$ due to a local NO density $\rho_{NO}(x, y)$ can be written as

$$S_{LIF}(x, y) = \varphi I_L(x, y) A_F(x, y) g(\nu_L, \nu_0) f_{vJ}(T) \rho_{NO}(x, y) \frac{A}{A + Q}, \quad (1)$$

in which x and y are the spatial coordinates within the plane illuminated by the laser and φ is a proportionality constant including experimental parameters like optics collection efficiency, camera sensitivity, absorption line strength, etc. $I_L(x, y)$ denotes the local laser beam intensity, $A_F(x, y)$ describes the attenuation of the induced fluorescence emitted at (x, y) and $g(\nu_L, \nu_0)$ is the overlap integral of the laser line profile with the NO absorption spectrum. The temperature-dependent fractional population of the probed rovibrational state is described by the Boltzmann fraction $f_{vJ}(T)$ and the fluorescence yield is determined by the Stern-Vollmer factor $A/(A + Q)$, in which A denotes the spontaneous emission rate on the vibronic transition that is monitored and Q the effective non-radiative decay rate. The non-radiative decay processes that reduce the fluorescence yield are a result of intermolecular collisions and include both Electronic Energy Transfer (EET; notably $D \rightarrow A$ and $D \rightarrow C$) and quenching ($D \rightarrow X$).

In order to extract the NO density from the LIF signal S_{LIF} , all factors in eq. 1 have to be known.

Most of these factors depend on the position (x, y) and/or on the in-cylinder conditions (pressure, temperature, volume and laser beam intensity), and can therefore not be calibrated by *e.g.* an exhaust gas measurement. The evaluation of the individual factors of eq. 1 is discussed shortly below, a more extensive description is given by Stoffels et al. (1998).

Local laser intensity $I_L(x, y)$, Fluorescence attenuation $A_F(x, y)$: The laser intensity suffers severe attenuation on its way through the combustion chamber. Also the induced fluorescence is attenuated on its way to the top window. At larger crank angles (*i.e.* later in the stroke) these attenuations are expected to be caused mainly by scattering off and absorption by particulates, whereas at smaller crank angles absorption by still unburned fuel will also contribute as reported by Sick (1997). For the purpose of imaging an independent measure of the local laser intensity and the fluorescence attenuation is provided by Mie scattering, here understood to comprise elastic light scattering off small particles (regardless of their size). (Note, that in this case the little difference in wavelength between the laser radiation and the induced fluorescence is neglected.) On the assumption *i*) that laser intensity and fluorescence attenuation is mainly due to scattering off and absorption by small particles (oil, soot, fuel droplets) and *ii*) that there exists a linear relationship between scattering and absorption cross sections of these particles as described in Bohren and Huffman (1983), the local laser intensity and the fluorescence attenuation can be reconstructed from measurements of the local Mie scattered intensity combined with overall transmission measurements. Details of the reconstruction method will be published elsewhere by Stoffels et al. The overall transmission of 193 nm light through the firing engine is measured by coupling in and out the laser beam through the side windows and detecting the transmitted radiation behind the outcoupling window by a CCD camera. The result is given in fig. 2c. The rise in transmission around 60° aTDC coincides with the end of the visible combustion, suggesting that unburned fuel indeed plays an important part in absorption of 193 nm laser radiation (see also Sick (1997)). In the case that dispersed fluorescence spectra are obtained only the overall transmission is used to calculate the local laser beam intensity and the attenuation of the induced fluorescence.

Overlap integral $g(\nu_L, \nu_0)$: The overlap integral is calculated by assuming Gaussian profiles for both the laser emission line and the NO absorption line. Lacking data on the pressure broadening and shift of transitions in the $D(v' = 0) \leftarrow X(v'' = 1)$ band, for

the present purpose the functional pressure and temperature dependence of the $A \leftarrow X$ band as derived by Chang et al. (1992) is taken in combination with a proportionality factor that is derived from own measurements on the $D \leftarrow X$ band in the engine.

Boltzmann fraction $f_{vJ}(T)$: The temperature dependent fractional population of the probed state ($v''=1, J=26.5$) can be calculated using the well established spectroscopic data of the NO electronic ground state given in Huber and Herzberg (1979).

Stern-Vollmer factor $A/(A + Q)$: The spontaneous emission rate on the $D(v' = 0) \rightarrow X(v'')$ transition can be estimated from the radiative lifetime of the D-state ($\tau = 18$ nsec given in Radzig and Smirnov (1985)) and the appropriate Franck-Condon factor (0.165 for $v'' = 3$, calculated using the approximation by Nicholls (1981) and molecular data from Huber and Herzberg (1979)), yielding $A_{03} = 9.2 \cdot 10^6 \text{ sec}^{-1}$. The non-radiative decay rate Q poses a more serious problem. Although there is a considerable amount of data available for the NO A-state quenching (see *e.g.* Paul et al. (1993)), data for the D-state are all but lacking. Preliminary results of measurements on the D-state fluorescence yield under conditions of elevated temperature and pressure indicate that $D \rightarrow A$ EET by collisions with N_2 provide a very efficient decay channel as measured by Van den Boom et al. (1998). For the present purpose, we have simply assumed

$$Q = \bar{v}_{\text{rel}} \rho \sigma \gg A = A_{03}, \quad (2)$$

with $\bar{v}_{\text{rel}} = (8kT/\pi\mu)^{1/2}$ the relative velocity between collision partners, ρ the total number density and σ an effective quenching cross section taken to be independent of pressure and temperature.

In summary, using the above assumptions the local NO number density can be extracted from PLIF images and dispersed fluorescence spectra as

$$\rho_{\text{NO}}(x, y) \propto \frac{PT^{-1/2}}{g(\nu_L, \nu_0)f_{vJ}(T)} \frac{S_{\text{LIF}}(x, y)}{I_L(x, y)A_F(x, y)}, \quad (3)$$

where in the case of imaging $I_L A_F$ is reconstructed from separately recorded Mie scattering images as discussed above. Assuming the average NO density in an image or spectrum to also represent the average NO density in the whole cylinder, the total amount of NO can be written as

$$N_{\text{NO}} \propto V_{\text{cyl}} \rho_{\text{NO}}(x, y), \quad (4)$$

in which V_{cyl} is the in-cylinder volume (depends on crank angle).

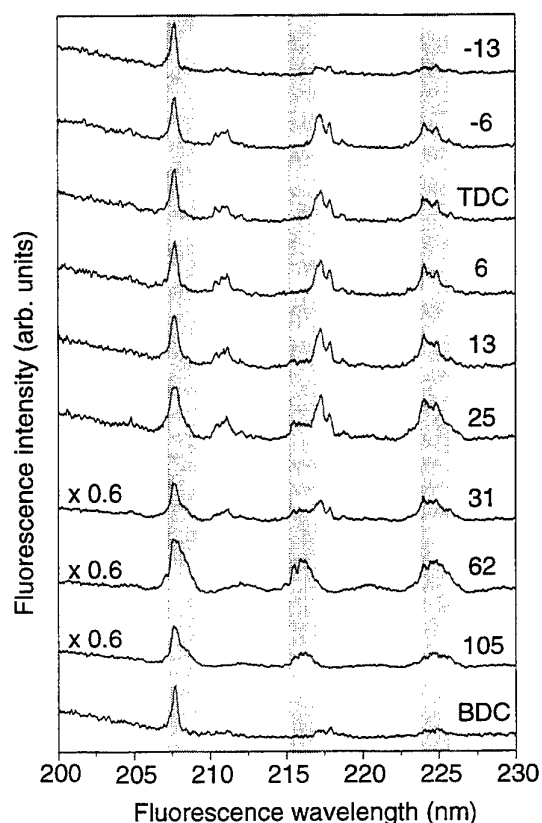


Figure 3: Dispersed fluorescence spectra of NO for different crank angles ($^{\circ}$ aTDC, indicated at the right), obtained by illuminating the combustion through the top window. All spectra are to the same scale unless indicated otherwise. The increasing intensity at the blue end of the spectra is due to directly scattered laser light. The persistent peak at 207.8 nm is due to quartz phosphorescence. The grey bars indicate the positions of the $D^2\Sigma^+(v'=0) \rightarrow X^2\Pi(v''=3,4,5)$ bands of NO.

4. RESULTS AND DISCUSSION

4.1 Dispersed Fluorescence Spectra

Figure 3 shows a typical series of dispersed fluorescence spectra (averaged over 100 engine cycles) for different crank angles, recorded with the OMA system ($50\text{ }\mu\text{m}$ entrance slit) and illuminating the combustion through the top window (fig. 1). All these spectra show a persistent peak at 207.8 nm, which, however, is an unfortunate artefact caused by laser induced phosphorescence of the quartz observation window. The spectral structure shows a considerable qualitative change around 30° aTDC. For $\Theta \lesssim 30^{\circ}$ aTDC two prominent fluorescence features are found at 211 and 217.5 nm, the latter with a persistent doublet structure even at TDC. Both features can be ascribed to fluorescence of hot Oxygen

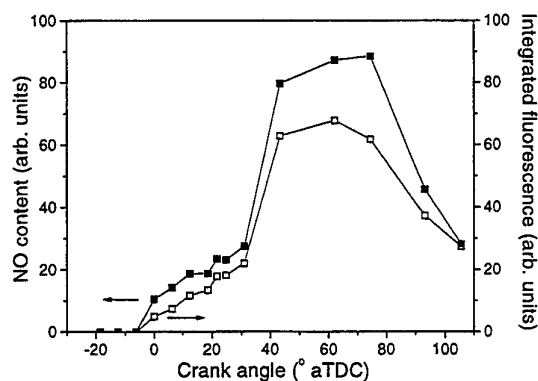


Figure 4: The integrated fluorescence signal of NO present inside the cylinder of the engine as a function of crank angle obtained from the spectra given in fig. 3 (\square). The NO content curve derived from the integrated fluorescence signal processed for the change in pressure, temperature, volume and laser intensity during the stroke (\blacksquare).

(O_2) that is also excited by the laser radiation from $v''=2,3$ as reported by Lee and Hanson (1986) and Shimauchi et al. (1994). For $\Theta \gtrsim 30^{\circ}$ aTDC these O_2 features disappear and are replaced by somewhat broader spectral structures around 208 nm (red shoulder on the quartz phosphorescence peak), 216 and 225 nm. These features arise from fluorescence out of the laser-excited $D(v'=0)$ -state to the $X(v''=3,4,5)$ -states, respectively. The two indistinct emission signals at 212.5 and 220 nm result from fluorescence out of the $C(v'=0)$ -state, populated by Electronic Energy Transfer (EET), to the $X(v''=3,4)$ -states. Fluorescence bands of NO and O_2 coincide in the 225 nm region, which is the reason why the spectrum in this wavelength region is relatively invariant. The shape of the 225 nm band does, however, change from a multiple-peaked structure (characteristic for O_2 , due to strong predissociation of the upper state described in e.g. Kruppenie (1972) and Wodtke et al. (1988)) for $\Theta \lesssim 30^{\circ}$ aTDC to a structureless bump (characteristic for NO) at $\Theta \gtrsim 30^{\circ}$ aTDC.

Even though the NO fluorescence is most evident in the spectra for $\Theta \gtrsim 30^{\circ}$ aTDC, it should be stressed that NO fluorescence can be recognized in all spectra for $\Theta \geq \text{TDC}$.

4.2 The in-cylinder NO content

The intensity of the NO fluorescence peaks in the dispersed fluorescence spectra provide information about the amount of NO present inside the cylinder at different crank angles. To compare the

peaks of the spectra at different crank angles and engine conditions it is necessary to convert the NO fluorescence into more quantitative data. To this end the NO fluorescence signal of the $D(v' = 0) \rightarrow X(v'' = 4)$ band at 216 nm (right at the blue side of the O_2 band at 217.5 nm and clearly visible in the spectra for $\Theta = 25^\circ$ aTDC and $\Theta = 31^\circ$ aTDC) is fitted to a Gaussian curve taking into account the structures due to O_2 fluorescence. The integrated fluorescence yield obtained from the spectra presented in fig. 3 is given in fig. 4 (\square). To arrive at a measure for the NO density as a function of crank angle (eqs. 3 and 4) the integrated fluorescence yield has been processed according to the prescriptions discussed above (Data evaluation section). In the processing the in-cylinder pressure, mean gas temperature and transmission data given in fig. 2 are used. A curve that is proportional to the NO content within the cylinder, obtained from evaluation of the integrated fluorescence signal of the spectra in fig. 3 (given as (\square) in fig. 4) is also presented in fig. 4 (\blacksquare). It shows a steep rise starting at $\Theta \approx 30^\circ$ aTDC and reaches a maximum around 75° aTDC followed by a more gradual decline during the later part of the stroke. Similar curves have been measured in several different runs, as well as for various engine operating conditions and fuels. Because the fluorescence yield curves obtained for several engine runs reproduce well, the accuracy of the NO content curve will be determined mainly by the precision of the fluorescence yield processing method. Although the general relationship between the fluorescence yield and the NO content is well established (eq. 1) some errors will be introduced by the uncertainties involved in some of the factors of the signal processing. Another systematic error will be caused by the use of the mean gas temperature. During the actual combustion, the local temperature at the place the NO is formed is probably higher, as the cylinder contents are not in thermal equilibrium at that moment. Because the NO molecules are excited from a vibrationally excited state results the use of the mean gas temperature to calculate the population of the lower level in a too low population around TDC, where the actual temperature is probably higher. This may lead to an overestimation of the relative NO density at smaller crank angles. However because these are systematic errors that appear in all NO content curves they do not affect the relative differences between curves and NO content curves at different engine conditions can be compared. The curve in fig. 4 (which is typical for this engine) shows that, in this particular engine, the bulk of NO formation takes place

relatively late in the stroke, indicating that the premixed combustion contributes only little and most of the NO is formed during the diffusion burning phase. This result is in agreement with theoretical predictions by the group of Pitsch et al. (1997). They also agree with recent results from Dec and Canaan (1998) and Nakagawa et al. (1997). Images presented by Dec and Canaan (1998) showed that NO formation starts around the jet periphery just after the diffusion flame forms and continues in the hot post-combustion gases, at places where the reacting fuel jet had traveled. However, it is in contrast with the models that predict that the premixed combustion has a large contribution to the NO formation and NO_x emissions correlate with the amount of fuel consumed during the initial premixed burn as described in e.g. Heywood (1988) and Warnatz et al. (1996).

A second conspicuous feature of the NO curves in fig. 4 is their decline towards larger crank angles. This can partly be explained by the fact that NO is chemically not particularly stable, and will be converted to NO_2 during the colder part of the stroke. (Note that Diesel engines operate under lean conditions, so there will be O_2 left after the combustion has subsided; see e.g. Heywood (1988).) This would lead to a reduction of the NO content in the engine, which has, in fact, been predicted by calculations of Pitsch et al. (1997), albeit not to the extent observed in fig. 4.

4.3 Two-dimensional NO distributions

The spectra shown in fig. 3 have some consequences for PLIF measurements that aim at recording 2D NO distributions. Excitation-emission spectra recorded in the two-stroke engine at $\Theta = 43^\circ$ aTDC have shown that all strong NO transitions (within the ArF laser tuning range) lie close to some O_2 resonance, so that efficient excitation of NO unavoidably also involves some overlap with an O_2 transition within the laser bandwidth as also reported by Lee and Hanson (1986) and Shimauchi et al. (1994). Evidently, since O_2 excitation can not completely be avoided, the NO band(s) should be filtered out of the total fluorescence. In our case, the $D(v' = 0) \rightarrow X(v'' = 3)$ NO fluorescence band at 208 nm was used for imaging, because it lies relatively isolated from O_2 fluorescence bands (nearest neighbours observed at 205 nm and 211 nm), and is also sufficiently distant from the excitation wavelength to avoid contributions of Mie scattered laser radiation.

However, the fluorescence distributions recorded this way cannot immediately be interpreted as NO

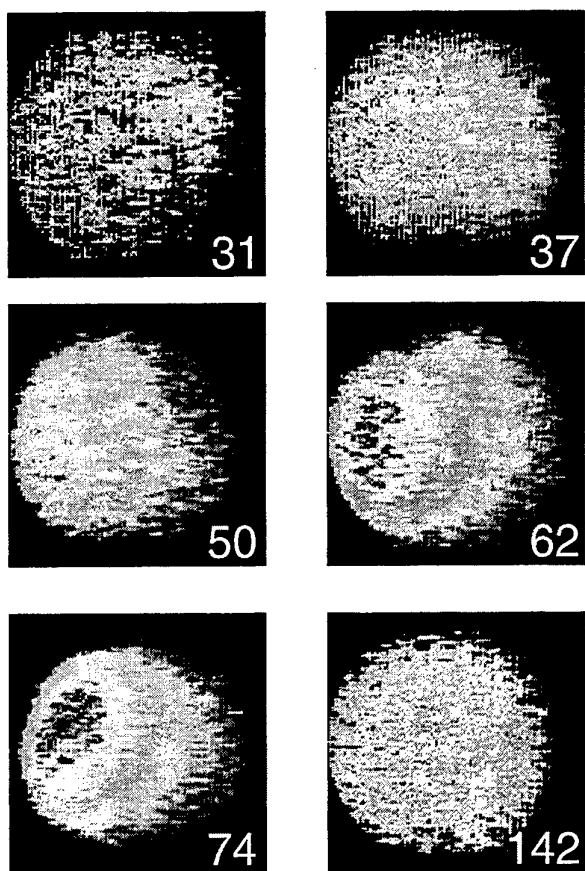


Figure 5: NO distributions, averaged over 25 engine cycles, corrected for local laser intensity variations. Crank angles are indicated in the images. The laser beam travels from left to right and fuel is injected from the bottom of the images upwards. Images are individually scaled.

density distributions, because the intensity of the laser beam is not uniform over the whole image. The local laser intensity was reconstructed from the local Mie scattered intensity by the method briefly discussed above. NO distributions (diameter 25 mm, individually scaled) averaged over 25 engine cycles processed for the local laser intensity are given in figure 5. To the extent that quenching and other collisional energy transfer processes are, at least on average, uniform over the field of view, the images represent NO distributions in arbitrary units (that is, the local pixel values are proportional to the local NO density). Since they are individually scaled to enhance contrast, only the distributions should be compared, not the intensities.

For $\Theta \lesssim 35^\circ$ aTDC the NO fluorescence signal is weak, and, since at these crank angles the Mie scattering images used for reconstruction of the lo-

cal laser intensity may contain a contribution from the flame luminosity, the fluorescence distribution is hard to interpret. At larger crank angles the signal level improves considerably. The formation of NO is seen to be concentrated in the leftmost part of the observation area, slowly spreading into a more uniform distribution as the crank angle increases. At 142° aTDC, when both inlet and outlet ports are open, a uniform distribution of the remaining NO is seen. (Note that the plane of observation is located high in the cylinder, whereas the scavenging ports are located near the position of the piston at BDC.) Since also the distribution of scattering particles is concentrated in the left-hand part of the observation region (data not shown), the images point to the occurrence of a reproducible flow pattern inside the cylinder of this engine.

5. CONCLUSION

The NO formation inside the combustion chamber of a DI Diesel engine operated on standard Diesel fuel has been studied throughout the whole engine cycle using ArF excimer laser induced fluorescence. LIF images visualise the two-dimensional NO distribution in a plane located 6 mm below the fuel injector. Dispersed fluorescence spectra have been used to obtain a semi-quantitative measure (up to a calibration constant) for the amount of NO present in the cylinder at any crank angle. The post-processing procedures that must be used to extract a NO content from the LIF signal strength are discussed. The results for this particular engine show a relatively late start of the NO formation with a steep rise at about 30° aTDC. The NO content reaches a maximum at about 75° aTDC after which it gradually decreases.

Our results show the feasibility of obtaining semi-quantitative data on the NO distribution in a fairly realistic Diesel engine by means of ArF laser diagnostics. Great care must be taken to avoid spectroscopic interference of, particularly, Oxygen. In order to arrive at these data, a number of assumptions has had to be made, the substantiation of which has to be part of future research. Notably, this concerns *i*) information on collisional energy transfer involving both the ground state (RET) and the electronically excited $D^2\Sigma^+$ -state (EET) for different collision partners, *ii*) data on pressure broadening and shifting of NO absorption lines and *iii*) methods to assess the local in-cylinder laser intensity.

ACKNOWLEDGEMENTS

It is a pleasure to acknowledge the expert technical assistance of especially L. Gerritsen and P. van

Dijk of the workshop of the University of Nijmegen, as well as the help of E. van Leeuwen during the build-up phase of the project. This research is supported by the Technology Foundation (STW), the Netherlands Organization for Applied Scientific Research (TNO) and Esso.

REFERENCES

- Bohren, C.F. & Huffman, D.R. 1983, Absorption and scattering of light by small particles, Wiley, New York.
- Chang, A.Y., DiRosa, M.D. & Hanson, R.K. 1992, Temperature Dependence of Collision Broadening and Shift in the NO A \leftarrow X (0,0) Band in the Presence of Argon and Nitrogen, J. Quant. Spectrosc. Radiat. Transfer vol. 47, pp. 375-390.
- Dec, J.E. & Canaan, R.E. 1998, PLIF Imaging of NO Formation in a DI Diesel Engine, SAE transactions, pp. 79-105, paper no. 980147.
- Eckbreth, A.C. 1988, Laser Diagnostics for Combustion Temperature and Species, Abacus Press, Tunbridge Wells, UK.
- Heywood, J.B. 1988, Internal Combustion Engine Fundamentals, McGraw-Hill, Singapore.
- Huber, K.P. & Herzberg, G. 1979 Molecular spectra and molecular structure IV. Constants of diatomic molecules, van Nostrand Reinhold, New York.
- Kruppenie, P.H. 1972, The Spectrum of Molecular Oxygen, J. Chem. Phys. Ref. Data, vol 1, pp. 423-534.
- Lee, M.P. & Hanson, R.K. 1986, Calculations of O₂ Absorption and Fluorescence at Elevated Temperatures for Broadband Argon-Fluoride Laser Source at 193 nm, J. Quant. Spectrosc. Radiat. Transfer, vol. 36, pp. 425-440.
- Nicholls, R.W. 1981, Approximate Formulas for Frank-Condon factors, J. Chem. Phys., vol. 74, pp. 6980-6981.
- Nakagawa, H., Endo, H., Deguchi, Y., Noda, M., Oikawa, H. & Shimada, T. 1997, NO Measurements in Diesel Combustion Based on Laser-Sheet Imaging, SAE transactions, pp. 187-196, paper no. 970874.
- Paul, P.H., Gray, J.A., Durant Jr, J.L. & Thoman Jr, J.W. 1993, A Model for Temperature-dependent Collisional Quenching of NO A² Σ^+ , Appl. Phys. B, vol.57, pp. 249-259.
- Pitsch, H., Barths, H. & Peters, N. 1997, Modellierung der Schadstoffbildung bei der Dieselmotorischen Verbrennung, in Berichte zur Energie- und Verfahrenstechnik, ed. Leipertz, A., Heft 97.1, pp. 139-163, ESYTEC GmbH, Erlangen, Germany.
- Radzig, A.A. & Smirnov, B.M. 1985, Reference data on atoms, molecules and ions, Springer Verlag, Berlin.
- Rothe, E.W. & Andresen, P. 1997, Application of Tunable Excimer Lasers to Combustion Diagnostics: A Review, Appl. Opt., vol 36, pp. 3971-4033.
- Shimauchi, M., Miura, T. & Takuma, H. 1994, Absorption Lines of Vibrationally excited O₂ and HF in ArF Laser Spectrum, Jpn. J. Appl. Phys., vol. 33, pp. 4628-4635.
- Sick, V. 1997, Mehrdimensionale Laserspektroskopische Messung von Stickoxid in der Motorischen Verbrennung, in Berichte zur Energie- und Verfahrenstechnik, ed. Leipertz, A. Heft 97.1, pp. 177-190, ESYTEC GmbH, Erlangen, Germany.
- Stoffels, G.G.M., van den Boom, E.J., Spaanjaars, Dam, N., Meerts, W.L., & ter Meulen, J.J., In-Cylinder Measurements of NO Formation in a Diesel Engine, submitted to SAE.
- Van den Boom, E.J. et al. 1998, To be published.
- Versluis, M., Ebben, M., Drabbels, M. & ter Meulen, J.J. 1991, Frequency Calibration in the ArF Laser Tuning Range Using Laser-Induced Fluorescence of NO, Appl. Opt., vol. 30, pp. 5229-5232.
- Warnatz, J., Maas, U. & Dibble, R.W. 1996, Combustion, Springer Verlag, Berlin.
- Wodtke, A.M., Huwel, L., Schlüter, H., Voges, H., Meijer, G. & Andresen, P. 1988, predissociation of O₂ in the B-State, J. Chem. Phys., vol. 89, pp. 1929-1935.

INVESTIGATION OF OIL TRANSPORT MECHANISMS ON THE PISTON SECOND LAND OF A SINGLE CYLINDER DIESEL ENGINE, USING TWO-DIMENSIONAL-LASER-INDUCED FLUORESCENCE

Benoist Thirouard, Douglas P. Hart.

Sloan Automotive Laboratory
Massachusetts Institute of Technology
Cambridge, MA, U.S.A.

ABSTRACT

A two-dimensional-Laser-Induced-Fluorescence (LIF) system was developed to visualize the oil distribution and study the oil transport in the piston ring pack of a single-cylinder diesel engine through an optical window on the liner. The system gives high spatial and intensity resolutions so that detailed oil distribution on the piston as well as between the rings and the liner can be studied. This work primarily focused on investigating different oil transport mechanisms on piston second land under various engine operating conditions. Two mechanisms for the oil flow on the second land were identified, namely, inertia driven oil flow in the axial direction and oil dragging by gas flow in the circumferential direction. Finally, the effects of ring rotation were investigated.

1. INTRODUCTION

Reduction of oil consumption is required to satisfy three factors that currently govern the development of automotive engines: utilization of hydrocarbon resources, protection of the environment, and customer satisfaction. It is estimated that more than 50% of the engine oil consumption in automotive engines is from the piston ring pack. Consequently, the investigation of oil transport mechanisms at the interface between piston and liner is of critical importance.

The ring and groove geometry along with temperature and pressure conditions at the interface between piston and liner are the governing factors in oil flow. Due to lack of experimental data, the effects of these parameters on oil transport in the piston ring-pack were poorly understood. Thus, accurate prediction of oil consumption is nearly impossible.

LIF technique have been used for measuring oil film thickness of the piston ring-pack for some time [Hoult and Takigushi (1991), Shaw *et al* (1992),

Tamai (1995), Casey (1998), Takigushi *et al* (1998)]. In early works, LIF was implemented to make point measurements. A great deal of knowledge on the oil film thickness between rings and the liner and on the piston was gained by using these systems. However, the obvious limitation of point LIF is that it can only display the oil film at one location and is thus not able to simultaneously show the oil distribution in the piston ring-pack. When one intends to study oil transport in piston ring-pack, it was often found to be very difficult to interpret the data from these measurements without knowing the oil film in the surrounding region [Casey (1998)].

Inagaki *et al.* (1995) developed a two-dimensional oil film distribution measuring system, where a flash lamp was used as the light source. Even with a narrow window, their system demonstrated the benefits of having a two-dimensional view of oil distribution on a piston. In the current study, a two-dimensional oil distribution measuring system was developed utilizing a pulsed laser. The system was implemented in a single cylinder diesel engine with a 7mm wide window on the cylinder liner. Studies were conducted at varying engine operating conditions and utilizing different ring configurations. Several important oil transport mechanisms were identified. Theoretical models are presented to describe oil flow due to different driving forces.

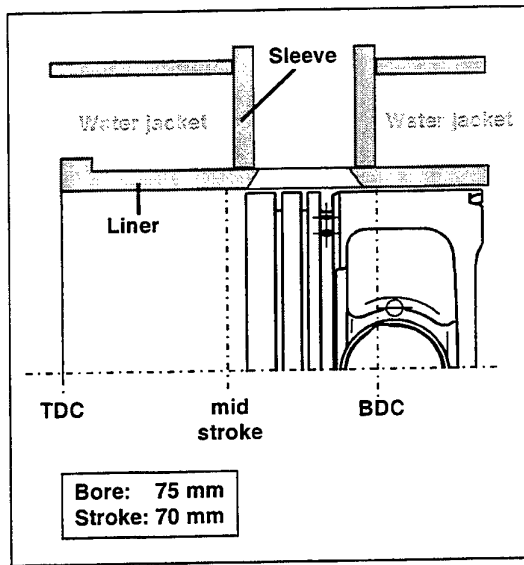


Fig. 1 Engine Setup

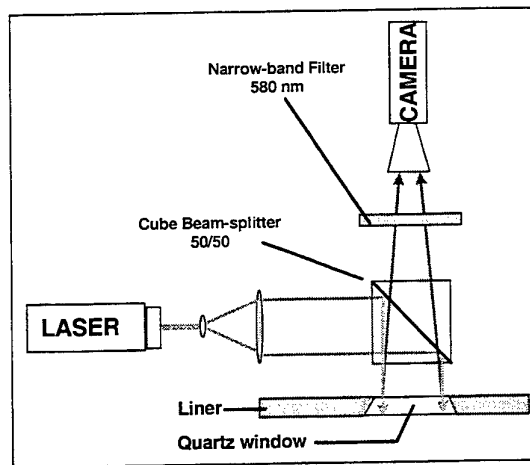


Fig. 2 Optical Setup

2. EXPERIMENT SETUP

2.1 Engine Setup

The engine used in this study was a 300 cc Kubota single-cylinder diesel. The liner was equipped with a quartz window on the anti-thrust side (Fig 1). The window is located between mid-stroke and the BDC so that the entire axial extent of the piston ring-pack can be observed at 88 degree of crank angle before or after the TDC. The window was glued in the liner with Epoxy. Although, the window and the liner were honed together in order to obtain a flush surface, the window was still a few

micron protruded after honing. However, ring profiles showed no damage after more than 20 hours running.

2.2 Optical Setup

Laser induced fluorescence was used to observe oil behavior in the piston ring pack. As reported by Röhrle (1995), temperature in the piston ring pack can vary from 80°C on the piston skirt up to 280°C on the crown land. Hence, to resolve all the regions in the piston ring-pack, the sensitivity of the LIF signal to oil temperature must be minimized. The dyes commonly used for this type of experiment are Coumarin 540 and 523 [Hoult and Takigushi (1991), Shaw *et al* (1992), Inagaki *et al* (1995), Takigushi *et al* (1998)]. These dyes, however, are sensitive to temperature. In this work, Rhodamine 590 was chosen for its strong stability with temperature up to 250°C. The implemented dye concentration was $5 \cdot 10^{-4}$ mol/liter of oil. The wavelength of maximum absorption for rhodamine 590 is 528 nm. Accordingly, the second harmonic of a Nd YAG laser (532 nm) was used to excite the doped oil. The fluorescence signal was acquired with an intensified CCD camera (Princeton Instrument ICCD 576 SE) through a narrow band filter centered on 580 nm (Fig. 2). The purpose of the narrow band filter was to suppress any effect of direct reflection from the quartz window.

The acquisition frequency was limited by the camera characteristics to 1 frame per second. High spatial resolution was obtained at 0.04 mm/pixel (Fig 3). In the images, the brighter the signal is, the higher the film thickness is. No calibration was attempted in this work. Therefore, observation were qualitative. The system was only able to detect accumulation of the oil in liquid form. As described by Burnett (1992), oil can also be vaporized or be transported as an oil mist in air stream. The current system is not able to detect oil in gaseous and mist forms.

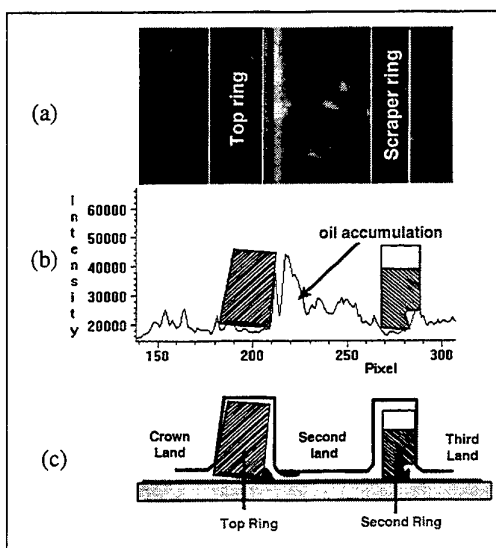


Fig. 3

- (a)- Oil distribution image
- (b)- Fluorescence intensity across the image
- (c)- Ring pack geometry

2.3 Test Specifications

For the experimental results discussed in this paper the engine was equipped with standard rings. Three different ring configurations were tested.

- Configuration 1: top two rings pinned with gaps located on the window side (Fig 4).
- Configuration 2: top two rings pinned with gaps located on the side opposite to the window (Fig 4).
- Configuration 3: standard configuration, non-pinned rings.

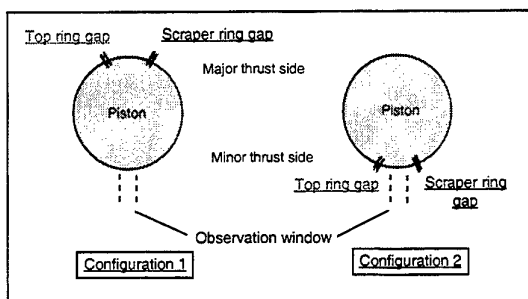


Fig.4 Ring gap location in configurations 1 and 2.

Experiments were conducted from 1200 rpm to 2800 rpm and from no load to 60% load. Coolant temperature was kept constant at 50°C. SAE 10W30

oil was used. Due to the pollution by combustion soot, oil had to be changed every 8 hours.

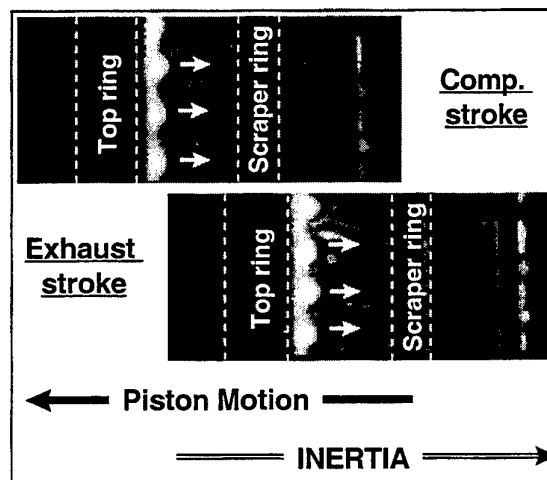


Fig. 5 Inertia driven flow on the second land (1200 rpm - no load - Configuration 3).

3. OIL BEHAVIOR ANALYSIS

Images acquired in configuration 3 during the four strokes of a engine cycle, at 1200 and 1700 rpm, and no load, have shown two important types of oil flows occurring on the piston second land:

- 1- Oil flow in the cylinder axis direction,
- 2- Oil flow around the piston circumference.

3.1 Oil Flow in the Axial Direction

Oil flow in the axial direction, driven by the inertia force due to piston acceleration/deceleration was observed. The images shown in Figure 5 were acquired around mid-stroke during the compression and exhaust strokes. The direction of the inertia force switches to the downward direction after the middle of the down-strokes until the middle of the next up-stroke. Since the images are acquired at 88 degree before the TDC for both compression and exhaust stroke, they should show the maximum effects of downward inertia force on the oil accumulation. As seen in figure 5, the pattern of the oil accumulation below the top ring clearly shows that the oil was moving toward the second ring.

The velocity of oil moving on a flat area under inertia force can be estimated from Tian (1995).

$$V_{oil} = \frac{a \cdot h^2}{\nu} \quad (\text{Eq. 1})$$

where V: Oil velocity.

a : Acceleration .

h : Thickness of the oil accumulation.

ν : Kinematic viscosity.

This equation can be established from a balance of inertia and shear stress, and neglecting the effect of surface tension. The displacement of oil accumulation during the period between a mid down-stroke and mid up-stroke (180 crank angle degrees) was calculated at 1200 rpm for two different oil accumulation thickness:

- $h = 10 \mu\text{m}$, oil displacement = 0.3 mm
- $h = 20 \mu\text{m}$, oil displacement = 4 mm.

These results show a very strong effect of oil film thickness on the oil velocity. During the experiments with non-pinned rings (configuration 3), the thickness of the oil on the piston second land was changing continuously so that it was possible to see different oil accumulation patterns at different oil film thickness. As shown in figure 6, with a thicker oil film thickness on the second land (bottom figure), indicated by a strong fluorescence signal, oil motion could be identified from the oil pattern. In the top figure where a thinner oil film thickness exists, no oil flow in the axial direction was observed.

One characteristics of the inertia driven oil flow is that the net displacement of the oil in the axial direction over an engine cycle is not significant, as inertia switches direction after every half engine revolution. Unless the film thickness is large enough so that inertia can drive the oil out of the second land, oil would always move back and forth on the second land.

3.2 Oil Transport in the Axial Direction

Strong oil motion around the piston circumference was observed on the second land. The images shown in figure 7 were acquired 10 engine cycles apart. A clear 3 mm/s circumferential flow can be identified on the second land.

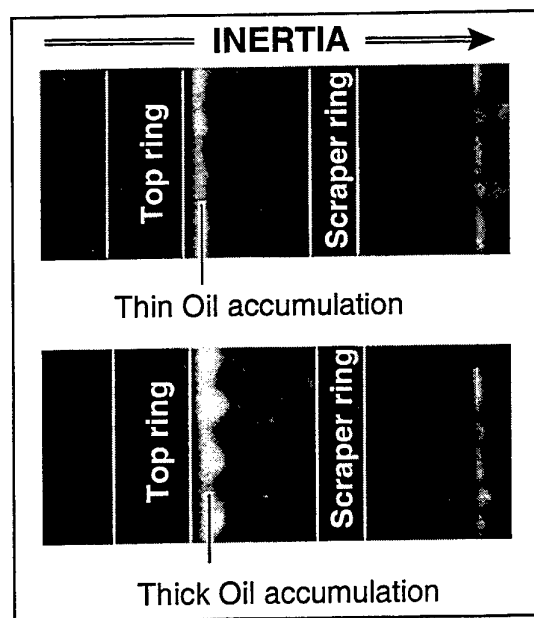


Fig. 6 Inertia driven flow on the second land (1200 rpm - no load - Configuration 3).

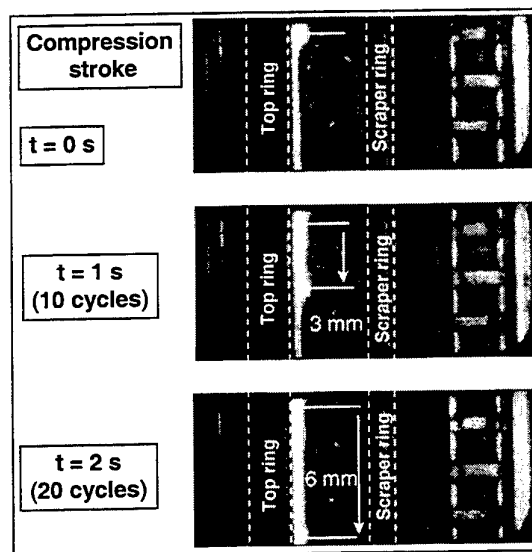


Fig. 7 Oil transport on the second land in the circumferential direction. (1200 rpm - no load - Configuration 3)

The oil flow in the circumferential direction can be driven by the gas flow. When the cylinder pressure is high, there is a gas flow on the second land from the top ring gap to the second ring gap. The shear stress at the interface of gas and oil drags the oil along with gas. Here, estimation is made to relate the velocity of the oil flow to the gas flow by

balancing the shear stress at the gas-oil interface. Because the clearance between the second land and the liner is of the order of 0.2 mm and the axial width of the second land is of the order of 3mm, the gas flow in the circumferential direction can be approximated as uniform across the axial extent of the second land. Thus, the Reynolds number of the gas flow in the channel between the second land the liner can be estimated as:

$$Re = \frac{\dot{V} \rho}{L \mu}$$

where \dot{V} : Volumetric flow rate.
 ρ : Gas density.
 μ : Gas viscosity.
 L : Axial width of the second land.

Using the blow-by value of this engine as the estimation of the volumetric flow rate \dot{V} , we found that the Reynolds number is below 1000. Consequently, the gas flow in the second land is laminar. Approximating the gas flow in the second land as a Poiseuille flow and the oil flow as a Couette flow, balancing the shear stress at the gas/oil interface gives the following relationship:

$$\text{-shear stress balance: } \frac{dP}{dx} \cdot \frac{h_{gas}}{2} = \mu \cdot \frac{V_{oil}}{h_{oil}} \quad (\text{Eq. 2})$$

where

P : Pressure.
 V_{oil} : Oil velocity at the gas/oil interface.
 h_{gas} : Thickness of the gas layer between the piston and the liner.
 h_{oil} : Thickness of the oil layer on the second land.

$$\dot{V} = \frac{L}{12 \cdot \mu} \cdot \frac{dP}{dx} \cdot h_{gas}^3 \quad (\text{Eq. 3})$$

- Combining Eq. 2 and 3, we obtained:

$$V_{oil} = \frac{6 \cdot \dot{V} \cdot h_{oil}}{L \cdot h_{gas}^2}$$

Assuming an oil film thickness of 40 μm , the calculated oil velocity is about 2 mm/s. This result is of the same order of magnitude as the observed velocity. Consequently, it can be concluded that the

gas dragging effect is the main force driving oil in the circumferential direction.

There are two characteristics of this oil flow dragged by the gas flow:

- After one engine cycle, positive blow-by implies that there is more gas flow from the top ring gap to the second ring gap than the other way around despite a reversed gas flow starts at around 50 degree after the TDC of the expansion stroke. Thus, the mean oil transport due to the gas dragging effect is directed toward the third land.
- When gas flows down through the top ring gap during the later part of the compression stroke and early part of the expansion stroke, the pressure difference between the combustion chamber and second land pressure is high (Fig. 8). Consequently, the downward gas flow through the top ring gap is usually choked. Thus, the gas velocity in the second land and oil velocity moving by gas dragging is constant with engine speed. The results shown in Figure 8 have been computed using MIT models developed by Tian (1996).

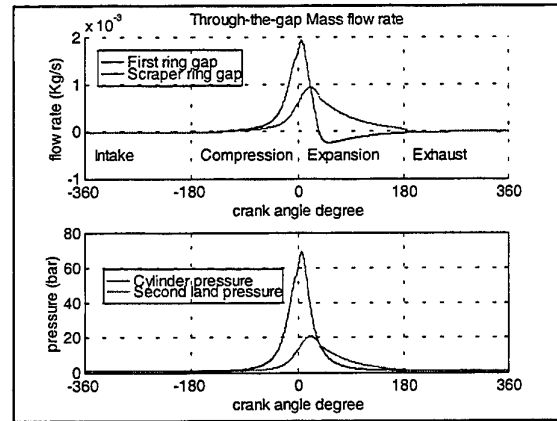


Fig. 8 Mass gas flow through the top two ring gaps and pressure difference at the top ring gap. (1200 rpm - no load).

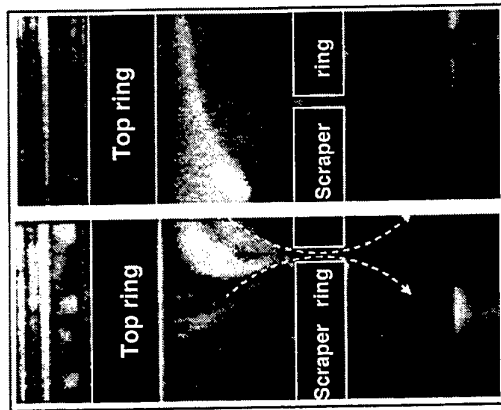


Fig 9 - Oil flow through the scraper ring gap
(1200 rpm - no load - compression stroke -
Configuration 3).

Occasionally, a clear oil flow pattern just above the second ring gap is observed when the second ring gap rotates to the window location. As shown in Figure 9, oil is pulled toward the scraper ring gap by the gas flow during the compression stroke. However, no oil accumulation was detected in the third land just below the second ring gap (Figure 10). The reason is that the high velocity gas flow in the gap is able to break up the oil and create an oil mist. Oil mist can not be observed on the third land due to low dye concentration.

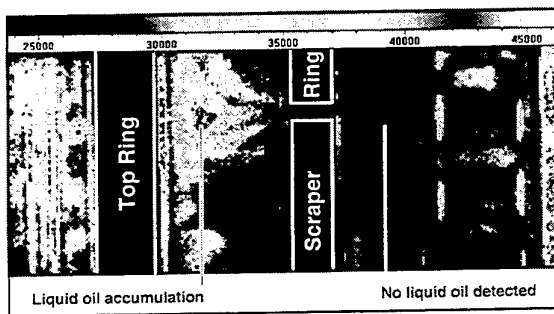


Fig. 10 Oil break up in the scraper ring gap,
(1200 rpm - no load - compression stroke -
Configuration 3).

3.3 Comparison between Inertia and Gas Dragging Effect

Using the equation proposed to evaluate velocity of oil motion on the second land in the axial direction, the contribution of inertia and gas dragging effects was compared. The following assumptions were made:

- second land width 3 mm,

- oil accumulation lying in the middle of the second land,
- constant blow-by gas velocity on the second land.

If the alternating oil motion induced by inertia is not strong enough for the oil to reach either a ring or a groove, the mean oil axial displacement will be zero. In this case, the gas dragging effect, which continuously drives the oil toward the scraper ring gap, is the main oil transport mechanism on the second land. If inertia can push the oil in one of the two top ring grooves within half an engine revolution, however, the major flow is in the axial direction and the inertia driven transport becomes the dominant one. In figure 16, a line is drawn to separate two regions where different oil transport mechanisms dominate, based on Eq. 2. In the domain where inertia effect is dominant, oil can be moved across the second land and possibly be transported into the grooves of the top two rings. Part of the oil that flows into the top ring groove then can be transported to the crown land and consumed. In the other domain, the effect of gas dragging is the main mechanism of oil transport in the second land. Effect of the gas dragging eventually removes the oil out of the second land through the ring gaps.

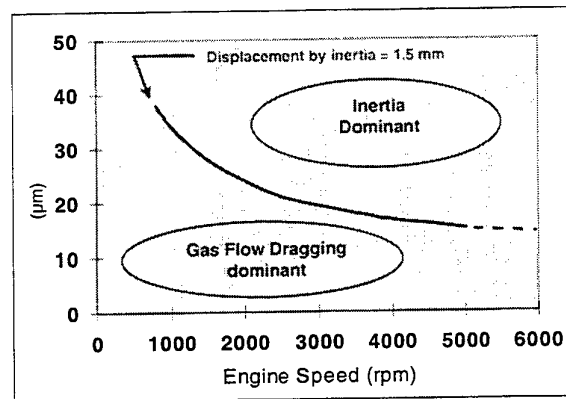


Fig 16 - Comparison of gas dragging and inertia effect on oil transport on the second land.

4. EFFECTS OF RING GAP LOCATION AND RING ROTATION ON SECOND-LAND OIL DISTRIBUTION

4.1 Oil Behavior in Configuration 1

In configuration 1 (Fig. 4), the two top ring gaps were located on the thrust-side, away from the window. In this configuration, strong gas flows do not occur on the second land in front of the observation window. In this case, oil motion on the second land only occurred in the axial direction.

4.2 Oil Behavior in Configuration 2

In configuration 2 (Fig. 4), the top two ring gaps were located on each side of the window, 7 mm away from the window edges. In this configuration, the main gas flow on the second land occurs within the observation window on the anti-thrust side. When the two rings were pinned in configuration 2, no oil accumulation was detected on the piston second land. The strong gas flow which occurs between the two top ring gaps when they are close to each other carries oil into the third land and thus leaves no oil accumulation on the second land at the window location.

4.3 Ring Rotation Effect

In the experiments with non-pinned rings (configuration 3), strong unsteady oil transport was observed. The amount of oil accumulated on the second land changed significantly over several minutes whereas engine parameters were kept constant. In the experiments conducted with the two top rings pinned, however, the oil distribution on the second land was steady. Therefore, it was concluded that ring rotation was responsible for unsteady oil accumulation and oil transport on the second land.

5. CONCLUSIONS

A two-dimensional visualization system using laser-induced-fluorescence was developed to provide detailed images of oil distribution in the piston ring pack of a single cylinder diesel engine. Several mechanisms of liquid oil transport on the piston second land were identified and studied.

Oil was observed moving on the second land in both axial and circumferential direction.

- 1- Oil moves in the axial direction when the lubricant accumulation is thick. This was

found to be consistent with the fact that inertia driven flows are strongly dependent on oil accumulation thickness.

- 2- It was observed that the blow-by gas flow drags the oil on the second land in the circumferential direction. This phenomena creates oil accumulation around the second ring gap.

Comparison of both phenomena showed that the gas dragging effect should over take inertia effects at high engine speed.

Finally ring rotation was found to be responsible for unsteady oil behavior on the second land.

ACKNOWLEDGMENTS

This work is sponsored by the MIT Consortium on Lubrication in Internal Combustion Engines. Current members include Dana Corporation, Mahle GmbH, PSA Peugeot Citroën, Renault and Volvo.

REFERENCES

- Hoult, D.P., Takigushi, M., 1991, "Calibration of Laser Fluorescence Technique Compared with Quantum Theory," STLE Tribology Transactions, Volume 34 (1991), 3, pp440-444.
- Shaw, B.T., Hoult, D.P., Wong, V.W., 1992, "Development of Engine Lubricant Film Thickness Diagnostics Using Fiber Optics and Laser Fluorescence," SAE Paper 920651.
- Tamai, G., 1995, "Experimental Study of Engine Oil Film Thickness Dependency on Liner Location, Oil Properties, and Operating Conditions," M.S. Thesis, Department of Mechanical Engineering, MIT.
- Casey, S., 1998, "Analysis of Lubricant Film Thickness and Distribution along the Piston/Ring/Liner Interface in a Reciprocating Engine," M.S. Thesis, Department of Mechanical Engineering, MIT.
- Takiguchi, M., Nakayama, K., Furuhashi, S., Yoshida, H., 1998, "Variation of Piston Ring Oil Film Thickness in an Internal Combustion Engine," SAE Paper 980563.

Inagaki, H., Saito, A., Murakami, M., and Konomi, T., 1995, "Development of Two-Dimensional Oil Film Thickness Distribution Measuring System," SAE Paper 952346.

Röhrle, M.D., 1995, "Pistons for Internal Combustion Engines", MAHLE GmGh, Printed in Germany 930513.

Burnett, P.J., 1992, "Relationship Between Oil Consumption, Deposit Formation and Piston Motion for Single-Cylinder Diesel Engines," SAE Paper 920089.

Tian, T., Noordzij, B., Wong, V.W., Heywood, J.B., 1996, "Modeling Piston-ring Dynamics, Blow-by, and Ring Twist Effects," ASME ICE Fall Technical Conference, October 1996.

Tian, T., 1995, "Modeling Oil-Transport and Oil-Consumption Mechanisms and the Influence of Piston and Ring Dynamics," Consortium on Lubrication in Internal Combustion Engines, Massachusetts Institute of Technology, June 13 1995, Internal Report.

SESSION 38

FREE FLOWS II

WEAKLY INTERACTING TWO PARALLEL PLANE JETS

Joseph C.S. Lai and Asghar Nasr

School of Aerospace & Mechanical Engineering
University College, The University of New South Wales
Australian Defence Force Academy
Canberra, ACT 2600, AUSTRALIA.

ABSTRACT

The mean velocity field of unventilated two parallel plane jets for large nozzle spacing ratios has been studied using a two-component laser Doppler anemometer. Results show that by comparison with small s/w (less than 5), the interactions between the inner shear layer and the recirculation zone for large s/w are weaker. The initial peaks of turbulence intensities and Reynolds shear stress corresponding to the nozzle inner and outer edges tend to persist downstream from the location of the vortex centre without being overwhelmed by the influences caused by the recirculating flow in the recirculation zone. The lateral turbulence intensities and Reynolds shear stress in the outer shear layer spread and decay more rapidly than in the inner shear layer. The attraction of the two individual jets towards each other is clearly illustrated by the mean velocity vector field and supported by static pressure measurements. Comparisons of the results of the unventilated jets with those of ventilated jets in the literature indicate there is no recirculation zone in the ventilated jets and the unventilated jets combine to develop into a single free jet much earlier than ventilated jets.

1. INTRODUCTION

Two parallel plane jets play an important role in numerous technological applications such as entrainment and mixing processes in boiler and gas turbine combustion chambers and injection systems and thrust-augmenting ejectors for V/STOL aircraft. The flow patterns of unventilated two parallel plane jets are shown schematically in Fig. 1. Here, two identical plane nozzles each of width w are separated in the lateral (y) direction by a distance s , giving a nozzle

spacing ratio of s/w . The origin of the Cartesian coordinate system (x - y) is located at the nozzle plate and the x -axis is in the plane of symmetry which bisects the two nozzles. Owing to the mutual entrainment between the two jets, a sub-atmospheric pressure zone is formed close to the nozzle plate. The sub-atmospheric pressure causes individual jets to curve towards each other in a region close to the nozzle plate known as the converging region. In the recirculation zone, the mean streamwise velocity on the x -axis (U_c) is negative. The two inner shear layers merge at the merging point (mp) where U_c is zero. Downstream from the merging point, in the merging region, the two jets continue to interact with each other and U_c increases until it reaches a maximum value (U_{cmax}) at the combined point (cp). The streamwise distances from the nozzle plate to the merging and combined points are referred to as the merging length (x_{mp}) and the combined length (x_{cp}) respectively. Downstream from the combined point is the combined region where the two jets combine together to resemble a single free jet flow.

Although two parallel plane jets have been experimentally investigated by many researchers such as Miller and Comings (1960), Tanaka (1970, 1974), Murai et al. (1976), Militzer (1977), Ko and Lau (1989) and Lin and Sheu (1990, 1991), these studies were conducted using either hot-wire or Pitot tube which are subject to severe errors in the converging and merging regions. Recently, two component LDA measurements of unventilated two parallel plane jets were reported by Nasr & Lai (1997a, b, c) for small s/w (less than 5). By examining the strength of the interactions between the recirculating flow and the inner shear layer in terms of the turbulence intensities

and Reynolds shear stress distributions for various s/w , Nasr & Lai (1997b) classified unventilated two parallel plane jets into weakly interacting and strongly interacting jets according to whether s/w exceeds 5.

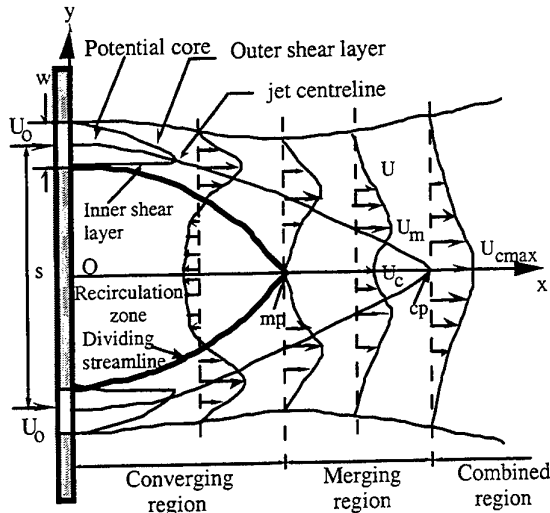


Fig. 1 Schematic of unventilated two parallel plane jets.

Details of strongly interacting two parallel plane jets for s/w less than 5 are given by Nasr & Lai (1997b). The primary objective of this paper is, therefore, to present the velocity field of weakly interacting unventilated two parallel plane jets with large nozzle spacing ratio (namely, $s/w=7.5$ and 11.25) measured with a two-component laser Doppler anemometer (LDA) for a nozzle exit Reynolds number of 11,000. These data are hitherto not available in the literature and will provide a useful database for validating turbulence models for complex shear flows. Comparisons are also made with ventilated two parallel plane jets.

2. APPARATUS AND EXPERIMENTAL CONDITIONS

Experiments were conducted for two-dimensional nozzles each with width 6 mm and two different nozzle spacing ratios, namely, $s/w=7.5$ and 11.25 . The nozzle exit Reynolds number was 11,000 and the exit streamwise turbulence intensity was 2% at the centreline. Velocity measurements were made with a two-component Dantech LDA and were corrected with the residence time weighting function. The uncertainty in mean velocities and turbulence intensities is within ± 0.08 m/s and that of Reynolds shear stress is within ± 0.4 m²/s². In order to measure the static pressure distributions in the jets, a disc type static pressure probe was designed and validated against a standard Pitot-static tube in the test section of a low turbulence

subsonic wind tunnel. Detailed experimental procedures and experimental set-up were given by Nasr & Lai (1996, 1977a).

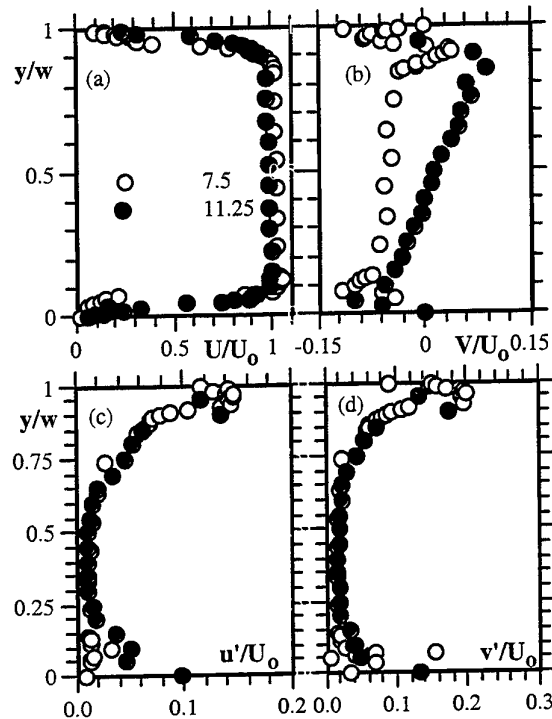


Fig. 2 Nozzle exit conditions for various s/w
(a) U/U_0 (b) v/U_0 (c) u'/U_0 (d) v'/U_0 .

3. RESULTS

3.1 Mean flow characteristics at the nozzle exit

Figure 2 displays the nozzle exit conditions for unventilated two parallel plane jets with $s/w = 7.5$ and 11.25 . Here, the origin of the coordinate system is located at the nozzle inner edge. The streamwise velocity profiles (Fig. 2a) have a top-hat shape similar to that of a single free jet flow, thus indicating the existence of a potential core in the main flow near the nozzle plate. The exit streamwise velocity near the nozzle inner edge is slightly higher for $s/w = 7.5$ than for $s/w = 11.25$, indicating higher flow acceleration due to the sub-atmospheric pressure zone near the nozzle plate. The lateral velocity profiles at the nozzle exit in Fig. 2(b) show that the individual jet deflects towards the x-axis even at the exit plane. Higher flow deflection can be observed for $s/w = 7.5$ as the lateral velocity is negative across over 90% of the nozzle width at the nozzle exit. For $s/w = 11.25$, both streamwise and lateral velocity profiles at the nozzle exit appear to be similar to those of a single free jet. This is deduced from the observation of both positive and negative mean lateral velocity at the nozzle exit in the outer and inner edges of the jet. The distributions of

the streamwise and lateral turbulence intensities at the nozzle exit in Figs. 2(c) and (d) show that their values at the central streamline and at the nozzle exit are quite low, being about 2 %. The peaks of u'/U_0 and v'/U_0 in these figures identify the inner and outer shear layers at the nozzle exit.

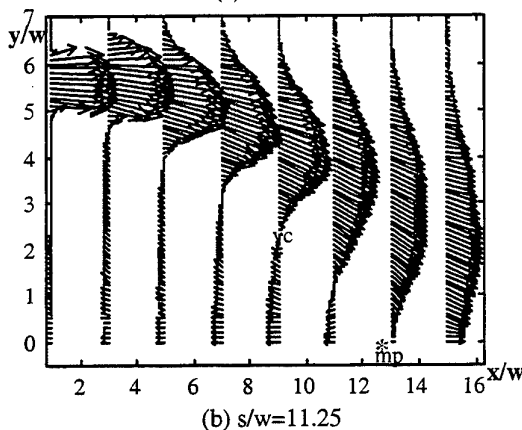
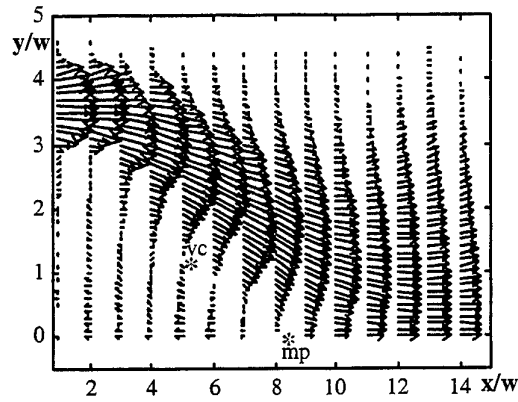


Fig. 3 Mean velocity vectors.

3.2 Mean velocity vectors

The mean velocity vector field of two parallel jets for $s/w = 7.5$ and 11.25 is shown in Fig. 3. These vectors have been determined from the simultaneous measurements of mean streamwise and lateral velocity components. Reversed flow and streamline deflection towards the x-axis are evident. The dividing streamline, standing vortex centre and merging point can be easily identified. The merging length is found to be about $8.3w$ for $s/w=7.5$ compared with $12.5w$ for $s/w=11.25$. The absolute magnitude of the reversed flow along the x-axis increases downstream from the nozzle plate until it reaches a maximum value of about $0.17U_0$ at a streamwise distance corresponding to the location of the standing vortex centre ($x_{vc}/w = 5.25$) for $s/w=7.5$. These compare with $0.23U_0$ at ($x_{vc}/w = 9$,

$y_{vc}/w=2$) for $s/w=11.25$. U_0 then decreases as the flow proceeds downstream and becomes zero at the merging point. The mean streamwise velocity along the x-axis then increases downstream from the merging point until it becomes maximum at the combined point.

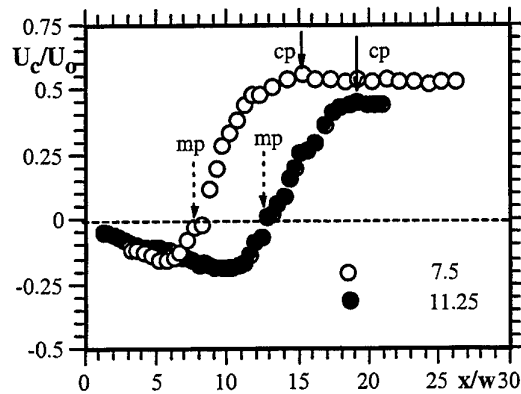


Fig. 4 Distribution of U_c/U_0 for various s/w .

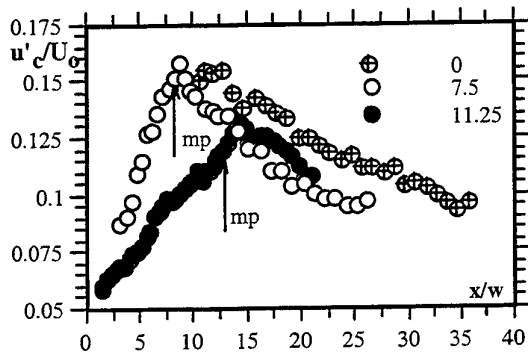
3.3 Mean streamwise velocity distributions along the x-axis

The distributions of the mean streamwise velocity along the x-axis, U_c/U_0 , are shown in Fig. 4 for $s/w = 7.5$ and 11.25 . The negative mean streamwise velocity close to the nozzle plate for both jet configurations indicates the existence of contra-rotating standing vortices which recirculate air on the concave side of the jets. The magnitude of the maximum negative velocity along the x-axis for $s/w = 7.5$ is less than that for $s/w = 11.25$. The merging point for each s/w , where U_c/U_0 is zero, can be identified by the intersection of the zero velocity dashed line with the corresponding velocity profile. Due to the interaction of the two jets, the velocity along the x-axis then increases from the merging point and becomes maximum at the combined point, where the two jets combine together to resemble a single jet flow. It can be seen from Fig. 4 that, the maximum mean streamwise velocity along the x-axis at the combined point, U_{cmax}/U_0 , is less for $s/w = 11.25$. This is because the jet width is greater at the combined point for larger s/w . However, the velocity decay rate along the x-axis downstream from the combined point seems to be nearly the same for both s/w .

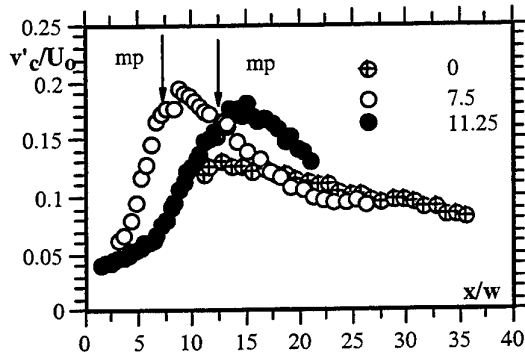
3.4 Turbulence intensity distributions along the x-axis

Distributions of streamwise and lateral turbulence intensity on the x-axis, (u'_c/U_0 and v'_c/U_0) are shown in Figs. 5(a) and (b) respectively for $s/w = 7.5$, 11.25 and

0 (single jet). It can be seen that, u'_c/U_0 increases with x/w up to a point immediately downstream from the merging point where high velocity streamlines collide. The streamwise turbulence intensity then decreases as the flow proceeds further downstream and its decay approaches that of a single free jet. The reduction of the streamwise turbulence intensity in the merging region close to the combined point is primarily due to the relaxation effect of the merging processes on the turbulence activities. Fig. 5(a) also indicates that the maximum value of u'_c/U_0 is significantly greater for $s/w = 7.5$ than for 11.25. Similar to u'_c/U_0 , v'_c/U_0 increases with x/w and reaches a maximum value immediately downstream of the merging point where the flow collision is maximum. The value of the maximum lateral turbulence intensity is slightly less for $s/w = 11.25$ than 7.5. As the flow proceeds downstream, the decay of v'_c/U_0 approaches that of a single free jet. Comparison between Figs. 5(a) and (b) reveals that, v'_c/U_0 is considerably higher than u'_c/U_0 for both s/w because of higher momentum transfer in the lateral direction in the merging region.



(a) Streamwise turbulence intensity.

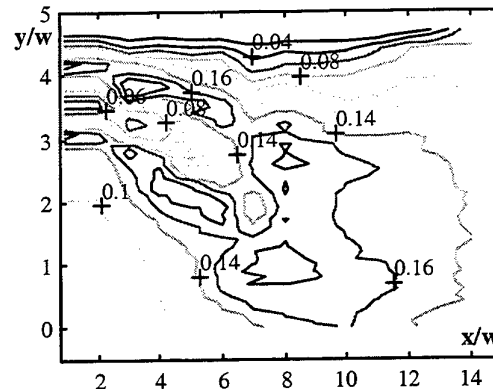


(b) Lateral turbulence intensity.

Fig. 5 Distribution of the turbulence intensity on the x -axis for various s/w .

3.5 Spatial distribution of streamwise turbulence intensity

Contours of normalised streamwise turbulence intensity, u'/U_0 , in the converging and merging regions are depicted in Figs. 6(a) and (b) for $s/w = 7.5$ and 11.25 respectively. The inner and outer shear layers can be clearly identified by the u'/U_0 peaks. Unlike the two parallel jets of $s/w = 2.5$ and 4.25, discussed in Nasr & Lai (1997b) where the inner shear layer initial peaks were overwhelmed by the strong effects of the recirculating flow, they persist downstream beyond the standing vortex centre ($x_{vc}/w = 5.25$ and 9 for $s/w = 7.5$ and 11.25 respectively). An additional small peak in u'/U_0 within the recirculating flow region can be detected at $x/w = 6$ (Fig. 6a). Due to the mutual interaction between the inner and outer shear layers, their peaks begin to merge by $x/w = 8$. It can be observed that further downstream from the merging point ($x_{mp}/w = 8.3$ and 12.5 for $s/w = 7.5$ and 11.25 respectively), the turbulence in the central region of the flow decreases owing to the relaxation effect of the merging process. Downstream from the combined point, in the combined region, the streamwise turbulence intensities normalised by the local maximum mean streamwise velocity follow those of a single free jet.



(a) $s/w = 7.5$

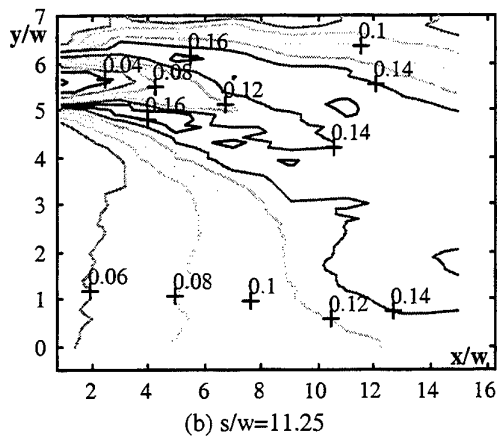


Fig. 6 Contours of streamwise turbulence intensity.

Fig. 6 also shows that u/U_0 in the inner shear layer peak is slightly higher than that in the outer shear layer. As the flow proceeds downstream, the magnitude of the inner and outer shear layer peaks approaches each other.

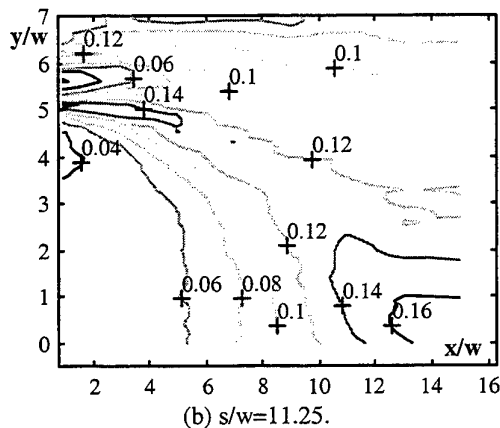
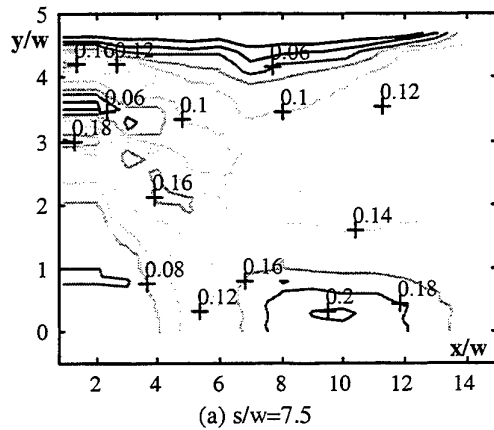
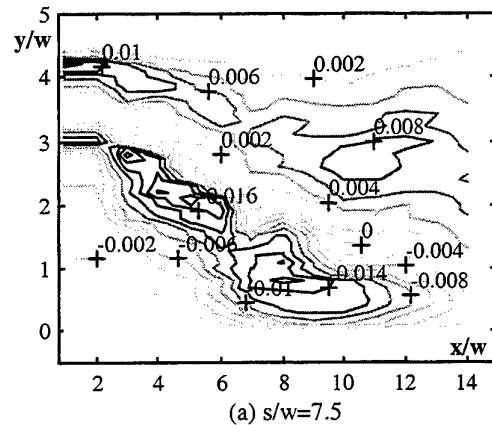


Fig. 7 Contours of lateral turbulence intensity.

3.6 Spatial distribution of lateral turbulence intensity

Figures 7(a) and (b) display the contours of the lateral turbulence intensity v/U_0 for $s/w = 7.5$ and 11.25 respectively. The initial peak of v/U_0 corresponding to the lip of the nozzle outlet is smaller in the outer shear layer than in the inner shear layer. This is due to the initial convergence of the jet towards the x -axis close to the nozzle plate as a result of the lateral pressure gradient. As the jets curve towards the x -axis, the two peaks slowly disappear and by $x/w = 8$ and 12 for $s/w = 7.5$ and 11.25 respectively, v/U_0 becomes maximum due to the collision of the two inner shear layers on both sides of the x -axis. Comparison of u/U_0 and v/U_0 in Figs. 6 and 7 reveals that, downstream from merging point, v/U_0 is larger than u/U_0 in the vicinity of the x -axis. However u/U_0 is considerably higher than v/U_0 in the outer part of the flow. Hence, strictly speaking, the turbulence field is not isotropic like a single free jet.



3.7 Spatial distribution of Reynolds shear stress

Contours of the normalised Reynolds shear stress, $-\overline{uv}/U_0^2$ are shown in Figs. 8(a) and (b) for $s/w = 7.5$ and 11.25 respectively. The positive and negative Reynolds shear stresses indicate the outward and inward momentum transfer in the outer and inner shear layers respectively. As the jet curves towards the x-axis, the outer shear layer peak of $-\overline{uv}/U_0^2$ becomes less distinct. On the other hand, as the inner shear layer develops, its peak first decreases with downstream distance and then increases to a maximum value around the merging point where the momentum transfer is maximum, owing to the collision of the two inner shear layers on both sides of the x-axis.

3.8 Static pressure measurements

Figure 9 shows the lateral distributions of the mean static pressure P/P_0 measured with a disc type static pressure probe at $x/w = 0.5$ for $s/w = 7.5$ and 11.25. Compared with strongly interacting two parallel jets of $s/w = 2.5$ and 4.25 reported by Nasr & Lai (1997b), the static pressure in the recirculation zone close to the nozzle plate is considerably higher for weakly interacting jets than for strongly interacting jets. Unlike strongly interacting two parallel jets where the static pressure increases continuously from the x-axis to the outer edge of the jet, P/P_0 is nearly constant along the lateral direction in the recirculation zone close to the nozzle plate. For both $s/w = 7.5$ and 11.25, in the region close to the inner edge of the jet, the static pressure increases and then decreases again in the main flow before recovering to atmospheric pressure at the outer edge of the jet.

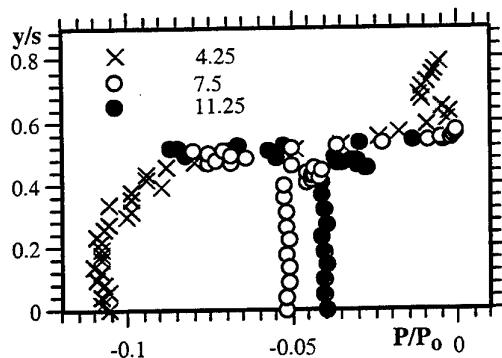


Fig. 9 Static pressure distribution at $x/w=0.5$ for various s/w .

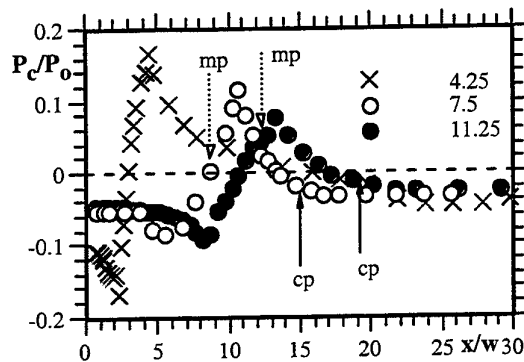


Fig. 10 Static pressure distribution on the x-axis for various s/w .

Distributions of the normalised mean static pressure along the x-axis P_c/P_0 are presented in Fig. 10 for $s/w = 7.5$ and 11.25. For $s/w = 7.5$ and 11.25, the static pressure along the x-axis behaves quite similar to that of strongly interacting jets ($s/w = 4.25$). However, the positive and negative peaks of P_c/P_0 are relatively smaller than the corresponding peaks observed for $s/w = 4.25$.

3.9 Comparison of unventilated and ventilated two parallel plane jets

Unlike unventilated two parallel jets (Fig. 1) where the surrounding air entrainment between the two jets is prevented by the nozzle plate, the inter-jet entrainment in ventilated jets (secondary flow) issuing from free-standing nozzles eliminates the formation of standing vortices (recirculating flow region) upstream of the merging point. Owing to a higher static pressure in the zone between the two jets in the converging region, the flow curvature in the ventilated two parallel jets is less than that in the unventilated jets. It is generally accepted that, in the combined region, both unventilated and ventilated two parallel jets resemble a single free jet. In the near field, however, the flow properties of unventilated and ventilated jets are quite different from each other. This has not been quantitatively examined by previous researchers and will, therefore, be considered here.

Figure 11 depicts the mean streamwise velocity profiles U/U_0 for unventilated two parallel jets with $s/w = 11.25$ and those of ventilated jets with $s/w = 12.5$ measured by Elbanna et al. (1983) using constant temperature hot-wire anemometry. Here, the ordinate is normalised by the lateral distance (s) between the nozzles. Except in the region between the two jets where U/U_0 is higher for ventilated parallel jets, downstream from the nozzle exit plane up to $x/w = 7$ the profiles of the mean streamwise velocity in the main jet are quite similar for both jet configurations.

However, the effect of a higher flow curvature for unventilated jets is evident at $x/w = 10$ and 15 as the velocity profiles are deflected more towards the x -axis. It can be observed from Fig. 11 that, near the nozzle exit, the decay of the local maximum streamwise velocity U_m/U_o is similar for both unventilated and ventilated jets and as the flow approaches the merging point, it becomes greater for the former.

Fig. 12 compares the LDA results of the mean streamwise velocity along the x -axis, U_c/U_o , for unventilated two parallel jets with $s/w = 11.25$ with the hot-wire results of Elbanna et al. (1983) for ventilated two parallel plane jets with $s/w = 12.5$. It can be seen that, for ventilated jets, the normalised secondary flow velocity along the x -axis, U_c/U_o , is about 0.14 at the nozzle exit and decreases with x/w down to a value of about 0.06 at the merging point ($x_{mp}/w = 12$). Downstream from the merging point, U_c/U_o begins to increase with x/w up to a maximum value of about $U_{cmax}/U_o = 0.42$ at the combined point ($x_{cp}/w = 30$). On

the other hand, for the unventilated two parallel jets, the maximum magnitude of the reversed flow is about -0.2 which is about 30% higher than that for ventilated jets. In the merging region, U_c/U_o increases considerably faster (owing to a higher flow collision and momentum transfer) and reaches a maximum value ($U_{cmax}/U_o = 0.46$) slightly higher than that for ventilated jets. The measured combined length of $x_{cp}/w = 30$ for ventilated two parallel jets with $s/w = 12.5$, is significantly higher than that of $x_{cp}/w = 19$ for unventilated jets with $s/w = 11.25$. This 63% longer combined length agrees with the results of Lin and Sheu (1991), Elbanna et al. (1983) and Marsters (1977). However, the merging length of $x_{mp}/w = 12$ for ventilated jets of Elbanna (1983) measured by hot-wire is shorter than the merging length $x_{mp}/w = 12.5$ of the unventilated jets measured by LDA in the present study. This could be due to the errors in hot-wire measurements as the flow angle, turbulence intensity, and probe interference are high near the merging point.

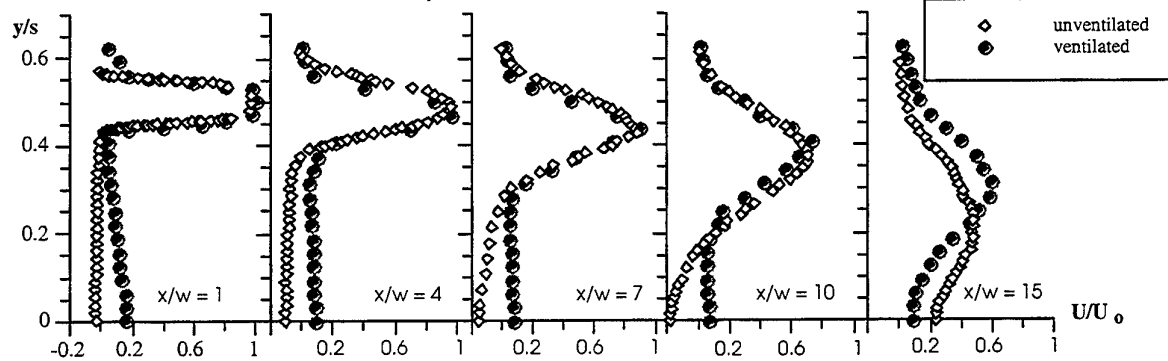


Fig. 11 Comparisons of mean streamwise velocity profiles between ventilated and unventilated jets.

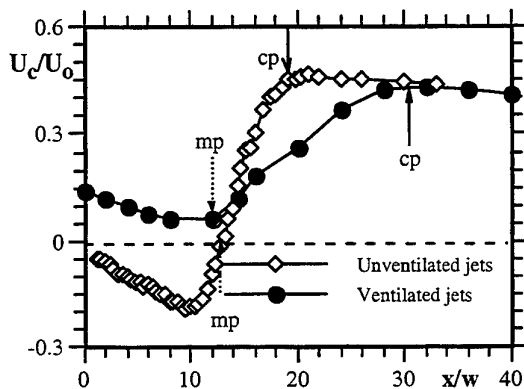


Fig. 12 Distribution of mean streamwise velocity on the x -axis.

The distributions of the mean static pressure along the x -axis, P_c/P_o , for unventilated two parallel jets of $s/w = 11.25$ of the present study and for ventilated two parallel jets of Marsters (1977) with $s/w = 11$ are compared in Fig. 13. For ventilated jets, P_c/P_o is minimum at the nozzle exit plane and it increases with x/w to a maximum at a location downstream from the merging point. The minimum normalised static pressure of about -0.027 for ventilated parallel jets is significantly greater than -0.098 for unventilated jets. The maximum static pressure along the x -axis, P_{cmax}/P_o , of about 0.038 is also considerably lower for ventilated jets than 0.08 for unventilated jets which is due to the higher flow collision for the latter. Examination of the wall static pressure data for ventilated two parallel plane jets by Marsters (1977) suggests that the ratio of the streamwise distance from the nozzle exit at which the maximum static pressure

occurs to the merging length is about 1.3 which is higher than that of 1.15 for unventilated jets reported by Tanaka (1970). This is due to the higher tendency of the two jets to deflect towards each other in unventilated jets.

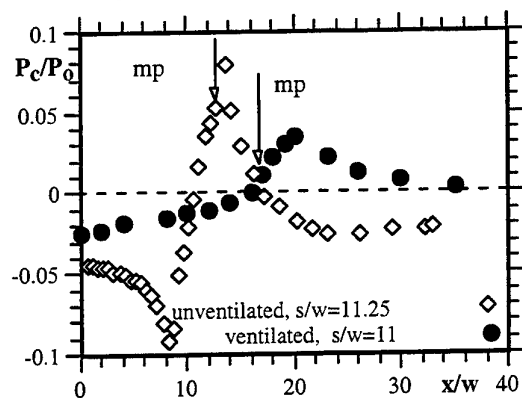


Fig. 13 Static pressure distribution on the x-axis

4. CONCLUSIONS

Mean velocity vectors determined from simultaneous LDA measurements of streamwise and lateral velocities have been presented for two parallel plane jets with $s/w = 7.5$ and 11.25 . The converging and merging regions, recirculation zone, merging and combined lengths, location of the vortex centre and magnitudes of the maximum and minimum velocities along the symmetry axis (x -axis) have been determined.

Distributions of turbulence intensities and Reynolds shear stress in the converging and merging regions and recirculation zone of two parallel jets show that the initial peaks of these turbulence properties corresponding to the nozzle inner and outer edges tend to persist downstream from the location of the vortex centre without being overwhelmed by the influences caused by the recirculating flow in the recirculation zone. The peaks of lateral turbulence intensities and Reynolds shear stress in the outer shear layer spread and decay more rapidly than in the inner shear layer.

Lateral distribution of the mean static pressure P/P_0 measured using a disc type static pressure probe at $x/w = 0.5$ shows that P/P_0 in the recirculation zone is considerably higher for weakly interacting jets of $s/w = 7.5$ and 11.25 than for strongly interacting jets of $s/w = 2.5$ and 4.25 examined by Nasr & Lai (1977b). It has been shown that P/P_0 at $x/w = 0.5$ is nearly constant along the lateral direction in the recirculation zone close to the nozzle plate and reaches its minimum value in the main flow followed by recovery to atmospheric pressure at the outer edge of the jet. The distributions of the static pressure along the x -axis show that the

positive and negative peaks of P_c/P_0 are also relatively smaller for $s/w = 7.5$ and 11.25 than those observed for $s/w = 2.5$ and 4.25 .

LDA results of unventilated two parallel jets with $s/w = 11.25$ of the present study and hot-wire data of Elbanna et al. (1983) for ventilated two parallel plane jets with $s/w = 12.5$ have been compared. It has been shown that the maximum normalised secondary flow velocity of about 0.15 for ventilated jets is relatively smaller than the absolute value of the maximum reversed flow velocity of 0.2 for unventilated jets. The maximum mean streamwise velocity at the combined point, U_{cmax}/U_0 , has been found to be 0.42 and 0.44 for ventilated and unventilated jets respectively. Comparisons of the static pressure along the x -axis P_c/P_0 for unventilated two parallel jets of $s/w = 11.25$ of the present study and for ventilated two parallel jets of Marsters (1977) for $s/w = 11$ show that for ventilated jets, P_c/P_0 has a minimum of about -0.027 which is significantly greater than -0.098 for unventilated jets. The maximum normalised static pressure on the x -axis of 0.038 is also considerably lower for ventilated jets than 0.08 for unventilated jets.

REFERENCES

- Elbanna H. and Gahin S. (1983) Investigation of Two Plane Parallel Jets. AIAA J., 21 (7), 986-991.
- Ko N. W. M. and Lau K. K. (1989) Flow Structures in Initial Region of Two Interacting Parallel plane Jets. Experimental and Fluid Science, 2, 431-449.
- Lin Y. F. and Sheu M. J. (1990) Investigation of two plane parallel unventilated jets. Experiments in Fluids 10, 17-22.
- Lin Y. F. and Sheu M. J. (1991) Interaction of Parallel Jets. AIAA J 29(9), 1372-1373.
- Marsters G. F., (1977) Interaction of Two Plane Parallel Jets AIAA J., 15(12), 1756 - 1762.
- Militzer J.(1977) Dual plane parallel jets. Ph. D. Thesis, University of Waterloo, Canada.
- Miller D. R. and Comings E. W., (1960) Force-momentum field in a dual-jet flow Journal of fluid mechanics. 7, 237.
- Murai, K., Taga, M. & Akagawa, K. (1976) An Experimental Study on Confluence of Two-Dimensional Jets. Bull. JSME, 19, 956 - 964.

Nasr, A. and Lai, J.C.S. (1996) The effect of offset ratio on the mean flow characteristics of turbulent offset jets. Proceedings of ICAS96, Sorrento, Napoli, Italy, Sept. 8-13, vol. 2, 1968-1978.

Nasr A. and Lai J. C. S. (1997a) Two parallel plane jets: mean flow and effects of acoustic excitation. Experiments in Fluids 22, 251-260.

Nasr A. and Lai J. C. S. (1997b) Strongly interacting two parallel jets. Proceedings of JSME Centennial Grand Congress, Int. Conf. on Fluid Eng., Tokyo, Japan, July 13-16, 1997, I, 117-122.

Nasr A. and Lai J. C. S. (1997c) Comparison of flow characteristics in the near field of two parallel plane jets and an offset plane jet. Physics of Fluids, 9(10), 2919-2931.

Tanaka E. (1970) The Interference of Two - Dimensional Parallel Jets. (1st Report, Experiments on Dual Jet), Bull. JSME, 13, 272-280.

Tanaka E. (1974) The Interference of Two - Dimensional Parallel Jets. (2nd Report, Experiments on the Combined flow of Dual Jet), Bull. JSME, 17, No.109, 920-927.

AN IMAGE PROCESSING APPROACH TO THE STUDY OF TURBULENT STRUCTURES ASSOCIATED WITH A JET IN A CROSSFLOW

S. McCusker, N. Toy and E. Savory
Fluid Mechanics Research Group
Department of Civil Engineering
University of Surrey,
Guildford, Surrey, UK

ABSTRACT

The following paper outlines a method of creating a thin light sheet, using a low-cost, low-power, laser light source without the use of complex electronic circuitry. The main body of the paper will discuss the application of this technique to a digital image processing study of the large-scale turbulent structures within the shear layer of the classical configuration of a low speed circular jet in a crossflow. It will be shown that the analysis procedure presented is capable of providing instantaneous, full field measurements which are not obtainable with standard hot-wire anemometry techniques. Furthermore, the results are based on data acquisition over a flow field of a much larger scale than attainable by most PIV methods. The image processing technique is extended to encompass a box-counting method of fractal analysis, from which information concerning the length scales of turbulent structures within a field of view can be inferred.

The method developed identifies the length scales of the large-scale turbulent structures at the outer edge of a jet in a crossflow and calculates the instantaneous velocities of these structures on an individual basis. From this information, turbulence characteristics for these structures are quantified and these results are then compared to hot-wire measurements taken in the same flow regime. The fractal analysis approach identifies a wider range of structure sizes on a more global basis, yielding information concerning the complete range of length scales which exist at the outer edge of the shear layer. The paper demonstrates the validity of the new techniques and highlights the value of full-field, instantaneous measurements when studying turbulent flows.

NOMENCLATURE

D	Jet nozzle diameter
I	Turbulence Intermittency
K_t	Kolmogorov time scale
L	X-direction length scale - measured by image processing
L_i	Integral length scale - measured by hot-wire
$N(h)$	Number of boxes of size, h, containing the fractal boundary
U	Average velocity in the downstream direction.
U_s	Average velocity of turbulent structures in the downstream direction.
X	Horizontal distance from the jet exit in the downstream direction
Y	Vertical distance from the jet exit, measured from the ground plane
b	Fractal equation constant - related to interface length
d	Fractal dimension
h	Fractal box size
n	Order of iteration for Koch curve construction
u	Fluctuating component of velocity in X-direction (Hot-Wire)
u'	R.M.S. of u
u_s	Instantaneous structure velocity in the X-direction.
u'_s	R.M.S. of u_s
u'/U	Turbulence Intensity (Hot - Wire)
$u'/(U * I)$	Turbulence Characteristic - Turbulence Intensity divided by Turbulence Intermittency (Hot-Wire)
u'_s / U_s	Turbulence Characteristic - Turbulence Intensity of Large-Scale Structure

1. INTRODUCTION

Conventional flow measurement techniques such as hot-wire anemometry and, more recently, Laser Doppler Anemometry (LDA) have been used extensively in the study of turbulent flows. Whilst these techniques provide a great deal of data concerning the time history of the flow behaviour, they fail to provide information reflecting the instantaneous characteristics of the flow. The foundation of such techniques is that they are point-based and so they fail to provide a 'picture' of the flow. Established flow visualisation techniques such as Particle Image Velocimetry (PIV) do produce full-field quantitative data concerning a flow field. However, such techniques require very high resolution imaging for accurate data acquisition and, as a result, the field of analysis is generally very small and does not reflect the large-scale behaviour of the flow. Such techniques are very effective when studying small scale turbulent structures but are not viable for studies of large-scale turbulence as will be presented here.

The phenomenon of a jet in a crossflow has been studied by many authors, Keffer & Baines (1963), Pratte & Baines (1967), Fearn & Weston (1974) and Fric & Roshko (1989) amongst others. The main features of the flow regime have been well established, Margason (1993). The application of these studies is very diverse, from combustion chamber mixing to atmospheric dispersion from chimney plumes. Because of its wide range of applications the jet in a crossflow has been of interest to the present authors for a long time. Many investigations have been carried out by applying digital image processing techniques to studies of turbulence within a jet in a crossflow Toy et al. (1992), Toy et al. (1993) and McCusker et al. (1996). These have shown the advantages of novel approaches to turbulence investigations. The current approach requires the acquisition of a large number of images of the turbulent / non-turbulent interface between the jet and the crossflow. This, combined with the image processing equipment available, made possible the application of the relatively new field of fractal analysis to the stored images. Some work has already been carried out in this area, most notably that summarised by Sreenivasan (1991) in a review of fractal analysis approaches to turbulence studies. In his paper he covered many aspects, including a high resolution box-method applied to flow visualisation images of a turbulent / non-turbulent boundary which showed a fractal dimension of 1.36 for a two-dimensional cut of an axi-symmetric free water jet over a range of turbulent length scales from the integral length scale down to the Kolmogorov length scale.

The current work is a consolidation of three different approaches to the quantification of turbulence characteristics of a jet in a crossflow. Firstly, a Lagrangian approach to turbulent convection is developed. Secondly, the images acquired for this technique are examined by the box-method of fractal analysis and, thirdly, the results of these two new techniques are compared to those acquired by conventional, crossed hot-wire anemometry.

2. EXPERIMENTAL DETAILS

2.1. Smoke Tunnel Facility

All of the experiments were carried out in a purpose built open-circuit smoke tunnel facility (Figure 1). The tunnel has working section dimensions of 0.75m height, 0.62m width and 3.6m length. High efficiency filters are fitted to the tunnel outlet to remove practically all of the smoke introduced into the flow. Optical access to the working section was provided by a removable 'Perspex' side wall panel and a glass floor section. The smoke was provided by a Concept 'Genie' smoke generator which produced particles of which 90% were of diameter less than 1 μ m. The jet was seeded at source and created by a small centrifugal fan supplying the pipework which consisted of copper tubing of 32.5mm internal diameter with a 325mm straight section leading into a 90° bend of 135mm radius. This was followed by a vertical section of 425mm, ending in a contraction of 6.25:1 area ratio with a 25mm straight outlet. The result of this network was a 13mm diameter jet with a 'top hat' velocity profile at the exit. The apparatus was configured such that the jet entered the crossflow through a nozzle with the exit flush with the roof plane of the tunnel. The experiments described here were carried out with a jet nozzle exit velocity of 6m/s and a freestream crossflow velocity of 1m/s.

2.2. Image Processing Equipment

The image processing equipment used was a Series 151 Image Processing Module, supplied by Imaging Technology, consisting of an arithmetic logic unit pipeline processor (ALU), a frame buffer capable of holding 16 frames of 512 x 512 pixels x 8 bits and a high performance analogue to digital interface (ADI) module which also controlled the time base for the image processing unit. The system was controlled by a desktop PC via a VME-bus and received input either via a CCD camera or VHS VCR. A diagram of the apparatus is shown in Figure 2. The analysis software was written in Microsoft C, using some of the dedicated image processing routines provided with the unit.

2.3. Light Sheet Arrangement

A schematic of the arrangement for creating a light sheet is shown in Figure 3. The system driving the light sheet arrangement was an Amplicon PC30AT, analogue/digital I/O board. The major problem to be overcome in creating the light sheet was producing sufficient intensity so that the seeded flow was well illuminated. Given that the highest power laser light source available for the work was a 50mW diode laser with a wavelength of 790nm, it was realised that beam splitting would so greatly diffuse the light intensity that it would not be practical. The selected method was to scan the light beam using an oscillating mirror. To achieve a sharp, clear image it was necessary to scan the mirror through the field of view of the camera only once during the image acquisition. Any more sweeps would result in a double image on the CCD receptors. This was achieved by coupling the

output of the camera, via an amplifier, to the input of the A/D converter on the PC30AT board as well as to its normal destination of the VCR. The laser was directed at the mirror, which was mounted on a stepper motor, and positioned so that the beam was reflected along a path out of the range of view of the camera. The custom-written software continuously sampled the output from the camera, waiting for the severe voltage drop associated with the blanking pulse of the camera output. The end of this blank was used as the trigger for the mirror to start moving. This was also controlled by the PC30AT card. When the end of the blanking pulse was detected, a signal was sent via the digital I/O port to the stepper motor control box which turned the stepper motor through its sweep and stopped it when the beam had passed through the camera viewing field. Again, the software waited for a blanking pulse before returning the mirror to its starting position, so completing one cycle during which two images were acquired. In this way the sweep of the laser was synchronised with the acquisition period of the camera.

2.3. Fractal analysis of turbulence

It has long been acknowledged that, in turbulent flows, energy is transferred, on balance, from large eddies, through progressively smaller eddies until it is dissipated at turbulence length scales around the Kolmogorov microscale. The model of turbulence as a field that is made up of a number of eddies of varying size, allows the application of fractal analysis to an instantaneous image of turbulence which has been acquired via flow visualisation.

Digitised images are stored as pixel maps, which conveniently allow the application of the box-counting method of fractal analysis. In this technique, a progressively more refined grid is laid over the instantaneous flow visualisation image. The number of boxes straddling the interface between rotational and irrotational flow in each instance is counted and used to calculate the fractal dimension.

For a clearer understanding of the box-method of fractal analysis, consider the Koch curve shown in Figure 4. In the first case, where $n=0$, the number of squares of side, h , required to cover the line can be shown to be $b(h)$, where b , is the length of the line. However, after the first iteration, when $n=1$, the number of boxes required would no longer follow a simple inverse relationship, rather, the number of boxes required would follow a law of $N(h)=b(1/h)^d$. This is because in each successive iteration, a similar substitution is made as in the first. This law holds throughout as long as the box size is smaller than the shortest lengths in the line. In a theoretical Koch curve $n=\infty$, so a log-log plot of $N(h)$ against $1/h$ would yield a constant gradient of d , the fractal dimension. However, it can be seen from Figure 5-Figure 8 that, whilst a turbulent boundary may contain a series of progressively smaller structures, it is not completely fractal in nature in the way that the Koch curve is. Furthermore, the length scales of the structures do not become infinitely small and, as such, there is a limit to the fractal dimension of such a line. Fractal analysis of such a shape shows that there is a range of structure sizes for which it can be said that there is a similarity from one

scale to the next. Clearly, when the resolution of the fractal grid is such that the size of the boxes is greater than that of the largest structures in the image, a change in box size will yield no information concerning the size of the structures. In fact, the interface will be treated as a straight line and yield a dimension of 1. Similarly, when the box size is less than the smallest structures there is no more information to be gained by increasing resolution and, again, the fractal dimension returned is 1. By using these criteria, it is then possible to find the range of structure sizes which exist within a section of the flow visualisation image. To gain further information about these structures a technique has been developed by which individual structures can be tracked over a period of 60ms.

2.4. Structure Tracking

The structure tracking routine begins by acquiring four consecutive images of the wake of the model at intervals of 20ms. A binary thresholding routine is then carried out which reduces the image to regions of smoke and no-smoke. A region containing a distinct turbulent structure is identified by the user and the pixel intensities within this region are stored in the PC memory as the primary image. The software then scans the near region of the subsequent image, at each location comparing the intensities of the primary image with the area under interrogation. The region of greatest correlation, that is the region where there is the greatest overlap between the primary and secondary images, is then identified as the region containing the structure in its second position. The pixel intensities within this area are written to the PC memory and this region is used as the primary image when searching for the structure in its third position. This process is repeated until the location of the turbulent structure is identified in all four images (Figure 5-Figure 9). The software then proceeds to find the centre of area of all four instances of the structure so that the translation of the structure can be quantified in pixel locations which can be converted to a length by a simple scaling technique. The outline of the structure in all four positions is copied and written to a second frame buffer (Figure 9), so that the position, size and shape of the structure in all four instances can be viewed simultaneously. From this image the velocity and deformation of the structure can be assessed both quantitatively and qualitatively.

2.5. Sources of Error

The use of camera and image processing equipment will always lead to blur errors, caused by movement of the object during image acquisition. The error margin in the technique presented is a function of the sweep speed of the laser beam and the downstream velocity of the object. During the experiments carried out within this study, the blurring error was found to be 4%, regardless of image size. This is a constant error, which 'stretches' the image. Whilst this would result in shift of the calculated location of the structure, it has no effect on the calculation of the convection velocities, as the same shift occurs at all four locations where the turbulent structure is identified. The blurring effect would, of course,

influence the results of the fractal analysis technique. However, this method is used to indicate the range of scales existing within an image and, hence, in these circumstances a 4% error is negligible. One further source of error in the tracking technique is in the identification of the centroids of the turbulent structures. The difficulty lies in the identification of the turbulent structure, independent of its visualised connectivity to other adjacent structures. For the purposes of tracking the position of the structure, however, this is not a significant problem. Reference to the images in Figure 5 to Figure 8 shows that whilst there is significant distortion of the structure over the 60ms sampling period, there is very little deformation between any two consecutive images. This allows the structure and connectivity to be treated as one entity, where there is no relative movement between the connectivity and the structure. As a result, the rate of convection of the structure can be assumed to be the same as that of the structure and connectivity combined. In cases where the deformation is significant, the tracking software would not recognise the flow structure in the second position and the routine would fail. This accounts for the number of tracked structures being less than 40 at some locations. The difficulty in distinguishing the structure from its connectivity will affect the precision of the absolute location of the structure in that the calculated centroid will be biased towards the connectivity section. In the worst possible case, where this section takes up 25% of the enclosing box, the greatest error in absolute location is of the order of 8% of the structure length. To minimise this effect, every effort was made to select structures which were as discrete from other structures as possible.

3. RESULTS AND DISCUSSION

The area under investigation in the current work is the shear layer of the interface region between the jet and the crossflow. This is the region in which entrainment of the surrounding flow into the jet takes place. To demonstrate the validity of the current technique results are presented which were obtained in an X-Z plane on the centre-line at approximately $X/D=20$ downstream of the nozzle. However, similar results have been achieved at all 6 downstream locations studied. The chart in Figure 10 shows the locations of approximately 240 turbulent structures which have been tracked. The spread of the data in the direction normal to the freestream can be seen to increase with downstream displacement. This width is an indication of the depth of the shear layer of the outer edge of the jet along its axis of symmetry.

Before discussing the behaviour of the turbulent structures, the range of structures tracked in relation to those captured using conventional measurement techniques must be established. Figure 11 shows the cumulative distribution function (CDF) of the size of the 240 structures which were studied. A similar distribution is achieved when using a smaller sample set, down to less than 30 structures at each of the 6 downstream locations. From this it can be seen that 90% of the structures were of a length scale between 1D and 4D, with an essentially Gaussian distribution within that range

(Figure 12). By associating the measured length scales with a nominal frequency (Figure 13) it is possible to place the range of structures within the energy cascade emphasised by the hot-wire technique (Figure 14). The structure frequency is termed nominal, because a true frequency of occurrence of the structures cannot be implied by length scale alone. The nominal result was arrived at by using a simple relationship of $U=f \cdot L$. Whilst this does not give an absolute result, it at least identifies a high limit for the frequency of the structure of size L . A comparison between Figure 13 and Figure 14 indicates that the structures which were chosen were generally at the low frequency end of the energy cascade. Reference to Table 1 and Figure 10 quite clearly place the size of the structures tracked in a range between the integral length scale (calculated from hot-wire results) and the shear layer width of approximately 4.5D. Figure 11 and Figure 13 also show that there is very little variation in the size of the large-scale turbulent structures with downstream position.

The question of the adequacy of the sample size is addressed by Figure 15 and Figure 16, in which mean velocity and a turbulence characteristic (u'_s / U_s) are plotted against the number of samples used in the calculation. It may be seen that both approach asymptotic values, with a variation of less than 4% after 90 measurements. This reflects a sample size of 30 structures as each structure yields three velocity and turbulence values. The results presented here are calculated from sample sets of up to 40 structures. Figure 15 shows that image processing techniques can be used to measure the convection velocities of the large-scale structures in the flow. In the general case the velocity measured by the present technique, is within 5% of the freestream velocity of 1m/s. No variation in downstream velocity with downstream position is indicated. Perhaps more interesting are the fluctuations in the velocity of the turbulent structures as they move downstream. The statistical definition of turbulence is, after all, a measure of fluctuations in velocity. The technique presented here restricts the measurement of these fluctuations to sections of the flow which are purely turbulent. In this way a measure of the turbulence contribution of the large-scale structures is achieved (Figure 16). A direct comparison with hot-wire measurements is not possible as the hot-wire measures turbulence at all scales within the sampling range of the measurement technique. The drawback of the hot-wire technique is that it is based on a time-average of fluctuations of velocity. A turbulence measure obtained by hot-wire anemometry provides a statistic which also takes into account the sections of the flow which are nominally non-turbulent. As a result, the turbulence level measured is an attenuation of the velocity fluctuations in the turbulent region by the flow in the non-turbulent region. This effect would be particularly high in regions of low turbulence intermittency, such as the one being studied here. If comparisons between the two techniques must be made, a more similar comparison would be to divide the hot-wire turbulence intensity by the intermittency at the same point. This would provide an indication of the turbulence intensity of the turbulent regions. By consulting Table 1, this turbulence characteristic can be seen to generally be between 10% and 15% in the region from 15D to 19D from the ground plane, 20D downstream of the jet

exit. This result compares well with the turbulence characteristic of 11.5% measured by the image processing method.

Figure 17 is representative of the results achieved by applying the box method of fractal analysis to the images acquired for the study outlined above. Whilst an ideal result for fractal analysis is that of a straight line, the gradient of which is the fractal dimension, in reality nothing is fractal to an infinite scale. Beyond the fractal limit of any interface, that is when the resolution of the boxes is smaller than the smallest discontinuity, the number of boxes encompassing the interface increases linearly with grid resolution. The result of this is that the fractal dimension is measured as 1. In Figure 17 this point can be seen to be reached when the box size is of the order of 0.2D or 2.6mm. This value is well above the pixel resolution of the imaging equipment which is approximately 0.36mm/pixel. Thus, the limit indicated by the fractal analysis is a reflection of the lower limit of the structure sizes at the outer edge of the jet image. It can be seen that this 2.6mm limit is above the Kolmogorov length scale and so it can be stated that the flow seeding does not distinguish structures of that size. The limit of the fractal analysis method indicates the smallest size of turbulent structures found on the turbulent/non-turbulent interface. Similarly, for a grid of low resolution, with box size greater than the largest discontinuities, a reduction in box size will also produce a linear relationship between the number of boxes and the resolution. Therefore a gradient of 1 on the log-log curve will occur once more. This can just be seen in Figure 17 between the last two points, which indicate that within the flow visualisation images, the largest structure sizes are of the order of 4D. This result is supported by the image tracking technique discussed earlier.

4. CONCLUSIONS

A low-cost method of light sheet illumination has been demonstrated. A procedure was outlined for setting up the apparatus so that laboratories with the most basic equipment would be able to produce light sheets of the intensity which would usually be prohibitively costly.

The illumination method was a means of creating an environment for a series of flow visualisation experiments. The main aim of this paper was to show that large-scale digital image processing which has, in the past, been generally for qualitative analysis only, can be used to produce quantitative data. Furthermore, the techniques outlined herein have been shown to be capable of eliciting results which are not achievable with conventional measurement techniques. The paper has shown that instantaneous measurements of velocity and length scale based on individual structures is possible. It has demonstrated that time-averaged techniques have a tendency to produce results which have been smoothed out and are not a true representation of the flow. The current work was born of the realisation of the drawbacks in conventional, point-based and statistical approaches to turbulence studies. This new method allows the investigation

of discrete constituents of turbulence and, therefore, may lead to a greater understanding of turbulent flows.

REFERENCES

- Fearn R.L. and Weston R.P., 1974, Vorticity Associated with a Jet in a Crossflow, *AIAA J.*, Vol 12 pp 1666-1671
- Fric T.F. and Roshko A., 1989, Structure in the Near Field of a Transverse Jet, *7th Symp. on Turbulent Shear Flow, Stanford University*, Aug 21-23. pp 6.4.1-6.4.6
- Keffer, J.F. and Baines W.D. 1963, The Round Turbulent Jet in a Crosswind, *J. Fluid Mech.*, Vol 15 pp 481-486
- Margason R.J., 1993, Fifty Years of Jet in Crossflow Research, *AGARD Conf. Proc. 534 Computational and Experimental Assessment of Jets in a Crossflow.*, Winchester UK 19-22 April, pp 1.1 -1.30
- McCusker S., Savory E. and Toy N., 1996 A Digital Image Processing Analogy to Hot-Wire Anemometry I.MECH.E Conf. Trans. *Int. Seminar on Optical Methods and Data Processing in Heat and Fluid Flow.*, City University., pp 469-474
- Pratte B.D. and Baines W.D., 1967, Profiles of the Round Turbulent Jet in a Crossflow, *Proc ASCE. J. of the Hydraulics Division*, HY6, Vol 92. pp 53-64
- Sreenivasan K. R. 1991, Fractals and Multifractals in Fluid Turbulence., *Ann. Rev. Fluid Mech.*, 23., pp 539-600
- Toy N., Disimile P. J., Savory E. and McCusker S., 1992, The Development of the Interface Between Twin Circular Jets and a Normal Crossflow, *Proc. of the 13th Biennial Symp. on Turbulence, University of Missouri-Rolla.*, Paper B10
- Toy N., Savory E. and McCusker S., 1993, The Penetration of Twin Turbulent Jets in a Crossflow, *ASME FED*, Vol. 174, pp 71-76

Y/D	U (m/s)	$\frac{u'}{U}$	I	Turbulence Characteristic $\frac{u'/U}{I}$	Kolmogorov Frequency (1/Kt) (Hz)	Integral Length Scale (L_i/D)
15.0	1.002	0.062	0.499	0.124	61.63328	1.0095
15.5	0.996	0.047	0.450	0.104	49.95005	0.8691
16.0	0.996	0.048	0.351	0.137	47.40685	1.0887
16.5	0.993	0.029	0.272	0.107	40.64875	0.8488
17.0	0.996	0.014	0.111	0.126	36.63809	1.0623
17.5	0.991	0.013	0.077	0.169	36.43253	0.8393
18.0	0.993	0.014	0.123	0.114	36.34513	0.8763
18.5	0.990	0.011	0.086	0.128	36.90173	0.8068
19.0	0.990	0.014	0.109	0.128	36.53769	0.7619

Table 1 - Table of Hot-Wire Data at X/D = 20

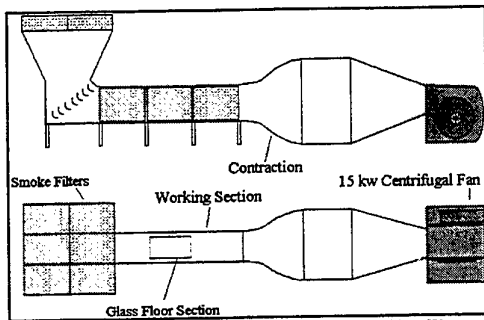


Figure 1-Diagram of Smoke Tunnel Facility

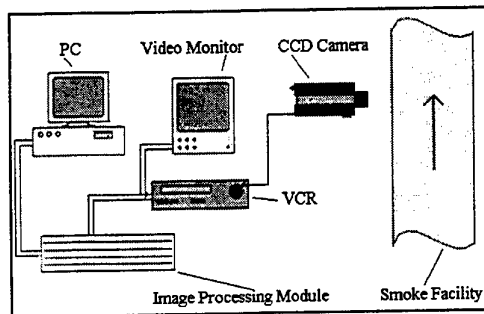


Figure 2 - Diagram of Image Processing Equipment

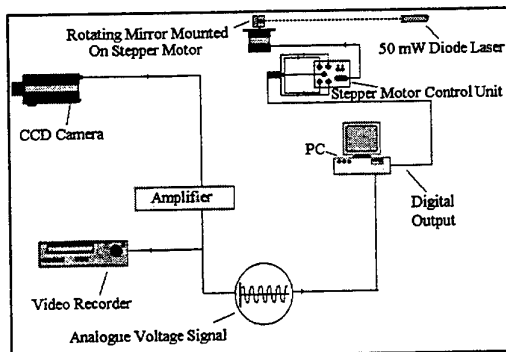


Figure 3 - Schematic of Light Sheet Arrangement

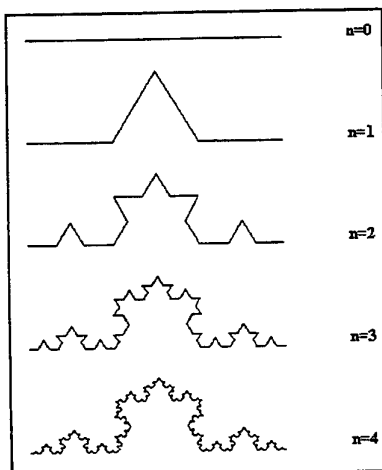


Figure 4 - Triadic Koch Curve



Figure 5 - 1st of 4 Images of Turbulent Structure



Figure 6 - 2nd of 4 Images of Turbulent Structure



Figure 7 - 3rd of 4 Images of Turbulent Structure



Figure 8 - 4th of 4 Images of Turbulent Structure

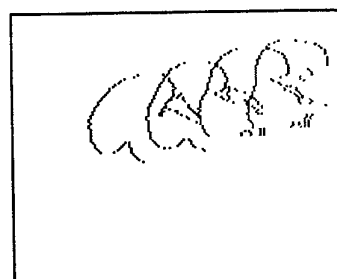


Figure 9 - Combined Image of Structure Path

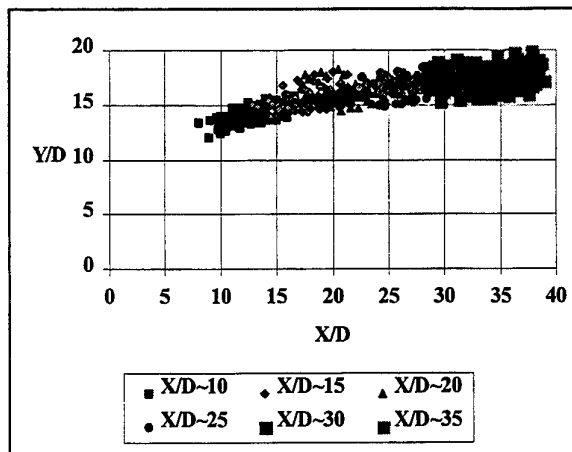


Figure 10 - Location Of Of Turbulent Structures

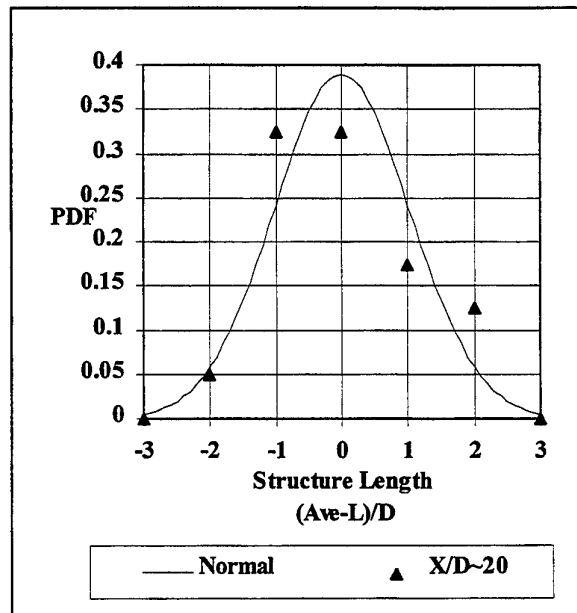


Figure 12 - Probability Density Function of Length Scales
(Y/D=15 - 20)

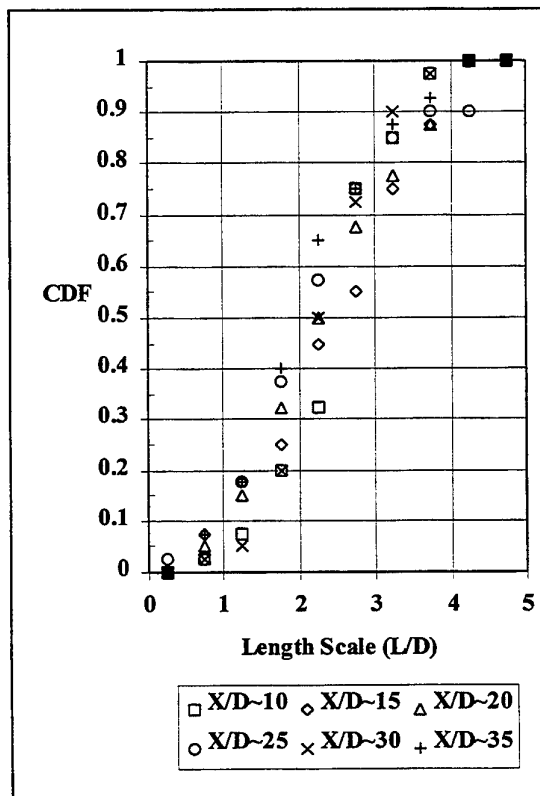


Figure 11 - Cumulative Distribution Function of Length Scales (Y/D =15 - 20)

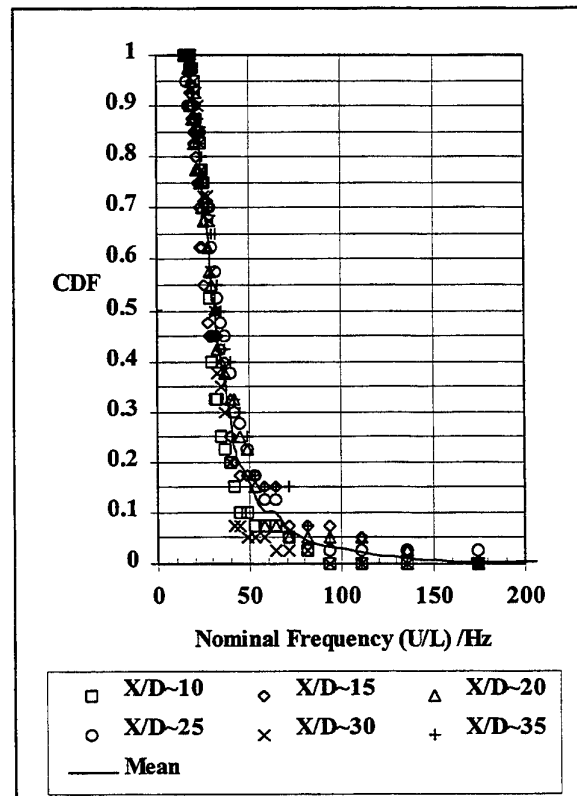


Figure 13 - Cumulative Distribution Function of Frequencies (Y/D =15 - 20)

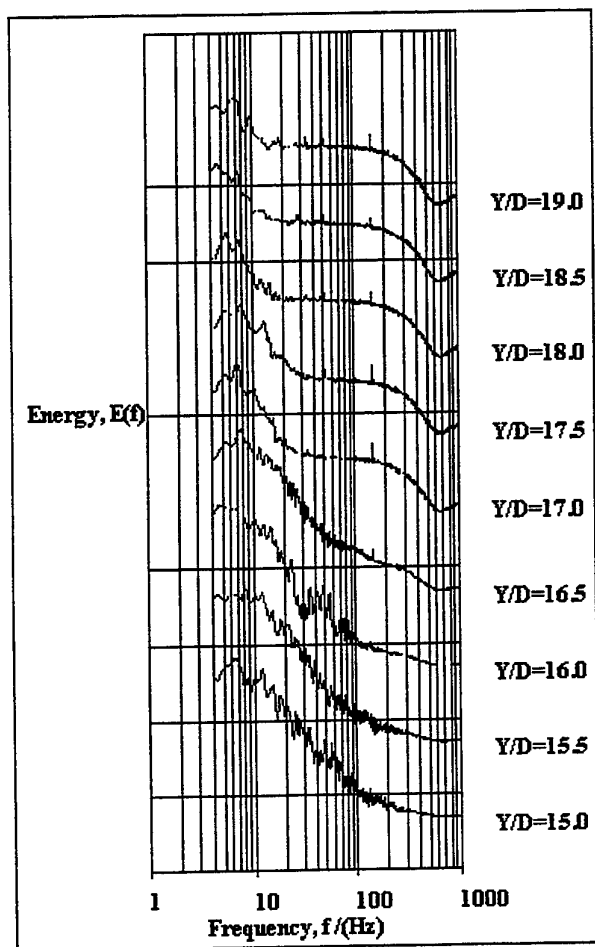


Figure 14 - Power Spectra at $X/D=20$

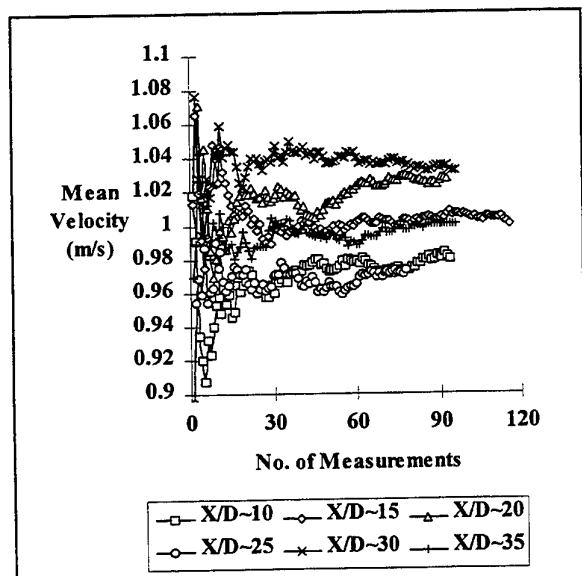


Figure 15 - Mean Velocity Estimations From Structure Positions

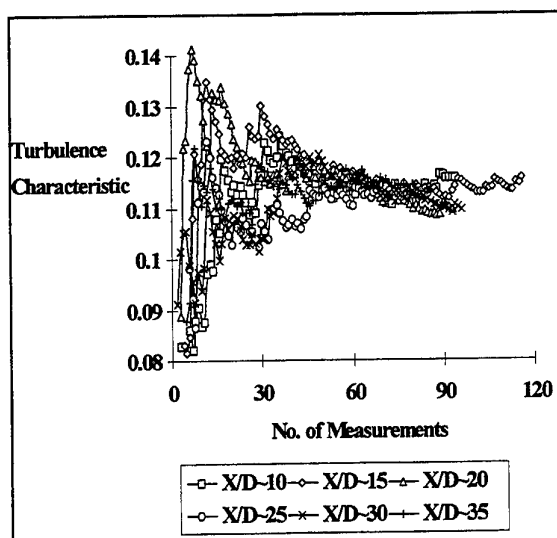


Figure 16 - Turbulence Characteristic Estimations From Structure Velocities

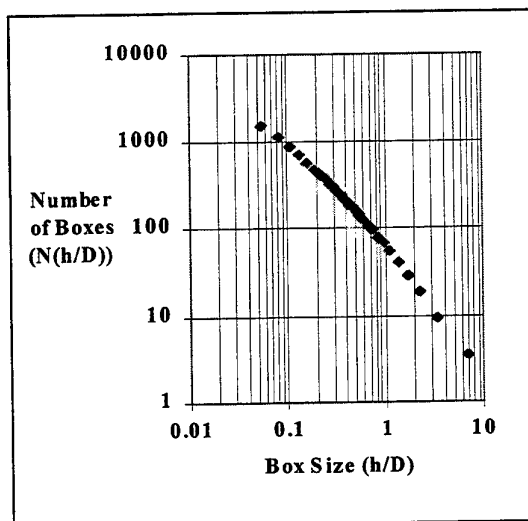


Figure 17 - Log - Log Plot of Number of Boxes against Grid Resolution Average of 40 Images @ $X/D \sim 20$

PTV Analysis of Jets in Cross-flow

G. Carlomagno*, A. Cenedese**, G. De Angelis**

*DETEC Università "Federico II", Piazzale Tecchio 80, 80125 Napoli

**DITS Università "La Sapienza", Via Eudossiana 18, 00184 Roma

ABSTRACT

A jet in a cross-flow is a fully three dimensional flow where different vortex structures are generated from the interaction between the main flow and the jet. In order to analyse such a complex flow, the particle tracking velocimetry (PTV), based on the analysis of successive images, is utilised. Since the frame is analysed one at a time in sequence the ambiguity in the velocity versus is solved. Also the dynamic range in the velocity measurements is increased by one order of magnitude compared to those obtained by means of the analysis of a multiexposed image.

1. INTRODUCTION

Jets in cross-flow are an interesting flow for various engineering applications:

- environmental: smoke dispersion from chimneys and volcanoes, liquid dispersion in lakes and rivers;
- petrol industry: oil and gas jets in the main flow of pipe withdrawal;
- engines: surface cooling, fluid injection;
- aeronautics: rocket direction control, vehicles V/STOL.

In this paper the near field of the jet in cross flow is experimentally analysed by means of Particle Tracking Velocimetry (PTV) which allows a quantitative velocity measurement in a plane to be obtained. In such an area a strong interaction between main flow and jet produces a very complex field where these kinds of different vortex structures can be identified (Fig. 1 Fric and Roshko, 1994):

- jet shear layer vortices: are the dominating element in the initial part of the jet, due to Kelvin-Helmholtz instability and are identical to those generated by coaxial jets;

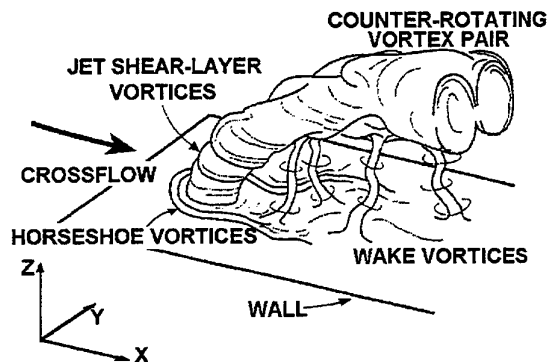


Fig. 1 Near field representation of a jet in a cross flow (from Fric and Roshko, 1994)

- horse-shoe vortices: are due to an adverse gradient near the wall close to the jet again, such vortices are found in a very limited zone corresponding to a distance of some jet diameter from the jet entrance;
- counter-rotating vortex pair: occurs due to interaction between main currents and the jet, they develop in the near field and become the main element in the far field;
- wake vortices: occur due to interaction between the jet and the boundary layer at the wall.

Jets in cross flow are widely studied with empirical models, integral models, numerical models and with experimental simulations.

The empirical models (Margason (1968), Pratte e Baines (1967), Kamotani e Greber (1972), Rajaratnam e Gangadharaiiah (1981)) are the simpler way to obtain information on the jet axis geometry. For a circular jet perpendicular to the main flow the following relationship is proposed :

$$\frac{z}{D} = aR^\alpha \frac{F_x}{F_D} \frac{F}{K}$$

where:

- x is the direction along the main flow;
- z is the direction orthogonal to the wall;
- R is the ratio between the velocity of the jet and the velocity of the mean flow;
- D is the jet diameter;
- a , α , β are constants suggested by different authors (Tab.1).

Author	R	a	α	β
Kamotani & Greber	4÷10	0.89	0.94	0.36
Pratte & Baines	5÷35	2.05	0.72	0.28
Margason	2÷10	1.59	0.67	0.33

Tab. 1

The integral models (Abramovich (1963), Rajaratnam (1976), Schetz (1980), Demuren (1985)) are based on the utilisation of the momentum balance equation to a volume banded by planes orthogonal to the jet axis. In order to reduct to one dimensional situation, it is necessary to make an hypothesis on the velocity distribution in the transversal sections: usually the form of the sections is chosen to be elliptical. Also from these models the trend of the axis is obtained.

More recently numerical relations of the three dimensional balance equation have been proposed utilising different turbulence closures. In this case no hypothesis is necessary for geometry of the transversal section which is possible to determinate in one more realistic way (kidney-shape cross section) (Jones e McGuirk (1979), Leonard (1979), Schetz (1980), Launder e Spalding (1980), Sikes et al. (1986), Demuren (1992)(1994), Alvarez e Jones (1993)).

In the 1970 studies focused on the mean trajectory of the jets and the evolution of the flow along the mean trajectory. Ramsey e Goldstein (1971) used a subsonic wind tunnel capable of air velocities of up to 70 m/s in the test section. The test section of the wind tunnel was 20.3 cm x 20.3 cm in cross section. The injection of the air jet was through a 23.5 mm diam stainless steel tube approximately 1 m long. Fully developed turbulent flow was present at the tube exit. The blowing rate $M = \rho_j U_j / \rho_f U_f$ ranged from 0.1 to 2 and the air jet entered at an angle of either 35 or 90 deg to the main flow. A hot-film probe with a 0.025 mm diam x 0.51 mm long sensor was used for velocity measurements. the probe was positioned along the tunnel center line. Kamotani e Greber (1972) performed their experiments in a 771 mm² cross section subsonic wind tunnel. The jet was

injected perpendicularly. Velocity and turbulence intensity were measured by a hot wire probe. The mean flow direction was measured by a small yaw angle meter made of two hypodermic needles of 0.71 mm diam with bevelled open ends. Detailed measurements were performed using jets having momentum fluxes ranging from about 15 to 60 times the cross flow momentum flux.

In the 1980, Crabb et al. (1981) used an open circuit wind tunnel with a free stream velocity of 12 m/s. The dimensions of the working section of the wind are 0.46 m wide, 0.30 m high and 1.8 m long. A single tube, 25.4 mm inside diameter and a 0.75 m long was used to inject the jet normal to the free stream with velocity ratio 1.15 and 2.3. The jet was located at a distance 0.15 m downstream of a 25 x 460 mm emery paper trip. The jet was supplied from a centrifugal fan. Hot-wire measurements were made laterally across the jet and the cross-flow. Laser Doppler anemometer and hot wire anemometry were used to make measurements. Andreopoulos and Rodi (1984) utilised a closed-circuit wind tunnel with an octagonally shaped working section 6 m long and 1.5 m in diameter. The jet discharge was placed 10 exit diameters downstream from the leading edge of a plate installed 0.28 m above the floor of the tunnel. The jet exited normally from a brass pipe of 50 mm internal diameter, the exit plane of the pipe being 12 diameters downstream of the plenum chamber, which was fed by a two-stage compressor. The mean and turbulent velocity components in the jet in a cross flow interaction region were measured with anemometers, cross and triple wire probes for the three velocity ratio $R=0.5$, 1 and 2.

In the latter years, Fric and Roshko (1994) made use of an open-return low-speed wind tunnel of cross-section 0.5 m x 0.5 m. The velocity ratio ranged between 2 and 10 and nominal mean cross flow velocities ranged from 1.5 to 4.5 m/s. The incompressible jet which issued orthogonally into the crossflow was supplied by a 3.8 cm exit-diameter nozzle. The jet was powered by a radial vane centrifugal blower. In that study the smoke-wire visualisation technique, which places closely spaced streaklines into the flow, was used extensively. Kelso et al. (1996) made visualisation experiments with a closed-return water channel. The study was restricted to jet to freestream velocity ratios R ranging from 2 to 6. The pipe, which was orthogonal to the channel floor and very short (3.5D long) had an internal diameter of 25 mm. The jet's water supply was isolated from the main channel circuit by a constant-head tank. A narrow circumferential slot in the pipe

wall allowed dye to be injected directly into the pipe boundary layer. Moveable dye injection tubes were also used to introduce dye into the cross-flow from points away from the wall. Dyes with specific gravity 1 were used to visualise the flow.

2. EXPERIMENTAL SET-UP

Experiments have been carried out in a water tunnel maintaining constant the velocity of the main flow ($u_f = 10$ cm/s at the channel centre) and varying the jet velocity u_j from 20 cm/s to 100 cm/s ($R = u_j/u_f = 2\div 10$). The tunnel, made in perspex, has a rectangular section (10 cm x 15 cm).

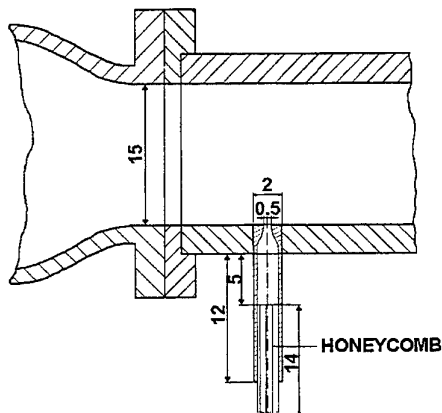


Fig. 2 Jet test section (the dimensions are in cm).

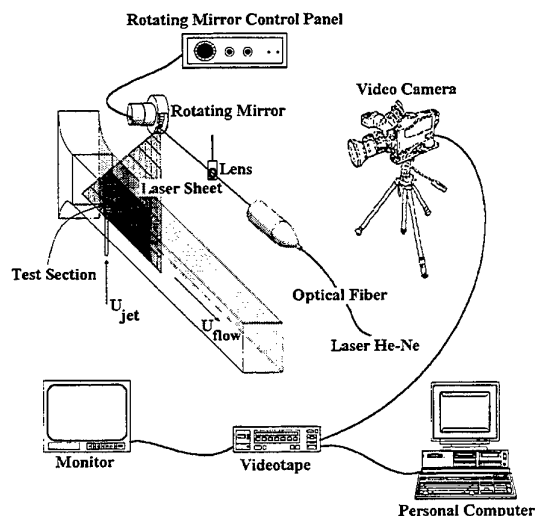


Fig. 3 Experimental apparatus for lighting test section and for images acquisition

The circular jet, whose initial dimension is 0.5 cm, has the axes perpendicular to the main flow. So as to avoid secondary flow in the jet and reduce turbulence level at the inlet a suitably convergent preceded by a honeycomb was used. Moreover, to limit the boundary layer effect, the jet is placed immediately downstream to the convergent section of the tunnel (Fig. 2).

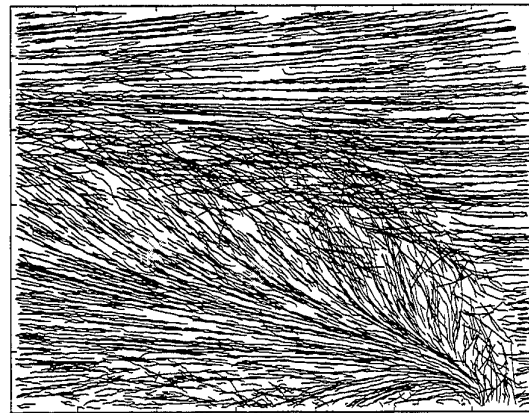


Fig. 4 Trajectories evaluated for 20 s ($R=4$).

In Fig. 3 the test section lighting system and the major acquisitions are shown. The light sheet is obtained by means of laser beam (Argon 512 nm wavelength) and rotating mirror. The jet liquid (water) is seeded by pollen particles ($70 \mu\text{m}$) which assume the same specific weight of the liquid. The images are acquired with a standard video camera at a speed of 50 images/second (25 interlaced) and stored in a videotape.

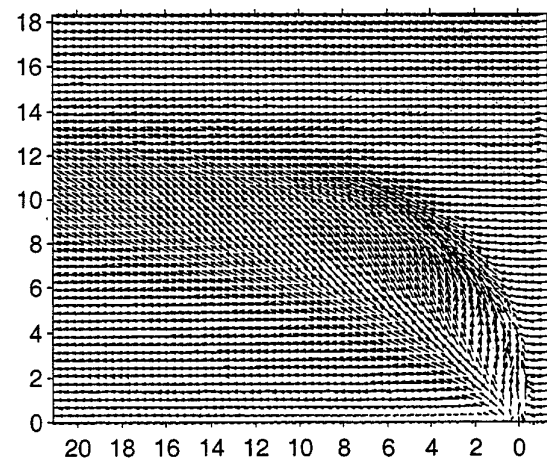


Fig. 5 Velocity flow field reconstructed in a regular grid ($R=4$).

The images are subsequently analysed off line performing the following operation:

- filters and thresholds in order to reduce noise level;
- identification of each particle barycenter;
- trajectories reconstruction;
- velocity evaluation;
- reconstruction of velocity field in a regular grid using a gaussian filter.

3. RESULTS

The images for PTV analyses are obtained with two different light sheet positions:

- longitudinal light sheet in the plane xz of water tunnel and jet axes;
- transversal light sheet in the plane yz perpendicular to the mean flow direction; the images are acquired at different distances from the jet entrance.

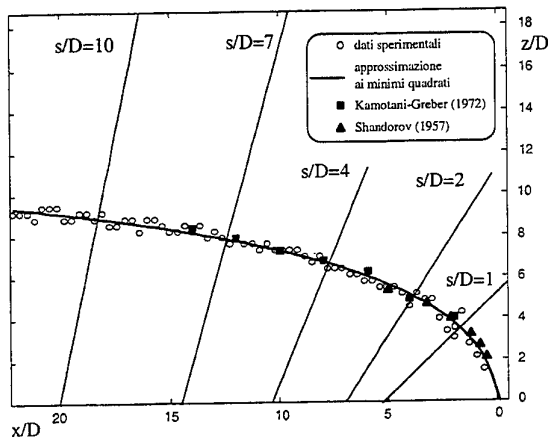


Fig. 6 Axes of the jet: comparison between theoretical approximation and experimental data ($R=4$).

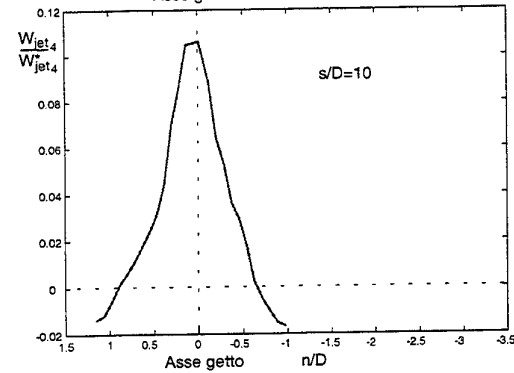
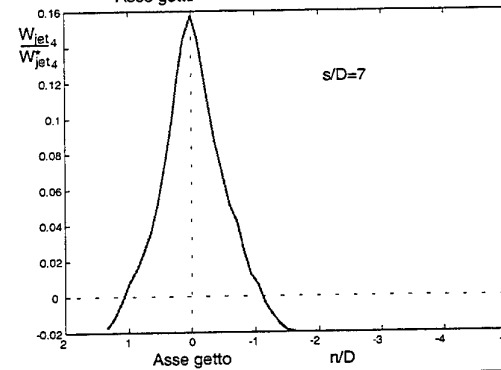
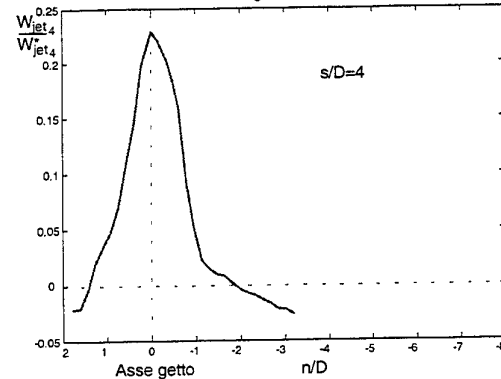
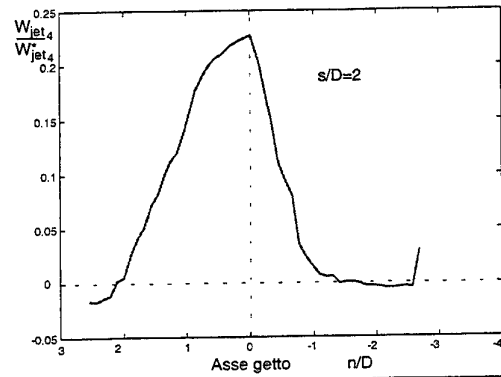
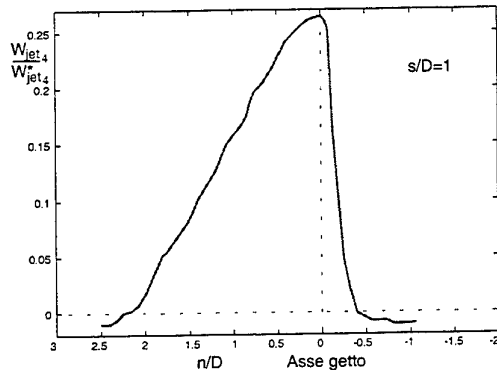


Fig. 7 Velocity profiles in some transversal sections of the jet ($R=4$). W_{jet4}^* is the velocity measured at the exit of the nozzle.

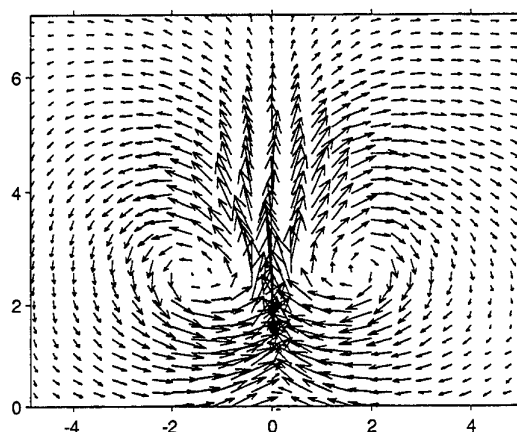


Fig. 8 Detail of the velocity field in a plane perpendicular to the mean velocity ($R=4$)

In Fig. 4 an example of the results obtained by means of a longitudinal light sheet is shown. Starting from the trajectories, the mean velocity and turbulence intensity field in a regular grid can be obtained (Fig. 5). From an analysis of this data it is possible to evaluate the position of the jet axis. The

jet axis is defined as the points location where the mean velocities assume the maximum values in a transversal section of the same jet.

In Fig. 6 the results obtained for $R = 4$ are shown. These results are compared with those obtained by other authors (Kamotani e Greber, 1972; Shandorov, 1957) and with the trend resulting from use of an integral method, due to Vizel and Mostinskii (1965):

$$\frac{F_y}{F_x} = aR^2 \log \frac{F}{H} + b \frac{x}{D}$$

where a and b are constant values which can be determined by means of a least squares method.

The trend of the velocity (Fig. 7) in the direction of the jet axis for different cross sections show an evident skewness for small values of s/D (s is the curvilinear abscissa). Further analysis in the longitudinal plane were carried out on transversal planes (orthogonal to the velocity of the main flow).

Fig. 8 shows the velocity field obtained

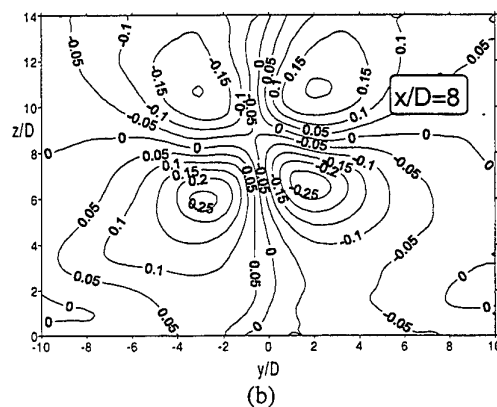
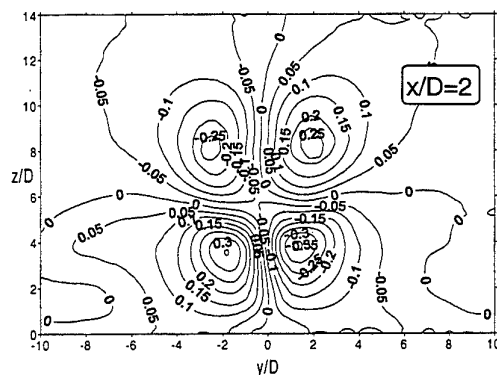
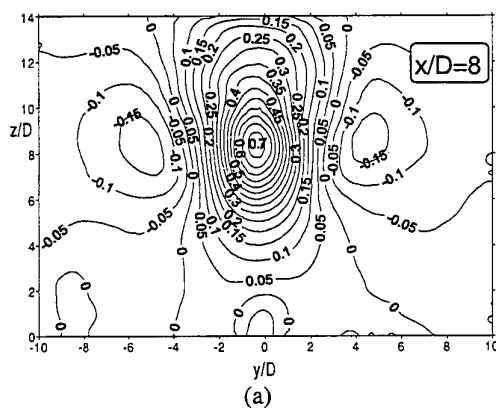
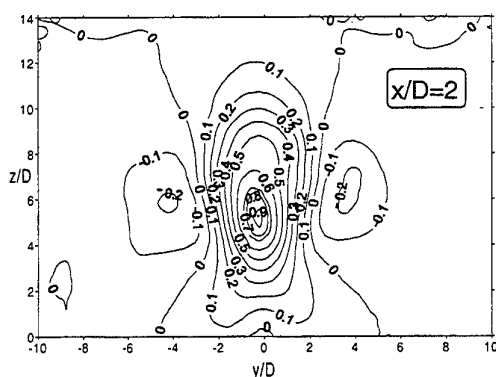


Fig. 9 (a) Costant w values
(b) Costant v values
for two different distance from the jet-exit ($R=4$)

Jones W.P.,
McGuirk J.J.,
1979, Computation
of a round

likewise by means of tracking analysis and subsequently reconstructed using in a regular grid a suitable interpolation technique. Two opposite rotating vortical structures are clearly visible. In fig. 9, referring to z axis, it is possible to see for two different sections x/D how the velocity component w shows an evident symmetry whereas the velocity component v shows an anti symmetrical trend.

turbulent jet discharging into a confined cross flow, Turbulent Shear Flows II, Springer Verlag, New York.

Kamotani Y., Greber I., 1972, Experiments on a turbulent jet in a cross flow, AIAA J., vol.10, no.11.

Kelso R.M., T.T. Lim, A.E. Perry, 1996, An experimental study of round jets in cross-flow, J. Fluid Mech., vol. 306.

Fric T.F., Roshko A., 1994, Vortical structure in the wake of a transverse jet, J. Fluid Mech., vol.279.

Launder B.E., Spalding D.B., 1980, The numerical computation of turbulent flows, Comp. Meths. Appl. Mech. Eng. vol.3.

Leonard B.P., 1979, A stable and accurate convective modelling procedure based on quadratic upstream interpolation, Compt. Meths. Appl. Mech. Engrg.

Margason R.J., 1968, The path of a jet directed at large angles to a subsonic stream, NASA.TN.D.-4919, Langley Research Center, Hampton, Virginia.

Pratte B.D., Baines W.D., 1967, Profiles of the round turbulent jets in a cross flow, J. Hydr. Div., Proc. ASCE, vol.93.

Rajaratnam N., 1976, Turbulent jets, Elsevier Scientific Publishing Company, New York.

Rajaratnam N., Gangadharaiah T., 1981, Scales for circular jets in cross flow, J. Hydr. Div., ASCE, vol.107.

Ramsey J.W., Goldstein R.J., 1971, Interaction of a heated jet with a deflecting stream, ASME. J. Heat Transfer.

Schetz J.A., 1980, Injection and mixing in turbulent flow, AIAA, New York.

Shandorov G.S., 1957, Flow from a channel into stationary and moving media, Zh. Tekhn. Fiz.

4. CONCLUSION

Experimental analysis of a jet in a cross flow points out a very complex vortex structure which is connected with a non gaussian velocity distribution in space.

PTV based on the analysis of a large quantity of images is utilised in order to have the average of the velocity values and evidence the formation of two counter-rotating vortexes in the transversal section.

REFERENCES

Abramovich G.N., 1963, The theory of turbulent jets, MIT Press, Cambridge, MA.

Alvarez J., Jones W.P., 1993, Computation of a jet discharging into a cross-flow with a second moment turbulence closure and a low-diffusive convection-discretization scheme, in: Engineering Turbulence Modeling and Experiments 2, Elsevier Publishers.

Andropoulos J., Rodi W., 1984, Experimental investigation of jets in a crossflow, J. Fluid Mech., vol.138.

Crabb D., Durao D.F.G., Whitelaw J.H., 1981, A round jet normal to a crossflow, ASME. J. Fluids Eng., vol. 103.

Demuren A.O., 1985, Modeling turbulent jets in crossflow, in: Encyclopedia of Fluid Mechanics, vol.2, cap.17.

Demuren A.O., 1992, 1994, Calculations of 3D impinging jets in crossflow with Reynolds stress models, Proceedings. Inter. Symposium on Heat Transfer in Turbomachinery, Marathon, Grecia.

Sykes R.I., Lewellen W.S., Parker S.F., 1986, On the vorticity dynamics of a turbulent jet in a cross flow, J. Fluid Mech., vol.168.

Vizel Y.M., Mostinskii I.L., 1965, Deflection of a jet injected into a stream, Fluid Dynamics, vol.8.

A 30° INCLINED WALL JET

Joseph C.S. Lai and Deshan Lu

School of Aerospace & Mechanical Engineering
University College, The University of New South Wales
Australian Defence Force Academy
Canberra, ACT 2600, AUSTRALIA.

ABSTRACT

The mean velocity field of a 30° inclined wall jet has been investigated using a two-component laser Doppler anemometer. The role of coherent structures arising from initial instabilities has been explored by hot-wire spectra measurements. Results indicate that the fundamental vortex roll-up frequency in both the inner and outer shear layer corresponds to a Strouhal number (based on nozzle exit momentum thickness and velocity) of 0.012. The spatial development of instabilities in the jet has been studied by introducing acoustic excitation at a frequency corresponding to the shear layer mode. The formation of the fundamental and its first subharmonic has been identified in the outer shear layer. However, the development of the first subharmonic in the inner shear layer has been severely suppressed. Distributions of mean velocities, turbulence intensities and Reynolds shear stress indicate that controlled acoustic excitation enhances the development of instabilities and promotes jet reattachment of the wall, resulting in a substantially reduced recirculation flow region.

1. INTRODUCTION

Turbulent wall jets have been extensively studied both theoretically and experimentally. However, a review by Launder (1983) on turbulent wall jets has revealed that despite over two hundred publications on the topic, accurate data particularly on the distribution of turbulence stresses are lacking and the physics of the flow is still not well understood. With very few exceptions, all the measurements so far were conducted in the fully-developed region of the jet where self preservation is being approached or has already been

attained. Some of the more recent studies, such as Matsuda et al (1990), Katz et al (1992), Hsiao & Sheu (1994), Schneider & Goldstein (1994) and Zhou et al (1996) have been directed at studying the flow structures in plane wall jets. In most practical applications, a jet is injected at an angle to a solid boundary and the region of interest is within the first ten nozzle widths.

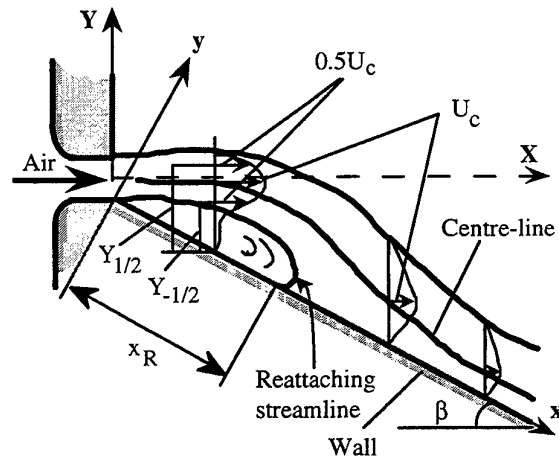


Fig. 1 Model of an inclined wall jet.

Forthmann (1934) conducted the first experimental study of an inclined wall jet and the Coanda effect (in which a jet reattaches to a nearby solid surface) has attracted considerable attention. Based on surface pressure measurements, Newman (1961) proposed a flow model (Figure 1) that provides an estimate of the reattachment distance. His results were in fair agreement with experimental data for $\beta > 45^\circ$ and for jet exit

Reynolds number > 8000 . The effect of the wall angle (β) on the development of the velocity field of an inclined wall jet was first investigated using constant temperature hot-wire anemometry by Lai & Lu (1996) for $\beta = 0^\circ, 15^\circ, 30^\circ$ and 45° and a nozzle exit Reynolds number of 10,000. Although surface pressure measurements and flow visualisation results as documented by Lai & Lu (1992) seem to correlate quite well with the hot-wire measurements, the hot-wire data cannot discriminate against reversed flow in the recirculation flow region between the main jet flow and the wall. It is, therefore, essential to use an instrument such as laser Doppler anemometer (LDA) capable of resolving such flow ambiguities. Furthermore, the instability characteristics of an inclined wall jet have never been reported in the literature. The objectives of this paper are, therefore,

- (i) to study the velocity field of a 30° two-dimensional wall jet using a two-component LDA;
- (ii) to present the instability characteristics of a 30° inclined wall jet; and
- (iii) to demonstrate how the spatial development of this jet can be controlled through acoustic excitation.

APPARATUS AND INSTRUMENTATION

Apparatus

The two-dimensional nozzle facility comprised a blower, a perspex jet settling chamber and a rectangular nozzle with profiles based upon the British Standard BS1042. The nozzle dimensions were: length $l = 300$ mm, width $h = 5$ mm, giving an aspect ratio of 60. The perspex jet settling chamber is 770 mm long, 150 mm wide and 400 mm high. The air flow rate can be adjusted to give various nozzle exit velocities up to 50 m/s. Air from the blower was passed through a series of grids which reduced the turbulence intensity at the nozzle exit for the steady jet to about 0.3 % at the centre-line, as described by Lai & Simmons (1985). The wall length was $L = 500$ mm, giving $L/h = 100$. The wall angle β was set at 30° . No side plates were used to enhance the two-dimensionality of the flow. Hot-wire and LDA probes, controlled by an NEC 386/20 computer, were traversed in the streamwise and transverse directions by two stepping motors. The smallest step in each direction was 0.015 mm. The nozzle exit Reynolds number (based on nozzle width h and exit velocity (U_0)) was 6,700. The variation of the ambient temperature was within $\pm 1^\circ\text{C}$. Lai & Lu (1998) have shown that for $L/h = 30$, the jet is essentially two-dimensional even without side plates installed. Furthermore, for $6,670 < R_0 < 13,340$ and $\beta < 50^\circ$, the reattachment length is virtually independent of R_0 .

Instrumentation

Hot-wire anemometry (HWA) The frequency spectra in the shear layer of the jet were obtained using a single hot-wire, operated at an overheat ratio 1.3 with a TSI IFA100 constant temperature anemometer and an OnoSokki CF-350 FFT analyser. X-wires were also used in some measurements.

Laser Doppler anemometry (LDA) The LDA system comprised a Coherent's INNOVA 70 series Argon ion laser and two DANTEC 57N10 Burst Spectrum Analysers (BSA). A smoke generator was used for seeding the flow. The liquid used to produce smoke was non-poisonous Rosco "FOG FLUID". Seeding particles (smoke) were introduced into the flow through both sides of the jet settling chamber. The Burst Spectrum Analysers were operated in the continuous mode and the number of burst samples for each measurement was at least 2000. The raw velocity data were corrected by applying a weighting function using the time between particle arrivals in order to reduce the velocity bias errors. The LDA measurement technique was first validated by theoretical results and hot wire data made in a single free jet at 15 nozzle widths downstream from the nozzle plate (Lu (1994)).

RESULTS AND DISCUSSIONS

Initial Conditions

It is well known that the spatial development of free shear flows is dependent on the initial conditions. For an inclined wall jet, initially at the nozzle exit, there are two distinctive boundary layers: the inner and the outer shear layers. Fig. 2 shows the mean streamwise velocity profiles measured by a single hot-wire in the two initial boundary layers at $x/h = 0$.

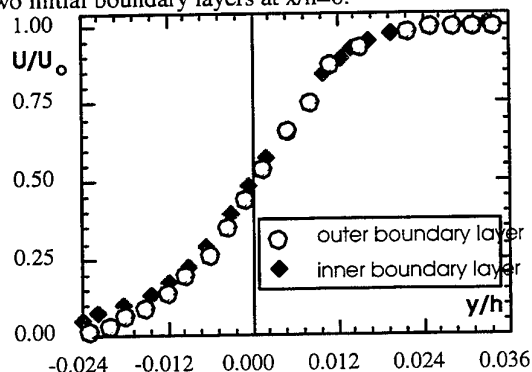


Fig. 2 Mean streamwise velocity profiles at the nozzle exit.

It can be seen that the differences between the inner and outer boundary layers velocity profiles are not significant. The shape factor is 2.85. The initial momentum thickness θ_0 for $\beta = 30^\circ$ and 90° (free jet) was measured by a single hot-wire when the nozzle exit Reynolds number was varied from 3,000 to 10,000. As shown in Fig.3, the initial momentum thickness for the free jet (90°) is proportional to $(U_0)^{-1/2}$, in agreement with results of Gutmark & Ho (1983) and Hsiao & Huang (1990) and the results for $\beta=30^\circ$ also obeys the same relationship.

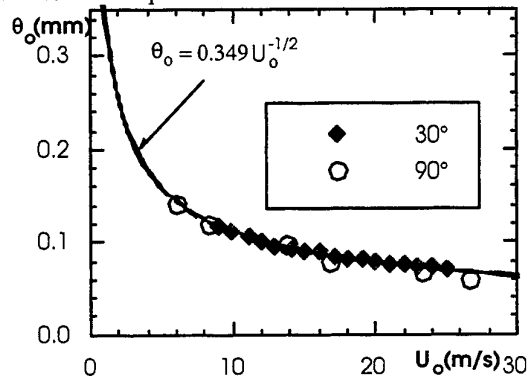


Fig. 3 Variation of the initial momentum thickness θ_0 with the nozzle exit velocity.

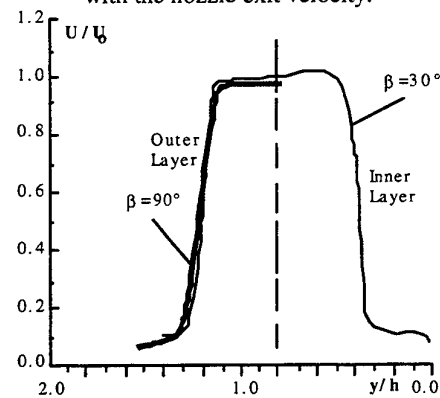


Fig. 4 (a) Mean streamwise velocity at $x/h=0.5$.

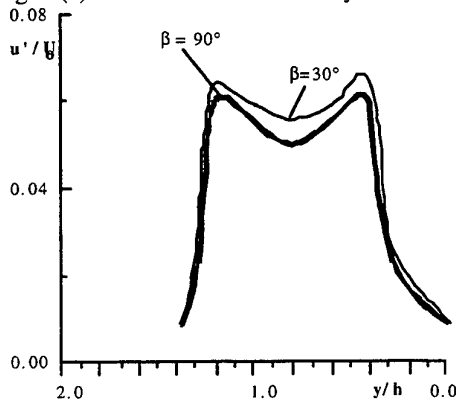


Fig. 4 (b) Streamwise turbulence intensity at $x/h=0.5$.

The mean streamwise velocity and turbulence intensity profiles measured by LDA at $x/h=0.5$ for $\beta = 30^\circ$ are shown in Figs. 4(a) and (b) respectively. Compared with a free jet ($\beta = 90^\circ$) which has top-hat velocity distributions in the potential core, the inclined wall jet has inclined velocity distributions near the nozzle exit, indicating that the jet is deflected towards the wall. This is known as the Coanda effect which may be explained as follows. As the jet leaves the nozzle, the fluid which is entrained in the confined region between the jet and the wall is accelerated near the wall and since the flow is two-dimensional, a pressure lower than that of the surroundings is produced on the wall. Consequently the jet curves towards the wall and reattaches to the wall if the wall is long enough.

Instability Characteristics of the Natural Jet

In order to observe the development of instabilities in the shear layers in free jet flows, measurements were made at $y = y_{0.9}$ in the inner edge of the shear layer where large momentum transfer occurs between the flow in the potential core and the flow in the shear layer (Hussain 1983, Zaman & Hussain 1984). Here U_m is the local x-maximum velocity and $U = 0.9U_m$ at $y = y_{0.9}$. Figs. 5 shows the spatial development of the frequency spectra, $u'(f)/U_m$ for $\beta = 90^\circ$ (free jet). It can be seen that the fundamental vortex roll-up frequency f_m ($=2475$ Hz) is saturated at $x/h = 2.0$, has started to merge to form the first subharmonic $f_m/2$ at $x/h = 3.0$, and by $x/h = 6.0$ the third sub-harmonic $f_m/8$ has emerged (Fig. 5).

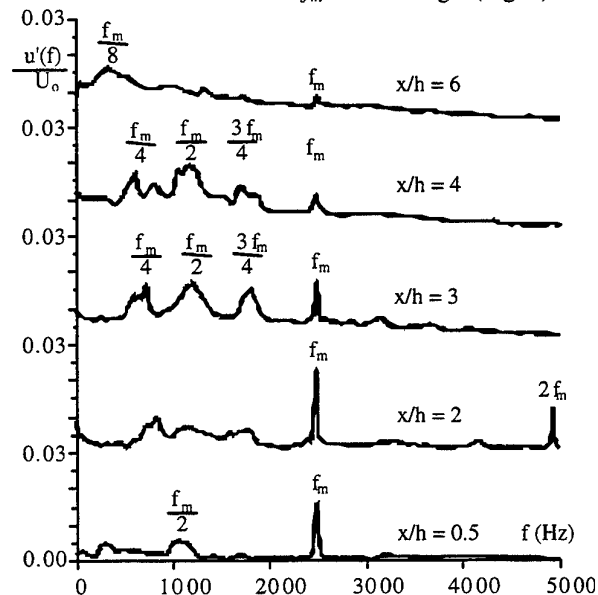
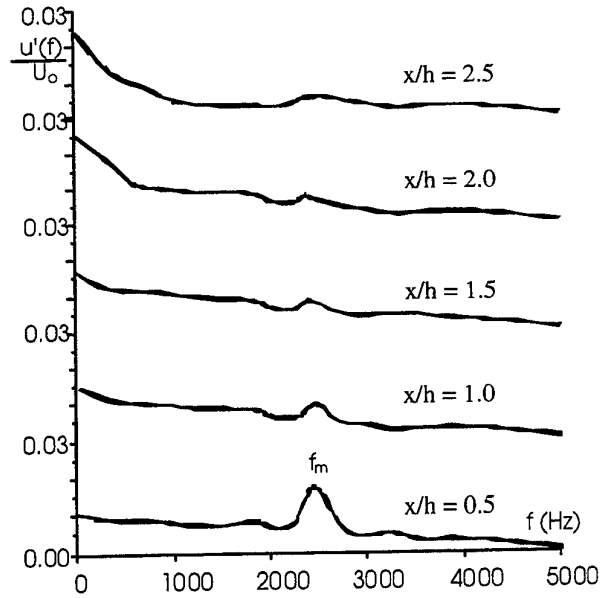
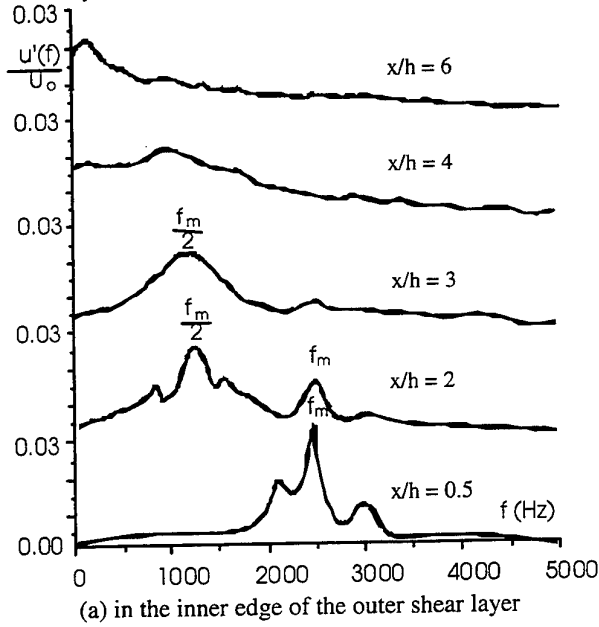


Fig. 5 Frequency spectra $u'(f)/U_o$ in the inner edge of the shear layer for a free jet.

Fig. 6 (a) shows the frequency spectra of $u'(f)/U_o$ at $y = y_{0.9}$ in the outer shear layer for $\beta = 30^\circ$. The fundamental frequency f_m in the outer shear layer for the inclined wall jet equals that in the free jet ($\beta = 90^\circ$). However, the amplitude of $u'(f_m)$ is different for $\beta = 30^\circ$ and 90° . This is because the coordinate system (x - y) is dependent on the wall angle β ; the shift of maximum $u'(f_m)$ observed in Figs. 5 and 6(a) is due to the rotation of the (x - y) coordinate system. If the locations of maximum $u'(f_m)$ are evaluated under the (X - Y) coordinate system, they are nearly the same for different β . Fig. 6(a) shows that for $\beta = 30^\circ$, only the fundamental frequency f_m and its first sub-harmonic $f_m/2$ are found in the flow development region in the outer shear layer.



(b) in the inner edge of the inner shear layer
Fig. 6 Frequency spectra $u'(f)/U_o$ for $\beta = 30^\circ$.

Spectra measurements for the inner shear layer edge made at $y = y_{0.9}$ for $\beta = 30^\circ$ are shown in Fig. 6(b). The fundamental frequency of 2475 Hz can be identified at $x/h = 0.5$. However, unlike in the outer shear layer, there is no evidence of the formation of subharmonics in the inner shear layer primarily because of the constraint imposed by the wall.

In two-dimensional free jets, the flow patterns within two symmetrical shear layers have the same mechanism in the development of instabilities. On the other hand, in an inclined wall jet, the flow mechanism between the inner and outer shear layers is quite different because of the asymmetrical structure and the presence of the wall. A principal distinction of free- and wall-bounded flows is derived from their different instability characteristics (Fiedler & Fernholz 1990). While wall-bounded flows are Orr-Sommerfeld unstable, with viscosity playing a crucial role, free flows are in essence Rayleigh unstable. There the effect of viscosity is only of damping influence and the primary instability is characterised by vortical induction.

Fig. 7 shows the variation of f_m with the nozzle exit velocity U_o . It is clear that for $\beta = 30^\circ$, f_m varies with $(U_o)^{3/2}$, which is the same as for free jets reported by Hsiao and Huang (1990). By combining the results of the initial momentum thickness θ_o in Fig. 3 and f_m in Fig. 7, the fundamental mode expressed in terms of the Strouhal number $St_\theta (= \theta_o f_m / U_o)$ for $\beta = 30^\circ$ is approximately 0.012, virtually independent of Re in the range $3000 < Re < 11,000$. These results are in good agreement with those for free shear layer flows reported

by Fiedler & Fernholz (1990), Hussain & Zaman (1978) and Hussain (1983).

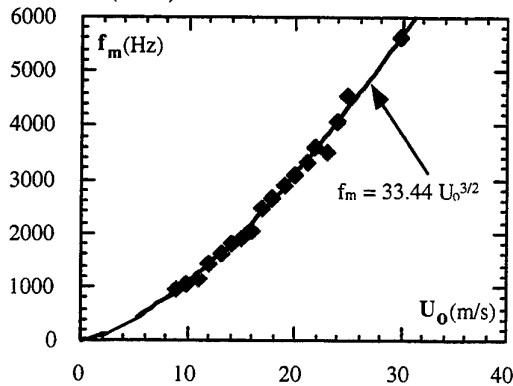


Fig. 7 Variation of f_m with U_o .

Mean Velocity Field

Fig. 8 displays the general flow pattern of a 30° inclined wall jet by injecting smoke at the lips of the nozzle and illuminating it with a laser sheet. The general features of an inclined wall jet, such as the inner shear layer, the outer shear layer and the recirculation flow region as shown schematically in Fig. 1, can be discerned. It can be seen that the jet is separated from the wall as soon it leaves the nozzle, then curves towards the wall and reattaches to it at some distance downstream. Further downstream the jet develops into a wall jet flow. The flow field of the inclined wall jet may be controlled by acoustically exciting it at a frequency f_e equal to the fundamental frequency of 2475 Hz, to promote the development of the outer free shear layer mode. Following Vlasov and Ginevski (1976), the excitation level ϵ was defined in terms of $v'(f_e)/U_o$, where $v'(f_e)$ is the rms transverse fluctuation velocity at f_e measured at $x/h=0.8$. It was found by Lu (1994) that u'/U_o increases with ϵ until $\epsilon = 0.06$ and remains relatively constant up to about 0.06. Hence an excitation level of 0.016 was used. As shown in Fig. 9(b), while the excited jet displays essentially the same flow features as the unexcited jet, the recirculation flow region has been substantially reduced in size by the excitation.

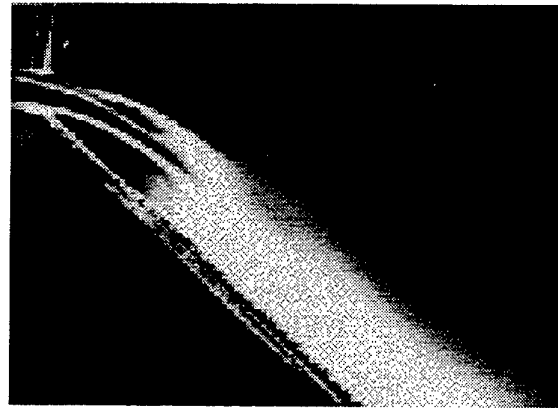


Fig. 9(a) Unexcited 30° inclined wall jet.



Fig. 9(b) Excited 30° inclined wall jet.

Mean streamwise and transverse velocity profiles measured by LDA at various streamwise distances (x/h) for the unexcited and excited jets are shown in Figs. 10(a) and (b) respectively. It can be seen from Fig. 10(a) that the mean streamwise velocities near the wall and immediately downstream of the nozzle are negative for both the unexcited and excited jets, indicating reversed flow and the presence of a recirculation flow region as observed in Fig. 9. However, Fig. 10(a) clearly shows that the excitation promotes the deflection of the jet towards the wall and earlier reattachment. This result is further supported by the mean transverse velocity profiles shown in Fig. 10(b). Under controlled acoustic excitation, V starts to turn largely negative near the wall by $x/h = 3$, indicating a strong flow towards the wall. By comparisons, for the unexcited jet, V does not turn negative until about $x/h=5$.

Turbulence field

Turbulence intensities The spatial development of streamwise and transverse turbulence intensities (u'/U_o and v'/U_o) in the x - and y -directions for unexcited and excited jets is displayed in Figs. 10(c) and (d)

respectively. The turbulence intensity distributions exhibit two peaks in u' and v' , which are associated with the inner and outer shear layers. Moreover, initially, for $x/h = 3$, under both natural and excited conditions, the peak of u'/U_0 in the inner shear layer is higher than that in the outer shear layer whereas the peak of the transverse turbulence intensity distributions v'/U_0 in the outer shear layer is higher than that in the inner shear layer. This is because the flow is constrained in the

inner shear layer in the y -direction, and the flow in the outer shear layer is relatively "free". Furthermore, initially, the streamwise and turbulence intensities in both the outer and inner shear layer under excitation are higher than those of the unexcited jet. These differences are significantly reduced by $x/h = 10$ where both the unexcited and excited jets have started to develop into an ordinary wall jet.

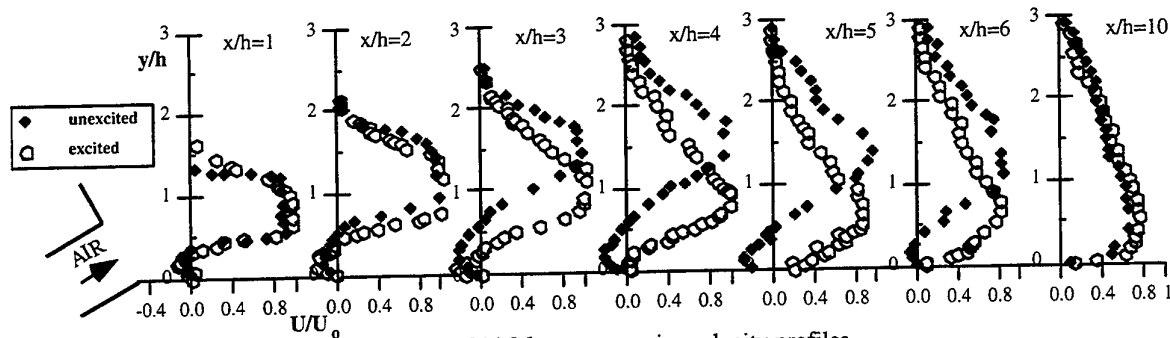


Fig. 10(a) Mean streamwise velocity profiles.

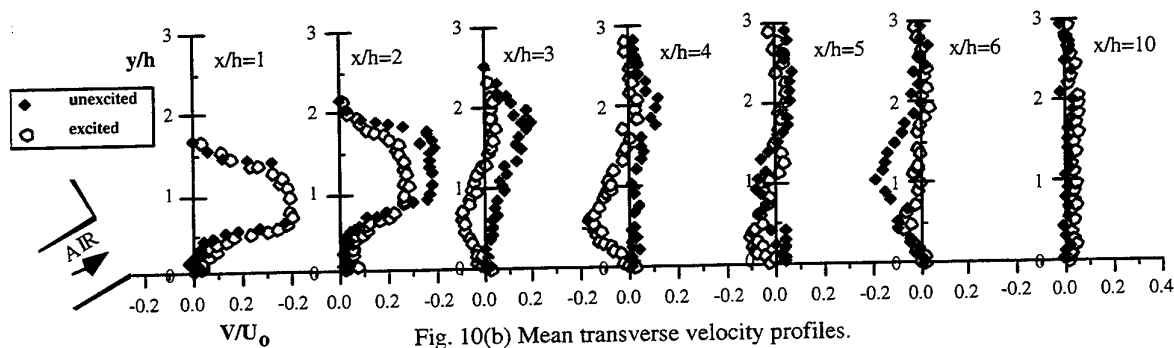


Fig. 10(b) Mean transverse velocity profiles.

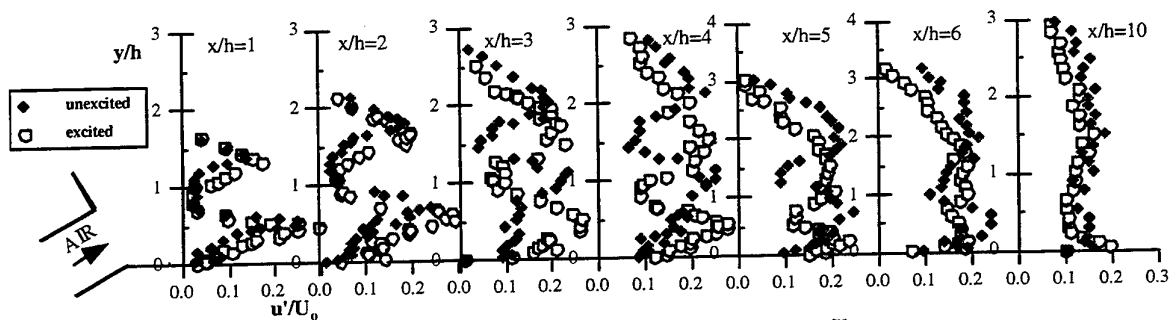


Fig. 10(c) Streamwise turbulence intensity profiles.

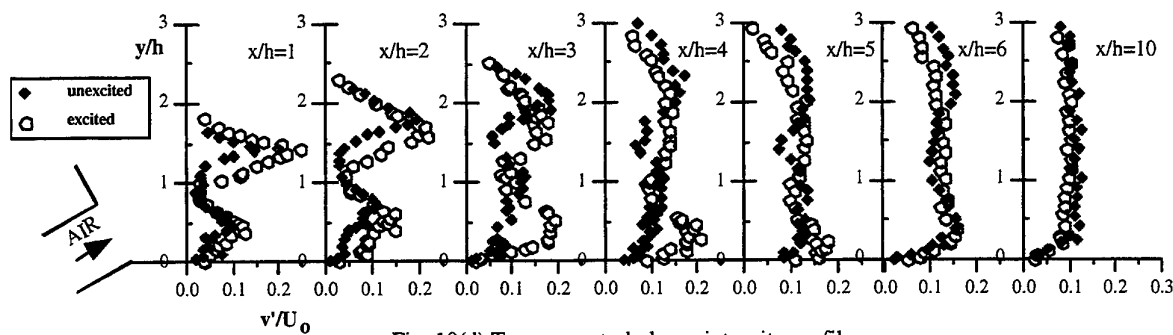


Fig. 10(d) Transverse turbulence intensity profiles.

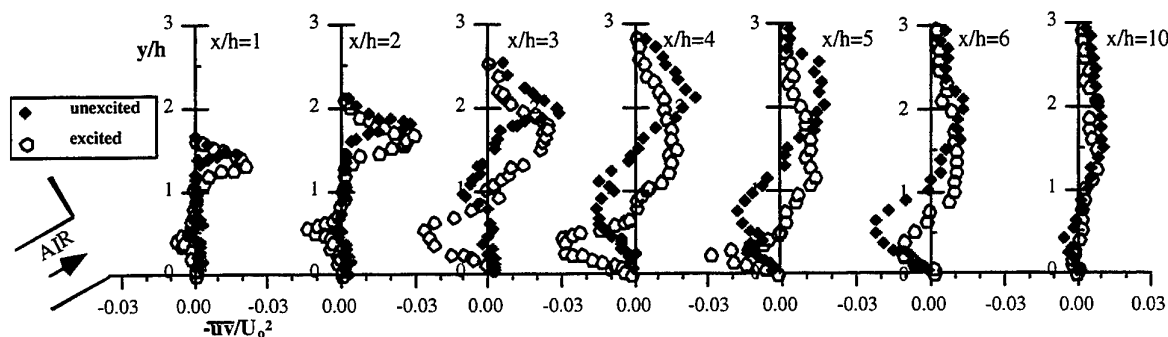


Fig. 10(e) Reynolds shear stress profiles.

Comparisons of the spatial development of Reynolds stress $-uv'/U_{2,0}$ between the unexcited and excited jets are made in Fig. 10(e). Similar to the turbulence intensity profiles, the inner and outer shear layers can be identified by the peaks in $-uv'/U_{2,0}$. As the flow proceeds downstream, large negative values of $-uv'/U_{2,0}$ can be identified near the wall, characterising the momentum transfer between the inner shear layer and the recirculation flow region. As shown below, reattachment has been determined to occur at $x/h = 4.5$ under excitation compared with $x/h = 6.2$ for the unexcited jet. For both the unexcited and excited jets, the magnitude of the Reynolds shear stress reaches a maximum value in the vicinity of the reattachment point, indicating high momentum transfer due to the jet impinging on the wall.

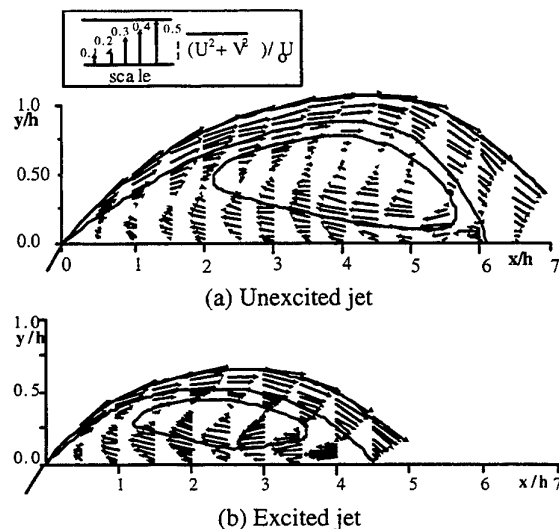


Fig. 11 Velocity vectors in the recirculation flow region.

Recirculation Flow Region

Figs. 11(a) and (b) display the mean velocity vectors constructed from the mean streamwise and transverse velocities determined by LDA in the recirculation flow region for the unexcited and excited jets respectively. The reversed flow region covers the initial area in the vicinity of the nozzle exit bounded by

the wall, the nozzle plate and the inner shear layer. High reversed flow velocity occurs just upstream of the reattachment point where there is high momentum transfer. The local maximum reversed flow velocity decreases as the fluid flows upstream in the recirculation flow region. It is interesting to note that the location of maximum reversed flow velocity is shifted away from the wall surface as the flow reverses from the reattachment point. The reversed flow velocity gradient near the wall is highest just upstream of the reattachment point and then decreases as x decreases. It can be determined from Figs. 11(a) and (b) that the time-averaged position of the reattachment point is located at $x/h = 6.2$ for the unexcited jet, compared with $x/h = 4.5$ under acoustic excitation. The size of the recirculation flow region has been substantially reduced by acoustic excitation.

Instability development

In order to study the instability development of the inner and outer shear layers, the 30° jet was excited acoustically with $f_e = 2475$ Hz, $\epsilon = 0.016$ at $Re = 6700$. Contours of the spatial development of the fundamental $u'(f_m)$ and the first subharmonic $u'(f_{m/2})$ are shown in Figs. 12(a) and (b) respectively. These contour plots show that the instabilities undergo only two stages of evolution of instabilities in the outer shear layer: the formation of the fundamental instability and its first subharmonic. While the development of the fundamental instability in the inner shear layer can be observed, the formation of its subharmonic is just detectable.

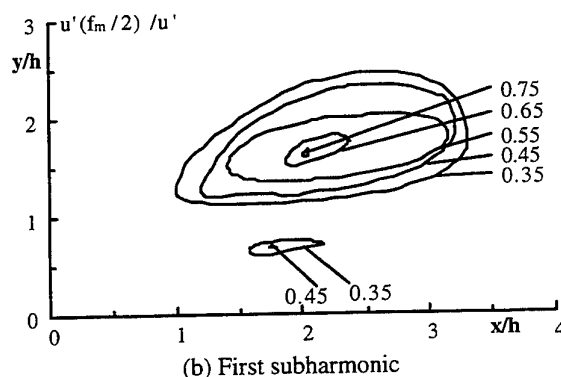
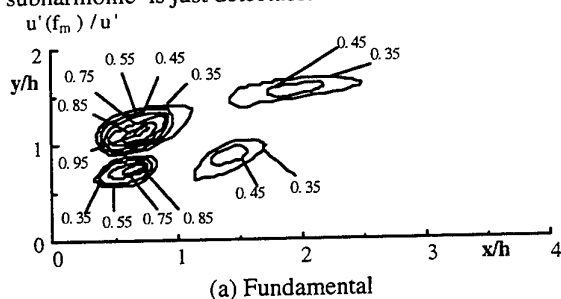


Fig. 12 Spatial development of instability modes.

In the outer shear layer, the fundamental instability wave $u'(f_m)$ appears to saturate at about $x/h = 0.8$ but it is still detectable by $x/h = 2$. By comparisons, in the inner shear layer, the fundamental $u'(f_m)$ structure is much smaller in size. While the first subharmonic instability in the outer shear layer has developed into a very large structure by $x/h=2$, its counterpart in the inner shear layer is virtually suppressed. The development of instability waves in the inner layer is inhibited because of the constraint imposed by the wall and the recirculation flow.

CONCLUSIONS

The mean velocity and turbulence field of a 30° inclined wall jet has been measured using hot-wire and laser Doppler anemometry for a nozzle exit Reynolds number of 6,700. The LDA results indicate that the jet is separated from the wall as soon as it leaves the nozzle but due to the subatmospheric pressure in the region confined between the wall, the nozzle plate and the inner shear layer of the jet, the jet is attracted towards the wall and reattaches to it at 6.2 nozzle widths downstream. Hot-wire spectra measurements in the inner and outer shear layers indicate that the fundamental vortex roll-up frequency (corresponding to the shear layer mode) is the same as that for a free jet with a Strouhal number of 0.012. The spatial development of the fundamental and first subharmonic instabilities was investigated by acoustically exciting the jet at a frequency corresponding to the shear layer model with an excitation level based on normalised transverse velocity fluctuation of 0.016 at the nozzle exit. While the formation of the fundamental vortex roll up and the merging of the fundamental to form the first subharmonic have been identified in the outer shear layer, the formation of the first subharmonic in the inner shear layer is barely detectable because of the constraint imposed by the wall and the recirculation flow region. LDA results indicate that acoustic

excitation introduced at the shear layer mode enhances the development of instabilities and promotes jet reattachment to the wall, thus reducing substantially the size of the recirculation flow region.

REFERENCES

- Fiedler, H. E. and Fernholz, H. H. (1990) *On management and control of turbulent shear flows*. Prog. Aerosp. Sci., **27**, 305 - 387.
- Forthmann, E. (1934) *Über Turbulente Strahlkreisbreitung*. Ing-Arch., **5**, 42.
- Gutmark, E. and Ho, C.M. (1983) *Preferred modes and the spreading rates of jets*. Physics Fluids, **26**(10), 2932-2943.
- Hsiao F.B. and Huang, J.M. (1990) *On the evolution of instabilities in the near field of a plane jet*. Physics Fluids, **A2**, 400-412.
- Hsiao, F.B. and Sheu, S.S. (1994) *Double row vortical structures in the near field region of a plane wall jet*. Expts. Fluids, **17**, 291-301.
- Hussain, A.K.F.M. (1986) *Coherent structures and turbulence*. J. Fluid Mech., **173**, 303 - 356.
- Katz, Y., Horev, E. and Wygnanski, I. (1992) *The forced turbulent wall jet*. J. Fluid Mech., **242**, 577-609.
- Lai, J.C.S. & Lu, D. (1992) *An inclined two-dimensional wall jet*. Proc. 5th Asian Congress of Fluid Mechanics, **1**, 195-98.
- Lai, J.C.S. & Lu, D. (1996) *Effect of wall inclination on the mean flow and turbulence characteristics in a two-dimensional wall jet*. Int. J. Heat & Fluid Flow **17**(4), 377-385.
- Lai, J.C.S. & Lu, D. (1998) *Reattachment of an inclined wall jet* Proc. ICAS 98, Melbourne, Australia, Sept. 13-18, 1998.
- Lai, J.C.S. & Simmons (1985) *Instantaneous velocity measurements in a vane-excited plane jet*. AIAA J, **23**(8), 1157-1164.
- Launder, B.E. (1983) *The turbulent wall jet - measurements and modelling*. Ann. Rev. Fluid Mech. **19**, 81-128.
- Lu, D. (1994) *Inclined wall jets*. PhD thesis, The University of New South Wales.
- Matsuda, H., Iida, S. and Hayakawa, M. (1990) *Coherent structures in a three-dimensional wall jet*. Trans. ASME J Fluids Eng. **112**, 462-467.
- Newman, B.G. (1961) *The deflection of plane jet by adjacent boundaries - Coanda effect*. Boundary Layer and Flow Control (ed. G.V. Lachmann), Pergamon Press **1**: 232 - 265.
- Schneider, M.E. and Goldstein, R.J. (1994) *Laser Doppler measurement of turbulence parameters in a two-dimensional plane wall jet*. Phys. Fluids, **6**, 3116-3129.
- Vlasov, E. V. and Ginevski, A. S. (1976) *The dual nature of acoustic effect on free turbulent jets*. Fluid Mech., Soviet Res. **5**(6).
- Zaman, K. B. M. Q. and Hussain, A. K. M. F. (1984) *Natural large-scale structures in the axisymmetric mixing layer*. J. Fluid Mech., **138**, 325 - 351.
- Zhou, MD, Heine, C and Wygnanski, I (1996) *The effects of excitation on the coherent and random motion in a plane wall jet*. J. Fluid Mech. **310**, 1-37.

SESSION 39

COMPLEX FLOWS IV

CLASSIFICATION OF TSUNAMI WAVE TO RUNUP TRANSITION USING LASER-INDUCED FLUORESCENCE TECHNIQUE

K. M. Mok¹ and Harry Yeh²

¹Faculty of Science and Technology, University of Macau, PO Box 3001, Macau

²Box 352700, Dept. of Civil Engr., Univ. of Washington, Seattle, WA 98195-2700, USA

ABSTRACT

Using the laser-induced fluorescence technique, the detailed transition of tsunami to runup process is observed and classified. For the generated waves with offshore Froude numbers ranging from 1.10 to 1.46, it is found that there are basically four types of wave-to-runup transition modes namely, collision type, plunging type, collapsing type, and gradual type.

1. INTRODUCTION

When a tsunami wave approaches the shore, it can be in the form of a nonbreaking wave, a breaking wave, or a broken wave (bore). The transition of these waves to their corresponding runup processes could have significant effects on the runup flow velocities and the final maximum runup height, which will affect the design of tsunami-proof structures as well as the determination of the extent of coastal flooding. Due to the horizontal characteristic length scale of a tsunami is much larger than the vertical one, most of the mathematical models for tsunami propagation and runup are based on the shallow-water wave theory.

For a simple nonbreaking wave (e.g. solitary and cnoidal waves), the shallow-water wave theory can predict not only the maximum runup height but also the runup process itself on a plane beach (Synolakis, 1991). Nevertheless Synolakis (1991) also pointed out that the apparent excellent predictive capability of the shallow-water wave equations on the evolution of the maximum wave height and on the maximum runup should not be extrapolated to conclude that the details of the evolution are also modeled equally well in all cases, especially the wave to runup transition process at the shoreline.

Once the incoming tsunami wave breaks offshore, the shallow-water wave theory predicts the runup motions poorly; the maximum runup heights in a

laboratory are always less than the prediction based on the shallow-water wave theory (Miller, 1968). The discrepancy was addressed as the effects of friction by Hibberd and Peregrine (1979). Then Packwood and Peregrine (1981) modified Hibberd and Peregrine's (1979) numerical model by incorporating the friction effects with the Chézy friction term. Even with a reasonable value of Chézy friction coefficient, their model predictions still considerably exceed Miller's (1968) experimental results which indicate that the friction effects alone cannot be the explanation for the discrepancy. Yeh and Ghazali (1986, 1988) suspected that the discrepancy in the maximum runup height prediction may be caused by the bore to runup transition process that occurs near the shoreline. They experimentally examined the "bore collapse" process described in many mathematical models. Note that the theoretical 'bore collapse' process is due to Whitham (1958) and Ho and Meyer (1962) who applied the jump conditions at the bore front, and found that the bore height vanishes as it approaches the shoreline while the fluid velocity and the bore propagation velocity merge to a common finite value. However, acceleration of the fluid parcels at the shoreline is singular. In short, the 'bore collapse' process is a rapid conversion of potential to kinetic energy. Yeh and Ghazali (1986, 1988) found that the theoretical 'bore collapse' never exits, and the transition of bore to runup mode is different between developed and undular bore. For fully developed bore, its front does not reach the shoreline directly but, instead, pushes a small wedge of quiescent water in front. This transition process involves 'momentum exchange' between the bore and the water wedge ahead of it (Yeh and Ghazali: 1986, 1988). On the other hand, the 'momentum exchange' does not take place in an undular bore, its front face overturns directly onto the dry beach and initiates the runup motion. Yeh et al (1989) furthered their studies to the runup process by measuring the runup speed. They found that the

maximum runup height of a fully developed bore is found to be about 60% of the value predicted by the inviscid theory. The reduction of the kinetic energy available for the runup process partly results from the 'momentum exchange' initiated by the pressure gradient which, in turn, plays an important role at the early stage of the runup mode.

Since the detail transition of tsunami wave to runup appears to play an important role on the subsequent runup process and there is no theoretical or numerical model which can describe it properly, experimental observation will certainly give further insight in this highly nonlinear and complex problem. The present study focuses on the experimental observation of the tsunami wave to runup transition using laser-induced fluorescence technique with the objective to classify their types.

2. EXPERIMENT

A series of experiments was performed in a 9.0 m long, 1.2 m wide, and 0.9 m deep water tank situated at the Harris Hydraulic Laboratory of the University of Washington. A schematic view of the experimental setup is shown in Fig. 1. A 7.5° uniformly sloping beach is constructed by 1.9 cm thick Plexiglas plates bolted on an aluminum frame. A tsunami is generated by lifting a 12.7 mm thick aluminum gate which initially separates the quiescent water on the beach side from the deeper water behind. This wave-generation scheme has an advantage since the theoretical prediction of the waves (especially bores) can be made from the classical dam-break problem. A pneumatic cylinder which is electrically activated by a single solenoid valve with 650 kPa operating air pressure is used to lift the gate in a controlled manner. The distance from the gate to the beach toe was 1.5 m in order to provide a sufficient

distance for the generated wave to separate from the disturbance produced by the gate uplift. Note that the wave generation scheme in the present study was adopted from Yeh et al. (1989).

A 4-watt Argon-ion laser is used for the visualization of wave profile. The emitted laser beam is converted to a thin sheet (1-mm thick) of laser light through a resonant scanner. The scanner is capable of sweeping the beam at 1200 Hz with a maximum of a 50° peak-to-peak angle. The generated laser sheet is projected from above in the cross-shore direction and illuminates the vertical longitudinal plane of the water dyed with fluorescein along the centerline of the tank. The detailed wave-to-runup transition process illuminated with the laser-induced fluorescence were recorded by a high speed 3-CCD video camera for analysis.

3. RESULTS

The generated waves have offshore Froude numbers $F = U_o/(gh_o)^{1/2}$ ranging from 1.10 to 1.46, where U_o is the speed of the wave front in the uniform water depth offshore. The results indicate that there are basically four types of wave-to-runup transition modes; i.e. (1) collision type, (2) plunging type, (3) collapsing type, and (4) gradual type. Each of the cases is described below.

- i) The collision type ($1.34 \leq F \leq 1.46$): The wave is broken and is fully developed into a bore before it reaches the shoreline; i.e. the bore has an entirely turbulent front face. As the bore approaches the shoreline, there is a momentum exchange between the bore and the water body ahead of it; the bore keeps pushing the initially quiescent mass of water in front of it as it advances to shore, so the bore front itself never reaches the shoreline directly and the subsequent

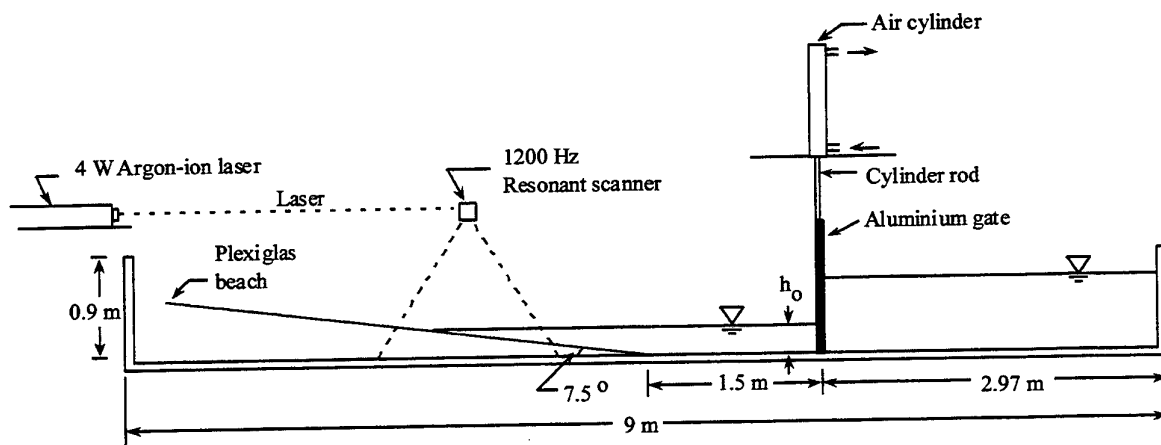
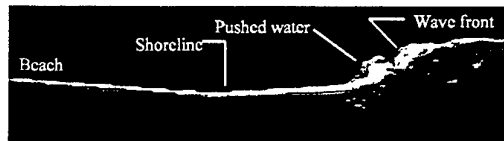


Figure 1. A schematic view of the experimental apparatus.

runup is led by the pushed water. The present observation is consistent with that observed by Yeh et al (1989). (Figure 2, $F = 1.46$)

- ii) The plunging type ($F = 1.24$): The generated wave is unborken before reaching the shoreline.

As the wave shoals, its front face starts to steepen and eventually reaches to almost vertical at location very close to the shoreline. Then the bore front overturns directly onto the dry beach and initiates the runup process. (Figure 3)



$t = 0.000$ sec.



$t = 0.100$ sec.



$t = 0.133$ sec.



$t = 0.167$ sec.



$t = 0.200$ sec.



$t = 0.267$ sec.

Figure 2. Collision-type wave to runup transition process. Offshore Froude number, $F = 1.46$.



$t = 0.000$ sec.



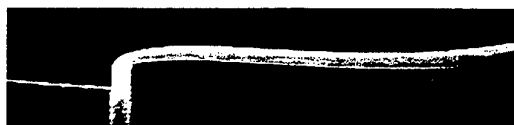
$t = 0.033$ sec.



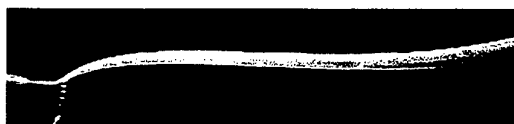
$t = 0.067$ sec.



$t = 0.100$ sec.



$t = 0.167$ sec.



$t = 0.200$ sec.

Figure 3. Plunging-type wave to runup transition process. Offshore Froude number, $F = 1.24$.

- iii) The collapsing type ($F = 1.18$): The generated wave is unbroken before reaching the shoreline. As the wave shoals, its front face starts to steepen and eventually reaches to almost vertical at location very close to the shoreline. Then the upper part of the bore front curves forward to initiate the overturning motion similar to the plunging type transition. However, the bore collapses before the overturning process starts by shooting the bore front toe up the dry bed to initiate the runup process. (Figure 4)
- iv) The gradual type ($F = 1.10$): The generated

wave is smooth and its steepness is small at all time. As the wave shoals, its front face steepens as it reaches to the shoreline. Unlike the plunging type, its front face slope never reaches to vertical and it does not overturn onto the dry beach. Instead, when the steepened wave front reaches the shoreline, its toe starts to move up the dry bed and the rest of the wave follows. During the entire process, the water surface appears to be smooth and continuous and the transition from wave to runup is gradual. (Figure 5)

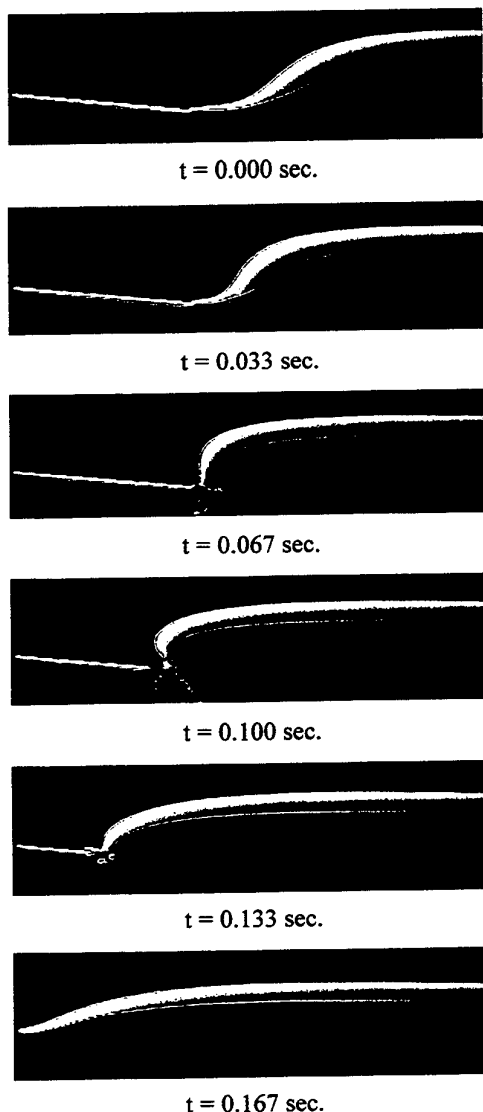


Figure 4. Collapsing-type wave to runup transition process. Offshore Froude number, $F = 1.18$.

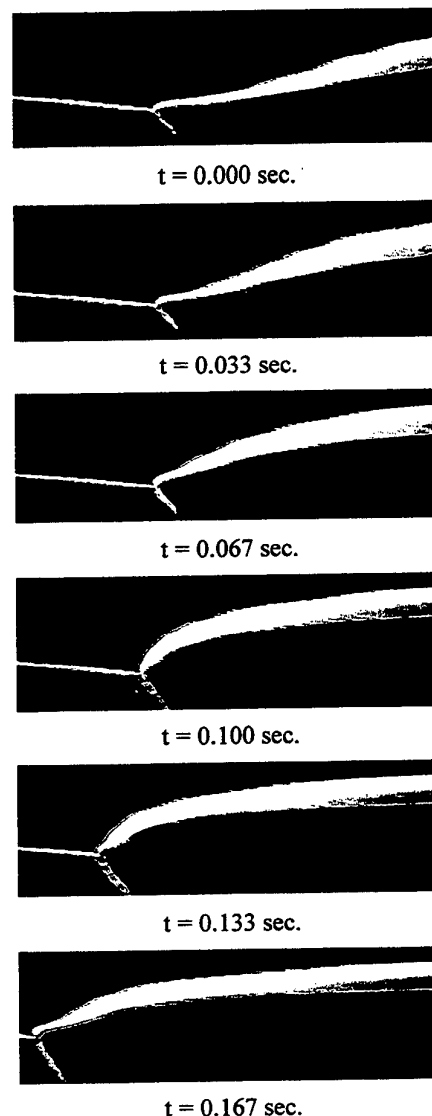


Figure 5. Gradual-type wave to runup transition process. Offshore Froude number, $F = 1.10$.

4. CONCLUDING REMARKS

The detailed process of the transition from tsunami wave to runup mode was revealed and classified. It was found that there are four transition processes for waves with offshore Froude number ranging from 1.10 to 1.46. These different transition processes for different waves may give additional explanations for the discrepancies or agreements of the resulting maximum runup height between the theory and measurements. For the cases with breaking incoming waves, it should be noted that the turbulence generated by the wave breaking action, in addition to the wave-to-runup transition, may play important role in affecting the resulting maximum runup height as pointed out by Yeh et al (1989). For the cases with small Froude number ($F < 1.20$), the wave is nonbreaking and its transition to runup process appears to be smooth. This may be the reason that the maximum runup height can be modeled rather accurately even with the linear theory (Synolakis, 1991). Nevertheless the detailed evolution from wave to runup transition for these waves are mainly affected by viscosity, surface tension and consequently the water-air-beach contact line, which many mathematical models do not take into account and therefore cannot be modeled adequately.

ACKNOWLEDGMENTS

The authors wishes to thank Mr. T. McKay of the University of Washington for his assistance in setting up the experimental facilities. Ms. C. Grandinetti is thanked for running the experiments. The work for this paper was supported by the US National Science Foundation Grant no. CMS-9614120. The preparation and publication fee of this paper is kindly supported by the University of Macau.

REFERENCES

- Hibberd, S. & Peregrine, D. H. 1979, Surf and run-up on a beach : a uniform bore, J. Fluid Mech. vol. 95, pp. 323-345.
- Ho, D. V. & Meyer, R. E. 1962, Climb of a bore on a beach. Part 1 : Uniform beach slope, J. Fluid Mech. vol. 14, pp. 305-318.
- Miller, R. L. 1968, Experimental determination of run-up of undular and fully developed bores, J. Geophys. Res. vol. 73, pp. 4497-4510.
- Packwood, A. R. & Peregrine D. H. 1981, Surf and run-up on beaches : models of viscous effects, Rep. AM-81-07. University of Bristol. 34 pp.
- Synolakis, C. E. 1991, Tsunami runup on steep slopes: How good linear theory really is, Natural Hazards, vol. 4, pp. 221-234.
- Whitham, G. B. 1958, On the propagation of shock waves through regions of non-uniform area of flow, J. Fluid Mech. vol. 4, pp. 337-360.
- Yeh, H. H. & Ghazali, A. 1986, Nearshore behavior of bore on a uniformly sloping beach, Proc. 20th Conf. Coastal Engng. pp. 877-888.
- Yeh, H. H. & Ghazali, A. 1988, On Bore Collapse, J. Geophys. Res., vol. 93, pp. 6930-6936.
- Yeh, H. H., Ghazali, A. & Marton, I. 1989, Experimental study of bore run-up, J. Fluid Mech. vol. 206, pp. 563-578.

Characterisation of the interaction between a boundary layer and a cavity using Digital Particle Velocimetry with Optical Flow

G. Quénot*, A. Rambert**, P. Gougat**, T. Kowalewski***

*CLIPS-IMAG, Grenoble, France

**LIMSI-CNRS, France

***IPPT PAN, Centre of Mechanics, Polish Academy of Sciences, Poland

ABSTRACT

An Optical Flow technique based on the use of Dynamic Programming has been applied to Particle Image Velocimetry yielding a significant increase in the accuracy and spatial resolution of the velocity field. Results are presented for an interaction between a laminar boundary layer and a cavity.

The experimental characterisation of the interaction between a boundary layer and a cavity was developed in order to valid a three dimensional computation code based on the L.E.S. method (Large Eddies Simulation). The main application of this work is the study of the pollutant transport and dispersion in a canyon street.

INTRODUCTION

The aim of this investigation is to explore the possibility of using an optical flow technique in measuring fluid flow velocity. Classical flow visualisation is based on direct observation of tracer particles. Analysis of subsequent images searching for local displacements allows quantitative measurement of two-dimensional flow fields. The optical flow method offers a new approach for analysing flow images. It largely improves spatial accuracy and minimises the number of spurious vectors. Application of this method may help in quantitative analyses of several challenging problems of fluid mechanics, as well as in full plane validation

of their numerical counterparts. This technique has been tested for calibrated synthetic sequences of images (Quénot et al., 1998). It was observed that the accuracy remains better than 0.5 pixels/frame.

The study of the interaction between a boundary layer and a cavity is an approach in characterisation of flow regimes within the urban canyon (Hunter et al., 1991).

Much attention has been directed to the study of the various canyon flow regimes (DePaul and Sheih, 1986; Oke, 1988) since air flow is responsible for the transport of properties such as pollutants, heat and moisture. A number of studies have referred to the existence of a vortex cell within an urban street canyon when ambient winds aloft are perpendicular to the street.

Canyon geometry is an important determinant of characteristic airflow observed within urban canyons. Three principal flows regimes are "skimming" flow, "wake interface" flow and "isolated roughness" flow, following the nomenclature of Oke (1987). The transition between flows is determined by canyon geometry and can be described in terms of threshold height/width (H/W) ratios for an arbitrary length (L/H) ratio.

Previous studies used a k- ϵ turbulence model of air flow to confirm the wind tunnels observations. The model was based on that developed by Paterson and Apelt (1989) to predict pressure experienced by walls of buildings within cities. It solves the Navier-Stokes equations for momentum and the equations for the transportation and dissipation of turbulent kinetic energy.

An approach Large Eddies Simulation was proposed (Chabni, 1997) which predict the large eddies structures characterised by a higher turbulent kinetic energy and it models only the little scales (not accessible to the numerical discretisation). The aim of our study is to provide experimental results in order to valid the numerical model. The results obtained by optical flow technique was compared with those obtained by classical DPIV (Digital Particle Image Velocimetry) based on cross-correlation (Hiller et al., 1993) and then with the numerical results.

Optical Flow for DPIV

Optical flow computation consists in extracting a dense velocity field from an image sequence assuming that the intensity is conserved during the displacement. Several techniques have been developed for the computation of optical flow. In a survey and comparative performance study, Barron et al. (1994) classify them in four categories: differential, correlation based, energy based and phase based. Not all of these are well suited for the DPIV problem. Many of these require long image sequences that are not easily obtained experimentally. The technique that was chosen for DPIV application was introduced by Quénot (1992) as Orthogonal Dynamic Programming (ODP) algorithm for optical flow detection from a pair of images. It has been extended to be able to operate on longer sequences of images and to search for subpixel displacement (Quénot, 1996). The ODP based DPIV will referred to as ODP-DPIV. Compared with other optical flow approaches or to the classical correlation based DPIV, the ODP-DPIV has the following advantages: (i) it can be applied simultaneously to sequences of more than two images; (ii) it performs a global image match by enforcing continuity and regularity constraints on the flow field. This helps in ambiguous or low particle density regions; (iii) It provides dense velocity fields (neither holes nor border offsets); (v) local correlation is iteratively searched for in regions whose shape is modified by the flow, instead of being searched by fixed windows. This greatly improves the accuracy in regions with strong velocity gradients.

The orthogonal algorithm

Strip to strip alignment

The algorithm is based on the search of a transformation that relates the second image to the first one and minimises the Minkowski distance of first and second order, L_1 and L_2 .

The matching is global and does not require any previous segmentation or features extraction. The main idea is to transform the search problem for two-dimensional displacements into a carefully selected sequence of search problems for one dimensional displacement, thereby decreasing greatly the complexity.

First, the two images are identically sliced into several parallel overlapping strips (Fig. 1). Then, for every pair of strips, an optimal match is searched for with displacement allowed only in the slicing direction and identical for all the pixels in the same column in the orthogonal direction (Fig. 2)

A dense field of displacements (between column vectors) is found for every pair of strips minimising the Minkowski distance between them with help of a dynamic programming algorithm (Dynamic Programming is used in the orthogonal algorithm because it appeared to be the most efficient way for performing an optimal strip to strip matching). This gives us a displacement value at every point of the central fibre of all strips. Then displacement values for all other pixels of the image are interpolated from the pixel values of the central fibre of the nearest strips. a dense displacement field is obtained for the whole image. This displacement field is then smoothed before the following steps of the algorithm are applied.

Orthogonal iterations

The displacement field found in the first step is used to deform the second image relative to the first one. An image $I_2(i,j)$ is built from the $(dx(i,j), dy(i,j))$ displacement field and the image $I_1(i,j)$ as $I_2(i,j) = I_1(i+dx(i,j), j+dy(i,j))$. The image $I_2(i,j)$ instead of $I_1(i,j)$ is now compared and aligned to $I_1(i,j)$. Then the previously steps are repeated with the slicing performed in the orthogonal direction and the alignment results are used to update and refine the (dx, dy) displacement field. The combination of a horizontal and vertical pass results in an alignment in both directions. After both passes are executed, the initial orthogonal shift is reduced in both directions. To refine the accuracy of the matching result, the whole process is reiterated several times in a pyramidal fashion by reducing the spacing and width of the strips.

Experimental device

The experiments were performed in a wind tunnel for different mean velocities from 1 to 5 m/s.

The velocity profiles in the boundary layer were obtained by hot wire and Laser Doppler Velocimetry. The cavity placed at 200 mm from the leading edge has the characteristic dimensions: $H=50$ mm, $L=100$ mm, $W=300$ mm, where H is the height, L the length and W the width of the cavity.

Experimental results

At the entry of the cavity, the boundary layer is still laminar and it is matching with a Blasius profile. Measurements made after the cavity showed that the boundary layer was no longer laminar. A spectral frequency analysis of the hot wire signals was realised which showed that the frequencies were in the low frequency domain (<200 Hz). This perturbation of the boundary layer was due to the exit of the vortex structures from the cavity.

The velocity field inside the cavity was measured using an Argon laser and a Pulnix digital camera (768×484 pixels). *Lycopodium* particles were used as seeding.

The velocity field was computed using ODP-DPIV and classical DPIV based on cross-correlation techniques. An example of a velocity field corresponding to the left part of the cavity (A, Fig. 6) obtained by DPIV for a mean velocity of 1 m/s is presented in Fig.3 For the same pair of images, the results obtained using optical flow, is presented in the Fig. 4. We can observe the good concordance between the two velocity fields. For DPIV technique the cross-correlation window size was 16×16 pixels. In Fig.4 the vectors are presented in the same range. The result of a zoom made in a region with a velocity gradient is presented in Fig.5; the spatial resolution obtained by optical flow is higher, one vector corresponds to a 4×4 pixels search window.

A numerical result corresponding to the experimental configuration is presented in Fig. 6. Two counter rotating vortex are observed with eddies of smaller dimensions turning around them. The flow visualisation (Fig. 7) confirms the perturbation of the laminar boundary layer numerically observed.

In the same conditions of mean flow velocity and at the same location a couple of images was recorded using smoke as seeding (Fig. 8). In these conditions, the DPIV based on the cross-correlation technique is unable to compute an accurate velocity field. However the DPIV based on the optical flow could furnish interesting results in these seeding conditions (Fig. 9). Even if the image processing was made in the same flow conditions and at the same location, it is difficult to compare the velocity fields obtained with *Lycopodium* particles

and with smoke because the flow inside the cavity is very unsteady. Experiments with smoke used as seeding are currently performed in simple experimental configurations in steady flows in order to valid the optical flow method in these experimental conditions.

CONCLUSION

An Optical Flow technique based on the use of Dynamic Programming has been successfully applied to Digital Particle Image Velocimetry yielding a significant increase in the accuracy and spatial resolution. Results have been presented for an interaction between a boundary layer and a cavity modelling the flow in a canyon street. Using this algorithm, a dense velocity vector field for every pixel of the image could be obtained.

Preliminary experimental investigations show that optical flow method can be successfully applied to extract velocity fields on smoke seeding image sequences on which classical cross-correlation DPIV fails.

Future work will be conducted in order to obtain a better characterisation of the results quality: statistical estimation of the accuracy of the velocity field from the particle density, the smoothness of extracted field and the reconstruction error.

An important future development of the optical flow technique is its extension to three-dimensional velocity fields computation for which Dynamic Programming search is very well suited.

REFERENCES

- Chabni, A. 1997, Etude par méthodologie de type Simulation des Grosses structures de la dynamique de l'interaction et des échanges entre une couche limite et une encoche, Ph.D. thesis Université Paris Sud, France.
- DePaul F. T. and Sheih C.M. 1986 Measurements of wind velocity in a street canyon Atmospheric Environment vol. 20, pp. 455-459.
- Hiller, W.J., Kowalewski, T., Stella, F. 1993, Onset of natural convection in a cube, Int. J. Heat Mass Transfer, vol. 36 pp. 3251-3263.
- Hunter, L.J., Watson, I.D. and Johnson, G.T. 1991, Modelling airflow regimes in urban canyons, Energy Bldn., 15-16, pp. 315-324.

Oke, T.R. 1988, Street design and urban canopy layer climate, Energy Bldng. vol. 11, pp. 103-113.

Paterson, D.A. and Apelt C.J. 1989, Simulation of wind flows over three dimensional buildings, Bldng. Envir. vol. 24, pp. 39-50.

Quénot, G.M., Pakleza, J. and Kowalewski, T. 1998, Particle Image Velocimetry with Optical Flow, Experimental in Fluids (in press).

Quénot, G.M. 1996, Computation of Optical Flow using Dynamic Programming, IAPR Workshop on Machine Vision Applications, Tokyo.

Quénot, G.M. 1992, The Orthogonal Algorithm for Optical Flow detection using Dynamical Programming, Proc. IEE ICASSP, San Francisco, vol. 3, pp. 249-252.

FIGURES

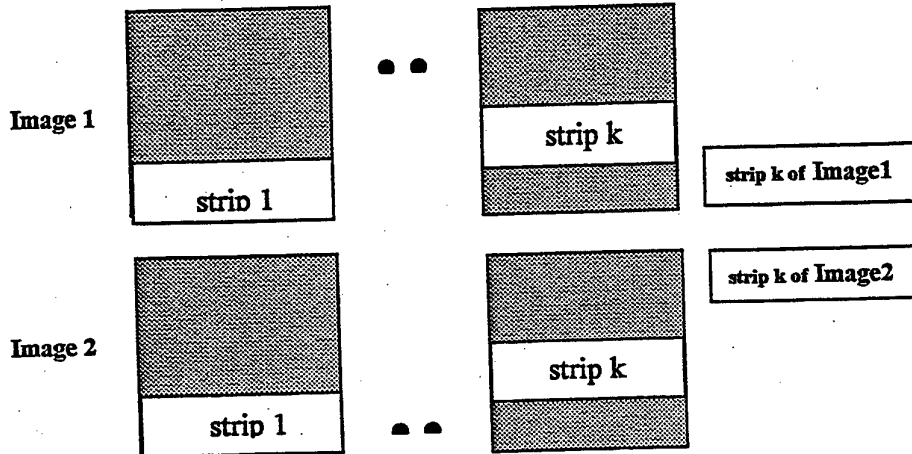


Fig1. Image slicing

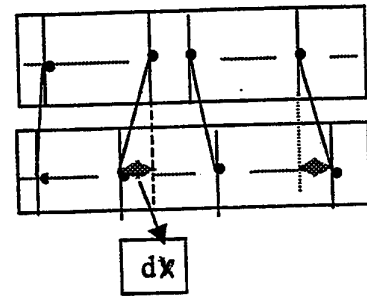


Fig2. Strip alignment

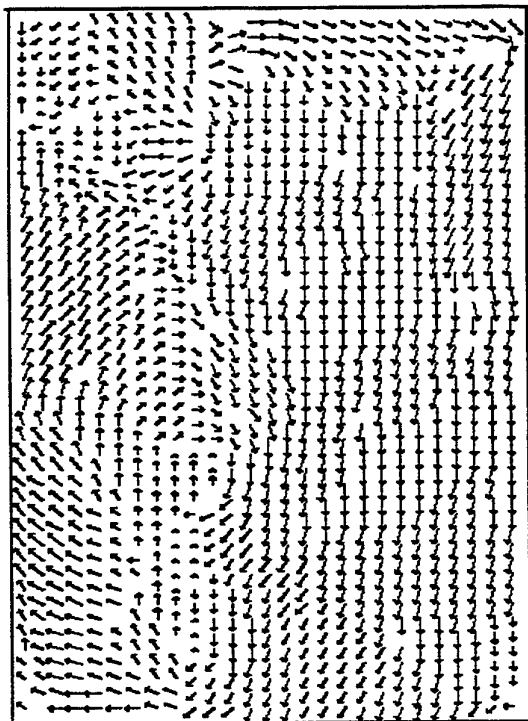


Fig 3. Flow velocity field using DPIV based on cross-correlation

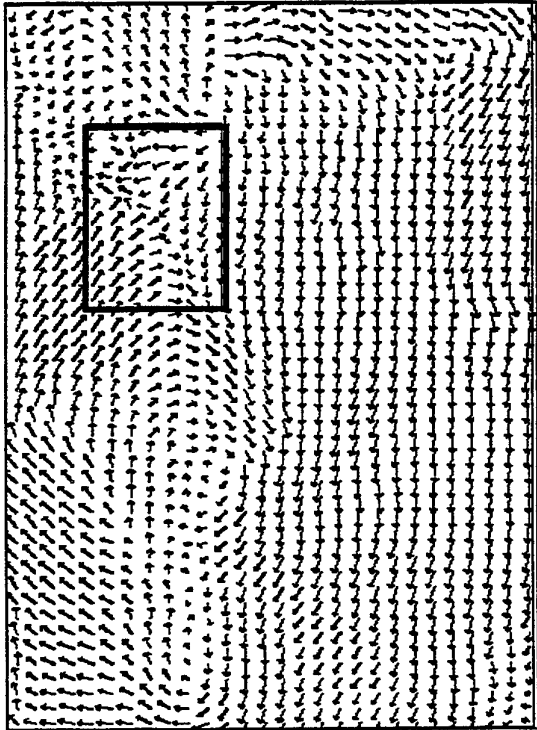


Fig. 4 Flow velocity field using DPIV based on Optical Flow

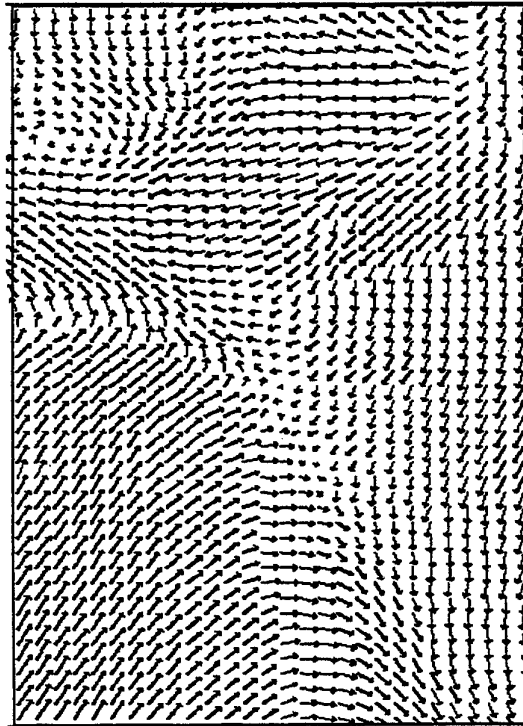


Fig.5 Zoom of the velocity field of the indicated region

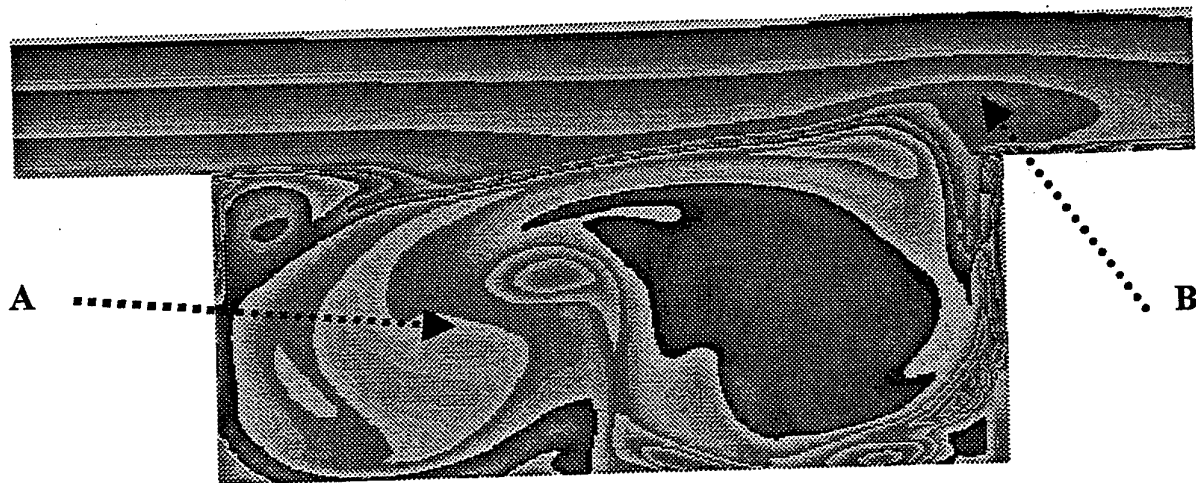


Fig.6 Numerically vorticity field



Fig.7 Vortex structures at the interaction region (zone B)

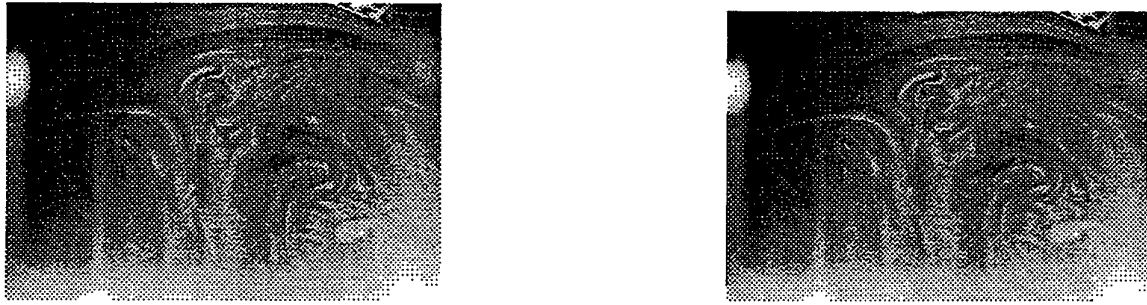


Fig 8. Couple of images inside the cavity (same location as in Fig. 3-4) using smoke as seeding

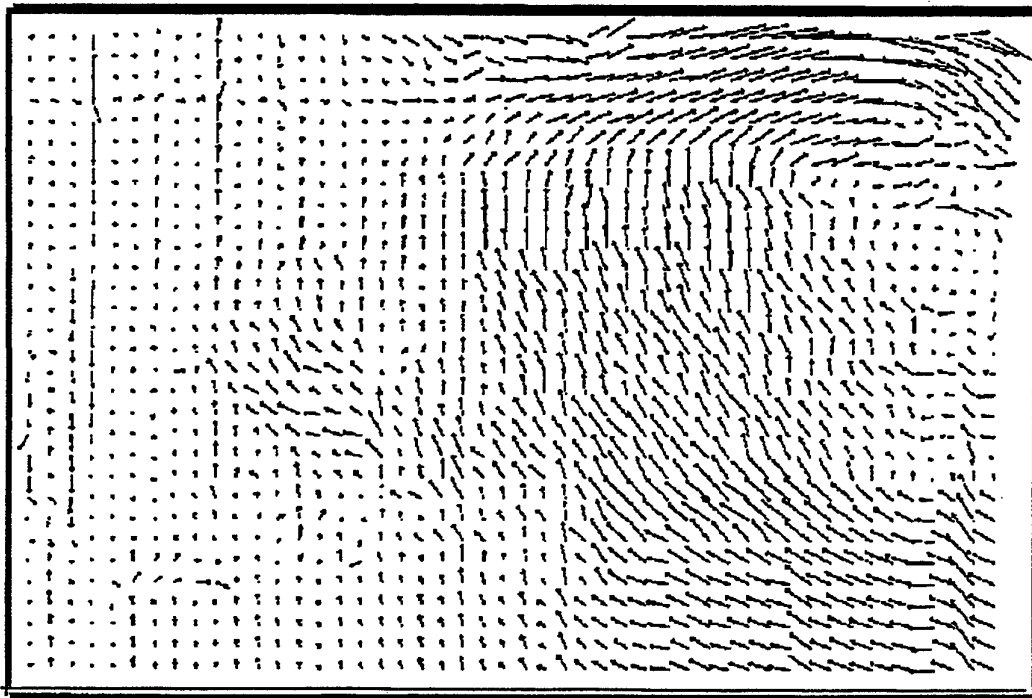


Fig.9 Flow field velocity using DPIV based on Optical Flow and using smoke as seeding

AUTHORS' INDEX

- Abe, M., 6.1.1
Adrian, R.J., 6.4.1, 6.6.1, 11.1.1, 14.1.1, 16.1.1, 17.4.1
Ajayi, K.T., 22.1.1
Akamatsu, F., 35.3.1
Alkislal, M.B., 13.5.1
Allain, C., 19.5.1
Allen, J.T., 23.3.1
Alvarez, M.P., 16.4.1
Anacleto, P., 25.7.1
Andrés, N., 16.4.1
Antonia, R.A., 2.1.1
Aoki, T., 4.5.1
Araneo, L., 7.4.1
Aroussi, A., 33.4.1
Arregle, J., 7.6.1
Arroyo, M.P., 16.4.1
Arsié, A., 39.2.1
Augenstein, E., 2.3.1
Auger, P.L., 28.4.1
Azzazy, M., 23.1.1, 34.3.1
- Baetz, W., 6.2.1
Barreras, F., 2.5.1, 24.2.1
Barrientos, A., 33.5.1
Barros, A.N., 21.3.1
Bar-Ziv, E., 35.5.1
Batliwala, F., 34.1.1
Baur, T., 20.6.1
Beale, A., 3.5.1
Becker, J., 34.5.1
- Belghit, A., 31.2.1
Bélorgey, M., 39.2.1
Bench, P., 28.4.1
Benedict, L., 32.5.1
Bergounoux, L., 9.2.1
Berkner, L., 15.2.1
Berry, J.D., 1.1.1
Berton, E., 19.5.1
Bettis, R.J., 23.3.1
Beylich, A.E., 23.4.1
Bjorkquist, D.C., 6.5.1
Böhm, C., 20.3.1
Bolcs, A., 8.2.1
Bolinder, J., 29.2.1
Boree, J., 24.4.1
Borg, A., 29.2.1
Brehm, C., 7.2.1
Brenier, Y., 18.5.1
Brenn, G., 21.1.1
Britan, A.B., 26.5.1
Bröder, D., 27.2.1
Brücker, Ch., 27.4.1
Brun, M., 7.5.1
Buckberry, C.H., 12.5.1, 31.5.1
Burnett, M., 36.3.1
Bütefish, K.A., 24.6.1
- Caldas, F., 17.3.1
Carlier, J., 11.2.1
Carlomagno, G., 38.3.1
Cartallier, A., 28.4.1
Carter, C.D., 35.1.1
Carvalho, I.S., 24.1.1
Cater, J., 4.2.1
Cattanei, A., 20.2.1, 36.4.1
Catton, I., 23.1.1, 34.3.1
Cenedese, A., 38.3.1
Cessou, A., 25.3.1
Champagne, J.Y., 36.2.1

*Ninth International Symposium on
Applications of Laser Techniques to Fluid Mechanics*

- Changsong, G., 29.1.1
Charbonnier, J.M., 2.6.1
Chiné, B., 33.5.1
Christensen, K.T., 16.1.1
Christnacher, F., 2.3.1
Coghe, A., 7.4.1
Cognet, G., 18.5.1
Cossali, G.E., 7.4.1
Coustols, E., 19.3.1
Cross, P.B., 36.3.1
Czarske, J.W., 15.3.1, 32.3.1
- Da Costa, G., 26.4.1
Dahoe, A.E., 35.6.1
Dakemoto, Y., 21.4.1
Dam, N., 37.3.1
Damp, S., 2.3.1
Dawson, J.R., 3.3.1, 3.5.1, 3.6.1
Day, S., 29.3.1
De Angelis, G., 38.3.1
De Gregorio, F., 19.6.1
Delfos, R., 24.3.1
Deljouravesh, R., 18.7.1
Derksen, J.J., 4.3.1, 14.5.1
Desantes, J.M., 7.6.1
Dias, I., 12.1.1
Diertele, L., 19.2.1
Dinkelacker, F., 25.4.1, 25.6.1
Djenidi, L., 2.1.1
Doelman, M.S., 14.5.1
Dölle, O., 32.3.1
Domnick, J., 21.1.1
Donbar, J.M., 35.1.1
Dopazo, C., 2.5.1
Dopheide, D., 15.4.1, 18.3.1
DrBarber, P.A., 34.1.1
Duarte, D., 25.5.1
Dullenkopf, K., 1.3.1, 31.3.1
Dupont, P., 4.1.1, 11.2.1
Duport, I.S., 28.4.1
Durst, F., 9.1.1, 11.3.1, 14.2.1, 21.1.1, 22.1.1
- Ebner, J., 1.3.1
Egbers, C., 4.6.1, 20.3.1, 28.2.1
Ehrenfried, K., 19.2.1, 19.6.1
Einav, S., 29.4.1
El Hajem, M., 36.2.1
Elia, N., 20.2.1
Elsässer, A., 1.3.1
Elvarasan, R., 2.1.1
Entwistle, J.D., 6.3.1
Escudier, M.P., 8.3.1
- Falgayrettes, P., 18.5.1
Fandrey, C., 9.3.1
Fanouille, P., 24.4.1
Favier, D., 19.5.1
Feldmann, O., 14.4.1
Fernandes, E.C., 3.3.1
Fernholz, H.H., 20.5.1
Ferrão, P., 17.3.1, 25.5.1
Fick, W., 3.2.1
Fiechtner, G.J., 35.1.1
Firpo, J.L., 9.2.1
Fischer, M., 11.3.1, 8.1.1
Fitzpatrick, J.A., 3.6.1, 20.7.1
Flack, R.D., 8.1.1
Fleming, G.A., 1.1.1
Foucaut, J.M., 11.2.1
Four, I., 24.4.1
Freek, C., 4.4.1, 13.1.1, 22.4.1
Fuchs, L., 29.2.1
Funke, S., 12.3.1
Furuichi, N., 22.2.1
- Garib, M., 13.6.1
Gentner, C. 36.5.1
Geropp, D., 2.2.1
Gharib, M., 16.5.1
Gicquel, P., 8.6.1
Gindele, J., 31.1.1
Girardot, L., 36.7.1
Göde, E., 36.5.1
Gökalp, I., 17.2.1
Golovanevsky, B., 34.7.1

*Ninth International Symposium on
Applications of Laser Techniques to Fluid Mechanics*

- Gomes, F.V., 39.1.1
Góngora, H.G.C., 7.5.1
Gonzalez, U., 7.6.1
Gord, J.R., 35.1.1
Gorton, S.A., 1.1.1
Gougat, P., 39.3.1
Gouldson, I.W., 8.3.1
Grabow, J., 15.1.1
Grad, Y., 29.4.1
Greated, C.A., 6.3.1
Griffths, A.J., 3.2.1
Grosche, G., 18.3.1
Gui, L., 10.5.1
- Hachiga, T., 22.2.1
Hackert, G., 35.4.1
Hand, D.P., 6.3.1
Hanson, R.K., 25.2.1
Hardalupas, Y., 3.4.1
Hargrave, G.K., 9.4.1
Hart, D.P., 13.3.1, 37.4.1
Hassan, Y.A., 27.5.1
Hasselbrink, E.F., 25.2.1
Havermann, M., 23.4.1
Heath, J., 9.4.1
Hein, D., 23.2.1
Heitor, M.V., 3.3.1, 17.3.1, 24.1.1, 25.7.1
Hentschel, W., 13.1.1
Hess, C., 18.1.1
Hino, M., 26.3.1
Hishida, K., 6.1.1, 16.2.1, 22.2.1, 26.6.1
Hoekstra, A.J., 4.3.1
Holler, V., 25.6.1
Holzapfel, W., 6.2.1
Honore, D., 25.1.1
Hsu, C.T., 9.5.1
Huang, Z., 16.3.1
Hubner, W., 13.2.1
Huckle, E., 34.3.1
- Iked, Y., 12.2.1, 12.6.1, 21.5.1
Immohr, J., 28.2.1
Ishima, T., 7.1.1, 24.4.1
- Ismailov, M., 7.1.1
Israel, A.T., 4.3.1
- Jackson, D.A., 29.5.1
Jaffre, D., 25.1.1
Javanovic, J., 11.3.1
Jingui, C., 29.1.1
Jones, J., 6.3.1
- Kadambi, J.R., 12.4.1
Kähler, C., 11.1.1, 19.6.1
Kantorovich, I., 35.5.1
Karatekin, Ö., 2.6.1
Karl, J., 23.2.1
Kataoka, K., 4.5.1
Katayama, K., 10.3.1
Katsuki, M., 35.3.1
Kawaguchi, T., 26.6.1
Kawahara, N., 12.2.1
Keicher, M., 14.7.1
Keller, J., 31.4.1
Kerrigan, S., 6.6.1
Kim, J.H., 21.5.1
Kim, K.C., 14.1.1
Kim, M.S., 2.2.1
Kobayashi, K., 7.1.1
Kobayashi, T., 13.4.1, 13.6.1
Kockx, J.P., 24.3.1
Kompenhans, J., 10.1.1, 13.6.1, 19.2.1, 19.6.1
Köngeter, J., 20.6.1, 33.1.1
Korenaga, K., 28.3.1
Kowalewski, T.A., 34.7.1, 39.3.1
Kozlov, P.V., 26.5.1
Kremer, H., 35.4.1
Kuhn, A., 6.3.1
Kumada, M., 22.2.1
Kuzmanovski, A., 10.4.1
- Lai, J.C.S., 38.1.1, 38.4.1
Lai, W., 6.6.1
Lam, D.H., 10.2.1

*Ninth International Symposium on
Applications of Laser Techniques to Fluid Mechanics*

Lang, N., 19.4.1
Lanzetta, F., 36.7.1
Larsen, P.S., 17.4.1
Lawes, M., 35.2.1
Le Coz, J.F., 7.3.1
Le Mironet, S., 4.1.1
Lee, K.C., 14.2.1
Lee, W.K., 36.3.1
Lehmann, P., 32.3.1, 33.2.1
Lein, G., 36.5.1
Leipertz, A., 25.4.1, 25.6.1
Leopold, F., 2.3.1
Levin, V.A. 26.5.1
Levy, Y., 34.7.1
Li, E.B., 15.5.1
Lim, T.T., 4.2.1
Limberg, W., 19.4.1
Liu, Z.C., 6.6.1, 16.2.1
Liubao, Z., 29.1.1
Lixin, Y., 29.1.1
Löber, W., 6.2.1
Lourenco, L.M., 13.5.1
Lozano, A., 2.5.1, 24.2.1
Lu, D., 38.4.1
Lund, C., 2.4.1
Luxton, R.E., 3.1.1

Madarame, H., 26.1.1
Maeda, M., 6.1.1, 16.2.1, 26.6.1
Maia, R., 8.4.1
Maison, L., 39.2.1
Maresca, C., 19.5.1
Martin, W.T., 12.4.1
Matos, M., 17.3.1
Matsumoto, K., 4.5.1
Maurey, C., 25.3.1
Mayinger, F., 14.4.1
McCluskey, D.R., 8.5.1
McCusker, S., 38.2.1
Meerts, W., 37.3.1
Meinhart, C.D., 6.4.1, 16.2.1
Melling, A., 9.1.1
Mendoza, J., 23.1.1
Meng, H., 16.3.1, 20.4.1
Menon, R., 36.1.1, 36.7.1

Merzkirch, W., 10.5.1, 13.1.1
Meyer, K.E., 20.1.1
Meyers, J.F., 1.1.1
Miles, P., 37.2.1
Miranda, P., 8.4.1
Mitichkin, S.Y., 26.5.1
Modares, D., 16.5.1
Mok, K.M., 39.2.1
Möller, T.J., 24.6.1
Moreira, A.L.N., 21.3.1
Morel, R., 36.2.1
Morikita, H., 14.7.1
Most, D., 25.6.1
Mounaïm-Rousselle, C., 18.2.1
Mouqallid, M., 31.2.1
Muller, E., 32.1.1
Muller, H., 18.3.1, 15.4.1
Mungal, M.G., 17.1.1, 25.2.1

Nakajima, T., 12.6.1, 21.5.1
Nakatani, N., 34.6.1
Naqwi, A., 9.3.1, 15.2.1
Nasr, A., 38.1.1
Nath, B., 6.2.1
Nathan, G.L., 3.1.1
Nijenboer, F.J., 32.2.1
Nino, E., 11.4.1
Nishio, S., 13.4.1
Nishiyama, M., 28.3.1
Nitsche, W., 19.1.1
Nobach, H., 32.1.1
Nonn, T.I., 27.3.1

Obermayer, K., 10.4.1
Obokata, T., 7.1.1
O'Doherty, T., 3.2.1, 3.5.1
Ohba, K., 21.4.1, 28.3.1
Ohmi, K., 10.2.1
Ohmura, N., 4.5.1
Okamoto, K., 10.6.1, 13.4.1, 26.1.1
Oliemans, R.V.A., 24.3.1
Onofri, F., 9.2.1, 24.5.1
Oschwald, M., 23.5.1

- Ottmann, M., 23.2.1
- Pagé, J., 17.2.1
- Pailhas, G., 19.3.1
- Pajot, O., 18.2.1
- Pallacin, I.G., 24.2.1
- Pantaloni, J., 24.5.1
- Pastor, J.V., 7.6.1
- Pekalski, A.A., 35.6.1
- Pengel, K., 19.6.1
- Pereira, A.S., 22.3.1
- Pereira, F., 16.5.1, 22.4.1, 33.3.1,
- Perrin, M., 25.1.1
- Petrak, D., 18.4.1
- Pickering, S.J., 33.4.1
- Pinho, F.T., 8.4.1, 22.3.1
- Pinto, F.T., 39.1.1
- Pitz, R.W., 34.1.1
- Plamann, K., 15.3.1
- Podoleanu, A.G., 29.5.1
- Posylkin, M., 7.2.1
- Prenel, J.P., 36.7.1
- Proença, M.F., 8.4.1, 39.1.1
- Przybilla, E., 18.4.1
- Pu, Y., 16.3.1
- Qiu, H., 9.5.1, 21.2.1
- Quénol G., 39.3.1
- Raffel, M., 10.1.1, 19.2.1, 19.6.1
- Raimann, J., 21.1.1
- Rambert, A., 39.3.1
- Ramuzat, A., 29.3.1
- Raposo, J.M.F., 13.1.1, 33.3.1
- Rasmussen, J.J., 8.5.1
- Rath, H.J., 28.2.1, 20.3.1
- Razore, S., 20.2.1
- Reeves, M., 12.5.1, 31.5.1
- Resagk, C., 15.1.1
- Reuber, J., 33.1.1
- Reuss, D.L., 37.1.1
- Ribarov, L.A., 34.1.1
- Riethmuller, M.L., 12.1.1, 18.6.1, 22.5.1, 29.3.1
- Ripault, J.M., 9.2.1
- Rogers, J.A., 29.5.1
- Röhle, I., 33.2.1, 34.2.1
- Rolon, J.C., 35.1.1
- Romano, G.P., 32.4.1
- Rona, A., 11.5.1
- Ronneberger, O., 10.1.1
- Rosalik, M., 37.1.1
- Rosenfeld, K., 18.4.1
- Rottenkolber, G., 31
- Saarenrinne, P., 14.6.1
- Saga, T., 13.4.1
- Samenfink, W., 1.3.1
- Santiago, J.G., 6.4.1
- Santos, D., 24.1.1
- Sarh, B., 17.2.1
- Sato, Y., 26.3.1
- Sauvage, P., 19.3.1
- Savory, E., 38.2.1
- Scaramo, F., 22.5.1
- Scarlett, B., 35.6.1
- Schabacker, J., 8.2.1
- Schafer, M., 14.2.1
- Scheuerpflug, W., 12.3.1
- Schik, A., 23.5.1
- Schmidt, W.D., 27.5.1
- Schneider, G.M., 3.1.1
- Schodl, R., 34.2.1
- Schoepf, G., 3.2.1
- Sciacchitano, A., 20.2.1
- Selbach, A., 3.4.1
- Sellens, R., 18.7.1
- Sen, R., 13.5.1
- Serio, C., 11.4.1
- Servouze, Y., 8.6.1
- Sharp, K., 6.6.1, 14.1.1
- Sheng, J., 16.3.1
- Sheppard, C.G.W., 35.2.1, 35.7.1
- Siller, H.A., 20.5.1
- Sitte, B., 4.6.1
- Skarman, B., 34.5.1

*Ninth International Symposium on
Applications of Laser Techniques to Fluid Mechanics*

Soika, A., 25.4.1, 25.6.1
Sola, I.J., 16.4.1
Sollows, K.F., 33.6.1
Soloff, S.M., 16.2.1
Sommerfeld, M., 27.2.1
Son, P.H., 21.4.1
Soria, J., 4.2.1
Sousa, J.M.M., 4.4.1, 13.1.1, 22.4.1
Spaanjaars, C., 37.3.1
Spettel, F., 36.2.1
Spicher, U., 31.1.1
Stahlecker, D., 36.5.1
Stanislas, M., 4.1.1, 11.2.1, 13.6.1
Stefanini, J., 36.7.1
Stenum, B., 8.5.1
Stenzel, O., 2.4.1
Stepowski D., 25.3.1
Stoffels, G., 37.3.1
Strunck, V., 18.3.1
Susset, A., 25.1.1
Syred, N., 3.1.1, 3.5.1

Tadrist, L., 24.5.1
Tanaka, G., 26.1.1
Tanguy, B., 8.6.1
Tarr, S., 33.4.1
Taugwalder, F., 16.5.1
Taylor, A.M.K.P., 14.7.1
Teng-Yang, R., 33.6.1
Ter Meulen, J.J., 37.3.1
Testov, V.G., 26.5.1
Thirouard, B., 37.4.1
Tieu, A.K., 15.5.1
Tinapp, F., 19.1.1
Tobben, H., 15.4.1
Tomkins, C., 6.6.1
Tosiyasu, T., 10.3.1
Touvet, Y., 19.3.1
Towers, D.P., 12.5.1, 31.5.1
Toy, N., 38.2.1
Trinite, M., 25.1.1, 31.2.1
Tropea, C., 13.2.1, 31.4.1, 32.1.1, 32.5.1
Tsukagoshi, M., 7.1.1
Tsushima, S., 35.3.1

Tujeehut, T.D., 24.3.1

Ubaldi, M., 20.2.1, 36.4.1
Udrea, D., 36.3.1
Uemura, T., 10.3.1
Ullmun, U., 17.4.1
Urban, W.D., 17.1.1

Valeau, V., 20.7.1
Van Beeck, J.P.A.J., 18.6.1
Van den Akker, H.E.A., 4.3.1, 14.5.1
Van den Boom, E., 37.3.1
Van den Konijnenberg, J.A., 8.5.1
Van den Moortel, T., 24.5.1
Van Maanen, H.R.E., 32.2.1
Venart, J.E.S., 33.6.1
Villafuerte, J.O., 27.5.1
Voigt, S., 15.1.1, 26.2.1
Volkert, J., 13.2.1, 31.4.1
Volkholz, P., 9.1.1

Wachter, P., 14.2.1
Wang, F.Y., 2.6.1
Wehrmeyer, J.A., 34.1.1
Welling, H., 15.3.1
Wereley, S.T., 6.4.1
Wernet, M.P., 12.4.1
Werquin, O., 4.1.1
Westerweel, J., 1.2.1
Whitelaw, J.H., 3.4.1, 7.2.1
Wigley, G., 9.4.1
Wiles, D.P., 6.3.1
Willert, C.E., 11.1.1, 19.6.1, 34.2.1
Wirtz, S., 35.4.1
Wittig, S., 1.3.1, 31.3.1
Wolf, G., 21.1.1
Woolley, R., 35.2.1
Wozniak, G., 27.1.1, 34.5.1
Xianqiu, Y., 29.1.1

*Ninth International Symposium on
Applications of Laser Techniques to Fluid Mechanics*

Yamada, N., 12.2.1, 12.6.1

Yamaguchi, K., 16.2.1

Yang, W., 20.4.1

Yates, A., 2.5.1

Yeh, H., 39.2.1

Yeung, Y.F., 21.2.1

Yianneskis, M., 14.2.1

Yongda, S., 29.1.1

Yoshida, N., 6.1.1

Zellmer, H., 15.3.1

Zevenbergen, J.F., 35.6.1

Zhang, X., 11.5.1

Zhao, B., 35.5.1

Zijl, J.L.J., 24.3.1

Zunino, P., 20.2.1, P., 36.4.1